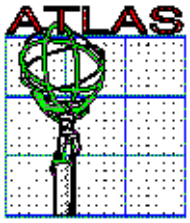

ATLAS DETECTOR AND PHYSICS PERFORMANCE

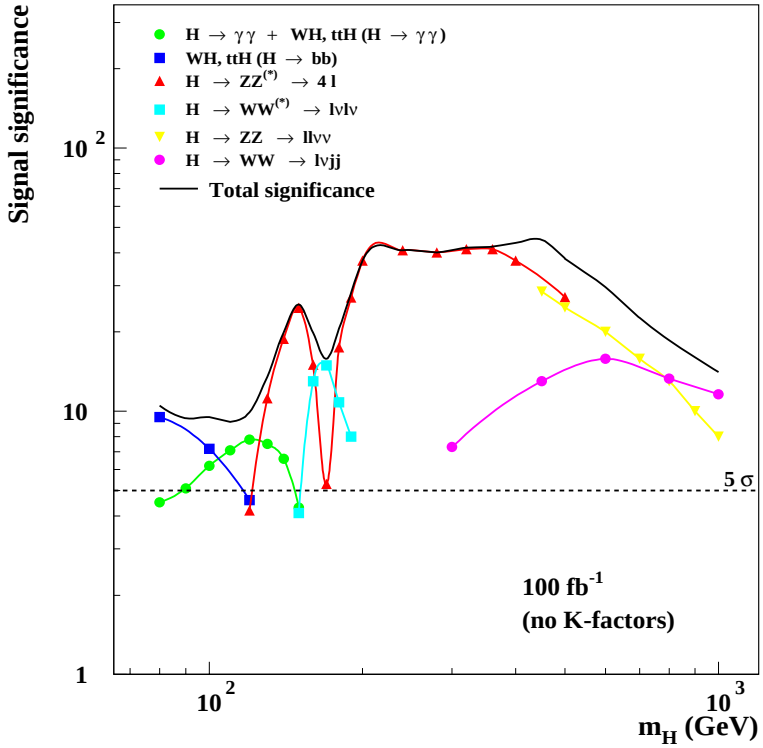

Technical Design Report

Volume II

Issue:	1
Revision:	0
Reference:	ATLAS TDR 15, CERN / LHCC 99-15
Created:	25 May 1999
Last modified:	25 May 1999
Prepared By:	ATLAS Collaboration

For this edition typing and typograhical errors have been corrected. Layout and pagination may therefore differ slightly with respect to the first, limited edition.

All trademarks, copyright names and products referred to in this document are acknowledged as such.

ATLAS Collaboration

Armenia
Yerevan Physics Institute, Yerevan

Australia
Research Centre for High Energy Physics, Melbourne University, Melbourne
University of Sydney, Sydney

Austria
Institut für Experimentalphysik der Leopold-Franzens-Universität Innsbruck, Innsbruck

Azerbaijan Republic
Institute of Physics, Azerbaijan Academy of Science, Baku

Republic of Belarus
Institute of Physics of the Academy of Science of Belarus, Minsk
National Centre of Particle and High Energy Physics, Minsk

Brazil
Universidade Federal do Rio de Janeiro, COPPE / EE / IF, Rio de Janeiro

Canada
University of Alberta, Edmonton
Department of Physics, University of British Columbia, Vancouver
University of Carleton / C.R.P.P., Carleton
Group of Particle Physics, University of Montreal, Montreal
Department of Physics, University of Toronto, Toronto
TRIUMF, Vancouver
University of Victoria, Victoria

CERN
European Laboratory for Particle Physics (CERN), Geneva

China
Institute of High Energy Physics, Academia Sinica, Beijing, University of Science and Technology of China, Hefei, University of Nanjing and University of Shandong

Czech Republic
Academy of Sciences of the Czech Republic, Institute of Physics and Institute of Computer Science, Prague
Charles University, Faculty of Mathematics and Physics, Prague
Czech Technical University in Prague, Faculty of Nuclear Sciences and Physical Engineering, Faculty of Mechanical Engineering, Prague

Denmark
Niels Bohr Institute, University of Copenhagen, Copenhagen

Finland
Helsinki Institute of Physics, Helsinki

France
Laboratoire d'Annecy-le-Vieux de Physique des Particules (LAPP), IN2P3-CNRS, Annecy-le-Vieux
Université Blaise Pascal, IN2P3-CNRS, Clermont-Ferrand
Institut des Sciences Nucléaires de Grenoble, IN2P3-CNRS-Université Joseph Fourier, Grenoble
Centre de Physique des Particules de Marseille, IN2P3-CNRS, Marseille
Laboratoire de l'Accélérateur Linéaire, IN2P3-CNRS, Orsay
LPNHE, Universités de Paris VI et VII, IN2P3-CNRS, Paris

CEA, DSM / DAPNIA, Centre d'Etudes de Saclay, Gif-sur-Yvette

Republic of Georgia
Institute of Physics of the Georgian Academy of Sciences and Tbilisi State University, Tbilisi

Germany
Physikalisches Institut, Universität Bonn, Bonn
Institut für Physik, Universität Dortmund, Dortmund
Fakultät für Physik, Albert-Ludwigs-Universität, Freiburg
Institut für Hochenergiephysik der Universität Heidelberg, Heidelberg
Institut für Physik, Johannes-Gutenberg Universität Mainz, Mainz
Lehrstuhl für Informatik V, Universität Mannheim, Mannheim
Sektion Physik, Ludwig-Maximilian-Universität München, München
Max-Planck-Institut für Physik, München
Fachbereich Physik, Universität Siegen, Siegen
Fachbereich Physik, Bergische Universität, Wuppertal

Greece
Athens National Technical University, Athens
Athens University, Athens
High Energy Physics Department and Department of Mechanical Engineering, Aristotle University of Thessaloniki, Thessaloniki

Israel
Department of Physics, Technion, Haifa
Raymond and Beverly Sackler Faculty of Exact Sciences, School of Physics and Astronomy, Tel-Aviv University, Tel-Aviv
Department of Particle Physics, The Weizmann Institute of Science, Rehovot

Italy
Dipartimento di Fisica dell' Università della Calabria e I.N.F.N., Cosenza
Laboratori Nazionali di Frascati dell' I.N.F.N., Frascati
Dipartimento di Fisica dell' Università di Genova e I.N.F.N., Genova
Dipartimento di Fisica dell' Università di Lecce e I.N.F.N., Lecce
Dipartimento di Fisica dell' Università di Milano e I.N.F.N., Milano
Dipartimento di Scienze Fisiche, Università di Napoli 'Federico II' e I.N.F.N., Napoli
Dipartimento di Fisica Nucleare e Teorica dell' Università di Pavia e I.N.F.N., Pavia
Dipartimento di Fisica dell' Università di Pisa e I.N.F.N., Pisa
Dipartimento di Fisica dell' Università di Roma 'La Sapienza' e I.N.F.N., Roma
Dipartimento di Fisica dell' Università di Roma 'Tor Vergata' e I.N.F.N., Roma
Dipartimento di Fisica dell' Università di Roma 'Roma Tre' e I.N.F.N., Roma
Dipartimento di Fisica dell' Università di Udine, Gruppo collegato di Udine I.N.F.N. Trieste, Udine

Japan
Department of Information Science, Fukui University, Fukui
Hiroshima Institute of Technology, Hiroshima
Department of Physics, Hiroshima University, Higashi-Hiroshima
KEK, High Energy Accelerator Research Organisation, Tsukuba
Department of Physics, Faculty of Science, Kobe University, Kobe
Department of Physics, Kyoto University, Kyoto
Kyoto University of Education, Kyoto-shi
Department of Electrical Engineering, Nagasaki Institute of Applied Science, Nagasaki
Naruto University of Education, Naruto-shi
Department of Physics, Faculty of Science, Shinshu University, Matsumoto
International Center for Elementary Particle Physics, University of Tokyo, Tokyo
Physics Department, Tokyo Metropolitan University, Tokyo
Department of Applied Physics, Tokyo University of Agriculture and Technology, Tokyo

Morocco
Faculté des Sciences Aïn Chock, Université Hassan II, Casablanca, and Université Mohamed V, Rabat

Netherlands
FOM - Institute SAF NIKHEF and University of Amsterdam / NIKHEF, Amsterdam
University of Nijmegen / NIKHEF, Nijmegen

Norway
University of Bergen, Bergen
University of Oslo, Oslo

Poland
Henryk Niewodniczanski Institute of Nuclear Physics, Cracow
Faculty of Physics and Nuclear Techniques of the University of Mining and Metallurgy, Cracow

Portugal
Laboratorio de Instrumentação e Física Experimental de Partículas (University of Lisboa, University of Coimbra, University Católica-Figueira da Foz and University Nova de Lisboa), Lisbon

Romania
Institute of Atomic Physics, National Institute of Physics and Nuclear Engineering, Bucharest

Russia
Institute for Theoretical and Experimental Physics (ITEP), Moscow
P.N. Lebedev Institute of Physics, Moscow
Moscow Engineering and Physics Institute (MEPhI), Moscow
Moscow State University, Institute of Nuclear Physics, Moscow
Budker Institute of Nuclear Physics (BINP), Novosibirsk
Institute for High Energy Physics (IHEP), Protvino
Petersburg Nuclear Physics Institute (PNPI), Gatchina, St. Petersburg

JINR
Joint Institute for Nuclear Research, Dubna

Slovak Republic
Bratislava University, Bratislava, and Institute of Experimental Physics of the Slovak Academy of Sciences, Kosice

Slovenia
Jozef Stefan Institute and Department of Physics, University of Ljubljana, Ljubljana

Spain
Institut de Física d'Altes Energies (IFAE), Universidad Autónoma de Barcelona, Bellaterra, Barcelona
Physics Department, Universidad Autónoma de Madrid, Madrid
Instituto de Física Corpuscular (IFIC), Centro Mixto Universidad de Valencia - CSIC, Valencia

Sweden
Fysiska institutionen, Lunds universitet, Lund
Royal Institute of Technology (KTH), Stockholm
University of Stockholm, Stockholm
Uppsala University, Department of Radiation Sciences, Uppsala

Switzerland
Laboratory for High Energy Physics, University of Bern, Bern
Section de Physique, Université de Genève, Geneva

Turkey
Department of Physics, Ankara University, Ankara
Department of Physics, Bogaziçi University, Istanbul

United Kingdom
School of Physics and Astronomy, The University of Birmingham, Birmingham
Cavendish Laboratory, Cambridge University, Cambridge
Department of Physics and Astronomy, University of Edinburgh, Edinburgh
Department of Physics and Astronomy, University of Glasgow, Glasgow
Department of Physics, Lancaster University, Lancaster
Department of Physics, Oliver Lodge Laboratory, University of Liverpool, Liverpool
Department of Physics, Queen Mary and Westfield College, University of London, London
Department of Physics, Royal Holloway and Bedford New College, University of London, Egham
Department of Physics and Astronomy, University College London, London
Department of Physics and Astronomy, University of Manchester, Manchester
Department of Physics, Oxford University, Oxford
Rutherford Appleton Laboratory, Chilton, Didcot
Department of Physics, University of Sheffield, Sheffield

United States of America
State University of New York at Albany, New York
Argonne National Laboratory, Argonne, Illinois
University of Arizona, Tucson, Arizona
Department of Physics, The University of Texas at Arlington, Arlington, Texas
Lawrence Berkeley Laboratory and University of California, Berkeley, California
Department of Physics, Boston University, Boston, Massachusetts
Brandeis University, Department of Physics, Waltham, Massachusetts
Brookhaven National Laboratory (BNL), Upton, New York
University of Chicago, Enrico Fermi Institute, Chicago, Illinois
Nevis Laboratory, Columbia University, Irvington, New York
Department of Physics, Duke University, Durham, North Carolina
Department of Physics, Hampton University, Virginia
Department of Physics, Harvard University, Cambridge, Massachusetts
Indiana University, Bloomington, Indiana
University of California, Irvine, California
Massachusetts Institute of Technology, Department of Physics, Cambridge, Massachusetts
University of Michigan, Department of Physics, Ann Arbor, Michigan
Michigan State University, Department of Physics and Astronomy, East Lansing, Michigan
University of New Mexico, New Mexico Center for Particle Physics, Albuquerque
Physics Department, Northern Illinois University, DeKalb, Illinois
Ohio State University, Columbus, Ohio
Department of Physics and Astronomy, University of Oklahoma
Department of Physics, University of Pennsylvania, Philadelphia, Pennsylvania
University of Pittsburgh, Pittsburgh, Pennsylvania
Department of Physics and Astronomy, University of Rochester, Rochester, New York
Institute for Particle Physics, University of California, Santa Cruz, California
Department of Physics, Southern Methodist University, Dallas, Texas
State University of New York at Stony Brook, Stony Brook, New York
Tufts University, Medford, Massachusetts
High Energy Physics, University of Illinois, Urbana, Illinois
Department of Physics, Department of Mechanical Engineering, University of Washington, Seattle, Washington
Department of Physics, University of Wisconsin, Madison, Wisconsin

Acknowledgements

The Editors would like to thank Mario Ruggier for his continuous help and competent advice on all FrameMaker issues. The Editors also warmly thank Michèle Jouhet and Isabelle Canon for the processing of the colour figures and the cover pages. Finally they would like to express their gratitude to all the Print-shop staff for their expertise in printing this document.

Table Of Contents

14 Physics overview

14.1 Introduction

The ATLAS physics programme has been already discussed in several documents, the most comprehensive ones being the Letter of Intent [14-1] and the Technical Proposal [14-2]. The goals which have been defined there and which have guided the detector optimisation procedure remain essentially the same, the most important one being measurements that will lead to an understanding of the mechanism of electroweak symmetry breaking.

The high energy and luminosity of the LHC offers a large range of physics opportunities, from the precise measurement of the properties of known objects to the exploration of the high energy frontier. The need to accommodate the very large spectrum of possible physics signatures has guided the optimisation of the detector design. The desire to probe the origin of the electroweak scale leads to a major focus on the Higgs boson; ATLAS must be sensitive to it over the full range of allowed masses. Other important goals are searches for other phenomena possibly related to the symmetry breaking, such as particles predicted by supersymmetry or technicolour theories, as well as new gauge bosons and evidence for composite quarks and leptons. The investigation of *CP* violation in *B* decays and the precision measurements of *W* and top-quark masses and triple gauge boson couplings will also be important components of the ATLAS physics programme.

As discussed in the previous volume, and as also will be illustrated several times throughout this one, excellent performance of the detector is needed to achieve these physics goals.

- The various Higgs boson searches, which resent some of the most challenging signatures, were used as benchmark processes for the setting of parameters that describe the detector performance. High-resolution measurements of electrons, photons and muons, excellent secondary vertex detection for τ–leptons and *b*-quarks, high-resolution calorimetry for jets and missing transverse energy (E_T^{miss}) are essential to explore the full range of possible Higgs boson masses.
- Searches for SUSY set the benchmarks on the hermeticity and E_T^{miss} capability of the detector, as well as on *b*-tagging at high luminosity.
- Searches for new heavy gauge bosons provided benchmark requirements for high-resolution lepton measurements and charge identification in the p_T range as large as a few TeV.
- Signatures characteristic for quark compositeness set the requirements for the measurement of very high-p_T jets.
- The precision measurements of the *W* and top-quark masses, gauge boson couplings, *CP* violation and the determination of the Cabibbo-Kobayashi-Maskawa unitarity triangle yielded benchmarks that address the need to precisely control the energy scale for jets and leptons, determine precisely secondary vertices, reconstruct fully final states with relatively low-p_T particles and trigger on low-p_T leptons.

14.2 Theoretical picture

The Standard Model (SM) [14-3] is a very successful description of the interactions of the components of matter at the smallest scales (10^{-18} m) and highest energies (~200 GeV) accessible to current experiments. It is a quantum field theory which describes the interaction of spin-1/2 point-like fermions, whose interactions are mediated by spin-1 gauge bosons. The bosons are a consequence of local gauge invariance applied to the fermion fields and are a manifestation of the symmetry group of the theory, *i.e.* SU(3)xSU(2)xU(1) [14-3] [14-4].

The fundamental fermions are leptons and quarks. The left-handed states are doublets under the SU(2) group, while the right-handed states are singlets. There are three generations of fermions, each generation identical except for mass: the origin of this structure, and the breaking of generational symmetry (flavour symmetry), remain a mystery. There are three leptons with electric charge -1, the electron (e), muon (μ) and tau lepton (τ) and three electrically neutral leptons, the neutrinos ν_e, ν_μ and ν_τ. Similarly, there are three quarks with electric charge 2/3, up (u), charm (c) and top (t), and three with electric charge -1/3, down (d), strange (s) and bottom (b). The quarks are triplets under the SU(3) group and thus carry an additional 'charge', referred to as colour. There is mixing between the three generations of quarks, which is parametrised by the Cabibbo-Kobayashi-Maskawa (CKM) [14-5] matrix whose origin is not explained by the Standard Model.

The SU(2)xU(1) symmetry group (which describes the so-called electroweak interaction) is spontaneously broken by the existence of a (postulated) Higgs field with non-zero expectation value [14-6]. This leads to the emergence of massive vector bosons, the W and Z, which mediate the weak interaction, while the photon of electromagnetism remains massless. One physical degree of freedom remains in the Higgs sector, which should manifest as a neutral scalar boson H^0, which is presently unobserved. The SU(3) group describes the strong interaction (quantum chromodynamics or QCD) [14-4]. Eight vector gluons mediate this interaction. They carry colour charges themselves, and are thus self-interacting. This implies that the QCD coupling α_s is small for large momentum transfers but large for small momentum transfers, and leads to the confinement of quarks inside colour-neutral hadrons. Attempting to free a quark produces a jet of hadrons through production of quark-antiquark pairs and gluons.

The success of the SM of strong, weak and electromagnetic interactions has drawn increased attention to its limitations. In its simplest version, the model has 19 parameters, the three coupling constants of the gauge theory SU(3)xSU(2)xU(1), three lepton and six quark masses, the mass of the Z boson which sets the scale of weak interactions, and the four parameters which describe the rotation from the weak to the mass eigenstates of the charge -1/3 quarks (CKM matrix). All of these parameters are known with varying errors. Of the two remaining parameters, a *CP*-violating parameter associated with the strong interactions must be very small. The last parameter is associated with the mechanism responsible for the breakdown of electroweak SU(2)xU(1) to $U(1)_{em}$. This can be taken as the mass of the, as yet undiscovered, Higgs boson. The couplings of the Higgs boson are determined once its mass is given.

The gauge theory part of the SM has been well tested, but there is no direct evidence either for or against the simple Higgs mechanism for electroweak symmetry breaking. All masses are tied to the mass scale of the Higgs sector. Although within the model there is no guidance about the Higgs mass itself, some constraints can be delivered from the perturbative calculations within the model requiring the Higgs couplings to remain finite and positive up to an energy scale Λ [14-7]. Such calculations exists at the two-loop level for both lower and upper Higgs mass bounds. With present experimental results on the SM parameters, if the Higgs mass is in the

range 160 to 170 GeV [14-8] then the renormalisation-group behaviour of the Standard Model is perturbative and well behaved up to Planck scale $\Lambda_{\rm Pl} \sim 10^{19}$ GeV. For smaller or larger values of m_H new physics must set in below $\Lambda_{\rm Pl}$.

As its mass increases, the self couplings and the couplings to the W and Z bosons grow [14-9]. This feature has a very important consequence. Either the Higgs boson must have a mass less than about 800 GeV, or the dynamics of WW and ZZ interactions with centre-of-mass energies of order 1 TeV will reveal new structure. It is this simple argument that sets the energy scale that must be reached to guarantee that an experiment will be able to provide information on the nature of electroweak symmetry breaking.

The presence of a single elementary scalar boson is unsatisfactory to many theorists. If the theory is part of some more fundamental theory, which has some other larger mass scale (such as the scale of grand unification or the Planck scale), there is a serious 'fine tuning' or naturalness problem. Radiative corrections to the Higgs boson mass result in a value that is driven to the larger scale unless some delicate cancellation is engineered ($(m_0^2 - m_1^2) \sim m_W^2$ where m_0 and m_1 are order 10^{15} GeV or larger). There are two ways out of this problem which involve new physics on the scale of 1 TeV. New strong dynamics could enter that provides the scale of m_W, or new particles could appear so that the larger scale is still possible, but the divergences are cancelled on a much smaller scale. In any of the options, Standard Model, new dynamics or cancellations, the energy scale is the same; something must be discovered at the TeV scale.

Supersymmetry [14-10] is an appealing concept for which there is so far no experimental evidence. It offers the only presently known mechanism for incorporating gravity into the quantum theory of particle interactions and provides an elegant cancellation mechanism for the divergences, provided that at the electroweak scale the theory is supersymmetric. The successes of the Standard Model (such as precision electroweak predictions) are retained, while avoiding any fine tuning of the Higgs mass. Some supersymmetric models allow for the unification of gauge couplings at a high scale and a consequent reduction of the number of arbitrary parameters.

Supersymmetric models postulate the existence of superpartners for all the presently observed particles: bosonic superpartners of fermions (squarks and sleptons), and fermionic superpartners of bosons (gluinos and gauginos). There are also multiple Higgs bosons: h, H, A and $H^{\pm}$. There is thus a large spectrum of presently unobserved particles, whose exact masses, couplings and decay chains are calculable in the theory given certain parameters. Unfortunately these parameters are unknown. Nonetheless, if supersymmetry is to have anything to do with electroweak symmetry breaking, the masses should be in the region below or order of 1 TeV.

An example of the strong coupling scenario is 'technicolour' for models based on dynamical symmetry breaking [14-11]. Again, if the dynamics is to have anything to do with electroweak symmetry breaking we would expect new states in the region below 1 TeV; most models predict a large spectrum of such states. An elegant implementation of this appealing idea is lacking. However, all models predict structure in the WW scattering amplitude at around 1 TeV centre-of-mass energy.

There are also other possibilities for new physics that are not necessarily related to the scale of electroweak symmetry breaking. There could be new neutral or charged gauge bosons with mass larger than the Z and W; there could be new quarks, charged leptons or massive neutrinos, or quarks and leptons could turn out not to be elementary objects. While we have no definitive expectations for the masses of these objects, the LHC experiments must be able to search for them over the available energy range.

Results on precision measurements within the Standard Model, as well as limits on new physics, from present experiments are presented, case by case, in the relevant chapter of this volume.

14.3 Challenges of new physics

This volume presents examples of the physics programme which should be possible with the ATLAS detector. The channels studied in previous documents [14-1][14-2] are re-examined and many new strategies proposed.

In the initial phase at low luminosity, the experiment will function as a factory for QCD processes, heavy flavour and gauge bosons production. This will allow a large number of precision measurements in the early stages of the experiment.

A large variety of QCD related processes will be studied. These measurements are of importance as studies of QCD 'per se' in a new energy regime with high statistics. Of particular interest will be jet and photon physics, open charm and beauty production and gauge bosons production. A study of diffractive processes will present significant experimental challenges itself, given the limited angular coverage of the ATLAS detector. Several aspects of diffractive production of jets, gauge bosons, heavy flavour partons will be nevertheless studied in detail. LHC will extend the exploration of the hard partonic processes to large energy scales (of few hundred GeV^2), while reaching small fractional momentum of the proton being carried by a scattered partons (of 10^{-5}). Precise constraints on the partonic distribution functions will be derived from measurements of Drell-Yan production, of W and Z bosons production, of production of direct photons and high-p_T jets, heavy flavours and gauge boson pairs. Deviation from the theoretical predictions for QCD processes themselves might indicate the onset of new physics, such as compositeness. Measurement and understanding of these QCD processes will be essential as they form the dominant background searches for new phenomena.

Even at low luminosity, LHC is a beauty factory with 10^{12} $b\bar{b}$ expected per year. The available statistics will be limited only by the rate at which data can be recorded. The proposed B-physics programme is therefore very wide. Specific B-physics topics include the search for and measurement of CP violation, of B_s^0 mixing and of rare decays. ATLAS can perform competitive high-accuracy measurements of B_s^0 mixing, covering the statistically preferred range of the Standard Model predictions. Rare B mesons such as B_c will be copiously produced at LHC. The study of B-baryon decay dynamics and spectroscopy of rare B hadrons will be also carried out.

LHC has a great potential for performing high precision top physics measurements with about eight million $t\bar{t}$ pairs expected to be produced for an integrated luminosity of 10 fb^{-1}. It would allow not only for the precise measurements of the top-quark mass (with a precision of ~2 GeV) but also for the detailed study of properties of the top-quark itself. The single top production should be observable and the high statistics will allow searches for many rare top decays. The precise knowledge of the top-quark mass places strong constraints on the mass of the Standard Model Higgs boson, while a detailed study of its properties may reveal as well new physics.

One of the challenges to the LHC experiments will be whether the precision of the W-mass measurement can be improved. Given the 300 million single W events expected in one year of data taking, the expected statistical uncertainty will be about 2 MeV. The very ambitious goal for both theory and experiment is to reduce the individual sources of systematic errors to less

than 10 MeV, which would allow for the measurement of the *W* mass with precision of better than 20 MeV. This would ensure that the precision of the *W* mass is not the dominant source of errors in testing radiative corrections in the SM prediction for the Higgs mass.

The large rate of gauge boson pair production at the LHC enables ATLAS to provide critical tests of the triple gauge-boson couplings. The gauge cancellations predicted by the Standard Model will be studied and measurements of possible anomalous couplings made. These probe underlying non-standard physics. The most sensitive variables to compare with Standard Model predictions are the transverse momentum spectra of high-p_T photons or reconstructed *Z* bosons.

If the Higgs boson is not discovered before LHC begins operation, the searches for it and its possible supersymmetric extensions in the Minimal Supersymmetric Standard Model (MSSM) will be a main focus of activity. Search strategies presented here explore a variety of possible signatures, being accessible already at low luminosity or only at design luminosity. Although the cleanest one would lead to reconstruction of narrow mass peaks in the photonic or leptonic decay channels, very promising are the signatures which lead to multi-jet or multi-τ final states. In several cases signal-to-background ratios much smaller than one are expected, and in most cases detection of the Higgs boson will provide an experimental challenge. Nevertheless, the ATLAS experiment alone will cover the full mass range up to 1 TeV for the SM Higgs and also the full parameter space for the MSSM Higgs scenarios. It has also a large potential for searches in alternative scenarios.

Discovering SUSY at the LHC will be straightforward if it exists at the electroweak scale. Copious production of squarks and gluinos can be expected, since the cross-section should be as large as a few pb for squarks and gluinos as heavy as 1 TeV. Their cascade decays would lead to a variety of signatures involving multi-jets, leptons, photons, heavy flavours and missing energy. In several models, discussed in detail in this volume, the precision measurement of the masses of SUSY particles and the determination of the model parameters will be possible. The main challenge would be therefore not to discover SUSY itself, but to reveal its nature and determine the underlying SUSY model.

Other searches beyond the Standard Model have been also investigated. Throughout this volume are presented strategies for searching for technicolour signals, excited quarks, leptoquarks, new gauge bosons, right-handed neutrinos and monopoles. Given the large number of detailed models published in this field, the task of evaluating each of them is beyond the scope of this document. Rather an exploratory point of view is taken, examples are used and in some cases a detailed study is performed.

14.4 Simulation of physics signals and backgrounds

In the process of evaluation of the physics potential of the ATLAS experiment, Monte Carlo event generators were used to simulate multiparticle production in physics processes appearing in the *pp* collisions. Detailed or parametrised simulation of the detector response to this multiparticle stream was then used to evaluate the possible observability of the signal.

In the full detector simulation, described in Section 2.2, the detailed geometry of the detector is implemented and the interactions of particles with the material of the detector are modelled. Results from full-simulation studies have been described in Chapters 3-10 for several crucial

benchmark signatures and physics processes, *e.g.* mass resolutions, acceptances and identification efficiencies for $H \to \gamma\gamma$, $H \to ZZ^* \to 4l$, $H \to b\bar{b}$, $H \to \tau\tau$ decays, E_T^{miss} resolution, *b*-jet and τ-jet identification capability.

However, in most of the cases presented in this volume, evaluation of the expected signals and backgrounds has been done with the fast simulation described in Section 2.5. This simulation includes, in a parametrised way, the main aspects related to the detector response: jet reconstruction in the calorimeters, momentum / energy smearing for leptons and photons, reconstruction of missing transverse energy and charged particles. It is tuned to reproduce as well as possible the expected ATLAS performance, and this tuning has been verified with several benchmark processes as described in Section 2.5.

The fast simulation was used very extensively for estimating the expected backgrounds from physics processes. Such approach was particularly useful for channels requiring large event samples, which one could not process with the much more time-consuming full simulation. Many of these studies are presented in this volume, *e.g.* for Higgs searches in Chapter 19, where, in some cases, both irreducible and reducible backgrounds required simulations of several million events.

14.4.1 Event generators

There are several available Monte Carlo event generators for *pp* collisions, the most exhaustive ones, with respect to available physics processes and complexity in modelling hadronic interactions, being: HERWIG [14-14], ISAJET[14-12] and PYTHIA[14-13]. Each of these simulates a hadronic final state corresponding to some particular model of the underlying physics. The details of the implementation of the physics are different in each of these generators, however the underlying philosophy of the generators is the same.

- The basic process is a parton interaction involving a quark or gluon from each of the incoming protons. Elementary particles in the final state, such as quarks, gluons or $W/Z/\gamma$-bosons, emerge from the interaction. The fundamental process is calculated in perturbative QCD, and the initial momentum of the quarks or gluons is given by structure functions.
- Additional QCD (gluon) radiation takes place from the quarks and gluons that participate in the basic scattering process. These parton showers are based on the expansions around the soft and collinear limits and can be ascribed to either the initial or final state. The algorithm used by HERWIG includes some effects due to quantum interference and generally produces better agreement with the data when detailed jet properties are studied. The showering continues down to some low energy cut-off. For some particular cases the matrix element calculations involving higher-order QCD processes are used. The events that have more energy in the parton process have more showering, and consequently more jet activity.
- The collection of quarks and gluons must then be hadronised into mesons and baryons. This is done differently in each of the event generators, but is described by a set of (fragmentation) parameters that must be adjusted to agree with experimental results. HERWIG looks for colour singlet collections of quarks and gluons with low invariant mass and groups them together; this set then turns into hadrons. PYTHIA splits gluons into quark-antiquark pairs and turns the resulting set of colour singlet quark-antiquark pairs into hadrons via a string model. ISAJET simply fragments each quark independently paying no attention to the colour flow. In ISAJET the underlying event that arises from the re-

maining beam fragments must be added. The other generators tie these fragments back into the partonic system in order to neutralise the colour.

Matrix elements are likely to provide a better description of the main character of the events, *i.e.* the topology of well separated jets, while parton showers should be better at describing the internal structure of these jets.

The above model(s) describe events where there is a hard-scattering of the incoming partons; either a heavy particle is produced or the outgoing partons have large transverse momentum. While these are the processes that are of most interest, the dominant cross-section at the LHC consists of events with no hard scattering. There is little detailed theoretical understanding of these minimum-bias events and the event generators must rely on data at current energies. These minimum-bias events are important at LHC, particularly at design luminosity, as they overlap interesting hard-scattering events such as the production of new particles. The generators use a different approach in this case. ISAJET uses a pomeron model that has some theoretical basis. HERWIG uses a parametrisation of data mainly from the CERN $p\bar{p}$ Collider. PYTHIA uses a mini-jet model where the jet cross-section is used at very low transverse momenta, *i.e* the hard scattering process is extrapolated until it saturates the total cross-section. Whenever relevant, ATLAS has used the PYTHIA approach with dedicated modifications that agree with present data from Tevatron [14-17]. The multiplicity in minimum-bias events predicted by this approach is larger than that predicted by ISAJET or HERWIG (see Chapter 15), hence issues associated with pile-up are treated conservatively.

The generators differ in the extent to which non-standard physics processes are included. The most complete implementation of the Standard Model processes are available in PYTHIA, while ISAJET has the most complete implementation of SUSY scenarios.

In the physics evaluation presented in this volume, the Standard Model physics and Higgs searches were mostly simulated with PYTHIA. ISAJET was used extensively for the supersymmetry studies but some analyses have been done also with the supersymmetric extension of PYTHIA [14-23]. HERWIG has been used for some of the QCD studies. The model of the hadronic interactions implemented in the physics generator has a direct impact on physical observables such as jet multiplicity, their average transverse momentum, internal structure of the jets and their heavy flavour content. That was one of the reasons why, whenever possible, PYTHIA was used enabling a consistent set of signal and background simulations to be generated.

Theoretical precision of the existing Monte Carlo generators is far from adequate for the challenging requirements of the LHC experiments. Despite the huge efforts which have been put into developing of physics generators for hadron colliders over the last years, the precision with which *e.g.* present data can be reproduced is not better than 10-30%, and in some cases is not better than a factor of two.

Table 14-1 shows a few examples of important signal and background processes with their predicted cross-sections, as used in the simulations discussed in this volume. If not explicitly stated otherwise, these are calculated using leading-order QCD as implemented in PYTHIA 5.7, using the CTEQ2L set of structure functions as the reference one. Whenever better or more appropriate calculations were available, the production cross-section from PYTHIA was suitably normalised, or a different Monte Carlo generator was used.

- The QCD multi-jet production is a dominant background for *e.g.* Higgs searches in the multi-jet final state. The production of events with three or more high-p_T jets is not well modelled by lowest-order di-jet processes convoluted with parton showers. To illustrate the large discrepancy between exact matrix element calculations and parton shower ap-

proaches in this case, Table 14-1 gives rates for one, three and four jet final states as given by the exact multi-parton matrix element NJETS Monte Carlo [14-15] and PYTHIA. On the other hand, heavy flavour content of jets is not modelled with the NJETS Monte Carlo. Simulation of four *b*-jet final states has been therefore only possible with the PYTHIA generator, which has the heavy flavour content of the partonic shower implemented.

- In the case of di-jet production in association with a *W* or *Z*, the VECBOS Monte Carlo [14-16], dedicated to this process, has been used. Exact matrix-element calculations were used also for estimating the expected cross-section in the case of W$b\bar{b}$ [14-18] and $Zb\bar{b}$ [14-19] production. In the first case a modified version of HERWIG [14-18] was used, while in the second case the EUROJET Monte Carlo [14-21] was adopted.
- The leading order $t\bar{t}$ cross-section is quoted in Table 14-1 since it has been used for all the background studies to new physics. For the specific case of top physics studies in Chapter 18, a more accurate NLO calculation of 833 pb has been used, except for the case of single-top production, for which the NLO terms are not yet known.
- The total $b\bar{b}$ cross-section is also quoted in Table 14-1. For the *B*-physics studies, much more detailed work reported in Chapter 17 has shown that for high-p_T *b*-quark production, which can provide a Level-1 trigger with a high-p_T muon, the PYTHIA model as used by ATLAS [14-20] reproduces quite well the $b\bar{b}$ production as measured at the Tevatron [14-21] [14-22]. In this case, only a small fraction of the total cross-section quoted in Table 14-1 is relevant for physics, and many of the large theoretical uncertainties inherent to the calculations of the total $b\bar{b}$ production are very significantly reduced. A more detailed discussion of $b\bar{b}$ production at the LHC is discussed in Section 15.8.

The list above collects some relevant examples of the attempts which have been made to estimate as correctly as possible the expected production rates at the LHC. More details can be found in the specific Chapters of this volume discussing particular physics processes

Large uncertainties in the signal and background production cross-sections, due to missing higher-order corrections, structure function parametrisations, energy scale for the QCD evolution, as well as models used for full event generation, remain. In addition, despite the existence of many higher-order QCD correction (*K*-factor) calculations, not all processes of interest at the LHC have benefited from this theoretical effort. In most cases they have also not been embodied in the Monte Carlo generator, so that proper studies of their impact on the observed rates cannot be undertaken. Therefore, the present studies consistently and conservatively avoided the use of *K*-factors, resorting to Born-level predictions for both signal and backgrounds.

14.4.2 Signal observability

In the following sections, most of the results will be given for integrated luminosities of 30 fb^{-1} and 100 fb^{-1}, which are expected to be collected in three years of data taking at the initial (low) luminosity and one year of data taking at the design (high) luminosity respectively. The ultimate discovery potential is evaluated for an integrated luminosity of 300 fb^{-1}.

In most cases, the event selection for signal and background has been performed as it might be expected for off-line analysis. The foreseen trigger LVL1/LVL2 menus were used for the discussed channels. The possible irreducible and reducible backgrounds are extensively discussed. Given that the presently available tools for physics modelling have inherent uncertainties, analyses in most cases are straightforward; sophisticated statistical methods and very detailed optimisation of cuts are not applied.

Table 14-1 Leading order cross-sections for some typical processes at the LHC. Unless stated otherwise, these numbers have been obtained by using PYTHIA 5.7 with CTEQ2L structure functions.

Process	Cross-section	Comments
Inclusive H m_H = 100 GeV	27.8 pb	
WH with $W \to l\nu$ m_H = 100 GeV	0.40 pb	
$t\bar{t}H$ with one $W \to l\nu$ m_H = 100 GeV	0.39 pb	
Inclusive SUSY $m_{\tilde{g}}$, $m_{\tilde{q}}$ ~ 1 TeV	3.4 pb	ISAJET or PYTHIA
Inclusive $b\bar{b}$	500 μb	All di-jet processes used
Inclusive $t\bar{t}$ (m_t = 175 GeV)	590 pb	
Di-jet processes: 1 jet p_T^j > 180 GeV, $\|\eta\|$ < 3.2	13 μb	PYTHIA
3 jets p_T^j > 40 GeV, $\|\eta\|$ < 3.2	2.0 μb (0.7 μb)	NJETS (PYTHIA)
4 jets p_T^j > 40 GeV, $\|\eta\|$ < 3.2	0.4 μb (0.1 μb)	NJETS (PYTHIA)
Inclusive W	140 nb	
Inclusive Z	43 nb	
Wjj with $W \to l\nu$ with 2 jets p_T^j > 15 GeV, $\|\eta\|$ < 3.2	4640 pb	VECBOS
$Wb\bar{b}$ with $W \to l\nu$	69.3 pb	Matrix element [14-18]+ HERWIG
Zjj with $Z \to ll$ with 2 jets p_T^j > 15 GeV, $\|\eta\|$ < 3.2	220 pb	VECBOS
$Zb\bar{b}$ with $Z \to ll$	36 pb	EUROJET + [14-19]
WW	71 pb	
WZ	26 pb	
$W\gamma$ with $W \to l\nu$ with p_T^γ > 100 GeV, $\|\eta\|$ < 2.5	210 fb	

The observation of a given signal will be considered as possible if a significance of five standard deviations, defined according to the naive estimator $S/\sqrt{B}$, where S (B) is the expected number of signal (background) events, can be obtained. This includes the relevant systematic uncertainties. If the number of expected signal and background events is smaller than 25, Poisson statistics has been used to compute the equivalent Gaussian significance.

14.5 Outline

This volume reviews the potential of the ATLAS detector for the observability of a variety of physics processes, starting from the studies of hadronic physics, precision measurements in the Standard Model sector and *CP*-violation phenomena, continuing through the searches for the Higgs boson(s) and supersymmetry, and ending with a discussion of physics beyond the Standard Model.

The volume begins with a discussion of QCD processes (Chapter 15), which have the largest rate and represent the dominant background for new physics searches. Next is a discussion of the properties of the *W* and *Z* gauge bosons and how ATLAS can improve the precision measurements of the masses and couplings (Chapter 16). This is followed by a presentation of the *B*-physics programme; methods for the measurement of *CP* violation, mixing and rare decays are discussed (Chapter 17). Next, measurements related to the top quark and searches for other heavy quarks / leptons are described (Chapter 18). The Standard Model Higgs boson and its variants in the minimal supersymmetric model provide a benchmark for LHC physics; the large number of possible discovery channels are analysed in detail (Chapter 19). Physics beyond the Standard Model is the subject of the final two sections; the most popular extension to Supersymmetry is discussed in detail and many signatures that allow precise measurements in this sector are presented (Chapter 20). Finally, signatures for other extensions to the Standard Model, such as new gauge bosons and technicolour, are discussed (Chapter 21).

14.6 References

14-1 ATLAS Letter of Intent, CERN / LHCC / 92-4, CERN 1992.

14-2 ATLAS Technical Proposal, CERN / LHCC 94-43, CERN 1994.

14-3 S. Glashow, Nucl. Phys. **22** (1961) 579;
S. Weinberg, Phys. Rev. Lett. **19** (1967) 1264;
A. Salam, in: 'Elementary Particle Theory', W. Svartholm,ed., Almquist and Wiksell, Stockholm,1968;
H.D. Politzer, Phys. Rev. Lett **30** (1973) 1346;
D.J. Gross and F.E. Waltzed, Phys. Rev. Lett. **30** (1973)1343.

14-4 H. Fritzsh and M. Gell-Mann, Proc. XVI Int. Conf. on High Energy Physics, eds. J. D. Jackson and A. Roberts (Fermilab 1972).

14-5 M. Kobayashi and T. Maskawa, Prog. Theor. Phys. **49** (1973) 652;
N. Cabibbo, Phys. Rev. Lett. **10** (1963) 531.

14-6 P. W. Higgs, Phys. Rev. Lett. **12** (1964) 132; Phys. Rev. **145** (1966) 1156;
F. Englert and R. Brout, Phys. Rev. Lett **13** (1964) 321;
G. S. Guralnik, C. R. Hagen and T. W. Kibble, Phys. Rev. Lett **13** (1964) 585.

14-7 L. Maiani, G. Parisi and R. Petronzio, Nucl. Phys. **B136** (1979) 115;
N. Cabbibo, L. Maiani, G. Parisi and R. Petronzio, Nucl. Phys. **B158** (1979) 295;
R. Dashen and H. Neuberger, Phys. Rev. Lett. **50** (1983) 1897;
D. J. E. Callaway, Nucl. Phys. **B233** (1984) 189;
M. A. Beg, C. Panagiatakopolus and A. Sirlin, Phys. Rev. Lett **52** (1984) 883;
M. Lindner, Z. Phys. **C31** (1986) 295.

14-8 T. Hambye and K. Riesselmann, Phys. Rev. **D55** (1997) 7255.

14-9 C. Quigg, B.W. Lee and H. Thacker, Phys. Rev. **D16** (1977) 1519;
M. Veltman, Acta Phys. Polon. **B8** (1977) 475.

14-10 J. Wess and B. Zumino, Nucl. Phys. **B70** (1974) 39.

14-11 For a review, see K.D. Lane hep-9605257 (1996).

14-12 F. Paige and S. Protopopescu, in Supercollider Physics, p. 41, ed. D. Soper (World Scientific, 1986).

14-13 T. Sjostrand, Comp. Phys. Comm. **82** (1994) 74.

14-14 G. Marchesini *et al.*, Comp. Phys. Comm. **67** (1992) 465.

14-15 F.A. Berends and H. Kuijf, Nucl.Phys.**B353** (1991) 59.

14-16 F.A. Berends, H. Kuijf, B. Tausk and W.T. Giele, Nucl.Phys.**B357** (1991) 32;
W. Giele, E. Glover, D. Kosower, Nucl. Phys. **B403** (1993) 633.

14-17 The CDF Collaboration, F. Abe *et al.*, Phys. Rev. **D41** (1990) 2330; Phys. Rev. Lett. **61** (1988) 1819.

14-18 M.L. Mangano, Nucl. Phys. **B405** (1993) 536.

14-19 B. van Eijk and R. Kleiss, in [14-24], page 183.

14-20 S. Baranov and M. Smizanska, 'Beauty production overwiew from Tevatron to LHC', ATLAS Internal Note ATL-PHYS-98-133 (1998);
P. Eerola,' The inclusive muon cross-section in ATLAS', ATLAS Internal Note ATL-PHYS-98-120 (1998).

14-21 D0 Collaboration, S. Abachi *et al.*, Phys. Rev. Lett. **74** (1996) 3548; Phys. Lett. **B370** (1996) 239.

14-22 CDF Collaboration, F. Abe *et al.*, Phys. Rev. Lett. 71 (1993) 500; Phys. Rev. Lett. **71** (1993) 2396; Phys. Rev. Lett. **71** (1993) 2537; Phys. Rev. Lett. **75** (1995) 1451; Phys. Rev. **D50** (1996) 4252; Phys. Rev. **D53** (1996) 1051.

14-23 T. Sjostrand, Comp. Phys. Comm. **82** (1994) 74. The supersymmetry extensions are described in S. Mrenna, Comp. Phys. Comm. **101** (1997) 232.

14-24 Proceedings of the Large Hadron Collider Workshop, Aachen, 1990, edited by G. Jarlskog and D. Rein, CERN 90-10 / ECFA 90-133.

15 QCD processes at the LHC

15.1 Introduction

The study of QCD processes at the LHC will serve two main goals. First the predictions of QCD will be tested and precision measurements will be performed, allowing additional constraints to be established *e.g.* on the distribution of partons in the proton, or providing measurements of the strong coupling constant α_s at various scales. Second QCD processes represent a major part of the background to other Standard Model processes and signals of new physics at the LHC and thus need to be understood precisely in the new kinematic region available here. Deviations from the QCD expectations might themselves also indicate the occurrence of new physics, as in the case of compositeness for the jet transverse energy and di-jet invariant mass and angular distributions. Furthermore, the production cross-sections for almost all processes are controlled by QCD.

Tests of QCD can be performed by comparing measurements to fixed order (either LO (leading order) or NLO (next-to-leading order)) calculations or to leading-log Monte Carlo programs which contain $2 \rightarrow 2$ LO matrix elements and approximate higher orders through the use of parton showers (and also include the hadronisation of the partonic system). Perturbative QCD can also be tested by extracting (or constraining) the fundamental parameter α_s. The difference between a LO and a NLO calculation is quantified in the *K*-factor; the *K*-factor is defined as the ratio between the cross-section at NLO to the one at LO. The *K*-factor can become significantly larger than 1, especially when new sub-processes appear at next-to-leading order. Calculations at next-to-leading order are mostly restricted to parton level and often performed by numerical integration of the corresponding matrix elements.

This chapter gives an overview of different measurements of QCD processes [15-1], [15-2], [15-3] to be performed with ATLAS, classified by the main characteristics (or main selection criteria) of the final state. Besides a qualitative overview, a few examples are given where first quantitative investigations of the potential of ATLAS have been performed. The organisation of the chapter is as follows: the next section contains a brief summary on the present knowledge of parton densities and some perspectives for improvements before the start of LHC. Then measurements of properties of minimum-bias events (Section 15.3) are discussed, followed by a description of studies of hard diffractive scattering (Section 15.4). Next, the information to be deduced from the measurement of jets (Section 15.5) is described, followed by a section on photon physics (Section 15.6) and one concerning the production of Drell-Yan pairs and heavy gauge bosons (Section 15.7). Before concluding, the production of heavy flavours (charm, bottom and top, Section 15.8) is discussed.

Unless stated differently in the corresponding sections, the standard trigger settings have been used. The signatures listed in [15-4] for the first level (and the second level) of the trigger system consist mainly of inclusive signatures. It is foreseen to accept a fraction of events with lower thresholds and it is possible to include specific signatures (esp. at the higher levels of the trigger system) combining different objects and thus allowing lowering of the corresponding thresholds. One important exception is the case of hard diffraction and the case of minimum-bias events, where dedicated triggers will have to be employed.

15.2 Knowledge of the proton structure

15.2.1 Global parton analyses and parton kinematics at the LHC

The calculation of the production cross-section at the LHC both for interesting physics processes and their backgrounds relies upon a knowledge of the distribution of the momentum fraction x of the partons in the proton in the relevant kinematic range. These parton distribution functions (pdf's) are determined by global fits (see [15-5] for a pedagogical overview) to data from deep-inelastic scattering (DIS), Drell-Yan (DY), jet and direct photon production at current energy ranges. Two major groups, CTEQ [15-6] and MRS [15-7], provide regular updates to the parton distributions when new data and / or theoretical developments become available.

Lepton-lepton, lepton-hadron and hadron-hadron interactions probe complementary aspects of perturbative QCD (pQCD). Lepton-lepton processes provide clean measurements of $\alpha_s(Q^2)$ and of the fragmentation functions of partons into hadrons. Measurements of deep-inelastic scattering structure functions (F_2,F_3) in lepton-hadron scattering and of lepton pair production cross-sections in hadron-hadron collisions provide the main source of information on quark distributions $q^a(x,Q^2)$ inside hadrons. At leading order, the gluon distribution function $g(x,Q^2)$ enters directly in hadron-hadron scattering processes with direct photon production and jet final states. Modern global parton distribution fits are carried out to next-to-leading order (NLO) which allows $q^a(x,Q^2)$, $g(x,Q^2)$ and the strong coupling $\alpha_s(Q^2)$ to all mix and contribute in the theoretical formulae for all processes. Nevertheless, the broad picture described above still holds to some degree in global pdf analyses. In pQCD, the gluon distribution is always accompanied by a factor of α_s, in both hard scattering cross-sections and in the evolution equations for the parton distributions. Thus, the determination of α_s and the gluon distribution is, in general, a strongly coupled problem. One can determine α_s separately from e^+e^- interactions or determine α_s and $g(x,Q^2)$ jointly in a global pdf analysis. In the latter case, though, the coupling of α_s and the gluon distribution may not lead to a unique solution for either (see *e.g.* in [15-8]).

Currently, the world average of $\alpha_s(M_Z)$ is of the order of 0.118 – 0.119 [15-9]. The average value from LEP is 0.121 while the DIS experiments prefer a somewhat smaller value (of the order of 0.116 – 0.117). Since global pdf analyses are dominated by the high statistics DIS data, they would favour the values of α_s closer to the lower DIS values. The more logical approach is to adopt the world average and concentrate on the determination of the pdf's. This is what both CTEQ and MRS currently do. One can either quote a value of $\alpha_s(M_Z)$ or the value of Λ_{QCD}. For the latter case, however, the renormalisation scheme used together with the number of flavours has to be clearly specified. Usually the $\overline{MS}$ scheme is used. The specification of the number of flavours is important as the value of α_s has to be continuous across flavour thresholds. A range of $\alpha_s(M_Z)$ of 0.105 to 0.122 corresponds to the range of $100 < \Lambda_{QCD} < 280$ MeV for five flavours and to $155 < \Lambda_{QCD} < 395$ MeV for four flavours.

The data from DIS, DY, direct photon and jet processes utilised in pdf fits cover a wide range in x and Q. The kinematic 'map' in the $(1/x,Q)$ plane of the data points used in a recent parton distribution function analysis is shown in Figure 15-1. The HERA data (H1 and ZEUS) are predominantly at low x, while the fixed target DIS and DY data are at higher x. There is considerable overlap, however, with the degree of overlap increasing with time as the statistics of the HERA experiments increases. The DGLAP equations [15-10] in pQCD describe the change of the parton distributions with Q^2. The NLO DGLAP equations should describe the data over the whole kinematic range shown in Figure 15-1. At very low x, however, the DGLAP evolution is believed to be no longer applicable and a BFKL [15-11] description must be used. No clear evi-

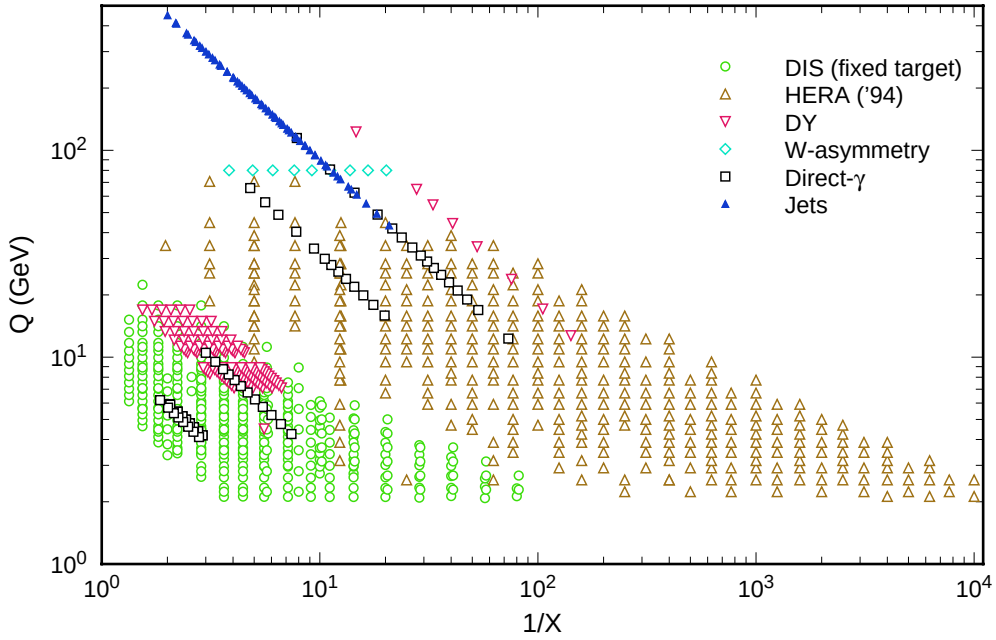

Figure 15-1 A kinematic map of data points in the *(1/x,Q)* plane from different processes used in a global fit of parton densities (from [15-5]).

dence of BFKL physics is seen in the current range of data; thus all global analyses use conventional DGLAP evolution of the pdf's. There is a remarkable consistency between the data in the pdf fits and the NLO QCD theory to fit these. Over 1300 data points are shown in Figure 15-1 and the χ^2 / DOF for the fit of theory to data is of the order of 1.

In Figure 15-2 the kinematics appropriate for the production of a state with mass M and rapidity y at the LHC is shown [15-12]. For example, to produce a state of mass 100 GeV at rapidity $y = 2$ requires partons of x values 0.05 and 0.001 at a Q^2 value of 10^4 GeV^2. The figure also shows another view of the kinematic coverage of the fixed target and the HERA experiments used in the pdf fits.

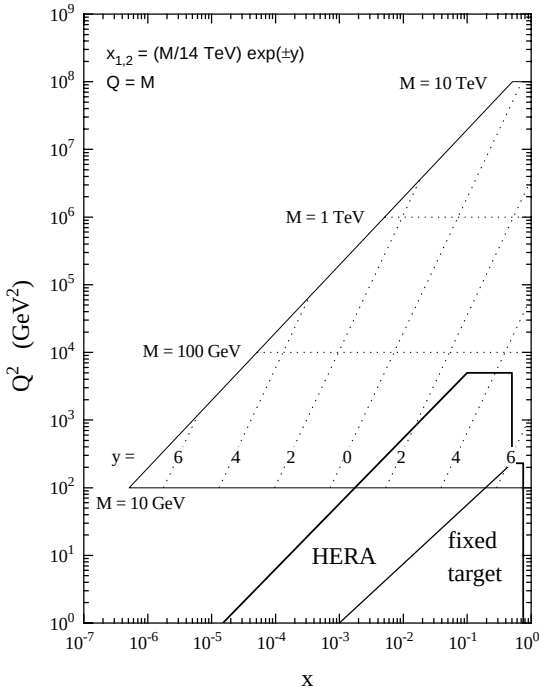

Figure 15-2 Parton kinematics at the LHC (from [15-12]) in the *(x,Q²)* kinematic plane for the production of a particle of mass M at rapidity y (dotted lines).

15.2.2 Properties and uncertainties of parton distribution functions

Figure 15-3 shows the parton distributions for the different quark flavours and the gluon as obtained from the CTEQ4M distribution [15-8] for a scale of $Q^2 = 20$ GeV^2, in Figure 15-4 the corresponding distributions are shown for a scale of $Q^2 = 10^4$ GeV^2. Clearly visible is the dominance of the gluon distribution for small parton momenta. In addition the violation of the flavour symmetry for $\bar{u}$ and $\bar{d}$ sea quarks can be seen.

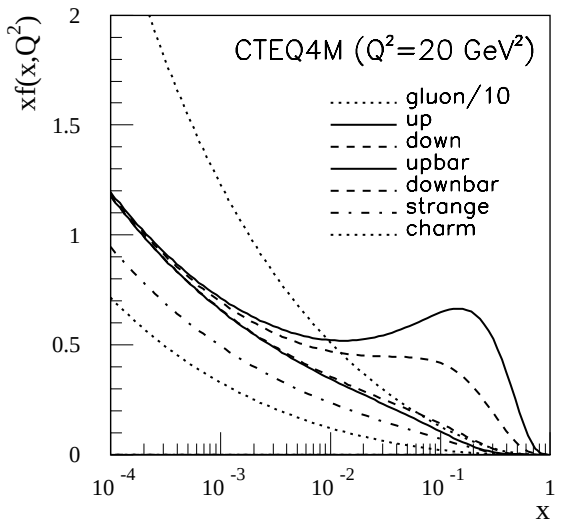

Figure 15-3 Parton distributions for the CTEQ4M pdf at Q^2 = 20 GeV^2. The gluon distribution has been reduced by a factor of 10.

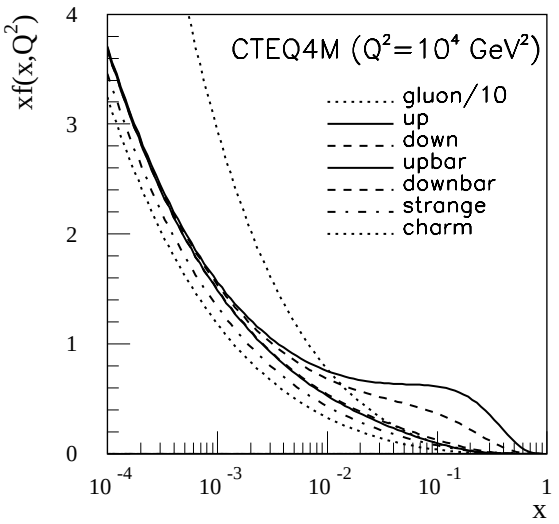

Figure 15-4 Parton distributions for the CTEQ4M pdf at Q^2 = 10^4 GeV^2. The gluon distribution has been reduced by a factor of 10.

Parton distribution determined at a given x and Q^2 'feed-down' to lower values of x at higher values of Q^2. The accuracy of the extrapolation to higher Q^2 depends both on the accuracy of the original measurement and any uncertainty on $\alpha_s(Q^2)$. For the structure function F_2, the typical measurement uncertainty at medium to large x is of the order of 3%. At high Q^2 (about 10^5 GeV^2) there is an extrapolation uncertainty of 5% in F_2 due to the uncertainty in α_s.

Figure 15-6 shows the gluon distribution as a function of x for five different values of Q^2, using the CTEQ4M distribution. Most of the evolution takes place at low Q^2 and there is only little evolution for x values around 0.1. In contrast, at an x value of 0.5, the gluon distribution decreases by a factor of approximately 30 from the lowest to the highest Q^2.

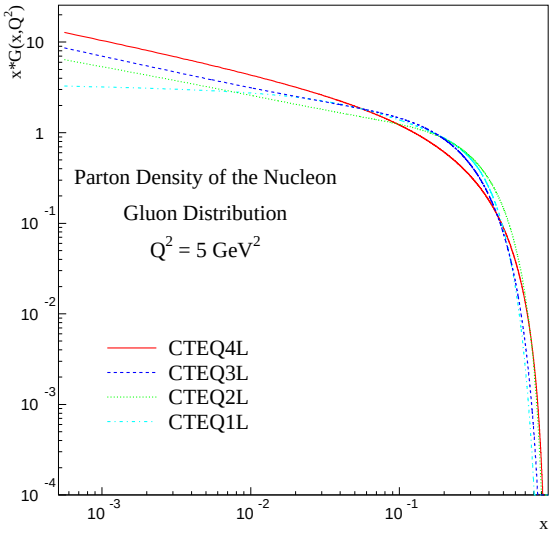

Figure 15-5 Gluon distribution for the CTEQ1L, CTEQ2L, CTEQ3L and CTEQ4L pdf's at a value of Q^2 = 5 GeV^2 (from [15-5]).

Global fits can also be performed using leading-order (LO) matrix elements, resulting in leading-order parton distribution functions. Such pdf's are preferred when leading order matrix element calculations (such as in Monte Carlo programs like HERWIG [15-13] and PYTHIA [15-14]) are used. The differences between LO and NLO pdf's, though, are formally NLO; thus the additional error introduced by using a NLO pdf should not be significant. A comparison of the LO and NLO gluon distribution is shown in Figure 15-7 for the CTEQ4 set, where the LO distribution is CTEQ4L and the NLO distribution is CTEQ4M. The differences get even smaller at larger Q^2 values.

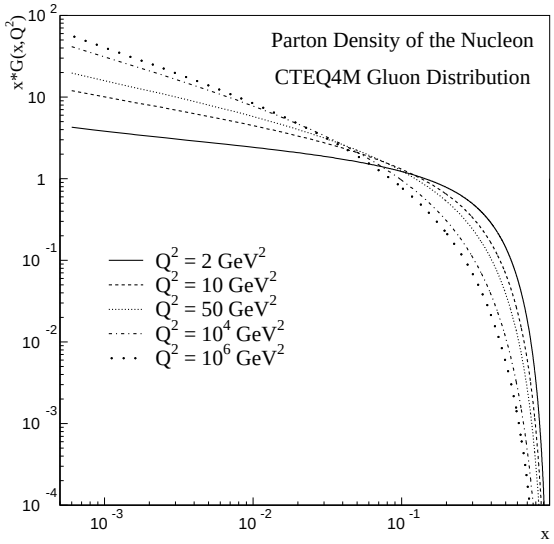

Figure 15-6 Gluon densities as a function of x from the CTEQ4M parton distribution set for five different Q^2 values: 2, 10, 50, 10^4 and 10^6 GeV^2 (from [15-5]).

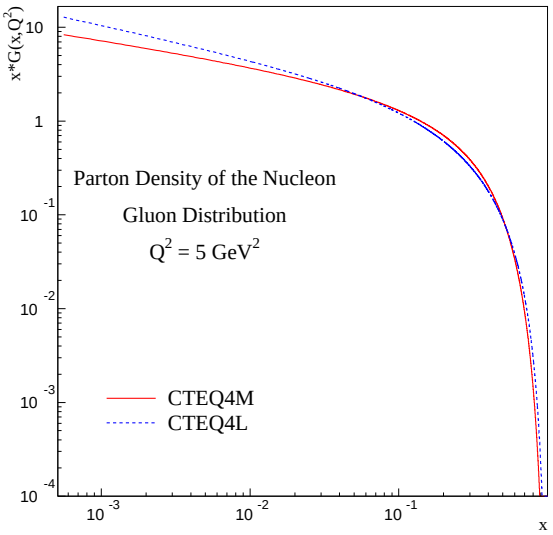

Figure 15-7 Comparison of the gluon distribution from the CTEQ4L (leading order) and the CTEQ4M (next-to-leading order) global fit (from [15-5]).

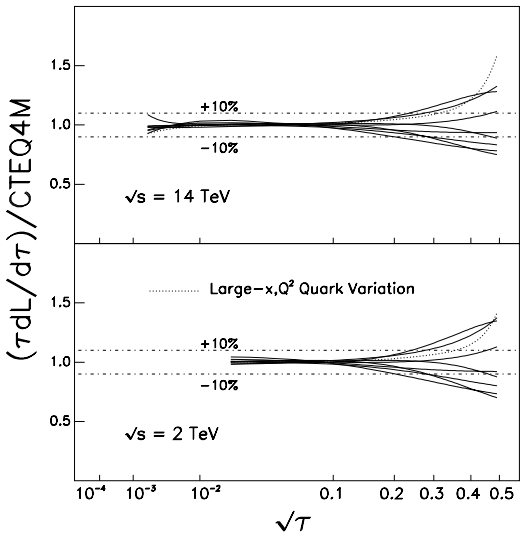

Figure 15-8 Normalised quark-gluon luminosity function (as a function of $\sqrt{\tau} = \sqrt{x_1 \cdot x_2}$) for variations in the gluon distribution which are consistent with existing DIS and DY datasets (from [15-17]). The dotted curve shows a toy model with more quarks at $x > 0.5$ for large Q^2 than in CTEQ4M.

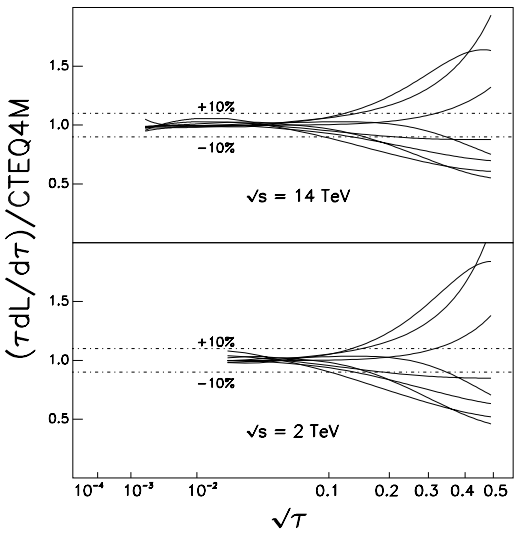

Figure 15-9 Normalised gluon-gluon luminosity function (as a function of $\sqrt{\tau} = \sqrt{x_1 \cdot x_2}$) for variations in the gluon distribution, which are consistent with existing DIS and DY datasets (from [15-17]).

Many of the comparisons in this document have been performed with the CTEQ2L pdf, a pdf that is on the order of five years old [15-15]. A comparison of the gluon distribution for CTEQ1L, CTEQ2L, CTEQ3L and CTEQ4L is shown in Figure 15-5. With increasing amounts of data included from HERA, the tendency has been for the low x pdf's to increase. The relative increases are reduced at higher values of Q^2.

In addition to having the best estimate for the values of the pdf's in a given kinematic range. it is also important to understand the allowed range of variation in the pdf's, *i.e.* their uncertainties. The conventional method of estimating parton distribution uncertainties is to compare different published parton distributions. This is unreliable since most published sets of parton distributions (*e.g.* from CTEQ and MRS) adopt similar assumptions and the differences between the sets do not fully explore the uncertainties that actually exist. Ideally, one might hope to perform a full error analysis and provide an error correlation matrix for all the parton distributions (see *e.g.* [15-16]). This goal may be difficult to carry out for two reasons. Experimentally, only a subset of the experiments usually involved in the global analyses provide correlation information on their data sets in a way suitable for the analysis. Even more important, there is no established way of quantifying the theoretical uncertainties for the diverse physical processes that are used and uncertainties due to specific choices of parametrisations. Both of these are highly correlated.

As the LHC is essentially a gluon-gluon collider and many hadron collider signatures of physics both within and beyond the Standard Model involve gluons in the initial state, it is important to estimate the theoretical uncertainty due to the uncertainty in the gluon distribution. The momentum fraction carried by gluons is 42% with an accuracy of about 2% (at Q = 1.6 GeV in the CTEQ4 analysis), determined from the quark momentum fraction using DIS data. This important constraint implies that if the gluon distribution increases in a certain x range, momentum conservation forces it to decrease in another x range. To estimate the uncertainty on the gluon distribution, an alternative approach has been carried out [15-17]: the (four) parameters of the gluon distribution (based on the CTEQ4 set) have been varied systematically in a global analysis and the resulting parton distributions have been compared to the DIS and Drell-Yan datasets making up the global analysis database. Only DIS and Drell-Yan datasets were used, as the experimental and theoretical uncertainties for these processes are under good control. Only those pdf's that do not clearly contradict any of the (DIS and Drell-Yan) data sets in the global analysis database were kept. The variation of the gluon distribution obtained with this procedure is less than 15% (10%) for low Q (high Q), except for large values of $x > 0.2$ (and very small ones $x < 10^{-4}$). In addition Figure 15-8 shows the effect of uncertainties on the quark distribution for x > 0.5, as obtained from a toy model (more details can be found in [15-17]).

To assess the range of predictions on physics cross-sections for a hard scattering process, it is more important to know the uncertainties on the gluon-gluon and the gluon-quark luminosity functions in the appropriate kinematic region of $\sqrt{\tau} = \sqrt{x_1 \cdot x_2}$. The relevant integrated parton-parton luminosity function is (in case of the gluon-gluon luminosity) defined as

$$\tau \frac{dL}{d\tau} = \int_{\tau}^{1} G(x, Q^2) G(x/\tau, Q^2) dx/x$$

This quantity is directly proportional to the cross-section for the *s*-channel production of a single particle and it also gives a good estimate for more complicated production mechanisms. In Figure 15-8 the allowed range of quark-gluon luminosities (normalised to the CTEQ4M values) is shown for the variations discussed above (for LHC and for Tevatron). The scale Q^2 is taken as τs, which naturally takes into account the Q^2 dependence of the gluon distribution as τ changes. The quark distributions in this case are taken to have no uncertainty, which is a reasonable assumption since the uncertainty on the gluon distribution is much larger. Figure 15-9 shows the corresponding variations in the gluon-gluon luminosity (normalised again to the values of the CTEQ4M distribution). For values of $\sqrt{\tau} < 0.1$ the resulting variation in the gluon-gluon and

quark-gluon luminosity function is less than 10%, for values of $\sqrt{\tau}$ between 0.1 and 0.2 (0.2 and 0.3) the variation increases to 20% (30%) for the gluon-gluon luminosity and 10% (15%) for the quark-gluon luminosity.

15.2.3 Expected improvements before the LHC start-up

DGLAP-based pQCD calculations have been extremely successful in describing data in DIS, DY and jet production, as well as describing the evolution of parton distributions over a wide range in x and Q^2 (for a recent review see *e.g.* [15-18]). From the pdf point-of-view, one of the current problems lies in the determination of the gluon density at high x. Fixed target direct photon cross-sections can serve as a primary probe of the gluon distribution at high x. However, rigorous theoretical treatment of soft gluon effects (requiring both k_T and Sudakov resummation) will be required before the data can be used with confidence in pdf fits [15-19].

Differential di-jet data from the Tevatron explore a wider kinematic range than the inclusive jet cross-sections. Both CDF and D0 have di-jet cross-section measurements from Run I which may also serve to probe the high x gluon distribution, in regions where new physics is not expected to contribute (*i.e.* at moderate E_{T}), but where any parton distribution shifts would be observable. The ability to perform such cross-checks is essential.

CDF and D0 will accumulate on the order of 2-4 fb^{-1} in Run II (2000-2003), a factor of 20-40 greater than the current sample. This sample should allow for more detailed information on parton distributions to be extracted from direct photon and DY data, as well as from jet production. Run III (2003-2007) could offer a data sample potentially as large as 30 fb^{-1}.

The luminosity upgrade foreseen at HERA in the year 2000 [15-20] should deliver to the experiments a luminosity of about 150 pb^{-1} / year, allowing for an integrated luminosity of about 1 fb^{-1} by 2005. This will allow an error of a few percent on the structure function F_2 for scales Q^2 up to 10^4 GeV^2. The gluon density, derived from the scaling violations of F_2, should be known to an accuracy of less than 3% in the kinematic range $10^{-4} < x < 10^{-1}$.

15.2.4 The role of data from ATLAS

ATLAS measurements of DY (including W and Z), direct photon, jet and top production will be extremely useful in determining pdf's relevant for the LHC. This data can be input to the global fitting programs, where it will serve to confirm / constrain the pdf's in the kinematic range of the LHC. Again, DY production will provide information on the quark (and anti-quark) distributions while direct photon, jet and top production will provide, in addition, information on the gluon distribution. Also the precise measurement of beauty production could be used to provide constraints on the gluon, however, in this case the present discrepancy between the theoretical prediction and the data from the Tevatron (which are a factor of 2 or more larger than the prediction) has to be resolved.

Another possibility that has been suggested is to directly determine parton-parton luminosities (and not the parton distributions per se) by measuring well-known processes such as W / Z production [15-21]. This technique would not only determine the product of parton distributions in the relevant kinematic range but would also eliminate the difficult measurement of the proton-proton luminosity (see Chapter 13). It may be more pragmatic, though, to continue to separate

out the measurements of parton pdf's (through global analyses which may contain LHC data) and of the proton-proton luminosity. The measurement of the latter quantity can be pegged to well-known cross-sections, such as that of the W/Z, as has been suggested for the Tevatron.

15.3 Properties of minimum–bias events

15.3.1 Importance of minimum–bias studies

Due to the high luminosity at the LHC, there will be up to an average of 25 inelastic collisions per bunch-crossing. The knowledge of the structure of these 'minimum-bias' events is of great importance for all physics studies to be carried out by ATLAS as well as a powerful diagnostic tool on the performance of the detector. Besides the properties of charged (and neutral) particle production, the understanding of jet structures with small transverse momentum ('mini-jets') is needed if vetoes on jet activity are to be used in physics analyses.

In this section, the selection of minimum-bias events is described (Section 15.3.2), followed by a brief overview of generators for minimum-bias events (Section 15.3.3) and a discussion of possible measurements (Section 15.3.4), including a comparison of the predictions by the different models.

15.3.2 Selection of minimum–bias events

In order to have an efficient detection of minimum-bias events, and to allow for a minimisation of uncertainties in the extrapolation due to the modelling of minimum-bias events, a very small acceptance loss is desirable. Given the angular acceptance in pseudorapidity of $|\eta| < 5$ in the ATLAS detector, the installation of additional detectors in the very forward region close to the beam-pipe is desirable. Possible locations along the beam-pipe outside of the ATLAS detector for such detectors can be found in Section 13.3.1, where also the acceptance for inelastic events as a function of the lower and upper limit on the pseudorapidity is described.

A trigger demanding signals in coincidence on both sides of the interaction region can select non-diffractive inelastic interactions with an acceptance loss of about 0.4%, if tagging is available in the region $3 < |\eta| < 7.5$. The acceptance of this coincidence for single-diffractive, double diffractive and central diffractive events is smaller and leads to an overall acceptance for inelastic events of about 90%. A large part of the diffractive inelastic events can be recovered by requiring activity in at least one of the two sides of the interaction point, *i.e.* a single arm trigger. If these dedicated forward detectors would not be available at the trigger, a selection of minimum-bias events could also be obtained from a trigger on random bunch crossings, taking into account only those crossings, where both proton bunches are filled.

15.3.3 Modelling of minimum-bias events

There are several models available, which can generate minimum-bias events and have been tuned to existing data up to highest available energies from Tevatron. The following four models have been considered HERWIG [15-13], ISAJET [15-22], PYTHIA [15-14] (a short description of these three models can be found in Section 14.4) and PHOJET [15-23]. The last generator is a

combination of ideas from the Dual Parton Model [15-24] approach to hadronic interactions at high energies and aspects of perturbative QCD (following very closely the approach of DTUJET [15-25]). The aim is to provide an almost complete picture of hadron-hadron, photon-hadron and photon-photon interactions at high energies.

The different settings used for these generators are summarised and commented in [15-26]. In the case of ISAJET and HERWIG, only simple models for minimum-bias events are used, which are restricted to soft physics processes. They do not attempt to connect soft and hard process. In PYTHIA and PHOJET on the other hand, this connection is made. PHOJET uses the Dual Parton Model for particle production at low transverse momentum and leading order QCD matrix elements for large transverse momentum processes (including parton showers to approximate higher order corrections). PYTHIA uses the leading order QCD matrix elements with a very low p_T cutoff to model low p_T non-diffractive physics. Both PHOJET and PYTHIA include multiple interactions.

In the case of PYTHIA, two different approaches to handle the divergences in the matrix elements have been considered: a sharp cut-off (‘Model1‘) and a smoothly varying cut-off (‘Model4’), corresponding to the value of the parameter MSTP(82) being equal to 1 or 4. The first setting significantly overestimates [15-26] the charged particle density as measured at the Tevatron (see below) and is not investigated further. In case of PYTHIA version 5.724, which is used in this document to model minimum-bias events (for more details see Section 2.3.2), the setting MSTP(82) = 4 is used together with the following two settings (as recommended): MSTP(2) = 2 (two loop expression for α_s in the matrix element) and MSTP(33) = 3 (inclusion of the *K*-factor in the hard scattering cross-section), which is labelled as ‘PYTHIA 5.724 - ATLAS’ in the figures. The most recent version 6.122 of PYTHIA has been also used. One important change for the generation of minimum-bias events is the introduction of an energy dependence for the transverse momentum cut-off. For the setting MSTP(82) = 4 it is recommended for PYTHIA 6.122 not to change the default parameters (shown as ‘PYTHIA 6.122 - Model4’). As will be shown below, using the parameters MSTP(2) = 2 and MSTP(33) = 3 in PYTHIA 6.122 for MSTP(82) = 4 (labelled ‘PYTHIA 6.122 - A’) is not able to describe the Tevatron data. For illustration, the predictions with these settings will however be shown (more details can be found in [15-26]).

15.3.4 Measurements

15.3.4.1 Total cross-section

The determination of the total cross-section in a luminosity independent way requires the simultaneous measurement of the elastic and the inelastic scattering rate. Details of this method can be found in Section 13.3.1. One important uncertainty in this measurement is the precise knowledge of the acceptance for inelastic events (minimum-bias events, single and double diffractive dissociation events as well as central diffractive events) and any possible model dependence for the acceptance determination.

15.3.4.2 Charged particle spectra and energy flow

At the LHC, minimum-bias events will make up the 25 interactions per bunch-crossing at high luminosity. In order to understand precisely their contribution to the measured quantities for the hard scattering events of interest, a detailed knowledge of the structure of the minimum-bias events is required. These measurements can in turn be used to verify and tune the corresponding models.

The event selection could be based on a trigger on random bunch crossings or on the tagging of minimum-bias events by demanding a coincidence in the forward detectors to be possibly placed outside the acceptance of ATLAS. For non-inclusive measurements further selection criteria have to ensure that only a single interaction has taken place in the bunch-crossing (*e.g.* by demanding only one reconstructed vertex in the event). One important aspect is the effect of the strong solenoidal field in ATLAS, which will lead to a decrease in acceptance for low p_T particles. Their detection could be improved by running in a special mode with the solenoidal field off, which should allow to measure the multiplicity as a function of pseudorapidity, without any measurement of the particle momenta.

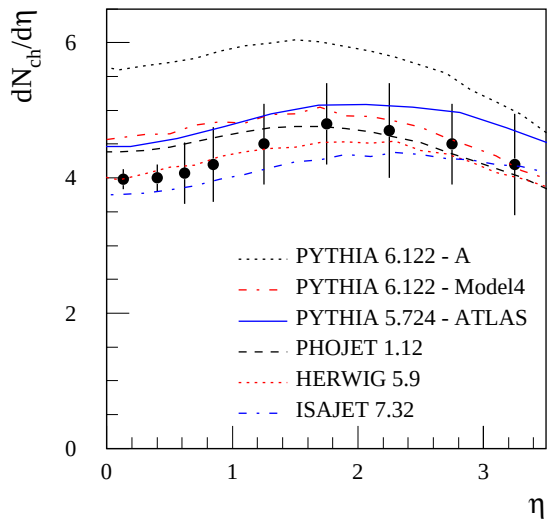

Figure 15-10 Charged particle density in minimum–bias events at Tevatron energies as a function of pseudorapidity (points, as measured by CDF [15-27]) and six model calculations (various curves). The PYTHIA 6.122-A model is shown for illustration only, as a non-recommended parameter setting was used.

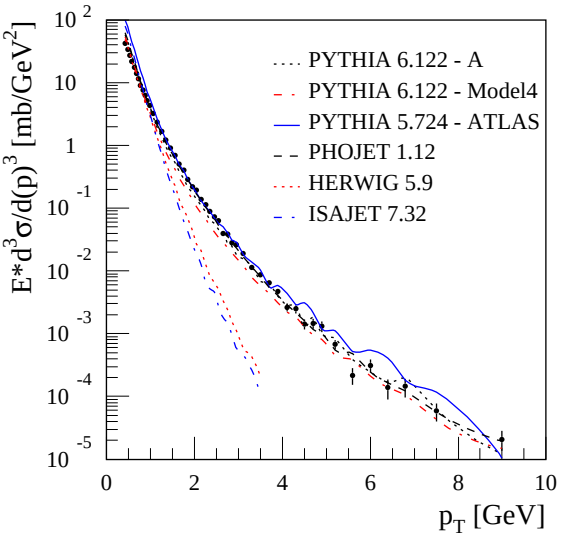

Figure 15-11 Transverse momentum spectrum of charged particles in minimum–bias events at Tevatron energies (points, as measured by CDF [15-28]) and six model calculations (various curves). For the HERWIG and ISAJET calculations, no hard scattering processes have been included.

In Figure 15-10 the charged particle density in minimum-bias events is shown as a function of pseudorapidity as measured by the CDF collaboration [15-27]. The data show a rather flat dependence on pseudorapidity with an average charged particle density of slightly more than 4 per unit of pseudorapidity. The data are well described by the HERWIG, ISAJET, PHOJET and PYTHIA (5.724-ATLAS and 6.122-Model4) calculations, whereas the new PYTHIA version 6.122 with the 'A' settings overestimates the Tevatron data significantly. For the central region ($\eta = 0$) the PYTHIA and PHOJET calculations slightly overestimate the data. Figure 15-11 shows the transverse momentum spectrum of charged particles in minimum-bias events as measured by CDF [15-28]. The two models where no hard processes have been included (HERWIG and ISA-

JET) clearly fail to describe the large transverse momentum part of the cross-section. Were a matching scheme (similar to the ones used *e.g.* in PYTHIA) between the soft process and the hard processes be provided, they should be able to also describe the transverse momentum spectrum. In contrast, the data are well described by PHOJET and the various PYTHIA calculations.

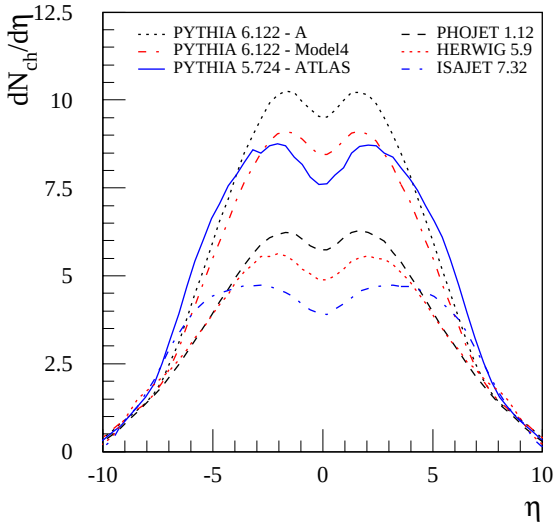

Figure 15-12 Charged particle density in minimum–bias events at LHC energies as a function of pseudorapidity, for six model predictions. The PYTHIA 6.122-A model is shown for illustration only, as a non-recommended parameter setting was used.

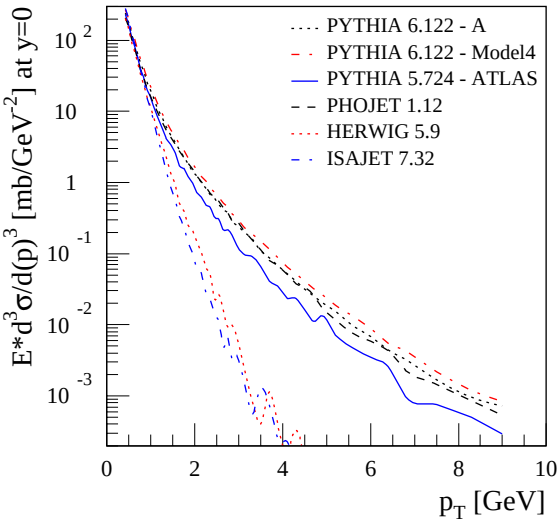

Figure 15-13 Transverse momentum spectrum of charged particles in minimum–bias events at LHC energies, for six model predictions. For the HERWIG and ISAJET calculations, no hard scattering processes have been included.

These six models are then used to give predictions for the LHC. In Figure 15-12 the expected charged particle density is shown as a function of the pseudorapidity and Figure 15-13 shows the cross-section for charged particle production as a function of transverse momentum. For the latter case, the two models (HERWIG and ISAJET), which failed to described the measured transverse momentum spectrum at the Tevatron, predict a very soft momentum spectrum. The reason is the same as for Tevatron energies: hard processes have not been included. It should be kept in mind however that they are able to describe the density of charged particles and their pseudorapidity distribution.

The predictions of HERWIG and ISAJET show very little dependence on the centre-of-mass energy in the average charged particle multiplicity. In the case of ISAJET the density is almost constant and for HERWIG it increases by about 1, similar is the case of PHOJET. The PYTHIA model predicts a larger increase in the charged particle multiplicity, going from about 4–5 at Tevatron energies to 8–9 at LHC energies (in the central region). The LHC predictions, shown over the full pseudorapidity range, show similar shapes for the different models (except for ISAJET and PYTHIA 5.724, which give a broader distribution). The largest charged particle density is predicted by the PYTHIA 6.122 calculation, using the ‘A’ settings. This is shown for illustration only, as the calculation overestimates already the Tevatron data. In case of the transverse momentum spectrum, the newest PYTHIA version predicts a slightly harder spectrum than the old version 5.724. Within the models presented, the calculation based on PYTHIA 5.724 with the ‘ATLAS’ settings appears to be a conservative estimate of the charged particle density in minimum-bias events.

Additional measurements could include the charged particle multiplicity as a function of the pseudorapidity, the scaled multiplicity distribution $n_{ch}/<n_{ch}>$ and the study of correlations between different particles, as was done at the Tevatron [15-29]. A differentiation between types of charged particles might be possible using a *dE/dx* measurement, as discussed in Section 3.4.4.

15.3.4.3 Jet structure and fragmentation functions at small transverse energy

The occurrence of jets with small transverse momenta (so called 'mini-jets') poses a challenge to QCD predictions. In order to study the transverse correlation between partons (see Section 15.5.6), jets with small transverse momentum have to be selected. At LHC energies, extrapolations predict that up to 50% of all inelastic events contain jets with transverse energies larger than 7 GeV. The understanding of the event structure in terms of jets with small transverse energy is important for the use of jet vetoing (see Section 9.1.3) or the identification of muons in the Tile calorimeter (see Section 5.3.3).

As the triggering of low energy jets in the LHC environment is an experimental challenge, the information obtained from a minimum-bias trigger at LVL1 (using either random bunch crossing or the information from additional dedicated detectors in the forward region) can be used to study the properties of these inelastic events not only in terms of particle production, but also in terms of jets with small transverse momenta and their properties. The higher level triggers of ATLAS could be used to provide an enriched sample of minimum-bias events with jet activity, by performing a jet reconstruction. Further studies are needed to quantify the reach in the minimum transverse energy to be accepted with such a selection scheme.

15.4 Measurements of hard diffractive scattering

15.4.1 Overview

In the 60s and 70s the Regge model provided a simple and efficient description of many measurements and phenomena in soft hadronic interactions. It was based on the principles of unitarity, analyticity and crossing symmetry. In addition to the Regge trajectories corresponding to the known mesons and baryons, an additional trajectory had to be introduced to describe deviations from a fall of the total cross-section nucleon-nucleon scattering like $s^{-1/2}$ and latter also the unexpected rise of the total cross-section with energy, as first noticed from the ISR data. This trajectory was named the Pomeron trajectory. It carries the quantum numbers of the vacuum and thus it can also be used to describe elastic scattering. Furthermore it also turned out to be a useful concept for the description of diffractive phenomena. Until recently there has been lack of interest in diffraction. The understanding of diffractive phenomena from first principles (*i.e.* from the Langrangian of QCD) is a 'first class challenge' to theory, which in the last few years has received revived attention due to the appearance of hard diffractive processes, *i.e.* diffractive processes in which a hard scatter takes place.

In terms of final state properties, diffractive events are characterised by the occurrence of rapidity gaps which are not exponentially suppressed with increasing gap size, as would be expected for gaps produced by fluctuations in the hadronisation of a non-diffractive event. Another characteristic property of the final state of single-diffractive (and central-diffractive) events is the appearance of a leading hadron, *i.e.* a hadron with a momentum close to the beam momentum (*e.g.*

$pp \rightarrow pX$). This hadron scatters quasi-elastically and is (due to kinematics) separated from the diffractive final state X by a distance $\Delta\eta$ in pseudorapidity. The value of $\Delta\eta$ depends on the centre-of-mass energy $\sqrt{s}$ and the invariant mass M of the system X through the relation: $\Delta\eta = \ln(s/M^2)$. At the LHC, typical values of $\Delta\eta$ are about 5.3 for $M = 1$ TeV and 9.9 for $M = 100$ GeV.

The name diffraction is related to the behaviour of the cross-section for these events as a function of the momentum transfer. An exponential fall-off with increasing momentum transfer is observed, reminiscent of the properties of the diffraction of light on a circular aperture. A further characteristic of diffractive processes is a slow dependence on the centre-of-mass energy.

The first indication for a partonic structure in diffractive processes (as suggested in [15-30]) has been obtained by the UA8 collaboration [15-31], studying single diffractive dissociation of protons and finding evidence for jets in the diffracted final state. This class of diffractive processes is called hard diffractive scattering, due to the presence of a hard (short distance) scale. Hard diffractive scattering is expected to be part of the inclusive hard scattering cross-section [15-32], and the measurement of jets, W/Z, direct photon and heavy flavour production has been suggested to provide information about the dynamics of the process. The UA8 data furthermore suggested that in part of the events almost the full Pomeron momentum participates in the hard scattering. This was named the ‘superhard Pomeron’.

The observation of deep-inelastic scattering (DIS) events at HERA with a rapidity gap revived interest in diffractive physics. This class of events was predicted by only a few people (*e.g.* in [15-30], [15-33] and [15-34]) and has now become a major part of the HERA physics programme [15-35]. One of the main motivations is to use deep-inelastic scattering as a probe of the colourless exchange governing diffractive scattering, which often appears under the name of the Pomeron. At HERA, typically about 10% of deep-inelastic scattering events can be attributed to a diffractive process.

The occurrence of hard scattering can be related to a partonic structure and a variety of measurements (production of jets, W and Z bosons and of Drell-Yan pairs [15-36] and the production of heavy flavours [15-32]) can be used in a similar way as in non-diffractive inelastic proton-proton interactions to provide constraints on parton densities. Given a set of derived parton distribution functions, a whole set of questions can be addressed: are these described by QCD evolution in the Q^2 dependence, is there agreement (universality of) between pdf’s extracted in different reactions (photon-Pomeron, proton-Pomeron or Pomeron-Pomeron), and are the pdf’s independent of the description of the coupling of the Pomeron to hadrons and so forth?

The inclusive single diffractive dissociation $pp \rightarrow pX$ is described by two variables: the (longitudinal) momentum fraction ξ and the square t of the momentum transfer at the vertex of the quasi-elastically scattered proton. The fraction ξ is related to the momentum fraction x_L of the scattered proton by $\xi = 1 - x_L$. Regge factorisation states the universality of the Pomeron trajectory (and other Regge trajectories) and assumes that only the coupling of the trajectory to a hadron depends on the nature of the hadron. This implies a decomposition of the inclusive cross-section for single diffractive dissociation into two factors: one describes the coupling of the Pomeron to the hadron (the flux factor), the second represents the inelastic cross-section between the Pomeron and the other hadron leading to the diffractive final state.

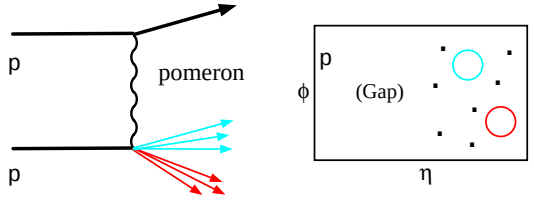

Figure 15-14 Single diffractive dissociation with jet production (adapted from [15-37]).

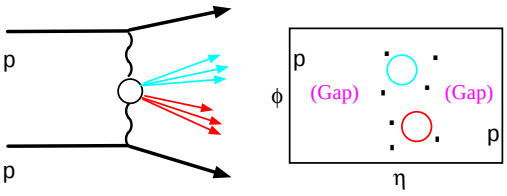

Figure 15-15 Central diffraction (double Pomeron exchange) with jet production (adapted from [15-37]).

In Figure 15-14 a sketch of a single diffractive dissociation event is shown, containing a hard scattering process leading to the production of two jets. In the η-ϕ phase space, the diffracted final state contains the two jets and is separated by a rapidity gap from the scattered proton. A similar sketch is given in Figure 15-15 for central diffraction (double Pomeron exchange), where the diffracted system is separated by two gaps from the two scattered protons.

15.4.2 Existing studies of hard diffraction

Detailed measurements of diffractive DIS (inclusive cross-section and final state studies) at HERA [15-35] supported the partonic interpretation and found that the process is dominated by gluons. A further area of investigation at HERA is the production of vector mesons (like ρ, ω, ϕ, J/ψ) which allows studies of the transition between soft and hard processes due to several available scales (mass M_V^2 of the meson, photon virtuality Q^2, momentum transfer t at the proton vertex) [15-38]. The HERA data are compatible with a factorisation of the measured diffractive cross-section into a flux factor and a term describing the partonic structure. However, it is necessary to invoke the contribution of non-leading trajectories besides the Pomeron to maintain the factorisation hypothesis. Assuming the validity of this approach, a structure function can be extracted, which exhibits clear scaling violations (different from those of a nucleon structure function, rather resembling those of a photon). The data indicate a dominance of the gluon distribution for all Q^2 [15-39]. These observations are supported by various measurements of final state properties in diffractive scattering at HERA, like topological variables, jet and heavy flavour production.

At the Tevatron, diffractive events in $p\bar{p}$ scattering were also observed by selecting events with a rapidity gap. Several classes were studied, including single diffractive dissociation with di-jet production [15-40], diffractive production of W bosons, double Pomeron exchange [15-41] and events with a rapidity gap between two jets [15-42][15-43][15-44]. The fraction of diffractive events for a given process (relative to the inclusive cross-section for this process) amounts to about 1%. Comparing this number to the results from HERA indicates a different survival probability for an event with a rapidity gap. At the end of run I, CDF installed a Roman Pot spectrometer to select elastically scattered anti-protons. Recently CDF observed also the diffractive production of J/ψ mesons and bottom quarks [15-45].

Measurements at the Tevatron of diffractive di-jet production and diffractive W production indicate a substantial difference in the rate compared to the prediction obtained using a factorisable model (see below) and the parton distributions as determined from the HERA data. The measured cross-sections are about a factor of 3 - 10 smaller [15-46]. One possible explanation is the (expected) breakdown of the (hard diffractive) factorisation model (which has been proven [15-47] only for the case of a single hadron beam in the initial state) in the case of hadron-hadron interactions. An interpretation of this factorisation breakdown is that spectator effects imply ad-

ditional soft interactions, which no longer lead to the diffractive final state. This would for example imply a different survival probability for the rapidity gap. A similar study for the di-jet production in double Pomeron scattering [15-48] leads to a factor of 10-100 with respect to the expectation in case of factorisation.

Indications for a perturbative behaviour in diffractive processes have been obtained from elastic photoproduction of J/ψ mesons in the reaction $\gamma p \rightarrow J/\psi p$ at HERA. The dependence on the photon-proton centre-of-mass energy $W_{\gamma p}$ due to exchange of a Regge trajectory is $d\sigma/dt = f(t)W^{2(2\alpha(t)-2)}$, where $\alpha(t)$ indicates the trajectory (*e.g.* the Pomeron trajectory as the leading one). Using HERA data to determine $\alpha(t)$, it was found [15-49] that the slope of the trajectory vanishes, *i.e.* there is no dependence on t. This behaviour not expected in the framework of the Regge model, where the diffraction peak (the sharp maximum of $d\sigma/dt$ for small $|t|$) 'shrinks' with increasing energy. Also in the measurement of single diffractive dissociation in $p\bar{p}$ collisions it was observed [15-50] that the differential cross-section as a function of x and t can best be described with a Pomeron trajectory containing a quadratic term, indicating either the onset of a perturbative Pomeron or the occurrence of multiple Pomeron exchange.

15.4.3 Models for hard diffractive scattering

Diffractive hard scattering, *i.e.* a diffractive process where in addition a hard scale is present, can be modelled under the assumption of diffractive factorisation. In this case, the cross-section for the process $pp \rightarrow pX$, where X contains a hard scattering, is given by the product of a diffractive parton distribution function, a parton distribution function for the proton and the hard scattering cross-section.

A relation to a partonic approach (similar to the quark parton model for the nucleons) has been proposed by several authors. One of the earliest ideas is due to Low [15-51] and Nussinov [15-52], who proposed as a QCD model for the Pomeron the exchange of a two gluon system in a colourless configuration. Bjorken and Kogut predicted the occurrence of hard diffractive processes in the context of the Aligned Jet Model [15-53] and the approach by Ingelman and Schlein [15-30] introduced the concept of parton densities for the Pomeron. The case of a 'superhard Pomeron' as mentioned above would imply in the partonic picture that one out of the two gluons carries almost the full momentum and the second gluon is a very soft one, which mainly neutralises the colour charge of the first one.

There are two places where factorisation might occur. Firstly, there is the so called Regge factorisation, which assumes that in a single diffractive process ($pp \rightarrow pX$) the vertex of the elastically scattered proton can be described independently of the reaction leading to the dissociative system. The proton-Pomeron vertex is described by a flux factor, depending only on the variables ξ and t. The inelastic reaction of the Pomeron with the second proton leads then to the dissociative final state X. The third ingredient is the Pomeron propagator.

Secondly, there is the hard scattering factorisation, which has been proven to be valid in the case where there is only one hadron beam involved (*e.g.* diffractive deep-inelastic scattering)[15-47]. In this case, the hard scattering cross-section is similar to a standard hard scattering cross-section with one of the two parton distribution functions replaced by a diffractive parton density. This parton density gives the distribution of a parton in a hadron under the condition that the outgoing diffracted hadron is detected and allows a separation of soft and hard processes. These diffractive parton densities avoid the concept of a Pomeron flux and the notion of Pomer-

on parton densities (as done in the Ingelman-Schlein model [15-30]), they are furthermore valid for all values of ξ. In the case of the Ingelman-Schlein model this is only true for small enough values of ξ, where Pomeron exchange is expected to dominate.

Based on a model for diffractive deep-inelastic scattering [15-54] which does not refer to the notion of a Pomeron, a model of soft colour rearrangement for hadron-hadron collisions has been proposed [15-55]. The model [15-54] for diffractive DIS assumes that after a normal hard scattering of the virtual photon on a parton of the proton, in part of the events, the exchange of a soft gluon (without changes to the momentum configuration of the partons) leads to the creation of two colour neutral systems, which then hadronise independently. In the case of hadron-hadron collision a similar mechanism could lead to the production of rapidity gaps in the case of a hard scattering process.

For the studies done on hard single diffraction (Section 15.4.5) and on hard central diffraction (Section 15.4.6), the PHOJET Monte Carlo program [15-23] has been used. The modelling of hard diffractive scattering is based on the approach of diffractive hard scattering factorisation, where the Pomeron is treated as a 'quasi-particle' and is assigned parton densities. Three possible parametrisations have been used (where in the case of the first two the Pomeron contains only gluons): a 'soft' gluon distribution ($xg(x) \propto (1-x)^5$), a 'hard' gluon distribution ($xg(x) \propto x(1-x)$) and a distribution ('CKMT parametrisation') containing both quarks and gluons in the Pomeron including the evolution according to the DGLAP equations. The hard scattering is described by leading order matrix elements, with parton showers added to approximate higher order corrections and hadronisation in the Lund String model. A comparison of the predictions of the PHOJET program to data obtained at the Tevatron can be found in [15-56].

15.4.4 Trigger and event selection

15.4.4.1 Rapidity gap signature

One of the possible ways to select diffractive scattering is to demand the presence of a rapidity gap in the final state, *i.e.* a region in phase space without particle production. The occurrence of such regions in 'normal' hard scattering events is expected to be suppressed strongly with growing size of the region in rapidity. In order to have good acceptance it is desirable to cover a large region in rapidity, going beyond the ATLAS acceptance of $|\eta| < 5$. An example for such detectors can be found in [15-57], where the TOTEM collaboration describes the integration of their inelastic detectors (covering the region $3 < |\eta| < 7$) into the environment of the CMS detector at interaction region IR5.

By tagging events only through the existence of a rapidity gap in the forward region (without observing the leading system), it cannot be completely excluded (due to the limited acceptance of the detector in the forward direction) that the unobserved leading system is, instead of a proton, a low mass proton excitation or a dissociative system of small mass. When a cross-section is measured, this contribution has to be estimated and subtracted. The acceptance for such forward going dissociative systems (as a function of their invariant mass) depends on the coverage in pseudo-rapidity in the forward direction. This acceptance can be obtained from a simulation of the detectors used for tagging and could be cross-checked (in case a leading-proton measurement is possible) using events with a measured scattered proton. The measurement of the proton momentum allows the determination of the mass of the forward-going system and with this the acceptance can be obtained from data.

15.4.4.2 Leading–proton detection

A very clean way of selecting single-diffractive events is the tagging and measurement of a leading proton, *i.e.* a quasi-elastically scattered proton with an energy close to the nominal beam energy. This can be achieved by placing position-sensitive detectors downstream of the interaction point close to the nominal beam trajectory. These detectors are usually put into so called 'Roman Pots' [15-58], in order to move them away from their nominal position during injection and tuning of the beam. The insertion of such detectors should not increase the background significantly. The detectors would also probably only be installed (or moved close to the beam) in the case of low-luminosity running. Further studies need to be performed to determine the impact of beam-halo interactions with the Roman Pots.

The momentum loss $\xi = \Delta p/p_0$ ($\xi = 1 - x_L$) of a proton can be obtained from a measurement of the displacement (transverse to the beam) away from the interaction point. The acceptance in ξ is limited by the transverse beam size σ_{beam} (this determines how close to the nominal beam position the detectors can be placed – usually up to (10–20)×σ_{beam}) and the dispersion of the machine. The resolution in ξ has a fundamental limit, which is the natural momentum spread of the beam, expected to be about 10^{-4} at the LHC. This limit can only be reached if several independent measurements are performed to determine the position and the angle of the proton at the interaction point. The use of a single measurement is limited by the width of the beam of scattered protons. A study [15-59][15-60] of the low β insertions at the LHC showed that, at a distance of about 200 m from the interaction point, a minimal ξ of $\xi_{\min} = 0.01$ can be reached (the ξ range for 80% acceptance is $0.01 < \xi < 0.09$). Going to distances larger than 300 m from the interaction point, gives a lower limit of $\xi_{min} = 2 \times 10^{-3}$ (80% acceptance for $0.002 < \xi < 0.015$). The acceptance in ξ could be increased to smaller values of ξ only for finite values of t.

A selection of leading protons by demanding $x_L > 0.9$ selects the kinematic region where Pomeron exchange is expected to dominate the diffractive process. This corresponds roughly to a demand for a rapidity gap of at least 4 units. The region of smaller x_L values is of interest for the studies of non-leading trajectories. For the studies presented in the next sections, it is assumed that Roman Pots will be able to measure scattered protons with $x_L > 0.9$ and $0.01\ \text{GeV}^2 < |t| < 1\ \text{GeV}^2$ on both sides of ATLAS. Further studies need to be performed when a more detailed design of a possible Roman Pot system is available, to determine in more detail the acceptance and the resolution to be obtained. Given the large separation of the detectors from the ATLAS interaction point (about 200 m), it is not yet clear whether it is possible to include a trigger on track segments in the Roman Pots at the first level of the ATLAS trigger system, which has a maximum latency of 2.5 μs [15-61]. Although a large fraction of this latency would be used for the protons to arrive at the detectors and for the signals to be brought back to the trigger electronics, it may be possible to provide a fast decision and to distribute this to the front-end electronics. However, a detailed feasibility study has not yet been performed.

More details on the layout of the LHC interaction regions (IR1 and IR5) can be found in [15-57]. In the proposal for the measurement of the elastic and total cross-sections by the TOTEM collaboration a detailed description of the planned Roman Pot detectors for the interaction region IR5 (CMS) is given, which can be transferred identically to the ATLAS interaction region (IR1). For the measurement of elastic scattering, a station of two Roman Pots is foreseen in front of the dipole D2, measuring the transverse displacement. For elastic scattering, the acceptance in momentum transfer strongly depends on the value β^* (being the value of the β function at the interaction region). For the high-luminosity running mode ($\beta^* = 0.5$ m, corresponding to small transverse beam sizes) the minimal $|t|$ is about 200 GeV^2. At injection, a value of $\beta^* = 18$ m is foreseen, implying an acceptance in $|t|$ between 1 GeV^2 and 10 GeV^2, whereas for $\beta^* = 1100$ m a range of $0.02\ \text{GeV}^2 < |t| < 1.4\ \text{GeV}^2$ is covered. To measure protons from single-diffractive

scattering, a spectrometer consisting of up to three stations (each consisting of two Roman Pots) is proposed. The machine optics close to the interaction point (as viewed from the interaction point) are composed of the quadrupoles Q1 – Q3 (strong focusing triplet to achieve the small beam sizes), the bending dipoles D1 and D2 (to get the orbits into collision and separated back) and the quadrupoles Q4 – Q7 (to adapt the machine optics to the arcs). A figure of the arrangement of these magnets can be found in [15-57] (Figure 6). The first two locations are situated between the dipoles D1 and D2; the first before the neutral particle absorber (TAN), the second behind the TAN. The third possible location is found between the quadrupoles Q4 and Q5. For leading protons, *e.g.* from single diffractive scattering, the acceptance in t extends to smaller values than listed above for the case of elastic scattering. A detailed study of the machine layout is needed to obtain the acceptance (as a function of ξ and t) for the different values of β^*, as described above.

15.4.4.3 Final–state requirements

Given the large cross-sections for diffractive processes, even after taking into account the small acceptance for the detection of leading protons, it is obvious that for normal running conditions additional conditions on the final state have to be applied (in order to avoid prescaling). These will be done *e.g.* by requiring the presence of jets in the final state. The cut on the jet transverse energy will be lower than in the case of inclusive jet production in 'normal' QCD events. A possible requirement would be at least one (or two) jets together with either a leading-proton tag or a rapidity gap signature from the forward detectors (as mentioned in Section 15.3.2). Whether the first possibility would be available at the first trigger level, has to be determined (see Section 15.4.4.2). If this were not the case, a refinement of the gap selection at the higher levels of the trigger system would happen, where the Roman Pot information would be available. In any case, pre-scaled triggers using the Roman Pots and / or the inelastic detectors alone should be available, as also should be the case for diffractive triggers where the jet energy threshold is further lowered.

15.4.4.4 Background sources

The following sources of background to the production of diffractive events have to be considered: pile-up, in which a diffractive event without jet production and a non-diffractive event with jet production coincide. This would fake a signal for hard diffractive scattering and would occur dominantly in low-mass diffractive events. The simultaneous occurrence of a hard diffractive event and a minimum-bias event would be a real hard diffractive scattering, but could obscure the properties of the event (*e.g.* by filling the gap). A selection on a single interaction (by requiring only a single primary vertex be reconstructed) would remove most of these overlays. Also other physics processes with similar signatures such as events due to meson exchange or double diffractive dissociation, where a leading particle of one of the dissociated systems fulfils the selection criteria, will take place.

15.4.5 Single hard diffractive dissociation

The measurement of di-jet production in single diffractive dissociation by the CDF collaboration [15-62] used a sample of same-side ($\eta_1 \cdot \eta_2 > 0$) di-jet events with a minimum transverse energy of 20 GeV for each jet. Using the information on charged particles from the tracking detectors, on calorimeter towers and hits in the scintillators of the beam-beam counters, multi-

plicity distributions on the side opposite to the jet system were studied and a clear excess of events with zero multiplicity was observed. The fraction of di-jet events that are diffractive (normalised to the non-diffractive events) was determined to be $(0.75 \pm 0.05 \pm 0.09)\,\%$ [15-62]. A further study by CDF [15-40] used a sample of events at 630 GeV and at 1800 GeV, where a leading anti-proton ($0.04 < \xi < 0.095$ and $|t| < 1\ \mathrm{GeV}^2$) has been measured. This allows tagging of colourless *t*-channel exchange in the kinematic region where Pomeron exchange should dominate. In both samples, large E_T jet pairs are observed, with a distribution of transverse energy similar (with a slightly steeper slope) to the one of jets in non-diffractive events.

The measurement of the longitudinal momentum x_L of the scattered proton gives the momentum fraction ξ of the proton momentum which is taken by the Pomeron: $\xi = 1 - x_L = P_{IP}/P_p$. Reconstruction of the two jets in the final state system with transverse energies $E_{T\ 1,2}$ and pseudorapidities $\eta_{1,2}$ determines the momentum fraction β of the parton in the Pomeron participating in the hard scattering:

$$\beta = \frac{E_{T1}e^{-\eta_1} + E_{T2}e^{-\eta_2}}{2\sqrt{\xi}P_{beam}}$$

The shape of the β distribution gives information about the partonic structure of the Pomeron.

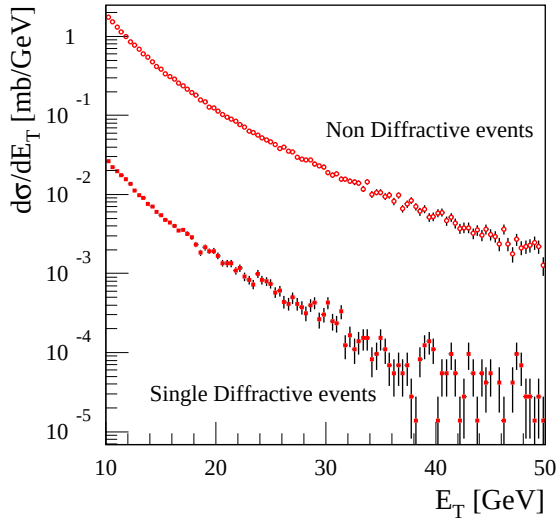

Figure 15-16 Cross-section for di-jet production ($|\eta^{jet}| < 3.2$) as a function of the jet transverse energy for non-diffractive and single diffractive events, obtained from the PHOJET Monte Carlo model.

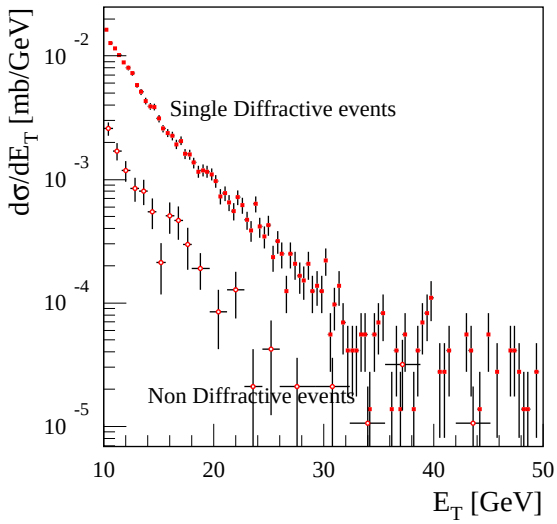

Figure 15-17 Visible cross-section for di-jet production ($|\eta^{jet}| < 3.2$) as a function of the jet transverse energy for non-diffractive and single diffractive events, when the detection of a leading proton is required (as obtained from the PHOJET Monte Carlo model).

Triggering of events with a hard diffractive interaction requires low transverse energy thresholds for the jets, due to the small invariant mass of the diffractive system. In Figure 15-16 the expected cross-sections for di-jet production with $E_T > 10\ \mathrm{GeV}$ and $|\eta| < 3.2$ are shown as a function of the minimum transverse energy (more details are to be found in [15-63]). As expected, the non-diffractive contribution has a cross-section which is almost two orders of magnitude larger than the single diffractive contribution. The rate for a di-jet trigger with low energy threshold would completely saturate the bandwidth of the trigger system. It can however be reduced by demanding the detection of a leading proton, as shown in Figure 15-17. This figure

shows the visible cross-section for the production of two jets with the same cuts as for Figure 15-16, but with the tagging of a leading proton with $x_F > 0.9$ and $0.01 < |t| < 1$ GeV^2 also being required. The non-diffractive cross-section is now smaller by about one order of magnitude than the single diffractive cross-section, although the ratio will be model dependent and needs to be verified using different models for the beam fragmentation region of the non-diffractive events.

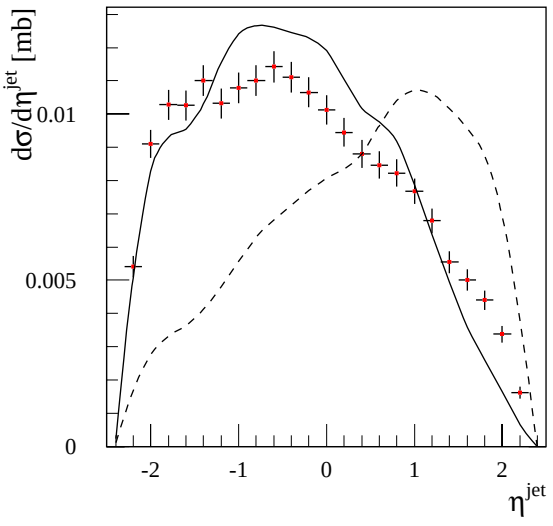

Figure 15-18 Cross-section for di-jet production ($|\eta^{jet}| < 3.2$ and $E_T > 10$ GeV) in single diffractive events with a tagged leading proton as a function of the jet pseudorapidity. Three different assumptions on the partonic structure of the Pomeron are shown: the CKMT parametrisation (points), a 'soft' gluon (solid line) and a 'hard' gluon distribution (dashed line).

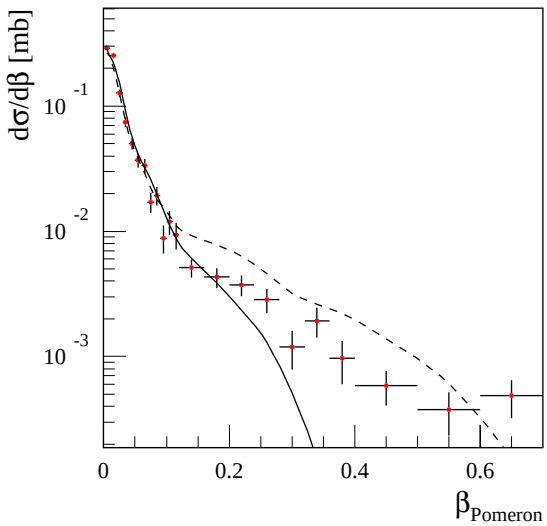

Figure 15-19 Cross-section for di-jet production ($|\eta^{jet}| < 3.2$ and $E_T > 10$ GeV) in single diffractive events with a tagged leading proton as a function of the momentum fraction variable β. Three different assumptions on the partonic structure of the Pomeron are shown: the CKMT parametrisation (points), a 'soft' gluon (solid line) and a 'hard' gluon distribution (dashed line).

In Figure 15-18 the cross-section for single diffractive events (tagged with a leading proton) with at least two jets with $E_T > 10$ GeV and $|\eta| < 3.2$ is shown as a function of the pseudorapidity of the two leading jets. Probably the actual minimum transverse momentum of the jets will be larger than 10 GeV, firstly due to constraints on the trigger rate and secondly due to the challenges in reconstructing jets with small transverse energy, where in addition the jet energy resolution is getting worse. Three different assumptions on the partonic structure of the Pomeron have been used: the CKMT parametrisation (shown as points), a soft gluon distribution (the solid line) and a hard gluon distribution (the dashed line). Between the last assumption and the first two, a very different shape is observed. Measuring the pseudorapidities of the two jets and their transverse energies allows the determination of the momentum fraction β of the partons in the hard scattering (assuming hard scattering factorisation). Figure 15-19 indicates the cross-section for single diffractive di-jet production as a function of β, for the same three assumptions on the partonic structure of the Pomeron. The differences between the assumptions are not as pronounced as in the case of the jet pseudorapidity distribution. More detailed studies are needed to assess the accessible kinematic range.

A further aspect of single diffractive dissociation is the production of a Higgs boson. The expected fraction of events with a Higgs boson being produced diffractively ranges between 10% and 25% (for $90 < m_H < 130$ GeV) [15-64] and 5% to 15% for a larger value of m_H [15-65]. The size

of the rapidity gap expected is small and no significant improvement in the signal-to-background ratio is expected, for the Higgs decays to two photons and to two Z bosons in the intermediate Higgs mass range.

15.4.6 Double Pomeron exchange

Double Pomeron exchange at the LHC is expected to give rise to final states of much larger invariant mass (up to 700 GeV) than at the Tevatron (with about 90 GeV), assuming a selection by demanding two leading protons with $x_F > 0.95$. The production of events with di-jets due to double Pomeron exchange, as suggested in [15-66], has been observed at the Tevatron [15-41]. In comparison with single diffractive hard scattering, an advantage of double Pomeron exchange is that almost no effects from underlying events or soft colour exchange are expected. The survival probability for the gaps should therefore not be influenced by these effects, as it is the case for single diffractive hard scattering. Taking into account $q\bar{q}$ production only, a cross-section of 5 nb at Tevatron energies has been calculated [15-66]. Events corresponding to double Pomeron exchange have been observed at the Tevatron, a study [15-41] by the CDF collaboration started from a sample of events with a tagged leading anti-proton ($0.05 < \xi < 0.1$ and $|t| < 1$ GeV^2), which contained at least two jets with $E_T > 7$ GeV. A study of the multiplicities of calorimeter towers and hits in the beam-beam counter scintillators on the outgoing proton side gave an excess at zero multiplicity, indicating the presence of double Pomeron exchange. The transverse energy spectra of the jets resembles those of single diffractive and non-diffractive events, but are more back-to-back in azimuth. The observed number of events is significantly smaller than expected from HERA data, assuming factorisation. Good agreement [15-41] can be obtained by reducing the prediction by a factor of 0.18^2, the square of the factor found in single diffractive di-jet production.

The study of double Pomeron exchange at LHC energies can be done in an inclusive way by demanding the presence of a leading proton in both 'Roman Pot' detectors (together with or without some activity in the central detector) or by taking a sample where at least one leading proton together with jet activity in the central part of ATLAS is required. The latter selection resembles the single hard diffractive selection, a lower jet E_T cut could be used by demanding in addition a rapidity gap opposite the leading proton.

Figure 15-20 shows the cross-section for central diffraction, resulting from Pomeron-Pomeron interactions, as a function of the invariant mass distribution of the final state. The solid line shows the cross-section without cuts on the outgoing protons, the dashed line has been obtained assuming that both protons are tagged with momenta corresponding to the values of $x_F > 0.9$ and $0.01 < |t| < 1$ GeV^2. As mentioned earlier, large invariant masses of the diffractive final state can be reached. This obviously implies the availability of the phase space for hard processes leading to the production of jets or electroweak bosons, which then can be used to probe the partonic structure. Requiring, in addition, the production of at least two jets with $E_T > 10$ GeV and $|\eta| < 3.2$ (indicated by the points in Figure 15-20), reduces the cross-section significantly and restricts the accessible invariant mass range to masses above 100 GeV.

Figure 15-21 shows for the selection of central diffractive events using two tagged protons and at least two jets, the cross-section as a function of the jet pseudorapidity for three different assumptions on the partonic structure of the Pomeron. The points corresponds to CKMT parametrisation, the solid line is a parametrisation using gluons only with a soft momentum distribution, *i.e.* most gluons have a small momentum fraction. These two assumptions give a

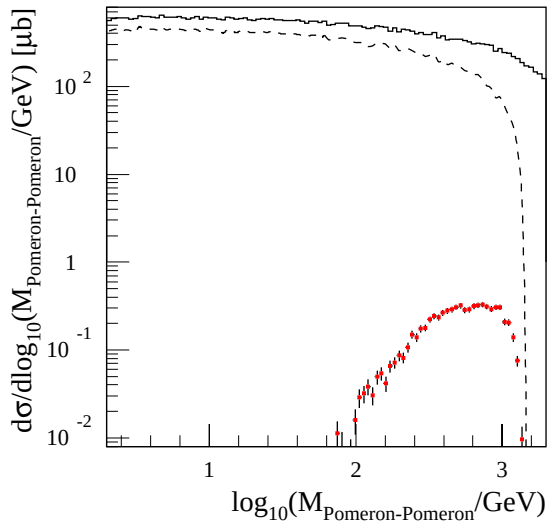

Figure 15-20 Cross-section for central diffraction as a function of the invariant mass of the diffractive system (the Pomeron-Pomeron invariant mass) for three assumptions: without final state requirements (solid line), requiring the detection of two leading protons (dashed line) and requiring in addition at least two jets with $|\eta| < 3.2$ and $E_T > 10$ GeV (points).

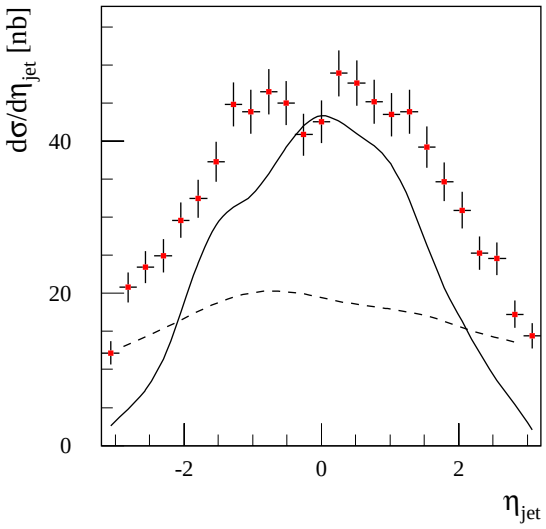

Figure 15-21 Cross-section for central diffraction (with both protons being tagged and at least two jets with $|\eta_{jet}| < 3.2$ and $E_T > 10$ GeV being found) as a function of the pseudorapidity of the jets. Three different assumptions on the partonic structure of the Pomeron are shown: the CKMT parametrisation (points), a 'soft' gluon (solid line) and a 'hard' gluon distribution (dashed line).

similar shape and differ mainly in the visible cross-section. The third assumption, shown as the dotted line, contains a hard distribution of gluons and exhibits a much flatter dependence of the cross-section on pseudorapidity.

Besides providing additional tests of the flux renormalisation (checks of factorisation breaking) the study of jet production in double Pomeron exchange allows studies of the partonic structure in a similar way to the ones done in non-diffractive proton-proton collisions. Selecting leading protons on both sides with $x_F > 0.9$ corresponds to having effectively a Pomeron-Pomeron collider with a maximal centre-of-mass energy of 1400 GeV. Calculations for the cross-section of double Pomeron events with di-jet production [15-67] indicate a cross-section between 0.05 and 0.3 nb for the kinematic range $0.002 < \xi_{1,2} < 0.03$, $|y_{jet\ 1,2}| < 1$ and $E_{T\ jet\ 1,2} > 20$ GeV.

The production of Higgs bosons via vector boson fusion can also lead to final states containing two scattered protons together with jets at large rapidities (in case of W and Z) and the Higgs decay products in the central gap region. As discussed in [15-68], the rapidity gap signature could be useful in improving the signal-to-background ratio. In double Pomeron scattering there is also the possibility to produce a Higgs boson in this reaction [15-69], leading to a final state with two quasi-elastically scattered protons and the decay products of the Higgs boson, separated by two gaps in rapidity from the protons, in contrast to the case of $WW \rightarrow H$ and $ZZ \rightarrow H$, where the protons are expected to scatter mainly incoherently.

About 1% of all events are predicted to be due to double Pomeron scattering [15-70]. Estimates of the cross-section for the process $pp \rightarrow ppH$, where the Higgs is produced and both protons are scattered quasi-elastically, give values of 0.3 to 0.02 pb for Higgs masses between 100 GeV and 1 TeV. The calculation is based on lowest order QCD diagrams, higher order corrections are expected to increase the cross-section. Backgrounds are due to the production of heavy-quark

pairs via the same mechanism, and should mainly contribute for small Higgs masses. Another issue is the survival probability of the rapidity gap. Allowing for proton dissociation, and demanding a rapidity of at least 6 units within which the Higgs is produced, increases the cross-section by up to a factor of 10 [15-71].

The mass resolution (using the missing mass technique) expected when both protons are detected is dominated by the beam divergencies at the interaction point [15-72]. In the case of the Tevatron, the expected mass resolution is about 300 MeV (for $\xi = 0.05$ and $|t| < 1\ \mathrm{GeV}^2$). The advantage of this method would be to avoid the small branching ratio for the decay of a Higgs to two photons by using the decay mode to $b\bar{b}$, while possibly allowing for small transverse momentum thresholds for the $b\bar{b}$ reconstruction. A trigger could be built from a coincidence between tags for leading proton in the Roman Pot spectrometers on both sides of the ATLAS detector, this selection could be refined by final state requirements using the central detector.

15.4.7 Colour-singlet exchange

Jet production in hadron-hadron collisions mainly proceeds by the exchange of a quark or a gluon between two partons, leading to a flow of colour between the two partons that give rise to the observed jets. Between the two jets therefore the production of particles is expected. If the exchange is a Pomeron or an electroweak gauge boson (W, Z or γ^*), a rapidity gap between the two jets is expected.

At Tevatron energies, the ratio of di-jet events with a gap to all di-jet events is expected to be of order 1% and probes the nature of the colourless exchange by studying the properties of the produced di-jet system. Different models for the colourless exchange predict different dependencies of the ratio on the size of the central gap and on the E_T of the jets. In case of electroweak exchange, the fraction is expected to be about 10^{-4}.

The production of events with a central rapidity gap (defined by measuring the multiplicity of calorimeter towers and charged particle tracks) between two jets has been observed at the Tevatron both by CDF [15-43][15-44] and D0 [15-42]. The measurement by D0 requires two jets of at least 30 GeV transverse energy. The colour singlet fraction determined from the data is $(0.94 \pm 0.04 \pm 0.12)\,\%$ [15-42]. This fraction is found to increase with increasing values either of the minimum E_T for the jets or the separation $\Delta\eta$ in rapidity of the two jets. This dependence can be used to discriminate between different models for the colour singlet exchange. The present D0 data disfavour a model based on two-gluon exchange, and favour a model using soft colour rearrangement. In contrast to the D0 data, the CDF collaboration does not find a significant dependence of the colour singlet fraction on E_T or $\Delta\eta$. The measurement [15-43] requires two opposite side jets with $E_T > 20$ GeV and $1.8 < |\eta_{jet}| < 3.5$. The colour singlet fraction amounts to $(1.13 \pm 0.12 \pm 0.11)\,\%$. A trigger for ATLAS could be based on the energy deposition in the forward calorimeters, which cover the range $3 < |\eta| < 5$. More details on such a trigger are given in Section 15.5.4.3, in the context of the study of BFKL signatures in di-jet production at large angular separation. The final event selection for studies of colour singlet exchange would - in contrast to the BFKL selection - require a gap in the central rapidity region.

15.4.8 Diffractive *W* and *Z* production

As in the case of inclusive *W* (and *Z*) production (see Section 15.7.3) for inelastic proton-proton scattering, the diffractive production of *W* (and *Z*) bosons constrains parton densities in single diffractive dissociation, as discussed in [15-73]. At the LHC it is not possible to make use of the correlation between the *W* charge (*i.e.* the charge of the decay lepton) and the out-going proton (anti-proton), as it was done in the measurement by CDF [15-74]. In this measurement, CDF observed that a fraction of $R_W = 1.15 \pm 0.55\,\%$ of all events with a *W* boson are of diffractive nature (under the assumption of a hard partonic structure of the Pomeron with quarks and gluons).

The production of diffractive di-jets is expected to be dominated by gluons, whereas the diffractive *W* production is dominated by quarks. The relative contribution of quarks and gluons can thus be constrained by a combination of both measurements. Results from the TEVATRON obtained by CDF [15-62] indicate a gluon fraction $f_g = 0.7 \pm 0.2$. This is compatible with the results obtained at HERA ($0.3 < f_g < 0.8$ obtained by the ZEUS collaboration, combining a measurement of the diffractive structure function F_2^D and of diffractive di-jet photoproduction [15-75]). The fraction of the momentum of the Pomeron carried by partons was determined to be $D = 0.18 \pm 0.04$, which reflects the fact that the observed cross-section is smaller than the one expected from the HERA data, assuming hard scattering factorisation. This indicates a breakdown of factorisation.

At ATLAS, the experimental selection of diffractive *W* and *Z* boson production could be based on the inclusive lepton triggers for inclusive vector boson production, as described in Section 15.7.3 and Section 15.7.4. The analysis of these events would then require a rapidity gap signature. Smaller transverse momenta could be accessed with prescaled triggers or by including in the trigger requirements for the selection of a leading proton or a rapidity gap in the forward direction, if the information from these dedicated detectors became available.

15.4.9 Diffractive heavy flavour production

Another tool to get information on the parton content in diffractive processes is the study of heavy flavour production [15-76]. A calculation of the cross-section for single ($pp \rightarrow p + Q\overline{Q} + X$) and double diffractive ($pp \rightarrow p + Q\overline{Q} + X + p$) heavy quark production [15-77] at an centre-of-mass energy of 10 TeV lead to the following predictions, which should increase slightly for LHC energies:

- charm production: $\sigma_{\text{single diffractive}} = 2 - 4\ \mu\text{b}$ (20 - 40%),
  $\sigma_{\text{double diffractive}} = 40 - 65\ \text{nb}$ (0.4 - 0.7%)
- bottom production: $\sigma_{\text{single diffractive}} = 0.5 - 1\mu\text{b}$ (15 - 40%),
  $\sigma_{\text{double diffractive}} = 6 - 15\ \text{nb}$ (0.2 - 0.5%)
- top production: $\sigma_{\text{single diffractive}} = 1 - 5\ \text{pb}$ (0.3 - 2%),
  $\sigma_{\text{double diffractive}} < 10\ \text{fb}$ ($< 6 \times 10^{-3}$)

where the numbers in brackets denote the fraction of the diffractive process with respect to the total cross-section. In the calculation, three models for the Pomeron parton distributions have been used, which differ in the parton content at the starting scale of the parametrisation (using quarks only, quarks and gluon and mainly hard gluons).

The detection of diffractive charm production could use the signature of a semi-leptonic decays or the reconstruction of charmed mesons (like D^{*+-}). Especially for the latter case, feasibility studies have to be performed. In the case of *b* quark production inclusive signatures (muon production) or the tagging of *b*-jets could be studied. At the Tevatron, the CDF collaboration has observed the diffractive production of *b* quarks as well as the diffractive production of J/ψ mesons [15-45].

A detailed study of the diffractive production of *b* quarks at the LHC and their properties has been performed in [15-60]. The cross-section for diffractive masses M_{diff} between 1.4 and 4.4 TeV amounts to 7.1 μb, the one for $0.44 < M_{diff} < 1.4$ TeV to 3.3 μb and for $140 < M_{diff} < 440$ GeV to 1.2 μb. The fraction of events with *b* quark production to the total diffractive cross-section varies between 3×10^{-4} (M_{diff} = 140 GeV) and 6×10^{-3} (M_{diff} = 4.4 TeV). The average pseudorapidity of beauty particles depends on the diffractive mass, but shows also sensitivity to parton distributions of the Pomeron. For a hard (soft) gluon distribution in the Pomeron, the average pseudorapidity of the beauty particles changes from -4 (-5) at M_{diff} = 140 GeV to 3.5 (0.5) at M_{diff} = 4.4 TeV when the leading proton is at positive pseudo-rapidity. For the acceptance of the Inner Detector of $|\eta| < 2.5$ a value of the diffractive mass between 700 and 4 TeV is expected. The ratio of the diffractive charm production to the diffractive beauty production ranges from a factor of about 15 at M_{diff} = 140 GeV to about 50 at M_{diff} = 4.4 TeV.

As in the case of diffractive vector boson production, a sample of diffractive heavy flavour production could be obtained from the triggers for *b* production (as mentioned in Section 15.8.3). For the case of diffractive charm production, the first level trigger would have to start with a rapidity gap signature or a leading proton candidate. Next the higher trigger levels could try to reconstruct final state signatures indicating the presence of open charm.

15.4.10 Summary on hard diffractive scattering

The increase of centre-of-mass energy from the Tevatron to the LHC could allow for more precise studies of hard diffractive scattering, and further understanding of the transition between perturbative and non-perturbative QCD. The advantage of the LHC is in the production of diffractive final states with larger masses, allowing the probing of partonic structure with a variety of different processes. A selection of events with two leading protons (or rapidity gaps on both sides of the detector) transforms the proton-proton collider into a Pomeron-Pomeron collider (with variable beam energy), where the maximal centre-of-mass energy ranges between the one of the S$p\bar{p}$S and the Tevatron collider.

Many open questions need to be addressed in further studies. This especially concerns the experimental selection of diffractive events, either using a leading proton signature or the presence of a rapidity gap. In the first case, the kinematic reach for the low β^* configuration of the interaction region needs to be determined, assuming the positions of the Roman Pot detectors as described in [15-57]. The reconstruction of the hard scattering in the central detector has to be studied for lower thresholds on transverse energy and momenta than in the case of proton-proton collisions, to take into account the effectively smaller centre-of-mass energy.

15.5 Jet physics

15.5.1 Overview

At hadron colliders, the most prominent signature for a hard scattering process to take place is the production of particles with a large total transverse momentum, *i.e.* the jets. The measurement of jets allows to draw conclusions about the hard scattering process. To do so one has to take into account the evolution of the partonic system from the hard scattering to the observed set of hadrons. This evolution includes parton showering (the creation of additional partons, typically with decreasing transverse momenta), the fragmentation (of coloured partons to the colourless hadrons), short lived particle decays and the effects of the underlying event as well as the ones of multiple interactions in a single bunch crossing.

In this section, several observables for jet production will be discussed: inclusive jet cross-section (Section 15.5.2), inclusive di-jet production (Section 15.5.4) and multi-jet production (Section 15.5.5). Further topics include aspects of jet fragmentation (Section 15.5.3) and the measurement of multiple parton scattering (Section 15.5.6).

15.5.2 Inclusive jet cross-section

15.5.2.1 Results from the Tevatron

The recent measurement of the inclusive jet cross-section by the CDF collaboration [15-78] up to transverse energies of 450 GeV showed an excess over the theoretical expectation from a NLO calculation at large transverse energies (> 250 GeV). This excess could be interpreted as a sign of new physics. However it could also be due to a lack of understanding of the underlying QCD process (*e.g.* the parton distributions in the proton). The CTEQ4 and CTEQ5 pdf fits have included the inclusive jet data both from CDF and D0 [15-79]. The high E_{T} jet data have little statistical weight, however, and the CDF excess remains when comparing to predictions using these pdf's. In the CTEQ4HJ fit, the high E_{T} jet data from CDF were given an enhanced weight. Using this distribution, the discrepancy between theory and data is reduced, but still present. The increase in the predicted cross-section comes about because of an increase in the gluon distribution at high x (a factor of two at $x = 0.5$). A similar measurement by the D0 collaboration [15-79] showed good agreement of the NLO calculation with the D0 data up to transverse energies of 450 GeV. The best agreement with the D0 data, however, is obtained with the CTEQ4HJ (and CTEQ5HJ) pdf's. A comparison of the data from the two experiments yields a 42% probability [15-80] that they are compatible, when taking into account the systematic errors and their correlations.

A further test of QCD can be performed by comparing the inclusive jet cross-sections for different centre-of-mass energies. This is best done by determining the ratio of the cross-sections from the data at 630 GeV and at 1800 GeV, and studying the ratio as a function of x_T, where x_T is the scaled transverse momentum of the jet: $x_T = 2p_T/\sqrt{s}$. The ratio is less sensitive to experimental and theoretical uncertainties, its value is determined by the evolution of parton densities, the amount of gluon emission and the running of the strong coupling constant. For values of $x_T > 0.1$, the CDF and D0 measurements agree; at lower x_T, some differences are present [15-80]. The theoretical expectation (based on NLO QCD) for the ratio is larger than the measured one, with a significance of about 3σ.

15.5.2.2 Experimental selection

The selection of inclusive jet production will be based on an inclusive jet trigger (at LVL1, for more details see Section 11.3.2) with a threshold of 180 GeV at low luminosity (290 GeV at high luminosity), where the jets have to be within $|\eta| < 3.2$. To cover a wider range in jet transverse energy (towards lower values), prescaled triggers will be used. At the higher levels of the ATLAS trigger and in the analysis, different jet algorithms can be applied. In the following a 'simple' cone algorithm [15-81] is assumed. Future studies have to show the advantages of using a recombination algorithm, like *e.g.* the k_T algorithm [15-82].

The details of the jet algorithm used in an individual analysis may depend on whether the jets are used for precision QCD comparisons and measurements or for jet spectroscopy. In leading-order predictions, each theoretical jet consists of a single parton. To completely reconstruct final states (for $t\bar{t} \rightarrow$ jets) one wants to correct the experimental jet 4-vector back to the parton value. At NLO, a jet can consist of two partons and for the first time structure can be explored. One does not want to correct for the energy 'out-of-cone' since this is at least partially described by the NLO calculation. The NLO calculation for three jet production has been recently completed. In this calculation [15-83], there are up to three partons in a jet, presumably allowing for a more detailed probe of the jet structure. It includes the one loop corrections to the $2 \rightarrow 3$ diagrams and the real emission in the $2 \rightarrow 4$ process. A NNLO calculation for the inclusive jet cross-section is still some time in the future since it involves the very difficult calculation of two-loop corrections. At NLO and beyond, the details of the jet algorithm become important, in particular if the calculations are to remain infrared safe.

15.5.2.3 Experimental uncertainties

One important aspect in all jet studies is the relation between the jet transverse energy measured in the detector and the 'true' transverse energy of the parton in the hard scattering process. The measured energy can differ from the 'true' one due to the following experimental effects (more details *e.g.* on the jet energy scale determination can be found in Section 12.5.1), not including theoretical uncertainties:

- the calorimeter response: deviation from uniform response over the acceptance (due to dead material, gaps and intercalibration errors), non-linearities in the response to low and high p_{T} particles, the knowledge of the e/π ratio and the p_{T} dependence of the jet particle content;
- the effect of the magnetic field in providing a p_{T} cut-off for particles to reach the calorimeter;
- the effect of the underlying event (in the same interaction as the hard scattering) and / or the contribution of other interactions in the same bunch-crossing;
- the production of neutrinos and muons inside a jet, which lead to a smaller energy deposition in the calorimeter;
- the finite size of the jet reconstruction volume, leading to a loss of energy not being attributed to the jet or to fluctuations of particles from other jets into the volume. This is only a problem if it is not modelled correctly by the NLO calculation.

All these effects lead to a smearing and shift of the jet energy. The correction for these effects has to be determined and be applied. The correction leads to the following sources of systematic uncertainties, which need to be quantified:

- knowledge of the jet energy scale of the calorimeters;
- knowledge of the energy resolution for jets;
- knowledge of the linearity of the calorimeter response (low and high p_T);
- understanding of the calorimeter response to hadrons, electrons and photons;
- knowledge of the jet trigger efficiency;
- knowledge of the luminosity for the overall normalisation.

The expected statistics at large jet E_T values implies a desirable control of the systematic uncertainties to a precision of less than 1% for energies below 1 TeV and to about 10% for transverse energies of about 3 TeV. The strategy for the determination of the jet energy scale is discussed in Section 12.5.1.

15.5.2.4 Theoretical uncertainties

The inclusive jet cross-section is calculated at next-to-leading order [15-84], this includes the one loop corrections to the tree level diagram of the $2 \rightarrow 2$ process and the real emission diagram in the $2 \rightarrow 3$ process. Due to the possible appearance of more than two partons in the final state, a jet algorithm has to be applied in the case of a NLO calculation. Comparison of a simple cone algorithm for the NLO partons with the experimental jet definition showed that the latter fails to merge sub-jets which are rather far separated. To cure this problem, an additional parameter was introduced in the jet definition at parton level: R_{sep}. Two partons are not joined in a single jet if their distance in η–ϕ space is larger than $R_{sep} \times R$, where R is the radius used for the cone definition. A value of R_{sep} of 1.3 approximately mimics the CDF and D0 experimental jet analyses. The knowledge of the theoretical prediction of the inclusive jet cross-section at NLO depends on the following uncertainties:

- renormalisation and factorisation scale dependence, where usually both scales are taken to be identical and only the common variation is investigated;
- jet definition for the NLO calculation (*e.g.* the R_{sep} parameter);
- knowledge of the parton distribution functions;
- the value of the strong coupling constant;
- uncertainties in the parton shower modelling;
- the impact of non-perturbative hadronisation effects, which are expected to be power suppressed ($1/Q$);
- modelling of the underlying event and modelling of minimum-bias events (pile-up due to multiple interactions per bunch-crossing).

The largest theoretical uncertainty in the prediction for the Tevatron jet cross-section comes at high E_T and is due to the uncertainty in the gluon distribution at high x. The next important uncertainty is due to the renormalisation scale dependence (as discussed in [15-85]), which does not show a strong E_T dependence.

15.5.2.5 Expected cross-section

The following results have been obtained using the ATLFAST simulation (see Section 2.5) of the ATLAS detector response and a leading order QCD calculation (PYTHIA [15-14]) of jet production, based on the CTEQ2L parton distribution [15-15]. Four samples with increasing cuts on the minimum transverse momentum of the hard scattering matrix element ($\hat{p}_T > 180$, 500, 1000 and 1380 GeV) have been generated, including the effects of initial and final state interactions, and of multiple parton scattering. This procedure has been chosen to produce a reasonable number of simulated events for large transverse momenta. However, threshold effects which lead to a distortion of the spectrum could not be avoided completely. The pile-up contribution to the energy resolution due to minimum-bias events was taken into account. The detector response has been unfolded from the result of the simulation to a cross-section at the hadron level. In addition, a pseudo *K*-factor (obtained from the JETRAD NLO result [15-84] and the PYTHIA LO result) was included to the unfolded cross-section, where details are described in [15-86]. Jets were defined using a cone algorithm with a cone size of R = 0.8. This value of 0.8 was obtained as a result of an optimisation procedure to achieve a compromise between out-of-cone losses and contamination from sources not related to the jet, *e.g.* from the underlying event, other jets or initial state radiation. More details on this optimisation can be found in [15-86].

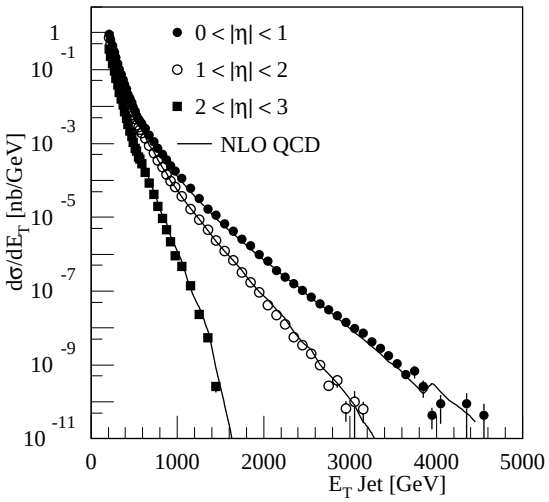

Figure 15-22 Inclusive jet cross-section (at hadron level) for different ranges of the jet pseudorapidity obtained from a PYTHIA calculation (points) and from a NLO Monte Carlo calculation (solid line).

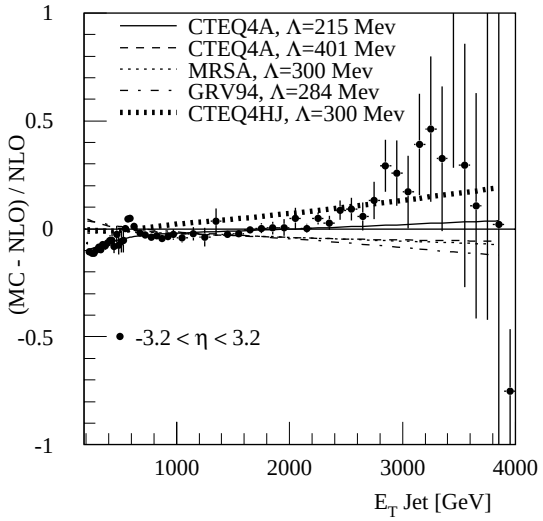

Figure 15-23 The ratio of the inclusive jet cross-section from PYTHIA (including a pseudo *K*-factor) to the one at NLO from the JETRAD calculation (including a hadronisation correction) is shown as points. Also shown is the relative difference to the NLO calculation for a variation of Λ_{QCD} and for different pdf's (the various curves).

In Figure 15-22 the inclusive jet cross-section is shown as a function of the transverse energy of the jet for three different bins in η: $0 < |\eta| < 1$, $1 < |\eta| < 2$ and $2 < |\eta| < 3$. The statistical error of the simulated events corresponds (for high E_T values) to the one expected for an integrated luminosity of 300 fb^{-1}. At small E_T values the statistical error is negligible. The expected statistics for an integrated luminosity of 30 fb^{-1} amounts to 4×10^5 events with $E_T^{jet} > 1$ TeV, 3000 events for $E_T^{jet} > 2$ TeV and about 40 events with $E_T^{jet} > 3$ TeV. Also shown in the figure is the

prediction of a NLO calculation (JETRAD) [15-84], using the CTEQ4M parton distribution set. This calculation of inclusive jet production at the parton level has been corrected for hadronisation effects, details are discussed in [15-86].

In Figure 15-23 the normalised difference of the simulated data to the NLO calculation is shown, as obtained from the CTEQ4M distribution and setting Λ_{QCD} (for five flavours) to a value of 300 MeV. This figure shows clearly the threshold effects that appear for transverse energies close to the matrix element cut-off $\hat{p}_T$. Further sources which could lead to a distortion of the spectrum are the parametrisation of the pseudo *K*-factor used to correct the PYTHIA cross-section and the hadronisation correction applied to the JETRAD calculation. The other curves indicate the relative difference between this reference NLO calculation and NLO calculations using different values for Λ_{QCD} (215 and 401 MeV) as well as using two other parton distribution functions (MRSA [15-87] and GRV94 [15-88]). The largest effect is observed when the CTEQ4HJ parton distribution is used. Based on the expected statistical accuracy in the region between 1 TeV and 2 TeV of transverse energy, the data should allow distinguishing between current distributions, like CTEQ4HJ and CTEQ4M. More studies are needed, however, to assess the expected systematic uncertainties.

15.5.2.6 Determination of α_s

An investigation has been carried out [15-89] as to whether it is possible to determine α_s and parton distribution functions from the collider data alone, without input from other experiments. As processes initiated by gluons play an important role and a strong correlation between α_s and the gluon distribution is expected, this probably excludes an independent determination of either quantity.

An extraction of the strong coupling constant α_s will not be able to compete with the precision measurements available from e^+e^- annihilation and deep-inelastic scattering. However the scale dependence of α_s could be determined in a single experiment (even a single process) over a large range in scale, including the highest achievable values of several TeV. This verification of the running of α_s implies a check of QCD at the smallest distance scales. As the running 'slows down' at large scales, this task is made more difficult. For a value of $\alpha_s = 0.118$ at 100 GeV the corresponding value at 4 TeV is about 0.075. A further possibility for an α_s determination is the production of multi-jets, as mentioned in Section 15.5.5. In the following, a possible procedure for a determination of α_s based on the inclusive or the triple differential jet cross-section is described. More studies are needed to arrive at quantitative conclusions about the potential accuracy.

The determination of α_s is based on the assumption, that the data can be described by perturbation theory with only small corrections for non-perturbative effects. The differential cross-section for inclusive jet production at next-to-leading order is the sum of two terms:

$$\frac{d\sigma}{dE_T} \sim \alpha_s^{\,2}(\mu_R)A(E_T) + \alpha_s^{\,3}(\mu_R)B(E_T)$$

where the functions *A* and *B* are calculated using parton distribution functions [15-89]. Fitting this expression to the measured inclusive cross-section gives for each E_T bin a value of $\alpha_s(E_T)$, which should show the running of the coupling constant. These values can then be evolved to the value of the coupling constant at the M_Z scale. The calculation of the functions *A* and *B* actually involves an assumption on the strong coupling constant, as global fits of parton densities are made for a certain value of α_s. To overcome this coupling between parton densities (espe-

cially the gluon density) and the strong coupling constant, a multi-step approach has been proposed in [15-89]. Firstly, parton distribution functions and the associated α_s value should be used to compare theory with data and to put constraints on the parton densities. In the next step, a particular set of parton distribution functions should be assumed as being correct and the strong coupling constant be extracted simultaneously for scales between several tens of GeV and several TeV (at the LHC). The third step would be a simultaneous determination of the strong coupling constant and the parton distribution functions from the triple differential di-jet cross-section. This step could be divided into two smaller levels: firstly, the quark distributions would be assumed as correct from the deep-inelastic scattering data and the gluon distribution would be determined. Secondly, information from other processes (like W/Z + jet production) would be included to also determine the quark distributions from the hadron collider data alone.

15.5.3 Jet shape and fragmentation

The definition of jets depends on their internal structure. Thus, it is important to provide direct measurements of it. The measurements will include the study of the jet shape, defined as the fraction of energy inside a cone of radius r ($r < R$) with respect to the cone of size R defining the jet. Existing measurements show broader jets at the Tevatron [15-90] than predicted by the HERWIG model. A comparison of the jet shape as a function of the jet transverse energy and the pseudorapidity of the jet with a next-to-leading order calculation [15-91] finds good agreement between the data and the calculation, provided that in the calculation the R_{sep} parameter determining the merging of partons is varied with the transverse energy and the pseudorapidity of the jets to take into account effects of jet broadening. Such a flexibility allows for few definite predictions. Furthermore similarities between the jet shapes in low Q^2 electron proton interactions and $p\bar{p}$ collisions were found. Jets do get narrower with increasing E_{T} and for a fixed value of E_{T}, jets are narrower in the forward region with respect to the central region.

When a k_T algorithm [15-82] is used to define a jet, sub-jets can be defined and their multiplicity being studied as a function of a resolution parameter as discussed in [15-92]. Recently, the NLO 3-jet calculation has been completed [15-83], which involves the 1-loop correction to the 3-jet cross-section. With up to four partons in the final state (and up to three in an individual jet), a more quantitative comparison with the experimentally measured shape of a jet is possible.

The measurement of charged particles in the Inner Detector will allow measurement of fragmentation functions. Since differences in the fragmentation function are expected for gluon and quark jets, the tagging of quark and gluon jets could provide additional information. Studies have to be performed to indicate the range in E_{T} where an efficient tagging is possible. From the fragmentation functions obtained, the information on scaling violations might lead to a determination of the strong coupling constant. An important application of a measurement of the fragmentation functions to charged particles for jets is the determination of the jet energy scale. The CDF collaboration uses this measurement to model the response of the calorimeter to jets in their determination of the energy scale [15-93]. An example for the measurement of charged particles inside jets is described in Section 3.5.2, using jets from the decay of a Higgs boson to $q\bar{q}$ and searching for tracks with $p_{\mathrm{T}} > 1$ GeV. Track reconstruction efficiencies of about 90% are obtained, together with a small probability of less than 0.4% for fake tracks.

15.5.4 Di-jet production

15.5.4.1 Triple differential cross-section

The measurement of the di-jet differential cross-section [15-94] for different values of the minimal E_T for both jets and of the two jet pseudorapidities $\eta_{1,2}$ allows selection of various kinematic regions in Q^2 and the parton momenta. At leading order, the parton momenta $x_{1,2}$ are then given by:

$$x_{1,2} = \frac{E_T}{\sqrt{s}}(e^{\pm\eta_1} + e^{\pm\eta_2})$$

Here the transverse energy of the leading jet is E_T and the pseudorapidities of the jets are given by $\eta_{1,2}$.

This relation expands to

$$x_{1,2} = \frac{1}{\sqrt{s}}\sum_{jets} E_{Tjet}e^{\pm\eta_{jet}}$$

for the case of NLO when more than two partons are produced. Their energies are assumed to be ordered in decreasing E_T. Theoretically it might be preferable [15-95] to measure the cross-section for di-jet production as function of the following three variables, $\eta^* = 0.5 \times |\eta_1 - \eta_2|$, and the two momentum fractions $X_{A,B} = \sum(E_{Ti}/\sqrt{s})e^{\pm\eta_i}$, depending on the transverse energies and pseudorapidities of the jets. The cross-section as a function of the leading jet transverse energy and the two pseudorapidities is not well behaved for large E_T, as there are large NLO corrections and consequent large uncertainties. In this region of phase space, the NLO cross-section is effectively a leading order cross-section, as the region is kinematically inaccessible at leading order.

Figure 15-24 shows examples of the differential cross-section for different jet rapidities, as obtained from a PYTHIA simulation (and compared to the results of the NLO calculation of JETRAD) using a similar approach as discussed in Section 15.5.2.5. Jets are pre-selected within the pseudorapidity range of $|\eta| < 3.2$ and the minimal transverse energy is 180 GeV.

In Figure 15-25 the expected range in x and Q^2 is shown, where for a given event the parton momentum fractions $x_{1,2}$ are calculated according to the formula mentioned above. The value shown has been chosen randomly between the two values available for the event, and the value of Q^2 has been calculated according to the expression

$$Q^2 \sim -\hat{t} = 2E_T^2\cosh\eta^{*2}(1 - \tanh\eta^*)$$

The size of the boxes is proportional to the number of events with these values. For a transverse energy threshold of 180 GeV, most of the events have Q^2 values of about 10^5 GeV^2 and values of $0.1 < x < 0.01$. Clearly visible is the kinematic boundary due to the centre-of-mass energy, which for a given momentum fraction leads to an upper limit on Q^2, where the latter increases with increasing x.

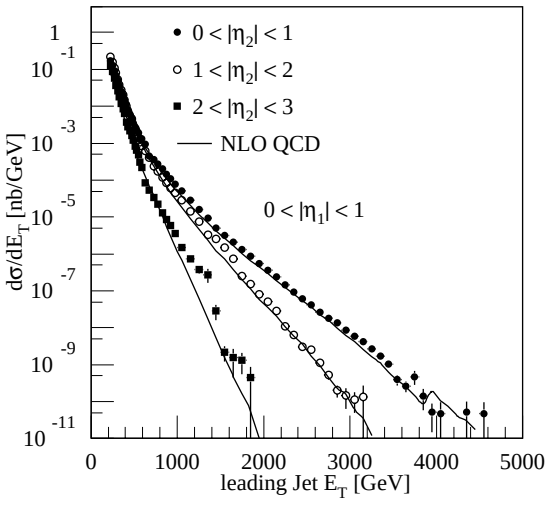

Figure 15-24 Di-jet cross-section (at hadron level with a leading jet $|\eta_1| < 1$) for different ranges of the pseudorapidity of the second leading jet obtained from a PYTHIA calculation (points) and from a NLO Monte Carlo calculation (solid line).

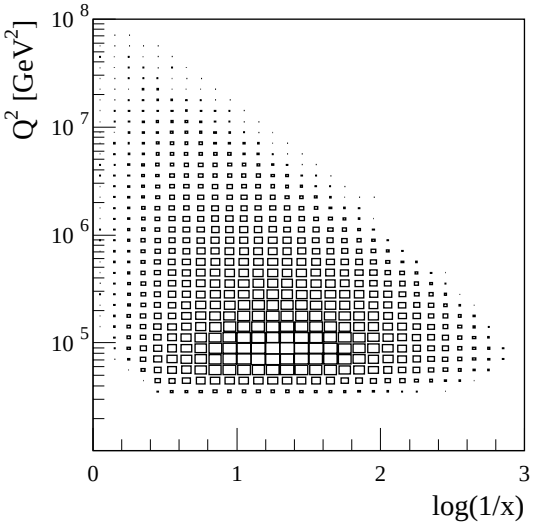

Figure 15-25 Range in *1/x* and Q^2 for the di-jet differential cross-section measurement. Only those bins are shown which contain more than 100 events for an integrated luminosity of 300 fb^{-1}.

At the Tevatron, the CDF collaboration chose to study the ratio of cross-sections where the leading jet is required to be central and the second jet is restricted to four slices in pseudo-rapidity [15-96] based on an integrated luminosity of less than 10 pb^{-1}. A cross-section based on the full statistics from Run I is to be published soon. Leaving the leading jet pseudorapidity fixed, the D0 collaboration studied the signed pseudorapidity distribution of the second jet [15-97]. Ultimately it should be possible to derive from the triple differential cross-section both the strong coupling constant and parton distribution functions. A summary of the recent measurements by the CDF and D0 collaborations of the triple differential cross-section can be found in [15-98].

15.5.4.2 Di-jet invariant mass and angular distribution

As in the case of the inclusive jet cross-section, the di-jet invariant mass and angular distributions are used to search for new physics. The expected sensitivity to new physics is discussed in Chapter 21. The invariant mass of the di-jet system is calculated from the two leading jets found using a cone algorithm with a radius of 0.8, treating the jets as massless objects.

Figure 15-26 shows the cross-section for di-jet production (restricted to jet pseudorapidities of $|\eta| < 1$) as a function of the invariant mass of the di-jet system, as obtained from the PYTHIA calculation (using the CTEQ2L pdf), including the simulation of detector effects. As discussed before, the cross-section obtained after the detector simulation (using ATLFAST) has been corrected to the hadron level. The error bars indicate (for large masses) the achievable statistical accuracy for 300 fb^{-1}. Also shown for comparison is the result of a NLO calculation based on JETRAD [15-84], using the CTEQ4M parton distribution. The partonic cross-section has been corrected for hadronisation effects. In Figure 15-27 the ratio of the di-jet invariant mass cross-section from PYTHIA (corrected with a pseudo *K*-factor) to the one from this NLO calculation (including a hadronisation correction) is shown, together with the ratio of NLO calculations using different parton distribution functions and different values of the strong coupling constant

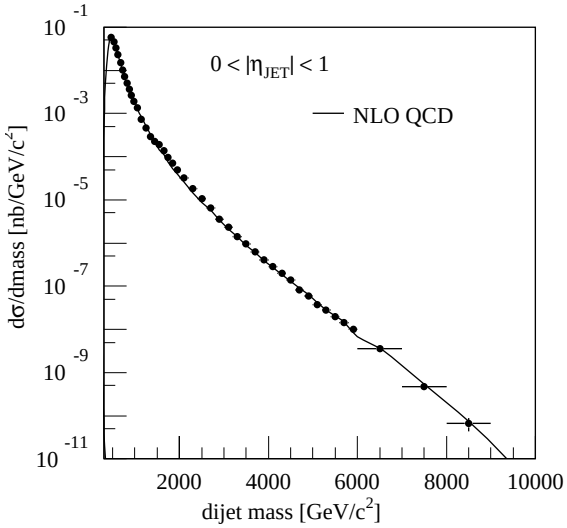

Figure 15-26 Di-jet invariant mass cross-section (at hadron level) for centrally produced jets ($|\eta| < 1$) obtained from a PYTHIA calculation (points) and from a NLO Monte Carlo calculation (solid line).

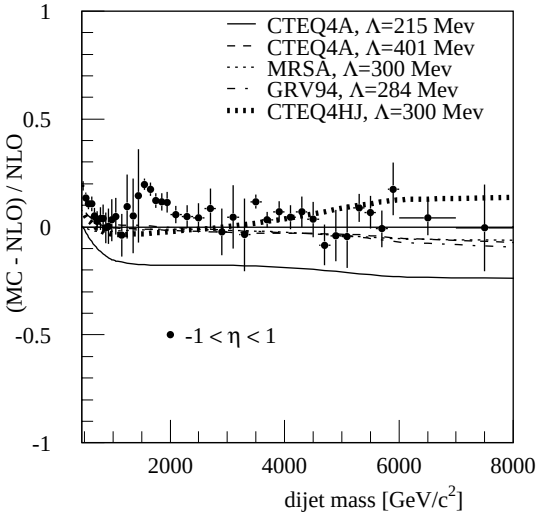

Figure 15-27 The ratio of the di-jet invariant mass cross-section from PYTHIA (including a pseudo *K*-factor) to the one at NLO from the JETRAD calculation (including a hadronisation correction) is shown as points. Also shown is the relative difference to the NLO calculation for a variation of Λ_{QCD} and for different pdf's (various curves).

(normalised to the CTEQ4M parton distribution and a value of Λ_{QCD} = 300 MeV). Clearly visible are the threshold effects close to the cut-offs on $\hat{p}_T$, where the statistical errors for masses smaller than about 4 TeV correspond to integrated luminosities much smaller than 300 fb^{-1}. Furthermore, this ratio is formed between a LO and a NLO calculation, which could produce additional distortions. The two largest effects are observed for a small value of Λ_{QCD} (CTEQ4A with 215 MeV) and for the CTEQ4HJ distribution, which allowed more freedom in the gluon distribution at large x to accommodate the excess of large E_T jets at the Tevatron. The errors bars shown indicate the statistical uncertainty at design luminosity only for invariant masses larger than 5 TeV, below the final statistical uncertainty will be smaller than the one shown. A measurement of the di-jet invariant mass distribution at the Tevatron by the D0 collaboration [15-99] showed good agreement of a NLO calculation with the data up to di-jet masses of 900 GeV. The data are at large masses slightly larger than the prediction based on the CTEQ3M distributions, here the CTEQ4HJ distributions give a better agreement.

15.5.4.3 Di-jet production at large angular separation

In a di-jet event, the two jets are expected to be balanced in E_T and to be back-to-back in azimuth. The configuration expected to dominate at leading order is central production of the di-jet system. It has been proposed [15-100] to study configurations where both jets are produced in the forward direction, being separated in rapidity by $\Delta = y_1 - y_2$. With increasing values of Δ, terms of the form $\log(s/Q^2)$ become more important in the partonic cross-section and can be resummed using the techniques of the BFKL approach. These terms appear only in certain regions of phase space and resummation should restore in this case the predictive power of the calculation. It is at present unclear, whether these regions can be probed by measurements at HERA or the Tevatron. The observation of the increase in the cross-section for large separation in rapidity (in fixed order QCD the partonic cross-section should remain constant) is difficult, since at larg-

er values of Δ the parton momentum fractions become large and the observable cross-section gets smaller. As observed at the Tevatron, additional radiation leads to a decorrelation in azimuth between the two jets [15-101][15-102], but in a manner correctly described by DGLAP kinematics.

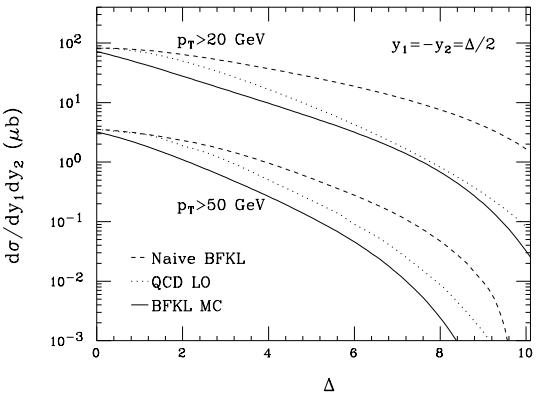

Figure 15-28 Differential cross-section for the production of two jets separated by Δ in rapidity. Three models are shown: a LO QCD calculation, a BFKL prediction and a BFKL Monte Carlo calculation (from [15-103]).

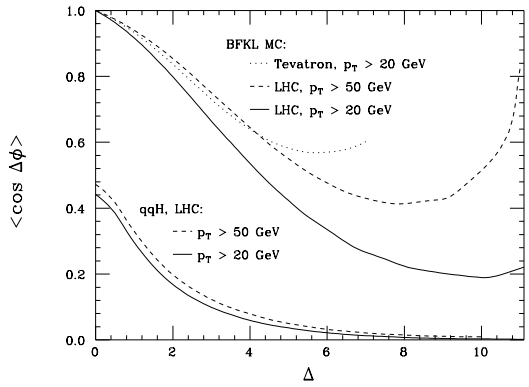

Figure 15-29 Azimuthal decorrelation in the production of two jets separated by Δ in rapidity. Shown are the results for the Tevatron and for the LHC from a BFKL Monte Carlo calculation (from [15-103]).

The cross-section for the production of two jets separated by a value of Δ in rapidity is shown in Figure 15-28 as a function of Δ. Three different calculations are shown for two cuts on the p_T of the most forward going jets: a LO QCD calculation, a 'naive' BFKL calculation (which contains only the resummation without taking into account kinematical constraints) and a realistic BFKL MC implementation [15-103], all using the CTEQ4L distribution. The decorrelation should be insensitive to the parton distribution functions. Figure 15-29 shows the expected azimuthal decorrelation in terms of <cos(π - Δφ)> (where Δφ is the angular separation between the two jets in azimuth) as a function of the separation Δ. The decorrelation increases (<cos(π - Δφ)> decreases) with increasing Δ. Shown are the predictions for Tevatron energies and for LHC energies, for the latter two values of the minimal jet transverse energy are used. Also shown is the expected decorrelation for the production of a heavy Higgs boson via gauge boson fusion in the process $qq \rightarrow qqH$, giving rise to two jets separated by Δ.

From the measurement of the D0 collaboration[15-104] (using jets with E_T > 20 GeV and a range of 0 < Δ < 6) it is known that a NLO calculation predicts too little decorrelation, whereas a 'naive' BFKL calculation predicts too much decorrelation at large separations. The HERWIG and PYTHIA models are able to describe the D0 data quite well.

The experimental challenge consists in selecting events where there is one jet on each side of the detector in the far forward region and trying to allow for as low transverse momentum of the jets as possible. The measurement requires in addition a good resolution in azimuthal angle to measure the decorrelation. The ATLAS forward calorimeter could provide a trigger on summed transverse energy in the region 3 < |η| < 5, as mentioned in [15-61] with a possible azimuthal division. The threshold on the jet energy will be restricted by the energy deposition in the forward calorimeter due to the underlying event and due to multiple interactions per bunch crossing. A LVL1 trigger would require a coincidence between energy depositions in the forward calorimeters at both sides of the detector, at the higher levels of the trigger a more refined jet selection could be applied, where the non-projective geometry of the calorimeter cells is taken

into account (see Section 9.1.4). In addition, the lateral size of the hadronic shower gets important. Without the use of the information of the forward calorimeter, the event selection would be restricted to values $\Delta < 6$. The fundamental selection for these events resembles the one for the study of colour singlet exchange at large momentum transfer, as discussed in Section 15.4.7. In the case of BFKL studies however, no requirements on the central rapidity region are made.

15.5.5 Multi-jet production

Possible measurements include the measurement of the cross-section for the production of *n* jets, along with a detailed analysis of the topological properties of the events. These can be used to constrain contributions from new physics, leading to final states with many jets. In the rest frame of the n-jet system, there are 4*n*-4 independent variables. These are typically divided into angular and fractional momentum variables, as well as invariant mass variables of combinations of different jets. The CDF collaboration has published a detailed study of multi-jet events (up to 6 jet events) and their topological properties [15-105]. The jet multiplicity distribution and the shape of the multi-jet mass and leading jet angular distribution shave been compared to a full leading order matrix element calculation [15-106][15-107] as well as to a leading order matrix element calculation (HERWIG) [15-13] for the $2 \rightarrow 2$ hard scattering, supplemented with parton showers. Both calculations agree well with the data. The inclusive p_T distribution is found to be able to discriminate between the two models, the HERWIG calculation overestimates the number of 3 and 4 jets at intermediate p_T. Multi-jet production can also be used to study effects of colour coherence, as discussed later.

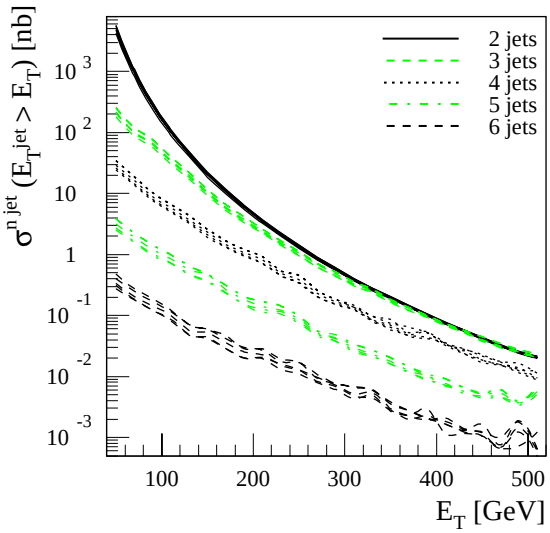

Figure 15-30 Cross-section for the exclusive production of *n* jets (*n* = 2,3,4,5,6 and $|\eta| < 3.2$) as a function of the minimum jet transverse energy at parton level for different parton distributions (CTEQ2L, CTEQ4L, CTEQ4HJ, MRSA and GRV94) from a LO calculation.

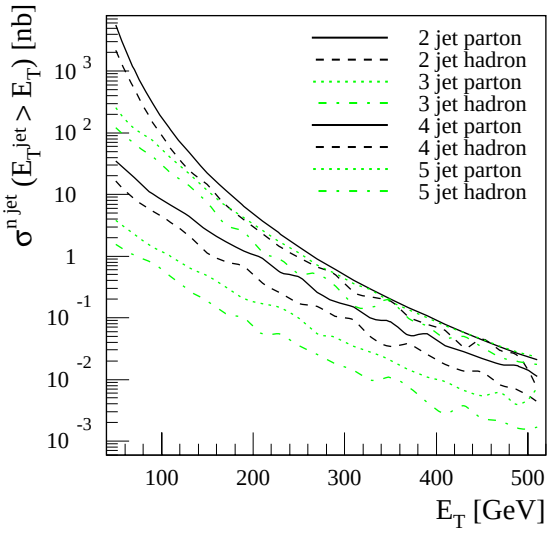

Figure 15-31 Cross-section for the exclusive production of *n* jets (*n* = 2,3,4,5 and $|\eta| < 3.2$) as a function of the minimum transverse energy of each jet comparing parton to hadron level. The hadron level cross-section has parton showers and hadronisation added to the LO result.

A thorough understanding of the properties and cross-sections for multi-jet production is important for several other physics studies, *e.g.* $t\bar{t}$ production with hadronic final states, the search for R-parity violating SUSY (where around 8 - 12 jets are expected for a signal) and for Higgs production in association with heavy quark pair ($b\bar{b}$ or $t\bar{t}$), where the Higgs decays to $b\bar{b}$. As mentioned previously in Section 15.5.2.6, the ratio of the cross-section for the production of 3 jets to the one of 2 jets might be used to extract the strong coupling constant.

The cross-sections for the production of n jets (n = 2,3,4,5,6) are shown in Figure 15-30 as a function of the jet transverse energy. They have been obtained from a leading order calculation[15-106] and [15-107]. In Figure 15-30 the differential cross-section for the production of n jets at the parton level is shown as a function of the transverse energy of the jets. Several parton distributions have been used: CTEQ2L, CTEQ4L, CTEQ4HJ, MRSA and GRV94. In the calculation, a minimal angular separation of 40 degrees between two partons was required. The experimental selection can be found in the trigger menu in Section 11.7. Multi-jet triggers with smaller thresholds will be available, although they will be subjected to a pre-scaling. A comparison between the cross-section at parton level and the one at hadron level is shown in Figure 15-31. The multi-jet cross-section at hadron level was obtained by adding parton showers to the partons from the NJETS calculation and hadronising the partonic system. Jets were defined using a cone algorithm with a radius of R = 0.4. The hadron level cross-sections are slightly smaller than the parton level ones for all jet multiplicities shown (n = 2,3,4,5).

Effects of colour coherence are expected to lead to an inhibition of soft gluon radiation (for example observed in the ‘string’ effect [15-108] in e^+e^- annihilation). The measurement of such effects in a hadron-hadron collider environment is difficult due to the many colour flow patterns present. The CDF collaboration tried to avoid these difficulties by selecting events where the leading jet has a large enough energy, so that the soft radiation becomes hard enough to form secondary jets. The measurement [15-109] of kinematical correlations between the second and third most energetic jet indicated the contribution of the interference between initial and final state gluon emission from the colour connected partons. A comparable investigation by D0 [15-110] arrived at similar conclusions.

15.5.6 Double parton scattering

Given the large density of partons with small longitudinal momenta in the proton, there exists the possibility of two (or more) hard interactions taking place in a high energy collision. The cross-section for double parton scattering can be expressed in terms of a two-parton distribution function $D(x,x',b)$ [15-111] depending on two momentum fractions and a transverse distance scale. In the case of no correlation between the partons, this function factorises and the double parton scattering cross-section σ_D can be written in terms of the single parton scattering cross-section σ_S and an effective cross-section σ_{eff}. This effective cross-section contains information about the spatial distribution of partons in the proton. Its value will increase with the uniformity of the spatial distribution and will decrease with increasing concentration of ‘clumpy’ regions containing a high density of partons. In the latter case the probability for a double parton scattering is larger, as the first scatter selected a region of high parton density. The ultimate goal will be to derive from measurements not only the occurrence of multiple parton scattering, but to extract parton densities containing the information about the correlation between several partons.

The occurrence of double parton scattering has been measured by the CDF collaboration, using events with exactly three jets and a photon (or a π^0) [15-112]. Requiring a transverse energy of the photon of more than 16 GeV and of the second and third jet of 5 to 7 GeV, an effective cross-section of $\sigma_{eff} = 14.5 \pm 1.7^{+1.7}_{-2.3}$ mb was extracted. No dependence of the process on the value of x was observed.

At the LHC the experimental challenge is to select events with mini-jets, *i.e.* jets which do not have a very large transverse energy. Besides the actual reconstruction of such jets the triggering of these events has to be studied in more detail. Based on a minimum-bias trigger for the first level of the ATLAS trigger, the higher levels, which have access to the full granularity of the sub-detectors, could try to enhance the signal by reconstructing jets with low transverse energy. More studies have to be performed to assess the minimal transverse energies for the jet reconstruction. In the context of low p_T jet tagging at low luminosity (more details can be found in Section 9.1.4) a minimal value of about 15 GeV was studied.

15.6 Photon physics

15.6.1 Overview

The detection of photons at a hadron collider is a challenging task due to the large background from jet production, where fluctuations can mimic the signature of a photon. ATLAS with its fine granularity calorimeters extending to $|\eta| < 2.5$ offers the possibility for a large rejection factor against this background (see Section 7.6). The advantage of photon measurements is the better energy determination in comparison to jet measurements. In addition the definition of a jet leads to ambiguities. Direct photon measurements can provide important constraints on parton distributions, especially on the gluon distribution in the proton. In case of photons, however, the experimental background due to jets containing a leading π^0 has to be understood well. The signal-to-background ratio can be improved significantly by requiring the photon candidate to be isolated, *i.e.* there should be no significant hadronic activity in a cone around the photon direction. Searches for the Higgs boson in the decay to two photons require a good understanding of the irreducible background from photon pair production.

In this section, the measurement of the inclusive prompt photon production (Section 15.6.2) and the production of photon pairs (Section 15.6.3) will be discussed. Additional topics include the production of photons with an associated final state property, like jets (Section 15.6.4) or open charm (Section 15.6.5).

15.6.2 Inclusive photon production

The production of direct photons has two main contributions, the QCD Compton process ($qg \rightarrow q\gamma$) and the annihilation graph ($q\bar{q} \rightarrow g\gamma$). In the case of Tevatron energies and small to moderate transverse momentum of the photon, the Compton process dominates. Also at the LHC the Compton process dominates in most of the kinematical region. Only this process provides a sensitivity to the gluon distribution. A calculation of direct photon production including next-to-leading-logarithms [15-113] starts from the two lowest order processes listed above (a similar calculation can be found in [15-114]). The calculation is based on a Monte-Carlo approach, allowing for the inclusion of cuts. Calculations at next-to-leading order include the one-

loop corrections to the $2 \rightarrow 2$ process and the tree level calculation of the $2 \rightarrow 3$ processes. The bremsstrahlung process corresponds to the emission of a photon from a final state parton. For large angles, this contribution is included in the $2 \rightarrow 3$ diagrams, for small angles only a phenomenological treatment via a non-perturbative fragmentation function is available. In [15-115] the calculation for isolated prompt photon production is shown, including studies on the uncertainties due to the scale dependence, the isolation criteria and the fragmentation contribution. The differences between the data at low photon transverse momenta at the Tevatron and the NLO expectation (which is lower than the data) can possibly be explained by the effects of initial state gluon radiation.

The usual measurement of prompt photon production requires in the experimental selection an isolated photon, by demanding no significant hadronic energy deposition inside an isolation cone around the photon direction. This definition is not simply transferrable to a perturbative QCD calculation, as the cancellation of infrared divergences [15-116] must not be spoilt, which would happen if a sharp isolation of the photon from other partons is made. Not applying a sharp isolation however allows contributions from photon fragmentation and from jet background to appear. Two approaches have been suggested: a cone based approach, where only a small amount of hadronic energy in a cone around the photon direction is allowed and the 'democratic' approach, where the photon is treated as a parton in performing a jet clustering. Then a cut on the hadronic energy of the jet containing the photon is applied. In the case of photon and associated jet production, a procedure has been suggested which is infrared safe to all orders and minimises the fragmentation contribution[15-116]. The cone approach is extended by requiring an upper limit on the hadronic energy in a cone around the photon for all cone sizes δ smaller than a fixed value δ_0. The upper limit on the hadronic energy E_{max} depends on the cone size: $E_{max} = f(\delta)$, where the function f goes to 0 when the size δ approaches 0. The jet finding is performed on all partons, but only those jets which are outside the isolation cone are accepted. This method allows hadrons to be close to the photon, as long as their energies get smaller as they get closer.

The primary background to direct photon production is due to jet fragmentation into a leading π^0 or η. The imposition of an isolation cut greatly discriminates against this jet fragmentation background, while having little effect on the prompt photon signal. Studies at the Tevatron (*e.g.* by CDF for $p_T^{\gamma} > 12$ GeV) have shown that after an isolation cut (less than 2 GeV in a cone of radius 0.7) the signal fraction (of the direct photon candidates) increases by up to several orders of magnitude (to ~20% at low p_T, approaching 100% at high p_T). For larger transverse momenta, the EM showers generated in the calorimeter overlap significantly and an analysis of the shower shape is necessary to allow a statistical subtraction of this background source. Another estimate of the background can be obtained from the measured converted photons in the tracking detectors.

In the kinematic range of the photon transverse momentum between 100 and 500 GeV the expected ratio between the inclusive direct photon cross-section (at NLO for $|\eta| < 0.7$, as shown in Figure 15-32) and the inclusive jet cross-section (at NLO [15-84] for $|\eta| < 0.7$) is about 1.5×10^{-3}. For photon transverse energies between 40 and 100 GeV a rejection of about 3000 against jets is achieved. More details on the separation between photons and jets can be found in Section 7.6.

The minimal parton momentum x_{min} is determined by the transverse energy threshold E_T^{min} and the maximal pseudorapidity η_{max} of the photon via the relation $x_{min} = 2(E_{Tmin}/\sqrt{s})e^{-\eta_{max}}$, the maximal momentum fraction x_{max} via $x_{max} = 2(E_{Tmax}/\sqrt{s})e^{\eta_{max}}$. The selection at ATLAS will be based on a trigger demanding an isolated photon of transverse energy larger than 40 GeV (low luminosity) or 60 GeV (high luminosity) within $|\eta| < 2.5$. This gives a value of

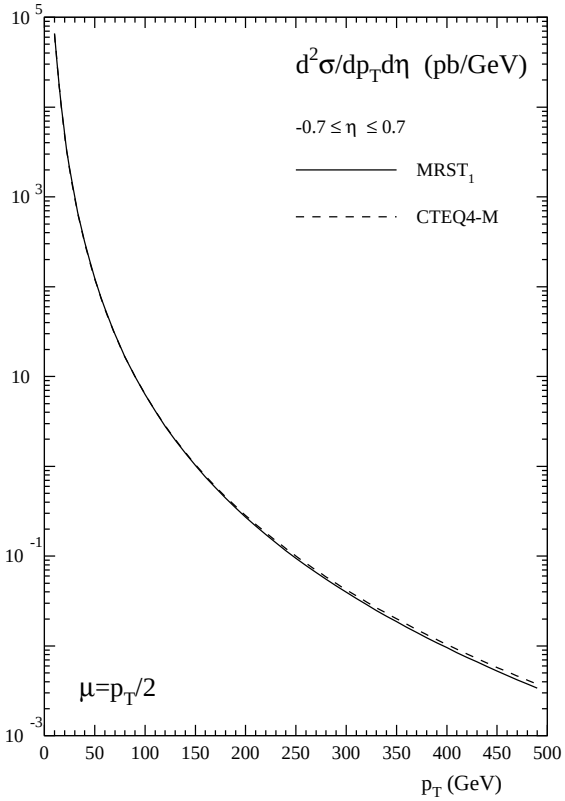

Figure 15-32 Inclusive direct photon cross-section (for central photon production $|\eta| < 0.7$) at next-to-leading order as a function of p_T (from [15-117]) for two pdf's.

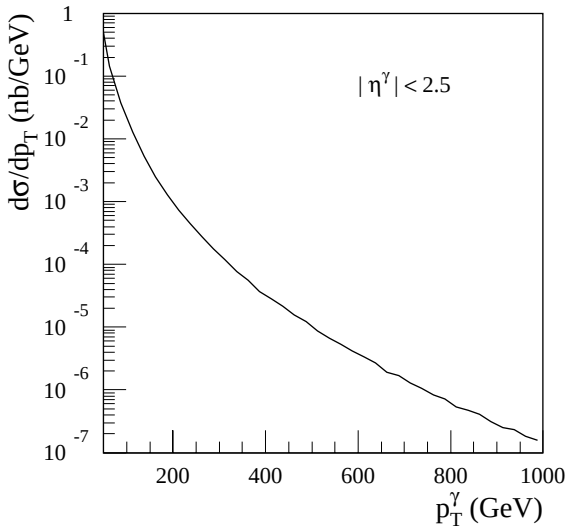

Figure 15-33 Inclusive direct photon cross-section at leading order (from PYTHIA, including the ATLFAST detector simulation) as a function of p_T for the CTEQ3L pdf.

$x_{min} = 5 \times 10^{-4}$, lower values could be reached by using lower thresholds, which will however be subjected to a prescaling. For a photon transverse energy of 500 GeV, a value of $x_{max} = 0.2$ is obtained. In Figure 15-32 the cross-section for prompt isolated photon production is shown as a function of the transverse momentum of the photon, as obtained from a next-to-leading order calculation [15-117] for central photon production ($|\eta| < 0.7$). Figure 15-33 shows the same cross-section, as obtained from a leading order calculation including a detector simulation (using ATLFAST), using the CTEQ3L parton distribution set. The photon was required to have a transverse momentum of at least 40 GeV and be within $|\eta| < 2.5$. Further an isolation criteria was applied. A comparison of the NLO and the LO calculation gives a *K*-factor of about 1.5, however it has to be taken into account that the NLO calculation is restricted to the central pseudorapidity region ($|\eta| < 0.7$), whereas the leading order calculation reaches up to $|\eta| < 2.5$.

15.6.3 Photon pair production

Effects of soft gluon emission can be studied directly by measuring the production of pairs of photons. The transverse momentum of the photon pair and the azimuthal angular difference between the two photons are sensitive to these emissions.

As in the case of inclusive photon production, the main experimental challenge is to reduce the background of fake photon pairs (*i.e.* processes producing two jets or a jet and a photon, where the jet(s) lead to one(two) fake photon(s)). The selection will be based on a trigger requiring two isolated photon candidates within $|\eta| < 2.5$. The threshold on the transverse energy will be 20 GeV for each photon (for low and high luminosity running conditions).

A calculation of the di-photon production at next-to-leading order including the resummation of soft gluon emission is presented in [15-118]. The resummation is performed on initial state gluon emission for $q\bar{q}$, qg and gg initial states, treating the di-photon system in a similar manner as a Drell-Yan virtual photon. The production of one photon via a fragmentation process is taken into account, the NLO contributions for the $q\bar{q}$ and qg initial states are determined exactly and for the gg box diagram NLO contributions are included in an approximation.

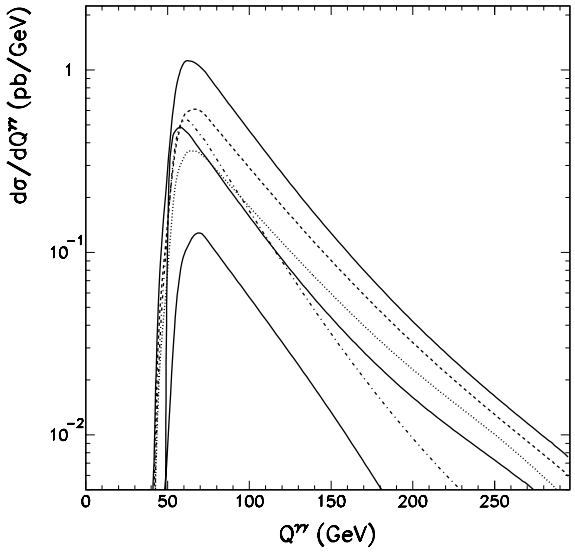

Figure 15-34 Cross-section for photon pair production from [15-119] as a function of the invariant mass $Q^{\gamma\gamma}$ of the pair. The upmost solid curve shows the total NLO prediction, whereas the LO contribution is represented by the middle solid curve. The other curves are explained in the text.

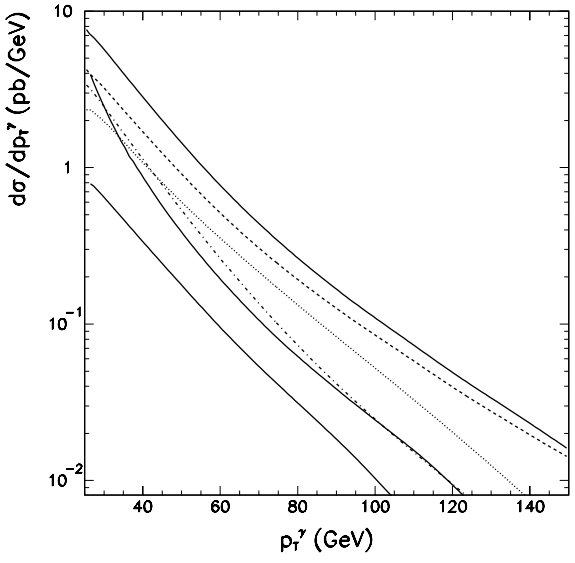

Figure 15-35 Cross-section for photon pair production from [15-119] as a function of the photon transverse momentum p_T^{γ}. The upmost solid curve shows the total NLO prediction, whereas the LO contribution is represented by the middle solid curve. The other curves are explained in the text.

Figure 15-34 shows the cross-section for di-photon production as a function of the invariant mass of the di-photon system. This calculation [15-119] includes the NLO contributions and the resummation of soft gluon emission. The following cuts have been applied to the photons: $p_T > 25$ GeV, $|\eta| < 2.5$, $\Delta R(\gamma,\gamma) > 0.4$ and $p_T^1/(p_T^1 + p_T^2) < 0.7$, where p_T^1 is the transverse momentum of the leading photon (this cut is not used in the analysis of the Higgs decay to two photons, as described in Section 19.2.2). The upmost solid line corresponds to the total cross-section, the dashed line represents the resummed part for $q\bar{q} + gg \rightarrow \gamma\gamma X$. The part of the resummed process due to the $q\bar{q}$ initial state is shown as a dotted line, the one due to the gg initial state as a dash-dotted line. The lowest solid curve shows the fragmentation contribution and the leading order contribution is indicated by the middle solid curve. The importance of the gg initial state for lower di-photon masses should be noted.

A total cross-section of about 61 pb is obtained (using the CTEQ4M distribution), where the leading order part amounts to about 22 pb (CTEQ4L). The total cross-section splits into the contributions from the three initial states as follows: 20.5 pb for $q\bar{q}$, 23.9 pb for gg and 16.6 pb for qg, where the latter includes a fragmentation contribution of 6.8 pb.The understanding of this distribution (representing the irreducible background contribution) is important in estimating the reach in the search for a light Higgs boson, which decays to two photons, or in setting limits on the Higgs production cross-section. The *K*-factor has a value of about two, being rather independent of the photon pair mass.

In Figure 15-35 the distribution of the transverse momentum of the photons is shown, where the labelling of the curves is described above. The comparison of the LO and the NLO result shows a large *K*-factor, which increases with the transverse momentum of the photon up to values of about five.

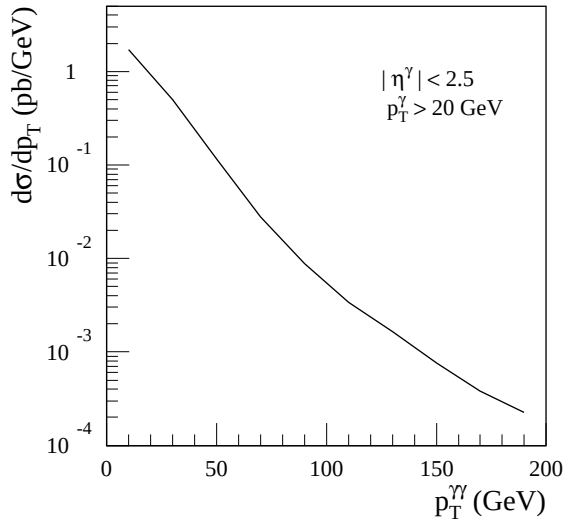

Figure 15-36 Cross-section for photon pair production from a leading order calculation (PYTHIA with ATLFAST) as a function of the transverse momentum $p_T^{\gamma\gamma}$ of the pair.

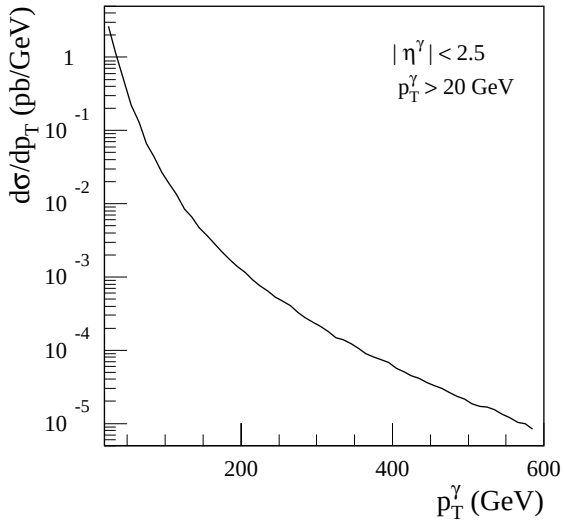

Figure 15-37 Cross-section for photon pair production from a leading order calculation (PYTHIA with ATLFAST) as a function of the transverse momentum p_T^{γ} of the photons.

In Figure 15-38 the cross-section for photon pair production is shown as a function of the invariant mass of the photon pair for masses up to 1 TeV. This cross-section was obtained from a leading order calculation using PYTHIA, including a simulation of the detector response (using ATLFAST). Photons were required to have at least 20 GeV transverse energy, to be isolated and to be restricted to pseudorapidities of $|\eta| < 2.5$. The CTEQ3L parton distributions were used. For the same cuts, Figure 15-36 shows the cross-section as a function of the transverse momentum of the photon pair, indicating that large transverse momenta can be studied with reasonable statistics. In Figure 15-37 the cross-section is shown as a function of the transverse momentum of a photon.

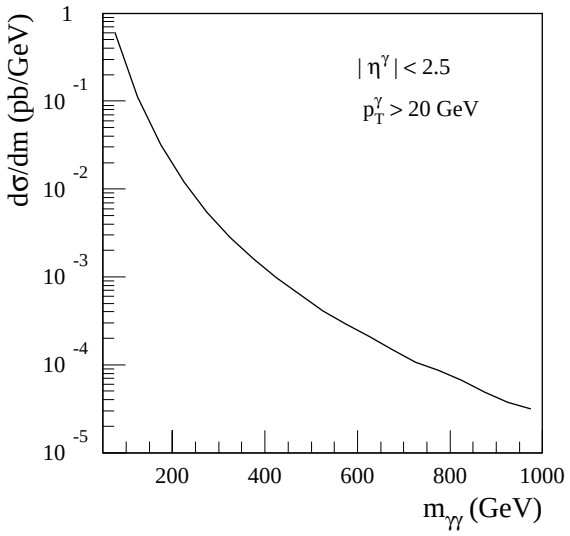

Figure 15-38 Cross-section for photon pair production from a leading order calculation (PYTHIA with ATLFAST) as a function of the invariant mass $m_{\gamma\gamma}$ of the pair.

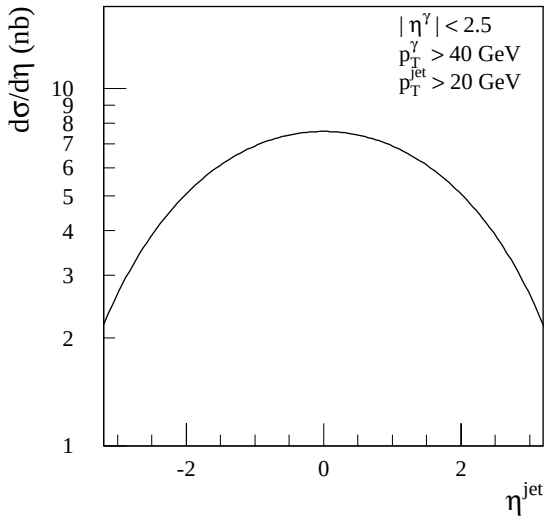

Figure 15-39 Cross-section for direct photon + jet production (PYTHIA with ATLFAST) as a function of the pseudorapidity η^{jet} of the jet, as obtained from a leading order calculation.

15.6.4 Photon + jet production

The measurement of an associated jet for photon production allows better constraints of the parton distribution functions, since both parton momenta of the hard scattering can then be reconstructed. When both the jet and the photon are centrally produced, the x values of the partons are of similar magnitude. The angular distribution is given by the quark propagator, similar to the case of W + jet production. A leading order calculation for photon + n jet production (n = 1,2,3) is available [15-120], the next-to-leading order corrections have been calculated [15-121]. In Figure 15-39 the cross-section for the production of a direct photon and a jet is shown as a function of the pseudorapidity of the jet. The figure has been obtained from a PYTHIA calculation, based on the CTEQ2L parton distributions and taking into account the ATLAS detector response. For the photon a minimal transverse energy of 40 GeV and a limit of $|\eta| < 2.5$ were required, the jet had to have a transverse energy of at least 20 GeV.

The occurrence of double parton scattering represents a source of background for this process. It can be studied by selecting events with a photon and three jets. For two hard scattering processes, the angular difference between the system of photon + leading jet and the second jet is expected to be flat. For a p_T cut of about 40 GeV on the photon transverse momentum, this effect should give a minimal contribution only.

A CDF measurement of the triple differential cross-section for photon + jet production [15-122] (as a function of p_T, η_γ and η_{jet}) allows to cover different ranges in parton momentum x by varying the jet pseudorapidity η_{jet}. Within the errors, this measurement does not discriminate between different parton distribution functions, where the highest sensitivity is expected at large jet pseudorapidities.

In order to quantify the contribution of the bremsstrahlung process ($qg \to qg\gamma$) to the direct photon production, relative to the Compton and the annihilation graph, the CDF collaboration measured the production of photons in association with 2 jets [15-123]. The two dominant sources of systematic uncertainty are the knowledge of the energy scale and the contribution from double hard scattering background. The data are best described with a 50% contribution of the Bremsstrahlung process to the isolated photon cross-section.

A further use of the photon + jet final state is the deduction of information on the $\bar{u}$ content of the proton [15-124]. The two dominant contributions to the production of a high p_T photon and an associated jet are $ug \to u\gamma$ and $u\bar{u} \to g\gamma$. These two processes are enhanced relative to the *d* and *s* quark contribution due to the electric charge of the *u* quarks and the smaller amount of *d* and *s* quarks in the proton.

15.6.5 Photon + charm and photon + beauty production

The production of charm in association with a photon can be used to constrain the charm content of the proton. Leading order calculations of prompt photon and charm production were carried out using two approaches [15-125]. The first approach included Compton scattering off a charm sea quark $gc \to \gamma c$, taking into account also the effect of gluon splitting $g \to c\bar{c}$ and of photons from fragmentation. The second approach is based on a massive charm quark at low energies, including the two following processes: $gg \to \gamma c\bar{c}$ and $q\bar{q} \to \gamma c\bar{c}$ as well as the fragmentation contribution. A non-negligible contribution to the inclusive prompt photon production is expected. For Tevatron energies, both approaches give similar results, indicating that the observation of prompt photon + charm production not necessarily implies a non-vanishing charm sea quark distribution. An analytical next-to-leading order calculation [15-126] indicates a *K*-factor of about 1.5 to 1.9 for Tevatron energies, which decreases with increasing photon transverse momentum. The calculation includes the one loop corrections to $gc \to \gamma c$, the leading order fragmentation graphs and the NLO contributions, like $gg \to \gamma c\bar{c}$, $gc \to \gamma gc$ and so on, which give rise to the large *K*-factor. Differential distributions are available and can be used to test correlations in the matrix elements. The dominant contribution is found to be due to the scattering off a charm sea quark. An implementation of this calculation by combining the analytic and the Monte-Carlo approach is available [15-127] and allows an implementation of experimental cuts.

The tagging of charm production can be done by measuring the associated production of a muon (or an electron) with a photon (inclusive detection of semi-leptonic decays) or by exclusive decay reconstruction (*e.g.* the non-leptonic decay of a D^{*+-} meson) together with a photon in the final state. Measurements done by CDF at the Tevatron for photon + muon production [15-128] and for photon + D^* production [15-129] show an excess of the measured cross-section (about a factor of 2) relative to the prediction of a PYTHIA calculation, the data are however in agreement with the NLO calculation.

The associated production of a photon together with a *b* quark contributes to the γ + charm production. A measurement of this contribution could be based on a selection of a photon together with the tagging of beauty production, as discussed in Section 15.8.3. In comparison to the case of inclusive photon production, in this case lower transverse momentum thresholds for the photon candidate should be possible.

15.7 Drell-Yan physics and gauge-boson production

15.7.1 Overview

The production of Drell-Yan pairs proceeds by the annihilation of quark and anti-quarks via an intermediate vector boson (γ^*/Z or W). This probes the proton structure at a scale Q^2 equal to the mass squared of the lepton pair. In proton-proton collisions, the production of lepton pairs proceeds via γ^*/Z bosons and starts from a combination of a valence quark and a sea quark (or a quark and an anti-quark from the sea) of the same flavour (*e.g.* $u\bar{u}$, $d\bar{d}$, ...). In the case of W production, a valence quark and a sea quark (or a quark and an anti-quark from the sea) of different flavour annihilate. QCD effects enter the cross-section for Drell-Yan production only in the initial state and thus make the predictions less uncertain.

Given the different average momentum fraction carried by valence and sea quarks, in most cases an asymmetric configuration will be preferred, where one momentum fraction is small, and the other large. At leading order, the rapidity y of the lepton pair is related to the momentum fractions $x_{1,2}$ via: $y = 0.5 \ln(x_1/x_2)$ and the invariant mass of the pair is given by $M^2 = x_1 x_2 s$. For a lower bound of 14 GeV on the mass M of the lepton pair, the product of the parton momentum fraction $x_1 x_2$ has to be larger than 10^{-6}. Assuming that the reconstruction of Drell-Yan pairs is done up to rapidities of 2.5, the maximum ratio possible between the two parton momenta is of the order of 150.

In this section, the production of Drell-Yan pairs over the full range of the invariant mass of the lepton pair will be discussed (Section 15.7.2), followed by the presentation of W boson production (Section 15.7.3). Next a discussion of Z boson production is presented (Section 15.7.4) and finally the pair production of vector bosons is described (Section 15.7.5).

15.7.2 Drell-Yan production

15.7.2.1 Di-lepton mass spectrum

The measurement of the lepton pair properties (lepton rapidities and invariant mass of the pair) allows the reconstruction of the parton momenta and thus can give constraints on the parton distribution for quarks. The two leptons are expected to be well separated from jets and other particles. A selection will start from trigger on di-leptons, where details on the thresholds and cuts can be found in Section 11.7. For the lepton pair production, a resummation of soft gluon emission contributions exists [15-130].

Besides the background from cosmic rays for the case of muon pairs, two classes of background sources can be distinguished: the misidentification of leptons and leptons originating from heavy quark decays. In both cases, the main source is the production of QCD jets and thus these (fake) leptons are expected not to be isolated, as are those from Drell-Yan production. Furthermore, the leptons from Drell-Yan production are of opposite charge. The background from misidentification can be determined by studying the same charge lepton pairs. Background of opposite charge lepton pairs from heavy quark decays ($b\bar{b}$ and $t\bar{t}$ production) can be estimated using $e\mu$ events. Measurements of the Drell-Yan pair production have been performed by CDF [15-131] and D0 [15-132].

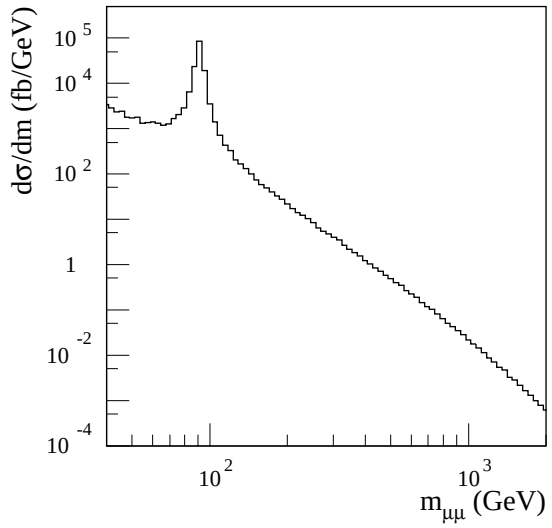

Figure 15-40 Cross-section for Drell-Yan muon pairs as a function of the invariant mass $m_{\mu\mu}$ of the muon pair from a leading order calculation (PYTHIA with ATLFAST) for the following cuts: $p_T^{\mu} > 6$ GeV and $|\eta_{\mu}| < 2.5$.

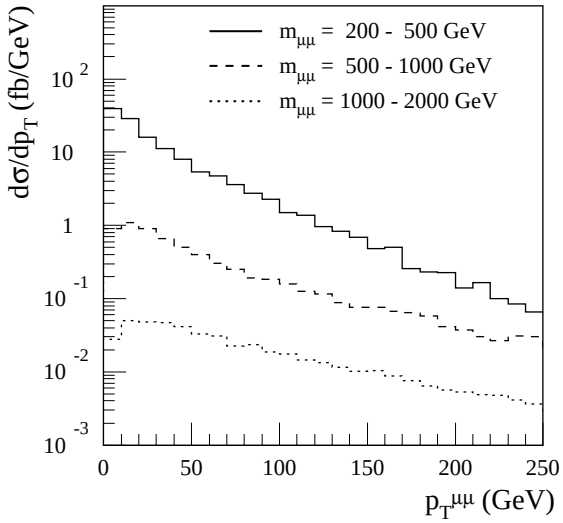

Figure 15-41 Distribution of the transverse momentum $p_T^{\mu\mu}$ of the lepton pair produced in a Drell-Yan process from a leading order calculation (PYTHIA with ATLFAST) for three ranges of $m_{\mu\mu}$. The following cuts have been applied: $p_T^{\mu} > 6$ GeV and $|\eta_{\mu}| < 2.5$.

Figure 15-40 shows the expected cross-section for Drell-Yan production as a function of the invariant mass of the Drell-Yan pair, as obtained from PYTHIA using the CTEQ2L parton distributions [15-15]. Clearly visible is the resonance contribution due to production of the Z boson, which will be discussed in more detail in Section 15.7.4.

15.7.2.2 p_T distribution of lepton pair

In Figure 15-41 the distribution of the transverse momentum of the muon pair produced via the Drell-Yan process is shown for three different ranges of the invariant mass of the two muons: 200-500, 500-1000 and 1000-2000 GeV. The prediction is based on the same cuts as in the previous section. The figure shows that with the LHC statistics a significant number of high mass Drell-Yan pairs will be produced with transverse momenta larger than 100 GeV.

The angular distribution of the leptons (and the lepton pair) produced in a Drell-Yan process should be sensitive to effects of non-perturbative QCD. For these angular observables, next-to-leading order calculations exist [15-133]. As shown by the CDF collaboration[15-134], the forward-backward asymmetry of the lepton pair produced can be used to verify the expected contribution due to the γ^* / Z interference for lepton pair masses significantly larger than the Z pole. Furthermore, the value of the forward-backward asymmetry could be modified in the presence of heavy neutral gauge bosons.

15.7.3 *W* production

15.7.3.1 Cross-section

At the LHC the cross-section for the production of the W^+ is larger than the one for the production of W^- bosons. The contribution from $c\bar{s}$ (and $s\bar{c}$) initial states amounts to 10% at LHC energies (about 2% for the Tevatron). The latter contributions mainly contribute to the central production of W's, whereas forward W production is mostly due to $u\bar{d}$ ($d\bar{u}$) states. The product $x_1 \cdot x_2$ of the parton momenta is fixed to a value of about 3×10^{-5} at leading order.

The experimental selection will start from a trigger on a single lepton (electron or muon) within the pseudorapidity range of $|\eta| < 2.4$ for muons and $|\eta| < 2.5$ for electrons, respectively. Details on the thresholds for these triggers can be found in Section 11.7.3, the selection will then require in addition missing transverse energy (as discussed in more detail in Section 16.1.2). Due to the large statistics expected for the LHC, a restriction to the clean leptonic decay channels (involving an electron or a muon) is possible.

The dominant sources of background are the decay $W \to \tau\nu$ for the electron and the muon channel, and the decay $Z \to \mu\mu$ (where one of the muons is outside the acceptance) for the muon channel. Due to the excellent electron-jet separation (as described in Section 7.4, where it has been shown that jet rejection factors of the order of 10^5 can be achieved, while having an efficiency of about 70% for electrons from W (and Z) decays) the background from QCD multi-jet events is negligible. More details on these and other background sources can be found in Section 16.1.3.7. The efficiency for the lepton detection can be derived from experimental data using the copious production of Z bosons and their decay to two leptons. The dominant systematic uncertainty for the cross-section measurement is expected due to the determination of the absolute luminosity.

15.7.3.2 Rapidity distribution

In contrast to the case of proton anti-proton collisions (as in the case of Tevatron), at the LHC there is no rapidity asymmetry for the produced W's. However, the shape of the rapidity distributions (being symmetric with respect to $\eta = 0$) is different for W^+ and W^-, where the total cross-section is larger for W^+ than for W^-. The difference in the shape of the rapidity distribution should survive in the detectable decay lepton. It is a direct consequence of the parton distribution functions responsible for W^+ ($u\bar{d}$) and W^- ($d\bar{u}$) production.

In Figure 15-42 the expected shape of the rapidity distribution for W^+ and W^- production is shown. The cross-section times leptonic branching ratio has been obtained from PYTHIA using the CTEQ2L parton distributions, without applying cuts on the decay lepton. In Figure 15-43 the corresponding distribution for the decay lepton is shown, where for the lepton (electron or muon), a minimal transverse momentum of 20 GeV and $|\eta| < 2.5$ were required. Furthermore a missing transverse energy of at least 20 GeV was demanded. In both figures the different shapes of the W^+ and the W^- are visible; the W^+ goes further out in rapidity and has a maximum at $|y| = 3$. The central region ($|y| = 0$) corresponds to a symmetric configuration of the parton momenta ($x_{1,2} \sim 0.005$), whereas at $|y| = 2.5$ an asymmetric configuration can be found ($x_1 \sim 0.1$, $x_2 \sim 0.0007$). The precise measurement of these rapidity distributions can be used to constrain the u and $\bar{d}$ (resp. d and $\bar{u}$) distributions.

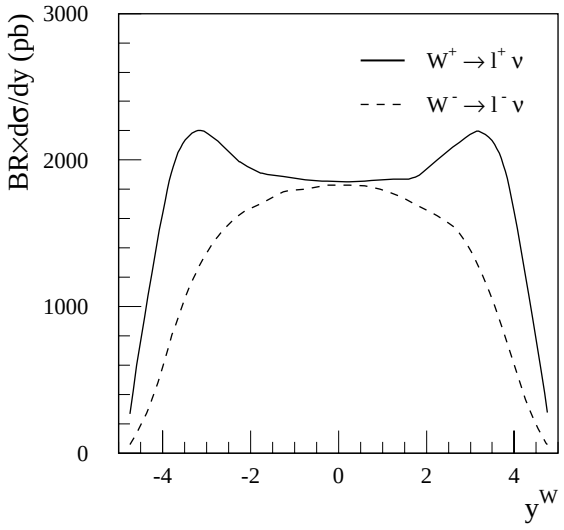

Figure 15-42 Differential cross-section for W^+ and W^- production as a function of the vector boson rapidity y^W from a leading order calculation (PYTHIA).

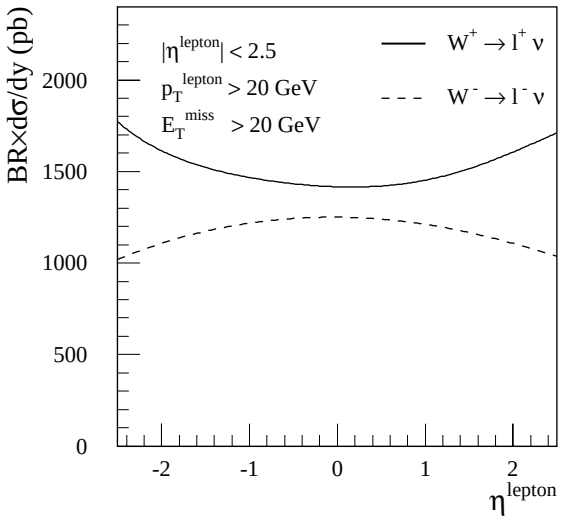

Figure 15-43 Differential cross-section for W^+ and W^- production as a function of the pseudorapidity η^{lepton} of the decay lepton of the W (PYTHIA and ATLFAST).

15.7.3.3 p_T distribution

The transverse momentum of the boson is due to associated production of quarks or gluons. A detailed understanding of the transverse momentum is important for a precise measurement of the W boson mass at hadron colliders. In the case of large q_T (the W transverse momentum) where mostly a single high p_T parton is radiated, an $O(\alpha_s^2)$ calculation exists. This is a one scale problem ($q_T \sim M_W$), where fixed order calculations are reliable. In the case of low q_T, multiple soft gluons can be emitted, leading to the appearance of large logarithms $\log(M_W^2/q_T^2)$. This two scale problem (q_T and M_W) can be solved by a resummation of these logarithmic terms. To provide a scheme for all q_T, a matching procedure has to be devised. These effects do also apply for the production of Z boson, as described in Section 15.7.4.2.

Data from the Tevatron on the W boson p_T show that a fixed order NLO calculation does not reproduce the measured spectrum. The comparison of data from D0 [15-135] to the prediction of Ref. [15-136], where a next-to-leading order calculation has been matched with the resummed calculation (introducing parameters for non-perturbative effects) shows consistency with the data. A second calculation [15-137] performs the matching at a scale where the W transverse momentum is close to the W mass. Using the data from D0, these two cannot be distinguished [15-138]. The non-perturbative part of the prediction has been obtained from a fit to the transverse momentum distribution of Z bosons, at small p_T the two calculations give different predictions. Even more uncertain is whether these non-perturbative parameters can be used universally, *e.g.* when going to LHC energies [15-139].

If the resummation of these logarithms is performed in the q_T space (where q_T is the transverse momentum of the vector boson) [15-140], a unified description of the production of vector bosons both for small and for large q_T is obtained without the need for a matching procedure. In Figure 15-44 the cross-section for inclusive W production is shown as a function of the transverse momentum of the W boson, as obtained from the calculation by Ellis and Veseli [15-140], using the MRS-R1 parton distributions [15-141]. The non-perturbative parameters (for the form factor) were set to the following values: $q_T^{lim} = 4$ GeV and $\tilde{a} = 0.1$ GeV^{-2}. They control the inter-

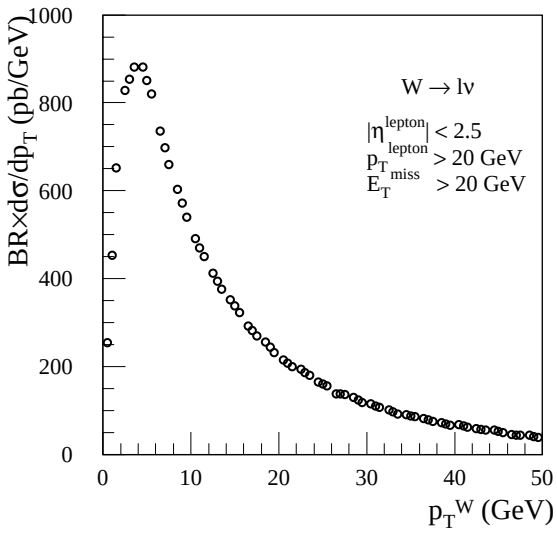

Figure 15-44 Differential cross-section for *W* production (with decay to either an electron or a muon) as a function of the transverse momentum p_T^W of the *W* boson from a next-to-leading order calculation (including resummation of large logarithms).

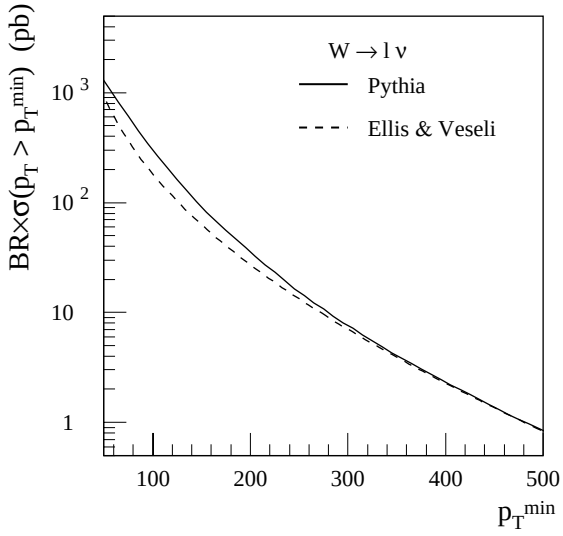

Figure 15-45 Cross-section for *W* production (with decay to either a muon or an electron) as a function of the minimum transverse momentum p_T^{min} of the *W* boson from a NLO calculation (Ellis and Veseli) and from a leading order calculation (PYTHIA).

cept and the first derivative of the differential cross-section for $p_T = 0$. The decay of the *W* boson, leading to a charged lepton (electron or muon) and a neutrino, is included using the following cuts: $p_T > 20$ GeV and $|\eta| < 2.5$ for the charged lepton and $p_T > 20$ GeV for the neutrino, approximating the experimental cut of missing transverse energy. Figure 15-45 shows the corresponding cross-section for *W* production up to transverse momenta of 500 GeV. Two calculations are shown: the resummed calculation from Ellis and Veseli and a leading order calculation from PYTHIA (including effects of parton showers and fragmentation). The cuts are identical to the ones used for Figure 15-44; in the case of PYTHIA a cut on the missing transverse energy (of at least 20 GeV) is performed, instead of the cut on the p_T of the neutrino in case of the Ellis-Veseli calculation. For large transverse momenta both calculations agree, as expected since in this region both are of $O(\alpha_s)$.

15.7.3.4 *W* + jet production

Measurements of the production of W bosons with associated jets were thought to have the potential to be used in a determination of the strong coupling constant. The cross-section for exclusive production of $W + n$ jets (n = 1,2,3,4) has been calculated at leading order [15-142]. A similar calculation [15-143] at leading order for LHC energies predicts for $p_T^W > 20$ GeV a cross-section of about 200 pb for W + 1 jet, about 50 pb for W + 2 jets and about 10 pb for W + 3 jets, where for the last two cross-sections a minimal jet transverse momentum of 19 GeV is required. The inclusive production of a *W* boson with at least one jet is calculated at next-to-leading order [15-84]. The study of the dependence of the associated jet rates in *W* production for different cone sizes defining the jet can give information on the ability of a next-to-leading order calculation to model the jet shape and to describe the overall production rate.The major source of background is the production of multi-jet final states, where one of the jets fakes an electron candidate and the event contains missing transverse energy.

A measurement of the ratio R_{10} of the inclusive cross-sections for W + 1 jet production to the one for W production [15-144] by the D0 collaboration using a cone size of 0.7 for the jet definition showed a NLO prediction being a factor of 2 smaller than the data in the range of 20 - 60 GeV for the minimal jet transverse energy. Furthermore the studies indicated no sensitivity of this ratio to the value of the strong coupling constant. The CDF collaboration measured the same ratio for two cone size: R = 0.4 [15-145] and R = 0.7 [15-146]. In the first case good agreement with the NLO calculation is found for minimal jet transverse energies between 15 and 95 GeV. For the case of R = 0.7, good agreement is observed for small transverse jet energies (< 35 GeV), at larger energies, the NLO prediction is smaller than the data by about 15%, being a 1σ difference. Comparing the results for the two cone sizes, an increase in R_{10} is found when going from 0.4 to 0.7 of about 30% for the data, whereas the NLO calculation only predicts about 10% increase. In both cases, CDF does not find a significant dependence of the ratio on the value of α_s.

Events with a W and associated jets can be used to study effects of colour coherence, which should lead to specific patterns in the parton flow from constructive or destructive interference between soft gluon emissions, as observed in e^+e^- annihilation ('string' effect). An important aspect is whether this pattern survives the hadronisation, as conjectured in the context of local parton hadron duality. The D0 collaboration has compared the distribution of soft particles in a disc of $0.7 < R < 1.5$ around the W and around the opposing jet [15-147], using the W as a template (since it is a colourless object). The data shows an enhancement of particle production around the tagged jet (with respect to the region around the W), as expected if colour coherence occurs. It has been suggested [15-148] to use these W + jet events to get information on properties of the soft gluon radiation. Using relevant event variables it is claimed that one could distinguish between the three partonic subprocesses contributing at lowest order: $qg \rightarrow Wq$, $gq \rightarrow Wq$ and $q\bar{q} \rightarrow Wg$. Possible applications are the derivation of constraints on the quark and gluon parton densities in the initial state and studies of the properties of quark and gluon jets.

The final state containing a W boson and four jets represents the dominant source of background for the top physics in the single lepton final state. The knowledge of the production of $Wb\bar{b}$ and $Wb\bar{b}$ + jet is important for the study of single top production and of the Wtb vertex. It has been calculated at leading order [15-149] (including, besides QCD processes, also the top signal, electroweak and Higgs contributions).

15.7.3.5 *W* + charm and *W* + bottom production

The production of W bosons with associated open charm production can be used to constrain the strange quark content of the proton [15-150]. The dominant production process is the QCD Compton graph with scattering on strange quarks: $gs \rightarrow Wc$. Background is expected from the production of $W + c\bar{c}$ $(b\bar{b})$, where the $c\bar{c}$ $(b\bar{b})$ pair is produced in the jet recoiling against the W and only one of the two heavy quarks is detected. The tagging of charm production could be done by searching for displaced vertices, by an exclusive reconstruction of non-leptonic decays of charmed baryons or mesons (*e.g.* the $D^* \rightarrow K\pi\pi$ decay) or by inclusive semi-leptonic decays.

The production of a W boson with an associated heavy quark pair can be used to deduce information on the gluon splitting to heavy quarks. The process proceeds via the annihilation of a quark-anti quark pair into a W and an off-shell gluon, where the latter splits into a heavy quark pair: $q\bar{q} \rightarrow Wg^* \rightarrow WQ\bar{Q}$. A selection would start from the decay lepton of the W. Next, requirements to identify two heavy quark decays would be added. This could be done by exclusive reconstruction of the decays or by demanding inclusive signatures like impact parameter significance.

For these channels additional studies are needed to assess the reach in kinematics, based on an inclusive trigger selection based on a lepton signature alone. In addition, the feasibility of reconstructing open charm has to be investigated and possibilities for an enrichment of such samples using the higher level triggers could be devised.

15.7.4 *Z* production

15.7.4.1 Cross-section

Besides the absence of final state interactions, the signature of a lepton pair from the production of a *Z* boson provides an unambiguous identification, in contrast to jet physics. Compared to the case of *W* boson production, for *Z* bosons the kinematics can be reconstructed accurately, since there is no neutrino carrying part of the boson momentum.

The cross-section for *Z* production at LHC energies is expected to have a contribution of more than 10% due to $s\bar{s}$ initial states. The product $x_1 \cdot x_2$ of the parton momenta is fixed to a value of about 4×10^{-5} at leading order. The major background sources are similar to the ones relevant for the inclusive *W* production (see Section 15.7.3.1). The experimental selection of *Z* production in ATLAS will be based on triggers requiring two leptons (electrons or muons), where a detailed description can be found in Section 11.7. This restriction to the clean leptonic decay mode of the Z is possible due to the large statistics expected for the LHC.

15.7.4.2 p_T distribution

Figure 15-46 shows the cross-section for production of *Z* bosons as a function of the transverse momentum $p_T{}^Z$, as obtained from a next-to-leading order calculation, including the resummation of large logarithms in the q_T space [15-140]. The various approaches to calculate the transverse momentum have been discussed for the case of *W* boson production in Section 15.7.3.3. The parton distribution MRS-R1 [15-141] has been used. For the decay leptons (electrons or muons) a minimal transverse momentum of 20 GeV was required and the leptons had to be produced within $|\eta| < 2.5$. The invariant mass of the lepton pair had to be within ±6 GeV of the nominal *Z* boson mass. The corresponding cross-section for larger transverse momentum of the *Z* boson is shown in Figure 15-47, both for the Ellis-Veseli calculation and the leading order calculation from PYTHIA (including parton showers and fragmentation effects). A cross-check with ISAJET gave cross-sections consistent with the ones obtained from PYTHIA.

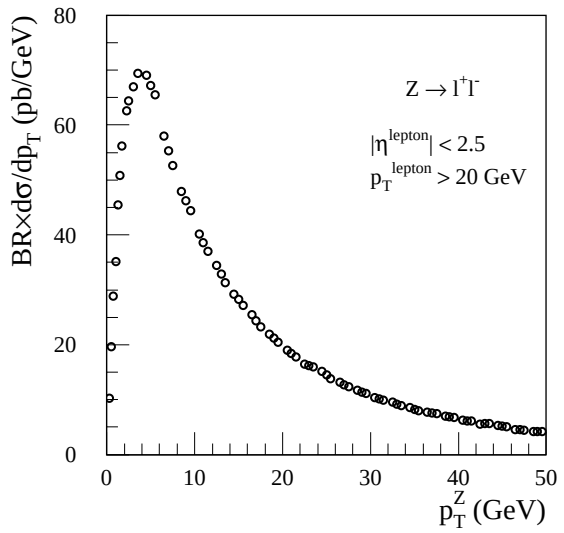

Figure 15-46 Differential cross-section for Z production (decay into either an electron or a muon pair) as a function of the transverse momentum p_T^Z of the Z boson from a next-to-leading order calculation including resummation of large logarithms.

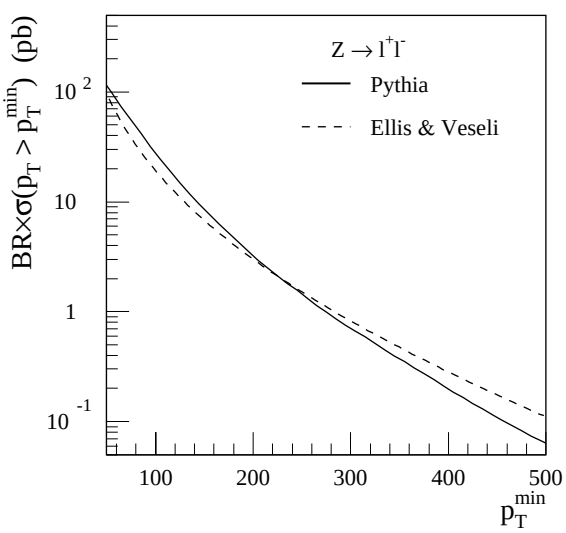

Figure 15-47 Cross-section for Z production (decay into either an electron or a muon pair) as a function of the minimum transverse momentum p_T^{min} of the Z boson from a NLO calculation (Ellis and Veseli) and from a leading order calculation (PYTHIA).

15.7.4.3 Forward-backward asymmetry

In Figure 15-48 the expected forward-backward asymmetry of Drell-Yan lepton pair production in the mass region of the Z resonance is shown as a function of the Z boson rapidity. The asymmetry A_{FB} is defined as the ratio of cross-sections $A_{FB} = (\sigma_F - \sigma_B)/(\sigma_F + \sigma_B)$, where $\sigma_{F/B} = \int_{0/-1}^{1/0} (d\sigma/d\cos\hat{\theta}) d\cos\hat{\theta}$ is the integrated cross-section for the angular distribution in the lepton pair centre-of-mass system. The prediction has been obtained using PYTHIA with the CTEQ2L parton distribution set and requiring the leptons to have $p_T > 20$ GeV and $|\eta| < 2.5$. The lepton pair mass had to be within ±6 GeV of the nominal Z boson mass. The errors shown correspond to the statistical uncertainty for an integrated luminosity of 30 fb^{-1}.

At the Tevatron, the measurement of the forward-backward asymmetry by CDF [15-151] has been used to determine the effective Weinberg angle $(\sin\theta_W)^2$. The determination of the effective Weinberg angle requires the subtraction of contributions to A_{FB} from background

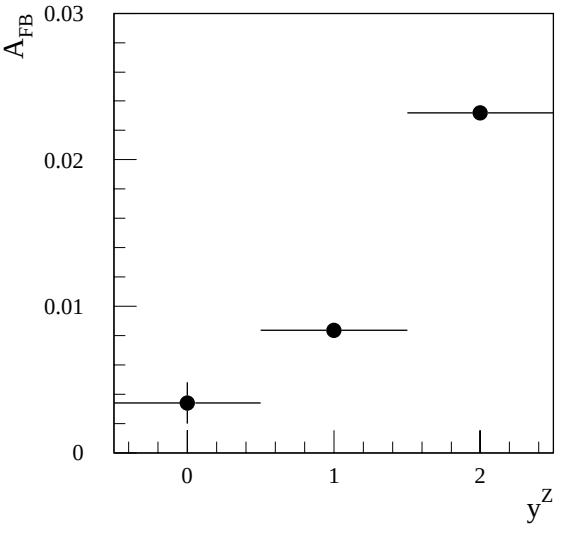

Figure 15-48 Expected forward-backward asymmetry of Z production as a function of the Z boson rapidity y^Z. For the PYTHIA (and ATLFAST calculation, the following cuts have been applied: $|\eta| < 2.5$, $p_T > 20$ GeV and $|M_{ll} - M_Z| < 6$ GeV.

processes as well as from higher QCD, QED and weak processes. The measurement performed by CDF reached a systematic uncertainty of about 1% on $(\sin\theta_W)^2$. This uncertainty is dominated by the uncertainty on the knowledge of the QCD background and on the QCD corrections.

15.7.4.4 *Z* + jet production

The exclusive production of a *Z* boson with *n* associated jets (*n* = 1,2,3,...) is known at leading order[15-142] while the inclusive production of a *Z* boson with at least one associated jet has been calculated at next-to-leading order[15-84]. An accurate measurement of *Z* + jet production can be used (in the case of four jets) to normalise the background from *W* + 4 jets to top quark production in the case of a single lepton and *b*-tag final state. In addition for gluino pair production leading to final states with four jets and missing E_T, the dominant background from the standard model is *Z* + 4 jet production, with an invisible decay of the *Z* to neutrinos. The calculation of the ratio of *W* + 4 jet to *Z* + 4 jet process [15-152] is insensitive, for Tevatron energies, to experimental cuts and theoretical ambiguities. Both processes are also calculated including heavy quark flavour identification.

15.7.5 Gauge boson pair production

15.7.5.1 *WW* and *ZZ* production

The production of gauge boson pairs [15-153] is used to study the triple gauge boson couplings (the result of the non-Abelian nature of the theory) and to derive limits on new interactions in Chapter 16. Boson pair production in hadronic collisions is dominated by the quark-antiquark annihilation process. In the case of *ZZ* and *WW* production the gluon-gluon fusion process also contributes (at $O(\alpha_s^2)$). However, even at LHC energies, it never dominates the $q\bar{q}$ annihilation. The experimental selection of gauge boson pair production will use criteria very similar to the inclusive *W* and *Z* production, based on leptonic decay modes. A detailed study of the *ZZ* production is important as the final state *ll*νν from *ZZ* represents a background to Higgs searches.

The production of *WW* boson pairs is in leading order due to the process $q\bar{q} \rightarrow WW$, either via *t*-channel quark exchange or via *s*-channel production of a γ^*/Z boson. The detection of the *WW* pair can proceed via a leptonic final state (*lνl'*ν') or semi-leptonic (*lνqq̄*).

The calculation of the cross-section for the pair production of the heavy gauge bosons has been performed in NLO. The results [15-154] are given for the following cuts: $p_T^l > 25$ GeV, missing transverse momentum > 50 GeV, $|\eta| < 3$ and an isolation cut for the leptons. At LO, the cross-section for *ZZ* production is found to be 36 fb, at NLO it increases to 43 fb. In the case of W^+W^-, the values are 470 fb at LO and 960 fb at NLO. The calculation has also includes results on kinematical distributions, like the transverse momentum spectrum for a pair of gauge bosons with (or without) an associated jet.

In Figure 15-49 the cross-section for *WW* production is shown as a function of the transverse momentum of the lepton from the *W* decay. The following cuts have been applied: the leptons (*l* = *e*, μ) are required to have a minimal transverse momentum of 20 GeV and have to be within $|\eta| < 2.5$. A missing transverse energy of at least 20 GeV is demanded in addition. The calculation is based on [15-155]; shown are the results at leading order and at next-to-leading order. Figure 15-50 shows the corresponding cross-section as a function of the missing transverse momentum. For a lepton transverse momentum of 100 GeV, the *K*-factor is about 1.5 and rises to

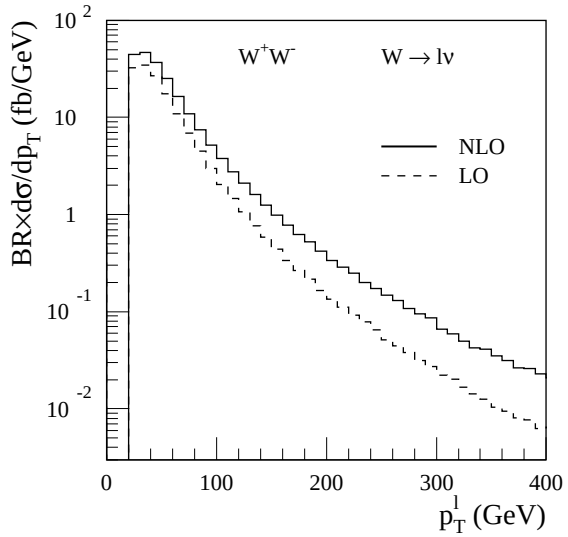

Figure 15-49 Differential cross-section for W^+W^- production and decay to leptons (where $l = e, \mu$) at leading and next-to-leading order as a function of the lepton transverse momentum p_T^l for the following cuts: $|\eta^l| < 2.5$, $p_T^l > 20$ GeV and $p_T^{miss} > 20$ GeV.

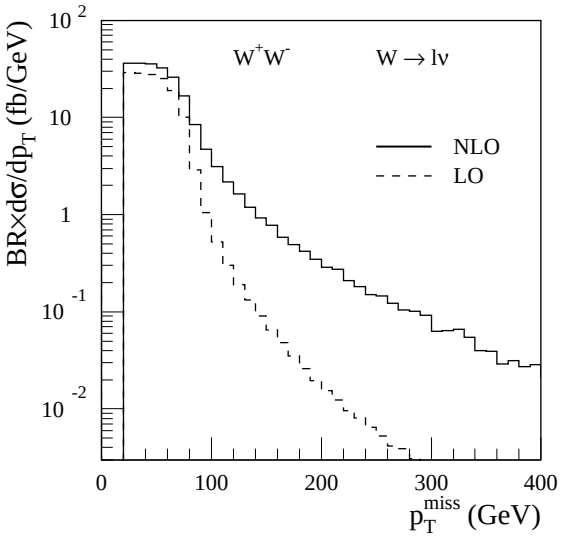

Figure 15-50 Differential cross-section for W^+W^- production and decay to leptons (where $l = e, \mu$) at leading and next-to-leading order as a function of the missing transverse momentum p_T^{miss} for the following cuts: $|\eta^l| < 2.5$, $p_T^l > 20$ GeV and $p_T^{miss} > 20$ GeV.

about three at $p_T = 400$ GeV. At a missing transverse momentum of 300 GeV, a huge *K*-factor of about 90 is obtained. These *K*-factors (which change also the shape of the distribution) are partially due to the appearance of real emission diagrams at next-to-leading order ($q\bar{q} \rightarrow WWg$ and $qg \rightarrow WWq$). In the latter diagram, one *W* boson is produced at large transverse momentum and recoils against the *q*, which radiates a soft *W* boson (almost collinear to the quark).

The selection criteria for the pure leptonic final state require two isolated leptons (*ee*, *e*μ, μμ) together with missing transverse energy to account for the neutrinos. The dominant background is due to top pair production (being larger than the *WW* signal), to a lesser extent also $Z \rightarrow \tau\tau$ and Drell-Yan production of *ee* and μμ contribute. Further sources of background include the production of multi-jets or *W* + jets, where jets are misidentified as electrons or heavy quark production whose decay leads to muons in the final state.

In case of the final state with two jets, the efficiency to resolve the two jets from the *W* decay drops significantly for values of $p_T^W > 200$ - 300 GeV (as discussed in Section 9.3.1). The production of a W boson with two or more associated jets dominates as background, multi-jet configurations with a jet being misidentified as an electron and with missing transverse energy can fake this signature too.

A next-to-leading order calculation of *ZZ* production [15-119] with subsequent decay to an electron pair and a muon pair has been performed restricting the leptons to $p_T^l > 25$ GeV, $|\eta^l| < 3$, requiring a separation of at least 0.4 in η–φ between the leptons and missing transverse energy of at least 50 GeV. The range in pseudo-rapidity for the leptons is slightly larger than the actual acceptance of $|\eta| < 2.5$. In Figure 15-51 the cross-section for the production of *ZZ* pairs is shown as a function of the invariant mass of the *ZZ* pair, in Figure 15-52 the cross-section for *ZZ* production is shown as a function of the transverse momentum of the *Z* boson. The calculation is based on the full NLO contributions, including a resummation of large logarithmic terms due to soft gluon radiation. For an integrated luminosity of 30 fb^{-1}, about 5×10^5 *ZZ* pairs are ex-

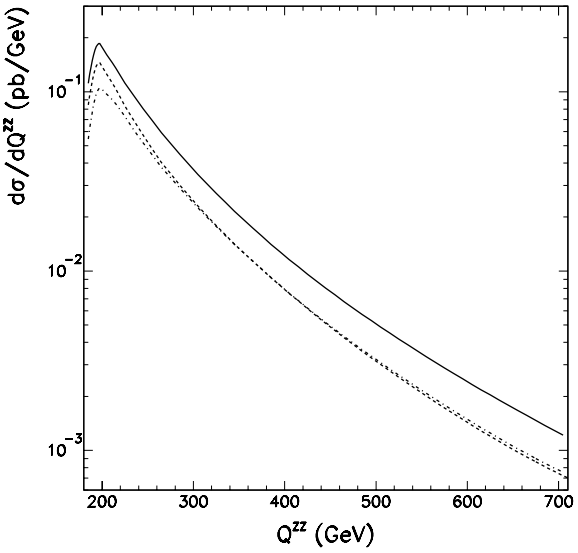

Figure 15-51 Cross-section for ZZ production as a function of the invariant mass Q^{ZZ} of the ZZ boson pair for a resummed calculation (from [15-119]). The cuts used in the calculation are: $p_T^l > 25$ GeV, $|y| < 3$ and $p_T^{miss} > 50$ GeV. The solid line shows the NLO results, the other curves are explained in the text.

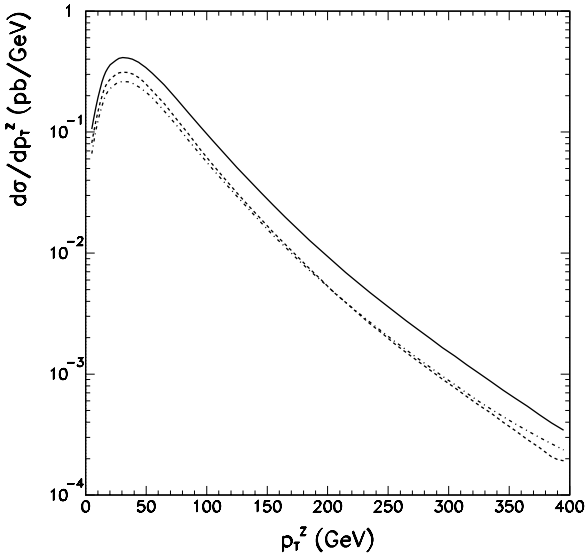

Figure 15-52 Cross-section for ZZ production as a function of the transverse momentum p_T^Z of one Z boson for a resummed calculation (from [15-119]). The cuts used in the calculation are: $p_T^l > 25$ GeV, $|y| < 3$ and $p_T^{miss} > 50$ GeV. The solid line shows the NLO results, the other curves are explained in the text.

pected to be produced at the LHC. For both figures, the rapidity of the Z boson produced has been restricted to $|y| < 3$, giving a total cross-section of 14.8 pb (with the CTEQ4M parton distributions), which is dominated by the $q\bar{q}$ initial state (10.9 pb) wrt the qg initial state (3.9 pb). The leading order contribution amounts to about 9 pb (for the CTEQ4L parton distributions). In both figures, the solid curve represents the full calculation, the dashed curve the contribution from the $q\bar{q}$ initial state and the dash-dotted curve the leading order part for the $q\bar{q}$ initial state.

15.7.5.2 $W\gamma$ and $Z\gamma$ production

The measurement of $W\gamma$ production can be used to probe to the $WW\gamma$ coupling. A typical selection will require a final state with a lepton, a photon and missing transverse energy. The dominant background source is due to W + jet production, where the jet fakes a photon. Smaller contributions are expected from $Z\gamma$ production and $W\gamma$, where the W decays via $\tau\nu$ to $l\nu\nu$. The calculation of $W\gamma$ production has been performed at NLO for several differential distributions [15-156]. An additional study at next-to-leading order has investigated the rapidity correlations between the lepton and the photon at LHC energies [15-157]. Using cuts on the photon ($p_T > 100$ GeV and $|\eta| < 2.5$), on the lepton ($p_T > 25$ GeV and $|\eta| < 3$), demanding a separation of at least 0.7 in η–ϕ between the lepton and the photon and requiring missing transverse energy of at least 50 GeV, it has been found that the QCD corrections lead to a K-factor of about 3. Although the actual acceptance in pseudo-rapidity is slightly smaller ($|\eta| < 2.5$), none of the conclusions will change. The differential distribution of the rapidity difference between photon and lepton shows that at the LHC the radiation zero amplitude is obscured by NLO corrections. The radiation zero amplitude (at parton level all helicity amplitudes vanish at lowest order for a certain value of the scattering angle between quark and photon) is one reason for the large K-

factor. A second reason is the collinear enhancement in $qg \rightarrow qW\gamma$, where a soft W is radiated off the quark (at the LHC the qg luminosity is large). As in the case of WW, this real emission diagram appears only at next-to-leading order.

The production of $Z\gamma$ can be used to study the triple boson couplings of $ZZ\gamma$ and $Z\gamma\gamma$, which at tree level in the Standard Model are zero. A similar selection as in the case of $W\gamma$ is required, except for the missing energy cut, which is replaced by demanding a second charged lepton. Background from Z + jet events, where the jet fakes a photon or an electron (in the latter case, this is being misidentified as a photon) dominates. Smaller contributions are due to multi-jet production and direct photon production. A calculation of the differential cross-section as a function of the transverse momentum of the photon at next-to-leading order, including the decay of the Z to leptons is available [15-158]. Applying the following cuts on the photon ($p_T^{\gamma} > 100$ GeV, $|\eta^{\gamma}| < 3$, isolation), on the leptons ($p_T^{l} > 20$ GeV, $|\eta^{l}| < 3$) and requiring a separation of at least 0.7 in η–ϕ between the photon and each lepton and an invariant mass of the photon-lepton pair of at least 100 GeV, a K-factor between 1.4 (for $p_T^{\gamma} = 100$ GeV) and 2 ($p_T^{\gamma} = 1$ TeV) is found. A previous calculation [15-159] gave a total cross-section of 230 fb at leading order and of 310 fb at next-to-leading order, using the following cuts: $p_T^{\gamma} > 50$ GeV, $|\eta^{\gamma}| < 2.5$, $p_T^{l} > 25$ GeV, $|\eta^{l}| < 3$, a separation of at least 0.7 between lepton and photon and a cut of 15% of the photon energy on the hadronic energy in a cone of 0.7 around the photon direction. As in the case of $W\gamma$ and WZ, the large NLO corrections at high transverse momentum of the photon are due to collinear enhancement in a real emission diagram ($qg \rightarrow Z\gamma q$) and the large qg luminosity at the LHC. The high p_T photon recoils against the quark, which radiates a soft Z boson. Due to the absence of a radiation zero amplitude at tree level, the K-factor for the $Z\gamma$ case is smaller than *e.g.* for $W\gamma$ or WZ.

15.7.5.3 *WZ* production

The measurement of WZ production probes the WWZ coupling. A calculation at next-to-leading order [15-160] is available, including the leptonic decays of the W and of the Z. A leading order cross-section of about 26 fb is obtained, using the following cuts: $p_T^{l} > 25$ GeV, $|\eta^{l}| < 3$, separation in η-ϕ of at least 0.4 between the leptons and missing transverse energy of at least 50 GeV. The total next-to-leading order cross-section (with the same cuts) amounts to about 52 fb. Lowering the cut on the missing transverse energy to 20 GeV increases the cross-section to about 81 fb at leading order. In Figure 15-53 the cross-section for WZ production as a function of the missing transverse momentum is shown, in Figure 15-54 the corresponding distribution as a function of transverse momentum of the lepton. The following cuts have been applied: the leptons ($l = e,\mu$) are required to have a minimal transverse momentum of 20 GeV and have to be within $|\eta| < 2.5$. A missing transverse energy of at least 20 GeV is demanded in addition. Both figures show large NLO corrections for large transverse momenta, *e.g.* for the lepton transverse momentum dependence the K-factor is about 2 at 100 GeV and rises to more than 5 at 400 GeV. In the case of the missing transverse momentum dependence, the K-factor amounts to about 4 at 400 GeV. The reason for these large K-factors is on one hand due to the radiation zero amplitude at tree level and on the other hand due to a collinear enhancement in the process $q_1 g \rightarrow WZq_2$, where at large p_T of the Z boson this is balanced by the quark, which then radiates a soft W boson. These real emission diagrams only appear at next-to-leading order and are further enhanced due to the large qg luminosity at the LHC.

For the final state of a lepton pair and an additional charged lepton at the Tevatron the CDF collaboration has one candidate event with three electrons and missing transverse energy [15-161]. The dominant background source for this channel is similar to the WW production for the semi-leptonic final state.

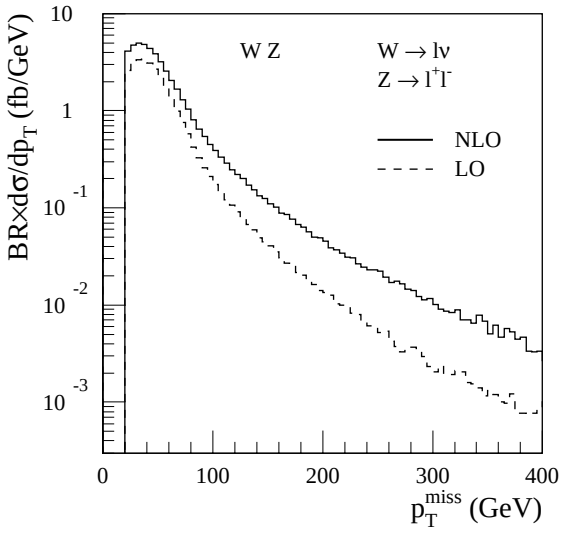

Figure 15-53 Differential cross-section for *WZ* production and decay to leptons (where $l = e, \mu$) at leading and next-to-leading order as a function of the missing transverse momentum p_T^{miss} for the following cuts: $|\eta^l| < 2.5$, $p_T^l > 20$ GeV and $p_T^{miss} > 20$ GeV.

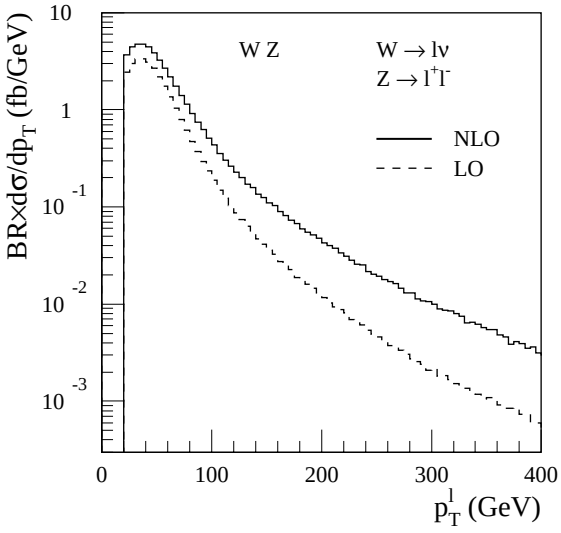

Figure 15-54 Differential cross-section for *WZ* production and decay to leptons (where $l = e, \mu$) at leading and next-to-leading order as a function of the lepton transverse momentum p_T^l for the following cuts: $|\eta^l| < 2.5$, $p_T^l > 20$ GeV and $p_T^{miss} > 20$ GeV.

15.8 Heavy flavour physics

15.8.1 Overview

Due to the quark mass involved, the production of heavy quarks (charm, bottom and top) provides an important process for the study of perturbative QCD and of the effects of non-perturbative aspects [15-162]. A perturbative approach is justified for large transverse momenta. In Figure 15-55 the differential cross-section for the production of a heavy quark pair is shown as a function of the transverse momentum of the heavy quark for *c*, *b* and *t* quarks (from [15-163], based on the calculations of [15-164] and [15-165]). Except for very small p_T ($p_T < 20$ GeV) the cross-sections for charm and bottom production are identical, showing that for transverse momenta much larger than the quark mass effects of the quark mass can be neglected. When higher-orders than NLO are included, the spectrum for *c* quarks is expected to become softer and differ-

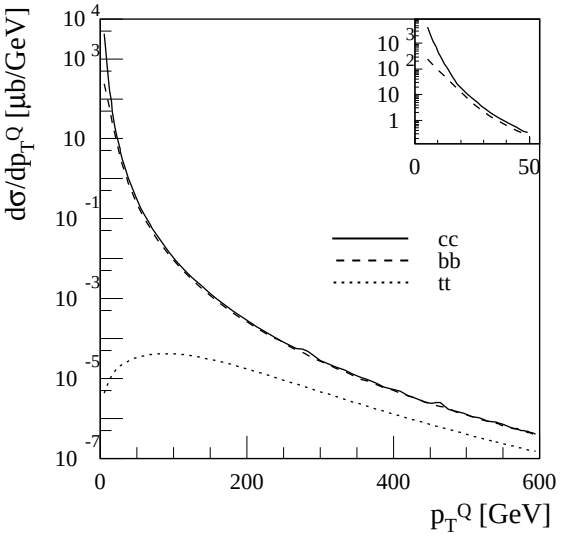

Figure 15-55 Differential cross-section for heavy quark pair production as a function of the transverse momentum p_T^Q of the heavy quark (for charm, bottom and top pair production, from [15-163]). The smaller figure shows for charm and bottom production the region of $p_T^Q < 50$ GeV.

ences might be visible even for larger p_T values. The total cross-sections for charm production is 7.8 mb, the one for bottom production 0.5 mb. The top-pair production cross-section is only 0.8 nb.

In this section, the production of charm quarks is discussed first (Section 15.8.2), concentrating mainly on the production of charmonium states (J/ψ and ψ'). Next, the production of b quarks is discussed (Section 15.8.3), where the emphasis lies on open bottom production, related to the studies of B physics as discussed in Chapter 17. Finally, the QCD related issues of top pair production will be presented (Section 15.8.4).

15.8.2 Charm production

15.8.2.1 Prompt J/ψ production

The direct production of J/ψ mesons can be studied due to the availability of vertexing detectors, which allow the separation of the contribution due to the production of B mesons with subsequent decay into final states containing a J/ψ. Further background is due to the production of χ_c mesons [15-166], which decay radiatively to a J/ψ meson. Measurements at the Tevatron [15-167],[15-168] have shown that the prediction of the colour-singlet model underestimates the data. This model uses perturbative QCD for the production of a colour-singlet state for the $c\bar{c}$ pair, which then can hadronise in a non-perturbative way to a charmonium state.

The discrepancy of the Tevatron data from this prediction led to a modified approach [15-55]; firstly all diagrams of perturbative QCD leading to a $c\bar{c}$ state are taken into account, whether or not the state forms a colour-singlet. Next the transformation of this state into a colour-singlet state is performed, assuming non-perturbative processes [15-169] (*e.g.* the colour-octet state is changed into a singlet state by emission of a very soft gluon). This leads to an expected similarity in the shape of the p_T distribution for different charmonium states, which is supported by the data. These models were then tuned to the data obtained at the Tevatron and subsequently used to extrapolate to LHC energies. This assumes that the non-perturbative contributions are universal.

Figure 15-56 shows the cross-section for direct J/ψ production (times the branching ratio for the decay to muons) [15-170] as a function of p_T. The calculation uses the CTEQ2L distribution and a cut on $|y| < 2.5$. The cross-section is decomposed into the contributions from the colour-singlet part and two colour-octet parts, which appear in the expansion as a function of the relative velocity of the two quarks: the ${}^1S_0^{(8)}$ '+' ${}^3P_J^{(8)}$ part and the ${}^3S_1^{(8)}$ part. These in total three parts can be determined from the Tevatron data and are then used to make the predictions shown above.

15.8.2.2 Prompt ψ(2S) production

In Figure 15-57 the cross-section for direct ψ' production [15-170] is shown, as a function of the p_T of the ψ' meson. The rapidity acceptance for the mesons is restricted to $|y| < 2.5$ and the CTEQ2L distribution has been used. For comparison, the cross-section for J/ψ production is also shown. Both give a similar shape and differ by about a factor of ten in absolute value.

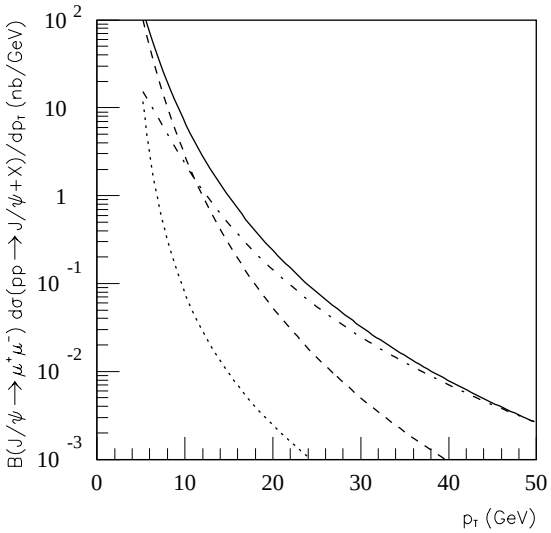

Figure 15-56 The cross-section for direct *J/ψ* production (with the decay to two muons) at the LHC a function of the *J/ψ* transverse momentum (from [15-170]). Shown are the total cross-section (solid), the colour-singlet contribution (dotted) and two colour-octet contributions (dashed for the ${}^1S_0^{(8)}$ '+' ${}^3P_J^{(8)}$ contribution and dot-dashed for the one of ${}^3S_1^{(8)}$).

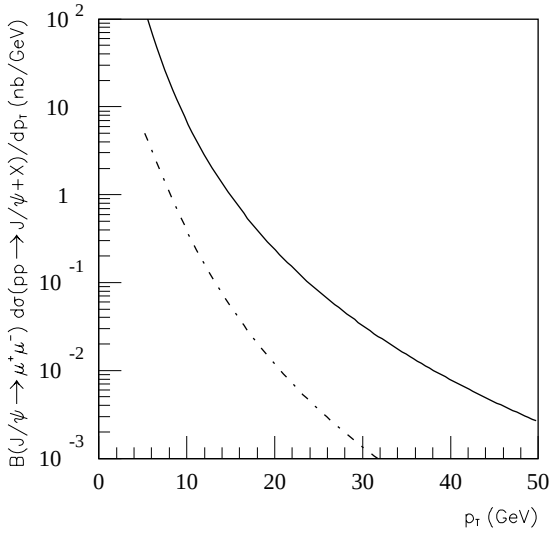

Figure 15-57 The cross-section for direct ψ' production (with the decay to two muons, the dash-dotted line) at the LHC as a function of the ψ' transverse momentum (from [15-170]). Also shown is the corresponding cross-section for *J/ψ* production (the solid line) as a function of the *J/ψ* transverse momentum.

15.8.2.3 Production of J/ψ with a photon or a massive vector boson

The associated production of a *J/ψ* meson at the LHC, together with a photon, should not be dominated by fragmentation contributions up to p_T values of 50 GeV [15-171]. This should be due to the fact that $q\bar{q}$ initial states are suppressed at the LHC. The more abundant *gg* initial states do not contribute to this process at leading order, higher order corrections are expected to be negligible. The expected differential cross-section (with the restriction $|y| < 2.5$) ranges from about 0.1 pb / GeV for p_T = 20 GeV to 0.5 nb / GeV at 100 GeV transverse momentum. A further possibility is the associated study of the production of *J/ψ* mesons with a *W* or *Z* boson, as discussed in [15-172], which can be used to cross-check the predictions of the colour octet model.

15.8.2.4 Open $c\bar{c}$ production

As discussed in [15-55], the production of open charm (*i.e.* the production of $D\overline{D}$ pairs) is expected to show a similar kinematical dependence on x_F as the production of *J/ψ* mesons. This can be used as a further constraint to verify predictions of different models. The experimental challenge is the selection of a sample of open charm production. When the *D* meson decays are reconstructed via π and *K* final states, there is no trigger available to select these. One possibility would be to use a sample of minimum-bias events (selected either by a trigger on random bunch crossings or by a trigger using information from dedicated detectors in the forward region, as mentioned in Section 15.3.2) where $c\bar{c}$ should contribute to a sizeable fraction of the total cross-section. To enrich this sample of events, it could be helpful to do a reconstruction of

charged tracks in the Inner Detector at the higher trigger levels and to pre-select *D* meson decay candidates. Further studies have to be performed in order to quantify the possible reach of such a selection.

15.8.3 Bottom production

15.8.3.1 Prompt Υ production

The production of bottomonium states should proceed either directly or via the decay of higher mass $b\bar{b}$ states. It exhibits similar discrepancies with respect to the predictions of the colour-singlet model. The cross-sections measured at the Tevatron for the production of the Υ(1S), Υ(2S) and Υ(3S) states [15-173] are larger then the predicted ones, with the discrepancy factor depending on the transverse momentum of the Υ resonance and increasing with increasing p_T (exceeding a factor of ten in the case of the Υ(1S)). An advantage of using Υ production, with respect to the production of charmonium states, is the possibility to reach smaller transverse momenta in case of the Υ, due to experimental selection requirements.

The associated production of an Υ meson together with a *W* or *Z* boson has been proposed [15-174] as a possible check for different model predictions. The dominant contribution to this process is expected from the production of a $b\bar{b}$ colour-octet state, which then binds to a *P*-wave state, that subsequently decays to an Υ. The expected cross-section amounts to 44 fb for Υ + *W* and 7 fb for Υ + *Z* production. This channel could also be used to search for heavy particles, decaying into a *W* or *Z* boson together with a $b\bar{b}$ pair.

15.8.3.2 Beauty production features

ATLAS will observe *B*-hadrons produced in proton-proton collisions at $\sqrt{s}$ = 14 TeV in the central rapidity region, $|\eta| < 2.5$. The lower limit for the *B*-hadron transverse momentum $p_T(B)$ is set by the trigger requiring a muon with $p_T(\mu) > 6$ GeV. This corresponds to approximately $p_T(B) > 10$ GeV. The specific property of this kinematical region is that beauty production should be governed mostly by perturbative QCD. Contributions from non-perturbative diffractive processes are expected to be small, and the interaction between the reaction products and the beam remnants is negligible.

The observed particle spectra represent a composite effect of three factors: the parton densities, the hard partonic subprocess and the hadronisation or fragmentation. The quark distribution functions are measured precisely in deep-inelastic scattering (see Section 15.2) over a range in x from 10^{-1} to 10^{-5}, which fully includes the range $10^{-4} < x < 10^{-1}$ accessible in *B* production at ATLAS. The fragmentation functions are clearly determined at LEP in e^+e^- annihilation. In the cases when the hard QCD dynamics is well understood, LHC gives access to direct measurements of gluon densities by means of the dominant gluon-gluon fusion process.

The present experimental results at Fermilab [15-175][15-176] indicate that the theory of beauty production is still not complete, suggesting important contributions from higher-order corrections beyond the LO and NLO calculations [15-164][15-177]. At the phenomenological level, the higher-order QCD contributions are interpreted in terms of additional production mechanisms, such as the Flavour Excitation and Parton Showering [15-14]. Methods of experimental separation of different production mechanisms based on the observation of specific phase space regions are discussed in the next sections.

15.8.3.3 Single *b* differential cross-section

The inclusive single *b* quark (or *B*-hadron) distributions together with the total visible production cross-section provide the simplest test of theoretical consistency. Typically the shape of the differential cross-section $d^2\sigma / dp_T d\eta$ shows only little sensitivity to the details of the production mechanism. The difference between models is mainly in the overall cross-section normalisation and usually does not exceed the inherent theoretical uncertainties. In this sense, the single *b* distributions can not be easily used to discriminate between different theories, unless a significant discrepancy is observed.

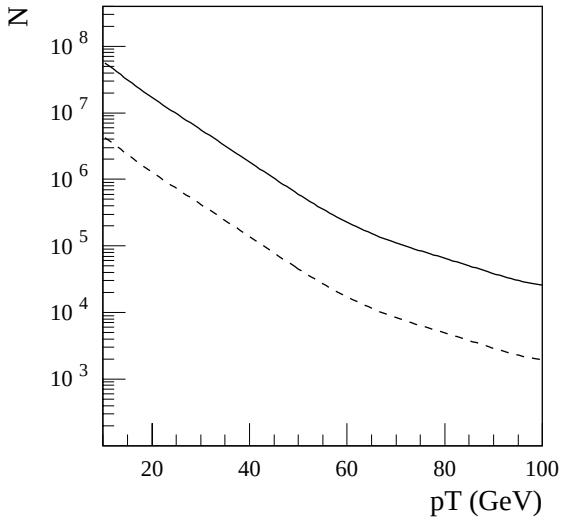

Figure 15-58 Number of reconstructed inclusive and exclusive *B*-hadron decays to $J/\psi(\mu\mu)$ for 30 fb^{-1}, as a function of the minimum transverse momentum of the *B*-hadron. The solid line corresponds to inclusive events ($b\bar{b} \rightarrow J/\psi\, X$ with $J/\psi \rightarrow \mu\mu$). The sum of the following exclusive channels is shown as the dashed line: $B_d \rightarrow J/\psi\, K^0(\pi\pi)$, $B_d \rightarrow J/\psi\, K^{0*}(K^+\pi^-)$, $B^+ \rightarrow J/\psi\, K^+$, $B_s \rightarrow J/\psi\, \phi(KK)$ and $\Lambda_b \rightarrow J/\psi\, \Lambda^0(p\pi^-)$, always with $J/\psi \rightarrow \mu\mu$.

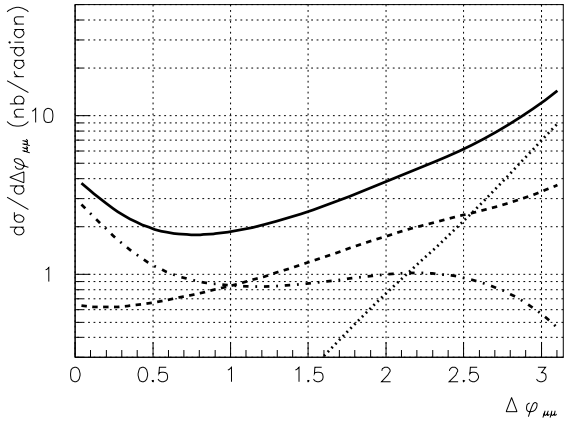

Figure 15-59 Azimuthal μμ correlations at the LHC (from [15-179]). Shown are the different mechanisms contributing in PYTHIA to the $\Delta\phi_{\mu\mu}$ spectrum: flavour excitation $gb \rightarrow gb$ (dash-dotted curve), gluon–gluon fusion $gg \rightarrow b\bar{b}$ (dotted curve), gluon–gluon scattering followed by gluon splitting $gg \rightarrow gg$ with $g \rightarrow b\bar{b}$ (dashed curve) and the sum of all contributions (solid curve).

Due to a large beauty production cross-section and a selective trigger, ATLAS can reconstruct large samples of exclusive *B*-hadron decays. Statistically dominant, with the trigger criteria that have been considered so far, are the exclusive channels with $J/\psi \rightarrow \mu\mu$ (Figure 15-58), which will allow measurements up to $p_T \sim 100$ GeV with negligible statistical errors (about 2000 events with $p_T > 100$ GeV). The region of higher p_T can be covered by inclusive $J/\psi \rightarrow \mu\mu$ measurements. It has been shown that a J/ψ vertex cut will remove the direct J/ψ contribution. A comparison with exclusive decays can be used for calibration.

Using $b\bar{b} \rightarrow J/\psi(\mu\mu)\, X$ events (where the *b* quark was required to have a transverse momentum larger than 40 GeV), which were passed to a full detector simulation, the efficiency for the reconstruction of muons using the combined information from the muon chambers, the Inner Detector and the calorimeters was studied (for more details on the combined reconstruction procedure see Section 8.1). As seen in Figure 15-60, the muons from the J/ψ decay can be identified with high efficiency, despite the large transverse momentum of the *b* jet. For a transverse momentum of the muon larger than 10 GeV the efficiency reaches a value of about 85%. In

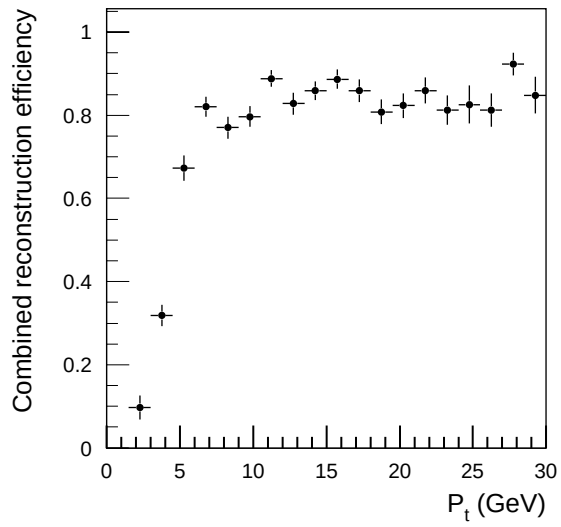

Figure 15-60 Reconstruction efficiency for muons from $b\bar{b} \rightarrow J/\psi(\mu\mu)\,X$ events (with a minimal transverse momentum of the b quark of 40 GeV) as a function of the minimum muon transverse momentum p_T.

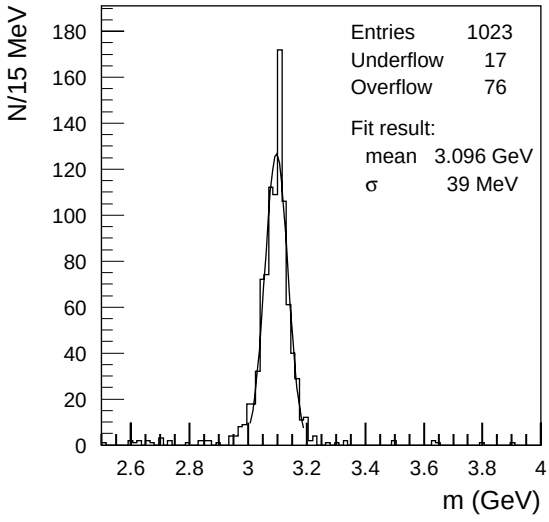

Figure 15-61 Mass resolution for muon pairs from $b\bar{b} \rightarrow J/\psi(\mu\mu)\,X$ events (with a minimum transverse momentum of the b quark of 40 GeV). Shown is the distribution of the invariant mass m of the muon pair.

Figure 15-61 the resolution in the invariant mass of the muon pair is shown, from a fit of a Gaussian a resolution of 39 MeV is obtained. The resolution does not degrade in comparison with the case when the J/ψ is reconstructed from the tracks of the Inner Detector (using information from the event simulation for the identification of the muons, as discussed in Section 6.6.1 of [15-178]). The probability to lose an event due to the matching of a muon (from the muon system) to a wrong track in the Inner Detector is only about 10%, leading to events where the invariant mass of the muon pair is outside a 3σ window around the nominal J/ψ mass. This is the result of a first study, where further improvements, especially on the loss of events, are expected.

The lower p_T limit on channels with $J/\psi \rightarrow \mu\mu$ comes from the muon trigger and muon identification performance. There are exclusive channels with electrons and hadrons reconstructed with $p_T < 10$ GeV, but they are biased by a LVL1 p_T cut on the muon coming from the associated B hadron. These events can be used for b-$\bar{b}$ correlation measurements, as discussed below.

15.8.3.4 $b - \bar{b}$ correlations

The correlations between the b and $\bar{b}$ quarks are usually presented in terms of the azimuthal angular difference $\Delta\phi$. In Figure 15-59 the expected azimuthal correlation $\Delta\phi_{\mu\mu}$ between the muons from the b and $\bar{b}$ decay is shown, which can be used to get information about the correlation between the b and $\bar{b}$. The domain of back-to-back kinematics, $\Delta\phi_{\mu\mu} \sim \pi$, is mostly populated by the LO QCD contribution. On the contrary, the effects of higher orders are most pronounced in the deviations from this back-to-back configuration. The region of $\Delta\varphi_{\mu\mu} \sim 0$ is free of the LO contribution, and so is only sensitive to the NLO contributions.

b-$\bar{b}$ correlations can be measured by full reconstruction of one of the associated B hadrons and by the inclusive reconstruction (lepton) of the other B hadron (see Section 17.1.1). After the exclusive reconstruction of a B hadron, no isolation cuts are needed to separate an accompanying lepton. This type of event gives a possibility to detect b and $\bar{b}$ quarks produced close to each other. There will be approximately 5×10^5 events of this type after three years, however, they are

mostly concentrated at $\Delta\varphi \sim \pi$, with only a minor part contributing to the region of interest $\Delta\varphi \sim 0$. Besides that, the angular correlations should be studied for different transverse momenta of b and $\bar{b}$ quarks. All this requires high statistics, which can be obtained by an inclusive reconstruction of J/ψ from B hadrons and a lepton from the semileptonic decays of the associated anti-B hadrons. The argument for not requiring the lepton to be isolated from J/ψ is still valid. The expected number of events as listed in Table 15-1 is of the order of 6×10^6. The exclusive decays can be used for calibration. For large transverse momenta the statistics can be extended by using inclusive events with two muons of opposite charge coming from semileptonic decays of two B hadrons. The selection of these events at the trigger is under study; as discussed in Section 11.6 the second level trigger is capable to accept the expected rate of two muon events. Requiring for the second muon a threshold of $p_T(\mu) > 5$ GeV will give in 3 years of the order of 10^9 events (after the second level trigger) with two muons from $b\bar{b}$ events (including the contribution from minimum bias events). More studies are needed to assess the final contribution from $c\bar{c}$ production and from π/K decays.

Table 15-1 Expected number of inclusive $b\bar{b} \rightarrow J/\psi X$ events (where the J/ψ decays to leptons) reconstructed after 3 years. These events will be used for $b - \bar{b}$ correlations studies. For each inclusive channel the number of exclusive events with the same lepton content is given. Here '*had*' denotes any of K^0, K^{0*}, K^+, Λ^0 or ϕ, and '*B*' stands for either B^0, B^+, B_s or Λ_b.

Inclusive decay channel	Number of events for inclusive reconstruction	Exclusive channels with the same lepton content	Number of events in reconstructed exclusive channels
$b\bar{b} \rightarrow \mu\ \ J/\psi(\mu\mu)\ X$	2.8×10^6	$bB \rightarrow \mu\ \ J/\psi(\mu\mu)\ had$	2.1×10^5
$b\bar{b} \rightarrow e\ \ J/\psi(\mu\mu)\ X$	3.6×10^6	$bB \rightarrow e\ \ J/\psi(\mu\mu)\ had$	2.1×10^5
$b\bar{b} \rightarrow \mu\ \ J/\psi(ee)\ X$	0.6×10^6	$bB \rightarrow \mu\ \ J/\psi(ee)\ had$	0.9×10^5

15.8.3.5 Production asymmetry

The B-hadron production asymmetry is defined as the difference of the probabilities of B and $\overline{B}$ hadron production in pp collisions. From the theoretical point of view, the asymmetry can provide information on the effects of soft dynamics during the fragmentation (*i.e.* the soft interactions between the produced b quark and the remnants of the disrupted proton). However, the relevant physical effects are expected [15-14],[15-180],[15-181] to be unimportant [15-182],[15-183] in the central rapidity region covered by ATLAS.

A production asymmetry always occurs at the presence of a *CP*-violation asymmetry originating from the B-hadron decays (see Section 17). In some cases these two effects are expected to be of the same order, for instance in the channels $B^0 \rightarrow J/\psi(\mu\mu)\, K^{0*}$, $B^+ \rightarrow J/\psi(\mu\mu)\, K^+$ and $\Lambda_b \rightarrow J/\psi(\mu\mu)\, \Lambda^0$. These channels are expected to have small CP violation (< 1%) due to interference between the lowest and higher-order decay amplitudes. A method of separation of these two effects is considered, which is based on the fact that the production asymmetry varies with transverse momentum and the rapidity of produced b quark, while the decay process should remain the same.

However, measurements of such small effects will require very good understanding of the possible detection asymmetries. For the selected channels the LVL1 trigger asymmetries due to muon charge are not relevant, as a muon comes from the decay of the J/ψ. In the Inner Detector

the asymmetry may come from differences in hadron reconstruction with opposite charges, *e.g.* due to strong interaction cross-sections. More details on systematic uncertainties can be found in Chapter 17.

15.8.3.6 Production polarisation

The polarisation phenomenon is closely related to the production mechanism and, probably, includes an interplay between 'hard' and 'soft' interactions. This topic is addressed in Section 17.5.

15.8.3.7 Double beauty production

The production of two heavy-quark pairs is a fourth-order QCD process, and so provides a sensitive test of perturbative QCD. The full fixed-order $O(\alpha_s^4)$ calculation [15-184] for $p\,p$ collisions at the LHC gives a cross-section of about 440 nb which contrasts with a value of 3800 nb predicted by PYTHIA. This difference maybe due to an underestimation of higher order effects in the fixed order QCD calculation, together with an overestimation of these by PYTHIA.

Even the larger (PYTHIA) cross-section prediction is, however, too small to allow the double beauty production detection and its separation from the background processes. For the *B* physics studies requiring tagging of *B* flavour it was shown [15-184] that the probability of a wrong tag due to double *b* production will be negligible: 10^{-4} - 10^{-3}, as also discussed in more detail in Section 17.2.2.4.

15.8.4 Top production

15.8.4.1 Total cross-section

Within perturbative QCD, higher order corrections to the total cross-section for top pair production are under control and the scale uncertainty for a NLO calculation is of the order of 10% at Tevatron energies and similar for the LHC. When taking into account a resummation of soft gluon effects [15-185], the uncertainty is decreased to about 5% for LHC energies. The inclusion of the soft gluon resummation leads to an increase of the cross-section for a large scale and even to a decrease at a small scale, thus reducing the scale dependence. The total cross-section for $t\bar{t}$ production (assuming a top quark mass of 175 GeV and using the MRSR2 parton distribution set [15-141]) is 803 pb at NLO and 833 pb for NLO including the NLL resummation [15-185]. In Figure 15-62 the dependence of the total $t\bar{t}$ cross-section on the top mass, m_{top}, is shown for the NLO calculation including the NLL resummation. In addition, the predictions of the NLO+NLL as well as the one of the NLO calculation alone are shown, for setting the scale μ to the values $\mu = 2\mu_0$ and $\mu = \mu_0/2$ (where $\mu_0 = m_{top}$). As mentioned above, the sizeable scale dependence at NLO is reduced when the NLL resummation is included.

An uncertainty of similar size (to the one of the scale uncertainty) arises due to the choice of the parton distribution function. The precision on the measurement of the total cross-section is expected to be dominated by the knowledge of the absolute scale of the luminosity. More details on the experimental selection and the study of systematic uncertainties can be found in Section 18.1.4.1. An error of 5% on the total $t\bar{t}$ cross-section corresponds (when the validity of the NLO+NLL calculation is assumed) to an error of 1% on the top mass.

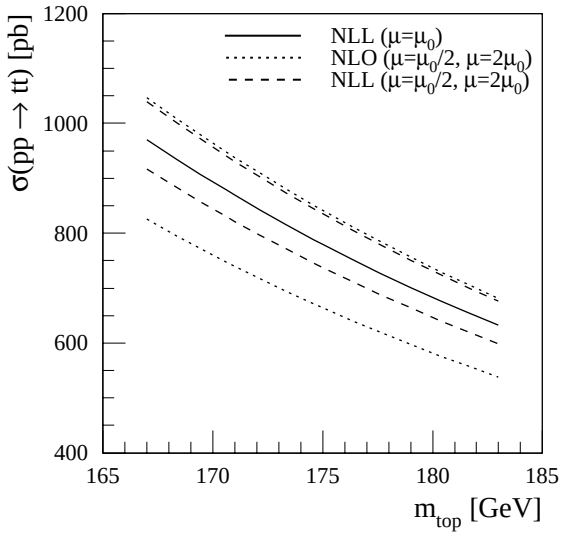

Figure 15-62 Total cross-section for top pair production as a function of the top mass, m_{top}. The solid line shows the cross-section at NLO, including the resummation of soft gluon contributions (NLL), based on [15-185]. The dashed (dotted) line indicates the scale uncertainty for the NLO+NLL (NLO only) calculation.

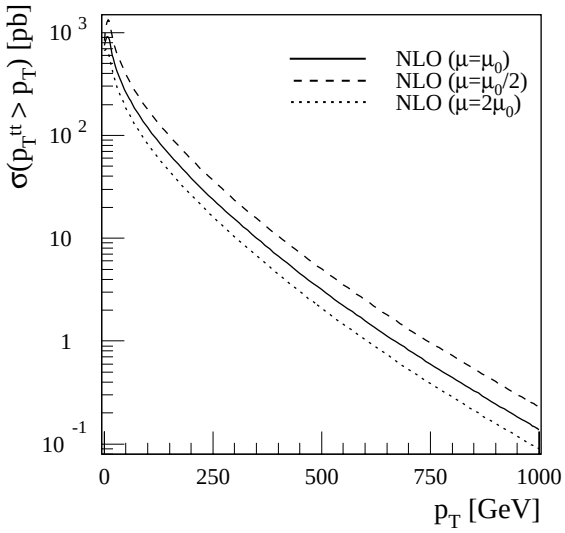

Figure 15-63 Cross-section for top pair production as a function of the minimum transverse momentum of the top pair from a NLO calculation (solid line). The dashed and the dotted lines indicate the scale uncertainty of the NLO calculation [15-177], using the MRST pdf.

15.8.4.2 Inclusive p_T distribution of the $t\bar{t}$ pair

The measurement of the p_T of the top quark for the top pair production is important for the understanding of the top production efficiencies needed for a precise cross-section measurement. In contrast to the measurement of the inclusive p_T distribution for b quark production (which can be done using the inclusive measurement of the transverse momentum of muons), this measurement will start from a reconstructed top quark decay, where details on the cuts for the selection of top quarks are given in Section 18.1.2.

In Figure 15-63 the integrated cross-section for $t\bar{t}$ production is shown as a function of the minimal transverse momentum of the $t\bar{t}$ pair. The NLO calculation [15-177] (using the MRST parton distribution set) is shown for a value of the scale μ being equal to μ_0, where μ_0 is given by $\mu_0^2 = m_{top}^2 + p_{T,\,top}^2$. The scale uncertainty is obtained by choosing the settings $\mu = 2\mu_0$ and $\mu = \mu_0 / 2$ for the scale μ.

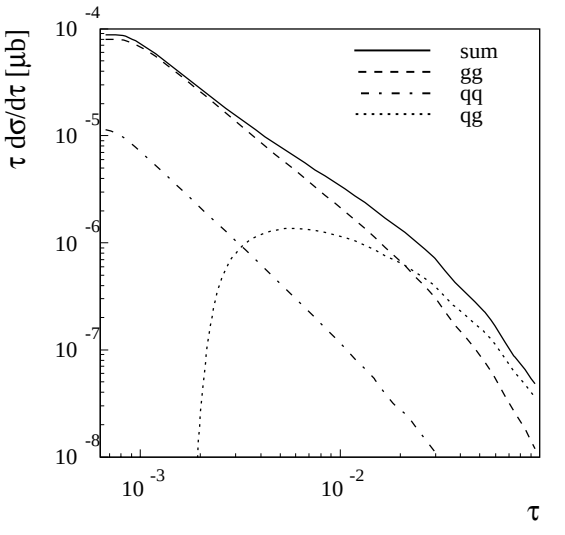

Figure 15-64 Differential cross-section for $t\bar{t}$ production as a function of the normalised centre-of-mass energy $\sqrt{\tau}$ (where $\tau = \hat{s}/s$) of the partonic initial state for the three different parton-parton initial states (from [15-163], using the MRST pdf).

15.8.4.3 $t\bar{t}$ mass distribution

A clarification of possible deviations in the production cross-section regarding new physics needs to study kinematical distributions, like the invariant mass of the $t\bar{t}$ pair. Deviations from the QCD expectation (like new *s*-channel resonances) should give characteristic signatures in the invariant mass distribution. Furthermore the extraction of Higgs decay into $t\bar{t}$ (at low tanβ) requires a precise knowledge of the invariant mass distribution. More details can be found in Section 18.1.4.

The precise measurement of the production of top quark pairs can be used to put constraints on the gluon density. Figure 15-64 shows the differential cross-section for top pair production at the LHC as a function of the normalised hard process centre-of-mass energy $\sqrt{\tau} = \sqrt{x_1 \cdot x_2}$. For value of $\sqrt{\tau} < 0.1$ the cross-section is dominated by the gluon-gluon initial state, for larger values of $\sqrt{\tau}$ the quark-gluon initial state starts to dominate.

15.9 Conclusion

The overview presented in this section illustrates the variety of QCD related processes that can be studied using the ATLAS detector. These measurements are of importance as a study of QCD at the LHC, accessing a new kinematic regime at the highest energy accessible in the laboratory. On the other hand, a precise knowledge and understanding of QCD processes is important for the studies of the Higgs boson(s) and searches for new physics beyond the Standard Model, where QCD represents a large part of the background.

The study of diffractive processes, which allows to access the hard and soft regime of QCD at the same time, presents a significant experimental challenge in the LHC environment and given the limited angular acceptance of the ATLAS detector. More detailed studies are needed to quantify and prove the ideas sketched in this section and to validate the design of the additional detectors envisaged.

At the present stage of these studies of QCD related processes, the possible constraints on parton density functions are difficult to quantify. Given more precise information about the actual measurement range possible and the achievable accuracy (obtained from detailed simulation of the detector response), it will be necessary to perform ‘global fits’ to determine the impact of the LHC measurements. As a further study one should investigate the amount of information on the parton distributions, that can be deduced from the LHC data alone.

Candidate signatures to provide constraints on the quark and anti-quark distributions are the production of *W* and *Z* bosons via the Drell-Yan process as well as lepton pair production in general. On the other hand, the production of direct photons, of jets and of top quarks can be used to get information on the gluon distribution.

The LHC will extend the kinematic range to larger values of Q^2, the hard scale of the partonic process, reaching scales of the order of TeV^2. The fraction of the proton momentum attributed to a parton will allow access to values below 10^{-5}, while keeping the scale above 100 GeV^2, in contrast to HERA measurements, where these small momentum fractions are only reached for hard scales close to or even below 1 GeV^2.

15.10 References

15-1 J.E. Huth and M.L. Mangano, Ann. Rev. Nucl. Part. Sci. **43** (1993) 585.

15-2 R.K. Ellis, W.J. Stirling, B.R. Webber, 'QCD and Collider physics', Cambridge, UK, Univ. Pr. (1996).

15-3 J. Huston, 'QCD at High Energies', plenary talk at the XXIX International Conference on High Energy Physics (ICHEP 98), Vancouver, Canada, 23-29 Jul 1998, preprint hep-ph/9901352 (1999).

15-4 ATLAS Collaboration, Trigger Performance Status Report, CERN/LHCC/98-15 (1998).

15-5 J. Huston, 'LHC Guide to Parton Distribution Functions and Cross Sections', ATLAS Internal Note ATL-PHYS-99-008 (1999).

15-6 H.L. Lai *et al.*, preprint hep-ph/9903282 (1999).

15-7 A.D. Martin *et al.*, Eur. Phys. J. **C4** (1998) 463.

15-8 H.L. Lai *et al.*, Phys. Rev. **D55** (1997) 1280.

15-9 Yu. L. Dokshitzer, preprint hep-ph/9812252, (1998).

15-10 Yu.L. Dokshitzer, Sov. Phys. JETP **46** (1971) 641;
V.N. Gribov and L.N. Lipatov, Sov. J. Nucl. Phys. **15** (1972) 438 und 675;
G. Altarelli and G. Parisi, Nucl. Phys. **B126** (1977) 298.

15-11 E.A. Kuraev, L.N. Lipatov and V.S. Fadin, Zh. Eksp. Teor. Fiz. **71** (1976) 840;
E.A. Kuraev, L.N. Lipatov and V.S. Fadin, Zh. Eksp. Teor. Fiz. **72** (1977) 377;
Ya.Ya. Balitsky and L.N. Lipatov, Yad. Fiz. **28** (1978) 1597.

15-12 W.J. Stirling, 'Structure Functions', Talk given at the LHCC workshop 'Theory of LHC processes', Feb. 1998, CERN.

15-13 G. Marchesini *et al.*, Comp. Phys. Comm. **67** (1992) 465.

15-14 T. Sjostrand, Comp. Phys. Comm. **82** (1994) 74.

15-15 Wu-Ki Tung, 'Perspectives on Global QCD Analyses', in Proceedings of the International Workshop on Deep Inelastic Scattering and Related Subjects, Eilat, Israel (1994), ed. A. Levy, World Scientific Publishing Co., Singapore.

15-16 W.T. Giele and S. Keller, Phys. Rev. **D58** (1998) 94023.

15-17 J. Huston *et al.*, Phys.Rev. **D58** (1998) 1140.

15-18 A.M. Cooper-Sarkar, R.C.E. Devenish and A. De Roeck, Int. J. Mod. Phys. **A13** (1998) 3385.

15-19 L. Apanasevich *et al.*, Phys. Rev. **D59** (1999) 074007.

15-20 G. Ingelman, (ed.), A. De Roeck, (ed.) and R. Klanner, (ed.), 'FUTURE PHYSICS AT HERA', preprint DESY 96-235 (1996), Hamburg, Germany.

15-21 M. Dittmar, F. Pauss, D. Zuercher, Phys. Rev. **D56** (1997) 7284.

15-22 F. Paige and S. Protopopescu, in Supercollider Physics, p. 41, ed. D. Soper, World Scientific, (1986).

15-23 R. Engel, Z. Phys. **C66** (1995) 203;
R. Engel, 'PHOJET manual', preprint SI-95-05, University of Siegen (1995).

15-24 A. Capella *et al.*, Phys. Rep. **236** (1994) 227.

15-25 P. Aurenche *et al*., Phys. Rev. **D45** (1992) 92;
P. Aurenche *et al*., Comp. Phys. Comm. **83** (1994) 107

15-26 A. Kupco, 'MC event generators and their predictions for minimum bias events at LHC energies', ATLAS Internal Note ATL-COM-PHYS-99-023 (1999).

15-27 F. Abe *et al.*, Phys. Rev. **D41** (1990) 2330.

15-28 F. Abe *et al.*, Phys. Rev. Lett **61** (1988) 1819.

15-29 N. Moggi (for the CDF collaboration), Nucl. Phys. B Proc. Suppl. **71** (1999), 221.

15-30 G. Ingelman and P. Schlein, Phys. Lett. **152B** (1985), 256.

15-31 R. Bonino *et al.*, Phys. Lett. **211B** (1988) 239.

15-32 E.L. Berger *et al.*, Nucl. Phys. **B286** (1987) 704.

15-33 J.D. Bjorken, 'Final state hadrons in deep inelastic processes and colliding beams', publ. in Proc. of Int. Symposium on Electron and Photon Interactions at High Energies, p. 281, Cornell, (1971).

15-34 A. Donnachie and P.V. Landshoff, Phys. Lett. **B191** (1987) 309;
A. Donnachie and P.V. Landshoff, 'Hard Diffraction at HERA', Proc. of the HERA Workshop, ed. R.D. Peccei, DESY, Hamburg (1987) 351.

15-35 P. Marage, preprint hep-ph/9810551, (1998).

15-36 A. Donnachie and P.V. Landshoff, Nucl. Phys. **B303** (1988) 634.

15-37 A. Brandt *et al.*, 'A Forward Proton Detector at D0', preprint FERMILAB-Pub-97/377 (1997).

15-38 J.A. Crittenden, 'Exclusive Production of Neutral Vector Mesons at the Electron-Proton Collider HERA', preprint DESY-97-068 (1997).

15-39 C. Adloff *et al.*, Z.Phys. **C76** (1997) 613.

15-40 CDF collaboration (M.G. Albrow, for the collaboration), 'Diffractive Dijet Production in CDF', preprint FERMILAB-CONF-98-134-E (1998).

15-41 CDF collaboration (M.G. Albrow, for the collaboration), 'Di-Jet Production by Double Pomeron Exchange', preprint FERMILAB-CONF-98-138-E (1998).

15-42 B. Abbott *et al.*, Phys. Lett. **B440** (1998) 189.

15-43 F. Abe *et al.*, Phys. Rev. Lett **80** (1998) 1156.

15-44 C. Adloff *et al.*, Eur. Phys. J. **C6** (1999) 587.

15-45 K. Terashi (for the CDF and D0 collaborations), 'Rapidity Gap Results from Tevatron', proceedings 13th Topical Conference on Hadron Collider Physics, Mumbai, India, Jan. 14-20, 1999;
K. Goulianos, 'Diffractive Production of Jets, Di-Jets, W+jets and b', XXXIVe Rencontres de Moriond, Les Arcs, France, Mar. 20-27, 1999.

15-46 L. Alvero *et al.*, preprint hep-ph/9805268 (1998).

15-47 J.C. Collins, Phys.Rev. **D57** (1998), 3051.

15-48 L. Alvero *et al.*, preprint hep-ph/9806340 (1998).

15-49 A. Levy, Phys. Lett. **B424** (1998) 191.

15-50 A. Brandt *et al.*, Nucl. Phys. **B514** (1998) 3.

15-51 F.E. Low, Phys. Rev. **D12** (1975) 163.

15-52 S. Nussinov, Phys. Rev. Lett. **34** (1974) 1286.

15-53 J.D. Bjorken and Kogut, Phys. Rev. **D8** (1973) 1341.

15-54 W. Buchmuller, Phys. Lett. **B353** (1995) 335;
W. Buchmuller and A. Hebecker, Phys. Lett **B355** (1995) 573.

15-55 O.J.P. Eboli *et al.*, '(No) Colour in QCD: Charmonium, Charm and Rapidity Gaps', preprint MADPH 96-965 (1996).

15-56 R. Engel and J. Ranft, 'Hard Diffraction and Central Diffraction in Hadron-Hadron and Photon-Hadron Collisions', preprint SI-97-17, University of Siegen, Nov. 1997;
F.W. Bopp *et al.*, 'Rapidity Gaps and the PHOJET Monte Carlo', preprint SI-98-25, University of Siegen, Mar. 1998.

15-57 TOTEM Collaboration, Technical Proposal, CERN / LHCC / 99-07 (1999).

15-58 A. Brandt *et al.*, Nucl. Instr. and Meth. **A327** (1993) 412.

15-59 K. Eggert and G. Morsch, 'Leading Proton Detection in Diffractive Events for an LHC Low-Beta Insertion', preprint CERN-AT-94-09-DI, (1994).

15-60 K. Eggert and G. Morsch, Nucl. Instr. and Meth.**A351** (1994) 174.

15-61 ATLAS Collaboration, First-Level Trigger Technical Design Report, CERN / LHCC / 98-14 (1998).

15-62 F. Abe *et al.*, Phys. Rev. Lett. **79** (1997) 2636.

15-63 G. Ballistoni and S. Tapprogge, 'Studies of Hard Diffraction in ATLAS', ATLAS Internal Note ATL-COM-PHYS-99-022 (1998).

15-64 D. Graudenz and G. Veneziano, Phys. Lett. **B365** (1996) 302.

15-65 M. Heyssler *et al.*, Phys. Lett. **B406** (1997) 95.

15-66 J. Pumplin, Phys. Rev. **D47** (1993) 4820;
J. Pumplin, Phys. Rev. **D52** (1995) 1477.

15-67 A. Berera and J.C. Collins, 'An Estimate of the Double Pomeron Dijet Cross Section at FELIX', preprint VAND-TH-97-07 (1997).

15-68 J.D. Bjorken, Phys. Rev. **D47** (1992) 101.

15-69 A. Schaefer *et al.*, Phys. Lett. **B249** (1990) 331.

15-70 A. Bialas and P.V. Landshoff, Phys. Lett. **B256** (1991) 540.

15-71 J.R. Cudell, O.F. Hernandez, Nucl. Phys. **B471** (1996) 471.

15-72 M.G. Albrow and A. Rostovtsev, private communication.

15-73 P. Bruni and G. Ingelman, Phys. Lett. **B311** (1993) 317.

15-74 F. Abe *et al.*, Phys. Rev. Lett. **78** (1997) 2698.

15-75 M. Derrick *et al.*, Phys. Lett. **B356** (1995) 129.

15-76 H. Fritzsch and K.-H. Streng, Phys. Lett. **B164** (1985) 391.

15-77 M. Heyssler, Z. Phys. **C73** (1997) 299.

15-78 F. Abe *et al.*, Phys. Rev. Lett **77** (1996) 438.

15-79 B. Abbott *et al.*, Phys. Rev. Lett. **82** (1999) 2451.

15-80 G.C. Blazey (for the D0 collaboration), 'Inclusive Jet Production at 630 and 1800 GeV', preprint FERMILAB-CONF-98-367-E (1998).

15-81 J. Alitti *et al.*, Phys. Lett. **B257** (1991) 232.

15-82 S. Catani *et al.*, Nucl. Phys. **B406** (1993) 187.

15-83 W.B. Kilgore and W.T. Giele, preprint hep-ph/9903361 (1999).

15-84 W.T. Giele *et al.*, Nucl. Phys. **B403** (1993) 633.

15-85 B. Abbott *et al.*, Eur. J. Phys. **C5** (1998) 687.

15-86 H. Stenzel and S. Tapprogge, 'Prospects of Studies with QCD Jets in ATLAS', ATLAS Internal Note ATL-COM-PHYS-99-021 (1999).

15-87 A.D. Martin *et al.*, Phys. Rev. **D50** (1994) 6734.

15-88 M. Gluck *et al.*, Z. Phys. **C67** (1995) 433.

15-89 W.T. Giele, E.W.N. Glover and J. Yu, Phys.Rev. **D53** (1996) 120.

15-90 F. Abe *et al.*, Phys. Rev. Lett **70** (1993) 713.

15-91 M. Klasen and G. Kramer, Phys. Rev. **D56** (1997) 2702.

15-92 M.H. Seymour, Nucl. Phys. **B513** (1998) 269.

15-93 H. Akimoto *et al.*, Phys. Rev. **D**, in preparation.

15-94 W.T. Giele, E.W.N. Glover and D.A. Kosover, Phys.Rev. **D52** (1995) 1486.

15-95 S.D. Ellis and D.E. Soper, Phys. Rev. Lett. **74** (1995) 5182.

15-96 F. Abe *et al.*, 'The Two-Jet Differential Cross-Section at CDF', preprint FERMILAB-CONF-93-201-E (1993).

15-97 S. Abachi *et al.*, 'Measurement of the Inclusive Triple Differential Dijet Cross Section, $d^3\sigma/dE_T d\eta_1 d\eta_2$ in $p\bar{p}$ Collisions at $\sqrt{s}$ = 1.8 TeV', preprint FERMILAB-CONF-95-217-E (1995).

15-98 T. Asakawa (for the CDF and D0 collaborations), 'Dijet Results from CDF and D0', proceedings 13th Topical Conference on Hadron Collider Physics, Mumbai, India, Jan. 14-20, 1999.

15-99 B. Abbott *et al.*, 'The Dijet Mass Spectrum and a Search for Quark Compositeness in $p\bar{p}$ Collisions at $\sqrt{s}$ = 1.8 TeV', preprint FERMILAB-PUB-98-220-E (1998).

15-100 A.H. Mueller and H. Navelet, Nucl. Phys. **B282** (1987) 727.

15-101 W.J. Stirling, Nucl. Phys. **B423** (1994) 56.

15-102 V. Del Duca and C.R. Schmidt, Phys. Rev. **D51** (1995) 2150.

15-103 L.H. Orr and W.J.Stirling, Phys.Lett. **B436** (1998) 372.

15-104 B. Abbott *et al.*, 'The Azimuthal Decorrelation of Jets Widely Separated in Rapidity', preprint FERMILAB-CONF-97-371-E (1997).

15-105 F. Abe *et al.*, Phys. Rev. Lett **75** (1995) 608;
F. Abe *et al.*, Phys. Rev. **D54** (1996) 4221.

15-106 F.A. Berends *et al.*, Phys. Lett. **B232** (1989) 266.

15-107 F.A. Berends and H. Kuijf, Nucl. Phys. **B353** (1991) 59.

15-108 B. Andersson, G. Gustafson and T. Sjostrand, Phys. Lett. **B94** (1980) 211

15-109 F. Abe *et al.*, Phys. Rev. **D50** (1994) 5562.

15-110 B. Abbott *et al.*, 'Colour Coherent Radiation in Multi-jet Events from $p\bar{p}$ Collisions at $\sqrt{s}$ = 1.8 TeV', preprint FERMILAB-Pub-97/201-E (1997).

15-111 G. Calucci and D. Treleani, Nucl. Phys. B, Proc. Suppl. **71** (1999) 392.

15-112 F. Abe *et al.*, Phys. Rev. **D56** (1997) 3811.

15-113 H. Baer *et al.*, Phys. Rev. **D42** (1990) 61.

15-114 P. Aurenche *et al.*, Phys. Rev. **D42** (1990) 1440.

15-115 E.L. Berger and J. Qiu, Phys. Rev. **D44** (1991) 2002.

15-116 S. Frixione, Phys. Lett. **B429** (1998) 369.

15-117 L.E. Gordon and W. Vogelsang, Phys. Rev. **D50** (1994) 1901.

15-118 C. Balazs *et al.*, Phys. Rev. **D57** (1998) 6934.

15-119 C. Balazs and C.-P. Yuan, preprint hep-ph/9810319 (1999).

15-120 V. Barger *et al.*, Phys. Lett. **B232** (1989) 371.

15-121 H. Baer *et al.*, Phys. Lett **B234** (1990) 127.

15-122 F. Abe *et al.*, Phys. Rev. **D57** (1998) 1359.

15-123 F. Abe *et al.*, Phys.Rev. **D57** (1998) 67.

15-124 R.G. Badalian and S. Heppelmann, Phys. Rev. **D57** (1998) 4367.

15-125 M. Stratmann and W. Vogelsang, Phys. Rev. **D52** (1995) 1535.

15-126 E.L. Berger and L.E. Gordon, Phys. Rev. **D54** (1996) 2279.

15-127 B. Bailey *et al.*, Phys. Rev. **D54** (1996) 1896.

15-128 F. Abe at al., preprint hep-ex/9902001 (1999).

15-129 F. Abe *et al.*, Phys. Rev. Lett. **77** (1996) 5005.

15-130 C. Balazs and C.-P. Yuan, Phys. Rev. **D56** (1997) 5558.

15-131 F. Abe *et al.*, 'Measurement of Z^0 and Drell-Yan Production Cross Section Using Dimuons in $p\bar{p}$ Collisions at $\sqrt{s}$ = 1.8 TeV', preprint FERMILAB-PUB-98-280-E (1998).

15-132 B. Abbott *et al.*, 'Measurement of the High-Mass Drell-Yan Cross Section and Limits on Quark-Electron Compositeness Scales', preprint FERMILAB-PUB-98-391-E (1998).

15-133 E. Mirkes and J. Ohnemus, Phys.Rev. **D51** (1995) 4891.

15-134 F. Abe *et al.*, Phys. Rev. Lett. **77** (1996) 2616.

15-135 B. Abbott *et al.*, Phys. Rev. Lett. **80** (1998) 5498.

15-136 P.B. Arnold and R. Kauffmann, Nucl. Phys. **B349** (1991) 381.

15-137 G.A. Ladinsky and C.P. Yuan, Phys.Rev. **D50** (1994) 4239.

15-138 C.E. Gerber (for the CDF and D0 collaborations), 'Review of W and Z production at the Tevatron', preprint FERMILAB-Conf-98-148-E (1998).

15-139 C.-P. Yuan, 'Gluon Resummation in Vector Boson Production and Decay', preprint CTEQ-851 (1998), Talk given at the XXXIIIe Rencontres de Moriond 'QCD and High Energy Hadronic Interactions', 21-28 March 1998, Les Arcs, France.

15-140 R.K. Ellis and S. Veseli, Nucl. Phys. **B511** (1998) 649.

15-141 A.D. Martin, R.G. Roberts and W.J. Stirling, Phys. Lett. **B387** (1996) 419.

15-142 F.A. Berends *et al.*, Nucl. Phys. **B357** (1991) 32.

15-143 V. Barger *et al.*, Phys. Rev. **D40** (1989) 2888.

15-144 B. Abbott *et al.*, 'A Measurement of the Ratio of Production Cross Sections for W+1 Jet to W+0 Jets and Comparisons to QCD', preprint FERMILAB-Conf-97/369-E (1997).

15-145 F. Abe *et al.*, Phys. Rev. Lett. **81** (1998) 1367.

15-146 CDF collaboration (B. Flaugher, for the collaboration), 'Measurement of $R_{10}(\sigma(W+ \geq 1 \text{ jet})/\sigma(W))$ at CDF', preprint FERMILAB-CONF-98-339-E (1998).

15-147 B. Abbott *et al.*, 'Colour Coherence in W + Jet Events', preprint FERMILAB-Conf-97/372-E(1997).

15-148 J. Amundson *et al.*, Phys. Rev. **D57** (1998) 527.

15-149 E. Boos *et al.*, preprint hep-ph/9903215 (1999).

15-150 U. Baur *et al.*, Phys.Lett.**B318** (1993) 544.

15-151 F. Abe *et al.*, Phys. Rev. Lett. **67** (1991) 1502.

15-152 V. Barger *et al.*, Phys. Lett. **B338** (1994) 336.

15-153 J. Ellison and J. Wudka, 'Study of Trilinear Gauge Boson Couplings at the Tevatron Collider', preprint UCR-D0-98-01 (1998).

15-154 J. Ohnemus, Phys.Rev. **D50** (1994) 1931.

15-155 U. Baur *et al.*, Phys. Rev. **D53** (1996) 1098.

15-156 U. Baur *et al.*, Phys. Rev. **D48** (1993) 5140.

15-157 U. Baur *et al.*, Phys. Rev. **D50** (1994) 1917.

15-158 U. Baur *et al.*, Phys. Rev. **D57** (1998) 2823.

15-159 J. Ohnemus, Phys. Rev. **D51** (1995) 1068.

15-160 U. Baur *et al.*, Phys. Rev. **D51** (1995) 3381.

15-161 J. Huston, private communication.

15-162 S. Frixione, M.L. Mangano, P. Nason and G. Ridolfi, in 'Heavy Flavours II', eds. A.J. Buras and M.Lindner, Advanced Series on Directions in High Energy Physics, World Scientific Publishing Co., Singapore.

15-163 M. Mangano, 'Heavy flavour production', Talk given at the LHCC workshop 'Theory of LHC processes', Feb. 1998, CERN.

15-164 P. Nason *et al.*, Nucl. Phys. **B303** (1988) 607;
P. Nason *et al.*, Nucl. Phys. **B327** (1989) 49;
erratum *ibid.*, Nucl. Phys. **B335** (1990) 260.

15-165 W. Beenakker *et al.*, Nucl. Phys. **B351** (1991) 507.

15-166 F. Abe *et al.*, Phys. Rev. Lett. **79** (1997) 578.

15-167 F. Abe *et al.*, Phys. Rev. Lett. **79** (1997) 572.

15-168 S. Abachi *et al.*, Phys. Lett. **B370** (1996) 239;
B. Abbott *et al.*, 'Small Angle J/ψ Production in $p\bar{p}$ Collisions at $\sqrt{s}$ = 1.8 TeV', preprint FERMILAB PUB-98/237-E (1998).

15-169 K. Sridhar, Mod. Phys. Lett. **A11** (1996) 1555.

15-170 B. Cano-Coloma and M.A. Sanchis-Lozano, Nucl. Phys. **B508** (1997) 753.

15-171 P. Mathews *et al.*, preprint hep-ph / 9901276 (1999).

15-172 V. Barger *et al.*, Phys. Lett **B371** (1996) 111.

15-173 F. Abe *et al.*, Phys. Rev. Lett. **75** (1995) 4358.

15-174 E. Braaten *et al.*, 'Associated Production of Y and Weak Gauge Bosons in Hadron Collisions', preprint UTPT-98-18 (1998).

15-175 S. Abachi *et al.*, Phys. Rev. Lett. **74** (1995) 3548.

15-176 F. Abe *et al.*, Phys. Rev. Lett. **71** (1993) 500;
F. Abe *et al.*, Phys. Rev. Lett. **71** (1993) 2396;
F. Abe *et al.*, Phys. Rev. Lett. **71** (1993) 2537;
F. Abe *et al.*, Phys. Rev. Lett. **75** (1995) 1451;
F. Abe *et al.*, Phys. Rev. **D50** (1994), 4252.

15-177 M. Mangano *et al.*, Nucl. Phys. **B373** (1992) 295.

15-178 ATLAS Collaboration, Inner Detector Technical Design Report Vol. I, CERN / LHCC 97-16 (1997).

15-179 S. Baranov and M. Smizanska, 'Beauty production overview from Tevatron to LHC', ATLAS Internal Note ATLAS-PHYS-98-133 (1998).

15-180 R. Vogt and S.J. Brodsky, Nucl. Phys. **B438** (1995) 261.

15-181 R.C. Hwa, Phys. Rev. **D51** (1995) 85.

15-182 G.A. Alves *et al.*, Phys. Rev. Lett. **72** (1994) 812.

15-183 M. Adamovich *et al.*, Phys. Lett. **B305** (1993) 402.

15-184 A. Likhoded and A. Berezhnoy, private communication.

15-185 R. Bonciani *et al.*, Nucl. Phys. **B529** (1998) 424.

15-186 W. Bernreuther *et al.*, Phys. Lett. **B368** (1996) 153.

16 Physics of electroweak gauge bosons

Gauge bosons and gauge-boson pairs will be abundantly produced at the LHC. The large statistics and the high centre-of-mass energy will allow several precision measurements to be performed, which should improve significantly the precision achieved at present machines. Two examples of such measurements are discussed in this Chapter: the measurement of the W mass, which will benefit mainly from the large statistics, and the measurement of Triple Gauge Couplings (TGCs), which will benefit from both the large statistics and the high centre-of-mass energy.

In addition, measurements related to inclusive gauge boson production, gauge-boson pair production and gauge boson plus jet(s) production will be important to understand the underlying physics and measure the background for new particle searches. These issues are discussed in Section 15.7. Finally, Z production will be one of the main tools for the *in situ* calibration of the detector mass scale (Chapter 12).

16.1 Measurement of the W mass

At the time of the LHC start-up, the W mass will be known with a precision of about 30 MeV from measurements at LEP2 [16-1] and Tevatron [16-2]. The motivation to improve on such a precision is discussed briefly below. The W mass, which is one of the fundamental parameters of the Standard Model, is related to other parameters of the theory, *i.e.* the QED fine structure constant α, the Fermi constant G_F and the Weinberg angle $\sin\vartheta_W$, through the relation

$$m_W = \sqrt{\left(\frac{\pi\alpha}{G_F\sqrt{2}}\right)}\frac{1}{\sin\vartheta_W\sqrt{1-\Delta R}}$$

where ΔR accounts for the radiative corrections which amount to about 4%. The radiative corrections depend on the top mass as $\sim m_{top}^2$ and on the Higgs mass as $\sim log\ m_H$. Therefore, precise measurements of both the W mass and the top mass allow constraining the mass of the Standard Model Higgs boson or of the h boson of the MSSM. This constraint is relatively weak because of the logarithmic dependence of the radiative corrections on the Higgs mass.

Equivalent errors in the above relation arising from the uncertainties in the top mass and in the W mass imply that the precision on the top mass and on the W mass should be related by the expression

$$\Delta m_W \approx 0.7 \times 10^{-2} \Delta m_{top}$$

Since the top mass will be measured with an accuracy of about 2 GeV at the LHC (see Chapter 18), the W mass should be known with a precision of 15 MeV or better, so that it does not become the dominant error in the Higgs mass estimation. Such a precision is beyond the sensitivity of Tevatron and LEP2.

A study was performed to assess whether ATLAS will be able to measure the W mass to better than 20 MeV [16-3]. This measurement, which will be performed in the initial phase at low luminosity as the top mass measurement, would constrain the mass of the Higgs boson to better than 30%. When and if the Higgs boson will be found, such constraints would provide an im-

portant consistency check of the theory, and in particular of its scalar sector. Disentangling between the Standard Model and the MSSM might be possible, since the radiative corrections to the W mass are expected to be a few percent larger in the latter case.

The measurement of the W mass at hadron colliders is sensitive to many subtle effects which are difficult to predict before the experiment starts. However, based on the present knowledge of the ATLAS detector performance and on the experience from the Tevatron, it should be possible to make a reasonable estimate of the total uncertainty and of the main contributions to be expected. In turn, this will lead to requirements for the detector performance and theoretical inputs which are needed to achieve the desired precision. This is the aim of the study which is described in the next Sections.

16.1.1 The method

The measurement of the W mass at hadron colliders is performed in the leptonic channels. Since the longitudinal momentum of the neutrino cannot be measured, the transverse mass $m_T{}^W$ is used. This is calculated using the transverse momenta of the neutrino and of the charged lepton, ignoring the longitudinal momenta:

$$m_{\mathrm{T}}^{W} = \sqrt{2 p_{\mathrm{T}}^{l} p_{\mathrm{T}}^{\nu} (1 - \cos\Delta\phi)} \qquad 16\text{-}1$$

where $l = e, \mu$. The lepton transverse momentum $p_{\mathrm{T}}{}^l$ is measured, whereas the transverse momentum of the neutrino $p_{\mathrm{T}}{}^\nu$ is obtained from the transverse momentum of the lepton and the momentum $\bar{u}$ of the system recoiling against the W in the transverse plane (hereafter called 'the recoil'):

$$p_{\mathrm{T}}^{\nu} = -\left|\bar{p}_{\mathrm{T}}^{l} + \bar{u}\right|$$

The distribution of $m_{\mathrm{T}}{}^W$, and in particular the trailing edge of the spectrum, is sensitive to the W mass. Therefore, by fitting the experimental distribution of the transverse mass with Monte Carlo samples generated with different values of m_W, it is possible to obtain the mass which best fits the data. The trailing edge is smeared by several effects, such as the W intrinsic width and the detector resolution. This is illustrated in Figure 16-1, which shows the distribution of the W transverse mass as obtained at particle level (no detector resolution) and by including the energy and momentum resolution as implemented in ATLFAST. The smearing due to the finite resolution reduces the sharpness of the end-point and therefore the sensitivity to m_W.

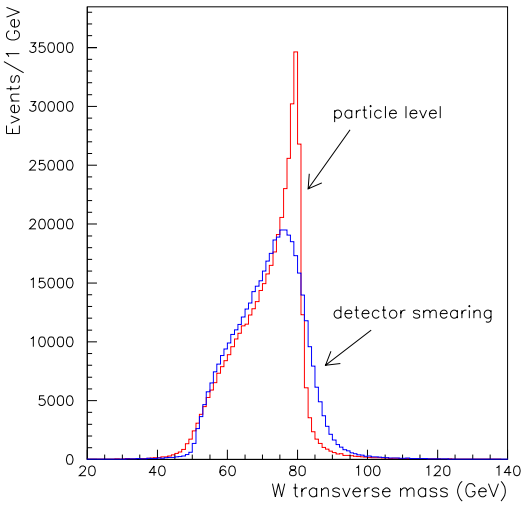

Figure 16-1 Distribution of the W transverse mass as obtained at particle level and by including the expected ATLAS detector resolution.

When running at high luminosity, the pile-up will smear significantly the transverse mass distribution, therefore the use of the transverse-mass method will probably be limited to the initial phase at low luminosity. Alternative methods are mentioned in Section 16.1.4.

16.1.2 *W* production and selection

At the LHC, the cross-section for the process $pp \rightarrow W+X$ with $W \rightarrow l\nu$ and $l = e, \mu$ is 30 nb. Therefore, about 300 million events are expected to be produced in one year of data taking at low luminosity. Such a cross-section is a factor of ten larger than at the Tevatron ($\sqrt{s}$ = 1.8 TeV).

To extract a clean *W* signal, one should require:

- An isolated charged lepton (*e* or μ) with $p_T > 25$ GeV inside the region devoted to precision physics $|\eta| < 2.4$.
- Missing transverse energy $E_T^{miss} > 25$ GeV.
- No jets in the event with $p_T > 30$ GeV.
- The recoil should satisfy $|\vec{u}| < 20$ GeV.

The last two cuts are applied to reject *W*'s produced with high p_T, since for large $p_T{}^W$ the transverse mass resolution deteriorates and the QCD background increases. The acceptance of the above cuts is about 25%. By assuming a lepton reconstruction efficiency of 90% and an identification efficiency of 80%, a total selection efficiency of about 20% should be achieved. Therefore, after all cuts about 60 million *W*'s are expected in one year of data taking at low luminosity (10 fb^{-1}), which is a factor of about 50 larger than the statistics expected from the Tevatron Run 2.

16.1.3 Expected uncertainties

Due to the large expected event sample, the statistical uncertainty on the *W* mass should be smaller than 2 MeV for an integrated luminosity of 10 fb^{-1}.

Since the *W* mass is obtained by fitting the experimental distribution of the transverse mass with Monte Carlo samples, the systematic uncertainty will come mainly from the Monte Carlo modelling of the data, *i.e.* the physics and the detector performance. Uncertainties related to the physics include the knowledge of: the *W* p_T spectrum and angular distribution, the parton distribution functions, the *W* width, the radiative decays and the background. Uncertainties related to the detector include the knowledge of: the lepton energy and momentum scale, the energy and momentum resolution, the detector response to the recoil and the effect of the lepton identification cuts. At the LHC, as now at the Tevatron, most of these uncertainties will be constrained *in situ* by using data samples such as $Z \rightarrow ll$ decays. The latter will be used to determine the lepton energy scale, to measure the detector resolution, to model the detector response to the *W* recoil and the p_T spectrum of the *W*, *etc.*

The advantages of ATLAS with respect to the Tevatron experiments are:

- The large number of *W* events mentioned above.
- The large size of the 'control samples'. About six million $Z \rightarrow ll$ decays, where $l = e, \mu$, are expected in one year of data taking at low luminosity after all selection cuts. This is a factor of about 50 larger than the event sample from the Tevatron Run 2.
- ATLAS is more powerful than CDF and D0 are, in terms of energy resolution, particle identification capability, geometrical acceptance and granularity. Maybe more important for this measurement is the fact that ATLAS will benefit, when data taking will start, from extensive and detailed simulation and test-beam studies of the detector performance.

Nevertheless, ATLAS is a complex detector, which will require a great deal of study before its behaviour is well understood [16-4].

To evaluate the expected systematic uncertainty on the W mass, $W \rightarrow l\nu$ decays were generated with PYTHIA and processed with ATLFAST. After applying the selection cuts discussed above, a transverse mass spectrum was produced for a reference mass value (80.300 GeV). All sources of systematic uncertainty affecting the measurement of the W mass from CDF Run 1A [16-5] were then considered (recent CDF and D0 results based on the full Run 1 statistics can be found in [16-6]). Their magnitude was evaluated in most cases by extrapolating from the Tevatron results, on the basis of the expected ATLAS detector performance. The resulting error on the W mass was determined by generating new W samples, each one including one source of uncertainty, and by comparing the resulting transverse mass distributions with the one obtained for the reference mass. A Kolmogorov test [16-7] was used to evaluate the compatibility between distributions.

Since the goal is a total error of ~20 MeV, the individual contributions should be much smaller than 10 MeV. A large number of events was needed to achieve such a sensitivity. With three million events after all cuts, corresponding to twelve million events at the generation level, a sensitivity at the level of 8 MeV was obtained.

The main sources of uncertainty and their impact on the W mass measurement are discussed one by one in the next Sections. The total error and some concluding remarks are presented in Section 16.1.4.

16.1.3.1 Lepton energy and momentum scale

This is the dominant source of uncertainty on the measurement of the W mass from Tevatron Run 1, where the absolute lepton scale is known with a precision of about 0.1% [16-5][16-8]. Most likely, this will be the dominant error also at the LHC. Indeed, in order to measure the W mass with a precision of 20 MeV or better, the lepton scale has to be known to 0.02%. The latter is the most stringent requirement on the energy and momentum scale from LHC physics. It should be noted that a precision of 0.04% must be achieved by the Tevatron experiments in Run 2, in order to measure the W mass to 40 MeV [16-2].

The lepton energy and momentum scale will be calibrated *in situ* at the LHC by using physics samples, which will complement the information coming from the hardware calibration and the test-beam measurements. The methods and preliminary results from full-simulation studies are discussed in Chapter 12. The muon scale will be calibrated by using mainly $Z \rightarrow \mu\mu$ events, and the EM Calorimeter scale will be calibrated by using mainly $Z \rightarrow ee$ events or E/p measurements for isolated electrons. The main advantage of the LHC compared to the Tevatron is the above-mentioned large sample of $Z \rightarrow ll$ decays. The Z boson is close in mass to the W boson, therefore the extrapolation error from the point where the scale is determined to the point where the measurement is performed is small. In Run 1A, due to the small number of Z events, the central tracker of CDF was calibrated by using $J/\psi \rightarrow \mu\mu$ decays, whereas the calorimeter scale was transferred from the tracker by using E/p measurements for isolated electrons [16-5]. The extrapolation error from the J/ψ mass to the W mass is one of the dominant sources of uncertainty in the CDF measurement of the W mass from Run 1A. For Run 1B [16-6], $J/\psi \rightarrow \mu\mu$ and $Y \rightarrow \mu\mu$ decays were used as cross-checks, but $Z \rightarrow \mu\mu$ was used as the reference mass to determine the momentum scale, thanks to the larger statistics compared to Run 1A. For what concerns the energy scale, inconsistencies in the E/p scale determination have not been resolved, therefore the

calorimeter scale is based solely on the $Z \rightarrow ee$ mass. In the absence of a magnetic field, D0 can only use $Z \rightarrow ee$ events to calibrate the EM Calorimeter [16-8]. The resulting uncertainty is dominated by the limited statistics of the Z sample.

The error on the absolute lepton scale to be expected in ATLAS was evaluated by extrapolating from the CDF uncertainties for Run 1A. It was found that, both for electrons and muons, an uncertainty of 0.02% is difficult to achieve but not impossible. This has been confirmed by full-simulation studies (Chapter 12). To reach such a precision, however, several experimental constraints, *e.g.* knowledge of the magnetic field to the 0.1% level [1] and of the Inner Detector material to ~1%, should be satisfied. Indeed, only in an overconstrained situation will it be possible to disentangle the various contributions to the detector response, and therefore to derive a reliable systematic error.

16.1.3.2 Lepton energy and momentum resolution

To limit the uncertainty on the W mass from the lepton resolution to less than 10 MeV, the EM Calorimeter energy resolution and the Inner Detector and Muon System momentum resolutions have to be known with a precision of better than 1.5%.

The lepton energy and momentum resolution will be determined at the LHC by using information from test-beam and from Monte Carlo simulations of the detector, as well as *in situ* measurement of the Z width in $Z \rightarrow ll$ final states. These methods are used presently at the Tevatron. As an example, the statistical error on the momentum resolution obtained by CDF in Run 1A is 10%, whereas the systematic error is only 1% and is dominated by the uncertainty on the radiative decays of the Z [16-5]. Since the performance of the ATLAS Inner Detector in terms of momentum resolution is expected to be similar to that of CDF, and since the statistical error at the LHC will be negligible, a total error of less than 1.5% should be achieved. There is even the possibility that this uncertainty decreases, if improved theoretical calculations of radiative Z decays will become available.

16.1.3.3 W p_T spectrum

The modelling of ${p_T}^W$ in the Monte Carlo is affected by both theoretical and experimental uncertainties. Theoretical uncertainties arise from the difficulty in predicting the non-perturbative regime of soft-gluon emission, as well as from missing higher-order QCD corrections (see Section 15.7.3). Experimental uncertainties are mainly related to the difficulty of simulating the detector response to low-energy particles.

Therefore, the method used by CDF to obtain a reliable estimate of ${p_T}^W$ for Run 1A consisted of measuring the p_T distribution of the Z boson from $Z \rightarrow ll$ events in the data, and using the ${p_T}^Z$ spectrum as an approximation for the ${p_T}^W$ spectrum in the Monte Carlo, exploiting the fact that both gauge bosons have similar p_T distributions. The ${p_T}^W$ distribution obtained in this way can be further improved by requiring that the recoil distributions in the Monte Carlo and in the W data agree [16-5]. The resulting error on the W mass from CDF Run 1A is about 45 MeV per channel and is dominated by the limited statistics of the Z and W samples in the data [16-5]. For

1. In order to meet this requirement, one month during detector installation will be devoted to the measurement of the magnetic field.

Run 1B an improved method was adopted, which consisted of using the theoretical prediction for the ratio $p_T{}^W / p_T{}^Z$ (in this ratio several uncertainties cancel) to convert the measured $p_T{}^Z$ into $p_T{}^W$.

At the LHC, the average transverse momentum of the W (Z) is 12 GeV (14 GeV), as given by PYTHIA. Over the range p_T (W,Z) < 20 GeV, both gauge bosons have p_T spectra which agree to within ±10%. By assuming a negligible statistical error on the knowledge of $p_T{}^Z$, which will be measured with high-statistics data samples, and by using the $p_T{}^Z$ spectrum instead of the $p_T{}^W$ distribution, an error on the W mass of about 10 MeV per channel was obtained without any further tuning. Although the leading-order parton shower approach of PYTHIA is only an approximation to reality (see Section 15.7.3), this result is encouraging. Furthermore, improved theoretical calculations for the ratio of the W and Z p_T should become available at the time of the LHC, so that the final uncertainty will most likely be smaller than 10 MeV.

16.1.3.4 Recoil modelling

The transverse momentum of the system recoiling against the W, together with the lepton transverse momentum, is used to determine the p_T of the neutrino (see Equation 16-1). The recoil is mainly composed of soft hadrons from the underlying event, for which neither the physics nor the detector response are known with enough accuracy. Therefore, in order to get a reliable recoil distribution in the Monte Carlo, information from data is used at the Tevatron, and will most likely be used also at the LHC. More precisely, in each Monte Carlo event with a given $p_T{}^W$, the recoil is replaced by the recoil measured in the data for Z events characterised by a p_T of the Z boson similar to the above-mentioned $p_T{}^W$. The resulting error on the W mass from CDF Run 1A is 60 MeV per channel, and is dominated by the limited statistics of Z data. Results from CDF and D0 based on the full statistics of Run 1[16-6] show that this uncertainty scales with $\sqrt{N}$, where N is the number of events. Extrapolating to the LHC data sample, an error of smaller than 10 MeV per channel should be achieved. It should be noted that the recoil includes the contribution of the pile-up expected at low luminosity (two minimum-bias events per bunch crossing on average).

16.1.3.5 *W* width

The intrinsic width of the W, which is known with a precision of 85 MeV from measurements at the Tevatron, translated into an error of 20 MeV per channel on the W mass measurement from CDF Run 1A [16-5].

At hadron colliders, the W width can be obtained from the measurement of R, the ratio between the rate of leptonically decaying W's and leptonically decaying Z's:

$$R = \frac{\sigma_W}{\sigma_Z} \times \frac{BR(W \to l\nu)}{BR(Z \to ll)}$$

where the Z branching ratio (BR) is obtained from LEP measurements, and the ratio between the W and the Z cross-sections is obtained from theory. By measuring R, the leptonic branching ratio of the W can be extracted from the above formula, and therefore Γ_W can be deduced assuming Standard Model couplings for the W. The precision achievable with this method is limited by the theoretical knowledge of the ratio of the W to the Z cross-sections. Another method consists of fitting the high-mass tails of the transverse mass distribution, which are sensitive to the W width.

At the Tevatron Run 2 the *W* width should be measured with a precision of 30 MeV by using both the above-mentioned methods [16-2], which translates into an error of 7 MeV per channel on the *W* mass. This is however a conservative estimate for the LHC, since one could also use the *W* width as predicted by the Standard Model, as it has been done by CDF for Run 1B. Furthermore, the *W* width should be measured at the LHC with high precision by using the high-mass tails of the transverse mass distribution, as mentioned above.

16.1.3.6 Radiative decays

Radiative $W \rightarrow l\nu\gamma$ decays produce a shift in the reconstructed transverse mass, which must be precisely modelled in the Monte Carlo. Uncertainties arise from missing higher-order corrections, which translated into an error of 20 MeV on the *W* mass as measured by CDF in Run 1A. Improved theoretical calculations have become available since then [16-9]. Furthermore, the excellent granularity of the ATLAS EM Calorimeter, and the large statistics of radiative Z decays (Section 12.3.2), should provide useful additional information. Therefore, a *W* mass error of 10 MeV per channel was assumed in this study.

16.1.3.7 Background

Backgrounds distort the *W* transverse mass distribution, contributing mainly to the low-mass region. Therefore, uncertainties on the knowledge of the background rate and shape translate into an error on the *W* mass. This error is at the level of 10 MeV (25 MeV) in the electron (muon) channel for the measurement performed by CDF in Run 1A, where the background was known with a precision of about 15% [16-5].

A study was made of the main backgrounds to $W \rightarrow l\nu$ final states to be expected in ATLAS. The contribution from $W \rightarrow \tau\nu$ decays should be of order 1.3% in both, the electron and the muon channel. The background from $Z \rightarrow ee$ decays to the $W \rightarrow e\nu$ channel is expected to be negligible, whereas the contribution of $Z \rightarrow \mu\mu$ decays to the $W \rightarrow \mu\nu$ channel could amount to 4%. The difference between these two channels is due to the fact that the Calorimetry coverage extends up to $|\eta| \sim 5$, whereas the coverage of the Muon System is limited to $|\eta| < 2.7$. Therefore, muons from Z decays which are produced with $|\eta| > 2.7$ escape detection and thus give rise to a relatively large missing transverse momentum. On the other hand, electrons from Z decays produced with $|\eta| > 2.4$ are not efficiently identified, because of the absence of tracking devices and of fine-grained Calorimetry, however their energy can be measured up to $|\eta| \sim 5$. Therefore these events do not pass the E_T^{miss} cut described in Section 16.1.2. Finally, $t\bar{t}$ production and QCD processes are expected to give negligible contributions.

In order to limit the error on the *W* mass to less than 10 MeV, the background to the electron channel should be known with a precision of 30%, which is easily achievable, and the background to the muon channel should be known with a precision of 7%. The latter could be monitored by using $Z \rightarrow ee$ decays.

16.1.4 Results

The expected contributions to the uncertainty on the *W* mass measurement, of which some are discussed in the previous Sections, are presented in Table 16-1. With an integrated luminosity of 10 fb^{-1}, and by considering only one lepton species (*e* or μ), the total uncertainty should be about 25 MeV. By combining both lepton channels, which should also provide useful cross-checks

since some of the systematic uncertainties are different for the electron and the muon sample, an error of about 20 MeV should be achieved by ATLAS alone. This error should decrease to about 15 MeV by combining ATLAS and CMS together. Such a precision would allow the LHC to compete with the expected precision at a Next Linear Collider [16-10].

The most serious challenge in this measurement is the determination of the lepton absolute energy and momentum scale to 0.02%. All other uncertainties are expected to be of the order of (or smaller than) 10 MeV. Preliminary results from CDF including the full statistics from Run 1 [16-6] indicate that many of the errors in the second column of Table 16-1 have indeed approached the ATLAS expected uncertainties given in the third column. For instance, the present CDF error coming from uncertainties in the parton distribution functions is only 15 MeV.

To achieve such a goal, improved theoretical calculations of radiative decays, of the W and Z p_T spectra, and of higher-order QCD corrections will be needed.

The results presented here have to be considered as preliminary and far from being complete. It may be possible that, by applying stronger selection cuts, for instance on the maximum transverse momentum of the W, the systematic uncertainties may be reduced further. Moreover, two alternative methods to measure the W mass can be envisaged. The first one uses the p_T distribution of the charged lepton in the final state. Such a distribution features a Jacobian peak at

Table 16-1 Expected contributions to the uncertainty on the W mass measurement in ATLAS for each lepton family and for an integrated luminosity of 10 fb^{-1} (third column). The corresponding uncertainties of the CDF measurement in the electron channel, as obtained in Run 1A [16-5], are also shown for comparison (second column).

Source	Δm_W (CDF)	Δm_W (ATLAS)
Statistics	145 MeV	< 2 MeV
E-p scale	120 MeV	15 MeV
Energy resolution	80 MeV	5 MeV
Lepton identification	25 MeV	5 MeV
Recoil model	60 MeV	5 MeV
W width	20 MeV	7 MeV
Parton distribution functions	50 MeV	10 MeV
Radiative decays	20 MeV	< 10 MeV
${p_T}^W$	45 MeV	5 MeV
Background	10 MeV	5 MeV
TOTAL	230 MeV	25 MeV

$p_T^l \sim m_W/2$ and has the advantage of being affected very little by the pile-up, therefore it could be used at high luminosity. However, the lepton momentum is very sensitive to the p_T of the W boson, whereas the transverse mass is not, and hence a precise theoretical knowledge of the W p_T spectrum would be needed to use this method. Another possibility is to use the ratio of the transverse masses of the W and Z bosons [16-11]. The Z transverse mass can be reconstructed by using the p_T of one of the charged leptons, whilst the second lepton is treated like a neutrino

whose p_T is measured by the first lepton and the recoil. By shifting the m_T^Z distribution until it fits the m_T^W distribution, it is possible to obtain a scaling factor between the W and the Z mass and therefore the W mass. The advantage of this method is that common systematic uncertainties cancel in the ratio. The main disadvantage is the loss of a factor of ten in statistics, since the $Z \rightarrow ll$ sample is a factor of ten smaller than the $W \rightarrow l\nu$ sample. Furthermore, differences in the production mechanism between the W and the Z (p_T, angular distribution, *etc.*), and possible biasses coming from the Z selection cuts, will give rise to a non-negligible systematic error.

The final measurement will require using all the methods discussed above, in order to cross-check the systematic uncertainties and to achieve the highest precision.

16.2 Gauge-boson pair production

The principle of gauge invariance is used as the basis for the Standard Model. The non-Abelian gauge-group structure of the theory of Electroweak Interactions predicts very specific couplings between the Electroweak gauge bosons. Measurements of these Triple Gauge-boson Couplings (TGC) and Quadruple Gauge-boson Couplings (QGC) of the W, Z and γ gauge-bosons provide powerful tests of the Standard Model.

Any theory predicting physics beyond the Standard Model, while maintaining the Standard Model as a low-energy limit, may introduce deviations in the couplings. Precise measurements of the couplings will not only be a stringent test of the Standard Model and the electro-weak symmetry breaking, but also probe for new physics in the bosonic sector, and will provide complementary information that given by direct searches for new physics. Radiative corrections within the Standard Model also introduce small deviations in the values of the couplings from those expected at lowest order. The deviations are typically of order of O(0.001); deviations due to corrections from supersymmetric or technicolour theories are comparable to this [16-12]. Experiments that can reach this sensitivity could provide powerful constraints on these models.

In the most general Lorentz invariant parametrisation, the three gauge-boson vertices, $WW\gamma$ and WWZ, can be described by fourteen independent couplings [16-13], seven for each vertex. The possible four quadruple gauge-boson vertices: $\gamma\gamma WW$, $Z\gamma WW$, $ZZWW$ and $WWWW$ require 36, 54, 81 and 81 couplings, respectively for a general description. However, on very general theoretical grounds [16-14], it is not possible to introduce QGCs which would not affect the TGCs. In view of this the study presented here concentrate on the TGCs.

Assuming electromagnetic gauge invariance, C- and P-conservation, the set of 14 couplings for the three gauge-boson vertices is reduced to 5: g_1^Z, κ_γ, κ_Z, λ_γ and λ_Z [16-15], where their Standard Model values are equal to $g_1^Z = \kappa_\gamma = \kappa_Z = 1$ and $\lambda_\gamma = \lambda_Z = 0$ at tree level.

The TGCs related to the $WW\gamma$ vertex determine properties of the W, such as its magnetic dipole moment μ_W and electric quadrupole moment q_W:

$$\mu_W = \frac{e}{2m_W}(g_1^Z + \kappa_\gamma + \lambda_\gamma)$$

$$q_W = \frac{e}{m_W^2}(\kappa_\gamma - \lambda_\gamma)$$

In the following the TGCs are denoted Δg_1^Z, $\Delta\kappa_\gamma$, $\Delta\kappa_Z$, λ_γ and λ_Z, where the Δ denotes the deviations of the respective quantity from its Standard Model value.

The values of the TGCs in the Standard Model are such that scattering processes involving gauge bosons at high energy respect unitarity. Modification of the couplings leads to a potential violation of unitarity since the effective parametrisation does not provide the cancellations at very high energies occur in the Standard Model. To restore unitarity at high energies the TGCs are modified by a dipole form factor with a scale Λ, such that $TGC \rightarrow TGC/(1+s/\Lambda^2)^2$, where $\sqrt{s}$ is the centre-of-mass energy of the hard scattering process. Unless otherwise stated, the scale, Λ, is 10 TeV in the study presented here, corresponding to the point where the unitarity limit and the experimental precision are comparable.

The current limits on the TGCs obtained from the combined Tevatron and LEP2 measurements range from O(0.1) for $\Delta\kappa_\gamma$ to O(0.01) for λ_γ. Extrapolating to the year 2005 leads one to expect that these limits will improve by a a factor 10.

The measurement of the TGCs presented here concentrates on fully leptonic final states of $W\gamma$ and WZ production. Backgrounds are expected to be higher in the WW channel and in final states involving jets.

16.2.1 $W\gamma$ Production

The characteristic features of leptonic final states of $W\gamma$ di-boson events, that is, $W\gamma \rightarrow l\nu\gamma$ where $l = e$ or μ, imply that extraction of the signal should be straightforward as it involves a high p_T lepton and γ in connection with large missing p_T. On the other hand, the expected signal cross section is small, about 350 fb for $p_T^\gamma > 100$ GeV; several orders of magnitude below the dominant heavy flavour production processes of QCD that can also lead to events with isolated leptons and large missing energy. The background can be split in one set of events with prompt leptons and γ's and another set of events where one or more jets have been mis-identified as leptons or γ's. Both sets have their main contribution from heavy flavour pair production, $b\bar{b}$ and $t\bar{t}$, with possible hard QED γ's. Additional contributions to the latter set of events come from prompt γ production, $q\gamma$, and W production. The following selection is made [16-16].

- Only one γ with high p_T ($p_T > 100$ GeV);
- Only one high p_T lepton ($p_T > 40$ GeV) (efficiency of 90% has been assumed);
- Both the lepton and the γ should be isolated, $E_{cone} < 12$ GeV for a cone of radius 0.2;
- Large transverse mass of the lepton and missing p_T system, $m_T^W > 35$ GeV;
- No remaining large jet activity, $E_{T,max}(\text{jet}) < 20$ GeV.

These requirements bring the background down to about 20% of the signal, and reduce the expected number of events for an integrated luminosity of 30 fb^{-1} to slightly less than 3000. The very efficient mis-identification rejection in ATLAS (see Sections 7.4, 7.6 and 7.7) implies that the dominant background comes from events with prompt leptons and γ's which populate the lower end of the p_T spectrum. In contrast, the contribution from events with high-p_T jets mis-identified as leptons or γ is much smaller, but their p_T range is larger.

16.2.1.1 Kinematic reconstruction

In purely leptonic final states from $W\gamma$ di-boson events the momentum of the neutrino can be reconstructed by using the W mass as a constraint and assuming that the missing transverse energy is carried off by the neutrino. There is a a two-fold ambiguity in this reconstruction. In the following all distributions that depend explicitly on the neutrino momentum have two entries with equal weight corresponding to this ambiguity. The finite W width is not included in the reconstruction hypothesis and there exist events without a physical solution. For the majority of these events a unique solution is found by neglecting the imaginary part of the complex solution, corresponding to a minimal change of the W mass hypothesis in order to obtain a physical solution.

16.2.2 *WZ* Production

In analogy with the $W\gamma$ analysis, only leptonic final states from WZ production, $WZ \rightarrow lll\nu$, where $l = e$ or μ, have been studied. The signal cross section of WZ production is approximately 26 pb at the LHC, reducing to almost 95 fb for $p_T^Z > 100$ GeV. Fully leptonic final states from WZ production are identified by having three energetic leptons, of which two are of equal flavour and opposite charge, in addition to missing p_T. As in $W\gamma$ production case, the dominant background sources are heavy flavour pair production; additional contributions from prompt $Z\gamma$ and Z production with jet mis-identification also contribute. These can be reduced by requiring [16-16]

- Exactly three high p_T leptons ($p_T > 25$ GeV);
- At least one pair of leptons should have same flavour and opposite sign and have an invariant mass consistent with that of a Z, $|m_{l\bar{l}}-m_Z| > 10$ GeV;
- Large transverse mass of the lepton and missing p_T system, $m_T^W > 40$ GeV;
- No remaining large jet or γ activity, $p_T^\gamma < 50$ GeV and $E_{T,max}(\text{jet}) < 20$ GeV.

After this selection, about 1200 events remain with a purity of approximately 70% for an integrated luminosity of 30 fb^{-1}.

The reconstruction of the WZ event kinematics follows the same procedure as for the $W\gamma$ reconstruction (Section 16.2.1.1).

16.2.3 Determination of Triple Gauge Couplings

The experimental sensitivity to the TGCs comes from the increase of the production cross section and the alteration of differential distributions for non-standard TGCs. The sensitivity is further enhanced at high centre-of-mass energies of the hard scattering process; This effect is more significant for λ type TGCs than for κ type TGCs. As a consequence an increase of in the number of events with large di-boson invariant masses is a clear signature of non-standard TGCs as illustrated on Figure 16-2, where the invariant mass of the hard scattering is shown for $W\gamma$ events simulated with the ATLFAST detector simulation program for the Standard Model and non-standard TGCs. For non-standard values of the TGCs the simulation of the hard scattering is based on a leading order calculation [16-15]. In this way, limits on the TGCs can be obtained from event counting in the high-mass region. The disadvantage of such an approach alone is that the behaviour of the cross section as function of the TGCs is such that the ability to disen-

tangle the contributions from different TGCs and even their sign (with respect to SM) is poor. It is therefore advantageous to combine it with information from angular distributions, including the boson decay angles; this improves the sensitivity and enables the f the contributions from non-standard TGCs to be separated.

One observable, p_T of the γ or Z, traditionally used at hadron colliders, has sensitivity from a combination of high mass event counting and angular distributions. The enhanced sensitivity to the TGCs is due to the vanishing of helicity amplitudes in the Standard Model prediction at small $|\eta|$ [16-15]. Non-standard TGCs may partially eliminate this 'zero radiation', although the zero radiation prediction is less significant when including NLO corrections. Several variables and combinations thereof have been studied to assess the possible sensitivity to the TGCs. For both $W\gamma$ and WZ events the variables are very similar; the γ momentum is simply replaced with that of the Z reconstructed from the two leptons. The actual behaviour of the variables as function of the couplings and the energy is slightly different for the two processes, due to the mass of the Z. In this study two sets of variables have been used (and the equivalent set for WZ): ($m_{W\gamma}$, $|\eta_\gamma^*|$), and (p_T^γ, θ^*), where $|\eta_\gamma^*|$ is the rapidity of the γ with respect to the beam direction in the $W\gamma$ system, and θ^* is the polar decay angle of the charged lepton in the W rest-frame. Both sets consist of one variable sensitive to the energy behaviour and one sensitive to the angular information.

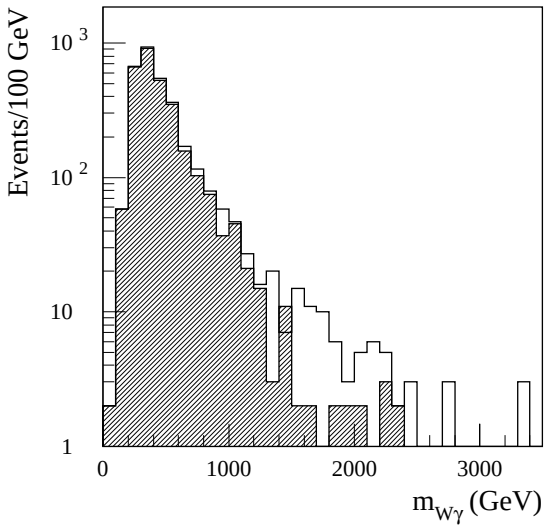

Figure 16-2 The distribution of the invariant mass of the $W\gamma$ system for the Standard Model (shaded histogram) and a non-standard value of 0.01 for $\lambda\gamma$ (white histogram). The number of events corresponds to an integrated luminosity of 30 fb^{-1}.

In principle, it possible is to reconstruct the four (six) variables for a $W\gamma$ (WZ) event, but lack of statistics make multidimensional binned fits using all information difficult. Alternatively, probability distributions can be constructed by integrating over the initial parton configuration using Monte Carlo.

Distributions of some of the variables used in this analysis are shown in Figures 16-3 and 16-4, for both the standard model expectation and different non-standard TGCs. The strong enhancement for non-standard TGCs at high p_T is clearly visible and, furthermore, the qualitative behaviour is the same for different TGCs. The high sensitivity to the TGCs from $|\eta_\gamma^*|$ is due to the characteristic 'zero radiation' gap. In contrast the sensitivity to the TGCs from the decay polar angle, θ^* is weak; it primarily serve as a projector of different helicity components and thereby enhances the sensitivity from other variables.

The determination of the couplings from the different event channels studied in this analysis is done by binned maximum-likelihood fits to distributions of the variables, combined with the total cross-section information. The likelihood function is constructed by comparing the fitted histogram with a reference histogram using Poisson probabilities. The reference distributions are obtained for different values of the couplings by reweighting at generator level.

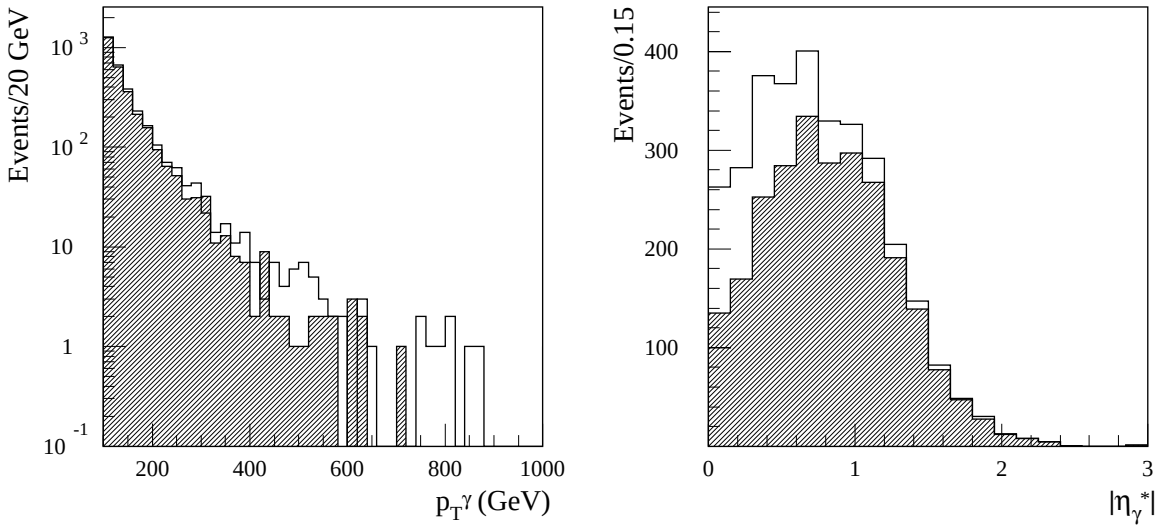

Figure 16-3 Distribution of p_T^γ (left) and $|\eta_\gamma^*|$ (right) from $W\gamma$ events for an integrated luminosity of 30 fb^{-1}. Distributions are shown for the Standard Model (shaded histograms) and for non-standard values (white histograms) $\lambda_\gamma = 0.01$ (left) and $\Delta\kappa_\gamma = 0.2$ (right).

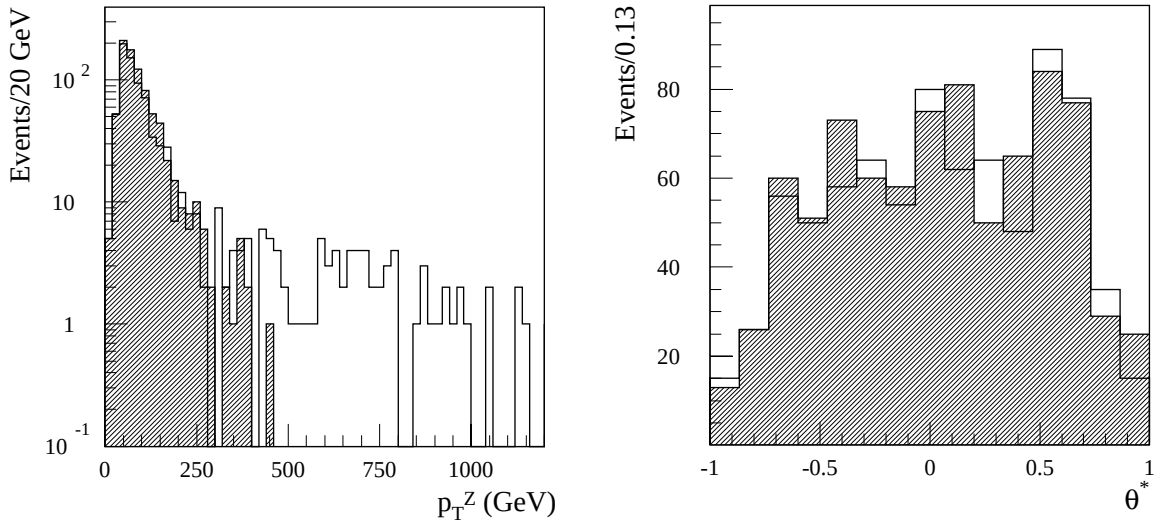

Figure 16-4 Distribution of p_T^Z (left) and θ^* (right) from WZ events for an integrated luminosity of 30 fb^{-1}. Distributions are shown for the Standard Model (shaded histograms) and for non-standard values (white histograms) $\Delta g_1^Z = 0.05$ (left) and $\Delta\kappa_Z = 0.2$ (right).

16.2.4 Systematic uncertainties

At the LHC, the sensitivity to the TGCs is a combination of the very high energy and high luminosity. As the main sensitivity is given by the very high end of the p_T distributions, the important sources of systematic error are those which affect the high energy spectrum. Consequently, the uncertainty arising from the imprecise knowledge of the background is expected to be quite small in the measurement of the TGCs as the dominant background is concentrated at low p_T;

non-standard TGCs would increase the number of events in the high end of the p_T spectrum. For example, the precision on λ_γ was estimated for a sample with a tighter cut on p_T^γ (>200 GeV). The corresponding change in sensitivity is less than 1%, despite a reduction by more than a factor 10 in the total number of signal events. In the case of $\Delta\kappa_\gamma$ the change in sensitivity is larger; about 50%. The reason for this difference between λ-type and κ-type TGCs is that the precision on λ-type TGCs arises from the high energy behaviour, whereas the limits on the κ-type TGCs benefit from angular information, and, hence, are statistically limited.

Of more theoretical oriented uncertainties to the p_T distribution is the choice of pdf and higher order corrections. Higher order corrections have been calculated [16-17] and give substantial contributions, up to a factor 3 (Section 15.7.5), and also alter the differential distributions leading to a loss in precision, with the possibility of mimicking non-standard TGCs if not properly accounted for in the fit to data [16-17]. The combination of all these effects will manifest themselves to lowest order as uncertainties in the a p_T scale.

Finally, it should be stressed that not all observables are equally susceptible to systematic uncertainties. The requirement of a complete reconstruction of the event kinematics introduces many additional sources of systematic errors as it can be seen from the W mass measurement (Section 16.1.2), favouring the more robust measurement of distributions of p_T of either γ or Z, where the exact knowledge of the W kinematics is less important.

16.2.5 Results

The expected 95% C.L. limits on the TGCs obtained from fits to binned distributions of observables are listed in Table 16-2 for fits where one coupling is allowed to vary at the time, with the other couplings held fixed at their Standard Model values. For comparison, the ideal case with maximal sensitivity using an unbinned fit to the complete 6 (8) dimensional phase- space distribution of $W\gamma$ (WZ) production at generator level is also shown. Such a method relies on the complete reconstruction of the event including the knowledge of the initial partonic configuration and will not be applicable to data. From Table 16-2 it is clear that a part of the sensitivity to the κ type TGCs come from the angular information, whereas sensitivity to the λ type TGCs is completely dominated by the very high energy tails.

Table 16-2 The envisaged statistical precision from single parameter fits for a given coupling, assuming an integrated luminosity of 30 fb^{-1}. The limits are presented for the different sets of variables and the ideal case denote fits at generator level using all available information.

Coupling	95% C.L. ($m_{W\gamma}$, $\lvert\eta^*\rvert$)	95%C.L. (p_T^γ, θ^*)	95%C.L. Ideal case
$\Delta\kappa_\gamma$	0.035	0.046	0.028
λ_γ	0.0025	0.0027	0.0023
Δg_1^Z	0.0078	0.0089	0.0053
$\Delta\kappa_Z$	0.069	0.100	0.058
λ_Z	0.0058	0.0071	0.0055

The single parameter limits shown in Table 16-2 represent the best possible precision in the search for anomalous TGCs. In the case of non-standard TGCs, a general multiparameter fit is the only way to establish the nature of the non-standard contribution. For the $WW\gamma$ TGCs the correlation between $\Delta\kappa_\gamma$ and λ_γ is small and the two parameter limits are close to the limits in Table 16-2. In contrast the correlation between Δg_1^Z and $\Delta\kappa_Z$ is quite large (~50%) worsening the general three parameter limits with about 25%.

In summary a precision of O(0.001) for the best constrained couplings, comparable to the world-limit at the time of the LHC start-up, can be achieved with only 10 fb^{-1} corresponding to one year of running at low luminosity.

16.3 Conclusions

Preliminary studies indicate that measuring the *W* mass with a precision of about 20 MeV will be challenging. The biggest single advantage of the LHC is the large statistics, which will permit small statistical errors and good control of the systematic uncertainties.

The study of gauge boson pair production in the first years of the LHC will provide a unique opportunity to perform high precision measurements, which will put stringent constraints on the electroweak symmetry breaking and the gauge group structure of the Standard Model, well beyond the precision at the time of the LHC start-up.

To achieve such unprecedented precision, improved theoretical calculations in many areas will be needed, and several challenging experimental requirements will have to be satisfied.

16.4 References

16-1 G. Altarelli, T. Sjöstrand and F. Zwirner, 'Physics at LEP2', CERN 96-01 (1996).

16-2 D. Amidei and R. Brock, 'Future electroweak physics at the Fermilab Tevatron', FERMILAB-PUB-96/082 (1996).

16-3 F. Gianotti, 'Measurement of the *W* mass at the LHC', ATLAS Internal Note ATL-COM-PHYS-99-063 (1999).

16-4 S. Haywood, 'Offline calibration and alignment of the Inner Detector', ATLAS Internal Note ATL-INDET-99-001 (1999).

16-5 CDF Collaboration, Phys. Rev. **D 52** (1995) 4784.

16-6 M. Lancaster, 'New results on W mass', talk given at the XXXIV Rencontres de Moriond, March 1999, Les Arcs, France.

16-7 Eadie *et al.*, 'Statistical methods in experimental physics', North-Holland, (1971) 269.

16-8 D0 Collaboration, Phys. Rev. Letters **80** (1998) 3008.

16-9 U. Baur *et al.*, Phys. Rev. **D56** (1997) 140.

16-10 E. Accomando *et al.*, 'Physics with e^+e^- Linear Colliders', DESY 97-100, hep-ph/9705442 (1997).

16-11 S. Rajagopalan and M. Rijssenbeek, 'Measurement of m_W using the transverse mass ratio of *W* and *Z*', in Proceedings of the Workshop on New Directions in High Energy Physics, Snowmass 1996.

16-12 J. Ellison and J. Wudka, Ann. Rev. Nucl. Part. Sci. **48** (1998) 33.

16-13 K.Hagiwara, R.Peccei, D. Zeppenfeld and K.Hikasa, Nucl. Phys. **B282** (1987) 253.

16-14 D. Zeppenfeld, private communication.

16-15 U. Baur and D. Zeppenfeld, Nucl. Phys. **B308** (1988) 127.

16-16 D. Fouchez, 'Gauge bosons pair production study with ATLAS', ATLAS Internal Note ATL-PHYS-NO-060 (1994).

16-17 U. Baur, T. Han and J. Ohnemus, Phys. Rev. **D48** (1993) 5140; Phys. Rev. **D51** (1995) 3381.

17 *B*-physics

17.1 Introduction

The rate of *B*-hadron production at the LHC is enormous thanks to the large hadronic cross-section for *b*-quark production and the high luminosity of the machine ($L = 10^{33}\,\mathrm{cm}^{-2}\mathrm{s}^{-1}$ even at so-called low luminosity). About one collision in every hundred will produce a *b*-quark pair, which is a considerably better signal-to-noise ratio than at lower-energy hadron machines such as the Tevatron. In ATLAS, an inclusive-muon trigger with a p_{T} threshold of 6 GeV will make an initial selection of *B*-events. Using this inclusive selection, about 25% of the muon-trigger events will contain *b*-quarks. In the first year of operation, some $2.3\text{x}10^{10}$ *b*-quark pair events will be selected for more detailed analysis in the LVL2 trigger and event filter, that are focused on the selection of specific classes of final states. This event rate will be higher than in any accelerator presently operating, or in any accelerator in operation before the start-up of the LHC.

Although the main focus of the ATLAS physics programme is the search for and study of physics beyond the Standard Model, through the production and decay of new types of particles, an important range of *B*-physics studies is planned, as discussed in this Chapter. In fact, an important aim of the *B*-physics work is to test the Standard Model through precision measurements of *B*-hadron decays that together will over-constrain the CKM matrix, possibly giving indirect evidence for new physics. This programme of work will include the following: precise measurements of *CP* violation in *B*-meson decays, which in the Standard Model is due to a single phase in the CKM matrix; precise measurements of the periods of flavour oscillations in B_s^0 as well as B_d^0 mesons, and of relative decay rates – such measurements constrain the elements of the CKM matrix; searches for and measurements of very rare decays which are strongly suppressed in the Standard Model and where significant enhancements could provide indirect evidence for new physics. Many of the ATLAS measurements will be more precise than those from experiments at lower-energy machines, thanks to the greater available statistics.

At the LHC, the general-purpose experiments ATLAS and CMS will face stiff competition from LHCb, which is a dedicated *B*-physics experiment. However, even though a dedicated experiment can be better optimised for certain event types, ATLAS will be competitive in several channels. ATLAS will thus play an important role in maximising the combined precision of *B*-physics measurements from the LHC.

In the following, the *B*-physics potential of ATLAS is presented. The remainder of this section introduces the framework concerning the production and triggering of *B* hadrons. Section 17.2 discusses *CP*-violation measurements in a number of channels, and also addresses the decay channel $B_s^0 \to J/\psi\phi$ more generally, including a discussion on the measurement of $\Delta\Gamma_s$. B_s^0-oscillation measurements provide information complementary to the *CP*-violation measurements, and the capabilities of measuring the oscillation parameter are described in Section 17.3. Rare decays of the type $B \to \mu\mu(X)$ are described in Section 17.4, and finally, other precision measurements are briefly discussed in Section 17.5.

17.1.1 General features of beauty production in ATLAS

ATLAS will observe decays of *B* hadrons, that are centrally produced in proton–proton collisions at 14 TeV centre-of-mass energy. Events will be selected initially by an inclusive-muon trigger with a p_T threshold of 6 GeV in the pseudorapidity range $|\eta| < 2.4$. Further selections at the trigger level focus on specific final states. For the selected events, the Bjorken *x*-variable of the colliding partons will be between 10^{-4} and 10^{-1} – this range is an order of magnitude broader than in collider experiments at the Tevatron. The mean value of the *B*-hadron transverse momentum with respect to the beam in the statistically dominant channels is 16 GeV or more, which is high enough to justify the perturbative QCD approach [17-1]. At the phenomenological level, the role of higher-order corrections to *b*-quark production may be understood in terms of additional production mechanisms, such as flavour excitation and parton showering [17-2].

At the LHC, many studies can be made of *B*-hadron production. Measurements include *b*-jet differential cross-sections, differential cross-sections of single particles in *b*-jets, production asymmetries, production polarisation, b–$\bar{b}$ correlations, $b\bar{b}g$ final states, doubly-heavy-flavoured hadrons, double *b*-quark-pair production, and prompt J/ψ production. The *B*-hadron production features are discussed in more detail in Chapter 15. It is worth noting that the *B*-production cross-section is not well understood at the phenomenological level, and that predictions are uncertain to a factor of two or more.

17.1.2 Model used for simulation studies

About 1.5 million *B*-hadron events have been simulated using the PYTHIA 5.7 and JETSET 7.4 programs [17-3] for event generation. The flavour-creation, flavour-excitation and gluon-splitting production mechanisms of *b*-quarks were included. The simulations were performed with the CTEQ2L set of parton-distribution functions and the default set of PYTHIA parameters, the most important ones being the *b*-quark mass ($m_b = 5$ GeV) and the factorisation scale ($\mu = p_T^{\text{hard}}$). The fragmentation of *b*-quarks to *B*-hadrons was simulated according to the Peterson function with $\varepsilon_b = 0.007$, as supported by LEP measurements. The choice of parameters was motivated by the fact that the corresponding simulation results reproduce the *b*-quark production cross-section at the Tevatron [17-4].

The total $b\bar{b}$ cross-section is not well defined in PYTHIA when one includes processes other than the lowest-order one for $b\bar{b}$ production, since PYTHIA takes the partons to be massless, and therefore the cross-section diverges when the transverse momentum approaches to zero. However, what is relevant for ATLAS is the part of the cross-section that passes the trigger – this is 2.3 μb when the $b\bar{b}$ events are triggered requiring a muon with $p_T > 6$ GeV and $|\eta| < 2.4$.

About 30% of all the generated events were processed with a detailed detector-simulation program (the remaining events were used for larger-statistics studies using a parametrisation of the detector performance). The simulation software, based on the GEANT 3 package and described in [17-5], was used to simulate the detector response. For most of the events, only the Inner Detector was simulated, since the analyses rely mostly on charged particles reconstructed in the Inner Detector. For the *B*-physics studies presented in this chapter, pile-up (average 2.3 events at low luminosity) was not included in the simulation unless stated explicitly.

Information about particles resulting from all types of secondary interactions inside the Inner Detector was stored if the energy of the incident particle was above 300 MeV (10 MeV for bremsstrahlung). Also, information was stored on particle decays anywhere in the ATLAS detector for use in the study of background muons coming from decays of charged kaons and pions.

Backgrounds which require large rejection factors in the analysis were simulated using a fast Monte Carlo simulation program [17-6]. This included a parametrisation of the detector performance, which was tuned to reproduce the results from reconstruction of fully simulated *B*-physics events in the Inner Detector [17-7]. More detailed information about the production and data samples is given in [17-8].

17.1.3 Trigger

The triggers for *B*-physics studies are described in Chapter 11 and more details can be found in [17-9]; only a brief description is given here.

As indicated above, the LVL1 trigger for all *B*-physics studies in ATLAS will be an inclusive muon trigger, with a transverse-momentum threshold of 6 GeV in the pseudorapidity range $|\eta| < 2.4$. At LVL2, the LVL1 muon is first confirmed before proceeding to a track search in the Inner Detector. The cross-section for $b\bar{b}$ events passing this initial stage of the LVL2 trigger is 2.3 μb. Note that the LVL1 trigger muon, which must be confirmed at LVL2, may come either from the *B*-decay of interest, or from the decay of the other *B*-hadron in the event.

At LVL2, ATLAS expects to trigger on both $J/\psi \to \mu\mu$ and $J/\psi \to ee$. In the case of $J/\psi \to \mu\mu$, the LVL1 trigger muon may come from the J/ψ or from the decay of the other *B*-hadron in the event. A trigger on $J/\psi \to \mu\mu$ may be achieved by requiring a second muon of $p_T > 3$ GeV, using information from the muon chambers in the end-cap and from the Tile hadronic calorimeter in the barrel. The feasibility of such a trigger over the full $|\eta| < 2.5$ region is currently under study. Using the muon chambers alone, it would be possible to trigger over the whole $|\eta| < 2.5$ region down to a p_T threshold of 5 GeV. In the $B_d^0 \to J/\psi\, K_S^0$ analysis, results will be presented for both trigger-threshold possibilities. The dimuon trigger covers rare *B*-decays, $B_{d,s} \to \mu\mu(X)$, in addition to the numerous final states containing J/ψ that are considered in the study of *CP* violation and other topics. With $J/\psi \to \mu\mu$ giving the LVL1 trigger muon, the event may be selected if there is a $p_T > 5$ GeV electron identified at LVL2, even if the second muon from the J/ψ does not pass the LVL2 selection. Such events are useful for *CP*-violation studies with electron tagging; the second muon from the J/ψ decay can be reconstructed in the event filter with relaxed cuts.

The trigger on $J/\psi \to ee$ is implemented at LVL2, using information from the Inner Detector and, in particular, relying on the electron–hadron separation provided by the TRT (see Chapter 10 of [17-9]). With this technique, it will be possible to use an electron p_T threshold of 0.5 GeV (the minimum track p_T reconstructible in the Inner Detector). The $J/\psi \to ee$ events will always be required to contain the LVL1 trigger muon in addition to the J/ψ.

$B^0 \to \pi^+\pi^-$ candidates are searched for at LVL2 by combining pairs of opposite-charge particles with $p_T > 4$ GeV, requiring the sum of p_T moduli to be above 10 GeV and the invariant mass of the pair to be in the range 4.5–6.5 GeV. The distance of both pions to the triggering muon should satisfy $\Delta R > 0.4$ to reject candidates with one or both pions belonging to the trigger *B*-jet. The option of lowering the minimum pion p_T to increase the event yield is being studied. With the

minimum pion p_T set to 1.5 GeV, the acceptance for signal events would triple. However, additional trigger requirements, such as a cut on the transverse impact parameter, would be needed to maintain an acceptable trigger rate.

For all the channels considered for the measurement of Δm_s, the LVL2 trigger is a D_s^- mass trigger. The baseline is to use the decay mode $D_s^- \rightarrow \phi^0 \pi^-$. This is done by considering combinations of oppositely charged tracks and applying kaon hypotheses to reconstruct the ϕ^0. The D_s^- is subsequently reconstructed from combinations of ϕ^0 with another track, applying a pion hypothesis. It would be possible to use the decay mode $D_s^- \rightarrow K^{*0} K^-$ as well, but since the K^{*0} is a much wider resonance than the ϕ^0, and pion–kaon separation is not available, the p_T thresholds for the particles would have to be raised to a point where the increase in statistics for the Δm_s measurement would be marginal.

After the LVL2 trigger, more refined selections can be made in the event filter, relying on improved track-reconstruction performance for making selections based, for example, on invariant-mass and vertexing cuts.

17.2 *CP*-violation studies

17.2.1 Overview

Within the Standard Model, *CP* violation in weak decays is introduced by the phase of the CKM quark-mixing matrix. The unitarity of the CKM matrix can be used to derive triangle relations between the matrix elements. The unitarity relation,

$$V_{ub}^* V_{ud} + V_{cb}^* V_{cd} + V_{tb}^* V_{td} = 0$$

provides the so-called unitarity triangle. The angle α is opposite to the side $V_{cb}^* V_{cd}$, β is opposite to the side $V_{ub}^* V_{ud}$ and γ is opposite to the side $V_{tb}^* V_{td}$. These angles can be measured, for example, in neutral B decays to final states f which can be reached by both B^0 and $\overline{B}^0$. Due to *CP* violation, the rates of B^0 and $\overline{B}^0$ decays are different, resulting for some decay modes in a measurable asymmetry A, defined as:

$$A(t) = \frac{N(\overline{B}^0 \rightarrow f)(t) - N(B^0 \rightarrow f)(t)}{N(\overline{B}^0 \rightarrow f)(t) + N(B^0 \rightarrow f)(t)} = a\cos(\Delta m t) + b\sin(\Delta m t), \qquad 17\text{-}1$$

where a is the direct *CP*-violation amplitude, b is the mixing-induced *CP*-violation amplitude and Δm is the mass difference of the $B^0 - \overline{B^0}$ system. B^0 and $\overline{B}^0$ refer to the B-flavours at production, which must be determined using tagging techniques. In the simplified case of pure mixing-induced *CP* violation, the asymmetry reduces to

$$A(t) = b\sin(\Delta m t) .$$

An important consideration of many *CP*-violation studies, and also for B^0-oscillation measurements, is the determination of the flavour of a B-hadron at production; this is referred to as flavour tagging and various methods are available as discussed below. Limitations in the tagging purity, as well as the presence of background, dilute the observed asymmetry, and this must be

taken into account in the analysis. Also, in proton–proton collisions, B and $\overline{B}$ hadrons are produced with different probabilities. This production asymmetry, which has been estimated to be of the order of 1% or less, has to be subtracted from the measured asymmetry.

Considering the simplified example of pure mixing-induced *CP* violation in the case of B_d^0 decays where the oscillation period is comparable with the lifetime, the time-integrated asymmetry can also be used for *CP*-asymmetry measurements ('event counting'). Starting from the expression $A(t) = b\sin(\Delta m t)$, the time-integrated asymmetry is $A = D_{int} b$, where $D_{int} = x/(1+x^2)$ is the dilution factor due to integrating over time from $t = 0$ and $x = \Delta m/\Gamma$. Note that, in contrast to experiments at e^+e^- machines where B-mesons are produce via Υ(4S) decays, the time-integrated asymmetry is non-zero. Taking into account the other dilution factors, the observable asymmetry is

$$A^{obs} = D_{tag} D_{back} (D_{int} b + A^P),$$

where D_{tag} is the dilution factor from tagging ($D_{tag} = 1 - 2\omega_{tag}$, where ω_{tag} is the wrong-tag fraction), and D_{back} is the dilution factor from background ($D_{back} = N_S/(N_S+N_B)$, where N_S and N_B are the numbers of signal and background events, respectively). A^P is the production asymmetry. Using the formula above, the statistical error on the *CP*-violation parameter b is:

$$\delta b \approx \frac{1}{D_{tag} \cdot \sqrt{D_{back}} \cdot D_{int} \cdot \sqrt{N_S}} \qquad 17\text{-}2$$

17.2.2 Measurement of asymmetry in $B_d^0 \to J/\psi K_S^0$

The measurement of the time-dependent *CP*-violating asymmetry in the decay $B_d^0 \to J/\psi K_S^0$ can provide a clean measurement of the angle β of the unitarity triangle. To a very good approximation, the Standard Model prediction for the asymmetry in this channel is given by:

$$A(t) = \sin 2\beta \sin(\Delta m_d t)$$

where Δm_d is the mass difference in the $B_d^0 - \overline{B_d^0}$ system. The predicted asymmetry is insensitive to the contribution from penguin diagrams. This makes the $B_d^0 \to J/\psi K_S^0$ decay the so-called gold-plated mode to measure the angle β.

The $B_d^0 \to J/\psi K_S^0$ decay, with $J/\psi \to \mu\mu$ or $J/\psi \to ee$, and $K_S^0 \to \pi^+\pi^-$, is also experimentally very clean, and data samples can be reconstructed with relatively low background. It is worth noting that, recently, the CDF Collaboration has measured $\sin 2\beta = 0.79^{+0.41}_{-0.44}$ (stat+syst), using a sample of about 400 events collected during the Run 1 Tevatron data-taking period [17-10]; the error is dominated by the statistical contribution. This demonstrates the feasibility of analysing this channel in the environment of a hadron collider. The current Standard Model best estimate of the unitarity triangle gives $\sin 2\beta = 0.725^{+0.055}_{-0.060}$ [17-11]. Several experiments are expected to make measurements of $\sin 2\beta$ before LHC starts operation; for example BaBar expects to achieve a precision of about 5% [17-12]. However, as discussed below, ATLAS should be able to make a considerably more precise measurement of this parameter.

In the following, the analysis using various tagging methods for the $J/\psi \to \mu\mu$ and $J/\psi \to ee$ samples is discussed. Due to the LVL1 trigger requirement, the $J/\psi \to ee$ events must also contain a muon candidate with $p_T > 6$ GeV and $|\eta| < 2.4$, as discussed in Section 17.1.3. This muon, which usually comes from the decay of the second b-quark in the event, can be used to tag the

flavour of the B_d^0 at production. For $J/\psi \to \mu\mu$, the trigger muon may come either from the decay of the second *b*-quark in the event or from the J/ψ decay. In the former case, the muon may be used to tag the flavour of the B_d^0 at production, as for $J/\psi \to ee$. In the latter case, additional tagging methods can be used to enhance the statistics and provide valuable cross-checks of systematics. As discussed in Section 17.2.2.4 below, the additional methods of tagging that can be used are electron tag, *B*–π tag and jet-charge tag.

17.2.2.1 *J/ψ* reconstruction

The reconstruction of J/ψ decays was investigated using samples of $B_d^0 \to J/\psi K_s^0$ events, generated with PYTHIA in both J/ψ decay channels considered, and fully simulated with GEANT. The events were generated as explained in Section 17.1.2 and include the underlying event as simulated by PYTHIA; no additional pile-up events were added for this analysis. Studies have not yet been performed to evaluate the feasibility of continuing the analysis of this channel after the initial running at low luminosity, *i.e.* at luminosities above $10^{33}\,\mathrm{cm}^{-2}\mathrm{s}^{-1}$. Offline cuts on the transverse momenta of the leptons from the J/ψ decay are the same as those imposed by the LVL1 and LVL2 thresholds described in detail above. Track reconstruction in the entire Inner Detector was performed using the xKalman algorithm (see Section 3.1.2). For the $J/\psi \to ee$ case, a special electron fit option was used in xKalman: for identified electrons, the reconstruction program included, directly in the track-fitting procedure, a correction for possible energy losses due to bremsstrahlung.

Pairs of opposite-charge electrons or muons were fitted to a common vertex and their invariant mass calculated. Successful fits (χ^2 / d.o.f.<6) were retained and, for the muon case, an invariant-mass cut with a $[-3\sigma, +3\sigma]$ window around the nominal *J/ψ* mass was applied. For the electron case, the window was set to be asymmetric in order to take into account the bremsstrahlung energy losses that create a long tail at small invariant masses. This energy loss depends on the amount of material traversed by the electrons and is larger in the end-cap than in the barrel region of the Inner Detector. To take this into account, the mass window was set to $[-5\sigma, +3\sigma]$ ($[-7\sigma, +3\sigma]$) if the J/ψ was produced within the range $|\eta| < 0.7$ ($|\eta| > 0.7$). Finally, the transverse decay length of the reconstructed J/ψ was required to be greater than 250 μm.

For events passing the LVL1 trigger requirement (muon with $p_T > 6$ GeV in $|\eta| < 2.4$), the J/ψ reconstruction efficiency is about 50% in the electron channel and 80% in the muon channel (LVL2 trigger muon threshold at 3 GeV). These figures do not include the lepton trigger and identification efficiencies (see Section 17.2.2.3). The lower reconstruction efficiency in the electron channel is due to bremsstrahlung energy-loss effects causing the electrons to be lost in the reconstruction and causing the J/ψ to fail some of the cuts (mainly the mass-window cut). Further optimisation is needed, both in the track-reconstruction phase and in the selection cuts, to improve the efficiency for reconstructing J/ψ.

The invariant-mass distributions for the electron and muon case are shown in Figures 17-1 and 17-2, respectively. The distributions include only events in which the two reconstructed leptons have been successfully matched with the true generated leptons from J/ψ decay. The resolutions were estimated to be about 40 MeV (muons) and 60 MeV (electrons). For the electron case, the resolution was estimated by fitting only the symmetric core of the distribution.

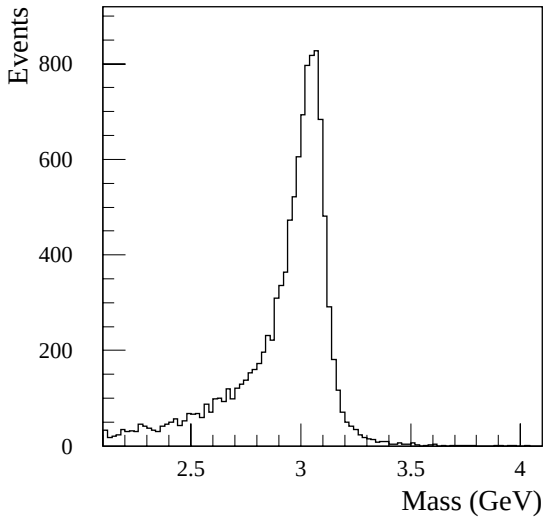

Figure 17-1 Invariant-mass distribution of $J/\psi \to ee$ (signal only).

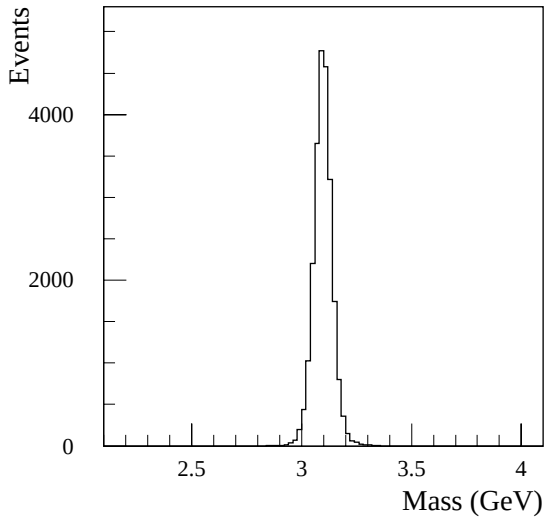

Figure 17-2 Invariant-mass distribution of $J/\psi \to \mu\mu$ (signal only) for events with the LVL2 trigger muon p_T threshold at 3 GeV.

The reconstructed resolution obtained for electrons from full simulation was parametrised as a function of $|\eta|$ and p_T in the fast simulation program ATLFAST. This provides a fast simulation description for background analyses. Since the distributions are non-Gaussian due to interactions in the Inner-Detector material, they were parametrised based on the location of a single hard bremsstrahlung, chosen at random from the appropriate distribution. The parametrisation gave the five fitted track parameters and the correlation matrix. The agreement between the full and the fast simulation is good as can be seen from Figure 17-3.

A similar fast-simulation parametrisation as a function of $|\eta|$ and p_T was made for muons. However, here, the distributions are very close to Gaussian, not having any significant tails in the absence of pattern-recognition problems.

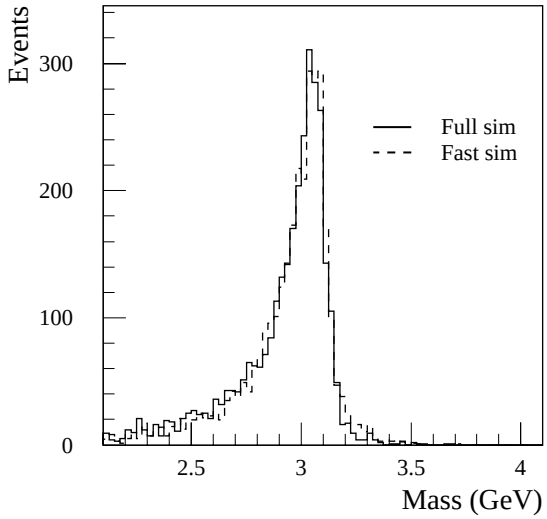

Figure 17-3 Comparison between full (solid line) and fast (dashed line) simulation for $J/\psi \to ee$.

17.2.2.2 K_S^0 reconstruction

The reconstruction of the decay $K_S^0 \to \pi^+\pi^-$ is described in detail in Section 3.6.2.1. The decay vertex was reconstructed using three-dimensional vertexing, and the pair was chosen as a K_S^0 candidate if a good vertex was found at a decay radius R between 1 cm and 37 cm and with $|z| < 210$ cm, and if the invariant mass of the pair was compatible with the K_S^0 mass.

For events in which a J/ψ has been successfully reconstructed, the total K_s^0 reconstruction efficiency is about 41%. This figure includes the acceptance for a K_s^0 decay inside the fiducial volume delimited by the R and z cuts listed above, the tracking efficiency and the efficiency of the selection cuts (cuts on fit probability, mass-window and transverse decay length from the primary vertex). The K_s^0 mass resolution is about 4.5 MeV for K_s^0 decays at low radii and increases to up to 7 MeV towards the external border of the fiducial decay volume.

In order to be able to perform a reliable estimation of the background to the $B_d^0 \to J/\psi K_s^0$ decay, using samples for which full GEANT simulation was not available, a fast simulation for charged pions, similar to the one for muons and electrons briefly described in the previous section, was developed. The parametrisation was established studying the resolutions of the five track parameters for pions in fully-simulated samples. The total sample was divided into bins of p_T, η and, in order to be able to describe also the pions from K_s^0, decay radius. In each bin, the track parameter resolutions were described as the sum of two Gaussians in order to take into account also the presence of tails. While an exponential description of the tails might have been more appropriate in some cases, the two-Gaussian description provides good results and allows one to take into account correlations in a more straightforward way. As discussed in [17-7], this method allows one to obtain a parametrisation of the full covariance matrix (including the correlation terms) as a function of p_T, η and R. This parametrisation was used to smear the five generated pion-track parameters in the fast-simulation program. The K_s^0 mass distribution obtained using this method is compared in Figure 17-4 to the one obtained with full simulation; reasonable agreement is observed between the two.

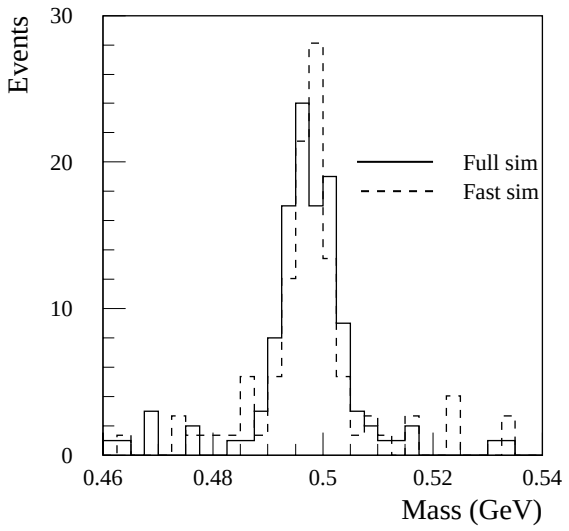

Figure 17-4 Comparison between full (solid line) and fast (dashed line) simulation for $K_s^0 \to \pi^+\pi^-$.

17.2.2.3 B_d^0 reconstruction

Leptons and pions coming from J/ψ and K_s^0 candidates which survived the selections described above were used in reconstructing $B_d^0 \to J/\psi K_s^0$ decays. The B_d^0 was reconstructed by performing a three-dimensional kinematic fit to the four tracks and applying vertex and mass constraints on both the ll and $\pi^+\pi^-$ systems. At the same time, the momentum of the K_s^0 (B_d^0) was required to point to the J/ψ (primary) vertex. The proper decay time of the B_d^0 was required to be greater than 0.5 ps and the transverse momentum was required to be greater than 5 GeV. A mass resolution of 19 (26) MeV and a transverse decay-length resolution of 64 μm (68 μm) were estimated for the reconstructed B_d^0 meson in events in which the J/ψ decayed to muons (electrons).

After the first three years of running at low luminosity, corresponding to an integrated luminosity of 30 fb^{-1}, it is estimated that ATLAS will reconstruct 14400 $J/\psi K_s^0$ decays in the $J/\psi \to ee$ channel and 473 550 (219 690) events in the μμ channel, assuming a LVL2 trigger threshold of 3 GeV (5 GeV) for the second muon. The relatively low number of $J/\psi \to ee$ events is due to the requirement of an additional muon which provides the LVL1 trigger and can be used for tag-

ging the flavour of the B_d^0 at production. Besides all the selection cuts described above, these numbers also include the estimated efficiencies of the detector to identify electrons and muons: ε = 85% for the LVL1 trigger muon, ε = 95% for other muons with p_T > 5 GeV, ε = 90% for muons with 3 GeV< p_T<5 GeV, and ε = 75% for all electrons.

17.2.2.4 Flavour tagging

To perform a measurement of the *CP*-violating asymmetry, it is necessary to know the flavour of the neutral *B* meson at production. Various methods have been developed for this purpose along the years, mainly by the LEP experiments and by CDF. Flavour tagging can be divided in two categories – Opposite-Side Tagging (OST) and Same-Side Tagging (SST) – depending on whether the algorithm deduces the flavour by looking at the products of the other *b*-quark in the event (the opposite side) or at the particles accompanying the *B*-meson under study (the same side). In this section, a brief description of the tagging algorithms developed so far for this analysis is given and the performance summarised. Each algorithm has been optimised by adjusting parameters to maximise the quality factor $Q = \varepsilon D_{\mathrm{tag}}^2$ that determines the statistical precision on the asymmetry measurement. Here, ε is the tagging efficiency defined as the fraction of reconstructed *B* candidates with a tag, and D_{tag} is the dilution factor due to mistags.

In the lepton-tagging technique, an additional lepton is searched for in the event, with the assumption that this tag lepton originates from a semi-leptonic decay of the other *b*-quark in the event. This method is known to have low efficiency (due to the low B_d^0 semi-leptonic branching ratio of about 10% and the kinematic cuts), but good purity. However, in the $J/\psi \to ee$ sample this method is fully efficient due to the presence of the trigger muon. In the $J/\psi \to \mu\mu$ sample, an additional lepton (muon or electron) with p_T > 5 GeV is searched for. In case the tag lepton was a muon (so that there are three muons in the event), the LVL1 trigger muon could be either one of the J/ψ legs or the tag muon. The total lepton-tagging efficiency in the $J/\psi \to \mu\mu$ sample is about 0.04 (electron or muon tag).

The mistag rate with lepton tagging was extensively studied in a large inclusive-muon sample and double-checked, with smaller statistics, in samples of $B_d^0 \to J/\psi K_s^0$ decays. The dependence of the mistag rate on the tag lepton transverse-momentum threshold is shown in Figures 17-5 and 17-6 for electrons and muons respectively. It can be seen that the wrong-tag fraction decreases with increasing tag p_T threshold. The mistag rate depends on p_T of the signal *B*-hadron as well as on the p_T of the tag lepton. With increasing p_T of the signal *B*-hadron, the wrong-tag fraction increases for a fixed tag p_T threshold. This is due to the fact that, as the p_T of the signal *B*-hadron increases, the p_T of the other *B* tends to increase as well, resulting in a higher probability for the leptons from cascade decays to pass the p_T threshold for the tag. This can be seen in Figure 17-7, which shows the wrong-tag fraction as a function of the signal *B*-hadron p_T, when the tag p_T was fixed to 6 GeV. For the hadronic channels $B_d^0 \to \pi^+\pi^-$ and $B_s^0 \to D_s^-\pi^+$ ($B_s^0 \to D_s^- a_1^+$), the average p_T of the signal *B* was about 20 GeV, and the wrong muon tag fraction was taken to be 0.22.

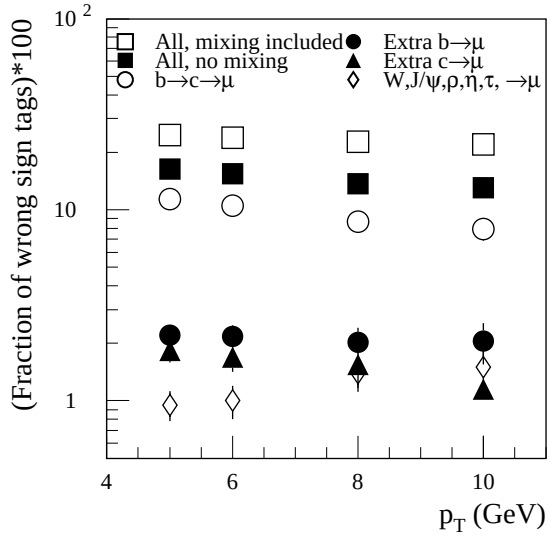

Figure 17-5 Muon wrong-tag fraction as a function of the tag p_T threshold. This plot is made for the case where the decay $J/\psi \to \mu\mu$ gives rise to a muon with p_T > 6 GeV. At tag p_T > 6 GeV, the average p_T of the signal-*B* is 26 GeV.

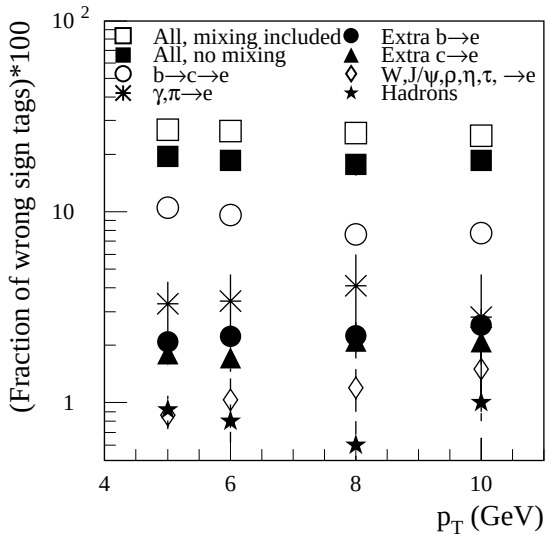

Figure 17-6 Electron wrong-tag fraction as a function of the tag p_T threshold. This plot is made for the case where the decay $J/\psi \to \mu\mu$ gives rise to a muon with p_T > 6 GeV. At tag p_T > 5 GeV, the average p_T of the signal-*B* is 25 GeV.

For muon tagging of the $J/\psi \to \mu\mu$ sample, a mistag rate of $\omega_{tag} = 0.24$ was applied in the analysis. Here the average p_T of the B_d^0 is about 25 GeV. For muon tagging of the $J/\psi \to ee$ sample, the wrong-tag fraction was lower, $\omega_{tag} = 0.21$, due to the lower p_T of the signal-*B* (17 GeV on average). Contributions to the mistag rate from hadrons misidentified as muons and from decays in flight of pions and kaons were found to be negligible. The mistag rates are also given in the summary in Table 17-1.

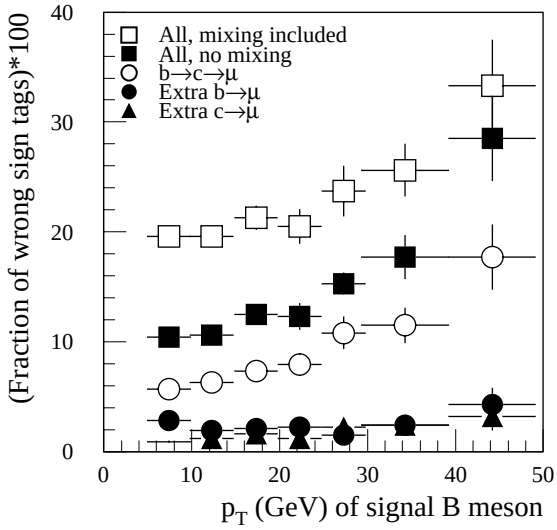

Figure 17-7 Muon wrong-tag fraction as a function of the signal *B*-hadron p_T. The tag muon was required to have p_T > 6 GeV.

For electron tagging of the $J/\psi \to \mu\mu$ sample, the fraction of wrong tags was 0.27 with a 5 GeV threshold. The contributions to the mistag rate from misidentified hadrons (about 1%) and from conversions (about 2%) were estimated using fully simulated Monte Carlo samples. The hadron rejection factor was about 1800, corresponding to a 75% electron efficiency. The electron was identified by using both the e.m. calorimeter and the TRT (see Section 7.3.1). The conversion-removal algorithm, similar to the one described in Section 7.5.1, has not yet been fully optimised for this analysis. The mistag rates are summarised in Table 17-1.

The B-π correlation tagging is an SST technique as it uses charged pions associated with the B_d^0 that has decayed to $J/\psi K_s^0$. The algorithm exploits the correlation between the flavour of the b-quark and the charge sign of a particle produced nearby in phase-space. Such charge–flavour correlations are expected to come both from particles produced in the fragmentation and from the decays of B^{**} resonances [17-13]. No attempt was made to separate the two contributions. In both cases, a positively-charged particle is correlated to a B_d^0 and a negatively-charged one to a $\overline{B_d^0}$. This particle will be referred to as a 'pion' in the following discussion, although it is not identified as such.

The algorithm selects charged-particle tracks contained in a cone $\Delta R < 0.7$ around the reconstructed B meson direction, with $|d_0|/\sigma_{d_0} < 3$ (where d_0 is the transverse impact parameter of the pion) and with 0.5 GeV < p_T < 4.0 GeV. If more than one particle survives this selection, the one with the highest p_L^{rel} (the momentum component along the reconstructed B direction) is selected. This set of cuts provides the highest quality factor, although other choices provided similar results within the statistical uncertainty. The results for the efficiency and the dilution factor for this algorithm are presented in Table 17-1.

As in the B-π algorithm, jet-charge tagging exploits the correlation between the charge of a jet (defined as a kinematically-weighted average of the charge of the particles in the jet) and the charge of the quark producing the jet. Although jet-charge tagging can be applied to both the B_d^0 jet and to the opposite jet, for the time-being it was applied only to the same-side jet. In the analysis, the signal is tagged as a B_d^0 ($\overline{B_d^0}$) if the jet-charge tag has $Q_{jet} > +c$ ($Q_{jet} < -c$), where c is a tunable cut.

The algorithm included in the jet all tracks with $p_T > 0.5$ GeV, $|d_0| < 1$ cm and $|\Delta z| < 5$ cm (where Δz is the difference between the z_0 of the track and the z-coordinate of the primary vertex), contained inside a cone $\Delta R < 0.8$ around the B direction. The four particles identified as the B_d^0 decay products were excluded. This set of cuts, together with the definition of the weights $w_i = p_T^k$, where $k = 1.25$ (1.0) for the $J/\psi \to ee$ ($J/\psi \to \mu\mu$) sample, and cut value $c = 0.26$ for both J/ψ decay channels, were chosen to maximise the quality factor Q. Different sets of cuts provided similar results within the statistical uncertainties. The results are summarised in Table 17-1.

Table 17-1 Efficiencies and dilution factors for the tagging algorithms considered in the analysis (n/a = not available). The notation μ6μ3 (μ6μ5) means that in the corresponding sample, the LVL2 trigger threshold for the second muon has been assumed to be 3 (5) GeV.

Tag	$B_d^0 \to J/\psi(ee)K_s^0$		$B_d^0 \to J/\psi(\mu 6 \mu 3)K_s^0$		$B_d^0 \to J/\psi(\mu 6 \mu 5)K_s^0$	
	ε_{tag}	D_{tag}	ε_{tag}	D_{tag}	ε_{tag}	D_{tag}
OST: electron tag	n / a	n / a	0.012	0.46	0.016	0.46
OST: muon tag	1.0	0.57	0.025	0.52	0.025	0.52
SST: B–π	0.80	0.14	0.82	0.16	0.84	0.17
SST: Jet-charge	0.71	0.12	0.64	0.17	0.66	0.18

It is worth noting that the performance shown in Table 17-1 for the various tagging methods is quite consistent with that achieved by CDF [17-10]. For example, for the SST methods, CDF obtains a dilution factor of 0.166 ± 0.022 for SVX tagged events or 0.174 ± 0.036 for non-SVX events, where SVX refers to the CDF Silicon Vertex Detector.

Note that there is scope to improve on the tagging performance by using an event-by-event likelihood analysis and including additional information such as $p_{\mathrm{T}}^{\mathrm{rel}}$ measurements, although this remains to be studied.

17.2.2.5 Event yields

The total number of events after tagging is summarised in Table 17-2 for each sample for an integrated luminosity of 30 fb^{-1}.

Table 17-2 Expected number of tagged events and relative background for each sample for an integrated luminosity of 30 fb^{-1}. The notation $\mu 6 \mu 3$ ($\mu 6 \mu 5$) means that in the corresponding sample, the LVL2 trigger threshold for the second muon has been assumed to be 3 (5) GeV. The *e*- and μ-tag samples are subclasses of the lepton-tagged sample, and the sample '*B*-π tagged events with no lepton tags' is a subclass of the sample '*B*-π tagged events'. The lepton tagged sample and the *B*-π tagged sample with no lepton tags are independent and can be combined in a straightforward way.

Event class	$B_d^0 \to J/\psi(ee)K_S^0$		$B_d^0 \to J/\psi(\mu 6 \mu 3)K_S^0$		$B_d^0 \to J/\psi(\mu 6 \mu 5)K_S^0$	
	Signal	Background	Signal	Background	Signal	Background
Lepton tagged events	14 400	900	17 700	1 600	8800	500
e tags	n / a	n / a	5 800	500	3 500	210
μ tags	14 400	900	11 900	1 100	5 300	310
B-π tagged events	11 600	900	390 700	15 300	184 100	5 000
B-π tagged events with no lepton tags	n / a	n / a	376 100	13 700	176 700	4 500

Since the lepton tag purity is much higher than the *B*-π tag purity, the lepton tag was used whenever it was available. The *B*-π tag was used only if there was no lepton tag. The highest statistical tagging power would be achieved by combing all available tagging information on an event-by-event basis. A study of the tag combination has not yet been performed. Jet-charge tags are not listed in this table. Jet-charge tags have proven, as expected, to be highly correlated with *B*-π tags, and since the *B*-π tag purity was higher that the jet-charge-tag purity, only *B*-π tags were used.

17.2.2.6 Background estimate

The background to the $B_d^0 \to J/\psi K_S^0$ decay was studied using large samples of J/ψ *X* and $\mu 6X$ events. The inclusive sample of J/ψ decays from *B*'s was produced with the same lepton-p_{T} thresholds as for the signal sample. This sample was used to give an estimate of the background coming from *B* decays containing a true J/ψ in the final state. Background contributions come from the combination of a true J/ψ with K_S^0 candidates from various sources: true K_S^0 from *B*-hadron decays, true K_S^0 from the fragmentation, and fake K_S^0.

The $\mu 6X$ sample contained events with muons from semileptonic B-hadron decays with a minimum muon transverse momentum of 6 GeV. This sample was used to estimate the background from fake J/ψ's (arising from lepton–lepton, lepton–hadron and hadron–hadron pairs) reconstructed in association with a true or a fake K_s^0.

The background samples were processed using the fast simulation program. However, good agreement was found with results obtained from smaller-statistics samples of fully-simulated background events. The total number of background events is presented in Table 17-2. Conservatively, a pessimistic 95% B-π tagging efficiency has been assumed for the background events. In all the samples, the biggest background contribution comes from true J/ψ background events. Background from fake J/ψ's was found to be about 5% of the total background. The background level under the $B_d^0 \to J/\psi K_s^0$ peak is rather small including all samples (see Figure 17-8).

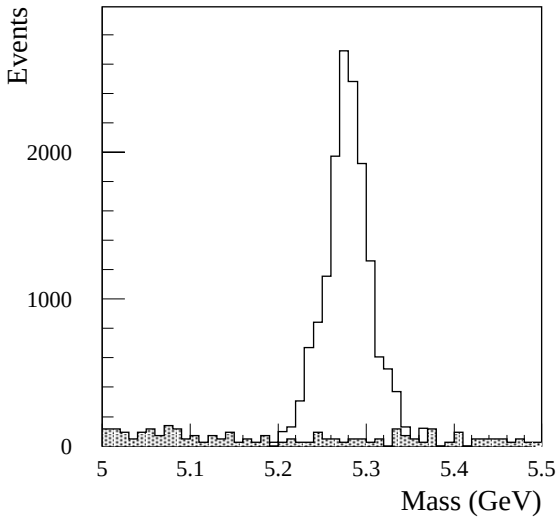

Figure 17-8 Invariant-mass distribution of the B_d^0 peak in the muon-tagged $J/\psi \to ee$ channel (open histogram) with superimposed the estimated background contribution (shaded histogram). Note that the selection includes a decay-time cut on the B_d^0.

The background from prompt J/ψ's has not yet been studied for this channel. This is a potential background source for the hadron-tagged samples, while the lepton-tagged samples with three leptons per event are very unlikely to be affected. However, the background from prompt J/ψ production was studied for the untagged decay $B_s \to J/\psi\phi$ (see Section 17.2.4.2), which is experimentally similar, and it was found to be negligible.

17.2.2.7 The statistical accuracy of the sin2β measurement

The accuracy of the $\sin 2\beta$ measurement was estimated with a fit to the time-dependent asymmetry distribution with a function of the form $A = D \sin 2\beta \sin(\Delta m_d t)$, where D is the overall dilution factor. For this analysis time dependence of the dilution due to background has been neglected. The time-dependent asymmetry was modelled including dilution factors from background and from tagging. An input value of $\sin 2\beta = 0.6$ was assumed for the only free parameter of the fit. The proper time of the B-decay was histogrammed using bins of width 0.83 ps (corresponding to about 250 μm in decay length). Due to the cut on the decay proper time used in the selection, the measurement was made for $t(B) > 0.5$ ps. The proper-time resolution, estimated using the fully-simulated signal sample, is 0.073 ps.

The results of the fit using lepton tagging and B–π tagging in the various samples considered are presented in Table 17-3, where the lepton-tagged events have been removed from the B-π tagged samples, leaving statistically independent samples. Since in the class $J/\psi(ee)$ all the events have a muon tag, no events are left in the B-π tagged sample. Note that the statistical precision from a number of different samples and tagging methods is comparable, allowing meaningful cross-checks to be made between them.

Table 17-3 Estimate of the error on sin2β using a time dependent analysis in each of the samples considered for lepton tagging and *B*–π tagging with an integrated luminosity of 30 fb^{-1}. Note that the J/ψ(μ6μ5) sample is a subset of the J/ψ(μ6μ3) one.

Tag	*J/ψ(ee)* sample	*J/ψ(*μ6μ3) sample	*J/ψ(*μ6μ5) sample
Lepton tags	0.018	0.023	0.030
B–π tag	n / a	0.015	0.019

As the $B_d^0 \to J/\psi(ee)K_s^0$ sample is statistically independent from the $B_d^0 \to J/\psi(\mu\mu)K_s^0$ ones, results from the two samples can be combined in a straightforward way. Using lepton tagging combined with *B*-π tagging, the estimated uncertainty on $\sin 2\beta$, with 30 fb^{-1} of data is $\delta(\sin 2\beta) = 0.010$ (stat) assuming a LVL2 trigger p_T threshold of 3 GeV for the second muon or $\delta(\sin 2\beta) = 0.012$ (stat) with a threshold of 5 GeV.

17.2.2.8 Systematic uncertainty

Previous studies have shown that the overall systematic error in the $\sin 2\beta$ measurement is small [17-14]. Contributions come from the production asymmetry of B_d^0 and $\overline{B_d^0}$ mesons, from asymmetries in the tagging efficiency and in the background, and from uncertainties in the determination of the various dilution factors. All these uncertainties need to be controlled, in order not to spoil the excellent statistical precision achievable on this measurement.

Many of the potential sources of systematic uncertainty can be controlled using the channels $B^+ \to J/\psi(\mu\mu)K^+$ and $B_d^0 \to J/\psi(\mu\mu)K^{*0}$ (where $K^{*0} \to K^+\pi^-$). For the first channel the results for charged *B*-mesons need to be extrapolated to the neutral case which may introduce some model dependence. For the second channel, the results are obtained directly for B_d^0 particles, allowing for the flavour oscillations. The reconstruction of these so-called control channels is discussed below before estimates of the systematic uncertainties are presented.

The availability of many tagging algorithms and the large statistics of tagged and untagged signal and control samples provide the flexibility to perform internal cross-checks of the analysis. The $B^+ \to J/\psi(\mu\mu)K^+$ and $B_d^0 \to J/\psi(\mu\mu)K^{*0}$ samples can be used to measure the wrong-tag fraction for the various tagging methods and also the charge asymmetry in the tagging efficiencies. For all these studies, it is important to reconstruct large statistics of control samples, so that the systematic errors will not appreciably degrade the statistical error on $\sin 2\beta$.

17.2.2.9 Reconstruction of $B^+ \to J/\psi(\mu\mu)K^+$

As discussed above, the decay channel $B^+ \to J/\psi(\mu\mu)K^+$ can be used to measure parameters that relate the observed asymmetry in $B_d^0 \to J/\psi K_s^0$ decays (and other channels) to the true *CP* asymmetry. The $B^+ \to J/\psi(\mu\mu)K^+$ decay (as well as the $B_d^0 \to J/\psi(\mu\mu)K^{*0}$ decay described below) was studied using a sample of events generated with PYTHIA and fully simulated inside the Inner Detector. Only J/ψ decays to muon pairs were considered. Muon identification efficiencies were included when calculating the expected number of signal events.

The trigger selection for this channel was the same as for the $B_d^0 \to J/\psi(\mu\mu)K_s^0$ decay channel. The J/ψ vertex was fitted and selection cuts were applied as described in Section 17.2.2.1. Once a J/ψ was successfully reconstructed, the event was searched for a track (the 'kaon') with transverse momentum greater than 1.5 GeV. The track was required to be inconsistent with coming from the primary vertex at the one standard deviation level ($|d|/\sigma_d > 1$). The two muons and the kaon were then fitted to a common vertex applying a mass constraint to the J/ψ and requiring the total momentum at the B vertex to point to the primary event vertex. The normalised χ^2 of the fit was required to be less than six. Finally, a cut $p_T(B) > 5$ GeV was applied and the mass was required to be within three standard deviations of the nominal B^+ mass.

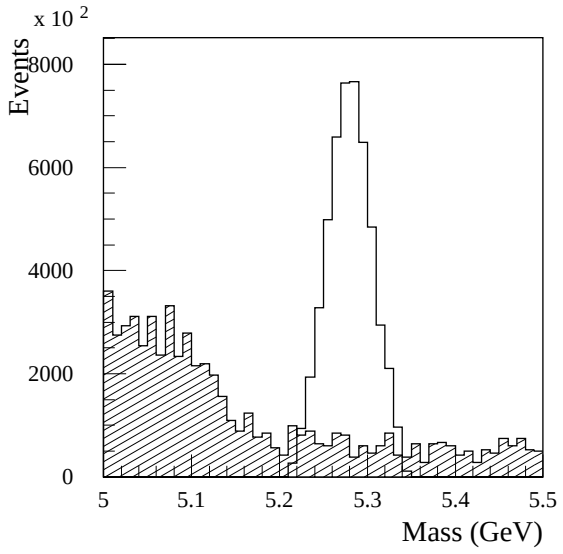

Figure 17-9 Invariant-mass distribution for the decay $B^+ \to J/\psi(\mu\mu)K^+$ (open histogram) with superimposed the estimated background contribution (shaded histogram).

The mass peak is shown in Figure 17-9; the mass resolution is about 26 MeV. The number of signal events expected for an integrated luminosity of 30 fb^{-1} is given in Table 17-4 for both LVL2 trigger options. Also given in this table are the numbers of untagged background events estimated using the inclusive $J/\psi X$ sample. The backgrounds from fake J/ψ and prompt J/ψ have not yet been included in this study. However, in the background estimate for the signal $B_d^0 \to J/\psi(\mu\mu)K_s^0$, the dominant background was found to originate from real J/ψ from B-decays. The selection cuts for this channel may need further optimisation to improve the signal-to-background ratio; tighter cuts should be feasible given the large statistics.

Table 17-4 Total number of events expected in the control samples (30 fb^{-1}).

Sample	Untagged signal	Untagged background	Lepton tagged signal	Lepton tagged background	B-π tagged signal	B-π tagged background
$B^+ \to J/\psi(\mu 6\mu 3)K^+$	5 078 000	929 000	198 000	13 800	4189 000	882 000
$B^+ \to J/\psi(\mu 6\mu 5)K^+$	2 471 000	509 000	122 000	8 500	2070 000	484 000
$B_d^0 \to J/\psi(\mu 6\mu 3)K^{*0}$	2 631 000	608 000	115 000	24 400	2170 000	578 000
$B_d^0 \to J/\psi(\mu 6\mu 5)K^{*0}$	1 292 000	311 000	63 600	12 200	1083 000	295 000

Also given in Table 17-4 are the numbers of tagged events and respective backgrounds, both for lepton tagging and B–π tagging. As in the $B_d^0 \to J/\psi(\mu\mu)K_s^0$ analysis, both muons and electrons with $p_T > 5$ GeV are used for tagging. A complete study of B–π tagging has not been performed for these channels, and tagging efficiencies on both signal and background equal to those estimated for the $B_d^0 \to J/\psi(\mu\mu)K_s^0$ case have been used. In Table 17-4, lepton tagged events have not been removed from the B–π tagged events. About 4% (5%) of the B–π tagged events in the $\mu 6\mu 3$ ($\mu 6\mu 5$) class have a lepton tag in addition to the B–π tag.

17.2.2.10 Reconstruction of $B_d^0 \to J/\psi(\mu\mu)K^{*0}$

Triggering of these channels and the J/ψ reconstruction were the same as for the $J/\psi(\mu\mu)K^+$ analysis. After the J/ψ was successfully reconstructed, all track pairs with $p_T > 0.5$ GeV were fitted to a common vertex. The normalised χ^2 of the fit was required to be less than 6 and the p_T of the reconstructed K^{*0} was required to be greater than 3 GeV. Candidates inside a three standard deviation mass window around the nominal K^{*0} mass were retained. In the fit, both pion and kaon mass assignments were tried. If both combinations passed all the K^{*0} selection cuts listed above, only the combination yielding the mass closest to the nominal K^{*0} mass was retained.

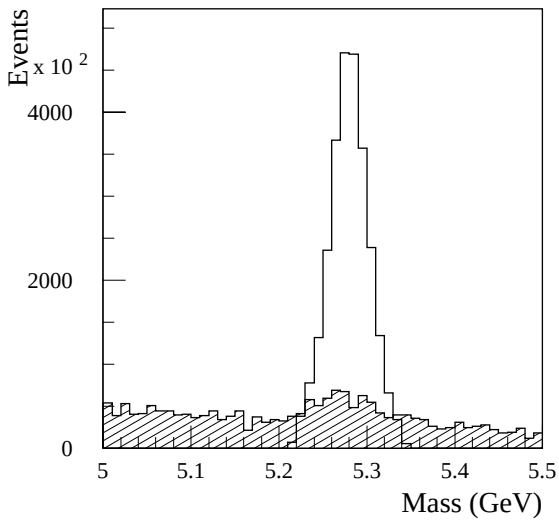

Figure 17-10 Invariant-mass distribution of the decay $B_d^0 \to J/\psi(\mu\mu)K^{*0}$ (open histogram) with superimposed the estimated background contribution (shaded histogram).

The two muons and the two hadron tracks were then fitted to a common vertex. Due to the large K^{*0} width, a mass constraint was applied only to the J/ψ vertex. The final cuts on the B vertex were similar to those described for the $J/\psi(\mu\mu)K^+$ analysis (χ^2/dof < 6, three standard deviation mass window and $p_T(B) > 5$ GeV).

The mass peak is shown in Figure 17-10; the mass resolution is about 23 MeV. The number of expected signal events for an integrated luminosity of 30 fb^{-1} is given in Table 17-4. The background shown in the figure and in the table includes the contribution from the reflection of the signal, where the π and K masses are wrongly assigned in the K^{*0} fit, as well as the contribution from other $B \to J/\psi X$ final states. Note that the peak in the background distribution near the B_d^0 mass is due to the K^{*0} reflection.

The numbers of tagged events (lepton tagging and B–π tagging) and the respective numbers of background events are also given in Table 17-4. The signal and background B–π tagging efficiencies have been deduced from the results obtained in the $B_d^0 \to J/\psi(\mu\mu)K_S^0$, as a complete study of the algorithm for this sample has not been performed yet.

17.2.2.11 Uncertainty on the production asymmetry

The production asymmetry, A^P, is not expected to exceed about 1% and it can be measured by using the decay channels discussed above which are expected to have negligible *CP* violation. It can be measured in the untagged control samples by counting the numbers of reconstructed B and $\bar{B}$ mesons, taking account of the flavour oscillations in the case of B_d^0. The statistical uncertainty on this measurement will be around $\delta A^P = 0.05\%$ (0.07%) from the $B^+ \to J/\psi(\mu\mu)K^+$ sample and about 0.07% (0.10%) from the $B_d^0 \to J/\psi(\mu\mu)K^{0*}$ sample, for a LVL2 trigger muon threshold of 3 GeV (5 GeV). It is assumed that any *CP*-violation effects in the two control samples can be neglected. Note that the large numbers of events available in these channels would be sufficient to study the p_T dependence of any observed production asymmetry.

Systematic effects due to small differences in the reconstruction efficiencies for K^+ and K^- remain to be evaluated. A cross-check of corrections for such effects may be made by using the flavour oscillations in the decays $B_d^0 \to J/\psi(\mu\mu)K^{*0}$, for example.

17.2.2.12 Uncertainties from tagging

Systematic effects on the *CP*-violation asymmetry measurement related to tagging can be studied using the $B^+ \to J/\psi(\mu\mu)K^+$ and $B_d^0 \to J/\psi(\mu\mu)K^{*0}$ events for lepton (electron and muons) tagging, and $B_d^0 \to J/\psi(\mu\mu)K^{*0}$ for *B*–π tagging.

In all tagging methods, a fraction of the produced *B* mesons are mistagged, as discussed in Section 17.2.2.4. The wrong-tag fraction can be measured by comparing the numbers of positive-charge and negative-charge tags associated with the decays $B^+ \to J/\psi(\mu\mu)K^+$ and $B_d^0 \to J/\psi(\mu\mu)K^{*0}$, allowing for the oscillations in the case of B_d^0. The wrong-tag fraction can be measured separately for the tagging of *B* and $\bar{B}$ mesons, and the average value can be computed. By using the numbers of tagged signal and background events listed in Table 17-4, the statistical uncertainty on the measurement of the dilution due to tagging is estimated to be $\delta(D_{\rm tag})/D_{\rm tag} = 0.0038$ (0.0048) for lepton tagging using the $B^+ \to J/\psi(\mu\mu)K^+$ sample with a LVL2 trigger $p_{\rm T}$ threshold of 3 GeV (5 GeV) for the second muon. For *B*–π tagging the result is $\delta(D_{\rm tag})/D_{\rm tag} = 0.0028$ (0.0037) for a 3 GeV (5 GeV) trigger threshold. Slightly larger uncertainties are obtained using the $B_d^0 \to J/\psi(\mu\mu)K^{*0}$ sample.

17.2.2.13 Uncertainties from background

Another contribution to the systematic error on sin2β comes from the uncertainty on the backgrounds to the signal and the control samples. Assuming conservatively a 5% uncertainty on the normalisation of the signal background, this propagates to give an uncertainty on the dilution from background of about $\delta(D_{\rm back})/D_{\rm back} = 0.0065$ (0.0055) for the 3 GeV (5 GeV) trigger threshold. The systematic uncertainty is smaller for the latter sample, because the signal-to-background ratio is better with a 5 GeV cut on the second muon. Here it is assumed that there is no *CP*-violation in the background. As in the case of the $B_d^0 \to \pi^+\pi^-$ analysis discussed in Section 17.2.3, it should be possible to measure the background using sidebands.

17.2.2.14 Summary of the sin2β measurement precision

Combining the various sources of uncertainty discussed above, one obtains an overall precision for the sin2β measurement as follows. The statistical precision of the sin2β measurement is $\delta(\sin 2\beta)$ (stat.) = 0.010 (0.012) for a LVL2 muon-trigger threshold of 3 GeV (5 GeV). The total systematic uncertainty is $\delta(\sin 2\beta)$ (syst.) = 0.005, independent of the LVL2 muon-trigger threshold. This level of precision is considerably better than at e^+e^- *B*-factories that will run before the start-up of ATLAS. For example BaBar expects to achieve a precision of about 0.05 [17-12].

17.2.3 Measurement of asymmetry in $B_d^0 \to \pi^+\pi^-$

The channel $B_d^0 \to \pi^+\pi^-$ is more complicated than the $B_d^0 \to J/\psi K_S^0$ one, both from the theoretical and the experimental point of view.

From the theoretical point of view, $B_d^0 \to \pi^+\pi^-$ is more complicated because of the interplay between *CP*-violation induced via tree-level and penguin diagrams, giving an observed time-dependent asymmetry that depends on a total of three parameters. The asymmetry *A(t)* for $B_d^0 \to \pi^+\pi^-$ is given by Equation 17-1. The two coefficients *a* and *b* that can be determined experimentally are related to the angle α in the unitarity triangle (where $\alpha = \pi - \beta - \gamma$ is assumed) by

$$a = 2\frac{A_P}{A_T}\sin\delta\sin\alpha \qquad 17\text{-}3$$

$$b = -\sin(2\alpha) - 2\frac{A_P}{A_T}\cos\delta\cos(2\alpha)\sin\alpha, \qquad 17\text{-}4$$

where A_T and A_P are the tree and penguin amplitudes, and δ is the phase difference between them. In this decay mode, the direct *CP*-violation component *a* may be sizeable.

The parameters *a* and *b* can be extracted from a fit to the observed asymmetry as a function of proper decay time. Since there are three unknowns, α, δ and A_P/A_T, and since δ is not believed to be calculable A_P/A_T must be given by theory. The evaluation of this quantity is currently the subject of intensive theoretical studies which will soon be aided by new measurements, for example from the BaBar collaboration [17-12]. Fleischer and Mannel [17-15] estimate that, with the help of measurements of the $B^+ \to \pi^+K^0$ and $B^+ \to \pi^+\pi^0$ branching ratios, the theoretical uncertainty on the penguin contribution would yield an uncertainty on α of less than 3º. The current best Standard Model fit of the unitarity triangle yields an estimate $\sin 2\alpha = -0.26^{+0.29}_{-0.28}$ [17-11]. A small value of $\sin 2\alpha$ could mean no observable *CP* asymmetry in this channel, but a tight bound on $\sin 2\alpha$ would nevertheless be a valuable constraint on the unitarity triangle.

Experimentally, the $B_d^0 \to \pi^+\pi^-$ signal must be extracted from the huge combinatorial background; this can be achieved using a combination of cuts, including vertexing. In the case of ATLAS, a more difficult physics background is other two- and three-body decays, which cannot be removed given the poor *K*/π separation. A simple event-counting method would rely too much on the background description, so an overall fit, using all available information, is necessary. It is likely that some of the background channels will themselves exhibit *CP*-violation effects, requiring a sophisticated analysis that fits the contribution to the observed asymmetry from the different channels.

17.2.3.1 Reconstruction

To select B_d^0 candidates, the presence of a pair of oppositely-charged particles each with $p_T > 4$ GeV was required. The pair should form a vertex with a χ^2 of the fit corresponding to a probability of more than 5%, and the invariant mass of the pair must be in the range 4.6–6.0 GeV [17-16]. The B_d^0 flight direction was required to be aligned in the transverse plane with the direction from the beam-line to the decay vertex. Tracks were not considered if they were consistent with originating from a low-mass displaced vertex; a track is eliminated if it forms with any other track a vertex where the two tracks had $p_T > 1$ GeV, separation $\Delta R < 0.5$, invariant mass less than 2 GeV, the vertex of the pair had a χ^2 probability of more than 1%, and the vertex was separated from the beam-line by more than ten standard deviations. This requirement also removed efficiently *B* decays with three or more prongs. The resolutions for the mass and decay time are $\sigma_m = 70$ MeV and $\sigma_t = 0.065$ ps respectively.

17.2.3.2 Backgrounds

The list of signal and background branching ratios and yields is given in Table 17-5. As the final results were obtained from an overall fit of the mass histograms, the yields in the mass histogram and in a $\pm 1\sigma_m$ mass window around the B_d^0 mass are listed separately. The $B_d^0 \to K^+\pi^-$ branching ratio is a recent, still imprecise, first measurement from CLEO [17-17]. The $B_d^0 \to \pi^+\pi^-$ branching ratio was inferred from the CLEO upper limit. The other branching ratios were inferred from the first two with a simple SU(3) symmetry assumption, except for the Λ_b decays which were set to their experimental upper limits [17-18]. It should be noted that these branching ratios are much less favourable than the estimated ones used in the ATLAS Technical Proposal [17-14]. Charmless decays to three-body final states other than $B \to \pi^+\pi^-\pi$ and $B \to \rho\pi^-$ involving charged kaons were neglected. The most abundant background is the decay $B_d^0 \to K^+\pi^-$, because of the absence of π/K separation, and because the mass resolution (σ_m = 70 MeV) is worse than the separation between the peaks (~40 MeV).

Table 17-5 Branching ratios and yields in the $\pi^+\pi^-$ sample for an integrated luminosity of 30 fb^{-1}. The *B* Comb. component corresponds to cases not explicitly listed when the pion candidates come from the same *B* hadron, while the Comb. component is the combinatorial background from all other sources (see text).

Channel	*BR*'s ($\times 10^{-5}$)	Yield 4.6–6.0 GeV	Yield $\pm 1\sigma_m$
$B_d^0 \to \pi^+\pi^-$	0.7	9500	6500
$B_d^0 \to K^+\pi^-$	1.5	19 800	12 100
$B \to \rho\pi^-$	2.5	8100	200
$B \to \pi^+\pi^-\pi$	5.0	2100	0
$B_s^0 \to \pi^+K^-$	0.7	2500	1400
$B_s^0 \to K^+K^-$	1.5	5200	3400
$\Lambda_b \to p\pi^-$	8.0	15 900	1100
$\Lambda_b \to pK^-$	8.0	16 700	2500
B Comb.	-	36 400	200
Comb.	-	19 500	2600

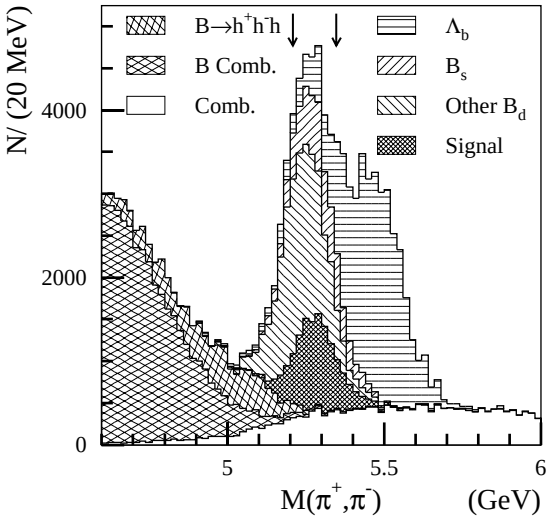

Figure 17-11 $\pi^+\pi^-$ mass spectrum. The arrows indicate a $\pm 1\sigma$ window.

The *B* combinatorial background is important below 5 GeV but does not contribute to the peak. It involves a variety of decays with three or four particles in the final state, such as $B_d^0 \to D^+\pi^-$ followed by $D^+ \to K^0\pi^+$, or $B_d^0 \to \pi^+\pi^-\pi\pi$. Usually, in these cases, the B_d^0 candidate does not fulfil the pointing requirement, unless the additional particles have low momentum. The truly combinatorial background is the random coincidence of high-impact-parameter tracks. The use of full simulation and reconstruction was mandatory to parametrise the tracking resolution, including exponential tails in addition to the parametrisation described in Section 17.2.2.2. A high-statistics sample was then simulated with fast simulation to demonstrate the required greater than 10^7 rejection factor on the LVL1 trigger output. About 50% of the combinatorial background involves a track from additional primary *D* mesons, 25% involves tracks from different *B* hadrons and the remainder involves a

track from a *B* hadron and a primary track. The shape of the combinatorial background is due to a kinematic effect – tracks with $p_T > 4$ GeV from different jets were combined. Figure 17-11 shows the final mass spectrum.

17.2.3.3 Results from event counting

Using Equation 17-2, results were first obtained using a simple event-counting method. The number of signal events found in the one-standard-deviation mass window around the nominal B_d^0 mass was 6500, and the background dilution was $D_{\text{back}} = 0.22$. Initial-state tagging was performed with the triggering muon, yielding a tagging dilution of $D_{\text{tag}} = 0.56$ (see Section 17.2.2.4). The time-integrated method yielded a dilution of $D_{\text{int}} = 0.59$. The statistical sensitivity to $\sin 2\alpha$ was then, in the absence of penguin decays, $\delta_{stat}(\sin 2\alpha) = 0.080$. Systematic uncertainties arising from the lepton tagging are expected to be of order 0.01, as in the $B_d^0 \rightarrow J/\psi K_s^0$ channel.

By the year 2005, the branching ratios of the two-body decay channels will have been measured at the *B* factories and at the Tevatron. A 5% relative uncertainty on these branching ratios will give a relative uncertainty on the asymmetry of less than 5% considering only the uncertainty on dilution from the background. However, it is possible that these backgrounds will exhibit some *CP* asymmetry themselves in which case the event-counting method will yield some linear combination of the signal and background *CP* asymmetries.

17.2.3.4 Results from time-dependent fit, allowing for *CP* violation in the background and using hadron identification

To be able to cope with the possible background *CP* asymmetry, and to use fully the time information and the one-standard-deviation π/K separation (see Section 3.4.4), an unbinned maximum-likelihood fit was performed (see [17-16] for more details) for events with mass above 5 GeV. For each event, the likelihood is the sum of the likelihoods of each decay hypothesis (as listed in Table 17-5 plus the charge-conjugated modes, three-body final states being neglected). The likelihood of a given decay hypothesis is computed using the corresponding event fraction, the proper-time and its uncertainty, and, for the corresponding particle-type assignment, the invariant mass of the pair and the measured specific ionisation, as well as the flavour at production and decay time. The flavour information was used to distinguish decays of the Λ_b (which does not oscillate) and the B_s^0 (which oscillates rapidly, with a period of about 0.4 ps for $\Delta m_s = 15\ \text{ps}^{-1}$) from those of the B_d^0 (which oscillates slowly with a period of about 14 ps).

The *CP* asymmetry parameters for all of the decays modes were free parameters of the fit. The time-dependent asymmetry for the non-flavour specific states (namely $B_d^0 \rightarrow \pi^+\pi^-$ and $B_s^0 \rightarrow K^+K^-$) are of the form given in Equation 17-1. *CP* asymmetry for decays to flavour-specific states is time independent and can originate only from direct *CP* violation, since no interference can occur through mixing. Other free parameters were the numbers of events for each decay channel. The total number of events was constrained to the observed one using the Poisson likelihood. The number of events for each channel (except for the combinatorial background) was constrained by the branching ratios given in Table 17-5, with a 5% uncertainty corresponding to the expected uncertainty on these branching ratios in the year 2005. The validity of the fitting method was checked by performing Monte-Carlo experiments with event statistics corresponding to 30 fb^{-1}, with randomised input *CP* asymmetry for signal and all backgrounds. The differ-

ence between the fitted asymmetry and the input asymmetry divided by the fit uncertainty was a normal Gaussian. The fit uncertainties on the *CP* parameters were almost independent of the input *CP* asymmetries, and were symmetric to a very good approximation.

If only the *b* coefficient for the decay $B_d^0 \to \pi^+\pi^-$ was fitted (which equals to sin 2α in the absence of penguin diagrams), fixing the other parameters at their true values, the uncertainty was $\delta b(B_d^0 \to \pi^+\pi^-) = 0.059$. This represents a 25% gain compared to the simple event counting method. If penguins were allowed (*i.e.* the *a* coefficient for $B_d^0 \to \pi^+\pi^-$ was also allowed to vary), the precision on *b* degraded to 0.070. Fitting simultaneously all the background asymmetries degraded the precision on *b* to 0.083. Note that a good accuracy of about 0.02 can also be obtained on the asymmetry in some of the background channels such as $B_d^0 \to K^+\pi^-$, which could be interesting in itself (the asymmetry in $B_d^0 \to K^+\pi^-$ could help in constraining the angle γ [17-19]).

If the numbers of events of each of the decay channels were also included in the fit, constraining the branching ratios with fractional errors of 5%, the final statistical uncertainty obtained was $\delta b(B_d^0 \to \pi^+\pi^-) = 0.085$, showing that there is little dependence on the input branching ratios. In fact, if no input branching ratio information was used, the uncertainty degraded only to 0.090, and the number of events of the various channels can be obtained from the data (provided the list of decays in Table 17-5 is complete).

The uncertainty on the *CP* parameters with and without specific ionisation information is shown on Table 17-6. If specific ionisation were not used, the sensitivity would be $\delta b(B_d^0 \to \pi^+\pi^-) = 0.117$, *i.e.* 35% worse, mainly because of the increased correlation of *b* with the *CP* asymmetry in the backgrounds $B_d^0 \to K^+\pi^-$ and $B_s^0 \to \pi^+K^-$. Furthermore, in this case, the fit did not converge unless the branching ratio information was included. The robustness of the fit was tested by degrading the assumed mass resolution, the proper-time resolution or specific ionisation resolution by 10% (in reality, these resolutions would be measured from reference samples with better accuracy). In all cases, this induced a shift of less than 0.01 in $b(B_d^0 \to \pi^+\pi^-)$.

Table 17-6 Sensitivity to *CP* asymmetries using the 5% constraint on the branching ratios, with and without using specific-ionisation (*dE/dx*) information.

Parameter	Sensitivity (with *dE/dx*)	Sensitivity (no *dE/dx*)
$a(B_d^0 \to \pi^+\pi^-)$	0.065	0.078
$b(B_d^0 \to \pi^+\pi^-)$	0.085	0.117
$a(B_d^0 \to K^+\pi^-)$	0.020	0.027
$a(B_s^0 \to \pi^+K^-)$	0.150	0.251
$a(B_s^0 \to K^+K^-)$	0.097	0.111
$b(B_s^0 \to K^+K^-)$	0.097	0.111
$a(\Lambda_b \to p\pi^-)$	0.022	0.032
$a(\Lambda_b \to pK^-)$	0.023	0.036
a(Comb.)	0.014	0.014

The precision on $b(B_d^0 \to \pi^+\pi^-)$ quoted above does not depend on the actual values of α, A_P/A_T and δ, but the resulting sensitivities on α and δ do. Figure 17-12 shows the precision on α for various input values of α and δ, and various values of the uncertainty on A_P/A_T, when the fit was performed using the specific-ionisation information. A precision of better than 5° was obtained for α in most cases, except when α was close to 45° or 135°, which corresponds to $|\sin 2\alpha| \sim 1$ which is strongly disfavoured by the Standard Model fit [17-11].

Due to the form of Equation 17-3 and Equation 17-4, a four-fold ambiguity in the result is unavoidable. For example, for input values $\alpha = 90°$, $\delta = 30°$ and $A_P/A_T = 0.2$, the solutions $(\alpha,\delta) = (90°, 30°)$, $(109°, 148°)$, $(270°, 210°)$ and $(289°, 330°)$ have the same χ^2-minimum. Additional secondary χ^2 minima sometimes cannot be excluded from the χ^2 difference – in the above example, solutions $(167°, 79°)$ and $(347°, 259°)$ have $\chi^2 - \chi^2_{\min} \sim 3$. Only an overall CKM unitarity-triangle fit can resolve these ambiguities.

Depending on the exact values of α and δ, and provided that A_P/A_T can be theoretically calculated to within 10%, the analysis of the decay $B^0_d \to \pi^+\pi^-$ could provide a constraint on α with a precision approaching 2° after three years of low-luminosity running, with the help of the specific-ionisation measurement in the TRT.

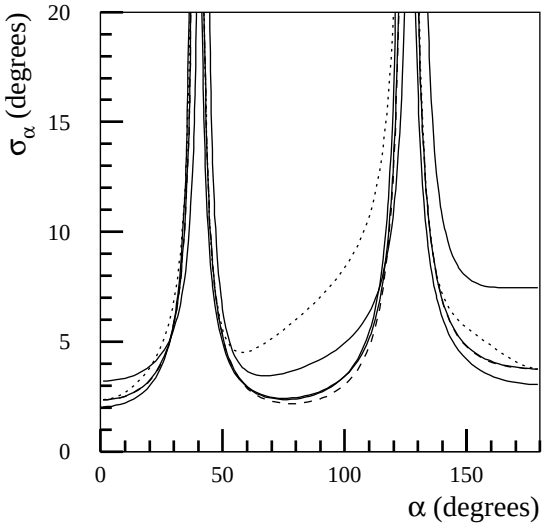

Figure 17-12 Precision for measuring α as a function of α after three years of low-luminosity data-taking. The three solid lines were obtained (from bottom to top) with phase values $\delta = 0°$,30° and 60°, and with $A_P/A_T = 0.2\pm0.02$. The dashed lined was obtained with $\delta = 30°$ and no uncertainty on A_P/A_T and the dotted line with 50% uncertainty on A_P/A_T. Note that the precision in the [-180º–0º] range is symmetric to the one shown.

17.2.4 Analysis of the decay $B^0_s \to J/\psi\,\phi$

17.2.4.1 Introduction

The channel $B^0_s \to J/\psi\phi$ can be used for various studies. Only a very small *CP* asymmetry is predicted in the Standard Model as discussed below, and the observation of a sizeable effect would be a clear sign of new physics. Measurement in ATLAS of the *CP* asymmetry at the level predicted by the Standard Model for this channel is marginal. However, a number of other parameters can be determined within the Standard Model, for example the width difference $\Delta\Gamma_s$. Although these other measurements do not strictly belong in this section, they are covered here since many aspects of the different analyses are coupled.

In the Standard Model, the interference term between the amplitudes for the direct weak decay $B^0_s \to J/\psi\phi$ and the same decay via B^0_s mixing is proportional to

$$e^{-i\xi} = (V^*_{ts}V_{tb}\,V^*_{cs}V_{cb})/(V_{ts}V^*_{tb}V_{cs}V^*_{cb}).$$

This measures the weak-interaction-induced phase that is expected to give rise to a rather small *CP*-violation asymmetry. The phase ξ is related to the angle γ of the unitarity triangle ($\xi = 2\lambda\sin\gamma|V_{ub}|/|V_{cb}|$, where λ is the sine of the Cabibbo angle), but the small expected value of ξ (0.024 – 0.054, see [17-20]) makes the extraction of γ via a measurement of ξ difficult. Larger than expected *CP* violation in the decay $B^0_s \to J/\psi\phi$ would indicate that processes beyond the Standard Model are involved. Tagged samples of $B^0_s \to J/\psi\phi$ decays are needed for the measurement of ξ.

The decay $B_s^0 \to J/\psi\phi$ is also very useful for measuring several, as yet unmeasured, parameters in the B_s^0-meson system. The different masses of the *CP*-even ($B_s{}^L$) and *CP*-odd ($B_s{}^H$) mass eigenstates give rise to mixing between B_s^0 and $\bar{B}_s^0$ mesons. The difference of widths, $\Delta\Gamma_s = \Gamma_H - \Gamma_L$, could be as much as 20% of the average B_s^0 width $\Gamma_s = (\Gamma_H + \Gamma_L)/2$ [17-21]. The angular distribution of the $B_s^0 \to J/\psi\phi$ decay products can be expressed in terms of the amplitudes $A_\parallel$ and A_0 for decays to *CP*-even, and $A_\perp$ for decays to *CP*-odd $J/\psi\phi$ configurations. The expression for the angular distribution contains time-dependent terms proportional to $e^{-\Gamma_H t}$ or to $e^{-\Gamma_L t}$, allowing $\Delta\Gamma_s$ to be determined experimentally. The phase differences between the amplitudes $A_\parallel$, A_0 and $A_\perp$, caused by strong final-state interactions, are parametrised by δ_1 and δ_2, and are measured through their effect on the interference between the amplitudes. Measurements of these parameters require no tagging of the B_s^0 flavour at production.

The B_s^0 decay proper time and the angular distributions of the secondary particles in the decay channel $B_s^0 \to J/\psi\phi$ thus carry information about eight independent parameters of physics interest:

- $\Delta\Gamma_s = \Gamma_H - \Gamma_L$;
- $\Gamma_s = (\Gamma_H + \Gamma_L)/2$;
- two independent *CP* amplitudes $A_\parallel$ and $A_\perp$ (A_0 is constrained by a normalisation condition);
- the strong phase differences δ_2, δ_1;
- the weak phase difference ξ;
- the B_s^0 mixing parameter $x_s = \Delta m_s/\Gamma_s$.

Measurements exist at present only for the B_s^0 lifetime. A method is proposed, based on earlier theoretical works [17-22], to measure some of these parameters, and estimate the expected precision.

The discussion of the $B_s^0 \to J/\psi\phi$ channel is arranged as follows. Firstly the experimental aspects of reconstructing $B_s^0 \to J/\psi\phi$ decays are addressed in Section 17.2.4.2. Then, Section 17.2.4.3 describes how the flavour at production can be tagged for this channel; tagging is used for the extraction of the weak phase difference, ξ, associated with *CP*-violation (Section 17.2.4.5). In Section 17.2.4.4, the maximum-likelihood method that is used to determine the various parameters from the measured angular distributions is described. This is followed in Section 17.2.4.5 by a discussion of how the parameters are determined in two steps, first using the full sample without tagging to determine Γ_s, $\Delta\Gamma_s$, $A_\parallel$, $A_\perp$ and δ_2-δ_1, and then using the subset of tagged events to determined the additional parameter ξ. The conclusions for this channel are presented in Section 17.2.4.6.

17.2.4.2 Reconstruction of $B_s^0 \to J/\psi\,\phi$

The decay $B_s^0 \to J/\psi(\mu\mu)\phi(KK)$ was used for this investigation. Simulated events were generated with PYTHIA and fully simulated with GEANT. The expression $\mu 6\mu 3$ implies the presence of one muon with p_T of at least 6 GeV and one muon with p_T of at least 3 GeV. All of the particles were required to have $|\eta| < 2.5$, and the p_T of each kaon from the ϕ decay was required to be greater than 0.5 GeV. The selection procedure followed quite closely that for the $B_d^0 \to J/\psi K_s^0$ study, and, from the point of view of the experimental techniques, the channels are similar in many ways.

The reconstruction of the J/ψ proceeded as described for $B_d^0 \to J/\psi K_s^0$. Successful fits were retained if the invariant mass was within three standard deviations of the nominal J/ψ mass ($\sigma = 39$ MeV). In the ϕ reconstruction, pairs of oppositely-charged $p_T > 0.5$ GeV particles were fitted to a common vertex and their invariant mass was calculated assuming kaon hypotheses. Successful fits were retained within the mass interval [1.0092–1.0296] GeV. The particles were also required to be collimated within 15 degrees in φ and 10 degrees in θ.

The muons and kaons coming from the J/ψ and ϕ candidates were assumed to come from a $B_s^0 \to J/\psi\phi$ decay and a three-dimensional kinematic fit was performed. The four particles were required to be consistent with coming from a common vertex (probability larger than 0.02), and the momentum of the B_s was required to point to the primary vertex. Cuts on the p_T of the B_s^0 (greater than 10 GeV) and on the proper time (longer than 0.5 ps) were also applied. The resolution on the reconstructed B_s^0 mass was 27 MeV. The residual distribution of the proper lifetime of the reconstructed B_s^0 was well described by a double Gaussian function (Figure 17-13). In the modelling of the angular distributions, described below, a simplified parametrisation of the proper-time resolution was used with a single-Gaussian of width 0.063 ps (see Figure 17-14).

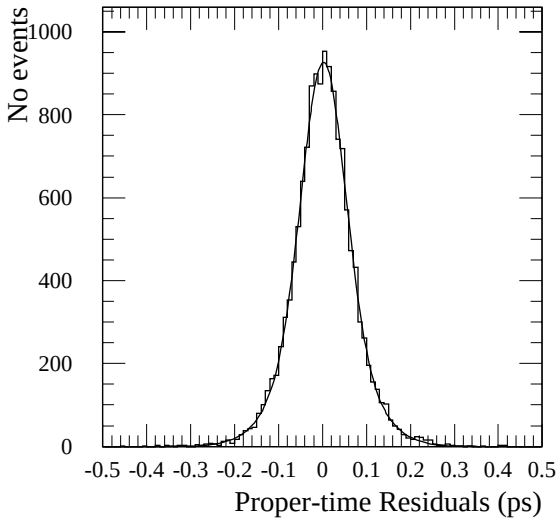

Figure 17-13 Residual distribution of the proper lifetime of the reconstructed B_s^0, fitted with a double Gaussian of widths 0.05 ps and 0.09 ps.

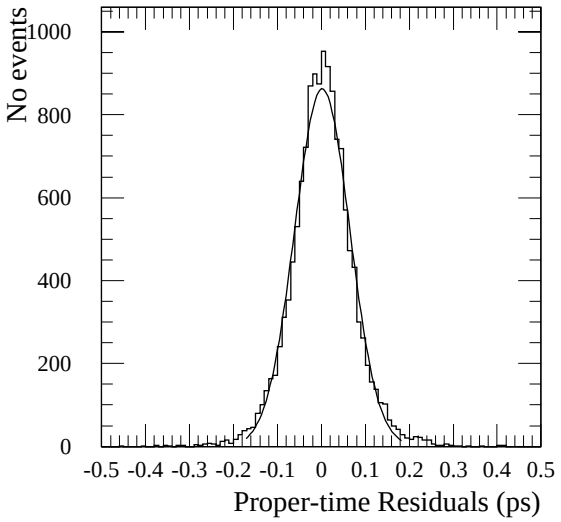

Figure 17-14 Residual distributions of the proper lifetime of the reconstructed B_s^0, fitted with a single Gaussian of width 0.063 ps.

The backgrounds from other processes were estimated using the following Monte Carlo samples: an inclusive sample of $c\bar{c}$ events containing a J/ψ produced by a direct colour-octet model implemented in PYTHIA [17-23]; an inclusive sample of $b\bar{b}$ events giving rise to a J/ψ; and a sample of $B_d^0 \to J/\psi K^{*0}$ decays. The number of events selected for each sample is given in Table 17-7. Essentially all the background came from events containing a b-quark, with the reconstructed J/ψ being genuine and the ϕ being fake. The dominant channel giving rise to such backgrounds is $B_d^0 \to J/\psi K^{*0}$. Typically, the fake ϕ contains one genuine and one misassigned charged kaon. The use of specific ionisation could help in controlling the K^{*0} reflection, but this is still to be studied.

The background studies were mainly done with the fast-simulation program. A smaller sample of inclusive $b\bar{b} \to J/\psi X$ events was, however, studied with full simulation and reconstruction, and the results obtained were found to be consistent with the fast-simulation study.

Table 17-7 Signal statistics and background composition after the acceptance cuts in $|\eta|$ and p_T (first two columns), and after the reconstruction of simulated events (last column). Note that the $B_d \to J/\psi\, K^{*0}$ background is included in the inclusive $b\bar{b} \to J/\psi X$ samples, and should not be double counted.

Process	Cross-section [μb]	N events for 30 fb^{-1}	Reconstruction efficiency	N rec. events for 30 fb^{-1}
signal $B_s^0 \to J/\psi\phi$	2.7 x 10^{-5}	810 000	0.39	318 000
$pp \to J/\psi(\mu 6 \mu 3)X$	1 x 10^{-2}	3 x 10^{8}	<3x10^{-5}	<9400
$b\bar{b} \to J/\psi(\mu 6 \mu 3)X$	4 x 10^{-3}	12 x 10^{7}	4x10^{-4}	47 000
$B_d^0 \to J/\psi(\mu 6 \mu 3)K^{0*}$	2.5 x 10^{-4}	7.5 x 10^{6}	3x10^{-3}	21 000

17.2.4.3 Tagging

Much of the analysis described below can be performed without tagging the flavour at production of the B_s^0 that decayed to $J/\psi\phi$. However, the measurement of the weak phase, described at the end of Section 17.2.4.5, requires tagging. Here some issues of tagging that are specific to the $B_s^0 \to J/\psi\phi$ analysis are addressed.

Events with an additional lepton can provide a subsample of tagged events. However, the efficiency of lepton tagging is low due to the relatively small semileptonic branching ratios of B-mesons and the effects of the p_T and η cuts. The tagging efficiency can be increased by using the jet charge to determine the flavour of the B at production. Note that the mass of the resonance B^{**} is expected to be such that the decay to $B_s^0 K$ is not kinematically possible [17-24], and therefore, the jet-charge tag can exploit only the fragmentation correlation in case of B_s^0 mesons.

The jet charge Q_{jet} is defined by:

$$Q_{jet} = \frac{\sum_i q_i p^{\kappa}{}_i}{\sum_i \left| p^{\kappa}{}_i \right|}$$

where q_i is the charge of the i^{th} particle, and p_i is a momentum measure. According to fragmentation models, the particles are ordered in the momentum component parallel to the original quark direction. On the other hand, maximising the momentum component transverse to the beam-line would guarantee that no very hard forward particles are wrongly assigned to the jet. Various options were considered, and the best results were obtained by using the momentum component parallel to the reconstructed B-meson direction, which is used in the following. The parameter κ controls the relative influence of the soft and hard tracks in the jet charge. Using Monte Carlo models, the optimum performance was obtained with a value of κ near to 0.5, though in principle additional information could be extracted by considering a range of κ values.

Only particles which satisfied the general acceptance requirements of $p_T > 0.5$ GeV and $|\eta| < 2.5$ were considered. Particles were required to be in a cone with $\Delta R<0.8$ of the reconstructed B-meson momentum vector, and particles from the $B_s^0 \to J/\psi\phi$ decay were excluded. Particles with impact parameters $|d_0| > 1$ cm were also excluded, as they probably originate from decays rath-

er than the fragmentation process. After these selections, there were cases where there were no particles remaining to form the jet charge, and also cases where the charge was based only on one particle.

The algorithm was optimised by minimising the estimate of the statistical error on the *CP*-violating weak phase measurement by adjusting the square of the dilution factor D_{tag} and the tag efficiency ε. This resulted in a lower efficiency (62%) and a higher purity (D_{tag} = 0.23) than for jet-charge tagging in the $B_d^0 \to J/\psi K_S^0$ analysis. In principle, the algorithm could be further optimised by excluding cases where the estimated jet charge is near to zero where the chances of incorrect assignment are high. Preliminary studies indicate that the performance is enhanced with the exclusion of cases with $|Q_{jet}| < 0.3$. This will be optimised further using higher statistics.

17.2.4.4 Modelling of $B_s^0 \to J/\psi\,\phi$ decays and the likelihood function

The precision of the experimental determination of the parameters describing the $B_s^0 \to J/\psi\phi$ decay was estimated using a maximum-likelihood fit to Monte Carlo simulated data. The decay $B_s^0 \to J/\psi\phi$ was modelled according to a probability density function:

$$F^{\pm}(t,\Omega) = \frac{1}{4\pi^2} \times \frac{9}{8} \times \sum_{i=1}^{8} f_i^{\pm}(t) \times F_i(\Omega) \qquad 17\text{-}5$$

where the superscript +(-) indicates B_s^0 ($\bar{B}_s^0$), the functions f_i are bilinear combinations of time-dependent decay amplitudes, and $\Omega = (\theta_1,\theta_2,\varphi)$, where θ_1,θ_2 and φ are angles describing the direction of the secondary particles in the decay $B_s^0 \to J/\psi(\mu\mu)\,\phi(KK)$ as defined in Figure 17-15. The functions F_i are trigonometric functions of the decay angles. The functions f_i and F_i are defined in [17-25]. In the simulation, the values of the eight unknown independent parameters (two amplitude values $A_{||}$ and $A_{\perp}$, two strong phase differences δ_2 and δ_1, the mixing parameter x_s, the weak phase ξ and the two decay rates Γ_H and Γ_L) were chosen based on the latest theoretical and experimental results ([17-21], [17-22] and [17-26]).

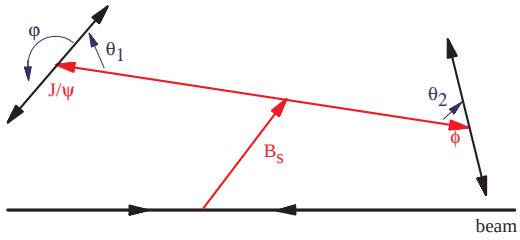

Figure 17-15 Definition of the three angles: θ_1 is the angle of the muon momentum in the J/ψ rest frame with the *z*-axis parallel to the J/ψ momentum in the B_s^0 rest frame; θ_2 is defined in a similar way for the φ decay; φ is the angle between the J/ψ and the φ decay planes.

The simulation took into account the proper-time resolution approximated by a single Gaussian function as obtained from the full detector simulation and reconstruction. The acceptance as a function of proper time and the three angles was included. The background was also simulated, and was taken to be flat in the decay angles. The time dependence of the background was assumed to have a form $e^{-\Gamma t}$ where Γ corresponds to the average neutral *B*-hadron lifetime. The level of background, *b*, will be determined from the invariant-mass distribution, and was fixed in the fit. The likelihood function had the form:

$$L = \prod_{i=1}^{N} \frac{\int_0^{\infty}\left(\varepsilon_1 F^{+}(t_i,\Omega_i) + \varepsilon_2 F^{-}(t_i,\Omega_i) + be^{-\Gamma t_i}\right)\times e^{-(t_i-t')^2/2\delta t^2}\,dt'}{\int_{t_{min}}^{\infty}\left(\int_0^{\infty}\left(\varepsilon_1 F^{+}(t,\Omega) + \varepsilon_2 F^{-}(t,\Omega) + be^{(-\Gamma t)}\right)\times e^{-(t-t')^2/2\delta t^2}\,dt'\right)dt}$$

where for untagged events $\varepsilon_1 = \varepsilon_2 = 0.5$; for events with a B_s^0 tagged as a particle $\varepsilon_1 = 1\text{-}\omega$ and $\varepsilon_2 = \omega$, where ω is the wrong-tag fraction; for a B_s^0 tagged as an antiparticle $\varepsilon_1 = \omega$ and $\varepsilon_2 = 1\text{-}\omega$. The index i is running over the events. Finally, t_{min} is the minimum proper lifetime allowed in the event selection.

17.2.4.5 Parameter determination and estimation of precision

The most complete analysis would include both tagged and untagged events in a single maximum-likelihood fit. It became clear, however, that the expected experimental precision was not sufficient to allow the simultaneous determination of all eight unknown parameters. Instead, the analysis was divided into two steps. In the first step, the full event statistics were used. In the second step only the events with a tag were analysed. This allowed several useful approximations to be made.

The full event statistics, including both tagged and untagged events, were modelled according to Equation 17-5. Five parameters, $\Delta\Gamma_s$, Γ_s, $A_{\|}$, $A_{\perp}$ and δ_2-δ_1, were determined in the fit assuming $\varepsilon_1 = \varepsilon_2 = 0.5$, which leads to the cancellation of the oscillatory terms in the likelihood function. With this assumption, the three other parameters ξ, x_s and $\delta_2+\delta_1$ have a negligible influence on the likelihood function, and so were fixed in the fit.

The rate difference $\Delta\Gamma_s = \Gamma_H - \Gamma_L$ could be determined by this method with a relative statistical error of less than 12% with 30 fb^{-1}, corresponding to 300 000 signal events (see Figure 17-16). The result depends strongly on the value of $\Delta\Gamma_s/\Gamma_s$, while the decay-time resolution is not critical here (see Figure 17-17). The relative statistical errors on the other free parameters are summarised in Table 17-8. The statistical errors are typically a few percent, except for the strong phase difference $\delta_2 - \delta_1$, for which the probability density function is insensitive if $(\delta_2 - \delta_1) \sim \pi$, as suggested by theoretical models (see Dighe, Dunietz and Fleischer in [17-22], and references therein).

Table 17-8 Summary of the analysis of the full sample with 30 fb^{-1}.

Number of signal events	300 000
Number of background events	45 000
$\delta t/t$	4.4%
Input parameters	$\Delta\Gamma_s/\Gamma_s = 0.15$, $x_s = 20$, $\xi = 0.039$, $\delta_2+\delta_1 = -\pi$
$\delta(\Delta\Gamma_s)/\Delta\Gamma_s$	12%(stat.)+7%(syst.)
$\delta(\Gamma_s)/\Gamma_s$	0.7%(stat.)+0.3%(syst.)
$\delta(A_{\|})/A_{\|}$	0.7%(stat.)+0.3%(syst.)
$\delta(A_{\perp})/A_{\perp}$	3%(stat.)+1%(syst.)

Several sources of systematic errors were considered. The mean lifetime in the background sample must be known, and will be determined from sidebands in the reconstructed mass distribution. If this mean lifetime was overestimated by 3% in the likelihood function, the measured value of $\Delta\Gamma_s$ was shifted downwards by 0.04, giving a 7% systematic error. The likelihood fit also used the measured proper decay time and its error for each event. The error depends on the position uncertainty on the secondary

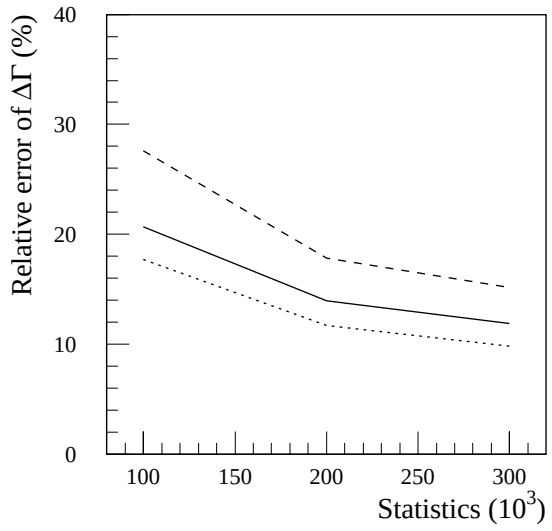

Figure 17-16 The relative error of $\Delta\Gamma_s$ as a function of signal statistics for three levels of background: 15% (full line), 30% (dashed line) and no background (dotted line). $\Delta\Gamma_s$ was determined by a maximum-likelihood fit. The four other parameters of the fit were Γ_s, $A_{\|}$, $A_{\perp}$ and δ_2-δ_1.

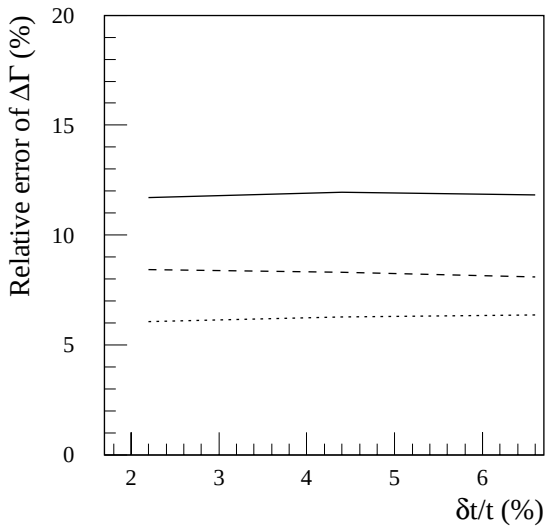

Figure 17-17 The relative error of $\Delta\Gamma_s$ as a function of the relative precision of the proper-lifetime measurement for three values of the ratio $\Delta\Gamma_s/\Gamma_s$. The full line corresponds to $\Delta\Gamma_s/\Gamma_s$ = 15%, the dashed line to $\Delta\Gamma_s/\Gamma_s$ = 20%, and the dotted line to $\Delta\Gamma_s/\Gamma_s$ = 25%. The statistics here is 300 000 signal events, and the background is 15% of the signal.

vertex and on the momentum error, and a mis-estimation of either can introduce a systematic error on the $\Delta\Gamma_s$. This effect was tested by assuming a proper decay-time uncertainty in the likelihood fit that was 5% larger than the uncertainty used in the simulation; this conservative estimate resulted in a negligible systematic error.

The angular distribution of the background may have a complicated shape. Decay channels that are flat in decay angle (*e.g.* the decay to non-resonant states $B \to J/\psi K\pi$) will gain apparent structure due to incorrect mass assignments. Background channels with polarisation (such as $B_d^0 \to J/\psi K^{*0}$) will have an intrinsic angular structure and will also be deformed by incorrect mass assignments. However, the actual background shape can be estimated from the side bands. Also, if the background composition is well determined, the background shape can be calculated from the measured distributions of the background channels. No estimate is included as yet for the systematic effects of the non-flat background distributions.

The second part of the analysis was done for tagged events only, using the jet-charge-tag method described in Section 17.2.4.3 (there is scope to improve the measurement by using other tagging methods in addition). In order to give an estimate of the performance in a simple case, seven of the eight parameters were fixed, leaving only the weak phase ξ free. This was based on the assumption that the values of the other parameters can be determined in other measurements (using untagged $B_s^0 \to J/\psi\phi$, and $B_d^0 \to J/\psi K^{*0}$, and $B_s^0 \to D_s\pi$ events). For this ideal case, where all other parameters were measured with negligible errors, the weak phase can be obtained with a statistical precision $\delta(\xi) \sim 0.03$, assuming the Standard Model expected values: $\xi = 0.039$, $x_s = 20$ and $\Delta\Gamma_s/\Gamma_s = 0.15$. The errors obtained for different values of the mixing parameter and proper decay-time resolutions are shown in Figure 17-18. The results for the tagged analysis are summarised in Table 17-9.

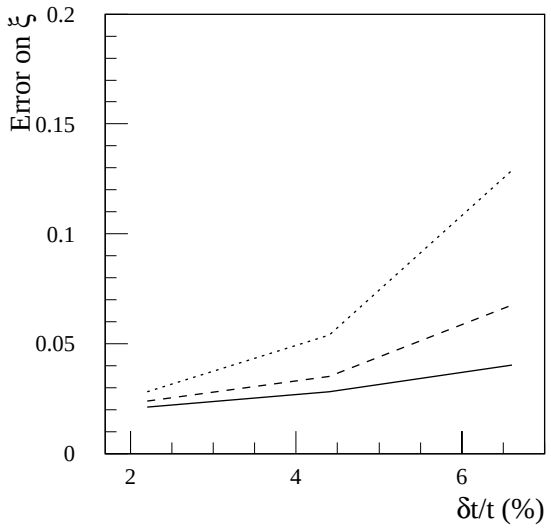

Figure 17-18 The error on the weak phase ξ as a function of the relative precision of proper-lifetime measurement for three values of the B_s^0 mixing parameter x_s. The full line corresponds to $x_s = 20$, the dashed line to $x_s = 30$ and dotted line to $x_s = 40$. The weak phase ξ was determined by a maximum-likelihood fit, while all other seven parameters were fixed.

Table 17-9 Summary of the tagged-sample analysis with 30 fb^{-1} data.

Number of signal events	180 000
Number of background events	27 000
Proper-time resolution	4.4%
Input parameters	$\Delta\Gamma_s/\Gamma_s = 0.15$, $x_s = 20$, $\tau_{Bs} = 1.61$ ps, $\delta_2 = 0$, $\delta_1 = -\pi$ $\lvert A_\parallel \rvert / \lvert A_0 \rvert = 0.8$; $\lvert A_\perp \rvert / \lvert A_0 \rvert = 0.37$ $\xi = 0.039, \tau_B = 1.58$ ps.
$\delta(\xi)$	0.03 (stat.)

The results presented above are derived in the context of the Standard Model. However, it is possible to express the *CP* asymmetry purely in terms of the helicity amplitudes, Γ_s, $\Delta\Gamma_s$, x_s and the phase ξ. The precision of the asymmetry measurement can be studied, independent of the model, as a function of any triplet of $\Delta\Gamma_s$, x_s and ξ values, using the already-measured value of Γ_s. Table 17-10 shows results for some examples of input parameters. The first row in the Table shows the case of the Standard Model, with the input parameters based on an overall fit to existing experimental data. The second and third rows show two examples for non-standard models [17-27], [17-28]. As expected, there is some degradation of the precision on the measurement of ξ with increasing x_s, due to the difficulty in resolving the rapid oscillations. On the other hand, the precision of the measurement of ξ is not strongly dependent on the value of ξ. For example, keeping $x_s = 20$, $\Delta\Gamma_s/\Gamma_s = 0.15$ and using an input value $\xi = 0.16$ (instead of 0.04 in the Standard Model), leaves the precision unchanged at $\delta(\xi) = 0.03$. Thus, the analysis gives high sensitivity to any new physics that significantly enhances the *CP* asymmetry in this channel over a wide range of x_s values.

Table 17-10 Precision on measurement of *CP*-violation parameter, ξ, as a function of $\Delta\Gamma_s/\Gamma_s$, x_s and the true value of ξ.

x_s	$\Delta\Gamma_s/\Gamma_s$	Input value of ξ	δ(ξ)
20	0.15	0.04 (SM)	0.03
33	0.15	0.08 ([17-27])	0.05
39	0.15	0.17 ([17-28])	0.07

17.2.4.6 Conclusions

The main results of the $B_s^0 \to J/\psi\phi$ study are summarised in Tables 17-8 and 17-9. ATLAS can measure $\Delta\Gamma_s$ with a relative error $\delta(\Delta\Gamma_s)/\Delta\Gamma_s$ = 12% (stat.)+7% (syst.). The fit allows the simultaneous determination of other parameters (the average B_s^0 width Γ_s and the amplitudes $A_\parallel$ and $A_\perp$ for the decays to *CP*-even and *CP*-odd $J/\psi\phi$ configurations). Making use of events tagged using the jet-charge technique, the *CP*-asymmetry parameter ξ can be measured with high precision (δ(ξ) = 0.03 for x_s = 20).

17.2.5 Analysis of the decay $B_d^0 \to D^0K^{*0}$

The use of the decay amplitudes of several neutral B_d^0 decays in determining the angle $\gamma = \arg(-V_{ud}V^*_{ub}/V_{cd}V^*_{cb})$ was investigated. The following relations hold between six decay modes of the B_d^0 to neutrals:

$$A(B_d{}^0 \to \bar{D}^0 K^{*0}) = A(\bar{B}_d{}^0 \to D^0 \bar{K}^{*0}),$$

$$A(B_d{}^0 \to D^0 K^{*0}) = A(\bar{B}_d{}^0 \to \bar{D}^0 \bar{K}^{*0}),$$

$$A(B_d{}^0 \to D^0{}_{CP} K^{*0}) \neq A(\bar{B}_d{}^0 \to D^0{}_{CP} \bar{K}^{*0}),$$

when D^0 and K^{*0} decay into $K\pi$, and $D^0{}_{CP}$ indicates a decay to *CP* eigenstates ($\pi\pi$, KK). Two triangles can be constructed, which differ in the length of one side only [17-29]. The angle 2γ is formed as shown in Figure 17-19. Thus, by measuring the decay rates in the different channels, the angle γ could be determined.

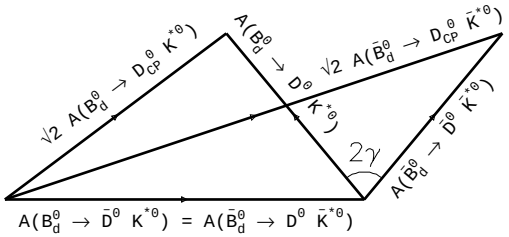

Figure 17-19 The two triangles formed of decay amplitudes of six possible decays of the form $B^0{}_d \to D^0K^{*0}$.

The assumed branching ratios used in the study were agreed between the LHC experiments (see [17-30]); some of the expected branching ratios are very low, in particular that for $B_d^0 \to D^0K^{*0}$, which is of the order of 10^{-6}. After the requirement that the events contained a trigger muon with $p_T > 6$ GeV and that the four final-state particles were within the detector acceptance, approximately 60 events were retained per year in the rarest decay mode. Furthermore, the LVL2 trigger for this decay, based on the D^0 and K^{*0} invariant masses, would have to operate with high p_T thresholds for the hadrons in or-

der to limit the rate from the combinatorial background. It can be concluded that the measurement of all the six decay modes by ATLAS alone would not be feasible assuming Standard Model branching ratios.

17.2.6 Conclusions on *CP* violation

The angle β of the unitarity triangle is expected to be measured with a precision of

$$\delta(\sin 2\beta) = 0.012 \text{ (stat.)}$$

with an integrated luminosity of 30 fb^{-1}, collected at low-luminosity data-taking. The precision can be improved further to about 0.010, if triggering on muons with p_T>3 GeV can be achieved at LVL2. Systematic uncertainties arising from the production asymmetry, flavour tagging and background are expected to be controlled to better than 1% by using the non-*CP*-violating decays $B^+ \to J/\psi(\mu\mu)K^+$ and $B_d^0 \to J/\psi(\mu\mu)K^{*0}$ (where $K^{0*} \to K^+\pi^-$). Furthermore, the availability of many tagging algorithms and the large statistics of tagged and untagged signal and background samples provide the flexibility to perform internal cross-checks of the analysis.

Since the ATLAS Technical Proposal, significant progress has been made in the analysis of the decay $B_d^0 \to \pi^+\pi^-$ to overcome problems associated with the large background. An effort has been made to use the specific ionisation in the TRT to separate pions, kaons and protons on a statistical basis. A sophisticated fitting method has been developed to use maximally the event-by-event information: each event was assigned a probability to belong to any of the decay classes (signal and backgrounds), based on the probability distribution functions on proper time and its uncertainty, the invariant mass, the specific ionisation of the two particles and the flavour at production and at the decay time. Possible *CP* asymmetries in the background were taken into account. With an integrated luminosity of 30 fb^{-1}, the fit gave a statistical precision on the mixing-induced *CP*-violation amplitude *b* of:

$$\delta b(B_d^0 \to \pi^+\pi^-) = 0.085 \text{ (stat.)}.$$

The branching ratios of the signal and background channels were constrained to estimated values within 5% uncertainty, since the branching ratios are expected to be measured before ATLAS can proceed to the *CP*-violation measurement of this channel. However, if the branching fractions were left completely free in the fit, the precision would degrade only to 0.090. On the other hand, if no *dE/dx* information were used, the precision would degrade to 0.117. The sensitivity to the direct *CP*-violation amplitude *a* was 0.065. If there were no penguin graphs contributing to this decay, the *b* coefficient would be equal to $\sin 2\alpha$, which could be measured with a precision of 0.059.

The sensitivity to the angle α of the unitarity triangle depends on the value of α, on the ratio of the penguin and tree-level amplitudes, and on the strong phase δ. Nevertheless, over most of the range, the precision on α approaches 2° after three years of low luminosity running.

The third angle of the unitarity triangle, γ, is difficult to measure. Using tagged $B_s^0 \to J/\psi\phi$ decays, the weak phase $\xi = 2\lambda\sin\gamma|V_{ub}|/|V_{cb}|$ can be measured with a statistical precision of 3% (x_s = 20) using the 180 000 reconstructed events expected for an integrated luminosity of 30 fb^{-1}. Nevertheless, there is no sensitivity to the angle γ in the Standard Model. The use of the six decays $B_d^0 \to D^0K^{*0}$ does not seem feasible for γ measurement either. The unitarity triangle will, however, already be overconstrained by the measurements of the two angles α and β, and the B_s^0-mixing measurement (see following section), which measures a side of the unitarity trian-

gle. The current Standard Model best estimate for the angle γ yields $\gamma = (59.5\,^{+8.5}_{-7.5})^{o}$ [17-11]. Furthermore, it has been proposed that the ratio of the branching fractions of charged and neutral B mesons into $K\pi$ final states would constrain $\sin^2\gamma$, but there are diverging views on the theoretical validity of the proposal (see [17-11] and references therein).

The $B_s^0 \to J/\psi\phi$ decays are also useful for various other measurements of the B_s^0-meson system, and an angular-analysis technique was developed. Since tagging is not needed, the statistics are fairly large – 300 000 events for an integrated luminosity of 30 fb^{-1}. The width difference of the B_s^0-meson eigenstates, $\Delta\Gamma_s$, is expected to be measured with a relative statistical precision of 12%, and Γ_s can be measured with a relative statistical precision of 0.7%. In addition, the decay amplitudes to *CP*-even and *CP*-odd final states can be measured with a relative precision of 0.7% and 3%, respectively.

17.3 Measurements of B_s^0 oscillations

17.3.1 Introduction

The observed B_s^0 and $\bar{B}_s^0$ states are linear combinations of two mass eigenstates, denoted here as H and L. Due to the non-conservation of flavour in charged weak-current interactions, transitions between B_s^0 and $\bar{B}_s^0$ states occur with a frequency proportional to $\Delta m_s = m_H - m_L$.

Experimentally, these $B_s^0 - \bar{B}_s^0$ oscillations have not yet been observed directly. In the Standard Model, their frequency is predicted in [17-11] to be between 12.0 ps^{-1} and 17.6 ps^{-1} with 68% CL, and lower than 20 ps^{-1} at 95% CL, significantly larger than the corresponding value Δm_d in the $B_d^0 - \bar{B}_d^0$ system. From measurements done by the ALEPH, DELPHI and OPAL experiments at LEP, by SLD at SLC, and by CDF at the Tevatron, a combined lower bound of $\Delta m_s > 12.4$ ps^{-1} at 95% CL has been established [17-31]. In the $B_d^0 - \bar{B}_d^0$ system, the oscillations have been directly observed and a rather precise value $\Delta m_d = 0.464 \pm 0.018$ ps^{-1} [17-32] has been measured.

The values for Δm_d and Δm_s predicted in the Standard Model by computing the corresponding box diagrams, with the top-quark contribution assumed to be dominant, are proportional to $|V_{td}|^2$ and $|V_{ts}|^2$ respectively. The direct determination of V_{td} and V_{ts} from Δm_d and Δm_s is, however, hampered by hadronic uncertainties. These uncertainties partially cancel in the ratio:

$$\frac{\Delta m_s}{\Delta m_d} = \frac{M_{B_s}}{M_{B_d}} \frac{\hat{B}_{B_s} f_{B_s}^2}{\hat{B}_{B_d} f_{B_d}^2} \left|\frac{V_{ts}}{V_{td}}\right|^2 ,$$

where M_B are the B-meson masses, $\hat{B}_B$ are the bag parameters, and f_B are the B-meson form factors. Using the experimentally-measured masses and a value for the ratio $\xi = (\sqrt{\hat{B}_{B_s}} f_{B_s})/(\sqrt{\hat{B}_{B_d}} f_{B_d})$ which can be computed in lattice QCD, a better constraint for $|V_{ts}/V_{td}|$ can be obtained, which can then be converted into a constraint of $|V_{td}|$, the worst-measured side of the unitarity triangle.

The probability density to observe an initial B_s^0 meson decaying at time t after its creation as a $\bar{B}_s^0$ meson is given by:

$$P_{B^0\bar{B}^0}(t) = \frac{\Gamma_s^2 - \left(\frac{\Delta\Gamma_s}{2}\right)^2}{2\Gamma_s} e^{-\Gamma_s t}\left(\cosh\frac{\Delta\Gamma_s t}{2} + \mu_0 \cos\Delta m_s t\right),$$

where $\mu_0 = -1$, $\Delta\Gamma_s = \Gamma_H - \Gamma_L$ and $\Gamma_s = (\Gamma_H + \Gamma_L)/2$. For an initial B_s^0 meson, the probability density $P_{B^0B^0}(t)$ to decay as a B_s^0 meson at time t is given by the above expression with $\mu_0 = +1$. The small effects of *CP* violation are neglected in the above relation. Unlike $\Delta\Gamma_d$ which can be safely neglected, the width difference in the $B_s^0 - \bar{B}_s^0$ system $\Delta\Gamma_s$ could be as much as 20% of the total width Γ_s [17-21].

Experimentally, Δm_s can be determined by measuring the asymmetry:

$$A(t) = \frac{P_{B^0B^0}(t) - P_{B^0\bar{B}^0}(t)}{P_{B^0B^0}(t) + P_{B^0\bar{B}^0}(t)} \sim \frac{\cos\Delta m_s t}{\cosh\frac{\Delta\Gamma_s t}{2}}.$$

B_s^0 ($\bar{B}_s^0$) is tagged at the production point by the muon used for the LVL1 trigger; at the decay vertex, the meson's state is given by the charge-sign of one of the decay products. From the fit of the measured asymmetry, the oscillation period can be determined.

17.3.2 Event reconstruction

The signal channels considered for the measurement of $B_s^0 - \bar{B}_s^0$ oscillations were $B_s^0 \to D_s^- \pi^+$ and $B_s^0 \to D_s^- a_1^+$, with $D_s^- \to \phi\pi^-$ followed by $\phi \to KK$ (called ϕ mode in the following). For both B_s decay channels, the decay mode $D_s^- \to K^{*0}K^-$ with $K^{*0} \to K^+\pi^-$ (called K^{*0} mode in the following) may also be considered in order to increase the signal statistics. The K^{*0} mode analysis for $B_s^0 \to D_s^- a_1^+$ decay channel is discussed in this report. However, since this mode is not yet included in the LVL2 trigger, the maximum value of Δm_s which can be measured by ATLAS was computed without the K^{*0} mode, and the effect of including this decay mode is shown separately. Using a 3 GeV cut on the p_T of the three tracks from $D_s^- \to K^{*0}K^-$ and other cuts similar to those for the ϕ-mode trigger, an increase of around 235 Hz would be expected in the LVL2 trigger rate from adding the K^{*0} mode.

The simulated events were generated using PYTHIA 5.7 in the framework of ATGEN-B (ATLAS program for *B*-event generation), and then passed through the ATLAS simulation program DICE (Inner Detector only). Details about the general physics parameters used in ATGEN-B may be found in Section 17.1.2. In the simulation, the *b*-quark was forced to decay semileptonically giving a muon with $p_T > 6.0$ GeV and $|\eta| < 2.5$. The $\bar{b}$ was forced to produce the required *B*-decay channel. All the final-state particles from the *B* decay were required to have $p_T > 0.5$ GeV and $|\eta| < 2.5$. The simulated events were reconstructed using the xKalman package from ATRECON.

17.3.2.1 Reconstruction of the D_s^- decay vertex in the $D_s^- \to \phi\pi^-$ decay mode

The reconstruction of the D_s^- vertex in the $D_s^- \to \phi\pi^-$ decay mode proceeded via two steps (here and in the following charge-conjugate states are implicitly included). The ϕ decay vertex was first reconstructed by considering all combinations of pairs of oppositely-charged tracks with $p_T > 1.5$ GeV for both tracks. Kinematic cuts on the angles between the two tracks

$\Delta\theta_{KK} < 10°$ and $\Delta\varphi_{KK} < 10°$ were also imposed. The two-track vertex was then fitted assigning the kaon mass to both tracks. Combinations passing a fit-probability cut of 1% with the invariant mass within $3\sigma_{\phi}$ of the nominal ϕ mass were selected as ϕ candidates. To all accepted ϕ candidates, a third negative track with $p_T > 1.5$ GeV from the remaining ones was added. The pion mass was assigned to the third track and a three-track vertex was refitted. Combinations of three tracks which had a fit probability greater than 1% and an invariant mass within $3\sigma_{D_s}$ of the nominal D_s^- mass were selected as D_s^- candidates. Figure 17-20 and Figure 17-21 show the reconstructed invariant-mass distributions for ϕ and D_s^-, respectively, in the channel $B_s^0 \to D_s^-(\phi\pi^-)a_1^+$. Similar distributions were obtained in the decay channel $B_s^0 \to D_s^-(\phi\pi^-)\pi^+$.

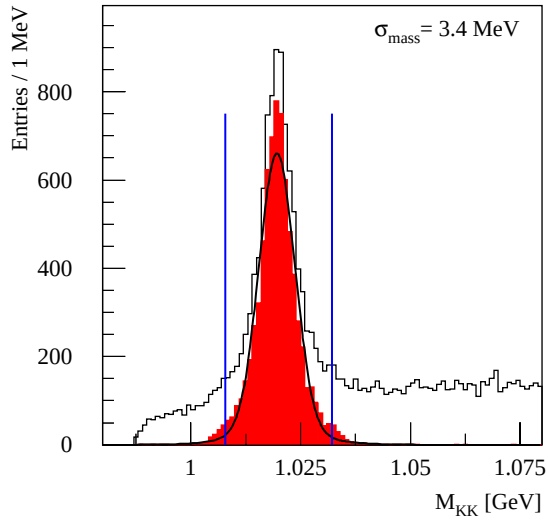

Figure 17-20 Reconstructed ϕ invariant-mass distribution in the channel $B_s^0 \to D_s^-(\phi\pi^-)a_1^+$. In the dark histogram, the reconstructed ϕ matches a generated ϕ. The distributions only include the contribution from Monte Carlo events for the indicated signal channel.

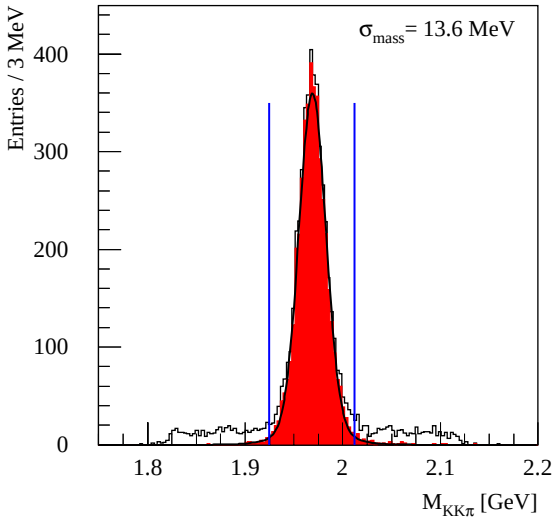

Figure 17-21 Reconstructed D_s^- invariant-mass distribution in the channel $B_s^0 \to D_s^-(\phi\pi^-)a_1^+$. In the dark histogram, the reconstructed D_s^- matches a generated D_s^-. The distributions only include the contribution from Monte Carlo events for the indicated signal channel.

17.3.2.2 Reconstruction of the D_s^- decay vertex in the $D_s^- \to K^{*0}K^-$ decay mode

The reconstruction of the D_s^- decay vertex in the decay mode $D_s^- \to K^{*0}K^-$ was performed using similar techniques to those used in the $D_s^- \to \phi\pi^-$ case. First, K^{*0} candidates were reconstructed from combinations of pairs of oppositely-charged tracks, with $p_T > 3.0$ GeV for each track, and $\Delta\theta_{K\pi} < 10°$ and $\Delta\varphi_{K\pi} < 20°$ assuming that the positive-charge track was a kaon and the negative-charge one was a pion. The two tracks were required to originate from the same vertex (vertex fit probability greater than 1%) and have an invariant mass within one Γ_{BW} of the nominal K^{0*} mass.

Additional negative-charge tracks with $p_T > 3.0$ GeV were combined with K^{*0} candidates, applying the kaon hypothesis for the additional tracks. The three tracks were then fitted as originating from a common vertex; no mass constraint was required for the tracks from K^{*0}, due to the large K^{*0} natural width. Combinations with a fit probability greater than 1% and with an invariant mass within $3\sigma_{D_s}$ of the nominal D_s^- mass were selected as D_s^- candidates.

The invariant-mass distributions of the reconstructed K^{*0} and D_s^- candidates are shown in Figure 17-22 and Figure 17-23, respectively.

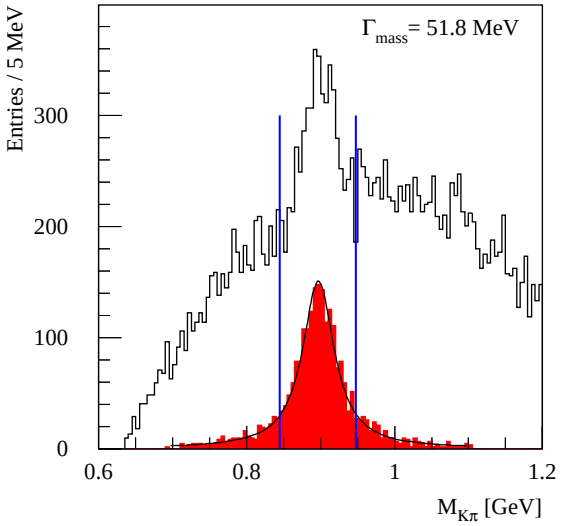

Figure 17-22 Reconstructed K^{*0} invariant-mass distribution in the $B_s^0 \to D_s^-(K^{*0}K^-)a_1^+$ channel. In the dark histogram, the reconstructed K^{*0} matches a generated K^{*0}. The distributions only include the contribution from Monte Carlo events for the indicated signal channel.

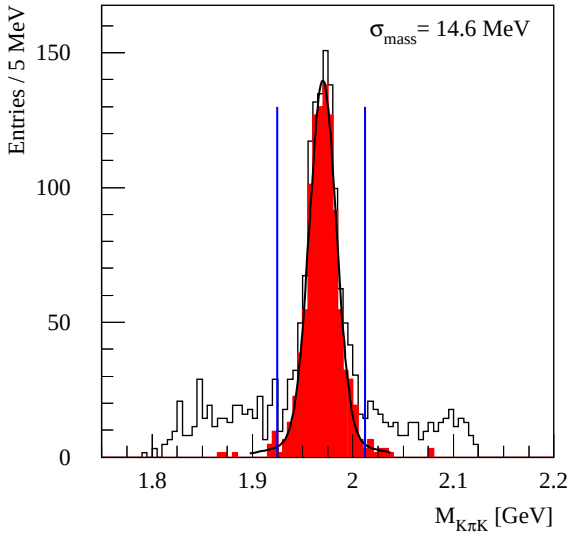

Figure 17-23 Reconstructed D_s^- invariant-mass distribution in the $B_s^0 \to D_s^-(K^{*0}K^-)a_1^+$ channel. In the dark histogram, the reconstructed D_s^- matches a generated D_s^-. The distributions only include the contribution from Monte Carlo events for the indicated signal channel.

17.3.2.3 Reconstruction of the a_1^+ decay vertex

For each reconstructed D_s^- meson, a search was made for a_1^+ candidates in three-particle combinations of the remaining charged tracks. In a first step, ρ^0 mesons were reconstructed from all combinations of two tracks with opposite charges and with $p_T > 0.5$ GeV for both tracks, each particle in the combination being assumed to be a pion. Kinematic cuts $\Delta\theta_{\pi\pi} < 15°$ and $\Delta\varphi_{\pi\pi} < 35°$ were used to reduce the combinatorial background. The two selected tracks were then fitted as originating from the same vertex; from the combinations passing a fit probability cut of 1%, those with an invariant mass within 1.5 Γ_{BW} of the nominal ρ^0 mass were selected as ρ^0 candidates.

Next, a positive track with $p_T > 0.5$ GeV from the remaining charged tracks was added to the ρ^0 candidate, assuming the pion hypothesis for the extra track. The three tracks were then fitted as originating from a common vertex, without any mass constraints. Combinations with a fit probability greater than 1% and with an invariant mass within 300 MeV of the nominal a_1^+ mass were selected as a_1^+ candidates.

The invariant-mass distributions of the reconstructed ρ^0 and a_1^+ candidates are shown in Figure 17-24 and Figure 17-25, respectively.

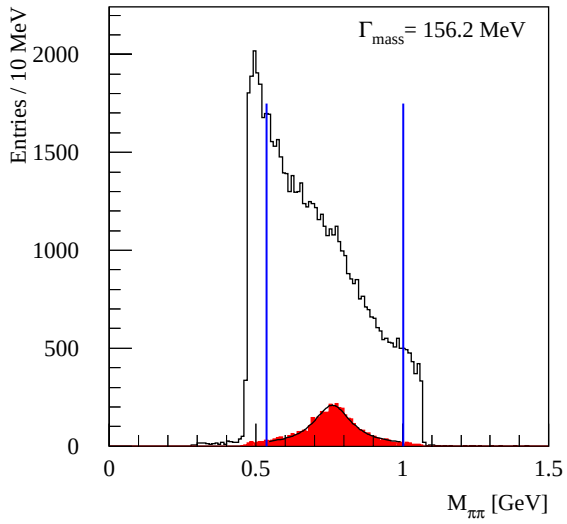

Figure 17-24 Reconstructed ρ^0 invariant-mass distribution in the channel $B_s^0 \to D_s^-(\phi\pi^-)a_1^+(\rho^0\pi^+)$. In the dark histogram, the reconstructed ρ^0 matches a generated ρ^0. The distributions only include the contribution from Monte Carlo events for the indicated signal channel.

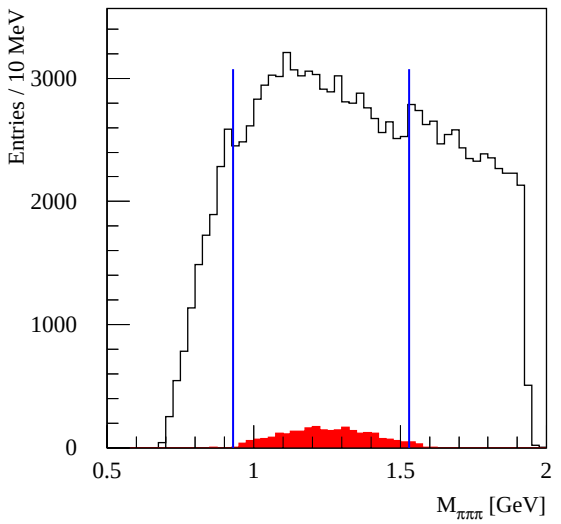

Figure 17-25 Reconstructed a_1^+ invariant-mass distribution in the channel $B_s^0 \to D_s(\phi\pi^-)a_1^+(\rho^0\pi^+)$. In the dark histogram, the reconstructed a_1^+ matches a generated a_1^+. The distributions only include the contribution from Monte Carlo events for the indicated signal channel.

17.3.2.4 Reconstruction of the B_s^0 decay vertex

For the $B_s^0 \to D_s^-\pi^+$ channel, the B_s^0 decay vertex was reconstructed by considering all D_s^- candidates and adding a fourth track from the remaining tracks in the event. This track was required to have opposite charge with respect to the pion track from the D_s^- and $p_T > 1.0$ GeV. The four-track decay vertex was refitted including ϕ and D_s^- mass constraints, and requiring that the total momentum of the B_s^0 vertex pointed to the primary vertex and the momentum of D_s^- vertex pointed to the B_s^0 vertex.

For the $B_s^0 \to D_s^- a_1^+$ channel, the B_s^0 candidates were reconstructed combining the D_s^- candidates with the a_1^+ candidates. A six-track vertex fit was then performed with mass constraints for the tracks from ϕ and D_s^-; due to the large a_1^+ natural width, the three tracks from the a_1^+ were not constrained to a_1^+ mass. Similarly, for the K^{*0} mode, the tracks from K^{*0} were not constrained to the K^{*0} mass. As in the $B_s^0 \to D_s^-\pi^+$ channel, the total momentum of the B_s^0 vertex was required to point to the primary vertex and the momentum of D_s^- vertex was required to point to the B_s^0 vertex.

In order to be selected as B_s^0 candidates, the four-track and six-track combinations were required to give a probability greater than 1% for the vertex fit. The signed separation between the reconstructed B_s^0 vertex and the primary vertex, and between the D_s^- and B_s^0 vertex were required to be positive (the momentum should not point backward to the parent vertex). To improve the purity of the sample, further cuts were imposed: the accepted B_s^0 candidates were required to have a proper decay time greater than 0.4 ps, an impact parameter smaller than 55 μm and $p_T > 10$ GeV.

17.3.3 Background analysis

Background to the channels being considered for the measurement of Δm_s can come from two sources: from other four- or six-body B-hadron decay channels, and from combinatorial background (random combinations with some or all particles not originating from a B decay).

For $B_s^0 \to D_s^- \pi^+$, the following four-body decay channels were considered as potential sources of background: $B_d^0 \to D_s^- \pi^+$, $B_d^0 \to D^- \pi^+$ (with $D^-, D_s^- \to \phi\pi^-$ and $\phi \to KK$) and $\Lambda_b^0 \to \Lambda_c^+ \pi^-$ followed by $\Lambda_c^+ \to pK^-\pi^+$. The similar six-body decay channels considered as potential sources of background for $B_s^0 \to D_s^- a_1^+$ were: $B_d^0 \to D_s^- a_1^+$, $B_d^0 \to D^- a_1^+$ (with $D^-, D_s^- \to \phi\pi^-$, $\phi \to KK$ for the ϕ mode and $D^-, D_s^- \to K^{*0}K^-$, $K^{*0} \to K^+\pi^-$ for the K^{*0} mode) and $\Lambda_b^0 \to \Lambda_c^+ \pi^-$ followed by $\Lambda_c^+ \to pK^-\pi^+\pi^+\pi^-$. The simulated four- and six-body background events were passed through the detailed detector-simulation program, reconstructed and analysed using the same programs, the same conditions and the same cuts as the signal events.

In order to study the combinatorial background, a very large sample of simulated inclusive-muon events is needed. The results presented here are based on a sample of 1.1 million $b\bar{b} \to \mu X$ events, with $p_T > 6$ GeV and $|\eta| < 2.4$ for the muon corresponding the trigger conditions. Even with this large sample, the background estimate is based on very low statistics.

The $b\bar{b} \to \mu X$ sample was analysed in the framework of the fast-simulation program ATLFAST++ (see Section 2.5), applying the same algorithms and the same cuts that were used for the fully-simulated samples. A careful check was made of the performance of the fast-simulation program by running it on signal and six-body background samples, and comparing the results with those from the detailed simulation. Good agreement was obtained for the number of reconstructed events and the widths of the mass peaks for the reconstructed particles.

17.3.4 Evaluation of signal and background statistics

The reconstructed B_s^0 invariant-mass distributions in the decay channels $B_s^0 \to D_s^-(\phi\pi^-)\pi^+$, $B_s^0 \to D_s^-(\phi\pi^-)a_1^+(\rho^0\pi^+)$ and $B_s^0 \to D_s^-(K^{*0}K^-)a_1^+(\rho^0\pi^+)$ are shown in Figure 17-26, Figure 17-27 and Figure 17-28, respectively, for an integrated luminosity of 10 fb^{-1}.

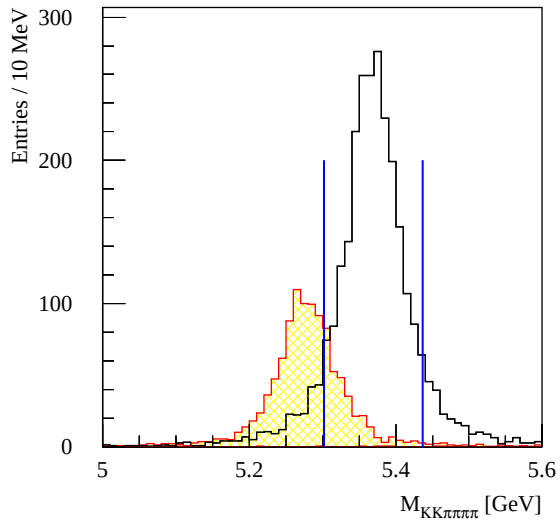

Figure 17-26 Reconstructed B_s^0 invariant-mass distribution for $B_s^0 \to D_s^-(\phi\pi^-)\pi^+$ decays. The open histogram shows the signal, the hatched histogram shows the background from $B_d^0 \to D_s^-(\phi\pi^-)\pi^+$ decays and the dark histogram shows the fake reconstructed B_s^0 decays from the signal sample. The combinatorial background is not shown here.

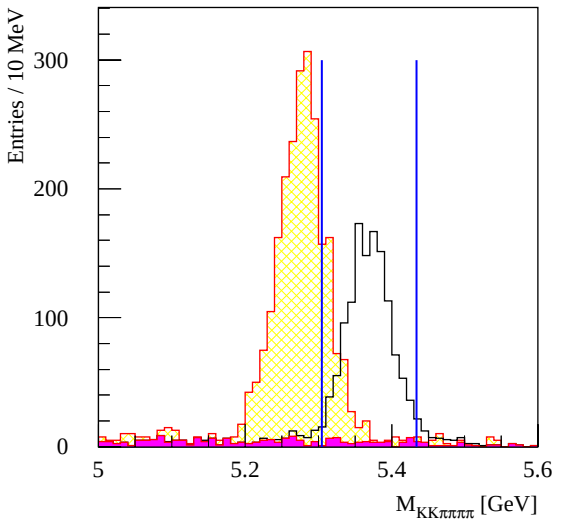

Figure 17-27 Reconstructed B_s^0 invariant-mass distribution for $B_s^0 \to D_s^-(\phi\pi^-)a_1^+(\rho^0\pi^+)$ decays. The open histogram shows the signal, the hatched histogram shows the background from $B_d^0 \to D_s^-(\phi\pi^-)a_1^+(\rho^0\pi^+)$ decays and the dark histogram shows the fake reconstructed B_s^0 decays from the signal sample. The combinatorial background is not shown here.

For $B_s^0 \to D_s^-(\phi\pi^-)a_1^+$ and $B_s^0 \to D_s^-(K^{*0}K^-)a_1^+$ the results are from fully-simulated samples; for $B_s^0 \to D_s^-(\phi\pi^-)\pi^+$ they are from a fast-simulation analysis. The reconstructed mass distributions for the four- and six-body background channels are also shown in the figures. The combinatorial background, for which only very limited statistics are available, is not shown in these figures; its distribution is expected to be flat in the relevant mass range. The mass resolutions of the reconstructed B_s^0 mesons were obtained by fitting single-Gaussian distributions. The results are 33.5 MeV for $B_s^0 \to D_s^-(\phi\pi^-)\pi^+$, 32.2 MeV for $B_s^0 \to D_s^-(\phi\pi^-)a_1^+(\rho^0\pi^+)$ and 30.5 MeV for $B_s^0 \to D_s^-(K^{*0}K^-)a_1^+(\rho^0\pi^+)$.

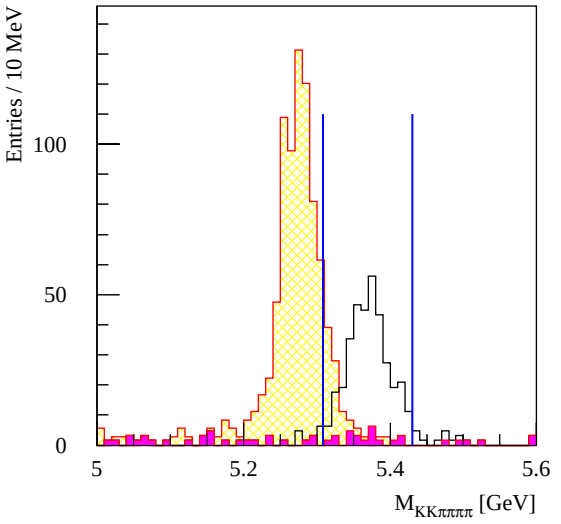

Figure 17-28 Reconstructed B_s^0 invariant-mass distribution for $B_s^0 \to D_s^-(K^{*0}K^-)a_1^+(\rho^0\pi^+)$ decays. The open histogram shows the signal, the hatched histogram shows the background from $B_d^0 \to D_s^-(K^{*0}K^-)a_1^+(\rho^0\pi^+)$ decays and the dark histogram shows the fake reconstructed B_s^0 decays from the signal sample. The combinatorial background is not shown here.

The numbers of events expected for the various signal and background channels that have been analysed are given in Table 17-11 for an integrated luminosity of 30 fb^{-1}. The cross-sections and

Table 17-11 Signal and background samples analysed for the study of $B_s^0 - \bar{B}_s^0$ oscillations. The numbers presented for the combinatorial background are for the sum of the $B_s^0 \to D_s^-(\phi\pi^-)\pi^+$ and $B_s^0 \to D_s^-(\phi\pi^-)a_1^+$ analysis channels.

Process	Cross-section [μb]	Events for 30 fb^{-1}	Simulated events	Rec. events	Rec. events for 30 fb^{-1}
$B_s^0 \to D_s^-(\phi\pi^-)\pi^+$	1.281x10^{-5}	384 180	47 775	5 018	6 750
$B_s^0 \to D_s^-(\phi\pi^-)a_1^+$	1.281x10^{-5}	384 180	18 784	1 506	3 620
$B_s^0 \to D_s^-(K^{*0}K^-)a_1^+$	1.589x10^{-5}	476 970	9 988	208	1 000
$B_d^0 \to D_s^-(\phi\pi^-)\pi^+$	4.519x10^{-6}	135 570	24 698	694	710
$B_d^0 \to D_s^-(\phi\pi^-)a_1^+$	2.098x10^{-5}	629 460	9 699	186	1 390
$B_d^0 \to D_s^-(K^{*0}K^-)a_1^+$	2.605x10^{-5}	781 500	9 988	41	345
$B_d^0 \to D^-(\phi\pi^-)a_1^+$	8.204x10^{-6}	246 135	9 949	1	3
$B_d^0 \to D^-(K^{*0}K^-)a_1^+$	7.651x10^{-6}	229 530	9 989	6	15
$\Lambda_b^0 \to \Lambda_c^+(pK\pi\pi\pi)\pi^-$	1.968x10^{-6}	59 040	10 994	0	0
Comb. background sum (φ mode only)			1.1x10^6	see text	14 500

the numbers of events for 30 fb^{-1} are calculated after the following cuts: one *b*-quark is required to decay semileptonically giving a muon with $p_T > 6.0$ GeV and $|\eta| < 2.5$; the other *b*-quark is required to give rise to the given *B*-hadron decay channel. In addition, in the simulated samples the final-state particles from the given *B*-hadron decay channel are required to have $p_T > 0.5$ GeV and $|\eta| < 2.5$.

The events reconstructed from the samples for the exclusive decay modes were counted in a $\pm 2\sigma_{B_s}$ window around the nominal B_s^0 mass. Using the fraction of events reconstructed in the simulated sample and the number of events expected for an integrated luminosity of 30 fb^{-1}, the expected number of reconstructed events was estimated. The numbers or reconstructed events given in the table have been corrected for the additional cuts imposed on the simulated sample using the cross-section given by PYTHIA, for muon efficiency (on average 0.85) and for LVL2 trigger efficiency (0.85).

A total of 10370 reconstructed events is expected for the φ mode of the $B_s^0 \to D_s^-\pi^+$ and $B_s^0 \to D_s^- a_1^+$ decay channels for an integrated luminosity of 30 fb^{-1}. An increase of around 30% in the number of events could be obtained by including the K^{*0} mode for both B_s decay channels.

The only significant backgrounds come from the $B_d^0 \to D_s^- a_1^+$ and $B_d^0 \to D_s^-\pi^+$ channels, and from the combinatorial background. Note that the number of reconstructed events from the two B_d^0 decay channels is conservative since the branching-ratio values used are upper limits. As expected, due to the combination of the D^- mass shift ($M_{D^-} - M_{D_s^-} = 90$ MeV) and B_d^0 mass shift ($M_{B_s} - M_{B_d} \approx 100$ MeV), very few $B_d^0 \to D^- a_1^+$ events are reconstructed in a $\pm 2\sigma_{B_s}$ window

around B_s^0 nominal mass. Due to the different decay topology, the $\Lambda_b^0 \to \Lambda_c^+ \pi^-$ channel does not give any contribution to the background. No contribution to the background for $B_s^0 \to D_s^- \pi^+$ is expected from $B_d^0 \to D^- \pi^+$ and $\Lambda_b^0 \to \Lambda_c^+ \pi^-$ decays.

The statistics available for estimating the combinatorial background are very limited, despite the large size (1.1 million events) of the $\mu 6X$ sample. Each simulated event was therefore passed 20 times through the fast-simulation program, different random smearing of the track parameters being applied each time. The number of background events was counted in an enlarged mass window ($[M_{B_s} - 150$ MeV, $M_{B_s} + 150$ MeV$]$). On average, 0.4 events per pass were reconstructed in the mass window summing the $B_s^0 \to D_s^- \pi^+$ and $B_s^0 \to D_s^- a_1^+$ channels for the ϕ mode. Normalising to the number of $\mu 6X$ events expected for an integrated luminosity of 30 fb^{-1}, applying correction factors for the reconstruction and trigger efficiencies, and scaling for the size of the mass window, the combinatorial background was estimated to be 14 500 events in a $\pm 2\sigma_{B_s}$ window around the B_s^0 mass, and the range of variation was estimated to be between 9600 and 20 900 event at 90% CL. Correlations between the results from the 20 passes were taken into account. The corresponding background for the K^{*0} mode of the $B_s^0 \to D_s^- a_1^+$ is 5600 events.

17.3.5 Determination of the proper-time resolution

The proper time of the reconstructed B_s^0 candidates was computed from the reconstructed transverse decay length, d_{xy}, and from the B_s^0 transverse momentum, p_T:

$$t = \frac{d_{xy} M_{B_s^0}}{c p_T} \equiv d_{xy} g$$

where $g = M_{B_s^0}/(c p_T)$.

The transverse decay length is the distance between the interaction point and the *b*-hadron decay vertex, projected onto the transverse plane. Figure 17-29 shows, for the example of the $B_s^0 \to D_s^-(\phi\pi^-) a_1^+(\rho^0\pi^+)$ decay mode, the difference $d_{xy} - d_{xy}^0$ fitted with two Gaussian functions, where d_{xy}^0 is the true transverse decay length. For each event, the decay-length uncertainty, $\sigma_{d_{xy}}$, was estimated from the covariance matrices of the tracks associated with the vertices. The pull of the transverse decay length, $(d_{xy} - d_{xy}^0)/\sigma_{d_{xy}}$, was found to have a Gaussian shape with a width of $S_{d_{xy}} = 0.958 \pm 0.020$.

The distribution for $(g - g_0)/g_0$, shown in Figure 17-30, also has a Gaussian shape, with a width of $S_g = (0.631 \pm 0.013)\%$. Here $g_0 = t_0/d_{xy}^0$, with t_0 being the true proper time. The proper-time resolution function $\mathrm{Res}(t, t_0)$ was parametrised, in close analogy with [17-33], with a Gaussian function:

$$\mathrm{Res}(t, t_0) = \frac{1}{\sqrt{2\pi}\sigma(t_0)} \exp\left[-\frac{1}{2}\left(\frac{t - t_0}{\sigma(t_0)}\right)^2\right],$$

with the width $\sigma(t_0)$ computed event-by-event as:

$$\sigma(t_0) = \sqrt{(g S_{d_{xy}} \sigma_{d_{xy}})^2 + (t_0 S_g)^2}.$$

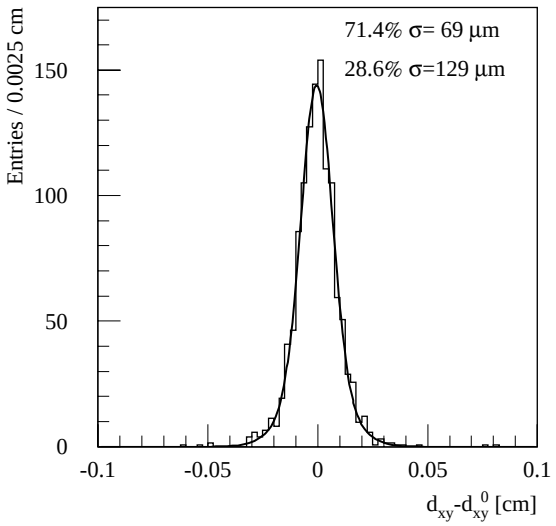

Figure 17-29 Decay-radius resolution for the decay channel $B_s^0 \to D_s^-(\phi\pi^-)a_1^+(\rho^0\pi^+)$

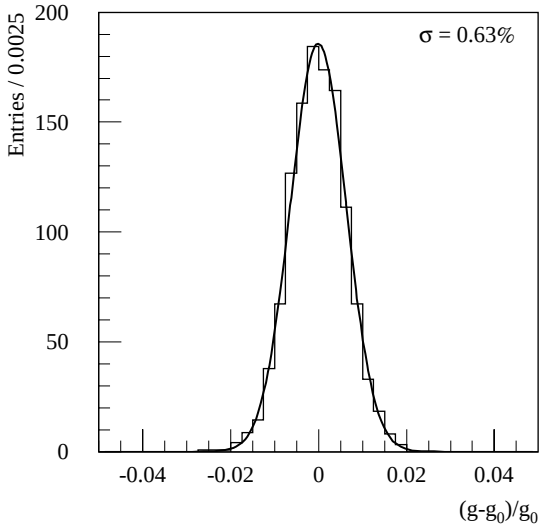

Figure 17-30 Fractional resolution on g-factor for the decay channel $B_s^0 \to D_s^-(\phi\pi^-)a_1^+(\rho^0\pi^+)$

Figure 17-31 shows, for the example of the $B_s^0 \to D_s^-(\phi\pi^-)a_1^+(\rho^0\pi^+)$ decay mode, the proper-time resolution together with the parametrisation obtained from the $\mathrm{Res}(t, t_0)$ function given above. The parametrisation reproduces well the tails seen in the distribution for reconstructed events. The $t - t_0$ distribution has an rms of 0.071 ps. To illustrate the deviations from the Gaussian shape, when the distribution was fitted with two Gaussian functions, the widths obtained were 0.050 ps for the narrow Gaussian function (60.5%) and 0.093 ps for the broader one (39.5%). Similar distributions were obtained for the other two analysed channels.

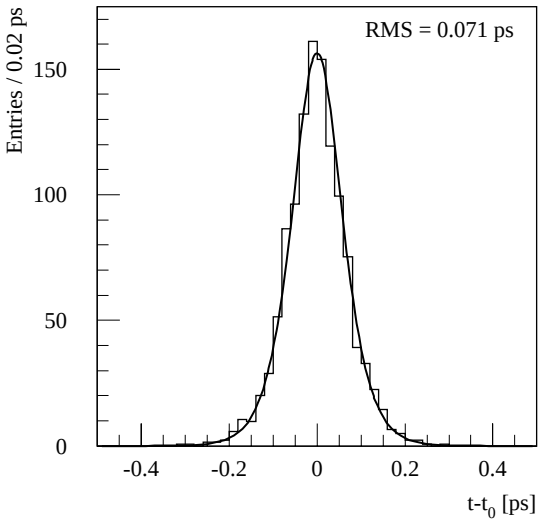

Figure 17-31 Proper-time resolution for the decay channel $B_s^0 \to D_s^-(\phi\pi^-)a_1^+(\rho^0\pi^+)$. The curve displays the resolution as obtained from the $\mathrm{Res}(t, t_0)$ function given in the text.

17.3.6 Extraction of Δm_s reach

The maximum value of Δm_s measurable in ATLAS was estimated using a simplified Monte Carlo model. The input parameters of this model were: the number of signal events, N_{sig}, the number of background events from B_d^0 decays, N_{B_d}, and the number of events for the combinatorial background, N_{comb}; the characteristics of the events involved in the computation of the proper-time resolution (see below); the wrong-tag fraction. The wrong-tag fraction was assumed to be the same for both B_s^0 and B_d^0 mesons: $\omega_{\mathrm{tag}} = 0.22$ (see Section 17.2.2.4). The proper-time resolution obtained with detailed simulation for the $B_s^0 \to D_s^-(\phi\pi^-)a_1^+(\rho^0\pi^+)$ decay channel was assumed for all signal events.

Monte Carlo experiments with $N_{\rm sig}$ signal events oscillating with a given frequency Δm_s, together with N_{B_d} B_d^0 background events oscillating with frequency Δm_d and $N_{\rm comb}$ combinatorial events (no oscillations), were generated in the following way. For each event with an oscillating b hadron, the true proper time t_0 was generated according to an exponential distribution using the slope obtained from a fit of the true proper time of the simulated sample. The uncertainty on the measurement of the transverse decay length, $\sigma_{d_{xy}}$, and the true value of the g-factor, g_0, were generated at random according to the distributions obtained from the simulated samples (the distributions were fitted with the sum of three and two Gaussian functions for $\sigma_{d_{xy}}$ and g_0, respectively). From the computed true decay length, $d_{xy}^0 = t_0/g_0$, the corresponding reconstructed decay length was generated as $d_{xy} = d_{xy}^0 + S_{d_{xy}}\sigma_{d_{xy}}\Omega$, with Ω being a random number distributed according to the normal distribution. The reconstructed g-factor was generated as $g = g_0 + g_0 S_g \Omega'$, with Ω' a random number distributed according to the normal distribution function. From the transverse decay length and g-factor, the reconstructed proper time was then computed as $t = g d_{xy}$. The probability for the event to be mixed or unmixed was determined from the t_0 and Δm_s values (Δm_d value if the event was a B_d^0 event). For a fraction of the events, selected at random, the state was changed between mixed and unmixed, according to the wrong-tag fraction, $\omega_{\rm tag}$. For the combinatorial background, the reconstructed proper time was generated assuming that it has the same distribution as the one for B_s^0 mesons. Half of the combinatorial events were added to the mixed events and half to the unmixed events.

The asymmetry

$$A(t) = \frac{\frac{dn(++)}{dt} - \frac{dn(+-)}{dt}}{\frac{dn(++)}{dt} + \frac{dn(+-)}{dt}} \sim D \frac{\cos\Delta m_s t}{\cosh\frac{\Delta\Gamma_s t}{2}}$$

was computed for the 'generated events' for $t > 0.4$ ps, in agreement with the experimental cut on the reconstructed proper time. Here *n(++)* is the number of events with the tagging muon and the reconstructed D_s having the same sign ($B_{s_0}^0$ meson did not oscillate), and *n(+–)* is the number of events in which they have unlike sign (B_s^0 meson oscillated). The asymmetry distribution $A(t)$ was then analysed with a method based on the amplitude fit proposed in [17-34]. According to this method, $A(t)$ was fitted with the function $A_{\rm fit}\cos(\Delta m_s t)/\cosh(\Delta\Gamma_s t/2)$ where Δm_s and $\Delta\Gamma_s$ were constant values and $A_{\rm fit}$ was the only free parameter. The fit was repeated for different values of Δm_s and an $A_{\rm fit}(\Delta m_s)$ distribution was obtained ($\Delta\Gamma_s$ was a constant parameter). The value of Δm_s which gave the maximum $A_{\rm fit}$ was considered as the Δm_s measured in that experiment.

The experiment was performed for different true Δm_s values. For each true Δm_s value, the experiment was repeated 1000 times. The fitted amplitude distribution was averaged over these 1000 experiments as a function of the Δm_s value in the asymmetry fit function $A_{\rm fit}(\Delta m_s)$; the average distribution was then fitted with a Gaussian function and the width σ of the distribution was determined. An experiment was called 'successful' if the measured Δm_s value was within $\pm 1.96\sigma$ of the true Δm_s value, corresponding to a 95% probability that the measured Δm_s value would fall within $\pm 1.96\sigma$ of the true value given Gaussian errors. The maximum value of Δm_s for which 95% of the generated experiments were successful was taken as the maximum value of Δm_s which is expected to be measurable. For each experiment, the difference between the reconstructed Δm_s and the true Δm_s was computed; this distribution was fitted with a Gaussian function and its width was taken as the accuracy of the Δm_s measurement.

With an integrated luminosity of 30 fb^{-1}, the maximum value of Δm_s that is expected to be measurable is 38.5 ps^{-1}.The expected accuracy of the Δm_s measurement is 0.04 ps^{-1} for Δm_s = 12 ps^{-1}, 0.05 ps^{-1} for Δm_s = 20 ps^{-1}, 0.10 ps^{-1} for Δm_s = 30 ps^{-1}, and 0.16 ps^{-1} for Δm_s = 38.5 ps^{-1}. The time-dependent asymmetry for a single 'experiment' with an integrated luminosity of 30 fb^{-1} is shown in Figure 17-32, when Δm_s = 38.5 ps^{-1}.

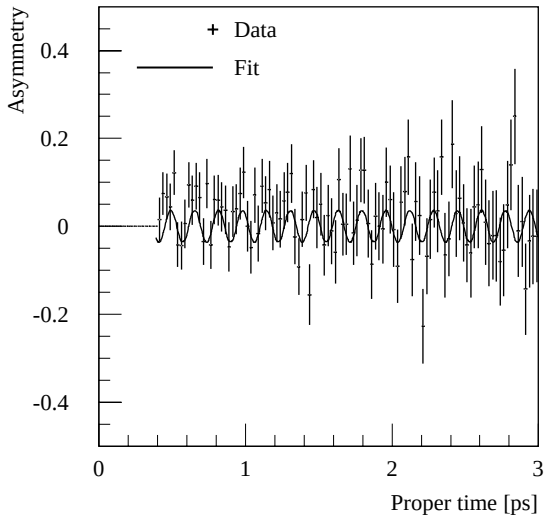

Figure 17-32 The time-dependent asymmetry for Δm_s = 38.5 ps^{-1} in a single 'experiment' for an integrated luminosity of 30 fb^{-1}. The crosses correspond to 'simulated data' and the line to the fit with a cosine function.

17.3.7 Dependence of Δm_s reach on experimental quantities

The previous analysis was repeated for different values of the integrated luminosity 5 fb^{-1}, 10 fb^{-1}, 20 fb^{-1} and 30 fb^{-1}. The proper-time resolution was also varied, by changing the widths $S_{d_{xy}}$ and S_g by the same factor. The values of the scaling factors used were 0.75 and 1.5. For these values, the proper-time resolution, fitted with two Gaussian functions with the same normalisation ratio as for the nominal values, had the widths 0.033 ps (0.074 ps) and 0.064 ps (0.138 ps), respectively, to be compared with the nominal 0.050 ps (0.093 ps); the value in parenthesis is the width of the second, broader Gaussian function. All combinations given by these proper-time resolution values and integrated luminosity values were tried. The dependence of the Δm_s reach on the integrated luminosity is shown in Figure 17-33 for different values of the proper-time resolution, and assuming that $\Delta\Gamma = 0$.

The dependence of the maximum value of Δm_s which can be measured on the fraction of signal events in the sample of reconstructed events is shown in Figure 17-34 for the nominal proper-time resolution. The values in the plot were obtained assuming that the number of signal events remains constant at the values given in Table 17-11 and that the numbers of combinatorial background events and of background events coming from B_d^0 change with the same factor. The dependence on the background is not very strong for the assumed conditions; however, this dependence could change if the combinatorial background has some asymmetry or if it has a different proper time dependence. If the combinatorial background was taken to be 20 900 events, which was estimated to be the 90% CL upper limit for the combinatorial background, while the numbers of signal events and background events from other sources were as in Table 17-11, the maximum value of Δm_s that is expected to be measurable would be 36.0 ps^{-1} with an integrated luminosity of 30 fb^{-1}.

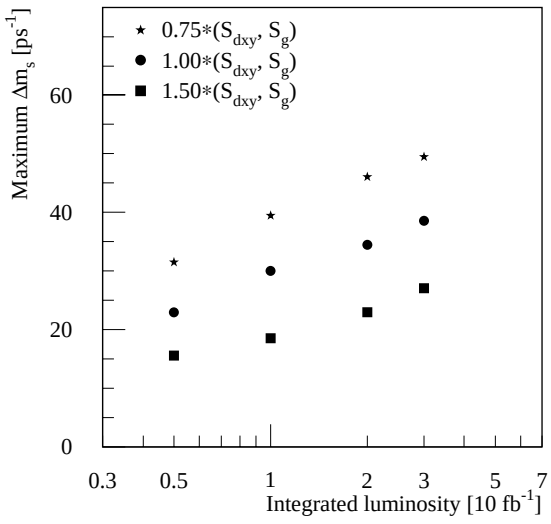

Figure 17-33 Sensitivity range of ATLAS for the Δm_s measurement as a function of the integrated luminosity for various proper-time resolutions.

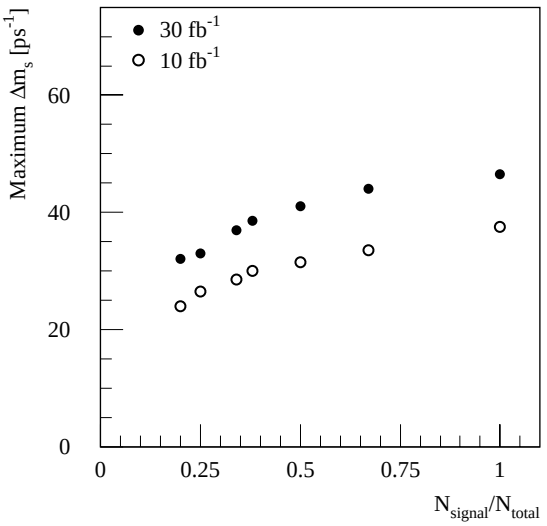

Figure 17-34 Sensitivity range of ATLAS for the Δm_s measurement as a function of the signal content of the sample, for nominal proper-time resolution and integrated luminosities of 10 fb^{-1} and 30 fb^{-1}.

For values of $\Delta\Gamma/\Gamma_s \leq 0.2$ no significant change in the sensitivity range was observed. If the K^{*0} mode was also considered, the Δm_s limit did not improve, mainly due to the decrease in the signal-to-background ratio resulting from the conservative estimate of the combinatorial background to be added to the sample.

17.3.8 Conclusions

The maximum value of Δm_s which we expect to be able to measure with 30 fb^{-1} data, with the performance of the detector presented in the previous sections and with the assumed cross-sections of the involved processes, is 38.5 ps^{-1}. The expected accuracy of the Δm_s measurement is 0.16 ps^{-1} for Δm_s = 38.5 ps^{-1}, and better for lower values of Δm_s. The dependence of the Δm_s sensitivity range on various parameters shows that we should be able to measure Δm_s over the whole range predicted in the Standard Model.

17.4 Rare decays $B \rightarrow \mu\mu(X)$

17.4.1 Introduction

Certain rare decays, for which the decay products themselves provide a distinctive signature that can be used in the LVL1 trigger, can be studied very effectively in ATLAS making use of the high rate of *B*-hadron production. These so-called 'self-triggering' modes include decays of the type $B_{d,s} \rightarrow \mu\mu(X)$. Such decays involve flavour-changing neutral currents (FCNC) and are

strongly suppressed in the Standard Model, with predicted branching ratios typically in the range 10^{-5}–10^{-10}. New physics might result in significant enhancements compared to the Standard Model predictions.

The potential to study rare decays of the type $B_{d,s} \to \mu\mu(X)$ is discussed in the following. For the purely muonic decays, ATLAS will be sensitive to branching ratios of order 10^{-9} and should be able to measure the branching ratio for $B_s \to \mu\mu$ assuming the Standard Model prediction. Large-statistics samples will be collected for decays of the type $b \to (s, d)ll$ that give final states such as $B_d^0 \to K^{*0}\mu\mu$, $B_d^0 \to \rho^0\mu\mu$ and $B_s^0 \to \phi^0\mu\mu$. This will allow precise measurements to be made of the decay dynamics, as well as of the branching ratios, giving significant constraints on new physics.

These rare decay modes are forbidden at the tree level in the Standard Model, so the decays involve loop diagrams. In non-standard models of electroweak interactions, FCNC processes can be allowed at the tree level and thus, the branching ratios of these rare decays would not be so suppressed. In addition, in the presence of new physics, additional particles may be present in the loops again enhancing the decay probability. Due to the very low Standard Model predictions for the branching fractions for purely muonic decays, a significant enhancement in measured branching fractions would clearly demonstrate the effects of new physics. The measurement of the lepton forward–backward asymmetry in semimuonic B decays is another promising tool to probe the new physics beyond the Standard Model.

In the context of Standard Model, the principal interest lies in the measurement of the branching fractions of the $B \to \mu\mu(X)$ channels. The measurement of the branching fractions of the decays $B_d^0 \to \rho^0\mu\mu$ and $B_d^0 \to K^{*0}\mu\mu$ allows the CKM matrix-element ratio $|V_{td}|/|V_{ts}|$ to be determined. The square of this ratio is useful also for the estimation of the ratio of the mass differences $\Delta m_s/\Delta m_d$ in the $B_d^0 - \bar{B}_d^0$ and $B_s^0 - \bar{B}_s^0$ systems (see [17-35]), complementary to direct measurements of the oscillation periods.

17.4.2 Theoretical approach

In the theoretical approach used here, the effective Hamiltonian which governs the $b \to q$ transition has the following structure [17-36]:

$$H_{eff} = \frac{G_F}{\sqrt{2}} V_{tb} V_{tq}^* \sum_i C_i(\mu) O_i(\mu)$$

where $q = d, s$, G_F is the universal Fermi constant, $C_i(\mu)$ are the Wilson coefficients which contain the information on the short-distance dynamics of the theory, and $O_i(\mu)$ are the basis operators. The parameter μ in the equation is a typical scale which separates the long and short-distance (LD and SD) physics. For B decays it is convenient to choose this scale $\mu \sim m_b$. The contributions of the LD effects are contained in the $B \to M$ transition form factors that enter in the calculation of the Wilson coefficients, where B is the B-meson and M is any other meson. These form factors are the main source of uncertainties in the theoretical predictions for exclusive decays (see, *e.g.* [17-37] and references therein).

Table 17-12 presents theoretical predictions for the branching ratios of $B \to K^*\gamma$ and $B \to K^*\mu\mu$. The columns ‘QM’ and ‘Lat’ present the results obtained with the two sets of transition form factors taken from [17-37]. The column ‘Ali’ refers to the results in [17-38]. In order to estimate

the uncertainties in the CKM matrix elements V_{td} and V_{ts}, the uncertainty on the form factors is required. One can see from the table that the results obtained with the different theoretical approaches agree within the errors and are consistent with the experimental data.

Table 17-12 Non-resonant branching fractions of radiative and rare *B*-decays.

Decay mode	QM $BR \times \lvert V_{ts}/0.038\rvert^2$	Lat $BR \times \lvert V_{ts}/0.041\rvert^2$	Ali $BR \times \lvert V_{ts}/0.033\rvert^2$	Experimental *BR*
$B \to K^*\gamma$	4.2×10^{-5}	4.2×10^{-5}	$(4.9 \pm 2.0) \times 10^{-5}$	$(4.0 \pm 1.9) \times 10^{-5}$ [17-32]
$B \to K^*ee$	1.50×10^{-6}	1.45×10^{-6}	$(2.3 \pm 0.9) \times 10^{-6}$	$< 2.9 \times 10^{-4}$ [17-32]
$B \to K^*\mu\mu$	1.15×10^{-6}	1.10×10^{-6}	$(1.5 \pm 0.6) \times 10^{-6}$	$< 2.3 \times 10^{-5}$ [17-32]

For studies of SD effects, information about the Wilson coefficient $C_{7\gamma}$ is important. The experimental measurement of the lepton forward–backward asymmetry in semileptonic *B*-decays caused by FCNC transitions will provide information on this coefficient. To illustrate the possible sensitivity to new physics, one can compare the Minimal Supersymmetric Standard Model (MSSM) with the Standard Model. In each case, a range of allowed values of $C_{7\gamma}$ is provided by CLEO results on rare radiative decays [17-39]. The quantity $R_{7\gamma} = C_{7\gamma}^{MSSM}(M_W)/C_{7\gamma}^{SM}(M_W)$ lies in one of the following intervals

$$-4.2 < R_{7\gamma} < -2.4 \qquad 0.4 < R_{7\gamma} < 1.2$$

The shape of the differential forward–backward asymmetry distribution turns out to be qualitatively different for positive and negative values of $R_{7\gamma}$ [17-40]. The lepton forward–backward asymmetry remains sensitive to the value of the Wilson coefficient after the experimental cuts, and thus it will be possible for ATLAS to test the Standard Model in the exclusive $B \to Ml^+l^-$ decays.

17.4.3 Simulation of rare *B*-decay events

17.4.3.1 Simulation of $B_{d,s} \to \mu\mu$

Purely muonic *B*-decays are predicted to have very low branching fractions within the Standard Model (10^{-9}–10^{-10}), whereas they may have significantly higher ones in non-standard models. The following Standard Model branching ratios were assumed for the present study [17-41]: $Br(B_d \to \mu\mu) = 1.5 \times 10^{-10}$, $Br(B_s \to \mu\mu) = 3.5 \times 10^{-9}$. Simulations were made with the PYTHIA event generator. The Inner-Detector response was simulated fully and the particles were reconstructed in the Inner Detector. The muon reconstruction efficiency was assumed to be 85% for the LVL1 trigger muon, and 95% for the other muon. About 1500 signal events were simulated in

Table 17-13 Efficiencies of selection cuts for $B_{d,s} \to \mu\mu$

Cut	Efficiency
Decay length of B^0 > 0.7 mm, χ^2/dof < 3	0.70
Angle between p_T of B^0 and line joining primary and B^0 decay vertices $\alpha < 1^o$	0.94
Isolation: $n_{ch}(p_T > 0.8$ GeV) = 0 in a cone $\theta < 20^o$	0.40

each channel, with $p_T(\mu) > 6$ GeV and $|\eta(\mu)| < 2.5$ for each muon. About 9000 background events were simulated and reconstructed with the same criteria. The sensitivity of signal events to cuts is shown in Table 17-13.

After applying all the cuts, the numbers of events expected for 30 fb^{-1} at low luminosity are shown in Table 17-14. The $B_s \to \mu\mu$ channel can be observed, assuming the branching fraction predicted by the Standard Model. The significance of the signal, however, is only 2.8σ.

Table 17-14 Number of expected events after three years of LHC running at low luminosity (30 fb^{-1})

Channel	Signal	Background
$B_d^0 \to \mu\mu$	4	93
$B_s^0 \to \mu\mu$	27	93

The feasibility to reconstruct the purely muonic decays $B_{d,s}^0 \to \mu\mu$ at high luminosity was also estimated. This estimation was based on the assumption that the pixel *B* layer will be operational at high luminosity, and that no degradation of the impact-parameter and p_T resolutions will occur. For each channel, 1000 signal events with corresponding pile-up were fully simulated and reconstructed in the Inner Detector. The background was studied at the particle level using the parametrisation for p_T and impact parameter resolutions from ATLFAST. A sample of 10 000 background events with pile-up was used for this study. The numbers of events for both channels and the corresponding backgrounds expected for 100 fb^{-1} are given in Table 17-15.

Table 17-15 Number of expected events after one year of LHC running at high luminosity (100 fb^{-1}).

Channel	Signal	Background
$B_d^0 \to \mu\mu$	14	660
$B_s^0 \to \mu\mu$	92	660

Combining the low- and high-luminosity samples, a 4.3σ significance can be obtained for the channel $B_s^0 \to \mu\mu$. The 95% CL upper limit for the branching fraction for $B_d^0 \to \mu\mu$ obtained with the combined sample would be $3\text{x}10^{-10}$. It should be noted, however, that the *B* mass resolution of 69 MeV is not good enough to separate B_s and B_d on an event-by-event basis, but their relative fractions would have to be fitted from the joint mass distribution. The study of rare muonic *B* decays at high luminosity will significantly improve the results which can be obtained at low luminosity, especially if data collection is continued for several years.

17.4.3.2 Simulation of $B_d^0 \to K^{*0}\mu\mu$, $B_d^0 \to \rho^0\mu\mu$ and $B_s^0 \to \phi^0\mu\mu$

Studies have been performed for the rare-decay channels $B_d^0 \to K^{*0}\mu\mu$, $B_d^0 \to \rho^0\mu\mu$, and $B_s^0 \to \phi^0\mu\mu$. In the future, the potential for studying $B_s^0 \to K^{*0}\mu\mu$ and $B_d^0 \to \omega\mu\mu$ decays will also be evaluated. The following predicted values for the branching ratios were assumed: $Br\ (B_s^0 \to \phi^0\mu\mu) = 1\times10^{-6}$, $Br(B_d^0 \to K^{*0}\mu\mu) = 1.5\times10^{-6}$ and $Br(B_d^0 \to \rho^0\mu\mu) = 1\times10^{-7}$. Events were simulated fully and then reconstructed in the Inner Detector. For each channel, 1500 signal events were analysed with the following experimental cuts: both muons were required to have $p_T(\mu) > 6$ GeV and $|\eta(\mu)| < 2.5$, and both hadrons were required to have $p_T(h) > 1$ GeV and $|\eta(h)| < 2.5$. The same reconstruction and trigger efficiencies for the muons were assumed as above. The reconstruction efficiency for hadrons was found to be 90% averaged over the full pseudorapidity region for $p_T > 1$ GeV.

The uncertainty in the theoretical predictions for the transition form-factors influences strongly the dimuon q^2-distributions (where q^2 is the invariant-mass squared of the muon pair) and the branching ratios. Different analytical expressions for the matrix element for $B_d^0 \to K^{*0}\mu\mu$ were

implemented in PYTHIA and the results were compared. It was found that the individual-muon p_T distributions remain essentially unaffected by the choice of form factors. An important conclusion from this study was that, although the q^2-dependence of form factors affects q^2-dependence of the events, it does not influence the efficiency of triggering and reconstructing the signal events, or the rejection of the background [17-42].

The mass resolutions obtained by the Gaussian fit with the full reconstruction were: $\sigma(\phi^0)$ = 3 MeV, $\sigma(B_s^0 \to \phi^0\mu\mu)$ = 52 MeV, $\sigma(K^{*0})$ = 30 MeV, $\sigma(B_d^0 \to K^{*0}\mu\mu)$ = 50 MeV, and $\sigma(B_d^0 \to \rho^0\mu\mu)$ = 55 MeV. In case of the ρ^0 resonance, requiring the mass to be in the interval [0.60,0.94] MeV corresponded to 82% efficiency. In order to exclude the reflection of K^* to ρ^0, hadron pairs forming an invariant mass within two standard deviations around the nominal K^* mass using the K/π mass assignments were excluded. For the remaining pairs, both hadrons were assumed to be pions and the effective mass of the pair was required to be within the ρ^0 mass window. The possible reflections from $B_s^0 \to \phi^0\mu\mu$ to $B_d^0 \to \rho^0\mu\mu$ and $B_d^0 \to K^{*0}\mu\mu$ were found to be negligible.

For background studies, the following reactions were simulated by PYTHIA: B_d^0-meson decays $B_d^0 \to J/\psi K_S^0$, $B_d^0 \to \rho^0\mu\mu$ and $B_d^0 \to \omega^0\mu\mu$, B_s^0-meson decays $B_s^0 \to K^{*0}\mu\mu$ and $B_s^0 \to \phi^0\mu\mu$, semimuonic decays of one of the *b*-quarks, and semimuonic decays of both *b*-quarks. It was found that the last reaction gave the main contribution to the background. Therefore, 13000 events of this type were simulated and analysed similarly to the signal events.

The mass distributions for the $B_{d,s}^0$ signals are shown, together with those for the backgrounds, in Figure 17-35, Figure 17-36 and Figure 17-37. The sensitivity of signal events to the applied cuts is shown in Table 17-16. The application of all cuts leaves about 9% of the simulated signal events. The expected numbers of signal and background events after three years of LHC running at low luminosity are presented in Table 17-17.

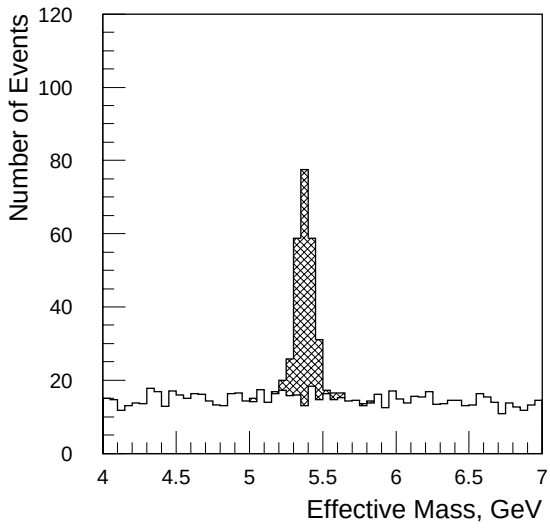

Figure 17-35 Reconstructed signal (cross-hatched) and background for $B_s^0 \to \phi^0\mu\mu$ with 30 fb^{-1}.

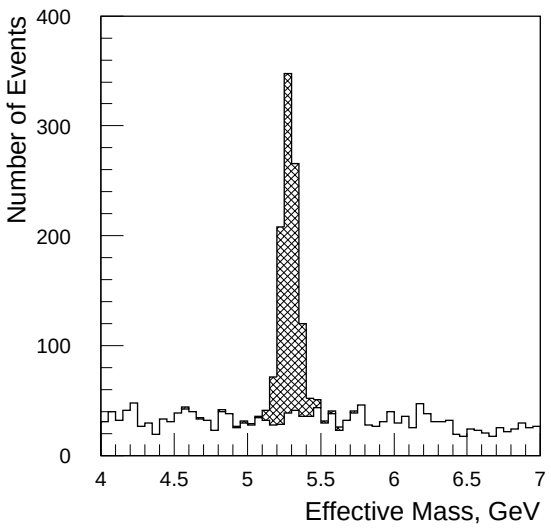

Figure 17-36 Reconstructed signal (cross-hatched) and background for $B_d^0 \to K^{*0}\mu\mu$ with 30 fb^{-1}.

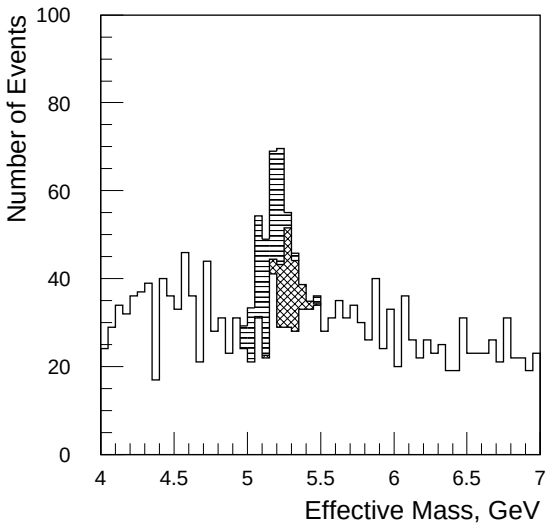

Figure 17-37 Reconstructed signal (cross-hatched) and background for $B_d^0 \to \rho^0\mu\mu$ with 30 fb^{-1}. The horizontally hatched histogram shows the reflection from $B_d^0 \to K^{*0}\mu\mu$.

Table 17-16 Efficiencies of selection cuts for $B_d^0 \to K^{*0}\mu\mu$, $B_d^0 \to \rho^0\mu\mu$ and $B_s^0 \to \phi^0\mu\mu$.

Cut	$B_d^0 \to K^{*0}\mu\mu$	$B_d^0 \to \rho^0\mu\mu$	$B_s^0 \to \phi^0\mu\mu$
$m(hh) = m\ (K^{*0}, \varphi^0) \pm 2\sigma$ OR $m(\pi\pi) \in [0.60, 0.94]$ MeV	0.81	0.82	0.82
Decay length of $B^0_d > 0.8$ mm, χ^2/ d.o.f <10, angle between p_T of B^0_d and line joining primary and B^0_d decay vertices $\alpha < 1^o$	0.45	0.40	0.43
$m(\mu\mu) \notin J/\psi$, $m(\mu\mu) \notin \psi'$ $	0.85	0.86	0.85
$n_{ch}(p_T>0.8$ GeV) = 0 in a cone $\theta< 5^o$	0.65	0.67	0.65
p_T of $K^{*0} > 5$ GeV	0.71		
$m(hh\mu\mu) = m(B_d^0)^{+\sigma}_{-2\sigma}$	0.74	0.75	0.75

Table 17-17 Number of events expected after 30 fb^{-1} of low-luminosity running.

Channel	*Br*	Signal	Background
$B_d^0 \to \rho^0\mu\mu$	10^{-7}	220	950
$B_d^0 \to K^{*0}\mu\mu$	1.5×10^{-6}	2000	290
$B_s^0 \to \phi^0\mu\mu$	10^{-6}	410	140

From the ratio of the branching fractions for the two decay modes $B_d^0 \to K^{*0}\mu\mu$ and $B_d^0 \to \rho^0\mu\mu$, the ratio $|V_{td}|/|V_{ts}|$ can be determined, since the decay rates are proportional to the respective CKM matrix elements:

$$\frac{N(B_d^0 \to \rho^0\mu\mu)}{N(B_d^0 \to K^{0*}\mu\mu)} = \kappa_d \frac{|V_{td}|^2}{|V_{ts}|^2},$$

where κ_d is the ratio of form factors squared.

The theoretical uncertainty of the form factor for the decay $B_d^0 \to \rho^0\mu\mu$ is large due to the *u*-loop matrix-element contribution to the $b \to dll$ process. It was shown in [17-43], that the $|V_{td}|/|V_{ts}|$ ratio can be determined experimentally with a small theoretical uncertainty arising from hadronic form factors in the dimuon kinematic mass region 16.5 GeV^2 < q^2 < 19.25 GeV^2. The fraction of signal events in this kinematic region was estimated using the GI form factor parametrisation [17-42] and found to be 24% of the total number of events. With these events, the ratio $|V_{td}|/|V_{ts}|$ can be measured with a statistical accuracy of 14% for 30 fb^{-1} of low-luminosity data; the theoretical systematic uncertainty is about 7% [17-43].

Note that the reflection from $B_d^0 \to K^{*0}\mu\mu$ to $B_d^0 \to \rho^0\mu\mu$ is sizeable (see Figure 17-37) due to the large difference in the branching ratios assumed for the two channels. After assigning the wrong mass hypotheses to the K^{*0} decay products, the decay $B_d^0 \to K^{*0}\mu\mu$, reconstructed as $B_d^0 \to \rho^0\mu\mu$, gives a mass peak below, but close to, the $B^0{}_d$ mass. In contrast, the combinatorial background is approximately flat. Taking into account that the branching ratio for $B_d^0 \to K^{*0}\mu\mu$ can be measured with high accuracy, it is assumed that the $B_d^0 \to \rho^0\mu\mu$ signal can be extracted from an overall fit.

17.4.4 The measurement of the forward–backward asymmetry

The forward–backward (*FB*) charge asymmetry $A_{FB}(\hat{s})$ in the decays $B_d^0 \to M\mu\mu$ is defined by the following equation:

$$A_{FB}(\hat{s}) = \frac{\int_0^1 \left(\frac{d^2\Gamma}{ds\,d\cos\theta}\right) d\cos\theta - \int_{-1}^0 \left(\frac{d^2\Gamma}{ds\,d\cos\theta}\right) d\cos\theta}{\int_0^1 \left(\frac{d^2\Gamma}{ds\,d\cos\theta}\right) d\cos\theta + \int_{-1}^0 \left(\frac{d^2\Gamma}{ds\,d\cos\theta}\right) d\cos\theta}$$

where θ is the angle between the lepton l^+ and the *B*-meson direction in the rest frame of the lepton pair, and $\hat{s} = q^2/M_B^2$. In Figure 17-38 the theoretical curves for $A_{FB}(\hat{s})$ in the Standard Model and MSSM for $B_d^0 \to K^{*0}\mu\mu$ [17-37] are presented. These curves include the resonant contributions for J/ψ and ψ'.

The general trend of the behaviour of A_{FB} for Standard Model is that the asymmetry is positive at low q^2, has a zero at $\hat{s} \approx 0.14$, and then becomes negative, irrespective of the details of the form-factor behaviour (except for the resonant region – for a detailed analysis of the behaviour of *FB* asymmetry in this region, see [17-40]). The maximum of $A_{FB}(\hat{s})$ occurs at $\hat{s} = 0.05$. For the

MSSM, the shape of A_{FB} is sensitive to the value of $C_{7\gamma}$, or equivalently to the value of $R_{7\gamma}$. For $R_{7\gamma} > 0$ the shape is similar to that in the Standard Model, but for $R_{7\gamma} < 0$ the asymmetry is negative at low q^2.

In the simulation, the resonant region $0.33 < \hat{s} < 0.55$ was excluded from the analysis. To estimate the experimental resolution of A_{FB} measurements in $B_d^0 \to K^{*0}\mu\mu$ decays, the total numbers of signal and background events after three years of low-luminosity running were used (see Table 17-17). The numbers of signal and background events for each $\hat{s}$-region were estimated assuming that the signal $d\Gamma/d\hat{s}$ distribution is similar to the one presented in [17-44], and that the background distribution is flat. The sensitivity to the asymmetry was then the calculated, and results are presented in Table 17-18 where it can be seen that three regions are useful for measurements. If negative values of A_{FB} are experimentally observed in the first $\hat{s}$-region, this will demonstrate a clear signal of non-standard physics. The measurements in the second and third $\hat{s}$-regions, which practically do not depend on the models, will show possible systematic uncertainties in the experimental data.

In Figure 17-38, the average values of A_{FB} and the expected errors on A_{FB} for three $\hat{s}$-regions are shown. One can see that the expected measurement accuracy is sufficient to separate the Standard Model and the MSSM in the case $R_{7\gamma} < 0$ using measurements in the first $\hat{s}$-region.

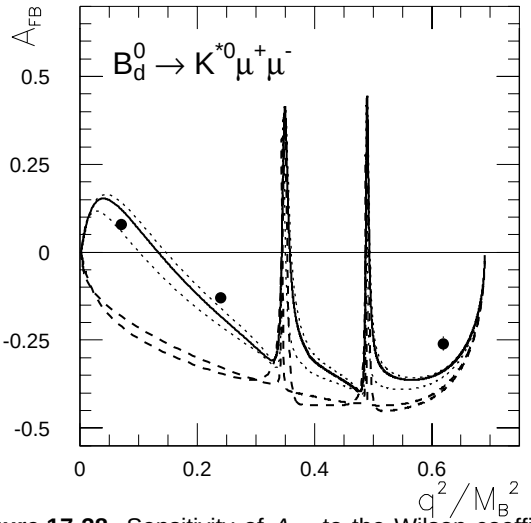

Figure 17-38 Sensitivity of A_{FB} to the Wilson coefficient $C_{7\gamma}$. The three points are the simulation results. The solid line shows the Standard Model prediction, the dotted lines show the range predicted by the MSSM for $R_{7\gamma} > 0$ and the dashed lines show the range predicted by the MSSM for $R_{7\gamma} < 0$.

Table 17-18 Expected sensitivity for asymmetry measurements after three years at low luminosity (30 fb^{-1}) and theoretical predictions of the asymmetry. Here $\hat{s}_{min} = 4m_l^2/M_B^2$, where m_l is the lepton mass and $\hat{s}_{max} = (M_B - M_K^*)^2/M_B^2$.

Quantity	$\hat{s}_{min} \div 0.14$	$0.14 \div 0.33$	$0.55 \div \hat{s}_{max}$
δA_{FB}(stat.)	5%	4.5%	6.5%
SM A_{FB}	10%	-14%	-29%
MSSM A_{FB}	$(-17 \div 0.5)$ %	$(-35 \div -13)$ %	$(-33 \div -29)$ %

17.4.5 Conclusions

ATLAS will be able to study rare semi-muonic and muonic *B*-decays. It will be possible to measure branching ratios of the decay channels $B_s^0 \to \phi^0 \mu\mu$, $B_d^0 \to K^{*0} \mu\mu$ and $B_d^0 \to \rho^0 \mu\mu$. From the ratio of branching fractions for the two latter channels, it will be possible to determine the ratio $|V_{td}|/|V_{ts}|$ with a 14% statistical accuracy within the Standard Model. Measurements of the forward–backward charge asymmetry in the decay $B_d^0 \to K^{*0} \mu\mu$ will also be feasible and may reveal new physics effects, for example in some parameter-space regions of the MSSM.

Combining three years of low-luminosity and one year of high-luminosity data taking, the decay $B_s \to \mu\mu$ would be observed and a stringent upper limit for the decay $B_d \to \mu\mu$ would be set, assuming Standard Model branching ratios. Given that these decays are highly suppressed in the Standard Model, there are hopes that any non-standard physics effects would significantly enhance the branching ratios, in which case the signals would be easier to detect.

17.5 Precision measurements of *B* hadrons

Precision measurements of *B*-hadrons are important to validate the Standard Model and to search for new physics. As discussed above, ATLAS can make a significant contribution to the study of *CP*-violation in *B*-meson decays. It will also be able to measure the oscillation parameter of the B_s meson for values of Δm_s well beyond the range predicted in the Standard Model, and the corresponding mass difference $\Delta\Gamma_s$. In addition, measurements of very rare decays to final states with muon pairs will be possible, testing and constraining parameters of the Standard Model, and possibly revealing new physics. In this Section some additional physics topics are presented that can be addressed by ATLAS.

Many precision measurements will be made in other experiments before 2005 when ATLAS is expected to take its first data. For example, the BaBar, Belle and CLEO experiments at e^+e^- machines will address in detail the decays of the B^0 and B^+ mesons, while experiments at hadron machines will also study B_s and B_c mesons and *B*-baryons. Nevertheless, given the large statistics available in a variety of exclusive final states (see Table 17-19), ATLAS may be able to improve the precision of mass, lifetime and other measurements in some cases. For example, ATLAS is expected to measure the B_s lifetime with a statistical accuracy of 0.7% after three years at low luminosity with the $B_s^0 \to J/\psi\phi$ channel.

In the following two examples of precision studies are discussed: the analysis of the B_c meson, and measurements of Λ_b polarisation.

17.5.1 Measurements with the B_c meson

The B_c meson exhibits some unique features regarding both its production and decay properties, due to its explicit double-heavy-flavour content. In addition, in hadronic spectroscopy the properties of B_c can be used in interpolating between charmonium and bottomonium resonances, and QCD-inspired potential models can be scrutinised with different combinations of charm and bottom constituent masses. Since m_c/m_b is small, the B_c system enables testing the heavy-quark symmetries and understanding better the next-to-leading terms in the heavy-quark effective theory, and its application to heavy–light *B* mesons.

The expected large production rates should bring the possibility of detecting the non-leptonic decay mode $B_c \to J/\psi\pi$, or the semileptonic one $B_c \to J/\psi\mu\nu$, through charmonium decaying into a muon pair [17-45]. With the foreseen statistics, the former channel would allow a very precise determination of the B_c mass. The latter one could be useful to extract the CKM matrix element V_{cb} [17-46], provided that the B_c production cross-section can be determined elsewhere. Furthermore, the B_c lifetime measurement is a very clean test of the interplay between strong and weak interactions inside hadrons, as both quarks can undergo a weak decay inside the same particle, in contrast to usual singly-heavy *D* or *B* mesons. Doubly-heavy baryons [17-47] are potentially detectable at the LHC, completing the interesting panorama of heavy–heavy systems.

Table 17-19 Number of reconstructed events with ATLAS with an integrated luminosity of 30 fb^{-1}.

Decay mode	Branching fraction	*N* of events
$B_d^0 \to \pi\pi$	$0.7\text{x}10^{-5}$, estimated from limit in [17-17]	6 500
$B_d^0 \to J/\psi K_s^0$	$4.45\text{x}10^{-4}$ [17-32]	630 000
$B_s^0 \to D_s\pi$	$3.0\text{x}10^{-3}$, same as for $B_d^0 \to D\pi$ in [17-32]	6 800
$B_s^0 \to J/\psi\phi$	$9.3\text{x}10^{-4}$ [17-32]	300 000
$B_s^0 \to D_s a_1$	$6.0\text{x}10^{-3}$, same as for $B_d^0 \to D a_1$ in [17-32]	3600
$B_d^0 \to D_s a_1$	$< 2.6\text{x}10^{-3}$ [17-32]	5 900
$\Lambda_b \to J/\psi\Lambda^0$	$3.7\text{x}10^{-4}$ [17-49]	75 000
$B_c \to J/\psi\pi$	$0.2\text{x}10^{-2}$ estimate based on [17-47] and [17-48].	12 000
$B_c \to J/\psi\mu\nu$	$2\text{x}10^{-2}$ estimate based on[17-47] and [17-48].	300 000 (inclusive reconstruction)

17.5.2 Λ_b polarisation measurement

17.5.2.1 Introduction

Polarisation measurements of *B*-hadrons could clarify the problems of different polarisation models [17-50] that failed to reproduce the existing data on strange-hyperon production [17-51]. In particular, information about the quark-mass dependence of polarisation effects could be obtained. Hadrons with non-zero spin can be polarised perpendicularly to their production plane. For symmetry reasons, in *pp* collisions this polarisation vanishes as the Feynman variable x_F approaches zero, so that the expected observed polarisation in ATLAS is smaller than in experiments covering more forward regions (for example LHCb). Thus, a polarisation measurement in ATLAS will require very high precision.

17.5.2.2 Method of polarisation measurement

A polarisation measurement can be obtained with Λ_b baryons via the angular distributions of the cascade decay $\Lambda_b \to J/\psi\Lambda^0$, $J/\psi \to \mu\mu$, $\Lambda^0 \to p\pi$. The decay is described by the Λ_b polarisation, P_b, four helicity amplitudes and the known asymmetry parameter for the $\Lambda^0 \to p\pi$ decay, $\alpha(\Lambda^0) = 0.646$. The $J/\psi \to \mu\mu$ decay depends only on one amplitude which is absorbed into the normalisation.

The angular distribution function, ω, can be written in terms of five measurable angles that are defined in Figure 17-39:

$$\omega(\theta, \theta_1, \theta_2, \varphi_1, \varphi_2) = \frac{1}{4\pi^2} \sum_{i=1}^{19} \alpha_i f_i \times F_i(\theta, \theta_1, \theta_2, \varphi_1, \varphi_2) ,$$

where the α_i are bilinear combinations of the four helicity amplitudes, the f_i are combinations of P_b and $\alpha(\Lambda^0)$, and the F_i are functions of the five angles θ, θ_1, θ_2, φ_1 and φ_2. The expressions for α_i, f_i and F_i can be found in [17-52]. From the measured angular distributions, 19 independent moments $\langle F_i \rangle$ can be obtained. Since the system of equations is over-constrained, the polarisation, P_b, can be determined.

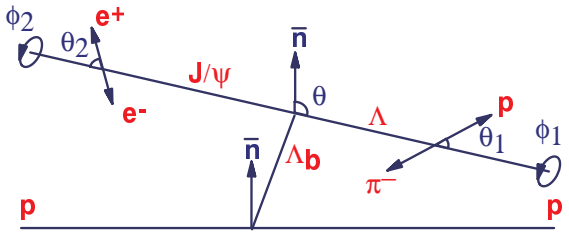

Figure 17-39 The definition of the five angles. θ is the polar angle of the Λ^0 momentum $\bar{p}_\Lambda$ in the Λ_b rest frame relative to the normal $\bar{n}$ to the production plane. θ_1 and φ_1 are the angles of the proton in Λ^0 rest frame, with the *z*-axis being parallel with p_Λ and the *y*-axis being parallel to $\bar{n} \times \bar{p}_\Lambda$. θ_2 and φ_2 are defined for the J/ψ decay in a similar way.

17.5.2.3 Event selection, background and estimation of precision

The events were simulated within the Inner Detector only. Efficiency factors were applied for muon reconstruction and identification. The LVL2 trigger will select $J/\psi \to \mu\mu$ decays with p_T larger than 6 GeV for one muon and 3 GeV for the other muon. The muon tracks in the Inner Detector were fitted requiring that they originate from a common point. A simultaneous J/ψ mass and vertex constrained fit was performed. The transverse flight distance from the primary vertex to the Λ_b decay point was required to be larger than 250 μm and, for the Λ^0 candidate, a transverse flight distance in the range 1 – 42 cm was required. A second fit then constrained the J/ψ mass and Λ^0 momentum to point to the dimuon vertex. The J/ψ–Λ^0 invariant-mass spectrum had a Gaussian core with σ = 22 MeV. The proper decay-time of the Λ_b candidate was required to be larger than 0.5 ps. Within the mass region of three standard deviations around the Λ_b mass, the background was ~2% and it was dominated by J/ψ's from B-hadrons combined with Λ^0's coming from the fragmentation. The Λ_b reconstruction properties and background composition are summarised in Table 17-20. After three years of low-luminosity data-taking, the number of reconstructed $\Lambda_b \to J/\psi\Lambda^0$ events will be ~75 000. The branching ratio for $\Lambda_b \to J/\psi\Lambda^0$ was taken to be 3.7×10^{-4}, as measured by CDF [17-49].

Table 17-20 Summary of the Λ_b analysis with an integrated luminosity of 30 fb^{-1}.

Number of reconstructed $\Lambda_b \to J/\psi\,\Lambda^0$ decays.	**75 000**
Number of background events, dominated by $J/\psi+\Lambda^0$, where the J/ψ is from a *B*-decay and the Λ^0 is from fragmentation.	1 500
Reconstruction efficiency of $J/\psi \to \mu\mu$ for decays with $p_T(\mu_1) > 6$ GeV and $p_T(\mu_2) > 3$ GeV. Efficiency includes the trigger and the combined muon identification, including calorimetry.	0.78
Reconstruction efficiency of $\Lambda^0 \to p\pi$ with $p_T(p) > 0.5$ GeV and $p_T(\pi) > 0.5$ GeV. Reconstructed Λ^0 candidate must have decay radius $1 < r < 42$ cm and invariant mass within $\pm 3\sigma$ from the Λ_b mass.	0.56
Efficiency of final cuts on Λ_b proper lifetime $\tau > 0.5$ ps, invariant mass within $\pm 3\sigma$ from the Λ_b mass.	0.48
J/ψ mass resolution, $\sigma_{J/\psi}$	39 MeV
Λ^0 mass resolution, $\sigma_{\Lambda 0}$	2.5 MeV
Λ_b mass resolution, $\sigma_{\Lambda b}$	22 MeV
Resolution on Λ_b proper decay-time τ, σ_t	0.073 ps
Statistical error on Λ_b polarisation P_b, σ_{Pb}	0.016

The estimated statistical precision of the polarisation measurement using the above method of moments was $\sigma(P_b)$~0.016. Some of the Λ_b baryons are produced indirectly through the decays of heavier states $\Sigma_b \to \Lambda_b \pi$, $\Sigma^*_b \to \Lambda_b \pi$. Thus, the observed Λ_b polarisation will be diluted and, according to the present models, the dilution factor is expected to be in the range 0.34–0.67 [17-52]. The lower value corresponds to the case in which the polarisations of the Λ_b, Σ_b and Σ^*_b are in the relation $P_b = P(\Sigma_b) = -P(\Sigma^*_b)$, and the upper limit corresponds to $P_b = -P(\Sigma_b) = P(\Sigma^*_b)$.

The large Λ_b sample, characterised by a small background, can be used for a precise determination of the Λ_b lifetime. The maximum-likelihood fit, taking into account the proper decay time resolution and assuming a single exponential for the background with mean decay time the same as for the neutral *B* hadrons, gives a statistical precision of 0.3%.

17.6 Conclusions on the *B*-physics potential

The expected *B*-physics performance of ATLAS is summarised in the Table 17-21. High-statistics studies of *CP* violation in various *B*-decay channels will give measurements of the unitarity-triangle angles α and β, and will search for deviations from the Standard Model. These measurements will be complemented by the measurement of the B_s-oscillation parameter Δm_s. Several other measurements will be made with the B_s and Λ_b, thus complementing the data from e^+e^- *B*-factories. Finally, very rare *B* decays will be accessible as well.

Table 17-21 Summary of the *B*-physics potential. The assumed integrated luminosity is 30 fb^{-1}, except for the rare dimuon decays, where 130 fb^{-1} is assumed.

Observable	Expected accuracy or value	World data (situation in 1999)
$\sin 2\alpha$	$\delta_{stat}(\alpha) \approx 2°$	Estimated to be in the range $\sin 2\alpha = -0.26^{+0.29}_{-0.28}$ [17-11]
$\sin 2\beta$	$\delta_{stat}(\sin 2\beta) = 0.010$	$\sin 2\beta = 0.79^{+0.41}_{-0.44}$ [17-10]
Angle γ		Estimated to be in the range $\gamma = (59.5^{+8.5}_{-7.5})°$ [17-11]
$\xi = 2\lambda \sin\gamma \lvert V_{ub}\rvert / \lvert V_{cb}\rvert$	$\delta(\xi)$=0.03 (stat.)	ξ = 0.024–0.054 [17-32]
Δm_s	Measured up to 38.5 ps^{-1}	Δm_s > 12.4 ps^{-1} [17-31]
$\tau(B_s^0)$	$\delta\Gamma_s/\Gamma_s$=0.7% (stat.)	$\tau(B_s^0) = 1.54 \pm 0.07$ ps [17-32]
$\Delta\Gamma_s$ in the B_s-meson system	$\delta(\Delta\Gamma_s)/\Delta\Gamma_s$=12% (stat.)	$\Delta\Gamma_s/\Gamma_s$ < 0.83 [17-53]
$\lvert V_{td}\rvert / \lvert V_{ts}\rvert$ from rare decays	$\delta(\lvert V_{td}\rvert / \lvert V_{ts}\rvert)$=14% (stat.)	$\lvert V_{td}\rvert / \lvert V_{ts}\rvert$ < 0.27 [17-32]
$\tau(\Lambda_b)$	$\delta(\tau(\Lambda_b))/\tau(\Lambda_b)$ =0.3% (stat.)	$\tau(\Lambda_b) = 1.24 \pm 0.08$ ps [17-32]
$Br(B_s^0 \to \mu\mu)$	4.3σ signal (SM)	Not measured yet
$Br(B_d^0 \to \mu\mu)$	Upper limit 3x10^{-10} (SM)	Not measured yet
A_{FB} of muons in rare semileptonic decays	$\delta(A_{FB})$< 5%(stat.)	Not measured yet

17.7 References

17-1 M. Mangano, 'Heavy Flavour Production', talk given at the LHCC Workshop 'Theory of LHC processes', CERN, 9–13 February 1998.

17-2 B. L. Combridge, J. Kripfganz and J. Ranft, Phys. Lett. **B70** (1977) 234;
R. Cutler, D. Sivers, Phys. Rev. **D17** (1978) 196;
H. U. Bengtsson, Computer Physics Communications **31** (1984) 323.

17-3 T. Sjostrand, 'PYTHIA 5.7 and JETSET 7.4: Physics and manual', LU-TP-95-20 (1995).

17-4 P. Eerola, 'The inclusive muon cross-section in ATLAS', ATLAS Internal Note ATL-PHYS-98-120 (1998);
S. P. Baranov and M. Smizanska, 'Beauty production overview from Tevatron to LHC', ATLAS Internal Note ATL-PHYS-98-133 (1998).

17-5 A. Dell'Acqua, 'DICE manual version 0.10', ATLAS Internal Note ATL-SOFT-95-011 (1995).

17-6 E. Richter-Was, D. Froidevaux and L. Poggioli, 'ATLFAST 2.0 a fast simulation package for ATLAS', ATLAS Internal Note ATL-PHYS-98-131 (1998).

17-7 E. J. Buis *et al.*, 'Update of Inner Detector performance parameterisations', ATLAS Internal Note ATL-INDET-98-215 (1998).

17-8 M. Smizanska *et al.*, 'Overview of simulations for ATLAS *B*-physics studies in period 1996-1999', ATLAS Internal Note ATL-COM-PHYS-99-042 (1999).

17-9 ATLAS Collaboration, Trigger performance status report, CERN / LHCC / 98-15 (1998).

17-10 CDF collaboration, 'A Measurement of sin2β from $B \to J/\psi K^0_S$ with the CDF Detector'. CDF internal note CDF/PUB/BOTTOM/CDF/4855, Feb 1999.

17-11 F. Parodi, P. Roudeau and A. Stocchi, 'Constraints on the parameters of the CKM matrix by end 1998', hep-ex/9903063 (1999).

17-12 P. F. Harrison (ed.) *et al.*, BaBar Collaboration, 'The BaBar Physics Book: Physics at an Asymmetric *B* Factory', SLAC-R-0504, Oct 1998.

17-13 M. Gronau, A. Nippe and J. L. Rosner, Phys. Rev. **D47** (1993) 1988.

17-14 ATLAS Collaboration, Technical Proposal, CERN/LHCC/94-43 (1994).

17-15 R. Fleischer and T. Mannel, Phys. Lett. **B397** (1997) 269.

17-16 D. Rousseau and P. Sherwood, 'Measurement of sin(2α) in the $B^0_d \to \pi\pi$ channel', ATLAS-COM-PHYS-99-012 (1999).

17-17 R. Godang *et al.*, CLEO Collaboration, Phys. Rev. Lett. **80** (1998) 3456.

17-18 D. Buskulic *et al.*, ALEPH Collaboration, Phys. Lett. **B384** (1996) 471.

17-19 R. Fleischer, CERN-TH/98-60 (1998), to appear in Eur. Phys. J. **C.**

17-20 A. Ali and D. London, 'Profiles of the Unitarity Triangle and CP-violating Phases in the Standard Model and Supersymmetric Theories', DESY preprint 99-042, UdeM-GPP-TH-99-58, hep-ph/9903535 (1999).

17-21 M. Beneke, G. Buchalla and I. Dunietz, Phys. Rev. **D54** (1996) 4419;
M. Beneke *et al.*, 'Next-to-leading order QCD corrections to the lifetime differences of B_s mesons', CERN-TH 98-261 (1998).

17-22 I. Dunietz, Phys. Rev. **D52** (1995) 3048;
A. S. Dighe *et al.*, 'Angular distributions and lifetime differences in $B_s \to J/\psi\phi$ decays', FERMILAB-PUB 95-345 T (1995);
A. S. Dighe, I. Dunietz and R. Fleischer, 'Resolving a discrete ambiguity in the CKM angle β through $B_{(u,\,d)} \to J/\psi K^*$ and $B_s \to J/\psi\phi$ decays', CERN-TH 98-85 (1998).

17-23 B. Cano-Coloma and M. A. Sanchez-Lozano, Nucl. Phys. **B508** (1997) 753.

17-24 E. J. Eichten, C. H. Hill and C. Quigg, Phys. Rev. Lett. **71** (1993) 4116;
E. J. Eichten, C. H. Hill and C. Quigg, 'Orbitally Excited Heavy-Light Mesons Revisited', FERMILAB-CONF-94/118-T (1994).

17-25 M. Smizanska, 'Determination of $\Delta\Gamma_s$ by ATLAS and the impact of non-zero $\Delta\Gamma_s$ on other B^0_s studies', ATLAS Internal Note ATL-PHYS-99-003 (1999).

17-26 CDF Collaboration, Phys. Rev. Lett. **75** (1995) 3068.

17-27 G. Barenboim, J. Bernabeu, J. Matias and M. Raidal, '*CP* asymmetries in B_s decays and spontaneous *CP* violation', hep-ph/9901265 (1999).

17-28 G. Barenboim, J. Bernabeu and M. Raidal, Phys. Rev. Lett. **80** (1998) 4625.

17-29 I. Dunietz, Phys. Lett. **B270** (1991) 75.

17-30 LHCb Collaboration, Technical Proposal, CERN/LHCC/98-4 (1998).

17-31 The LEP *B* Oscillation Working Group, 'Combined Results on B^0 oscillations: Results for Summer 1998 Conferences', LEPBOSC 98/3 (1998).

17-32 C. Caso *et al.*, Particle Data Group, Eur. Phys. J. **C3** (1998) 1.

17-33 D. Buskulic *et al.*, ALEPH Collaboration, Eur. Phys. J. **C7** (1999) 553.

17-34 H. G. Moser and A. Roussarie, Nucl. Instr. and Methods **A384** (1997) 491.

17-35 A. Ali, 'Flavour changing neutral current processes and CKM phenomenology', DESY preprint 97-256 (1997), hep-ph/9801270. To be published in the Proceedings of the First APCTP Workshop Pacific Particle Physics Phenomenology, Oct. 31- Nov. 2, 1997, Seoul, South Korea.

17-36 B. Grinstein, M. B. Wise and M. J. Savage, Nucl. Phys. **B319** (1989) 271.

17-37 D.Melikhov, N.Nikitin and S.Simula, Phys. Rev. **D57** (1998) 6814.

17-38 A.Ali, '*B* Decays, Flavour Mixings and *CP* Violation in the Standard Model', DESY preprint 96-106 (1996), hep-ph/9606324. Published in the Proceedings of the XX International Nathiagali Summer College on Physics and Contemporary Needs, Bhurban, Pakistan, June 24–July 13, 1995, eds. Riazuddin, K.A. Shoaib *et al.*; Nova Science Publishers, New York.

17-39 P. Cho, M. Misiak and D. Wyler, Phys. Rev. **D54** (1996) 3329.

17-40 D. Melikhov, N. Nikitin and S.Simula, Phys. Lett **B430** (1998) 332.

17-41 A. Ali, Nucl. Instr. and Methods **A384** (1996) 8.

17-42 D. Melikhov *et al.*, 'Studying the physics beyond the Standard Model in rare semileptonic *B*-decay $B \to K^* \mu^+ \mu^-$ with ATLAS detector', ATLAS Internal Note PHYS-98-123 (1998).

17-43 T. M. Aliev, C. S. Kim and M. Savci, Phys. Lett. **B441** (1998) 410.

17-44 D. Melikhov, N. Nikitin and S. Simula, Phys. Lett **B410** (1997) 290.

17-45 F. Albiol *et al.*, 'Searching for B_c mesons in ATLAS', ATLAS Internal Note ATL-PHYS-94-058 (1994).

17-46 M. Galdon and M. A. Sanchis-Lozano, Z. Phys. **C71** (1996) 277.

17-47 M. A. Sanchis-Lozano, Nucl. Phys. **B440** (1995) 251.

17-48 M. Lusignoli and M. Masetti, Z. Phys. **C51** (1991) 549.

17-49 CDF collaboration, Phys. Rev. **D55** (1997) 1142.

17-50 T.A. De Grand and H.I. Miettinen, Phys. Rev. **D24** (1981) 2419;
Y. Hama and T. Kodama, Phys. Rev. **D48** (1993) 3116;
J. Ellis, D. Kharzeev and A. Kotzinian, Z. Phys. **C69** (1996) 467;
W.G.D. Dharmaratna and G.R. Goldstein, Phys. Rev. **D53** (1996) 1073.

17-51 J. Lach, 'Hyperon polarisation: an experimental overview', FERMILAB-CONF-92-378, Dec 1992. Invited talk given at International Workshop on Flavour and Spin in Hadronic and Electromagnetic Interactions, Turin, Italy, 21-23 Sep 1992.

17-52 J. Hrivnac, R. Lednicky and M. Smizanska, J. Phys. **G21** (1995) 629.

17-53 CDF collaboration, 'Measurement of the B_s^0 meson lifetime using semileptonic decays', to be published in Phys. Rev. **D59** (1999).

18 Heavy quarks and leptons

The top quark is the only known fundamental fermion with a mass on the electroweak scale. As a result, study of the top quark may provide an excellent probe of the sector of electroweak symmetry breaking (EWSB), and new physics may well be discovered in either its production or decay. The LHC will be a 'top quark factory', and a very large variety of top physics studies will be possible with the high statistics samples which will be accumulated.

Figure 18-1 shows the expected cross-section for the pair production of heavy quarks at the LHC for quark masses in the range from 175 to 1000 GeV. For the case of the top quark, with $m_t \approx 175$ GeV, the next-to-leading order (NLO) prediction including gluon resummation is $\sigma(t\bar{t}) = 833$ pb [18-1]. In addition to the detailed studies of top quark physics which this large cross-section will allow, the LHC will be an excellent place to search for the possible existence of fourth generation quarks and leptons. Approximately 1000 events would be produced per low luminosity year for a quark mass of 900 GeV.

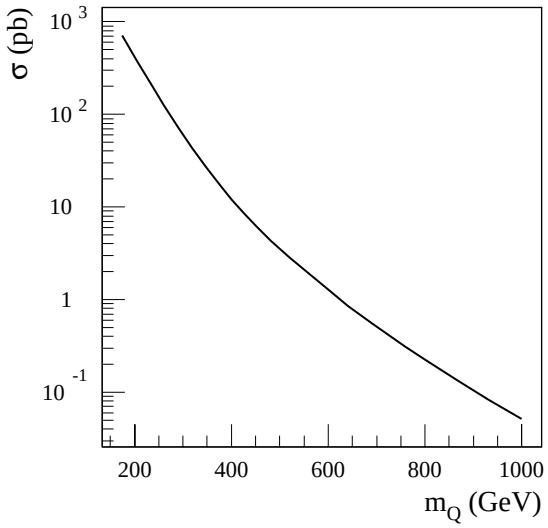

Figure 18-1 Predicted Standard Model cross-section, versus quark mass, for pair production of heavy quarks at the LHC.

Section 18.1 discusses the ATLAS sensitivity to many topics related to top quark physics. Section 18.2 presents the ATLAS discovery potential for fourth generation quarks, and Section 18.3 briefly develops ideas on searching for heavy leptons.

The results presented in this chapter are obtained predominantly using ATLFAST [18-2], the parametrised ATLAS detector simulation (see Section 2.5). Cross-checks of the results, particularly for the case of the measurement of the top quark mass, have been made using the detailed GEANT simulation of the ATLAS detector.

18.1 Top quark physics

18.1.1 Introduction

With the discovery of the top quark at Fermilab [18-3][18-4], top physics has moved from the search phase into the study phase. The NLO prediction that $\sigma(t\bar{t}) = 833$ pb at the LHC [18-1] implies production of more than 8 million $t\bar{t}$ pairs per year at low luminosity (and, of course, ten times that number per year at high luminosity). The motivations for detailed studies of the top quark are numerous. Within the Standard Model (SM), an accurate measurement of the top quark mass (m_t) helps constrain the mass of the SM Higgs boson (m_H). The large value of m_t implies the top quark may provide an excellent probe of EWSB, fermion mass generation, and the possible existence of other massive particles. In addition, top quark events will be the dominant background in many searches for new physics at the TeV scale; extraction of new physics will

therefore require detailed measurement and understanding of the production rate and properties of top quark events. Also, the $W \rightarrow jj$ decays in top quark events provide an important *in situ* calibration source for calorimetry at the LHC (see Section 9.3.1 and Section 12.5).

The next section describes briefly the kinematics of $t\bar{t}$ events at the LHC, and presents estimates of the event samples which will be accumulated. Section 18.1.3 discusses in detail the estimated precision which can be achieved in the measurement of the mass of the top quark, one of the fundamental parameters of the SM. In Section 18.1.4, studies of $t\bar{t}$ production are presented. Section 18.1.5 then presents results related to top quark decays and couplings. Finally, Section 18.1.6 describes studies of electroweak single top production, and of the variety of physics topics which can be best (or only) studied using this channel.

Apart from the analyses of single top production, where a variety of Monte Carlo signal generators have been used (see Section 18.1.6 for details), top quark signal processes have been simulated with the PYTHIA Monte Carlo program [18-5], including initial- and final-state radiation, hadronisation and decays. Most background processes have also been generated with PYTHIA, with the exception of $Wb\bar{b}$, which has been produced using HERWIG [18-6], where the correct matrix-element calculation of that process is available. For most top physics analyses, the backgrounds from non-top final states are small after selection cuts and the remaining background is dominated by top events themselves. Therefore, unlike most of the other chapters in the TDR which use leading-order (LO) predictions for cross-sections since NLO predictions are not available for all the relevant backgrounds, the top quark analyses use the NLO prediction that $\sigma(t\bar{t}) = 833$ pb. All analyses assumed efficiencies for charged lepton reconstruction and identification of 90%.

18.1.2 $t\bar{t}$ selection and event yields

At the LHC, the largest source of top quarks is from $t\bar{t}$ production. According to the SM, the top quark decays almost exclusively to Wb. The final state topology of $t\bar{t}$ events then depends on the decay modes of the W bosons. In approximately 65.5% of $t\bar{t}$ events, both W bosons decay hadronically via $W \rightarrow jj$, or at least one W decays via $W \rightarrow \tau\nu$. These events are difficult to extract cleanly above the large QCD multi-jet background, and are for the most part not considered further. Instead, the analyses presented here concentrate on 'leptonic $t\bar{t}$ events', where at least one of the W bosons decays via $W \rightarrow l\nu$ (with the charged lepton either an electron or muon). The lepton plus large $E_{\mathrm{T}}^{\mathrm{miss}}$, due to the escaping neutrino(s), provide a large suppression against multi-jet backgrounds. The leptonic events, which account for approximately 34.5% of all $t\bar{t}$ events, can be subdivided into a 'single lepton plus jets' sample and a 'dilepton' sample, depending on whether one or both W bosons decay leptonically.

18.1.2.1 Single lepton plus jets sample

The single lepton plus jets topology, where one W decays leptonically and the other W decays hadronically via $W \rightarrow jj$, arises in $2 \times 2/9 \times 6/9 \approx 29.6\%$ of all $t\bar{t}$ events. One expects, therefore, production of almost 2.5 million single lepton plus jet events for an integrated luminosity of 10 fb^{-1}. The presence of a high p_{T} isolated electron or muon allows these events to be triggered efficiently, using, for example, the single lepton triggers discussed in Section 11.7.3. Furthermore, the complete final state can be reconstructed (with a quadratic ambiguity), despite the missing neutrino, by assuming $E_{\mathrm{T}}^{\mathrm{miss}} = E_{\mathrm{T}}(\nu)$ and applying the constraint that $m_{l\nu} = m_W$.

An important tool for selecting clean top quark samples, particularly in the single lepton plus jets mode, is the ability to identify *b*-quarks. As discussed in detail in Chapter 10, with a tagging efficiency of 60% for *b*-jets, a rejection of at least 100 can be achieved against prompt jets (*i.e.* jets containing no long-lived particles) at low luminosity. At high luminosity, a rejection factor of around 100 is obtained with a reduced *b*-tagging efficiency of 50%.

Requiring an isolated lepton with p_T > 20 GeV, E_T^{miss} > 20 GeV, and at least four jets with p_T > 20 GeV, including at least one *b*-tagged jet, a sample of about 820 000 single *b*-tagged events would be selected for an integrated luminosity of 10 fb^{-1}. Figure 18-2 and Figure 18-3 show the p_T(lepton) and jet multiplicity distribution for events with p_T(lepton) > 20 GeV, normalised to an integrated luminosity of 10 fb^{-1}. For the jets distribution a p_T(jet) > 20 GeV has been required.

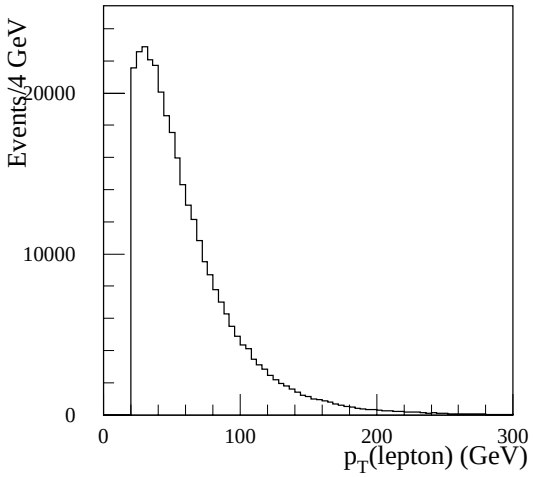

Figure 18-2 p_T(lepton) distribution for single lepton plus jet events with a lepton p_T > 20 GeV, normalised to an integrated luminosity of 10 fb^{-1}.

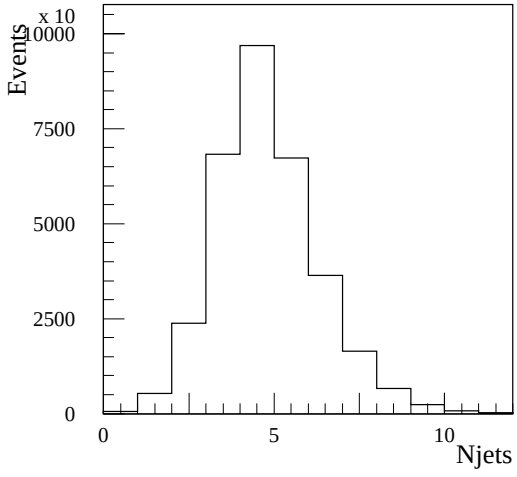

Figure 18-3 Distribution of jet multiplicity (threshold at p_T > 20 GeV) for single lepton plus jet events with a lepton p_T > 20 GeV, normalised to an integrated luminosity of 10 fb^{-1}.

18.1.2.2 Dilepton sample

Dilepton events, where each *W* decays leptonically, provide a particularly clean sample of $t\bar{t}$ events, although the product of branching ratios is small, 2/9 x 2/9 ≈ 4.9%. With this branching ratio, one expects the production of over 400 000 dilepton events for an integrated luminosity of 10 fb^{-1}. The presence of two high p_T isolated leptons allows these events to be triggered efficiently, using the single or double lepton triggers discussed in Section 11.7.3.

18.1.2.3 multi-jet sample

The largest sample of $t\bar{t}$ events consists of six-jet events from the fully hadronic decay mode, $t\bar{t} \rightarrow WWb\bar{b} \rightarrow (jj)(jj)b\bar{b}$. With a branching ratio of 6/9 x 6/9 ≈ 44.4%, it corresponds to the production of 3.7 million multi-jet events for an integrated luminosity of 10 fb^{-1}. However, these events suffer from a very large background from QCD multi-jet events. In addition, the all-jet final state poses difficulties for triggering. The trigger menus discussed in Section 11.7.3 consider

multi-jet trigger thresholds only up to four jets, for which a jet E_T threshold of 55 GeV is applied at low luminosity. Further study is required to determine appropriate thresholds for a six-jet topology.

A very preliminary investigation [18-7] has been made of a simple selection and reconstruction algorithm for attempting to extract the multi-jet $t\bar{t}$ signal from the background. Hadronic $t\bar{t} \rightarrow WWb\bar{b} \rightarrow (jj)(jj)b\bar{b}$ events were selected by requiring six or more jets with $p_T > 15$ GeV, with at least two of them tagged as b-jets. Jets were required to satisfy $|\eta| < 3$ ($|\eta| < 2.5$ for b-jet candidates). In addition, the scalar sum of the transverse momenta of the jets was required to be greater than 200 GeV. The $t\bar{t}$ signal efficiency for these cuts was 19.3%, while only 0.29% of 1.8 million QCD multi-jet events survived. With this selection, and assuming a QCD multi-jet cross-section of 1.4×10^{-3} mb for p_T(hard process) > 100 GeV, one obtains a signal-to-background ratio S / B ≈ 1 / 57.

Reconstruction of the $t\bar{t}$ final state proceeded by first selecting di-jet pairs, from among those jets not tagged as b-jets, to form $W \rightarrow jj$ candidates. A χ^2_W was calculated from the deviations of the two m_{jj} values from the known value of m_W. The combination which minimised the value of χ^2_W was selected, and events with $\chi^2_W > 3.5$ were rejected. For accepted events, the two W candidates were then combined with b-tagged jets to form top and anti-top quark candidates, and a χ^2_t calculated as the deviation from the condition that the top and anti-top masses are equal. Again, the combination with the lowest χ^2_t was selected, and events with $\chi^2_t > 7$ were rejected. After this reconstruction procedure and cuts, the value of S / B improved to 1 / 8 within the mass window 130-200 GeV, or slightly better for higher p_T(jet) thresholds (see Table 18-1).

Table 18-1 For different p_T(jet) thresholds, the efficiency of the selection cuts and reconstruction algorithm described in the text, for the $t\bar{t}$ multi-jet signal and the background from QCD multi-jets. Also included is the resulting ratio of $t\bar{t}$ signal to QCD background (S/B) within a mass window $130 < m_{jjb} < 200$ GeV.

p_T(jet) threshold	Signal (%)	QCD (%)	S/B
15 GeV	7.2	.028	1 / 8
20 GeV	4.3	.014	1 / 7
25 GeV	2.5	.0056	1 / 6

The isolation of a top signal can be further improved in a number of ways, such as using a multivariate discriminant based on kinematic variables like aplanarity, sphericity or ΔR(jet-jet), or restricting the analysis to a sample of high p_T top events. These techniques are undergoing further investigation, but it will be very difficult to reliably extract the signal from the background in this channel. In particular, the multi-jet rates and topologies, as generated by PYTHIA, suffer from very large uncertainties. Comparisons with the NJETS [18-8] matrix-element calculations have shown [18-9] that these uncertainties are about a factor of three for three- or four-jet final states. In the case of six-jet final states, the uncertainties could be expected to be even larger.

18.1.3 Measurement of the top quark mass

The most recent combined value of the top quark mass from CDF and D0 is $m_t = 174.3 \pm 3.2 \pm 4.0$ GeV [18-10]. The mass of the top quark is a fundamental parameter of the SM and should be measured as accurately as possible. As is well known, radiative corrections in the SM relate the mass of the top quark and the mass of the W to the mass of the SM Higgs boson. Assuming that m_W can be measured with a precision of ±20 MeV (see Section 16.1), a determination of m_t with a precision of $\delta m_t \leq \pm 2$ GeV would be required to match that from m_W and from the current theoretical uncertainties. Models beyond the SM which attempt to explain in a

more fundamental way the origin of mass and the observed fermion mass hierarchy, such as top-bottom-tau Yukawa coupling unification in a supersymmetric SO(10) GUT [18-11], would profit from a precision of the order $\delta m_t \approx \pm 1$ GeV.

With the large number of top quark events which will be available at the LHC, the uncertainty in the measurement of m_t will be dominated by systematic errors. Several different data samples and methods, with somewhat differing sensitivities to systematic errors, can be used, and the resulting measurements can then be combined for optimal precision.

The studies presented in this section were performed predominantly using ATLFAST [18-2], since they concentrated on the influence on the m_t measurement of various 'physics-related' sources of uncertainties, such as initial and final state radiation, and uncertainties in the knowledge of *b*-quark fragmentation. As discussed in Section 18.1.3.5, some cross-checks of the results have been made with results from a detailed GEANT simulation of the ATLAS detector. However, detailed studies of 'detector-related' effects, and in particular of the calibration and understanding of the jet energy scale, are not discussed here, but in Chapter 9 and Chapter 12. The top mass measurement is assumed to be performed using data taken during low luminosity running, and so pile-up has not been included. Detector noise is also not included, but should not significantly affect the results.

18.1.3.1 Inclusive single lepton plus jets channel

The process $pp \rightarrow t\bar{t} \rightarrow WWb\bar{b} \rightarrow (l\nu)(jj)b\bar{b}$ provides a large sample of top quark events. The presence of a high p_T isolated lepton provides an efficient trigger. The lepton and the high value of E_T^{miss} give a large suppression of backgrounds from QCD multi-jets and $b\bar{b}$ production. The major sources of backgrounds are W+jet production with $W \rightarrow l\nu$ decay, and Z+jet events with $Z \rightarrow ll$. Potential backgrounds from WW, WZ, and ZZ gauge boson pair production have also been studied, but are reduced to a negligible level after cuts.

For the single lepton plus jets sample, it is possible to fully reconstruct the $t\bar{t} \rightarrow WWb\bar{b} \rightarrow (l\nu)(jj)b\bar{b}$ final state. The four-momentum of the missing neutrino can be reconstructed by setting $m_\nu = 0$, assigning $E_T(\nu) = E_T^{miss}$, and calculating $p_z(\nu)$, with a quadratic ambiguity, by applying the constraint that $m_{l\nu} = m_W$. If one applies the further kinematic constraints that $m_{jj} = m_W$ and $m_{jjb} = m_{l\nu b} = m_t$, the top mass can be determined using a three-constraint fit. This kinematic fit technique currently gives the most precise determination of m_t at the Tevatron [18-12], where statistics are limited. However, if the systematic errors are to be kept small, this method requires an excellent modelling and understanding of the E_T^{miss} distribution and resolution, which is beyond the scope of the studies reported here. The discussion presented here (for more details, see [18-13]) will focus on the method where the isolated lepton and large E_T^{miss} are used to tag the event, and the value of m_t is extracted as the invariant mass of the three jet system arising from the hadronic top quark decay (*i.e.* $m_t = m_{jjb}$).

Events were selected by requiring an isolated lepton with $p_T > 20$ GeV and $|\eta| < 2.5$, and $E_T^{miss} > 20$ GeV. Jets were reconstructed using a fixed cone algorithm. Cone sizes of $\Delta R = 0.4$ and 0.7 were investigated. At least four jets with $p_T > 40$ GeV and $|\eta| < 2.5$ were required, and at least two of the jets were required to be tagged as *b*-jets. In Table 18-2, the selection efficiencies for the signal and background processes after each successive cut are presented, together with the expected S/B ratio.

For an integrated luminosity of 10 fb^{-1}, a signal of 126 000 $t\bar{t}$ events was obtained after selection cuts, with a small background of 1,922 events, yielding a value of S/B = 65.

Table 18-2 Efficiencies (in percent), not including branching ratios, for the inclusive $t\bar{t}$ single lepton plus jets signal and for background processes, as a function of the selection cuts applied. The last column gives the equivalent number of events for an integrated luminosity of 10 fb^{-1}, and the signal-to-background ratio.

Process	p_T^l > 20GeV E_T^{miss} > 20GeV	As before, plus $N_{jet} \geq 4$	As before, plus $N_{b\text{-}jet} \geq 2$	Events per 10 fb^{-1}
$t\bar{t}$ signal	64.7	21.2	5.0	126 000
W+jets	47.9	0.1	0.002	1658
Z+jets	15.0	0.05	0.002	232
WW	53.6	0.5	0.006	10
WZ	53.8	0.5	0.02	8
ZZ	2.8	0.04	0.008	14
Total background				1922
S/B				65

For accepted events, the decay $W \rightarrow jj$ was reconstructed from among those jets that were not tagged as b-jets. The jet pair with an invariant mass m_{jj} closest to m_W was selected as the W candidate. The invariant mass distribution of the selected di-jet combinations is shown in Figure 18-4. Fitting the distribution with a Gaussian plus a third order polynomial yielded a W mass consistent with the generated value and a m_{jj} mass resolution of 7.8 GeV. Within a mass window of ±20 GeV around m_W, the purity (P) and efficiency (ε) of the W reconstruction, determined by comparing with the parton level information, were P = 67% and ε = 90%, respectively. The background is dominated by wrong combinations in the $t\bar{t}$ events themselves. Other selection criteria, such as requiring that the highest p_T jet be part of the combination, did not improve significantly the purity nor efficiency, and therefore are not considered in the following.

Events with $|m_{jj} - m_W| < 20$ GeV were retained, and the W candidate was then combined with one of the b-tagged jets to attempt to reconstruct $t \rightarrow Wb$. If one does not do anything to choose between the b-tagged jets, one reconstructs at least two jjb combinations per event. In this case, the right combination is always selected but the purity is only 30%. To choose the correct jjb combination, a variety of criteria were tried, including choosing the jjb combination which gave the highest p_T for the reconstructed top candidate, or using the b-jet which was furthest from the isolated lepton. Similar results were obtained for these various methods. Figure 18-5 presents the reconstructed m_{jjb} distribution using the jjb combination which gives the highest p_T for the reconstructed top candidate. Fitting the distribution with a Gaussian plus a third order polynomial yielded a top mass consistent with the generated value of 175 GeV, and a m_{jjb} mass resolution of 11.9 GeV.

Normalising to an integrated luminosity of 10 fb^{-1}, about 32 000 signal events were reconstructed, of which 30 000 yielded a value of m_{jjb} within a window of ±35 GeV around the generated value of m_t = 175 GeV. In addition, 34 000 'wrong combinations' in $t\bar{t}$ events were obtained (where the incorrect jet-parton assignment was made), of which 14 000 were in the mass window around m_t. The total background from processes other than $t\bar{t}$ summed up to only 115 events. In the mass window defined above, the signal purity and overall efficiency were P = 68% and ε = 69%, respectively. The determination of m_t by fitting the peak in the measured m_{jjb} spectrum resulted in a statistical uncertainty of δm_t(stat.) = ±0.070 GeV for an integrated luminosity of 10 fb^{-1}.

Performing the same analysis, but relaxing the *b*-tagging criterion to require at least one *b*-jet, yielded 80 000 signal events, with 76 000 having m_{jjb} within a window of ±35 GeV around the generated value of m_t = 175 GeV. In addition, 166 000 wrong $t\bar{t}$ combinations were accepted, with 58 000 in the mass window, and 6 000 events from other background processes. The resultant statistical error on m_t was reduced to δm_t(stat.) = ±0.042 GeV.

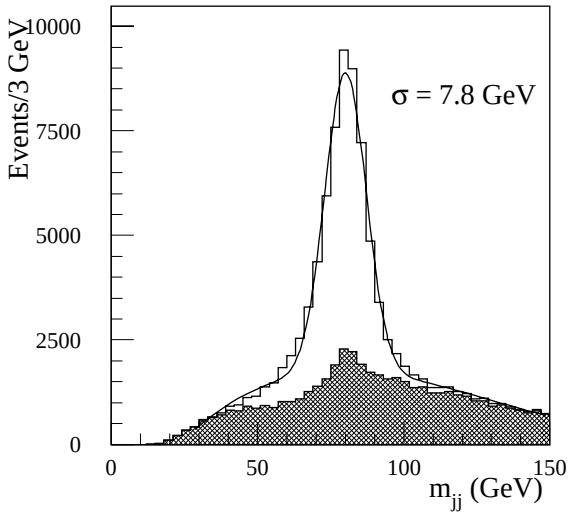

Figure 18-4 Invariant mass distribution of the selected *jj* pairs for the inclusive sample, normalised to an integrated luminosity of 10 fb^{-1}. The shaded histogram shows the background, which is dominated by 'wrong combinations' from $t\bar{t}$ events.

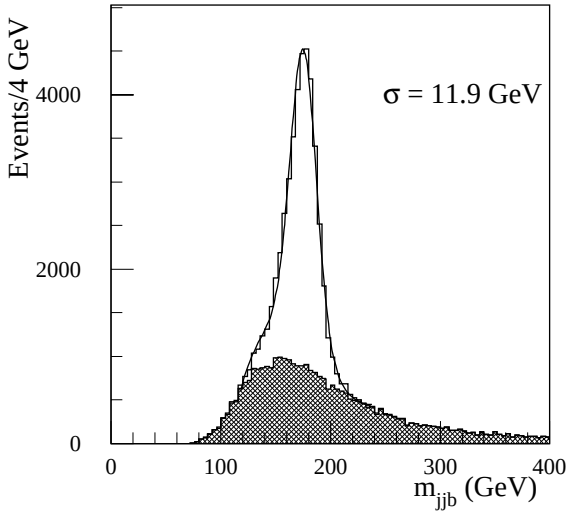

Figure 18-5 Invariant mass distribution of the accepted *jjb* combinations for the inclusive sample, normalised to an integrated luminosity of 10 fb^{-1}. The shaded histogram shows the background, which is dominated by 'wrong combinations' from $t\bar{t}$ events. Only the *jjb* combination with the highest p_T is shown for each event.

The dependence of the reconstructed top mass on the generated value was checked using several samples of $t\bar{t}$ events with different values of m_t ranging from 160 to 190 GeV. The results are shown in Figure 18-6, and demonstrate a linear dependence of the reconstructed value of m_t on the generated top mass. The stability of the reconstructed value of m_t was also checked as a function of p_T(top). As shown in Figure 18-7, no significant p_T(top) dependence was observed. The systematic errors on the measurement of m_t are discussed in Section 18.1.3.3.

18.1.3.2 High p_T single lepton plus jets channel

At the LHC, the $t\bar{t}$ production rate is sufficiently large that one can make very tight cuts and still accept a sample of events for which the statistical error on m_t will be small compared to the systematic error. One could, for example, require that the top and anti-top quarks have high p_T. In this case, they would be produced back-to-back, and the daughters from the two top decays would appear in distinct 'hemispheres' of the detector. This topology would greatly reduce the combinatorial background from having to select which jets have to be combined to reconstruct the $t \rightarrow jjb$ candidate. Backgrounds from processes other than $t\bar{t}$ would also be reduced at high p_T. Furthermore, the higher average energy of the jets to be reconstructed should reduce the sensitivity to systematic effects due to the jet energy calibration and to effects of gluon radiation.

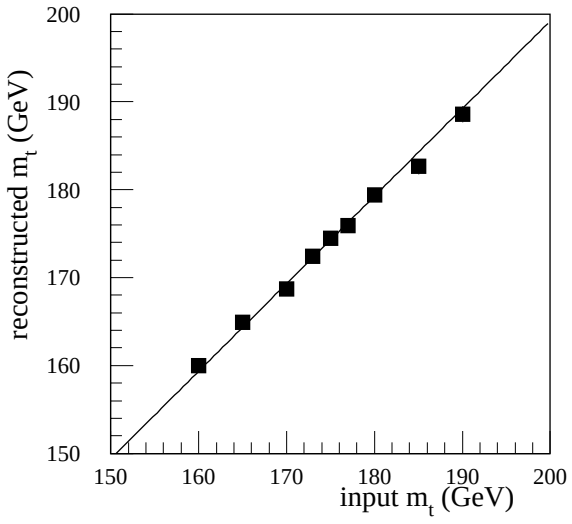

Figure 18-6 Dependence of the reconstructed value of m_t on the generated value of m_t for the inclusive single lepton plus jets sample.

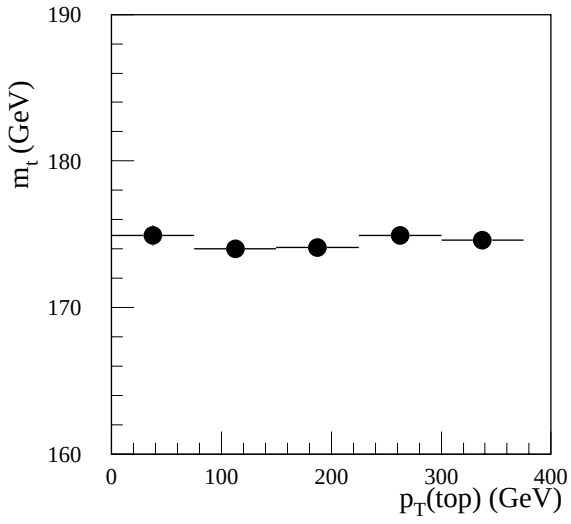

Figure 18-7 Dependence of the reconstructed value of m_t on the generated value of p_T(top) for the inclusive single lepton plus jets sample.

High p_T $t\bar{t}$ events were generated using PYTHIA 5.7 with a p_T cut on the hard scattering process above 200 GeV. The expected cross-section in this case is about 120 pb, or about 14.5% of the total $t\bar{t}$ production cross-section. The selection cuts required the presence of an isolated lepton with $p_T > 30$ GeV and $|\eta| < 2.5$, and $E_T^{miss} > 30$ GeV. The total transverse energy of the event was required to be greater than 450 GeV. Jets were reconstructed using a cone algorithm with radius $\Delta R = 0.4$.

The plane perpendicular to the direction of the isolated lepton was used to divide the detector into two hemispheres. Considering only jets with $p_T > 40$ GeV and $|\eta| < 2.5$, the cuts required one *b*-tagged jet in the same hemisphere as the lepton, and three jets, one of which was *b*-tagged, in the opposite hemisphere. Di-jet candidates for the $W \rightarrow jj$ decay were selected from among those jets in the hemisphere opposite to the lepton which were not tagged as jets. The resultant m_{jj} invariant mass distribution is shown in Figure 18-8. Fitting the six bins around the peak of the mass distribution with a Gaussian, yielded a *W* mass consistent with the generated value, and a m_{jj} resolution of 7 GeV, in good agreement with that obtained for the inclusive sample in Figure 18-4.

Di-jets with 40 GeV < m_{jj} < 120 GeV were then combined with the *b*-tagged jet from the hemisphere opposite to the lepton to form $t \rightarrow jjb$ candidates. Finally, the high p_T(top) requirement was imposed by requiring $p_T(jjb) > 250$ GeV. With these cuts, the overall signal efficiency was 1.7%. Background from sources other than $t\bar{t}$ was reduced to a negligible level. The invariant mass distribution of the accepted *jjb* combinations is shown in Figure 18-9. Fitting the six bins around the peak of the mass distribution with a Gaussian, yielded a top mass consistent with the generated value of 175 GeV, and a m_{jjb} mass resolution of 11.8 GeV, in good agreement with that obtained for the inclusive sample in Figure 18-5. For an integrated luminosity of 10 fb^{-1}, a sample of 6 300 events would be collected, leading to a statistical error of δm_t(stat.) = ±0.25 GeV, which remains well below the systematic uncertainty (see Section 18.1.3.3).

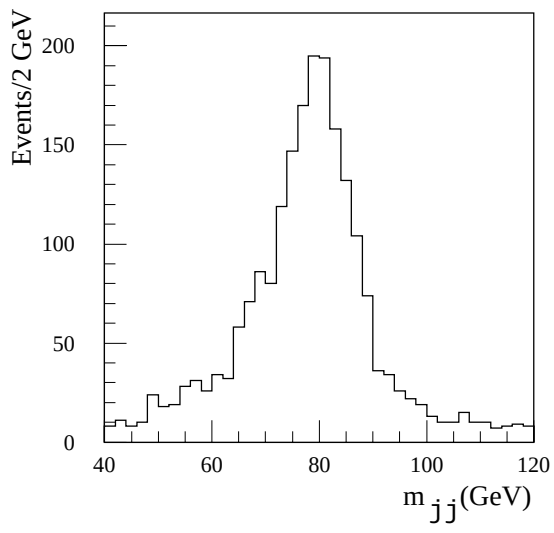

Figure 18-8 Invariant mass distribution of the selected di-jet combinations for the high p_T(top) sample, normalised to an integrated luminosity of 10 fb^{-1}.

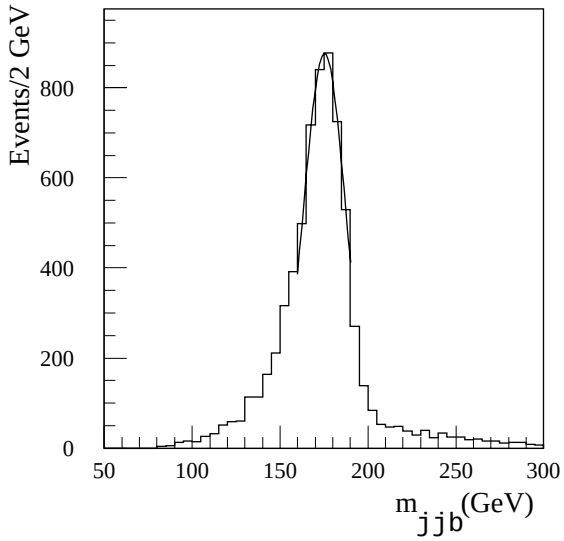

Figure 18-9 Invariant mass distribution of the accepted combinations for the high p_T(top) sample, normalised to an integrated luminosity of 10 fb^{-1}.

Three Monte Carlo data sets, with top masses of 170, 175 and 180 GeV, were used to verify that the reconstructed top mass depends linearly on the Monte Carlo input value. As a stability check of the measurement and of the calibration procedure, the reconstructed value of m_t was determined as a function of $p_T(jjb)$ for the data set with input value m_t = 175 GeV. As in the inclusive sample, no strong p_T dependence was observed.

18.1.3.3 Systematic uncertainties on the measurement of m_t in the single lepton plus jets channel

As discussed below, a number of sources of systematic error on the measurement of m_t using the single lepton plus jets channel have been studied using samples of events generated with PYTHIA and simulated with ATLFAST. In addition, over 60 000 signal events were simulated through the GEANT-based full simulation to allow cross-checks of the ATLFAST results. The results of these comparisons are presented following the discussion of the systematic errors.

The measurement of m_t via reconstruction of $t \rightarrow jjb$ relies on a precise knowledge of the energy calibration for both light quark jets and *b*-jets. The jet energy scale depends on a variety of detector and physics effects, including non-linearities in the calorimeter response, energy lost outside the jet cone (due, for example, to energy swept away by the magnetic field or to gluon radiation at large angles with respect to the original parton), energy losses due to detector effects (cracks, leakage, *etc.*), and 'noise' due to the underlying event. As discussed in Section 9.1 and Section 12.5, the goal is to understand the jet energy scale at the level of 1% for both light quark jets and *b*-jets.

The energy scale of *b*-jets enters in a direct way into the measurement of m_t and must be calibrated from other sources. In contrast, the energy of the two light quark jets can be calibrated event-by-event using the constraint that $m_{jj} = m_W$, at least for the inclusive single lepton plus jets sample, where the jets tend to be well separated. Indeed, the $W \rightarrow jj$ decays in $t\bar{t}$ events provide an essential *in situ* calibration tool for the ATLAS calorimetry system. For the high p_T(top) sample, the two light quark jets from the *W* decay tend to be very close to each other. The ener-

gy sharing between the two jets due to their spatial proximity in the detector complicates the calibration using the m_W constraint, as discussed in Section 9.3.1. A systematic error for the high p_T(top) sample based on the assumption that the W mass constraint cannot be used to perform an event-by-event calibration, is conservatively assumed in the following.

To estimate the effect of an absolute jet energy scale uncertainty, different 'miscalibration' coefficients were applied to the measured jet energies. Effects due to miscalibration of light quark jets and of b-jets were studied separately, and a top mass shift per percent of miscalibration was determined in each case. For example, Figure 18-10 demonstrates the observed linear dependence of the top mass shift on the b-jet absolute scale error for the inclusive sample. Table 18-3 summarises the systematic errors on m_t, defined as the top mass shifts resulting from assumed 1% jet scale errors.

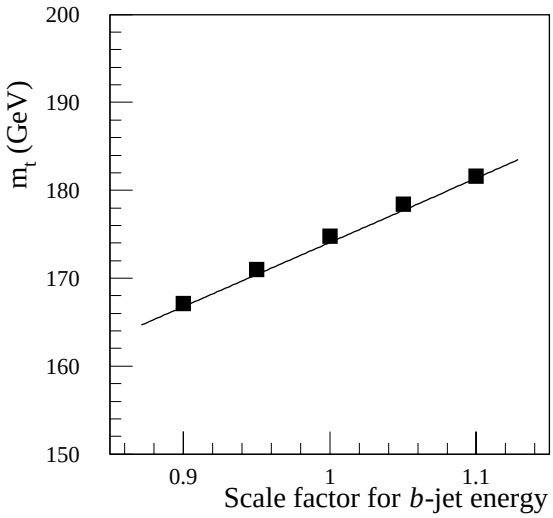

Figure 18-10 Reconstructed top mass for the inclusive single lepton plus jets $t\bar{t}$ sample, as a function of the systematic uncertainty on the energy scale for b-jets.

The fraction of the original b-quark momentum which will appear as visible energy in the reconstruction cone of the corresponding b-jet depends on the fragmentation function of the b-quark. This function is usually parametrised in PYTHIA in terms of one variable, ε_b, using the Peterson fragmentation function [18-14]. The experimental uncertainty on ε_b used here is 0.0025 [18-15]. The value of ε_b usually used in the simulations was ε_b = -0.006. Another sample of signal events was generated with ε_b = (-0.006+0.0025) = -0.0035. The difference between the values of m_t determined with these two samples was taken as the systematic error, $\delta m_t(\varepsilon_b)$, due to uncertainties in the knowledge of ε_b.The resultant systematic uncertainties are summarised in Table 18-3 for the inclusive sample and the high p_T(top) sample.

The presence of initial state radiation (ISR) and final state radiation (FSR) can impact the measurement of m_t. A top mass shift due to ISR, Δm_t(ISR), was defined as the difference between the value of m_t determined for the usual data set with ISR switched on, and the value measured using a sample of events generated with ISR switched off. A similar definition was used to define a shift due to FSR, Δm_t(FSR). In the case of FSR a large mass shift occurs, of order 10 GeV for a jet cone size of ΔR = 0.4. As expected, this large shift is considerably reduced if the cone size to reconstruct the jet is increased to ΔR = 0.7 (see Table 18-3). The level of uncertainty on the knowledge of ISR and FSR is of order 10%, reflecting the uncertainty on α_s. As a more conservative estimate of the resultant systematic errors in m_t, 20% of the Δm_t(ISR) and Δm_t(FSR) mass shifts defined above have been taken. The mass shifts and corresponding systematic errors are summarised in Table 18-3. The systematic errors estimated in this way are less than 0.3 GeV for ISR, while 1-2 GeV errors result from effects due to FSR.

An alternative approach uses the measured jet multiplicity to search, event-by-event, for the presence of hard gluon radiation. Following the convention for this approach adopted at the Tevatron [18-12], the mass shift would be defined not by comparing events with radiation switched on and events with radiation switched off, but by the difference, Δm_t, between the value of m_t determined from events with exactly four jets and that determined from events with

more than four jets. The systematic error due to effects of initial and final radiation would then be considered as $\delta m_t = \Delta m_t / \sqrt{12}$. Such a calculation would yield systematic errors of approximately 0.4 - 1.1 GeV, smaller than the more conservative approach adopted here.

Uncertainties in the size and shape of the background, which is dominated by 'wrong combinations' in $t\bar{t}$ events, can affect the top mass reconstruction. The resultant systematic uncertainty on m_t was estimated by varying the assumptions about the background shape in the fitting procedure. Fits of the m_{jjb} distribution were performed assuming a Gaussian shape for the signal and either a polynomial or a threshold function for the background. Varying the background function resulted in a systematic error on m_t of 0.2 GeV.

The structure of the 'underlying event' can affect the top mass reconstruction. However, as discussed in Section 18.1.3.4, it is possible to estimate and correct for this effect using data. Given the large statistics available at the LHC, it is assumed that the residual uncertainty from the underlying event will be small compared to the other errors (note that the 'underlying event' denotes here a minimum bias event, since the impact of ISR has already been accounted for).

The individual contributions to the systematic error of the inclusive and high p_T(top) samples are summarised in Table 18-3. For the inclusive sample, the systematic errors are reported for the analysis using jet cone sizes of ΔR = 0.4 and ΔR = 0.7. For the high p_T(top) sample, only ΔR = 0.4 was used since the jets are close in space.

Table 18-3 Top mass shift (Δm_t) and resulting systematic error on m_t (δm_t) due to the various source of systematic errors, for both the inclusive sample (for jet cone sizes of ΔR = 0.4 and 0.7) and the high p_T(top) sample. The light quark jet energy scale error for the high p_T(top) sample assumes that the W mass constraint cannot be used for an event-by-event calibration, due to the overlapping of the jets. See the text for more details.

Source of uncertainty	Comment on method	Inclusive sample		High p_T(top) sample	
		$\lvert\Delta m_t\rvert$ (GeV) ΔR=0.4 (0.7)	δm_t (GeV) ΔR=0.4 (0.7)	$\lvert\Delta m_t\rvert$ (GeV)	δm_t (GeV)
Light jet energy scale	1% scale error	0.3 (0.3)	0.3 (0.3)	1.3	1.3
b-jet energy scale	1% scale error	0.7 (0.7)	0.7 (0.7)	0.7	0.7
b-quark fragmentation	(ε_b=-0.006)-(ε_b=-0.0035)	0.3 (0.3)	0.3 (0.3)	0.5	0.5
Initial state radiation	ISR ON - ISR OFF	0.2 (1.3)	0.04 (0.3)	0.4	0.1
Final state radiation	FSR ON - FSR OFF	10.2 (6.1)	2.0 (1.2)	7.9	1.6
Background	-	0.2 (0.2)	0.2 (0.2)	< 0.2	< 0.2

In summary, the jet energy scale and FSR dominate the systematic errors. The jet corrections required are a function of the p_T of the jet (see Chapter 9), and are smaller for high p_T jets. For this reason, it is hoped that ongoing studies of the jet calibration might allow one to reduce this source of systematic error for the high p_T(top) sample with respect to the inclusive one. However, results are presented here, assuming a 1% scale uncertainty, independent of jet p_T. For the high p_T(top) sample, the light quark jet scale is also significant, if the constraint $m_{jj} = m_W$ cannot be used to calibrate the light quark jets event-by-event. The tightly collimated jets in the high p_T(top) sample require the use of a relatively small jet cone (ΔR = 0.4), resulting in a significant sensitivity to FSR effects.

18.1.3.4 High p_T single lepton plus jets analysis with a large calorimeter cluster

For the high p_T(top) sample, the large boost forces the jets from the hadronic top decay close to each other in the detector, where they overlap. While this causes some difficulties for the standard reconstruction, where m_t is reconstructed as the invariant mass of the *jjb* system (as presented above), it gives rise to the possibility to reconstruct the top mass by collecting all the energy deposited in the calorimeter in a large cone around the top quark direction. Such a technique has the potential to reduce the systematic errors, since it is less sensitive to the calibration of jets and to the intrinsic complexities of effects due to leakage outside the smaller cones, energy sharing between jets, etc. Some results from a preliminary investigation [18-16] of the potential of this technique are discussed below.

The event selection was performed as in Section 18.1.3.2, although the p_T cut on the isolated lepton and the E_T^{miss} cuts were lowered to 20 GeV, and the jets were required to have $p_T > 20$ GeV. A jet cone of $\Delta R = 0.4$ was used for the lepton hemisphere, where, apart from radiation effects, only the *b*-jet is expected. In the hemisphere opposite to the lepton, where the three jets from the hadronic top decay are expected, a smaller jet cone size of $\Delta R = 0.2$ was used.

For accepted events, the two highest p_T non-*b*-tagged jets were combined with the highest p_T *b*- jet candidate in the hemisphere opposite to the lepton to form candidates for the *jjb* hadronic top decay. The selected *jjb* combination was required to have $p_T > 150$ GeV and $|\eta| < 2.5$. With these selection criteria, about 13 000 events would be expected in the mass window from 145 to 200 GeV, with a purity of 90%, for an integrated luminosity of 10 fb^{-1}. The reconstructed invariant mass of the *jjb* combination is shown in Figure 18-11. The direction of the top quark was then determined from the jet momenta. Figure 18-12 shows the distance ΔR in pseudorapidity azimuthal angle space between the reconstructed top direction and the true direction at the parton level, demonstrating good agreement between the measured direction and the true direction.

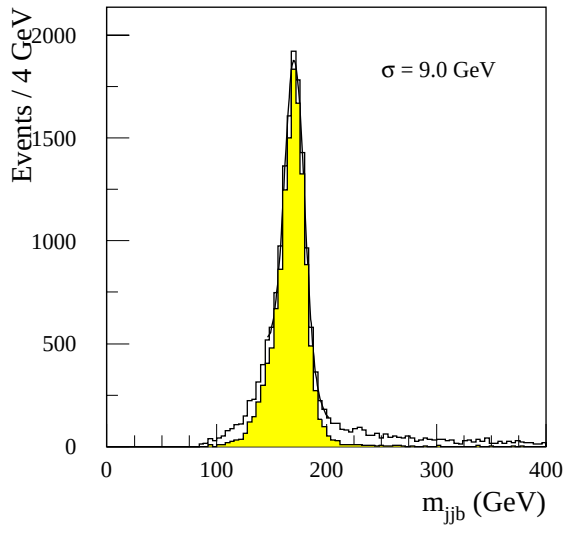

Figure 18-11 Invariant mass distribution of the selected *jjb* combination, using $\Delta R = 0.2$ cones for the high p_T (top) sample, normalised to an integrated luminosity of 10 fb^{-1}. The shaded area corresponds to the combinations with the correct jet-parton assignments.

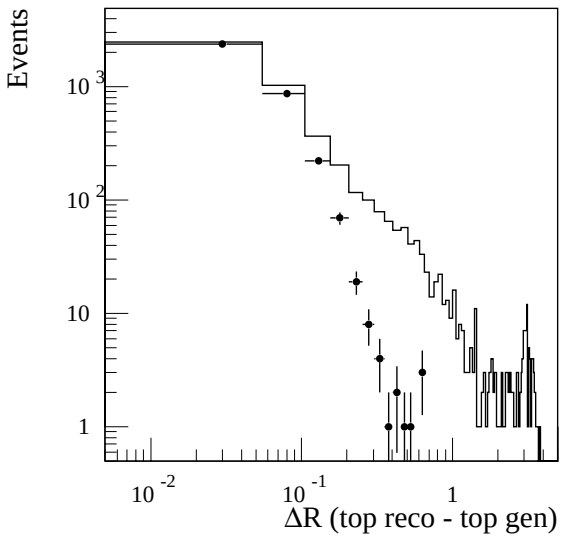

Figure 18-12 Distance ΔR between the top quark direction reconstructed using $\Delta R = 0.2$ cones and the parton level direction of the top quark. The dots correspond to the correct *jjb* combinations.

A large cone of radius ΔR was then drawn around the top quark direction as determined with jets of size 0.2. The top mass was determined by adding the energies of all calorimeter 'cells' within the cone (a calorimeter cell has a size $\Delta\eta x\Delta\phi$ = 0.1x0.1). The effective invariant mass of the cells was then calculated according to the formula:

$$m_{jjb} = (E^2 - p^2) = \left(\sum_{i=1}^{n} E_i\right)^2 - \left(\sum_{i=1}^{n} \vec{p}_i\right)^2 \quad ,$$

where the sum runs over all cells with energy above threshold inside the cone, the energies are those deposited in the cells, and the cell momenta are calculated from their energy and position, assuming the energy in each cell was deposited by a massless particle. The invariant mass spectrum is shown in Figure 18-13 for a cone size ΔR= 1.3, and exhibits a clean peak at the top quark mass.

The fitted value of the reconstructed top mass is shown in Figure 18-14, where it displays a strong dependence on the cone size. It has been checked that, if only the hard process (HP) in PYTHIA is enabled, the fitted mass remains constant (within 2%) independent of cone size. However, once effects of the 'underlying event' (UE) from multiple interactions (MUI) among the partons of the colliding pair of protons are included, a dependence on cone size appears. Additional shifts in the top mass result from initial and final state radiation (ISR / FSR).

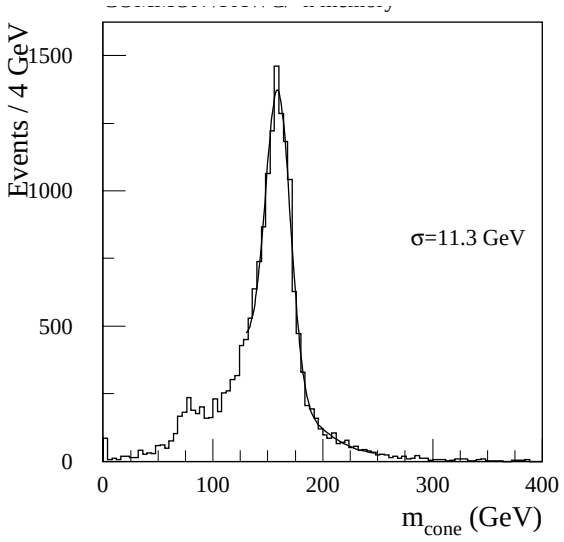

Figure 18-13 Reconstructed $t \rightarrow jjb$ mass spectrum obtained using cells in a single cone of size ΔR = 1.3, normalised to an integrated luminosity of 10 fb^{-1}.

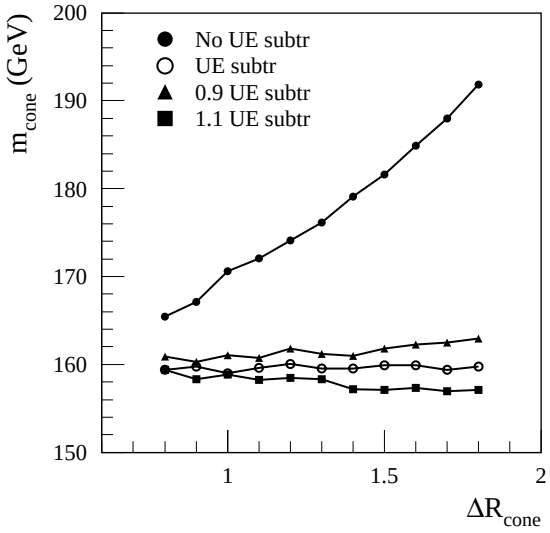

Figure 18-14 The fitted top mass using cells in a single cone, before and after the underlying event (UE) subtraction and as a function of the cone size.

In the absence of the underlying event, and for cone sizes which are sufficiently large to contain all three jets from the hadronic top decay, the fitted mass should be independent of the cone size. Therefore, a method has been developed to subtract the contribution from the underlying event, by using the calorimeter cells not associated with the products of the top quark decay. The UE contribution was calculated as the average E_T deposited per calorimeter cell, averaged over those cells which were at least a distance ΔR away from the impact points of the daughters of the partons in the hard scattering process. In Figure 18-15, the values obtained for different settings of the PYTHIA generator are shown. As expected, the average E_T per calorimeter cell

increases as more activity is added, especially in the case of ISR. Only a rather small dependence is observed on the radius ΔR used to isolate the cells associated with the hard scattering process.

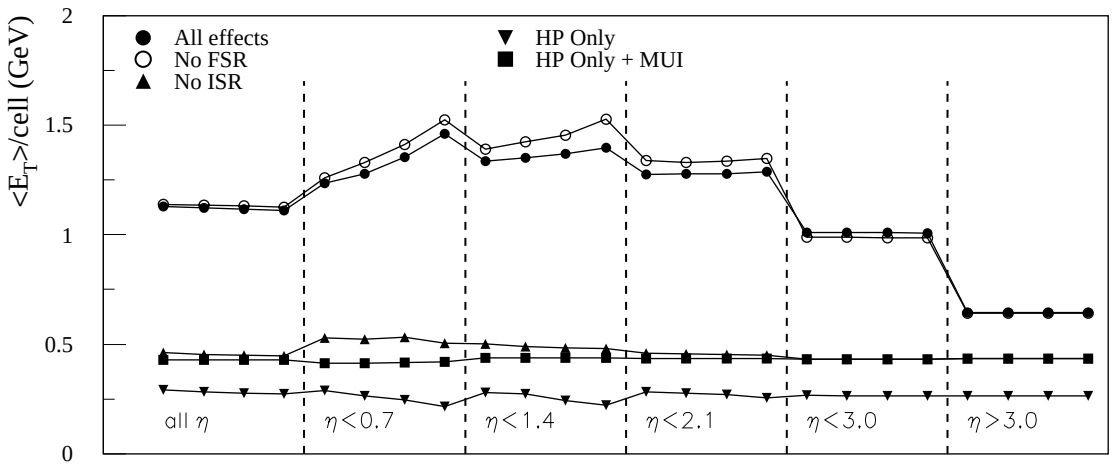

Figure 18-15 Estimator of the average E_T deposited per cell from the underlying event as a function of η for different settings of the PYTHIA event generator. In each η range, the four symbols correspond to different ΔR values, within which cells were flagged as belonging to partons from the hard scattering process (ΔR = 0.7, 0.8, 0.9, and 1.0) and therefore not used to compute the average E_T per cell. The acronyms of HP (hard-scattering process), MUI (multiple interactions), ISR (initial state radiation) and FSR (final state radiation) refer to the options enabled in PYTHIA for the various data sets.

For the remainder of the analysis, the average E_T per cell in the case of HP+MUI only (0.429 GeV per cell) was used as the UE estimator and was subtracted from each cell (assuming no pseudorapidity dependence) used in the invariant mass calculation. The resulting value of the reconstructed mass (m_{cone}), with and without UE subtraction, is shown in Figure 18-14 as a function of the cone radius. As can be seen, after the UE subtraction, the reconstructed top mass is independent of the cone size used. As a cross-check, the mean E_T per cell was varied by ±10% and the top mass recalculated in each case. As shown superimposed on Figure 18-14, these 'miscalibrations' lead to a re-emergence of a dependence of m_t on the cone size. While the prescription for the UE subtraction does lead to a top mass which is independent of the cone size, it should be noted that the reconstructed mass is about 15 GeV (or 8.6%) below the nominal value, m_t = 175 GeV, implying that a rather large correction would be needed.

To investigate if this correction can be calibrated, the same procedure was applied to a sample of W+jet events generated with a range of p_T comparable to that of the top sample. The W was forced to decay hadronically into jets. Events were selected by requiring the presence of at least 3 jets (using a cone size of 0.4) with $p_T > 30$ GeV and $|\eta| < 2.5$. The highest p_T jet was required to satisfy $p_T > 40$ GeV. The W decay was reconstructed from the second and third highest p_T jets, since in general the highest p_T jet was the jet balancing the p_T of the W boson.

As for the high p_T(top) analysis, the direction of the reconstructed W was measured from the jets, and all cells within a distance ΔR were used to calculate the W invariant mass. The underlying event contribution was estimated with the same algorithm as described above, averaging over those cells which were far away from the reconstructed jets. The results agreed within 1% with the values determined for the high p_T(top) sample. This is not surprising since the underlying event contribution measured without ISR is expected to be basically identical for all processes.

In Figure 18-16, the reconstructed W mass as a function of the cone size is plotted before and after the UE event subtraction. As in the case of the top events, the reconstructed W mass after UE subtraction is independent of the cone size. The average value of m_{jj} after the UE subtraction is about 8.5 GeV (or 10.6%) below the nominal value of m_W.

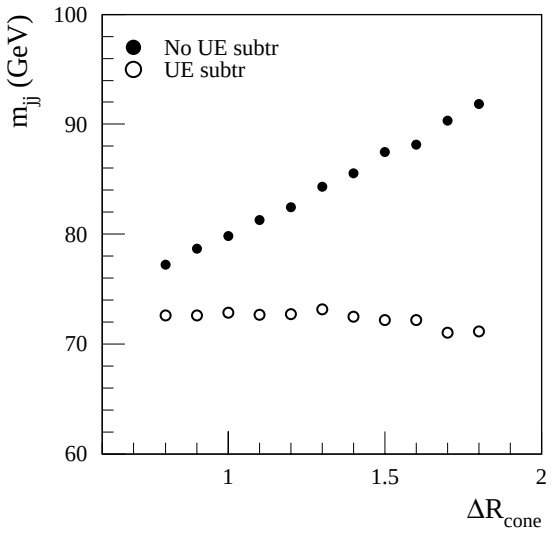

Figure 18-16 For the W+jet sample, the fitted W mass, using cells in a single cone, before and after the UE event subtraction and as a function of the cone size.

The fractional error on m_{jj}, as measured with the W+jet sample, was used as a correction factor to m_{cone} in the high p_T(top) sample. For a cone of radius ΔR = 1.2, the top mass after UE subtraction increases from 160.1 GeV to 177.0 GeV after rescaling. Similarly, the value of 159.9 GeV, obtained after UE subtraction with a cone of radius ΔR = 1.3, gives a value of 176.0 GeV after rescaling. The rescaled values of m_{cone} are about 1% higher than the generated top mass. This over-correction of m_t using the value of m_W measured with the same method, is due to ISR contributions to the cone used to measure m_t. If ISR is switched off, the rescaling procedure works to better than 1%. This can be understood, since the contributions from ISR to high p_T $W \rightarrow jj$ decays, whether produced directly or in top decay, should be similar to first order in energy, but not in mass.

The systematic errors were evaluated as described in Section 18.1.3.3 and are summarised in Table 18-4. Varying the energy scale of the calorimeter cell calibration by 1% resulted in an error in m_t of 0.6 GeV. As expected, the use of a large cone substantially reduces the effects of FSR and b-quark fragmentation, each of which gives rise to a systematic error of 0.1 GeV. The uncertainty arising from ISR, which can affect the determination of the UE subtraction, is about 0.1 GeV. The main uncertainty in this technique comes from the calibration procedure. The calibration with the W+jet sample produces a value of m_t which is about 1% above the generated value. Furthermore, the $W \rightarrow jj$ events would suffer from background from QCD multi-jet events. Ongoing studies suggest one could calibrate using $W \rightarrow jj$ decays from the high p_T(top) events themselves, selecting those events in which the b-tagged jet is far away from the other two jets of the W decay and then reconstructing the $W \rightarrow jj$ decay using a single cone of size ΔR = 0.8. For example, requiring that the minimum separation between the light quark jets and the b-tagged jets satisfy $\Delta R > 1.5$, one can see a clear W mass peak, as shown in Figure 18-17. Further study is required to reliably estimate the potential of this calibration procedure, and a systematic uncertainty of 1% is assigned to it in Table 18-4.

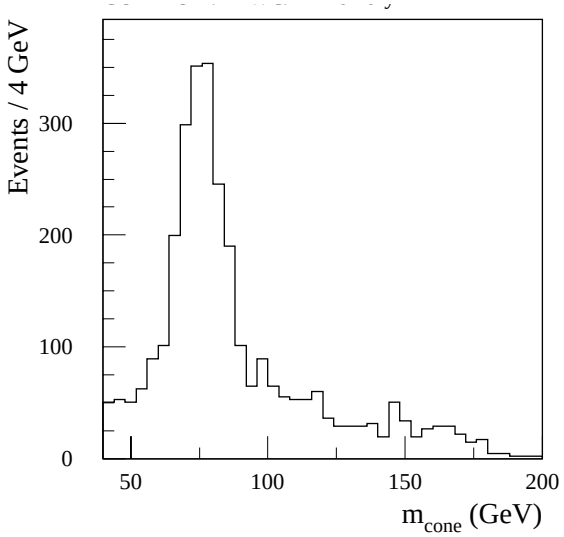

Figure 18-17 Reconstructed $W \rightarrow jj$ mass spectrum obtained using cells in a single cone of size ΔR = 0.8, for those events of the high p_T(top) sample where the b-tagged jets are a distance of at least ΔR = 1.5 away from the light quark jets. The figure is normalised to an integrated luminosity of 10 fb^{-1}.

Table 18-4 Top mass shift (Δm_t) and resulting systematic error on m_t (δm_t) due to the various sources of systematic errors (see text), for the high p_T(top) sample analysed using cells in a large cone ΔR = 1.3.

Source of uncertainty	Comment on method	Cone size ΔR = 1.3	
		$\lvert\Delta m_t\rvert$ (GeV)	δm_t (GeV)
Cell energy scale	1% scale error	0.6	0.6
b-quark fragm.	(ε_b=-0.006)-(ε_b=-0.0035)	0.1	0.1
Initial state radiation	ISR ON - ISR OFF	0.7	0.1
Final state radiation	FSR ON - FSR OFF	0.2	0.1
Calibration of method	High p_T $W \rightarrow jj$ decays	1.6	1.6

18.1.3.5 Comparison between fast and full simulation for the single lepton plus jets sample

The computing power required to generate sufficiently large $t\bar{t}$ samples to perform all the systematic studies would be prohibitive. However, in order to be able to cross-check the results obtained with ATLFAST, a total of over 60 000 $t\bar{t}$ events were processed through DICE, the GEANT-based ATLAS detector simulation, and then the ATLAS reconstruction package, ATRECON. The event samples included approximately 30 000 inclusive single lepton plus jet events, and an equal number of events generated with p_T(top) > 200 GeV.

To avoid simulating events through GEANT which would later likely fail the selection criteria, cuts on the transverse momentum and pseudorapidity of the $t\bar{t}$ daughters have been applied at the generator level. The fully simulated events have, therefore, been generated under somewhat more restrictive conditions than used for the ATLFAST simulations described previosuly. In order to make consistent comparisons between fast and full simulation, the events which have been passed through the full GEANT simulation and reconstruction package were also run through the fast simulation package (ATLFAST), so that the exact same events can be compared (see also Section 9.3.4).

For the inclusive channel, in the top mass window 175 ± 35 GeV, the signal purity and overall efficiency were P = 79% and ε = 6.4% for fast simulation and P = 78% and ε = 5.7% for full simulation. Figure 18-18 and Figure 18-19 show the m_{jj} mass distributions for the two reconstructions. The resulting m_W resolutions were 7.3 and 8.1 GeV for fast and full simulation, respectively. The reconstructed m_{jjb} invariant mass distributions are shown in Figure 18-20 and Figure 18-21. The m_{jjb} invariant mass resolutions were 11.4 GeV and 13.4 GeV for fast and full simulation, respectively .

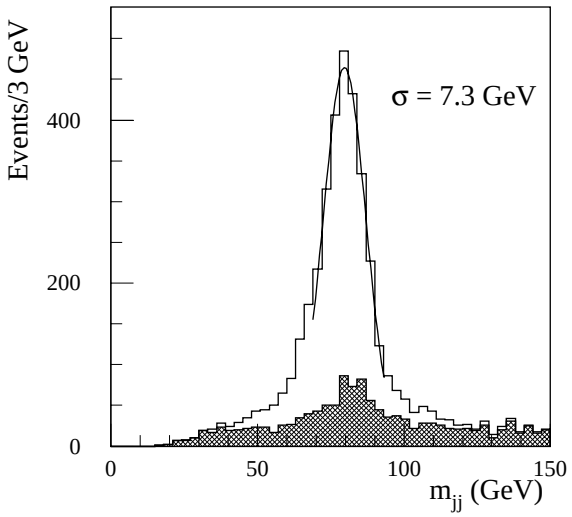

Figure 18-18 Invariant di-jet mass distribution obtained from fast simulation for the same sample of 30 000 inclusive single lepton plus jet events which were fully simulated. The shaded histogram shows the background from wrong combinations.

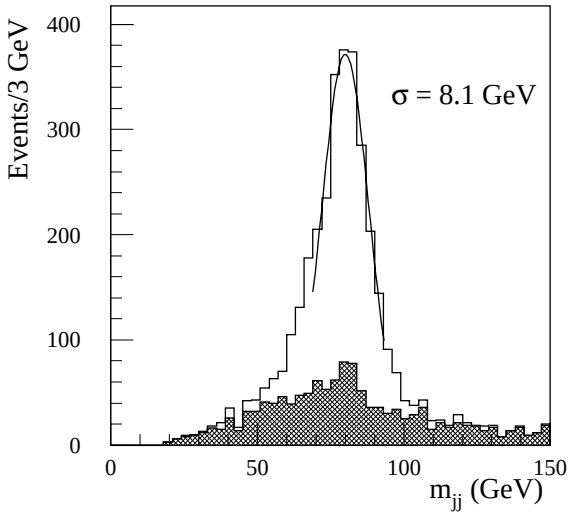

Figure 18-19 Invariant di-jet mass distribution obtained from full simulation for the sample of 30 000 inclusive single lepton plus jet events. The shaded histogram shows the background from wrong combinations.

In summary, the predictions from the two simulations are in good agreement for the signal efficiencies and purities. The amount and shape of the combinatorial background under the W and top mass peak are in good agreement as well. The m_W and m_t mass resolutions are in reasonable agreement, with the full simulation predicting resolutions which are 10-20% worse than those from the fast simulation.

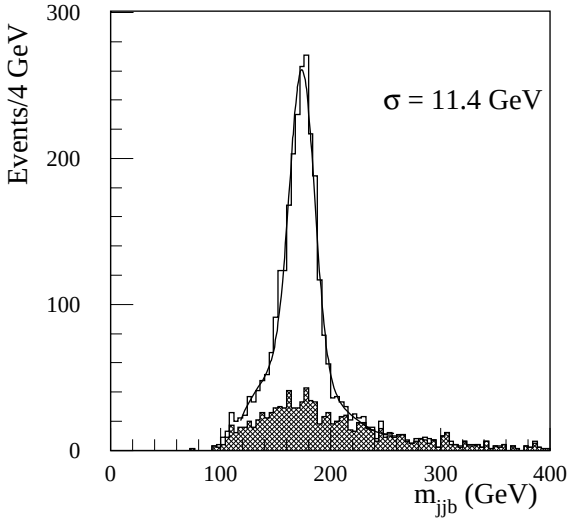

Figure 18-20 Invariant *jjb* mass distribution obtained from fast simulation for the same sample of 30 000 inclusive single lepton plus jet events which were fully simulated. The shaded histogram shows the background from wrong combinations.

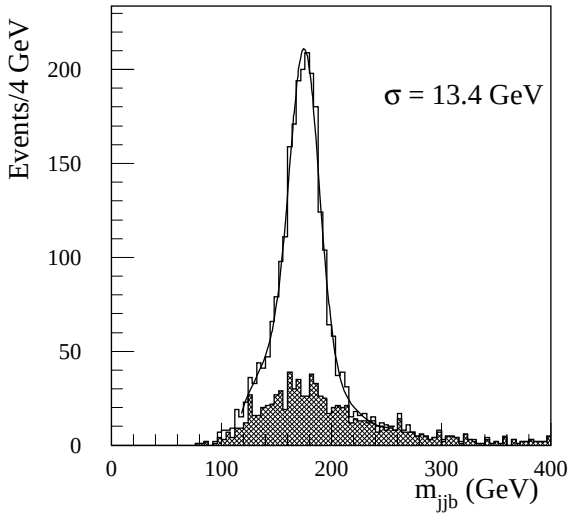

Figure 18-21 Invariant *jjb* mass distribution obtained from full simulation for the sample of 30 000 inclusive single lepton plus jet events. The shaded histogram shows the background from wrong combinations.

18.1.3.6 Dilepton channel

Dilepton events can provide a measurement of the top quark mass complementary to that obtained from the single lepton plus jets mode. The signature of a dilepton event consists of two isolated high p_T leptons, high E_T^{miss} due to the neutrinos, and two jets from the fragmentation of the *b*-quarks. Measurement of m_t using dilepton events is complicated by the fact that one cannot fully reconstruct either of the top quarks, due to the undetected neutrinos in the final state. This problem can be dealt with by weighting each solution based on some dynamical information, and thus obtaining a preferred mass for each event. Alternatively, one can take advantage of the fact that the kinematical distributions of the top decay products depend on m_t, and attempt to obtain the most likely top mass for a set of events. The mass determination depends on the assumption that the kinematical distributions for top production are reproduced by the Monte Carlo simulation.

About 400 000 dilepton $t\bar{t}$ events are expected to be produced in a data sample corresponding to an integrated luminosity of 10 fb^{-1}. Backgrounds arise from Drell-Yan processes associated with jets, $Z \rightarrow \tau\tau$ associated with jets, WW+jets and $b\bar{b}$ production. The event selection criteria required two opposite-sign leptons within $|\eta| < 2.5$, with $p_T > 35$ and 25 GeV respectively, and with $E_T^{miss} > 40$ GeV. Two jets with $p_T > 25$ GeV were required in addition. After the selection cuts, 80 000 signal events survived, with *S/B* around 10.

Of the many possible kinematic variables which could be studied, preliminary analyses [18-17] of three have been performed: the mass m_{lb} of the lepton-*b*-jet system, the energy of the two highest E_T jets, and the mass m_{ll} of the dilepton system formed with both leptons coming from the same top decay (*i.e.* $t \rightarrow lvb$ followed by $b \rightarrow lvc$).

Top mass measurement using m_{lb}

In this analysis, the value of m_t was estimated using the expression

$$m_t^2 = m_W^2 + 2 \cdot \langle m^2_{lb} \rangle / [1 - \langle \cos\theta_{lb} \rangle]$$

Here, $<m_{lb}^2>$ is the squared mean invariant mass of the lepton and *b*-jet from the same top decay. The mean value of $\cos\theta_{lb}$, the angle between the lepton and the *b*-jet in the *W* rest frame, can be regarded as an input parameter to be taken from Monte Carlo.

To obtain a very clean sample, the two highest p_T jets were required to be tagged as *b*-jets, leaving a total of about 15,200 signal events per 10 fb^{-1}. One cannot determine, in general, which lepton should be paired with which *b*-jet. The pairing which gave the smaller value of m_{lb}^2 was chosen, and checking the parton-level information showed that this criterion selected the correct pairing in 85% of the cases, for a generated top mass of 175 GeV. The mean value $<m_{lb}^2>$ was measured for samples generated with different top masses *m*, and then m_t was calculated from the expression above. The resultant m_t is a function of $<\cos\theta_{lb}>$ and *m*. A χ^2 was defined and minimised with respect to $<\cos\theta_{lb}>$ in order to determine the best value of $<\cos\theta_{lb}>$. The value of m_t was corrected to compensate for the shift, less than 0.6 GeV, produced by using a fixed $<\cos\theta_{lb}>$, and for not distinguishing between *b* and $\bar{b}$.

For an integrated luminosity of 10 fb^{-1}, the expected statistical uncertainty on m_t using this method is about 0.9GeV. Major sources of systematics include uncertainty on the *b*-quark fragmentation function, which produces a systematic error on m_t of 0.7 GeV if defined as described in Section 18.1.3.3. Systematic errors due to the effects of FSR and ISR together are about 1 GeV, while that due to varying the jet energy scale by 1% is 0.6 GeV. Further studies are required to estimate the uncertainties due to the reliance upon the Monte Carlo modelling of the $t\bar{t}$ kinematics.

Top mass measurement using energy of two leading jets

Increased sensitivity could be obtained with a technique which utilizes not only the mean, but also the shape of the kinematic distribution. As an example, a study has been made of the sensitivity to m_t obtained by comparing to 'template' distributions the energy of the two highest E_T jets. The template distributions were made by generating PYTHIA samples of $t\bar{t}$ events with different values of m_t in the range 160-190 GeV, in steps of 5 GeV. Figure 18-22 shows, as an example, the templates obtained for m_t = 165 GeV and 175 GeV.

For each possible top mass value m, a $\chi^2(m)$ was obtained by comparing the kinematical distribution of the simulated data with the templates of mass m. The best value for the mass was the value which, for the 'data' set, generated with m_t = 175 GeV, gave the minimum χ^2.

For an integrated luminosity of 10 fb^{-1}, the expected statistical sensitivity on m_t corresponds to about 0.4 GeV. Varying the calorimeter jet energy scale by 1% produced a systematic error on m_t of 1.5 GeV. Other sources of systematic error result from dependence of the method on the Monte Carlo modelling of the $t\bar{t}$ kinematics, and require further study. As an example, changing the choice of the structure functions used in the Monte Carlo simulation (for example, from CTEQ2L to CTEQ2M or EHQL1) led to differences in the top mass of ±0.7 GeV.

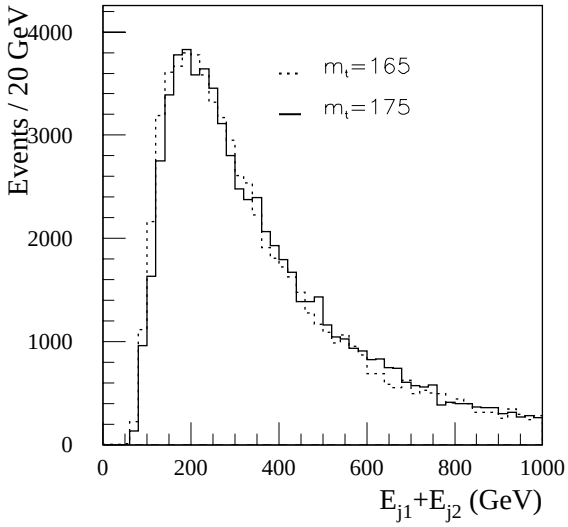

Figure 18-22 Template distributions of the total energy of the two leading jets in $t\bar{t}$ events for top quark masses of 165 and 175 GeV. The two distributions are normalised to the same area.

Top mass measurement using m_{ll} in tri-lepton events

The invariant mass distribution of the two leptons from the same top quark decay (*i.e.* $t \to lvb$ followed by $b \to lvc$) is quite sensitive to m_t. It has been shown that the mass distribution of lepton pairs from the same top quark decay is much less sensitive to the top quark transverse momentum distribution than that of lepton pairs from different top quarks [18-18].

Signal events are expected to contain two leptons from the decay of the W bosons produced directly in the top and anti-top quark decays, and one lepton from the b-quark decay. In addition to the cuts described above, one non-isolated muon with $p_T > 15$ GeV was required.

For an integrated luminosity of 10 fb^{-1}, the expected signal would be about 7,250 events, yielding a statistical uncertainty on the measurement of m_t of approximately ±1 GeV. This technique is insensitive to the jet energy scale. The dominant uncertainties arise from effects of ISR and FSR and from the b-quark fragmentation, which sum up to about 1.5 GeV.

18.1.3.7 Summary of top mass studies

The very large samples of top quark events which will be accumulated at the LHC will allow a precision measurement of the top quark mass. More than 120 000 single lepton plus jet events would be selected, with a signal-to-background ratio of over 60, within a single year of running at low luminosity. Measuring m_t by reconstructing the invariant mass of the $t \to jjb$ candidates in these events would yield a statistical error below 0.1 GeV. Studies of the systematic errors indicate a total error below 2 GeV should be obtainable, provided the energy scales for jets and b-jets can be understood at the 1% level (see Chapter 12). A substantial contribution to the systematic error for the inclusive sample comes from FSR. A method to reconstruct m_t in the high p_T(top) sample using the cells within a single large cone, succeeds in substantially reducing the

sensitivity to FSR. Further study is required to reliably estimate the potential of this method. Complementary measurements of m_t can be performed with the sample of 80 000 dilepton events selected for an integrated luminosity of 10 fb^{-1}.

18.1.4 Top quark pair production

The NLO prediction for $t\bar{t}$ production at the LHC is quite precisely known. At the LHC, the gluon-gluon fusion process $gg \rightarrow t\bar{t}$ accounts for about 90% of the total $t\bar{t}$ production, with $q\bar{q}' \rightarrow t\bar{t}$ accounting for the rest. (Note that these fractions are approximately reversed in the case of $p\bar{p} \rightarrow t\bar{t}$ at the Tevatron, where $q\bar{q}'$ annihilation dominates). Measurements of the total cross-section, as well as differential cross-sections, are discussed in Section 15.8.4, including implications for QCD measurements, such as the determination of parton distribution functions. Here some examples of possible signatures of new physics in $t\bar{t}$ production are presented.

18.1.4.1 $t\bar{t}$ production cross-section measurements

Physics beyond the SM could affect cross-section measurements for $t\bar{t}$ production in a variety of ways. For example, existence of a heavy resonance decaying to $t\bar{t}$ might enhance the cross-section, and might produce a peak in the $t\bar{t}$ invariant mass spectrum (this possibility is discussed in more detail in the next section). Deviations from the SM top quark branching ratios, due for example to a large rate of $t \rightarrow H^+b$, could lead to an apparent deficit in the $t\bar{t}$ cross-section measured with the assumption that BR($t \rightarrow W^+b$) ≈ 1.

The NLO prediction of $\sigma(t\bar{t})$ = 833 pb [18-1] implies production of over 8 million $t\bar{t}$ pairs in one year at low luminosity. Measurements of $\sigma(t\bar{t})$ will be limited by the uncertainty of the integrated luminosity determination, which is currently estimated to be 5%-10% (see Chapter 13). The cross-section relative to some other hard process, such as Z production, should be able to be measured more precisely.

18.1.4.2 Search for $t\bar{t}$ resonances

A number of theoretical models predict the existence of heavy resonances which decay to $t\bar{t}$. An example within the Standard Model is the SM Higgs boson, which will decay to $t\bar{t}$ provided the decay is kinematically allowed. However, the strong coupling of the SM Higgs boson to the W and Z implies that the branching ratio to $t\bar{t}$ is never very large. For example, for m_H = 500 GeV, the SM Higgs natural width would be 63 GeV, and BR($H \rightarrow t\bar{t}$) ≈ 17%. The resulting value of $\sigma \times$ BR for $H \rightarrow t\bar{t}$ in the SM is not sufficiently large to see a Higgs peak above the large background from continuum $t\bar{t}$ production. In the case of MSSM, however, if m_A,$m_H > 2m_t$, then BR($H/A \rightarrow t\bar{t}$) ≈ 100% for tan$\beta \approx 1$. For the case of scalar or pseudoscalar Higgs resonances, it has been pointed out [18-19] that interference can occur between the amplitude for the production of the resonance via $gg \rightarrow H/A \rightarrow t\bar{t}$ and the usual gluon fusion process $gg \rightarrow t\bar{t}$. The interference effects become stronger as the Higgs' mass and width increase. Searches for these decays are discussed in detail in Section 19.3.2.7, in the context of MSSM.

The possible existence of heavy resonances decaying to $t\bar{t}$ arises in technicolor models [18-20] as well as other models of strong electroweak symmetry breaking [18-21][18-22]. In Section 21.2.1.5, the production and decay into $t\bar{t}$ of a colour octet techni-eta (η_8) particle of mass 500 GeV was studied. Recent variants of technicolor theories, such as Topcolor [18-23], posit

new interactions which are specifically associated with the top quark, and could give rise to heavy particles decaying to $t\bar{t}$. Since $t\bar{t}$ production at the LHC is dominated by gg fusion, colour octet resonances ("colourons") could also be produced [18-24].

Because of the large variety of models and their parameters, a study was made of the sensitivity to a 'generic' narrow resonance decaying to $t\bar{t}$ (more details can be found in reference [18-25]). Events of the single lepton plus jets topology $t\bar{t} \rightarrow WWb\bar{b} \rightarrow (l\nu)(jj)b\bar{b}$ were selected by requiring $E_T^{miss} > 20$ GeV, and the presence of an isolated electron or muon with $p_T > 20$ GeV and $|\eta| < 2.5$. In addition, it was required that there were between four and ten jets, each with $p_T > 20$ GeV and $|\eta| < 3.2$. At least one of the jets was required to be tagged as a b-jet. After these cuts, the background to $t\bar{t}$ resonant production was dominated by continuum $t\bar{t}$ production.

The momentum of the neutrino was reconstructed, as described previously, by setting $m_\nu = 0$, assigning $E_T(\nu) = E_T^{miss}$, and calculating $p_z(\nu)$ (with a quadratic ambiguity) by applying the constraint that $m_{l\nu} = m_W$. The hadronic $W \rightarrow jj$ decay was reconstructed by selecting pairs of jets from among those not tagged as b-jets. In cases where there were at least two b-tagged jets, then candidates for $t \rightarrow Wb$ were formed by combining the $W \rightarrow l\nu$ and $W \rightarrow jj$ candidates with each of them. In events with only a single b-tagged jet, this was assigned as one of the b-quarks and each of the still unassigned jets then was considered as a candidate for the other b-quark.

Among the many different possible jet-parton assignments, the combination was chosen that minimised the following χ^2:

$$\chi^2 = (m_{jjb} - m_t)^2 / \sigma^2(m_{jjb}) + (m_{l\nu b} - m_t)^2 / \sigma^2(m_{l\nu b}) + (m_{jj} - m_W)^2 / \sigma^2(m_{jj})$$

Events were rejected if either $m_{l\nu b}$ or m_{jjb} disagreed with the known value of m_t by more than 30 GeV.

For events passing the reconstruction procedure, the measured energies were rescaled, according to their resolution, to give the correct values of m_W and m_t for the appropriate combinations. This procedure improved the resolution of the mass reconstruction of the $t\bar{t}$ pair to $\sigma[m_{t\bar{t}}] / m_{t\bar{t}} \approx 6.6\%$. As an example, Figure 18-23 shows the reconstructed $m_{t\bar{t}}$ distribution for a narrow resonance of mass 1600 GeV. The width of the Gaussian core is well described by the resolution function described above. The size of the tails, which are dominated by incorrect jet-parton assignments, is such that approximately 65% of the events are contained within $\pm 2\sigma$ of the peak.

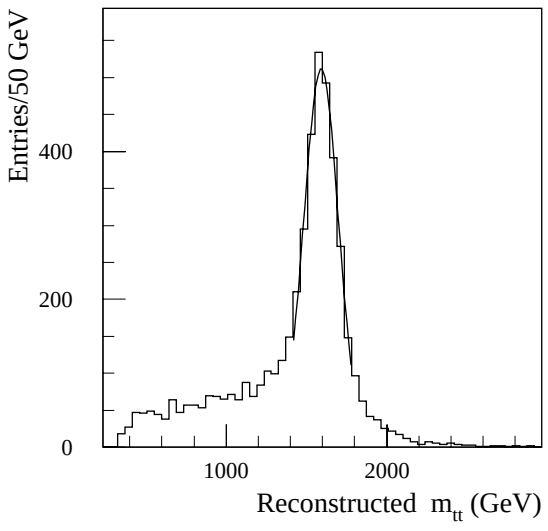

Figure 18-23 Measured $t\bar{t}$ invariant mass distribution for reconstruction of a narrow resonance of mass 1600 GeV decaying to $t\bar{t}$.

The reconstruction efficiency, not including branching ratios, for $t\bar{t} \rightarrow WWb\bar{b} \rightarrow (l\nu)(jj)b\bar{b}$ was about 20% for a resonance of mass 400 GeV, decreasing gradually to about 15% for $m_{t\bar{t}} = 2$ TeV.

For a narrow resonance X decaying to $t\bar{t}$, Figure 18-24 shows the required $\sigma \times \mathrm{BR}(X \rightarrow t\bar{t})$ for discovery of the resonance. The criterion used to define the discovery potential was observation within a $\pm 2\sigma$ mass window of a signal above the $t\bar{t}$ continuum background, where the required signal must have a statistical significance of at least 5σ and must contain at least ten events. Results are shown versus m_X for integrated luminosities of 30 fb^{-1} and 300 fb^{-1}. For example, with 30 fb^{-1}, a 500 GeV resonance could be discovered provided its $\sigma \times \mathrm{BR}$ is at least 2,560 fb. This value decreases to 830 fb for m_X = 1 TeV, and to 160 fb for m_X = 2 TeV. The corresponding values for an integrated luminosity of 300 fb^{-1} are 835 fb, 265 fb, and 50 fb for resonances masses m_X = 500 GeV, 1 TeV, and 2 TeV.

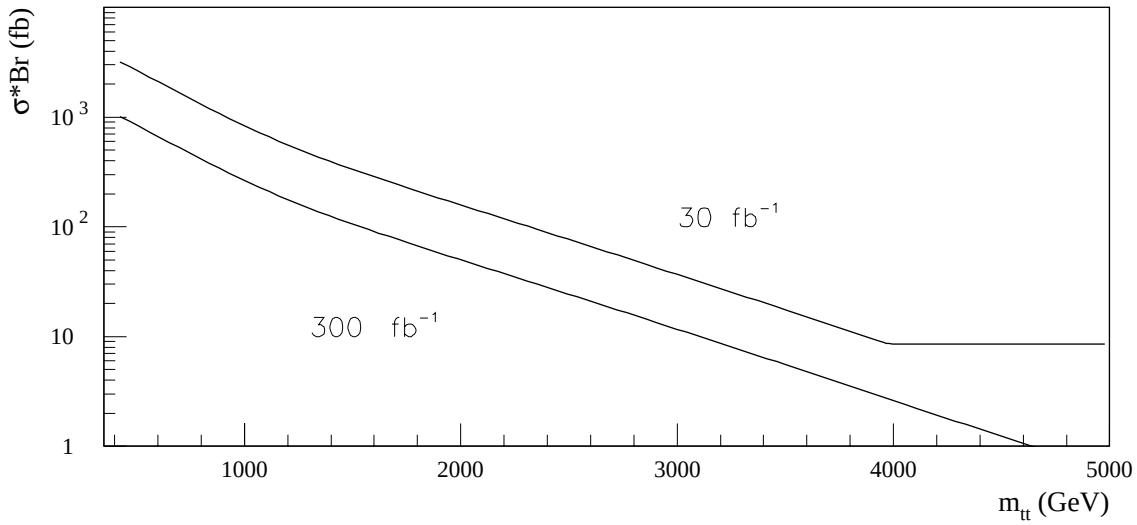

Figure 18-24 Value of $\sigma \times \mathrm{BR}$ required for a 5σ discovery potential for a narrow resonance decaying to $t\bar{t}$, as a function of $m_{t\bar{t}}$, and for an integrated luminosity of either 30 or 300 fb^{-1}.

Once predictions from models exist for the mass, natural width, and $\sigma \times \mathrm{BR}$ for a specific resonance, the results in Figure 18-24 can be used to determine the sensitivity and discovery potential for those models. As discussed above, extra care must be taken in the case of spin zero resonances, due to possible interference effects. While such effects are small for the case of a narrow resonance, they can be significant once the finite widths of heavy resonances are taken into account.

18.1.4.3 $t\bar{t}$ spin correlations

The SM prediction of the top quark width, given the large value of m_t, is $\Gamma_t \sim 1.5$ GeV. Thus, the top quark lifetime is very short in comparison with the hadronisation time ($\sim 1/\Lambda_{\mathrm{qcd}}$), and the top quark decays as a "bare quark" before hadronising. In addition, the top quark decays before the strong interaction has time to depolarise its spin. As a consequence, the spin orientation of the top quark should be preserved in its decay. The weak decay of the top quark implies the daughters in the decay chain can be used to analyze its spin orientation.

To lowest order, top quarks produced via the strong processes $gg / q\bar{q} \rightarrow t\bar{t}$ are unpolarised, and the transverse polarisation effects due to loop diagrams are predicted to be very small. However, the spins of the t and $\bar{t}$ are correlated. At the LHC, the top and anti-top quarks tend to be produced with the same helicity, thus favouring the production of 'Left-Left' (LL) or 'Right-Right' (RR) $t\bar{t}$ pairs. For example, for $m_{t\bar{t}} < 500$ GeV, about 80% $t\bar{t}$ pairs are predicted [18-26] to be pro-

duced with either LL or RR helicities. This fraction falls slowly to a little under 70% for $m_{t\bar{t}} < 1000$ GeV. A measurement of this spin correlation would check whether the top quark does indeed decay before the strong interaction has time to depolarise its spin, and thereby would allow a lower limit to be set on Γ_t. Furthermore, new physics, such as large CP violation in the top system, could alter the spin correlations predicted by the SM. Such effects could result, for example, from additional phases in the EWSB sector which, due to the large value of m_t, could produce large effects in top physics while still satisfying bounds from data on the lighter quarks (see, for example, [18-27]).

The angular distribution of the ith decay product with respect to the top spin vector is given, in the top quark rest frame, by the expression:

$$\frac{1}{N}\frac{dN}{d\cos\theta_i} = \frac{1}{2}(1 + \alpha_i \cos\theta_i)$$

The coefficients α_i are characteristic for each particle produced in the decay ($\alpha = 1$ for charged leptons, $\bar{d}$ and $\bar{s}$ quarks; $\alpha = -0.33$ for neutrinos, u and c quarks; $\alpha = -0.41$ for the b-quark). From these values, it is apparent that the charged lepton, in addition to being the simplest to tag experimentally, also provides the most undiluted measure of the top spin direction. Therefore, the analysis presented here will consider only the correlations between the pair of charged leptons produced in 'dilepton' $t\bar{t}$ events where both W bosons decay via $W \rightarrow l\nu$.

For dilepton $t\bar{t}$ events, the angular distribution of the two charged leptons is described by:

$$\frac{1}{N}\frac{d^2N}{d(\cos\theta_{l_1})d(\cos\theta_{l_2})} = \frac{1}{4}(1 - \kappa \cos\theta_{l_1}\cos\theta_{l_2})$$

with $\kappa = A\alpha_{l1}\alpha_{l2}$, where $A = (2P-1)$ and P is the fraction of the events where the top and anti-top quarks are produced with the same helicity. As discussed above, $\alpha_{l1} = 1$ and $\alpha_{l2} = -1$.

For this analysis [18-28], Monte Carlo events have been generated with the default version of PYTHIA, which does not incorporate spin correlations, and also with a modified version where the matrix element for top decay takes into account the top polarisation:

$$|M|^2 \sim \frac{m_t^2 E_l (m_t - 2E_l)}{(q^2 - m_W^2)^2 + \Gamma^2 m_W^2}(1 + h_t \cos\theta_l)$$

where E_l and θ_l are the energy and the angle with respect to the top spin direction of the lepton, as measured in the top rest frame, and q is the lepton+neutrino 4-momentum. Predictions from the standard non-correlated PYTHIA matrix elements (NC) would correspond in this approach to the choice $(h_t, h_{\bar{t}}) = (0, 0)$. The SM prediction would correspond to $(h_t, h_{\bar{t}}) = (+1, -1)$. CP violation in top production and decay could give rise to different values for $(h_t, h_{\bar{t}})$. To investigate the effects of CP violation, the sets of values $(h_t, h_{\bar{t}}) = (0.2, -0.8)$ (referred to hereafter as 'CP28') and $(h_t, h_{\bar{t}}) = (0.9, -0.6)$ (dubbed 'CP96') were considered.

Physical observables, such as the opening angle between the two isolated leptons ($\cos\theta_{ll}$) and the azimuthal angle difference (ϕ_{ll}), are sensitive to h_t and were therefore chosen as good experimental probes of the $t\bar{t}$ spin correlations. As mentioned previously, the predicted spin correlations are a function of $m_{t\bar{t}}$. For dilepton events, $m_{t\bar{t}}$ cannot be directly measured due to the

missing neutrinos. However, a variety of possible kinematic variables, such as the dilepton invariant mass, are loosely correlated with $m_{t\bar{t}}$, and can be used as a crude estimator of $m_{t\bar{t}}$ to enhance the expected spin correlations.

Dilepton events were selected with the criteria described in Section 18.1.3.6. Two high p_T (larger than 35 and 25 GeV respectively) isolated, opposite-sign leptons with $|\eta| < 2.5$ and with $|m_{ll} - m_Z| > 10$ GeV were required, together with $E_T^{miss} > 40$ GeV and two jets with $p_T > 15$ GeV. In order to preserve statistics, *b*-tagging was not required. For each model, these criteria selected about one million dilepton events for an integrated luminosity of 100 fb^{-1}, with $S/B = 7.8$.

Figure 18-25(a) shows the measured $cos\ \theta_{ll}$ distribution in the case of the various parameter sets. The bin-by-bin fractional differences between the measured distributions for the SM and those for the other models considered are shown in Figure 18-25(b) for the case of no correlations (NC), in Figure 18-25(c) for CP28, and in Figure 18-25(d) for CP96. The same distributions for the azimuthal angle difference ϕ_{ll} are shown in Figure 18-26. The solid line shows the case where all events are considered, while the dashed (dotted) lines shows the result for those events with $m_{ll} < m_Z$ ($m_{ll} > m_Z$) .

For both angles, differences at the level of a few percent are observable between the distributions measured for the different models. The differences for the CP96 model are somewhat less pronounced than for CP28, as expected given the smaller deviation of the spin parameters from the SM values. Further study is required to more fully explore the sensitivity to CP violation.

18.1.5 Top quark decays and couplings

Within the context of the Standard Model, the top quark decays as a 'bare quark' via a pure V-A interaction. The decay $t \to W^+b$ is dominant according to the SM, with a branching ratio of approximately 99.9%. Expectations for the CKM-suppressed decays are approximately 0.1% and 0.01% for $t \to W^+s$ and $t \to W^+d$, respectively. However, the large top mass implies that the top quark would tend to couple strongly to other massive particles. Therefore, determining whether the top quark has the couplings and decays predicted by the SM provides a sensitive probe of physics beyond the SM.

18.1.5.1 BR($t \to bX$) and measurement of V_{tb}

The SM prediction that BR($t \to W^+b$) ≈ 1 can be checked by comparing the number of $t\bar{t}$ events with a double *b*-tag to those with a single *b*-tag. In this manner, the first *b*-tag is used to identify the event as a $t\bar{t}$ event, and the presence of a second *b*-tag is then used to determine the fraction of top quark decays involving a *b*-quark, and hence a measurement of BR($t \to bX$). Within the three-generation SM,

$$R_{2b/1b} = BR(t \to Wb) / BR(t \to Wq) = |V_{tb}|^2 / (|V_{tb}|^2 + |V_{ts}|^2 + |V_{td}|^2) = |V_{tb}|^2.$$

Therefore, within the context of the SM, with unitarity of the three-generation CKM matrix, $R_{2b/1b}$ provides a measure of $|V_{tb}|$. Applying the unitarity constraint, the value of $|V_{tb}|$ is already very precisely known; the Particle Data Group [18-29] lists the allowed range of values from 0.9991 to 0.9994. However, new physics, such as the existence of a fourth generation of quarks, would imply the three-generation CKM matrix is not unitary, and could increase the relative branching ratios of $t \to W^+s(d)$ compared to $t \to W^+b$.

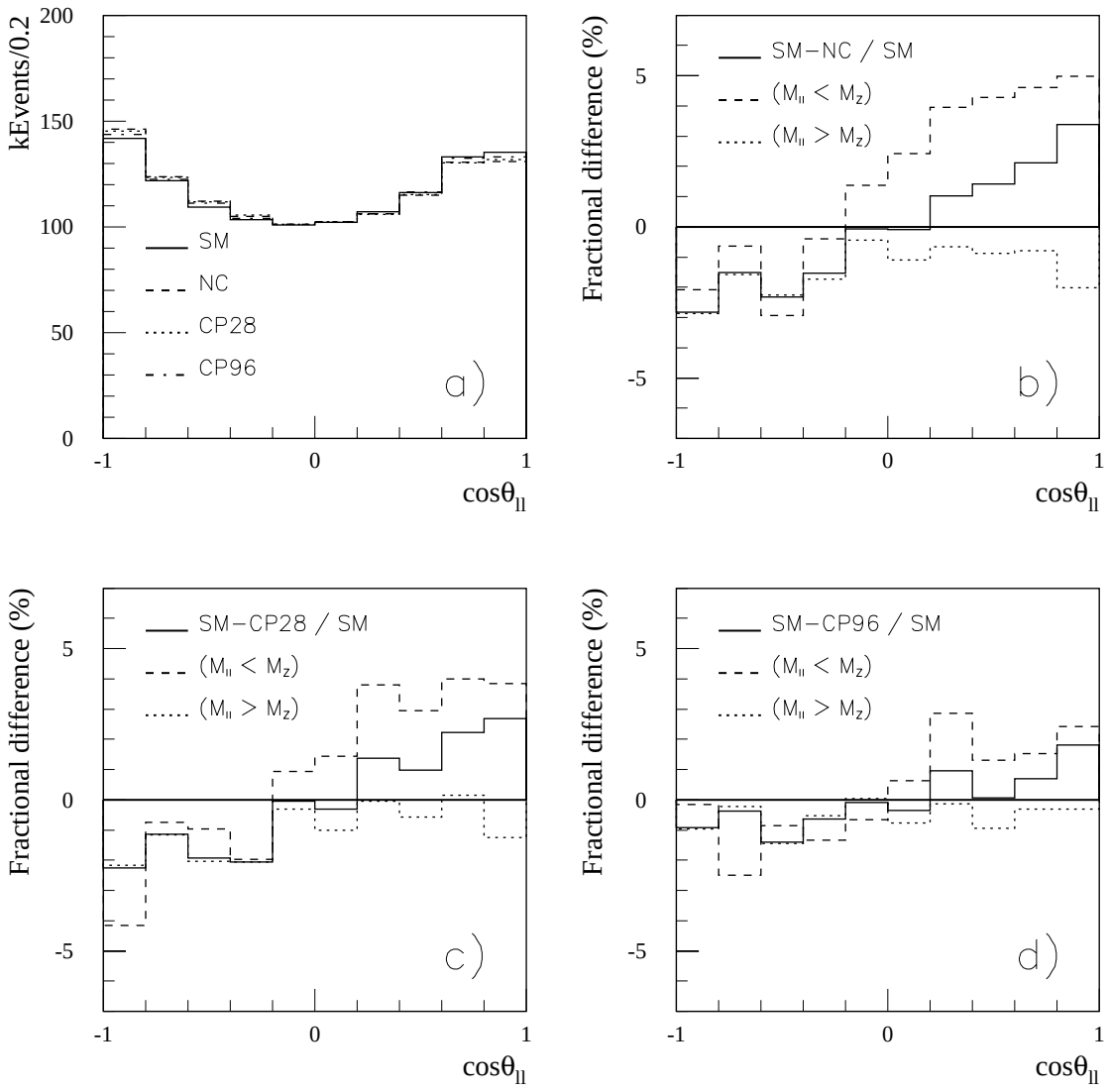

Figure 18-25 (a) Distribution of $cos\,\theta_{ll}$ as measured for the various parameter sets, normalised to 100 fb^{-1}. Also, fractional differences between the SM distribution and that measured with (b) no spin correlations (NC), (c) the CP28 parameter set, and (d) the CP96 parameter set. In each plot, the solid line shows the distribution for all events, and the dashed (dotted) line shows the results for events with $m_{ll} < m_Z$ ($m_{ll} > m_Z$). For more details, see the text.

CDF has measured the ratio of double *b*-tags to single *b*-tag in leptonic $t\bar{t}$ events, and determined a value of $R_{2b/1b} = 0.99 \pm 0.29$ [18-30], consistent with the SM expectation within the large (predominantly statistical) error. Within the SM, this measurement implies $|V_{tb}| > 0.76$ (95% C.L.). Without the SM three-generation unitarity constraint, the measurement implies only that $|V_{tb}|$ is much larger than either $|V_{ts}|$ or $|V_{td}|$.

The very large samples of $t\bar{t}$ events which will be accumulated at the LHC will allow a statistically sensitive measurement of $R_{2b/1b}$. For example, as discussed earlier, $t\bar{t}$ events in the single lepton plus jets mode can be selected by requiring an isolated electron or muon with $p_T > 20$ GeV, $E_T^{miss} > 20$ GeV, and at least four jets with $p_T > 20$ GeV. Requiring that at least one of the jets be tagged as a *b*-jet produces a clean sample of $t\bar{t}$ events, with $S/B = 18.6$, with the re-

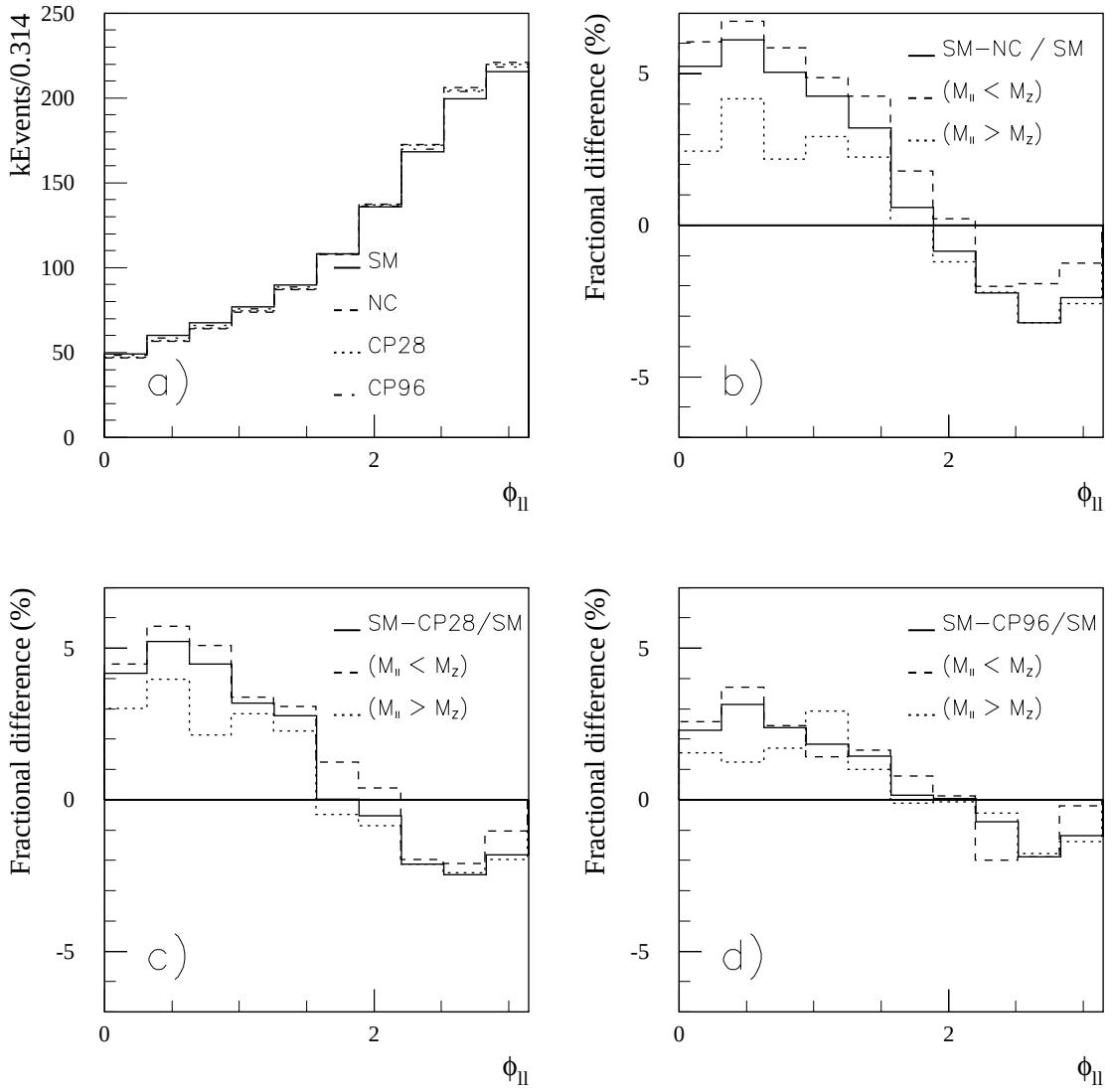

Figure 18-26 (a) Distribution of ϕ_{ll} as measured for the various parameter sets, normalised to 100 fb^{-1}. Also, fractional differences between the SM distribution and that measured with (b) no spin correlations (NC), (c) the CP28 parameter set, and (d) the CP96 parameter set. In each plot, the solid line shows the distribution for all events, and the dashed (dotted) line shows the results for events with $m_{ll} < m_Z$ ($m_{ll} > m_Z$). For more details, see the text.

maining background coming mostly from W+jet events. Assuming a b-tagging efficiency of 60%, a sample of 820 000 single b-tagged events would be selected for an integrated luminosity of 10 fb^{-1}. Of these, 276 000 would be expected to have a second b-tag, assuming the SM top quark branching ratios. Given these numbers, the statistical precision achievable would correspond to a relative error of $\delta R_{2b/1b} / R_{2b/1b}(\text{stat.}) \approx 0.2\%$ for an integrated luminosity of 10 fb^{-1}. The final uncertainty will be dominated by systematics errors due to the uncertainty in the b-tagging efficiency and fake b-tag rates, as well as correlations affecting the efficiency for b-tagging two different jets in the same event. Further study is needed to estimate the size of these systematic uncertainties.

18.1.5.2 BR($t \to WX$)

The measurement of the ratio ($R_{ll/l}$) of dilepton to single lepton $t\bar{t}$ events can be used to determine BR$(t \to WX)$. In this case, the first lepton tags the $t\bar{t}$ event, and the presence of a second lepton is used to determine the fraction of top quark decays producing an isolated lepton, which can be then be related to the presence of a W (or other leptonically decaying state) in the decay. The SM, for which BR($t \to WX$) = 100%, predicts $R_{ll/l}$ = BR($W \to l\nu$) ≈ 2/9. Deviations from this prediction could be caused by new physics. For example, the existence of a charged Higgs boson could lead to a large branching ratio for the decay $t \to H^+b$ if kinematically permitted. The dominant H^+ decays, in such instances, are usually considered to be $H^+ \to \tau\nu$ or $H^+ \to c\bar{s}$. In either of these cases, the number of isolated electrons and muons produced in top decay would be reduced, and so $R_{ll/l}$ would be less than the SM prediction. The existence of such a charged Higgs boson could also be probed by explicitly searching for an excess of τ production (see Section 18.1.5.4). However, it is possible the first sign of new physics could come from the more 'inclusive' measurement of $R_{ll/l}$.

As discussed above, with an integrated luminosity of 10 fb^{-1}, a clean sample of about 443 000 $t\bar{t}$ events in the single lepton plus jets mode could be selected by requiring an isolated electron or muon with p_T > 20 GeV, E_T^{miss} > 20 GeV, and at least two b-tagged jets with p_T > 20 GeV. To determine $R_{ll/l}$, one then measures how many of these events have a second isolated electron or muon, again with p_T > 20 GeV, and of the opposite sign of the first lepton. For an integrated luminosity of 10 fb^{-1}, and assuming the SM, one would expect a selected sample of about 46 000 dilepton events with these cuts. Given these numbers, the statistical precision achievable would correspond to a relative error of $\delta R_{ll/l} / R_{ll/l}$(stat.) ≈ 0.5% for an integrated luminosity of 10 fb^{-1}. Further study is required to estimate the systematic uncertainties in $R_{ll/l}$ due to the lepton identification and fake rates.

18.1.5.3 Top quark Yukawa coupling

In the SM, the mass of the top quark is due to its Yukawa coupling (y_t) to the Higgs boson. The values of the Yukawa couplings of the fundamental fermions are free parameters of the Standard Model. The measured value of m_t implies a value of the top quark Yukawa coupling of approximately unity. Alternative theories, such as Topcolor [18-23], explain the large top mass as arising, at least in part, from some new strong dynamics. Clearly, measuring independently the value of the Yukawa coupling would provide important information on the mechanism of fermion mass generation.

The value of the top quark Yukawa coupling can be accessed experimentally by searching for $t\bar{t}H$ production. One of the lowest order Feynman diagrams for this process of Higgs production in association with $t\bar{t}$ is shown in Figure 18-27. The top Yukawa coupling appears at the top-Higgs vertex. The reconstruction of this process is discussed in detail in Section 19.2.4.3 as part of the search strategy for both SM and MSSM Higgs bosons. Here the final results of the analysis are used to determine the precision implied for the determination of the top quark Yukawa coupling.

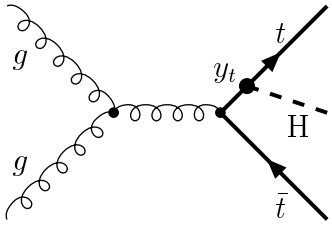

Figure 18-27 A lowest order Feynman diagram for $t\bar{t}H$ production.

The $t\bar{t}H$ analysis required one of the top quarks to decay via $t \to lvb$ and the other via $t \to jjb$. Since $t\bar{t}H$ production has a significant cross-section only for relatively light Higgs masses, the Higgs boson is detected through its decay $H \to b\bar{b}$, the dominant decay channel for the m_H range of interest. Thus, the final state contains an isolated lepton, missing p_T, two light quark jets, and a total of four b-jets. The resulting large combinatorial background was dealt with by first reconstructing both top quark decays. The combination which simultaneously best satisfied both the t and $\bar{t}$ mass constraints was used to assign jets to the top decays. A search was then made for a $H \to b\bar{b}$ signal using only the remaining unassigned b-jets.

Table 18-5 For an integrated luminosity of 30 fb^{-1}, and for three different values of m_H, the expected number of events for the signal from SM $t\bar{t}H$ production followed by the $H \to b\bar{b}$ decay. The final row provides the relative statistical uncertainty on the top quark Yukawa coupling.

	SM Higgs mass		
Process	**80 GeV**	**100 GeV**	**120 GeV**
$t\bar{t}H$ Signal	81	61	40
Total Backgnd	145	150	127
$\delta y_t/y_t$ (stat.)	9.3%	11.9%	16.2%

The expected numbers of signal and background events are summarised in Table 18-5 for SM Higgs masses of 80, 100, and 120 GeV, and for integrated luminosity of 30 fb^{-1}. The background events are mostly from $t\bar{t}$ production with additional jets. Results are given in Table 18-6 for 100 fb^{-1}.

Table 18-6 The same as Table 18-5, but for an integrated luminosity of 100 fb^{-1}.

	SM Higgs mass		
Process	**80 GeV**	**100 GeV**	**120 GeV**
$t\bar{t}H$ Signal	140	107	62
Total Backgnd	295	278	257
$\delta y_t/y_t$ (stat.)	7.4%	9.2%	14.4%

The implied statistical uncertainty in the determination of y_t is given in the last row in each table. For example, for m_H = 100 GeV, y_t could be measured with a relative statistical error of 11.9% for 30 fb^{-1}, improving to 9.2% for an integrated luminosity of 100 fb^{-1}. Many of the systematic errors, such as those associated with uncertainties in the integrated luminosity and in the $t\bar{t}$ reconstruction efficiency, could be controlled by comparing the $t\bar{t}H$ rate with the $t\bar{t}$ rate.

18.1.5.4 Top quark rare decays

With its large mass, the top quark will couple strongly to the sector of EWSB. Many models of physics beyond the SM include a more complicated EWSB sector, with implications for top quark decays. Examples include the possible existence of charged Higgs bosons, or possibly large flavor changing neutral currents (FCNC) in top decays. The sensitivity to some of these scenarios is discussed below.

$t \to H^+b$

If a sufficiently light charged Higgs boson exists, the decay $t \to H^+b$ could compete with the SM decay mode $t \to W^+b$. As discussed in Section 18.1.5.2, such a possibility could be seen by looking 'inclusively' at the ratio of dilepton to single lepton $t\bar{t}$ events. However, one could also look directly for evidence of this decay, for example by searching for a violation of lepton universality, whereby one finds an excess of τ production in $t\bar{t}$ events due to the decay $t \to H^+b$, followed by $H^+ \to \tau\nu$. The details of such an analysis for $t \to H^+b$ are presented in Section 19.3.2.11 in the context of exploring the Higgs sector of MSSM. As discussed in detail there, the limit on the sensitivity

to BR($t \to H^+b$) is dominated by systematic uncertainties, arising mainly from imperfect knowledge of the τ-lepton efficiency and of the number of fake τ-leptons present in the final sample. These uncertainties are estimated to limit the achievable sensitivity to BR($t \to H^+b$) = 3%.

Flavor Changing Neutral Currents (FCNC)

Within the SM, FCNC decays of the top quark are highly suppressed, and so any observation of FCNC top decays at the LHC would be an indication of new physics. For example, Table 18-7 summarizes branching ratios for FCNC top quark decays as predicted in the SM [18-31] and in the MSSM [18-32].

Table 18-7 Approximate branching ratios predicted for FCNC top quark decays in the SM and in MSSM. In each case, *q* is used to denote *u* or *c* quarks.

FCNC Decay	**BR** in SM	**BR** in MSSM
$t \to Zq$	$\approx 10^{-12}$	$\approx 10^{-8}$
$t \to \gamma q$	$\approx 10^{-12}$	$\approx 10^{-8}$
$t \to gq$	$\approx 10^{-10}$	$\approx 10^{-6}$

While the MSSM does enhance the branching ratios, they would still be too small to be observable. However, other extensions of the SM, including models with new dynamical interactions of the top quark, with multiple Higgs doublets, and with new exotic fermions, can lead to very significant enhancements of FCNC top decays [18-33]. Typically, the models include anomalous couplings with a coupling strength to quarks proportional to $\sqrt{m_q}$. These models can then accommodate large effects in top quark decays, while still satisfying the existing stringent limits on FCNC decays of the light quarks. Some of these models allow branching ratios for FCNC top decays of 10^{-3} - 10^{-2}, or even higher. The existing limits from CDF [18-34] are BR($t \to Zq$) < 33% and BR($t \to \gamma q$) < 3.3%, each at 95% CL, limited by the statistics of Run I at the Tevatron. The FCNC couplings can be parametrised in terms of the strength of the anomalous coupling κ and a scale Λ which characterizes the cut-off scale of new physics. For example, with this formulation, the partial width for the FCNC decay $t \to gq$ can be written as $\Gamma(t \to gq) = 4/3\ \alpha_s\ m_t^3\ (\kappa_g^2 / \Lambda^2)$, and similar expressions can be written for $\Gamma(t \to \gamma q)$ and $\Gamma(t \to Zq)$ (see [18-33] for more details).

$t \to Zq$ decay

The sensitivity to the FCNC decay $t \to Zq$ (with $q = u, c$) has been analysed [18-35] by searching for a signal in the channel $t\bar{t} \to (Wb)(Zq)$, with the boson being reconstructed via the leptonic decay $Z \to ll$. The selection cuts required a pair of isolated, opposite sign, same flavor leptons (electrons or muons), each with $p_T > 20$ GeV and $|\eta| < 2.5$ and with $|m_{ll} - m_Z| < 6$ GeV.

Due to the clean $Z \to ll$ signature, the dominant backgrounds are due to large cross-section processes with Z bosons in the final state, namely Z+jet and WZ production. These backgrounds, along with the signal process, were generated via PYTHIA 5.7 and simulated using ATLFAST. Cuts on the Zq final state are not sufficient to effectively reduce the large Z+jet background. Therefore, the analysis relied also on cuts based on the Wb decay of the other top quark in the event. Two different possible decay chains have been considered: the first ('leptonic mode') where the W decays leptonically $W \to l\nu$, and the second ('hadronic mode') with $W \to$ jj. The hadronic W decay signature has a much larger branching fraction, but suffers from larger backgrounds.

The search in the leptonic mode required, in addition to the leptons from the Z boson decay, an additional lepton with $p_T > 20$ GeV and $|\eta| < 2.5$, $E_T^{miss} > 30$ GeV, and at least two jets with $p_T > 50$ GeV and $|\eta| < 2.5$. In addition, exactly one of the high p_T jets was required to be tagged as a b-jet.

After these cuts, the invariant mass spectrum of each Zq combination was formed from the $Z \to ll$ candidates taken with each of the non b-tagged jets. The Zq invariant mass resolution was 10.1 GeV. Combinations were accepted if m_{Zq} agreed with the known top mass within ± 24 GeV. The signal efficiency, not including the branching ratios for $Z \to ll$ and $W \to l\nu$, is summarised in Table 18-9 as a function of the various cuts. Also shown are the number of accepted background events, assuming an integrated luminosity of 100 fb^{-1}. In this channel, a value of BR($t \to Zq$) as low as 1.1x10^{-4} could be discovered at the 5σ level with an integrated luminosity of 100 fb^{-1}.

Table 18-8 Signal efficiency for the analysis of $t\bar{t} \to (Wb)(Zq)$ with $W \to jj$ and $Z \to ll$. Also listed are the numbers of accepted background events, assuming an integrated luminosity of 100 fb^{-1}.

Description of Cut	$t \to Zq$ Effic.(%)	Bkgnd Events
2l, 4 jets	14.9	60394
m_Z cut	12.8	50973
m_W cut	5.4	14170
b-tag	2.5	1379
$t \to W^+b$ mass cut	0.6	90
m_{Zq} cut	0.4	2

The search in the hadronic mode required, in addition to the $Z \to ll$ candidate, at least four jets with $p_T > 50$ GeV and $|\eta| < 2.5$. One of the jets was required to be tagged as a b-jet. To further reduce the background, the decay $t \to jjb$ was first reconstructed. A pair of jets, from among those not tagged as a b-jet, was considered a W candidate if $|m_{jj} - m_W| < 16$ GeV. W candidates were then combined with the b-jet, and considered as a top candidate if $|m_{jjb} - m_t| < 8$ GeV. For those events with an accepted $t \to jjb$ candidate, the invariant mass of the Z candidate with the remaining unassigned high p_T jets was calculated to look for a signal from $t \to Zq$ decays. Combinations were accepted if m_{Zq} agreed with the known top mass within ±24 GeV.

The signal efficiency, not including the branching ratios for $Z \to ll$ and $W \to jj$, is summarised in Table 18-8 as a function of the various cuts. Also shown are the number of accepted background events, assuming an integrated luminosity of 100 fb^{-1}. The results in Table 18-8 demonstrate that, in this channel a BR as low as 2.3x10^{-4} could be discovered at the 5σ level.

Combining the results from the leptonic and hadronic modes, a branching ratio for $t \to Zq$ as low as 10^{-4} could be discovered at the 5σ level with an integrated luminosity of 100 fb^{-1}.

Table 18-9 Signal efficiency for the analysis of $t\bar{t} \to (Wb)(Zq)$ with $W \to l\nu$ and $Z \to ll$. Also listed are the numbers of accepted background events, assuming an integrated luminosity of 100 fb^{-1}.

Description of Cut	$t \to Zq$ Effic.(%)	Bkgnd Events		
		Z+j	*W+Z*	$t\bar{t}$
3 lep; p_T>20GeV	43.2	945	1778	1858
E_T^{miss} > 30GeV	32.7	80	1252	1600
2 j; p_T>50 GeV	19.7	31	225	596
m_Z cut	16.8	24	180	29
b-tag	8.2	10	14	10
m_{Zq} cut	6.1	0	2	5

t → γq decay

The sensitivity to the FCNC decay $t \to \gamma q$ (with q = u, c) was analysed [18-36] by searching for a peak above background in the $m_{\gamma j}$ spectrum in the region of m_t. The requirement of a high p_T isolated photon candidate in $t\bar{t} \to (Wb)(\gamma q)$ events is not sufficient to reduce the QCD multi-jet background to a manageable level. Therefore,

the $t \to Wb$ decay of the other top (anti-) quark in the event was reconstructed using the leptonic $W \to l\nu$ decay mode of the W boson decay. The final state sought was therefore $t\bar{t} \to (Wb)(\gamma q) \to (l\nu b)(\gamma q)$.

The event selection criteria required the presence of an isolated photon with $p_T > 40$ GeV and $|\eta| < 2.5$, an isolated electron or muon with $p_T > 20$ GeV and $|\eta| < 2.5$, and $E_T^{miss} > 20$ GeV. Exactly 2 jets with $p_T > 20$ GeV were required, in order to reduce $t\bar{t}$ background. At least one of the jets was required to be tagged as a b-jet, and to satisfy $p_T > 30$ GeV and $|\eta| < 2.5$.

The $t \to l\nu b$ candidate was first reconstructed. For the two possible solutions of the neutrino momentum (determined as described previously), the resultant W boson was combined with the b-tagged jet, and the combination accepted as a top quark candidate if $m_{l\nu b}$ agreed with m_t within ±20 GeV. For events with an accepted $t \to l\nu b$ candidate, the $t \to \gamma q$ decay was sought by combining the isolated photon with an additional hard jet with $p_T > 40$ GeV and $|\eta| < 2.5$.

The invariant mass of the γj system was required to agree with the known value of m_t within ±20 GeV. The $m_{\gamma j}$ resolution with the cuts described above was 7.7 GeV (see Figure 18-28), and the signal efficiency (not counting branching ratios) was 3.3%, including a b-tagging efficiency of 60%.

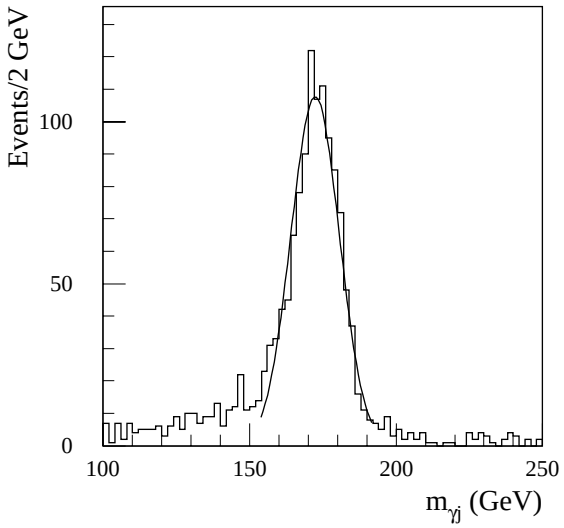

Figure 18-28 The $m_{\gamma j}$ invariant mass distribution resulting from the analysis of a sample of 10 000 signal events for the decay $t \to \gamma q$.

The background is dominated by events with a real $W \to l\nu$ decay and either a real or fake photon. These processes include $t\bar{t}$ and single top production as well as W+jets and $Wb\bar{b}$ production. The $t\bar{t}$ background was simulated with PYTHIA, while the other backgrounds were simulated as described in the discussion of the analysis of single top production presented in Section 18.1.6. After cuts, the background with real photons (normalised to an integrated luminosity of 100 fb^{-1}), consisted of 50 $t\bar{t}$ events, and negligible contributions from the other processes. Assuming a somewhat conservative jet rejection of about 2 900 for photons with $p_T > 40$ GeV (see Section 7.6), larger backgrounds resulted with fake photons, namely 90 $t\bar{t}$ events, 10 events from single top production, and about 5 events from W+jets including $Wb\bar{b}$. The total background was therefore 155 events, dominated by $t\bar{t}$ events. The corresponding 5σ discovery limit for an integrated luminosity of 100 fb^{-1} is BR($t \to \gamma q$) = 1.0×10^{-4}.

$t \to gq$ decay

A search for a FCNC t-gluon-q coupling (with $q = u,c$) through the decay $t \to gq$ would be overwhelmed by background from QCD multi-jet events. It has, however, been pointed out [18-37] that evidence for such a coupling can be sought through the production of like-sign top pairs, $pp \to ttX$ [$pp \to \bar{t}\bar{t}X$] (see Figure 18-29).

An experimentally clean signature of tt ($\bar{t}\bar{t}$) production would be the production of like-sign high p_T leptons, arising from events where the W bosons from both (anti-)top quarks decay leptonically. Such events would be expected to have, in addition to the like-sign lepton pair, two hard b-jets. The main sources of background are $qq \rightarrow Wq\mathrm{W}q$ and $qq' \rightarrow t\bar{t}\mathrm{W}$. The expected cross-section for each process producing W^+ pairs is about 0.5 pb, with that for W^- pairs about 0.25 pb.

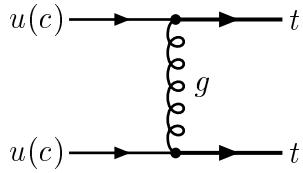

Figure 18-29 Feynman diagram depicting like-sign tt production via a FCNC t-gluon-q coupling (with $q = u, c$).

The initial selection required two like-sign isolated leptons with $p_T > 15$ GeV and $|\eta| < 2.5$. In addition, two jets with $p_T > 20$ GeV and $|\eta| < 2.5$ were required. Signal events should contain exactly two hard jets (due to the b-quarks), while the background events tend to contain additional jets. Thus, it was required that there exist no more than two jets with $p_T > 20$ GeV. These two leading jets were then required to have $p_T > 40$ GeV, and to have at least one tagged as a b-jet. In at least one of the two possible sets of lepton plus jet combinations, it was required that each of the lepton plus jet pairs have an invariant mass m_{lj} below 160 GeV, in order that they be kinematically consistent with originating from a top quark decay. Finally, it was required that the invariant mass of the $lljj$ system be greater than 500 GeV.

The effectiveness of the cuts in enhancing the signal relative to the background processes is summarised in Table 18-10. From initial samples of 10 000 events for each of the processes, 853 signal events survived all cuts, while only 15 $Wt\bar{t}$ and 12 $WqWq$ background events were retained. Scaling the backgrounds to their SM production cross-sections, a total of 10.8 $l^{\pm}l^{\pm}$ events (including all combinations of muons and electrons), would be expected for an integrated luminosity of 100 fb^{-1}. The results in Table 18-10 correspond to a 95% confidence level sensitivity to $|\kappa_g / \Lambda| = 0.091$ TeV^{-1}, corresponding to BR($t \rightarrow gq$) = 7.4 x 10^{-3}.

Table 18-10 Number of accepted same sign dilepton events for the same-sign top production signal and the $Wt\bar{t}$ and $WqWq$ backgrounds (out of an initial sample before cuts of 10 000 events in each case). The last line gives the equivalent number of accepted events assuming an integrated luminosity of 100 fb^{-1} and, in the case of the signal, for an anomalous coupling equal to unity.

Description of Cut	tt ($\bar{t}\bar{t}$) Signal	$Wt\bar{t}$ bkgnd	$WqWq$ bkgnd
Initial selection	3452	5354	5462
Exactly 2 jets	2095	712	3269
p_T(j) > 40 GeV	1221	316	118
$m_{lj} < 160$ GeV	1177	190	46
$m_{lljj} > 500$ GeV	853	15	12
Events / 100 fb^{-1}	22860	6.0	4.8

$t \rightarrow WbZ$ and $t \rightarrow WbH$

The 'radiative' top decay $t \rightarrow WbZ$ has been suggested [18-39] as a sensitive probe of the top quark mass, since the measured value of m_t is close to the threshold for this decay. For the top mass of (173 ± 5.2) GeV quoted by the 1998 Particle Data Group [18-29], the SM prediction is BR($t \rightarrow WbZ$) = (5.4$^{+4.7}_{-2.0}$) x 10^{-7} [18-39]. Thus, within the current uncertainty $\delta m_t \approx 5$ GeV, the predicted branching ratio varies by approximately a factor of three. A measurement of BR($t \rightarrow WbZ$) could, therefore, provide a strong constraint on the value of m_t. Similar arguments have been made for the decay $t \rightarrow WbH$, assuming a relatively light SM Higgs boson (*i.e.* for $m_H \approx m_Z$).

Sensitivity to the decay $t \to WbZ$ has been studied [18-36] using PYTHIA 6.1 and ATLFAST to simulate $t\bar{t} \to (WbZ)(Wb)$, with $Z \to ll$ and $W \to jj$. The efficiency for exclusively reconstructing $t \to WbZ$ is very low, due to the soft p_T spectrum of the b-jet in the $t \to WbZ$ decay. Instead, a 'semi-inclusive' technique was used, where a WZ pair close to threshold was searched for as evidence of the $t \to WbZ$ decay. Since the $t \to WbZ$ decay is so close to threshold, the resolution on m_{WZ} is not significantly degraded with respect to the exclusive measurement. The selection of $Z \to ll$ candidates required an opposite-sign, same-flavour lepton pair, each lepton having $p_T > 30$ GeV and $|\eta| < 2.5$. Since the $Z \to ll$ signal is so clean, a wide dilepton mass window was taken (60 GeV $< m_{ll} <$ 100 GeV) in order to have very high efficiency. Candidates for $W \to jj$ decay were formed by requiring at least two jets, each having $p_T > 30$ GeV and $|\eta| < 2.5$, and satisfying 70 GeV $< m_{jj} <$ 90 GeV. The $lljj$ invariant mass resolution was $\sigma[m_{WZ}] = 7.2 \pm 0.4$ GeV, and the signal efficiency was 4.3%.

The clean $Z \to ll$ signature means that the dominant backgrounds come from processes with a Z boson in the final state, primarily Z+jet production, and to a much lesser extent from WZ and $t\bar{t}$ production. In order to reduce the Z+jet background, an additional cut requiring a third lepton with $p_T > 30$ GeV was made. For the signal process $t\bar{t} \to (WbZ)(Wb)$, this cut selects events in which the W from the other top decays leptonically. The W leptonic branching ratio results in a corresponding drop in signal acceptance by a factor of about 2/9, but very effectively reduces the Z+jet background.

After the selection, and with a cut on m_{WZ} of ±10 GeV around the top mass, the total expected background was reduced to ≈1.5 events (mostly from WZ production) per 10 fb^{-1}. Requiring at least five events for signal observation leads to a branching ratio sensitivity of order 10^{-3}. Since the background has been reduced essentially to zero, the sensitivity should improve approximately linearly with integrated luminosity. However, even with a factor of ten improvement for an integrated luminosity of 100 fb^{-1}, the sensitivity would still lie far above the SM expectation of order 10^{-7}-10^{-6}.

Given this result, observation of the decay $t \to WbH$ does not look possible. The current LEP limit on m_H implies that the Higgs is sufficiently heavy that, in the most optimistic scenario that the Higgs mass is just above the current limit, BR(t $\to WbH$) ≈ BR(t $\to WbZ$). As m_H increases further, BR(t $\to WbH$) drops quickly. Assuming $m_H \approx m_Z$, one would have to search for $t \to WbH$ using the dominant decay $H \to b\bar{b}$. The final state suffers much more from background than in the case of $t \to WbZ$, where the clean $Z \to ll$ signature is a key element in suppressing background. Although BR($H \to b\bar{b}$) in this m_H range is much larger than BR($Z \to ll$), the large increase in background will more than compensate for the increased signal acceptance, and so one expects the sensitivity to BR($t \to WbH$) to be worse than for BR($t \to WbZ$). Therefore, the decay $t \to WbH$ has not been studied in further detail.

18.1.6 Electroweak single top quark production

As discussed above, the strong production of $t\bar{t}$ pairs yields large top quark samples, allowing detailed studies of many properties of top quark production and decay. However, the precise determination of the properties of the W-t-b vertex, and the associated coupling strengths, will more likely be obtained from measurements of the electroweak production of single top quarks. Single top quarks can be produced via three different reactions. These reactions are shown in Figure 18-30 from left to right in order of decreasing cross-sections.

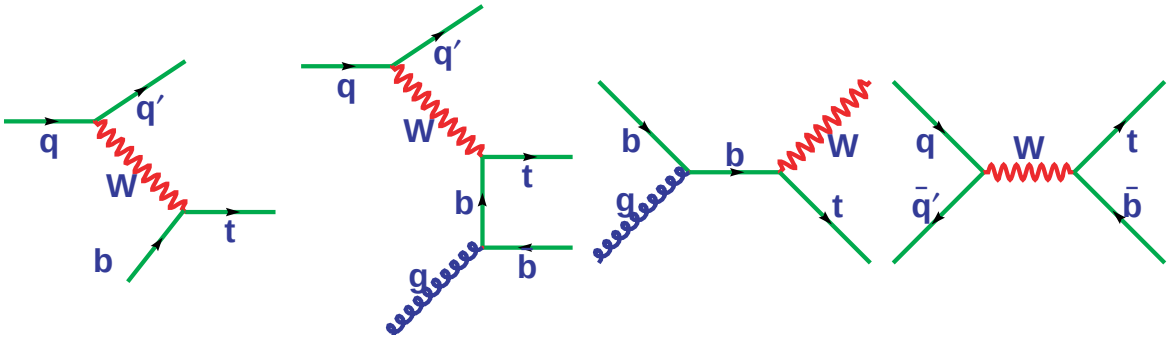

Figure 18-30 Feynman diagrams for the electroweak single top quark processes accessible at the LHC. The first two diagrams correspond to *W*-gluon fusion, the next to *Wt* production, and the final diagram to the *s*-channel or *W** process.

The first two graphs in Figure 18-30, usually referred to as the '2-2' and '2-3' processes, respectively, both refer to the same physical '*W*-gluon fusion' process. In this study the NLO correction as a separate process has been ignored. Rather, simulations based on the 2-2 process only have been used and normalised to the cross-section for a properly combined set of the two graphs. Since the *W*-gluon fusion process is the largest source of single top production at the LHC, with an expected cross-section of approximately 250 pb, it will be the source for much of the physics sensitivity, as well as a serious background for the other single top processes. The second production mechanism (the third graph from the left), referred to as the '*Wt*' process, is the direct production of a top quark and a *W* boson. This process is immeasurably small at the Tevatron, but is predicted to have a sizeable cross-section (≈60-110 pb) at the LHC. The third reaction proceeds via production of an off-shell *W* and will be called the '*W**' process. The cross-section for the *W** process is predicted to be only about 10 pb, since there are no valence anti-quarks in the initial state at the LHC.

Each process has a separate set of background sensitivities and experimental demands. Table 18-11 lists the cross-sections used in this study and the product of $\sigma \times BR$ for the case where one *W* decays leptonically via $W \to l\nu$, where the lepton is an electron or muon. This study is based upon an integrated luminosity of 30 fb^{-1}.

Table 18-11 Cross-sections used in the EW single top signal and background simulations.

Process	σ (pb)	$\sigma \times BR(W \to l\nu)$ (pb)
Wg (2-2 + 2-3)	244	54.2
Wt	60	17.8
W^*	10	2.2
$t\bar{t}$	833	246
$Wb\bar{b}$	300	66.7
Wjj	18000	4000

The primary physics interest in single top production is the ability to directly determine the coupling strength for the *t*-*W*-*b* vertex. The single top cross-section is unambiguously predicted by the SM (apart from the coupling), and it is important to cross check the *W*-gluon fusion, *Wt*, and *W** cross-sections separately. The various processes of single top production have different sensitivities to new physics. For example, the *W** channel is sensitive to an additional heavy *W'* boson, since new s-channel diagrams in which the W' is exchanged would occur. In contrast, additional contributions to the *W*-gluon fusion process from new t-channel diagrams with a *W'* would be suppressed by $1/m_{W'}{}^2$. Therefore, existence of a *W'* boson would be expected to produce an enhancement in both $\sigma(W^*)$ and $\sigma(W^*)/\sigma(Wg)$. On the other hand, the *W*-gluon fusion process channel is more sensitive to modifications of the top quark's couplings to the other SM particles. For example, an anomalous

chromo-magnetic moment in the top-gluon vertex [18-45], or a V+A contribution at the *t*-*W*-*b* vertex [18-46], could lead to both an increase in single top production and a modification of the decay angular distributions. Also, anomalous FCNC couplings could give rise to new contributions to single top production, such as $gu \rightarrow t$. These processes could modify the *W*-gluon process of single top production, while not affecting the rate of Wt and W^* channels. Therefore, in this case one would expect a decrease in the ratio of $\sigma(W^*)/\sigma(Wg)$.

Because it is an inherently weak production process, the *W* and top quark are produced in the appropriate mixture of helicities, as unambiguously predicted by the SM. A helicity analysis of top quark decay can check for new physics, such as right handed couplings, or an unexpected admixture of the left handed and longitudinal components for the *W*.

18.1.6.1 Monte Carlo generators

A variety of Monte Carlo generators have been employed to study electroweak single top production and the relevant backgrounds. The generators have been compared against one another for consistency and shown to be in reasonable agreement. All signal generators were interfaced to PYTHIA for showering and particle generation, with the PYTHIA output processed through ATLFAST for detector simulation. PYTHIA [18-5] includes the basic *W*-gluon fusion reaction according to SM assumptions. The SGPM package [18-47] is a parton-level generator for the Wt process, plus the $t\bar{t}$ and $Wb\bar{b}$ background processes. Also included are the FCNC processes, $gu \rightarrow t$ and $qq \rightarrow tt$. Decays are included and the reactions are implemented as external processes in PYTHIA. The ONETOP package [18-48] creates matrix elements at the parton level with the full density matrix for the 2-2, 2-3, W^* and Wt signal processes, as well as the $t\bar{t}$ and $Wb\bar{b}$ backgrounds. This is the only readily accessible generator which includes helicity information for all processes. Decays are included and all reactions are implemented as external processes in PYTHIA. HERWIG [18-6] has been used to produce *W*+jets background. *Wjj* events, involving the production of *W* in association with light quark jets, is a standard HERWIG process (iproc 2100). Background from $Wb\bar{b}$ is generated via a matrix element calculation interfaced to HERWIG.

Considerable effort was expended comparing the predictions of the various Monte Carlo generators. The results from PYTHIA, ONETOP, and SGPM for single top and $t\bar{t}$ production processes were very similar, agreeing typically within 10-15%. The predictions for the *Wjj* background were different by nearly 50%. The values from HERWIG are generally thought to be the most accurate, since HERWIG treats colour coherence more correctly, and were therefore used.

18.1.6.2 Signal and background separation strategies

In order to reduce the enormous QCD multi-jet backgrounds, as well as provide a high p_T lepton for trigger purposes, single top production with $t \rightarrow Wb$ followed by a leptonic decay $W \rightarrow l\nu$, where the charged lepton is a muon or an electron has been considered. The initial pre-selection cuts required the presence of at least one isolated lepton with $p_T > 20$ GeV, at least two jets with $p_T > 30$ GeV, and at least one *b*-tagged jet with $p_T > 50$ GeV. After these cuts, the dominant backgrounds are from processes with a real *W* in the final state, namely $t\bar{t}$ and *Wjj* (and in particular $Wb\bar{b}$) production. In the following, distributions are presented of variables which can be used to separate the various single top processes from these backgrounds and from each other.

Table 18-12 summarises the number of reconstructed jets per event, with $|\eta| < 5$ and $p_T > 15$ GeV, for the signal and background processes. It can be seen that the jet multiplicity would be a particularly useful variable for reducing the $t\bar{t}$ background, which has on average more jets than the single top processes.

Table 18-12 Fraction of events with different total reconstructed jet multiplicities for the various signal and background processes.

Process	njet = 2	njet = 3	njet > 3
W-g fusion	0.682	0.255	0.063
Wt	0.158	0.530	0.312
*W**	0.683	0.256	0.061
$t\bar{t}$	0.022	0.211	0.767
Wjj	0.446	0.323	0.231
W$b\bar{b}$	0.621	0.274	0.105

The number of jets per event tagged as *b*-jets, with $|\eta| < 2.5$, is presented in Table 18-13. It can be seen that requiring, for example, more than one *b*-tagged jet would enhance the *W** signal with respect to *Wjj* and *W*-gluon fusion. The reduction in the *W*-gluon fusion background is due to the fact that the second *b*-jet in *W*-gluon fusion events has low p_T and is often not tagged. In addition to the jet and *b*-jet multiplicities, the leading jet and *b*-jet p_T distributions are also useful discriminators. For example, the $Wb\bar{b}$ and *Wjj* events tend to have softer spectra than for single top and $t\bar{t}$ events.

Figure 18-31 shows the total event invariant mass, defined from the four vectors of all of the jets and leptons found in the event. A significant difference is observed between the invariant mass of events in the non-top backgrounds and in the signal processes.

This work focuses on single top signal events with a leptonic *W* decay. Therefore, apart from the *Wt* signal and the $t\bar{t}$ background, there should be no excess of di-jet combinations with m_{jj} near the value of m_W. Indeed, Figure 18-32 shows the distribution of di-jet masses obtained by choosing the di-jet with mass closest to m_W. It can be seen that *Wt* and $t\bar{t}$ have di-jet mass distributions which are significantly peaked near the *W* mass, while the other channels do not.

Table 18-13 Fraction of events with different total reconstructed *b*-jet multiplicities for the various signal and background processes.

Process	nb-jet = 1	nb-jet = 2	nb-jet > 2
W-g fusion	0.933	0.066	0.001
Wt	0.944	0.055	0.001
*W**	0.662	0.336	0.002
$t\bar{t}$	0.668	0.325	0.007
*W*jj	0.945	0.053	0.002
$Wb\bar{b}$	0.619	0.379	0.002

Another variable of interest is the reconstructed top mass (since there is no top quark in W*jj* and $Wb\bar{b}$ events). As described in previous sections, the top mass in the decay $t \to Wb$ followed by $W \to l\nu$ can be calculated by assigning $E_T(\nu) = E_T^{miss}$ and by calculating $p_z(\nu)$ (with a quadratic ambiguity) by applying the constraint that $m_{l\nu} = m_W$. Figure 18-33 shows the reconstructed $m_{l\nu b}$ distribution, where the $p_z(\nu)$ solution which gives $m_{l\nu b}$ closest to m_t has been chosen. In Figure 18-34, the scalar sum of the p_T of all of the jets in the event is plotted. Clearly the p_T in $t\bar{t}$ events is much higher on average than in the signal processes, while the *Wjj* events have lower average p_T .

Based on these kinematic distributions, cuts were optimised for each of the single top processes. In the case of *Wjj* production, the largest single top background, the cross-section at the LHC is currently not well known. Therefore, the usual procedure of minimising the relative error in the cross-section measurement by minimising $\sqrt{S+B}/S$ was not followed. Instead, the cuts were chosen to minimise the effect of the uncertainty on the W*jj* cross-section by optimising the *S/B*

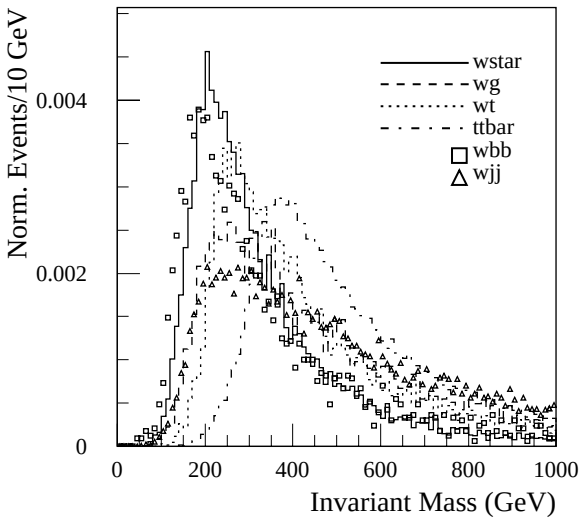

Figure 18-31 Total invariant mass of the event (see the text for more details), normalised to unity.

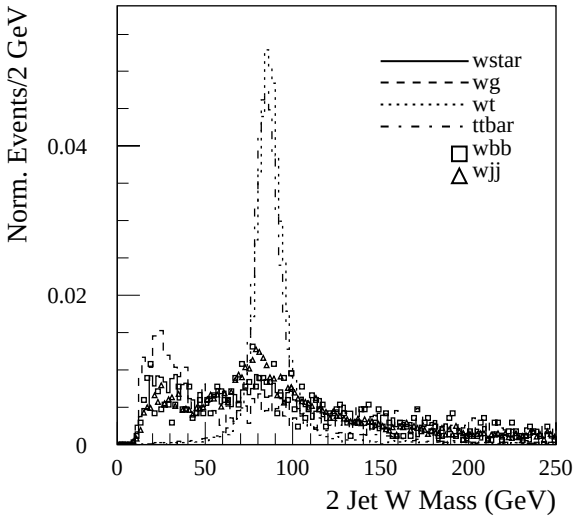

Figure 18-32 Invariant mass distribution of the di-jet with m_{jj} closest to m_W, normalised to unity.

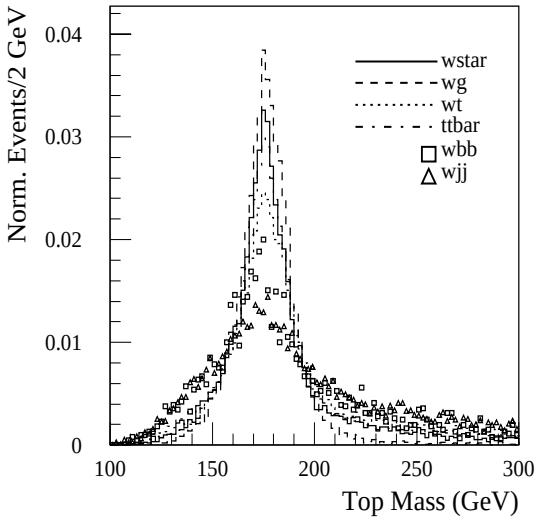

Figure 18-33 Invariant mass of the lνb combination with $m_{l\nu b}$ closest to m_t, normalised to unity.

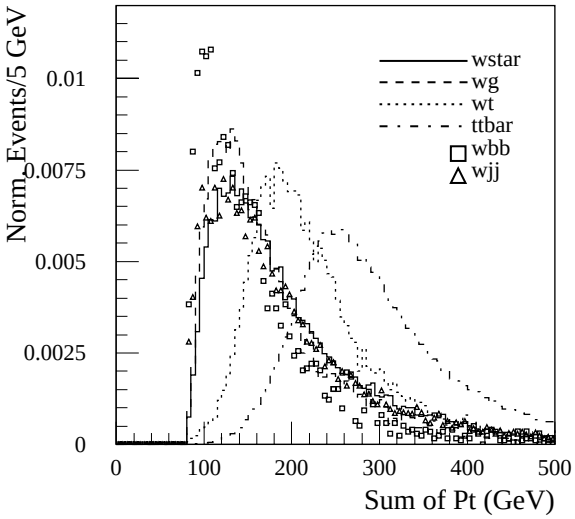

Figure 18-34 Scalar sum of p_T in each event, normalised to unity.

ratio. Analysis of each of the three single top production processes is presented in turn, followed in Section 18.1.6.6 by a discussion of the measurement of V_{tb}. The analysis of each process started with the pre-selection cuts presented earlier, namely the presence of at least one isolated lepton with $p_T > 20$ GeV, at least two jets with $p_T > 30$ GeV, and at least one *b*-tagged jet with $p_T > 50$ GeV.

18.1.6.3 Measurement of W-gluon fusion cross-section

The *W*-gluon signal is distinguished from backgrounds by the presence of a spectator quark jet which emerges in the forward direction. To isolate this signal, in addition to the pre-selection cuts, a forward jet with $|\eta| > 2.5$ and $p_T > 50$ GeV was therefore required. The total number of

jets was further required to be exactly two, to provide additional rejection of $t\bar{t}$ background, although it is recognised that comparison to a theoretical cross-section might be compromised by such a topological restriction. In addition, the central jet was required to be tagged as a *b*-jet, and to satisfy p_T > 50 GeV, in order to reduce *Wjj* background. Further rejection of the 'soft' *W*+jet backgrounds was accomplished by requiring the total invariant mass of the event be greater than 300 GeV and that H_T, the sum of the E_T values of all the jets and leptons in the event, satisfy H_T> 200 GeV. Finally, a top mass window was employed to reduce non-top backgrounds. These particular choices are not unique and a significant effort is still required to fully optimise these cuts. In particular, this will likely require a better understanding of the *Wjj* background.

Details of each cut are presented in Table 18-14 which shows the selection efficiency for the signal and background processes after each cut is applied, as well as the final number of events normalised to an integrated luminosity of 30 fb^{-1}. The number of events for the signal and $t\bar{t}$ background are taken as the average of results from ONETOP and PYTHIA. The number of events for the $Wb\bar{b}$ background are taken as the average of results from the HERWIG and ONETOP calculations. The result of 26 800 signal events and a total background of about 8 650 events, corresponds to a *S/B* = 3.1 and $S/\sqrt{B}$ = 286. The relative statistical uncertainty in the cross-section is 0.71%. If the high and low results of the *Wjj* calculation are used, the resulting values of S/B range from 4.3 down to 2.4.

Table 18-14 Cumulative efficiencies for the signal and background processes after each successive cut of the analysis to isolate the *W*-gluon fusion process. Also shown are the numbers of selected events after all cuts, normalised to an integrated luminosity of 30 fb^{-1}. The uncertainties are due to the Monte Carlo statistics. Note that the number of jets (Njets) includes any *b*-jets.

Description of cuts	Cumulative Selection Efficiency (%)			
	***W-g* fusion**	$t\bar{t}$	$Wb\bar{b}$	***Wjj***
Pre-selection cuts	20.0	44.4	2.49	0.667
Njets = 2; p_T>30GeV	13.2	0.95	0.99	0.37
Forward jet; p_T>50, $\|\eta\|$ >2.5	4.3	0.046	0.072	0.06
m_{tot}>300 GeV	3.58	0.025	0.043	0.048
H_T > 200 GeV	2.08	0.019	0.036	0.027
150 < m_t < 200 veto	1.64	0.01	0.0052	0.0066
Events / 30 fb^{-1}	26 800 ± 1000	720 ± 160	104 ± 60	7900 ± 1600

18.1.6.4 Measurement of *Wt* cross-section

The strategy for measuring the *Wt* cross-section is similar to that for *W*-gluon fusion, since they share the same backgrounds. However, the nature of *Wt* events makes them relatively easy to separate from *Wjj* and difficult to separate from $t\bar{t}$ events. Assuming the $t\bar{t}$ cross-section will be well measured at the LHC, this does not preclude performing a precise measurement of the *Wt* cross-section.

In addition to the pre-selection cuts, the number of jets in the central region was required to be exactly three, each with p_T > 50 GeV. Requiring at least three jets significantly reduces non-top backgrounds, while not allowing four or more jets reduces $t\bar{t}$ background. Exactly one of these jets was required to be tagged as a *b*-jet. By not allowing more than one *b*-tag the $t\bar{t}$ background

was reduced, while at least one *b*-tag was necessary to suppress *Wjj*. The total invariant mass of all reconstructed leptons and jets was required to be less than 300 GeV in a further attempt to reduce the $t\bar{t}$ background. Finally, the presence of a second *W* in *Wt* and $t\bar{t}$ events was exploited by requiring the reconstructed mass of the two untagged jets to be consistent with m_W by satisfying 65 GeV < m_{jj} < 95 GeV.

The samples of signal and background events surviving these cuts are summarised in Table 18-15. The only significant background remaining is from $t\bar{t}$ production, which is still more than a factor of four larger than the signal. Backgrounds from *Wjj* and from other single top processes are reduced to a negligible level. From Table 18-15, *S/B* = 0.22 and $S/\sqrt{B}$ = 39. The relative statistical error on the *Wt* cross-section is 2.8%.

Table 18-15 Cumulative efficiencies for the signal and background processes after each successive cut of the analysis to isolate the *Wt* process. Also shown are the numbers of selected events after all cuts, for an integrated luminosity of 30 fb^{-1}. The uncertainties listed are due to the Monte Carlo statistics. Note that the number of jets (Njets) includes any *b*-jets.

Description of cuts	Cumulative Selection Efficiency (%)		
	Wt	***tt̄***	***Wbb̄***
Pre-selection cuts	25.5	44.4	2.49
njets = 3; p_T > 50 GeV	3.41	4.40	0.05
n*b*-jet = 1	3.32	3.24	0.037
m_{tot} < 300 GeV	1.43	0.71	0.008
65 < m_{jj} < 95 GeV	1.27	0.41	0.003
Events / 30 fb^{-1}	6828 ± 269	30408 ± 742	58 ± 19

18.1.6.5 Measurement of *W** cross-section

Since the *W** signal has such a small cross-section relative to background, stringent cuts must be made to obtain a reasonable signal-to-background ratio (for details of this analysis see reference [18-49]). In addition to the pre-selection cuts, exactly two jets with $|\eta| < 2.5$ were required, in order to reduce the $t\bar{t}$ background, which tends to have more than two jets. Furthermore, both jets were required to have p_T > 75 GeV, and to be tagged as *b*-jets. This cut significantly reduces the *W*+jets background. This cut also reduces background from *W*-gluon fusion events since the second, lower p_T, *b*-jet from these events tends to be very soft and is often outside the *b*-tagging region ($|\eta|$<2.5). Those *W*-gluon fusion events for which both *b*-jets are tagged, are suppressed by the p_T cut. Further rejection of *Wjj* background is achieved by requiring the scalar sum of the jet p_T to be greater than 175 GeV, since the total jet p_T in *Wjj* events is generally lower than for events containing top quarks. The invariant mass of the event was required to exceed 200 GeV, again a cut predominantly against *Wjj* background events, which do not contain top quarks and so tend to have smaller invariant mass. Finally, a cut was placed on $m_{l\nu b}$, requiring it to lie within the range from 150-200 GeV.

The signal and background samples passing the successive cuts are summarised in Table 18-16. After all cuts, a value of S/B = 0.46 is achieved, with a significance of $S/\sqrt{B}$ = 23. The relative statistical error on the *W** cross-section is 5.4%.

Table 18-16 Cumulative efficiencies for the signal and background processes after each successive cut of the analysis to isolate the W^* process. Also shown are the numbers of selected events after all cuts, for an integrated luminosity of 30 fb^{-1}. The uncertainties listed are due to the Monte Carlo statistics. Note that the number of jets (Njets) includes any *b*-jets.

Description of cuts	Cumulative Selection Efficiency (%)					
	W*	***W-g* fusion**	***Wt***	$t\bar{t}$	$Wb\bar{b}$	***Wjj***
Pre-selection cuts	27.0	20.0	25.5	44.4	2.49	0.667
njets = 2; p_T > 30 GeV	15.7	6.8	3.79	0.93	1.35	0.201
n*b*-jet = 2; p_T > 75 GeV	2.10	0.05	0.018	0.023	0.038	0.0005
scalar sum of p_T >175 GeV	1.92	0.036	0.016	0.021	0.030	0.0004
m_{tot}>200GeV	1.92	0.036	0.014	0.021	0.025	0.0003
150<m_{lvb}<200 GeV	1.67	0.031	0.008	0.017	0.016	0.0002
Events / 30 fb^{-1}	1106 ± 40	510 ± 148	42 ± 21	1290 ± 228	328 ± 61	226 ± 113

18.1.6.6 Determination of V_{tb}

Given the results summarised above, the relative experimental statistical errors on the production cross-sections of the single top processes would be 0.71% for the *W*-gluon process, 2.8% for *Wt* production, and 5.4% for the *W** process. These results imply statistical uncertainties on the extraction of V_{tb} of 0.36% for *W*-gluon fusion, 1.4% for *Wt*, and 2.7% for *W**.

The errors in the extraction of V_{tb} would be dominated by uncertainties in the theoretical predictions of the cross-sections. These arise from uncertainties in the parton distribution functions (PDF), uncertainty in the scale (μ) used in the calculation, and the experimental error on the mass of the top quark. As summarised in Table 18-17, the reliance of the *W*-gluon fusion process on gluon PDFs leads to a higher error than in the *W** channel. However, the *W** cross-section has a greater relative dependence on the top mass. Despite this heightened dependence on the top mass, the overall theoretical error on the cross-section is lowest for *W** (assuming the top mass will be measured to ±2 GeV). For detailed discussions of the theoretical errors, see references [18-50], [18-51], [18-52] and [18-53]. The *Wt* cross-section at the LHC is not currently well known theoretically; the value of 50% quoted in the table reflects the range of values appearing in the literature. The measurement of V_{tb} is also sensitive to errors in the cross-sections of the backgrounds. In particular, the cross-section for the *Wjj* process at the LHC is not well known.

Table 18-17 Relative errors, and their sources, in the cross-sections for single top production. The error due to imprecision in the top mass is quoted assuming δm_t = 2 GeV. For more details, see the text.

Source	δσ/σ (%)		
of Error	***W****	***W-g* fusion**	***Wt***
Statistical	5.4	0.71	2.8
PDF	4	10	-
μ (scale)	4	5	-
δm_t	5	2	-
Total theory error	7.5	11	≈50

Another source of error is due to the kinematic modelling of the signal and backgrounds by the Monte Carlo generators. Rather harsh cuts are required to extract the signals from background, leading to signal efficiencies of typically of 1 - 3%. Extrapolating from the experimentally measured cross-section to the theoretical prediction will introduce additional uncertainty into the extraction of V_{tb}. Also, the only *Wjj* events which contribute to the background are in the far reaches of the tails of the invariant mass and transverse momentum distributions. Since these are extremely unusual events, it is not clear that the simulation is accurate in this regime. This problem of modelling the tails of high rate backgrounds is common among many ATLAS physics analyses and requires further study.

18.1.6.7 Measurements of *W* and top polarisation in *W*-gluon fusion

Single top production provides an opportunity to study the polarisation of top quarks as well as of the *W* bosons produced in their decay. As discussed below, the SM predicts that about 70% of *W* bosons produced in top decay will be longitudinally polarised. Furthermore, in the limit of zero *b*-quark mass, the SM predicts that the top quarks produced in the *W*-gluon fusion process at LO are almost 100% polarised. Since the top decays too quickly to hadronise or depolarize, its spin information is transmitted to its decay products. New physics, such as top production in the decay of a heavy charged Higgs boson or the existence of V+A couplings at the *W*-*t*-*b* vertex, could alter the decay angular distributions of either the *W* boson or the top quark. Investigations of the *W* and top polarisations (for more details, see reference [18-54]) are discussed below.

The polarisation of the *W* boson can be investigated through measurements of distributions of its decay products [18-27]. For example, the cosine of the decay angle of the lepton, $\cos_W\Theta_l$, measured in the *W* rest frame with respect to the direction of the *W* boson momentum vector in the top rest frame, can be readily obtained from the *l*-*b* invariant mass (m_{lb}) as: $\cos_W\Theta_l \cong 2 \cdot m_{lb}^2/(m_t^2 - m_W^2) - 1$. The differential angular distribution can be decomposed into three terms:

$$F_W(\cos_W\Theta_l) = \frac{3}{2} \cdot \left[f_{long} \cdot \left(\frac{\sin_W\Theta_l}{\sqrt{2}} \right)^2 + f_L \cdot \left(\frac{1 - \cos_W\Theta_l}{2} \right)^2 + f_R \cdot \left(\frac{1 + \cos_W\Theta_l}{2} \right)^2 \right]$$

where f_R, f_L and f_{long} are the fractions of right, left and longitudinal components of the *W* polarisation. According to the SM, $f_R = 0$ and $f_{long}/f_L = m_t^2/(2m_W^2)$. With m_t = 175 GeV, the SM predicts $f_{long} = 0.703$ and $f_L = 0.297$.

Events with right-handed *W* polarisation were introduced into the simulation by treating the neutrino in SM events as a charged lepton, and vice versa. In addition to a sample of events simulated with the SM prediction, a ‘SM-like’ scenario, in which the non-longitudinal fraction $1 - f_{long} = 0.297$ is shared by f_R and f_L, was simulated. The simulations were performed at the parton level. As an example, Figure 18-35 shows the distribution of $\cos_W\Theta_l$ for the Standard Model scenario and the more general situation with $f_{long} = f_{long}^{SM} = 0.703$, $f_L = 0.90 \times f_L^{SM} = 0.267$ and $f_R = f_L^{SM} - f_L = 0.030$.

Several functions were used to fit the $\cos_W\Theta_l$ distributions, including a pure SM fit which assumes f_R=0, a ‘SM-like’ fit with f_{long} fixed to the SM value and the fractions f_L and f_R being returned, and a more general fit in which all three components were left free. The results obtained with the SM sample yielded values for f_{long}, f_L and f_R which differed by less than 1.5% from the generated values. When using the mixed sample, the ‘SM-like’ and the more general fit both re-

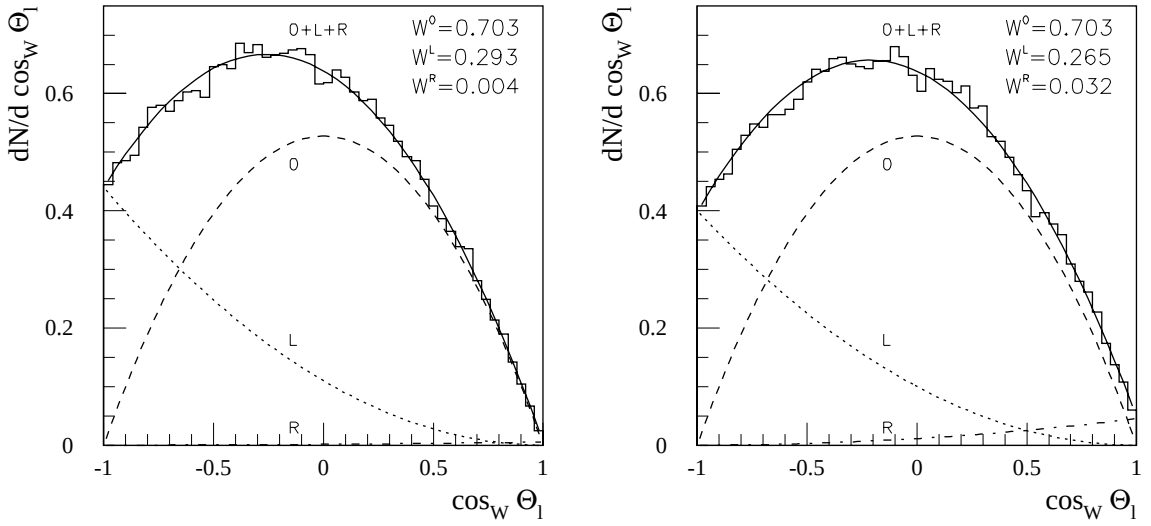

Figure 18-35 Distributions of the cosine of the lepton angle in the W rest frame for the SM scenario with f_R=0, (left figure) and a "SM-like" scenario in which there is a 3% right-handed component included at the expense of the left-handed fraction. The curves correspond to a SM-like fit (f_{long} = 0.703, f_L + f_R = 0.297) resulting in f_R= 0.004 (left) and f_R = 0.032 (right). In each figure, the contributions from longitudinal (O), left-handed (L) and right-handed (R) polarisations are shown separately, as well as their sum.

turned a non-zero value for f_R of ~11% (the 'SM-like' fit results are shown in Figure 18-35). In the non-SM scenario, a pure SM fit under the hypothesis of a zero f_R is clearly disfavoured, with a χ^2 per degree of freedom five times higher than obtained with the fit with f_R as a free parameter.

In addition to measuring the W helicity, the polarisation of the top quarks produced in W-gluon fusion can be observed by measuring the angular distribution of the lepton in the top rest frame with the polarisation axis defined by the direction of the top in the center-of-mass frame of the two incoming quarks. In this frame, the situation is like a 2-2 scattering in electron-positron annihilation. The distribution of $\cos_t\Theta_l$ in this frame is described by

$$F_t(\cos_t\Theta_l) = f_L \cdot \frac{1-\cos_t\Theta_l}{2} + f_R \cdot \frac{1+\cos_t\Theta_l}{2}$$

Unlike the decay scenario, which used a Lorentz invariant to define the angle, a boost is required which introduces a minor skewing of the distribution. Depending on how the neutrino longitudinal momentum is defined, this skewing is more or less pronounced. As can be seen from Figure 18-36, the skewing of the distribution due to the algorithm used to define the boost is minimal. The fits denoted on the figure show the fitted fractions of left- and right-handed components for the helicity of the top quark. Since these are Standard Model distributions, the right handed component is expected to be zero. The fitted RH helicity fractions, reflect the uncertainty from the Monte Carlo statistics. Further study is required to move beyond this parton-level study and to understand the final sensitivity to a right-handed component, including detector effects.

In principle, for polarised top quarks, the asymmetry in the number of events produced with a particular charged lepton into and out of the decay plane should be zero for a T-conserved process. Hence, a non-zero measurement of this asymmetry could be interpreted as evidence for CP-violation, given the assumption of conserved CPT. It has been estimated in the literature [18-27]

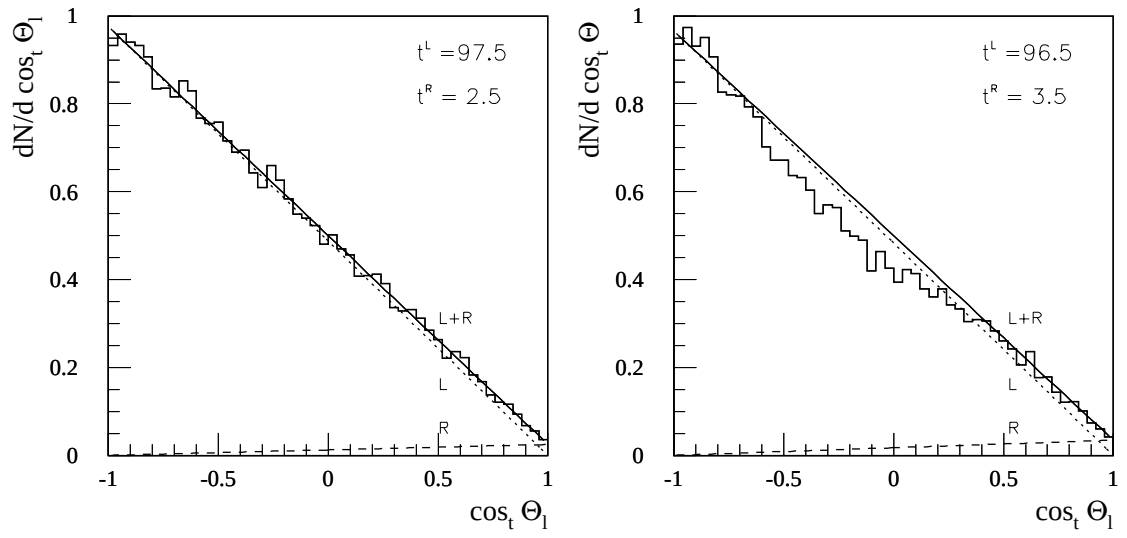

Figure 18-36 Distribution of the cosine of the lepton angle in the top rest frame, reconstructed using the true neutrino momentum (left figure) and using the longitudinal momentum for the neutrino which gives the best top quark mass fit (right figure). Superimposed on each figure are the results of the fit, showing the resulting left-handed (L) and right-handed (R) polarisations separately, as well as their sum.

that approximately 10^7-10^8 single top events would be required to detect CP violation at the level of 0.1-1%. While this is perhaps within reach of the statistics available over the lifetime of the LHC, such a study has not yet been carried out.

18.1.6.8 Conclusions of electroweak single top studies

While further work is required in order to fully understand the detector effects, the initial conclusions are that ATLAS is capable of extending the measurements expected from Fermilab into a new energy regime in which the cross-sections are very large. Backgrounds from $t\bar{t}$ production and W production with heavy flavor appear to be manageable, although detailed measurements of heavy quark production in association with W bosons will be necessary for precise control. Exploiting the three different single top production mechanisms, independent measurements of V_{tb} can be made which will provide both its definitive determination at the statistical level of a fraction of a percent as well as important tests of non-standard physics possibilities. The production of polarised top quarks is a unique feature of its weak production mechanism which will allow for precise helicity measurements at both the production and the decay vertices.

18.1.7 Conclusions of top quark physics studies

The large production cross-sections at the LHC for $t\bar{t}$ pair production and electroweak single top production imply that, in one year of running at low luminosity (10^{33} cm^{-2}s^{-1}), a sample of top quark events will be produced which is more than 10^4 times larger than the data set used at the Fermilab Tevatron to discover the top quark. Over the lifetime of the ATLAS experiment, samples of many millions of top quark events will be selected.

These large data sets will allow very sensitive studies of the properties of the top quark. The mass of the top quark will be measured with a precision of less than 2 GeV, dominated entirely by systematic errors. The top quark Yukawa coupling can be measured with a precision of less than 10% for a Higgs mass of 100 GeV. The $t\bar{t}$ spin correlations predicted in the SM can be observed, and used to probe for anomalous couplings or CP violation. Heavy resonances decaying to $t\bar{t}$ could be detected with masses up to 3 TeV for $\sigma \times$ BR greater than about 10 fb. Rare decays of the top quark can be probed down to branching ratios as low as of order a few times 10^{-5}. Finally, the detailed study of three different mechanisms of electroweak single top production will yield a wealth of information including precision measurements of V_{tb}, measurement of the W and t polarisations, and searches for anomalous couplings.

18.2 Fourth generation quarks

Data from LEP and SLC imply the existence of only three SM families with light neutrinos. However, extra generations with heavy neutrinos are not excluded, and models which include them have been proposed. The current experimental limits on fourth family quarks and leptons are $m_l > 80$ GeV and $m_Q > 128$ GeV [18-29]. The measurement of the ρ parameter [18-29] constrains the mass splitting between the doublet members of possible heavy generations of quarks: $\Sigma_i(c_i/3)\Delta m_i^2 < (49\ \text{GeV})^2, (83\ \text{GeV})^2$, where c_i is the colour factor, and where the first (second) limit corresponds to a Higgs mass of about 90 GeV (300 GeV). Considering only fourth family quarks, an analysis gives $\Delta m = |m(d_4) - m(u_4)| < 43$ GeV (72 GeV).

To take a specific model as an example, the democratic mass matrix (DMM) approach, developed as one possibility for solving the problem of the masses and mixings of the fundamental particles is considered. In the DMM approach, the SM is extended to include a fourth generation of fundamental fermions, with masses typically in the range from 300 to 700 GeV [18-55]. In order to avoid violation of partial wave unitarity, the quark masses should be smaller than about 1 TeV [18-56]. A few efforts have been made to parametrise the CKM matrix to take into account a possible fourth family [18-57][18-58]. These models predict that the fourth generation quark masses are close to each other, and that two-body decays of fourth family quarks are dominant over three-body decays. Guided by these models, two sets of mass values: $m(u_4) \approx m(d_4) \approx 320$ GeV and $m(u_4) \approx m(d_4) \approx 640$ GeV, together with the CKM values in references [18-59] and [18-57] are studied.

A fourth generation of fermions would contribute to the loop-mediated processes in Higgs production ($gg \rightarrow H$) and decay ($H \rightarrow \gamma\gamma$, $H \rightarrow$ gg) [18-61].

This effect would both enhance the Higgs production cross-section, and modify the branching ratios for Higgs decay. Table 18-18 summarises a few examples of the predicted enhancement, relative to the three-generation SM, a fourth generation would give in the values of $\sigma \times \mathrm{BR}$ for the channels $H \to \gamma\gamma$ and $H \to ZZ$. The enhancement is typically a factor of approximately 7-10 for the $H \to ZZ$ (and also $H \to WW$) channels, and up to 2 for $H \to \gamma\gamma$. The enhancements are almost independent of the assumed mass of the fourth family quarks or any other parameters.

Table 18-18 The enhancement, compared to the prediction of the three generation SM, in Higgs production and decay due to a fourth generation of fermions of mass 320 GeV or 640 GeV.

SM	**Enhancement in $\sigma \times$ BR**			
Higgs	**$\sigma \times$ BR($H \to \gamma\gamma$)**		**$\sigma \times$ BR($H \to ZZ$*)**	
Mass (GeV)	**m_4=320 GeV**	**m_4=640 GeV**	**m_4=320 GeV**	**m_4=640 GeV**
120	1.16	1.18	9.79	7.79
130	1.33	1.35	9.46	9.40
150	2.19	2.22	7.36	7.28
170			11.4	11.2
180			8.39	8.23

Of course, as discussed below, more clear evidence for the existence of a fourth generation of quarks could be obtained by searching for them directly. Fourth family quarks would be produced in pairs at the LHC. The expected production cross-section as a function of heavy quark mass was plotted in Figure 18-1, and shows that $\sigma \approx 10$ pb for a quark mass of 400 GeV, decreasing to ≈0.25 pb for a mass of 800 GeV.

18.2.1 Fourth family up quarks

The fourth generation up-type quark (u_4) would predominantly decay via $u_4 \to Wb$. The expected event topologies are thus the same as for $t\bar{t}$ production, except for the different mass of the u_4 quark. The best channel for observing $u_4\bar{u}_4$ production would be the 'single lepton plus jets' mode where one W decays leptonically ($W \to l\nu$) and the other hadronically ($W \to jj$) [18-60].

Events of the topology $u_4\bar{u}_4 \to WWb\bar{b} \to (l\nu)(jj)b\bar{b}$ were generated with PYTHIA and simulated with ATLFAST. Events were selected by requiring $E_{\mathrm{T}}^{\mathrm{miss}} > 20$ GeV and the presence of an isolated electron or muon with $p_{\mathrm{T}} > 50$ GeV and $|\eta| < 2.5$. The lepton isolation criteria required the separation in pseudorapidity / azimuthal angle space between the lepton and any jet to exceed 0.4, and that the total transverse energy deposition in cells within a cone $\Delta R < 0.2$ around the lepton not exceed 10 GeV. Two very hard ($p_{\mathrm{T}} > 250$ GeV) jets were required to be tagged as b-jets. An additional pair of jets, not tagged as b-jets, was required to satisfy 50 GeV $< m_{jj} <$ 100 GeV in order to be loosely consistent with m_W. Accepted W candidates were then combined with the b-tagged jets to search for evidence of $u_4 \to Wb \to jjb$. The mass resolution and efficiency were 21 GeV and 1.1%, respectively, for $m(u_4) = 320$ GeV. For $m(u_4) = 640$ GeV, the corresponding values were 40 GeV and 0.6%.

The background is dominated by $t\bar{t}$ production with subsequent decay $t\bar{t} \to (l\nu)(jj)b\bar{b}$. This background process has the same final state as the signal, as well as a large cross-section. In addition, there are smaller backgrounds from W + 4 jets, WW + 2 jets, and ZZ + 2 jets. The hard kinematic cuts are effective at reducing the backgrounds. The W and WW backgrounds are further suppressed by the requirement of two b-tagged jets. The background from ZZ + 2 jet production, with one Z decaying leptonically and the other to $b\bar{b}$, is very small after cuts.

Table 18-19 presents the expected number of observed events due to $u_4\bar{u}_4$ pair production for different u_4 masses and for an integrated luminosity of 100 fb^{-1}, together with the contributions from the background processes. Figure 18-37 shows the reconstructed m_{jjb} distributions for signal and background in the cases of u_4 quark mass of 320 GeV. In addition to a prominent top quark peak, an excess around the u_4 quark mass is observed.

Table 18-19 For three different u_4 masses, the expected number of selected events for the $u_4\bar{u}_4$ signal and the backgrounds in the single lepton plus jets mode, for an integrated luminosity of 100 fb^{-1}.

	Mass of u_4 quark	
Process	**320 GeV**	**640 GeV**
$u_4\bar{u}_4$ signal	7067	1060
$t\bar{t}$	12880	5953
W + 4 jets	507	218
WW + jj	75	32
ZZ + jj	11	4
Total Background	13473	6207
$S/\sqrt{\mathbf{B}}$	61.0	13.5
S/B	0.52	0.17

The corresponding values of $S/\sqrt{B}$ and S/B are also presented in Table 18-19. With an integrated luminosity of 100 fb^{-1}, a u_4 signal could in principle be discovered with greater than 5σ significance for both u_4 masses. However, as $m(u_4)$ increases, the decreasing value of S/B and the increasing width of the signal will make challenging the task of extracting the signal above background. An investigation is underway of the possibility to further improve extraction of the signal by simultaneously reconstructing the $u_4 \rightarrow$ lvb decay, and requiring that both decays give the same u_4 mass.

Events of the 'all jets' topology $u_4\bar{u}_4 \rightarrow WWb\bar{b} \rightarrow (jj)(jj)b\bar{b}$ with both W bosons decaying hadronically have also been studied [18-62]. The signature for this channel is characterised by six or more jets in the final state. QCD multi-jet events are the dominant source of background, with an estimated cross-section of about 5.5 μb. Other backgrounds sources include $t\bar{t}$ and W plus jet production.

In addition to the two very hard b-jets ($p_T > 250$ GeV) required above, the selection criteria demanded at least 6 jets with $p_T > 20$ GeV (including the two tagged b-jets) and no isolated lepton in the final state. Table 18-20 shows the number of generated signal and background events before and after applying these event selection cuts, and illustrates the effectiveness of the cuts in very significantly decreasing the backgrounds from QCD multi-jets and W+jets production.

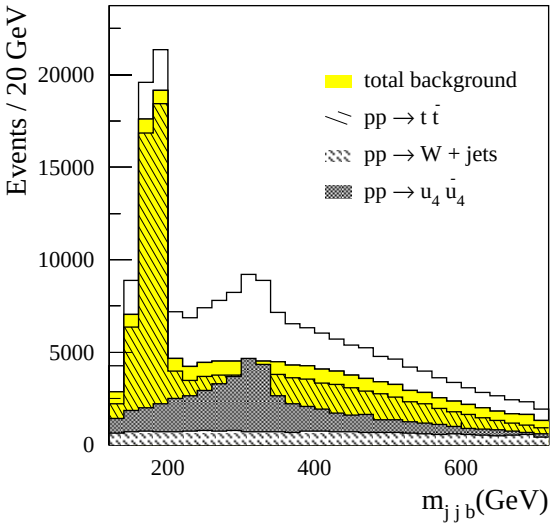

Figure 18-37 Invariant m_{jjb} mass distribution for selected single lepton plus jet events for $m(u_4)$ = 320 GeV, normalised to an integrated luminosity of 100 fb^{-1}.

The $W \rightarrow jj$ decay was reconstructed from the light quark jets. The combinations satisfying $|m_{jj} - m_W| < 15$ GeV were then combined with all b-tagged jets. Further background reduction was achieved by requiring $H_T > 500$ GeV, where H_T is defined as the scalar sum of the transverse energies of all the reconstructed jets. The resulting m_{jjb} mass resolution and signal efficiency were 22 GeV and 6.9%, respectively, for $m(u_4) = 320$ GeV. The corresponding values for $m(u_4) = 640$ GeV were 36 GeV and 0.4%.

Table 18-20 All jets $u_4\bar{u}_4$ signal and background event samples, before and after applying the selection cuts.

Process	Evts generated	Evts after cuts
$u_4\bar{u}_4$ Signal	$2.0{\cdot}10^6$	$6.8{\cdot}10^5$
QCD jets	$2.0\cdot10^8$	$3.9{\cdot}10^4$
$t\bar{t}$	10^7	$1.4{\cdot}10^6$
W + jets	$1.0\cdot 10^8$	10^4

Table 18-21 summarizes the number of signal and background events surviving these cuts. It is clear from the small S/B values that the backgrounds from QCD and from $t\bar{t}$ dominate over the signal. The QCD background is of particular concern, since its cross-section at the LHC is not well known. The rather broad m_{jjb} signal distribution, due to the many different combinations possible, also complicates efforts to extract the signal above background. For u_4 masses which are not too high, it is possible that the all-jets analysis could be used to support a discovery made in the single lepton plus jets decay channel.

Table 18-21 Expected rates of the fourth family up-quarks in all-jets mode and various backgrounds for an integrated luminosity of 100 fb^{-1}.

	Mass of u_4	
Process	**320 GeV**	**640 GeV**
$u_4\bar{u}_4$ signal	96.8k	2390
QCD multi-jets	491k	144k
$t\bar{t}$	296k	64k
W + jets	17.6k	7.2k
Total Bkgnd	804.6k	215.2k
S/B	0.12	0.01

18.2.2 Fourth family down quarks

Under the assumption that $m(d_4) \approx m(u_4)$, the dominant d_4 decay mode would be $d_4 \rightarrow tW^-$. The most promising final state to search for $d_4\bar{d}_4$ pair production is the single lepton plus jets channel $pp \rightarrow d_4\bar{d}_4 \rightarrow t\bar{t}W^+W^- \rightarrow W^+bW^-\bar{b}W^+W^-$, where one of the W decays leptonically and the others decay hadronically [18-62]. The dominant background for this channel is $t\bar{t}$ production with additional jets. Other sources of background, such as WW+jets and W+jets, do not contribute significantly.

Events satisfying the final state topology $d_4\bar{d}_4 \rightarrow l + 2b_{\text{jet}} + 6j + E_T^{\text{miss}}$ were required to have exactly eight jets with $p_T > 20$ GeV, including two b-tagged jets, and one isolated electron or muon with $p_T > 20$ GeV. In addition, a requirement was imposed that $E_T^{\text{miss}} > 20$ GeV. Di-jet pairs satisfying $|m_{jj} - m_W| < 15$ GeV were considered as $W \rightarrow jj$ candidates, and were combined with b-tagged jets to search for $t \rightarrow jjb$ candidates. Combinations with $|m_{jjb} - m_t| < 15$ GeV were considered as top quark candidates. Finally, $t \rightarrow jjb$ and $W \rightarrow jj$ candidates were combined to search for a signal from the hadronic decay $d_4 \rightarrow tW \rightarrow (jjb)jj$. The resulting mass resolution was 42 GeV, with a signal efficiency of 0.54%.

Figure 18-38 shows the invariant mass distributions of the (*jjb*)*jj* system for the signal and $t\bar{t}$ background in the case $m(d_4)$ = 320 GeV, assuming an integrated luminosity of 100 fb^{-1}. Within a mass window of 320 ± 60 GeV, a total of about 29 400 signal events were selected, with a background of about 39 000 events. The d_4 signal and $t\bar{t}$ background shapes are very similar. However, the size of the excess is much larger than the uncertainty in the knowledge of the $t\bar{t}$ cross-section. Observation of such an excess would be a clear signal of new physics, though further studies would be required to determine the cause of the enhancement. For the case with $m(d_4)$ = 640 GeV and an integrated luminosity of 100 fb^{-1}, 2 043 signal events would be accepted, with a background of 3 479 events in the mass interval 640 ± 75 GeV. The very broad signal shape would complicate detection of the signal above background.

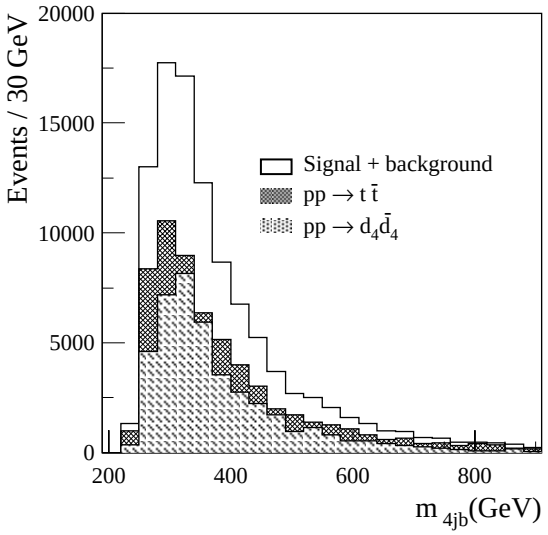

Figure 18-38 Invariant mass distribution of the *(jjb)jj* system for $m(d_4)$ = 320 GeV, normalised to an integrated luminosity of 100 fb^{-1}.

These results can be improved by more fully utilising the knowledge of the final state, and the resulting kinematic constraints (such as m_W and m_t constraints for the appropriate combinations). It has been shown in the analysis of $t\bar{t}H$ for example (see Section 19.2.4.3), that it is possible to simultaneously reconstruct both top quark decays, thereby reducing greatly the number of possible combinations. Application of such techniques here should improve the separation of the signal from background, and are being studied.

18.2.3 Bound states of fourth family quarks

If the decays of fourth generation quarks were suppressed, for example due to small inter-generation mixings, the resultant long quark lifetime could lead to formation of a $Q_4\overline{Q}_4$ bound state [18-63] such as a pseudoscalar quarkonium state η_4. As already said, the extension of the DMM model to include a fourth family predicts a mass difference between u_4 and d_4 of the order of 1 GeV. Given the expected experimental resolution of ATLAS, this mass difference would not allow the identification of the quark type which compose the quarkonium.

The production of a superheavy quarkonium via $gg \rightarrow \eta_4$ process has been implemented in PYTHIA. The decay $\eta_4 \rightarrow ZH$, followed by $Z \rightarrow ll$ and $H \rightarrow b\bar{b}$, has been studied [18-65] for $m(\eta_4)$ = 600 GeV and m_H = 150 GeV assuming $\sigma \times$ BR = 0.19 pb (including BR($Z \rightarrow ll$) and BR($H \rightarrow b\bar{b}$)). The main background for this channel is due to Z+jets production ($\sigma \sim 1.7\times10^4$ pb). Continuum ZH production does not contribute significantly ($\sigma \sim 6\text{x}10^{-3}$ pb).

The selection cuts required the presence of two isolated opposite-sign, same-flavour leptons with $p_T > 20$ GeV and satisfying $|m_{ll} - m_Z| < 10$ GeV. In addition, two jets with $p_T > 15$ GeV were required to be tagged as *b*-jets. Evidence for the decay $\eta_4 \rightarrow ZH$ was then searched for by reconstructing the $llb\bar{b}$ invariant mass. The resulting mass resolution was 25 GeV, with a signal efficiency of 7%.

As shown in Figure 18-39, a clear signal of $\eta_4 \rightarrow ZH$ can be seen near the mass $m(\eta_4)$ = 600 GeV. With an integrated luminosity of 100 fb^{-1}, the estimated number of signal and background events are 4660 and 573 events, respectively.

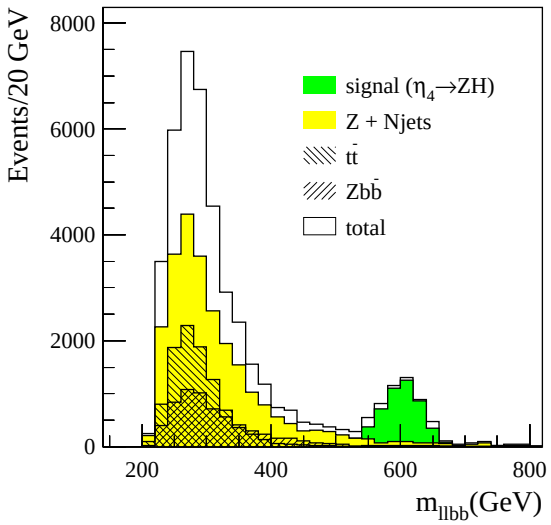

Figure 18-39 The $llb\bar{b}$ invariant mass distribution for the $\eta_4 \rightarrow ZH$ signal and background, normalised to an integrated luminosity of 100 fb^{-1}.

18.3 Heavy leptons

Accurate measurement of the parameters of Z decay have demonstrated that there exist only three light neutrinos coupling to the Z with SM couplings. The simplest supposition is then that the lepton sector comprises these three light neutrinos and their charged counterparts. However, it is quite possible that heavy leptons exist.

Many models, such as composite models [18-66], left-right symmetric models [18-67], grand unified theories [18-68], technicolor models [18-69], superstring-inspired models [18-70], and models of mirror fermions [18-71], predict the existence of new particles with masses around of the scale of 1 TeV and allow the possible existence of new generations of fermions. For illustration purposes, the case of heavy, 'fourth generation' leptons which have SM couplings is considered. In this case, production of a pair of heavy charged leptons (LL) or a pair of heavy neutrinos ($N\overline{N}$) at the LHC is dominated by the Drell-Yan process and by gluon-gluon fusion. The total production cross-section, $\sigma(LL)$, is of order 1 pb at the LHC for $m_L \approx 100$ GeV, decreasing to a few fb for $m_L \approx 700$ GeV, with similar predictions for $N\overline{N}$ production [18-72].

The experimental signatures for detection of these heavy leptons depends critically on their masses and decay modes. Searches for $L \rightarrow NW$ have been discussed in the literature [18-73], and have concluded that it would be very difficult to separate the signal from the large backgrounds from single and pair production of W and Z bosons. However, these analyses were performed with the assumption of a massless fourth-generation neutrino, and need to be repeated for a massive neutrino. In addition to this approach, the case where both the L and the N are massive gives rise to other possibilities. For example, if the L and N were roughly degenerate, the decay $L \rightarrow NW$ (and $N \rightarrow LW$) would be kinematically forbidden. Instead, the heavy leptons would decay predominantly through their mixing with the light lepton generations. In this case, the charged lepton decay $L \rightarrow \nu W$ could be suppressed by a small mixing angle so that the L could be relatively long-lived and would look like a muon escaping the detector. However, due to its large mass, the velocity distribution for L production would not be peaked as sharply at $\beta \approx 1$ as for muon production. Measurement of its time-of-flight with the muon spectrometer could then be used to identify and determine the mass of the heavy charged lepton. Such an analysis is reported in Section 20.3, where the situation with heavy long-lived charged sleptons was examined in the context of gauge-mediated supersymmetry breaking models. In the case where the decay $N \rightarrow lW$ (with l a light lepton) occurs inside the detector, an interesting signature of $N\overline{N} \rightarrow llWW$ production would be the production of high p_T lepton pairs in association with jets (for the case where both W bosons decay hadronically). The dominant background, arising from $t\bar{t}$ production, could be suppressed by requiring no E_T^{miss} and by trying to recon-

struct the N mass from ljj combinations. The cases of $pp \rightarrow N\overline{N} \rightarrow lljjjj$ and $pp \rightarrow e\overline{N} \rightarrow eejj$ in left-right symmetric models are presented in Section 21.6.2. Studies are underway of the ATLAS sensitivity to these and other possible experimental signatures of heavy lepton production.

18.4 Conclusions

The LHC, with its high beam energy and luminosity, will be an excellent place to search for, and explore the properties of, heavy quarks and leptons. The cross-section for $t\bar{t}$ production at the LHC is about 100 times larger than that at the Tevatron, and will lead to accumulation over the lifetime of ATLAS of millions of $t\bar{t}$ events. Studies of these events, and the large samples of electroweak single top quark events, will permit very detailed studies of the properties of the top quark, and will allow sensitive probes of the EWSB sector. In addition, the existence of fourth generation quarks will be probed for masses up to of order 700 GeV. A great discovery potential, not yet fully evaluated, also exists for heavy leptons.

18.5 References

18-1 R. Bonciani *et al.*, Nucl. Phys. **B529** (1998) 424.

18-2 E. Richter-Was, D. Froidevaux and L. Poggioli, 'ATLFAST 2.0 a fast simulation package for ATLAS', ATLAS Internal Note ATL-PHYS-98-131 (1998).

18-3 CDF Collaboration, Phys. Rev. **D50** (1994) 2966; Phys. Rev. **D51** (1995) 4623; Phys. Rev. Lett. **74** (1995) 2626.

18-4 D0 Collaboration, Phys. Rev. Lett. **74** (1995) 2422.

18-5 T. Sjostrand, Computer Physics Communications **82** (1994) 74.

18-6 G. Marchesini *et al*, Computer Phys. Commun. 67 (1992) 465.

18-7 Lj. Simic, G. Skoro and D. Popovic, 'Signal and background study for $t\bar{t}$ all hadronic decay at the LHC', ATLAS Internal Note ATL-COM-PHYS-99-057 (1999).

18-8 F.A. Berends and H. Kuijf, Nucl. Phys. **B353** (1991) 59.

18-9 E. Richter-Was and D. Froidevaux, 'MSSM Higgs searches in multi *b*-jets final states', ATLAS Internal Note ATL-PHYS-No-104 (1997).

18-10 K. Sliwa, 'Top mass and cross-section results from CDF and D0 at the Fermilab Tevatron', FERMILAB-CONF-99/086-E. Proceedings of the 13th Topical Conference on Hadron Collider Physics, Tata Institute of Fundamental Research, Mumbai, India (1999).

18-11 U. Sarid, 'Precision top mass measurements vs. Yukawa unification predictions', hep-ph/9610341.

18-12 CDF Collaboration, Phys. Rev. Lett. **80** (1998) 2767;
D0 Collaboration, Phys. Rev. **D58** (1998) 052001.

18-13 P. Grenier *et al.*, 'Measurement of the top quark mass in the inclusive single lepton plus jets channel', ATLAS Internal Note ATL-COM-PHYS-99-024 (1999).

18-14 C. Peterson *et al.*, Phys. Rev. **D27 (**1983) 105.

18-15 ALEPH Collaboration, Phys. Rep. **294** (1998) 1.

18-16 I. Efthymiopoulos, 'High p_T top mass reconstruction in the single lepton plus jets channel using a large calorimeter cluster', ATLAS Internal Note ATL-COM-PHYS-99-050 (1999).

18-17 A. Lagatta, L. La Rotonda and M. Cobal, 'Top mass evaluation in the $t\bar{t}$ dilepton channel', ATLAS Internal Note ATL-COM-PHYS-99-044 (1999).

18-18 G. Unal and L. Fayard, Proceedings of the Large Hadron Collider Workshop, Aachen, 1990, edited by G. Jarlskog and D. Rein, Volume II, p. 360.

18-19 K.J.F. Gaemers and G. Hoogeveen, Phys Lett. **146B** (1984) 347;
D. Dicus, A. Stange and S. Willenbrock, Phys. Lett. **B333** (1994) 126.

18-20 K. Lane and E. Eichten, Phys. Lett. **B352** (1995) 382;
E. Eichten and K. Lane, Phys. Lett. **B327** (1994) 129.

18-21 C.T. Hill and S.J. Parke, Phys. Rev. **D49 (**1994) 4454.

18-22 R. Casalbuoni *et al.*, Z. Phys. **C69** (1996) 519.

18-23 C.T. Hill, Phys. Lett. **B266** (1991) 419; Phys. Lett. **B345** (1995) 483.

18-24 E. Simmons, Phys. Rev. **D55 (**1997) 1678.

18-25 N. Cartiglia and J. Parsons, 'Study of ATLAS sensitivity to a heavy resonance decaying to $t\bar{t}$', ATLAS Internal Note ATL-COM-PHYS-99-038 (1999).

18-26 G. Mahlon and S. Parke, Phys. Rev. **D53** (1996) 4886.

18-27 G.L. Kane, G.A. Ladinsky and C.-P. Yuan, Phys. Rev. **D45** (1992) 124;
W. Bernreuther and. A. Brandenburg, Phys. Rev. **D49** (1994) 4481;
C.-P. Yuan, Mod. Phys. Lett. **A10** (1995) 627;
W. Bernreuther and A. Brandenburg, Phys. Lett. **B314** (1993)104.

18-28 A. Lagatta, V. Simak and J. Smolik, '$t\bar{t}$ spin correlations and the potential for observation of CP violation in the production vertex', ATLAS Internal Note ATL-COM-PHYS-99-049 (1999).

18-29 Particle Data Group, Review of Particle Physics, European Physical Journal **C3** (1998) 1.

18-30 J. Konigsberg, FERMILAB-CONF-99/129-E. Published Proceeding, 17th International Workshop on Weak Interactions and Neutrinos (WIN 99), Cape Town, South Africa, 1999.

18-31 B. Grzadkowski, J.F. Gunion, and P. Krawczyk, Phys. Lett. **B268** (1991) 106;
G. Eilam, J.L Hewett, and A. Soni, Phys. Rev. **D44** (1991) 1473;
M. Luke and M.J Savage, Phys. Lett. **B307** (1993) 387.

18-32 C.S Li, R.J Oakes, and J.M. Yang, Phys. Rev. **D49** (1994) 293;
J.M. Yang and C.S. Li, Phys. Rev. **D49** (1994) 3412;
G. Couture, C. Hamzaoui, and H. Koenig, Phys. Rev. **D52** (1995) 1713;
G. Couture, M. Frank, and H. Koenig, Phys. Rev. **D56** (1997) 4219;
G.M. de Divitiis, R. Petronzio, and L. Silvestrini, Nucl. Phys. **B504** (1997) 45.

18-33 R.D. Peccei and X. Zhang, Nucl. Phys. **B337** (1990) 269;
T. Han, R.D. Peccei, and X. Zhang, Nucl. Phys. **B454** (1995) 527;
T. Han *et al.*, Phys. Lett. **B385** (1996) 311;
M. Hosch, K. Whisnant, and B.L. Young, Phys. Rev. **D56** (1997) 5725;
V.F. Obraztsov, S.R. Slabospitsky, and O.P. Yushchenko, Phys. Lett. **B426** (1998) 393;
T. Han *et al.*, Phys. Rev. **D58** (1998) 73008;
B.A. Arbuzov and M. Y. Osipov, Phys. Atom. Nucl. **62** (1999) 495.

18-34 CDF Collaboration, Phys. Rev. Lett. **80** (1998) 2525.

18-35 L.D. Chikovani and T.D. Djobava, 'ATLAS sensitivity to the flavor-changing neutral current decay $t \rightarrow Zq$', ATLAS Internal Note ATL-COM-PHYS-99-034 (1999).

18-36 J. Dodd, S. McGrath and J. Parsons, 'Study of ATLAS sensitivity to rare top quark decays', ATLAS Internal Note ATL-COM-PHYS-99-039 (1999).

18-37 Y.P. Gouz and S.R. Slabospitsky, 'Double top production at hadron colliders', hep-ph/9811330.

18-38 E. Jenkins, Phys. Rev. **D56** (1997) 458.

18-39 G. Mahlon and S. Parke, Phys. Lett. **B347** (1995) 394;
G. Mahlon, 'Theoretical expectations in radiative top decays', hep-ph/9810485.

18-40 M. Jarabek and J.H. Kuhn, Phys. Lett. **B329** (1994) 317.

18-41 W.G.H. Dharmaratna and G. R. Goldstein, Phys. Rev. **D41** (1991) 1731.

18-42 B. Grzadkowski and J.F. Gunion, Phys. Lett. B287 (1992) 237.

18-43 A.P. Heinson, A.S. Belyaev, and E.E. Boos, Phys., Rev. D56 (1997) 3114.

18-44 V. Barger, J. Ohnemus and R.J.N. Phillips, Int. Journ. Mod. Phys. **A4** (1989) 617.

18-45 E. Malkawi and T. Tait, Phys. Rev. **D54** (1996) 5758;
T. Han et al, Phys. Rev. **D58** (1998) 073008.

18-46 D.O. Carlson, E. Malkawi and C.P. Yuan, Phys. Lett. **B337** (1994) 145;
D.O. Carlson, Ph.D. Thesis, Michigan State University (1995);
Tim Tait, Ph.D. Thesis, Michigan State University (1999).

18-47 SGMP is provided via private communication with authors at Protvino and is not currently publicly available.

18-48 S. Mrenna, T. Tait, C.P. Yuan, private communication.

18-49 D. O'Neil, B. Gonzalez-Pineiro and M. Lefebvre, 'Measuring V_{tb} via s-channel single top production with ATLAS', ATLAS Internal Note ATL-COM-PHYS-99-015 (1999).

18-50 S. Willenbrock, 'Overview of Single Top Theory - Measuring the Cross-section, Theoretical Uncertainties, $|V_{tb}|$, etc.', Talk presented at the 'Thinkshop, top quark Physics for Run II' at Fermi National Laboratory, Bhatavia, Illinois (1998).

18-51 M.C. Smith and S. Willenbrock, Phys. Rev. **D54** (1996) 6696.

18-52 T. Tait and C.P. Yuan, 'Single top production at the Fermilab tevatron', hep-ph/9710372.

18-53 J. Huston et al., Phys. Rev. **D58** (1998) 114034.

18-54 B. Gonzalez-Pineiro et al., 'Top and W polarization in electroweak top production at the LHC', ATLAS Internal Note ATL-COM-PHYS-99-027 (1999).

18-55 A. Celikel, A.K. Ciftci and S. Sultansoy, Phys. Lett. **B342** (1995) 257.

18-56 M.S. Chanowitz, M.A. Furman and I. Hinchliffe, Nucl. Phys. **B153** (1979) 402.

18-57 S. Atag *et al.*, Phys. Rev. **D54** (1996) 5745.

18-58 A. Datta and S. Raychaudhuri, Phys. Rev. **D49** (1994) 4762.

18-59 E. Arik *et al.*, 'A search for fourth family quarks at hadron colliders', ATLAS Internal Note ATL-PHYS-96-091 (1996).

18-60 E. Arik *et al.*, Phys. Rev. **D58** (1998) 117701.

18-61 E. Arik *et al.*, 'Enhancement of the Standard Model Higgs boson production cross-section with a fourth family of Standard Model quarks', ATLAS Internal Note ATL-PHYS-98-125 (1998).

18-62 E. Arik *et al.*, 'Observability of Standard Model fourth family quarks at the LHC', ATLAS Internal Note ATL-PHYS-99-005 (1999).

18-63 V. Barger *et al.*, Phys. ReV. **D35** (1987) 11.

18-64 H. Inzawa and T. Morii, Phys. Lett. **B70** (1993) 20.

18-65 E. Arik *et al.*, 'Production and decay properties of the pseudoscalar quarkonium associated with a fourth generation quark', ATLAS Internal Note ATL-PHYS-99-061 (1999).

18-66 L. Abbot and E. Farhi, Phys. Lett. **101B** (1981) 69; Nucl. Phys. **B189** (1981) 547;
W. Buchmueller, Acta Phys. Austriaca Suppl. XXVII (1985) 517.

18-67 J.C. Pati and A.Salam, Phys. Rev. **D10** (1974) 275;
R.N. Mohapatra and J.C. Pati, Phys. Rev. **D11** (1975) 566 and Phys. Rev. **D11** (1975) 2558;
G. Senjanovic and R.N. Mohapatra, Phys. Rev. **D12** (1975) 1502;
G. Senjanovic, Nucl. Phys. **B153** (1979) 334.

18-68 See, for example, P. Langacker, Phys. Rep. **72** (1981) 185.

18-69 S. Dimopoulos, Nucl. Phys. **B168** (1981) 69;
E. Farhi and L. Susskind, Phys. Rev. **D20** (1979) 3404;
J. Ellis *et al.*, Nucl. Phys. **B182** (1981) 529.

18-70 J.L. Hewett and T.G. Rizzo, Phys. Rep. **183** (1989) 193.

18-71 J. Maalampi, K. Mursula and M. Roos, Nucl. Phys. **B207** (1982) 233.

18-72 See for example P.H. Frampton *et. al.*, Phys. Rev. **D48** (1993) 3128 and references therein.

18-73 See for example V. Barger, T. Han and J. Ohnemus, Phys. Rev. **D37** (1988) 1174, and references therein.

19 Higgs Bosons

19.1 Introduction

The experimental observation of one or several Higgs bosons [19-1] will be fundamental for a better understanding of the mechanism of electroweak symmetry-breaking. In the Standard Model [19-2], one doublet of scalar fields is assumed, leading to the existence of one neutral scalar particle H. On the basis of present theoretical knowledge, the Higgs sector in the Standard Model remains largely unconstrained. The Higgs-boson mass, m_H, is not theoretically predicted. From unitarity arguments an upper limit of ~1 TeV can be derived [19-3]. The requirements of the stability of the electroweak vacuum and the perturbative validity of the Standard Model allow to set upper and lower bounds depending on the cutoff value chosen for the energy scale Λ up to which the Standard Model is assumed to be valid [19-4]. Such analyses exist at the two-loop level for both lower [19-5] and upper [19-6] Higgs mass bounds. If the cutoff value is chosen at the Planck mass, which means that no new physics appears up to that scale, the Higgs-boson mass is required to be in the range between $130 < m_H < 190$ GeV. This bound becomes weaker if new physics appears at lower mass scales. If the cutoff is chosen to be 1 TeV, the Higgs-boson mass is constrained to be in the range $50\ \text{GeV} < m_H < 800$ GeV. Experimentally, constraints on the Standard Model Higgs-boson mass are derived directly from searches at LEP2, which presently lead to $m_H > 90$ GeV [19-7]. It is expected that the sensitivity of LEP2 will be extended to ~105 GeV over the coming years [19-8], if the centre of mass energy of the LEP collider is raised to 200 GeV. Indirectly, high precision electroweak data constrain the Higgs-boson mass via their sensitivity to loop corrections. Assuming the overall validity of the Standard Model, a global fit to all electroweak data leads to $m_H = 76^{+85}_{-47}$ GeV [19-9].

In supersymmetric theories, the Higgs sector is extended to contain at least two doublets of scalar fields. In the minimal version, the so-called MSSM model [19-10], there are five physical Higgs particles: two *CP*-even Higgs bosons h and H, one *CP*-odd Higgs boson A, and two charged Higgs bosons $H^{\pm}$. Two parameters, which are generally chosen to be m_A and $\tan\beta$, the ratio between the vacuum expectation values of the two Higgs doublets, determine the structure of the Higgs sector at tree level. However, large radiative corrections affect the Higgs masses and couplings. The lightest neutral scalar Higgs-boson mass, m_h, is theoretically constrained to be smaller than ~150 GeV [19-11].

Alternative manifestations of electroweak symmetry-breaking mechanisms would probably involve a strongly interacting electroweak sector [19-12]. In this case, significant deviations from the Standard Model predictions would be observable in final states consisting of gauge boson pairs.

The aim of this Chapter is to review and assess the performance of the ATLAS detector in the search for a Standard Model Higgs boson, for the various supersymmetric Higgs bosons, and for alternative signals of electroweak symmetry breaking. Many results are based on studies which have been presented in earlier documents [19-13][19-14][19-15][19-16]. The main differences with respect to previous studies are:

- The significance of a Higgs discovery is evaluated for the final ATLAS detector configuration, as presented in the various Technical Design Reports.
- Improvements on theoretical calculations of cross-sections, branching ratios *etc*., which have appeared since the Technical Proposal, are taken into account.

- The study of the MSSM Higgs sector is extended by several channels, which had not been considered in the Technical Proposal. In addition, cases where SUSY particles are light and appear in Higgs decays and cases where Higgs bosons are produced in decays of SUSY particles are considered in some detail here.
- Finally, it is discussed how accurately Higgs boson parameters, such as mass, width, spin, and couplings to fermions and bosons, can be measured in the ATLAS detector.

The results presented in this Chapter are obtained predominantly from fast detector simulations [19-17] (see Section 2.5), where the detector response and resolution functions have been taken into account. However, the crucial detector-dependent performance parameters such as the mass resolutions, reconstruction and identification efficiencies for the signal events and the most important background rejections, were obtained from a detailed GEANT simulation of the ATLAS detector. Many of them have already been presented in the corresponding performance chapters of this document. Wherever relevant, they have been used for the evaluation of the signal significance.

Physics processes have been simulated with the PYTHIA Monte Carlo program, including initial- and final-state radiation, hadronisation and decays. The signal and background production cross-sections are affected by uncertainties due to higher-order corrections, structure function parametrisations and event generation. Over the recent years, there has been considerable progress in the calculation of higher-order QCD corrections to the cross-sections for the Higgs-boson production [19-18]. However, the higher-order QCD corrections to the production cross-sections are not known for all signal and background processes. Therefore, the present Higgs studies have consistently and conservatively refrained from using *K*-factors, resorting to Born-level predictions for both signal and backgrounds.

This Chapter begins with a discussion of the discovery potential of the ATLAS detector for the Standard Model Higgs boson (Section 19.2), followed by the discussion of the Higgs boson searches in the MSSM (Section 19.3). Searches in the framework of a strongly interacting Higgs sector are described in Section 19.4. A short summary and conclusions are given in Section 19.5.

19.2 Standard Model Higgs boson

19.2.1 Introduction

In this Section, the expected performance in the search for the Standard Model Higgs boson with ATLAS is discussed over the mass range from 80 GeV to 1000 GeV. Although the present LEP2 mass limit for a Standard Model Higgs boson is already higher than 90 GeV [19-7], masses as low as 80 GeV have been considered in the studies reported here in order to assess the detection capabilities in these difficult conditions. Such low masses remain relevant in some regions of the MSSM parameter space, where the same final state topologies from Higgs boson decays occur as in the Standard Model case. The Standard Model Higgs boson is searched for at the LHC in various decay channels, the choice of which is given by the signal rates and the signal-to-background ratios in the various mass regions.

These channels are:

- $H \rightarrow \gamma\gamma$ direct production;
- $H \rightarrow \gamma\gamma$ from the associated production WH, ZH and $t\bar{t}H$, using a lepton (e, μ) tag from the vector boson or top quark decay;
- $H \rightarrow b\bar{b}$ from the associated production WH, ZH and $t\bar{t}H$, using a lepton (e, μ) tag and b-tagging;
- $H \rightarrow ZZ^* \rightarrow 4l$;
- $H \rightarrow ZZ \rightarrow 4l$ and $H \rightarrow ZZ \rightarrow llν\nu$;
- $H \rightarrow WW \rightarrow lνjj$ and $H \rightarrow ZZ \rightarrow lljj$.

The search strategies and background rejection methods have been established through many studies over the past years. In addition to the well established channels listed above, the discovery potential is also reported for less promising channels, such as $H \rightarrow Z\gamma$. The associated production of a Higgs boson with QCD jets, where the Higgs boson decays to $\gamma\gamma$, has been also investigated. In addition, the discovery potential of the Higgs boson in the recently suggested $H \rightarrow WW^* \rightarrow lνlν$ channel [19-19] has been studied.

The total Higgs-boson production cross-section has contributions from various subprocesses, of which gg fusion and WW fusion are the most important ones. The WW fusion process is significant only in the high-mass region. The processes of $q\bar{q}$ and ZZ fusion also contribute to the total cross-section. For all Higgs studies reported here, the CTEQ2L structure function parametrisation has been used. The variation in the cross-section has been estimated [19-15] using four different sets of structure function parametrisations (namely the CTEQ2L, CTEQ2MS, CTEQ2M and MRSD sets); in the low-mass region ($m_H < 180$ GeV), a spread of only ~5% in the Higgs-boson production rates has been found. The decay branching ratios have been calculated using the program of Ref. [19-20], which includes all higher-order corrections presently available.

19.2.2 $H \rightarrow \gamma\gamma$

The decay $H \rightarrow \gamma\gamma$ is a rare decay mode, only observable over a limited Higgs boson mass region, where the production cross-section and the decay branching ratio are both relatively large. It is a promising channel for Higgs searches in the mass range $100 < m_H < 150$ GeV and places severe requirements on the performance of the EM Calorimeter. Excellent energy and angular resolution are needed to observe the narrow mass peak above the irreducible prompt $\gamma\gamma$ continuum. Powerful particle identification capability is also required to reject the large QCD jet background as well as the potentially dangerous resonant background from $Z \rightarrow ee$ decays, in the case where $m_H \approx m_Z$.

In the following, the search for $H \rightarrow \gamma\gamma$ decays is described separately for direct production of the Higgs boson (Section 19.2.2.1), for associated production of a Higgs boson with a W or Z boson or a $t\bar{t}$ pair (Section 19.2.2.2), and for production of a Higgs boson in association with QCD jets (Section 19.2.2.3). In each case, the signal reconstruction, the reducible and irreducible backgrounds and the signal observability are discussed.

19.2.2.1 Direct production

The direct production of a low-mass Higgs boson is dominated by the *gg* fusion process. The production cross-sections and the branching ratios for the $H \rightarrow \gamma\gamma$ decay are listed in Table 19-1 for $80 < m_H < 150$ GeV.

Signal Reconstruction

Very detailed and complete simulations have been performed to evaluate the reconstruction of photons in the ATLAS detector [19-21]. In the simulations done for this TDR, the most relevant changes and up-to-date details of the Inner Detector and of the calorimeters (*e.g.* the barrel cryostat) have been included. The impact of photon conversions on the mass resolution and on the signal reconstruction efficiency has thus been realistically evaluated.

Isolated photons have been reconstructed by applying the standard photon identification criteria, as described in Section 7.5.1. Both unconverted and converted photons have been used and the electromagnetic shower energy has been reconstructed using the procedures described in Chapter 7. The photon identification efficiency has been found to be 80%, approximately independent of p_T in the region of interest.

Simple kinematic cuts, which optimise approximately the significance of the $H \rightarrow \gamma\gamma$ signal over the mass range considered, have been applied:

- The photon candidates, ordered in p_T, were required to have transverse momenta in excess of 40 and 25 GeV ($p_T^1 > 40$ GeV and $p_T^2 > 25$ GeV).
- Both photon candidates were required to be in the pseudorapidity interval $|\eta| < 2.4$. Events with one or more photons in the region of the electromagnetic barrel/end-cap transition in an interval of $\Delta\eta = 0.15$, were rejected.

The acceptance of these kinematic cuts increases with m_H and ranges from 29% for $m_H = 80$ GeV to 58% for $m_H = 150$ GeV. It should be noted that, in comparison to the study presented in [19-14], the cut on the p_T-balance between the two photons has been removed [19-22]. This increases the signal acceptance by ~16% and the irreducible background by ~9%. The acceptance of the kinematic cuts is given in Table 19-1 as a function of m_H. In order to compute signal event rates, these numbers still have to be multiplied by the photon reconstruction efficiency. For $m_H = 90$ GeV, the photon reconstruction efficiency is somewhat lower than the nominal 80% because of the stringent cuts applied to remove the background from $Z \rightarrow ee$ decays (see the discussion of the $Z \rightarrow ee$ background below).

Table 19-1 Cross-sections (σ), branching ratios (BR), cross-sections times branching ratios ($\sigma \times$ BR), acceptances and expected mass resolutions at high luminosity for $H \rightarrow \gamma\gamma$ decays as a function of m_H.

Higgs mass (GeV)	80	90	100	110	120	130	140	150
Cross-section (pb)	38.4	32.4	27.8	24.2	21.2	18.8	17.0	15.4
Branching ratio (%)	0.089	0.119	0.153	0.190	0.219	0.222	0.193	0.138
$\sigma \times$ BR (fb)	34.2	38.6	42.5	46.0	46.4	41.8	32.8	21.2
Acceptance	0.29	0.38	0.44	0.48	0.51	0.53	0.55	0.58
Mass resolution (GeV)	1.11	1.20	1.31	1.37	1.43	1.55	1.66	1.74

The invariant mass of the two photons is reconstructed using the combined information of the EM Calorimeter and the Inner Detector, as discussed in Section 7.8.1.

An example of a reconstructed Higgs mass distribution, obtained after applying the kinematic and photon identification cuts as well as the photon conversion and primary vertex reconstruction algorithms, is shown in Figure 19-1. It has been obtained from a fully simulated sample of $H \rightarrow \gamma\gamma$ decays with m_H = 100 GeV, including the minimum-bias pile-up expected at high luminosity. The overall mass resolution, σ, is found to be 1.31 GeV. The various contributions to the total mass resolution are discussed in detail in Section 7.8.1. The interval of $\pm 1.4\sigma$ around the nominal Higgs mass, which is used for the evaluation of the signal significance, contains 79% of the fully simulated $H \rightarrow \gamma\gamma$ events. For a Gaussian distribution, this fraction is expected to be 83.8%. At low luminosity, the $\gamma\gamma$ mass resolution can be improved, since the pile-up contribution to the energy resolution of the calorimeter is largely reduced and the vertex can be reconstructed from the associated tracks. For example, for m_H = 100 GeV the mass resolution improves from 1.31 GeV to 1.10 GeV.

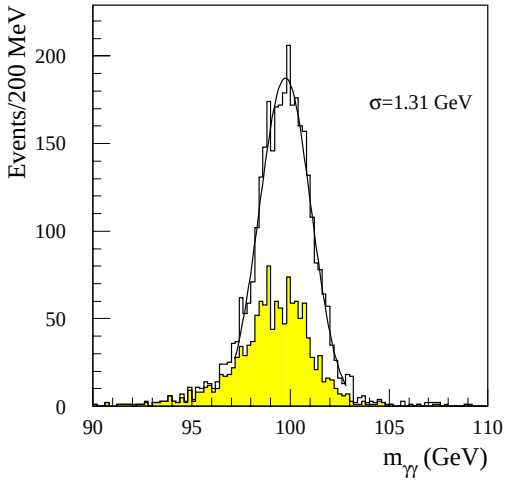

Figure 19-1 Reconstructed two-photon invariant mass for $H \rightarrow \gamma\gamma$ decays with m_H = 100 GeV at high luminosity. The shaded histogram represents events containing at least one converted photon.

Irreducible background

The irreducible background consists of genuine photon pairs produced via the following three processes: Born ($q\bar{q} \rightarrow \gamma\gamma$), box ($gg \rightarrow \gamma\gamma$), and quark bremsstrahlung ($qg \rightarrow q\gamma \rightarrow q\gamma\gamma$). The production cross-section for the sum of the Born and box processes is of the order of 1 pb / GeV in the two-photon mass range around 100 GeV. In the bremsstrahlung process, only the small fraction of events with isolated photons in the final state pass the selection criteria. It has been demonstrated [19-23] that their contribution, as generated using PYTHIA, is in good agreement with semi-analytical calculations [19-24]. After isolation cuts, this background amounts to about 50% of the combined Born plus box contribution, and has been included in the simulations by correspondingly scaling these backgrounds. The expected numbers of $\gamma\gamma$ background events in the relevant mass windows are given in Table 19-2.

Reducible background

In addition to the irreducible $\gamma\gamma$ background, other potentially large background sources have to be considered. These include jet-jet and γ-jet events in which one or both jets are misidentified as photons, as well as $Z \rightarrow ee$ decays, where both electrons are mistaken as photons. Since the production cross-sections for these processes are many orders of magnitude larger than the signal cross-sections, excellent photon / jet and photon / electron discrimination are required.

For pairs of calorimeter clusters which pass the kinematic cuts and have an invariant mass in the range from 70 GeV to 170 GeV, the ratios of the jet-jet and γ-jet cross-sections to the irreducible $\gamma\gamma$ cross-section are 2×10^6 and 8×10^2 respectively. There are large uncertainties on these ratios and on the fraction of jets which are expected to satisfy the photon identification criteria, arising

from higher-order corrections and from uncertainties in jet fragmentation. In order to reduce these backgrounds to a level well below that of the irreducible $\gamma\gamma$ continuum, rejection factors of $2\text{x}10^7$ and $8\text{x}10^3$ are required.

These rejection factors have been realistically evaluated by using large samples of fully simulated two-jet events, as described in Section 7.6. The rejection factors were then applied to estimate the cross-sections for the reducible jet-jet and γ-jet backgrounds relative to the irreducible $\gamma\gamma$-background. The results are shown in Figure 19-2 as a function of the two-photon invariant mass $m_{\gamma\gamma}$. After applying the full photon identification cuts from the calorimeter and the Inner Detector, the residual jet-jet and γ-jet backgrounds are found to be at the level of approximately 15% and 20%, respectively, of the irreducible $\gamma\gamma$ background over the mass range relevant to the $H \rightarrow \gamma\gamma$ search.

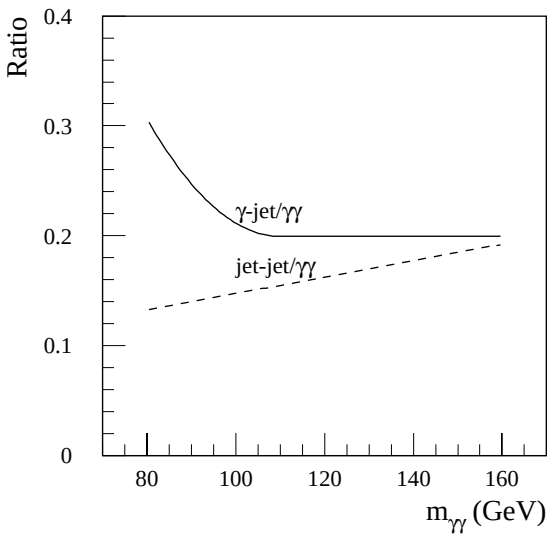

Figure 19-2 Expected ratios of the residual reducible jet-jet and γ-jet backgrounds to the irreducible $\gamma\gamma$-continuum background as a function of the invariant mass of the pair of photon candidates at high luminosity.

$Z \rightarrow ee$ background

For Higgs boson masses close to m_Z, the resonant background from $Z \rightarrow ee$ decays is potentially very dangerous. This background has a production cross-section roughly 25 000 times larger than that of the $H \rightarrow \gamma\gamma$ signal. Therefore, a rejection of ~ 500 per electron is needed to reduce it to a level below 10% of the expected $H \rightarrow \gamma\gamma$ signal. This requires that the Inner Detector vetoes electron tracks with very high efficiency.

Two classes of Z-decays have been studied with particular care in order to evaluate the expected veto efficiency. The first class consists of $Z \rightarrow ee$ (or $\mu\mu$) radiative decays with one or two photons in the final state. A careful study of these decays, which included initial- and final-state photon radiation [19-25], has shown that they produce final states for which the invariant mass of the $\gamma\gamma$ (or γe pair) is no longer resonant, as shown by the dashed histogram in Figure 19-3. If an electron veto efficiency of 99.8% is assumed, approximately equal contributions from $\gamma\gamma$ and γe radiative pairs are found. The contribution from $Z \rightarrow \mu\mu\gamma\gamma$ decays corresponds to about 20% of the total contribution from $Z \rightarrow ee$ radiative decays. Since the Z radiative decay background is smooth above 80 GeV, and is much smaller than the irreducible $\gamma\gamma$ background, it can be neglected.

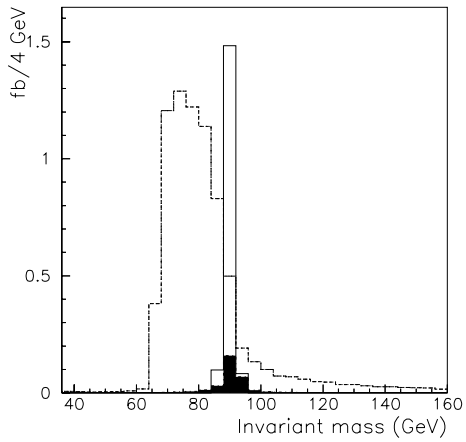

Figure 19-3 Reconstructed two-photon invariant mass for $H \rightarrow \gamma\gamma$ decays with m_H = 90 GeV (full histogram), for $Z \rightarrow ee\gamma$ (γ) and $Z \rightarrow \mu\mu\gamma\gamma$ decays (dashed histogram) and for $Z \rightarrow ee$ decays (black area) after electron veto cuts.

The second class of background from $Z \rightarrow ee$ decays consists of events where both electrons are misidentified as photons after undergoing very hard bremsstrahlung in the material of the Inner Detector at small radius (beam pipe and vertexing layers). As discussed in Section 7.7, detailed studies on the reconstruction of electrons with a p_T of 40 GeV over the full pseudorapidity coverage have been performed. Using an electron / photon separation algorithm based on two complementary pattern recognition programs and a photon conversion finder, an electron veto inefficiency as low as 0.19% can be reached for $Z \rightarrow ee$ events at the expense of an additional inefficiency for photon identification. The efficiency loss for photons depends on the luminosity. For a sample of $H \rightarrow \gamma\gamma$ events, it has been estimated to be 3.3% at low luminosity and 5.6% at high luminosity. The loss of signal efficiency has been included in the calculation of the expected event rates for m_H = 90 GeV. Figure 19-3 shows the expected $\gamma\gamma$ mass distribution for the remaining $Z \rightarrow ee$ events after applying the track veto described above. The rms width of the peak is found to be 4.4 GeV, which is therefore significantly larger than the expected one for normal $Z \rightarrow ee$ events and for $H \rightarrow \gamma\gamma$ events in this mass range. Although the residual $Z \rightarrow ee$ background remains resonant, its contribution to the $H \rightarrow \gamma\gamma$ signal for $m_H = m_Z$ is less than 10%.

Signal Observability

The expected $H \rightarrow \gamma\gamma$ signal significances, defined for each mass point as $S/\sqrt{B}$ where S and B are the numbers of accepted signal and background events in the chosen mass window of $\pm 1.4\sigma_m$, are given in Table 19-2 for an integrated luminosity of 100 fb^{-1}. The contributions from the irreducible and reducible backgrounds are accounted for in these estimates. In addition to the signal events from direct production, events from the associated production of a Higgs boson with a W or Z boson or a $t\bar{t}$-pair have been included in the signal. Due to the larger hadronic activity in the events arising from associated production, the efficiency of the photon isolation cuts is slightly lower than the values found for the direct production (see Section 19.2.2.2).

Table 19-2 Observability of the $H \rightarrow \gamma\gamma$ signal (direct and associated production) for 80 < m_H < 150 GeV. The expected numbers of signal and background events in the mass window, chosen to be $m_H \pm 1.4\sigma$, are given for an integrated luminosity of 100 fb^{-1}. The signal significances are given for integrated luminosities of 100 fb^{-1} (high luminosity) and 30 fb^{-1} (low luminosity).

Higgs mass (GeV)	**80**	**90**	**100**	**110**	**120**	**130**	**140**	**150**
Signal events (direct production)	502	655	947	1110	1190	1110	915	617
Signal events (WH, ZH, $t\bar{t}H$ production)	85	76	98	97	93	76	58	35
$\gamma\gamma$ background	41 700	41 000	41 400	35 000	29 000	24 700	20 600	16 900
Jet-jet background	5400	5600	5950	5300	4600	4100	3550	3050
γ-jet background	12500	10600	9100	7000	5800	4900	4100	3400
$Z \rightarrow ee$ background	-	< 70	-	-	-	-	-	
Stat. significance for 100 fb^{-1}	2.4	3.1	4.4	5.6	6.5	6.5	5.8	4.3
Stat. significance for 30 fb^{-1}	1.5	1.9	2.7	3.4	3.9	4.0	3.5	2.6

For an integrated luminosity of 100 fb^{-1}, a Standard Model Higgs boson in the mass range between 105 GeV and 145 GeV can be observed with a significance of more than 5σ by using the $H \rightarrow \gamma\gamma$ channel alone. Table 19-2 also contains the estimated significances of the $H \rightarrow \gamma\gamma$ channel for an integrated luminosity of 30 fb^{-1}, corresponding to the first three years of LHC operation. The significances at low luminosity have been evaluated by taking the resulting improvements in mass resolution and background rejection into account. A signal in the $\gamma\gamma$ channel can only be seen in this case with a significance of ~ 4σ over a narrow mass range between 120 and 130 GeV.

The significances quoted in Table 19-2 are slightly higher than the ones given in the Technical Proposal. The main reason for this is the removal of the so called p_T-balance cut, which was applied in order to suppress bremsstrahlung background. Although without this cut the background increases, there is a net gain in the significance. Another reason is the slightly improved mass resolution which is mainly due to a more sophisticated photon energy reconstruction, separating converted and non-converted photons. These gains are somewhat offset by the higher reducible background.

As an example of signal reconstruction above background, Figure 19-4 shows the expected signal from a Higgs boson with m_H = 120 GeV for an integrated luminosity of 100 fb^{-1}. The $H \rightarrow \gamma\gamma$ signal is clearly visible above the smooth $\gamma\gamma$ background, which is dominated by the irreducible continuum of real photon pairs.

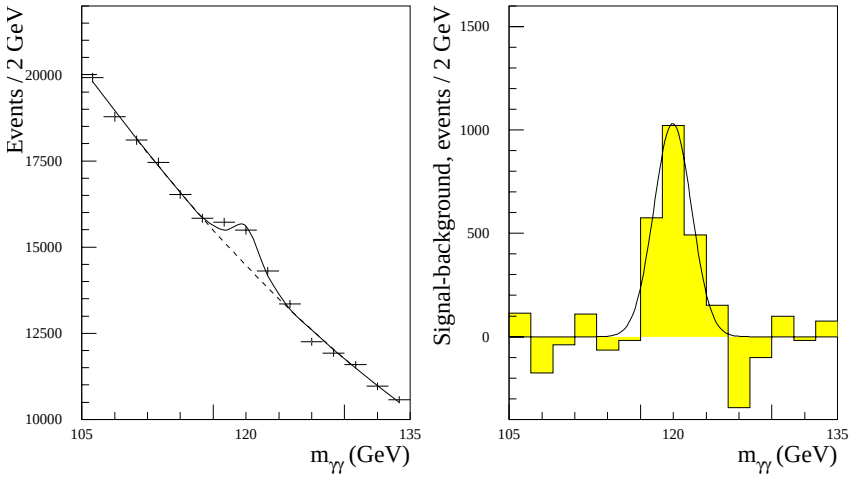

Figure 19-4 Expected $H \rightarrow \gamma\gamma$ signal for m_H = 120 GeV and for an integrated luminosity of 100 fb^{-1}. The signal is shown on top of the irreducible background (left) and after subtraction of this background (right).

19.2.2.2 Associated production: *WH*, *ZH* and $t\bar{t}H$

The production of the Higgs boson in association with a W or a Z boson or with a $t\bar{t}$ pair can also be used to search for a low-mass Higgs boson. The production cross-section for the associated production is almost a factor 50 lower than for the direct production, leading to much smaller signal rates. If the associated W / Z boson or one of the top quarks is required to decay leptonically, thereby leading to final states containing one isolated lepton and two isolated photons, the signal-to-background ratio can nevertheless be substantially improved with respect to the direct production. In addition, the vertex position can be unambiguously determined by the lepton charged track, resulting in better mass resolution at high luminosity than for the case of direct $H \rightarrow \gamma\gamma$ production.

There are many sources of reducible and irreducible backgrounds, which have been evaluated in a recent study [19-26]. The signal reconstruction proceeds along similar lines to the case of direct production. Two isolated photons and one lepton are searched for over $|\eta| < 2.4$. Simple kinematic cuts are applied, requiring that the transverse momenta of the photons and of the lepton exceed 25 GeV. As for direct $H \rightarrow \gamma\gamma$ production, events with one or more photons or the lepton in the crack region between the barrel and the end-cap calorimeter, in a region of $\Delta\eta = 0.15$, are rejected. In order to suppress the reducible background from QCD jet and $t\bar{t}$ production and from final-state photon radiation, additional isolation criteria are applied: the distance ΔR between each photon and each reconstructed jet cluster is required to be larger than 0.4. This separation criterion is also applied to the $\gamma\gamma$ and γl separation, *i.e.* $\Delta R_{\gamma\gamma} > 0.4$ and $\Delta R_{\gamma l} > 0.4$. After applying these cuts, the signal acceptance for $m_H = 100$ GeV is found to be 31% for WH and ZH events and 29% for $t\bar{t}H$ events. The slightly lower acceptance for $t\bar{t}H$ events is due to the larger jet activity in these events, which affects the efficiency of the separation criteria described above. These acceptances have to be multiplied by the reconstruction efficiencies for the photons and leptons. These have been estimated using fully simulated signal events and found to be compatible with those assumed for direct $H \rightarrow \gamma\gamma$ production, thereby indicating that the separation criteria quoted above lead to reconstructed final states with well isolated photons and leptons. The mass dependence of the acceptance is given in Table 19-3 for Higgs boson masses in the range between 80 and 140 GeV.

The irreducible background has been evaluated by considering the $W\gamma\gamma$, $Z\gamma\gamma$, $t\bar{t}\gamma\gamma$ and $b\bar{b}\gamma\gamma$ processes. In particular, radiation of photons from the leptons in the final state has been found to be important. They have been evaluated using the PYTHIA event generator in conjuction with the PHOTOS program [19-27]. After the kinematic cuts described above, the $Z\gamma\gamma$ background, where one photon is radiated from a final-state lepton, is dominant. This background has been further suppressed by requiring the lepton-photon mass, $m_{\gamma l}$, to be above a given threshold, $m_{\gamma l} > 25$ GeV, for any lepton-photon combination and to be outside a mass window of ± 8 GeV around the Z-boson mass. To further improve this rejection, events with a second lepton of the same flavour and opposite charge with $p_T > 10$ GeV are vetoed. These additional cuts reject the dominant $Z\gamma\gamma$ background by a factor 3.6, whereas the signal efficiency for $m_H = 100$ GeV is found to be 74%. The efficiency values as a function of m_H are given in Table 19-3.

There are also many sources of reducible backgrounds. Final states containing one, two or three jets in association with a lepton or a photon, such as $\gamma\gamma$-jet, γl-jet, γ-jet-jet, l-jet-jet and jet-jet-jet, have been considered [19-26]. In each case, the γ/jet or lepton/jet rejection factors, as determined from the full detector simulation (see Sections 7.4 and 7.6), have been applied. The total reducible background is estimated to be at the level of 20 - 30% of the irreducible one over the mass range considered, as shown in Table 19-3. The main contributions to the remaining reducible background arise from $t\bar{t} \rightarrow \gamma l$-jet final states, from associated $\gamma\gamma$-jet production, and from associated $W\gamma$+jet $\rightarrow l\gamma$+jet final states.

For the determination of the signal significance, only events in the mass window $m_H \pm 1.4\sigma$ are considered. Compared to direct $H \rightarrow \gamma\gamma$ production, the mass resolution at high luminosity is slightly improved, due to the precise determination of the z-position of the vertex by the lepton track. As an example, for $m_H = 100$ GeV, the mass resolution improves from 1.31 GeV to 1.23 GeV. Results from full simulation described in Section 19.2.2 show that, the acceptance in the mass window is 79%.

Table 19-3 Cross-sections times branching ratios, σ x BR, (sum of *WH*, *ZH* and $t\bar{t}H$), acceptances and expected numbers of signal and background events for associated Higgs production with $H \rightarrow \gamma\gamma$ decay and for $80 < m_H < 140$ GeV at high luminosity. The expected numbers of events and the statistical significances are given for an integrated luminosity of 100 fb^{-1}.

Higgs mass (GeV)	**80**	**100**	**120**	**140**
$\sigma \times$ BR (fb)	1.55	1.44	1.22	0.65
Acceptance of kin. cuts	0.24	0.30	0.31	0.32
Acceptance of mass cuts	0.70	0.74	0.78	0.79
Signal events	12.2	14.7	13.2	7.5
Irreducible background	6.0	5.7	4.4	3.2
Reducible background	1.3	1.4	1.3	1.3
Statistical significance	3.7	4.3	4.3	2.8

Using Poisson statistics, the probability to observe a statistical fluctuation in the background such that the total number of observed events would be larger than the sum of signal and background events, has been evaluated. The results, expressed in the usual units of Gaussian standard deviations, are given in the last row of Table 19-3. The statistical significances in this channel are found to be around 4.3σ for masses in the range between 100 and 120 GeV. The observation of this channel therefore represents an independent confirmation of a possible Higgs boson discovery for integrated luminosities above 100 fb^{-1}. It would also provide valuable information for the determination of the Higgs couplings to vector bosons and to the top quark. Because of the very small signal rate, this channel is not believed to have any discovery potential at low luminosity.

19.2.2.3 Associated production: *H* + jet $\rightarrow \gamma\gamma$ + jet

It has been argued that the observability of a Higgs boson in the γγ decay mode can be improved at the LHC by considering the associated production of a Higgs boson with one or two hard jets [19-28][19-29].

In addition to higher-order corrections to direct Higgs production (*e.g.* $gg \rightarrow Hg$), there are other production mechanisms which lead to the associated production of a Higgs boson with high-p_T jets. First there is the *WW* fusion process, which produces Higgs bosons in association with two jets which appear as tag jets in the forward regions of the detector (see Section 19.2.10). For a low-mass Higgs boson, this contribution to the total production cross-section is, however, only ~ 10%. Secondly, there is the associated production (*WH*, *ZH*, and $t\bar{t}H$), where jets from hadronic decays of the vector bosons or the top quarks are present in the final state. For these processes, jets appear in association with the Higgs boson already at the Born level, whereas they appear as a result of the higher-order QCD corrections for the dominant *gg* fusion process. Given the large contribution of the *gg* fusion to the total Higgs production cross-section, these higher-order QCD contributions are nevertheless expected to give a large contribution to inclusive *H*+jet production.

A study of the observability of *H+jet* with $H \rightarrow \gamma\gamma$ production has been recently carried out for the ATLAS detector [19-30]. The cross-sections for the associated production of a Higgs boson with a *W/Z* and a $t\bar{t}$ pair as well as for the *WW* fusion process have been obtained from the standard PYTHIA event generator. For the *gg* fusion process, the available first-order QCD ma-

trix-element calculation, *i.e.* at order α_s^3, [19-31] has been used. Unfortunately, such calculations are not available now for the dominant irreducible $\gamma\gamma$ background. A calculation exists for the $q\bar{q}$ subprocess, but not for the *gg* box-contribution. Due to the lack of a complete calculation for the $\gamma\gamma$ background, any such study would suffer at present from large uncertainties in the background estimates. A consistent treatment of the signal and the background can only be done when appropriate higher-order calculations will be available for both. In the analysis presented below, the signal contribution from direct $H \rightarrow \gamma\gamma$+jet production is estimated by using both the parton-shower approach and the available first-order matrix-element calculation. The results from both these approaches are used to estimate the uncertainties on the signal significance in this channel.

In the analysis, H+jet $\rightarrow \gamma\gamma$+jet final states are selected by applying the following criteria:

- Two isolated photons with $p_T^1 > 60$ GeV and $p_T^2 > 40$ GeV, within $|\eta| < 2.4$. As for the direct $\gamma\gamma$ analysis, events with photons in the barrel / end-cap transition region ($\Delta\eta = 0.15$) are rejected. In addition, a threshold on the transverse momenta of the photon system is also required $p_T^{(\gamma 1+\gamma 2)} > 50$ GeV.
- At least two reconstructed jets with:

  $E_T > 40$ GeV over $|\eta| < 2.4$ or $E > 800$ GeV over $2.4 < |\eta| < 4.6$.
- The distance ΔR between the jet and each photon is required to be $\Delta R > 1.5$. This cut is introduced to suppress bremsstrahlung contributions, where photons are radiated from the final-state quarks.

The expected numbers of signal and background events after applying this selection are given in Table 19-4 for an integrated luminosity of 100 fb^{-1}. The numbers shown in Table 19-4 for the expected signal rates demonstrate clearly that they depend strongly on the method chosen to generate the events. If the matrix-element approach is used, the *gg* fusion process accounts for most of the signal rate. The respective contributions of *WW* fusion and associated production amount to 35% and 10% of the total signal rate. In contrast, if the parton-shower approach is used, the contribution to the signal from direct H+jet production via *gg* fusion is decreased by a factor of 10, resulting in a total signal which is lower by a factor of two.

The dominant background contribution arises from quark bremsstrahlung. It should, however, be noted that, due to the lack of a complete higher-order calculation, the contribution from the $\gamma\gamma$ irreducible background has been estimated using the parton-shower approach, which most likely leads to an underestimate of the real contribution, as indicated by the results obtained for the signal.

Estimates of the signal significance are given in Table 19-4 for both approaches (matrix-element and parton-shower). In the absence of an appropriate $\gamma\gamma$ background calculation in the case of the matrix-element approach, the parton-shower estimate for this background has been scaled up by the same factor of 10 as found for the signal. In all cases, the significances shown in Table 19-4 are lower than those obtained for the inclusive direct $H \rightarrow \gamma\gamma$ signal, in addition to being affected by large theoretical uncertainties.

In summary, it might be possible to enhance the significance of a low-mass Higgs boson discovery in the $\gamma\gamma$ channel at the LHC, by looking for the associated production of $H \rightarrow \gamma\gamma$ decays with two jets. The simulated signal rate itself is very sensitive to the method used to generate the events. Given the large uncertainties reported here, this channel may be of interest as a confir-

Table 19-4 Expected rates for signal and background processes contributing to $\gamma\gamma$ + two jet final states for an integrated luminosity of 100 fb^{-1}. The signal contributions and statistical significances are given separately for the matrix-element and the parton-shower calculations of direct production of Higgs bosons associated with jets.

Higgs mass (GeV)	**100**	**120**	**140**
$gg, qg, q\bar{q} \rightarrow H + g\ (q)$ (matrix-element)	36	56	52
$gg, q\bar{q} \rightarrow H$ (parton-shower)	3	6	9
WW fusion ($qq \rightarrow qq\ H$)	24	35	30
Associated production ($WH/ZH, t\bar{t}H$)	9	10	8
Total signal (matrix-element)	70	101	90
Total signal (parton-shower)	36	51	47
$\gamma\gamma$ irreducible background	16	30	39
Bremsstrahlung: $qq \rightarrow g\ \gamma$, $qg \rightarrow q\ \gamma$	113	67	100
Total background	129	97	139
Total background (scaled, see text)	273	367	490
Statistical significance (matrix-element and scaled background, see text)	4.2	5.3	4.1
Statistical significance (parton-shower)	3.2	5.2	4.0

mation of a potential signal, but cannot at present be considered as a discovery channel. More solid conclusions may be drawn when higher-order calculations for all background processes and / or measurements from the Tevatron become available.

In a similar analysis, the associated production of a Higgs boson with a single jet, as suggested in [19-29], has also been investigated and the details are reported in [19-30]. In this case also, a better theoretical understanding is needed before large signal significances can be claimed.

19.2.3 $H \rightarrow Z\gamma$

$H \rightarrow Z\gamma$ is another rare decay mode of the Standard Model Higgs boson. As in the case of the $\gamma\gamma$ decay, the branching ratio for this channel is only significant in the limited mass range between 100 and 160 GeV. In addition, it has to be multiplied by the $Z \rightarrow ll$ branching ratio, which is about 6.6% (electrons and muons). The production cross-section times branching ratio is below 2.6 fb in the mass range 120 - 160 GeV. Both the signal and the backgrounds have been evaluated using the fast simulation, and the sensitivity is found to be below 1.4 σ with a signal-to-background ratio of 2.5% [19-32].

19.2.4 $H \rightarrow b\bar{b}$

19.2.4.1 General considerations

If the mass of the Standard Model Higgs boson is lighter than 2 m_W, the $H \rightarrow b\bar{b}$ decay mode is dominant with a branching ratio of ~ 90 %. The observation of such a characteristic signature would be important for both the Higgs discovery and for the determination of the nature of any resonance observed in this mass region. Since the direct production, $gg \rightarrow H$ with $H \rightarrow b\bar{b}$, cannot be efficiently triggered nor extracted as a signal above the huge QCD two-jet background, the associated production with a W or Z boson or a $t\bar{t}$ pair remains as the only possible process to observe a signal from $H \rightarrow b\bar{b}$ decays. The leptonic decays of the W boson or semi-leptonic decays of one of the top quarks provide an isolated high-p_T lepton for triggering. In addition, requiring this high-p_T lepton provides a large rejection against background from QCD jet production. The Higgs-boson signal might thus be reconstructed as a peak in the invariant jet-jet mass spectrum of tagged b-jets.

Both the WH and the $t\bar{t}H$ channels have already been studied for the ATLAS Technical Proposal [19-14]. The analysis was complex and it became clear that excellent b-tagging capabilities are needed. The major difficulties in extracting a reliable signal from either of these two channels are the combination of a small signal and the need for an accurate control of all the background sources. The analyses have been repeated for this document, using the expected performance of the final ATLAS detector configuration. In the case of the $t\bar{t}H$ channel, the analysis has also been significantly improved. In the new analysis presented here, both top-quark decays are completely reconstructed. This provides a significantly better signal-to-background ratio and a reduction of the combinatorial problem in the b-jet assignment to the Higgs boson decay.

Other channels involving $H \rightarrow b\bar{b}$ decays have been suggested in the literature [19-33]. They have so far not been considered by ATLAS for the following reasons:

- ZH production with $Z \rightarrow ll$: this channel would provide a rate about six times lower than the WH channel. In addition, although $t\bar{t}$ production does not contribute significantly to the background in this channel, gg $\rightarrow$ Z$b\bar{b}$ production with $Z \rightarrow ll$ is only a factor 1.8 smaller in rate than the W$b\bar{b}$ background with $W \rightarrow l\nu$, and the signal-to-background ratio would therefore not be significantly improved with respect to the WH channel.
- ZH production with Z $\rightarrow \nu\nu$: it would be difficult to trigger efficiently on such final states. In addition, this channel suffers from potentially very large experimental backgrounds, given the rather low E_T^{miss} expected for the signal.
- $b\bar{b}H$ production: this process is also difficult to trigger on with high efficiency. However, $b\bar{b}H$ production may be significantly enhanced in supersymmetric extensions of the Standard Model and a detailed study has been carried out in the MSSM framework (see Section 19.3.2.8). This study has shown that, even if the trigger problem is ignored, a signal can only be extracted for large values of tanβ, where the enhancement is large. Therefore, this channel does not provide any discovery potential for the Standard Model Higgs boson.

In the following, the main features of the analyses of the WH (search for $l\nu b\bar{b}$ final states [19-34]) and $t\bar{t}H$ (search for $l\nu jjb\bar{b}b\bar{b}$ final states [19-35]) channels are summarised. These analyses have been performed using the fast simulation (see Section 2.5). Crucial aspects of the b-tagging performance (see Section 10.6) and of the invariant mass reconstruction of b-jet pairs (see Section 9.3) are in agreement with the results obtained from the full detector simulation.

Table 19-5 shows the production cross-sections for the signal with m_H = 100 GeV and for some important background processes. The signal cross-sections for $l\nu b\bar{b}$ (WH production) and $l\nu jjb\bar{b}b\bar{b}$ ($t\bar{t}H$ production) final states are of the same order. The reducible backgrounds from W+jet and $t\bar{t}$ production are huge, with cross-sections orders of magnitudes larger than the signal cross-sections. In addition to the large non-resonant backgrounds, there is also WZ production, which constitutes a dangerous resonant background for the WH signal.

Table 19-5 Cross-sections times branching ratios for WH and $t\bar{t}H$ production and for various background processes. All relevant branching ratios ($W \to l\nu$, $W \to jj$, $H \to b\bar{b}$ and $Z \to b\bar{b}$) are included.

Final state: $l\nu b\bar{b}$ + X	**σ (pb)**
WH (m_H = 100 GeV)	0.40
WZ	0.86
W$b\bar{b}$	70
$t\bar{t}$	247
$W^* \to tb$	1.4
$qg \to tbq$	45
Wjj (two jets with p_T > 15GeV, $\|\eta\|$ < 3.2)	4640
Final state: $l\nu$ jj $b\bar{b}$ $b\bar{b}$ + X	
$t\bar{t}H$ (m_H = 100 GeV)	0.29
$t\bar{t}Z$	0.02

Some of the features of the event topology are common to both channels:

- One trigger lepton with p_T > 20 GeV (electron) or p_T > 6 GeV (muon) within $|\eta|$ < 2.5. At high luminosity, these respective p_T-thresholds are raised to 30 GeV and 20 GeV.
- Jets from $H \to b\bar{b}$ decay with p_T > 15 GeV and within $|\eta|$ < 2.5. Reconstructed jet energies are recalibrated on average back to the original parton energies. After recalibration, the jet-jet mass peak from $H \to b\bar{b}$ decays is positioned at the nominal Higgs-boson mass. About 85% of the events are reconstructed inside a mass window of ±22 GeV around the nominal Higgs-boson mass. The b-tagging performance is simulated assuming the nominal efficiencies of respectively 60% and 50% at low and high luminosity. It should be noted, that the expected numbers of signal and background events, and, in particular, the ratio of reducible to irreducible background, depend on the optimisation of the b-tagging efficiency versus the rejection of non-b jets. A detailed study of this important issue is presented in Chapter 10.

Because of the quite different final-state topologies and of the different backgrounds in the WH and $t\bar{t}H$ channels, the final selection criteria are different for each channel and are described in the following.

19.2.4.2 *WH* channel

The background to the WH channel can be divided into three classes.

- Irreducible background from $WZ \to l\nu b\bar{b}$ and from $Wb\bar{b}$ production. The former produces a peak at m_Z in the $b\bar{b}$ mass distribution, and is therefore of special concern. The latter is dominated by $q\bar{q} \to Wg \to Wb\bar{b}$, and also has a small contribution from $q\bar{q} \to W^* \to \bar{t}b \to Wb\bar{b}$.
- Reducible background with at least two b-quarks in the final state, which arises predominantly from $t\bar{t} \to WWb\bar{b}$ and, to a lesser extent, from single top production through $gq \to t\bar{b}q \to l\nu b\bar{b} + q$.
- Reducible background containing jets misidentified as b-jets, which arises mainly from W+*jet* production. Its magnitude depends critically on the quality of the b-tagging.

In order to reduce these large backgrounds, the following selection criteria are applied:

- At least one isolated trigger lepton, fulfilling the pre-selection requirements described above.
- Two tagged *b*-jets fulfilling the pre-selection requirements described above.
- Lepton veto: no additional lepton is reconstructed with $p_T > 6$ GeV and within $|\eta| < 2.5$.
- Jet veto: no additional jets are reconstructed with $p_T > 15$ GeV within $|\eta| < 5.0$. This veto is applied mostly to reject the large $t\bar{t}$ background.
- Mass cut: events are kept if the invariant mass of the two tagged *b*-jets is reconstructed in a mass window of ±22 GeV (*i.e.* around $\pm 2\sigma_m$) around the nominal Higgs-boson mass.

The total expected kinematic acceptances, excluding the *b*-tagging and lepton identification and reconstruction efficiencies, are 12.5% for signal, 1.4% for *Wjj* and 0.2% for $t\bar{t}$. The jet veto alone reduces the $t\bar{t}$ background by a factor of 30. The signal acceptance has been estimated to be 82% in a mass window of ±20 GeV from full simulation studies (see Section 9.3.2).

The expected numbers of signal and background events in the chosen mass window are given in Table 19-6 for three different Higgs-boson masses and for an integrated luminosity of 30 fb^{-1}. The background is dominated by *Wjj* events and decreases rapidly with increasing mass. Over the mass range considered here, the ratio between the reducible and irreducible background is about 70 %. With increasing m_H, the signal production cross-section decreases, but the backgrounds from W$b\bar{b}$, *Wjj* and *Wjb* are also about a factor of two lower for $m_H = 120$ GeV than for $m_H = 80$ GeV.

Table 19-6 Expected WH, $H \rightarrow b\bar{b}$ signal and background rates inside the mass window for three different Higgs-boson masses, assuming the nominal b-tagging performance and an integrated luminosity of 30 fb^{-1}.

Higgs mass (GeV)	**80**	**100**	**120**
$WH, H \rightarrow b\bar{b}$	650	416	250
$WZ, Z \rightarrow b\bar{b}$	540	545	220
$Wb\bar{b}$	3400	3650	2000
$t\bar{t} \rightarrow WWb\bar{b}$	2500	3700	3700
tb, tbq	500	740	740
Wbj, Wjj	12500	7600	4160
$R_{\text{red/irred}}$	0.75	0.70	0.65
Total background	19440	16235	10820
S/B	3.3%	2.5%	2.3%
$S/\sqrt{B}$	4.7	3.3	2.4
$S/\sqrt{B}$ incl. syst. (see text)	3.0	1.9	1.7

The invariant $b\bar{b}$ mass distributions for the signal and background events passing the selection criteria are shown in Figure 19-5. The residual $t\bar{t}$ and *Wjj* background distributions are reasonably flat. The W$b\bar{b}$ background peaks however around 60 GeV and the *WZ* resonant background obviously peaks around m_Z.

The expected *WZ* background contribution is shown above the sum of the non-resonant continuum backgrounds in Figure 19-6, for an integrated luminosity of 30 fb^{-1}. An example of the expected $H \rightarrow b\bar{b}$ signal is shown in Figure 19-7 for $m_H = 100$ GeV. These figures illustrate the difficulty of extracting a resonant signal from $b\bar{b}$ pairs in this mass range, due to the low expected signal-to-background ratios and the rapidly varying shape of the summed background, which for the present selection is peaked around 80 GeV. For more details see [19-36].

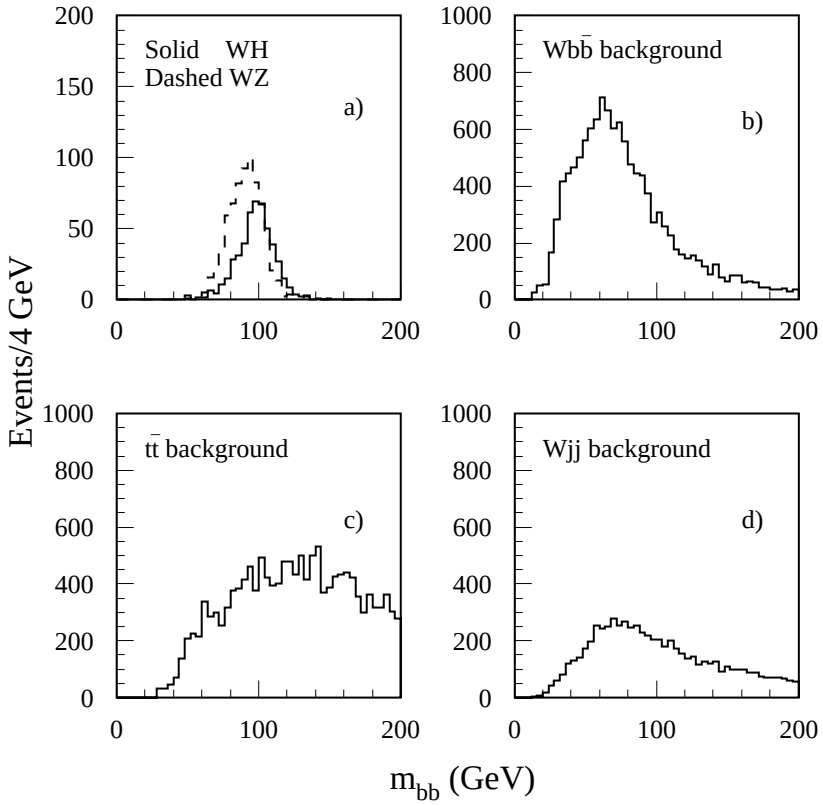

Figure 19-5 Invariant $b\bar{b}$ mass distributions for the *WH* signal and background events, after applying all selection criteria and for an integrated luminosity of 30 fb^{-1}: a) *WH* signal with m_H = 100 GeV (solid line) and resonant *WZ* background (dashed line), (b) $Wb\bar{b}$ background, (c) $t\bar{t}$ background, and (d) *Wjj* background.

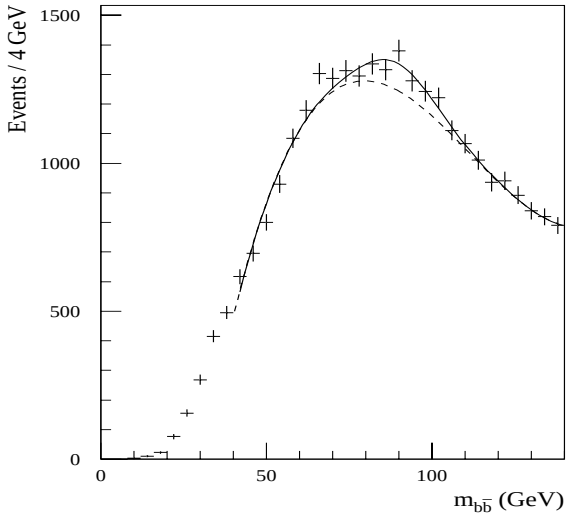

Figure 19-6 Expected *WZ* signal with $Z \rightarrow b\bar{b}$ above the summed background, for an integrated luminosity of 30 fb^{-1}. The dashed line represents the shape of the background.

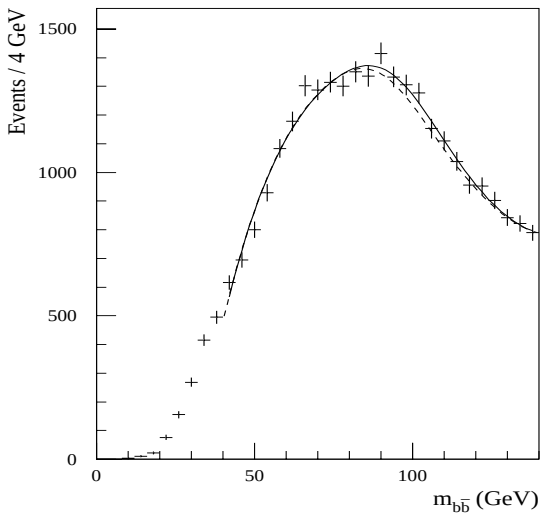

Figure 19-7 Expected *WH* signal with $H \rightarrow b\bar{b}$ above the summed background for m_H = 100 GeV and for an integrated luminosity of 30 fb^{-1}. The dashed line represents the shape of the background.

As shown in Table 19-6, a WH signal might be extracted if one assumes that the various background distributions are all perfectly known. Even in this optimistic scenario, the signal significance is at best 4.7σ for $m_H = 80$ GeV and is below 3σ for values of m_H above the ultimate sensitivity expected for LEP2. These numbers correspond to an integrated luminosity of 30 fb^{-1} expected to be reached over three years of initial operation at low luminosity. It is not clear in all cases how to achieve an accurate knowledge of the various backgrounds from the data.

- The most dangerous background from WZ production will be rather precisely measured through the background-free $WZ \rightarrow l\nu ll$ final states. Clearly, the observation of the WZ, $Z \rightarrow b\bar{b}$ final state above the continuum backgrounds would be an important first step in demonstrating the feasibility of extracting a WH signal at larger values of $m_{b\bar{b}}$.
- The shape and magnitude of the Wjj background can be constrained by varying the b-tagging cuts, assuming that this does not bias the $b\bar{b}$ mass distribution.
- The shape and magnitude of the $t\bar{t}$ background can be constrained by varying the jet-veto cuts, since it has by far the largest sensitivity to these cuts.
- The shape and magnitude of the W$b\bar{b}$ background cannot be obtained directly from the experimental data and one will have to rely on Monte Carlo simulations, which can to some extent be normalised to the experimental data in the mass regions where no signal from $H \rightarrow b\bar{b}$ decays is expected. If a systematic uncertainty of ±5% on the shape of the W$b\bar{b}$ background is assumed in the $H \rightarrow b\bar{b}$ signal region, the statistical significances are reduced considerably, as shown in Table 19-6.

Searches for WH, $H \rightarrow b\bar{b}$ final states at high luminosity will be further complicated by the impossibility of applying the tight jet-veto cuts described here (this would result in a substantial increase of the $t\bar{t}$ background) and by the need to increase the jet p_T threshold from 15 GeV to 30 GeV. In addition, the $H \rightarrow b\bar{b}$ mass resolution will be also somewhat degraded and this channel is not considered promising for searches at high luminosity.

In conclusion, the extraction of a signal from $H \rightarrow b\bar{b}$ decays in the WH channel will be very difficult at the LHC, even under the most optimistic assumptions for the b-tagging performance and calibration of the shape and magnitude of the various background sources from the data itself.

19.2.4.3 $t\bar{t}H$ channel

The cross-section for associated $t\bar{t}H$ production [19-34][19-35] is about the same as for WH production (see Table 19-5). The final state is however considerably more complex, since it consists of two W bosons and four b-jets. The W bosons and two b-jets come from the top-quark decays, and the other two b-jets from the Higgs boson decay. For trigger purposes, one of the W bosons is required to decay leptonically, whereas the other one is assumed to decay into a $q\bar{q}$ pair. In order to reliably extract the signal, the analysis requires that both top quarks be fully reconstructed. This method reduces considerably the large combinatorial background in the signal events themselves, since two of the b-jets are associated to the top decays, and therefore the remaining two should come from the Higgs boson decay. The signal should appear as a peak in the $m_{b\bar{b}}$ distribution, above the various background processes, which are classified as follows:

- Irreducible backgrounds, such as resonant $t\bar{t}Z$ and continuum $t\bar{t}b\bar{b}$ production. Since the $t\bar{t}Z$ cross-section is much smaller than the signal cross-section (see Table 19-5), the resonant background is not a problem in this channel.

- Reducible backgrounds containing jets misidentified as *b*-jets, such as $t\bar{t}jj$, *Wjjjjjj*, $WWb\bar{b}jj$, *etc*. The *Wjjjjjj* and $WWb\bar{b}jj$ backgrounds are suppressed to a large extent by the reconstruction of both top decays.

The following basic selection is applied before the *W* and top decay reconstruction are performed:

- One trigger lepton, fulfilling the pre-selection requirements described above.
- At least six jets with $p_T > 15$ GeV. The p_T threshold is raised to 30 GeV at high luminosity.
- Exactly four jets tagged as *b*-jets.

The *W* bosons are reconstructed from the jets not tagged as *b*-jets and from the reconstructed lepton and the neutrino. In the case of the leptonic decay, the *W* mass constraint is used to determine the longitudinal component of the neutrino. In order to improve the mass resolution for the reconstructed top quarks, the jet-jet invariant mass (within a ±25 GeV window around m_W) is also corrected to the nominal *W* mass, by scaling the corresponding four-vectors. Ambiguities arise in the pairing of the two *W* bosons with two of the four *b*-jets. These ambiguities are resolved by selecting from all *lνb-jjb* combinations the one which minimises $\chi^2 = (m_{jjb} - m_t)^2 + (m_{l\nu b} - m_t)^2$. It has been checked using the background samples [19-35], that this procedure does not introduce artificial peaks in the reconstructed mass spectrum of the two remaining *b*-jets. It should be noted that the reconstruction of the top signal is used to suppress background from *W+jet* events, but mainly to minimise the combinatorial background from the signal events themselves.

Most of the results presented below come from fast simulation of signal and background events. The quoted resolutions and acceptances have been confirmed with the full simulation of signal events for low-luminosity operation, see Section 9.3.4 and Section 2.5.

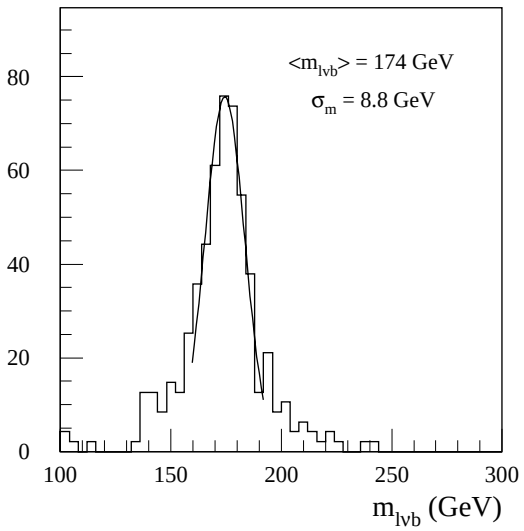

Figure 19-8 For fully simulated and reconstructed events (the $W \to l\nu$ reconstructed with fast simulation) the reconstructed top mass from $t \to l\nu b$ decays in $t\bar{t}H$ signal events with $m_H = 100$ GeV and for low-luminosity performance after the χ^2 selection (see text).

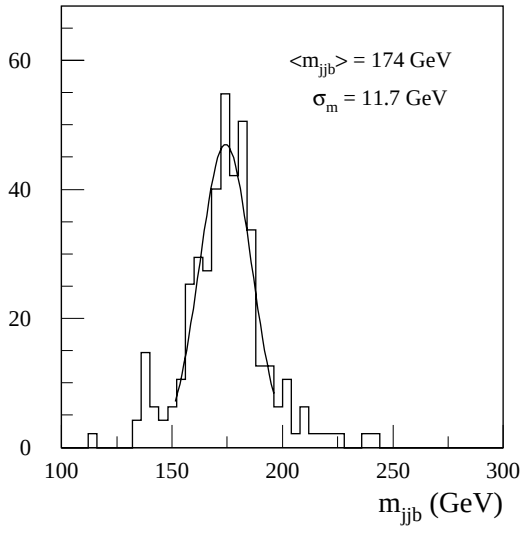

Figure 19-9 Same as Figure 19-8, but for the reconstruction of $t \to jjb$ decays.

The distributions of the reconstructed top masses ($m_{l\nu b}$ and m_{jjb}) for fully simulated events are shown in Figures 19-8 and 19-9 for $t\bar{t}H$ signal events with m_H = 100 GeV (see also Section 9.3.4). It should be noted that, due to the χ^2 selection, the mass distributions are somewhat biased towards the nominal top mass and therefore do not represent a true measure of the mass resolution. To further reject wrongly reconstructed top decays, only those events are kept, for which both top masses have been reconstructed to lie within ±20 GeV (*i.e.* ~ ±2σ) around the nominal top mass. This requirement is fulfilled by 66% of the reconstructed events. This acceptance must be convoluted with the acceptance of the kinematic cuts, which is 21.9%. This has still to be multiplied by the lepton and *b*-tagging efficiencies, for which the nominal values of 90% and 60% at low luminosity have been assumed. Multiplying these numbers leads to a total acceptance of 1.7% for $t\bar{t}H \rightarrow l\nu\, jj\, b\bar{b}\, b\bar{b}$ events at low luminosity.

At high luminosity, the p_T thresholds for the lepton and the jets are raised to 30 GeV. This results in a decrease of the acceptance of the kinematic cuts to 88% of their low luminosity value. In addition, the *b*-tagging efficiency is reduced from 60% to 50%. The top reconstruction efficiency is not significantly affected, and the total acceptance for $t\bar{t}H \rightarrow l\nu\, jj\, b\bar{b}\, b\bar{b}$ events is reduced to 0.7% at high luminosity.

For events passing all cuts, the $b\bar{b}$ invariant mass, $m_{b\bar{b}}$, is computed and a final cut is applied to select events in a mass window around the nominal Higgs-boson mass. The $m_{b\bar{b}}$ distribution of reconstructed fully simulated signal events is shown in Figure 19-10 for a Higgs-boson mass of 100 GeV at low luminosity. In the fast simulation used in this analysis, the Higgs-boson mass is reconstructed with a resolution of σ = 19 GeV, in good agreement with the results obtained from full simulation, σ = 20 GeV, which are discussed in Section 9.3.4 . For a significant fraction of the signal events, the assignment of the various jets is not correct, and results in the presence of non-negligible combinatorial background from the signal itself as shown in Figure 19-10. The shaded histogram represents those events for which the jet assignments in the Higgs boson reconstruction are correct.

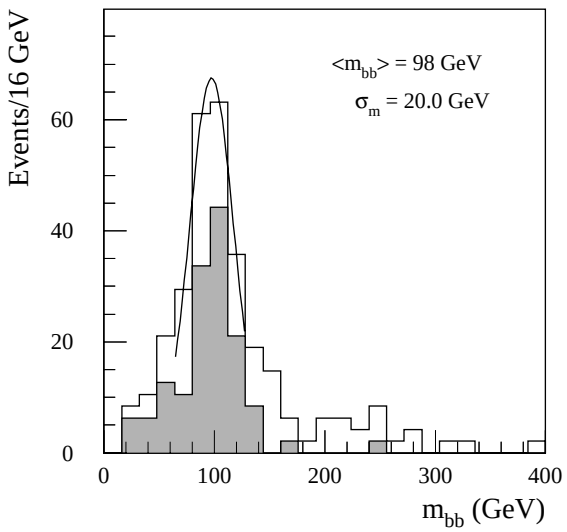

Figure 19-10 For fully simulated events, the reconstructed $m_{b\bar{b}}$ distribution for $t\bar{t}H$ with $H \rightarrow b\bar{b}$ signal events with both top-quarks being reconstructed inside a mass window m_{jjb}, $m_{l\nu b} = m_t \pm 20$ GeV and for low-luminosity performance. The shaded area denotes those events for which the jet assignment in the Higgs boson reconstruction is correct.

At low luminosity, the mass window cut is chosen to be ±30 GeV, and has an efficiency of 41% for signal events. For 64% of the events in this mass window, the jet assignment is correct. At high luminosity, the mass resolution is degraded from 19 GeV to 22 GeV. In this case, a mass window of ±45 GeV around the nominal Higgs-boson mass has been used, resulting in an acceptance of about 50%. At high luminosity, the fraction of events in the mass window, for which the jet assignments are correct, is reduced to about 50%. Detailed numbers for the fraction of correctly reconstructed $H \rightarrow b\bar{b}$ events in the signal are included in Tables 19-7 and 19-8, where the expected numbers of signal and background events are given at low and high luminosity, respectively.

The $m_{b\bar{b}}$ distributions for the summed signal and background events are shown in Figures 19-11 and 19-12, respectively for Higgs-boson masses of 100 and 120 GeV and for an integrated luminosity of 100 fb^{-1} (30 fb^{-1} with low-luminosity operation and 70 fb^{-1} with high-luminosity operation). The summed background is shown by the dashed line, and the points with error bars represent the result of a single experiment.

The expected numbers of signal and background events accepted by the full reconstruction chain are given in Tables 19-7 and 19-8, for Higgs-boson masses of 80, 100 and 120 GeV, and for integrated luminosities of 30 and 100 fb^{-1} respectively. The dominant background after these selection and reconstruction criteria is the irreducible, non-resonant $t\bar{t}jj$ background. Since top-quark production will be studied extensively in ATLAS (see Section 18.1), the shape of this background will be measured. To reject any potential contribution of a Higgs-boson signal in the determination of the background shape, a *b*-jet veto will most likely have to be used. Assuming that the shape of this background is known, the significance for the Higgs boson discovery in this channel exceeds 5σ in the low-mass range up to about 100 GeV for an integrated luminosity of 30 fb^{-1}.

Table 19-7 Expected *ttH* signal and background rates for three different Higgs-boson masses and for an integrated luminosity of 30 fb^{-1}. The numbers of events are given after all cuts, including the $m_{b\bar{b}}$ mass window cuts. The fraction of true $H \to b\bar{b}$ events ($S_{H \to b\bar{b}}/S_{\text{total}}$) in the signal peak is also given.

Higgs mass (GeV)	**80**	**100**	**120**
Signal *S*	81	61	40
$t\bar{t}Z$	7	8	2
Wjjjjjj	17	12	5
$t\bar{t}jj$	121	130	120
Total background *B*	145	150	127
S/B	0.56	0.41	0.32
$S/\sqrt{B}$	6.7	5.0	3.6
$S_{H \to b\bar{b}}/S_{\text{total}}$	0.67	0.64	0.59

The numbers given in Table 19-8 assume high luminosity performance. If the significance for an integrated luminosity of 100 fb^{-1} is computed from a combination of the significances reached for 30 fb^{-1} at low luminosity and for 70 fb^{-1} at high luminosity, the discovery window for a Standard Model Higgs boson, where the significance exceeds 5σ can be extended up to about 120 GeV. An ultimate integrated luminosity of 300 fb^{-1} at the LHC would extent the Higgs boson discovery window in this channel by another 10 GeV to about 130 GeV.

Table 19-8 Same as Table 19-7 for an integrated luminosity of 100 fb^{-1} (high luminosity operation).

Higgs mass (GeV)	**80**	**100**	**120**
Signal *S*	140	107	62
$t\bar{t}Z$	13	13	5
*W*jjjj	35	15	10
$t\bar{t}jj$	247	250	242
Total background *B*	295	278	257
S/B	0.47	0.38	0.24
$S/\sqrt{B}$	8.2	6.4	3.9
$S_{H \to b\bar{b}}/S_{\text{total}}$	0.57	0.53	0.50

It should be stressed that, due to the complete reconstruction of both top decays, the signal-to-background ratio has improved significantly compared to earlier studies [19-14], and lies in the range between 32% and 56% at low luminosity and between 24% and 47% at high luminosity.

In conclusion, the extraction of a Higgs-boson signal in the $t\bar{t}H$, $H \to b\bar{b}$ channel appears to be feasible over a wide range in the low Higgs-boson mass region, provided that the two top-quark decays are reconstructed completely with a reasonably high efficiency. This calls for excellent *b*-tagging capabilities of the detector. Another crucial item is the knowledge of the shape of the main residual background from $t\bar{t}jj$ production. If the shape can be accurately determined

using real data from $t\bar{t}$ production, a Higgs-boson signal could be extracted with a significance of more than 5σ in the mass range from 80 to 130 GeV, assuming an integrated luminosity of 300 fb^{-1}. For an uncertainty of ±5% on the absolute normalisation of the background shape, the discovery window would be reduced to the range between 80 and 125 GeV.

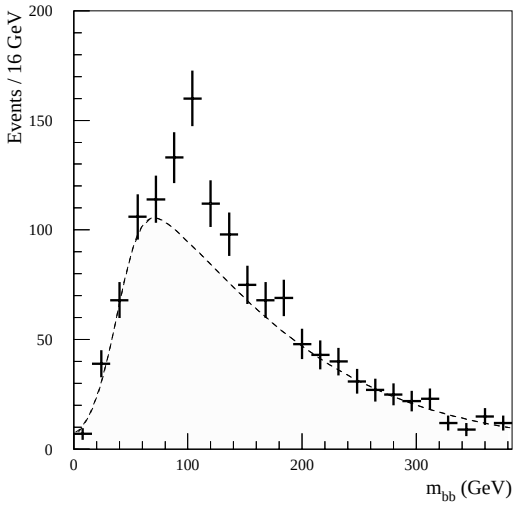

Figure 19-11 Invariant mass distribution, $m_{b\bar{b}}$, of tagged *b*-jet pairs in fully reconstructed $t\bar{t}H$ signal events with a Higgs-boson mass of 100 GeV above the summed background (see text), for an integrated luminosity of 100 fb^{-1} (30 fb^{-1} with low-luminosity operation and 70 fb^{-1} with high-luminosity operation). The points with error bars represent the result of a single experiment and the dashed line represents the background distribution.

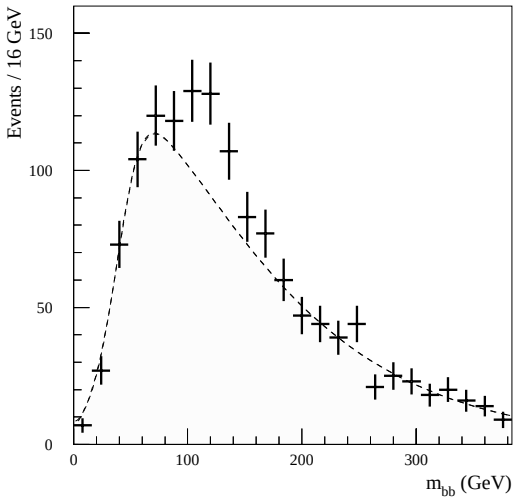

Figure 19-12 Same as Figure 19-11, but for a Higgs-boson mass of 120 GeV.

19.2.5 $H \rightarrow ZZ^* \rightarrow 4l$

The decay channel $H \rightarrow ZZ^* \rightarrow 4l$ provides a rather clean signature in the mass range between ~120 GeV and 2 m_Z, above which the gold-plated channel with two real Z bosons in the final state opens up. The branching ratio is larger than for the $\gamma\gamma$ channel and increases with increasing m_H up to $m_H \sim 150$ GeV. A pronounced dip appears, however, for $150 < m_H < 180$ GeV, because of the opening of the $H \rightarrow WW$ channel. In addition to the irreducible background from ZZ^* and $Z\gamma^*$ continuum production, there are large reducible backgrounds from $t\bar{t}$ and $Zb\bar{b}$ production. Because of the large top production cross-section, the $t\bar{t}$ events dominate at production level; the $Zb\bar{b}$ events contain, however, a genuine Z in the final state, which makes their rejection more difficult. In addition, there is a background from ZZ continuum production, where one of the Z bosons decays into a τ–pair, with subsequent leptonic decays of the τ–leptons, and the other Z decays into an electron or a muon pair.

In this Section, the potential for a Higgs boson discovery in the $H \rightarrow ZZ^* \rightarrow 4l$ channel is presented. Both electrons and muons are considered in the final state, thus yielding *eeee*, *ee*$\mu\mu$ and $\mu\mu\mu\mu$ event topologies. Since the detector performance is expected to be somewhat different for these various final states, they have been treated separately in the following. All results on the lepton and Higgs-boson mass reconstruction have been obtained from a full detector simula-

tion. Bremsstrahlung effects have also been taken into account, by using PYTHIA together with the PHOTOS package [19-27]. Background events have been generated using the exact matrix-element calculation [19-37] for the process $gg \rightarrow Zb\bar{b}$, which accounts for about 90% of the total $Zb\bar{b}$ cross-section. For both the $t\bar{t}$ and $Zb\bar{b}$ reducible backgrounds, leptons from cascade decays of *b*-quarks, *i.e.* not directly produced through *W*-boson or *b*-quark semi-leptonic decays, also contribute significantly to the background and have therefore been included in the event generation.

19.2.5.1 First stage of event selection

The signal reconstruction proceeds by selecting four leptons which pass the standard electron and muon identification criteria, as described in Sections 7.2 and 8.1, followed by the simple kinematic cuts:

- Two leptons with $p_T > 20$ GeV and $|\eta| < 2.5$ are required to trigger the experiment.
- Two additional leptons with $p_T > 7$ GeV and $|\eta| < 2.5$ are required.
- One pair of leptons of appropriate charge and flavour is required to have an invariant mass in a window around the *Z* mass, defined as $m_Z \pm m_{12}$. This cut rejects most of the non-resonant $t\bar{t}$ background.
- The other pair of leptons is required to have an invariant mass, above a certain threshold, defined as m_{34} threshold. This cut considerably reduces both the contributions from $t\bar{t}$ and $Zb\bar{b}$ cascade decays and from the $Z\gamma^*$ background.

The p_T thresholds for the leptons have been optimised to maintain a good acceptance for the signal at low m_H. By optimising the size of the m_{12} window as a function of the Higgs-boson mass, it is possible to recover partially acceptance losses due to $H \rightarrow ZZ^* \rightarrow 4l$ decays, which contribute significantly at the low end of the mass range [19-38]. The optimised values of m_{12} window and m_{34} threshold, used for the various Higgs-boson masses, are given in Table 19-9, together with the acceptance of the kinematic cuts, which is found to vary between ~27% and ~54% for masses between 120 and 180 GeV. The acceptance numbers are averaged over the three possible final-state topologies.

Table 19-9 For $H \rightarrow ZZ^* \rightarrow 4l$ final states, mass window, m_{12}, used around the Z mass and threshold, m_{34}, applied to the mass of the other lepton pair, together with the acceptance of the kinematic cuts as a function of m_H. The statistical error on the acceptances is ±0.003.

Higgs mass (GeV)	120	130	150	170	180
m_{12} window (GeV)	± 20	± 15	± 10	± 6	± 6
m_{34} threshold (GeV)	15	20	30	45	60
Acceptance of kinematic cuts	0.265	0.335	0.415	0.466	0.535

The Higgs-boson production cross-section times branching ratio to four leptons is given in Table 19-10 as a function of m_H, together with the cross-sections for the irreducible and reducible background contributions. The background cross-sections are given after the kinematic cuts have been applied and are integrated over a mass window of ±5 GeV around the corresponding Higgs-boson mass. Without further cuts, the reducible background is dominant, and a signifi-

cant fraction of these background events comes from cascade decays [19-39]. They can be further rejected by exploiting lepton isolation and vertexing criteria, as described in Section 19.2.5.3.

Table 19-10 Cross-section (σ) times branching ratio (*BR*) for $H \to ZZ^* \to 4l$ decays and for the various background processes (integrated over a mass window of ±5 GeV around the Higgs-boson mass) as a function of m_H. The acceptance of the kinematic cuts is included for all background processes.

Higgs mass (GeV)	**120**	**130**	**150**	**170**	**180**
$\sigma \times$ BR for Higgs signal (fb)	1.29	2.97	5.53	1.40	3.26
$\sigma \times$ BR for $ZZ^* \to 4l$ (fb)	0.16	0.28	0.28	0.26	0.24
$\sigma \times$ BR for $ZZ \to \tau\tau\, ll \to 4l$ (fb)	0.04	0.03	0.03	0.02	0.01
$\sigma \times$ BR for $t\bar{t} \to WbW\bar{b} \to 4l$ (fb)	1.2	1.9	2.5	1.9	1.7
$\sigma \times$ BR for $Zb\bar{b} \to 4l$ (fb)	0.9	1.3	1.7	1.3	1.2

19.2.5.2 Higgs-boson mass reconstruction

The results obtained from the full detector simulation and reconstruction of four-lepton final states are presented below. The reconstruction is based on the algorithms presented in Section 7.8.2 for electrons and Section 8.6.3 for muons. The following effects have been included in the evaluation of the mass resolution:

- Inner bremsstrahlung, *i.e.* radiative photon emission in Z decays, is included in the event generation; high-p_T photons ($p_T > 5$ GeV), which are identified and reconstructed, are included in the calculation of the four-lepton mass.
- Since the contribution from the experimental mass resolution is larger than that from the intrinsic width of the Z boson, a Z-mass constraint is applied, if the mass of the lepton pair is inside a window of ±6 GeV around the nominal Z-mass (see Section 7.8.2).
- Unlike the case of the $H \to \gamma\gamma$ analysis, where events are rejected if one or more photons are in the transition region between the barrel and end-cap calorimeters, events are not rejected for the $H \to ZZ^* \to 4l$ analysis (in the $H \to \gamma\gamma$ case, the quality of the γ/jet separation is crucial and tighter fiducial cuts are applied). Electrons in the transition region are measured with a somewhat worse energy resolution, and therefore they increase the non-Gaussian tails in the mass distributions.

The results are determined from full simulation at low and high luminosity for Higgs-boson masses of 130 GeV and 170 GeV. Based on these results, those for other masses are obtained by appropriate scaling of the results from the fast simulation. The results are discussed separately for the various final-state configurations, and a summary of all mass resolutions and of the relevant acceptances is given in Tables 19-11 and 19-12.

$H \to ZZ^* \to eeee$

An example of a reconstructed four-electron invariant mass distribution is shown for a Higgs-boson mass of 130 GeV in Figure 19-13. The mass resolution, obtained from a Gaussian fit in a window from -1.5σ to +2.5σ around the peak, is found to be (1.54 ± 0.06) GeV at low luminosity and (1.81 ± 0.07) GeV at high luminosity. Inner bremsstrahlung leads to a degradation of the mass resolution by about 0.1 GeV.

Within a mass window of $\pm 2\sigma$ around m_H, $(83.3 \pm 0.6)\%$ and $(84.7 \pm 0.6)\%$ of the events are retained at low and high luminosity respectively. This acceptance is about 12% lower than what is expected from a Gaussian distribution. The additional acceptance losses arise from inner bremsstrahlung (3%), from external bremsstrahlung in the Inner Detector (3%), from events for which no Z-mass constraint could be applied (5%), and from events for which one or more electrons are in the transition region between the barrel and end-cap calorimeters (1%). These individual fractions have been determined from the full detector simulation and reconstruction for $m_H = 130$ GeV. Most of these acceptance losses decrease as m_H increases.

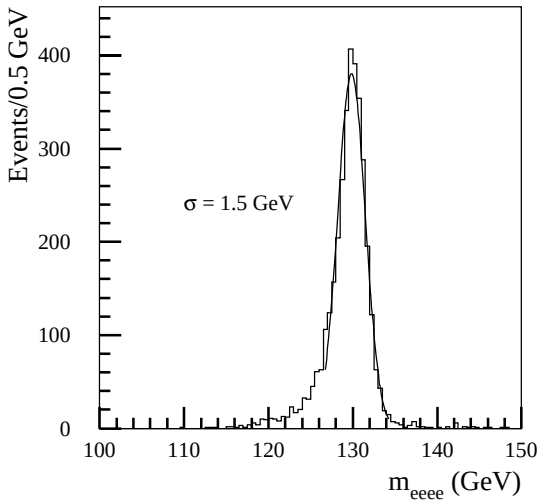

Figure 19-13 For fully simulated and reconstructed $H \rightarrow ZZ^* \rightarrow eeee$ decays with $m_H = 130$ GeV, four-electron invariant mass distribution at low luminosity (a Z mass constraint is applied).

The efficiency for the four-electron identification and reconstruction is found to be 69%, corresponding to an average of about 91% per electron.

$H \rightarrow ZZ^* \rightarrow \mu\mu\mu\mu$

The muon reconstruction is performed both in the Muon Spectrometer and in the Inner Detector. Details on the mass resolution obtained for the reconstruction in these two independent systems are given in Section 8.6.3. For the analysis presented here, the combination of the muon reconstruction in both systems has been used. In this case, the four-muon mass resolution is found to be (1.42 ± 0.04) GeV for a Higgs-boson mass of 130 GeV. The acceptance in the mass window of $\pm 2\sigma$ around m_H is about 83%. The individual contributions to the non-Gaussian part of the acceptance losses have been determined from full simulation and reconstruction: 4% of the events are lost due to inner bremsstrahlung, 5% are lost due to events for which no Z-mass constraint could be applied, and the remaining 3% are lost mainly due to non-Gaussian tails in the muon-momentum reconstruction. The effect of the inner bremsstrahlung is found to be slightly larger than in the four electron case, since low-energy photons, which are often recovered in the electron energy measurement in the EM Calorimeter, cannot be recovered in the track momentum measurement. For four-muon final states, the mass resolution is not affected by pile-up and is therefore identical at high luminosity.

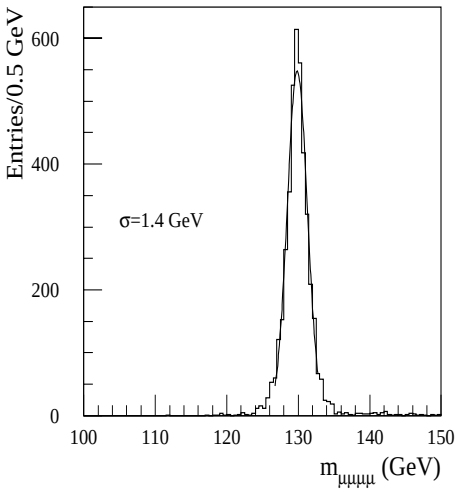

Figure 19-14 For fully simulated and reconstructed $H \rightarrow ZZ^* \rightarrow \mu\mu\mu\mu$ decays with $m_H = 130$ GeV, four-muon invariant mass distribution at low luminosity (a Z mass constraint is applied).

An example of a reconstructed mass peak for a Higgs-boson mass of 130 GeV is shown in Figure 19-14. The efficiency for the four-muon reconstruction is found to be 83.7%.

$H \rightarrow ZZ^* \rightarrow ee\mu\mu$

The $ee\mu\mu$ final state occurs in about one half of the total $H \rightarrow ZZ^* \rightarrow 4l$ event sample. The four-lepton mass resolution is found to be (1.39 ± 0.06) GeV for events where the on-shell Z decays to electrons, and (1.74 ± 0.07) GeV for events where it decays to muons. The difference between these two cases comes from the fact that the leptons from the on-shell Z have a harder p_T spectrum and that for the EM Calorimeter electron energy measurements, the relative resolution improves with increasing p_T, whereas it degrades for the magnetic muon-momentum measurements.

The average mass resolution at low luminosity is found to be (1.51 ± 0.06) GeV. The corresponding reconstructed four-lepton mass is shown in Figure 19-15 for a Higgs-boson mass of 130 GeV. In this case, (85.4 ± 0.6)% and (85.3 ± 0.6)% of the events are reconstructed within $m_H \pm 2\sigma$ at low and high luminosity, respectively. The non-Gaussian acceptance losses arise from inner bremsstrahlung (3%), from external bremsstrahlung in the Inner Detector (2%), from events for which no Z-mass constraint could be applied (4%), and from events for which one or more electrons are in the transition region between the barrel and end-cap calorimeters (0.5%).

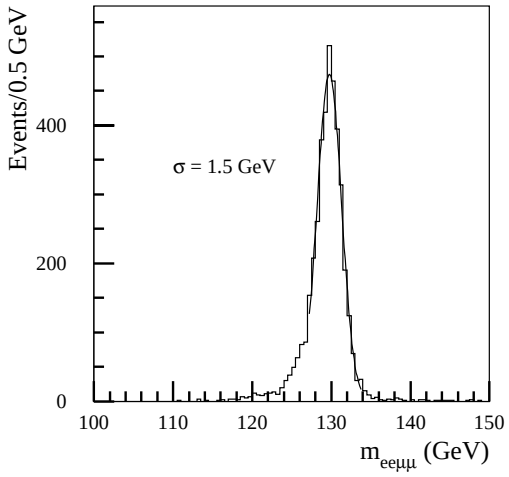

Figure 19-15 For fully simulated and reconstructed $H \rightarrow ZZ^* \rightarrow ee\mu\mu$ decays with $m_H = 130$ GeV, four-muon invariant mass distribution at low luminosity (a Z mass constraint is applied).

Summary of results

The results for the mass resolutions obtained for the various four lepton final states, for the overall efficiency for identifying and reconstructing them, and for the acceptances in the chosen mass windows, are summarised in Tables 19-11 and 19-12. As an example, for a Higgs-boson mass of 130 GeV, mass resolutions in the range between 1.42 GeV (in the case of four-muon final states) and 1.81 GeV (in the case of four-electron final states at high luminosity) are obtained. Electrons are more affected by pile-up effects than muons. In the four-muon final states, nearly all high-p_T photons from inner bremsstrahlung can be recovered and included in the four-muon invariant mass. In the electron case, this is only possible if the photons can be identified as separate clusters in the EM Calorimeter. Soft bremsstrahlung is, however, mostly recovered for electrons, since it is most often collinear and therefore automatically included in the EM Calorimeter energy measurement.

Table 19-11 Mass resolutions for the various four-lepton final states from $H \rightarrow ZZ^* \rightarrow 4l$ decays at low and high luminosity as a function of m_H. Bremsstrahlung effects are taken into account and a Z mass constraint is applied. The mass resolutions are obtained from full simulation and reconstruction for the events passing the kinematic cuts described in the text. The statistical error on the quoted resolution values is about ± 0.06 GeV.

Higgs mass (GeV)	Luminosity	120	130	150	170	180
σ(4*e*) (GeV)	Low	1.50	1.54	1.71	1.97	2.21
σ(4*e*) (GeV)	High	1.81	1.81	1.98	2.17	2.37
σ(4μ) (GeV)	Low / High	1.32	1.42	1.62	2.00	2.20
σ(2*e*2μ) (GeV)	Low	1.43	1.51	1.64	1.99	2.20
σ(2*e*2μ) (GeV)	High	1.64	1.68	1.84	2.10	2.28

Table 19-12 Overall efficiencies for identification and reconstruction of the various four-lepton final states from $H \rightarrow ZZ^* \rightarrow 4l$ decays with m_H = 130 GeV, together with the acceptances in the selected mass window (see text). The results are obtained from full simulation and reconstruction of events passing the kinematic cuts described in the text. The statistical error on the quoted acceptance numbers is about ± 0.006.

	4e		4μ		2e2μ	
	Low luminosity	High luminosity	Low luminosity	High luminosity	Low luminosity	High luminosity
Overall lepton efficiency	0.69	0.69	0.84	0.84	0.76	0.76
Acceptance in mass window	0.833	0.847	0.837	0.837	0.854	0.853

As discussed above, the lepton identification and reconstruction efficiencies have been evaluated from the full simulation and reconstruction. Although higher efficiencies of 91% per electron and 96% per muon have been obtained, the nominal value of 90% per lepton is used in Section 19.2.5.4 for the evaluation of the signal significances, for reasons of consistency with the other physics analyses in this document.

19.2.5.3 Rejection of reducible backgrounds

After the kinematic cuts are applied, the reducible backgrounds from $t\bar{t}$ and $Zb\bar{b}$ production are ten times higher than the irreducible one [19-40]. Since the overall uncertainties on these backgrounds are large, it is desirable to bring them well below the irreducible background from ZZ^* continuum production. To achieve this requires an additional rejection of 100, which can be obtained using lepton isolation and vertexing measurements, as described in this Section. All the results presented are based on the reconstruction of fully simulated large statistics samples of four-muon and four-electron final states from $H \rightarrow ZZ^* \rightarrow 4l$ events with m_H = 130 GeV and from $t\bar{t}$ and $Zb\bar{b}$ production.

Isolation cuts

In contrast to the Higgs-boson signal and the irreducible ZZ* continuum background, at least two of the selected leptons are non-isolated in the $t\bar{t}$ and $Zb\bar{b}$ backgrounds, since they originate from a *b*-quark decay. Isolation cuts are expected to reduce these backgrounds considerably. These cuts are applied to all four leptons in the final state and combine the information from:

- the calorimeter, where the summed transverse energy in a cone around the lepton can be required to be smaller than a given threshold E_T^{cut};
- the Inner Detector, where one may require that no charged track with p_T larger than a given threshold be reconstructed in a cone around the lepton.

These isolation criteria have been studied in detail in [19-40]. They are strongly correlated and the gain in combining them is small. The distribution of the maximal transverse momentum of all charged tracks reconstructed in the Inner Detector in a cone of radius ΔR = 0.2 around the leptons is shown in Figure 19-16, for the Higgs-boson signal and the reducible backgrounds. A significant background rejection can be achieved by this cut alone.

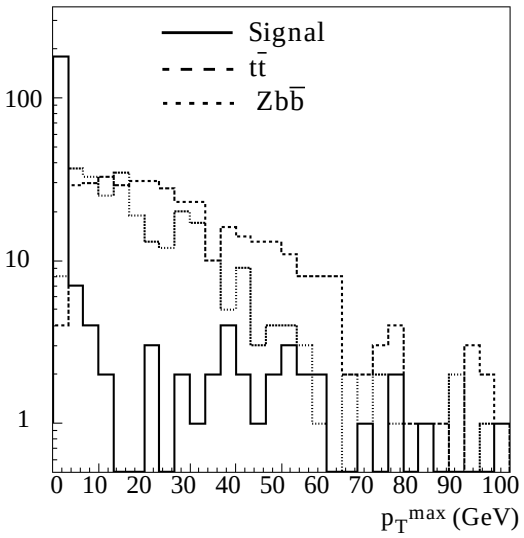

Figure 19-16 Distribution of the maximal transverse momentum, p_T^{max}, of all charged tracks reconstructed in the Inner Detector in a cone of radius $\Delta R = 0.2$ around the leptons for the $H \rightarrow ZZ^* \rightarrow 4l$ signal and the reducible backgrounds.

The p_T spectrum of *b*'s (and therefore of the leptons from *b*-decay) is softer in $Zb\bar{b}$ events than in $t\bar{t}$ events, leading to a less effective rejection of the non-isolated leptons using isolation cuts.

For the four-muon final state, the results for the background rejections as function of the efficiency for signal events with m_H = 130 GeV are shown separately for $t\bar{t}$ and $Zb\bar{b}$ events in Figure 19-17 both for low and high luminosity. At low luminosity, for a signal efficiency of 90%, a rejection of ~110 (~30) against $t\bar{t}$ ($Zb\bar{b}$) can be obtained. At high luminosity, similar rejections are obtained for an efficiency of 65% (75%) against the $t\bar{t}$ ($Zb\bar{b}$) backgrounds. For the four-electron final states, the results obtained are presented in Figures 19-18 and 19-19, respectively for the $t\bar{t}$ and $Zb\bar{b}$ backgrounds.

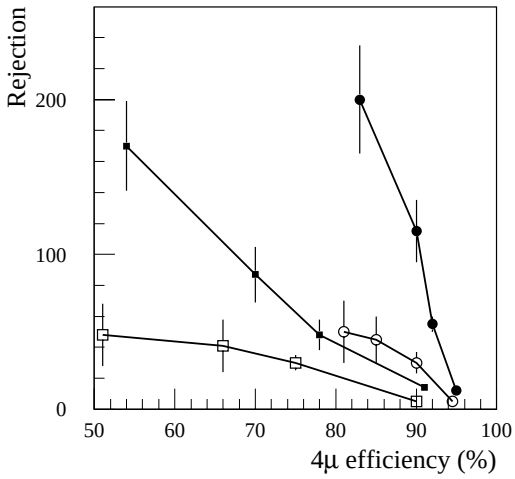

Figure 19-17 Rejection using track isolation of reducible backgrounds versus overall efficiency for $H \rightarrow ZZ^* \rightarrow \mu\mu\mu\mu$ final states with m_H=130 GeV. The results are shown for $t\bar{t}$ and $Zb\bar{b}$ as black and open symbols respectively and for both low (circles) and high (squares) luminosity.

The results are shown for track isolation at low luminosity and for calorimeter isolation at low and high luminosity.

- Compared to the results shown in Figure 19-17 for the four-muon final states, those for the four-electron final states using track isolation at low luminosity provide similar rejections at a somewhat lower efficiency. This is most likely due to the extra track multiplicity arising from conversions of bremsstrahlung photons in the four-electron case. The use of explicit electron-veto algorithms should improve the results of Figures 19-18 and 19-19 and bring them closer to the values of Figure 19-17.
- The calorimeter isolation at low luminosity is as effective as the track isolation for $t\bar{t}$ events. As mentioned above, the isolation cuts are much less effective for $Zb\bar{b}$ events because of the softer p_T spectrum of the b's.
- Finally, at high luminosity, the rejection using the calorimeter isolation is degraded in both cases because of the large fluctuations induced by pile-up noise in the energy depositions measured in the calorimeter towers.

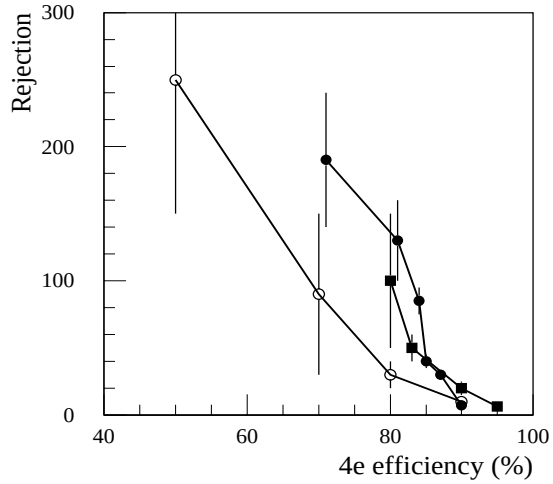

Figure 19-18 Rejection of $t\bar{t}$ background versus overall efficiency for $H \rightarrow ZZ^* \rightarrow eeee$ final states with m_H=130 GeV. The results are shown for track isolation at low luminosity (black circles), calorimeter isolation at low luminosity (black squares) and calorimeter isolation at high luminosity (open circles).

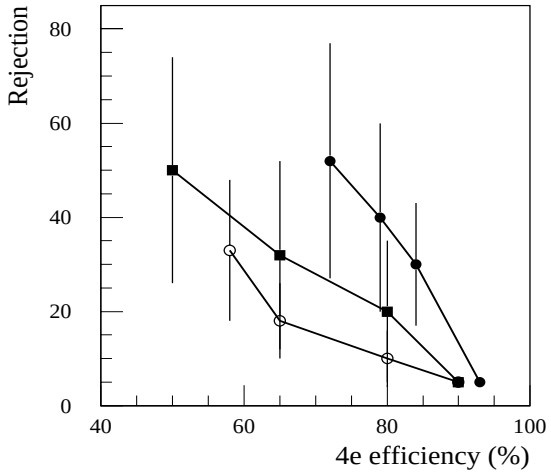

Figure 19-19 Same as Figure 19-18 for the $Zb\bar{b}$ background.

Impact parameter cuts

Further rejection against the reducible backgrounds can be obtained by using impact parameter cuts, since two of the leptons originate from b-decays. The largest of the normalised impact parameters (in the transverse plane) of the four reconstructed lepton tracks, is used as a discriminant variable. The distribution of this variable is shown in Figure 19-20 for four-muon final states from signal events and from the $t\bar{t}$ and $Zb\bar{b}$ reducible backgrounds. The long tails due to leptons from b-decays are clearly visible for both backgrounds.

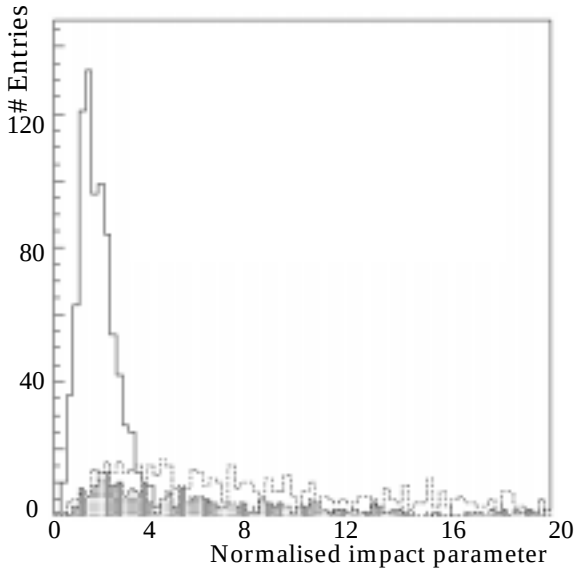

Figure 19-20 Largest of normalised impact parameters of the four muons, as reconstructed for fully simulated events from $H \rightarrow ZZ^* \rightarrow \mu\mu\mu\mu$ decays (solid histogram) and from the $t\bar{t}$ (dashed histogram) and $Zb\bar{b}$ (shaded histogram) backgrounds.

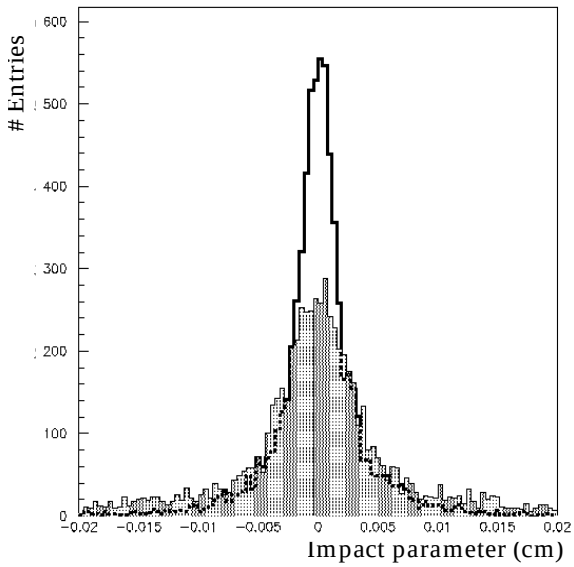

Figure 19-21 Distribution of largest (in absolute value) of the impact parameters of the four electrons as reconstructed for fully simulated events from $H \rightarrow ZZ^* \rightarrow eeee$ decays, before (shaded) and after (white) bremsstrahlung recovery.

For electrons, both inner and external bremsstrahlung induce tails in the impact parameter distributions. Figure 19-21 shows that these tails are significantly reduced by the bremsstrahlung recovery procedure of xKalman [19-41], see Section 7.2.1.1. The largest (in absolute value) of the impact parameters of the four reconstructed electron tracks is shown in Figure 19-21 before and after the recovery procedure is applied.

The spread of the primary vertex in x and y (in the transverse plane) induces a loss of impact parameter resolution. For four-muon final states, for example, the impact parameter resolution degrades from 19 μm to 29 μm if this spread is taken into account without correcting for it. This loss can be recovered by introducing the following kinematic variable [19-40]:

$$SUMDI = \sum_{i,\,j\,=\,1,\,4}^{i\,>\,j} \sqrt{(x_i - x_j)^2 + (y_i - y_j)^2}$$

where (x_i,y_i) are the coordinates in the transverse plane of the intersection point of two lepton tracks. Given the four tracks, there are six possible such intersection points. For signal events, for which all leptons come from the primary vertex, the intersection points of all lepton pairs should coincide, and hence the value of *SUMDI* is expected to be small. This is illustrated in Figure 19-22 for signal events and for $t\bar{t}$ and $Zb\bar{b}$ background events.

The rejection power of the lepton impact parameter information, as obtained from full simulation and reconstruction, is shown in Figure 19-23, for both $t\bar{t}$ and $Zb\bar{b}$ events as a function of the efficiency for the signal events. The results are shown for the normalised impact parameter method, both without and with vertex spread. The observed loss of rejection due to the vertex spread can be nearly fully recovered if the *SUMDI* variable is used. For the four-muon final states, a rejection of 12 against the $t\bar{t}$ background and of 5.5 against the $Zb\bar{b}$ background is ob-

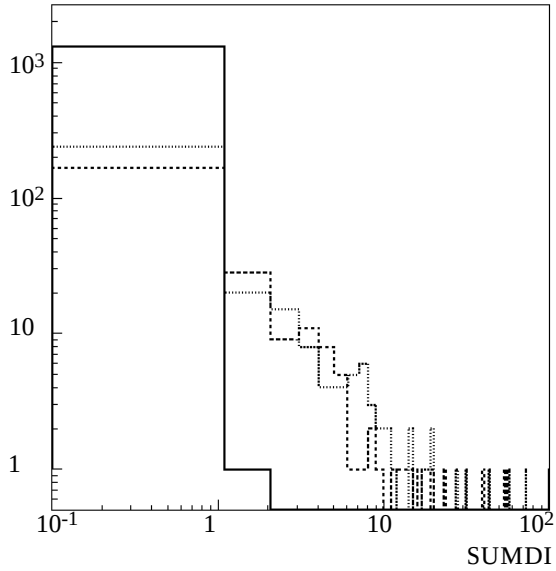

Figure 19-22 Distribution of *SUMDI* variable (cm) for $H \rightarrow ZZ^* \rightarrow \mu\mu\mu\mu$ signal events (solid) and for $t\bar{t}$ (dashed) and $Zb\bar{b}$ (dotted) background events (see text).

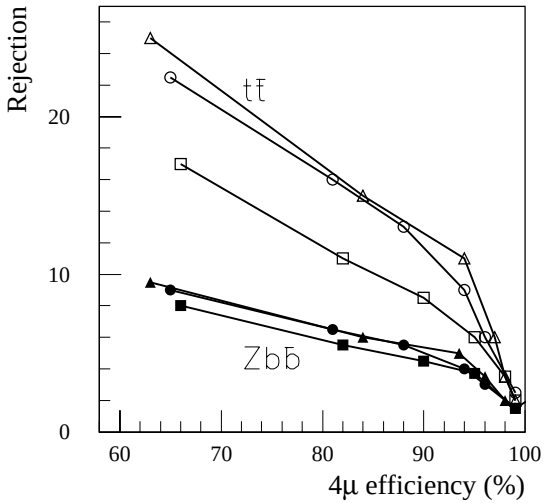

Figure 19-23 Rejection using impact parameter cuts of $t\bar{t}$ (open symbols) and $Zb\bar{b}$ (black symbols) backgrounds versus efficiency for $H \rightarrow ZZ^* \rightarrow \mu\mu\mu\mu$ final states with m_H = 130 GeV. The results are shown for the normalised impact parameter method without (triangles) and with (squares) vertex spread and for the method (circles) using the *SUMDI* variable (see text).

tained, for a signal efficiency of 90%. For the same rejection factors, the signal efficiency is degraded by about 20% for the four-electron final states. The rejection is significantly lower for $Zb\bar{b}$ events because of the lower average p_T of the leptons, which results in a worse impact parameter resolution, dominated by multiple scattering effects.

At high luminosity, the rejection of the impact parameter cuts is conservatively assumed to be degraded by about 35% (this was estimated by removing the information from the pixel *B*-layer when reconstructing the fully simulated events).

Combined rejection of reducible backgrounds

The results of the isolation and impact parameter studies reported above are combined together to provide estimates of the overall rejection against $t\bar{t}$ and $Zb\bar{b}$ backgrounds, which can be achieved as function of the efficiency for the $H \rightarrow ZZ^* \rightarrow 4l$ signal events and as a function of luminosity. The combined results are shown in Table 19-13, separately for the various four-lepton final states (the values for $H \rightarrow ZZ^* \rightarrow ee\mu\mu$ decays are derived by interpolation from the results obtained for the four-muon and four-electron final states). It is important to note that:

- The correlation between the isolation and impact parameter rejections (obtained separately in the studies reported above) is taken into account, since it is large, namely -10% for $t\bar{t}$ and -40% for $Zb\bar{b}$ events. This correlation is highest for $Zb\bar{b}$ events, since the isolation cuts soften the lepton p_T spectrum, which is in a range where the impact parameter resolution is limited by multiple scattering and therefore also dependent on p_T.
- The efficiency for four-electron final states is significantly lower than for four-muon final states (10% loss for isolation cuts and 20% loss for impact parameter cuts). The difference decreases at high luminosity because pile-up effects systematically degrade the isolation.

- The overall goal of a factor 100 rejection can be achieved, easily for the higher-p_T leptons from $t\bar{t}$ events, and also for the more difficult case of $Zb\bar{b}$ events (except for final states containing electrons at high luminosity).

Table 19-13 Combined rejections (using isolation and impact parameter cuts) against the $t\bar{t}$ and $Zb\bar{b}$ reducible backgrounds and efficiencies for the $H \rightarrow ZZ^* \rightarrow 4l$ final states with m_H=130 GeV. The results are given separately for the various four-lepton final states and for low and high luminosity.

	4e		**4μ**		**2e2μ**	
	Low luminosity	**High luminosity**	**Low luminosity**	**High luminosity**	**Low luminosity**	**High luminosity**
Signal efficiency	0.57	0.47	0.81	0.58	0.69	0.52
Rejection of $t\bar{t}$	1200	800	1200	800	1200	800
Rejection of $Zb\bar{b}$	130	50	110	90	120	70

It has also been investigated whether the background rejection could be further increased by using the missing transverse energy, E_T^{miss}. Although an E_T^{miss} cut would provide extra rejection, it would require the use of a very low cut, typically $E_T^{miss} < 20$ GeV. As shown in Section 19.2.5.4, the reducible backgrounds are rejected to a level well below the irreducible backgrounds, and this additional cut has therefore not been used. It could be used in future studies, however, to further optimise the signal efficiency with respect to the rejection of the reducible backgrounds.

19.2.5.4 Results

The numbers of signal and residual background events have been estimated for various Higgs masses in the range between 120 and 180 GeV. In order to compute the signal event rates, the cross-sections and kinematic cut efficiencies (Tables 19-9 and 19-10), the mass window acceptances (Table 19-12), the lepton identification and reconstruction efficiencies, and the isolation and impact parameter cut efficiencies (Table 19-13) are taken into account. For the evaluation of the signal significances, a lepton identification and reconstruction efficiency of 90% has been used to be consistent with the other results presented in this document. For this channel, this is conservative, given the results from the full simulation and reconstruction. The background numbers are computed from the cross-sections (Table 19-10), the mass windows (Table 19-11) the lepton identification and reconstruction efficiencies and the rejection factors obtained with the isolation and impact parameter cuts against the reducible backgrounds (Table 19-13).

The results are shown in Tables 19-14 and 19-15, respectively for integrated luminosities of 30 fb^{-1} and 100 fb^{-1}:

- the signal rates decrease very rapidly for $m_H < 130$ GeV and appear marginal for a Higgs boson discovery in this channel in this mass region;
- the dominant background is the irreducible continuum background from $ZZ^*/Z\gamma^*$ production;
- the reducible background is well below the irreducible background, thanks to the isolation and impact parameter cuts, and the dominant residual background remains the $Zb\bar{b}$ background;

- the significances have been evaluated using the Gaussian $S/\sqrt{B}$ approximation, but, given the small event rates, have also been calculated assuming Poisson statistics for both signal and background.

Table 19-14 Signal and background rates after all cuts and signal significances as a function of m_H, for $H \rightarrow ZZ^* \rightarrow 4l$ events and for an integrated luminosity of 30 fb^{-1} (low luminosity performance).

Higgs mass (GeV)	120	130	150	170	180
Signal	4.1	11.4	26.8	7.6	19.7
$t\bar{t}$	0.01	0.02	0.03	0.02	0.02
$Zb\bar{b}$	0.08	0.12	0.19	0.17	0.19
ZZ^*	1.23	2.27	2.51	2.83	2.87
$ZZ \rightarrow \tau\,\tau\,ll$	0.13	0.20	0.25	0.08	0.02
Significance ($S/\sqrt{B}$)	3.4	7.0	15.5	4.3	11.2
Significance (Poisson)	2.4	4.8	15.5	3.2	11.2

Table 19-15 Same as Table 19-14, but for an integrated luminosity of 100 fb^{-1} (high luminosity performance).

Higgs mass (GeV)	120	130	150	170	180
Signal	10.3	28.7	67.6	19.1	49.7
$t\bar{t}$	0.05	0.10	0.13	0.12	0.12
$Zb\bar{b}$	0.53	0.79	1.14	1.01	1.02
ZZ^*	3.53	6.36	7.03	7.54	7.61
$ZZ \rightarrow \tau\tau ll$	0.33	0.51	0.62	0.20	0.06
Significance ($S/\sqrt{B}$)	4.9	10.3	22.6	6.4	16.7
Significance (Poisson)	3.8	10.3	22.6	5.3	16.7

In conclusion, the $H \rightarrow ZZ^* \rightarrow 4l$ signal can be observed with a better than 5σ significance over most of the range $130 < m_H < 180$ GeV (except for a narrow region around 170 GeV) for an integrated luminosity of 30 fb^{-1}. For an integrated luminosity of 100 fb^{-1}, the signal can be observed with a better than 5σ significance over the complete mass range $125 < m_H < 180$ GeV.

19.2.6 $H \rightarrow WW^{(*)} \rightarrow l\nu l\nu$

For Higgs-boson masses close to 170 GeV, the signal significance in the $H \rightarrow ZZ^* \rightarrow 4l$ channel is reduced, due to the suppression of the ZZ^* branching ratio as the WW decay mode opens up (see Section 19.2.5). For $m_H = 170$ GeV, the $H \rightarrow WW^* \rightarrow l\nu l\nu$ branching ratio is approximately 100 times larger than that of the $H \rightarrow ZZ^* \rightarrow 4l$ channel. In the case of $H \rightarrow WW^* \rightarrow l\nu l\nu$ decays, however, it is not possible to reconstruct the Higgs-boson mass peak. Instead, an excess of events may be observed, and then used to identify the presence of a Higgs-boson signal and to extract information on its mass.

Based on the method suggested in [19-19], the potential for a discovery of the Higgs boson in the $H \rightarrow WW^* \rightarrow l\nu l\nu$ decay mode has been investigated for Higgs-boson masses in the range between 150 and 190 GeV [19-42]. The analysis presented here is based on fast detector simulation for final states containing electrons and muons. The signal cross-section times leptonic branching ratio for the $H \rightarrow WW^* \rightarrow l\nu l\nu$ decay is found to be between 0.55 and 0.80 pb over the mass range considered. Decays into τ-leptons, where the τ-leptons decay leptonically into electrons or muons have been taken into account in the analysis.

Table 19-16 Cross-sections for the most important background processes to the decay $H \rightarrow WW^* \rightarrow l\nu l\nu$ (leptonic τ-decays are included). The $W \rightarrow l\nu$ and the $\tau \rightarrow e\nu\bar{\nu}$, $\mu\nu\bar{\nu}$ branching ratios are included (leptonic branching ratios for b-decays are not included).

Process	$\sigma \times$ **BR (pb)**
$WW^* \rightarrow l\nu l\nu$	4.8
$WZ / ZZ \rightarrow ll\nu + X$	1.1
$t\bar{t} \rightarrow WWb\bar{b} \rightarrow l\nu l\nu + X$	38.6
$q\,g \rightarrow W\,t \rightarrow WW\,b \rightarrow l\nu l\nu + X$	4.8
$Wb\bar{b} \rightarrow l\nu b\bar{b} + X$	82.3
W+jet(s), $p_T > 10$ GeV	19300
$b\bar{b}$ inclusive (BR not included)	500×10^6

There are many irreducible and reducible background contributions, and the most important ones are listed in Table 19-16:

- The dominant irreducible background arises from WW continuum production, which has a cross-section times branching ratio between six and nine times larger than that of the Higgs-boson signal.
- WZ production with $W \rightarrow l\nu$, $Z \rightarrow ll$ and ZZ production with $Z \rightarrow ll$ and $Z \rightarrow \nu\nu$ also constitute a source of potentially irreducible background;
- $t\bar{t}$ and Wt production are the source of the largest reducible backgrounds with isolated leptons in the final state;
- $Wb\bar{b}$ and direct $b\bar{b}$ production, containing one or two leptons from semileptonic b-decays, are the dominant sources of reducible background with non-isolated leptons in the final state. These are considerably suppressed by the lepton p_T-threshold cuts and by isolation cuts.
- Finally, W+jet production, where a jet is mistaken as an electron, may also be a source of significant background.

In order to discriminate the signal from the most dangerous background processes, the following selection cuts are applied:

- Two isolated leptons with opposite sign are required within $|\eta| < 2.5$ and with transverse momenta, $p_T^1 > 20$ GeV and $p_T^2 > 10$ GeV. At high luminosity, the cut on the leading lepton is raised to 30 GeV for trigger purposes.
- Significant missing transverse momentum is required, $E_T^{miss} > 40$ GeV.
- The dilepton invariant mass is required to be smaller than 80 GeV.
- The opening angle ($\Delta\phi$) between the two leptons in the transverse plane is required to be smaller than 1.0 (measured in rad).
- The absolute value of the polar angle Θ_{ll} of the di-lepton system is required to be smaller than 0.9.
- The absolute value of the pseudorapidity difference ($\Delta\eta$) between the two leptons is required to be smaller than 1.5.

- Events with one or more jets with $p_T > 15$ GeV and $|\eta| < 3.2$ are rejected. At high luminosity, the p_T-threshold of this jet-veto cut is raised to 30 GeV.
- The transverse mass computed from the leptons and the missing transverse momentum,

$$m_T = \sqrt{2 p_T^{ll} E_T^{miss} (1 - \cos(\Delta\phi))}$$

  is required to fall in the mass window m_H - 30 GeV $< m_T < m_H$. Since the WW^* background is falling with increasing transverse mass, the lower cut value is reduced to m_H - 40 GeV for Higgs-boson masses above 170 GeV, in order to recover signal efficiency.

The dilepton invariant-mass cut mainly rejects background events where the lepton pair originates from a Z-boson. This cut has a large rejection against the WZ and ZZ background. The jet-veto cut is introduced to reject the $t\bar{t}$ and Wt backgrounds, which are characterised by large hadronic activity. The p_T-threshold of this jet-veto cut has unfortunately to be raised at high luminosity, which makes it much less effective and results in an increased residual $t\bar{t}$ background. The dominant irreducible background from WW* production is reduced by the angular cuts on the di-lepton system. The small angular separation between leptons in signal events results from the opposite spin orientation of the W pair originating from the decay of the scalar Higgs boson [19-43].

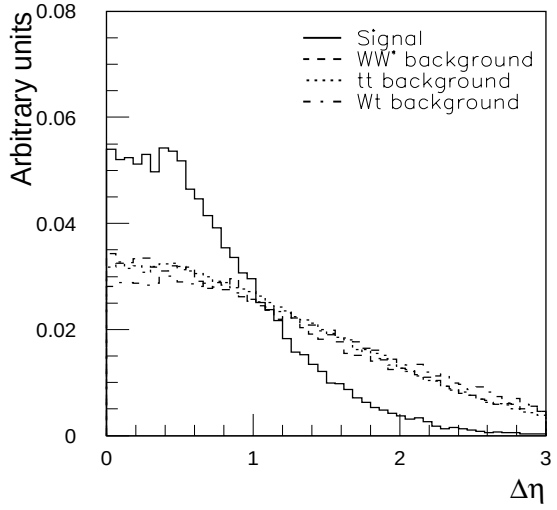

Figure 19-24 Difference in pseudorapidity between the two leptons for $H \rightarrow WW^* \rightarrow l\nu l\nu$ signal events with m_H = 170 GeV, and for the WW*, $t\bar{t}$ and Wt background events. All distributions are normalised to unity.

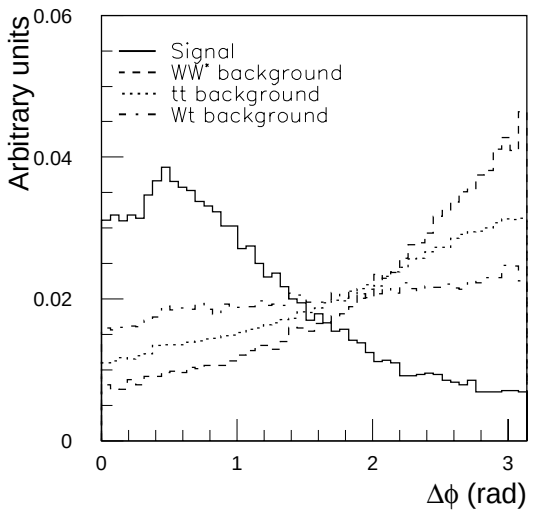

Figure 19-25 Difference in azimuth between the two leptons for $H \rightarrow WW^* \rightarrow l\nu l\nu$ signal events with m_H = 170 GeV and for the WW^*, $t\bar{t}$ and Wt background events. All distributions are normalised to unity.

The discrimination between the signal and the most important backgrounds is shown for the pseudorapidity difference, $|\Delta\eta|$, and the azimuthal difference, $\Delta\phi$, between the two leptons, respectively in Figures 19-24 and 19-25.

In Table 19-17, the cross-sections times branching ratios, the acceptances and the numbers of expected $H \rightarrow WW^* \rightarrow l\nu l\nu$ signal events are given as a function of m_H and for an integrated luminosity of 30 fb^{-1}. Over the mass range considered, the signal acceptance varies between 0.9 and 2.1%. In addition to this kinematic acceptance, a nominal identification and reconstruction efficiency of 90% per lepton has been assumed to obtain the signal event rates.

The numbers of expected background events in the selected transverse mass range are also given in Table 19-17, after all cuts are applied, for an integrated luminosity of 30 fb^{-1}. Due to the sliding window cut as a function of the Higgs-boson mass, also the background contribution is mass dependent. Thanks to the strict jet-veto cut applied at low luminosity, the $t\bar{t}$ background is at a level between 8 and 20 % of the irreducible WW^* background over the mass range considered. Single top production is found to be the dominant reducible background. A good signal-to-background ratio is obtained over this Higgs-boson mass range, with a maximum value of 0.7 for m_H = 170 GeV. At high luminosity, the $t\bar{t}$ and Wt background rejection is reduced and $t\bar{t}$ production is a significant reducible background, at the same level as the irreducible WW^* background.

The distribution of the transverse mass is shown in Figures 19-26 and 19-27 for the sum of signal plus background and for the background alone. The contribution from single top production and from $t\bar{t}$ production is also shown separately by the shaded histogram. The results are shown for m_H = 150 and 170 GeV and for an integrated luminosity of 30 fb^{-1}. Since there is no mass peak reconstructed in this channel, evidence for a Higgs-boson signal has to be deduced from an excess of events in the regions of transverse mass defined above. These regions are indicated by the two dotted lines.

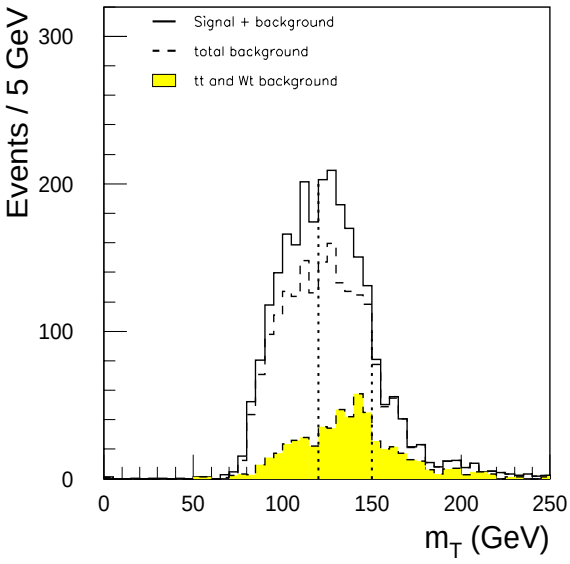

Figure 19-26 Transverse mass distribution for the summed $H \rightarrow WW^* \rightarrow l\nu l\nu$ signal (m_H = 150 GeV) and total background, for an integrated luminosity of 30 fb^{-1}. The distribution for the background alone is also shown separately. The shaded histogram represents the contributions from the Wt and $t\bar{t}$ background. The dashed lines indicate the selected signal region.

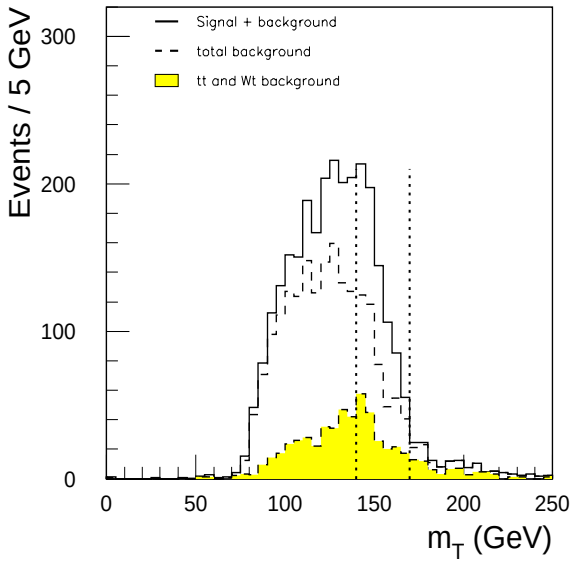

Figure 19-27 Same as Figure 19-26, but for m_H = 170 GeV.

The signal significance in this channel depends critically on the absolute knowledge of the various backgrounds. The cuts applied can be relaxed to some extent and a normalisation between the Monte Carlo prediction and the data can then be performed in regions, where only a small fraction of the signal is expected.

Table 19-17 Cross-sections times branching ratios, acceptances and numbers of expected signal and background events for $H \rightarrow WW^* \rightarrow l\nu l\nu$ decays and for an integrated luminosity of 30 fb^{-1}. The signal significances are computed assuming a systematic uncertainty of ±5% on the background.

Higgs mass (GeV)	**150**	**160**	**170**	**180**	**190**
$\sigma \times$ BR (fb)	610	790	800	705	550
Acceptance	0.016	0.021	0.017	0.016	0.009
Signal	240	400	337	276	124
WW* background	548	392	277	297	167
$t\bar{t}$ background	46	42	39	49	33
Wt background	215	195	149	163	85
WZ/ZZ background	25	17	9	10	6
W+jet background	< 10	< 10	< 10	< 10	< 10
Total background	844	656	484	529	301
Significance (including 5% systematic uncertainty)	4.7	9.6	10.3	7.8	5.4

Table 19-18 Same as Table 19-18, but for an integrated luminosity of 100 fb^{-1}.

Higgs mass (GeV)	**150**	**160**	**170**	**180**	**190**
Acceptance	0.024	0.032	0.027	0.026	0.016
Signal	1180	2050	1730	1490	700
WW* background	2320	1760	1200	1290	740
$t\bar{t}$ background	1010	960	850	1030	830
Wt background	2050	1890	1450	1590	920
WZ/ZZ background	105	75	45	50	35
W+jet background	25	25	25	25	25
Total background	5510	4710	3570	3985	2550
Significance (including 5% systematic uncertainty)	4.1	8.4	9.2	7.2	5.1
Significance (combined: 30 fb^{-1} + 70 fb^{-1}, including 5% systematic uncertainty)	5.4	11.4	12.7	9.7	7.2

To evaluate the significance, it has been optimistically assumed that such a normalisation can be performed to an overall accuracy of ±5%, *i.e.* that the summed WW*, $t\bar{t}$, and *Wt* background is known with a systematic uncertainty of ±5%. This uncertainty is larger than the statistical uncertainty on the background. Taking this into account, the signal significance estimated for an integrated luminosity of 30 fb^{-1} is above 5σ for ~150 < m_H < 190 GeV. Because of the less effective jet veto the residual $t\bar{t}$ and Wt backgrounds increase considerably at high luminosity. The numbers of expected signal and background events are given in Table 19-18, assuming high-luminosity running and an integrated luminosity of 100 fb^{-1}. Due to the strong increase of the $t\bar{t}$

and Wt background, the statistical significance does not improve compared to the low-luminosity running. The final signal significance which can be obtained with an integrated luminosity of 100 fb^{-1}, is computed from a combination of the significance achieved after low-luminosity operation over 30 fb^{-1} and high-luminosity operation over 70 fb^{-1}, assuming a fully correlated systematic error on the background.

The comparison of Tables 19-14 and 19-17 shows that the $H \rightarrow WW^* \rightarrow l\nu l\nu$ channel may have better sensitivity than the $H \rightarrow ZZ^* \rightarrow 4l$ channel for $160 < m_H < 175$ GeV, provided the small systematic uncertainty of ±5% Figure 19-28on the total background can be achieved.

Finally, it is important to note that constraints on the Higgs-boson mass can be extracted from the transverse mass distribution. As an example, the transverse mass distributions for m_H = 160 and 170 GeV are compared for the summed signal plus background in Figure 19-28. A sensitivity to the Higgs-boson mass is obtained from the upper edge of the distribution. The experimental resolution on the missing transverse energy defines the shape of this upper edge.

The distributions in Figure 19-28 can be separated with a purely statistical significance of 6σ [19-42]. Systematic uncertainties have not been studied yet, but the Higgs-boson mass can hopefully be constrained to better than ±5 GeV in this channel.

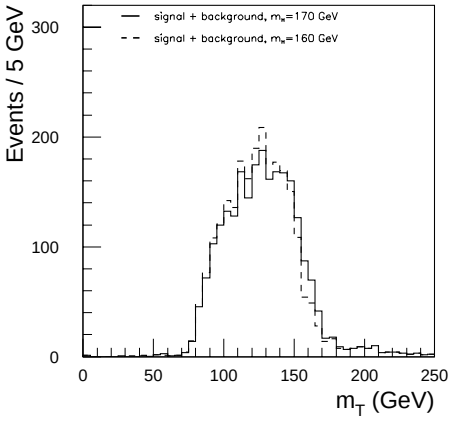

Figure 19-28 Transverse mass distributions of the summed signal plus background for m_H = 160 GeV (dashed histogram) and m_H = 170 GeV (full histogram).

19.2.7 WH with $H \rightarrow WW^* \rightarrow l\nu l\nu$ and $W \rightarrow l\nu$

It has been suggested recently [19-44], that the associated production of a Higgs boson with a W boson, with $W \rightarrow l\nu$ and $H \rightarrow WW^* \rightarrow l\nu l\nu$ provides an additional discovery channel at the LHC. The three-lepton final state appears as promising, since low background levels are expected. This channel is the associated production channel to the inclusive $H \rightarrow WW^* \rightarrow l\nu l\nu$ channel discussed in Section 19.2.6. Hence, the same general arguments about the signal extraction apply, and, in particular, evidence for a Higgs-boson signal has also in this case to be extracted from an excess of events above the expected background from Standard Model processes.

This channel is also interesting for the determination of the coupling parameters of the Higgs boson, since in its production and decay chain, only the couplings to gauge bosons appear. In almost all production and / or decay processes considered so far, Yukawa couplings of the Higgs boson to fermions are involved. In an extreme scenario, where there would appear only weak couplings of the Higgs boson to fermion pairs, this channel would remain unaffected, whereas all the others, except WH with $H \rightarrow \gamma\gamma$, would be suppressed.

A first study has been carried out [19-45], in which the ATLAS sensitivity in this channel has been investigated using fast simulation for Higgs-boson masses between 150 and 190 GeV. The signal cross-sections times leptonic branching ratios for this associated production channel are small, at the level of 4 fb. The values are given as a function of the Higgs-boson mass in Table 19-20.

There are two important backgrounds to this channel: WZ production, with a cross-section times leptonic branching ratio of 380 fb, and $t\bar{t}$ production with a cross-section times $W \rightarrow l\nu$ branching ratio of 28 pb. In the case of the $t\bar{t}$ background, the third lepton originates from semi-leptonic *b*-decays. In addition to these two major backgrounds, also the contributions from all other background sources studied for $H \rightarrow WW^* \rightarrow l\nu l\nu$ decays have been estimated. In order to achieve the necessary rejection against these backgrounds, the following cuts have been applied:

- Three isolated leptons (electrons or muons) with $p_T > 30$ GeV in the pseudorapidity interval $|\eta| < 2.5$.
- Same-flavour lepton veto: events which contain at least one pair of opposite-charge same-flavour leptons with an invariant mass between 60 and 120 GeV are rejected.
- $H \rightarrow WW$ tag: out of the three possible lepton pairs at least one should fulfil the tight angular cuts as used in the $H \rightarrow WW^* \rightarrow l\nu l\nu$ analysis (see Section 19.2.6). It is required that there is at least one pair with opposite charge, $\Delta\phi < 1.00$, $\Delta\eta < 1.5$ and an invariant dilepton mass smaller than 80 GeV. If none of the three possible lepton pairs fulfils these requirements the event is rejected.
- Jet veto: events with one or more jets with $p_T > 30$ GeV and $|\eta| < 3.2$ are rejected.

The second and third cut have a large rejection against the WZ background. The same flavour lepton veto rejects events containing $Z \rightarrow ll$ decays: this cut alone rejects the WZ background by about a factor 100 for a signal efficiency of about 70%. The residual WZ background contains either an off-shell Z or a $Z \rightarrow \tau\tau \rightarrow l\nu\, l\nu + X$ decay. Since the signal events contain two W bosons which originate from the decay of the scalar Higgs boson, the arguments on the angular separation between the decay leptons are still valid. The $H \rightarrow WW$ tag, based on this angular separation, therefore leads to another significant rejection of both the WZ and $t\bar{t}$ backgrounds for a reasonable signal efficiency. For the cuts applied, a rejection of about 3 is obtained for a signal efficiency of 85%. The large $t\bar{t}$ background can be further rejected in two different ways. A strict jet veto can be applied, where it is required that there be no jets with $p_T > 15$ GeV over $|\eta| < 3.2$. This jet veto can be applied at low luminosity, whereas at high luminosity the p_T-threshold has to be raised to 30 GeV. Since for $t\bar{t}$ events the third lepton originates from a semileptonic b-decay, the p_T-spectrum of the third lepton is more steeply falling for leptons from $t\bar{t}$ events than the one from signal events. There-

Table 19-19 Cross-sections times $W \rightarrow l\nu$ and $Z \rightarrow ll$ branching ratios and expected background rates for $WH \rightarrow WWW^* \rightarrow 3l$ decays. The rates are given for an integrated luminosity of 100 fb^{-1} and for various combinations of lepton and jet veto cuts. All other cuts are applied in addition, as described in the text.

Background process	**WZ**	**$t\bar{t}$**	**Wt**
σ x BR (fb)	380	28000	3500
Expected background events:			
$p_T(l) > 30$ GeV, Jet veto: 30 GeV	8.9	3.8	< 0.1
$p_T(l) > 20$ GeV, Jet veto: 15 GeV	4.7	8.1	10.0
$p_T(l) > 20$ GeV, Jet veto: 30 GeV	20.8	135	48.5

fore, a high p_T-threshold on the three leptons largely rejects the $t\bar{t}$ background, while keeping still a significant fraction of the signal. Both methods have been applied in the present study and the results are summarised in Table 19-19, where the expected background event rates are given for an integrated luminosity of 100 fb^{-1}. It should be noted that on top of the jet veto and lepton p_T-cuts indicated in the Table the same flavour lepton veto and the $H \rightarrow WW$ tag, as described above, have also been applied. As can be seen from these numbers, the largest background rejection is obtained if strict lepton p_T cuts are applied. For looser lepton cuts, the $t\bar{t}$ and Wt backgrounds are significant, in particular if a loose jet veto has to be applied, which is the case for high-luminosity operation. Since for these backgrounds the third lepton comes from a *b*-decay, an additional background rejection could be achieved using impact parameter and isolation criteria. An accurate estimation of these rejections requires a full simulation of the events. Since this has not yet been done, results based on the strict lepton cuts are quoted in the following.

The signal acceptance and the expected rates for signal and background events are summarised in Table 19-20 for Higgs boson masses in the range between 150 and 190 GeV and for an integrated luminosity of 100 fb^{-1}. For the cuts listed above, a total background of 12.7 events is found, which is dominated by the irreducible WZ background. The signal rate is largest for m_H =160 GeV, for which 28.5 signal events are expected. Therefore, a good signal-to-background ratio can be achieved in this channel for Higgs boson masses around 160 GeV. In the evaluation of the signal rates a lepton identification efficiency of 90% per lepton has been assumed.

The signal significance has been evaluated using Poisson statistics and assuming, as in the search for $H \rightarrow WW^* \rightarrow l\nu l\nu$ decays, a systematic uncertainty of ±5% on the total background. Due to the small background, however, this systematic uncertainty does not strongly degrade the significance. At high luminosity, a 5σ discovery of a SM Higgs boson in this channel seems to be possible in the mass range between ~155 GeV < m_H < 175 GeV, assuming an integrated luminosity of 100 fb^{-1}. For an ultimate integrated luminosity of 300 fb^{-1} the full range between 150 GeV and 190 GeV can be covered. For an integrated luminosity of 30 fb^{-1}, this channel is still rate-limited and a signal significance at the level of 3σ is obtained for m_H in the range between 160 and 170 GeV.

Table 19-20 Cross-sections times branching ratios, acceptances and numbers of expected signal and background events for WH, $H \rightarrow WW^* \rightarrow l\nu l\nu$ and $W \rightarrow l\nu$ decays and for an integrated luminosity of 100 fb^{-1}. The signal significances are computed assuming a systematic uncertainty of ±5% on the background and Poisson statistics.

Higgs mass (GeV)	**150**	**160**	**170**	**180**	**190**
σ × BR (fb)	3.95	4.60	4.10	3.30	2.35
Acceptance	0.063	0.085	0.084	0.077	0.067
Signal	18.1	28.5	25.2	18.5	11.5
Total background	12.7	12.7	12.7	12.7	12.7
Statistical significance (100 fb^{-1})	4.3	6.4	5.7	4.5	3.0
Statistical significance (30 fb^{-1})	2.2	3.3	3.0	2.3	1.5

Like for $H \rightarrow WW^* \rightarrow l\nu l\nu$ decays discussed in Section 19.2.6, the transverse mass of the E_T^{miss} and di-lepton system can be reconstructed for those di-lepton pairs fulfilling the angular separation and di-lepton mass cuts ($H \rightarrow WW$ tag). Although the E_T^{miss} is affected by the decay neutrino from the associated W boson, it is still peaked in the mass range between 100 and 200 GeV. As an example, the reconstructed transverse mass distribution is shown in Figure 19-29. The signal to background ratio can still be improved if appropriate transverse mass cuts are applied.

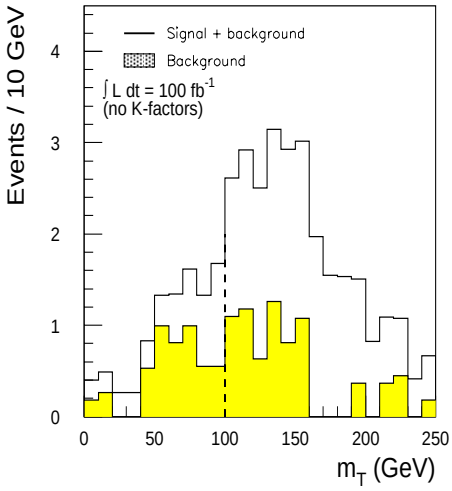

Figure 19-29 Transverse mass distributions of the summed signal plus background (histogram) for m_H = 160 GeV and for the background (shaded area).

In conclusion, the three-lepton channel represents an interesting possibility to enhance the observability of a Higgs-boson signal in the mass region between 150 and 190 GeV. It should finally be mentioned that, in addition to the three-lepton channel discussed here, the $WH \rightarrow WWW \rightarrow lljj$ channel with like-sign-leptons in the final state should also be considered. Although it suffers potentially from much larger backgrounds than the three-lepton channel, this channel is considered as interesting for Higgs-boson searches at the upgraded TeVatron collider [19-46].

19.2.8 Sensitivity to the SM Higgs boson in the intermediate mass range

The potential of the ATLAS experiment for the discovery of a SM Higgs boson in the intermediate mass range, 80 GeV < m_H < 2m$_Z$, is summarised in Figure 19-30 for integrated luminosities of 30 and 100 fb^{-1}. The signal significances are shown for individual channels, as well as for the combination of all channels.

For an integrated luminosity of 100 fb^{-1}, a SM Higgs boson can be discovered with a high significance over the full intermediate mass range. For all masses, the Higgs boson would be discovered in at least two different decay channels. A Higgs boson discovery with the ATLAS detector is already possible over the full intermediate mass range after a few years of running at low luminosity. It should be noted once again that no *K*-factors are included in the estimates of the signal significance, since these *K*-factors are generally not known for most background processes. This approach is conservative as long as the K-factor for the signal is larger than the square root of the *K*-factor for the background.

The most important channels in the intermediate mass region, for which a mass peak would be reconstructed, are the four-lepton channel, $H \rightarrow ZZ^* \rightarrow 4l$, the direct two-photon channel, $H \rightarrow \gamma\gamma$, as well as the associated production channels, where the Higgs boson is produced in association with a vector boson or a $t\bar{t}$ pair. In these channels, both the $\gamma\gamma$ and $b\bar{b}$ decay modes can be discovered at the LHC. For Higgs-boson masses around 170 GeV, for which the ZZ^* branching ratio is suppressed, the discovery potential can be enhanced by searching for the $H \rightarrow WW^* \rightarrow l\nu l\nu$ decay. In this case, the Higgs-boson signal would only be observed as an excess of events.

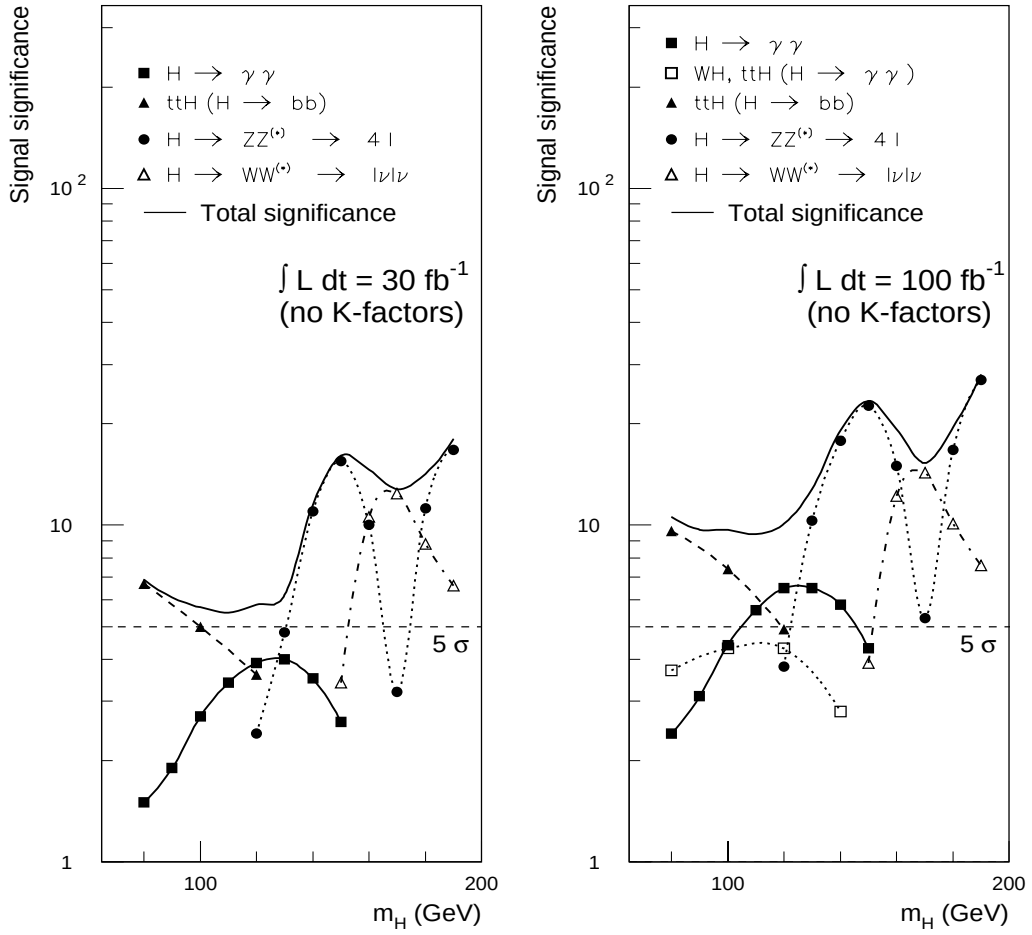

Figure 19-30 Sensitivity for the discovery of a Standard Model Higgs boson in the intermediate mass range. The statistical significances are plotted for individual channels as well as for the combination of all channels, assuming integrated luminosities of 30 fb^{-1} (left) and 100 fb^{-1} (right). Depending on the numbers of signal and background events, the statistical significance has been computed as $S/\sqrt{B}$ or using Poisson statistics. In the case of the $H \rightarrow WW^* \rightarrow l\nu l\nu$ channel, a systematic uncertainty of ±5% on the total number of background events has been included (see Section 19.2.6).

Most of the decay channels studied in the intermediate mass range are challenging in terms of detector performance. Even though the natural width of the Standard Model Higgs boson in this mass range is narrow, the backgrounds are relatively large and thus, an excellent detector performance in terms of energy resolution and background rejection is required. The $H \rightarrow \gamma\gamma$ decay mode requires high performance of the electromagnetic calorimetry in terms of photon energy resolution, photon direction measurements, and γ/jet separation. Impact parameter measurements in the Inner Detector are crucial for the discovery of the $b\bar{b}$ decay mode: efficient tagging of b-jets with a high rejection against light-quark and gluon jets allows a rather clean and complete reconstruction of $t\bar{t}$ final states together with the $b\bar{b}$ mass peak from Higgs boson decays. Finally, excellent performance in terms of the identification, reconstruction and measurement of isolated leptons with $p_T > 7$ GeV is required to discover the Higgs boson in the $H \rightarrow ZZ^* \rightarrow 4l$ channel. Due to the low expected rates over most of the mass range of interest, the Higgs boson cannot be discovered separately in the $H \rightarrow ZZ^* \rightarrow eeee$ or $H \rightarrow ZZ^* \rightarrow \mu\mu\mu\mu$ decay modes.

The performance of the ATLAS detector in its final optimised layout has been simulated in detail to assess whether it is able to meet the demanding requirements for the search for a Standard Model Higgs boson in the intermediate mass range. All the key performance characteristics have been evaluated with full GEANT simulation, both at low and high luminosity. These include the mass resolutions for the $H \rightarrow \gamma\gamma$, $H \rightarrow b\bar{b}$ and $H \rightarrow ZZ^* \rightarrow 4l$ channels, the performance of the *b*-tagging algorithms, and the rejections of many reducible backgrounds from various abundant Standard Model processes.

In conclusion, the ATLAS detector performance is adequate to guarantee that, if a Standard Model Higgs boson exists with a mass in the intermediate range, it will be discovered after only a few years of operation at low luminosity. Such a discovery would be confirmed and consolidated with better statistical significance at high luminosity. The results presented in the preceding Sections and summarised in Figure 19-30 could be compared to recent estimates based on work done in the context of studies performed for the future Tevatron runs [19-47]. Work is in progress to assess in a consistent way within ATLAS the comparative potentials of the detector to discover a SM Higgs boson in the intermediate mass range, in *pp* collisions at $\sqrt{s}$ = 14 TeV versus $p\bar{p}$ collisions at $\sqrt{s}$ = 2 TeV for an integrated luminosity of 30 fb^{-1} [19-48].

19.2.9 $H \rightarrow ZZ \rightarrow 4l$

For Higgs-boson masses in the range 180 GeV < m_H < ~700 GeV, the $H \rightarrow ZZ \rightarrow 4l$ decay mode is the most reliable channel for the discovery of a Standard Model Higgs boson at the LHC. The expected background, which is dominated by the continuum production of *Z* boson pairs, is smaller than the signal. In this mass range, the natural width of the Higgs boson grows rapidly with increasing m_H, and dominates the experimental mass resolution for m_H > 300 GeV. The momenta of the final-state leptons are high and their measurement does not put severe requirements on the detector performance. Therefore, the discovery potential in this channel is primarily determined by the available integrated luminosity.

The signal is reconstructed by requiring four identified leptons in the pseudorapidity range $|\eta| < 2.5$. The two leading leptons are required to have transverse momenta above 20 GeV, whereas the other two are required to have $p_T > 7$ GeV. For the lepton identification, an efficiency of 90% per lepton is assumed. The continuum $Z(\gamma^*)\, Z(\gamma^*) \rightarrow 4l$ production is the dominant background source in this mass range and its total production cross-section times branching ratio is 44 fb for $m_{ZZ} > 200$ GeV.

Since the Higgs-boson width varies rapidly over the mass range considered in this Section, a variable mass window of width σ_m, given by the convolution of the Higgs decay width and of the experimental resolution, $\sigma_m = ((\Gamma_H / 2.36)^2 + (0.02\ m_H)^2)^{1/2}$, was used to evaluate the observability of the signal. The acceptance was assumed to be 90% in a mass window of $\pm 1.64\ \sigma_m$ around m_H. Better estimates would require taking into account the correct line-shape for a broad Higgs boson, as well as interference effects between the resonant signal and the non-resonant background [19-49]. Given the very large sensitivity expected in this channel, these effects are not deemed critical for the evaluation of the signal observability, but would have to be included for *e.g.* a measurement of m_H.

The signal and background events expected in the mass window after applying only the simple kinematic cuts listed above are given in Table 19-21 (see [19-15] for more details). These numbers demonstrate that the signal can be easily identified above a small background over the full mass range from 200 to 600 GeV.

Since the Z-bosons from Higgs-boson decays are produced through the two-body decay of a heavy object, a significant rejection of the continuum ZZ background can be achieved by requiring that the transverse momentum of the harder of the two Z-bosons, $p_T^{max}(Z_1, Z_2)$, be larger than a given threshold value. As can be seen from the numbers in Table 19-21, the significance improves substantially if a moderate requirement, $p_T^{max}(Z_1, Z_2) > m_H/3$, is applied. Harder cuts on this maximum p_T would improve even further the signal significance. The efficiency of these harder cuts for the signal events is, however, subject to possibly significant theoretical uncertainties on the p_T distribution of the Higgs boson. In addition, the ZZ continuum background is known to be subject to higher-order QCD corrections [19-49], which increase substantially the background for high values of p_T^Z.

Table 19-21 Branching ratios and production cross-sections times branching ratios for the $H \rightarrow ZZ \rightarrow 4l$ decay mode, and expected numbers of signal and background events as a function of m_H. The expected event rates are given for an integrated luminosity of 30 fb^{-1} and for two sets of selection criteria, without and with an additional cut on the p_T of the harder of the two Z-bosons ($p_T^{max}(Z_1, Z_2) > m_H/3$).

Higgs mass (GeV)	**200**	**240**	**280**	**320**	**360**	**400**	**500**	**600**
$BR(H \rightarrow ZZ)$	0.26	0.29	0.30	0.31	0.30	0.28	0.27	0.27
$\sigma \times$ BR (fb)	12.4	11.2	9.6	8.9	8.7	6.8	3.2	1.6
Signal (no p_T cut)	134	127	110	105	105	86	44	23
Background (no p_T cut)	74	57	43	33	29	29	17	15
$S/\sqrt{B}$ (no p_T cut) for 30 fb^{-1}	15.6	16.8	16.8	18.2	19.3	15.9	10.7	5.9
Signal (with p_T cut)	54	88	90	90	91	76	39	19
Background (with p_T cut)	7	15	17	16	13	14	7	6
$S/\sqrt{B}$ (with p_T cut) for 30 fb^{-1}	20.4	22.7	21.8	22.5	25.2	20.3	14.7	7.8
$S/\sqrt{B}$ (with p_T cut) for 100 fb^{-1}	37.3	40.9	40.1	41.2	46.9	37.3	27.1	15.0

In conclusion, the $H \rightarrow ZZ \rightarrow 4l$ signal would be observed easily above the $ZZ \rightarrow 4l$ continuum background after less than one year of low luminosity operation for $200 < m_H < 600$ GeV. As an example of signal reconstruction above background, Figure 19-31 shows the expected signal from a Higgs boson with $m_H = 300$ GeV for an integrated luminosity of only 10 fb^{-1}. The signal is shown before (left) and after (right) the p_T^{max} cut is applied, and is clearly visible above the background from ZZ continuum production.

For larger values of m_H, the Higgs-boson signal becomes very broad and the signal rate drops rapidly, but a signal in the $H \rightarrow ZZ \rightarrow 4l$ channel could be observed up to $m_H \sim 800$ GeV, possibly even through the WW/ZZ fusion process if jet tagging in the forward regions is required [19-13].

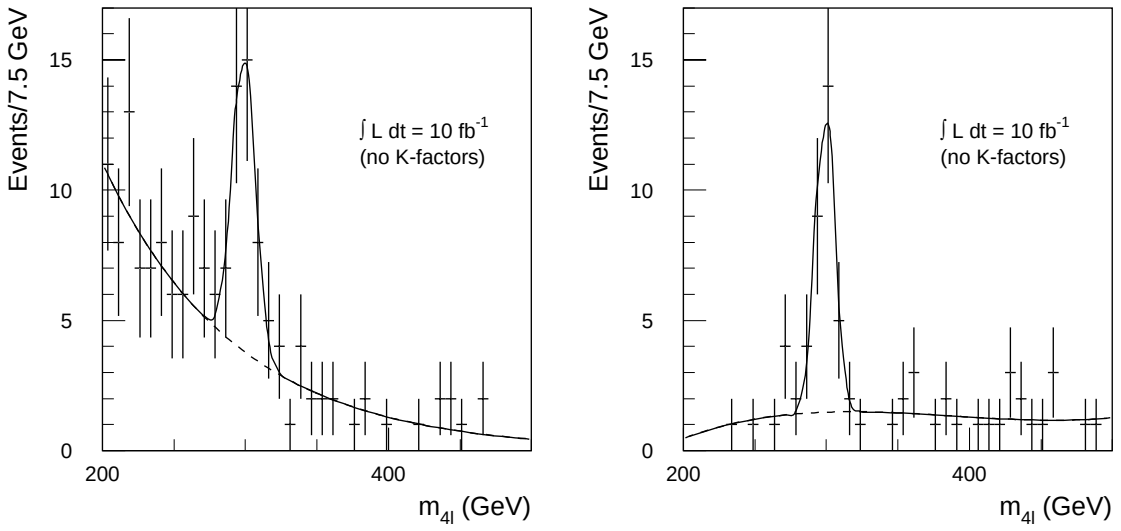

Figure 19-31 Expected $H \rightarrow ZZ \rightarrow 4l$ signal for m_H = 300 GeV and for an integrated luminosity of 10 fb^{-1}. The signal is shown on top of the ZZ continuum background before (left) and after (right) the $p_T^{max}(Z_1, Z_2)$ cut is applied (see text).

19.2.10 Heavy Higgs boson

As discussed in Section 19.2.9, the $H \rightarrow ZZ \rightarrow 4l$ decay mode can be observed up to $m_H \sim 800$ GeV, but it becomes rate-limited around $m_H = 700$ GeV. If no Higgs-boson signal were found for $m_H < 600$ - 800 GeV, searches in the TeV mass range would be essential to understand the electroweak symmetry-breaking mechanism. To access this mass range, one needs to detect Higgs-boson decays containing neutrinos or jets in the final state. If a Higgs-boson signal were found in the $H \rightarrow ZZ \rightarrow 4l$ channel, these channels could confirm the discovery and provide additional information on the Higgs couplings (WW-fusion production mechanism and $H \rightarrow WW$ decays).

The channels considered in this Section are the $H \rightarrow ZZ \rightarrow ll\nu\nu$ mode with a rate six times larger than the four-lepton mode and with a large E_T^{miss} signature, the $H \rightarrow WW \rightarrow l\nu jj$ mode with a rate 150 times larger than the four-lepton mode, and the $H \rightarrow ZZ \rightarrow lljj$ mode which has a rate 25 times larger than the four-lepton mode (six times smaller than the $H \rightarrow WW \rightarrow l\nu jj$ mode).

To reject the large QCD backgrounds in these channels excellent E_T^{miss} measurements and accurate reconstruction of $W/Z \rightarrow jj$ decays are needed. In addition, for the large values of m_H, a big fraction of the Higgs bosons are produced via gauge-boson fusion, materialised by forward-backward jets emitted at large pseudorapidities ($|\eta| > 2$). Good jet identification and energy measurements over $2 < |\eta| < 5$ are therefore essential [19-50].

19.2.10.1 *Search for $H \rightarrow ZZ \rightarrow ll\nu\nu$*

The signal in this channel is characterised by two high-p_T leptons from $Z \rightarrow ll$ decay in the central region and a large E_T^{miss} from $Z \rightarrow \nu\nu$ decay. The production cross-section times branching ratio is a few fb for $m_H \sim 500$ - 700 GeV, with a 25 - 30% contribution from vector boson fusion.

The largest background arises from reducible Z+jet production, where large E_T^{miss} can be created by neutrinos or by badly reconstructed jets due to cracks, dead material and the limited calorimeter pseudorapidity coverage. In addition, the ZZ irreducible continuum background, as well as the reducible $t\bar{t}$ and WZ/WW backgrounds have to be considered.

It has been shown in [19-51] and [19-52] (see also Section 9.2.2) that, for $E_T^{miss} > 150$ GeV, the instrumental background from jets mis-measured in the calorimeter or escaping outside the calorimeter coverage is much smaller than the background from Z+jet and ZZ production, where the E_T^{miss} is genuine (it originates from neutrinos produced in semi-leptonic decays of b-jets in the case of Z+jet production).

The selection cuts chosen for the $H \rightarrow ZZ \rightarrow ll\nu\nu$ channel are:

- Two same-flavour opposite-sign leptons with $p_T > 40$ GeV and $|\eta| < 2.5$ and no other isolated lepton.
- Z mass window: $m_{ll} = m_Z \pm 6$ GeV.
- Cut on p_T of $Z \rightarrow ll$: $p_T^{ll} >$ 150 (250) GeV for $m_H = 500$ (700) GeV.
- $E_T^{miss} > 150$ GeV.
- Forward jet tagging: one or two tag jets with $|\eta| > 2$ and $p_T > 25$ GeV.

The cumulative acceptances of these cuts, evaluated with fast simulation, are shown in Table 19-22. The efficiencies for the reconstruction of the tag jets in the signal events and the probabilities for fake tags in the background events are taken from fully simulated events [19-53][19-54] (see also Section 9.1.4).

Table 19-22 Cumulative acceptances (in %) of the various selection cuts for the $H \rightarrow ZZ \rightarrow ll\nu\nu$ signal and backgrounds.

Process	Lepton cuts	Z mass window	p_T^{ll} cut	E_T^{miss} cut	One tag jet	Two tag jets
$H \rightarrow ZZ \rightarrow ll\nu\nu$ ($m_H = 500$ GeV)	66.8	54.4	38.8	33.0	16.0	2.9
$H \rightarrow ZZ \rightarrow ll\nu\nu$ ($m_H = 700$ GeV)	70.4	57.4	45.7	41.1	21.6	4.8
ZZ continuum	36.2	29.2	1.9	1.4	0.24	0.016
WZ continuum	35.5	25.6	0.11	0.075	0.016	0.0018
WW continuum	36.7	1.1	0.005	0.002	0.001	$<< 10^{-3}$
$t\bar{t}$	3.1	0.09	0.005	3×10^{-4}	$< 10^{-5}$	$<< 10^{-5}$
Z+jets	64.0	51.6	3.4	1.6×10^{-5}	4×10^{-6}	1.3×10^{-6}

Figure 19-32 shows the E_T^{miss} distribution for the signal and various backgrounds which satisfy all the cuts of Table 19-22, including a double jet tag. The results are shown for $m_H = 600$ and 900 GeV. The signal appears as an excess of events with large E_T^{miss} above the backgrounds. After all selection cuts, including the double jet tag, the different backgrounds listed in Table 19-22 are all present (with the exception of the WW background) at approximately the same level.

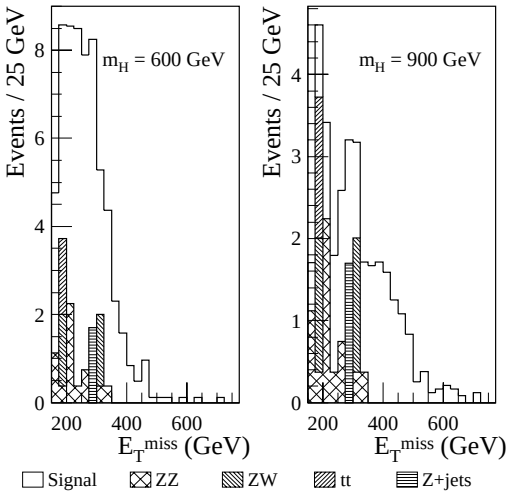

Figure 19-32 For an integrated luminosity of 100 fb^{-1} and for m_H = 600 GeV (left) and m_H = 900 GeV (right), reconstructed E_T^{miss} distribution for the $H \rightarrow ZZ \rightarrow ll\nu\nu$ signal and for the various backgrounds after requiring a double jet tag.

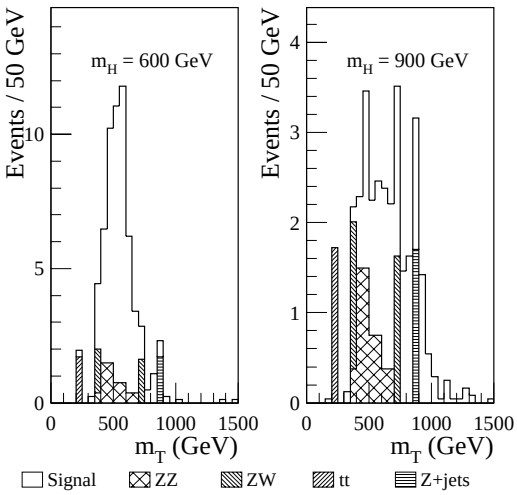

Figure 19-33 Same as Figure 19-32, but for the distribution of m_T, the transverse mass of the (ll E_T^{miss}) system.

In order to extract a more convincing signal, the transverse mass of the (ll E_T^{miss}) system, m_T, is calculated and shown in Figure 19-33. For m_H = 600 GeV, the width of the Higgs boson is still narrow enough that the peak of the m_T distribution can be observed close to the nominal Higgs-boson mass, and the signal is large with respect to the background. For m_H = 900 GeV, this is no longer the case, and a clear evidence for the signal would only be obtained if less stringent kinematic cuts (to provide a smoothly falling shape of the background as a function of E_T^{miss} or m_T) and variable jet tagging cuts (to vary the signal-to-background ratio) were studied, in a way similar to that described in more detail for the case of $H \rightarrow WW \rightarrow l\nu jj$ decays (see Section 19.2.10.2).

In addition, higher-order corrections to gauge-boson pair production (see Section 15.7.5) lead to significant increases in the background. For example, the E_T^{miss} distribution of the ZZ continuum background in Figure 19-32 corresponds to the p_T spectrum of the Z-boson decaying to a neutrino pair; for large values of E_T^{miss}, this spectrum might be underestimated by a factor of about two, in particular if the jet tagging cuts are assumed to be uncorrelated to the expected increase in rate due to the higher-order corrections.

With these caveats, the signal-to-background ratios and significances have been evaluated for the selection cuts described above and are shown in Table 19-23 as a function of the jet tagging cuts for m_H = 500 and 700 GeV and for an integrated luminosity of 100 fb^{-1}.

Without any jet tagging, the signal-to-background ratio is somewhat below one and decreases by a factor two when m_H increases from 500 to 700 GeV. The requirement of a single jet tag increases the signal-to-background ratio by a factor of about 2.5, and also increases the signal significance. As stated above, this significance does not correspond to a clear observation of a peak above a well-constrained background and should therefore be taken as an optimistic estimate. The requirement of a double jet tag further improves the signal-to-background ratio, and may be sufficient to demonstrate the discovery of a signal from $H \rightarrow ZZ \rightarrow ll\nu\nu$ decays.

Table 19-23 For an integrated luminosity of 100 fb^{-1}, expected numbers of $H \rightarrow ZZ \rightarrow ll\nu\nu$ signal and background events, signal-to-background ratios (*S/B*) and significances ($S/\sqrt{B}$), for m_H = 500 and 700 GeV and for various jet tagging cuts.

	Jet tagging	Signal	Background	*S/B*	$S/\sqrt{B}$
m_H = 500 GeV	None	707	763	0.9	25.6
	Single tag	345	147	2.4	28.5
	Double tag	66	12	5.3	18.7
m_H = 700 GeV	None	322	763	0.4	11.6
	Single tag	168	147	1.1	13.9
	Double tag	38	12	2.9	10.8

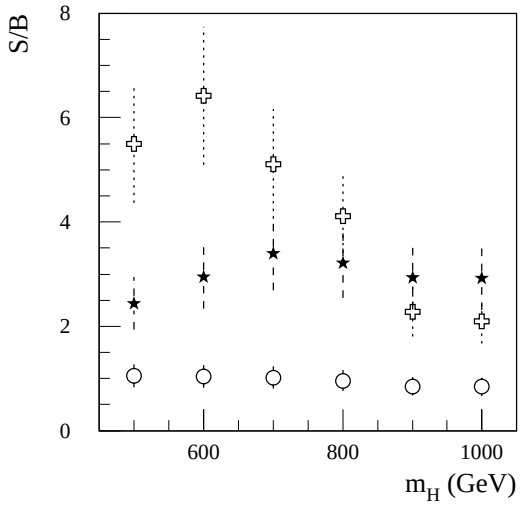

Figure 19-34 For an integrated luminosity of 100 fb^{-1} (high luminosity operation) and for the $H \rightarrow ZZ \rightarrow ll\nu\nu$ channel, optimised signal-to-background (*S/B*) ratio as a function of m_H for three jet tagging requirements: no jet tag (open circles), a single jet tag with p_T > 25 GeV (black stars), and a double jet tag with p_T > 25 GeV (open crosses).

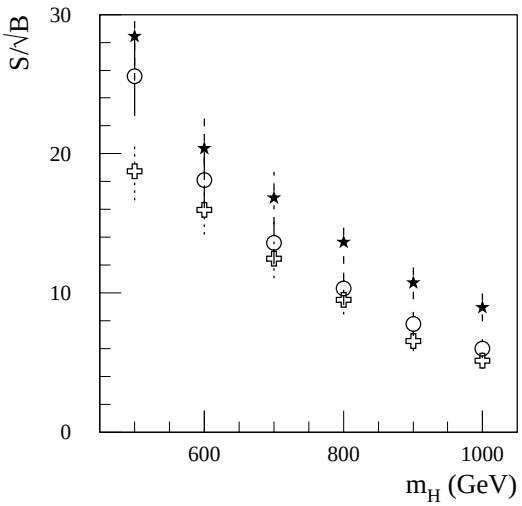

Figure 19-35 Same as Figure 19-34, but for the signal significance $S/\sqrt{B}$ as a function of m_H.

The p_T^{ll} and E_T^{miss} cuts have been varied as a function of m_H in an attempt to optimise the discovery potential of the $H \rightarrow ZZ \rightarrow ll\nu\nu$ channel over the range 400 < m_H < 1000 GeV. The results in terms of signal-to-background ratio and signal significance are shown in Figures 19-34 and 19-35, respectively, for an integrated luminosity of 100 fb^{-1}. All the results discussed above are obtained for high luminosity operation in the presence of pile-up, which affects the jet tagging efficiencies and fake tag rates (see Section 9.1.4). In the case of low luminosity operation, the signal-to-background ratios are therefore somewhat better than those of Figure 19-34, but the observability of a signal from $H \rightarrow ZZ \rightarrow ll\nu\nu$ decays would be limited to m_H < 600 GeV for an integrated luminosity of 30 fb^{-1}, due to the low rates expected after requiring a double jet tag.

If a signal is observed in this channel, the transverse mass of the (ll E_T^{miss}) system, m_T, can be used to measure the mass of the Higgs boson. Figure 19-36 shows as a crude example the variation of the average value of m_T as a function of m_H, including the expected purely statistical error for an integrated luminosity of 100 fb^{-1}.

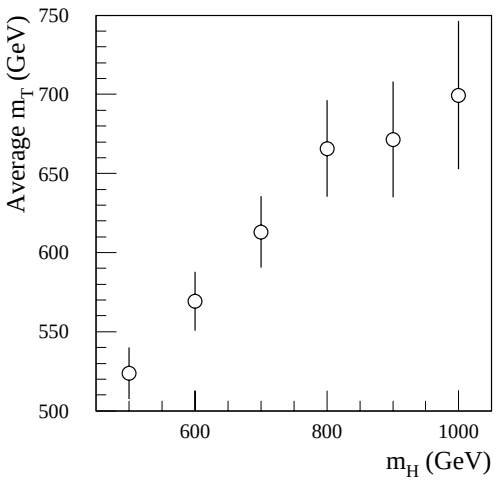

Figure 19-36 Average value of the reconstructed transverse mass, m_T, as a function of m_H, for the $H \rightarrow ZZ \rightarrow llνν$ signal with a double jet tag and for an integrated luminosity of 100 fb^{-1} (the error bars are purely statistical).

In conclusion, the $H \rightarrow ZZ \rightarrow llνν$ channel should be observable over a wide mass range from 400 to 900 GeV, and thus provide a reliable confirmation of the discovery of the Higgs boson in the gold-plated $H \rightarrow ZZ \rightarrow 4l$ channel for $m_H < 700$ GeV. For larger values of m_H, the demonstration of the observability of a convincing signal above the background requires careful studies of the evolution of the background shape as a function of the kinematic and jet tagging cuts, as well as a better understanding of the theoretical predictions for the p_T spectrum of individual vector bosons in gauge-boson pair production.

19.2.10.2 $H \rightarrow WW \rightarrow lνjj$ and $H \rightarrow ZZ \rightarrow lljj$ in $qq \rightarrow qqH$ production with $m_H \sim 1$TeV

The signal from this channel has a large enough rate to be observed during low luminosity operation and a very distinctive signature [19-55]:

- A high-p_T central lepton ($|\eta| < 2$).
- Large missing transverse energy from the escaping neutrino.
- Two high-p_T jets from the $W \rightarrow jj$ decay in the central region. Due to the large boost of the W-boson, the two jets are close-by in space ($\Delta R \sim 0.4$) and their energy deposition overlap.
- Two low-p_T tag jets in the forward regions ($|\eta| > 2$) coming from the WW/ZZ fusion production process.
- Small hadronic activity in the central region, except for the jets from $W \rightarrow jj$ decay.

The main backgrounds, before requiring any tag jets are:

- W+jet production with $W \rightarrow lν$. This background is potentially the largest and suffers from significant theoretical uncertainties due to higher-order corrections (K-factors) and to the procedure used to generate the events (see [19-56] for a comparison of the matrix-element and parton-shower approaches).
- $t\bar{t} \rightarrow lνjjb\bar{b}$ production. This background contains a real $W \rightarrow jj$ decay, but also additional hadronic activity from the b-jets when they fall in the central region.
- $WW \rightarrow lνjj$ continuum production, which has much lower rates than the W+jet and $t\bar{t}$ reducible backgrounds, but which is irreducible in the central region.

The main issues linked to the signal reconstruction and the background rejection are therefore the experimental efficiency and resolution for reconstructing high-p_T $W \to jj$ decays (see also Section 9.3.1.3) and the performance of the jet-veto cuts in the central region (see also Section 9.1.3). All the background processes will be rejected with high efficiency by the additional requirement of one or two tag jets in the forward region ($|\eta| > 2$) [19-50] and a realistic assessment of the performance of jet tagging has also to be included (see Section 9.1.4).

A set of cuts, called high-p_T central cuts, which are optimised exclusively in terms of the statistical significance of the signal above the background, without any study of the actual visibility of the signal, is used in the first stage of the analysis:

- Lepton cuts: p_T^l, $E_T^{miss} > 100$ GeV, $p_T^{W \to l\nu} > 350$ GeV.
- Jet cuts: two jets reconstructed within $\Delta R = 0.2$ with $p_T > 50$ GeV and $p_T^{W \to jj} > 350$ GeV.
- W mass window: $m_{jj} = m_W \pm 2\sigma$, where σ is the resolution on m_{jj} (see below).

Table 19-24 shows the cumulative efficiencies for $H \to WW \to l\nu jj$ decays with $m_H = 1$ TeV, as obtained for the high-p_T central cuts described above, for fast simulation compared to full simulation and reconstruction. The results are in good agreement for all cuts, and the full-simulation studies without and with pile-up show that these efficiencies are not affected strongly by pile-up, except possibly for the mass window on the W mass (see below).

Table 19-24 For the $H \to WW \to l\nu jj$ channel with $m_H = 1$ TeV, comparison of the cumulative efficiencies of the high-p_T central cuts (see text) for the fast and the full simulation and for low luminosity operation (no pile-up) and high luminosity operation (with pile-up).

Cuts	Fast simulation	Full simulation (no pile-up)	Full simulation (with pile-up)
Lepton cuts	43.3%	42.6%	42.6%
Jet cuts	29.0%	29.8%	29.8%
W mass window (no pile-up)	25.2%	24.8%	
W mass window (with pile-up)	23.6%		24.4%

The reconstruction of high-p_T $W \to jj$ decays is described in detail in Section 9.3.1.3. Various methods to overcome the problems of jet overlap and to optimise the resolution on the reconstructed W mass have been studied [19-54], and the one chosen for the studies reported here calculates the mass of the two jets, selected within a cone of size $\Delta R = 0.2$ and with $p_T > 50$ GeV, by using the four-momenta of each calorimeter cell (assumed to have zero mass) in two cones of size $\Delta R = 0.4$ with barycentres determined by the cones of size $\Delta R = 0.2$. Figure 19-37 shows the distributions of the reconstructed dijet mass with this method in the case of low luminosity operation (no pile-up) and of high luminosity operation (with pile-up). The distributions are obtained from a sample of fully simulated and reconstructed $H \to WW \to l\nu jj$ decays, and have been corrected as a function of the p_T of the dijet system for the systematic bias due to the finite size of hadronic showers, which results in a linear increase of the measured W mass as a function of the p_T of the W-boson (see Section 9.3.1.3).

Figure 19-37 shows that the resolution σ increases only from 5.0 GeV to 6.9 GeV when pile-up at high luminosity is added. The fraction of $W \to jj$ decays with $m_{jj} = m_W \pm 2\sigma$ decreases from 83% without pile-up to 82% with pile-up. The results for these efficiencies are also in good agreement between the fast and full simulation, as shown in Table 19-24.

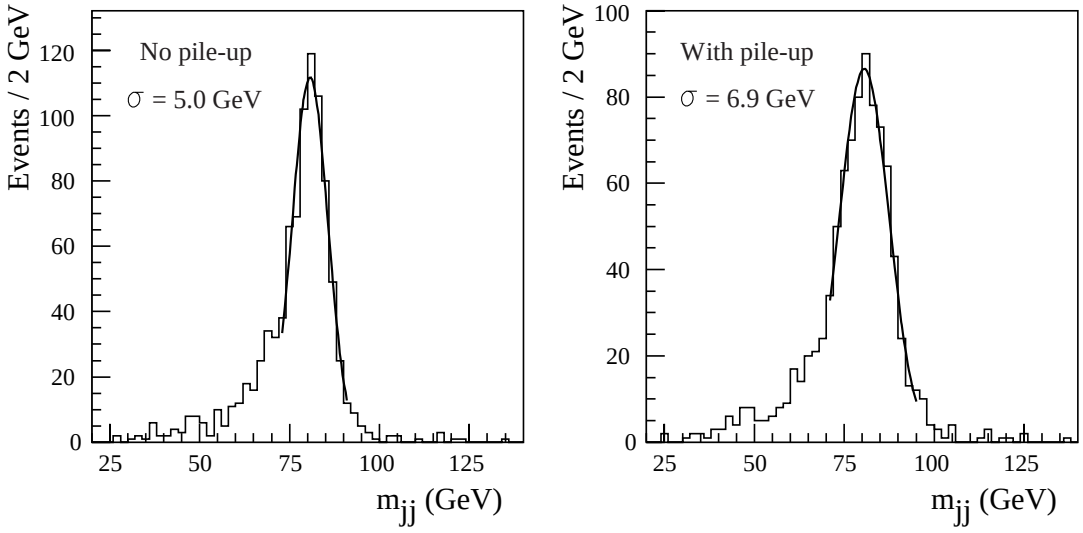

Figure 19-37 For fully simulated and reconstructed $H \rightarrow WW \rightarrow l\nu jj$ decays with m_H = 1 TeV, distributions of the dijet mass using the mass reconstruction method described in the text for low-luminosity operation (left) and high-luminosity operation (right).

Table 19-25 shows the numbers of signal and background events produced for an integrated luminosity of 30 fb^{-1}, the cumulative efficiencies of the high-p_T central cuts, and the numbers of events accepted after these cuts. Additional cuts are clearly needed, as mentioned above (jet veto in the central region and jet tagging in the forward regions).

Table 19-25 Numbers of events produced for an integrated luminosity of 30 fb^{-1} and cumulative efficiencies of the high-p_T central cuts (see text), as obtained from fast simulation for the $H \rightarrow WW \rightarrow l\nu jj$ signal with m_H = 1 TeV and for the $t\bar{t}$ and W+jet backgrounds.

	Higgs signal	**$t\bar{t}$ (p_T > 300 GeV)**	**W + jets (p_T > 250 GeV)**
Events produced	486	192 000	448 000
Efficiency of lepton cuts	43.3%	6.2%	11.5%
Efficiency of jet cuts	29.0%	3.3%	2.3%
Efficiency of W mass window	25.2%	1.0%	0.52%
Events accepted	122	1900	2300

Jet profile and asymmetry cuts have been investigated [19-54], to explore whether any significant additional rejection can be obtained against the dominant W+jet background. For the latter background the dijet system reconstructed with $m_{jj} = m_W \pm 2\sigma$ does not originate from the decay of a colour singlet and the jets are therefore expected to be broader than in the case of a real $W \rightarrow jj$ decay. Unfortunately, efficient cuts against the W+jet background would substantially bias the final mass distributions used to extract the signal (as described below) and this approach has not been pursued any further.

The performance of jet-veto cuts in the central region is described in detail in Section 9.1.3 as a function of the p_T threshold. Section 9.1.3 also compares the results from fast simulation to those from full simulation and reconstruction. The efficiency for signal events is found to be about 5% higher for fast simulation and is about 60% for a central jet veto ($|\eta| < 2$) with a p_T threshold of 25 GeV at low luminosity. The rejection of the $t\bar{t}$ background events is in excellent agreement between fast and full simulation.

This is illustrated in Figure 19-38 using a fast simulation, of the $H \rightarrow WW \rightarrow l\nu jj$ signal and of the $t\bar{t}$ and W+jet backgrounds. Efficiency here is defined as the fraction of events with no additional jet with p_T larger than threshold. The p_T thresholds chosen here are 15 GeV at low luminosity and 25 GeV at high luminosity, such that the efficiency for the $H \rightarrow WW \rightarrow l\nu jj$ signal is about 55%. The efficiency for the W+jet background is significantly lower than for the Higgs-boson signal because of the larger jet activity in these events. Finally, the central jet-veto cut provides a rejection factor of 10-15, depending on the p_T threshold at low and high luminosity, against the $t\bar{t}$ background which always has two additional b-jets in the final state.

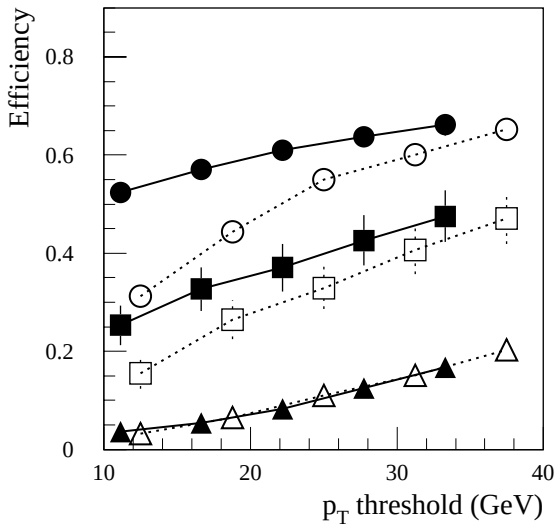

Figure 19-38 Efficiency of the central jet-veto cut as a function of the p_T threshold, as obtained from the fast simulation after the high-p_T central cuts (see text), for the $H \rightarrow WW \rightarrow l\nu jj$ signal (circles), the $t\bar{t}$ background (triangles) and the W+jet background (squares). The results are shown both without pile-up (black symbols) and with pile-up (open symbols).

Table 19-26 For an integrated luminosity of 30 fb^{-1} and for the $H \rightarrow WW \rightarrow l\nu jj$ channel with m_H = 1 TeV and 800 GeV, expected numbers of produced and accepted signal and background events, signal-to-background ratios and signal significances. The events are accepted if they pass all cuts, namely the high-p_T central cuts, the central jet veto and a double jet tag E_{tag} > 300 GeV (see text).

	Higgs signal	**$t\bar{t}$ (p_T > 300 GeV)**	**W+jets (p_T > 250 GeV)**	**WW (p_T > 50 GeV)**	**S/B**	**$S/\sqrt{B}$**
Events produced		192 000	448 000	255 000		
m_H = 1 TeV	486					
m_H = 800 GeV	1000					
Events accepted						
m_H = 1 TeV	37.9	3.3	9.2	1.0	2.8	10.3
m_H = 800 GeV	43.5	3.3	9.2	1.0	3.2	11.8

The final step of the event selection requires forward jet tagging (see [19-54] and Section 9.1.4 for details). The study is based on fully simulated and reconstructed events and includes the most up-to-date geometry of the forward calorimeters and a jet-finding algorithm optimised to minimise the effects of pile-up in the forward regions. The results presented in Section 9.1.4

show that the efficiency for reconstructing the tag jets is in agreement between fast and full simulation over $2 < |\eta| < 4$. For $|\eta| > 4$, the finite size of hadronic showers degrades the efficiency significantly and this effect has been corrected for in the fast simulation.

For the choice of a double jet tag requiring $E_{\mathrm{tag}} > 300$ GeV for both jets, the results are presented in Tables 19-26, for an integrated luminosity of 30 fb^{-1}. The expected numbers of produced and accepted signal events are shown for the $H \rightarrow WW \rightarrow l\nu jj$ signal with $m_H = 800$ and 1000 GeV. The same numbers are presented for the $t\bar{t}$, W+jet and WW backgrounds, which were generated with appropriate thresholds set on the p_{T} of the hard-scattering process. It is important to note that at the high luminosity the inclusion of all relevant pile-up effects and the use of a higher p_{T} threshold for the jet-veto cut reduces the signal-to-background ratio.

Large signal significances with a signal-to-background ratio around three can be obtained even at low luminosity. These values are optimistic, since the background rates suffer from significant uncertainties, but most of all because the broad signal expected from $H \rightarrow WW \rightarrow l\nu jj$ decays is difficult to separate clearly from the background. This is illustrated in Figure 19-39, which shows as an example the reconstructed spectrum of the invariant mass of the ($l\nu jj$) system, m_{lvjj}, summed for the $H \rightarrow WW \rightarrow l\nu jj$ signal with $m_H = 1$ TeV and for the backgrounds. The distributions are shown separately for the background and the summed signal+background, for an integrated luminosity of 30 fb^{-1} and for somewhat looser jet tagging cuts requiring two tag jets with $E_{\mathrm{tag}} > 100$ GeV. The signal and background shapes are very similar. This is due to the very strict central cuts applied to the reconstructed $W \rightarrow l\nu$ and $W \rightarrow jj$ decays. The thresholds of 350 GeV applied to ${p_{\mathrm{T}}}^{W \rightarrow l\nu}$ and ${p_{\mathrm{T}}}^{W \rightarrow jj}$ remove most of the background with $m_{\mathrm{lvjj}} < 800$ - 900 GeV.

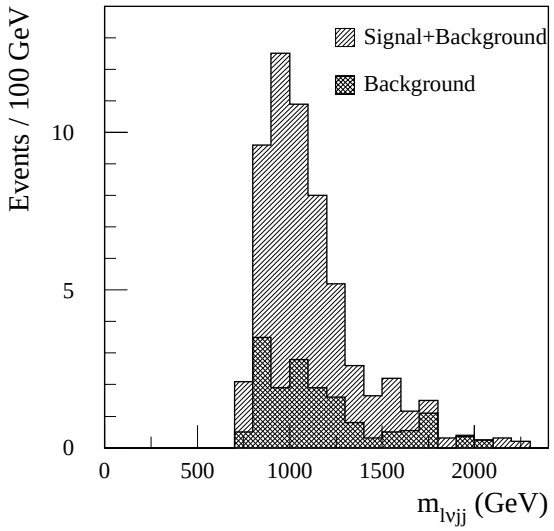

Figure 19-39 For an integrated luminosity of 30 fb^{-1} and for the $H \rightarrow WW \rightarrow l\nu jj$ channel with $m_H = 1$ TeV, distribution of reconstructed mass of the $l\nu jj$ system, m_{lvjj}, for the background (dark shaded histogram) and for the summed signal and background (light shaded histogram) after applying the high-p_{T} central cuts (see text), a central jet veto and a double jet tag ($E_{\mathrm{tag}} > 100$ GeV).

For the above reasons, a looser set of kinematic cuts in the central region, called loose central cuts, is defined:

- Lepton cuts: ${p_{\mathrm{T}}}^{l}$, ${E_{\mathrm{T}}}^{\mathrm{miss}} > 50$ GeV, ${p_{\mathrm{T}}}^{W \rightarrow l\nu} > 150$ GeV.
- Jet cuts: two jets reconstructed within $\Delta R = 0.2$ with $p_{\mathrm{T}} > 50$ GeV and ${p_{\mathrm{T}}}^{W \rightarrow jj} > 150$ GeV.
- W mass window: $m_{jj} = m_W \pm 2\sigma$, where σ is the resolution on m_{jj}.

The central jet-veto cut is applied with a p_{T} threshold of 20 GeV at low luminosity and two tag jets are required with $E_{\mathrm{tag}} > 300$ GeV. The results are shown in Table 19-27 for an integrated luminosity of 30 fb^{-1} and for $m_H = 1$ TeV. Table 19-27 shows the numbers of events produced, the acceptances of the loose central cuts, of the central jet veto and of the double jet tag, together with the numbers of events passing the successive sets of cuts for the signal and the various backgrounds.

Table 19-27 For an integrated luminosity of 30 fb^{-1} and for the $H \to WW \to l\nu jj$ channel with m_H = 1 TeV, expected numbers of signal and background events as a function of the cuts applied (see text). The acceptances and event rates are given separately for the loose central cuts, the central jet veto and the double jet tag.

	Higgs signal (m_H = 1 TeV)	**$t\bar{t}$ (p_T > 120 GeV)**	**W+jets (p_T > 100 GeV)**	**WW (p_T > 50 GeV)**
Events produced	486	2 250 000	10 400 000	255 000
After loose central cuts:				
Acceptance	45.7%	1.7%	0.15%	0.8%
Events	222	38,300	15,700	2070
After central jet veto (p_T > 20 GeV):				
Acceptance	64.5%	7.4%	44.0%	56.4%
Events	143	2800	6900	1170
After double jet-tag (E_{tag} > 300 GeV):				
Acceptance	50.7%	3.0%	0.9%	0.3%
Events	73	85	62	3

Compared to the results shown in Table 19-26 for the high-p_T central cuts, the signal-to-background ratio has degraded from about 3:1 to about 1:2 and the overall signal rate has increased by a factor 2. The choice of looser central cuts provides nevertheless the possibility to demonstrate the existence of a Higgs-boson signal from a study of the reconstructed invariant mass of the ($l\nu jj$) system, m_{lvjj}. Figure 19-40 shows the distribution of m_{lvjj} before and after the double jet tag is required for m_H = 1 TeV. The broad signal from $H \to WW \to l\nu jj$ decays now clearly emerges from the background, which is unbiased down to values of m_{lvjj} around 500 GeV.

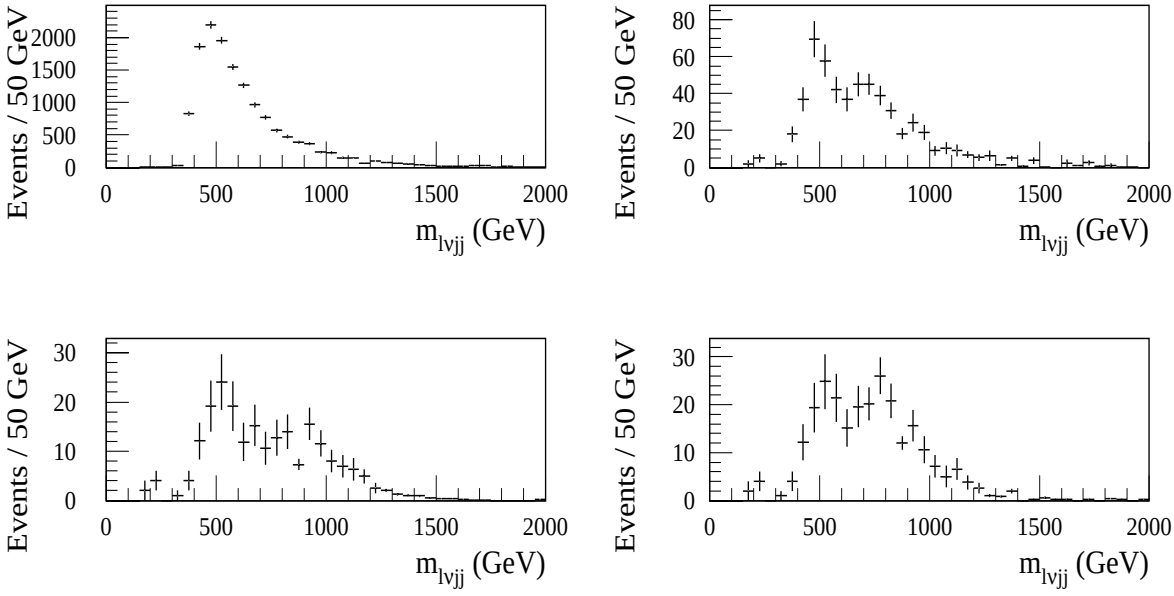

Figure 19-40 For an integrated luminosity of 30 fb^{-1} and for m_H = 1 TeV, distribution of m_{lvjj} for the summed signal+background before jet tagging cuts (top) and after requiring two tag jets with E_{tag} > 300 GeV (bottom). The results are obtained for the loose central cuts (see text).

Figure 19-41 For an integrated luminosity of 30 fb^{-1} and for m_H = 800 GeV, distribution of m_{lvjj} for the summed signal+background after requiring two tag jets with E_{tag} > 200 GeV (top) and E_{tag} > 400 GeV (bottom). The results are obtained for the loose central cuts (see text).

Figure 19-41 shows for m_H = 800 GeV, that the emergence of the signal can be further demonstrated by varying the energy threshold on the tag jets around its nominal value. As the threshold increases, the ratio between the signal peak around m_H and the kinematic peak of the background around 500 GeV increases significantly, thereby demonstrating the very different nature of the production mechanisms for the signal and background processes.

Preliminary studies have been done how well one could extract the main parameters of the observed resonance, namely its mass, width and height. A simple exponential fit is used for the m_{lvjj} distribution of the background and the signal shape is fitted to a Breit-Wigner with a width proportional to m_H^3. The results obtained for an integrated luminosity of 30 fb^{-1} indicates that the Higgs-boson mass would be measured with a statistical accuracy of about 5% and the signal rate would be measured to about 20%. A better description of the line shape of a very heavy Higgs boson would of course be needed to evaluate the systematic uncertainties on these difficult measurements of $H \rightarrow WW \rightarrow l\nu jj$ with $m_H \sim 1$ TeV.

The $H \rightarrow ZZ \rightarrow lljj$ channel cannot compete with the $H \rightarrow WW \rightarrow l\nu jj$ channel, since its rate is about six times lower. Nevertheless, it does not suffer from any significant $t\bar{t}$ background, and could be used for integrated luminosities above 100 fb^{-1} to confirm the observation of a signal in the $H \rightarrow WW \rightarrow l\nu jj$ channel, and thereby to compare the couplings of the Higgs boson to W and Z bosons.

Table 19-28 For an integrated luminosity of 100 fb^{-1} and for the $H \rightarrow ZZ \rightarrow lljj$ channel with m_H = 1 TeV and 800 GeV, expected numbers of produced and accepted signal and background events, signal-to-background ratios and signal significances. The events are accepted if they pass all cuts, namely the high-p_T central cuts, the central jet veto, and a double jet tag with E_{tag} > 600 GeV or E_{tag} > 300 GeV. Also shown are the results from full simulation and reconstruction for E_{tag} > 300 GeV.

	Higgs signal	Z+jets (p_T > 100 GeV)	S/B	Significance (Poisson)
Events produced		4 600 000		
m_H = 1 TeV	260			
m_H = 800 GeV	540			
m_H = 1 TeV				
E_{tag} > 600 GeV	9.2	2	4.6	4.3
E_{tag} > 300 GeV	17.3	8	2.2	4.7
Full simulation with pile-up (E_{tag} > 300 GeV)	14.7	18	0.8	2.9
m_H = 800 GeV				
E_{tag} > 600 GeV	9.4	2	4.7	4.3
E_{tag} > 300 GeV	19.2	8	2.4	5.2
Full simulation with pile-up (E_{tag}> 300 GeV)	16.3	18	0.9	3.3

The extraction of the signal proceeds along exactly the same lines as for the $H \rightarrow WW \rightarrow l\nu jj$ channel [19-55], except that a narrow mass window around the nominal Z mass is applied to the invariant mass of the lepton pairs. The only significant background then arises from Z+jet production, and the expected event rates before cuts and after all cuts, including a double jet tag with E_{tag} > 300 GeV and E_{tag} > 600 GeV, are shown in Table 19-28 for an integrated luminosity of 100 fb^{-1} and for the high-p_T central cuts described in the previous Section.

Since high-luminosity operation is discussed here, Table 19-28 also shows the results obtained from full simulation and reconstruction including pile-up. The efficiency of the jet-tagging cuts is 15% lower than that obtained with fast simulation and the background increases by a factor two due to fake tag jets.

In conclusion, the $H \rightarrow ZZ \rightarrow lljj$ channel with $m_H \sim 1$ TeV can only be observed for the ultimate integrated luminosity of 300 fb^{-1} presently envisaged for ATLAS.

19.2.10.3 $H \rightarrow WW \rightarrow l\nu jj$ for $m_H <$ 800 GeV

The results presented in Section 19.2.10.2 naturally call for an extension of the search for $H \rightarrow WW \rightarrow l\nu jj$ decays for Higgs-boson masses below 800 GeV. A very similar study has therefore been performed for m_H = 600 GeV [19-57].

- As shown in Table 19-29, central cuts on the reconstructed $W \rightarrow l\nu$ and $W \rightarrow jj$ decays are applied. These cuts have to be relaxed with respect to the values used for m_H = 1 TeV and the signal-to-background ratio is therefore much worse in this case.
- Although the same method is used for the $W \rightarrow jj$ reconstruction as that described in the case of $m_H \sim 1$ TeV, the cone size for the calculation of m_{jj} using the cells has to be increased from $\Delta R = 0.4$ to $\Delta R = 0.8$, since the boost of the W boson decreases as m_H decreases (see also Section 9.3.1).
- The central jet-veto cuts are the same as for m_H = 1 TeV (threshold of 15 GeV at low luminosity and of 25 GeV at high luminosity).
- Two forward tag jets are required and the signal observability is studied as a function of the energy threshold, E_{tag}, applied to these jets.

Table 19-29 Efficiencies of the central cuts at low luminosity and numbers of signal and background events accepted after all cuts, for an integrated luminosity of 30 fb^{-1} and for the $H \rightarrow WW \rightarrow l\nu jj$ channel with m_H = 600 GeV.

Cuts	Higgs signal	$t\bar{t}$	W+jets
Lepton cuts	58%	9.8%	2.7%
Jet cuts	68%	21.2%	4.3%
Events accepted	733	93 000	68 000

Tables 19-30 and 19-31 show the expected signal and background rates, before and after the successive cuts, respectively for integrated luminosities of 30 fb^{-1} (low-luminosity operation) and 100 fb^{-1} (high-luminosity operation). As already stated, jet tagging in the forward regions is necessary to achieve a sufficiently high signal-to-background ratio. The signal appears to be observable even for an integrated luminosity of 30 fb^{-1}.

This is confirmed by studying the shape of the m_{lvjj} spectrum. In contrast to Section 19.2.10.2, where the Higgs-boson width entirely dominates the quality of the reconstruction of the signal peak, the experimental resolution on m_{lvjj} begins to play a significant role for m_H = 600 GeV. The experimental resolution is approximately 40 GeV at low luminosity and 46 GeV at high luminosity, as obtained from full simulation and reconstruction. The dominant contributions to the experimental resolution arise from the $W \rightarrow jj$ mass resolution, the $E_{\mathrm{T}}^{\mathrm{miss}}$ resolution, and the reconstruction of the longitudinal momentum of the neutrino using the W-mass constraint. The overall experimental resolution is comparable to the effective rms of the Higgs-boson width, $\Gamma_{\mathrm{H}}^{\mathrm{tot}} \sim 120$ GeV. Figures 19-42 and 19-43 show the distribution of m_{lvjj} for the background and for the summed signal+background, respectively for integrated luminosities of 30 fb^{-1} and 100 fb^{-1}. In both cases, the signal is clearly visible above the background, which peaks around 500 GeV.

Table 19-30 For an integrated luminosity of 30 fb^{-1} (low-luminosity operation) and for $H \to WW \to l\nu jj$ decay with m_H = 600 GeV, expected numbers of signal and background events before cuts, after central cuts, after jet-veto cut and after requiring a double jet tag (see text). Also shown are the signal-to-background ratios and the signal significances.

Cuts	Higgs signal	$t\bar{t}$	W+jets	S/B	$S/\sqrt{B}$
Events produced	1860	4 440 000	56 820 000	0.00003	0.23
After central cuts	733	93 000	68 000	0.005	1.8
After central jet veto (p_T > 15 GeV)	466	6 200	29 000	0.013	2.5
After double jet-tag:					
E_{tag} > 100 GeV	323	680	1530	0.06	6.9
E_{tag} > 400 GeV	187	145	570	0.26	7.0
E_{tag} > 600 GeV	114	45	280	0.35	6.3

Table 19-31 Same as Table 19-30, but for an integrated luminosity of 100 fb^{-1} (high-luminosity operation)

Cuts	Higgs signal	$t\bar{t}$	W+jets	S/B	$S/\sqrt{B}$
Events produced	6200	14 800 000	189 400000	0.00003	0.43
After central cuts	2470	340 000	240 000	0.004	3.2
After central jet veto (p_T > 25 GeV)	1500	17 000	84 000	0.015	4.7
After double jet-tag:					
E_{tag} > 100 GeV	1060	3100	5900	0.11	11.0
E_{tag} > 400 GeV	642	1200	1470	0.26	12.9
E_{tag} > 600 GeV	398	460	630	0.36	12.0

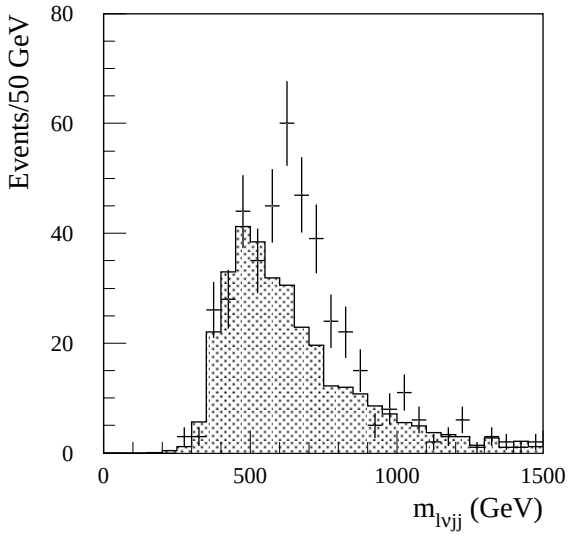

Figure 19-42 For an integrated luminosity of 30 fb^{-1} and for $H \to WW \to l\nu jj$ decays with m_H = 600 GeV, distribution of $m_{l\nu jj}$ for the background (shaded histogram) and for the summed signal+background (points with error bars).

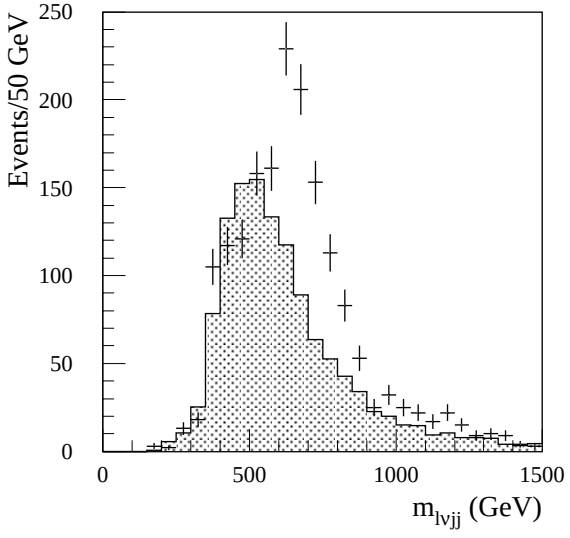

Figure 19-43 Same as Figure 19-42, but for an integrated luminosity of 100 fb^{-1}.

Finally, the study of the $H \rightarrow WW \rightarrow l\nu jj$ channel has been repeated for m_H = 300 GeV [19-57], to evaluate the overlap of this channel with the $H \rightarrow ZZ \rightarrow 4l$ and $H \rightarrow ZZ \rightarrow ll\nu\nu$ channels. For m_H = 300 GeV, the $W \rightarrow jj$ decays can be reconstructed using standard techniques, but the kinematic cuts have to be loosened even further, leading to an even lower signal-to-background ratio. Nevertheless, with the help of tight jet-veto and jet-tagging cuts, the signal can be observed above the background, as shown in Figure 19-44. The very similar shapes of the signal and background lead to the conclusion that this channel can only be used for confirmation of a discovery in another channel for m_H = 300 GeV.

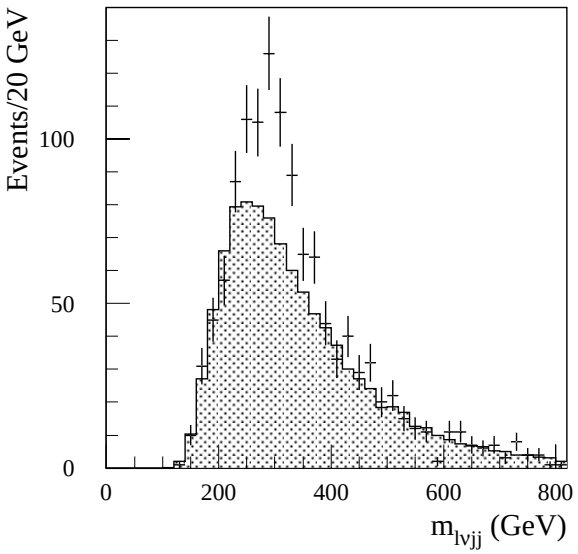

Figure 19-44 Same as Figure 19-42, but for m_H = 300 GeV.

19.2.10.4 Conclusions

The studies described above demonstrate that the SM Higgs boson would be observable in the $H \rightarrow ZZ \rightarrow ll\nu\nu$, $H \rightarrow ZZ \rightarrow lljj$ and $H \rightarrow WW \rightarrow l\nu jj$ decay modes, over most of the mass range from 300 GeV to 1 TeV. This can be achieved only through the requirement of two tag jets in the forward regions ($2 < |\eta| < 5$), which selects the $qq \rightarrow qqH$ production process and strongly reject the backgrounds from $t\bar{t}$ and W/Z+jet production.

The critical issues concerning the detector performance in these channels are the reconstruction of high-p_T $W \rightarrow jj$ decays, the efficiency of tight jet-veto cuts as a function of luminosity, the instrumental tails in the E_T^{miss} distribution from mis-measured jets, and the performance of jet tagging in the forward calorimeters. All these issues have been studied with full simulation and reconstruction, and the physics performance estimates have been updated to account for the results of these detailed studies.

The most recent efforts have concentrated on demonstrating the observability of the signal from $H \rightarrow WW \rightarrow l\nu jj$ decays above the background by using the reconstructed distribution of the mass of the $l\nu$jj system. At the same time, a first study of the sensitivity to the Higgs-boson mass, width and cross-section has been performed.

19.2.11 Overall sensitivity to the SM Higgs searches

The overall sensitivity for the discovery of a Standard Model Higgs boson over the mass range from ~80 GeV to ~1 TeV is shown in Figure 19-i. The sensitivity is given in units of $S/\sqrt{B}$ for the individual channels as well as for the combination of the various channels, assuming integrated luminosities of 30 and 100 fb^{-1}. A Standard Model Higgs boson can be discovered in the ATLAS experiment over the full mass range up to ~1 TeV with a high significance. A 5σ-discovery can already be achieved over the full mass range after a few years of running at low luminosity. As

already mentioned, no *K*-factors have been included in the evaluation of the signal significance. This is a conservative assumption, provided the *K*-factor for the signal process of interest is larger than the square root of the *K*-factor for the corresponding background process.

The requirements on the detector performance are the most demanding for the discovery of a Standard Model Higgs boson in the intermediate mass range, $80 < m_H < 2m_Z$, as discussed in Section 19.2.8. For $m_H > 2m_Z$, the dominant discovery channel is the four-lepton channel. In this case, the background is small and dominated by irreducible ZZ continuum production. For $m_H > 300$ GeV the requirements on the detector performance are rather modest in this channel, since the Higgs width is larger than the detector resolution. A high-significance discovery of the Higgs boson can be achieved for Higgs-boson masses up to 600 GeV over less than one year of data-taking at low luminosity.

A Standard Model Higgs boson in the mass range between 400 GeV and about 1 TeV would also be discovered with the $H \rightarrow WW \rightarrow l\nu jj$ mode providing the best discovery potential in this mass range. The good sensitivity to this channel for lower masses, provides independent and complementary information to the four-lepton channel. For $400 < m_H < 900$ GeV, the $H \rightarrow WW \rightarrow l\nu jj$ channel is complemented by the $H \rightarrow ZZ \rightarrow lljj$ and $H \rightarrow ZZ \rightarrow ll\nu\nu$ channels, which would provide additional robustness to a Higgs-boson discovery in this mass range.

As can be seen from Figure 19-i, at least two discovery channels are available over most of the Higgs-boson mass range. A comparison of the various production rates would provide valuable information for the determination of the Higgs-boson parameters, as discussed in the next Section.

19.2.12 Determination of the SM Higgs-boson parameters

Assuming that a Standard Model Higgs boson will have been discovered at the LHC, the ATLAS potential for the precision measurement of the Higgs parameters (mass, width, production rates, branching ratios) [19-58] is discussed in this section. Such measurements should give further insights into the electroweak symmetry-breaking mechanism and into the way the Higgs couples to fermions and bosons, and in some cases should allow a distinction between a SM and a MSSM Higgs boson (see also [19-59]).

The results presented here are limited to the mass region between 80 GeV and 700 GeV. For larger masses, the Higgs resonance becomes very broad ($\Gamma_H > 200$ GeV) and therefore precision measurements are meaningless. An integrated luminosity of 300 fb^{-1} is assumed in the following.

19.2.12.1 Measurement of the Higgs-boson mass

The ultimate experimental precision with which ATLAS should be able to measure the Higgs-boson mass is shown in Figure 19-45. The results obtained in the various decay channels, as well as the combination of all channels, are given. The quoted precision includes the statistical error in the determination of the peak position, coming from both the limited number of signal events and the error on the background subtraction (the background is assumed to be flat under the peak), and the systematic error on the absolute energy scale. The latter is assumed to be 0.1% for decay channels which contain leptons or photons (*e.g.* $H \rightarrow \gamma\gamma$, $H \rightarrow ZZ^{(*)} \rightarrow 4l$) and 1%

for decay channels containing jets (*e.g.* $H \rightarrow b\bar{b}$). Although the ATLAS goal is to determine the lepton energy scale to 0.02% (see Chapter 12 and Section 16.1), a more conservative error of 0.1% has been assumed as a baseline in this study.

For comparison, the precision of the Higgs-boson mass measurement has also been determined assuming a systematic uncertainty of 0.02% for the electromagnetic energy scale.

Figure 19-45 indicates that the Higgs mass can be measured with a precision of 0.1% up to masses of about 400 GeV if a scale uncertainty of ±0.1% is assumed. This number could be slightly improved in the mass range between ~150 and ~300 GeV if instead a better-scale uncertainty of ±0.02% could be achieved. For larger masses, the precision deteriorates because the Higgs-boson width becomes large and the statistical error increases. However, even for masses as large as 700 GeV, the Higgs-boson mass can be measured with an accuracy of 1%.

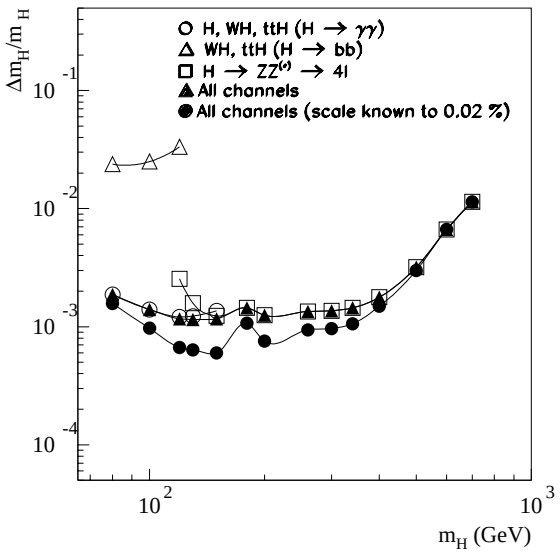

Figure 19-45 Relative precision $\Delta m_H/m_H$ on the measured Higgs-boson mass as a function of m_H, assuming an integrated luminosity of 300 fb^{-1}. The different open symbols correspond to different individual channels. The black triangles (black circles) correspond to the combination of all channels for an overall uncertainty of 0.1% (0.02%) on the absolute scale of the EM Calorimeter.

The precision of the measurement is determined by the four-lepton and two-photon channels, whereas the $H \rightarrow b\bar{b}$ channel contributes very little. This is due to both the larger systematic error on the absolute jet scale compared to the absolute lepton / photon scale and the larger statistical error because of worse mass resolution (~20 GeV for $H \rightarrow b\bar{b}$, compared to ~1.5 GeV for $H \rightarrow \gamma\gamma$ and $H \rightarrow ZZ^* \rightarrow 4l$).

No theoretical errors are included in the results presented in Figure 19-45. The uncertainty resulting from uncertainties on the structure functions is expected to be much smaller than 10 MeV [19-60]. A potentially larger error may come from the fact that, for $m_H > 700$ GeV, when the Higgs-boson width becomes large, interference effects between the resonant and the non-resonant processes tend to shift the position of the Higgs-boson peak towards lower values [19-49].

19.2.12.2 Measurement of the Higgs-boson width

The Higgs-boson width, Γ_H^{tot}, can be experimentally obtained from a measurement of the width of the reconstructed Higgs peak, after unfolding the contribution of the detector resolution. This direct measurement is only possible for Higgs-boson masses larger than 200 GeV, above which the intrinsic width of the resonance becomes comparable to or larger than the experimental mass resolution. This is the mass region covered mainly by $H \rightarrow ZZ \rightarrow 4l$ decays.

The ultimate precision on Γ_H, which can be achieved by ATLAS, is shown in Figure 19-46. These results include the statistical uncertainty coming from the number of signal events, and the systematic uncertainty coming from the measurement of the peak width and the knowledge of the detector energy and momentum resolution. In both cases, the systematic error is dominated by the uncertainty on the radiative decays and has been conservatively assumed to be 1.5% (see Section 16.1). As discussed in more detail in Section 16.1, the detector resolution will be obtained from the measurement of the Z width. The systematic uncertainty on the background subtraction has been neglected in this case since the signal-to-background ratio is large over most of the mass region relevant for this measurement.

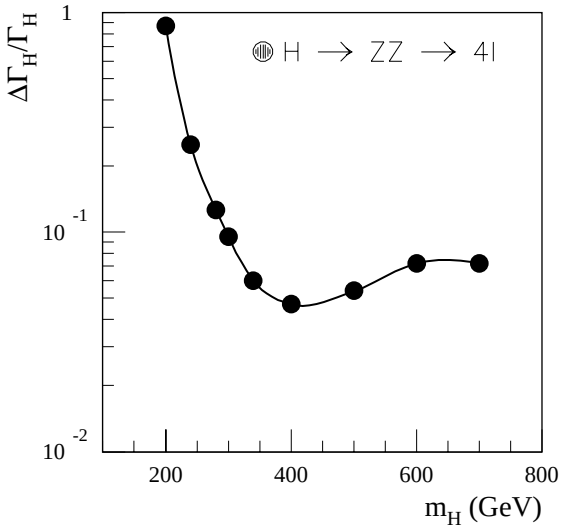

Figure 19-46 Relative precision $\Delta\Gamma_H/\Gamma_H$ on the measured Higgs-boson width as a function of m_H, assuming an integrated luminosity of 300 fb^{-1}.

Figure 19-46 shows that the precision improves with the Higgs-boson mass up to masses of ~300 GeV. For the higher masses the intrinsic width becomes larger and its contribution to the total resolution dominates compared to the detector resolution. Over the range $300 < m_H < 700$ GeV, the precision of the measurement is approximately constant and of the order of 6%.

19.2.12.3 Measurement of the Higgs-boson rate

The measurement of the Higgs-boson rate in a given decay channel provides a measurement of the production cross-section times the decay branching ratio for that channel. Such measurement in some cases would help to disentangle between SM and MSSM Higgs scenarios as discussed in Section 19.3.2.4.

The statistical error on such measurements is expected to be smaller than 10% over the mass region 120 - 600 GeV using the $\gamma\gamma$, $b\bar{b}$ and $4l$ final states. The main systematic error comes from the knowledge of the luminosity (see Chapter 13). Two values have been considered for the luminosity uncertainty: 5%, a somewhat ambitious goal, and 10% (a more conservative estimate).

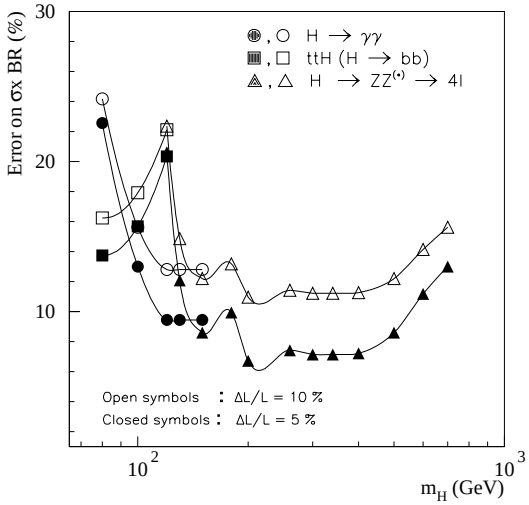

Figure 19-47 Relative precision on the measurement of the Higgs-boson rate ($\sigma \times$ BR) for various channels, as a function of m_H, for various channels, assuming an integrated luminosity of 300 fb^{-1}. The luminosity is assumed to be known to 10% (open symbols) or to 5% (black symbols).

An additional systematic error of 10% has been included to take into account the uncertainty on the background subtraction for channels where the background is not completely flat under the peak (*e.g.* $t\bar{t}H$ with $H \rightarrow b\bar{b}$).

Figure 19-47 shows the expected experimental uncertainty on the Higgs-boson rates, for various production and decay channels and for both assumptions on the luminosity uncertainty. Over the mass region 120 - 600 GeV, the Higgs-boson production rate can be measured with a precision of 12% (7%) if the luminosity is known to 10% (5%). These results stress the importance of future experimental and theoretical efforts to achieve a measurement of the absolute luminosity at the LHC to an accuracy at the level of a few percent.

19.2.12.4 Couplings and branching ratios

Once the Higgs-boson rate in a given decay channel is measured, an accurate theoretical prediction for the Higgs-boson production cross-section would allow a measurement of the branching ratio for the decay in that channel. Without theoretical assumptions, one can only measure ratios of rates for different channels, which in turn provide ratios of couplings and branching ratios. By performing these measurements for several channels, one can obtain several constraints on the Higgs-boson couplings to fermions and bosons, which can be used to test the theory.

A few examples of such measurements are given below, together with the expected precision for an integrated luminosity of 300 fb^{-1}:

- A measurement of the ratio of the $H \rightarrow \gamma\gamma$ and $H \rightarrow b\bar{b}$ rates in the associated production of Higgs bosons would provide the ratio between the $H \rightarrow \gamma\gamma$ and $H \rightarrow b\bar{b}$ branching ratios. Such a measurement can only be performed over the mass range, $80 < m_H < 120$ GeV, with an accuracy of about 30%, dominated by the statistical error.
- A measurement of the ratio between the $H \rightarrow \gamma\gamma$ and $H \rightarrow ZZ^* \rightarrow 4l$ rates would provide the ratio of the $H \rightarrow \gamma\gamma$ and $H \rightarrow ZZ^*$ branching ratios. Such a measurement can only be performed over the mass range $120 < m_H < 150$ GeV, with an accuracy of about 15%, dominated by the statistical error.
- A measurement of the ratio between the rate for $t\bar{t}H$ production and the rate for WH production both followed by $H \rightarrow \gamma\gamma$ or $H \rightarrow b\bar{b}$ decay, would provide the ratio of the Higgs couplings to the top quark (Yukawa coupling) and to the W boson. This measurement can only be performed over the mass range $80 < m_H < 120$ GeV, with an accuracy of about 25%, dominated by the statistical error.

In all the cases mentioned above, the statistical uncertainty dominates the measurement because the mass regions where two different channels overlap are at the edges of the sensitivity of one or the other channel. Furthermore, some systematic errors, such as the uncertainty on the absolute luminosity, cancel in the ratios.

It should be noted that, in addition to the measurements quoted above, other possibilities will also be studied. For example, the ratio between the $WW^{(*)}$ and $ZZ^{(*)}$ rates is sensitive to the couplings of the Higgs to the W and Z bosons. This ratio could be measured in the high mass region ($m_H > 300$ GeV) and, with a somewhat larger systematic uncertainty, in the mass range around 170 GeV. The $WH \rightarrow WWW^{(*)} \rightarrow 3l$ mode could provide additional information on the couplings of the Higgs boson to vector bosons. Finally, the ratio between the production cross-section via gg fusion and WW fusion can be measured, *e.g.* using forward jet tagging for $H \rightarrow ZZ \rightarrow 4l$. This could provide an indirect constraint on the Higgs-boson couplings to fermions and bosons.

19.2.12.5 Towards a determination of the spin and parity of the Higgs boson

The Standard Model predicts the Higgs boson to be a *CP*-even scalar particle. If the Higgs boson were discovered, these properties would have to be verified.

Only a few channels can give information on the spin and *CP*. *A priori* some general arguments, based on specific couplings, may be used to determine the spin. If, for example, the Higgs-boson is seen in the $H \rightarrow \gamma\gamma$ decay mode, then Yang's theorem implies that it is not a vector, and it must have a *CP*-even component. If the Higgs boson is observed in production and / or decay channels that require it to have substantial *WW* and / or *ZZ* couplings, it is very likely to have a large *CP*-even component, given that the *WW/ZZ* couplings of a pure *CP*-odd Higgs boson arise only at the one-loop level. Verifying that it is purely *CP*-even, as predicted by the Standard Model, will be much more challenging [19-61][19-62].

From the above, it is clear that a direct measurement of the Higgs-boson spin through the measurement of the angular distributions of its decay products is needed. A first study has therefore been performed [19-63], in which the sensitivity of the angular distributions to the spin of the Higgs boson is investigated. In this study, the $H \rightarrow \gamma\gamma$ and the $H \rightarrow ZZ \rightarrow 4l$ channels are used.

In the $H \rightarrow \gamma\gamma$ channel, the expected signal-to-background ratio is small, typically a few percent. This severely limits the potential to determine the spin structure from the angular distributions of the two photons. If only signal events are considered, it would be possible to discriminate with a significance of 10.7σ between the flat distribution, expected for the decay of a spin-zero particle, and a $(1+\cos^2\theta^*)$ distribution, where θ^* is the polar angle in the centre-of-mass of the decaying Higgs boson. The significance has been evaluated using a Kolmogorov-Smirnov test, assuming an integrated luminosity of 100 fb^{-1}. This sensitivity is substantially reduced, if the impact of the kinematic cuts, of the detector acceptance, and in particular of the background events are taken into account. The expected discrimination capability between the two hypotheses described above is reduced to a value below 1.5σ, even for an integrated luminosity of 300 fb^{-1}.

In the $H \rightarrow ZZ \rightarrow 4l$ channel, the expected signal-to-background ratio is much more favourable. For Higgs-boson masses between 200 and 400 GeV, it is about 20 (see Section 19.2.5). In this channel, in addition to the θ^* angular distribution of the Z bosons in the Higgs-boson centre-of-mass, the azimuthal separation $\Delta\phi$ between the two reconstructed Z bosons is sensitive to the spin of the Higgs-boson. For Higgs-boson decays into ZZ the azimuthal separation $\Delta\phi$ is expected to be smaller than for the ZZ continuum background. Both the $\cos(\theta^*)$ and the $\Delta\phi$ distributions depend on the ratio m_H / m_Z (particularly the θ^* distribution) and on the selection criteria. The optimisation of the signal-to-background ratio for higher Higgs-boson masses, with the selection cut requiring ${p_T}^Z{}_{\max} > m_H / 3$ causes the $\Delta\phi$ distribution to be more similar for the selected signal and background events. It can however still be demonstrated that, with a high significance, these angular distributions are incompatible with those expected for background events alone [19-63]. A more quantitative analysis of the discrimination between a spin-0 and a spin-1 particle, using this channel, is currently being carried out.

As suggested in [19-64], the $t\bar{t}H$ production channel could possibly be used to distinguish a *CP*-even from a *CP*-odd Higgs boson. This channel would however only provide sensitivity in the Higgs-boson mass window between 80 and 130 GeV. The method proposed requires the reconstruction of the momenta of both top quarks, which then could be used in a variety of simple variables. These variables are products of the reconstructed top-quark momenta and should

have sensitivity to the *CP* quantum number of the Higgs boson. Although this method looks interesting, its application at the LHC is difficult and might be limited by the available signal rates:

- For an integrated luminosity of 300 fb^{-1} and the $H \rightarrow \gamma\gamma$ decay mode the expected number of signal events is 20, before top-quark reconstruction, with a signal-to-background ratio of 1 (see Section 19.2.2). The expected efficiency for the reconstruction of both top-quarks (in the *jjb* and *lνb* channels) does not exceed 20% [19-35]. If *b*-tagging efficiencies are included, less than five reconstructed signal events are expected, with a signal-to-background ratio of about one.
- More events can be expected in the $H \rightarrow b\bar{b}$ mode, see Section 19.2.4.3. For an integrated luminosity of 30 fb^{-1} and m_H = 100 GeV, about 61 signal and 150 background events are expected to be reconstructed within the mass windows.

In addition, the systematic uncertainties linked to the reconstruction of the top-quark momenta have to be understood.

19.2.12.6 Conclusion

The results presented in the previous Sections demonstrate that ATLAS has a large potential, not only for the discovery of a Standard Model Higgs boson, but also for precision measurements of the Higgs-boson parameters. In particular, with an integrated luminosity of 300 fb^{-1} ATLAS would measure the Higgs-boson mass with a precision of 0.1% over the mass range 80 - 400 GeV, the Higgs-boson width with a precision of 6% over the mass range 300 - 700 GeV, the Higgs-boson production rate with a precision of 10%, and several of the most important couplings and branching ratios with a precisions of the order of 25%.

The determination of the spin and the *CP* quantum number of the Higgs boson from angular distributions is not straightforward at the LHC. Most channels suffer from too large backgrounds or too few events, and hence detailed studies of angular distributions are difficult. The most promising channel for a meaningful measurement is the $H \rightarrow ZZ^{(*)} \rightarrow 4l$ channel.

19.3 Minimal Supersymmetric Standard Model Higgs boson

19.3.1 Introduction

The investigation of the Higgs sector of the MSSM [19-10] is complex, since one has to deal with a rich spectrum of possible signals. The Higgs sector contains two charged ($H^{\pm}$) and three neutral (h, H, A) physical states. At the tree level, all Higgs-boson masses and couplings can be expressed in terms of two parameters only. They are usually chosen to be m_A, the mass of the *CP*-odd boson, and tanβ, the ratio of the vacuum expectation values of the Higgs doublets. However, the radiative corrections from loops containing top quarks or SUSY particles substantially modify the tree-level formulae for masses and mixing patterns in the Higgs sector [19-65][19-66] [19-67][19-68]. This has important implications for the strategies of MSSM Higgs-boson searches. At three-level the relation $m_h < m_Z \cos 2\beta$ holds, but the radiative corrections increase this upper limit to 150 GeV [19-11] in the most general case.

Over the past years, prospects for the detection of MSSM Higgs bosons at the LHC have been re-evaluated both theoretically [19-69] and experimentally [19-16]. These studies have selected sets of parameters, for which supersymmetric (SUSY) particle masses are large, so that Higgs-boson decays to SUSY particles are kinematically forbidden. The interest was focused on the discovery potential of various decay modes accessible also in the case of the SM Higgs boson: $h \to \gamma\gamma$, $h \to b\bar{b}$, $H \to ZZ \to 4l$, and of modes strongly enhanced at large tanβ: $H/A \to \tau\tau$, $H/A \to \mu\mu$. Much attention was given also to other potentially interesting channels such as: $H/A \to t\bar{t}$, $A \to Zh$, $H \to hh$. The conclusions drawn from these studies were that the complete region of parameter space, m_A = 50 - 500 GeV and tanβ = 1 - 50, should be accessible for Higgs-boson discovery by the ATLAS experiment. Over a large fraction of this parameter space, more than one Higgs boson and/or more than one decay mode would be accessible. The most difficult region was identified as the moderate tanβ and moderate m_A region, where only the lightest Higgs boson would be observable. Also, for larger values of m_A (m_A > 500 GeV), only the lightest Higgs boson, h, would most likely be observable. A summary of these studies is presented in Section 19.3.2 and Section 19.3.3.

If SUSY particles are light enough, decays of Higgs bosons to SUSY particles are kinematically allowed. The SM decay modes are then suppressed, competing in most cases with decays to charginos and neutralinos. The prospects for the observability of Higgs bosons under these conditions have also been evaluated [19-70] and are presented in Section 19.3.5. These studies have been performed using the more constrained SUGRA model [19-71]. With the allowed parameters combinations of SUGRA, the (m_A, tanβ) plane is still fully covered within the limits discussed above, but the possibility of discovering heavy Higgs bosons might be more limited. Some suppression of SM decay modes would occur in the low tanβ range, where, however new four-lepton signatures from Higgs-boson decays to SUSY particles would appear. Over a large fraction of the SUGRA parameter space, the possibility to observe the lightest Higgs boson, h, in SUSY cascade decays has also been systematically explored.

Some MSSM signatures have been investigated, even if the expected sensitivity is rather weak or if their observability is already almost excluded by searches at LEP2. These studies are nevertheless considered valuable, since they provide model-independent probes of possible Higgs-boson signatures and since they contribute to the general process of quantifying and optimising the detector performance for the exploration of new physics signatures.

Most studies presented below have been performed with the fast detector simulation, in particular to obtain a careful evaluation of the expected backgrounds. For several channels results obtained for mass resolutions, acceptances or reconstruction efficiencies have been confirmed with full simulation (see Section 2.5 and Section 9.3).

19.3.2 Scenarios with heavy SUSY particles

19.3.2.1 General considerations

In this study, two-loop equivalent calculations are used for the masses and couplings [19-66] [19-67][19-68], as well as one-loop calculations for some decay branching ratios [19-66][19-20]. QCD corrections are partially taken into account by including running quark masses in the calculations of branching ratios. As mentioned above, it is assumed that SUSY particles are sufficiently heavy that they do not play an important role in the phenomenology of MSSM Higgs-boson decays.

In addition, for the benchmark sets of MSSM parameters [19-11], where M_{SUSY} is fixed to 1 TeV, an extreme configuration of stop mixing parameters (A_t, μ) has been chosen, the so-called minimal mixing scenario (A_t, $\mu << M_{\mathrm{SUSY}}$). This scenario corresponds to the most pessimistic discovery scenario at the LHC, since these choices for the additional MSSM parameters give the lowest possible upper limit for m_h. This reduces the LHC potential for h-boson discovery in the $h \rightarrow \gamma\gamma$ channel, and also suppresses the $H \rightarrow ZZ^{(*)} \rightarrow 4\,l$ channel.

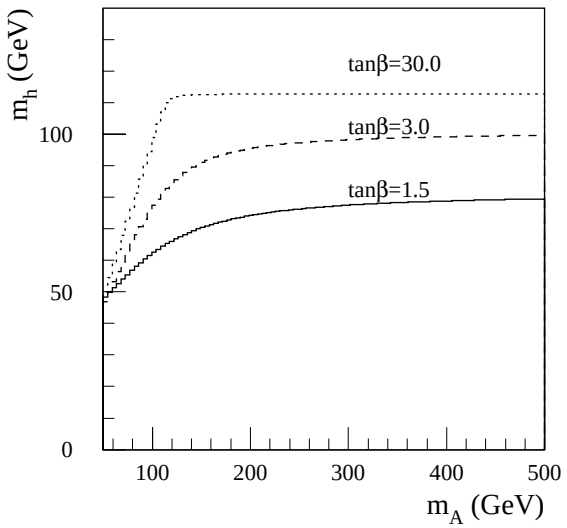

Figure 19-48 Two-loop equivalent predictions for m_h as a function of m_A and for tanβ = 1.5, 3, 30 in the minimal mixing scenario, as used throughout these studies.

In the minimal mixing scenario the predicted upper limit on m_h is 115 GeV for a top mass of 175 GeV [19-72]. This upper limit would increase to ~ 122 GeV, if maximal mixing were assumed. Figure 19-48 shows m_h as a function of m_A for three values of tanβ. The value of m_h depends very little on m_A for $m_A > 200$ GeV and reaches its maximum allowed value for $m_A > 200$ GeV and tanβ > 10. The masses of the charged Higgs-bosons $m_{H^{\pm}}$, and of the heavier neutral *CP*-even Higgs boson, m_H, vary nearly linearly with m_A. For large values of m_A all Higgs bosons except h are heavy and degenerate in mass.

The total decay widths of the MSSM Higgs bosons differ significantly from that of a SM Higgs boson of the same mass (see *e.g.* [19-16]). For large values of tanβ, the width of the h-boson is usually larger than that of a SM Higgs. However, it tends towards the SM value, as the h-boson mass approaches its maximal value for a given value of tanβ. This is the case for most of the relevant parameter space in the (m_A, tanβ) plane. Consequently, in most cases, the h-boson width is much smaller than the experimental resolutions expected for the decay modes observable at the LHC. The decay widths of the H- and A- bosons are also in general much smaller than that

of the SM Higgs boson of the same mass. However, they become relatively large with increasing m_A and / or tanβ. This has been taken into account whenever relevant for the evaluation of the significance of a possible signal from the decay of the heavy Higgs bosons.

In the (m_A, tanβ) region of parameter space relevant for the LHC searches, both the direct and associated production cross-sections and the branching ratios $h \to \gamma\gamma$ and $h \to b\bar{b}$ reach asymptotically the SM values as m_A and / or tanβ increases. In general, they are somewhat suppressed, except when m_h gets close to its maximum allowed value for a given value of tanβ. In this case, the $\sigma \times$ BR of the *h*-boson are even larger by 10 - 20% than the corresponding SM values. In this decoupling limit, the lightest MSSM Higgs-boson *h* behaves like a SM Higgs.

For the H / A bosons, the expected rates and decay channels vary rapidly with m_A and tanβ. As discussed in the next Sections, the variety of decay channels of interest is much richer than in the SM case. Typical features of MSSM Higgs decays are:

- the strong suppression of the HZZ and HWW coupling and absence of such couplings for the *A*-boson, which enhances the branching ratio of the other decay channels, such as $H/A \to \tau\tau$, $H/A \to t\bar{t}$;
- the strong enhancement of the $b\bar{b}H$, $b\bar{b}A$ coupling for large values of tanβ which leads to the dominance of this production mode;
- and the existence of decays with more than one Higgs boson involved, such as $H \to hh$ and $A \to Zh$.

19.3.2.2 h , H , $A \to \gamma\gamma$

h , $H \to \gamma\gamma$

The observability of the inclusive $H \to \gamma\gamma$ channel has been described in detail in Section 19.2.2.1 for the case of a SM Higgs boson. The search for the SM Higgs boson in $H \to \gamma\gamma$ decays can also be performed using associated WH and $t\bar{t}H$ production, as described in Section 19.2.2.2. The expected sensitivity for this channel can be combined with that for the inclusive one to improve the overall discovery potential for $H \to \gamma\gamma$ decays.

The expected MSSM rates, for both $h \to \gamma\gamma$ and $H \to \gamma\gamma$, are generally suppressed with respect to the SM case. However, they could also be slightly enhanced over limited regions of parameter space, as discussed above. In order to evaluate the overall sensitivity to γγ decays of the MSSM Higgs bosons, the results of the SM searches have been used. To obtain the 5σ-discovery contour curves in the (m_A, tanβ) plane, only *h*-boson masses above 70 GeV have been considered, since a proper experimental study of signal acceptance and background rates has not been performed for masses much below 80 GeV, and also since the present experimental limit from LEP2 is already of $m_h \sim 80$ GeV for any MSSM scenario [19-7].

The expected 5σ discovery contour curves in the (m_A, tanβ) plane are shown in Figures 19-49 and 19-50, respectively for integrated luminosities of 100 and 300 fb^{-1}. For the inclusive channel, the observability depends critically on the integrated luminosity. This is a consequence of the slow variation of m_h and $\sigma \times$ BR with increasing m_A.

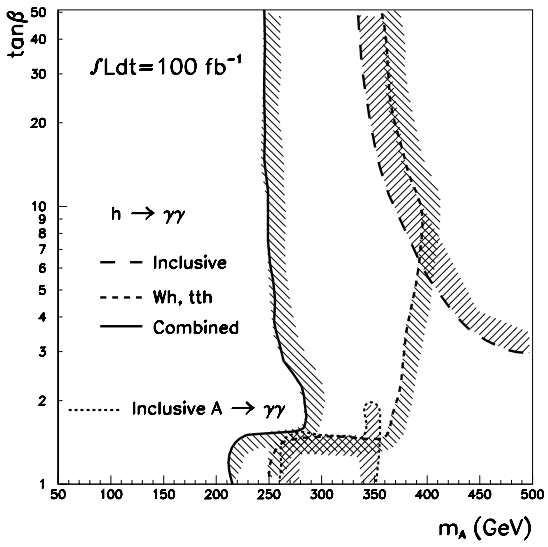

Figure 19-49 For an integrated luminosity of 100 fb^{-1}, 5σ-discovery contour curves for the $h \rightarrow \gamma\gamma$ (inclusive, associated *and* combined) and $A \rightarrow \gamma\gamma$ channels in the (m_A, tanβ) plane. The shaded areas indicate the side of the contour curves where the corresponding signal would be observable.

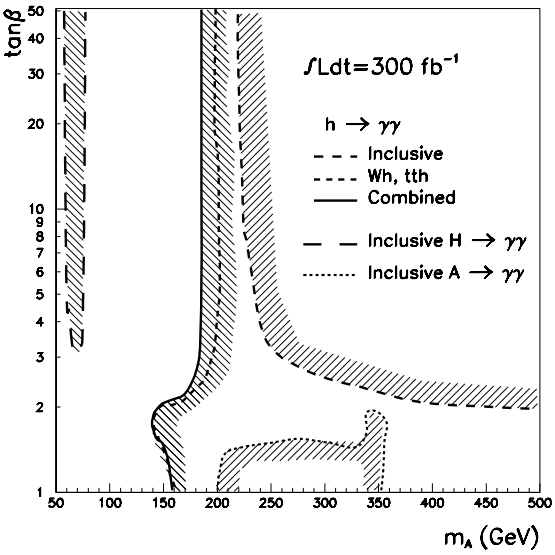

Figure 19-50 Same as Figure 19-49, but for an integrated luminosity of 300 fb^{-1}and including $H \rightarrow \gamma\gamma$.

Figures 19-49 and 19-50 show that a combined 5σ-discovery is possible for all values of tanβ provided m_A is larger than 180 GeV (260 GeV), for an integrated luminosity of 300 fb^{-1} (100 fb^{-1}). In the (m_A, tanβ) plane, the position of the 5σ-discovery contour curves is uncertain to $\sim \pm 30$ GeV along the m_A-axis, due to the rather large theoretical uncertainties still inherent to the calculation of m_h as a function of m_A.

The $h \rightarrow \gamma\gamma$ branching ratio has been computed here assuming that all SUSY particles have a mass of 1 TeV. More realistic mass spectra of SUSY particles usually contain lighter stop-quarks and charginos / neutralinos, and this may significantly decrease the $h \rightarrow \gamma\gamma$ branching ratio [19-73], which can also be affected by possible decays of the *h*-boson to the lightest neutralinos. In addition, SUSY particle masses lighter than 1 TeV could affect the $gg \rightarrow h$ production cross-section. For some specific choices of the SUSY model parameters, this cross-section could decrease by more than one order of magnitude. The $h \rightarrow \gamma\gamma$ channel would then only be observable at the LHC through the associated *Wh* and $t\bar{t}h$ production. While this would reduce the sensitivity, a significant fraction of the (m_A, tanβ) plane could still be covered with these processes alone. Since the SM and the MSSM h, $H \rightarrow \gamma\gamma$ rates are very similar over the accessible mass range, the observation of a Higgs boson decaying to γγ will not be sufficient to demonstrate the existence of a Higgs sector beyond the SM.

The heavy Higgs boson decay, $H \rightarrow \gamma\gamma$, would be observable only in a narrow strip for low m_A value (m_A = 70 - 80 GeV) corresponding to m_H = 110 - 120 GeV. This range of m_A is already almost excluded by searches at LEP2 [19-7].

$A \rightarrow \gamma\gamma$

The *CP*-odd Higgs boson A can also be searched for using the rare $\gamma\gamma$ decay mode. As in the case of the SM Higgs boson the $A \rightarrow \gamma\gamma$ decay mode is only observable over a limited region of parameter space, where the production cross-section (dominated by gg fusion) and the decay branching ratio are both relatively large. This region corresponds to small values of tanβ and to values of m_A between 200 - 350 GeV as shown in Table 19-32. For $m_A > 2m_t$ the $A \rightarrow t\bar{t}$ channel opens up and strongly suppresses the $A \rightarrow \gamma\gamma$ branching ratio.

Table 19-32 Cross-sections times branching ratios, acceptances and expected mass resolutions for the $A \rightarrow \gamma\gamma$ channel as a function of m_A.

m_A (GeV)	$\sigma \times$ BR (fb)	Accept.	σ_m (GeV)
200	7.3	15%	2.0
250	6.5	41%	3.0
300	10.3	57%	4.6
350	2.3	62%	6.3
400	0.2	66%	11.0

The signal reconstruction is performed exactly as for the SM $H \rightarrow \gamma\gamma$ decay mode, see Section 19.2.2. However, the p_T thresholds for the two photons can be raised considerably, given the higher Higgs-boson masses considered here. Thresholds of 125 GeV for the leading photon and 25 GeV for the second photon were found to give the best signal significance for 200 GeV < m_A < 400 GeV.

The acceptances of these simple kinematic cuts over this mass range are given in Table 19-32, which also includes the cross-sections and expected mass resolutions. Due to the narrow width of the A-boson in the MSSM, the mass resolution is determined by the experimental resolution of the EM Calorimeter.

Using a mass window of 1.4 σ_m and applying an efficiency factor of 80% for the photon identification, the expected numbers of signal and background events are given in Table 19-33 for an integrated luminosity of 100 fb^{-1}. The background is dominated by the irreducible $\gamma\gamma$ continuum, which itself is dominated by the $q\bar{q} \rightarrow \gamma\gamma$ Born process. As in the case of the search for SM $H \rightarrow \gamma\gamma$ decays, this background has been scaled up by a factor 1.5 to account for the quark-bremsstrahlung contribution. The reducible background is conservatively assumed to be 35% of the irreducible one, as estimated for lower masses in the SM Higgs case. Under these assumptions, the signal significances shown in Table 19-33 are expected.

Table 19-33 For the $A \rightarrow \gamma\gamma$ channel with tanβ = 1.1, expected number of reconstructed signal and background events inside the mass window, for an integrated luminosity of 100 fb^{-1}.

m_A (GeV)	Signal	Background	$S/\sqrt{B}$
200	52	210	3.6
250	121	1060	3.7
300	252	1660	6.2
350	68	810	2.4
400	5	130	0.5

The region of MSSM parameter space which can be covered by a search for the $A \rightarrow \gamma\gamma$ decay mode is shown in Figures 19-49 and 19-50 for integrated luminosities 100 fb^{-1} and 300 fb^{-1}, respectively. This channel is shown here for completeness as it provides coverage only over a limited range of m_A values for $m_A < 2m_t$ and for very low values of tanβ almost excluded already by LEP experiments.

19.3.2.3 $h \rightarrow b\bar{b}$

The SM $H \rightarrow b\bar{b}$ channel is discussed in detail in Section 19.2.4.2 for WH production (see also [19-34]) and in Section 19.2.4.3 for $t\bar{t}H$ production (see also [19-35]). Only the $t\bar{t}H$, $H \rightarrow b\bar{b}$ channel can be observed clearly above the background, provided the complete event is reconstructed. This requires excellent b-tagging performance (see Chapter 10 for more details), since each event contains four b-jets in the final state.

In the MSSM case, the rates can be enhanced by 10 - 20% compared to the SM, as discussed in [19-16]. The sensitivity to a $t\bar{t}h$, $h \rightarrow b\bar{b}$ signal has been computed from the results obtained for the SM search, after accounting for the different production and decay rates. The 5σ-discovery contours in the (m_A, tanβ) plane are shown in Figure 19-51. For an integrated luminosity of 30 fb^{-1}, the h-boson could be discovered in this channel for $m_A > 150$ GeV and tanβ < 4. For integrated luminosities above 100 fb^{-1}, the observability of the h-boson in this channel extends to 90% of the (m_A, tanβ) plane. For completeness, Figure 19-51 shows also the 5σ-discovery contour curve for the Wh, $h \rightarrow b\bar{b}$ channel for an integrated luminosity of 30 fb^{-1}, without including any systematic uncertainty on the background (see Section 19.2.4.2). This clearly demonstrates the superior discovery potential of the $t\bar{t}h$, $h \rightarrow b\bar{b}$ channel.

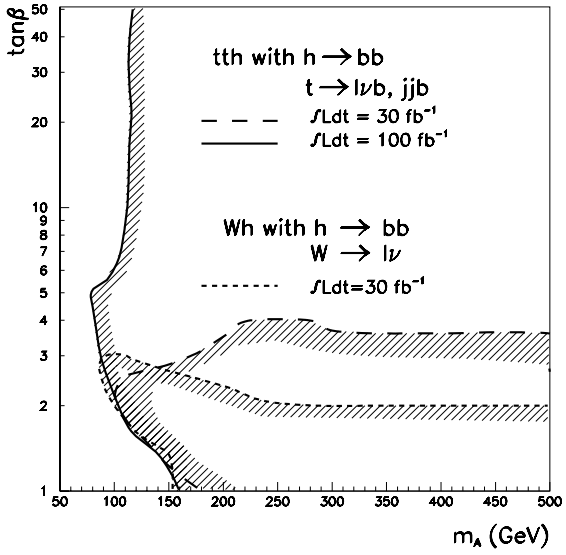

Figure 19-51 For integrated luminosities of 30 fb^{-1} and 100 fb^{-1}, the 5σ-discovery contour curves for the $t\bar{t}h$ and Wh with $h \rightarrow b\bar{b}$ channel in the (m_A, tanβ) plane.

In conclusion, the complete reconstruction of the $t\bar{t}h$, $h \rightarrow b\bar{b}$ final state has resulted in a very large improvement of the signal observability in this channel with respect to earlier studies [19-34], and the impact of this improvement is most striking in the MSSM case, as illustrated by Figure 19-51.

19.3.2.4 $H \rightarrow ZZ^{(*)} \rightarrow 4\,l$

As in the $h \rightarrow \gamma\gamma$ and $h \rightarrow b\bar{b}$ channels, the observability of the $H \rightarrow ZZ^{(*)} \rightarrow 4\,l$ channel in the MSSM is estimated by extrapolating the detailed studies performed in the SM case (see Section 19.2.5 and Section 19.2.9). For the intermediate mass range, 120 GeV < $m_H < 2m_Z$, the signal rates are small and the background rates are potentially very large. For the larger masses, above the ZZ threshold, the expected observability of this channel reaches values as high as 45σ, with a signal-to-background ratio of approximately 20:1. The only significant background arises from irreducible ZZ continuum production.

In the MSSM, the rates of $H \rightarrow ZZ^{(*)} \rightarrow 4\,l$ are strongly suppressed with respect to the SM case over the full tanβ range, except for values of tanβ smaller than one. This is due to the suppression of the HZZ coupling, to the opening of the $H \rightarrow hh$ decay channel, and to the enhancement of the $H \rightarrow t\bar{t}$ channel. These characteristics of the Higgs boson in the MSSM case limit the observability of this channel to the range $2m_h < m_H < 2m_t$ and to low values of tanβ.

Table 19-34 Observability of the $H \rightarrow ZZ^{(*)} \rightarrow 4\,l$ channels for an integrated luminosity of 30 fb^{-1}. The values for $\sigma \times$ BR are the ones for the SM Higgs boson and do not correspond to any fixed value of tanβ. For higher masses the numbers are given for the selection with the additional cut on $p_T{}^{max}(Z_1,Z_2)$ [19-16].

m_H (GeV)	130	150	170	200	240	300
$\sigma \times$ BR (fb)	3.0	5.5	1.4	12.4	11.2	9.1
Signal events	11.4	26.8	7.6	56	33	39
Background	2.6	3.0	3.2	5.3	1.1	1.2
Significance	4.8	15.5	3.2	24.2	31.8	36.1

In the SM case the Higgs-boson width increases rapidly with m_H, and therefore the chosen mass window is determined by the intrinsic Higgs-boson width for $m_H > 300$ GeV. Since the MSSM H-boson decay width remains much smaller than the experimental resolution over the relevant region of parameter space, the mass window chosen for the MSSM case is narrower. Since the observability in this channel is somewhat limited, cuts on the maximum p_T of the reconstructed Z-boson, $p_T{}^{max}(Z_1, Z_2)$, are used in the mass range $m_H > 200$ GeV [19-16]. Mass dependent requirements, $p_T{}^{max}(Z_1, Z_2) > m_H/3$ or $p_T{}^{max}(Z_1, Z_2) > m_H/2$, are applied to derive the observability in the MSSM case. The expected numbers of signal and background events are given in Table 19-34 for reference values of the cross-section times branching ratio, $\sigma \times$ BR, taken from the SM case. The expected 5σ-discovery contour curves are shown in Figure 19-52 for different values of the integrated luminosity. The highest possible integrated luminosity is needed to observe this channel in the MSSM case.

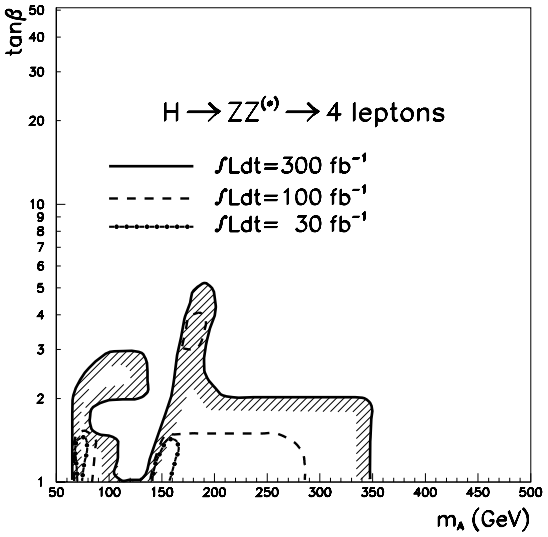

Figure 19-52 For integrated luminosities of 30 fb^{-1}, 100 fb^{-1} and 300 fb^{-1}, 5σ-discovery contour curves for the $H \rightarrow ZZ^{(*)} \rightarrow 4l$ channel in the (m_A, tanβ) plane.

If a signal were observed, the measured rate would provide the best information on its origin, since the $H \rightarrow ZZ^{(*)} \rightarrow 4\,l$ MSSM rates are suppressed by an order of magnitude with respect to the SM case over most of the parameter space. For values of m_H larger than ~250 GeV, the measured signal width would also distinguish between the SM Higgs boson with $\Gamma_H{}^{tot} \sim 10$ GeV and the MSSM Higgs boson with $\Gamma_H{}^{tot} << 10$ GeV for low values of tanβ.

19.3.2.5 *H/A* $\rightarrow \tau\tau$

Despite rather optimistic recent theoretical estimates [19-74], the $H \rightarrow \tau\tau$ decay mode is not expected to be observable at the LHC in the SM case, because the expected signal rates are too low compared to the large backgrounds from various SM processes [19-75]. However, in the MSSM case, the $H \rightarrow \tau\tau$ and $A \rightarrow \tau\tau$ rates are strongly enhanced over a large region of the parameter space. For low values of tanβ, the $gg \rightarrow A$, $A \rightarrow \tau\tau$ rates are dominant and significantly larger than in the SM case for a Higgs boson of the same mass. For large values of tanβ, the production is dominated by the strongly enhanced associated $b\bar{b}H$ and $b\bar{b}A$ production and the $H/A \rightarrow \tau\tau$

branching ratio is about 10% in the mass range 200 - 500 GeV. The relative contribution from the associated production is roughly 50% for $\tan\beta = 5$ and about 90% for $\tan\beta = 20$. For $m_A > 150$ GeV, the H and A bosons are almost degenerate in mass, so their signal rates in the $\tau\tau$-channel can be summed. A more complicated procedure, depending on the experimental resolution and on the mass difference $m_H - m_A$, has to be applied for $m_A < 150$ GeV [19-16]. Higgs-boson masses below 100 GeV have not been considered in this study due to the large resonant background from $Z \rightarrow \tau\tau$ decays.

This channel has been extensively used as a benchmark when optimising the detector for τ identification and E_T^{miss} reconstruction. The possible signal has improved as the detector design has evolved. Much effort has also gone into understanding in detail the topological features of the signal and background events. Since the ATLAS Technical Proposal [19-14] a combined analysis has been performed, using tagging of the spectator *b*-jets and a veto on the presence of other jets in the event. This has resulted in a significant improvement of the overall sensitivity to this channel.

The trigger for such decay modes is based on the leptonic decay of one of the τ-leptons. The other τ-lepton may then decay to hadrons (lepton-hadron channel) or to another lepton (lepton-lepton channel). The lepton-hadron channel turns out to provide the best sensitivity to a possible signal, due to both the larger rate (the fraction of $A \rightarrow \tau\tau$ resulting in a lepton-hadron final state is 46%) and to the more favourable kinematics of the τ-decay. This Section therefore only describes the extraction of the signal in this channel. The contribution from the lepton-lepton channel to the final observability is rather marginal and details on its analysis can be found in [19-76].

The backgrounds are a mixture of irreducible $Z \rightarrow \tau\tau$ background and of $t\bar{t}$, $b\bar{b}$ and *W+jet* processes, where a jet is misidentified as a τ–lepton. They can be significantly reduced by applying a selection based on a reconstructed lepton, τ identification and E_T^{miss}. Excellent τ identification performance to suppress the huge backgrounds containing hadronic jets from various sources [19-77], and excellent E_T^{miss}-resolution for the reconstruction of the $\tau\tau$ invariant mass, $m_{\tau\tau}$, are required to observe the signal [19-76].

A detailed discussion of the τ identification, the E_T^{miss} resolution and the reconstruction of the $\tau\tau$ invariant mass is presented already in Chapter 9. Only the main ingredients of the selection procedure are recalled here and only those aspects which are specific to the observability of this channel are discussed in some detail.

The standard $H/A \rightarrow \tau\tau$ analysis, as described already in [19-14] and [19-76], is based on a set of selection criteria, which include τ identification, kinematic cuts, and a mass window cut on the reconstructed $\tau\tau$ mass, $m_{\tau\tau}$. The energies of the two τ-leptons, used for the $m_{\tau\tau}$ calculation are evaluated from the energies of the τ decay products, which are assumed to have the direction of the parent τ-lepton, and the neutrino energies are obtained by solving a system of equations containing the two E_T^{miss} components (see the discussion on $Z \rightarrow \tau\tau$ mass reconstruction in Section 9.3.3.1).

This standard $H/A \rightarrow \tau\tau$ analysis includes the τ identification cuts described in detail in Section 9.1.5.2. Additional selections are then made:

- One isolated trigger lepton with $p_T > 24$ GeV within $|\eta| < 2.5$. The isolation requirement rejects leptons from $b\bar{b}$ production and decay by a factor of 100 for 90% efficiency for leptons from τ decays;
- $E_T^{jet} > 40$ GeV, $|\eta| < 2.5$ for the τ-jet;

- $E_T^{miss} > 18$ GeV;
- transverse mass m_T(lepton-E_T^{miss}) < 25 GeV;
- $1.8 < \Delta\phi^{(jet\text{-}lepton)} < 2.9$ or $3.4 < \Delta\phi^{(jet\text{-}lepton)} < 4.5$. This cut is necessary for the reconstruction of the ττ invariant mass.

Finally, events are accepted if the ττ invariant mass, $m_{\tau\tau}$, is within a mass window of $m_A \pm 1.5\,\sigma_m$.

The analysis presented above does not exploit the fact that the direct and associated production processes show substantial kinematic and topological differences. In associated production, spectator *b*-quarks are present in the signal events unlike in direct production. The $b\bar{b}H$ and $b\bar{b}A$ production processes can be selected by requiring a single tagged *b*-jet. This also reduces substantially the large W+*jet* and $Z \rightarrow \tau\tau$ backgrounds.

In $b\bar{b}H$, $b\bar{b}A$ events, the average transverse momentum of the Higgs boson is lower than in events from direct production. This difference increases with increasing Higgs-boson mass, from 14% to 42%, as m_H increases from 150 to 450 GeV. In $b\bar{b}H$, $b\bar{b}A$ events, the τ-leptons from the Higgs-boson decay are therefore more back-to-back, with the following consequences:

- A narrower $\Delta\phi^{(jet\text{-}lepton)}$ distribution, peaked around π, is observed for associated production with respect to direct production; the distribution is very similar to that of the $Z \rightarrow \tau\tau$ background.
- The fraction of events for which the neutrino system can be resolved is smaller by 30% for associated production compared to direct production (see Section 9.3.3.4).
- The ττ invariant mass resolution is degraded by about 50% for associated production compared to direct production (see Section 9.3.3.4).

Due to these topological features of the associated production the overall efficiency of the standard reconstruction procedure is reduced by 40 - 50% with respect to direct production.

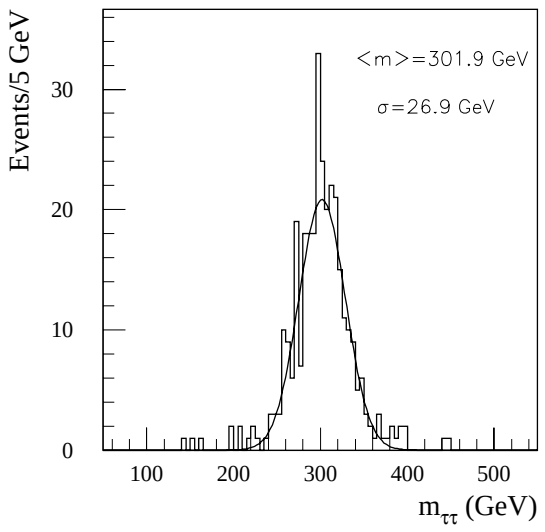

Figure 19-53 Reconstructed invariant mass, $m_{\tau\tau}$, from $A \rightarrow \tau\tau$ decays for direct Higgs-boson production and for m_A = 300 GeV.

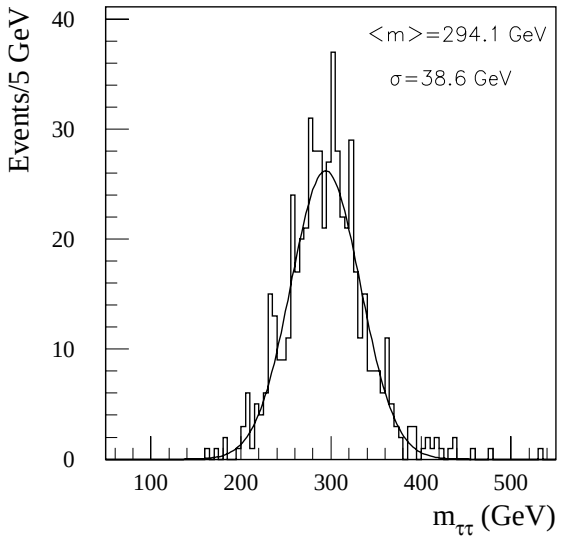

Figure 19-54 Same as Figure 19-53, but for associated Higgs-boson production.

Figures 19-53 and 19-54 show the $\tau\tau$ invariant masses obtained from fully simulated and reconstructed events at low luminosity for $m_A = 300$ GeV for events from direct and associated Higgs-boson production, respectively. Figure 19-55 shows the mass resolution, σ_m, expected at low luminosity as a function of m_A, separately for direct and associated Higgs-boson production. The general tendency of σ_m to increase with m_A is mostly due to the increase of $\sigma(E_T^{miss})$ as m_A increases (see Section 9.3.3.4).

Since the direct and associated production processes display substantial differences, both in their topological features and in the final state (two additional *b*-quarks in the case of associated production), a separate analysis for each production process has been performed to optimise the signal observability in the $H/A \rightarrow \tau\tau$ channel.

The analysis for direct production requires:

- A veto against *b*-jets for $p_T > 15$ GeV and $|\eta| < 2.5$ (to reject $t\bar{t}$ and $b\bar{b}$ backgrounds).
- Standard $H/A \rightarrow \tau\tau$ reconstruction (τ identification, kinematic and mass cuts).

The analysis for associated production requires:

- At least one tagged *b*-jet (to reject $Z \rightarrow \tau\tau$ and *W+jet* backgrounds).
- At most two non-*b* jets with $p_T > 15$ GeV and $|\eta| < 3.2$ (to reject $t\bar{t}$ backgrounds);
- Standard $H/A \rightarrow \tau\tau$ reconstruction (τ identification, kinematic and mass cuts), except for the $\Delta\phi^{(\text{jet-lepton})}$ cut.

In both analyses, the nominal *b*-tagging performance at low luminosity has been assumed (see Chapter 10).

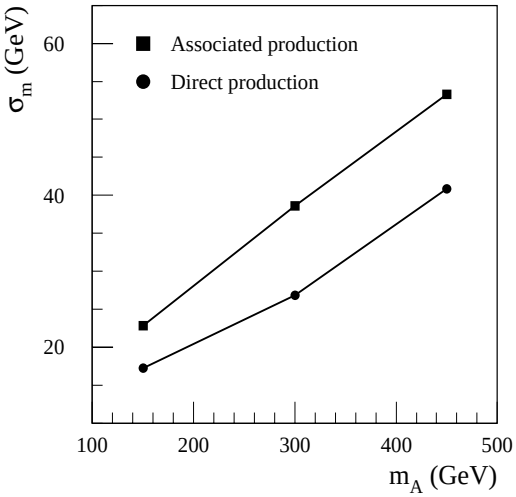

Figure 19-55 For $H/A \rightarrow \tau\tau$ decays at low luminosity, $\tau\tau$ invariant mass resolution, σ_m, as a function of m_A. The results are obtained from full simulation and reconstruction, and are shown separately for the direct (black circles) and associated (black squares) Higgs-boson production.

The analysis which enhances the fraction of events from direct production rejects more efficiently the $t\bar{t}$ and $b\bar{b}$ backgrounds because of the veto against *b*-jets. The analysis which selects mostly events from associated production will improve the sensitivity for moderate and large values of tanβ. In this case, the somewhat worse efficiency of the analysis is balanced by the improved *W+jet* and $Z \rightarrow \tau\tau$ background rejection.

Since events are accepted either by one analysis or the other, the expected overall signal significances are obtained by adding in quadrature the signal significances expected for each analysis separately. As explained in more detail in [19-78] and indicated in Table 19-35, the combination of these two analyses improves the overall sensitivity to the $H/A \rightarrow \tau\tau$ channel for masses in the range 150 - 450 GeV by 60 - 100% with respect to what would be obtained with the more inclusive analysis following the analysis presented in the ATLAS Technical Proposal.

Results at low luminosity

The $H/A \rightarrow \tau\tau$ reconstruction efficiency was estimated from high-statistics samples of fully simulated events for three different values of m_A (m_A = 150, 300 and 450 GeV) and separately for the direct and associated Higgs-boson production processes. High statistics samples of the various background processes (W+jet, $t\bar{t}$, $b\bar{b}$ and Z/γ^*) have also been fully simulated and reconstructed to evaluate the rejections of the two analyses described above as accurately as possible (see [19-78] for more details). Background from $Zb\bar{b}$ production has not been simulated in detail, since it has been shown to be very small in earlier studies [19-37]. The background rejections obtained after all the selection criteria (kinematic and topological cuts, mass window and τ identification) are very high for the reducible W+jet, $t\bar{t}$ and $b\bar{b}$ backgrounds. Therefore, for the background processes, the acceptance for the τ identification criteria has been factorised from the rest, since they are essentially uncorrelated to each other (the residual background from these processes contains only small contributions with real τ-leptons).

Table 19-35 Expected $H/A \rightarrow \tau\tau$ signal and background rates as a function of m_A for the lepton-hadron channel with tanβ = 10 and an integrated luminosity of 30 fb^{-1}. The rates are given separately for each production mechanism: direct ($gg \rightarrow H/A$) and associated ($b\bar{b}H$, $b\bar{b}A$) Higgs-boson production and for the direct/associated analyses (see text). The signal event rates correspond to the summed $H \rightarrow \tau\tau$ and $A \rightarrow \tau\tau$ rates. The expected signal significances are shown separately for the two analyses and for an integrated luminosity of 30 fb^{-1}. The overall combined significances are finally shown for integrated luminosities of 30 fb^{-1} and 300 fb^{-1}, accounting for the degraded performance expected at high luminosity (see text). For comparison the signal significance expected from an inclusive analysis, described in [19-76], is also shown.

m_A (GeV)	150	300	450
$\sigma \times$ BR for direct production (pb)	1.3	0.05	0.015
$\sigma \times$ BR for associated production (pb)	2.9	0.28	0.04
Mass window (GeV)	± 30 GeV	± 55 GeV	± 75 GeV
Inclusive analysis			
Signal significance for 30 fb^{-1}	5.7	1.2	0.6
Direct/associated analysis			
Event rates:			
Direct production	49 / 2	9.5 / 0.35	1.5 / 0.16
Associated production	56 / 72	6 / 18	1.3 / 6.3
Total signal	105 / 74	15.5. / 18	2.8 / 6.5
W+jet	530 / 46	740 / 43	228 / 22
$t\bar{t}$	7 / 6	9 /8	5 /4
$b\bar{b}$	14 / 29	4 / 21	1 / 6
$Z/\gamma^* \rightarrow \tau\tau$	163 / 5	41 / 2	7 / 0.5
Total background	714 / 86	794 / 74	241 / 32.5
Signal significance for 30 fb^{-1}	3.9 / 8.0	0.6 / 2.1	0.2 / 1.1
Combined significance for 30 fb^{-1}	8.9	2.2	1.2
Combined significance for 300 fb^{-1}	12.5	3.8	2.1

Table 19-35 gives the expected $H/A \rightarrow \tau\tau$ signal rates for three values of m_A and for an integrated luminosity of 30 fb^{-1}. The results are shown for tanβ = 10, separately for the direct and associated production processes and for each of the selection analyses. The signal from associated pro-

duction accounts for 70 - 80% of the total signal rate. The analysis requiring a tagged *b*-jet selects almost exclusively signal events from associated production, but a large fraction of these are also selected by the other analysis for low values of m_A, due to the limited acceptance in p_T and $|\eta|$ of the *b*-tagging algorithm.

The dominant background selected by the analysis optimised for direct Higgs-boson production arises from W+jet events, which have the largest production cross-section of all the background processes. For low values of m_A, the irreducible background from $Z \rightarrow \tau\tau$ is also significant for events selected with this analysis. In contrast, the analysis optimised for associated Higgs-boson production rejects much better the W+jet and $Z \rightarrow \tau\tau$ backgrounds, but due to their large production cross sections the dominant residual backgrounds remain to be W+jet and $b\bar{b}$ production.

In conclusion, the direct production analysis contributes significantly only for low values of m_A, but provides a signal-to-background ratio of only 0.15 for m_A = 150 GeV, even though it selects events with better mass resolution. In contrast, the associated production analysis provides a signal-to-background ratio close to 0.9 for the same values of m_A, and above 0.2 for the higher values of m_A.

Table 19-35 also shows the signal significances combined for both analyses for an integrated luminosity of 30 fb^{-1}. For m_A = 150 GeV, the inclusion of the direct production analysis improves the significance obtained with the associated production analysis by ~10%. This improvement increases as tanβ decreases, since the fraction of events arising from direct production increases. The combined method therefore improves the signal observability mostly for moderate values of tanβ. For large values of tanβ, the analysis requiring a tagged *b*-jet improves considerably the signal-to-background ratio and hence the signal observability with respect to previous more inclusive studies [19-14].

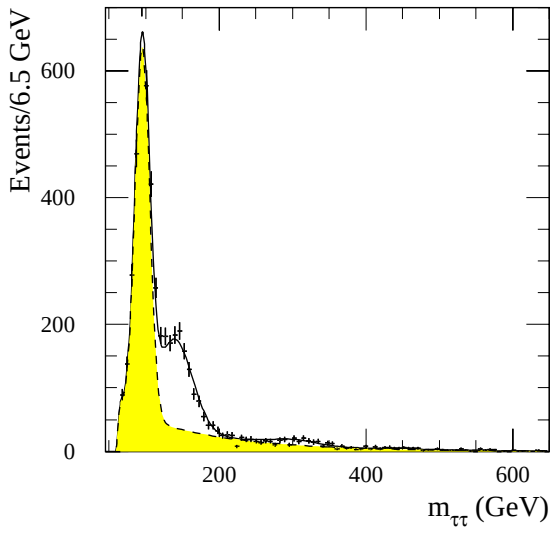

Figure 19-56 For the direct production analysis, for tanβ = 25 and for an integrated luminosity of 30 fb^{-1}, distribution of $m_{\tau\tau}$ shown for the total background (dashed shaded curve) and for the sum of the $H/A \rightarrow \tau\tau$ signals at m_A = 150, 300 and 450 GeV, and the background (solid curve and points with error bars).

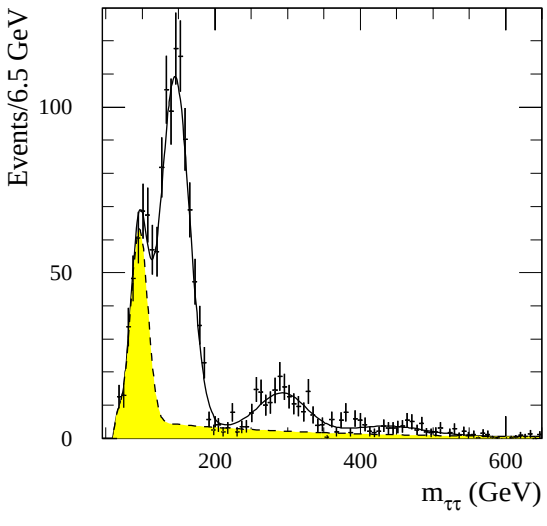

Figure 19-57 Same as Figure 19-56, but for the associated production analysis.

Table 19-36 shows for three values of m_A and for integrated luminosities of 30 fb^{-1} and 300 fb^{-1} the lower limit values of tanβ corresponding to a 5σ discovery for the $H/A \rightarrow \tau\tau$ channel. The errors assigned to the tanβ values are those which would arise if the overall background were assumed to have a systematic uncertainty of ±20%.

Table 19-36 For three values of m_A and for integrated luminosities of 30 fb^{-1} and 300 fb^{-1}, lower limits of tanβ corresponding to a 5σ discovery in the $H/A \rightarrow \tau\tau$ channel.

m_A (GeV)	30 fb^{-1}	300 fb^{-1}
150	7.5 ± 0.5	6.0 ± 0.5
300	14.5 ± 0.7	11.0 ± 0.5
450	19.5 ± 1.0	15.0 ± 0.6

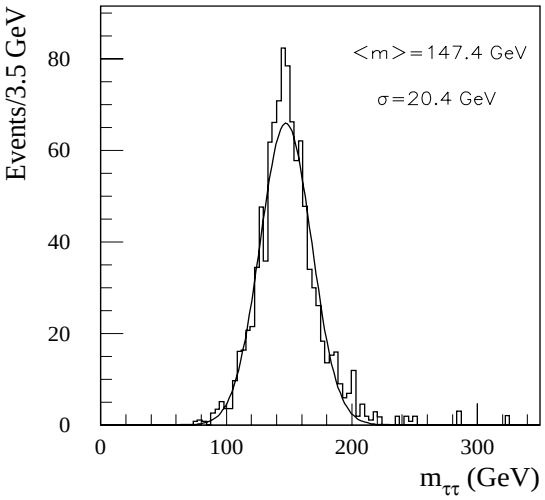

Figure 19-58 For the appropriate mixture of $H/A \rightarrow \tau\tau$ events from direct and associated production and for low-luminosity performance, distribution of reconstructed ττ mass for m_A = 150 GeV and tanβ = 7.5 (5σ discovery limit).

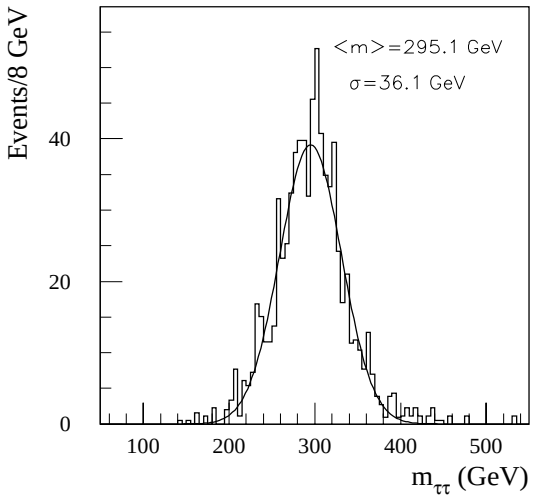

Figure 19-59 Same as Figure 19-58, but for m_A = 300 GeV and tanβ = 15.

Figures 19-56 and 19-57 show the $m_{\tau\tau}$ distributions expected for the summed signal and background, for three values of m_A with tanβ = 25 and for an integrated luminosity of 30 fb^{-1}, respectively for the direct and associated analyses. Finally, Figures 19-58, 19-59 and 19-60 show, respectively, for signal events with m_A = 150, 300 and 450 GeV, the $m_{\tau\tau}$ distribution for the appropriate mixture of direct and associated production events and for the value of tanβ corresponding to a 5σ-discovery for an integrated luminosity of 30 fb^{-1} (first column of Table 19-36).

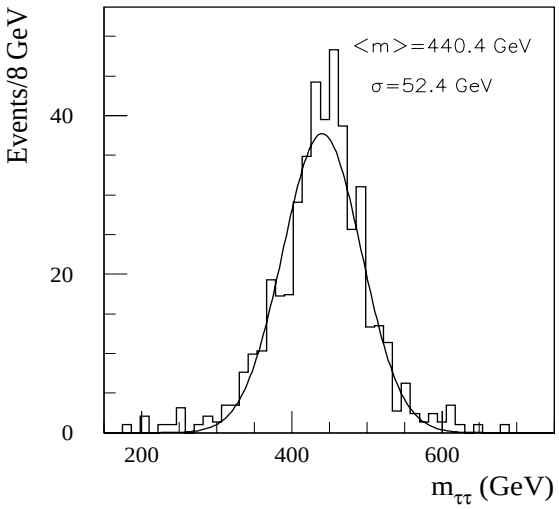

Figure 19-60 Same as Figure 19-58, but for m_A = 450 GeV and tanβ = 20.

Results at high luminosity

At high luminosity, the efficiency for τ identification and the background rejection can be maintained at their low-luminosity values, but the sensitivity to the $H/A \rightarrow \tau\tau$ channel is significantly degraded due to pile-up effects:

- The E_T^{miss} resolution is degraded by a factor of two at high luminosity and this directly affects the $m_{\tau\tau}$ reconstruction. The $m_{\tau\tau}$ resolution is degraded by a factor of two as can be seen from Figures 19-58 and 19-61.
- The acceptance in the mass window, which has to be twice as wide compared to its low-luminosity value, nevertheless decreases by about 30% (20%) for m_A = 150 GeV (m_A > 300 GeV).

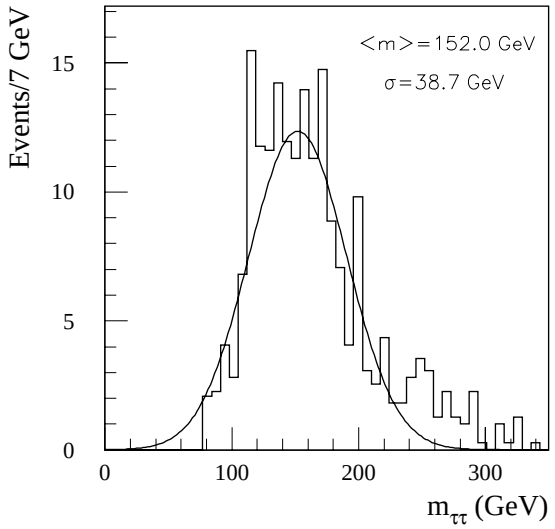

Figure 19-61 Same as Figure 19-58, but for tanβ = 6 and for high luminosity performance.

In addition, the acceptance for the signal is reduced at high luminosity due to:

- the reduced *b*-tagging efficiency (50% instead of 60%) for the same rejection of non-*b*-jets;
- the higher threshold on the jet p_T (30 GeV instead of 15 GeV);

The overall impact of high luminosity operation on the signal significance arises therefore mostly from the degradation of the ττ mass reconstruction due to pile-up and the *b*-tagging efficiency. The high luminosity signal significance is about 50% of the low luminosity significance for the same integrated luminosity. A real improvement on the 5σ discovery curve at low luminosity can be only expected after collecting the ultimate integrated luminosity of 300 fb^{-1}.

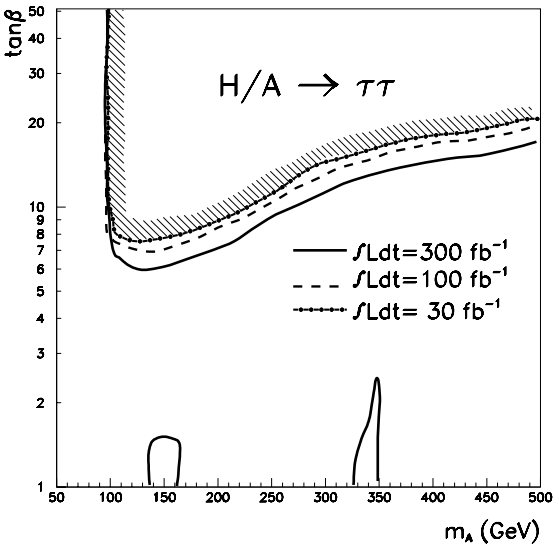

Figure 19-62 For integrated luminosities of 30 fb^{-1}, 100 fb^{-1} and 300 fb^{-1}, 5σ-discovery contour curves for the $H/A \rightarrow \tau\tau$ channel in the (m_A, tanβ) plane.

The expected 5σ discovery contour curves in the (m_A, tanβ) plane as a function of integrated luminosity are shown in Figure 19-62 for the combined $H/A \rightarrow \tau\tau$ signal. Even for a moderate integrated luminosity of 30 fb^{-1}, a signal should be observed over a large region of the (m_A, tanβ) plane. This region can be increased only for the largest integrated luminosities achievable with high luminosity operation, due to the degraded performance at high luminosity discussed above. For an integrated luminosity of 300 fb^{-1}, some sensitivity may also be achieved for low values of tanβ, in a region where the dominant signal contribution arises from direct $A \rightarrow \tau\tau$ production.

19.3.2.6 *H/A* $\rightarrow \mu\mu$

The $H \rightarrow \mu\mu$ decay channel cannot be observed for a SM Higgs because of both the very small signal rate and the large backgrounds from several SM processes. However, because of the large enhancement of rates through $b\bar{b}H$ and $b\bar{b}A$ production and of some enhancement of the branching ratio, both present at large tanβ, it can be observed in the MSSM case. The rates for this channel are governed by the same couplings as for the ττ channel, but the branching ratio scales as $(m_\mu/m_\tau)^2$.

This huge reduction in signal rates with respect to the ττ channel is compensated to some extent by the much better identification efficiency and experimental resolution, which can be achieved in the μμ channel. Also, in contrast to the $H/A \rightarrow \tau\tau$ channel, the efficiency of the reconstruction procedure and the mass resolution are comparable for the direct and associated production.

The final state contains isolated high-p_T muons and, for associated production, two additional spectator *b*-jets. In the standard event selection two muons with $p_T > 20$ GeV and $|\eta| < 2.5$ are required. This selection has a high acceptance, of 50 - 60%. The expected mass resolution, using the combined muon reconstruction, is σ_m / m = 2-3%. The intrinsic width of the Higgs boson increases with m_A and tanβ. It is of the order of ~1 GeV for tanβ = 10 and $100 < m_H < 500$ GeV and varies between 6 - 25 GeV for tanβ = 50. In the chosen mass window of $m_H \pm 1.64((\Gamma_H{}^{tot}/2.36)^2+\sigma_m{}^2)^{1/2}$, almost 90% of the signal events are contained, as described in Section 8.6.2.

The background in this channel is dominated by irreducible $Z/\gamma^* \rightarrow \mu\mu$ Drell-Yan production and reducible $t\bar{t}$ production with both top-quarks decaying into muons, $t \rightarrow \mu\nu b$. The expected cross-section for $Z/\gamma^* \rightarrow \mu\mu$ Drell-Yan production is 1400 pb for dimuon events with a mass above ~80 GeV and ~6 pb for $t\bar{t}$ events with two muons in the final state. A potential background source is also $b\bar{b}$ production with a total cross-section of 500 μb. After applying the kinematic cuts and muon isolation criteria, this background is found to be a negligible fraction of the total background. After an inclusive selection (see Table 19-37) the irreducible $Z/\gamma^* \rightarrow \mu\mu$ Drell-Yan background is dominant, while the $t\bar{t}$ background contributes only at the level of 20 - 30% of the total background over the mass range of interest. This fraction increases with increasing values of $m_{\mu\mu}$.

Since the direct and associated production result in substantially different final states, analyses, optimised separately for each production process [19-79], as in the $H/A \rightarrow \tau\tau$ case (see Section 19.3.2.5), are used. Moreover, it was found that both the irreducible and reducible backgrounds can be rejected further by applying cuts on the p_T of the dimuon system, $p_T{}^{\mu\mu}$, and on $E_T{}^{miss}$.

The optimised analyses require:

- $E_T{}^{miss} < 20$ GeV at low luminosity and $E_T{}^{miss} < 40$ GeV at high luminosity;
- $p_T{}^{\mu\mu} < 100$ GeV ;
- one *b*-tagged jet for the associated analysis, and a *b*-jet veto for the direct analysis. For low luminosity, the threshold on the *b*-tagged jet is set to 15 GeV, while for high luminosity, it is raised to 30 GeV.

Table 19-37 Expected $H/A \to \mu\mu$ signal and background rates within the chosen mass window as a function of m_A for tanβ = 15 and an integrated luminosity of 30 fb^{-1}. The rates are given separately for each production mechanism: direct ($gg \to H/A$) and associated ($b\bar{b}H$, $b\bar{b}A$) Higgs-boson production and for the direct/associated analyses (see text). The signal event rates correspond to the summed $H \to \mu\mu$ and $A \to \mu\mu$ rates. The expected signal significances are shown separately for the two analyses and for an integrated luminosity of 30 fb^{-1}. The overall combined significances are finally shown for integrated luminosities of 30 fb^{-1} and 300 fb^{-1}.

m_A (GeV)	125	150	200	300	450
σ × BR for direct production (fb)	9.6 (*A* only)	9.1	2.3	0.3	0.05
σ × BR for associated prod. (fb)	26 (*A* only)	24	10.	2.3	0.41
Inclusive analysis					
Events rates ($m_{\mu\mu} = m_A \pm 2\sigma$)					
Total signal	492	430	163	48.5	9.2
$Z/\gamma^* \to \mu\mu$	78 240	22 200	8 300	2 325	670
$t\bar{t}$	3 492	3 600	2 460	830	220
Total background	81732	25 800	10 760	3 150	890
Significance for 30 fb^{-1}	1.7	2.7	1.6	0.9	0.3
Direct/associated analysis					
Events rates ($m_{\mu\mu} = m_A \pm 2\sigma$)					
Direct production	121 / 2	116 / 2.8	29 / 0.7	2.7 / 0.07	0.4 / 0.01
Associated production	297 / 65	266 / 74	121 / 33	29.6 / 8.7	4.2 / 1.3
Total signal	418 / 67	382 / 77	150 / 33	32.3 / 8.7	4.6 / 1.3
$Z/\gamma^* \to \mu\mu$	60850 / 1180	15 300 / 430	8 840 / 220	1 700 / 27.4	102 / 7
$t\bar{t}$	57 / 137	56 / 174	41 / 98	12 / 32	1 / 4
Total background	60910 / 1317	15 354 / 604	8 880 / 318	1 712 / 59	103 / 11
Signal significance 30 fb^{-1}	1.7 / 1.9	3.1 / 3.1	1.6 / 1.9	0.8 / 1.1	0.4 / 0.4
Combined significance for 30 fb^{-1}	2.5 (*A* only)	4.4	2.4	1.4	0.6
Combined significance for 300 fb^{-1}	6.8 (*A* only)	11.6	6.4	3.3	1.8

Raising the E_T^{miss} threshold reduces the $t\bar{t}$ rejection, and thereby the sensitivity by 10%. Raising the jet threshold to 30 GeV implies an additional loss in significance of less than 10%. For high-luminosity operation, one expects a degradation of the nominal *b*-tagging efficiency from 60% to 50%, while the mass resolution and reconstruction efficiency for muons remain essentially the same.

The signal will be observed above the background as a narrow peak in the invariant dimuon mass distribution, $m_{\mu\mu}$, as shown in Figure 19-63. Table 19-37 gives the expected numbers of signal and background events in

Table 19-38 For five values of m_A and for integrated luminosities of 30 fb^{-1} and 300 fb^{-1}, lower limits of tanβ corresponding to a 5σ discovery in the $H/A \to \mu\mu$ channel.

m_A (GeV)	30 fb^{-1}	300 fb^{-1}
120	21.0	12.9
150	15.9	9.8
200	21.0	13.1
300	32.3	20.9
450	43.3	25.0

the appropriate mass window for an integrated luminosity of 30 fb^{-1} and tanβ = 15. For m_A = 120 GeV, only A-boson production is used, since the H and A masses are not degenerate and more complicated formulae have to be used for the calculation of the expected significance. For comparison, results are given for the inclusive analysis as well as for the more exclusive selections. There is a clear gain with the tighter selection, since the more favourable signal-to-background ratio leads to a better significance. Combining the results of both analyses enhances the sensitivity to this channel. Unlike in the $H/A \rightarrow \tau\tau$ case, there is no degradation in the mass resolution in the case of the associated production. The b-tagging of the spectator b-quark suppresses the dominant $Z/\gamma^* \rightarrow \mu\mu$ continuum background very effectively.

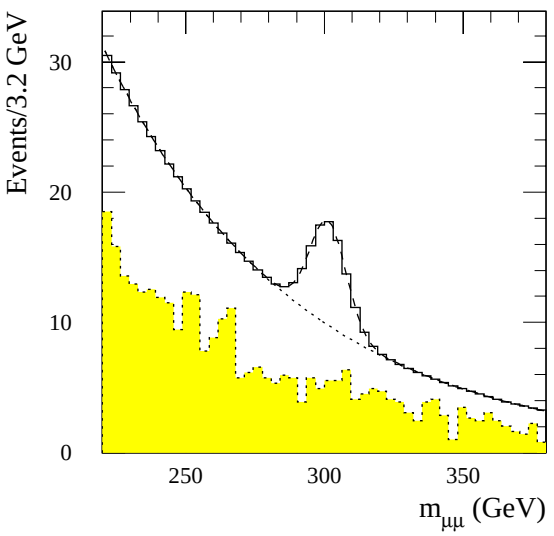

Figure 19-63 For an integrated luminosity of 30 fb^{-1} and for tanβ = 30, distribution of $m_{\mu\mu}$ shown for the reducible $t\bar{t}$ background (shaded histogram), for the total summed background (dashed curve) and for the sum of the $H/A \rightarrow \mu\mu$ signal with m_A = 300 GeV and the background (solid histogram). The $m_{\mu\mu}$ distribution is shown for the associated production analysis.

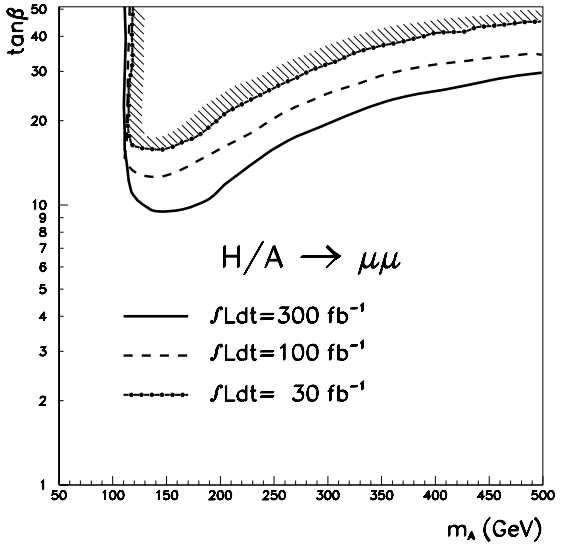

Figure 19-64 For integrated luminosities of 30 fb^{-1}, 100 fb^{-1} and 300 fb^{-1}, 5σ-discovery contour curves for the $H/A \rightarrow \mu\mu$ channel in the (m_A, tanβ) plane.

The expected significances for the inclusive, the associated and direct analyses and the combination of the latter two are given in Table 19-37 for integrated luminosities of 30 fb^{-1} and 300 fb^{-1}. The 5σ limit on tanβ for the combined analysis is given in Table 19-38 as a function of m_A. The expected 5σ-discovery contour curves for the combined $H/A \rightarrow \mu\mu$ signal are shown in Figure 19-64. The sensitivity to this channel is somewhat weaker than to the ττ channel as can be seen by comparing Tables 19-38 and 19-36. Nevertheless, the $H/A \rightarrow \mu\mu$ channel also covers a substantial fraction of the (m_A, tanβ) parameter space and provides a more precise measurement of the Higgs-boson mass (see Section 19.3.4.1).

19.3.2.7 $H/A \rightarrow t\bar{t}$

Due to the strong coupling of the SM Higgs boson to gauge-boson pairs, the $H \rightarrow t\bar{t}$ branching ratio is too small for this channel to be observable in the SM case. In the MSSM case, however, the $H \rightarrow t\bar{t}$ and $A \rightarrow t\bar{t}$ branching ratios are close to 100% for m_H, $m_A > 2\ m_t$ and for $\tan\beta \sim 1$. The $H \rightarrow t\bar{t}$ and $A \rightarrow t\bar{t}$ decays cannot be distinguished experimentally from each other, since the H- and A-bosons are almost degenerate in mass in the relevant region of parameter space.

As discussed in the literature [19-80], a signal from $H/A \rightarrow t\bar{t}$ decays would appear as a peak in the $t\bar{t}$ invariant mass spectrum above the $t\bar{t}$ continuum background for values of m_H smaller than 500 GeV. There is an interference between the signal and background amplitudes which causes an oscillating structure in the differential cross-section around $s = m_H^2$. This leads to a strong suppression of the observability of the signal at higher masses. As a consequence, for $m_H = 500$ GeV the total top-quark production cross-section differs very little from the cross-section with no Higgs boson being present. This interference effect is much stronger for the A than for the H boson. From the results presented in [19-80] this suppression of the total H+A rates is estimated to be roughly 30% for $m_H = 370$ GeV, 50% for $m_H = 400$ GeV and 70% for $m_H = 450$ GeV. These factors are taken into account in the analysis presented below (see also Table 19-39).

The signal is extracted [19-81] by searching for $WWb\bar{b}$ final states, with one $W \rightarrow l\nu$ and one $W \rightarrow jj$ decay. The lepton is required for the LVL1 trigger and all the jets, *i.e.* those from W-decay and the two b-jets, are required to have $p_T > 40$ GeV. It is expected that the experiment could trigger on such topologies and reconstruct them efficiently at both low and high luminosities. Both b-jets are required to be tagged, with an efficiency $\varepsilon_b = 60$ % (50%) at low (high) luminosity. Both top-quark decays are fully reconstructed (following the algorithm presented in Section 19.2.4.3) and a constraint on m_t is used to improve the resolution on the reconstructed $t\bar{t}$ invariant mass, $m_{t\bar{t}}$. The expected mass resolution, σ_m, on $m_{t\bar{t}}$ increases from 14 to 20 GeV as m_H increases from 370 to 450 GeV. After both top quark have been reconstructed, the background from continuum $t\bar{t}$ production is much larger than all other backgrounds (such as W+jet). The reconstructed $m_{t\bar{t}}$ distribution for signal and background events is shown in Figure 19-65 for $m_A = 370$ GeV and $\tan\beta = 1.5$.

The signal-to-background ratio varies between 9% and 1% over the mass range from 370 to 450 GeV. For an integrated luminosity of 30 fb^{-1} and $\tan\beta = 1.5$ about 2120 signal events and 4×10^4 background events are expected inside a mass windows of $\pm2\sigma_m$ around m_A for $m_A = 400$ GeV, see Table 19-39. For high luminosity operation and an integrated luminosity of 100 fb^{-1} one expects for a Higgs mass of 400 GeV about 4900 signal and 9×10^4 background events.

The mass resolutions quoted above imply that the width of a typical mass window for observing most of the signal would be between ±30 GeV and ±40 GeV. The extraction of the signal would only be possible for Higgs masses away from the kinematic peak of the background distribution, which is

Table 19-39 Observability of the $H/A \rightarrow tt$ channel for an integrated luminosity of 30 fb^{-1} and for $\tan\beta$ =1.5. The signal rates are computed using the rough estimate of the impact of the negative interference between the $H/A \rightarrow t\bar{t}$ signal and $t\bar{t}$ continuum production. For $m_A = 400$ GeV, a systematic uncertainty of 1% was assumed for the background.

m_A(GeV)	370	400	450
$\sigma \times$ BR (pb) (no interference)	11.8	8.4	4.8
$\sigma \times$ BR (pb) (with interference)	8.3	4.2	1.4
Signal	3190	2120	980
Background	34200	39500	52900
Significance	8.2	5.4	4.3

around $m_{t\bar{t}}$ = 400 GeV. Such an extraction assumes that the uncertainty on the shape of the continuum background is small and that it can be fitted from events outside the assumed Higgs mass window. Details on the fitting procedure can be found in [19-81]. This leads to the significance levels given in Table 19-39.

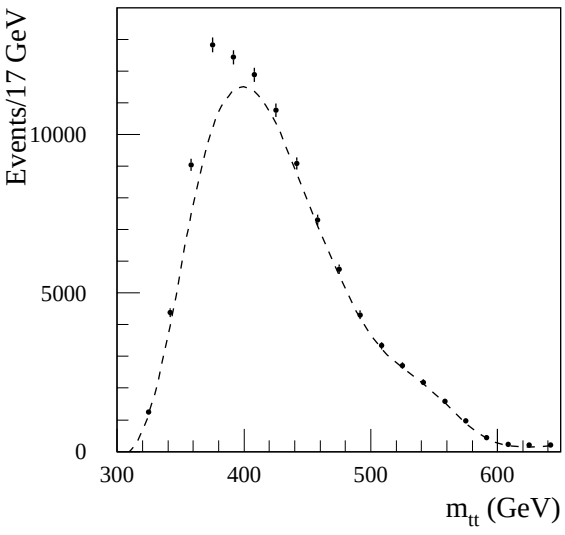

Figure 19-65 For an integrated luminosity of 30 fb^{-1} and for tanβ = 1.5, distribution of $m_{t\bar{t}}$ for the $t\bar{t}$ background (dashed histogram) and for the sum of the $H/A \rightarrow t\bar{t}$ signal with m_A = 370 GeV and of the signal+background (points with error bars).

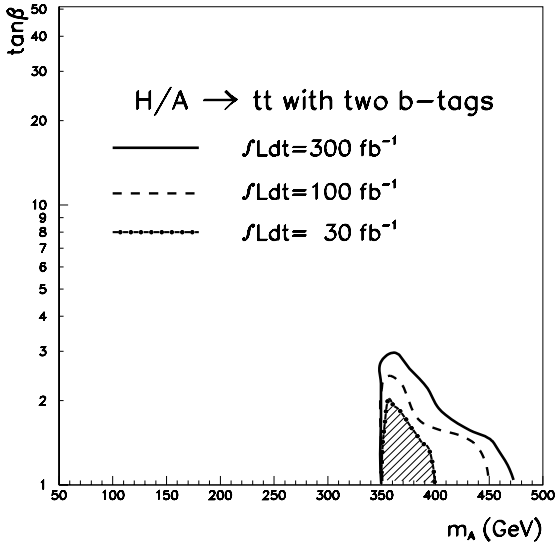

Figure 19-66 For integrated luminosities of 30 fb^{-1}, 100 fb^{-1} and 300 fb^{-1}, 5σ-discovery contour curves for the $H \rightarrow t\bar{t}$ channel in the (m_A, tanβ) plane.

For masses close to 400 GeV only an excess of events above the continuum background would be observed. This excess would be statistically significant, as shown in Table 19-39 and Figure 19-65, but this significance would only be meaningful if the theoretical uncertainties on the continuum background shape were not larger than about a percent. Although the theoretical uncertainties on the continuum $t\bar{t}$ production are much larger today, it is hoped that they would be reduced with time, and that the experimental data at the LHC would also contribute to a better understanding of heavy-flavour continuum production.

For the optimistic scenario assuming that the differential spectrum of $m_{t\bar{t}}$ would be known to better than 1% from a contribution of theory and experimental data, the signal significances including this systematic uncertainty for masses close to 400 GeV are shown in Table 19-39, and the 5σ-discovery contour curves in the (m_A, tanβ) plane for $H/A \rightarrow t\bar{t}$ decays are shown in Figure 19-66. These curves cover at best a limited region in parameter space, namely that corresponding to $2m_t < m_A < 470$ GeV. In conclusion, this channel will be only of very limited use as a discovery channel.

19.3.2.8 $b\bar{b}H$ and $b\bar{b}A$ production with $H/A \rightarrow b\bar{b}$

Final states containing four b-jets have been proposed in the literature [19-82] as signatures with a substantial discovery potential for heavy Higgs bosons in supersymmetric models. The channels of interest are:

- $b\bar{b}H$, $b\bar{b}A$ associated production with the subsequent $H/A \rightarrow b\bar{b}$ decay;

- $H \rightarrow hh \rightarrow b\bar{b}b\bar{b}$ (discussed in Section 19.3.2.9).

As described below, both channels have interesting features for the MSSM Higgs search. Their main drawback is the enormous background from QCD multijet production, and hence the very small signal-to-background ratio. In addition, triggering on purely hadronic final states is always a problem at hadron colliders. In order to maintain a LVL1 trigger rate from jets at a low enough level, rather high E_T thresholds have to be set on the individual jets [19-83] (see also Section 11.7.3). At present, ATLAS foresees three basic jet triggers at LVL1, a single jet trigger with a p_T threshold of 180 GeV, a three-jet trigger with a p_T threshold of 75 GeV on each jet, and a four jet-trigger with a p_T threshold of 55 GeV on each jet. These values apply to low-luminosity running. At high luminosity, they have to be raised to values of 290 GeV for single jet, 130 GeV for three jets and 90 GeV for four jets. These threshold settings limit the LVL1 jet trigger rate to the few kHz range, since the LVL2 trigger is not expected to reduce them by large factors.

For the particular Higgs-boson channels discussed here, these high thresholds lead to significant acceptance losses. If, on the other hand, efficient *b*-tagging could be performed with the LVL2 trigger, the LVL1 thresholds could be lowered. The possibility of applying *b*-tagging at LVL2 has been investigated already in some detail [19-83][19-84][19-85] and further work is in progress.

Given the difficulties described above, the analysis of these channels is performed in two steps. First, no acceptance losses at the trigger level are assumed, in order to determine the optimum physics coverage. In a second step, the events are subjected to the actual ATLAS LVL1 trigger thresholds, which represents a more realistic scenario, even if it could be considered pessimistic in certain cases (see below).

Analysis without trigger requirements

The $b\bar{b}H$ and $b\bar{b}A$ associated production with $H/A \rightarrow b\bar{b}$ is strongly enhanced for large values of tanβ and has been reported as a very promising channel [19-82]. This mode would be particularly interesting for large values of m_H and m_A for which the sensitivity to the $H/A \rightarrow \tau\tau$ channel slowly disappears (see Section 19.3.2.5). This channel has been studied carefully and the details are reported in [19-86].

For large values of m_A the final state has a very characteristic topology: the two hardest jets in the event come from the $H/A \rightarrow b\bar{b}$ decay, while the softer ones come predominantly from the associated $b\bar{b}$ pair and from initial / final-state radiation. These features can be used for the event selection, for which at least four reconstructed jets are required in the final state. A more favourable signal-to-background ratio is obtained, if the selection requires that the four jets of the highest transverse energies are tagged as *b*-jets. The background is dominated by events containing true *b*-jets. The contribution from events with at least one mis-identified jet is below 10%, if one assumes the default performance of the *b*-tagging algorithm at low luminosity (see Chapter 10).

The two leading jets are required to satisfy high p_T thresholds which are optimised as a function of m_A, as shown in Table 19-40. The p_T of the other two jets is required to be above 50 GeV and 30 GeV, respectively. For m_A = 200 GeV, the p_T threshold is lowered to 30 GeV for both jets. For the signal events, the expected acceptance, is of the order of 10% when four jets above these thresholds are required and the three most energetic ones are true *b*-jets (*b*-tagging efficiency is not included).

Table 19-40 p_T thresholds required for the two leading jets as a function of m_A for $H/A \rightarrow b\bar{b}$ decays from $b\bar{b}H$, $b\bar{b}A$ production.

m_A (GeV)	p_T^{min} (jet$_1$) (GeV)	p_T^{min} (jet$_2$) (GeV)
200	70	50
300	100	70
500	200	100
700	250	150
900	300	200

The two highest-p_T jets are used for the reconstruction of the Higgs-boson mass, $m_{b\bar{b}}$. The reconstructed $m_{b\bar{b}}$ peak, for tanβ = 50 and an integrated luminosity of 300 fb^{-1} is shown in Figure 19-67 for m_A = 500 GeV. Due to final-state radiation and hadronisation, the peak is rather broad, with a mass resolution of 50 GeV. About 20% of the $b\bar{b}$ combinations entering the distribution are incorrect. The acceptance in a mass window of ±80 GeV around m_A is about 70%.

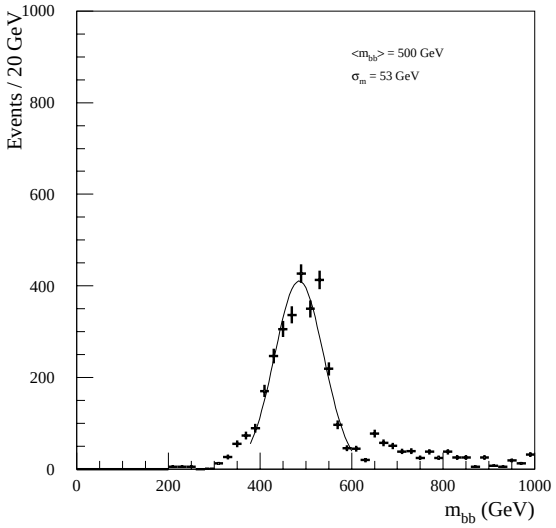

Figure 19-67 For $H/A \rightarrow b\bar{b}$ decays with m_A = 500 GeV from $b\bar{b}H$, $b\bar{b}A$ production with tanβ = 50 and for an integrated luminosity of 300 fb^{-1}, $m_{b\bar{b}}$ distribution obtained from the two leading *b*-jets in the event.

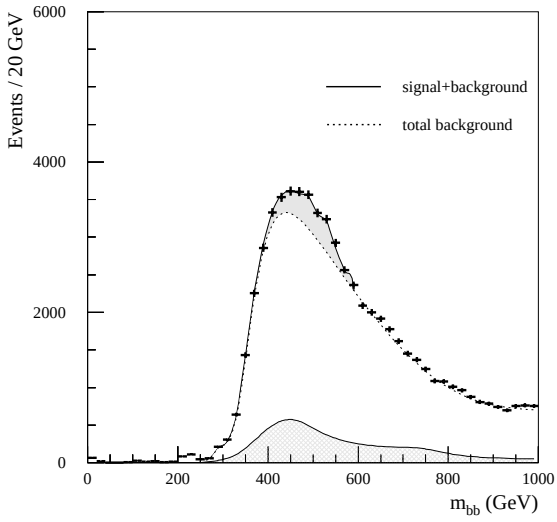

Figure 19-68 Same as Figure 19-67, but with the background included. The cross-hatched histogram shows the contribution from direct $b\bar{b}$ production and the dashed histogram represents the total background. The crosses show the summed signal and background. The signal events are clearly seen above the background (grey histogram).

This pure multi-*b*-jet final state will be very difficult to extract from the large QCD reducible and irreducible multi-jet background containing a variable number of real *b*-jets. A large sample of background events was generated using a shower approximation based on the hard-scattering dijet subprocess in the PYTHIA generator. The hard-scattering process was accompanied by initial- and final-state radiation, which both create additional jets with some fraction of *b*-jets from gluon splitting. After event selection but before applying the *b*-tagging procedure, the inclusive

background rates are approximately a factor of 10^4 to 10^5 higher than the signal rates in the mass window of interest. Requiring at least three identified *b*-jets reduces this factor to about 10^2 to 10^3.

Requiring in addition a fourth identified *b*-jet gains another factor of about two. In the sample containing at least three identified *b*-jets, approximately 40% of the background events contain at least three true *b*-jets, whereas in the sample containing at least four identified b-jets this fraction increases to 65%. The dominant remaining background arises from *gb* and *gg* production with gluon splitting into a $b\bar{b}$ pair. The contribution from direct $gg \rightarrow b\bar{b}$ production is found to be only at the level of 10% of the total background, as illustrated in Figure 19-68.

The final signal and background rates and the expected significances for an optimised selection procedure are given in Table 19-41 as a function of m_A, for $\tan\beta = 30$ and for integrated luminosities of 30 and 300 fb^{-1}.

As mentioned above, this channel has also been studied by requiring only 3 *b*-tagged jets [19-86]. Although the expected rates and significances are higher, the signal-to-background ratio is below 1%. It is rather unlikely that the systematic uncertainties on the background shape can be controlled to the precision required in this case. A selection requiring at least four identified *b*-jets, as presented in Table 19-41, yields a more favourable signal-to-background ratio (~3%) and also a more favourable ratio of irreducible-to-total background (~67%).

For a selection requiring four *b*-tagged jets and for an integrated luminosity of 300 fb^{-1}, a nominal significance larger than 5σ could be achieved for $\tan\beta > 29$ ($m_H = 500$ GeV) and for $\tan\beta > 20$ ($m_H = 300$ GeV), as illustrated in Figure 19-69. The overall conclusion is that, even for an integrated luminosity of 300 fb^{-1} and idealistic trigger conditions, the extraction of a $H/A \rightarrow b\bar{b}$ signal from $b\bar{b}$H, $b\bar{b}$A production will be very difficult. More detailed results are presented in [19-86].

The coverage in parameter space is smaller than the coverage of the $\tau\tau$ channel, see Section 19.3.2.5), which, for an integrated luminosity of 300 fb^{-1}, extends down to $\tan\beta > 11$ ($m_H = 300$ GeV) and to $\tan\beta > 15$ ($m_H = 500$ GeV). For an integrated luminosity of 30 fb^{-1}, the respective lower limits on $\tan\beta$ are $\tan\beta > 30$ and $\tan\beta > 50$ for the $b\bar{b}$ channel and $\tan\beta > 15$ and $\tan\beta > 20$ for the $\tau\tau$ channel.

It should be stressed that the significances quoted in Table 19-41 for the $b\bar{b}$ channel are rather optimistic, since the estimates of the QCD background are very uncertain (the background could be under-estimated by a factor of three) and the assumptions used for *b*-tagging are rather optimistic for such high-p_T jets. Systematic uncertainties due to the lack of knowledge of the background shape have not been taken into account in the significance estimates of Table 19-41**.** The results are optimistic also because the selection criteria are looser than those specified in the LVL1 / LVL2 trigger menu (see [19-83] and Section 11.7.3).

Acceptance with current trigger menu

If the currently planned LVL1 / LVL2 high-luminosity thresholds are applied (see Table 19-41), the acceptance for signal events is reduced by a factor of 4.7 (1.9) for $m_A = 300$ GeV ($m_A = 500$ GeV) while the background is reduced by a factor of three. This leads to a reduction in significance, for an integrated luminosity of 300 fb^{-1}, from 8.5 to 3.2 for $m_A = 300$ GeV and from 5.3 to 4.8 for $m_H = 500$ GeV. For $m_A = 200$ GeV the high-luminosity LVL1 / LVL2 thresholds reduce the acceptance for signal events by almost a factor of 18.

Table 19-41 Expected signal and background rates inside the signal mass window as a function of m_A, for $H/A \rightarrow b\bar{b}$ decays for $b\bar{b}H$ and $b\bar{b}A$ production with tanβ = 30, after applying an optimised selection procedure. The numbers are given for integrated luminosities of 30 fb^{-1} and 300 fb^{-1}(without and with the LVL1 trigger thresholds applied).

m_A(GeV)	200	300	500	700	900
σ × BR (pb)	107.0	29.0	3.5	0.9	0.2
Integrated luminosity of 30 fb^{-1}					
Signal	2 550	630	200	50	16
Background	43 000	24000	6100	1800	520
S/B	5.9%	2.6%	2.8%	2.8%	3.0%
$S/\sqrt{B}$	12.4	4.1	2.6	1.2	0.7
Integrated luminosity of 300 fb^{-1}					
Signal	12 440	3080	960	240	80
Background	230 000	130 000	33 000	10 000	2 800
S/B	5.4%	2.4%	2.9%	2.4%	2.8%
$S/\sqrt{B}$	26	8.5	5.3	2.4	1.5
Integrated luminosity of 300 fb^{-1} including LVL1 trigger thresholds					
Signal	710	650	510	240	80
Background	13 000	40 000	11 000	10 000	2 800
S/B	5.5%	1.6%	4.6%	2.4%	2.8%
$S/\sqrt{B}$	6.2	3.2	4.8	2.4	1.5

Figure 19-69 shows the 5σ-discovery contour curves in the (m_A, tanβ) plane before and after applying the LVL1/LVL2 trigger thresholds. The curves have not been extended to masses below m_A = 200 GeV since the acceptance of the LVL1/LVL2 trigger is reduced for m_A = 200 GeV to only 6% of that of the off-line selection.

In conclusion, the $b\bar{b}H$, $b\bar{b}A$ channel with $H/A \rightarrow b\bar{b}$ decay cannot be observed over most of the MSSM parameter space. Even for large values of m_A and tanβ, the large uncertainties on the QCD multijet backgrounds imply that the results shown in Figure 19-69 are optimistic and that therefore this channel cannot be considered as a discovery channel at LHC.

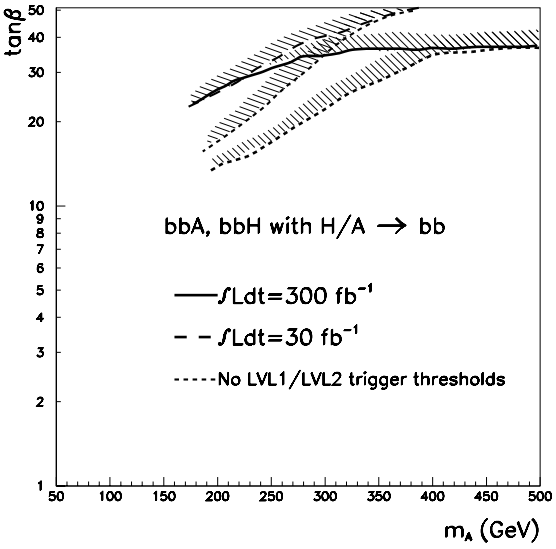

Figure 19-69 For integrated luminosities of 30 fb^{-1} and 300 fb^{-1}, 5σ-discovery contour curves in the (m_A, tanβ) plane for the $b\bar{b}H$, $b\bar{b}A$ with $H/A \rightarrow b\bar{b}$ channel. The dotted lines show the expected extension in coverage if the LVL1/LVL2 trigger thresholds are not applied.

19.3.2.9 $H \rightarrow hh$

This channel would be particularly interesting, since it would allow the simultaneous observation of two Higgs bosons. Possible final states of interest are:

- $H \rightarrow hh \rightarrow b\bar{b}b\bar{b}$. It would provide the largest signal rate, but would require a four-jet trigger with as low a p_T-threshold as possible and excellent *b*-tagging performance to control the overwhelming backgrounds from four-jet events.
- $H \rightarrow hh \rightarrow b\bar{b}\tau\tau$. The presence of at least one lepton from τ-decay would be required as a trigger, and the mass reconstruction of the ττ-pair would follow that described for $H/A \rightarrow \tau\tau$ decays. The dominant backgrounds would be from $t\bar{t}$ and *W+jet* production. This channel is difficult due to the poor mass resolution for the signal and the very large backgrounds.
- $H \rightarrow hh \rightarrow b\bar{b}\gamma\gamma$. This channel can be easily triggered upon and it offers good kinematic constraints and mass resolution for the reconstruction of m_H. The rate is however very limited.

The observability of the $H \rightarrow hh \rightarrow b\bar{b}\gamma\gamma$ and $H \rightarrow hh \rightarrow b\bar{b}b\bar{b}$ channels is discussed in this section. Similar final states occur from $A \rightarrow Zh$ decays. If the *Z*-boson and *h*-boson were degenerate in mass, the observability of the $H \rightarrow hh$ signal could be improved by $A \rightarrow Zh$ production with $Z \rightarrow b\bar{b}$ and $h \rightarrow \gamma\gamma$ or $h \rightarrow b\bar{b}$. The branching ratio $BR(A \rightarrow Zh) \times BR(Z \rightarrow b\bar{b})$ is much smaller than $BR(H \rightarrow hh) \times BR(h \rightarrow b\bar{b})$, but the cross-section for *A* production is larger than for *H* production, and therefore the additional contribution from the $A \rightarrow Zh$ channel would be at the level of 10 - 15%. This additional contribution has not been included in the studies presented below.

The $H \rightarrow hh \rightarrow b\bar{b}\gamma\gamma$ channel.

To extract a signal in this channel, events were selected to have:

- Two isolated photons, with $|\eta| < 2.5$ and $p_T > 20$ GeV which serve as a trigger.
- Two jets with $|\eta| < 2.5$ and $p_T > 15$ GeV ($p_T > 30$ GeV) at low (high) luminosity of which at least one is required to be tagged as a *b*-jet. The invariant mass of the two-jet system is denoted m_{bj} in the following.
- No other jet with $|\eta| < 2.5$ and $p_T > 15$ GeV ($p_T > 30$ GeV) at low (high) luminosity.
- The masses of the two-photon and dijet systems are required to be in a window of ±2 GeV and ±26 GeV around m_h, respectively. For events passing these cuts, the four-vectors of the photons and *b*-jets are rescaled to obtain $m_{\gamma\gamma} = m_{bj} = m_h$. This rescaling improves the invariant mass resolution for the $bj\gamma\gamma$ system, $m_{bj\gamma\gamma}$.
- The invariant mass of the $bj\gamma\gamma$ system is required to be within ±20 GeV of m_H. The signal acceptance in the mass window is 70% after the m_h constraints.

Figure 19-70 shows, for m_H = 300 GeV and m_h = 98 GeV, the reconstructed mass of the $\gamma\gamma$, *jb*, and $\gamma\gamma jb$ systems (without and with *h*-boson mass constraints).

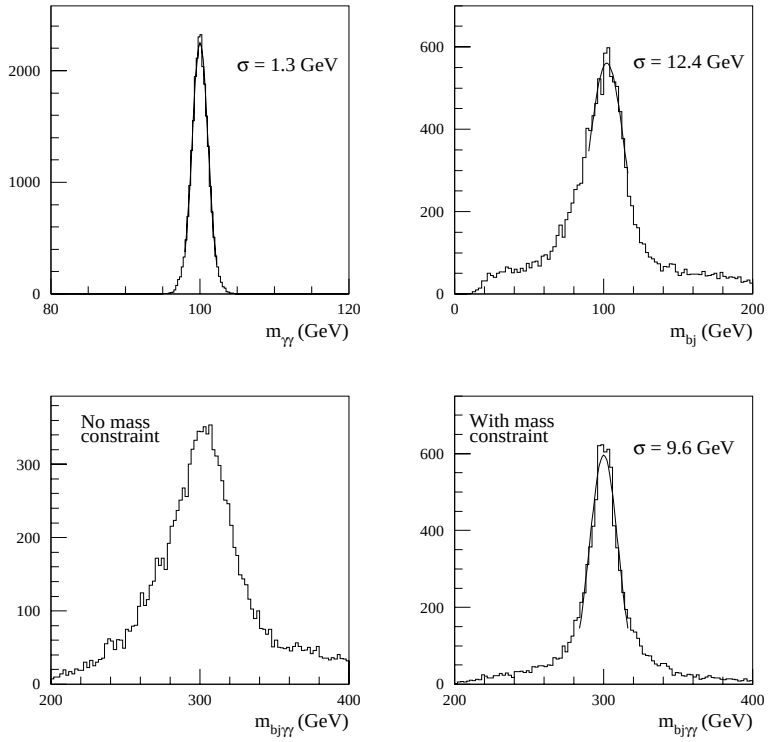

Figure 19-70 For m_H = 300 GeV and m_h = 98 GeV mass distributions from $H \rightarrow hh \rightarrow b\bar{b}\gamma\gamma$ decays (signal events only), shown for $m_{\gamma\gamma}$ (top left), m_{bj} (top right) and $m_{bj\gamma\gamma}$ before (bottom left) and after (bottom right) applying the *h*-boson mass constraints to $m_{\gamma\gamma}$ and m_{bj}.

At high luminosity, the expected $m_{bj\gamma\gamma}$ mass resolution increases by ~20% and the *b*-tagging efficiency decreases from 60% to 50%. In addition, since the p_T-thresholds on the jets have to be raised, the kinematic acceptance for the signal decreases from ~12% at low luminosity to ~6.5% at high luminosity.

The estimates for the observability of the $H \rightarrow bb\gamma\gamma$ signal given below can be considered as conservative at high luminosity, since a higher p_T threshold has been applied before recalibration of the jet energies.

Several background sources are considered: irreducible $b\bar{b}\gamma\gamma$ and reducible $bj\gamma\gamma$, $c\bar{c}\gamma\gamma$, $cj\gamma\gamma$ and jj$\gamma\gamma$, which are all estimated using the parton-shower approach in PYTHIA. There are large uncertainties on these background estimates, due to the poor knowledge of the total $b\bar{b}$, $c\bar{c}$ and jj cross-sections, and due to the procedure used to simulate photon bremsstrahlung in these processes. The various photon bremsstrahlung backgrounds were further reduced by requiring that the larger of the two h-boson transverse momenta be larger than a threshold value, typically of 60 - 80 GeV. Even for the requirement of only one tagged b-jet, the expected signal rates are rather low and they decrease rapidly with increasing tanβ.

For m_H = 320 GeV and an integrated luminosity of 300 fb^{-1}, about 106 events are expected for tanβ = 1 and 19 events for tanβ = 3, with a background of 1.7 and 4.2 events, respectively. Tables 19-42 and 19-43 give details on the number of expected signal and background events for an integrated luminosity of 30 fb^{-1} and 300 fb^{-1}, respectively. For a given value of m_H, the corresponding value of m_h increases as tanβ increases, and therefore the background rate varies.

The sensitivity to the $H \rightarrow hh \rightarrow b\bar{b}\gamma\gamma$ signal for a given value of m_H is estimated for two different values of m_h, and a simple linear interpolation or extrapolation is performed to obtain the 5σ-discovery contour curves in the (m_A, tanβ) plane. The result is shown in Figure 19-71. This channel is only observable for low values of tanβ, tanβ < 4, and for 2 $m_h < m_H < 2m_t$.

Table 19-42 Observability of the $H \rightarrow hh \rightarrow bb\gamma\gamma$ channel for an integrated luminosity of 30 fb^{-1} and for several values of m_H and m_h. The expected numbers of signal and background events are given together with the statistical significances (computed using Poisson statistics). The errors indicate the statistical precision of the simulation.

m_H (GeV)	230	270	320
m_h = 72 GeV	**(tanβ = 1)**		
σ × BR (fb)	6.0	5.0	4.6
Signal	18.4 ± 0.4	16 ± 0.3	16 ± 0.3
Background	1.7 ± 0.2	0.3 ± 0.05	0.3 ± 0.05
Significance	6.4	> 8.3	> 8.3
m_h = 97 GeV	**(tanβ = 3)**		
σ × BR (fb)	2.0	1.6	1.2
Signal	6.5 ± 0.1	4.8 ± 0.1	4.5 ± 0.1
Background	4.5 ± 0.4	1.5. ± 0.1	0.8 ± 0.1
Significance	2.1	2.0	2.7

Table 19-43 Same as Table 19-42, but for an integrated luminosity of 300 fb^{-1}.

m_H (GeV)	230	270	320
m_h = 72 GeV	**(tanβ = 1)**		
Signal	58.5 ± 1.2	40 ± 1.2	106 ± 0.3
Background	6.0 ± 0.7	2.1 ± 0.2	1.7 ± 0.3
Significance	23.5	26.1	77.8
m_h = 97 GeV	**(tanβ = 3)**		
Signal	16.5 ± 0.2	15.5 ± 0.2	18.6 ± 0.2
Background	8.8 ± 0.9	3.4 ± 0.3	4.2 ± 0.3
Significance	4.4	5.5	6.0

The $H \rightarrow hh \rightarrow b\bar{b}b\bar{b}$ channel

This channel, similarly to the channels $b\bar{b}A$, $b\bar{b}H$, presents another example of a multi-b-jet channel with no lepton present for triggering. It has been studied in some detail in [19-86], and the results of the analysis for m_H = 300 GeV and m_h = 80 GeV are presented below. As in Section 19.3.2.8, the discussion is split into two parts. First, an optimistic analysis without trigger requirements is presented, after which the impact of the current LVL1 / LVL2 trigger thresholds is discussed.

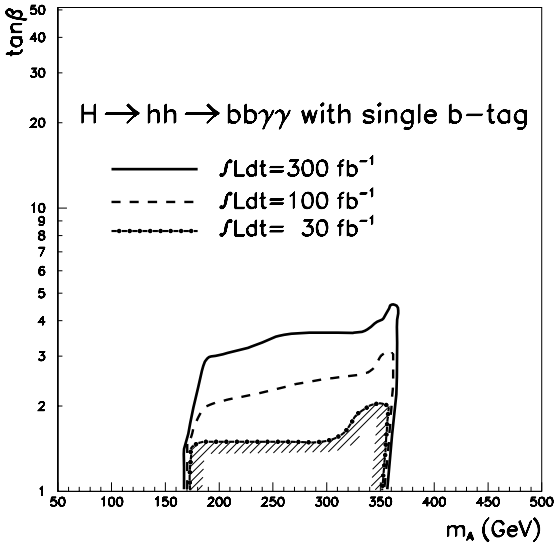

Figure 19-71 For integrated luminosities of 30 fb^{-1}, 100 fb^{-1} and 300 fb^{-1}, 5σ-discovery contour curves for the $H \rightarrow hh \rightarrow b\bar{b}\gamma\gamma$ channel in the (m_A, tanβ) plane.

Analysis without trigger requirements

The detector response is parametrised using fast simulation. Pile-up effects are included and a b-tagging procedure is applied to the reconstructed jets after recalibrating their four-momenta. For signal events, the jet spectrum is relatively hard, with an average p_T of 100 GeV for the hardest and 36 GeV for the fourth jet within $|\eta| < 2.5$. Requiring at least four jets reconstructed with $p_T > 40$ GeV (before energy recalibration) yields an acceptance of 25% for the signal events.

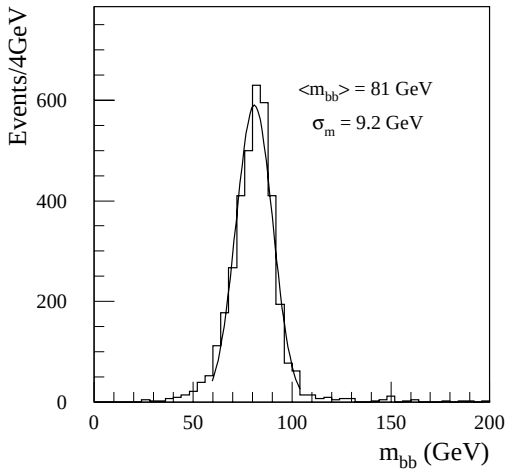

Figure 19-72 For fully simulated $H \rightarrow hh \rightarrow b\bar{b}b\bar{b}$ decays with m_H = 300 GeV and m_h = 80 GeV and for low-luminosity performance, distribution of $m_{b\bar{b}}$ for the best combination of two pairs of b-tagged jets (two entries per event).

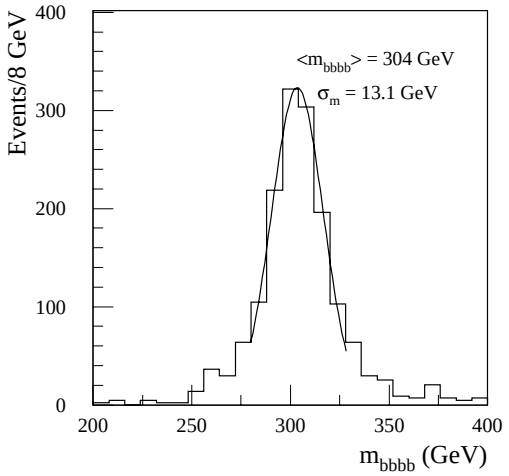

Figure 19-73 Same as Figure 19-72 but for the distribution of $m_{b\bar{b}b\bar{b}}$ after applying the h-boson mass constraint to both pairs of b-tagged jets.

The signal can be extracted by:

- Requiring the four highest-p_T jets to be identified as b-jets.
- Finding the best combination of two pairs of b-tagged jets with invariant masses, $m_{b\bar{b}} = m_h \pm 20$ GeV.

- Requiring $m_{b\bar{b}b\bar{b}} = m_H \pm 26$ GeV after applying the h-boson mass constraint to both pairs of b-tagged jets.

The results of this procedure for fully simulated and reconstructed events with $m_h = 80$ GeV and $m_H = 300$ GeV (see Section 9.3.2 and [19-87]) are illustrated in Figures 19-72 and 19-73 for the distributions of $m_{b\bar{b}}$ (two entries per event) and $m_{b\bar{b}b\bar{b}}$, respectively. At low luminosity, the acceptance for finding two $b\bar{b}$ pairs with $m_{b\bar{b}} = m_h \pm 20$ GeV is 76%, and that for finding $m_{b\bar{b}b\bar{b}} = m_H \pm 26$ GeV after applying the h-boson mass constraint in 82%.

Background events arise predominantly from QCD multijet production with a mixture of irreducible backgrounds (containing only b-jets) and reducible backgrounds (containing at least one non-b-jet in the final state). After requiring four jets within $|\eta| < 2.5$ and with $p_T > 40$ GeV, the expected number of inclusive four-jet events is $2\text{x}10^8$ from direct $gg \rightarrow b\bar{b}$ production, $1.2\text{x}10^9$ from $gb \rightarrow gb$ production and $1.7\text{x}10^{10}$ from $gg \rightarrow gg$ production.

Even though the direct $gg \rightarrow b\bar{b}$ production process contains initially two real b-jets, it contributes to only about 20% of the total background after requiring four b-tagged jets. Due to their much larger initial production rates, the dominant background arises from $gb \rightarrow gb$ and $gg \rightarrow gg$ production. The background from four real b-jets amounts to 70% of the total background.

Before any invariant mass combinations are selected, the multijet background is huge compared to the signal. As an example, for $m_H = 300$ GeV and $m_h = 97$ GeV ($\tan\beta = 3$), the signal-to-background ratio is about 0.1% after requiring events with four b-tagged jets with $p_T > 40$ GeV. This ratio increases to 1% after selecting the two best $b\bar{b}$ pairs in the mass window around m_h. These numbers show clearly that this channel cannot be used as a stand-alone discovery channel. Table 19-44 gives the expected signal and background rates for an integrated luminosity of 300 fb^{-1} and for two cases, $m_H = 300$ GeV and $m_h = 71$ GeV ($\tan\beta = 1.5$), and $m_H = 300$ GeV and $m_h = 97$ GeV ($\tan\beta = 3$). The signal observability is comparable to than that for $H \rightarrow hh \rightarrow b\bar{b}\gamma\gamma$

Table 19-44 For an integrated luminosity of 300 fb^{-1} and for $H \rightarrow hh \rightarrow b\bar{b}b\bar{b}$ decays with $m_H = 300$ GeV and two values of $\tan\beta$, $\tan\beta = 1.5$ and 3.0, expected cross-section times branching ratio, numbers of signal and background events, signal-to-background ratios and signal significances. No trigger requirements are imposed.

	$\tan\beta = 1.5$ ($m_h = 71$ GeV)	**$\tan\beta = 3.0$ ($m_h = 97$ GeV)**
$\sigma \times$ BR (pb)	1.73	0.76
Signal	1360	360
Background	4000	4000
S/B	34%	9.0%
$S/\sqrt{B}$	21.5	5.7

Table 19-45 For an integrated luminosity of 30 fb^{-1} and for $H \rightarrow hh \rightarrow b\bar{b}b\bar{b}$ decays with $m_H = 300$ GeV and $m_h = 97$ GeV ($\tan\beta = 3.0$), expected numbers of signal and background events, signal-to-background ratios and signal significances as a function of the p_T threshold for the softest jet.

p_T-threshold (GeV)	**20**	**30**	**40**
Signal	231	132	50
Background	48 000	10 000	800
S/B	0.5%	1.3%	6.2%
$S/\sqrt{B}$	1.1	1.3	1.8
$p_T^{bb} > 60$ GeV and $p_T > 80$ GeV			
Signal	132	75	30
Background	2 500	1 500	400
S/B	5.3%	5.0%	7.5%
$S/\sqrt{B}$	2.6	1.9	1.5

decays (see Table 19-43) but would be sufficient to confirm a discovery in this latter channel. However, the results of Table 19-44 are only indicative since they do not yet include any trigger requirements (see below).

Without optimised cuts, see upper part of Table 19-45, the background increases much faster than the signal as the p_T threshold is lowered and the sensitivity deteriorates rapidly. With optimised cuts, however, it would appear advantageous to lower the jet p_T threshold, but the already large uncertainties of about a factor of three on the modelling of the multijet background using the parton-shower approach would be even larger in this case. Even with optimised selection cuts, see lower part of Table 19-45, the sensitivity at low luminosity is weaker than or at most comparable to that for the $H \rightarrow hh \rightarrow b\bar{b}\gamma\gamma$ channels (see Section 19.3.2.9 and Table 19-42) and with much less favourable and more uncertain signal-to-background ratio.

Impact of current trigger menu

The present LVL1 trigger menu (see Section 11.7.3) imposes a p_T threshold of 90 GeV for the four-jet trigger at high luminosity, as compared to the 40 GeV threshold used in the analysis described above. The only other possibilities would be to trigger on single jets with $p_T > 290$ GeV or three jets with $p_T > 130$ GeV. These thresholds are very high compared to the expected p_T spectrum of jets from $H \rightarrow hh \rightarrow b\bar{b}b\bar{b}$ decays. Fulfilling the present LVL1 requirements would strongly suppress the possible sensitivity in this channel. A possible trigger on multijet final states including b-tagging at LVL2 is at present under study [19-83]. This would permit a lower threshold to be applied at LVL1.

19.3.2.10 $A \rightarrow Zh$

The observation of this channel would be particularly interesting, since it would correspond to the simultaneous discovery of two Higgs bosons. It is the dominant A-boson decay mode for low values of tanβ and for $m_Z + m_h < m_A < 2m_t$. Possible final states of interest are:

- $A \rightarrow Zh \rightarrow b\bar{b}b\bar{b}$. The channel is similar to $H \rightarrow hh \rightarrow b\bar{b}b\bar{b}$, but with smaller rates, because $BR(Z \rightarrow b\bar{b})$ is much smaller than BR($h \rightarrow b\bar{b}$). This would provide the largest signal rate, but would require a four-jet trigger with as low p_T-threshold as possible. Such a trigger is under consideration as discussed already in Section 19.3.2.9.
- $A \rightarrow Zh \rightarrow llb\bar{b}$. This channel is the only one discussed below, because it can be easily triggered upon and it offers the largest rates apart from the dominant four b channel.

Table 19-46 Expected cross-sections times branching ratios for background channels to the $A \rightarrow Zh \rightarrow llb\bar{b}$ searches.

Process ***lljj* final state**	$\sigma \times$ **BR (pb)**
$Zb\bar{b}$	36.0
Zjj with $m_{ll} > 80$ GeV	1880
ZZ with $Z \rightarrow bb$ $\sqrt{s'} > 150$ GeV	0.22
ZW, with $W \rightarrow jj$ $\sqrt{s'} > 150$ GeV	1.16
$t\bar{t}$	26.0

- $A \rightarrow Zh \rightarrow ll\gamma\gamma$. This channel would provide better kinematic constraints in the final state than the preceding one, but the expected rates are too low for it to be observable at the LHC.

The conclusions for the four-b channel are similar to that for the $H \rightarrow hh \rightarrow b\bar{b}b\bar{b}$ channel described previously. Below only the $A \rightarrow Zh \rightarrow llb\bar{b}$ channel is discussed.

The $A \rightarrow Zh \rightarrow llb\bar{b}$ events are selected to have [19-16]:

- Two isolated leptons, with opposite sign and same flavour in $|\eta| < 2.5$ and $p_T > 20$ GeV.
- Two additional jets with $|\eta| < 2.5$ and $p_T > 15$ GeV at low and $p_T > 30$ GeV at high luminosity. Both jets are required to be tagged as *b*-jets.
- The dilepton and dijet masses are required to be within ± 6 GeV and ± 22 GeV of m_Z and m_h respectively. For events in the mass window the four-vectors of the *b*-jets are rescaled, such that the peak position in the invariant mass of the $b\bar{b}$-system corresponds to the assumed nominal mass m_h.

After rescaling of the jet four-momenta a resolution of ~8 GeV is found for the reconstructed $llb\bar{b}$ invariant mass. These resolution has been confirmed with full simulation of the ATLAS detector [19-87]. The rescaling reduces significantly the non-Gaussian tails, as already illustrated in the case of $H \rightarrow hh \rightarrow b\bar{b}\gamma\gamma$.

The overall acceptance for the signal with $m_A = 300$ GeV is ~6.2% (3.0%) at low (high) luminosity including a lepton reconstruction efficiency of 90%, the *b*-tagging efficiency quoted above, and the acceptance of the selection cuts and mass windows. In this analysis, the threshold on the jet transverse momenta was applied, as for the $H \rightarrow hh \rightarrow b\bar{b}\gamma\gamma$ analysis, before energy recalibration. Since, in this channel, the average jet p_T is relatively low, such a procedure gives a significant loss of acceptance at high luminosity.

Several background sources have been considered: the irreducible $Zb\bar{b}$ and ZZ as well as the reducible ZW, Zjj and $t\bar{t}$ backgrounds. Cross-sections for these backgrounds are given in Table 19-46. After the selection cuts are applied, the $Zb\bar{b}$ and $t\bar{t}$ backgrounds are dominant.

Table 19-47 Cross-sections times branching ratios, expected number of signal and background events and statistical significance for the $A \rightarrow Zh \rightarrow llb\bar{b}$ channel for an integrated luminosity of 30 fb^{-1} and for several values of m_H and m_h (two different values of tanβ).

m_H (GeV)	200	250	300
m_h = 71 GeV tanβ = 1			
σ × BR (fb)	560	470	340
Signal	675	786	642
$Zb\bar{b}$	830	315	125
ZZ, Zjj	50	25	10
$t\bar{t}$	90	90	45
Total background	970	430	180
Significance	21.7	37.8	47.6
m_h= 97 GeV tanβ = 3			
σ × BR (fb)	9.0	21	17
Signal	15	39	37
Total background	1140	1120	650
Significance	0.5	1.2	1.4

Table 19-48 Same as Table 19-47, but for an integrated luminosity of 300 fb^{-1}, assuming high luminosity performance.

m_H (GeV)	200	250	300
m_h = 71 GeV tanβ = 1			
Signal	1008	2520	3000
$Zb\bar{b}$	375	375	60
ZZ, Zjj	20	20	10
$t\bar{t}$	210	405	190
Total background	600	800	260
Significance	40.8	89.0	186
m_h= 97 GeV tanβ = 3			
Signal	36	140	170
Total background	1830	2700	2000
Significance	0.8	2.7	3.8

The background can be further reduced by applying cuts on the transverse momenta of the reconstructed $h \to b\bar{b}$ or $Z \to ll$ and on the missing transverse momentum E_T^{miss}. A cut of $E_T^{miss} < 60$ GeV is found to optimise the signal-to-background ratio and leads to the event numbers given in Table 19-47. The results are given for two different values of tanβ and for an integrated luminosity of 30 fb^{-1}. The expected signal rates decrease rapidly with increasing tanβ, even though larger values of m_h improve the signal acceptance by nearly a factor of 2 between m_h = 70 GeV and m_h = 97 GeV. For tanβ = 1, the signal-to-background ratio increases from ~2:3 for m_A = 200 GeV to ~4:1 for m_A = 300 GeV. For a given value of m_A, the corresponding value of m_h increases with increasing tanβ and so the background rate varies also. At high luminosity, as presented in Table 19-48, the $t\bar{t}$ background becomes more important**.** For low tanβ values a clear mass peak can be reconstructed on top of the background, as shown in Figure 19-74 for a 300 GeV Higgs boson, tanβ =1 and an integrated luminosity of 30 fb^{-1}.

Given the rapid falling signal rates with increasing tanβ, the $A \to Zh \to llb\bar{b}$ channel can only be observed for low values of tanβ and for 200 GeV < m_A < 2 m_t. The sensitivity to the signal for a given value of m_A was estimated for two different values of m_h, and a simple linear interpolation or extrapolation was performed to obtain the 5σ-discovery contour curves in the (m_A, tanβ) plane which are presented in Figure 19-75.

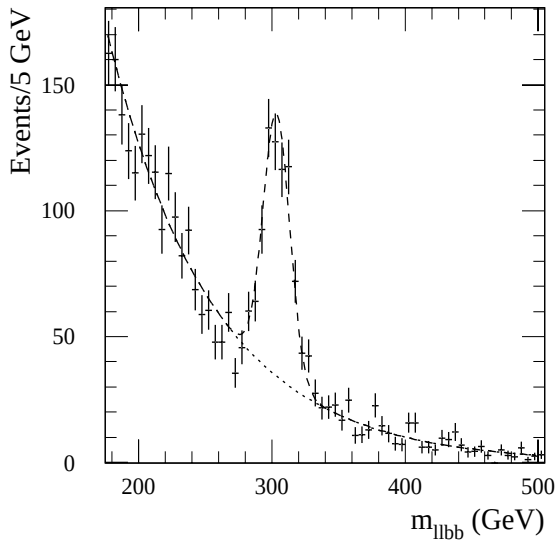

Figure 19-74 The expected signal+background distribution for $m_{llb\bar{b}}$ from a reconstruction of $A \to Zh \to llb\bar{b}$ events for m_A = 300 GeV and tanβ = 1 (m_h = 71 GeV) and for an integrated luminosity of 30 fb^{-1}.

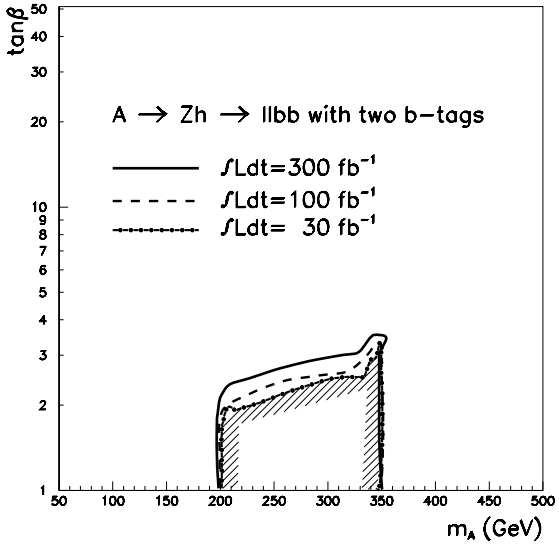

Figure 19-75 For integrated luminosities of 30 fb^{-1}, 100 fb^{-1} and 300 fb^{-1}, 5σ-discovery contour curves for the $A \to Zh \to llb\bar{b}$ channel in the (m_A, tanβ) plane.

19.3.2.11 Charged Higgs bosons

The charged Higgs bosons have masses which are almost degenerate with the masses of the *H*- and *A*-bosons. Although several mechanisms can be potential sources for their production, only a few seem promising for their detection:

- If the charged Higgs boson is lighter than the top quark, top quark decays represent a copious source of its production, via the decay $t \rightarrow H^+b$. Since top-quarks are expected to be produced with very large rates at the LHC, $\sigma_{t\bar{t}} \sim 600$ pb, a charged Higgs boson can be searched for in this channel for masses up to the kinematic limit imposed by the top-quark mass.
- If the charged Higgs boson is heavier than the top quark, it can be produced via the gluon-*b* and gluon-gluon fusion processes, $pp \rightarrow tH^{\pm}$ and $pp \rightarrow tbH^{\pm}$ respectively, in which the Higgs boson is emitted from a heavy quark [19-88].

The main decay channels of the charged Higgs bosons are the fermionic decays: $H^{\pm} \rightarrow \tau\nu$ below the *tb*-threshold and $H^{\pm} \rightarrow tb$ above. Below 150 GeV and for low values of tanβ, the $H^{\pm} \rightarrow cs$ and $H^{\pm} \rightarrow cb$ modes are not negligible. In the same mass range, the three-body off-shell decays $H^{\pm} \rightarrow hW^*$, $H^{\pm} \rightarrow AW^*$ and $H^{\pm} \rightarrow bt^* \rightarrow bbW$ [19-89] have also sizeable branching ratios. When the phase-space increases, 150 GeV < $m_{H^{\pm}}$ < 180 GeV, both the *bbW* and the *hW** mode could be enhanced with respect to the τν mode. Decays into the lightest chargino $\tilde{\chi}_1^{\pm}$ and neutralino $\tilde{\chi}_1^0$ or decays into sleptons would dominate whenever kinematically allowed. For large values of tanβ the importance of these SUSY decay modes would be reduced, however, for values as large as tanβ = 50, the decay $H^{\pm} \rightarrow \tilde{\tau}\,\tilde{\upsilon}$ would be enhanced, provided it is kinematically allowed and would lead to τ's in the final state. Their transverse momentum spectrum is, however, expected to be softer than that of τ's from the direct $H^{\pm} \rightarrow \tau\nu$ decays.

Charged Higgs lighter than the top-quark

The experimental strategies for the charged Higgs boson search below the top-quark mass rely on the $t \rightarrow H^+b$ decays, given the expected production of the $6\text{x}10^6$ $t\bar{t}$ pairs for an integrated luminosity of 10 fb^{-1}. Since the relevant $t \rightarrow H^+b$ branching ratio is proportional to ($m_t^2 \cot^2\beta + m_b^2 \tan^2\beta$), for a given value of $m_{H^{\pm}}$ the branching ratio for such decays is large at small and at large tanβ, but has a pronounced minimum at $\tan\beta \sim \sqrt{m_t/m_b} \sim 7.5$. The exact position of this minimum and its depth is sensitive to QCD corrections to the running *b*-quark mass.

Studies of $H^{\pm} \rightarrow \tau\nu$ and $H^{\pm} \rightarrow cs$ decay modes are presented below. The $H^{\pm} \rightarrow hW^*$, $H^{\pm} \rightarrow AW^*$ and $H^{\pm} \rightarrow bt^* \rightarrow bbW$ have not been studied so far by ATLAS. With the expected *b*-tagging efficiency, these multi-*b*-jets decays modes are very interesting for a more detailed investigation.

$H^{\pm} \rightarrow \tau\nu$

When the charged Higgs is produced in top decays, the $t \rightarrow H^+b$ decay competes with the standard $t \rightarrow Wb$ decay. The $H^{\pm} \rightarrow \tau\nu$ leads to an enhanced tau lepton rate in $t\bar{t}$ decays. The mass of the charged Higgs boson cannot, however, be directly reconstructed, because several neutrinos are produced in the final state.

The study was performed at the time of the Technical Proposal [19-14] (see also [19-90]), using a full detector simulation. Here only the main results are recalled and more details can be found in [19-90].

Events are selected to have:

- One isolated high p_T lepton within $|\eta| < 2.5$, which triggers the experiment. In signal events this lepton originates from semi-leptonic decays of the second top quark.
- One identified hadronic tau, using the same identification criteria as defined in Section 9.1.5 for the $H/A \rightarrow \tau\tau$ decays.
- At least three jets with $p_T > 20$ GeV and $|\eta| < 2.5$, of which two are required to be tagged as *b*-jets. This reduces the potentially large backgrounds from *W+jet* and $b\bar{b}$ production to a level well below the $t\bar{t}$ signal itself.

Table 19-49 Observability of the $H^{\pm} \rightarrow \tau\nu$ channel at low luminosity. The $\sigma \times$ BR values, the expected number of signal and background events and the signal significance are given for the production of one or two charged Higgs bosons in $t\bar{t}$ decay and for tanβ = 5. A systematic uncertainty of 3% on the background is assumed in the calculation of the signal significance.

m_{H^+} (GeV)	110	130	150
$\sigma \times$ BR (pb)	23.3	13.1	4.8
Signal	3050	1550	380
Background	7020	7170	9120
Significance	13.1	6.6	1.3

The selection cuts enhance the τ-lepton signal from $H^{\pm}$ decays with respect to that from *W* decay, and select mostly single-prong τ-decays.

As for the case of the $H/A \rightarrow \tau\tau$ decays discussed in Section 9.1.5 τ identification is a key element in extracting a possible signal from the large combinatorial background from jets. After the selection cuts and the τ identification criteria are applied, $t \rightarrow H^+b$ decays appear as final states with an excess of events with one isolated τ–lepton compared to those with an additional isolated electron or muon. Details on signal and background rates are given in Table 19-49 for tanβ = 5 and various H^+ masses. For example, for $m_{H^+} = 130$ GeV and tanβ = 5, an excess of ~1500 τ-leptons is expected from a charged Higgs-boson signal, above a background of ~3000 τ-leptons from *W*-decay, and of ~4000 fake τ-leptons.

When measuring such an excess, systematic uncertainties have to be taken into account. They arise mainly from the imperfect knowledge of the τ-lepton efficiency from fake τ-leptons present in the final sample. They were assumed to be ~3% from past experience [19-91], and were added to the statistical uncertainty to obtain the significances presented in Table 19-49. Since these systematic uncertainties dominate the overall uncertainty, the sensitivity to a charged Higgs-boson signal would not improve significantly with higher integrated luminosity unless increased statistics resulted in improved systematic uncertainties.

Figure 19-76 shows the expected 5σ-discovery contour curve for this channel in the (m_A, tanβ) plane for $m_t = 175$ GeV and for an integrated luminosity of 30 fb^{-1}. A signal from charged Higgs-boson production in $t\bar{t}$ decays

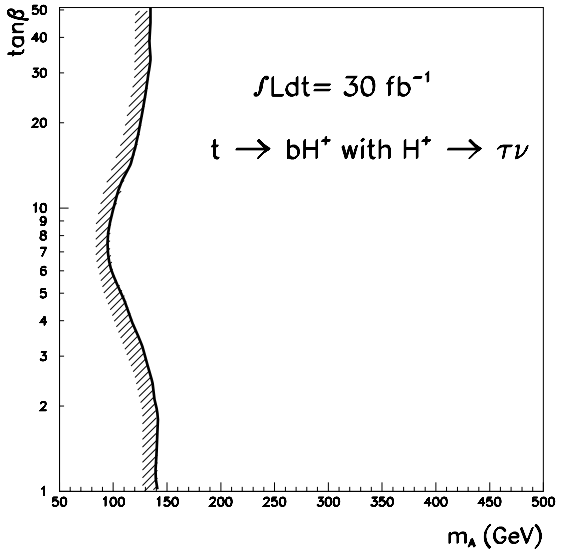

Figure 19-76 The 5σ-discovery contour curve for the $H^{\pm} \rightarrow \tau\nu$ channel in the (m_A, tanβ) plane for an integrated luminosity of 30 fb^{-1} and a top-quark mass of 175 GeV.

would be observed for all values of $m_{H^\pm}$ below m_t - 20 GeV over most of the tanβ-range. For moderate values of tanβ, for which the expected signal rates are lowest, the accessible values of $m_{H^\pm}$ are lower than this value by 20 GeV.

$H^\pm \to cs$

In the ATLAS Letter of Intent [19-13], the $H^\pm \to cs$ decay mode was considered as a complementary one to the $H^\pm \to \tau\nu$ channel for searches at low tanβ. Off shell decay modes such as $H^\pm \to hW^*$, $H^\pm \to AW^*$, $H^\pm \to bt^*$ were not considered in the original study. If these modes are taken into account, the prospects for the observability of the $H^\pm \to cs$ channel are reduced by a large factor. According to present theoretical calculations [19-89], assuming tanβ = 1.5 and $m_{H^\pm}$ = 110 - 150 GeV, for example, the $H^\pm \to cs$ branching ratio does not exceed ~3-6% while a branching ratio of ~26% is predicted by the default version of PYTHIA5.7, where off-shell decays are not included.

Table 19-50 Cross section times branching ratios for signal and $t\bar{t} \to WbWb$ background at tanβ = 1.5 and two different values of m_{H^+} for the production of a single charged Higgs boson in $t\bar{t}$ decays.

$t\bar{t}$ **with** $t \to Wb$, $W \to l\nu$ $t \to H^+b$, $H^\pm \to cs$	$t\bar{t}$ **with** $t \to Wb$, $W \to l\nu$ $t \to Wb$, $W \to jj$
m_{H^+} = 110 GeV	
$\sigma \times BR$ = 1.7 pb	$\sigma \times BR$ = 170 pb
m_{H^+} = 130 GeV	
$\sigma \times BR$ = 0.7 pb	$\sigma \times BR$ = 90 pb

The cross-section times branching ratios for the $H^\pm$ and the W decay modes of the top quark are compared in Table 19-50 for tanβ = 1.5 and two values of the $H^\pm$ mass. The original ratio of 1:10 of $t\bar{t} \to H^\pm bWb$ to $t\bar{t} \to WbWb$ events is reduced to 1:100 after branching ratios are taken into account. Given this ratio, the extraction of an $H^\pm \to cs$ peak in the m_{jj} distribution seems difficult.

For extracting this decay mode, the events are required to have:

- One isolated high p_T lepton within $|\eta| < 2.5$, to trigger the experiment. In signal events this lepton originates from semi-leptonic decays of the second top quark.
- Two b-tagged jet with $p_T > 15$ GeV and $|\eta| < 2.5$ and no additional b-jet.
- At least two non-b central jets $|\eta| < 2.0$ for the $H^\pm \to cs$ reconstruction, and no additional jets above 15 GeV in this central region.

Evidence for $H^\pm$ is searched for in the two-jet mass distribution. The mass peak from an $H^\pm$ decay can be reconstructed with a resolution of σ = 5 - 8 GeV if the mass of the $H^\pm$ is in the range between 110 and 130 GeV. In this mass range, the peak sits on the tail of the reconstructed $W \to jj$ distribution from $t\bar{t}$ background events which decay via a Wb instead of an H^+b. Examples are shown in Figures 19-77 and 19-78 for $H^\pm$ masses of 110 and 130 GeV. In this mass range the $H^\pm$ peak can be separated from the dominant $W \to jj$ background [19-92].

Table 19-51 The expected number of signal and background events for the $H^\pm \to cs$ channel for an integrated luminosity of 30 fb^{-1} and for m_H = 110 and 130 GeV and tanβ = 1.5.

m_{H^+} **(GeV)**	**110**	**130**
Signal	870	430
Background:	18 000	10 000
S/B	4.8%	4.5%
$S/\sqrt{B}$	6.5	4.4

The expected numbers of signal and background events for an integrated luminosity of 30 fb^{-1} are given in Table 19-51. This channel is complementary to the $H^{\pm} \rightarrow \tau\nu$ channel for low tanβ values. Whereas the $H^{\pm} \rightarrow \tau\nu$ channel allows only the observation of an excess of events, it is possible to reconstruct a mass peak in the $H^{\pm} \rightarrow cs$ decay mode, which makes a determination of the $H^{\pm}$ mass possible.

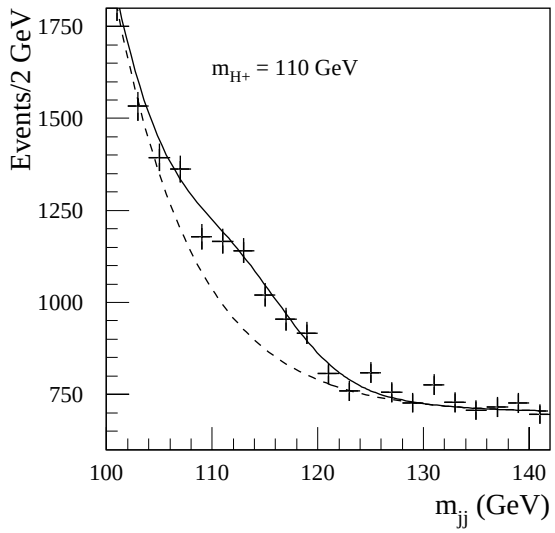

Figure 19-77 For the $H^{\pm} \rightarrow cs$ decays the expected m_{jj} distribution of signal+background events (solid line) and from the expected background (dashed) for $m_{H^{\pm}}$ = 110 GeV and tanβ = 1.5 and for an integrated luminosity of 30 fb^{-1}. The errors are statistical only.

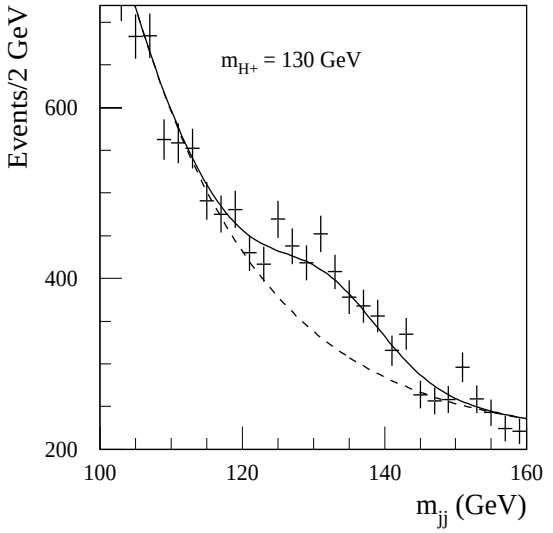

Figure 19-78 Same as Figure 19-77, but for m_{H^+} = 130 GeV.

Charged Higgs heavier than the top-quark

The possibility for discovering a charged Higgs heavier than the top-quark produced by *gg* and *gb* fusion [19-93] or by other *b*-quark initiated processes [19-94], has been investigated. Above the top-quark mass threshold the charged Higgs decays in almost 100% of the cases to *tb*. For charged Higgs bosons produced in *gb* fusion ($bg \rightarrow H^{\pm}t$) the final state would contain two top-quarks and a *b*-quark. The *gg* fusion with $H^{\pm}$ bremsstrahlung ($gg \rightarrow H^{\pm}tb$) would lead to two top-quarks and two *b*-quarks with the possibility of reconstructing top-quarks pairs. The $bq \rightarrow bH^{\pm}$ process would lead to two *b*-quarks and a top-quark in the final state. In all cases a multi-*b*-jet final state with at least one top-quark characterises the signal events. The only substantial background is expected to be the $t\bar{t}$ production.

The expected signal cross-section is driven by the $H^{\pm}$tb coupling squared, which is proportional to $(m_t^2 \cot^2\beta + m_b^2 \tan^2\beta)$. The cross-section reaches its minimum, for constant m_{H^+}, at $\tan\beta \sim \sqrt{m_t/m_b} \sim 7.5$. The branching ratio for $H^{\pm} \rightarrow tb$ decays is 100% for tanβ = 1.5 and decreases slowly to 80% with increasing tanβ where $H^{\pm} \rightarrow \tau\nu$ decays become relevant.

In the currently available Monte Carlo generator, PYTHIA 5.7, the $2 \rightarrow 2$ matrix-element for the process $bg \rightarrow H^{\pm}t$ has been implemented. The predicted rates for single $H^{\pm}$ production, including branching ratio for the semi-leptonic decay of one top-quark, are given in Table 19-52**.** More details on the analysis presented below can be found in [19-92].

Table 19-52 The expected cross section times branching ratios ($\sigma \times$ BR) for single charged Higgs production in $bg \rightarrow H^{\pm}t$ process with $H^{\pm} \rightarrow tb$ and one semi-leptonic top-quark decay $t \rightarrow l\nu b$ for various values of m_{H^+} and tanβ.

$m_{H^{\pm}}$	tanβ=1.5	tanβ= 10	tanβ= 30
200 GeV	3.4 pb	0.4 pb	1.6 pb
250 GeV	2.0 pb	0.18 pb	1.2 pb
300 GeV	1.2 pb	0.14 pb	1.0 pb
400 GeV	0.6 pb	0.08pb	0.4 pb

The applied reconstruction procedure requires:

- One isolated high p_T lepton within $|\eta| < 2.5$ to trigger the experiment. Both in signal and background events this lepton originates from semi-leptonic decays of one of the top quarks.
- Three b-tagged jets with $p_T > 30$ GeV, $|\eta| < 2.5$ and no additional b-jet.
- At least two non-b jets, which are used for the $W \rightarrow jj$ reconstruction of the second top quark.
- Both top-quarks must be reconstructed inside the mass window, as explained in Section 19.2.4.3.
- One of the reconstructed top-quarks is to be matched with the remaining b-jet for the reconstruction of the peak in the m_{tb} distribution from $H^{\pm} \rightarrow tb$ decay.

Thresholds on p_T are applied to improve the resolution of the reconstructed Higgs-boson mass ($p_T{}^t > 60$ GeV and $p_T{}^{H^{\pm}} > 80$ GeV).

For a Higgs boson mass of 200 GeV the initial signal-to-background ratio is in the order of 1:100 in the favourable low and high tanβ range. Requiring exactly three b-tagged jets improves this ratio to 1:20. The acceptance of the initial selection is about 2.5% (5.1%) for Higgs signal events of $m_{H^{\pm}} = 200$ GeV (500 GeV) and 0.1% for background events. After this selection, the background consists roughly of 70% $t\bar{t}b$ events and 30% $t\bar{t}j$ events. The mass resolution and acceptance of the top-pair reconstruction are comparable to those obtained in the $t\bar{t}H, H \rightarrow b\bar{b}$ analysis: namely, 12.5 GeV for $W \rightarrow jj$, ~10 GeV for $t \rightarrow jjb$ and $t \rightarrow l\nu b$ with ~60% acceptance for reconstructing both top-quarks inside their respective mass windows.

The mass resolution obtained for $H^{\pm} \rightarrow tb$, specified in Table 19-53, is not as good as could be expected from the reconstruction of other multi-jet multi-resonance channels, *e.g.* $H \rightarrow hh \rightarrow b\bar{b}b\bar{b}$ or $A \rightarrow t\bar{t}$. If only the true $H^{\pm} \rightarrow tb$ combinations are considered, the resolution is found to be $\sigma_m = 17$ GeV, with an acceptance of 86% inside a $\pm 2\sigma_m$ mass window for $m_H = 300$ GeV. When all combinations of the reconstructed tb events are allowed, including false $t \rightarrow Wb$ matching and/or false $H^{\pm} \rightarrow tb$ matching, a Gaussian peak with a resolution of $\sigma_m = 15$ GeV (39 GeV) is obtained, but with large tails. The event fraction inside a $\pm 2\sigma$ mass window becomes 42% (73%) for a Higgs-boson mass of 200 GeV (300 GeV). Nevertheless, the signal peak can be seen on top of the background as illustrated in Figures 19-79 and 19-80 for Higgs-boson masses of 200 and 300 GeV respectively.

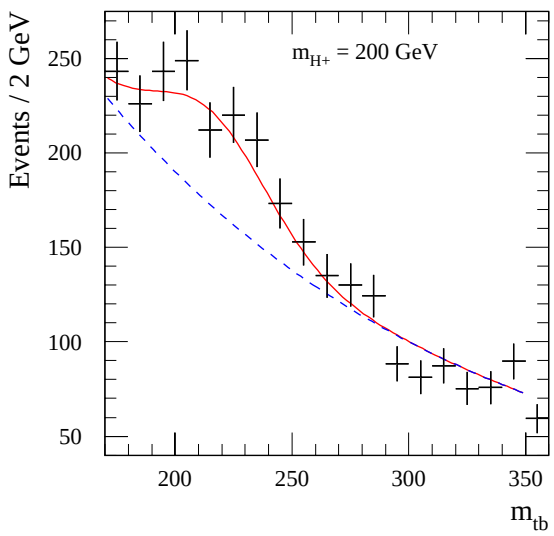

Figure 19-79 The signal+background (solid) and background only (dashed) distribution for reconstructed invariant mass m_{tb} for a Higgs boson mass of 200 GeV, tanβ = 1.5 and an integrated luminosity of 30 fb^{-1}. The errors are statistical only.

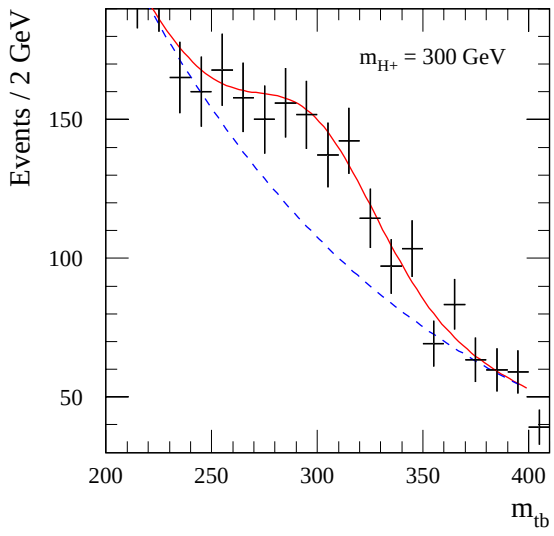

Figure 19-80 Same as Figure 19-79, but for a Higgs boson mass of 300 GeV.

Table 19-53 The mass resolution, acceptance inside the mass window, and the expected number of signal and background events for $H^{\pm} \rightarrow tb$ decays, for tanβ = 1.5 and 30 and for an integrated luminosity of 30 fb^{-1}.

$m_{H^{\pm}}$ (GeV)	200	250	300	400
σ_m (GeV)	15	37	39	49
Acceptance $m_{H^+} \pm 2\sigma_m$	42%	71%	73%	64%
tanβ = 1.5				
Signal	300	560	378	152
Background	760	1590	1650	1270
S/B	0.40	0.36	0.22	0.12
$S/\sqrt{B}$	10.9	14.0	9.3	4.3
tanβ = 30				
Signal	140	336	315	100
S/B	0.18	0.21	0.19	0.08
$S/\sqrt{B}$	5.4	8.4	4.4	2.8

The expected number of signal and background events in the mass window, which varies from ± 30 GeV for $m_{H^\pm}$ = 200 GeV to ±80 GeV for $m_{H^\pm}$ = 300 GeV, is given in Table 19-53 for an integrated luminosity of 30 fb^{-1} and for two different values of tanβ. The 5σ discovery contour curves in the (m_A, tanβ) plane are shown in Figure 19-81 for integrated luminosities of 30 fb^{-1}, 100 fb^{-1} and 300 fb^{-1} respectively. This channel would be observable for low and large values of tanβ. The kinematic limit for the on-shell $H^\pm \to tb$ decays is around m_A = 160 GeV.

Since not all the processes contributing to the single charged Higgs production were available for the Monte Carlo simulation, the signal rates given in Table 19-53 are underestimated. Therefore, the sensitivity to this channel, as presented above and shown in Figure 19-81, should be considered as a conservative estimate.

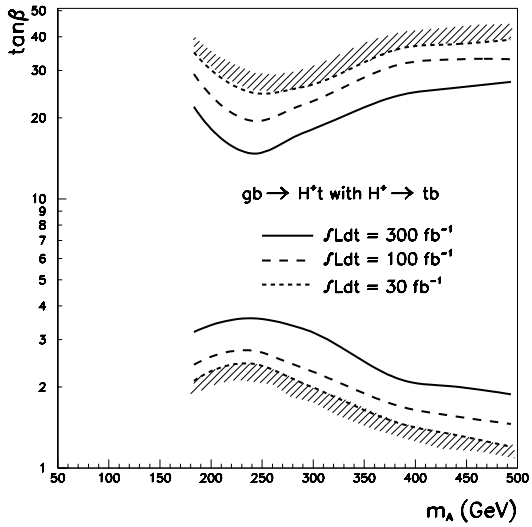

Figure 19-81 For integrated luminosities of 30 fb^{-1}, 100 fb^{-1} and 300 fb^{-1}, 5σ-discovery contour curves for the $H^\pm \to tb$ decays in the (m_A, tanβ) plane.

19.3.3 Overall sensitivity

The 5σ discovery contour curves, as determined in the previous Sections for the various channels in the (m_A, tanβ) plane, are superimposed in Figure 19-ii for integrated luminosities of 30 fb^{-1} and of 300 fb^{-1} and for the minimal mixing scenario (the most difficult case for the LHC). In Figure 19-82, the same overall picture is presented for the case of maximal mixing and an integrated luminosity of 300 fb^{-1}.

These Figures also display the present LEP2 limit ($\sqrt{s}$ = 189 GeV and 175 pb^{-1} per experiment), as well as the ultimate limit expected by the end of LEP2 operation in 2000 ($\sqrt{s}$ = 200 GeV and 200 pb^{-1} per experiment), assuming that no Higgs-boson discovery will be made. The present experimental limit from LEP2 already excludes values of tanβ below 2 - 3, and the expected ultimate limits will extend these excluded regions to tanβ < 3 (maximal mixing) or even tanβ < 7 (minimal mixing). This makes the prospects for the discovery of several channels presented in the previous Sections much less promising, since these channels do not provide any discovery potential for larger values of tanβ (this is the case for *e.g.* $H/A \to t\bar{t}$, $A \to Zh \to llb\bar{b}$ and $H \to hh \to b\bar{b}\gamma\gamma$).

Nevertheless these channels have been studied and presented here in some detail for two reasons.

- The level of detail with which the analyses of individual channels have been optimised at this stage is far below what has been done with LEP data for obvious reasons. The same is true for the scan of the (m_A, tanβ) parameter space. In addition, as discussed in Section 14.4, the presently available theoretical predictions for some of the signal process-

es and most of the background processes still suffer from large uncertainties. For these reasons, the signal observability reported here can be considered as conservative.

- More importantly, the MSSM scenario has been considered as a benchmark for the evaluation of the physics performance of the detector, given the rich spectrum of possible experimental signatures. The studies reported here would also be of interest for other models. Even if the search for a fundamental scalar particle with a mass below 130 GeV is considered to be the most important test of the MSSM [19-95], recent theoretical calculations show that this upper limit can be increased to masses of up to 200 GeV if additional Higgs doublets are introduced into the model [19-96]. The spectrum of possible scenarios is rather broad, whereas the spectrum of characteristic signatures is limited and the Standard Model background sources to such signatures are well established by now.

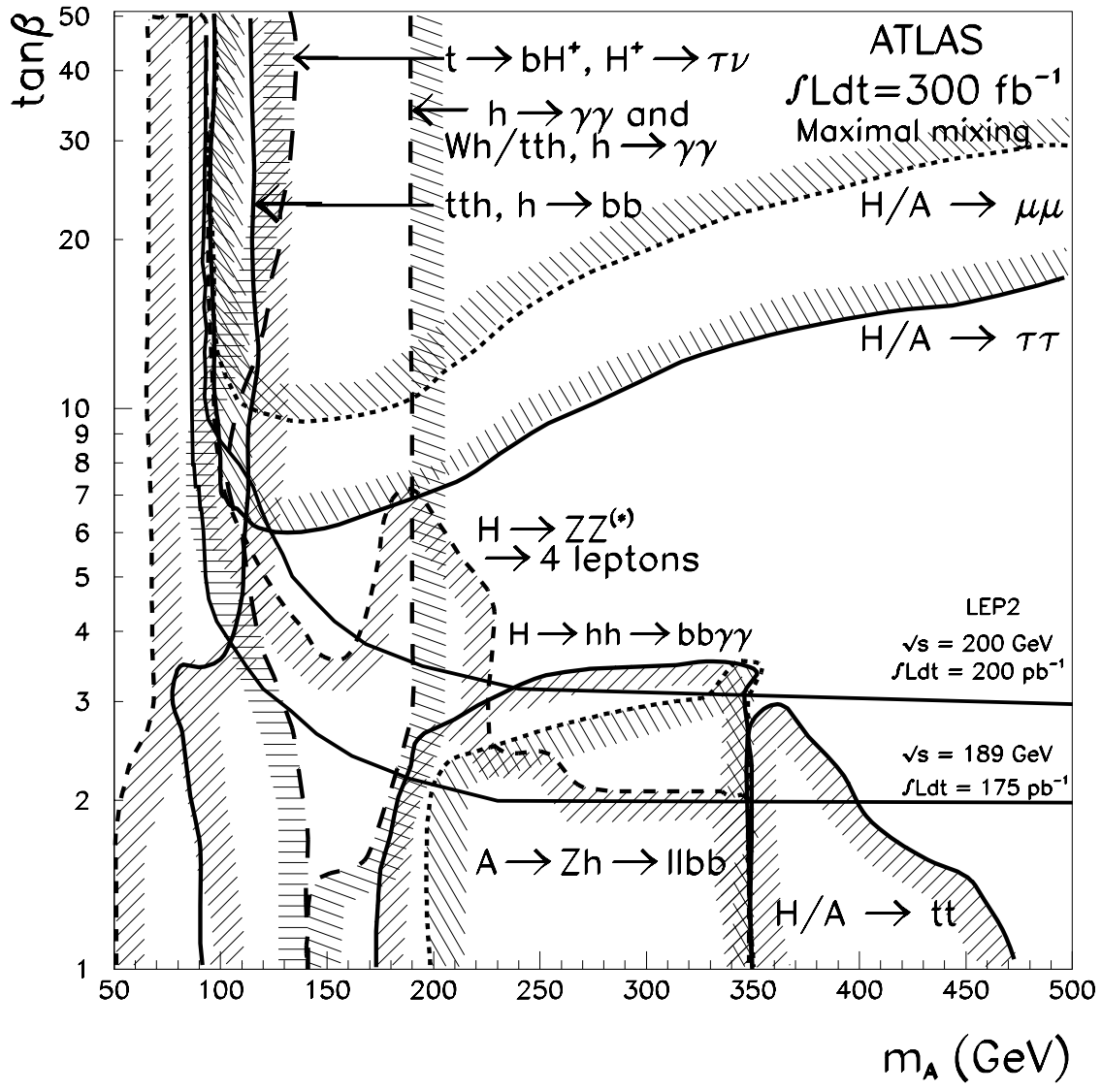

Figure 19-82 Same as Figure 19-ii, but for maximal mixing (see text).

Therefore, the conclusions concerning the observability of the various Higgs bosons in the MSSM are not limited by the strict validity of the model itself with respect to present (or expected) experimental limits. The goal was to evaluate the observability of a spectrum of signatures above the Standard Model background and to establish a full coverage of the parameter space.

As discussed already, the details of the 5σ-discovery contour curves presented in Figure 19-ii and Figure 19-82 may be affected by changes in some of the parameters in the MSSM model. This arises from kinematic shifts in the opening/closing of channels (determined by the value of m_h) or from changes in rates for signals or backgrounds. One of the important parameters governing such changes is the sensitivity to the mixing parameters A_t and A_b. As the so-called mixing varies from minimal to maximal, the predicted mass of the light *h*-boson rises for given values of m_A and tanβ, thereby increasing in many cases the discovery potential for the *h*-boson at the LHC and decreasing it at LEP.

The 5σ–discovery contour curves in the case of maximal mixing are shown in Figure 19-82. The main changes with respect to Figure 19-ii (bottom) arise from the fact that m_h is predicted to be 10 -20 GeV higher for the same values of m_A and tanβ. The expected coverage for $h \rightarrow \gamma\gamma$ is slightly degraded for $m_A \sim 150$ GeV and tanβ ~ 2. The coverage of the $H \rightarrow ZZ^{(*)} \rightarrow 4l$ channel is enhanced for low values of m_A, because the $H \rightarrow hh$ channel is closed for all values of tanβ. As a consequence, the $H \rightarrow hh$ and $A \rightarrow Zh$ channels become open only for higher values of m_A. More detailed differences between minimal and maximal mixing are beyond the precision of the evaluation presented here.

In summary, however, the overall picture remains the same:

- With a modest integrated luminosity of 30 fb^{-1}, the discovery potential covers a large fraction of the parameter space. For 80 % to 90 % of the cases, the discovery of a Higgs boson would allow discrimination between the SM and MSSM models.
- The overall discovery potential in the (m_A, tanβ) plane relies heavily on the $H/A \rightarrow \tau\tau$ channel and on the $t\bar{t}h$ with $h \rightarrow b\bar{b}$ and on the $h \rightarrow \gamma\gamma$ channels.
- For an integrated luminosity of 100 fb^{-1}, corresponding approximately to four years of LHC operation, the discovery potential covers the whole parameter space. For a very high integrated luminosity of 300 fb^{-1} the experiment would be able to distinguish between the SM and the MSSM models in most cases. In Figure 19-ii, the region with $m_A > 250$ GeV and $4 < \tan\beta < 5 - 10$ is only covered by the $h \rightarrow \gamma\gamma$ and $h \rightarrow b\bar{b}$ channels, and this distinction will be very difficult from these channels alone. However, $h \rightarrow b\bar{b}$ decays from SUSY particle decays should be observable above background in this region in many cases, thus providing a direct evidence for SUSY (see Section 19.3.5.4).
- In the case of the simultaneous discovery of the *h*- and *A*-bosons at LEP2, essentially only the charged Higgs boson would be seen directly in top-quark decays at the LHC. In the more likely case where only the *h*-boson was discovered at LEP2, several Higgs bosons would then be observed at the LHC (low tanβ region of Figure 19-ii).
- More generally, over large regions for $m_A > 160$ GeV, all three neutral Higgs bosons, and in some cases also the charged Higgs-boson would be discovered with ATLAS. Over most of this region, the *H*- and *A*- bosons are degenerate in mass and would be very difficult to distinguish. For ~10 % of the parameter space, *i.e.* for $\tan\beta > 7$ and $90 \text{ GeV} < m_A < 130$ GeV, the two heavy neutral Higgs bosons and the charged Higgs boson would be discovered with ATLAS.

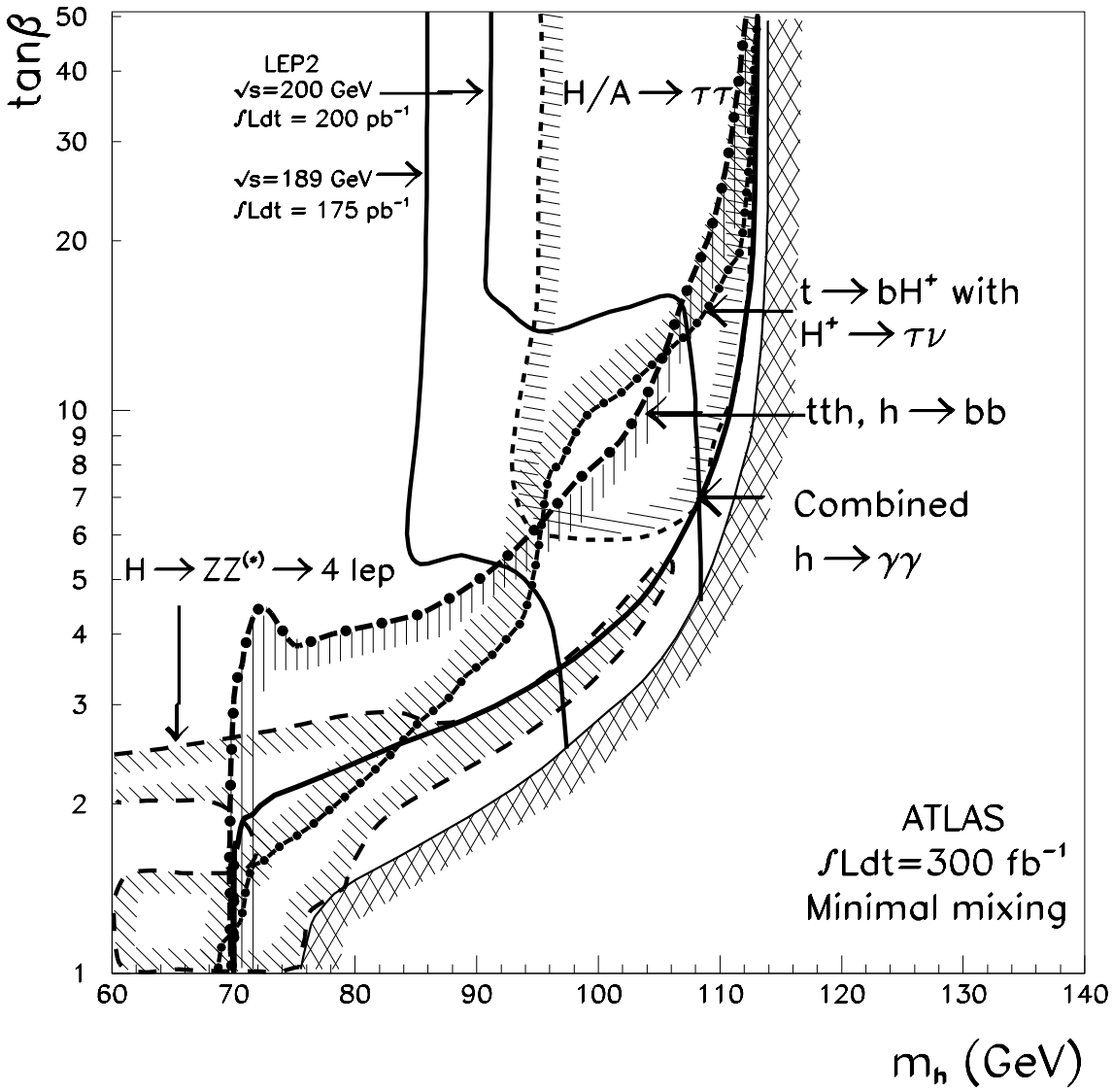

Figure 19-83 Same as Figure 19-ii but in the (m_h, tanβ) plane for an integrated luminosity of 300 fb^{-1}. The region on the right-hand side of the curve with the cross-hatched area is not allowed in the model (it corresponds to values of m_h larger than the maximum allowed value in the MSSM).

- The discovery potential of the heavy Higgs bosons for $m_A > 500$ GeV is limited to very large values of tanβ. In such cases the coverage of the (m_A, tanβ) plane would essentially be ensured only by the discovery of the h boson in the $h \to \gamma\gamma$ and $h \to b\bar{b}$ channels.
- The overall discovery potential can also be displayed in the (m_h, tanβ) plane, as shown in Figure 19-83 for an integrated luminosity of 300 fb^{-1}. This choice of parameter plane, although relevant for LEP2, where most of the sensitivity is related to the h-boson, is not the best one for displaying the LHC potential, because the large masses of the other Higgs bosons all collapse into the line delimiting the maximum allowed value of m_h. Figure 19-83 shows that, for large tanβ and for $m_h < 110$ GeV, a discovery of the h-boson through its direct production is not possible with ATLAS. However, if cascade decays of SUSY particles are also considered (see Section 19.3.5.4), the h-boson (produced in SUSY cascade de-

cays) would be discovered in the $h \rightarrow b\bar{b}$ channel in many SUSY scenarios, even for $m_h < 95$ GeV.

- The various channels described in the previous sections have also been studied for $\tan\beta < 1$ [19-16]. Even if such values are disfavoured for theoretical reasons, it is important to assess the experimental sensitivity in these cases. For this reason, each channel was studied for $0.3 < \tan\beta < 2$. In contrast to LEP2, which has very little sensitivity to values of $\tan\beta$ below ~ 0.8, the sensitivity with ATLAS is quite good for most channels of interest in this region of very low values of $\tan\beta$.
- It is important to recall here that all the SUSY particle masses were set to 1 TeV for this study. In some specific cases, the exact choice of the SUSY particle mass spectrum does affect the Higgs-boson production cross-sections and / or decay branching ratios, and therefore the discovery potential for specific channels. In particular, studies based on Minimal Supergravity (SUGRA) Models (see Section 19.3.5) indicate that the two heavy neutral Higgs bosons and the charged Higgs boson will have masses larger than 500 GeV in many cases and will therefore be outside the parameter space studied here. For given values of m_A and $\tan\beta$, different values of m_h would be allowed, depending on the exact mass spectrum of the SUSY particles, but, in most cases, these values would be close to the unique value allowed in the case of heavy SUSY particles.

19.3.4 Determination of the MSSM Higgs parameters

Assuming that a MSSM Higgs boson would be discovered, this section evaluates the potential for precision measurements of the model parameters, m_A and $\tan\beta$, and of the masses of the discovered Higgs bosons themselves (see [19-97] for more details).

The theoretical motivation for precision measurements in the MSSM is even stronger than in the Standard Model. In the SM, a precise knowledge of the profile of the Higgs boson (mass, width, branching ratios, couplings) would confirm the correctness of the model itself. However, since the sensitivity of the electroweak precision measurements to m_H through radiative corrections is only logarithmic, a precise knowledge of the Higgs-boson mass would not substantially overconstrain the model. The present data ($m_W = 80.394 \pm 0.042$ GeV and $m_t = 174 \pm 5$ GeV) and the electroweak precision measurements favour an area which is consistent with both the MSSM and the SM [19-98].

In the MSSM Higgs sector, the relations between the Higgs-boson masses, $\tan\beta$ and other parameters of the SUSY model are strongly constrained. Precise measurements of the Higgs-boson parameters and of the SUSY particle masses (see Chapter 20), if matched well by the precision of the theoretical calculations, would allow to overconstrain the SUSY model itself (see *e.g.* [19-99]).

If no SUSY particles are found, measurements of the Higgs-boson parameters should allow in some cases to distinguish between the SM and the MSSM models and to check the consistency with the relations between Higgs-boson masses predicted by the model. If, for example, the signal were to be observed in the $H \rightarrow ZZ^* \rightarrow 4l$ channel, the measured signal rate would provide the best tool to understand its origin, since the MSSM rates are suppressed by an order of magnitude with respect to the SM case over most of the parameter space. For values of m_H larger than ~250 GeV, the measured signal width would also provide a handle to disentangle the SM case ($\Gamma_H^{tot} \sim 10$ GeV) from the MSSM case ($\Gamma_H^{tot} < 1$ GeV).

The Higgs-boson couplings will be measured, but most likely with an accuracy not better than 10 - 20%, since in most cases these measurements will be based on signal rates. A measurement of obvious interest will be that of the Higgs-boson couplings to the top quark, either through the observation of $t\bar{t}h$ production with $h \to b\bar{b}$ decay, or through the observation of $H/A \to t\bar{t}$ decays.

As already discussed in Section 19.2.12 for the SM Higgs-boson, ratios of rates from different channels will also provide ratios of couplings in the MSSM. This would be the case of $H/A \to \tau\tau$ and $H/A \to \mu\mu$ for large values of tanβ. Over a very large range of tanβ and m_A values this would also be the case for the associated production with $h \to \gamma\gamma$ and $h \to b\bar{b}$ decay.

19.3.4.1 Measurement of the Higgs-boson masses

The precisions quoted in this section for Higgs-boson mass measurements are estimated with the same assumptions as already discussed in Section 19.2.12. They include the statistical error on the determination of the peak position, coming from both the limited number of signal events and from the error on the background subtraction (the background is assumed to be flat under the peak), and the systematic error on the absolute energy scale (see Chapter 12). This latter error is assumed to be 0.1% for decay channels which contain leptons or photons (*e.g.* $h \to \gamma\gamma$, $H \to ZZ^* \to 4l$) and 1% for decay channels containing jets (*e.g.* $h \to b\bar{b}$). No theoretical errors are included in the results presented below and an integrated luminosity of 300 fb^{-1} is assumed in the following.

In the MSSM model, the lightest Higgs boson is searched for over a very small range of mass values, with an upper limit of m_h = 115 - 130 GeV (depending on the model parameters) and a lower limit given by the experimental constraints. Since the present lower limit from LEP2 [19-11] is about 80 GeV for m_h and m_A, only results above these values are presented below. The couplings of the *h*-boson are similar to the couplings of the SM Higgs-boson over the accessible range of parameter space for the discovery channels: $h \to \gamma\gamma$ and $h \to b\bar{b}$. The precision expected for the mass measurements is therefore similar.

The heavy neutral Higgs bosons would be observable in decay channels not accessible otherwise for the SM Higgs-boson. The only exception is the $H \to ZZ^{(*)} \to 4l$ channel, for which, however, the expected rates are strongly reduced with respect to the SM case.

Table 19-54 Expected precision on the measurement of the MSSM Higgs boson masses for an integrated luminosity of 300 fb^{-1} and for the whole discovery region.

MSSM Higgs boson	Process	Precision $\Delta m/m$
h	Inclusive $h \to \gamma\gamma$	0.1% - 0.5%
	Wh, $t\bar{t}h$ with $h \to \gamma\gamma$	0.1% - 0.5%
	Wh, $t\bar{t}h$ with $h \to b\bar{b}$	1% - 3%
H	Inclusive $H \to \gamma\gamma$	0.1% - 0.5%
	$H \to ZZ^* \to 4l$	0.1% - 0.5%
	$H \to hh \to b\bar{b}\gamma\gamma$	1% - 2%
A	Inclusive $A \to \gamma\gamma$	0.1% - 0.5%
	$A \to Zh \to llb\bar{b}$	1% - 2%
H/A	$H/A \to \tau\tau$	1% - 12%
	$H/A \to \mu\mu$	0.1% - 2.0%

Table 19-54 summarises the expected precisions on the masses of the MSSM Higgs bosons over the complete set of possible discovery channels and over the full parameter space for an integrated luminosity of 300 fb^{-1}.

- If the *h* boson is discovered through the SM production processes (direct or associated production), the precision of the mass measurement is similar to that discussed already in Section 19.2.12. Over the range of parameter space covered by both the $h \to \gamma\gamma$ and $h \to b\bar{b}$

channels, the precision is determined by the $h \rightarrow \gamma\gamma$ channel and is ~0.1%. Over the region where only the $h \rightarrow b\bar{b}$ channel is observable the expected precision is 1 - 3%.

- Cascade decays of SUSY particles, discussed in Section 19.3.5.4, might be a source of copious production of $h \rightarrow b\bar{b}$ events. The precision which can be achieved in this channel varies with the rates associated with a given SUGRA parameter point (see Section 19.3.5.4). This channel is limited by the systematic error of 1% on the jet energy scale for signal rates above a few hundred events, which would be achieved over a large region of the SUGRA parameter space, for an integrated luminosity of 30 fb^{-1}.
- For low values of tanβ, the precision of the measurement of the mass of the H-boson will be determined by the $H \rightarrow ZZ^{(*)} \rightarrow 4l$ channel, if observable. It will vary strongly with tanβ, from 0.1% to 0.5%, following the rapid variation of rate. It will be worse than that expected for the SM Higgs-boson of the same mass, since the MSSM rates are strongly suppressed. If only the $H \rightarrow hh \rightarrow b\bar{b}\gamma\gamma$ decay mode were to be accessible, the expected precision would not be better than ~1%.
- The pseudoscalar A can be discovered for low values of tanβ in the $A \rightarrow Zh \rightarrow llb\bar{b}$ and $A \rightarrow \gamma\gamma$ modes with rates varying very rapidly with tanβ. The expected precision of the mass measurement is not better than 1 - 2% for $A \rightarrow Zh \rightarrow llb\bar{b}$ and 0.1% for the $A \rightarrow \gamma\gamma$ channel.
- For large values of tanβ, heavy Higgs bosons H and A will be discovered in the $\tau\tau$ or $\mu\mu$ decay mode. They cannot be disentangled from each other, being almost degenerate in mass and having almost identical decay modes. If both $H/A \rightarrow \tau\tau$ and $H/A \rightarrow \mu\mu$ decays are observable, the precision will be determined by the $\mu\mu$ decay mode, with a much better expected resolution and a smaller systematic error. For large values of tanβ where both channels are accessible, the precision is about 0.1%. For moderate values of tanβ, where the discovery reach of the $\tau\tau$ channel extends further than that of the $\mu\mu$ channel, the precision is degraded to 1-12%. For $H/A \rightarrow \tau\tau$ a systematic uncertainty of 1% coming from the jet energy scale has been included. The systematic uncertainty from the E_T^{miss} scale has not been included in the present study, but is expected to be of the same order of magnitude (see Section 12.5.2).

Figures 19-84 and 19-85 illustrate the expected precisions on the Higgs-boson masses discussed above, for an integrated luminosity of 300 fb^{-1} and for tanβ = 3 and tanβ = 30, respectively.

19.3.4.2 Measurement of tanβ

The measurement of the signal rates for the heavy Higgs bosons provides a good sensitivity to tanβ. The method proposed in [19-59] was followed for the evaluation of this sensitivity. The systematic error is dominated by the luminosity and is taken conservatively to be 10%. The expected precision on the measurement of m_A is also taken into account in the evaluation:

- If the signal were to be observed in the $H \rightarrow ZZ^{(*)} \rightarrow 4l$ channel, the measured signal rate would allow a measurement of tanβ with an accuracy of 10% to 25%, for an integrated luminosity of 300 fb^{-1}. For small tanβ its measurement is possible with the $H \rightarrow ZZ^{*} \rightarrow 4l$ channel. However, the precision is limited to 10% at best, since the signal rate for this channel is low.
- If the signal were to be obtained in the $H/A \rightarrow \tau\tau$ channel, the measured signal rate would provide good sensitivity to tanβ. As an example, for m_A = 150 GeV and an integrated luminosity of 300 fb^{-1}, tanβ can be measured to an accuracy of ±15 % for tanβ = 5 and of ±6 % for tanβ = 40.

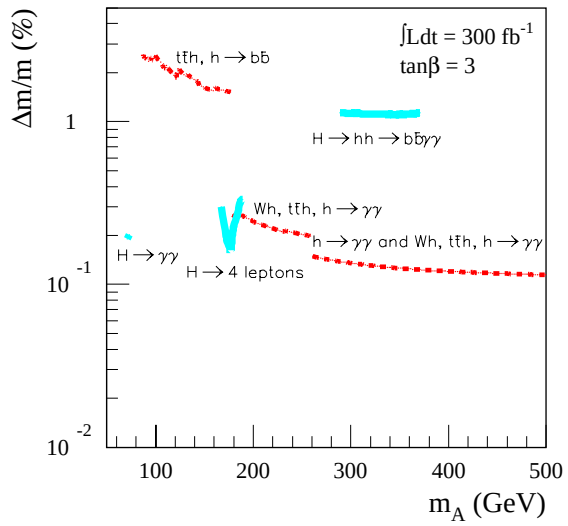

Figure 19-84 Expected precision on the measurement of the MSSM Higgs-boson masses for an integrated luminosity of 300 fb^{-1} and tanβ = 3.0

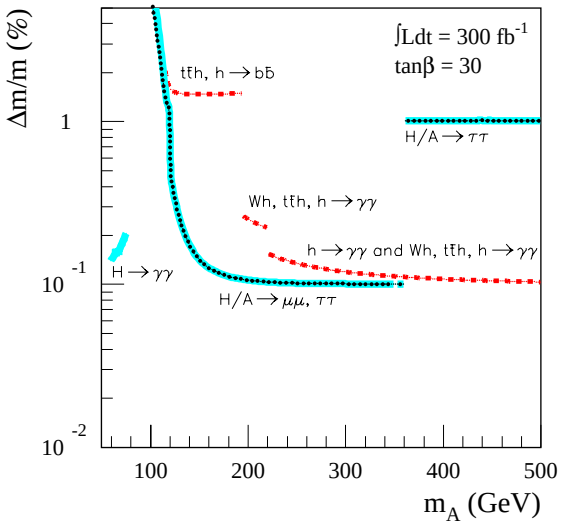

Figure 19-85 Same as Figure 19-84, but for tanβ = 30.

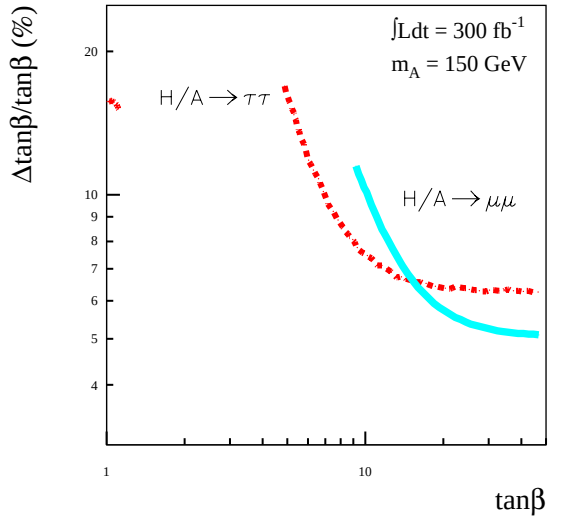

Figure 19-86 Expected precision on the measurement of tanβ, for an integrated luminosity of 300 fb^{-1} and for m_A = 150 GeV.

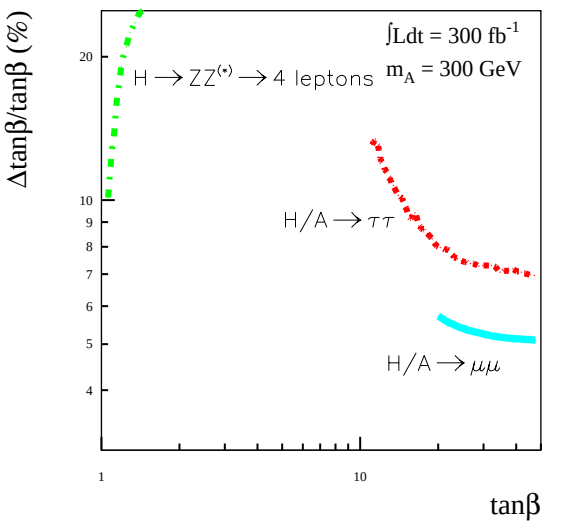

Figure 19-87 Same as Figure 19-84, but for m_A= 300 GeV.

- For large values of tanβ, a somewhat better sensitivity can be achieved with the $H/A \rightarrow \mu\mu$ channel, ±12 % for tanβ = 10 and ±5 % for tanβ = 40.

Figures 19-86 and 19-87 illustrate the expected precision on tanβ discussed above, for an integrated luminosity of 300 fb^{-1} and for m_A = 150 GeV and m_A = 300 GeV, respectively.

19.3.5 SUGRA scenarios

19.3.5.1 General considerations

As discussed in Section 19.3.3, the searches in the MSSM Higgs sector have been performed under the assumption that the SUSY mass scale is heavy and the influence of SUSY particles on the Higgs-boson decays could therefore been ignored. However, for a complete discussion of the MSSM Higgs sector, the influence of SUSY particles has to be considered [19-100]. In this section, other scenarii are discussed, where SUSY particles can appear among the decay products of supersymmetric Higgs bosons, and where the Higgs bosons themselves appear in the decays of SUSY particles. In general, the influence of the SUSY particle sector on the Higgs bosons arises from the following effects:

- Due to radiative corrections, the mass spectrum of the Higgs bosons is affected by the SUSY particle spectrum and the mixing parameters in the stop-sbottom sector [19-11].
- If SUSY particles are not too heavy, their contribution to loops can either enhance or suppress the $gg \rightarrow h, H, A$ production cross-sections and/or the branching ratios for the $\gamma\gamma$ channel [19-101].
- There are regions in parameter space, where the rates for Higgs-boson decays to SUSY particles are large and dominant. These decays reduce the rates for SM signatures, opening new modes for Higgs-boson detection [19-100][19-102]. Higgs-boson decays to charginos or neutralinos ($H \rightarrow \tilde{\chi}_2^0 \tilde{\chi}_2^0$, $\tilde{\chi}_1^\pm \tilde{\chi}_1^\pm$) which lead to multi-lepton final states, are among the most interesting signatures in this respect.
- There are regions in parameter space, where Higgs bosons are produced in decays of SUSY particles [19-100]. The most promising channel is the second lightest neutralino decay to the h-boson, followed by an $h \rightarrow b\bar{b}$ decay [19-103][19-104].

The many parameters of the MSSM render a systematic study of the interplay between the Higgs and SUSY sectors extremely difficult. Therefore these studies have been performed in the framework of the more constrained minimal SUGRA model [19-71]. For a detailed discussion of the parameters of this model, the reader is referred to Chapter 20.

Masses

The SUGRA parameters have been scanned over the ranges m_0, $m_{1/2}$ = 50 - 1000 GeV, tanβ = 1 - 50, for both signs of μ and for A_0 = 0. These ranges correspond to the region of parameter space over which SUSY would be discovered at the LHC (see Chapter 20). Parts of this parameter space are excluded theoretically or experimentally [19-105]. In the determination of these excluded parameter regions, the present experimental limit on m_h has not been included. Curves of constant m_h are

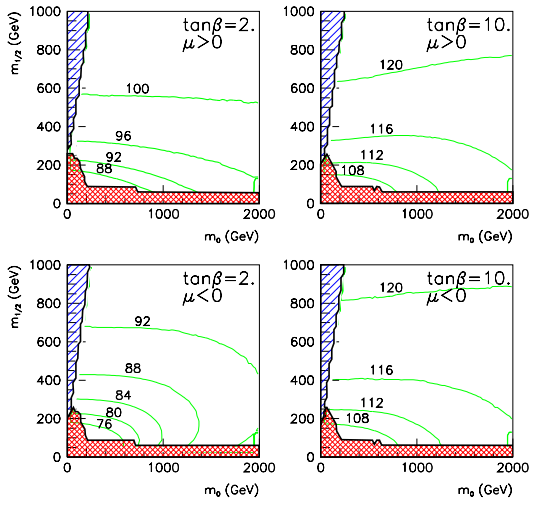

Figure 19-88 Curves of constant m_h in the (m_0, $m_{1/2}$) SUGRA parameter space for A_0 = 0, tanβ = 2 and 10, and for both signs of μ. The hashed and cross-hashed areas are excluded, respectively theoretically and experimentally.

shown over a subset of the SUGRA parameter space in Figure 19-88. For a given value of tanβ, these curves are almost independent of m_0 and increase only slowly with $m_{1/2}$. For low values of tanβ and for positive μ the predicted value for m_h is about 10 -15 GeV higher than for negative μ and for the same values of the m_0, $m_{1/2}$ parameters. This splitting disappears for large values of tanβ for which the mass of the *h*-boson reaches its upper limit.

The other supersymmetric Higgs bosons are predicted to be heavy in SUGRA models, even for relatively low values of (m_0, $m_{1/2}$). The *H*- and *A*- bosons are degenerate in mass over almost the whole parameter range. Curves of constant m_A are shown in Figures 19-89 and 19-90 for three values of tanβ (2, 10, 40) and for both signs of μ. For given values of m_0 and $m_{1/2}$, the predicted masses of the *H*- and *A*- bosons decrease with increasing tanβ. Note that the isoline m_A = 500 GeV reaches $m_{1/2} \sim 300$ GeV for tanβ = 10 and $m_{1/2} \sim 500$ GeV for tanβ = 40. For m_A = 500 GeV, the maximum possible value of $m_{1/2}$ increases from 250 GeV to 550 GeV when tanβ increases from 2 to 40. The heavy neutral Higgs bosons are only observable at the LHC for

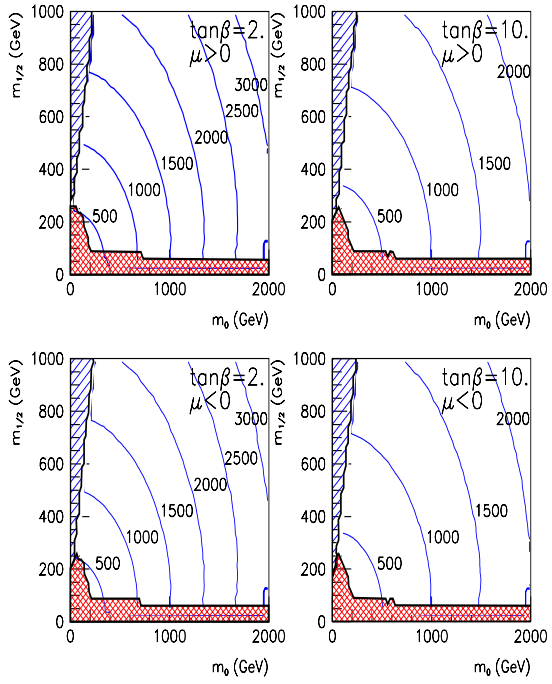

Figure 19-89 Same as Figure 19-88, but for curves of constant m_A.

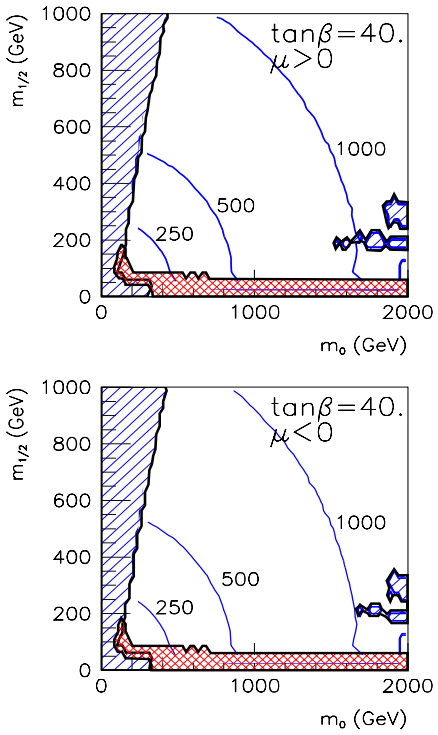

Figure 19-90 Same as Figure 19-89, but for tanβ = 40.

masses up to about 500 GeV, since their production cross-sections decrease rapidly with increasing mass. As shown in Figures 19-89 and 19-90, the region with m_A < 500 GeV represents, however, only a small fraction of the SUGRA parameter space.

If the excluded regions of the SUGRA parameter space are mapped onto the (m_A, tanβ) discovery plane discussed in Section 19.3.3, they correspond to regions with low values of m_A, so that only the region with m_A > 225 GeV is allowed. The discovery of a heavy neutral Higgs boson in SUGRA has therefore to rely on the $H/A \rightarrow \tau\tau$ and $H/A \rightarrow \mu\mu$ channels, or as shown in the next sections, on some of their possible SUSY decay modes [19-106].

Production and decay

For the evolution of the SUGRA parameters from the GUT scale to the weak scale, the ISASUSY package was used [19-107]. The output parameters were then used as input to the HDECAY package, which calculates the SUSY particle spectrum and the Higgs-boson branching ratios [19-20]. This package includes the most important higher-order QCD corrections to the decays into quark pairs and important decays to off-mass-shell particles. All SUSY particles contributions to the loop-mediated $h \to \gamma\gamma$ decay mode are included. The package calculates the Higgs-boson branching ratios in the so-called SUSY-ON and SUSY-OFF scenarios, where the latter omits SUSY particles in decays and loops but calculates the Higgs-boson masses and couplings for the chosen SUSY model.

Higgs-boson production via gluon-gluon fusion is a production process which is important to be estimated consistently in SUSY-ON / OFF scenarios. For this purpose, the decay width of the Higgs boson to *gg* pairs is calculated. A comparison of the cross-sections times branching ratios computed in the two scenarios provides an estimate of the difference between the effect of a variation of the couplings obtained from the MSSM parameters (m_A and tanβ) and the effect of SUSY loops or SUSY decay modes in the Higgs sector. The SUSY-OFF scenario is used as a reference model, since it corresponds to the one discussed extensively in Section 19.3.2. More details on the comparison between these two scenarios in SUGRA can be found in [19-70], where several plots illustrate the behaviour of $\sigma \times$ BR for different Higgs-boson decay channels in the SUGRA parameter space.

19.3.5.2 Standard Model decay modes

Observability of the h-boson

The SM decay modes of the *h*-boson may be suppressed due to the opening of SUSY decay modes or due to SUSY contributions to loops. Over the allowed SUGRA parameter space, the decay of $h \to \tilde{\chi}_1^0\ \tilde{\chi}_1^0$ (where $\tilde{\chi}_1^0$ denotes the lightest neutralino) is not accessible, and *h* only decays to SM particles.

The presence of SUSY particles in loops has a significant impact on the observability of the *h*-bosons over certain regions of the SUGRA parameter space:

- the $gg \to h$ production cross-section is somewhat enhanced;
- the $h \to \gamma\gamma$ branching ratio may be suppressed by up to 30%.

As a consequence, the $\sigma \times$ BR for $gg \to h \to \gamma\gamma$ is never below 90% of its SUSY-OFF value. The $\sigma \times$ BR for the *Wh* and $t\bar{t}h$ associated production with $h \to \gamma\gamma$ can be reduced to 70% of the SUSY-OFF values. The reduction of the $h \to \gamma\gamma$ rate occurs for low values of $m_{1/2}$ and is insensitive to m_0 [19-70]. On the other hand, the discovery potential for the $h \to b\bar{b}$ channel is essentially unaffected by the mass spectrum of the SUSY particles.

Figures 19-91 and 19-92 show how the 5σ-discovery contour curves in the (m_A, tanβ) plane for inclusive and associated $h \to \gamma\gamma$ searches, are modified by the changes in $\sigma \times$ BR from the SUSY-OFF values. In the SUGRA scenario, the region where m_A is less than 225 GeV, is excluded as explained in Section 19.3.5.1 and illustrated in Figures 19-91 and 19-92. Although the observability of the $h \to \gamma\gamma$ channel may be somewhat reduced the overall observability of the *h*- boson remains unchanged since the sensitivity of the $t\bar{t}h$, $h \to b\bar{b}$ channel is unaffected by SUSY particles.

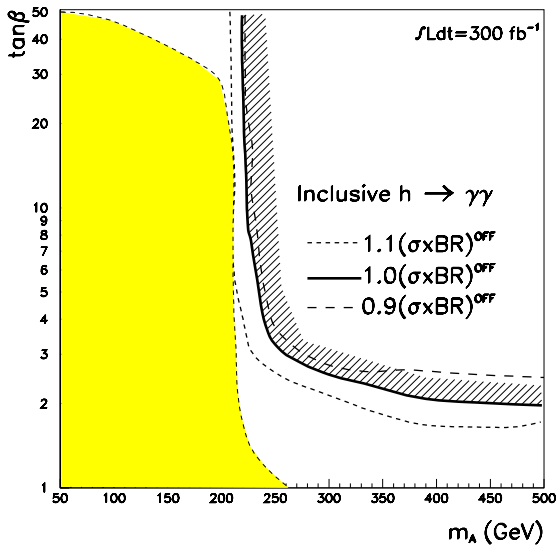

Figure 19-91 For an integrated luminosity of 300 fb^{-1}, 5σ-discovery contour curves for the inclusive $h \to \gamma\gamma$ channel in the (m_A, tanβ) plane as a function of $\sigma \times$ BR with respect to the SUSY-OFF scenario (see text).

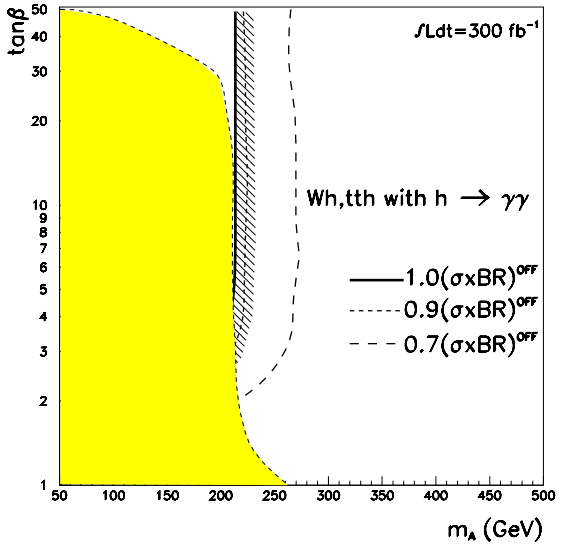

Figure 19-92 Same as Figure 19-91, but for the associated production of Wh and $t\bar{t}h$ with $h \to \gamma\gamma$.

Observability of the *H*- and *A*- bosons

In contrast to the h-boson, the SM decay modes of the heavy neutral Higgs bosons may be significantly affected by the opening of decay modes to SUSY particles (see Section 19.3.5.3). In many cases, the branching ratios to SM particles are strongly suppressed. These suppressions depend weakly on m_0 and are strongest for low values of $m_{1/2}$ and tanβ: for tanβ > 40, the suppression is always below 20% and for $m_{1/2} > 400$ GeV, it is always below 40% (see [19-70] for more details).

Figure 19-93 illustrates the impact of the opening of H/A SUSY decays modes on the observability of their SM decay modes in SUGRA. The top plots of Figure 19-93 show the possible regions of parameter space for a 5σ discovery of the heavy neutral Higgs bosons in the SUSY-OFF scenario (derived directly from the results reported in Section 19.3.2), both in the (m_0, $m_{1/2}$) and (m_A, tanβ) planes. The middle plots of Figure 19-93 indicate that these regions of possible discovery are not directly affected if SUSY decay modes are allowed, but the bottom plots of Figure 19-93 show that, over a large fraction of these regions, the suppression of the SM decay modes may be so large that their discovery is no longer possible.

Observability of the $H^{\pm}$ - boson

The production of a charged Higgs boson at the LHC can occur through $t\bar{t}$ production followed by a $t \to H^{+}b$ decay or through gg or gb fusion. A signal can be observed in the case of $t\bar{t}$ production in either the $H^{\pm} \to \tau\nu$ or $H^{\pm} \to cs$ decays. The decay $H^{\pm} \to tb$ is also observable for low and large values of tanβ (see Section 19.3.2.11).

In the SUGRA parameter region m_0, $m_{1/2}$ = 50 - 1000 GeV, the $H^{\pm}$ is heavier than the top quark, except at very large tanβ. $H^{\pm}$ could decay into charginos / neutralinos or squarks but, even above the top-quark threshold, the branching ratio to chargino / neutralino will not exceed 20 - 30%. Decay into stop-sbottom also may become important, with a branching ratio of the same order of magnitude as the branching ratio into SM fermions.

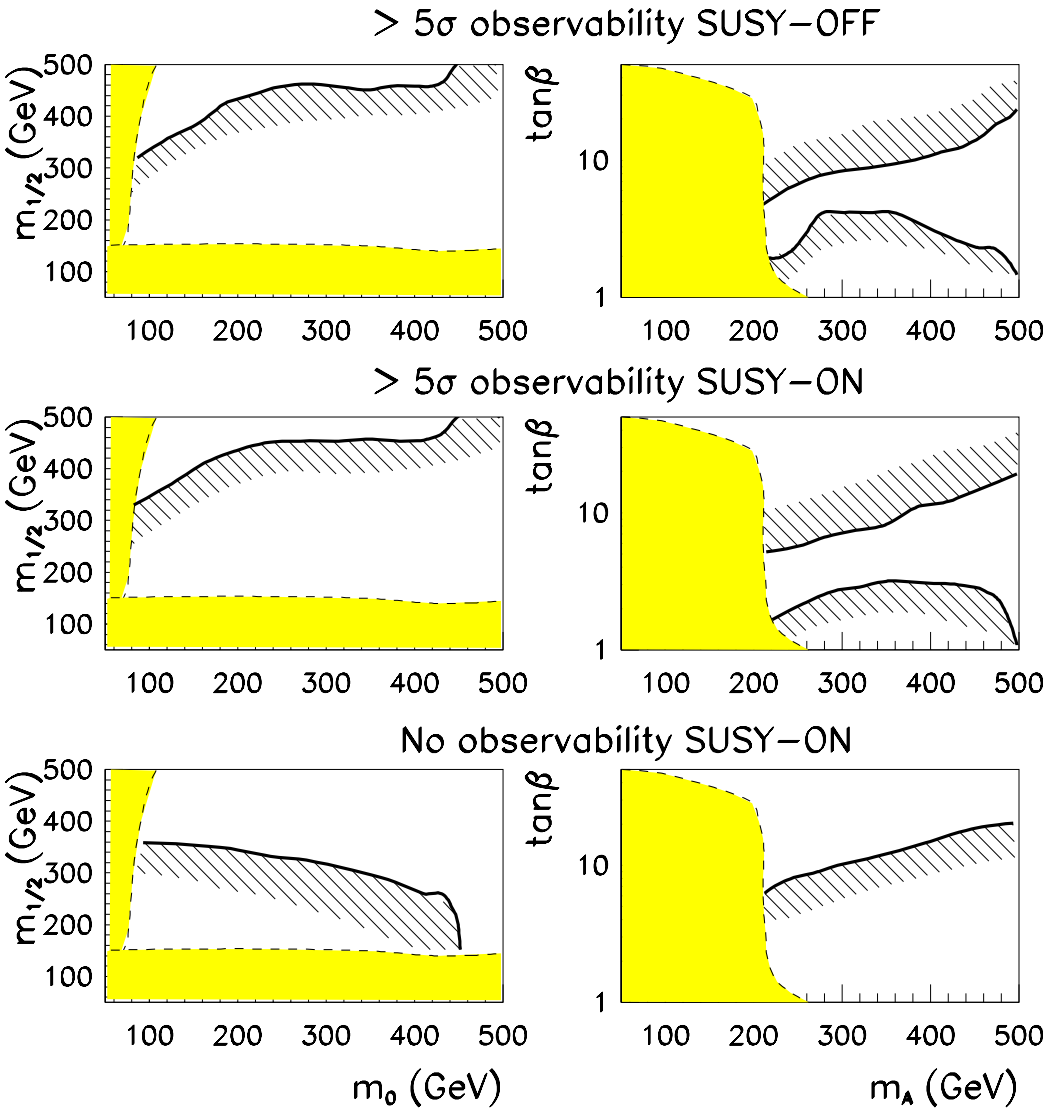

Figure 19-93 For SM decays of the heavy neutral Higgs bosons in SUGRA scenarios and for an integrated luminosity of 300 fb^{-1}, regions of the (m_0, $m_{1/2}$) plane (left) and of the (m_A, tanβ) plane (right), where a 5σ discovery would be possible in the absence of SUSY decay modes (top), in the presence of SUSY decay modes (middle) and where no discovery in SM decay modes would be possible in the presence of SUSY decay modes (bottom). The ττ, μμ, *tt* decays and $A \rightarrow Zh$ and $H \rightarrow hh$ modes are used. The shaded areas are excluded by theoretical and experimental constraints.

Overall sensitivity

Figure 19-94 shows the 5σ-discovery contour curves for SM decays of the various Higgs bosons and for an integrated luminosity of 300 fb^{-1}, as taken from the general MSSM studies reported in Section 19.3.2, but extrapolated to SUGRA scenarios with heavy SUSY particles (SUSY-OFF) and including the theoretical and experimental constraints described above.

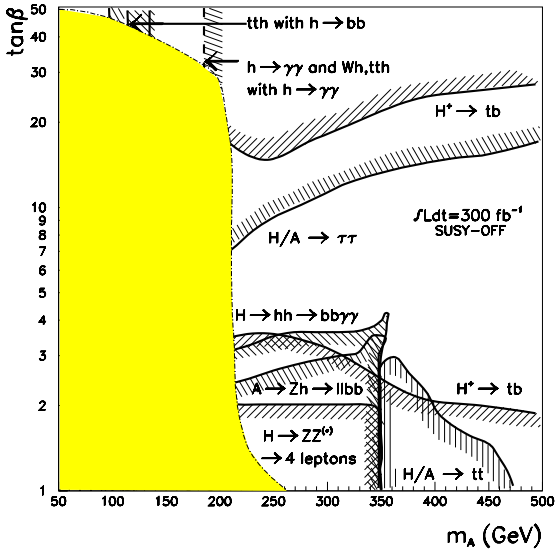

Figure 19-94 For an integrated luminosity of 300 fb^{-1} 5σ discovery contour curves for various SM Higgs-boson decay modes in the case of SUGRA scenarios with heavy SUSY particles (SUSY-OFF) and for an integrated luminosity of 300 fb^{-1}. The shaded area is excluded by theoretical and experimental constraints.

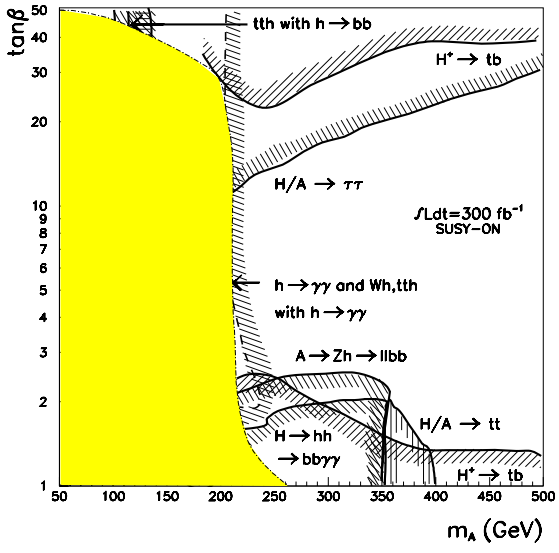

Figure 19-95 Same as Figure 19-94, but the impact of SUSY particles on Higgs-boson production and decay is included (SUSY-ON, see text).

In general, however, the other SUGRA parameters have an impact on these discovery curves through the opening of Higgs-boson decays to SUSY particles (mostly for H and A) and the presence of SUSY particles in loops. This impact is illustrated in Figure 19-95, where these effects are taken into account by reducing the SM decay rates of the heavy neutral Higgs bosons to 40% of their nominal SUSY-OFF values and by reducing the SM $h \to \gamma\gamma$ rates to their minimal predicted values (see Figures 19-91 and 19-92). Over most of the relevant region of SUGRA parameter space, the reduction is smaller so this is a conservative assumption. Despite the reduction in the decay rates of the Higgs bosons, the difference between Figures 19-94 and 19-95 is not very large (only the $H \to ZZ^{(*)} \to 4l$ channel disappears).

19.3.5.3 SUSY decay modes

In this section the sensitivity of the ATLAS experiment to decays of the heavy SUSY Higgs bosons via supersymmetric particles is discussed. There is a large branching ratio for neutralino and chargino decays, $H \rightarrow \tilde{\chi}_i^0 \tilde{\chi}_i^0$, or $H \rightarrow \tilde{\chi}_i^{\pm} \tilde{\chi}_i^{\pm}$, which could decay via cascades into multi-lepton final states. Such multi-lepton final states together with missing transverse energy provide a clean signature.

The strategy for the detection of these decays is shown first [19-106] for the SUGRA point 3 [19-108] (see Chapter 20). The method is then applied to other points in the SUGRA parameter space and the 5σ discovery regions are determined [19-109].

H/A $\rightarrow \tilde{\chi}\,\tilde{\chi}$ at SUGRA point 3

SUGRA point 3 [19-108] is characterised by the following parameters: m_0 = 200 GeV, $m_{1/2}$ = 100 GeV, A = 0, tanβ = 2 and sgn(μ) = -1. At this point the heavy Higgs bosons H and A are predicted to have masses of 375 GeV; decays: $H/A \rightarrow \tilde{\chi}_1^0 \tilde{\chi}_2^0$, $H/A \rightarrow \tilde{\chi}_2^0 \tilde{\chi}_3^0$ and $H/A \rightarrow \tilde{\chi}_2^{\pm} \tilde{\chi}_1^{\pm}$ are kinematically allowed and compete with the $t\bar{t}$ decay mode. The two lightest neutralinos have masses of 45 and 97 GeV, and the decay $\tilde{\chi}_2^0 \rightarrow \tilde{\chi}_1^0 l^+l^-$ has a relatively large branching ratio. The dominant contribution to the multi-lepton final states comes from the $H/A \rightarrow \tilde{\chi}_2^0 \tilde{\chi}_2^0$ decay, which leads to two lepton pairs with opposite sign and same flavour in 12% of the cases.

The dominant source of background are leptons produced in the decays of squarks and gluinos which cascade to charginos and neutralinos. Unlike the charginos / neutralinos from Higgs-boson decays they are however produced in association with quarks and gluons if they appear in the cascade of squarks / gluinos. This large hadronic activity can be used to suppress this type of SUSY background. An additional, smaller background source is the direct production of slepton or gaugino pairs via the Drell-Yan processes. Only a very small hadronic activity is expected in these events and their rejection is more difficult. The rate of direct production of $\tilde{\chi}_2^0$ pairs is comparable with the $H/A \rightarrow \tilde{\chi}_2^0 \tilde{\chi}_2^0$, also the background from the direct production of slepton / sneutrino pairs is non-negligible.

Events are selected as follows.

- Two pairs of isolated leptons with opposite sign and same flavour (OS-SF), with $p_T > 20$ GeV for the two hardest and $p_T > 7$ GeV for the other two leptons. The mass of the lepton pairs has to be above 4.5 GeV and outside of $m_Z \pm 10$ GeV.
- Jet veto of $p_T > 40$ GeV or 20 GeV in the pseudorapidity interval $|\eta| < 5$.

The jet veto acceptance for the signal is ~35% for the 40 GeV threshold and ~19% for the 20 GeV threshold, whereas the acceptance for the SUSY background is 0.56% and 0.025% respectively. The expected number of signal and background events passing these cuts are given in Table 19-55, assuming an integrated luminosity of 30 fb^{-1}. For the final selection a tight jet veto, 20 GeV for both low and high luminosity is needed. The expected additional loss in acceptance in the high luminosity case is 50% [19-110].

Table 19-55 Expected numbers of signal and background events with two OS-SF leptonic pairs for an integrated luminosity of 30 fb^{-1}.

Selection	Signal	Backg.	*S/B*
2 OS-SF pairs	493	3.6x10^5	0.001
Kinematic cuts	333	2.5x10^5	0.001
Jet veto 40 GeV	115	1545	0.07
Jet veto 20 GeV	80	140	0.57

With looser isolation criteria than those that were discussed in Section 19.2.5, the lepton reconstruction+isolation efficiency can be kept at the 66% per event (~90% per lepton) with still sufficient rejection power of 120 (20) against $t\bar{t}$ background and of 30 (10) against $Zb\bar{b}$ background for low (high) luminosity. The SM background (Z^*Z^*, $t\bar{t}$, $Zb\bar{b}$ events) is suppressed to a level below 10% (20%) of the SUSY background for low (high) luminosity.

In Figure 19-96 the invariant mass distribution of the four leptons, m_{llll}, is shown for the signal + background (black points) and for the background alone (histogram) after applying a jet-veto cut of 20 GeV and for an integrated luminosity of 300 fb^{-1}. The Higgs signal appears as an enhancement in the m_{llll} distribution and can be detected with a significance of $S/\sqrt{B}$ = 5.2 after 30 fb^{-1} and $S/\sqrt{B}$ = 11.9 after 300 fb^{-1} if the systematic error on the background is not taken into account. The shape of the distribution is sensitive to the Higgs-boson mass, as shown in Figure 19-97; a sensitivity of 10 GeV is expected for an integrated luminosity of 300 fb^{-1}.

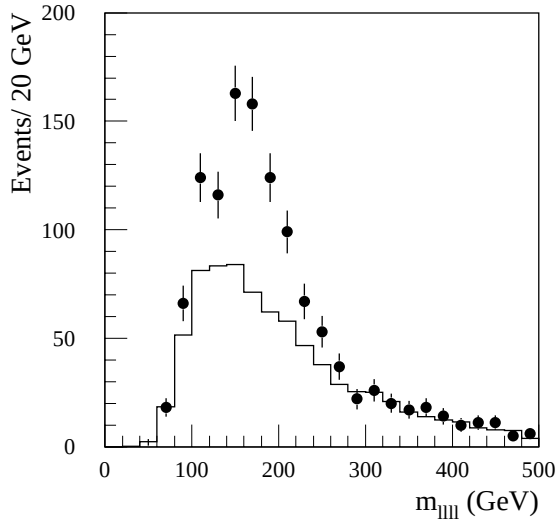

Figure 19-96 For $H/A \rightarrow \tilde{\chi}\,\tilde{\chi} \rightarrow 4l$+X decays with m_A = 371 GeV distribution of the four-lepton invariant mass for the background (solid line) and the summed signal+background (points with error bars) for an integrated luminosity of 300 fb^{-1}.

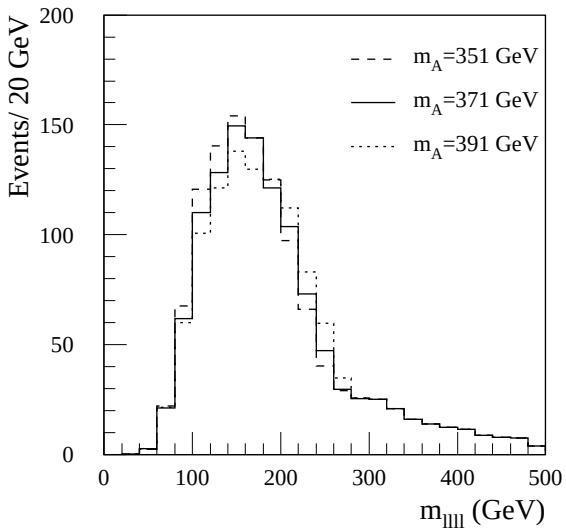

Figure 19-97 For $H/A \rightarrow \tilde{\chi}\,\tilde{\chi} \rightarrow 4l$+X and for an integrated luminosity of 300 fb^{-1}. The distribution is shown for three different values of m_A.

Complete reconstruction of the Higgs mass

If in the $\tilde{\chi}_2^0 \rightarrow \tilde{\chi}_1^0 l^+ l^-$ decay the dilepton pair has an invariant mass near its endpoint, then in the rest frame of the $\tilde{\chi}_2^0$ both the $\tilde{\chi}_1^0$ and the ll pair are forced to be at rest. One can then reconstruct the four-momentum of the $\tilde{\chi}_2^0$ if its mass is assumed. More details of this method can be found

in Section 20.2.4.1. The previous event selection was refined by requiring both OS-SF pairs to be in the $(m_{\tilde{\chi}_2^0} - m_{\tilde{\chi}_1^0}) - 10\ \text{GeV} < m_{ll} < (m_{\tilde{\chi}_2^0} - m_{\tilde{\chi}_1^0})$ window. To increase the statistics of the end-point events the jet veto is raised to 40 GeV.

The invariant mass of pairs of $\tilde{\chi}_2^0$'s is formed and shown in Figure 19-98. The mass distributions are shown for signal and background for values of the Higgs boson mass shifted by ±20 GeV around nominal one and for an integrated luminosity of 300 fb^{-1}. For a Higgs boson mass of m_A = 370 GeV 18 signal and 65 background events from the $ee\mu\mu$ sample are found in the mass window ±50 GeV around the nominal Higgs boson mass. This only corresponds to a signal significance $S/\sqrt{B}$ = 2.2. If all events with SF-OS lepton pairs are used about 33 signal and 132 background events are expected which give a statistical significance of $S/\sqrt{B}$ = 2.9. Figure 19-98 shows the expected distribution of the reconstructed Higgs boson mass for all OS-SF pairs and for three different values of the Higgs boson mass. Although the sensitivity in this particular point is rather weak for the full reconstruction of the Higgs boson mass, this method may be successfully used in other SUGRA scenarios.

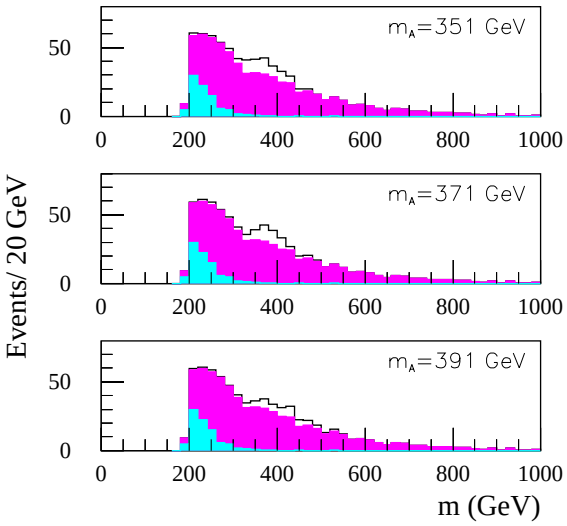

Figure 19-98 Expected reconstructed Higgs boson mass for all OS-SF pairs (see text) and an integrated luminosity of 300 fb^{-1}.

Scan of SUGRA parameter space

The same analysis as described above for the SUGRA point 3 has been applied to other points in the parameter space. The SUGRA parameter space has been scanned for fixed values of m_0 = 50, 100, 150, 200, 250 GeV in the range of $m_{1/2}$ = 100 - 300 GeV and tanβ = 1.5 - 50. The parameter A_0 had been set to zero. For this scan a dedicated package based on subroutines from ISAJET-7.37 was used. This calculates cross-sections and branching ratios for the signal and the SUSY backgrounds. Only the Higgs production via the gg fusion and the $b\bar{b}A$, $b\bar{b}H$ associated production gives a substantial contribution. The expected range in the SUGRA parameter space where the appropriate decay channel is open is determined. As the masses of the neutralinos $\tilde{\chi}_1^0$ and $\tilde{\chi}_2^0$ are proportional to $m_{1/2}$, the kinematic constraint $m_{\tilde{\chi}_2^0} - m_{\tilde{\chi}_1^0} < m_Z$, which is crucial for $\tilde{\chi}_2^0 \to \tilde{\chi}_1^0 l^+ l^-$ being dominant, gives the upper limit on $m_{1/2}$ of about 250 GeV for the Higgs searches in the four lepton channel.

Over most of the SUGRA parameter space the $H \to \tilde{\chi}_2^0\,\tilde{\chi}_2^0$ decay gives the main contribution to the four-lepton final state. In a small region of m_A in the range between 300 and 400 GeV and tanβ = 2, there is also a contribution from $H \to \tilde{\chi}_2^0\,\tilde{\chi}_3^0$ decays. If sleptons are lighter than the second lightest neutralinos, $m_{\tilde{e}_R}$ or $m_{\tilde{e}_L} < m_{\tilde{\chi}_2^0}$ the decay chain $\tilde{\chi}_2^0 \to \tilde{e}_R(\tilde{e}_L)^+\, e^-$ with the subsequent decay $\tilde{e}_R(\tilde{e}_L)^+ \to \tilde{\chi}_1^0\, e^+$ dominates the direct decay $\tilde{\chi}_2^0 \to \tilde{\chi}_1^0 l^+ l^-$.

The SUSY background was simulated including all SUSY production processes and those decay modes which give measurable contributions to the four lepton final state. For some SUGRA points the contributions from the neutralino/chargino production from sources other than $\tilde{\chi}_2^0\,\tilde{\chi}_2^0$-pair production are comparable with $\tilde{\chi}_2^0\,\tilde{\chi}_2^0$-pair production.

The $\tilde{\chi}\ \tilde{\chi}$, $\tilde{g}\ \tilde{\chi}$ and $\tilde{q}\ \tilde{\chi}$ production was included in the SUSY background. For large values of tanβ the $\tilde{\chi}$ decay to tau-leptons is dominant. For tanβ = 20 for example, the ratio $BR(\tilde{\chi}_2^0 \rightarrow \tilde{\chi}_1^0 \tau\tau) / BR(\tilde{\chi}_2^0 \rightarrow \tilde{\chi}_1^0 ee)$ is about 30 and the contribution from $\tau \rightarrow e\nu, \mu\nu$ decay is about 10% for the Higgs signal and about 30% for the background.

In some specific SUGRA parameter points the signal and background events were simulated and analysed with ATLFAST. The detection efficiencies depend on the particular parameters of the model. For example, the efficiency of the kinematic selection for leptons varies for signal events from ~40% for large m_A to ~10% for m_A = 200 GeV. For background events, the lepton cut efficiency is in the range 30 - 50% for most of the points. The analysis has been performed for jet-veto cuts, using thresholds of 20 and 40 GeV. At each point of parameter space the analysis with the higher significance is retained. For many SUGRA points, in contrast to the point 3 case, the SUSY background is not very high.

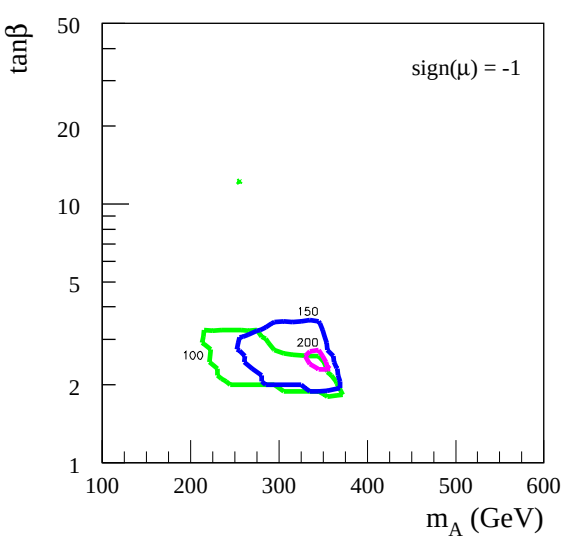

Figure 19-99 For an integrated luminosity of 30 fb^{-1}, 5σ-discovery contours for $H \rightarrow \tilde{\chi}\ \tilde{\chi} \rightarrow 4l$ channel in the (m_A, tanβ) plane for fixed m_0 = 50, 100, 150 and 200 GeV, and for sgn(μ) = -1.

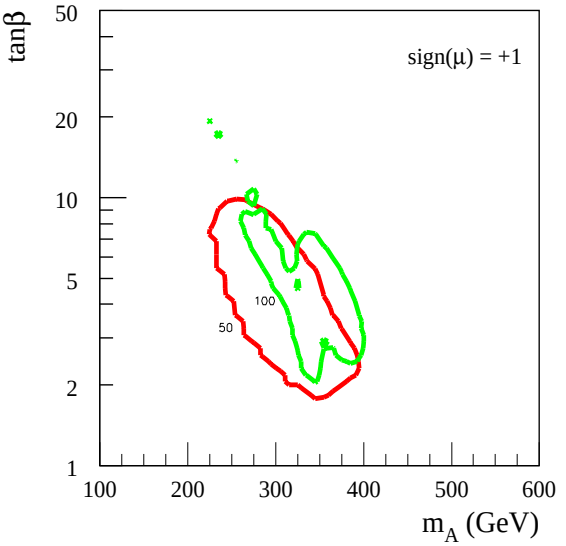

Figure 19-100 Same as Figure 19-99, but for sgn(μ) = +1.

The resulting 5σ-discovery contours are shown in Figure 19-99 to 19-102 projected onto the (m_A, tanβ) plane for both signs of μ, and for integrated luminosities of 30 fb^{-1} and 300 fb^{-1} [19-109]. The lines correspond to a 5σ significance. They are shown for fixed value of m_0 = 50, 100, 150 and 200 GeV. For positive μ values the significance is found to be slightly higher and a larger fraction of the (m_A, tanβ) plane can be covered. For both sgn(μ) the access to the large tanβ region, tanβ > 20, is restricted by the stau contribution. The complex structure of the significance region in the (m_A, tanβ) plane is mainly determined by the thresholds for the $\tilde{\chi}_2^0$ to sleptons decays.

In conclusion, while high luminosity running is required due to the small rate of Higgs production, this four lepton is promising for detection of heavy supersymmetric Higgs bosons via their decays to SUSY particles in the region of the (m_A, tanβ) plane which, using SM decay modes, was only accessible via the discovery of the light Higgs *h*. The sensitivity to the SUSY decay scenarios will be useful in the discrimination between the Standard Model and a supersymmetric Higgs model and for the investigation of the properties of the MSSM Higgs sector.

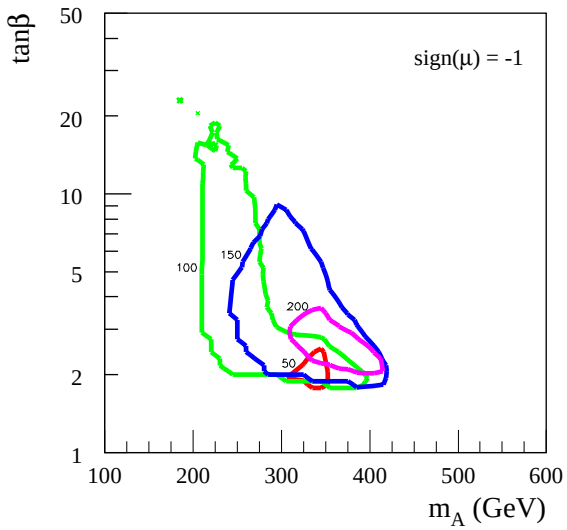

Figure 19-101 Same as Figure 19-99, but for an integrated luminosity of 300 fb^{-1}.

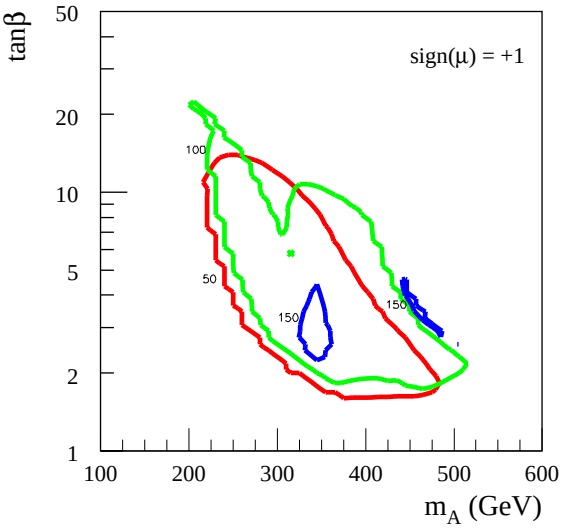

Figure 19-102 Same as Figure 19-100, but for an integrated luminosity of 300 fb^{-1}.

19.3.5.4 Higgs production in SUSY cascade decays

In this section the sensitivity to detect Higgs bosons in cascade decays of heavier SUSY particles is discussed. In particular, the lightest Higgs often appears at the bottom of cascades. One copious production source is the decay of the second lightest neutralino into the lightest neutralino, $\tilde{\chi}_2^0 \to \tilde{\chi}_1^0 h$; the former is produced with a large rate in the decays of squarks or gluinos such as $\tilde{q}_L \to \tilde{\chi}_2^0 q \to \tilde{\chi}_1^0 hq$. In R-parity conserving SUSY models the light Higgs h is always accompanied by missing transverse energy, carried away by the lightest SUSY particle. The presence of missing transverse energy and several energetic jets can be used to obtain a sample that consists mainly of the decay products of SUSY particles (see Section 20.2.5.). The discovery of the Higgs h in its dominant decay mode $h \to b\bar{b}$ without a lepton being present (as required in the Wh with $W \to l\nu$, case) then becomes possible.

In the following, the signal extraction is described using SUGRA point 1 as a typical example. The method established there [19-103] is then used at other points in the SUGRA parameter space and the discovery region in the SUGRA parameter space is determined [19-111].

$\tilde{\chi}_2^0 \to h\,(\to b\bar{b})\,\tilde{\chi}_1^0$ decay at SUGRA point 1

At point 1 (see Section 20.2) the SUSY particles are relatively heavy with squarks and gluinos in the 1 TeV range. The two lightest neutralinos have masses of 325 GeV and 170 GeV. Since the mass of the lightest Higgs h is 95 GeV, the decay $\tilde{\chi}_2^0 \to \tilde{\chi}_1^0 h$ is open and has a branching ratio of 90%. The Higgs boson h decays with a branching ratio of 80% into a $b\bar{b}$ pair.

The total cross-section for the production of SUSY particles is 3.6 pb and is dominated by squark-squark and squark-gluino production. About 25 000 events containing at least one h-boson are expected to be produced for an integrated luminosity of 30 fb^{-1}. About 90 % of them contain only one h-boson with an average p_T of about 200 GeV. In particular the cascade decay of the $\tilde{q}_L \to \tilde{\chi}_2^0 q \to \tilde{\chi}_1^0 hq$ leads to a very characteristic signature of multi-jet and multi-b-jet events associated with large E_T^{miss}. With further selection the reconstruction of the

$h \rightarrow b\bar{b}$ decays provides an accurate measurement of m_h, with a signal sample free of the large backgrounds from SM processes. Using this clean sample of $h \rightarrow b\bar{b}$ decays, a backward partial reconstruction of the SUSY cascade itself can also be performed (see Section 20.2.4.3).

Table 19-56 Numbers of expected events for SUSY and SM background events passing the selection cuts discussed in the text for an integrated luminosity of 30 fb^{-1} as a function of E_T^{miss} and *b*-jet-veto cuts. The third and fourth columns correspond to the choice of the final cuts.

Process	E_T^{miss} > 200 GeV Veto p_T^b > 15 GeV 30 fb^{-1}	E_T^{miss} > 300 GeV Veto p_T^b > 15 GeV 30 fb^{-1}	E_T^{miss} > 300 GeV Veto p_T^b > 50 GeV Final selection 30 fb^{-1}	E_T^{miss} > 300 GeV Veto p_T^b > 50 GeV Final selection 300 fb^{-1}
SUSY: $h \rightarrow b\bar{b}$	1190	920	980	6460
SUSY: other	190	160	180	1200
SM background	220	45	75	420
$S/\sqrt{B}$	59	64	61	160

To select a clean $h \rightarrow b\bar{b}$ signal above the SUSY combinatorial background and the SM background the following criteria are applied:

- $E_T^{miss} > 300$ GeV (or 200 GeV in some cases).
- Two tagged *b*-jets with $p_T > 50$ GeV, which are relatively close, $R^{b,b} < 2$. (The separation cut is mainly applied to reject $t\bar{t}$ background).
- There should be no additional *b*-jet with $p_T > 50$ GeV (or $p_T > 15$ GeV is some cases).
- Lepton-veto for isolated leptons with $p_T > 6$ GeV.
- Two additional jets with $p_T > 100$ GeV, one of them should be within $|\eta| < 2.0$.

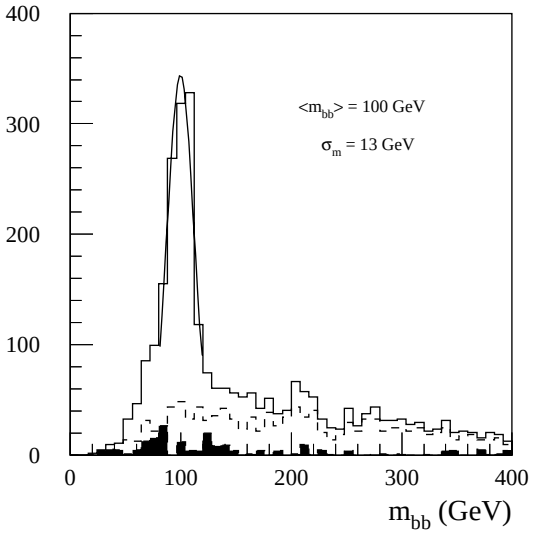

Figure 19-103 The reconstructed $m_{b\bar{b}}$ distribution for events passing the $h \rightarrow b\bar{b}$ selection cuts (see text). The distributions are shown for the SM background (shaded), the total SUSY+SM background (dashed) and the summed $h \rightarrow b\bar{b}$ signal and background for SUGRA point 1. An integrated luminosity of 30 fb^{-1} has been assumed.

Table 19-56 shows the number of expected events for the different selection cuts for integrated luminosities of 30 and 300 fb^{-1}. Already at low luminosity the signal can be clearly identified with a high significance above the backgrounds. At high luminosity, there is some degradation due to pile-up effects, and some degradation of the *b*-tagging efficiency which explains why the numbers in the Table do not scale with luminosity. In Figure 19-103 the reconstructed mass distributions $m_{b\bar{b}}$ of the two selected b-jets is shown after cuts. The contributions of the $h \rightarrow b\bar{b}$ signal + background (solid), of the Standard Model background (black) and of the total SM+SUSY background (dashed) are shown separately.

In the mass window $m_{b\bar{b}} = m_h \pm 25$ GeV, the SM background can be reduced well below 10% of the $h \to b\bar{b}$ signal. The SUSY combinatorial background is found to be small, at the level of 20% of the $h \to b\bar{b}$ signal itself.

Very similar conclusions are drawn from the analysis performed for SUGRA point 5 (see Section 20.2.5), where the SUSY particles have lower masses (gluino and squarks of 700 GeV) but similar cascade decay patterns [19-104].

Scan of SUGRA parameter space

The observability of the $h \to b\bar{b}$ signal was studied in the SUGRA parameter space for m_0 up to 2 TeV, $m_{1/2}$ up to 1 TeV, tanβ = 2, 10, and 30, sgn(μ) = ± 1 and $A_0 = 0$ [19-111]. For several points in the (m_0, $m_{1/2}$) plane where the channel $\tilde{\chi}_2^0 \to \tilde{\chi}_1^0 h$ is open, individual analyses similar to the one described above, were performed.

In most cases the same selection cuts were imposed. The E_T^{miss} threshold was increased with $m_{1/2}$ from 300 GeV for $m_{1/2}$ = 300 GeV to 600 GeV for $m_{1/2}$ = 1000 GeV. The E_T^{miss} cut was not so efficient at large m_0 and large $m_{1/2}$ where the E_T^{miss} results from the decay of rather light $\tilde{\chi}_2^0$, $\tilde{\chi}_i^{\pm}$ and not from decays of heavy $\tilde{q}$, as is the case for the low m_0, large $m_{1/2}$ region. The p_T thresholds for the *b* and non-*b* jets were optimised separately for different regions of the (m_0, $m_{1/2}$) parameter space.

Over a large region of the parameter space, the most important cascade for the *h* production, $\tilde{\chi}_2^0 \to \tilde{\chi}_1^0 h$, is open and has a branching ratio of about 90%. Also for $90 \le m_h \le 120$ GeV the branching ratio BR($h \to b\bar{b}$) is large and exceeds 75%. The total cross-section for SUSY production varies from ~ 10^3 pb at (m_0, $m_{1/2}$) ≈ (100 GeV, 100 GeV) to 10^{-1} pb for $m_{1/2} > 800$ GeV. The cross-section is almost independent of tanβ and sgn(μ).

All SUSY production processes available in PYTHIA 6.115 [19-112] were simulated, with $\tilde{q}\tilde{q}$, $\tilde{g}\tilde{q}$, $\tilde{g}\tilde{g}$, $\tilde{\chi}_1^{\pm}\ \tilde{\chi}_1^{\pm}$, $\tilde{\chi}_1^{\pm}\tilde{\chi}_2^0$ production being the most important ones. For low m_0 and large $m_{1/2}$, the $\tilde{q}\tilde{q}$ production is dominant (40%) since $m_{\tilde{g}} > m_{\tilde{q}}$, while at large m_0 and low $m_{1/2}$, where $m_{\tilde{g}} < m_{\tilde{q}}$, the $\tilde{g}\,\tilde{g}$ production is significant (30%). At the lower-left quarter of the (m_0, $m_{1/2}$) plane, where both the $\tilde{q}$ and the $\tilde{g}$ masses are low, $\tilde{g}\tilde{q}$ production contributions are larger than 35% of the total SUSY production. For large $\tilde{q}$ and $\tilde{g}$ masses, *i.e.*, at the upper-right part of the parameter space, gauginos lead the SUSY production via electroweak processes (50%). Mixed production processes, like $\tilde{g}\ \tilde{\chi}_1^{\pm}$, $\tilde{g}\,\tilde{\chi}_2^0$, $\tilde{q}\ \tilde{\chi}_1^{\pm}$, and $\tilde{q}\ \tilde{\chi}_1^0$ production, give contributions of order 1% or less.

In Figures 19-104 and 19-105 the 5σ-observability contours are shown for tanβ = 10, sgn(μ) = +1, and for integrated luminosity of 30 fb^{-1} and 300 fb^{-1} respectively. A line is superimposed which indicates where the branching ratio $BR(\tilde{\chi}_2^0 \to \tilde{\chi}_1^0 h)$ has a constant value of 50%. There is an obvious correlation between this branching ratio and the 5σ discovery contours. Once the channel $\tilde{\chi}_2^0 \to \tilde{\chi}_1^0 h$ is open, it quickly becomes dominant and the subsequent decay $h \to b\bar{b}$ becomes detectable. The expected number of $h \to b\bar{b}$ events, after selection cuts have been imposed, is indicated by the dashed and/or dotted lines in the figures. The 5σ discovery region depends only weakly on tanβ and sgn(μ). Similar plots exist for other values of tanβ and sgn(μ) and can be found in [19-111].

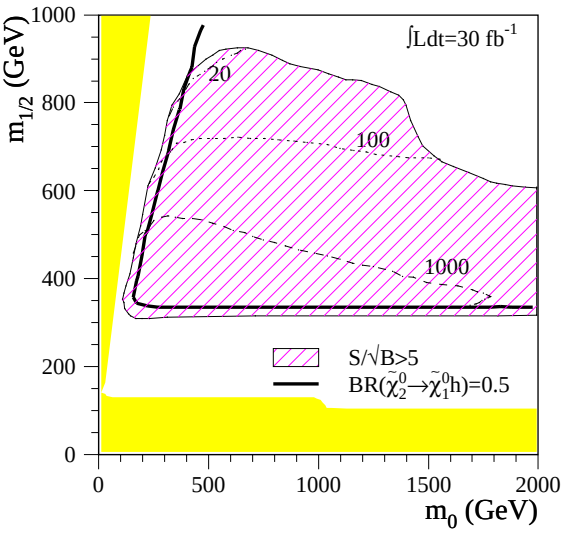

Figure 19-104 For an integrated luminosity of 30 fb^{-1}, 5σ-discovery area (hatched) for the $h \to b\bar{b}$ from SUSY cascade in the (m_0, $m_{1/2}$) plane for tanβ = 10, sgn(μ) = +1. The expected numbers of reconstructed $h \to b\bar{b}$ events are also shown. The dark shaded areas are excluded theoretically or experimentally.

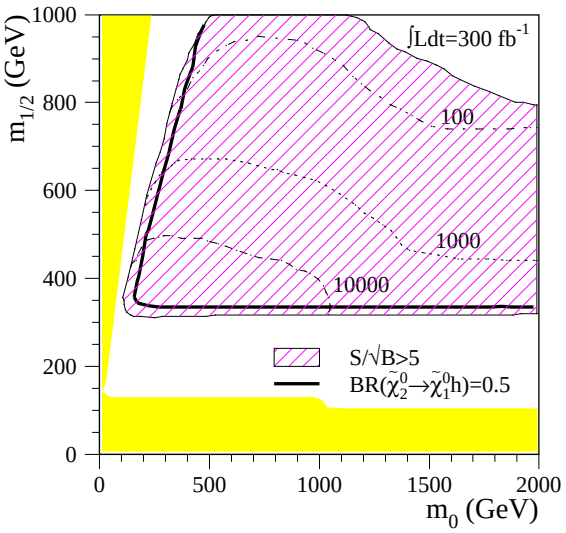

Figure 19-105 Same as Figure 19-104 but for an integrated luminosity of 300 fb^{-1}.

Outside the marked regions of the SUGRA parameter space the $h \to b\bar{b}$ decay will not be observed. Either the Higgs h is not produced in the SUSY cascade of heavy gaugino decays into lighter ones or a large $b\bar{b}$ irreducible background overwhelms the signal. This $b\bar{b}$ background arises from $\tilde{\chi}_2^0 \to \tilde{\chi}_1^0 Z \to \tilde{\chi}_1^0 b\bar{b}$, $\tilde{g} \to \tilde{\chi}_i^0 b\bar{b}$, or $\tilde{g} \to \tilde{\chi}_i^0 t\bar{t} \to \tilde{\chi}_i^0 WWb\bar{b}$ decays The non-observability of the signal in the upper right corner of the (m_0, $m_{1/2}$) plane is caused by a drop of the efficiency of the E_T^{miss} cut and by the lower cross-section for SUSY production. The results from the SUGRA parameter scan for both sgn(μ) were projected onto the (m_A, tanβ) plane. The results are shown in Figure 19-106 for integrated luminosities of 30 fb^{-1} and 300 fb^{-1}. In a large fraction of the (m_A, tanβ) parameter space above m_A= 500 GeV (m_A = 400 GeV) for tanβ > 5 (tanβ > 30) the $h \to b\bar{b}$ will be observable for an integrated luminosity of 30 fb^{-1}. It overlaps with the region where there is no sensitivity to the heavy Higgs bosons in the MSSM model.

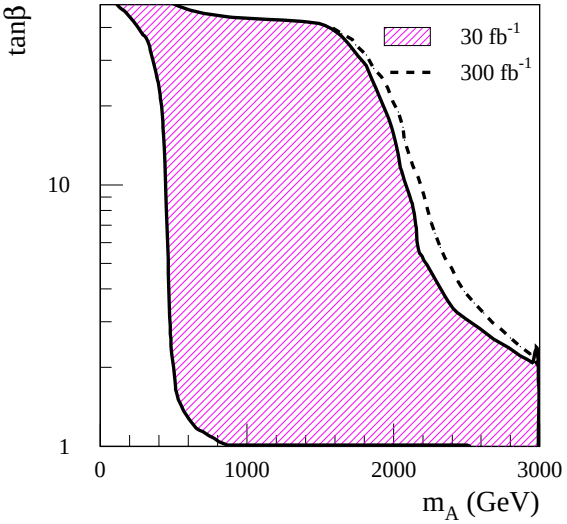

Figure 19-106 For integrated luminosities of 30 and 300 fb^{-1}, 5σ-discovery area (hatched) for the $h \to b\bar{b}$ from SUSY cascade in the (m_A, tanβ) plane. The dashed line indicates the improvement in the 5σ discovery for an integrated luminosity of 300 fb^{-1}

19.4 Strongly interacting Higgs sector

In the Standard Model, as the Higgs mass is increased, its coupling to gauge bosons increases, making the resonance wider and the interaction stronger, eventually leading to a violation of the unitarity bound ~1 TeV [19-3]. Requirements of vacuum stability and the validity of the running of the effective coupling, in next-to-leading order, should limit the allowed range for the mass of the Higgs boson [19-4], [19-5], [19-6].

While the Standard Model is renormalisable and consistent with all precision electroweak measurements, it has well known shortcomings [19-113]. It makes *ad hoc* assumptions about the shape of the potential, responsible for electroweak symmetry breaking, and provides no explanation for the values of the parameters. The theory becomes *trivial* (or non-interacting) if it is to remain valid at high energies. Radiative corrections to the Higgs mass diverge, leading to the *naturalness/hierarchy* problem. Supersymmetry is an appealing alternative which solves these problems, but at the cost of more particles and Higgs bosons, including a relatively light scalar not yet discovered.

It may well be, that no fundamental scalar particle exists. In that case, new physics must exist to account for the breaking of electroweak symmetry, for the regularisation of the vector boson coupling, and for generating fermion masses. In the absence of a low mass scalar Higgs particle, the study of electroweak symmetry breaking will require measurements, in the high energy regime, of the production rate of longitudinal gauge boson pairs since the longitudinal components are the Goldstone bosons of the symmetry breaking process. It will also be essential to search for the presence of new resonances which could exist in theories that regularise the vector boson scattering cross-section.

It has already been shown, in Section 19.2.10 that $V_L V_L$ fusion is detectable in the case of a heavy Higgs resonance, through the processes $H \rightarrow WW$ or $H \rightarrow Z\,Z$, up to $m_H \sim 1$ TeV. More generally, resonances could occur in vector, charged or neutral channels. Narrow resonances, predicted for example by technicolor models (see Section 21.2), should be detectable up to higher masses. Various other models exist for a unitarisation of the $V_L V_L$ coupling and experimental prospects have been evaluated in several recent reviews [19-114][19-115]. The search for a generic WZ resonance is presented below and the feasibility of measuring nonresonant behaviour of the $V_L V_L$ fusion process at high mass is assessed.

19.4.1 Detector performance issues

The same techniques are applied in the search for high mass gauge boson pairs as in the case of the heavy Higgs (see Section 19.2.10). Since the signals derive in large part from VV fusion, forward jet tagging is a powerful method of rejecting backgrounds. Central jet vetoing suppresses the large background from $t\bar{t}$ events, which produce pairs of W bosons accompanied by several jets. Searches which rely on reconstructing the hadronic decay of the W or Z will require optimisation of efficiencies and resolution in jet-jet masses.

19.4.2 Vector boson scattering in the Chiral Lagrangian model

Assuming an unbroken custodial $SU(2)_{L+R}$ symmetry, the scattering amplitudes for different $V_L V_L \to V_L V_L$ processes are related to each other by crossing. Defining a weak isospin I, the $W_L W_L$ scattering can be written in terms of isospin amplitudes, exactly as in low energy hadron physics. The isospin indices are assigned as follows,

$$W_L{}^a\, W_L{}^b \to W_L{}^c\, W_L{}^d$$

where W_L denotes either W_L or Z_L, where $W_L{}^{\pm} = (1/\sqrt{2})(W_L{}^1 \mp iW^2{}_L)$ and $Z_L = W_L{}^3$. The scattering amplitude is given by

$$M(W_L{}^a\, W_L{}^b \to W_L{}^c\, W_L{}^d) \sim A(s,t,u)\,\delta_{ab}\,\delta_{cd} + A(t,s,u)\delta_{ac}\delta_{bd} + A(u,t,s)\delta_{ad}\delta_{bc}$$

where a, b, c, d =1, 2, 3 and s, t, u are the usual Mandelstam kinematic variables.

Chiral Perturbation Theory (ChPT) [19-116] provides a theoretical framework capable of describing generically the strong interactions of electroweak gauge bosons [19-117]. In the chiral approach the low-energy Lagrangian is build as an expansion in derivatives of the Goldstone bosons fields. The form of the effective chiral Lagrangian, including operators up to dimension four, is only constrained by symmetry considerations which are common to any strong electroweak symmetry breaking sector [19-118]:

$$L^{(2)} = \frac{v^2}{4} trD_\mu U D^\mu U^\dagger$$

where $D_\mu U = d_\mu U - W_\mu U + UB_\mu$, $W_\mu = -(ig\sigma^a W_\mu^a)/2$, and $B_\mu = (ig\sigma^3 B_\mu)/2$. At higher-orders phenomenological parameters, L_1 and L_2 appear:

$$L^{(4)} = L_1(trD_\mu U D^\mu U^\dagger)^2 + L_2(trD_\mu U D^\nu U^\dagger)^2$$

The values of L_1 and L_2 depend on the model, but are expected to be in the range 10^{-2} to 10^{-3}. Given these parameters, it is possible to compute the function $A(s,t,u)$ in $O(p4)$ order [19-119]

$$A(s,t,u) = \frac{s}{v^2} + \frac{1}{4\pi v^4}(2L_1 s^2 + L_2(t^2+u^2)) + \frac{1}{16\pi^2 v^4}\left(-\frac{t}{6}(s+2t)\log\left(-\frac{t}{\mu^2}\right) - \frac{u}{6}(s+2u)\log\left(-\frac{u}{\mu^2}\right) - \frac{s^2}{2}\log\left(-\frac{s}{\mu^2}\right)\right)$$

The chiral Lagrangian approach does not respect unitarity. Among the methods used to unitarise chiral amplitudes, the Inverse Amplitude Method (IAM) [19-120][19-121], used here, has proved very successful in describing resonances in low energy π-π and πK scattering [19-122]. It is based on the assumption that the inverse of the amplitude has the same analytic properties as the amplitude itself.

In analogy to ππ scattering there are three possible isospin channels I = 0, 1, 2. At low energies states of lowest angular momentum J are most important, and thus only the $t_{I,J} = t_{0,0}$, $t_{1,1}$ and $t_{2,0}$ partial waves are considered here. The IAM is also able to reproduce, with proper choice of parameters, the broad Higgs-like resonance in the (I = 0, J = 0) channel. It has been shown [19-123]

that in the (I = 1, J = 1) channel there may exist narrow resonances up to masses of about 2500 GeV. The mass and width of this channel only depend on the combination $(L_2 - 2L_1)$ in this model and on v^2:

$$m_V^2 = \frac{v^2}{4(L_2 - 2L_1) - \frac{1}{18(4\pi)^2}} \text{ and } \Gamma_V = \frac{m_V^3}{96\pi v^2}$$

The $W_L Z_L \rightarrow W_L Z_L$ process is expected to be dominated by the (I = 1, J = 1) ρ-like resonance.

$W_L Z_L \rightarrow W_L Z_L \rightarrow lljj$

As a reference for this model, the process $W_L Z_L \rightarrow W_L Z_L$, with $Z \rightarrow ll$, $l = e, \mu$ and $W \rightarrow jj$ [19-124] is used. PYTHIA 5.7 was modified to generate the $V_L V_L$ scattering processes for any values of L_1 and L_2. The simulation was done for two values of $(L_2 - 2L_1) = 0.006$ and 0.01, which yield $\sigma \times$ BR of 1.5 fb and 2.8 fb, with mass peaks at 1.5 TeV and 1.2 TeV respectively.

The main features of the signal are:

- Two high-p_T leptons in the region $|\eta| < 2.5$ with the invariant mass consistent with the mass of Z-boson.
- Two high-p_T jets in the central region with the invariant mass consistent with the mass of W-boson.
- The presence of energetic jets in forward region ($|\eta| > 2$).

Requiring, at generator level, $\hat{s} > 1050$ GeV and $p_T^{\text{hard}} > 100$ GeV, the $\sigma \times$ BR of the Z+jet production, with leptonic decay of the Z boson is 0.276 pb. Irreducible background is from continuum WZ production and the main QCD background is from Z+multijet production. Two final-state jets can fake a W decay if the invariant mass of the jet pair is close to m_W. The $t\bar{t}$ background with leptonic decays of the W's is potentially dangerous because of the large cross-section, but can be efficiently suppressed by a cut on the invariant mass of the leptons from the W decay, since the two leptons have large transverse momenta and a wide opening angle. Figure 19-107 shows the invariant mass of two leptons from W decay for several values of the minimum lepton p_T allowed.

The vector bosons in $V_L V_L$ scattering are produced mostly in the central region and are characterised by large values of transverse momenta. These properties are used to suppress the background by selecting high p_T decay products. Figure 19-108 shows the p_T distribution of the leptons for the signal and Z+jet background (the background was generated here with a minimal p_T for Z of 30 GeV). The events are required to have two isolated and identified leptons of same flavour and opposite charge (e^+e^- or $\mu^+\mu^-$) in the region $|\eta| < 2.5$ with $p_T > 100$ GeV. The invariant mass of these two leptons was required to lie in the region $|m_{ll} - m_Z| < 6$ GeV. The total efficiency of this selection criteria was estimated at ~40% for signal events.

Jets were reconstructed by a cone algorithm with $\Delta R = 0.2$. Due to a large W boost, the cones of the jets could overlap. In that case, the reconstructed energy in the overlap region was shared between the jets according to their relative energies. A resolution of 10 GeV in the mass of the reconstructed W was obtained, consistent with what was found in Section 9.3.1. The events were required to have two jets with $p_T > 50$ GeV and $|\eta| < 2$ and the invariant mass of these two jets was $|m_{jj} - m_W| < 15$ GeV. Both Z and W bosons were required to have a transverse momentum larger than 200 GeV.

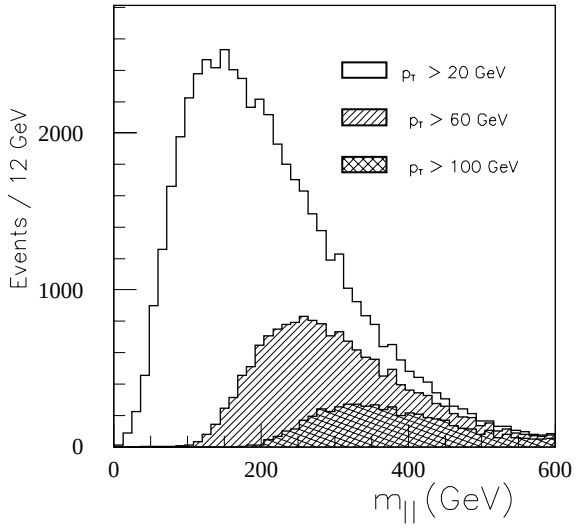

Figure 19-107 Invariant mass of the two leptons from the $t\bar{t}$ background, for the threshold on the leptons transverse momenta p_T = 20, 60 and 100 GeV.

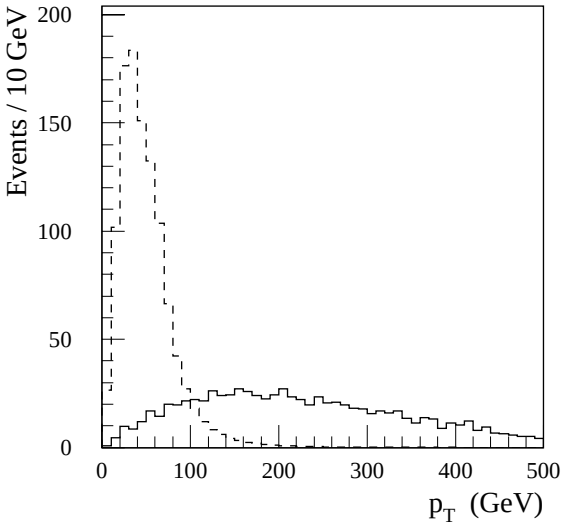

Figure 19-108 Transverse momentum distribution for leptons from signal (solid line) and from the Z+jet background (dashed). The histograms are normalised to a same number of events.

Forward jet tagging provides a powerful method of further rejecting background. Jets in the forward regions ($2 < |\eta| < 5$) were reconstructed by a cone algorithm with $\Delta R = 0.5$. Events were accepted if jets with $p_T >$ 30 GeV and energy larger than 500 GeV were present in each hemisphere. The total tagging efficiency of 0.25 for the signal process and 0.01 for Z+jet background was obtained.

The expected number of signal and background events after successively applied cuts and for an integrated luminosity of 100 fb^{-1} are presented in Table 19-57.

Table 19-57 Number of signal and background $W_L Z_L$ candidate events in a 2σ interval around the mass of the resonance, for an integrated luminosity of 100 fb^{-1}, for the cases (L_2 - 2L_1) = 0.01 and (L_2 - 2L_1) = 0.006, corresponding to Mρ = 1.2 TeV and 1.5 TeV respectively.

Number of events	**M_ρ = 1.2 TeV**		**M_ρ = 1.5TeV**	
	$W_L Z_L$	Z+jet	$W_L Z_L$	Z+jet
Central jets cut	284	2187	145	1781
$m_{jj} = m_W \pm 15$ GeV	101	154	46	82
Leptonic cuts	70	84	36	47
Forward jet tagging	14	3	8	1.3

The mass spectra for WZ candidates after all cuts show a clear peak with width 75 GeV for the 1.2 TeV resonance and 100 GeV for the 1.5 TeV resonance (Figure 19-109). The expected number of events in the window $|m_{WZ} - m_V| < 2\sigma$, for an integrated luminosity of 100 fb^{-1}, is 8 for m_V = 1.5 TeV and 14 for m_V = 1.2 TeV, with respectively 1.3 and 3 events from Z+jet background. The contribution from the irreducible continuum WZ background is negligible, below 0.05 events inside the mass window. It can therefore be concluded that such a narrow resonance process is detectable after a few years of high luminosity data taking.

The process of $W_L Z_L$ production can also be well measured in its purely leptonic final states, without jet tagging if the production by $q\bar{q}$ fusion dominates [19-14]. It is discussed in Section 21.2.1.1 in the framework of a multiscale technicolor model.

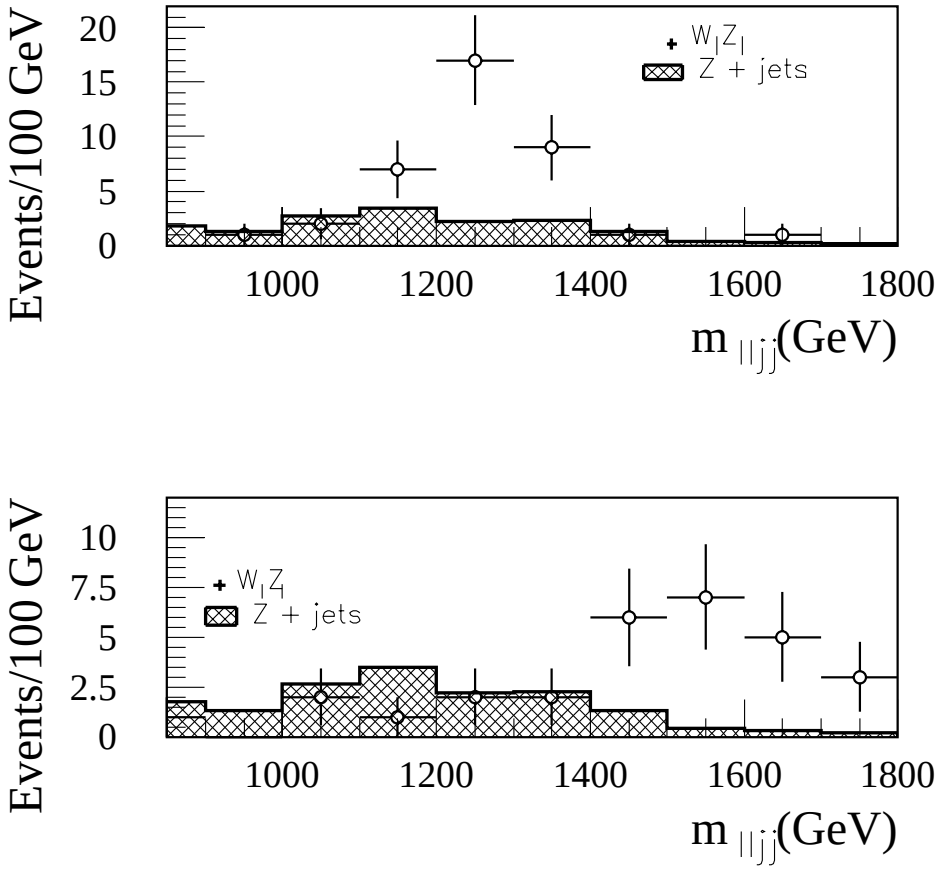

Figure 19-109 Reconstructed mass distribution for the WZ system for a 1.2 TeV and a 1.5 TeV resonance for an integrated luminosity of 300 fb^{-1}.

19.4.2.1 Non-resonant high mass gauge boson pairs

As a complement to measurements of resonances in $V_L V_L$ scattering, or in the absence thereof, the measurement of cross-sections at high mass for nonresonant channels will be a challenging task. It will be essential to understand very well the magnitude and energy dependence of backgrounds. Here, the observability of like-sign $W_L^{\prime}\ W_L^{\prime}$ production, followed by leptonic decay (μ or *e*) of the *W's* is discussed.This process has been considered in the literature as a potentially sensitive probe because of low background levels [19-125][19-126][19-127]. This channel can be particularly important since it has been shown that a complementary relationship between resonant *WZ* and nonresonant $W_L^{\prime}\ W_L^{\prime}$ exists [19-127].

As processes for the high mass $W_L\ W_L$ signal, the following are considered [19-128]:

- A t-channel exchange of a Higgs with m_H = 1 TeV, (W_LW_L only), simulated with PYTHIA: $\sigma \times \mathrm{BR}$ = 1.33 fb.
- A model with a K-matrix unitarised amplitude [19-127][19-129], $a_{IJ}^K = \frac{Re(a_{IJ})}{1 - iRe(a_{IJ})}$, with $\sigma \times \mathrm{BR}$ = 1.12 fb.
- The Chiral Lagrangian Model of Section 19.4.2, with the same parameters L1 = 0 and L2 = 0.006 or 0.01: $\sigma \times \mathrm{BR}$ = 0.484 fb and 0.379 fb respectively.

Backgrounds from continuum WW bremsstrahlung of $O(\alpha^2)$ in amplitude produce mostly transverse W's. Other backgrounds include processes involving non-Higgs exchange, as well as QCD processes of order $\alpha\alpha_s$ in amplitude, with gluon exchange and W bremsstrahlung from interacting quarks. The effects of $Wt\bar{t}$ and WZ backgrounds is also considered. The signal is generated with PYTHIA 6.2 [19-112], and backgrounds have been incorporated into PYTHIA using a generator code, obtained from [19-115], which takes into account all diagrams. The contributions from electroweak processes not involving the Higgs are estimated by assuming a low-mass Higgs (m_H = 100 GeV).

The analysis was performed using fast simulation. First, leptonic cuts were applied:

- Two positively charged isolated leptons in the central region (p_T > 40 GeV and $|\eta| < 1.75$).
- The opening angle between the two leptons, in the transverse plane must satisfy $\cos\Delta\phi < -0.5$. This cut selects preferentially events with longitudinal W's which have high p_T.
- The invariant mass of the two leptons m_{ll} > 100 GeV.

At the jet level, backgrounds can be reduced by requiring that:

- No jet (p_T > 50 GeV) be present in the central region ($|\eta| < 2$). This reduces significantly background from the $Wt\bar{t}$ process.
- Two of the jets must fall in the forward and backward regions: $\eta > 2$ and $\eta < -2$.
- A lower p_T is required from the forward jets: $p_T < 150$ GeV for the first and $p_T < 90$ GeV for the second.

The expected number of signal and background events is shown in Table 19-58, assuming an integrated luminosity of 300 fb^{-1}. Figure 19-110 displays the expected mass distribution of the $ll\nu\nu$ system (accounting only for transverse missing momentum). The major remaining background, especially at low values of $m_{ll\nu\nu}$ is from continuum transverse W's. Potentially large systematic uncertainties asso-

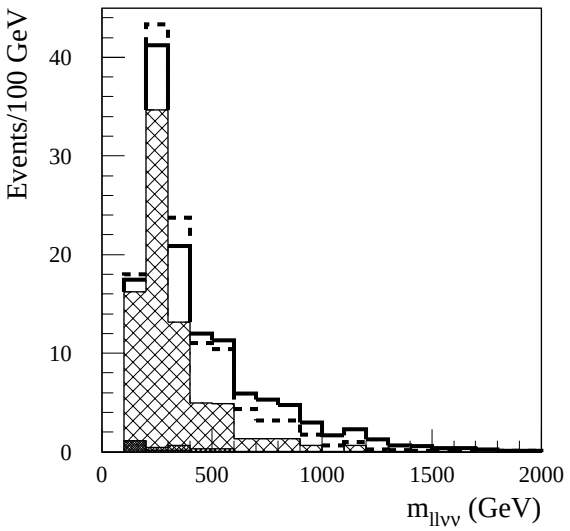

Figure 19-110 Distribution of invariant mass of the two leptons with E_T^{miss} in the $W_L\ W_L \rightarrow ll\nu\nu$ process expected for an integrated luminosity of 300 fb^{-1}. The scenarios are: K-matrix unitarisation (solid line) and 1 TeV Higgs (dotted histogram), shown on top of the backgrounds. The backgrounds are (from darkest to lightest): WZ, gluon exchange diagrams, and W_TW_T from electroweak bremsstrahlung.

ciated with the evaluated cross-section of this background, or of the cut efficiencies, can be estimated by analysing various distributions under different cut conditions.

The K-matrix scenario gives the highest signal, observable after a few years of high luminosity running, whereas a very low signal would be seen if the ρ resonance itself is clearly observable (Chiral Lagrangian Model, with L2 = 0.006 or 0.01 and L1 = 0, see Section 19.4.2).

Table 19-58 The expected number of events for the $W_L\ W_L$ signal and backgrounds after respective selection criteria and for an integrated luminosity of 300 fb^{-1}.

	Leptonic cuts	**Jet + leptonic cuts**	$m_{llνν}$**> 400 GeV**
Higgs m_H = 1 TeV	116	42.6	21.0
K-matrix	129	50.3	34.8
Chiral Lagrangian, L2 = 0.006	45	17.1	8.2
Chiral Lagrangian, L2 = 0.01	33.8	11.8	5.1
W_TW_T	648	76	14.5
Gluon exchange	127	1.35	0.54
Wt	281	0	0
WZ	555	1.2	0.3

19.5 Conclusions on the Higgs sector

The detailed studies described in this Chapter have demonstrated that the ATLAS detector has a large potential in the investigation of one of the key physics question at LHC, the origin of electroweak symmetry-breaking.

If a SM Higgs boson exists, discovery over the full mass range, from the LEP200 lower limit to the TeV scale will be possible after a few years of running at low luminosity.

- The most important channels in the intermediate mass region, $m_H < 2m_Z$, for which a mass peak would be reconstructed, are the four-lepton channel, $H \rightarrow ZZ^* \rightarrow 4l$, the direct two-photon channel, $H \rightarrow \gamma\gamma$, as well as the associated production channels, where the Higgs boson is produced in association with a vector boson or a $t\bar{t}$ pair. In these channels, both the γγ and $b\bar{b}$ decay modes can be discovered at the LHC. For Higgs-boson masses around 170 GeV, for which the ZZ^* branching ratio is suppressed, the discovery potential can be enhanced by searching for the $H \rightarrow WW^* \rightarrow l\nu l\nu$ decay. In this case, the Higgs-boson signal would only be observed as an excess of events.
- For $m_H > 2m_Z$ the dominant discovery channel is the four-lepton channel.
- In the mass range between 600 GeV and about 1 TeV, a Higgs boson would be discovered with the $WW \rightarrow l\nu jj$ mode. The sensitivity in this channel can also be extended down to lower masses, where it provides independent and complementary information to the four-lepton channel. For $400 < m_H < 900$ GeV the $H \rightarrow WW \rightarrow l\nu jj$ channel is complemented by the $H \rightarrow ZZ \rightarrow lljj$ and $H \rightarrow ZZ \rightarrow ll\nu\nu$ channels, which would provide additional robustness to a Higgs boson discovery in this mass range.

Over a large fraction of the mass range the discovery of a SM Higgs boson will be possible in two or more independent channels. It has also been shown that, if discovered, important Higgs-boson parameters like the mass and the width can be measured. Together with measurements of the production rates and some couplings and branching ratios they will provide useful constraints on the Higgs couplings to fermions and bosons which in turn can be used to test the Standard Model predictions and to determine the nature of the resonance.

The ATLAS experiment has also a large potential in the investigation of the MSSM Higgs sector. If the SUSY mass scale is large and supersymmetric particles do not appear in the Higgs decay products, the full parameter space in the conventional (m_A, tanβ) plane can be covered assuming an integrated luminosity of about 100 fb^{-1}.

- The interest was focused on the discovery potential of various decay modes accessible in the case of the SM Higgs boson: $h \to \gamma\gamma$, $h \to b\bar{b}$, $H \to ZZ \to 4l$, and of modes strongly enhanced at large *tan*β*: H/A* $\to \tau\tau$, *H/A* $\to \mu\mu$. Much attention was given to other potentially interesting channels such as: $H/A \to t\bar{t}$, $A \to Zh$, $H \to hh$, $H^{\pm} \to tb$.
- The overall discovery potential in the (m_A, tanβ) plane relies heavily on the $H/A \to \tau\tau$ channel, on the $t\bar{t}h$ with $h \to b\bar{b}$ and on the direct and associated $h \to \gamma\gamma$ channels.
- Over a large fraction of this parameter space more than one Higgs boson and / or more than one decay mode would be accessible.
- For almost all cases, the experiment would be able to distinguish between the SM and the MSSM models.

This complete coverage can also be reached independent on the mixing scenario in the stop-sbottom sector. The evidence for Higgs-boson signals would not constitute a direct proof of the existence of supersymmetry, unless supersymmetric particles are discovered themselves.

The interplay between SUSY particles and the Higgs sector has also been addressed. SUSY scenarios have an impact on the discovery potential through the opening of Higgs-boson decays to SUSY particles (mostly for *H* and *A*) and through the presence of SUSY particles in loops (mostly for production via *gg* fusion and for $h \to \gamma\gamma$ decays). Scenarios in which SUSY particles are light and appear as Higgs decay products have been studied in the framework of SUGRA models. The discovery potential of the lightest neutral Higgs *h* in the SM production processes would not be significantly different from what is obtained in the heavy SUSY scenario, since within the model, given present experimental constraints, the decay of *h* to the lightest SUSY particles is kinematically forbidden. Moreover, over a large fraction of the SUGRA parameter space, the *h*-boson would appear at the end of the decay cascade of SUSY particles in the channel $\tilde{\chi}_2^0 \to \tilde{\chi}_1^0 h$ which will be observable with the ATLAS detector. The neutral heavy Higgs bosons would be detected in some cases via their decays into neutralinos and charginos, using multi-lepton final states.

In the absence of a scalar Higgs boson, the principal probe for the mechanism of electroweak symmetry breaking will be gauge boson scattering at high energies. It has been shown that ATLAS will be sensitive to the presence of resonances, such as in the *WZ* system, up to masses around 1.5 TeV. Nonresonant processes, such as in the W^+W^+ production, will require a few years of high luminosity running and a good understanding of the underlying backgrounds.

Many scenarios discussed in this chapter have served as benchmark processes for optimising the detector design and performance. This includes the MSSM model, which should be considered as one theoretical model among many others, but one which provides a variety of signatures to test and to optimise the detector performance. The important detector requirements in

the investigation of electroweak symmetry breaking include electromagnetic calorimetry, jet-jet mass resolution in the reconstruction of multijet final states, good measurement of missing transverse energy, *b*-tagging, good electron, muon, tau and photon identification as well as forward jet tagging. The ATLAS detector in its final layout and optimisation is well matched to achieve the necessary requirements. It is also expected that the present design provides a firm basis for exploring areas of new and unexpected physics.

19.6 References

19-1 P.W. Higgs, Phys. Rev. Lett. **12** (1964) 132 and Phys. Rev. **145** (1966) 1156;
F. Englert and R. Brout, Phys. Rev. Lett. **13** (1964) 321;
G.S. Guralnik, C.R. Hagen and T.W. Kibble, Phys. Rev. Lett. **13** (1964) 585.

19-2 S. Glashow, Nuc. Phys. **22** (1961) 579;
S. Weinberg, Phys. Rev. Lett. **19** (1967) 1264; A. Salam, in: 'Elementary Particle Theory', W. Svartholm, ed., Almquist and Wiksell, Stockholm,1968;
H.D. Politzer, Phys. Rev. Lett. **30** (1973) 1346; D.J. Gross and F.E. Waltzed, Phys. Rev. Lett. **30** (1973)1343.

19-3 B.W. Lee *et al.*, Phys. Rev. Lett. **38** (1977) 883;
M. Quiros, 'Constraints on the Higgs boson properties from the effective potential', hep-ph/9703412;
A. Ghinculov and T. Binoth, Acta Phys. Polon. **B30** (1999) 99**.**

19-4 L. Maiani, G. Parisi and R. Petronzio, Nucl. Phys. **B136** (1979) 115;
N. Cabibbo *et al.* Nucl. Phys. **B158** (1979) 295;
R. Dashen and H. Neunberger, Phys. Rev. Lett. **50** (1983) 1897;
D.J.E. Callaway, Nucl. Phys. **B233** (1984) 189;
M.A. Beg *et al.*, Phys. Rev. Lett. **52** (1984) 883;
M. Linder, Z. Phys. **C31** (1986) 295.

19-5 G. Altarelli and G. Isidori, Phys. Lett. **B337** (1994) 141.
J.A. Casas, J.R. Espinosa and M. Quiros, Phys. Lett. **B342** (1995) 171; Phys. Lett. **B383** (1996) 374.

19-6 B. Grzadkowski and M. Linder, Phys. Lett. **B178** (1986) 81;
T. Hambye and K. Riesselmann, Phys. Rev. **D55** (1997) 7255.

19-7 The present LEP preliminary limits, presented at the 1999 winter conferences: ALEPH 99-007 CONF-99-003, March 1999; DELPHI 99-8 CONF-208; L3 Notes 2382,2383, March 1999; OPAL Note PN382, March 1999.

19-8 P. Janot, Proc. of the workshop on LEP-SPS performance, Chamonix IX, CERN-SL-99-007 DI (1999) and references therein.

19-9 The LEP Collaborations ALEPH, DELPHI, L3, OPAL, the LEP Electroweak Working Group and the Heavy Flavour and Electroweak Groups, CERN-EP/99-15.

19-10 For a review on the MSSM, see H. P. Nilles, Phys. Rep. **110** (1984) 1,
P. Nath, R. Arnowitt and A. Chamseed, *Applied N=1 Supergravity*, ICTP Series in Theoretical Physics, Vol. I (World Scientific, Singapore, 1984);
H.Haber and G. Kane, Phys. Rep. **117** (1985)

19-11 *E.g.* see 'Higgs Physics at LEP2', M. Carena, P. M. Zerwas (conv) *et al.*, Proceedings of the LEP2 Workshop, G. Altarelli, T. Sjöstrand and F. Zwirner (eds), CERN 1995.

19-12 S. Weinberg, Phys. Rev. **D13** (1979) 974, *ibid.* **D19** (1979) 1277;
L. Susskind, Phys. Rev. **D20** (1979) 2619.

19-13 ATLAS Letter of Intent, CERN / LHCC / 92-4, CERN 1992.

19-14 ATLAS Technical Proposal, CERN / LHCC 94-43, CERN 1994.

19-15 E.Richter-Was *et al.* 'Standard Model and Minimal Supersymmetric Standard Model Higgs rates and backgrounds in ATLAS', ATLAS Internal Note ATL-PHYS-95-048 (1995).

19-16 E. Richter-Was *et al.*, 'Minimal Supersymmetric Standard Model Higgs rates and backgrounds in ATLAS', ATLAS Internal Note ATL-PHYS-96-074 (1996), published in Int. J. Mod. Phys. **A13** (1998) 1371.

19-17 E. Richter-Was, D. Froidevaux and L. Poggioli, 'ATLFAST 2.0 a fast simulation package for ATLAS', ATLAS Internal Note, ATL-PHYS-98-131 (1998).

19-18 For a review see for example, M. Spira, Fortsch. Phys. **46** (1998) 203 and references therein.

19-19 M. Dittmar and H. Dreiner, Phys. Rev. **D55** (1997) 167; Contributed paper to the EPS Conference, hep-ph / 9703401.

19-20 A. Djouadi, J. Kalinowski and M. Spira, Comput. Phys. Commun. **108** (1998) 56.

19-21 ATLAS Collaboration, Calorimeter Performance Technical Design Report, CERN / LHCC 96-40 (1996).

19-22 V. Tisserand, 'The Higgs to Two Photon Decay in the ATLAS Detector', ATLAS Internal Note ATL-PHYS-96-090 (1996).

19-23 L. Fayard and G. Unal, 'Search for Higgs decays into photons with EAGLE', ATLAS Internal Note ATL-PHYS-92-001 and Addenda 1&2 (1992).

19-24 P. Aurenche *et al.*, in Proc. Large Hadron Collider Workshop, Aachen, 1990, edited by G. Jarlskog and D. Rein, CERN 90-10 / ECFA 90-133.

19-25 E. Richter-Was, 'Hard photon bremsstrahlung in the process $pp \rightarrow Z/\gamma^* \rightarrow l^+l^-$: a background for the intermediate mass Higgs' ATLAS Internal Note ATL-PHYS-94-034, published in Z. Phys. **C61** (1994) 323.

19-26 G. Eynard, 'Etude de la production associee du boson de Higgs WH, $t\bar{t}H$, ZH with $H \rightarrow \gamma\gamma$ avec le detecteur ATLAS, aupres du LHC', ATLAS Ph. D. Thesis 1997, LAPP Annecy.

19-27 E. Barberio and Z. Was, Comput. Phys. Commun. **79** (1994) 291; E. Barberio, B. van Eijk and Z. Was, Comput. Phys. Commun. **66** (1991) 115.

19-28 CMS Technical Proposal, CERN / LHCC 94-38, CERN 1994.

19-29 S. Abdulin *et al.*, INP MSU 98-13 / 514 (1998).

19-30 S. Zmushko,' Search for $H \rightarrow \gamma\gamma$ in association with jets', ATLAS Communication ATL-COM-PHYS-99-040 (1999).

19-31 R.K. Ellis, I. Hinchliffe, M. Soldate and J.J. van der Bij, Nucl. Phys. **B297** (1988) 221.

19-32 S. Kiourkos and J. Schwindling, 'H $\rightarrow$ Zγ channel in ATLAS. A study on the Standard Model and Minimal Supersymmetric SM case', ATLAS Communication ATL-COM-PHYS-99-009 (1999).

19-33 A. Stange, W. Marciano and S. Willenbrock, Phys. Rev. **D50** (1994); J. F. Gunion and T. Han, Phys. Rev. **D51** (1995) 1051.

19-34 D. Froidevaux and E. Richter-Was, 'Is the channel $H \to b\bar{b}$ observable at LHC ?', ATLAS Internal Note ATL-PHYS-94-043 (1994), published in Z. Phys. **C67** (1995) 213.

19-35 E. Richter-Was and M. Sapinski, 'Search for the SM and MSSM Higgs boson in the $t\bar{t}H$, $H \to b\bar{b}$ channel', ATLAS Internal Note ATL-PHYS-98-132 (1998), published in Acta Phys. Polon. **B30** (1999) 1001.

19-36 B.J. Dick, 'Further work on WH, $H \to b\bar{b}$', ATLAS Communication ATL-COM-PHYS-99-019 (1999).

19-37 B. van Eijk, R. Kleiss, in [19-130], vol. II, p. 183.

19-38 L. Guyot, D. Froidevaux and L. Poggioli, 'Physics Performance for Various Muon System Configurations', ATLAS Internal Note ATL-PHYS-95-076, (1995).

19-39 O. Linossier and L. Poggioli, 'Final state inner-Bremsstrahlung effects on $H \to ZZ^* \to 4l$ channel with ATLAS', ATLAS Internal Note ATL-PHYS-95-075, (1995).

19-40 O. Linossier and L. Poggioli,'H to ZZ^* to 4 leptons channel in ATLAS. Signal reconstruction and reducible backgrounds rejection ', ATLAS Internal Note ATL-PHYS-97-101, (1997).

19-41 I. Gavrilenko, 'Description of Global Patern Recongnition Program (xKalman)', ATLAS Internal Note ATL-INDET-97-165 (1997).

19-42 K. Jakobs and T. Trefzger, 'SM Higgs Searches for $H \to WW^* \to l\nu l\nu$ with a mass between 150-190 GeV at LHC', ATLAS Communications, ATL-PHYS-COM-99-031 (1999).

19-43 C.A. Nelson Phys. Rev. **D37** (1988) 1220).

19-44 H. Baer and J. D. Wells, Phys. Rev. **D57** (1998) 4446.

19-45 K. Jakobs, 'A study of the associated production WH, $H \to WW \to l\nu l\nu$', ATLAS Communication ATL-PHYS-COM-99-062 (1999); W. Bonivento, 'Higgs search in trilepton signal', ATLAS Communication ATL-PHYS-COM-99-046 (1999).

19-46 T. Han *et al.*, Phys. Rev. **D59** (1998).

19-47 Report of the Physics at RUN II Supersymmetry / Higgs Workshop, Fermilab,1999, eds. M. Carena and J. Lykken, in preparation; J. Conway, 'Higgs discovery potential in Run 2 at Tevatron', conference talks, La Thuile, 3 March 1999; Sitges, 30 April 1999; M. Carena, conference talk, PLANCK'99, 19 April, 1999.

19-48 D. Froidevaux *et al.*, 'Comparison of the physics potential of the ATLAS detector for searches for the intermediate Higgs boson in pp collision as $\sqrt{s}$ = 14 TeV and $p\bar{p}$ collision at $\sqrt{s}$ = 2 TeV', ATLAS Communication ATL-COM-PHYS-99-058.

19-49 U. Baur and E.W.N Glover, in [19-130], Vol. II, p.570.

19-50 R.H. Cahn *et al.*, Phys. Rev. **D35** (1987) 1626.

19-51 I. Zuckerman *et al.*,'MC simulation of backgrounds to the $H \to ZZ \to ll\nu\nu$ signal at the LHC', ATLAS Internal Note ATL-PHYS-92-007 (1992).

19-52 M. Bosman and M. Nessi, 'Study of *Z+jets* background to $H \to ZZ \to ll\nu\nu$ signal using full simulation of ATLAS calorimetry', ATLAS Internal Note ATL-PHYS-94-050, 1995.

19-53 H. Ruiz, 'Discovery potential of a heavy Standard Model Higgs boson through the $H \to ZZ \to ll\nu\nu$ channel at the LHC with the ATLAS detector', ATLAS Communication ATL-COM-PHYS-99-031 (1999).

19-54 P. Savard and G. Azuelos, 'The discovery potential of a Heavy Higgs (m_H= 800 GeV) using full GEANT simulation of ATLAS', ATLAS Internal Note ATL-PHYS-98-128 (1998).

19-55 S. Zmushko *et al.*, 'Study of $H \rightarrow WW \rightarrow l\nu jj$ and $H \rightarrow ZZ \rightarrow lljj$ decays for m_H = 1 TeV', ATLAS Internal Note ATL-PHYS-92-008 (1992).

19-56 M. Cobal *et al.*,' VECBOS: a Lowest Order Matrix Element Calculation to simulate direct QCD W + n jet events', ATLAS Internal Note ATL-PHYS-96-084 (1996).

19-57 V. Cavasinni *et al.*, 'Search for $H \rightarrow WW \rightarrow l\nu jj$ with the ATLAS detector (m_H= 300-600 GeV)', ATLAS Internal Note ATL-PHYS-98-127 (1998).

19-58 F. Gianotti, 'Precision physics at LHC', ATLAS Internal Note ATL-PHYS-99-001 (1999).

19-59 J.F. Gunion *et al.*, 'Higgs boson discovery and properties', Snowmass 96, hep-ph/9703330.

19-60 F. Abe *et al.*, CDF Collaboration, Phys. Rev. **D52** (1995) 4784.

19-61 J.F. Gunion, A. Stange, S. Willenbrock, 'Weakly Coupled Higgs boson', hep-ph/9602238

19-62 M. Kramer *et al.*, Z. Phys. **C64** (1994) 21.

19-63 E. Richter-Was, 'A first look at the Higgs spin determination with ATLAS', ATLAS Communication ATL-COM-PHYS-99-051 (1999).

19-64 J.F. Gunion and X-G. He, Phys.Rev.Lett.**76** (1996) 4468.

19-65 S. P. Li and M. Sher, Phys. Lett. **140B** (1984) 339;
Y. Okada, M. Yamaguchi and T. Yanagida, Prog. Theor. **85** (1991) 1;
H. E. Haber and R. Hempfling, Phys. Rev. Lett. **66** (1991) 1815;
P. Chankowski, S. Pokorski and J. Rosiek, Phys. Lett. **274B** (1992) 191; and Nucl. Phys. **B423** (1994) 437;
R. Hempfling and A. H. Hoang, Phys. Lett. **331B** (1994) 99;
J. Ellis, G. Ridolfi and F. Zwirner, Phys. Lett **257B** (1991) 83; and Phys. Lett **262B** (1991) 477.

19-66 J. Ellis, G. Ridolfi and F. Zwirner, Phys. Lett. **271B** (1991) 123;
M. Dress and M. Noijiri, Phys. Rev. **D45** (1992) 2482.

19-67 J. Kodaira, Y. Yasui and K. Sasaki, Phys. Rev. **D50** (1994) 7035. J. A. Casas, J.R. Espinosa, M. Quiros and A. Riotto, Nucl. Phys. **B436** (1995) 3.

19-68 M. Carena, J.R. Espinosa, M. Quiros and C.E.M. Wagner, Phys. Lett **355B** (1995) 209.

19-69 I. Dai, J. F. Gunion and R. Vega, Phys. Lett. **B315** (1993) 355. J. F. Gunion and L. Ohr, Phys. Rev. **D46** (1992) 2052; J. F. Gunion, in 'Perspectives on Higgs Physics', edited by G. Kane (World Scientific, Singapore, 1992) and references therein;
J. F. Gunion, R. Bork, H. E. Haber and A. Seiden, Phys. Rev. **D46** (1992) 2040;
J. F. Gunion, H. E. Haber C. Kao, Phys. Rev. **D46** (1992) 2907.

19-70 E. Richter-Was and D. Froidevaux, 'MSSM Higgs bosons in SUGRA model: observability in SM decay modes with ATLAS', ATLAS Communication ATL-COM-98-012 (1998).

19-71 L. Alvarez-Gaume, J. Polchinski, and M.B. Wise, Nucl. Phys. **B221** (1983) 495;
L. Ibanez, Phys. Lett. **118B** (1982) 73;
J. Ellis, D.V. Nanopolous, and K. Tamvakis, Phys. Lett. **121B** (1983) 123; K. Inoue *et al.*, Prog. Theor. Phys. **68** (1982) 927;
A.H. Chamseddine, R. Arnowitt, and P. Nath, Phys. Rev. Lett. **49** (1982) 970

19-72 The CDF Collaboration, W. Yao, 'Top mass at CDF', talk presented at ICHEP 98, Vancouver, B. C. Canada, 23-29 July, 1998.
The D0 Collaboration, B. Abbott *et al.*, Phys. Rev. **D58** (1998) 5201.

19-73 B. Kileng, Z. Phys. **C63** (1994) 87; B. Kileng *et al.*, Z. Phys. **C71 (1996)** 87.

19-74 D. Rainwater, D. Zeppenfeld, Phys. Rev. **D59** (1999) 14037.

19-75 L. Di Lella in [19-130], Vol. II, p.530.

19-76 D. Cavalli *et al.*, 'Search for $H/A \rightarrow \tau\tau$ decays', ATLAS Internal Note ATL-PHYS-94-051 (1994).

19-77 D. Cavalli and S. Resconi, 'Tau-jet separation in ATLAS detector ', ATLAS Internal Note ATL-PHYS-No-98-118 (1998).

19-78 D. Cavalli and S. Resconi, 'Combined Analysis of $A \rightarrow \tau\tau$ Events from Direct and Associated $b\bar{b}A$ Production ', ATLAS Communication ATL-COM-PHYS-99-010 (1999).

19-79 D. Cavalli and P. Bosatelli, 'Combined Analysis of $H/A \rightarrow \mu\mu$ Events from Direct and Associated $b\bar{b}A$ / $b\bar{b}H$ Production', ATLAS Communication, ATL-COM-PHYS-99-053 (1999).

19-80 K.J.F. Gaemers and G. Hoogeveen, Phys Lett. **146B** (1984) 347; D. Dicus, A. Stange and S. Willenbrock, Phys. Lett. **B333** (1994) 126.

19-81 S. Gonzalez de la Hoz, 'MSSM Higgs decay to top quarks', ATLAS Communication ATL-COM-PHYS-99-016 (1999).

19-82 J. Dai, J. F. Gunion and R. Vega, Phys. Lett. **B345** (1995) 29, Phys. Lett **B387** (1996) 801.

19-83 ATLAS Trigger performance Status Report, CERN-LHCC / 98-15 (1998).

19-84 ATLAS Collaboration, Inner Detector Technical Design Report, Volume I, CERN / LHCC / 97-16 (1997).

19-85 ATLAS Collaboration, Pixel Detector Technical Design Report, CERN / LHCC / 98-13 (1998).

19-86 E. Richter-Was and D. Froidevaux, 'MSSM Higgs searches in multi-b-jet final states', ATLAS Internal Note ATL-PHYS-97-104 (1997), published in Z. Phys. **C76** (1997) 665.

19-87 D. Cavalli and M. Sapinski, 'Full and fast simulation and reconstruction of Higgs decay channels with multi-b-jet final states', ATLAS Communication ATL-PHYS-COM-99-033 (1999).

19-88 J. Gunion, H. E. Haber, F. Paige, Wu-ki Tung and S. S. D.Willenbrock, Nucl. Phys. **B294** (1987) 621;
S. Moretti and K. Odagiri, Phys. Rev. **D55** (1997) 5627.

19-89 A. Djouadi, J. Kalinowski and M.P. Zerwas, Z. Phys. **C57** (1993) 569; Z. Phys. **C70** (1996**)** 435.

19-90 D. Cavalli *et al.*, 'Search for $H^{\pm} \rightarrow \tau\nu$ decays', ATLAS Internal Note ATL-PHYS-94-53 (1994).

19-91 UA2 Collaboration, Phys. Lett. **B280** (1992) 137.

19-92 K. Assamagan, 'The Charged Higgs in Hadronic Decays with the ATLAS Detector', ATLAS Communication ATL-COM-PHYS-99-030 (1999).

19-93 R.M. Barnett, H. E. Haber and D. E. Soper, Nucl. Phys **B306** (1988) 697.

19-94 S. Moretti and K. Odagiri, Phys. Rev. **D55** (1997) 55.

19-95 H. Baer, B. W. Harris and X. Tata, Phys. Rev. **D59** (1999) 15003; M. Carena, S. Mrenna and C.E.M. Wagner,' MSSM Higgs boson phenomenology at the Tevatron collider', ANL-HEP-PR-98-54, hep-9808312.

19-96 M. Quiros and J. R. Espinosa, 'What is the upper limit on the lightest supersymmetric Higgs mass?', CERN preprint CERN-TH-98-292 (1998), hep-ph / 9809269.

19-97 V. Mitsou, 'Precision measurements in MSSM with ATLAS', ATLAS Communication ATL-COM-PHYS-99-035 (1999).

19-98 W. Hollik, 29th International Conference on High-Energy Physics (ICHEP 98), Vancouver, British Columbia, Canada, July 23-30, 1998.

19-99 D. Froidevaux *et al.*,'Precision SUSY measurements with ATLAS: Extraction of SUGRA model parameters and conclusions', ATLAS Internal Note ATL-PHYS-97-112 (1997).

19-100 H. Baer, M. Bisset, X. Tata J. Woodside, Phys. Rev. **D46** (1992) 46.

19-101 G.L. Kane, G.D. Kribs, S.P. Martin, J.D. Wells, Phys. Rev. **D50** (1996) 213.

19-102 H. Baer, D. Dicus, M. Drees and X. Tata, Phys. Rev. **D36** (1987) 1363;
K. Griest and H. Haber, Phys. Tev. **D37** (1986) 719;
D. Choudhury, D. P. Roy, Phys. Lett. **B322** (1994) 368;
J. F. Gunion, Phys. Rev. Lett. **72** (1994) 199;
H. Baer, M. Bisset, C. Kao, X. Tata, Phys. Rev. **D50** (1994) 316.

19-103 E. Richter-Was, D. Froidevaux and J. Soderqvist, 'Precision SUSY measurements with ATLAS for SUGRA points 1 and 2', ATLAS Internal Note ATL-PHYS-97-108 (1997).

19-104 G. Polesello, L. Poggioli, E. Richter-Was and J. Soderqvist, 'Precision SUSY measurements with ATLAS for SUGRA point 5', ATLAS Internal Note ATL-PHYS-97-111 (1997).

19-105 J. Erler and D.M. Pierce, Nucl. Phys. **B526** (1998) 53.

19-106 S. Zmushko *et al.*, 'Search for the heavy Higgs in SUGRA point3', ATLAS Communication ATL-COM-PHYS-98-009 (1998).

19-107 F. Paige and Protopopescu, in Supercollider Physics, p.41, editor D. Soper, World Scientific Singapore, 1986.

19-108 I. Hinchliffe et al, 'Precision SUSY Measurements with ATLAS: Introduction and Inclusive Measurements', ATLAS Internal Note ATL-PHYS-97-107; 'Precision SUSY measurements at LHC: Point 3*', ATLAS Internal Note ATL-PHYS-97-109 (1997).

19-109 S. Zmushko et al, 'The $H \rightarrow \chi\chi \rightarrow 4l\ X$ observability with ATLAS (predictions within SUGRA model)', ATLAS Communication ATL-COM-PHYS-99-005 (1999).

19-110 S. Zmushko, D. Froidevaux and L. Poggioli,' $H \rightarrow WW \rightarrow l\nu jj$ and $H \rightarrow ZZ \rightarrow lljj$ Particle level studies', ATLAS Internal Note ATL-PHYS-97-103 (1997).

19-111 V. Mitsou, 'Observability of $h \rightarrow b\bar{b}$ in SUSY cascade in SUGRA parameter space', ATLAS Communication ATL-COM-PHYS-99-036 (1999).

19-112 T. Sjostrand, Comput.Phys.Commun. **82** (1994) 74. The supersymmetry extensions are described in S. Mrenna, Computer Physics Commun. **101** (1997) 232.

19-113 R.S. Chivukula, 'NATO Advanced Study Institute on Quantum Field Theory Since 1970: Perspective and Prospectives', Les Houches, 1998 (hep-ph/9803219).

19-114 R.S. Chivukula *et al.*, 'Strongly coupled electroweak symmetry breaking: implication of models', published in Electroweak Symmetry Breaking and New Physics at the TeV Scale, World Scientific, 2996, hep-ph/9503202;
T. Barklow, ed.; C.P. Yan, 'Proposals for studying TeV $W_L W_L \rightarrow W_L W_L$ interactions experimentaly', hep-ph/9712513,
M. Chanowitz, 'Strong WW scattering at the end of the 90's: theory and experimental prospects', hep-ph/9812215.

19-115 V. Barger, K. Cheung, A. Djouadi, B. A. Kniehl and P. M. Zerwas, Phys.Rev.**D49** (1994) 79.

19-116 S.Weinberg, Physica **96A** (1979) 327; J. Gasser and H. Leutwyler, Ann. of Phys. **158** (1984) 142; Nucl. Phys. **B250** (1985) 465 and 517.

19-117 A. Dobado and M.J. Herrero, Phys. Lett. **B228** (1989) 495 and **B233** (1989) 505; J. Donoghue and C. Ramirez, Phys. Lett. **B234** (1990) 361.

19-118 T. Appelquist and C. Bernard, Phys. Rev. **D22** (1980) 200, A. C. Longhitano, Nucl. Phys. **B188** (1981) 118.

19-119 M. Golden et al, UCD-95-32, hep-ph/9511206.

19-120 Tran N. Truong, Phys. Rev. Lett. **61** (1988) 2526; *ibid* **D67** (1991) 2260.

19-121 A. Dobado, M.J. Herrero and T.N. Truong, Phys.Lett **B235** (1990) 134.

19-122 A. Dobado and J.R. Pelaez, hep-ph/9604416.

19-123 J.R. Pelaez, Phys. Rev. **D55** (1997) 4193.

19-124 A. Miagkov, 'Vector boson scattering in Chiral Lagrangian model', ATLAS Internal Note ATL-PHYS-99-006 (1999).

19-125 V. Barger, K. Cheung, T. Han and R.J.N. Phillips, Phys. Rev. **D42** (1990) 3052.

19-126 J. Bagger *et al.*, Phys. Rev. **D52** (1995) 3878.

19-127 M.S. Chanowitz and W. Kilgore, Phys. Lett. **B322** (1994) 147.

19-128 G. Azuelos, A. Miagkov and R. Mazini, 'Measuring the rate of non-resonant high mass longitudinal gauge boson pairs in ATLAS', ATLAS Communication ATL-COM-PHYS-99-048.

19-129 M.S. Chanowitz, private communication.

19-130 Proceedings of the Large Hadron Collider Workshop, Aachen, 1990, edited by G. Jarlskog and D. Rein, CERN 90-10/ECFA 90-133.

20 Supersymmetry

20.1 Introduction

Supersymmetry – or SUSY – is one of the best motivated extensions of the Standard Model, so the study of SUSY is a primary goal of the LHC. If SUSY exists at the weak scale, $M \sim 1\text{TeV}$, then discovering evidence for SUSY particles at the LHC seems to be straightforward. Therefore, ATLAS has concentrated on the problems of making precision measurements of SUSY masses (or combinations thereof) and of using these to infer properties of the underlying SUSY model.

While the Standard Model has been tested to an accuracy of order 0.1% [20-1], the Higgs sector responsible for generating the masses of the W and Z bosons and of the quarks and leptons has not been tested yet. The Higgs boson is the only scalar field in the Standard Model. Scalar fields are special in that loop corrections to their squared masses are quadratically divergent: they are proportional to the cutoff Λ^2, while all other divergences are proportional only to $\log\Lambda^2$. Some new mass scale beyond the Standard Model must exist, if only the reduced Planck scale $M_P = (8\pi G_{\text{Newton}})^{-1/2} = 2.4 \times 10^{18}$ GeV associated with gravity, and the loop corrections to the Higgs mass are naturally of order this scale. This is known as the hierarchy problem [20-2]. The only known solutions – other than accepting an incredible fine tuning – are to embed the Higgs bosons in a supersymmetric theory or to replace the elementary Higgs boson with a dynamical condensate as in technicolor models.

SUSY [20-3, 20-4] is the maximal possible extension of the Lorentz group. It has fermionic generators $Q, \bar{Q}$ which satisfy

$$\{Q, \bar{Q}\} = -2\gamma_\mu P^\mu$$

$$[Q, P^\mu] = \{Q, Q\} = \{\bar{Q}, \bar{Q}\} = 0$$

where P^μ is the momentum operator and γ_μ are the Dirac matrices. SUSY therefore relates particles with the same mass and other quantum numbers differing by $\pm 1/2$ unit of spin,

$$Q|\text{boson}\rangle = |\text{fermion}\rangle, \qquad Q|\text{fermion}\rangle = |\text{boson}\rangle\,.$$

In the Minimal Supersymmetric extension of the Standard Model (MSSM) each chiral fermion $f_{L,R}$ has a scalar sfermion partner $\tilde{f}_{L,R}$, and each massless gauge boson A_μ with two helicity states ± 1 has a massless spin-$1/2$ gaugino partner with helicities $\pm 1/2$. There must also be two complex Higgs doublets and their associated Higgsinos to avoid triangle anomalies. The complete list of particles is shown in Tables 20-1 and 20-2. The interactions of SUSY particles are basically obtained from the Standard Model ones by replacing any two lines in a vertex by their SUSY partners; for example, the gluon-quark-quark and gluino-quark-squark couplings are the same. See [20-4] for the construction of the complete Lagrangian.

SUSY provides a solution to the hierarchy problem because it implies an equal number of bosons and fermions, which give opposite signs in loops and so cancel the quadratic divergences. This cancellation works to all orders: since the masses of fermions are only logarithmic divergent, this must also be true for boson masses in a supersymmetric theory. When SUSY is broken,

Table 20-1 Chiral supermultiplets in the Minimal Supersymmetric Standard Model. The squarks and sleptons come in three generations. The physical Higgs bosons after symmetry breaking are h, H, A, and $H^{\pm}$.

Name	Spin 0	Spin 1/2	$SU(3)\times SU(2)\times U(1)$
squarks, quarks	$\tilde{Q} = (\tilde{u}_L, \tilde{d}_L)$	$Q = (u_L, d_L)$	$(3, 2, 1/6)$
	$\tilde{u}_R^*$	$\bar{u}_R$	$(\bar{3}, 1, -2/3)$
	$\tilde{d}_R^*$	$\bar{d}_R$	$(\bar{3}, 1, 1/3)$
sleptons, leptons	$\tilde{L} = (\tilde{\nu}, \tilde{e}_L)$	$L = (\nu, e_L)$	$(1, 2, -1/2)$
	$\tilde{e}_R^*$	$\bar{e}_R$	$(1, 1, 1)$
Higgs, Higgsinos	$H_u = (H_u^+, H_u^0)$	$\tilde{H}_u = (\tilde{H}_u^+, \tilde{H}_u^0)$	$(1, 2, 1/2)$
	$H_d = (H_d^0, H_d^-)$	$\tilde{H}_d = (\tilde{H}_d^0, \tilde{H}_d^-)$	$(1, 2, -1/2)$

Table 20-2 Vector supermultiplets in the Minimal Supersymmetric Standard Model. After symmetry breaking, the winos and bino mix with the Higgsinos to give four neutralinos $\tilde{\chi}_i^0$ and two charginos $\tilde{\chi}_i^{\pm}$, and the W^0 and B mix as in the Standard Model.

Names	Spin 1/2	Spin 1	$SU(3)\times SU(2)\times U(1)$
gluino, gluon	$\tilde{g}$	g	$(8, 1, 0)$
winos, W's	$\tilde{W}^{\pm}, \tilde{W}^0$	$W^{\pm}, W^0$	$(1, 3, 0)$
bino, B	$\tilde{B}$	B	$(1, 1, 1)$

the corrections to the Higgs and other scalar masses become proportional to the SUSY mass scale rather than the Planck scale. If the Higgs is to be light without unnatural fine tuning, then the SUSY particles should have masses below about 1 TeV [20-5].

The particle content of the Standard Model is elegantly explained by Grand Unified Theories (GUT's), in which the $SU(3)$, $SU(2)$, and $U(1)$ gauge interactions all unify in a simple group such as $SU(5)$. This requires that their respective coupling constants all meet when evolved under the Renormalisation Group Equations (RGE's) to some high mass scale. The precision data at the Z mass collected at LEP and SLC are inconsistent with GUT's using the Standard Model RGE's but are consistent using the SUSY ones provided that the SUSY mass scale is in the 1 TeV range [20-1]. SUSY particles in this mass range are consistent with present direct [20-6, 20-7] and indirect [20-8] limits and with the constraints of fine tuning, and they would be readily observable at the LHC.

SUSY must of course be broken, since superparticles have not been observed: there is certainly no spin-0 selectron degenerate with the electron. Gauge invariance forbids mass terms in the Lagrangian for all Standard Model particles; masses can be introduced only by spontaneous symmetry breaking using the Higgs mechanism. In contrast, mass terms are allowed for all the SUSY particles. Thus, it is possible to parameterise SUSY breaking by introducing by hand SUSY-breaking mass terms for the squarks, sleptons, Higgsinos, and gauginos, all presumably at the TeV scale. Additional soft terms (bilinear B terms and trilinear A terms with dimension $d < 4$) consistent with gauge invariance can also be added without reintroducing quadratic divergences. Finally, a Higgsino mass term μ must be included; this must be of the same order as the SUSY breaking terms even though it is SUSY conserving.

The requirements of gauge invariance and renormalisability are sufficient to guarantee that the Standard Model Lagrangian conserves baryon and lepton number. In supersymmetric theories it is possible to violate both, potentially leading to disastrous weak-scale proton decay. The unwanted terms can be eliminated by imposing invariance under R-parity,

$$R = (-1)^{3(B-L)+2S},$$

where B, L, and S are the baryon number, lepton number, and spin. Hence $R = +1$ for all Standard Model particles and $R = -1$ for all SUSY particles. This has the consequence that SUSY particles must be produced in pairs and that the lightest SUSY particle (LSP) is absolutely stable. R-parity conservation holds automatically in many GUT models under rather general assumptions [20-9]. Weak-scale proton decay can also be avoided by imposing either baryon or lepton number conservation.

The Minimal Supersymmetric Standard Model (MSSM) is the supersymmetric extension of the Standard Model with the minimal particle content as listed in Tables 20-1 and 20-2 and R-parity conservation. The cancellation of quadratic divergences for scalar masses only requires supersymmetry for the terms with mass dimension four. In the MSSM, SUSY is broken 'by hand' by adding to the Lagrangian all possible soft terms consistent with $SU(3)\times SU(2)\times U(1)$ gauge invariance [20-4]. This includes mass terms for all the superpartners and trilinear A terms:

$$\begin{aligned}
L_{\text{soft}} = & -m_{H_d}^2|H_d|^2 - m_{H_u}^2|H_u|^2 + \mu B\varepsilon_{ij}(H_d^i H_u^j + h.c.) \\
& -\frac{1}{2}M_1\tilde{\bar{B}}\tilde{B} - \frac{1}{2}M_2\tilde{\bar{W}}\tilde{W} - \frac{1}{2}M_3\tilde{\bar{g}}\tilde{g} \\
& -M_Q^2(\tilde{u}_L^*\tilde{u}_L + \tilde{d}_L^*\tilde{d}_L) - M_U^2 u_R^* u_R - M_D^2\tilde{d}_R^*\tilde{d}_R \\
& -M_L^2(\tilde{l}_L^*\tilde{l}_L + \tilde{\nu}_L^*\tilde{\nu}_L) - M_E^2\tilde{l}_R^*\tilde{l}_R \\
& -\varepsilon_{ij}(-\lambda_u A_u H_u^i \tilde{Q}^j\tilde{u}_R^* + \lambda_d A_D H_d^i\tilde{Q}^j\tilde{d}_R^* + \lambda_l A_E H_d^i\tilde{L}^j\tilde{l}_R^*)
\end{aligned}$$

where Q, L, H_u, and H_d denote $SU(2)$ weak doublets as in Table 20-1 and a summation over generations is implied. All the parameters are in general matrices in flavour space and complex; there are a total of 105 new parameters [20-10] in addition to the Standard Model ones. One of these is the SUSY-conserving Higgsino mass μ, which must be of the same order as the SUSY breaking masses. Electroweak symmetry cannot be broken by hand in a similar way, since this would destroy gauge invariance. Instead, it is broken by the Higgs mechanism, giving rise to masses for the quarks, leptons, W and Z bosons. Supersymmetry requires two Higgs doublets and relates the Higgs self-coupling to gauge couplings:

$$\begin{aligned}
V_{\text{Higgs}} = & (m_{H_d}^2 + \mu^2)|H_d|^2 + (m_{H_u}^2 + \mu^2)|H_u|^2 - B\mu(\varepsilon_{ij}H_d^i H_u^j + h.c.) \\
& +\frac{1}{8}(g^2 + g'^2)(|H_d|^2 - |H_u|^2)^2 + \frac{1}{2}g^2|H_d^{i*}H_u^i|^2
\end{aligned}$$

It will be seen in Section 20.2 that the large top Yukawa coupling λ_t can naturally drive the Higgs squared mass negative, breaking electroweak symmetry.

Once SUSY and electroweak symmetry are broken, particles with the same quantum numbers will in general mix. The gauginos and Higgsinos mix to form two spin-1/2 'charginos' $\tilde{\chi}_i^{\pm}$ with the mass matrix in the $(\tilde{W}^+, \tilde{H}^+)$ basis

$$M_{\chi^+} = \begin{bmatrix} m_2 & \sqrt{2}M_W \sin\beta \\ \sqrt{2}M_W \cos\beta & \mu \end{bmatrix} \qquad 20\text{-}1$$

and four spin-1/2 'neutralinos' $\tilde{\chi}_i^0$ with the mass matrix in the (B, W^0, H_d, H_u) basis

$$M_{\chi^0} = \begin{bmatrix} m_1 & 0 & -M_Z \cos\beta \sin\theta_W & M_Z \sin\beta \sin\theta_W \\ 0 & m_2 & M_Z \cos\beta \cos\theta_W & -M_Z \sin\beta \cos\theta_W \\ -M_Z \cos\beta \sin\theta_W & M_Z \cos\beta \cos\theta_W & 0 & -\mu \\ M_Z \sin\beta \sin\theta_W & -M_Z \sin\beta \cos\theta_W & -\mu & 0 \end{bmatrix}. \qquad 20\text{-}2$$

In many models

$$\frac{M_1}{\alpha_1} \approx \frac{M_2}{\alpha_2} \approx \frac{M_3}{\alpha_s}$$

and μ is of order $M_{\tilde{g}}$, so that the two lighter neutralinos and the lighter chargino are dominantly gaugino, while the heavier states are dominantly Higgsino and weakly coupled to the first two generations.

While the chiral fermions f_L and f_R must have the same mass by Lorentz invariance, their superpartners $\tilde{f}_L$ and $\tilde{f}_R$ are scalars with separate masses. Their squared-mass matrix also gets off-diagonal contributions proportional to the fermion mass, *e.g.*

$$M_{\tilde{t}}^2 = \begin{bmatrix} M_{\tilde{Q}}^2 + m_t^2 + \frac{1}{6}(4M_W^2 - M_Z^2)\cos 2\beta & -m_t(A_t - \mu \cot\beta) \\ -m_t(A_t - \mu \cot\beta) & M_{\tilde{t}_R}^2 + m_t^2 - \frac{2}{3}(M_W^2 - M_Z^2)\cos 2\beta \end{bmatrix}. \qquad 20\text{-}3$$

The resulting left-right mixing is mainly important for the third generation; the eigenstates are called $\tilde{t}_{1,2}$, $\tilde{b}_{1,2}$, and $\tilde{\tau}_{1,2}$. There can also be mixings among generations of sfermions – including new sources of *CP* violation. For simplicity all flavour mixing and *L*-*R* mixing for the first two generations and all *CP*-violating phases will be ignored here.

Clearly it is not possible to explore the complete parameter space of the MSSM; in the absence of experimental help some theoretical prejudice must be imposed. Presumably supersymmetry should be broken spontaneously rather than by hand and should be unified with gravity. It does not seem possible to construct a phenomenologically acceptable model with spontaneous supersymmetry breaking using only the MSSM fields. Instead, it is necessary to introduce a hidden sector to break SUSY and then to communicate the breaking to the MSSM sector using some messenger interaction that couples to both. In supergravity (SUGRA) models gravity is the sole messenger [20-11]. Then the MSSM masses are scaled by the Planck scale,

$$M_{\text{MSSM}} \sim \frac{F}{M_P},$$

so the SUSY breaking scale in the hidden sector must be roughly $F \sim (10^{11}\,\text{GeV})^2$. In the minimal SUGRA model, it is assumed that all squarks, sleptons, and Higgs bosons have a common mass m_0 and that all gauginos have a common mass $m_{1/2}$ at the GUT scale. These masses are split when they are run down to the weak scale with the RGE's [20-12]. The squarks and gluinos

are relatively heavy but nevertheless dominate the SUSY production cross section at LHC energies because of their strong couplings. They typically decay via several steps into the lightest SUSY particle (LSP) $\tilde{\chi}_1^0$, which is stable. Since the LSP is neutral and weakly interacting, it escapes the detector, giving the characteristic SUSY signature of missing transverse energy E_T^{miss}. Signatures for SUGRA models are discussed in Section 20.2.

It is also possible that the SUSY breaking scale in the hidden sector is $F_m \ll (10^{11}\ \text{GeV})^2$ and that the MSSM particles get masses through $SU(3) \times SU(2) \times U(1)$ gauge interactions at a messenger scale $M_m \ll M_P$. This is known as Gauge Mediated Supersymmetry Breaking (GMSB) [20-13]. Since the gravitino $\tilde{G}$ gets its mass only through gravitational interactions, it is much lighter than all the MSSM particles, which eventually decay into it. In the minimal GMSB model the MSSM masses are proportional to $\Lambda \equiv F_m / M_m$; the gaugino masses are proportional to the number of messenger fields N_5, while the scalar masses are proportional to $\sqrt{N_5}$. The phenomenology is determined by whether the next lightest SUSY particle (NLSP) is a $\tilde{\chi}_1^0$ or a $\tilde{\tau}_1$ and by whether the NLSP decay $\tilde{\chi}_1^0 \to \tilde{G}\gamma$ or $\tilde{\tau}_1 \to \tilde{G}\tau$ occurs promptly or outside the detector. Signatures for the long-lived $\tilde{\chi}_1^0$ case are qualitatively similar to those for SUGRA, but the other three cases are quite different. Signatures for the minimal GMSB model are discussed in Section 20.3.

Finally, *R* parity may be broken, although there are strong constraints on many of the *R*-violating couplings [20-14]. If the *R*-violating couplings are small, then the main effect is to allow the LSP to decay, violating either baryon number, *e.g.* $\tilde{\chi}_1^0 \to qqq$, or lepton number, *e.g.* $\tilde{\chi}_1^0 \to l^+ l^- \nu$, but of course not both baryon and lepton number, since that would give rapid proton decay. Signatures for *R*-parity violation are discussed in Section 20.4.

Even if the general MSSM is correct, none of these models is likely to be the whole truth, but they do provide self-consistent frameworks in which to test the ability of the ATLAS detector to study supersymmetry at the LHC. In this chapter detailed studies are reported for several particular choices of the parameters in the minimal SUGRA, minimal GMSB, and *R*-parity violating scenarios. Discovery of signals for any of these at the LHC is straightforward. The main problem is not to distinguish SUSY from the Standard Model but to separate the many SUSY processes that occur. Hence, the emphasis here is on partial reconstruction of particular modes, measurement of combinations of masses from kinematic endpoints of the corresponding distributions, and global fits to these to determine the parameters of the underlying model. This approach is quite effective, but it utilises only part of the information that will be available at the LHC if SUSY in fact exists at the weak scale.

Since the main background for SUSY is SUSY itself, it is essential to generate the whole SUSY cross section, not just specific channels of interest. Typically, samples of 10^5 or more events have been generated for each point studied here using either ISAJET [20-15] or SPYTHIA [20-16]. Large samples of Standard Model events are also needed to assess potential backgrounds. Such large event samples necessitate using a fast detector simulation rather than a detailed, GEANT-based one. Most of the results given here are based on ATLFAST [20-17] or comparable particle-level detector simulations. These correctly describe the gross resolution and acceptance of ATLAS but not the effects of resolution tails, cracks, *etc.* The backgrounds for SUSY signatures after reasonable cuts appear however to be dominated by real physics events and not by such detector effects.

20.2 Supergravity models

The minimal supergravity (SUGRA) model [20-11] assumes that at the GUT scale all scalars (squarks, sleptons, and Higgs bosons) have a common mass m_0, all gauginos and Higgsinos have a common mass $m_{1/2}$, and all the trilinear Higgs-sfermion-sfermion couplings have a common value A_0. Such common masses are suggested by the fact that gravity is universal but are sometimes not found in models with realistic GUT-scale dynamics. The remaining parameters at the GUT scale are the bilinear SUSY breaking term B and the SUSY conserving Higgs mass μ. The 26 renormalisation group equations (RGE's) [20-12] are then solved iteratively between the weak and GUT scale. On each iteration the SUSY masses are calculated and used to determine the thresholds at which the masses and other parameters are frozen. Because of the specific form of the RGE's, the squared mass of the Higgs field is driven negative by the large top Yukawa coupling, causing electroweak symmetry breaking but leaving unbroken the col-

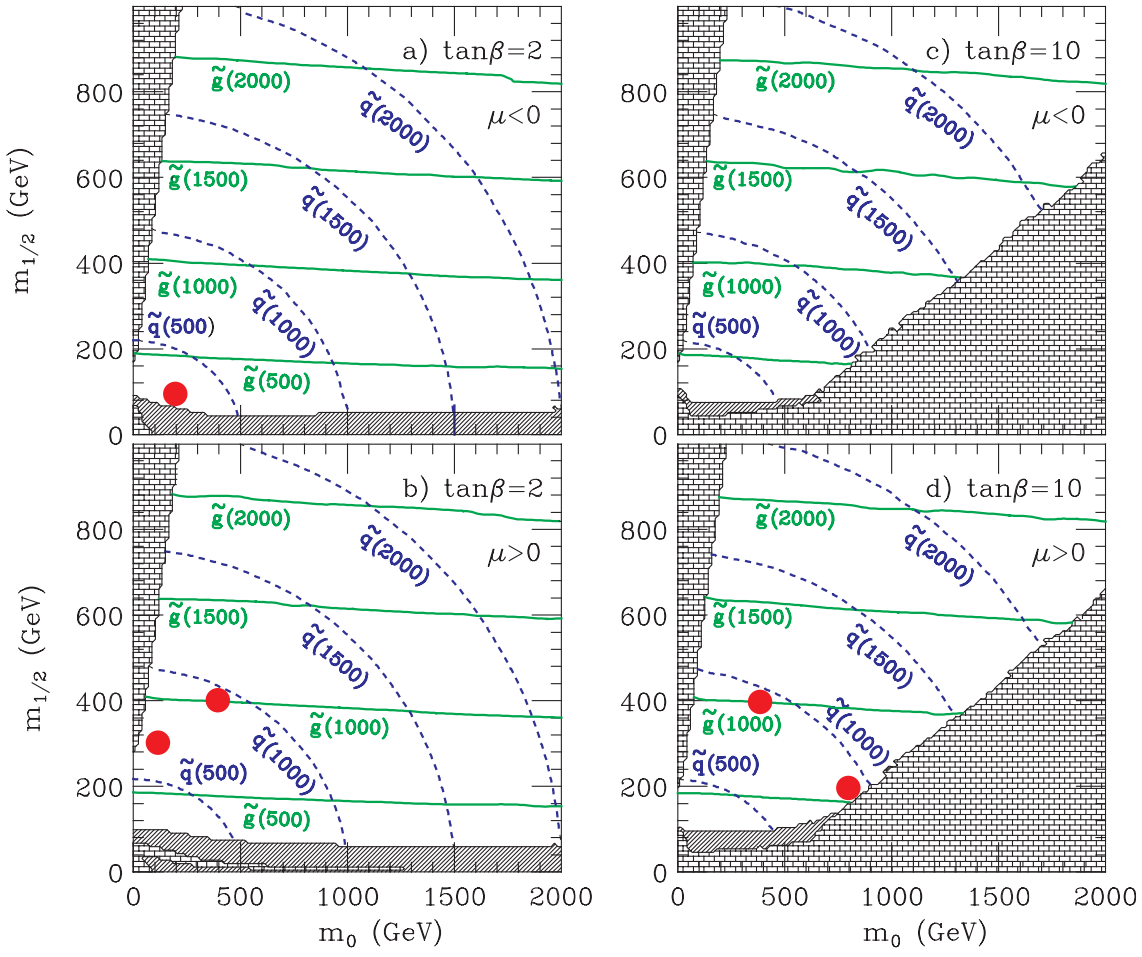

Figure 20-1 Contours showing gluino and squark masses in the m_0, $m_{1/2}$ plane for $A_0 = 0$ and representative values of $\tan\beta$ in the minimal SUGRA model. The bricked regions at small m_0 are excluded by the requirement that $\tilde{\chi}_1^0$ be the LSP. The bricked regions at large m_0 and $\tan\beta$ are excluded in ISAJET 7.22 by having no electroweak symmetry breaking; this is quite model dependent. The cross-hatched regions were excluded by experiment at the time of Ref. [20-18]. The dots represent the five minimal SUGRA points selected by the LHCC for detailed study by ATLAS and CMS.

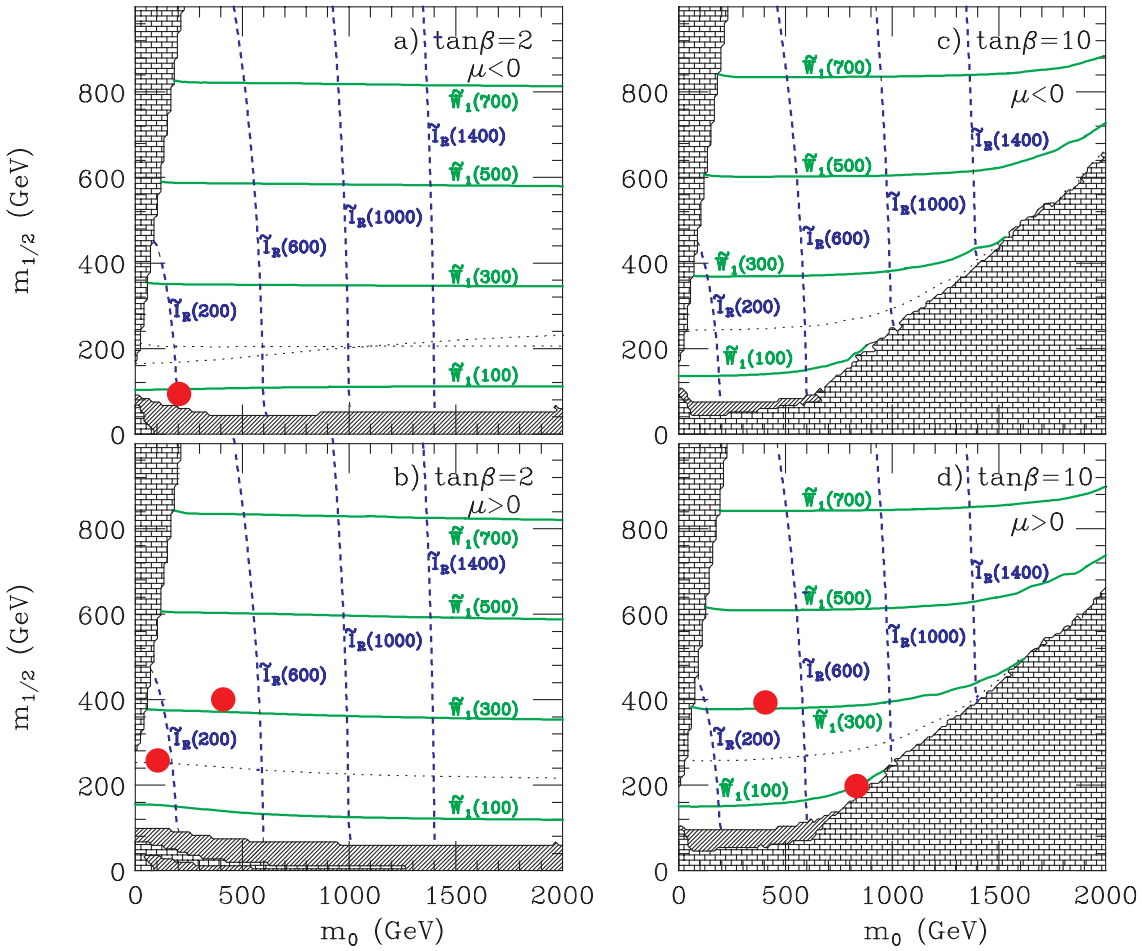

Figure 20-2 Contours showing wino and slepton masses in the m_0, $m_{1/2}$ plane for $A_0 = 0$ and representative values of $\tan\beta$ in the minimal SUGRA model. See Figure 20-1.

our and electromagnetic interactions. Then B and μ^2 can be eliminated in favour of M_Z and the ratio $\tan\beta = v_u/v_d$ of Higgs vacuum expectation values. The parameters of this minimal model are therefore

$$m_0, \qquad m_{1/2}, \qquad A_0, \qquad \tan\beta, \qquad \mathrm{sgn}\mu = \pm 1\,. \qquad \text{20-4}$$

The masses and mixings of all the SUSY and Higgs particles and hence also all their decays are determined in terms of these parameters. Some representative masses are shown in Figures 20-1 and 20-2. The shaded regions in the figures are excluded by theory or experiment. The dots represent the five minimal SUGRA points selected by the LHC Committee (LHCC) in 1996 for detailed study by the ATLAS and CMS Collaborations.

The parameters of the five LHCC points are listed in Table 20-3; the particle masses are listed in Table 20-4. The total SUSY cross-section ranges between a few picobarn for Points 1 and 2, with a SUSY mass scale of 1 TeV, to about one nanobarn for Point 3, with a mass scale of 300 GeV. Point 3 is the 'comparison point', selected so that other existing or proposed accelerators could find something. This point is already ruled out: LEP would have discovered the light Higgs with a mass of 68 GeV. Points 1 and 5 have light Higgs masses which are excluded by the pre-

Table 20-3 Parameters of the five minimal SUGRA points selected by the LHCC and a sixth SUGRA point with large $\tan\beta$ added later by ATLAS.

Point	m_0 (GeV)	$m_{1/2}$ (GeV)	A_0 (GeV)	$\tan\beta$	sgnμ
1	400	400	0	2	+
2	400	400	0	10	+
3	200	100	0	2	-
4	800	200	0	10	+
5	100	300	300	2.1	+
6	200	200	0	45	-

liminary limits of the LEP experiments [20-19]. In all three cases the Higgs mass can be increased by increasing $\tan\beta$ to about three. For Point 3 it might also be necessary to increase m_0 and $m_{1/2}$, since the charginos are in a mass region which can be explored by the next LEP run. As an example, the minimal SUGRA point

$$m_0 = 250\ \text{GeV} \qquad m_{1/2} = 125\ \text{GeV} \qquad A_0 = 0 \qquad \tan\beta = 5 \qquad \mu < 0$$

has a superparticle spectrum generally similar to Point 3 but a light Higgs mass of 98.6 GeV. The gluino mass is 350 GeV, and it has a high probability to decay via $\tilde{g} \to \tilde{b}_1 \bar{b} \to \tilde{\chi}_2^0 b \bar{b}$; the $\tilde{\chi}_2^0 \to \tilde{\chi}_1^0 l^+ l^-$ branching ratio is smaller but still large enough to be observable. Thus Point 3 remains useful even though it is ruled out by the Higgs search.

Points 1 and 2 both have gluino and squark masses near 1 TeV, about the upper limit expected from fine tuning arguments. Point 4 was chosen to be near the boundary for electroweak symmetry breaking, implying that μ is small so that there is quite strong mixing between gauginos and Higgsinos in Equations 20-1 and 20-2. This boundary turns out to be quite sensitive to the details of how electroweak symmetry breaking is implemented, so the properties of this point are quite model dependent. Point 5 was motivated by cosmology. There is strong evidence for non-baryonic cold dark matter in the universe [20-20], and the LSP is a good candidate for this cold dark matter. Point 5 gives a density of cold dark matter consistent with the universe having the critical density. The small value of m_0 produces light sleptons and so increases the annihilation cross section for $\tilde{\chi}_1^0$, reducing the cold dark matter to be consistent with the critical density, $\Omega = 1$. (One weakness of the GMSB and R-parity violating models considered in Section 20.3 and Section 20.4 is that they do not provide cold dark matter. Conversely, a very weak decay of the LSP via either gravitinos or R-parity violating interactions would remove the cold dark matter constraints on SUGRA models.) Point 6 was added later as an example with large $\tan\beta$. This point was selected so that the only two-body gaugino decays are $\tilde{\chi}_2^0 \to \tilde{\tau}_1 \tau$ and $\tilde{\chi}_1^\pm \to \tilde{\tau}_1 \nu$; these decays therefore dominate and give signatures involving τ's instead of the previous signatures. Point 6 is discussed separately in Section 20.2.8.

20.2.1 Inclusive SUGRA measurements

The first step in searching for SUSY at the LHC is to look for a deviation from the Standard Model. SUSY events are dominated by the production of gluinos and squarks, which decay through one or more steps to the LSP $\tilde{\chi}_1^0$, which escapes detection. Thus SUSY events are characterised by multiple jets, leptons, and missing transverse energy E_T^{miss}. Since the gluino is a

Table 20-4 Masses in GeV for the five LHCC SUGRA points and the large $\tan\beta$ SUGRA point listed in Table 20-3. The first and second generation squarks and sleptons are degenerate and so are not listed separately. The SUSY masses for the five LHCC points are from ISAJET 7.22 [20-15]; the Higgs masses are from SPYTHIA 2.08 [20-16] and use the approximate two-loop effective potential. The masses for Point 6 are from ISAJET 7.37 [20-15].

Particle	Point 1	Point 2	Point 3	Point 4	Point 5	Point 6
$\tilde{g}$	1004	1009	298	582	767	540
$\tilde{\chi}_1^{\pm}$	325	321	96	147	232	152
$\tilde{\chi}_2^{\pm}$	764	537	272	315	518	307
$\tilde{\chi}_1^0$	168	168	45	80	122	81
$\tilde{\chi}_2^0$	326	321	97	148	233	152
$\tilde{\chi}_3^0$	750	519	257	290	497	286
$\tilde{\chi}_4^0$	766	538	273	315	521	304
$\tilde{u}_L$	957	963	317	918	687	511
$\tilde{u}_R$	925	933	313	910	664	498
$\tilde{d}_L$	959	966	323	921	690	517
$\tilde{d}_R$	921	939	314	910	662	498
$\tilde{t}_1$	643	710	264	594	489	365
$\tilde{t}_2$	924	933	329	805	717	517
$\tilde{b}_1$	854	871	278	774	633	390
$\tilde{b}_2$	922	930	314	903	663	480
$\tilde{e}_L$	490	491	216	814	239	250
$\tilde{e}_R$	430	431	207	805	157	219
$\tilde{\nu}_e$	486	485	207	810	230	237
$\tilde{\tau}_1$	430	425	206	797	157	132
$\tilde{\tau}_2$	490	491	216	811	239	259
$\tilde{\nu}_\tau$	486	483	207	806	230	218
h	95	116	69	112	93	112
H	1046	737	379	858	638	157
A	1044	737	371	859	634	157
$H^{\pm}$	1046	741	378	862	638	182

Majorana fermion, it has equal branching ratios into l^+X and l^-X, giving rise to isolated like-sign dileptons for which the Standard Model background is small. To estimate the reach for each signature, events were generated for many SUGRA points and for Standard Model processes using ISAJET plus a simplified detector simulation. Events were selected to have [20-18]

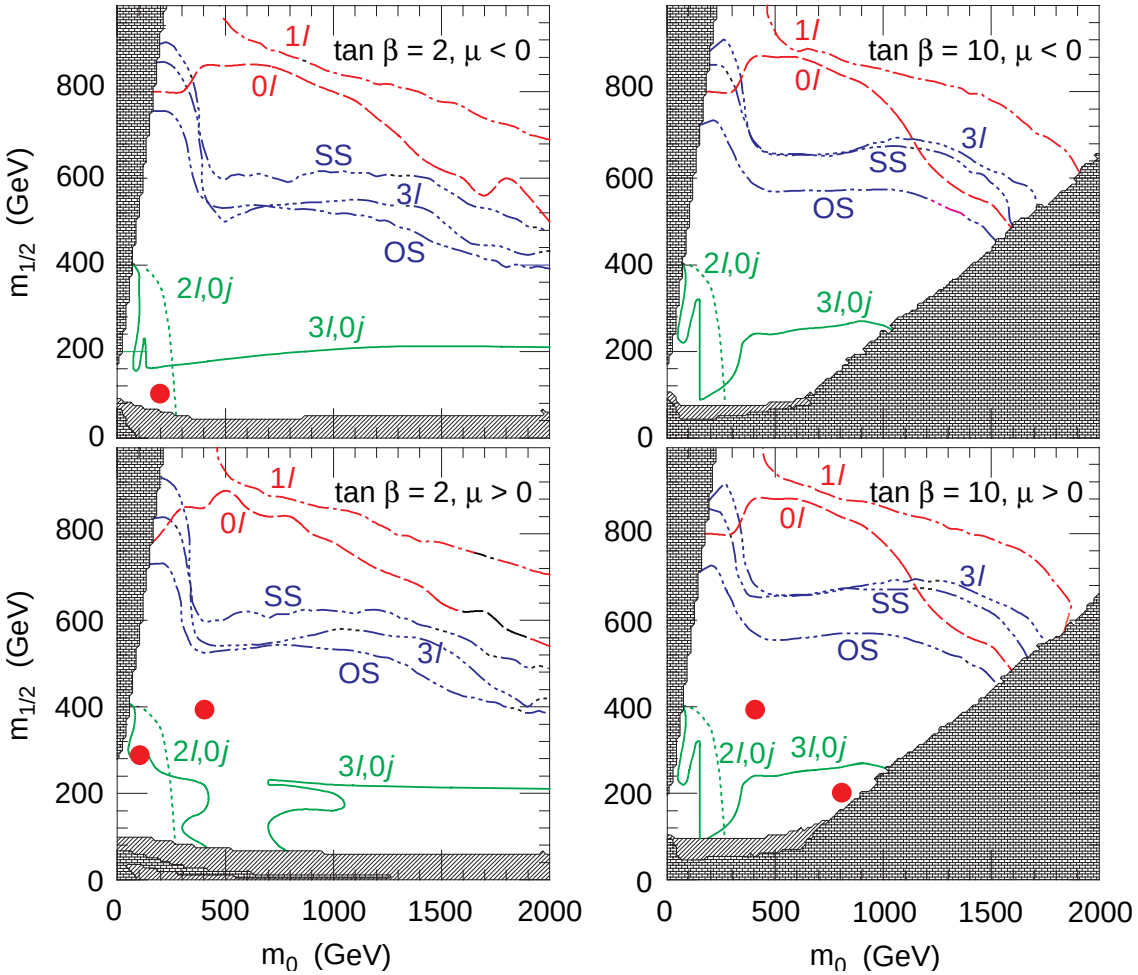

Figure 20-3 Reach for $S/\sqrt{B} > 5$ for various SUSY signatures in the SUGRA parameter space with $A_0 = 0$. 0l: Jets, E_T^{miss}, and no leptons. 1l: Jets, E_T^{miss}, and 1 lepton. SS: Same-sign dileptons. OS: Opposite-sign dileptons. 3l: trileptons. 3l,0j: trileptons with jet veto. 2l,0j: dileptons with jet veto. See Figure 20-1 for the explanation of the shaded regions.

- At least two jets with $p_T > E_T^c$ and $E_T^{miss} > E_T^c$, where for each SUGRA point the cut parameter $E_T^c \geq 100$ GeV was adjusted to maximise $S/\sqrt{B}$, where S is the SUSY signal, and B is the background.
- $S_T > 0.2$ to reduce the dijet background (where the 'transverse sphericity' $0 \leq S_T \leq 1$ is defined as $2\lambda_2/(\lambda_1 + \lambda_2)$, λ_1 and λ_2 being the eigenvalues of the 2×2 sphericity tensor $S_{ij} = \Sigma_k p_{ki} pkj$ formed by summing over the transverse momenta of all of the calorimeter cells).
- $p_T > 20$ GeV and $\eta < 2.5$ for any leptons.
- Transverse mass $M_T(l, E_T^{miss}) > 100$ GeV for the lepton plus jets channel to reduce the W + jets backgrounds.

The resulting reach [20-18], defined by at least 10 signal events and $S/\sqrt{B} > 5$ for an integrated luminosity of 10 fb^{-1}, is shown Figure 20-3 for the no lepton plus jets plus E_T^{miss}, one lepton plus jets plus E_T^{miss}, same-sign dilepton, opposite-sign dilepton and trilepton channels. By comparing this figure with the previous two, it can be seen that the reach in the jets plus E_T^{miss} chan-

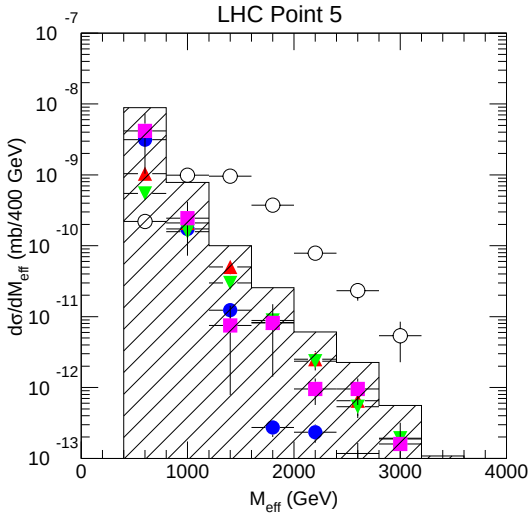

Figure 20-4 M_{eff} distribution for the Point 5 signal (open circles) and for the sum of all Standard Model backgrounds (histogram); the latter includes $t\bar{t}$ (solid circles), W + jets (triangles), Z + jets (downward triangles), and QCD jets (squares).

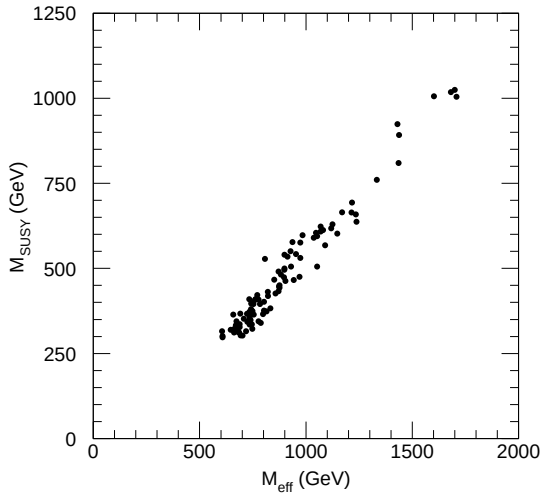

Figure 20-5 Peak of M_{eff} distribution as a function of. $M_{\mathrm{SUSY}} = \min(M_{\tilde{g}}, M_{\tilde{u}_R})$ for various models.

nels extends to squark and gluino masses greater than 2 TeV. Similar results were found in the ATLAS Technical Proposal [20-21]. The reach limits involve very hard jets and large $E_{\mathrm{T}}^{\mathrm{miss}}$, so they are determined mainly by the squark and gluino production cross sections and not by the detailed detector performance. The reach in the multi-lepton channels extends well beyond 1 TeV. Also shown in the figure is the reach for direct gaugino and slepton production in the dilepton and trilepton channels with a central jet veto. These channels generally provide the best reach at the Tevatron [20-6].

After finding one or more such inclusive signals, one would want to obtain a simple estimate of the SUSY masses involved. A good variable [20-22] for this purpose is the ‘effective mass’, the scalar sum of the missing energy and the transverse momenta of the four hardest jets:

$$M_{\mathrm{eff}} = E_{\mathrm{T}}^{\mathrm{miss}} + p_{\mathrm{T},1} + p_{\mathrm{T},2} + p_{\mathrm{T},3} + p_{\mathrm{T},4}\,. \qquad 20\text{-}5$$

This was calculated for the five LHCC SUGRA points listed in Table 20-3 and for the Standard Model backgrounds with the following cuts:

- $E_{\mathrm{T}}^{\mathrm{miss}} > \max(100\ \mathrm{GeV}, 0.2M_{\mathrm{eff}})$.
- At least 4 jets with $p_{\mathrm{T}} > 50\ \mathrm{GeV}$ and $p_{\mathrm{T},1} > 100\ \mathrm{GeV}$.
- Transverse sphericity $S_{\mathrm{T}} > 0.2$.
- No muon or isolated electron with $p_{\mathrm{T}} > 20\ \mathrm{GeV}$ and $\eta < 2.5$.

The M_{eff} distribution after these cuts for the Point 5 signal and the sum of all Standard Model backgrounds is shown in Figure 20-4. Note that $S/B \sim 10$ at large M_{eff} with an accepted cross section of more than 1 pb. For the other points the place where the signal emerges from the background is of course different, but the S/B ratio at large M_{eff} is similar. Discovering a signal using a variable and simple cuts such as these would be very easy for any of the five LHCC points. This is not very surprising: since squarks and gluinos are strongly interacting, they are

produced with cross sections comparable to the QCD background at the same Q^2, so rather simple cuts on $E_{\mathrm{T}}^{\mathrm{miss}}$ and the event topology are sufficient to separate the signal from the Standard Model background.

The peak of the effective mass distribution moves with the mass scale of the SUSY particles. To test this, 100 minimal SUGRA models were selected at random with m_0, $m_{1/2}$, and A_0 less than 500 GeV and with the constraint that they have the same light Higgs boson mass as Point 5 within ±3 GeV. (In retrospect it was inappropriate to include the Higgs mass constraint, since finding SUSY in this way is far easier than finding a light Higgs boson, but including it has no essential effect.) Figure 20-5 shows a scatter plot of the M_{eff} peak vs $M_{\mathrm{SUSY}} = \min(M_{\tilde{g}}, M_{\tilde{u}_R})$, which provides a measure of the mass scale of the strongly produced SUSY particles. The spread is remarkably small, about ±10%. The spread might be larger in a more general class of models, but it appears that simple distributions like this will provide a good first estimate of the SUSY mass scale.

One could produce many more inclusive distributions involving various combinations of jets, leptons, and $E_{\mathrm{T}}^{\mathrm{miss}}$ and attempt to fit all these to determine the SUGRA model parameters. It is more transparent, however, to use partial reconstruction of exclusive final states to determine precise combinations of masses from kinematic endpoints of distributions as discussed in the following subsections.

20.2.2 Exclusive SUGRA measurements for moderate tan β

If SUSY exists at the weak scale, it will presumably first be found using inclusive signatures such as the ones discussed in Section 20.2.1. To progress further, and in particular to understand how SUSY is broken, it is important to measure individual masses and decays. In the SUGRA model the decay products of a SUSY particles always include an invisible $\tilde{\chi}_1^0$, so no mass peaks can be reconstructed directly. It is possible, however, to pick out particular multi-body decay modes and then to determine combinations of masses by measuring the endpoints of the visible mass distributions [20-22, 20-23, 20-24, 20-25, 20-26, 20-27]. For example, in the decay $\tilde{\chi}_2^0 \to \tilde{\chi}_1^0 l^+ l^-$ the endpoint of the dilepton mass distribution measures $M(\tilde{\chi}_2^0) - M(\tilde{\chi}_1^0)$. In favourable cases, such measurements can be sufficient to fit the parameters of the model. If a long decay chain can be identified, it is even possible to determine the masses involved without relying on a model. This approach provides a much clearer physical interpretation than a global fit of a model to all possible distributions, although the latter will of course be part of any eventual analysis of data.

The starting point of such analyses is generally to reconstruct a specific mode at the bottom of a decay chain. The SUSY production cross section at the LHC is dominated by gluinos and squarks, which decay mainly through the lighter chargino and two neutralinos. For this reason many of the analyses involve decays of the second neutralino:

- $\tilde{\chi}_2^0 \to \tilde{\chi}_1^0 l^+ l^-$;
- $\tilde{\chi}_2^0 \to \tilde{l}^{\pm} l^{\mp} \to \tilde{\chi}_1^0 l^+ l^-$;
- $\tilde{\chi}_2^0 \to \tilde{\chi}_1^0 h \to \tilde{\chi}_1^0 b\bar{b}$.

Decays of charginos are more difficult to use because they involve either a missing neutrino or light quark jets. If the two-body decays of neutralinos are kinematically allowed, then they generally have substantial branching ratios. If they are not, then the three-body leptonic mode gen-

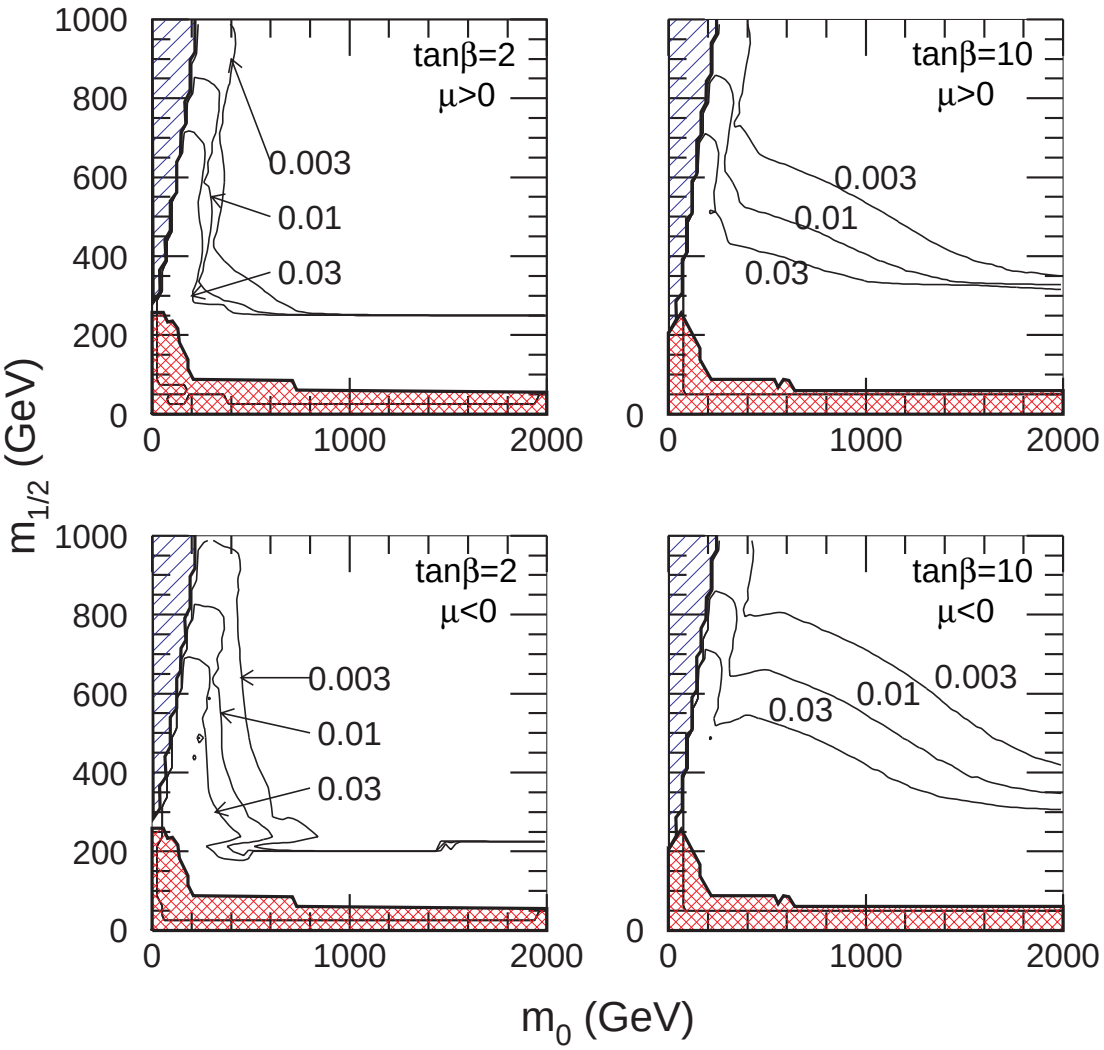

Figure 20-6 Contour plot of branching fraction times cross-section ($B\sigma$) in pb for $\tilde{\chi}_2^0$ to produce a dilepton pair in the minimal SUGRA model. This figure is based on a more recent implementation of electroweak symmetry breaking than Figures 20-1 – 20-3 that does not give an excluded region at large m_0 for $\tan\beta = 10$.

erally has a branching ratio either comparable to the Z leptonic branching ratio or larger if slepton exchange dominates. All of these modes will be illustrated in the following subsections by analyses for the five SUGRA points listed in Table 20-3.

For moderate $\tan\beta$ at least one of these decay modes is generally available. It is difficult to estimate a precise reach without a detailed study of many points since the backgrounds are dominated by SUSY, but a minimum requirement is that enough events be produced. The SUSY production cross section times combined branching ratio for the sum of all $\tilde{\chi}_2^0$ dilepton modes ($\tilde{\chi}_2^0 \to \tilde{\chi}_1^0 l^+ l^-$, $\tilde{\chi}_2^0 \to \tilde{l}^{\pm} l^{\mp} \to \tilde{\chi}_1^0 l^+ l^-$, and $\tilde{\chi}_2^0 \to \tilde{\chi}_1^0 Z \to \tilde{\chi}_1^0 l^+ l^-$) is shown in Figure 20-6, while that for $\tilde{\chi}_2^0 \to \tilde{\chi}_1^0 h \to \tilde{\chi}_1^0 b\bar{b}$ is shown in Figure 20-7. b-jet tagging assumed a tagging efficiency of 0.6 unless otherwise stated (see Chapter 10).

For very large $\tan\beta$ the splitting among the slepton masses becomes larger, and the only two-body decay available may be $\tilde{\chi}_2^0 \to \tilde{\tau}_1^{\pm}\tau^{\mp} \to \tilde{\chi}_1^0 \tau^+ \tau^-$.

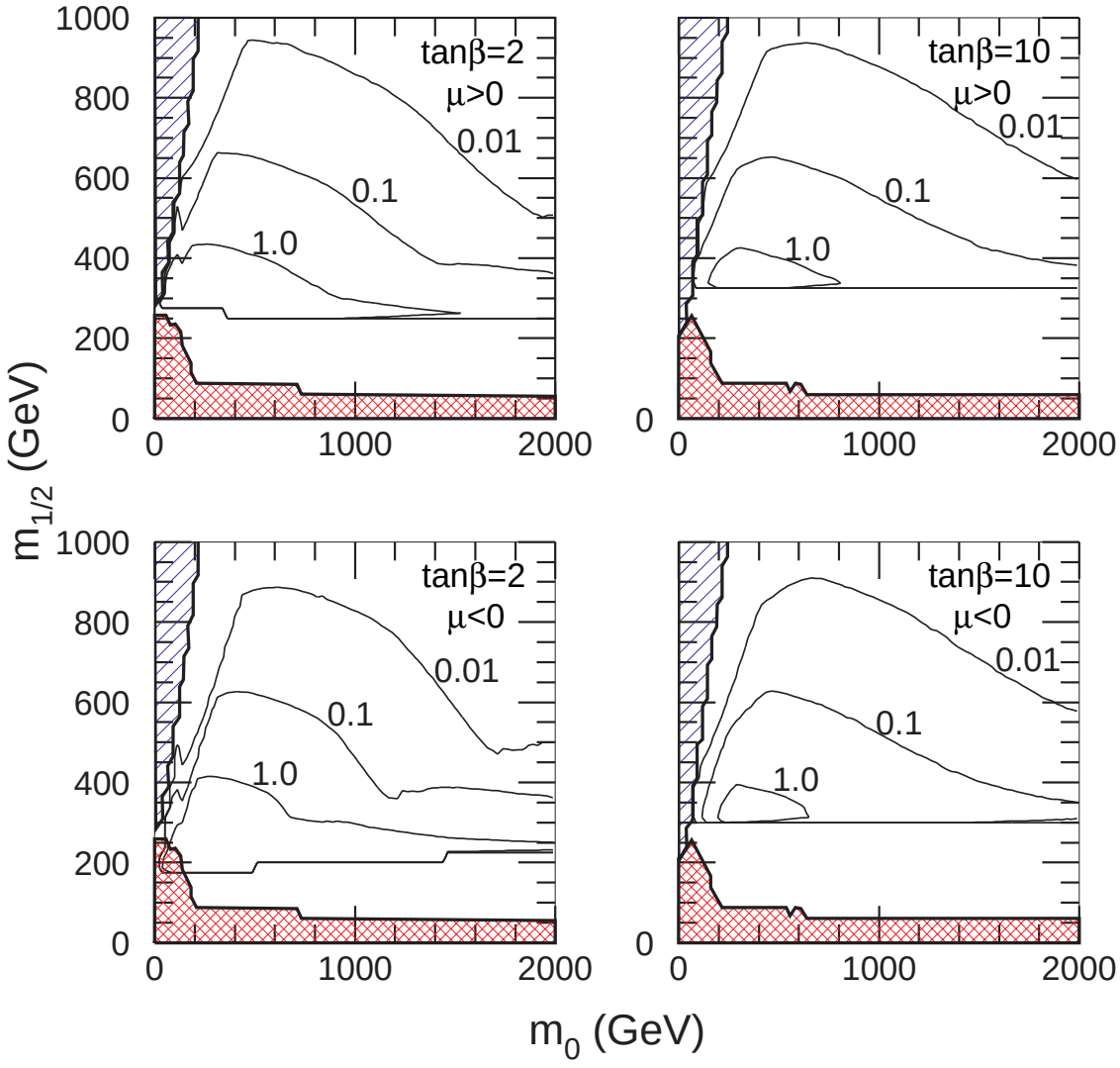

Figure 20-7 Contour plot of $B\sigma$ in pb for $\tilde{\chi}_2^0$ to decay via $h \to b\bar{b}$ in the minimal SUGRA model.

If this is the only two-body mode, its branching ratio will be nearly unity. This case is obviously more difficult and will be discussed separately in Section 20.2.8 below. Given a starting point, one then tries to work back up the decay chain to the primary gluinos and squarks, finding additional exclusive modes and mass constraints. In general the longer the chain that can be identified and reconstructed, the stronger the constraints will be. For this reason, SUGRA models generally are more difficult than GMSB models, which will be discussed in Section 20.3.

Sections 20.2.3–20.2.7 describe such analyses for the five LHCC SUGRA points based on this general approach. Unless otherwise stated, all the analyses described here are based on ISAJET 7.22 [20-15] or SPYTHIA 2.08 [20-16] plus ATLFAST [20-17] or a simple [20-22] particle-level parametrisation of the response of the ATLAS detector. Results are generally shown for integrated luminosities of 10 fb^{-1} to 30 fb^{-1}, corresponding to one to three years at low luminosity. Pileup is not properly taken into account, so the results given for high luminosity may be too optimistic. The statistics on the Standard Model backgrounds often correspond to much less than one year. They are sufficient to show that the background is small compared to the signal after the specified cuts but may exhibit large fluctuations.

20.2.3 l^+l^- SUGRA signatures

At Point 3 the light charginos and neutralinos have no two-body decays, so the three-body mode $\tilde{\chi}_2^0 \to \tilde{\chi}_1^0 l^+ l^-$ is relevant. The dominant SUSY cross section is gluino pair production. The $\tilde{b}_1$ is 20 GeV lighter than the gluino, but the first and second generation squarks are heavier than it, so the gluinos decay dominantly by $g \to \tilde{b}_1 \bar{b} + \text{h.c.}$, the only allowed two-body decay mode. Since the $\tilde{b}_1$ is mostly $\tilde{b}_L$, it decays mainly into $\tilde{\chi}_2^0$. Specifically, the branching ratios are [20-22, 20-24]

$$\begin{aligned} B(\tilde{g} \to \tilde{b}_1 b + \text{h.c.}) &= 89\% \\ B(\tilde{b}_1 \to \tilde{\chi}_2 b) &= 86\% \\ B(\tilde{\chi}_2 \to \tilde{\chi}_1^0 l^+ l^-) &= 2 \times 17\% \end{aligned}$$

Thus the SUSY events at Point 3 are characterised by multiple leptons and multiple b-jets. While these branching ratios are unusual because the gluino has just one two-body decay mode, it is common for heavy flavour and leptonic decays to be enhanced.

Given these decay modes, events were selected by requiring [20-22, 20-24]:

- A pair of isolated electrons or muons of opposite charge and the same flavour with $p_{\text{T},l} > 10$ GeV and $|\eta| < 2.5$.
- At least two jets tagged as b's having $p_{\text{T}} > 15$ GeV and $|\eta| < 2$.

The threshold on lepton p_{T} is such that only events containing muons will be selected with full efficiency by the trigger [20-28]. For electron pairs the p_{T} threshold should be raised to 15 GeV. Within these kinematic cuts a b-tagging efficiency of 60% and a lepton identification efficiency of 90% were assumed and included in all distributions; the backgrounds from misidentified leptons and b-jets are negligible. These cuts alone are sufficient to reject most of the Standard Model background, so no cut on $E_{\text{T}}^{\text{miss}}$ was used. The resulting dilepton distribution for the signal and for the sum of all Standard Model backgrounds is shown in Figure 20-8. The expected endpoint at

$$M_{\tilde{\chi}_2^0} - M_{\tilde{\chi}_1^0} = 52.47 \text{ GeV}$$

is very clear. The SUSY background comes mainly from two independent $\tilde{\chi}_1^{\pm}$ decays; it is responsible for the tail of events beyond this endpoint. The Standard Model background, which is tiny, comes mainly from $t\bar{t}$ events. If the branching ratios were less favourable, one could plot instead the flavour-subtracted combination $e^+e^- + \mu^+\mu^- - e^{\pm}\mu^{\mp}$ and cancel the background up to statistical fluctuations. Given the high statistics and small background, the endpoint can be determined with an accuracy limited only by systematics, estimated to be 0.1% or 50 MeV.

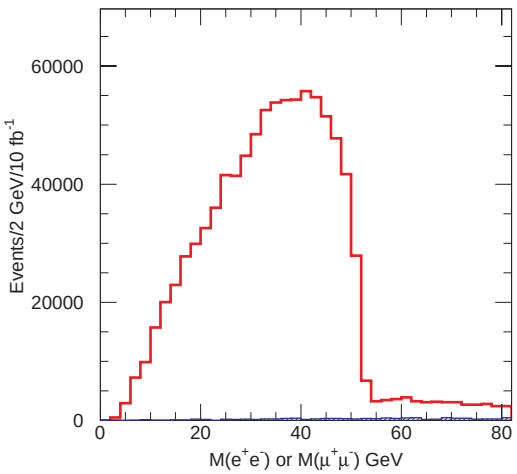

Figure 20-8 Dilepton mass distribution for Point 3 (solid) and Standard Model background (shaded).

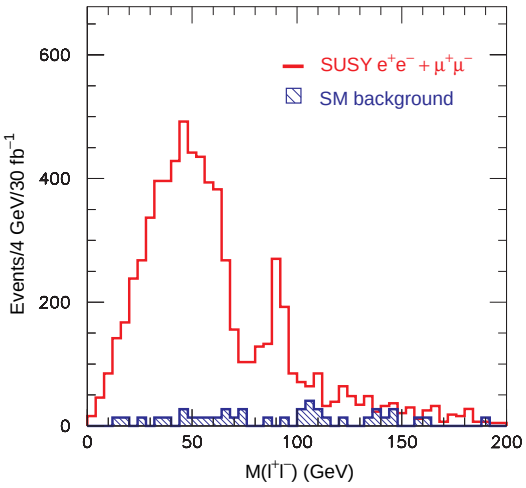

Figure 20-9 Dilepton distribution for Point 4 (solid) and Standard Model background (shaded).

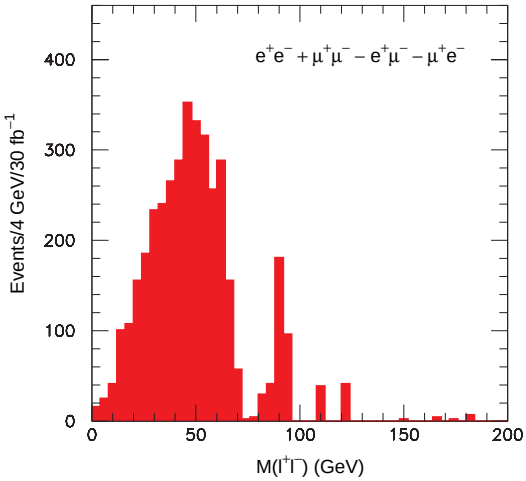

Figure 20-10 Flavour subtracted mass distribution for Point 4.

At Point 4 the light charginos and neutralinos also have no two-body decays. The three-body decay $\tilde{\chi}_2^0 \to \tilde{\chi}_1^0 l^+ l^-$ is again observable although at this point the sleptons are heavy, so the decay occurs through a virtual Z^* with a branching ratio of only $2 \times 3\%$. For the dilepton distribution at Point 4, events were selected by requiring [20-25]:

- Two isolated, opposite-sign, same-flavour electrons or muons with $p_{\mathrm{T},1} > 20$ GeV and $p_{\mathrm{T},2} > 10$ GeV; both leptons are required to have $|\eta| < 2.5$.
- $E_{\mathrm{T}}^{\mathrm{miss}} > 200$ GeV.
- At least four jets with $p_{\mathrm{T}} > 100$, 50, 50, and 50 GeV respectively and $|\eta| < 3.2$.

After these cuts, there are about 6500 signal events for an integrated luminosity of 30 fb^{-1}, with a total Standard Model background of 550 events, mainly from $t\bar{t}$. The mass distribution is shown in Figure 20-9. Note that in addition to the edge there is also a Z peak in the signal. This comes mainly from heavier gauginos: Point 4 is close to the boundary for radiative electroweak symmetry breaking, so μ is small. A small μ implies not only that the heavier charginos and neutralinos are relatively light but also that there is strong mixing between the gauginos and Higgsinos, so they have gauge-like rather than Higgs-like couplings to light flavours. Thus, the total production of the heavier gauginos is larger than is typical for SUGRA models. The heavy gaugino branching ratios into Z's are also quite large:

$$B(\tilde{\chi}_2 \to \tilde{\chi}_1 Z) = 32\%$$
$$B(\tilde{\chi}_3^0 \to \tilde{\chi}_{1,2}^0 Z) = 34\%$$
$$B(\tilde{\chi}_4^0 \to \tilde{\chi}_{1,2}^0 Z) = 5\%$$

The endpoint of the dilepton distribution, which again measures $M_{\tilde{\chi}_2^0} - M_{\tilde{\chi}_1^0}$, can be determined more accurately by plotting the combination $e^+e^- + \mu^+\mu^- - e^{\pm}\mu^{\mp}$, in which two independent decays – *e.g.*, of charginos or of top quarks – cancel. This distribution is shown in Figure 20-10. The

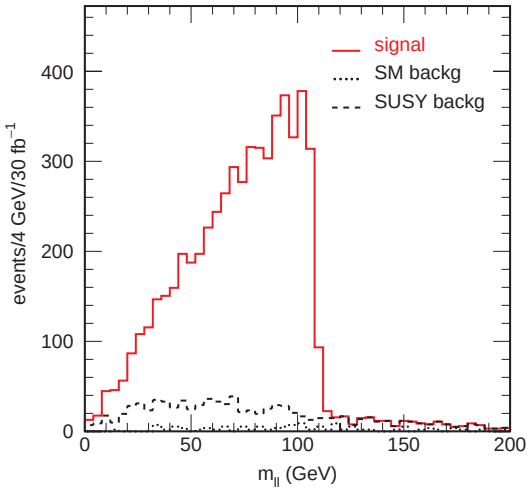

Figure 20-11 Dilepton $\tilde{\chi}_2^0 \to \tilde{l}_R^{\pm} l^{\mp} \to \tilde{\chi}_1^0 l^+ l^-$ signal at Point 5 (solid), background from other SUSY sources (dashed), and sum of Standard Model backgrounds (dotted) after cuts.

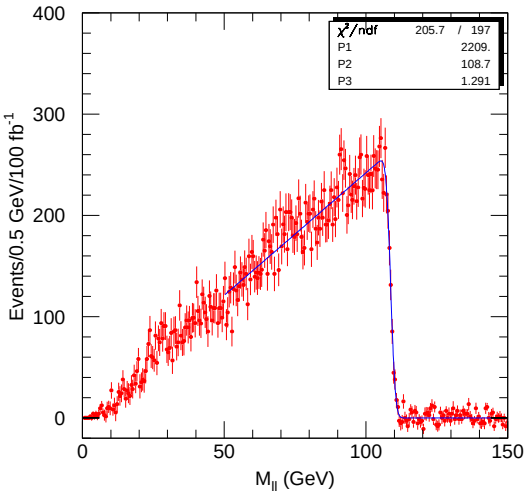

Figure 20-12 Minimum-χ^2 fit to flavour-subtracted dilepton signal for Point 5 for an integrated luminosity of 100 fb^{-1}.

error on the endpoint for three years at low luminosity was estimated [20-25] using a Kolmogorov test to be $(68.13^{+0.5}_{-1.0} \pm 0.07)$ GeV, where the first error is statistical and the second is systematic, coming mainly from the 0.1% uncertainty in the electromagnetic energy scale.

The size of the Z peak relative to the continuum and its p_T distribution can provide information on the masses and mixings of the heavier gauginos, albeit in a model dependent way. A full analysis would require generating many samples of events varying all the parameters of the minimal SUGRA or other SUSY model. To get an approximate indication of the sensitivity, only the $\tilde{\chi}_2^{\pm}$ mass was varied holding the other masses fixed. A Kolmogorov test was then used to determine the sensitivity of the p_T distribution of the Z to the $\tilde{\chi}_2^{\pm}$ mass. This analysis gave $M(\tilde{\chi}_2^{\pm}) = 315 \pm 21 \pm 9$ GeV for 30 fb^{-1} [20-25].

At Point 5 the right-handed sleptons are relatively light, so the decay $\tilde{\chi}_2^0 \to \tilde{l}_R^{\pm} l^{\mp} \to \tilde{\chi}_1^0 l^+ l^-$ is open; this is characteristic of SUGRA points that give an amount of cosmological cold dark matter consistent with the universe having the critical density, $\Omega = 1$, as predicted by inflation. Since the sleptons are light, the dilepton signal comes from a two-body intermediate state, not from a direct three-body decay. The signal comes mainly from squarks, either directly produced or from gluino decay, so the SUSY events also contain hard jets. Events were therefore selected to have [20-26]

- $E_T^{miss} > 300$ GeV;
- exactly two opposite-sign, same-flavour electrons or muons with $p_T > 10$ GeV and $|\eta| < 2.5$;
- at least two jets with $p_T > 150$ GeV.

The W and Z backgrounds are suppressed by the jet requirements and the $t\bar{t}$ background by the hard kinematics and the leptonic branching ratios. After these cuts, therefore, one is left with 5800 signal events with a background from other SUSY sources of 880 events and a Standard Model background of only 120 events. The mass distribution is shown in Figure 20-11. Because of the two-body kinematics, there is a very sharp edge at

$$M_{ll}^{\max} = M(\tilde{\chi}_2^0)\sqrt{1-\frac{M^2(\tilde{l}_R)}{M^2(\tilde{\chi}_2^0)}}\sqrt{1-\frac{M^2(\tilde{\chi}_1^0)}{M^2(\tilde{l}_R)}} = 108.93 \text{ GeV}$$

with a width set by the detector resolution. Most of the small remaining background can be removed by considering the flavour-subtracted combination $e^+e^- + \mu^+\mu^- - e^\pm\mu^\mp$. The position of this edge can therefore be measured to an estimated precision of 0.5 GeV with an integrated luminosity of 30 fb^{-1} [20-26].

Any difference in the location of this edge for the e^+e^- and $\mu^+\mu^-$ distributions would indicate a difference in the corresponding slepton masses, so it is interesting to measure the edge as accurately as possible [20-29]. Since the slepton is a scalar, the mass distribution before cuts is just given by phase space, *i.e.*

$$dM^2 = (M_{ll}^{\max})^2\frac{(1+z)}{2}dz\,, \qquad 20\text{-}6$$

where $z = \cos\theta^*$ is the decay angle in the slepton rest frame and is uniformly distributed. Acceptance cuts should not distort this form significantly in the vicinity of the edge. A sample of 1×10^6 events, corresponding to an integrated luminosity of about 75 fb^{-1}, was generated with ISAJET 7.37. For this analysis events were selected to have:

- $M_{\text{eff}} > 400$ GeV;
- $E_{\text{T}}^{\text{miss}} > \max(100\,\text{GeV}, 0.2M_{\text{eff}})$;
- at least four jets with $p_{\text{T}} > 100, 50, 50, 50$ GeV;
- two isolated, opposite-sign electrons or muons with $p_{\text{T}} > 10$ GeV and $|\eta| < 2.5$.

The dilepton mass for the $e^+e^- + \mu^+\mu^- - e^\pm\mu^\mp$ combination was then calculated. A minimum-χ^2 fit to the signal was made with MINUIT using the mass distribution from Equation 20-6 smeared with a Gaussian resolution; the errors were determined with MINOS [20-30]. It was not possible to generate enough background to include it in the fit with realistic errors. This fit is shown in Figure 22-12; it gave for an integrated luminosity of 100 fb^{-1}

$$M_{ll}^{\max} = 108.71^{+0.087}_{-0.088} \text{ GeV}$$

with a resolution of 1.29 GeV. A maximum likelihood fit gave a consistent value with slightly smaller errors. The effect of pileup was not taken into account in this analysis. The fitted values are not quite consistent with the expected 108.92 GeV, presumably because of small effects from the acceptance cuts and fitting procedure; this has not been investigated. The derivative of the edge position with respect to the slepton mass vanishes at the geometric mean of the $\tilde{\chi}_1^0$ and $\tilde{\chi}_2^0$ masses but in general is of order unity. For the masses at Point 5

$$\frac{dM_{ll}^{\max}}{dM_{\tilde{l}}} = 0.478\,.$$

Given the large sample of $Z \to l^+l^-$ events, it should be possible to control the systematic errors to less than 0.1%. Therefore, the dilepton endpoint would be sensitive to any difference in the right-handed slepton masses at about the 0.1% level, assuming of course the same event rates as at this point. The possibility of achieving an understanding of the energy and momentum scales at the level of 0.02% is investigated in detail in Chapter 9]. If this resolution could be achieved, the uncertainty on the edge measurement would be probably dominated by the statistical error, and by the uncertainties in the modelling of the background. No mass difference is expected in the minimal SUGRA model because of the postulated universality. However, mass differences and lepton flavour mixing can easily be present in more general SUGRA-type models with realistic GUT-scale dynamics and can give observable effects both at the LHC and in rare low-energy processes such as $\mu \to e\gamma$ and $\mu \to e$ conversion [20-31].,

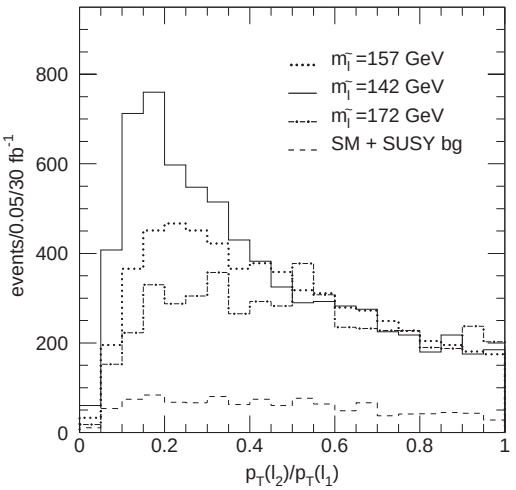

Figure 20-13 Ratio $p_{\mathrm{T},2}/p_{\mathrm{T},1}$ of the softer to the harder lepton for Point 5 and two other values of the slepton mass.

There is much more information available from the dilepton events. A variable that is particularly sensitive to the slepton mass is $p_{\mathrm{T},2}/p_{\mathrm{T},1}$, the ratio of the softer to the harder lepton; a slepton mass close to either the $\tilde{\chi}_1^0$ or the $\tilde{\chi}_2^0$ mass will obviously make one of the leptons soft. Figure 20-13 shows this ratio for the nominal slepton mass at Point 5, 157 GeV, and for two other masses [20-26]. This distribution should be sensitive to changes in the slepton mass of a few GeV fixing the masses of $\tilde{\chi}_1^0$ and $\tilde{\chi}_2^0$. A complete analysis would involve generating samples of events varying all the masses and the $p_{\mathrm{T}}(\tilde{\chi}_2^0)$ distribution and then fitting the resulting $M(ll)$, $p_{\mathrm{T}}(ll)$, and $p_{\mathrm{T},2}/p_{\mathrm{T},1}$ distributions plus the p_{T} distribution of the $h \to b\bar{b}$ signal from $\tilde{\chi}_2^0 \to \tilde{\chi}_1^0 h$ to be discussed in Section 20.2.5 below. Such an analysis has not yet been done.

20.2.4 More complex leptonic SUGRA signatures

The $\tilde{\chi}_2^0 \to \tilde{\chi}_1^0 l^+l^-$ or $\tilde{\chi}_2^0 \to \tilde{l}_R^{\pm} l^{\mp} \to \tilde{\chi}_1^0 l^+l^-$ decays discussed in the previous section can be the starting point for many more complex analyses that work back up the decay chain to obtain information on other SUSY particles. Examples will be given for all the points having such decays.

20.2.4.1 Squark and gluino reconstruction at Point 3

Most of the dileptons in Figure 20-8 for Point 3 come from the decay chain

$$\tilde{g} \to \tilde{b}_1\bar{b} \to \tilde{\chi}_2^0 b\bar{b} \to \tilde{\chi}_1^0 l^+l^- b\bar{b}\ .$$

To reconstruct the gluino and $\tilde{b}_1$ in this chain, events with two opposite-sign, same-flavour leptons (lepton $\equiv e, \mu$ in this section) and at least two b-jets were selected as before. The dilepton pair was required to be near the endpoint, $45\ \text{GeV} < M_{ll} < 55\ \text{GeV}$. Since the dilepton pair is near its maximum value, both the dilepton pair and the $\tilde{\chi}_1^0$ are forced to have low momentum in the rest frame of the $\tilde{\chi}_2^0$, so the $\tilde{\chi}_2^0$ momentum in the laboratory frame is determined to be

$$\vec{p}_{\tilde{\chi}_2^0} = \left(1 + \frac{M_{\tilde{\chi}_1^0}}{M_{ll}}\right)\vec{p}_{ll}\,. \qquad 20\text{-}7$$

Of course the $\tilde{\chi}_1^0$ mass is still unknown and must be determined from an overall fit; a first approximation would be to estimate it from the dilepton endpoint assuming $M(\tilde{\chi}_2^0) \approx 2M(\tilde{\chi}_1^0)$, as is generally true in models with gauge coupling unification. The energies and momenta of the tagged b-jets were corrected to the true energy (see Section 12.5.1.3), to account for losses from neutrinos and from energy leaking out of the $R = 0.4$ cone. This correction was actually derived for the $h \to b\bar{b}$ analysis and will be discussed in Section 20.2.5 below. The reconstructed $\tilde{\chi}_2^0$ momentum was combined with one b-jet to form the $\tilde{b}_1$ mass and then with a second b-jet to form the $\tilde{g}$ mass. Since the mass difference is small, the resolution on the difference is better than that on the individual masses; the kinematics is analogous to that familiar from $D^* \to D\pi$. The resulting scatter plot assuming the correct $\tilde{\chi}_1^0$ mass is shown in Figure 20-14, and the projections on the two axes are shown in Figures 20-15 and 20-16. While

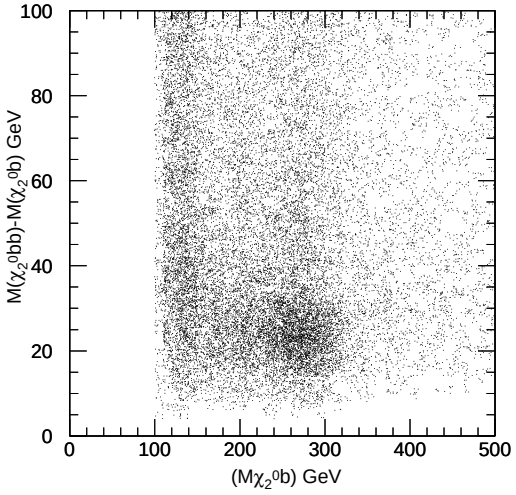

Figure 20-14 Difference of the reconstructed gluino and sbottom masses as a function of the reconstructed sbottom mass at Point 3. The nominal $\tilde{\chi}_1^0$ mass is used in the plot.

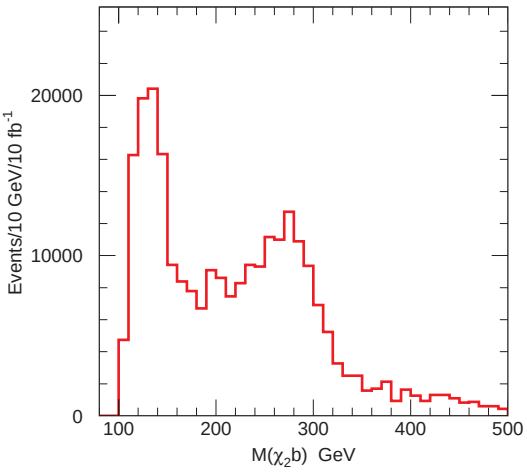

Figure 20-15 $M(\tilde{b}_1)$ projection of the scatter plot in Figure 20-14.

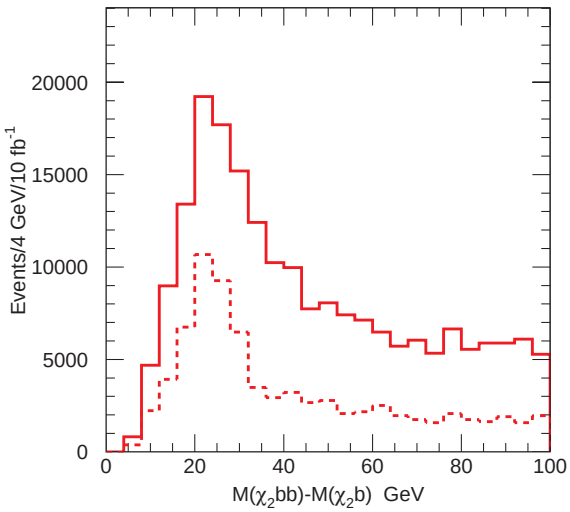

Figure 20-16 $M(\tilde{g}) - M(\tilde{b}_1)$ projection of Figure 20-14. The dashed curve shows the projection with a cut $230\ \text{GeV} < M(\tilde{b}_1) < 330\ \text{GeV}$.

there is a lot of combinatorial background, the peaks are clearly evident. The statistical errors are negligible, so the errors on the masses are determined by the systematic error on the jet energy scale and the dependence on the $\tilde{\chi}_1^0$ mass. The difference $M(\tilde{g}) - M(\tilde{b}_1)$ is insensitive to the assumed mass, while the reconstructed $\tilde{b}_1$ mass peak shifts linearly for events with $M(\tilde{g}) - M(\tilde{b}_1)$ within ±15 GeV of its peak value. Combining this with the energy scale uncertainty gives [20-24]

$$\Delta M(\tilde{b}_1) = 1.5\Delta M(\tilde{\chi}_1^0) \pm 3 \text{ GeV}$$

$$\Delta(M(\tilde{g}) - M(\tilde{b}_1)) = \pm 2 \text{ GeV}$$

where $\Delta M(\tilde{\chi}_1^0)$ is the difference between the true and assumed $\tilde{\chi}_1^0$ masses. At least within the context of the minimal SUGRA model the $\tilde{\chi}_1^0$ mass can be determined accurately by a global fit, as discussed in Section 20.2.9.

Light quarks at Point 3 can be reconstructed in a similar way using the decay $\tilde{q}_L \to \tilde{\chi}_2^0 q$, which has a branching ratio of about 10%. There is an enormous background from $\tilde{g} \to \tilde{b}_1 \bar{b}$, so events with b-jets must be vetoed. Based on the trade-off between tagging efficiency and light quark rejection found in the b-tagging studies documented in Chapter 10 and in the ATLAS Technical Proposal [20-21], this analysis assumed a 90% veto efficiency of b-jets with a 25% mistagging of light jets as b's. Events were selected to have

- at least one jet with $p_T > 125$ GeV and $|\eta| < 2$;
- no tagged b-jets with $p_T > 15$ GeV and $|\eta| < 2$;
- an opposite-sign, like-flavour l^+l^- pair with 45 GeV $< M_{ll} <$ 55 GeV.

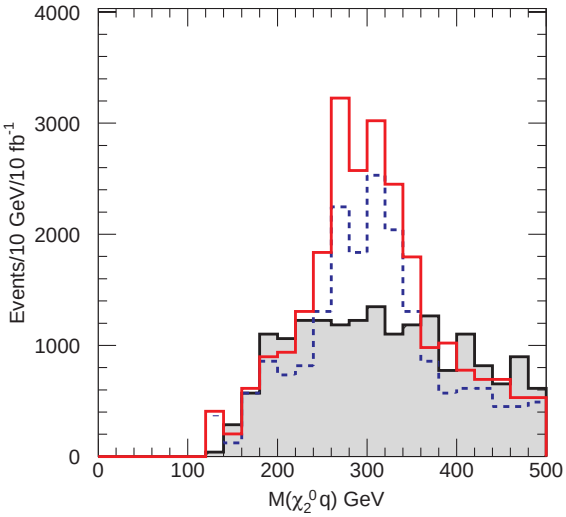

Figure 20-17 Reconstructed $\tilde{q}_L$ mass at Point 3. The combinatorial background is shown as a shaded histogram, and the signal due to real $\tilde{q}_L$'s as the dashed histogram. The remaining events are due to misidentified light quark jets.

The $\tilde{\chi}_2^0$ momentum was reconstructed as before from the visible dilepton momentum; it was then combined with any jet having $p_T > 125$ GeV and $|\eta| < 2$ to give the mass distribution shown in Figure 20-17. There is a clear signal. Even with a 90% veto efficiency there is a significant number of b-jets remaining in this plot. The signal for true light quark jets as determined from the event generator is shown as the dashed curve in the figure. If the veto efficiency were raised to 95% using an algorithm optimised for rejection rather than for tagging, then approximately half of this background would be removed, and the peak would shift upward, closer to the mean $\tilde{q}_L$ mass of 310 GeV. The combinatorial background, shown as the shaded histogram in Figure 20-17, was determined by mixing a $\tilde{\chi}_2^0$ from one event with a jet from another. Because there is a lot of background, the error on the $\tilde{q}_L$ mass is conservatively estimated to be ±20 GeV [20-24]; the purely statistical error would be much less than this.

20.2.4.2 Gluino reconstruction at Point 4

At Point 4, m_0 is large and the squarks are very heavy, so gluino pair production strongly dominates the SUSY cross section. Nevertheless, reconstructing gluinos is not trivial because of the many competing and complex decay modes. The approach used here is to select events with one gluino decaying via $\tilde{g} \to q\bar{q}'\tilde{\chi}_1^{\pm}$ and the other via $\tilde{g} \to q\bar{q}\tilde{\chi}_2^0$ with both gauginos decaying leptonically, giving three leptons and at least four jets. (Two neutralino leptonic decays could also be considered, but this has a smaller branching ratio.) Since the $\tilde{\chi}_1^{\pm}$ and $\tilde{\chi}_2^0$ are almost always nearly degenerate, the mass of the two jets from a single gluino has an endpoint at the difference between the gluino mass and the common gaugino mass. The goal of the analysis is to reconstruct this endpoint.

Events were selected to have:

- three isolated leptons with $p_T > 20$, 10, and 10 GeV and $|\eta| < 2.5$, with at least one opposite-sign, same-flavour pair;
- at least four jets with $p_T > 150$, 120, 70, and 40 GeV and $|\eta| < 2.5$;
- $M_{ll} < 72$ GeV for any opposite-sign, same-flavour lepton pair to reject Z backgrounds;
- no additional jets with $p_T > 40$ GeV and $|\eta| < 5$ to reduce combinatorial background. This jet veto cut has an efficiency of 35% for the signal.

The lepton and jet cuts eliminate the Standard Model background, so no E_T^{miss} cut is used in this analysis. For an integrated luminosity of 30 fb^{-1} there are after these cuts about 250 signal events, 30 SUSY events containing only one gluino, and 18 background events from $t\bar{t}$ and SUSY sources. There are three ways of combining the four jets into two pairs. The pairing of the two hardest and the two softest jets is less likely to be correct and so is excluded. The jet-jet mass distribution for the remaining two combinations is shown in Figure 20-18. This figure also shows the distribution for the correct pairing only, based on information from the generator.

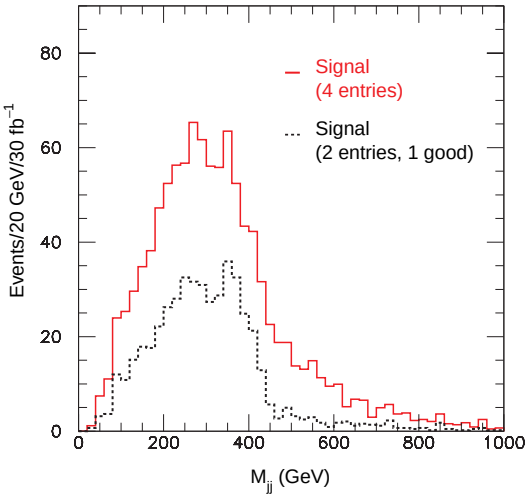

Figure 20-18 Dijet mass distribution for SUSY signal at Point 4 showing all combinations (solid) and only the correct combinations (dashed).

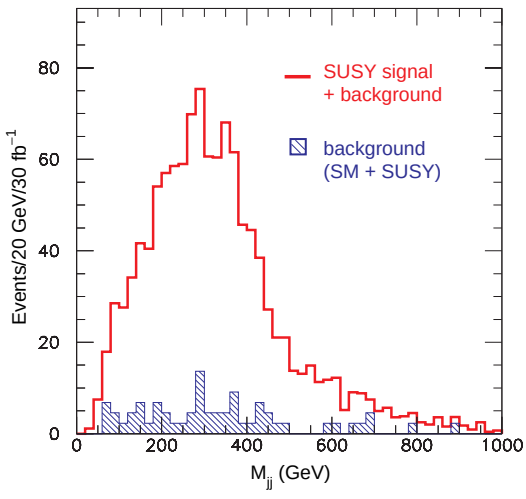

Figure 20-19 Dijet signal and sum of all backgrounds for Point 4.

The signal plus the sum of all Standard Model backgrounds is shown in Figure 20-19 compared to the background. There is clearly structure in the distribution at about the right mass, but it is not very sharp.

To test the sensitivity of this analysis, events were generated for several different gluino masses keeping all other parameters fixed, and the resulting distributions were compared using a Kolmogorov test. This leads to an estimated error for 30 fb^{-1} of [20-25]

$$M(\tilde{g}) - M(\tilde{\chi}_1/\tilde{\chi}_2^0) = 434^{+5.0}_{-16} \pm 4.5 \text{ GeV},$$

where the first error is statistical and the second is systematic. The statistical error is reduced to (+1.6,-5.0) GeV for 300 fb^{-1}. The systematic error is dominated by the 1% uncertainty on the jet energy scale.

20.2.4.3 Squark reconstruction at Point 5

At Point 5 gluinos are heavier than squarks and decay into them, so the three-step decay chain $\tilde{q}_L \to \tilde{\chi}_2^0 q \to l_R^{\pm} l^{\mp} q \to \tilde{\chi}_1^0 l^+ l^- q$ is the dominant source of the dilepton signal considered in Section 20.2.3. Long decay chains generically give multiple constraints; this one gives constraints from an $l^{\pm}q$ edge and an l^+l^-q four-body endpoint in addition to the dilepton endpoint. These provide three constraints on the four masses involved. (Additional constraints are discussed in Sections 20.2.5 and 20.2.6 below.)

The analysis used the same event sample as that which led to Figure 20-12. Events were selected to have [20-29]:

- at least four jets defined with an $R = 0.4$ cone, with $p_{\text{T, 1}} > 100$ GeV and $p_{\text{T, 2, 3, 4}} > 50$ GeV;
- $M_{\text{eff}} > 400$ GeV, where M_{eff} is defined by Equation 20-5;
- $E_{\text{T}}^{\text{miss}} > \max(100 \text{ GeV}, 0.2M_{\text{eff}})$;
- two isolated, opposite-sign leptons with $p_{\text{T}} > 10$ GeV and $|\eta| < 2.5$.

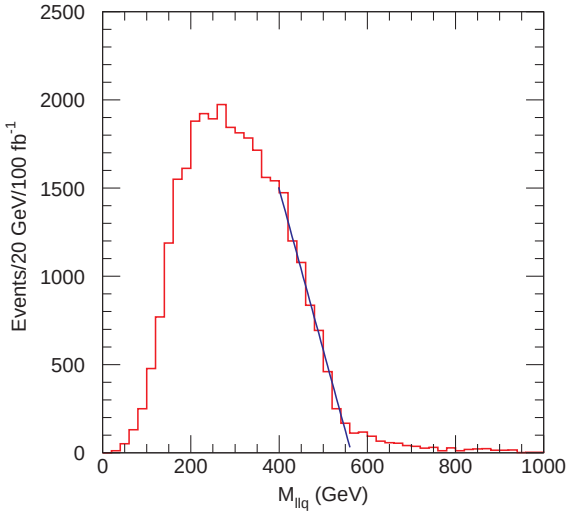

Figure 20-20 Smaller of the two l^+l^-q masses for the signal at Point 5.

In the cascade decays of squarks and gluinos in Point 5 the hardest jets in the event are typically produced in the decays $\tilde{q}_L \to \tilde{\chi}_2^0 q$ and $\tilde{q}_R \to \tilde{\chi}_1^0 q$. The leptons were therefore combined with each of the two hardest jets to extract information on the squark mass. The smaller of the two invariant masses should be less than the four-body endpoint for the $\tilde{q}_L$ decay chain, namely

$$M_{llq}^{\max} = \left[\frac{(M_{\tilde{q}_L}^2 - M_{\tilde{\chi}_2^0}^2)(M_{\tilde{\chi}_2^0}^2 - M_{\tilde{\chi}_1^0}^2)}{M_{\tilde{\chi}_2^0}^2} \right]^{1/2} = 552.4 \text{ GeV}.$$

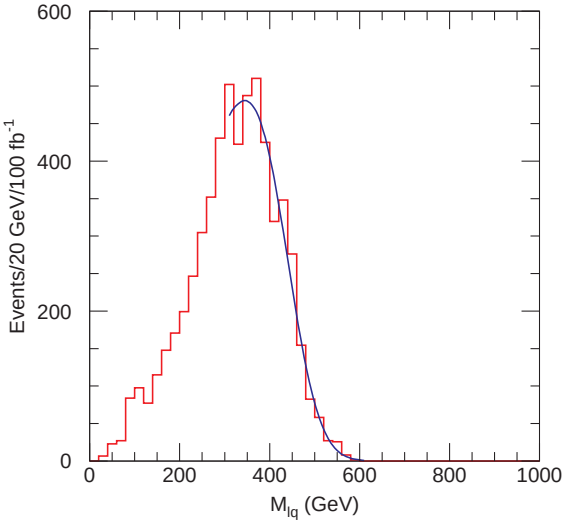

Figure 20-21 $l^{\pm}q$ mass distribution for combinations with $M_{l^+l^-q} < 600\text{GeV}$. The smooth curve is a fit to the theoretical form smeared with a Gaussian.

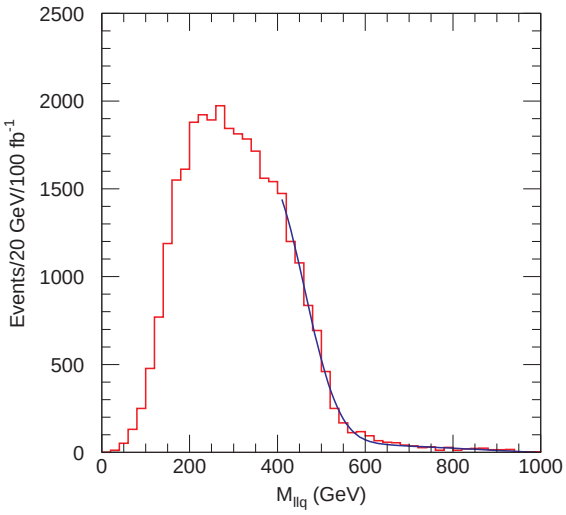

Figure 20-22 Fit described in the text to the smaller of the two l^+l^-q masses.

The distribution should vanish linearly at this endpoint as a result of the four-body phase space. The distribution of the reconstructed smaller mass is shown in Figure 20-20 for the combination $e^+e^- + \mu^+\mu^- - e^{\mp}\mu^{\pm}$. In this combination the background from two $\chi^{\pm}$ independent decays cancels out. The Standard Model background is not shown but is obviously small, as can be seen from the previous dilepton analysis. The figure also shows a linear fit near the endpoint. It extrapolates to 564.0 GeV, 2.1% above the nominal value, providing a first estimate of $M_{llq}^{\max}$.

The llq and lq endpoints can be determined more precisely using a fitting procedure that takes into account the smearing due to resolution and jet reconstruction. Events were selected in which one of the l^+l^-q masses is less than 600 GeV and the other is greater, so that only one pairing of the dilepton pair with one of the two hardest jets is kinematically consistent with the desired decay chain. The cut was chosen to be above the endpoint in Figure 20-20 but is otherwise somewhat arbitrary. The $l^{\pm}q$ distribution for this subsample, including both lepton-jet pairs from the low-mass l^+l^-q combination, is shown in Figure 20-21. It should have an edge from the combination of the quark and the 'right' lepton – *i.e.*, the one emitted first and so adjacent to the quark in the decay chain – which from two-body kinematics is

$$M_{lq}^{\max} = \left[\frac{(M_{\tilde{q}_L}^2 - M_{\tilde{\chi}_2^0}^2)(M_{\tilde{\chi}_2^0}^2 - M_{\tilde{l}_R}^2)}{M_{\tilde{\chi}_2^0}^2}\right]^{1/2} = 479.3 \text{ GeV} .$$

The edge in the figure is not very sharp, so its precise location is not obvious. A fit was therefore made using the theoretical shape of the edge, Equation 20-6 in Section 20.2.3, smeared with a Gaussian resolution. This procedure, which is similar to that for the fit shown in Figure 20-12, assumes that the jet mass can be neglected. The fit, which is shown as the smooth line in Figure 20-21, gives $M_{lq}^{\max} = 433.2^{+3.2}_{-3.3}$ GeV, which is 9.6% low, and $\sigma = 58.2$ GeV. The smearing will also shift the l^+l^-q endpoint. Figure 20-22 shows a fit using an empirical form with a linear plus a quadratic term near the endpoint,

$$\frac{dN}{dM} = [a_1(M_{llq}^{\max} - M) + a_2(M_{llq}^{\max} - M)^2]\vartheta(M_{llq}^{\max} - M) ,$$

smeared with the same Gaussian; a linear term was also included in the fit to describe the region beyond the endpoint. This fit produces the smooth curve in Figure 20-22 and $M_{llq}^{\max} = 498.0^{+7.2}_{-6.4}$ GeV, which is 9.9% low. Presumably the low values reflect energy loss out of the small jet cones, $R = 0.4$, and the neglect of the jet masses. To understand the shifts and the associated errors in detail, it would be necessary to generate and to analyse a number of different samples of events. This has not been done.

The ratio of the $l^{\pm}q$ and $l^{+}l^{-}q$ endpoints is independent of the squark mass,

$$\frac{M_{lq}^{\max}}{M_{llq}^{\max}} = \sqrt{\frac{M_{\tilde{\chi}_2^0}^2 - M_{\tilde{l}_R}^2}{M_{\tilde{\chi}_2^0}^2 - M_{\tilde{\chi}_1^0}^2}} = 0.868 ,$$

and it should be less sensitive to the jet energy scale and to jet clustering than either of the individual endpoints. The smeared fits give 0.870 for this ratio. This probably is fortuitously good agreement, although an analysis of the same data sample using jets defined with $R = 0.7$ gave an equally good result. More study of the systematic errors from the fitting procedure is needed.

There is also a linear vanishing of the distribution for the $l^{\pm}q$ mass combination formed with the 'wrong' lepton and the jet at

$$M'^{\max}_{lq} = \left[\frac{(M_{\tilde{q}_L}^2 - M_{\tilde{\chi}_2^0}^2)(M_{\tilde{l}_R}^2 - M_{\tilde{\chi}_1^0}^2)}{M_{\tilde{\chi}_2^0}^2}\right]^{1/2} = 274.5 \text{ GeV} .$$

Since this endpoint is below the edge of the distribution with the right lepton, it is not usable; an analogous endpoint is used for the GMSB model studied in Section 20.3.1.

20.2.5 $h \to b\bar{b}$ SUGRA signatures

If the two-body decay $\tilde{\chi}_2^0 \to \tilde{\chi}_1^0 h$ is kinematically allowed, it generally has a substantial branching ratio because the light neutralinos are dominantly gauginos. In many cases it is possible to reconstruct $h \to b\bar{b}$ as a resonance peak in the SUSY event sample. This signal may be easier to detect than $h \to \gamma\gamma$ and so provide the discovery mode for the light Higgs boson, although the $\gamma\gamma$ signal is still important to measure the mass precisely. The Higgs signal can also provide a good starting point for further analysis of SUSY particles. Points 1, 2 and 5 all have substantial $\tilde{\chi}_2^0 \to \tilde{\chi}_1^0 h$ decays that can be reconstructed and used in this way.

At Point 1 the branching ratio for $\tilde{\chi}_2^0 \to \tilde{\chi}_1^0 h$ is near unity; since the light neutralinos are mainly gauginos, the branching ratio for the only other two-body decay, $\tilde{\chi}_2^0 \to \tilde{\chi}_1^0 Z$, is small. Hence, about 20% of SUSY events contain at least one $h \to b\bar{b}$. The following cuts were chosen [20-29] to select the signal and eliminate Standard Model backgrounds:

- $E_{\mathrm{T}}^{\mathrm{miss}} > 300$ GeV;
- exactly two tagged b-jets with $p_{\mathrm{T}} > 50$ GeV (as usual a b-tagging efficiency of 60% is used);
- $\Delta R_{bb} < 2$ to help suppress $t\bar{t}$ background;
- a lepton veto, also to help suppress $t\bar{t}$ background;
- at least two additional jets with $p_{\mathrm{T}} > 100$ GeV, at least one of which has $|\eta| < 2$.

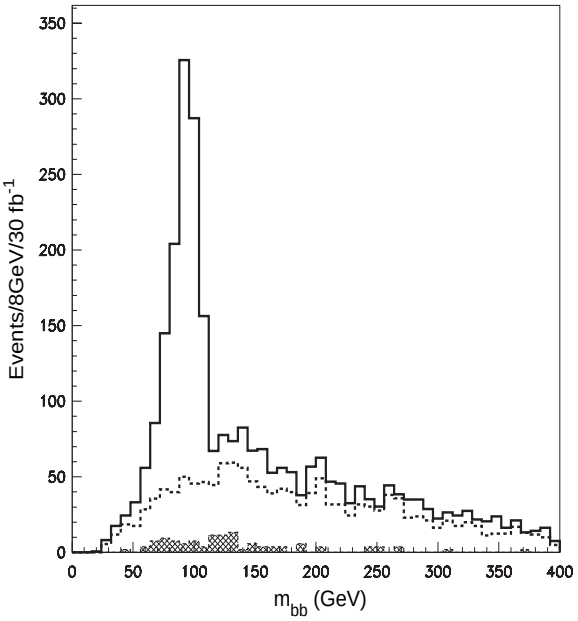

Figure 20-23 Mass distribution for two tagged b-jets at Point 1 for 30fb^{-1}. The dotted curve is the SUSY background, and the shaded histogram is the sum of all Standard Model backgrounds.

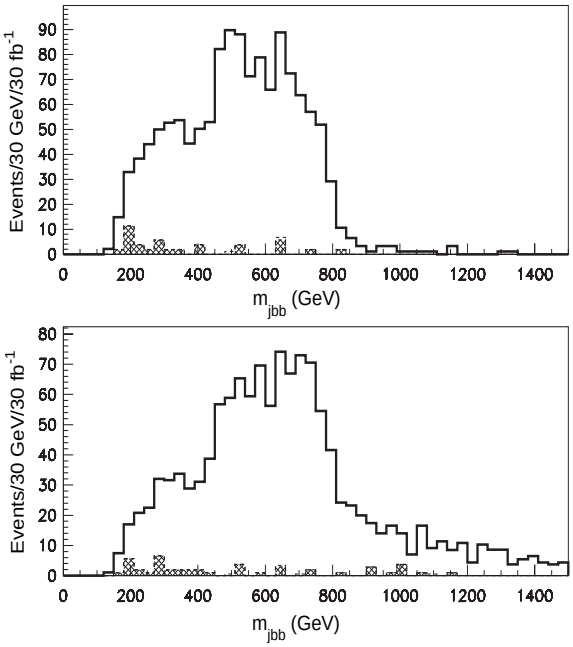

Figure 20-24 bbj mass distribution for events within $\pm 25\ \text{GeV}$ of the peak in Figure 20-23. Top plot: combination with smaller mass. Bottom plot: all combinations.

With these cuts the signal to background ratio is very good, as can be seen in Figure 20-23. For an integrated luminosity of $30\ \text{fb}^{-1}$ there are 980 signal events with a SUSY background of 180 events and a Standard Model background of only 75 events in a bin of $\pm 25\ \text{GeV}$ around the Higgs mass. Given this rate it would be much easier to discover the light Higgs by selecting SUSY events than in the inclusive $h \to \gamma\gamma$ mode.

Since the gluino is heavier than the squarks at this point, the dominant source of the signal is the decay chain $\tilde{q}_L \to \tilde{\chi}_2^0 q \to \tilde{\chi}_1^0 hq$, in which the squark may be produced either directly or from a gluino. For this decay chain there is a maximum value of the hq invariant mass that is determined by two-body kinematics [20-22]:

$$(M_{hq}^{\max})^2 = M_h^2 + (M_{\tilde{q}}^2 - M_{\tilde{\chi}_2^0}^2)\left[\frac{M_{\tilde{\chi}_2^0}^2 + M_h^2 - M_{\tilde{\chi}_1^0}^2 + \sqrt{(M_{\tilde{\chi}_2^0}^2 - M_h^2 - M_{\tilde{\chi}_1^0}^2)^2 - 4M_h^2 M_{\tilde{\chi}_1^0}^2}}{2M_{\tilde{\chi}_2^0}^2}\right]. \qquad 20\text{-}8$$

About 70% of the signal comes from $\tilde{q}_L\tilde{q}_R$ production, either directly or from gluino decays, with $\tilde{q}_L \to \tilde{\chi}_2^0 q$ and $\tilde{q}_R \to \tilde{\chi}_1^0 q$. Hence, it is advantageous to obtain a cleaner sample by selecting events with only two hard jets in addition to the pair of b-jets within $\pm 25\ \text{GeV}$ of the peak, vetoing events having any additional jets with $p_T > 50\ \text{GeV}$ and $|\eta| < 5$. Then the hard jets are likely to come from the squarks, so the smaller of the two $b\bar{b}q$ masses should be less than the endpoint for squark decay. As can be seen from Figure 20-24, the distribution for the smaller mass has a much better defined endpoint than that including both combinations. The estimated error [20-29] on this endpoint is $\pm 30\ \text{GeV}$ for $30\ \text{fb}^{-1}$. The improvement in the error for three years at high luminosity is estimated to be about a factor of two, limited both by the jet energy scale and by the reduced b-tagging efficiency at high luminosity.

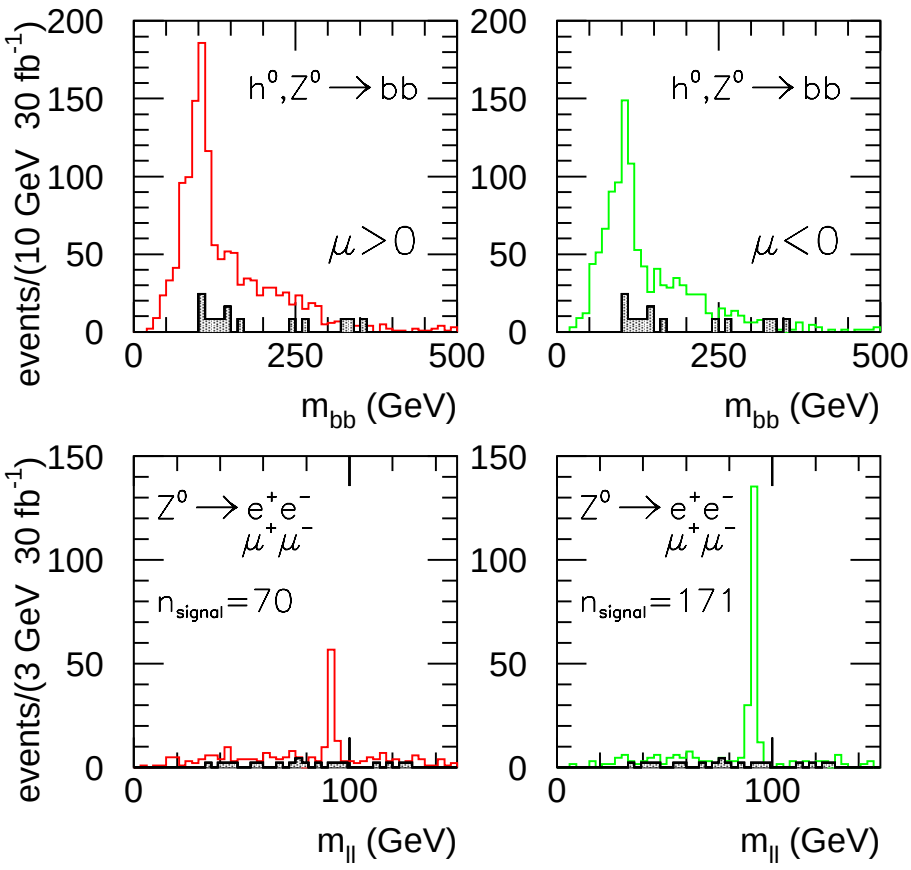

Figure 20-25 $b\bar{b}$ dijet and dilepton mass distributions for Point 2 and for a point with same parameters except $\mu < 0$. The shaded distributions show the Standard Model backgrounds.

For Point 2 with $\tan\beta = 10$ the light gauginos have more Higgsino content. Hence the branching ratio for $\tilde{\chi}_2^0 \to \tilde{\chi}_1^0 h$ is about 65%, with the rest of its decays being mainly $\tilde{\chi}_2^0 \to \tilde{\chi}_1^0 Z$. The $\tilde{\chi}_2^0 \to \tilde{\chi}_1^0 h$ branching ratio for the same parameters with $\mathrm{sgn}\mu = -1$ is about 91%. The dijet mass resolution is not good enough to separate the $\tilde{\chi}_2^0 \to \tilde{\chi}_1^0 h$ and $\tilde{\chi}_2^0 \to \tilde{\chi}_1^0 Z$ decays, so it is important to study the $Z \to l^+ l^-$ signal as well. For the $h \to b\bar{b}$ signal events are selected to have [20-23]

- $E_{\mathrm{T}}^{\mathrm{miss}} > 300$ GeV;
- at least two jets not tagged as b's with $p_{\mathrm{T}} > 100$ GeV;
- two tagged b-jets with $p_{\mathrm{T}} > 100$ GeV;
- $\Delta R_{bb} < 1.0$.

For the dilepton sample the cuts are

- $E_{\mathrm{T}}^{\mathrm{miss}} > 300$ GeV;
- at least two jets not tagged as b's with $p_{\mathrm{T}} > 100$ GeV;
- two opposite-sign, same flavour leptons with $p_{\mathrm{T}} > 10$ GeV.

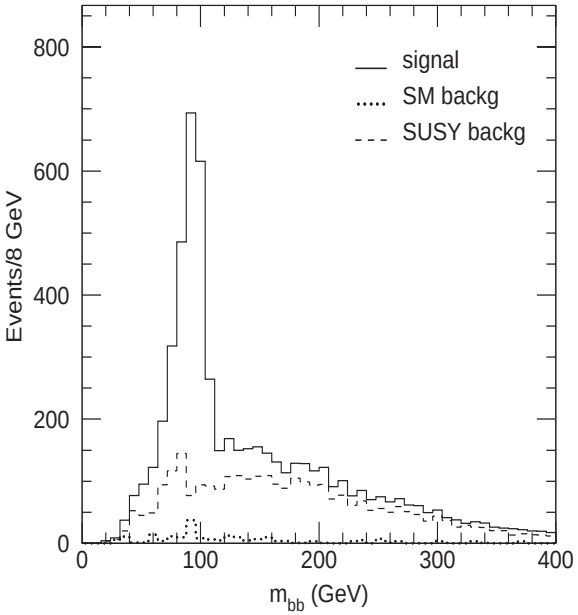

Figure 20-26 Corrected mass distribution for two b-jets for Point 5 Higgs SUSY signal (solid), SUSY background (dashed) and Standard Model background (dotted).

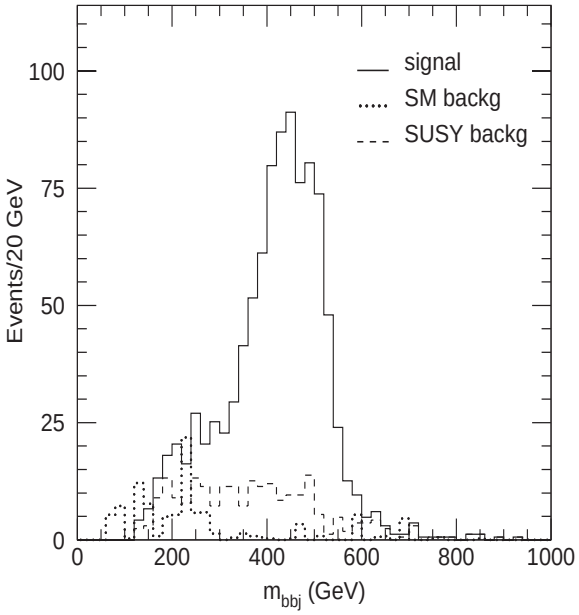

Figure 20-27 Smaller bbq mass for events in the Higgs peak in Figure 20-26.

The resulting dijet and dilepton mass distributions are shown in Figure 20-25 for both signs of μ. Even after correction for the kinematic cuts and for efficiencies these distributions do not directly measure the $\tilde{\chi}_2^0$ branching ratios, since there is a non-negligible contribution to the Z signals from $\tilde{\chi}_2^{\pm} \to \tilde{\chi}_1^{\pm} Z$. Hence, while the measurement is clearly useful, it is not easy to translate into limits on the SUSY model without a more detailed analysis.

The $h \to b\bar{b}$ analysis at Point 5 is quite similar to that at Point 1. The following selection cuts are made to select the signal and reject both SUSY and Standard Model backgrounds [20-26]:

- $E_{\mathrm{T}}^{\mathrm{miss}} > 300$ GeV;
- two tagged b-jets with $p_{\mathrm{T}} > 50$ GeV;
- no additional b-jets with $p_{\mathrm{T}} > 15$ GeV;
- at least two jets with $p_{\mathrm{T}} > 100$ GeV;
- no isolated leptons with $p_{\mathrm{T}} > 10$ GeV.

The signal and backgrounds after these cuts are shown in Figure 20-26. The event and detector Monte Carlos were used to derive a correction to the b-jet energy scale for losses from energy out of the cone used to define the jets and from neutrinos. With this correction, the mass of the Higgs can be measured with an estimated error of 1 GeV from this distribution with 30 fb^{-1} of luminosity. Again, it is easier to discover the Higgs in this channel than in $h \to \gamma\gamma$, although the latter will provide a much more accurate mass.

The Higgs signal comes from a mixture of gluino and squark production, but in most cases the two hardest jets come from the squark decays whether they are produced directly or in gluino decays. Therefore, the smaller of the two masses formed from the Higgs plus one of these two hardest jets should have an endpoint given by Equation 20-8. This distribution is shown in

Figure 20-27 and indeed exhibits the expected endpoint. If the remaining masses in Equation 20-8 are known from other measurements, then the estimated error on the $\tilde{q}_L$ mass is ± 10 GeV for 30 fb^{-1}, dominated by the jet energy scale [20-26].

20.2.6 Thresholds and model-independent SUGRA masses

In multi-step decays such as $\tilde{q}_L \to \tilde{\chi}_2^0 q, \tilde{\chi}_2^0 \to \tilde{\chi}_1^0 h$ or $\tilde{q}_L \to \tilde{\chi}_2^0 q, \tilde{\chi}_2^0 \to \tilde{\chi}_1^0 ll$, there is in general both a maximum and a minimum value of the observable mass as a consequence of two-body kinematics. The minimum value comes from a backwards decay of the second SUSY particle in the centre of mass of the first and can provide a measurable 'threshold' that determines a different combination of masses than the edges discussed previously [20-29]. This is analogous to the method proposed to measure SUSY masses at e^+e^- machines [20-32]. For $e^+e^- \to \tilde{\mu}^+\tilde{\mu}^- \to \tilde{\chi}_1^0\mu^+\tilde{\chi}_1^0\mu^-$ at a fixed centre-of-mass energy, the maximum and minimum values of the muon energy determine the $\tilde{\mu}$ and $\tilde{\chi}_1^0$ masses. For the LHC case, the squark mass plays the role of the initial energy, and invariant masses rather than laboratory energies must be used, but the basic idea is the same. At Point 5 the l^+l^-q threshold can be measured and combined with the results discussed previously to determine the $\tilde{q}_L$, $\tilde{\chi}_2^0$, $\tilde{l}_R$, and $\tilde{\chi}_1^0$ masses using only kinematics rather than relying on a fit to the minimal SUGRA as in Section 20.2.9 below. In this sense the determination of the masses is model independent; the feasibility of doing such an analysis is of course very model dependent.

At Point 5, the dilepton mass from $\tilde{\chi}_2^0 \to \tilde{l}_R^{\pm} l^{\mp} \to \tilde{\chi}_1^0 l^+ l^-$ is fixed by the $\tilde{\chi}_2^0$, $\tilde{l}_R$, and $\tilde{\chi}_1^0$ masses and by $z = \cos\theta^*$, where θ^* is the decay angle in the $\tilde{l}_R^{\pm}$ centre of mass relative to the $l^{\mp}$ direction. These quantities also determine the dilepton momentum in the $\tilde{\chi}_2^0$ centre of mass. If this momentum is not too large – *i.e.*, if the minimum dilepton mass is not too small – then there is obviously a minimum llq mass from the $\tilde{q}_L \to \tilde{\chi}_2^0 q \to l_R^{\pm} l^{\mp} q \to \tilde{\chi}_1^0 l^+ l^- q$ decay chain. The general expression is rather complicated but simplifies somewhat for $z = 0$:

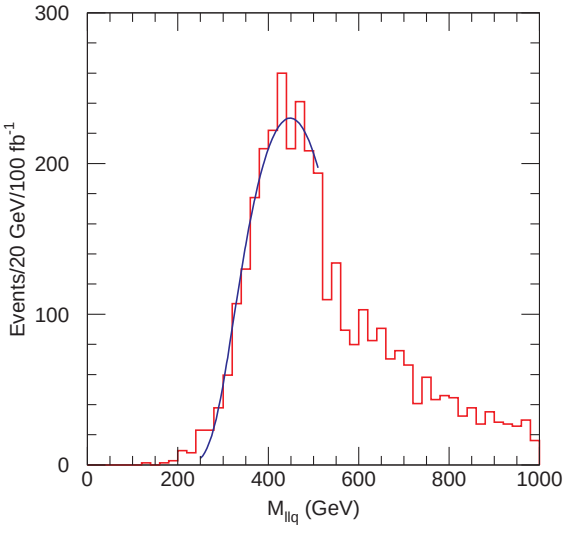

Figure 20-28 Distribution of the larger llq mass at Point 5 for $M_{ll} > M_{ll}^{\max}/\sqrt{2}$ and a fit described in the text.

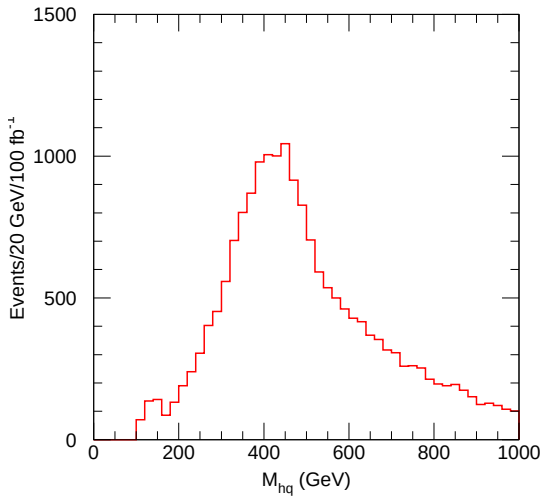

Figure 20-29 Distribution of the larger bbq mass at Point 5. No sideband subtraction or b-jet energy correction has been made.

$$(M_{llq}^{\min})^2 = \frac{1}{4M_2^2M_{\tilde{e}}^2}[-M_1^2M_2^4 + 3M_1^2M_2^2M_{\tilde{e}}^2 - M_2^4M_{\tilde{e}}^2 - M_2^2M_{\tilde{e}}^4 - M_1^2M_2^2M_q^2 - M_1^2M_{\tilde{e}}^2M_q^2 + 3M_2^2M_{\tilde{e}}^2M_q^2 - M_{\tilde{e}}^4M_q^2 + (M_2^2 - M_q^2) \times \sqrt{(M_1^4 + M_{\tilde{e}}^4)(M_2^2 + M_{\tilde{e}}^2)^2 + 2M_1^2M_{\tilde{e}}^2(M_2^4 - 6M_2^2M_{\tilde{e}}^2 + M_{\tilde{e}}^4)}]$$

where the shorthand notation $M_q = M_{\tilde{q}_L}$, $M_2 = M_{\tilde{\chi}_2^0}$, $M_{\tilde{e}} = M_{\tilde{e}_R} = M_{\tilde{\mu}_R}$, and $M_1 = M_{\tilde{\chi}_1^0}$ has been used and where all quark and lepton masses have been neglected. For the masses at Point 5, $M_{llq}^{\min} = 271.8$ GeV.

To extract this threshold, the same sample of events was used as for Figure 20-12. Events were selected as before with the additional requirement $M_{ll} > M_{ll}^{\max}/\sqrt{2}$, corresponding to $z > 0$. The cross section is dominated by squark pairs produced either directly or from gluino decay. Therefore, the larger of the two llq masses formed from the dilepton pair and one of the two highest p_T jets was selected; since the hardest jets presumably come directly from the squark, at least one of the two combinations should be greater than the minimum for squark decay. To extract the position of the edge, a fit was then made using the empirical functional form

$$[b_1(M - M_{llq}^{\min}) + b_2(M - M_{llq}^{\min})^2]\vartheta(M - M_{llq}^{\min})$$

smeared with a Gaussian resolution. The parameters are the desired $M_{llq}^{\min}$, the width of the Gaussian resolution, and the coefficients $b_{1,2}$. If the width was left free in the fit, then the result was quite sensitive to the interval included, so the width was constrained to be 10% of $M_{llq}^{\min}$, similar to what was found before. The distribution for 100 fb^{-1} and the resulting fit are shown in Figure 20-28. The fit with MINUIT and MINOS gave $M_{llq}^{\min} = 283.7^{+4.4}_{-4.5}$ GeV, a statistical error of about ±1.5%. The χ^2 of the fit is poor mainly because of the few bins near 200 GeV; these bins presumably also are responsible for the instability of the fit when the width was left free. Clearly more study is needed to understand the shape of this distribution and the optimal fitting procedure, but it seems plausible that this edge could be measured to ±2%.

Two-body kinematics implies that there is also a threshold for the hq mass from $\tilde{q}_L \to \tilde{\chi}_2^0 q \to \tilde{\chi}_1^0 hq$ at

$$(M_{hq}^{\min})^2 = \frac{(M_q^2 - M_2^2)}{2M_2^2}[M_2^2 + M_h^2 - M_1^2 - \sqrt{(M_2^2 - M_h^2 - M_1^2)^2 - 4M_1^2M_h^2}],$$

where the same shorthand notation as before is used. For Point 5, $M_{hq}^{\min} = 271.8$ GeV. Events were selected having exactly two b-jets with $70 < M_{bb} < 110$ GeV, and the larger of the two bbj masses formed by these and one of the two hardest jets in the event was taken. This distribution is shown in Figure 20-29 with no correction for the b-jet energy scale or sideband subtraction. Clearly this analysis could be improved, but it is unlikely to be as precise as the llq threshold. For now it is included in the analysis with a large error, ±5%.

For Point 5, although the l^+l^- edge, $l^\pm q$ edge, l^+l^-q 4-body endpoint, and hq edge described earlier give four constraints on the $\tilde{q}_L$, $\tilde{\chi}_2^0$, $\tilde{l}_R$, and $\tilde{\chi}_1^0$ masses, it turns out that there exists a solution for any value of the $\tilde{\chi}_1^0$ mass. Including the l^+l^-q threshold described here makes it possible to determine all the masses involved from kinematics alone. The errors for 100 fb^{-1} of luminosity are assumed to be 1% on the $l^\pm q$ and l^+l^-q edges, 2% on the l^+l^-q threshold, and negligible on the l^+l^- edge. These constraints were solved numerically: the $\tilde{q}_L$, $\tilde{\chi}_2^0$, and $\tilde{l}_R$ masses were generated with uniform random distributions within ±50% of their input values, and the $\tilde{\chi}_1^0$ mass was computed from these and the l^+l^- edge. The measured quantities were then

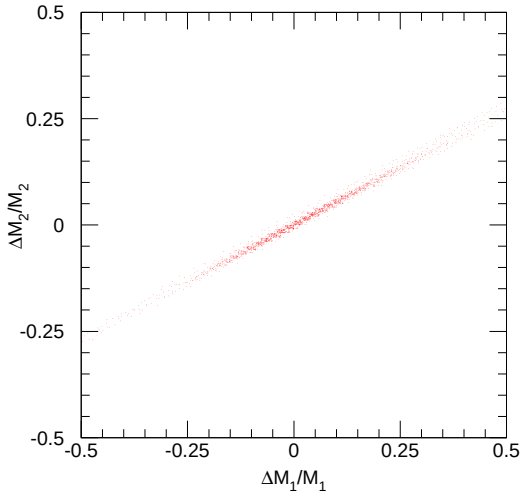

Figure 20-30 $\Delta M_{\tilde{\chi}_2^0}/M_{\tilde{\chi}_2^0}$ as a function of $\Delta M_{\tilde{\chi}_1^0}/M_{\tilde{\chi}_1^0}$ for masses from model-independent analysis for Point 5.

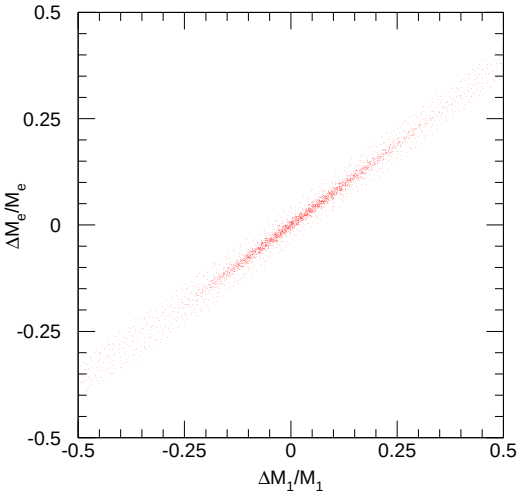

Figure 20-31 $\Delta M_{\tilde{l}_R}/M_{\tilde{l}_R}$ as function of $\Delta M_{\tilde{\chi}_1^0}/M_{\tilde{\chi}_1^0}$ for masses from model-independent analysis for Point 5.

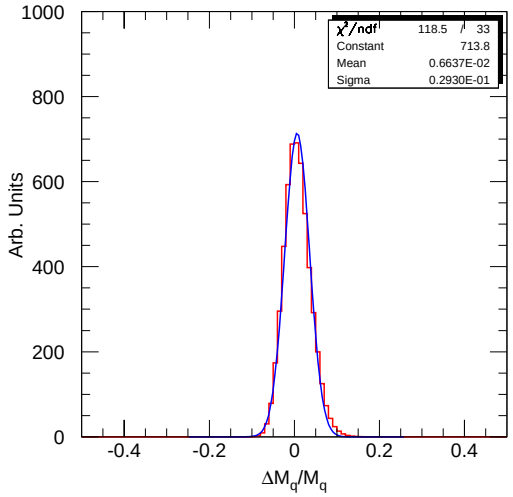

Figure 20-32 Distribution of the fractional difference between the reconstructed and the true squark mass from model-independent analysis for Point 5.

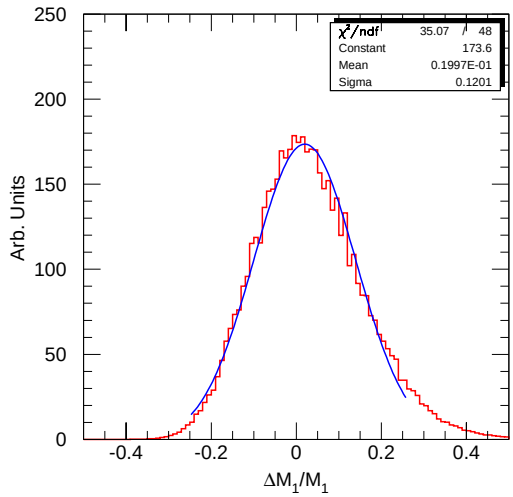

Figure 20-33 Distribution of the fractional difference between the reconstructed and the true $\tilde{\chi}_1^0$ mass from model-independent analysis for Point 5.

calculated, and the point was weighted using the assumed errors with Gaussian distributions. The resulting masses [20-29] are shown as scatter plots in Figures 20-30 and 20-31. Clearly the allowed masses are highly correlated. The width of the distributions of the difference between true and reconstructed mass is about ±3% for the squark mass, shown in Figure 20-32, ±6% for the $\tilde{\chi}_2^0$ mass, ±9% for the slepton mass, and ±12% for the $\tilde{\chi}_1^0$ mass, shown in Figure 20-33. The widths of these distributions are mainly controlled by the error on the l^+l^-q threshold. If this constraint were not included, the $\tilde{\chi}_1^0$ mass would be essentially undetermined. If this error could be reduced to ±1% with a more sophisticated fitting procedure and several years at full luminosity, the error on the $\tilde{\chi}_1^0$ mass would be reduced to about ±7%.

The errors obtained here are of course larger than those found in Section 20.2.9 below by fitting the minimal SUGRA model to the same measurements, but this analysis is done without assuming that the underlying model is known and would still be possible even if the model has a large number of parameters. The interpretations that $\tilde{q}_L$ rather than $\tilde{q}_R$ is the main source of $\tilde{\chi}_2^0$ and the lighter slepton is a $\tilde{l}_R$ rather than an $\tilde{l}_L$ are of course model dependent assumptions, although ones that are much more general than the minimal SUGRA model. While the specific results only apply to this particular point, any long sequence of decays like $\tilde{q}_L \to \tilde{\chi}_2^0 q \to \tilde{l}^{\pm} l^{\mp} q \to \tilde{\chi}_1^0 l^+ l^- q$ will in general give multiple constraints that potentially allow the individual masses to be determined through the measurement of several kinematic endpoints. Another example of the power of identifying long decay chains is presented for one of the GMSB points in Section 20.3.3.1.

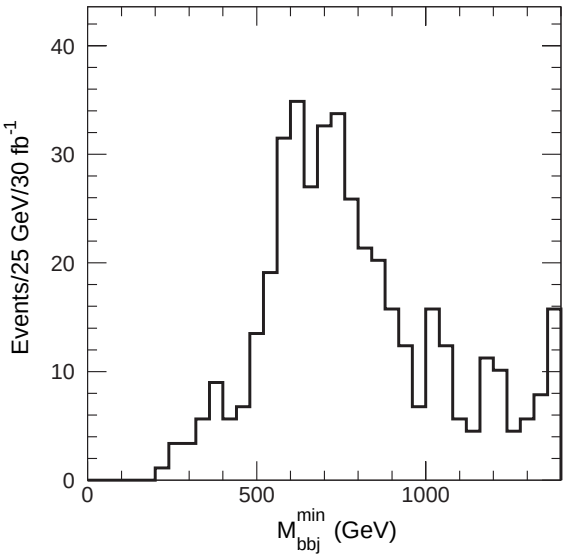

Figure 20-34 Distribution of the larger bbq mass at Point 1after rescaling the b-jets to M_h.

For Point 1 there is no dilepton signature, so the hq threshold, located at $M_{hq}^{\min} = 325.2$ GeV, is more useful. Events were selected with two b-jets near the Higgs mass, two hard jets, and no other jets with $p_T > 100$ GeV to reduce the combinatorial background. The momenta of the b-jets were then rescaled to give the correct Higgs mass, and the larger of the two masses formed by these and one of the hard jets was selected. This distribution is shown in Figure 20-34. More study is needed to understand how to extract the edge from this distribution, but it clearly contains useful information.

20.2.7 Other signatures for SUGRA Points 1 – 5

While signatures based either on $\tilde{\chi}_2^0 \to \tilde{\chi}_1^0 l^+ l^-$ or on $\tilde{\chi}_2^0 \to \tilde{\chi}_1^0 h$ are rather generally applicable, other exclusive modes can be reconstructed in special cases. This subsection contains a number of examples for the five LHCC points listed in Table 20-3. In some cases masses have been extracted by using the shapes of distributions and not just kinematic endpoints.

20.2.7.1 $q_R \to \tilde{\chi}_1^0 q$ signature at Point 1

At Points 1 and 2 the branching ratio for $q_R \to \tilde{\chi}_1^0 q$ is near unity, so production of $\tilde{q}_R$ pairs gives rise to events with two hard jets, no other jets except those from QCD radiation, and large missing transverse energy. The following cuts were made [20-23] to extract the signal and reject Standard Model backgrounds:

- $E_T^{\text{miss}} > 400$ GeV;
- two hard central jets with $p_T > 200$ GeV and $|\eta| < 2$;
- $p_{T,1} + p_{T,2} > 500$ GeV;
- $\Delta R > 1$ between the two jets;

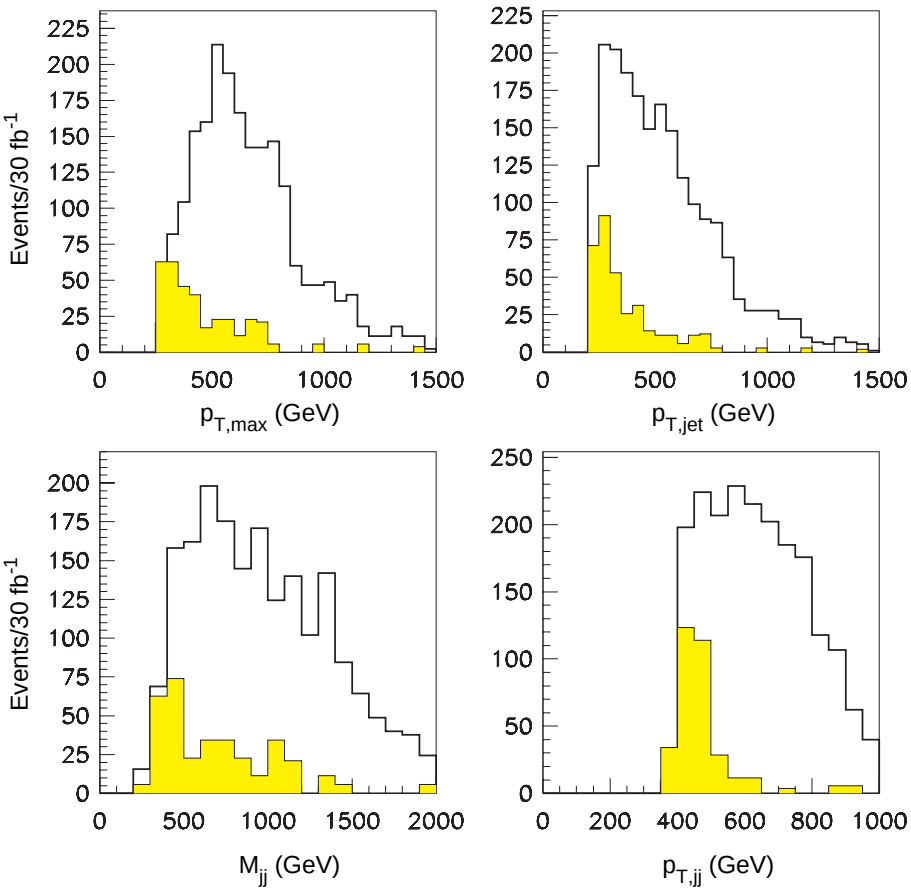

Figure 20-35 Distributions for the signal plus background (curves) and background (shaded) of the p_T of the hardest jet and the hardest two jets, the dijet mass, and the dijet p_T for the $\tilde{q}_R$ production signal at Point 1.

- no additional jets with $|\eta| < 5$ and $p_T > 15$ GeV at low luminosity or $p_T > 40$ GeV at high luminosity;
- no leptons or τ-jets.

After these cuts the SUSY signal is dominated by $\tilde{q}_R\tilde{q}_R$ pairs and $\tilde{q}_R$ associated production, and the Standard Model background is quite small. The resulting p_T and mass distributions for the two hard jets are shown in Figure 20-35. The relative backgrounds for high luminosity are slightly worse because of the need to relax the jet veto. While these distributions do not exhibit any endpoints or other structure that can be directly related to masses, they are still sensitive to the squark mass. Figure 20-36 shows the p_T distributions for three different squark masses; a Kolmogorov test using these shapes is able to distinguish masses differing by about ±25 GeV. After systematic effects – including the jet and E_T^{miss} energy scales, uncertainty in QCD effects such as initial state radiation, and the error in the $\tilde{\chi}_1^0$ mass – are taken into account, the sensitivity of this distribution to the $\tilde{q}_R$ mass is estimated to be about ±40 GeV for 30 fb^{-1} and about ±15 GeV for 300 fb^{-1} [20-23].

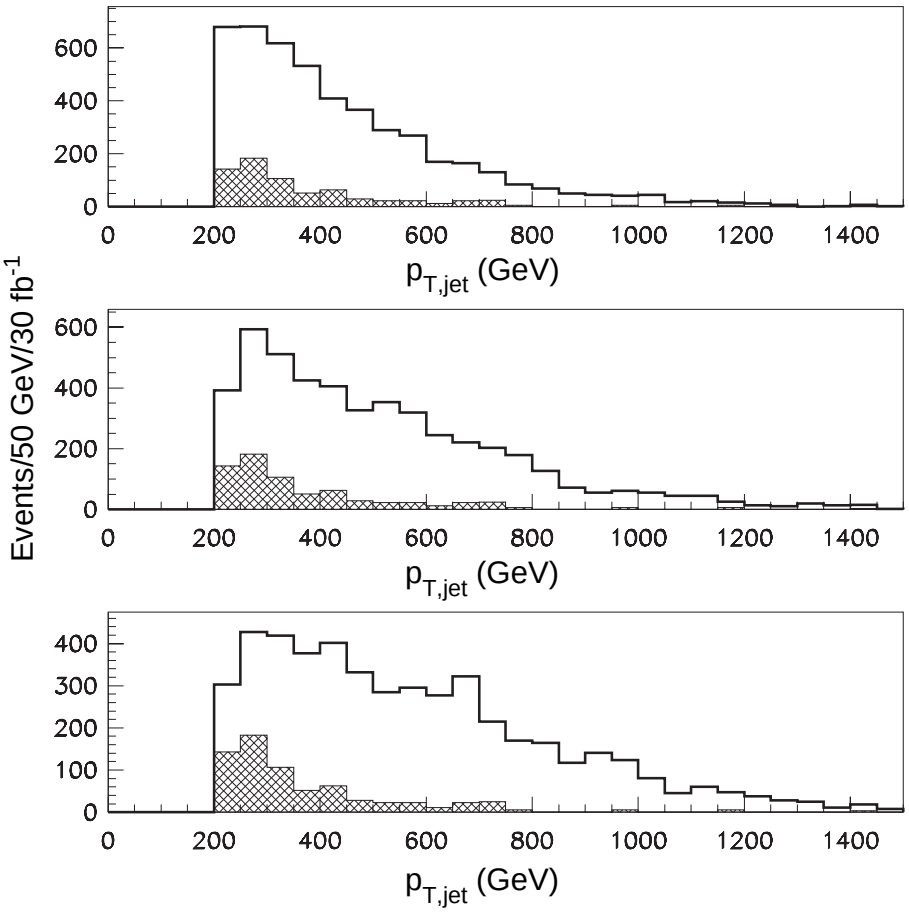

Figure 20-36 Jet p_T distributions for three different squark masses, 750, 950, and 1150 GeV, at Point 1 (full lines), and the sum of all backgrounds (hatched).

20.2.7.2 $\tilde{\chi}_2^{\pm}$ signature at Point 4

Point 4 was chosen to be close to the boundary for radiative electroweak symmetry breaking. Hence, μ is relatively small, and there is a large mixing between gauginos and Higgsinos. Production of the heavier charginos and neutralinos is therefore enhanced; about 85% of the $Z \to l^+l^-$ peak in Figure 20-10 comes from $\tilde{\chi}_2^{\pm} \to \tilde{\chi}_1^{\pm} Z$.

To select these events and reject Standard Model backgrounds the following rather tight requirements were imposed [20-25]:

- two isolated, opposite-sign, same-flavour leptons with $p_T > 20$ GeV and $|\eta| < 2.5$ having $87 < M_{ll} < 97$ GeV;
- a third isolated lepton with $p_T > 10$ GeV and $|\eta| < 2.5$;
- $E_T^{miss} > 100$ GeV;
- at least four jets with $p_T > 100, 50, 40, 40$ GeV and $|\eta| < 3.2$.

The last three cuts are mainly intended to remove the Standard Model backgrounds. After these cuts there about 250 signal events, 60 background events from other SUSY processes, and 4 $t\bar{t}$ events, the dominant Standard Model background, for an integrated luminosity of 30 fb^{-1}.

The rate for $Z \to l^+l^-$ in SUSY events provides a rough estimate of the $\tilde{\chi}_2^{\pm}$ mass, $240 < M(\tilde{\chi}_2^{+}) < 400$ GeV. The mean transverse momentum $\langle p_T^Z \rangle$ of the Z is also sensitive to the masses [20-25]. A full analysis would require comparing all the relevant distributions with many samples of events varying all the model parameters. As a first step, several SUSY samples were generated changing $M(\tilde{\chi}_2^{\pm})$ keeping everything else constant [20-25]. The $\langle p_T^Z \rangle$ for these samples is shown in Figure 20-37. The mean can be measured to an accuracy of ±7 GeV for 10 fb^{-1} and ±3 GeV for 100 fb^{-1}; the corresponding statistical errors on the mass are three times greater. The systematic errors are unimportant compared to the statistical errors. Various systematic effects on the relation between $\langle p_T^Z \rangle$ and $M(\tilde{\chi}_2^{\pm})$ could be important and were considered [20-25]. If initial state radiation is switched off completely, $\langle p_T^Z \rangle$ decreases by only 5 GeV. The corresponding error on the $\chi_2^{\pm}$ mass should be much smaller than this. The value of $\langle p_T^Z \rangle$ also depends on the gluino and $\chi_1^{\pm}$ masses. Within the minimal SUGRA framework, these have estimated errors from other measurements of ±10 GeV and ±2.5 GeV respectively, and variations within these limits have a negligible effect on the $\chi_2^{\pm}$ mass measurement. The final estimate of the result from this method is therefore $M(\tilde{\chi}_2^{\pm}) = 315 \pm 21 \pm 9$ GeV for low luminosity and $M(\tilde{\chi}_2^{\pm}) = 315 \pm 7 \pm 4$ GeV for high luminosity, where the first error is statistical and the second is systematic.

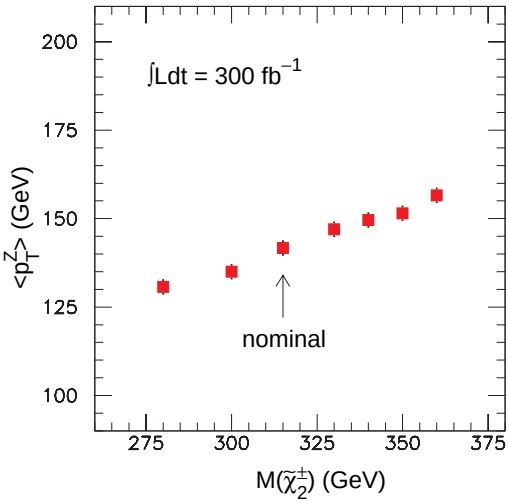

Figure 20-37 Variation of the mean $\langle p_T^Z \rangle$ with the $\tilde{\chi}_2^{\pm}$ mass at Point 4.

20.2.7.3 Top production signature at Point 5

At Point 5 there is significant top production in SUSY events from $\tilde{t}_1 \to \tilde{\chi}_i^0 t$ and $\tilde{b}_1 \to \tilde{\chi}_1^- t$, where the $\tilde{t}_1$ and $\tilde{b}_1$ may be produced either directly or from gluino decays. Since there are not enough constraints to reconstruct a missing neutrino, it is necessary to rely on hadronic top decays. The following cuts were used to make a first selection of events [20-26]:

- $E_T^{miss} > 200$ GeV;
- no leptons and τ-jets;
- two and only two tagged b-jets with $p_T > 30$ GeV;
- at least four additional central jets with $p_T > 30$ GeV and $|\eta| < 3.0$.

Top candidates were then selected from this sample of events:

1. Pairs jj of jets not tagged as b's with a mass $M_{jj} = M_W \pm 15$ GeV were selected, and the mass M_{jjb} of these with one of the tagged b-jets was calculated.
2. The pairings were required to be unique, so no jet is used twice.
3. The pairing that minimised $\chi^2 = (M_{jjb}^{(1)} - M_t)^2 + (M_{jjb}^{(2)} - M_t)^2$ was chosen.
4. The jj momenta were rescaled to obtain the correct W mass, and the jjb mass was recomputed.

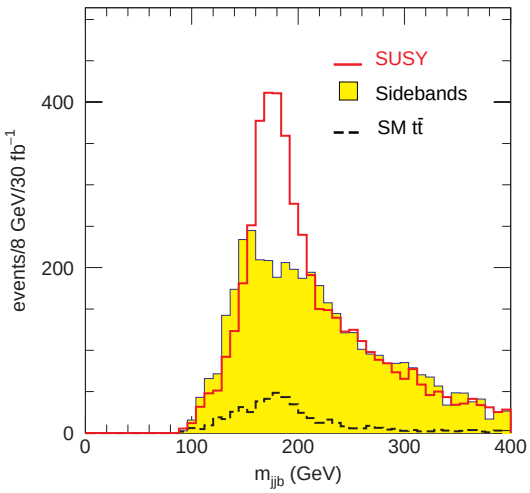

Figure 20-38 Top signal (open), estimated combinatorial background (shaded) at Point 5, and SM $t\bar{t}$ production.

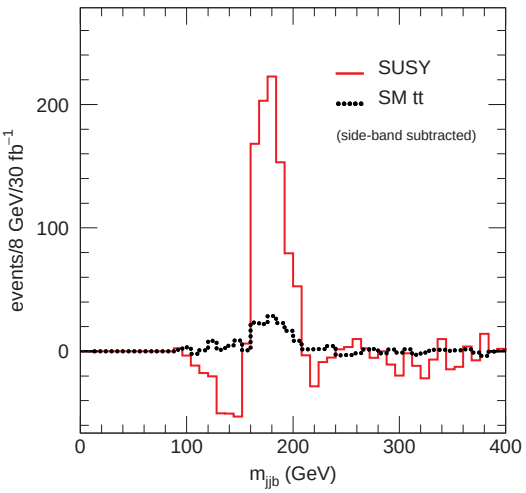

Figure 20-39 Background-subtracted top signal at Point 5.

Each step narrows the width of the M_{jjb} peak at the top mass. The final result after all four steps is shown in Figure 20-38, where the SUSY combinatorial background was estimated using the W sidebands $M_{jj} = 50 \pm 15$ GeV and $M_{jj} = 110 \pm 15$ GeV. The peak with the combinatorial background subtracted is shown in Figure 20-39. For an integrated luminosity of 30 fb^{-1}, 1200 SUSY events are expected having a $t\bar{t}$ pair with reconstructed masses within ±30 GeV of the top mass. (It should be noted, however, that this analysis is based on PYTHIA 2.08; ISAJET 7.27 predicts a smaller signal). Since direct $\tilde{t}_1$ production is small, the observation of $t\bar{t}$ provides an indication that $\tilde{g} \to \tilde{t}_1 \bar{t} \to \tilde{\chi}_1^0 t\bar{t}$ is kinematically allowed. Partial reconstruction of either the direct production or the gluino decay is not easy due to the large SUSY backgrounds but could provide additional constraints on the SUSY model [20-26].

20.2.7.4 Direct slepton production at Point 5

At Point 5, while the $\tilde{l}_R$ are copiously produced in cascade decays involving the $\tilde{\chi}_2^0$, the $\tilde{l}_L$ are produced mainly through the Drell-Yan process $q\bar{q} \to \gamma^*, Z^* \to \tilde{l}_L^+ \tilde{l}_{\bar{L}}$. Since the branching ratio for $\tilde{l}_L \to \tilde{\chi}_1^0 l$ is larger than 95%, the signature is an acoplanar pair of opposite-sign, same-flavour leptons, large $E_{\mathrm{T}}^{\mathrm{miss}}$, and no additional jets. The potential backgrounds from $t\bar{t}$ and from other SUSY processes are much larger than the signal, so rather hard cuts are necessary.

The signal and the Standard Model and SUSY backgrounds were generated with PYTHIA, and the detector response was simulated with ATLFAST. For low luminosity the following cuts were applied [20-26]:

- $E_{\mathrm{T}}^{\mathrm{miss}} > 120$ GeV;
- two opposite-sign, same-flavour leptons (lepton $\equiv e, \mu$) with $p_{\mathrm{T}} > 30$ GeV and $|\eta| < 2.5$;
- angular separation $\Delta\phi < 2$ for the two leptons;
- no jets with $p_{\mathrm{T}} > 15$ GeV and $|\eta| < 5$.

Such a strict jet veto is needed to reduce the $t\bar{t}$ background to an acceptable level, while the $\Delta\phi$ cut helps to reduce the WW background. These cuts also essentially eliminate the $\tilde{l}_R\tilde{l}_R$ background, which gives leptons that are softer and/or more collinear. The jet veto is sufficient to make the other SUSY backgrounds negligible. After these cuts, there is a total of 58 signal events, with backgrounds of 14 WW and four $t\bar{t}$ events for an integrated luminosity of 30 fb^{-1}.

Since the number of events is small, it is important to extend this search to high luminosity. This requires relaxing the jet veto. The last two cuts above were replaced by:

- angular separation $\Delta\phi < 2.5$ for the two leptons;
- no jets with $p_T > 40$ GeV and $|\eta| < 5$.

With these cuts there are a total of 600 signal events with backgrounds of 140 WW events and 140 $t\bar{t}$ events for an integrated luminosity of 300 fb^{-1}. While the signatures for sleptons are obviously difficult, it would be possible to detect the $\tilde{l}_L$ at this point with ATLAS using the full luminosity of the LHC.

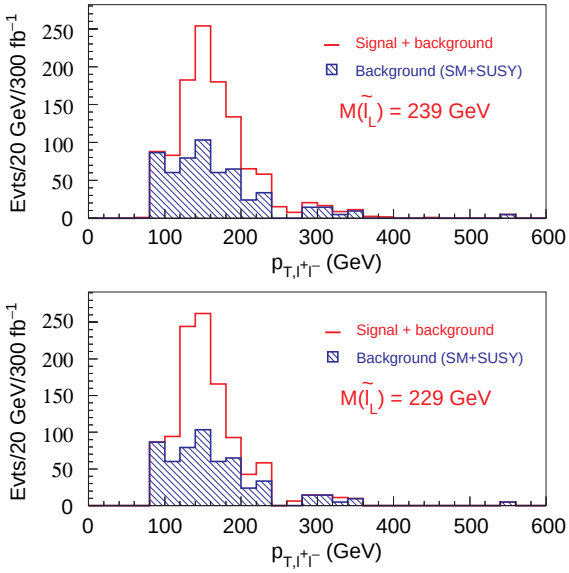

Figure 20-40 Distribution of the p_T of the selected dilepton pairs for two values of the l_R mass.

The dilepton signal does not provide a direct measurement of the slepton mass. Since the Drell-Yan cross section can be calculated with reasonable accuracy, it is possible to estimate the mass using the observed rate, but the accuracy will be limited by the knowledge of the efficiency of the cuts and by the uncertainty on the branching ratio and on the luminosity measurement (See Chapter 13). There is also sensitivity to the mass in the kinematic distributions, specifically in the p_T of the dilepton pair. This distribution is shown in Figure 20-40 for two different values of the slepton mass. A very precise measurement of the mass seems difficult.

If the $\tilde{l}_L$ were slightly heavier, then it would also be possible to search for a four-lepton signal from one $\tilde{l}_L \to \tilde{\chi}_1^0 l$ decay and one $\tilde{l}_L \to \tilde{\chi}_2^0 l \to \tilde{\chi}_1^0 lll$ decay. In principle the endpoint of the trilepton mass can be used to determine the slepton mass, although the rates are marginal. Such a case is discussed in Section 20.2.10 below.

20.2.8 Exclusive SUGRA measurements for large tan β

SUGRA phenomenology for $\tan\beta \geq 10$ is more complicated because of the need to include additional Yukawa couplings and mixings in the $\tilde{b}$ and $\tilde{\tau}$ sectors. For this technical reason the five LHCC SUGRA points were all selected to have $\tan\beta \leq 10$. Hence, at least one of the modes $\tilde{\chi}_2^0 \to \tilde{\chi}_1^0 ll$, $\tilde{\chi}_2^0 \to \tilde{l}l$, or $\tilde{\chi}_2^0 \to \tilde{\chi}_1^0 h$ was available for each point to provide a good starting point for exclusive measurements. There is, however, no reason to disfavour larger values of $\tan\beta$. The most important effect of large $\tan\beta$ is that the splitting between the $\tilde{\tau}_1$ and the other sleptons is increased. If $m_{1/2}$ is small enough so that $\tilde{\chi}_2^0 \to \tilde{\chi}_1^0 h$ and $\tilde{\chi}_2^0 \to \tilde{\chi}_1^0 Z$ are forbidden and m_0 large enough that $\chi_2^0 \to \tilde{l}_{L,R} l$ is also forbidden, then the only allowed two-body decays for the light gauginos can be $\tilde{\chi}_2^0 \to \tilde{\tau}\tau$ and $\chi_1^\pm \to \tilde{\tau}\nu_\tau$. These modes are then dominant, and none of the signatures discussed in Section 20.2.3 – 20.2.7 can be used.

SUGRA Point 6 in Table 20-3 is an example of such a point. The masses are listed in Table 20-4. Since the masses are light to avoid $\tilde{\chi}_2^0 \to \tilde{\chi}_1^0 h$, the cross section is large, 99 pb. Some of the most important branching ratios are

$$BR(\tilde{\chi}_2^0 \to \tilde{\tau}_1 \tau) = 99.9\% \qquad BR(\tilde{\chi}_1^{\pm} \to \tilde{\tau}_1 \nu_\tau) = 99.9\%$$
$$BR(\tilde{\chi}_3^0 \to \tilde{\chi}_2^0 Z) = 13\% \qquad BR(\tilde{\chi}_3^0 \to \tilde{\tau}_1 \tau) = 21\%$$
$$BR(\tilde{g} \to \tilde{b}_1 b) = 55\% \qquad BR(\tilde{g} \to \tilde{b}_2 b) = 10\%$$
$$BR(\tilde{g} \to \tilde{q}_L q) = 3\% \qquad BR(\tilde{g} \to \tilde{q}_R q) = 5.7\%$$

To study this point it is essential to use τ decays. Since SUSY events have additional missing energy from the $\tilde{\chi}_1^0$, it is not possible to reconstruct the τ momenta using the missing transverse energy as is done for $A \to \tau\tau$ in Section 9.3.3.4. Therefore, this analysis relies mainly on hadronic τ decays; the selection is biased towards multi-body decays, *e.g.*, $\tau \to \rho\nu$ or $\tau \to a_1\nu$, so that the visible momentum is closer to the true τ momentum.

ISAJET 7.37 was used [20-33] to generate a total of 600000 signal events. Because the masses are low, the cross section is large; this sample corresponds to an integrated luminosity of about 6 fb^{-1}. The response of ATLAS to these events was simulated with a simple particle-level simulation, including Gaussian resolutions and overall coverage but no cracks or non-Gaussian tails. Jets with $p_T > 25$ GeV were found using a simple fixed-cone jet algorithm with $R = 0.4$. Leptons were required to have $p_T > 10$ GeV and $|\eta| < 2.5$ and to be isolated, with $E_T < 10$ GeV in a $R = 0.2$ cone. An additional efficiency of 90% is included for each lepton. Where relevant, jets were assumed to be misidentified as photons with a probability of 10^{-3}, significantly worse than what is actually expected.

Such a simple, particle-level simulation is inadequate to describe the measurement of τ's; for example, the conversion of photons in the tracker has a non-trivial effect on the observed multiplicity in jets. Hence, a parametrisation of the τ response based on full GEANT simulation was developed [20-34]. Several samples of $Z \to \tau\tau$ events in various p_T ranges were generated with PYTHIA, and the ATLAS response was simulated with DICE and ATRECON. An algorithm to identify τ-jets based on the jet mass, multiplicity, and isolation criteria based on this simulation was then developed. The algorithm, described in Section 9.3.3.2, was optimised for $\tau\tau$ mass resolution rather than τ identification, so it is biased both against single pion decays and against jet masses greater than M_τ. It accepts 41% of the τ hadronic decays while giving a rejection of about 15 against light quark jets, which is adequate for the purpose. The mean value of the visible mass is $M_{\text{vis}} = 0.66 M_{\tau\tau}$ for all of the p_T ranges considered, and the resolution is approximately Gaussian with $\sigma / M_{\text{vis}} = 0.12$. The sign of the τ is identified correctly 92% of the time, from the charge of the tracks ascribed to the τ decay.

These results from full simulation provided the basis for τ identification and reconstruction in the SUSY and the Standard Model background samples. The jets found from the particle-level simulation were compared with the τ's from the event generator. If there was a τ within $\Delta R < 0.4$ of a jet and its hadronic decay products satisfied $E_\tau > 0.8 E_{\text{jet}}$, the jet was assumed to be a τ; otherwise it was assumed to be a normal jet. The τ identification or misidentification probabilities from the full simulation were then applied to obtain the reconstructed τ's. Masses for $\tau\tau$ pairs were calculated by smearing the generated masses with the resolution and shift from the full simulation rather than by using the jets. The charges were also assigned using the probabilities from the full simulation. This approach makes it possible to apply at least the main results from the GEANT simulation to large event samples.

20.2.8.1 Effective mass

The first step in the analysis is to look for a deviation from the Standard Model with a strategy similar to that for moderate $\tan\beta$. Gluinos and squarks decay to give signatures with multiple jets (including τ-jets) and missing energy. Events were selected with cuts very similar to those used in Section 20.2.1:

- at least four jets, some of which may be τ's, with $p_T > 100, 50, 50, 50$ GeV;
- $E_T^{miss} > \max(100\ \text{GeV}, 0.2M_{eff})$;
- transverse sphericity $S_T > 0.2$;
- no μ or isolated e with $p_T > 20$ GeV and $|\eta| < 2.5$.

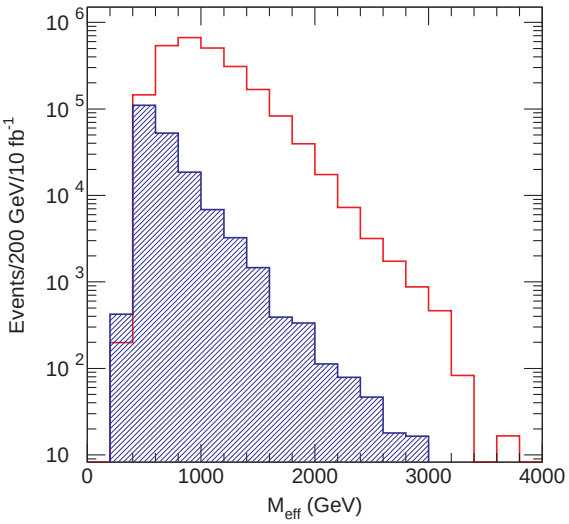

Figure 20-41 Effective mass distribution for Point 6 signal (open) and sum of Standard Model backgrounds (shaded) after cuts.

Figure 20-41 shows the distribution of effective mass M_{eff} after these cuts. As before, the signal dominates over the background for large M_{eff} by about a factor of ten. Since the masses must be fairly low to exclude $\tilde{\chi}_2^0 \to \tilde{\chi}_1^0 h$, the cross section is large. Discovery of this signal is therefore easy and does not depend on measuring τ's.

20.2.8.2 $\tau\tau$ mass distribution

It can be seen from Figure 20-41 that the SUSY signal dominates over the Standard Model background if the lepton cut is replaced by: $M_{eff} > 500$ GeV.

Two τ's are also required, and the lepton veto is then omitted. If the $\tau\tau$ mass distribution could be measured directly, it would show a sharp edge from $\tilde{\chi}_2^0 \to \tilde{\tau}\tau$ at

$$M_{\tau\tau}^{max} = M_{\tilde{\chi}_2^0}\sqrt{1-\frac{M_{\tilde{\tau}_1}^2}{M_{\tilde{\chi}_2^0}^2}}\sqrt{1-\frac{M_{\tilde{\chi}_1^0}^2}{M_{\tilde{\tau}_1}^2}} = 59.64\ \text{GeV}.$$

The selection discussed earlier is biased towards higher mass τ decays, for which the visible energy is closer to the true energy. The visible $\tau\tau$ mass distribution is shown in Figure 20-42 for real $\tau\tau$ pairs and for pairs made with a fake τ. The edge structure is clearly visible in the real distribution, although it is of course smeared out by the missing neutrinos. The fake mass distribution is concentrated at higher masses, reflecting the larger gluino and squark masses.

Figure 20-43 shows the distribution of visible masses resulting from scaling the generated masses by ±7.5% from the nominal values in order to test the sensitivity. These curves could be distinguished statistically, but understanding the background under the edge might be a problem since it is still quite large.

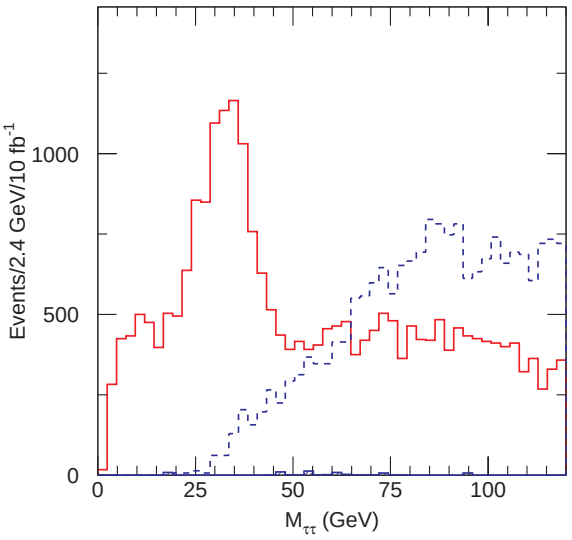

Figure 20-42 Visible $\tau\tau$ mass at Point 6 after cuts. The dashed curve is the background from fake τ's; the shaded histogram is the Standard Model background.

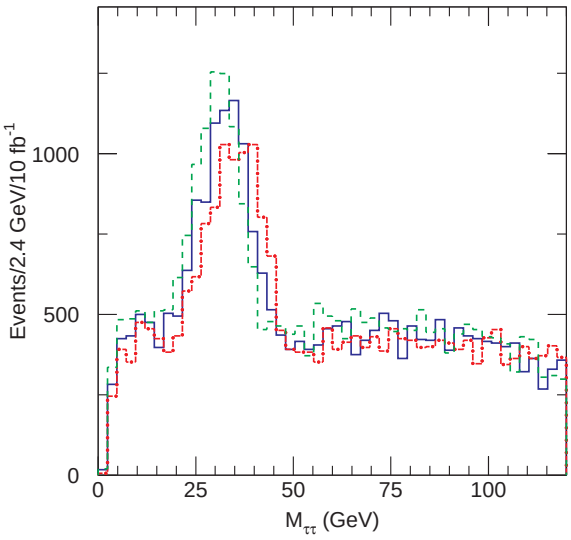

Figure 20-43 Visible mass distribution for real $\tau\tau$ pairs from Figure 20-42 compared with same distributions scaled by $\pm 7.5\%$.

Since the SUSY cross section is dominated by $\tilde{g}\tilde{g}$ and $\tilde{g}\tilde{q}$ production and the gluino is a Majorana fermion, most of the background from two $\chi_1^{\pm} \to \tilde{\tau}^{\pm}\nu$ decays cancels in the $\tau^+\tau^- - \tau^{\pm}\tau^{\pm}$ combination. The fake τ background has random signs, so it also cancels. The $\tau^+\tau^- - \tau^{\pm}\tau^{\pm}$ mass distribution is shown in Figure 20-44. The fake background is much smaller and the signal to background ratio for the edge is much better than in the previous figures. The signal beyond the endpoint is real and comes from $\tilde{\chi}_3^0$ and $\tilde{\chi}_4^0$ decays. Since the real fluctuations would be smaller than those in Figure 20-43, and τ decays are well understood, an error of 5% on the $\tau\tau$ endpoint should be achievable. The dominant error probably comes from the uncertainty on the effect of the τ identification cuts and so is difficult to estimate without much more study.

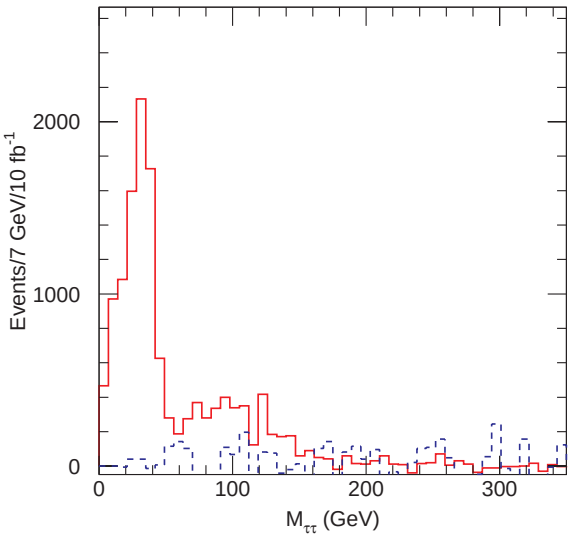

Figure 20-44 $\tau^+\tau^- - \tau^{\pm}\tau^{\pm}$ mass distribution for Point 6 signal (solid) and for background from fake τ's (dashed).

20.2.8.3 Reconstruction of $\tilde{g} \to \tilde{b}b \to \tilde{\chi}_1^0 \tau\tau bb$

At Point 5 it was possible to combine a l^+l^- pair with a hard jet to obtain a signal for $\tilde{q}_L$ (see Section 20.2.4.3). While a similar analysis is possible in principle for Point 6 using a $\tau^+\tau^-$ pair, it is much more difficult. It seems necessary both to use heavy flavour tagging and to reconstruct the gluino to get a good signal.

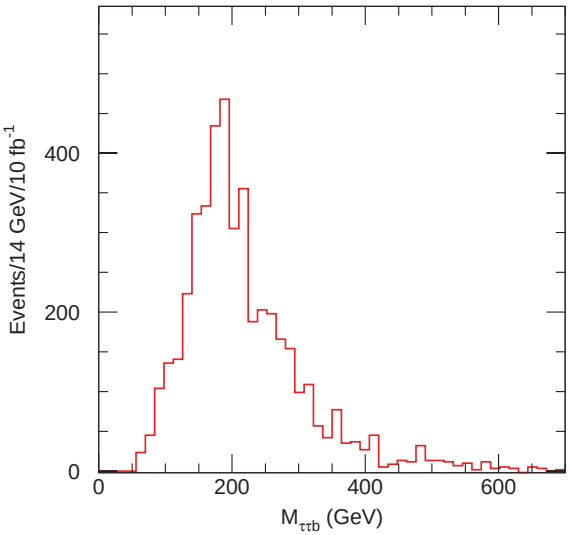

Figure 20-45 Visible $\tau^+\tau^- + \text{jet}$ mass at Point 6 for tagged b-jets. The distribution for like-sign τ pairs has been subtracted.

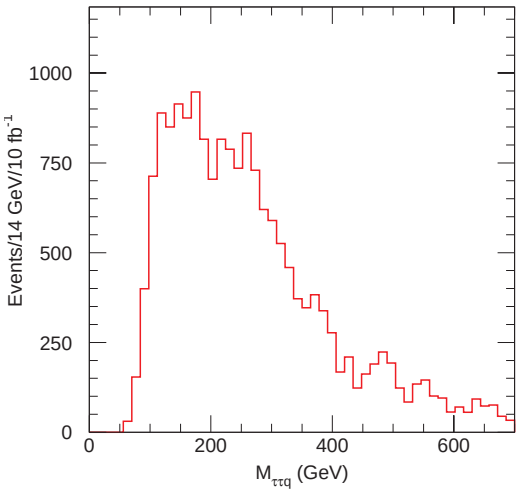

Figure 20-46 Visible $\tau^+\tau^- + \text{jet}$ mass at Point 6 for light quark jets.

The same jet, effective mass, and missing energy cuts were made as before. Events were then selected to have:

- two τ's with a visible $M_{\tau\tau}$ within 10 GeV of the peak in Figure 20-42;
- at least one tagged b-jet with $p_T > 25$ GeV.

The resulting $\tau^+\tau^- b - \tau^\pm\tau^\pm b$ visible mass distribution is shown in Figure 20-45. If the τ's were perfectly measured, this would have an endpoint at

$$M_{\tau\tau b}^{\max} = \left[\frac{(M_{\tilde{b}_1}^2 - M_{\tilde{\chi}_2^0}^2)(M_{\tilde{\chi}_2^0}^2 - M_{\tilde{\chi}_1^0}^2)}{M_{\tilde{\chi}_2^0}^2}\right]^{1/2}$$
$$= 303.9 \text{ GeV}$$

analogous to that for Point 5 in Figure 20-20. There is perhaps some structure but nothing like a real endpoint. The distribution is, however, clearly different from the same distribution with non-b jets shown in Figure 20-46.

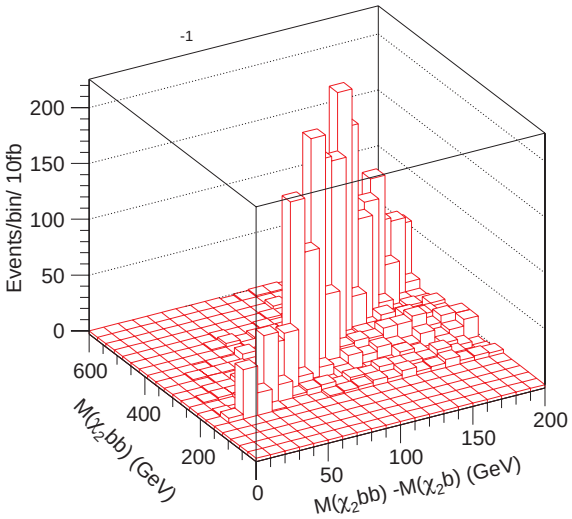

Figure 20-47 Lego plot of the reconstructed $M_{\tilde{g}}$ vs $M_{\tilde{g}} - M_{\tilde{b}_1}$ at Point 6.

A somewhat better signal can be obtained by requiring two tagged b-jets and reconstructing the gluino and squark simultaneously. This is similar to what was done for Point 3 in Section 20.2.4.1. Events were selected with a visible mass $40 < M_{\tau\tau} < 60$ GeV, and the momentum of the $\tilde{\chi}_2^0$ was estimated using the analog of Equation 20-7. This approximation is not as good as in the previous case: because this is a two-step decay, the $\tilde{\chi}_1^0$ momentum would not vanish at the endpoint even if the τ's were perfectly measured. Also, the difference $M_{\tilde{g}} - M_{\tilde{b}_1}$ is larger in this case, so the resolution on it is not as good. Nevertheless, the plot, Figure 20-47, of

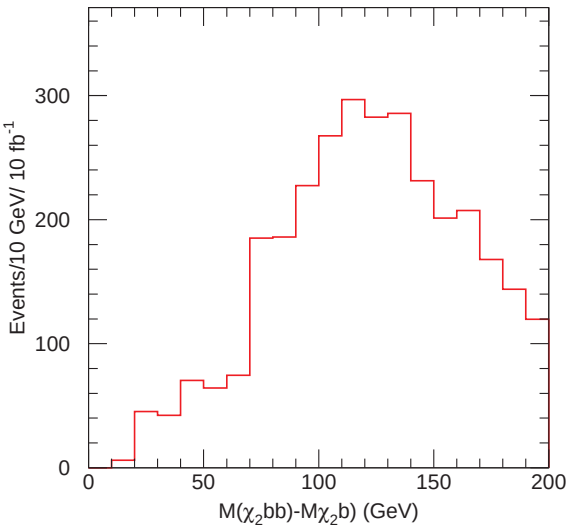

Figure 20-48 Projection of Figure 20-47 onto the $M_{\tilde{g}} - M_{\tilde{b}_1}$ axis.

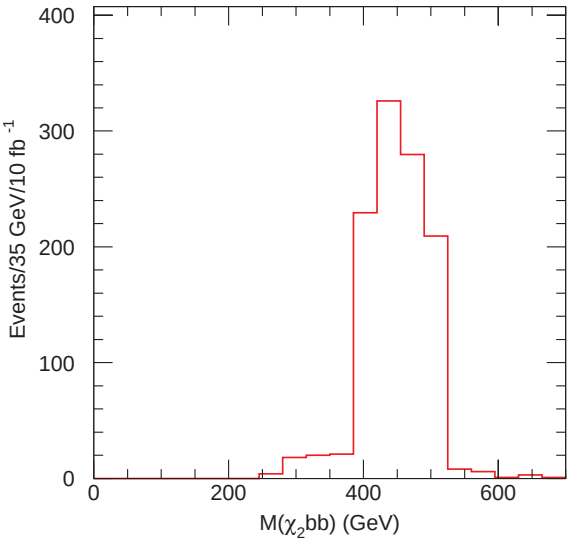

Figure 20-49 Projection of Figure 20-47 onto the $M_{\tilde{g}}$ axis with the cut $100\ \text{GeV} < M_{\tilde{g}} - M_{\tilde{b}_1} < 140\ \text{GeV}$.

$M_{\tilde{g}} - M_{\tilde{b}_1}$ vs $M_{\tilde{g}}$ reconstructed in this way does show a peak at the right place. The projection onto the $M_{\tilde{g}} - M_{\tilde{b}_1}$ axis is shown in Figure 20-48 and the second projection, after cutting on $M_{\tilde{g}} - M_{\tilde{b}_1}$, is shown in Figure 20-49.

A detailed estimate of the errors to be expected from this sort of analysis would require generating many signal samples and comparing the resulting distributions with the corresponding masses. This has not been done, nor has the analysis been optimised. It seems plausible, however, that for an integrated luminosity of 30 fb^{-1} the mass difference $M_{\tilde{g}} - M_{\tilde{b}_1}$ could be determined to about ± 20 GeV while $M_{\tilde{g}}$ could be determined to ± 60 GeV. These error estimates are used for the fits in Section 20.2.9 below.

20.2.8.4 Reconstruction of $\tilde{q}_R \to \tilde{\chi}_1^0 q$

The $\tau\tau$ signatures at Point 6 come primarily from $\tilde{q}_L$ decays. It is also possible to produce $\tilde{q}_R\tilde{q}_R$ pairs, either directly or from gluino decays. Since for squarks of the first two generations the decay $\tilde{q}_R \to \tilde{\chi}_1^0 q$ has a branching ratio of more than 95%, such events are characterised by two hard jets, no additional soft jets except those from gluino decay or initial state radiation, and large missing energy. The analysis is analogous to the one performed in Section 20.2.7.1. To select this signature, events were therefore selected to have:

- $E_{\mathrm{T}}^{\mathrm{miss}} > \max(200\ \mathrm{GeV}, 0.2M_{\mathrm{eff}})$;
- two jets with $p_{\mathrm{T}} > 150$ GeV;
- no additional jets with $p_{\mathrm{T}} > 25$ GeV;
- no leptons, b-jets, or τ-jets.

The p_{T} distribution for the two hardest jets in the events that are accepted by these cuts are shown in Figure 20-50. The mean p_{T} is a function of the squark mass, or rather of a complicated function of the squark production kinematics and of the energy release $M_{\tilde{q}_R}(1 - M_{\tilde{\chi}_1^0}^2 / M_{\tilde{q}_R}^2)$. The statistical error on the mean is tiny, so the only significant errors are systematic. The total systematic error on $M_{\tilde{q}_R}$ should be 25–50 GeV for 30 fb^{-1} and somewhat less for 300 fb^{-1} as the errors are better understood. These errors are used in the fits in Section 20.2.9 below.

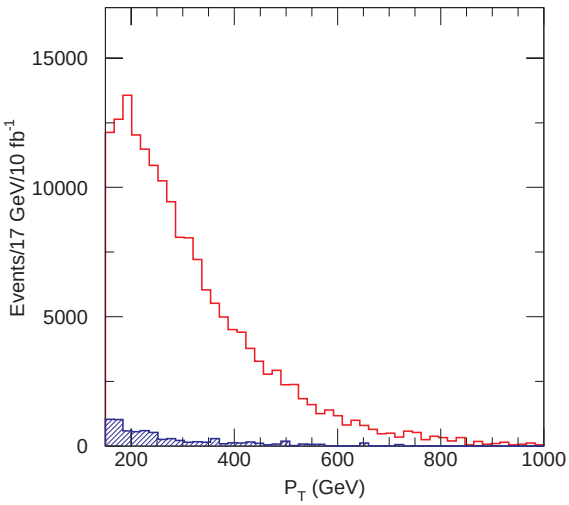

Figure 20-50 p_T distribution of two hardest jets for Point 6 signal (solid) and Standard Model background (shaded) after cuts described in the text.

20.2.9 Fitting minimal SUGRA parameters

Once a number of experimental constraints on combinations of masses have been set with methods like those described above, they can be used in a global fit to determine the parameters of a SUSY-breaking model [20-22, 20-27]. Clearly this requires that the model have only a limited number of parameters. This subsection gives the results of fitting the measurements discussed above to the minimal SUGRA model. This minimal model of course can fit the data by construction. Section 20.2.10 describes how well extra parameters corresponding to a few possible extensions of the minimal model could be constrained. A general treatment of non-minimal models seems very difficult without experimental data to provide guidance.

While some model-independent masses can be determined as described in Section 20.2.6, most of the measurements correspond to combinations of masses. Fitting masses or combinations of masses is much simpler than fitting kinematic distributions: for each point in the parameter space of the model it is sufficient to calculate the spectrum rather than generating and analysing a full sample of events. Also, expressing the results in terms of masses makes it easy to combine results derived using different event generators or different versions of the same generator. Thus, for simplicity all the fits have been done using only masses or combinations of masses. For a measurement such as the $\tilde{q}_R \to \tilde{\chi}_1^0 q$ signature described in Section 20.2.7.1, an approximate equivalent error on the squark mass was assigned. Measurements of this sort are noted below. Of course, if SUSY is discovered, a much more general analysis will be done using many event samples to fit all of the available data, also including the information from branching fractions and cross sections measurements.

The fits for Points 1–5 were made before a correct treatment of large $\tan\beta$ was available in the generator, so an artificial restriction on it had to be imposed. An initial scan of 300000 points was made covering the range

$$50 < m_0 < 1000 \text{ GeV}$$
$$100 < m_{1/2} < 700 \text{ GeV}$$
$$1 < \tan\beta < 15$$

for both signs of μ. The RGE's cause the parameters A_t, A_b, and A_τ that appear in the weak-scale mass matrices to evolve to approximate fixed points with very little dependence on the GUT-scale parameter A_0, which therefore cannot be determined and was not included in the scan. For each point in the scan, all the measured masses or combinations of masses were calculated, and the point was weighted using the estimated experimental errors, artificially inflated if necessary to obtain a reasonable number of solutions. After this initial scan found an approximate allowed region, more points were generated in this smaller region until the $\pm 1\sigma$ errors were determined for $30\ \text{fb}^{-1}$, corresponding to an initial three years at low luminosity, and for $300\ \text{fb}^{-1}$, corresponding to the ultimate reach of ATLAS. For Point 6 a similar method was used with the scan region extended to $\tan\beta < 60$.

The theoretical treatment used to calculate the masses is not perfect. The RGE's are calculated to two loops in gauge couplings and one loop in Yukawa couplings, the thresholds are treated as step functions, and no GUT-scale physics is included. It is assumed that these things can be improved, so no associated errors are included in the fits. The calculation of the light Higgs mass is more difficult. The one-loop effective potential used to calculate it is rather sensitive to the choice of scale, and the leading two-loop effects from the running top quark mass are known to be important. Since the expected experimental error on the mass from $h \to \gamma\gamma$ is at the 0.1% level (see Section 19.2.2), three cases are considered here:

- Low-L: includes statistical errors for low luminosity, $30\ \text{fb}^{-1}$, the systematic errors on the electromagnetic, muon, and jet energy scales previously mentioned, and a theory-dominated error of $\Delta M_h = \pm 1$ GeV on the light Higgs mass.
- High-L: includes statistical errors for high luminosity, $300\ \text{fb}^{-1}$, the systematic errors on the electromagnetic, muon, and jet energy scales previously mentioned, and a theory-dominated error of $\Delta M_h = \pm 1$ GeV on the light Higgs mass.
- Ultimate: The same as High-L but including only the experimental error $\Delta M_h = \pm 0.2$ GeV on the light Higgs mass.

The fits for each point will be described in turn.

Table 20-5 Inputs for the minimal SUGRA model fits at Points 1 and 2. The measurements listed below the heavy rule determine combinations of masses and production dynamics. The High-L and Ultimate measurements differ only in the error on the Higgs mass.

Quantity	Reference	Low-L	Ultimate
M_h (Point 1)	Section 19.2.2	95.4 ± 1.0 GeV	95.4 ± 0.2 GeV
M_h (Point 2)	Section 19.2.2	115.3 ± 1.0 GeV	115.3 ± 0.2 GeV
$M_{hq}^{\max}$	Section 20.2.5	758.3 ± 25 GeV	758.3 ± 13 GeV
$M_{\tilde{q}_R}$	Section 20.2.7.1	959 ± 40 GeV	959 ± 15 GeV
$M_{\tilde{g}}$	[20-23]	1004 ± 25 GeV	1004 ± 12 GeV
$M_{\tilde{t}_1}$ (Point 1)	[20-23]	none	647 ± 100 GeV
$M_{\tilde{t}_1}$ (Point 2)	[20-23]	none	713 ± 100 GeV

Table 20-6 Results of fits of the minimal SUGRA model to the measurements for Points 1 and 2 listed in Table 20-5.

Parameter	Low-L	High-L	Ultimate
m_0	400 ± 100 GeV	400 ± 100 GeV	400 ± 100 GeV
$m_{1/2}$	400 ± 10 GeV	400 ± 8 GeV	400 ± 8 GeV
$\tan\beta$ (Point 1)	2.00 ± 0.08	2.00 ± 0.08	2.00 ± 0.02
$\tan\beta$ (Point 2)	10.0 ± 2.0	10.0 ± 2.0	10.0 ± 1.2

20.2.9.1 Points 1 and 2

Points 1 and 2 are high-mass points with relatively small cross sections. The decay $\tilde{\chi}_2^0 \to \tilde{\chi}_1^0 h$ is completely dominant, so there are fewer well-measured quantities than at some of the other points. These two points differ only in $\tan\beta$ and the corresponding light Higgs mass, so they will be discussed together. The measurements are summarised in Table 20-5 together with references to the appropriate sections of this document or supporting notes. In addition, it should be possible to measure $M_{hq}^{\min}$ as discussed in Section 20.2.6, but not enough work has been done to assign a reliable error. The measurements listed below the line in Table 20-5 do not measure the masses directly. For example, the measurement described in Section 20.2.7.1 measures a combination of the $\tilde{q}_R$ and $\tilde{\chi}_1^0$ masses plus the production kinematics. Treating it as a measurement of a single mass is a reasonable first approximation and a necessary one to allow a scan of the whole parameter space to be made with moderate effort.

The results of the fit [20-27] are summarised in Table 20-6. The value of m_0 is not very well determined because sleptons do not occur in cascade decays at this point to any significant extent, and they are too heavy to be produced directly. Thus the only information on m_0 comes from the squark masses, which are dominated by $m_{1/2}$.

The determination of $\tan\beta$ comes mainly from the light Higgs mass, which also depends on $\mathrm{sgn}\mu$. Figure 20-51 shows the light Higgs mass and the branching ratio for $\tilde{\chi}_2^0 \to \tilde{\chi}_1^0 Z$ as functions of $\tan\beta$ for both signs of μ. Each curve consists of many points corresponding to choices of the other parameters that are consistent with all the measurements except the Higgs mass in Table 20-5. For Point 1, the lower part of the figure shows that the Higgs mass determines two different values of $\tan\beta$ corresponding to the two signs of μ. These values are indicated by the vertical lines in the upper half of the figure. Since the corresponding branching ratios for $\tilde{\chi}_2^0 \to \tilde{\chi}_1^0 Z$ are quite different, the two solutions can be distinguished by using the relative rates for $Z \to ll$ and $h \to b\bar{b}$.

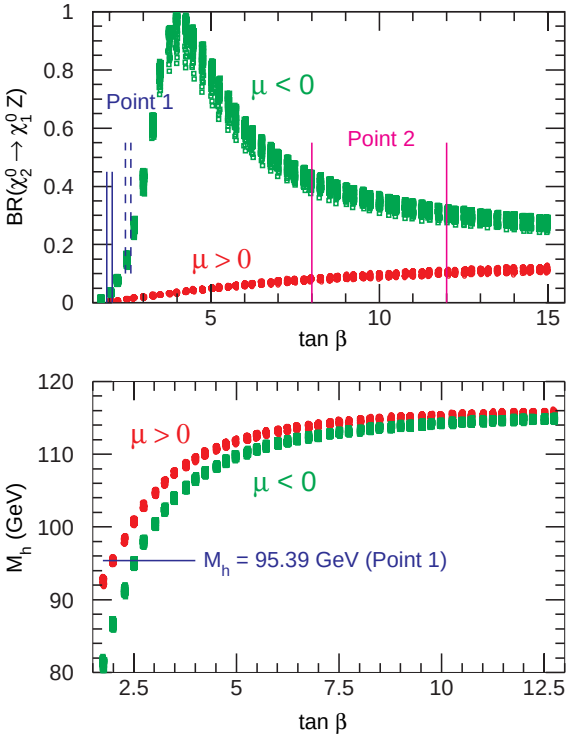

Figure 20-51 Higgs mass and $\tilde{\chi}_2^0 \to \tilde{\chi}_1^0 Z$ branching ratios as functions of $\tan\beta$ and $\mathrm{sgn}\mu$ scanned over the allowed values of the other parameters.

For Point 2, the Higgs mass has a much weaker dependence on $\tan\beta$ and is almost independent of $\mathrm{sgn}\mu$. The allowed region, again indicated by vertical lines, corresponds to different rates for $Z \to ll$ and $h \to b\bar{b}$. This can be used to determine $\mathrm{sgn}\mu$, as was discussed in Section 20.2.5. Presumably these branching ratios could also be used in a more quantitative way to improve the measurement of $\tan\beta$ at Point 2, but this has not been studied.

20.2.9.2 Point 3

Point 3 is a low-mass point with many well-measured quantities. The best-measured ones are summarised in Table 20-7. The measurements listed below the line in the table actually determine combinations of masses. For example, the scatter plot shown in Section 20.2.4.1 really measures $M_{\tilde{b}_1} - 1.5M_{\tilde{\chi}_1^0}$ rather than $M_{\tilde{b}_1}$. Within the minimal SUGRA model, however, $M_{\tilde{\chi}_1^0}$ is known since $M_{\tilde{\chi}_2^0} - M_{\tilde{\chi}_1^0}$ is accurately measured and the two gaugino masses are related by the GUT condition

$$m_1 \approx \frac{5}{3}\tan^2\theta_w m_2 \,.$$

Hence the distinction is less significant than for Points 1 and 2. While the fit is done including all the information simultaneously, $m_{1/2}$ is mainly determined by $M_{\tilde{\chi}_2^0} - M_{\tilde{\chi}_1^0}$, which is accurately measured from the dilepton endpoint. Then m_0 is determined by measuring a squark mass using either $M_{\tilde{b}_1}$ or $M_{\tilde{g}} - M_{\tilde{b}_1}$. Finally, $\tan\beta$ is determined by the Higgs mass, which also fixes the sign of μ. Given the tiny statistical errors for this low-mass point, it is therefore not surprising that all the parameters are accurately determined, as summarised in Table 20-8. The masses in this case are so light that all the errors are dominated by systematic effects, so there is little improvement with increasing luminosity.

Point 3 is of course somewhat unrepresentative, both because of its low masses and because of its unusual branching ratios. Detailed study of SUSY at the LHC will in general require the full luminosity available.

Table 20-7 Inputs for the minimal SUGRA model fit at Point 3. The measurements listed below the heavy rule really determine combinations masses and production dynamics.

Quantity	Reference	Low-L	Ultimate
M_h	Section 19.2.2	68.5 ± 3.0 GeV	68.5 ± 0.2 GeV
$M_{\tilde{\chi}_2^0} - M_{\tilde{\chi}_1^0}$	Section 20.2.3	52.42 ± 0.05 GeV	52.42 ± 0.05 GeV
$M_{\tilde{g}} - M_{\tilde{b}_1}$	Section 20.2.4.1	20.3 ± 2.0 GeV	20.3 ± 2.0 GeV
$M_{\tilde{b}_1}$	Section 20.2.4.1	278.1 ± 3.0 GeV	278.1 ± 3.0 GeV
$M_{\tilde{q}_L}$	Section 20.2.4.1	320.5 ± 20.0 GeV	320.5 ± 10.0 GeV

Table 20-8 Results of a fit of the minimal SUGRA model to the measurements in Table 20-7.

Parameter	Low-L	High-L	Ultimate
m_0	200.0 ± 10.0 GeV	200.0 ± 6.0 GeV	200.0 ± 5.0 GeV
$m_{1/2}$	100.0 ± 1.0 GeV	100.0 ± 1.0 GeV	100.0 ± 1.0 GeV
$\tan\beta$	2.00 ± 0.05	2.00 ± 0.05	2.00 ± 0.02

Table 20-9 Inputs for the minimal SUGRA model fit at Point 4. The measurements below the horizontal rule really determine combinations of masses and production dynamics.

Quantity	Reference	Low-L	Ultimate
M_h	Section 19.2.2	111.8 ± 1.0 GeV	111.8 ± 0.2 GeV
$M_{\tilde{\chi}_2^0} - M_{\tilde{\chi}_1^0}$	Section 20.2.3	68.7 ± 0.8 GeV	68.7 ± 0.25 GeV
$M_{\tilde{g}} - M_{\tilde{\chi}_2^0}$	Section 20.2.4.2	434.0 ± 12.0 GeV	434.0 ± 6.0 GeV
$M_{\tilde{\chi}_2^\pm}$	Section 20.2.7.2	315 ± 20 GeV	315 ± 7 GeV
$\langle M_{\tilde{q}} \rangle$	[20-25]	915 ± 25 GeV	915 ± 25 GeV

Table 20-10 Results of a fit of the measurements in Table 20-9 to the minimal SUGRA model.

Parameter	Low-L	High-L	Ultimate
m_0	800 ± 50 GeV	800 ± 45 GeV	800 ± 35 GeV
$m_{1/2}$	200.0 ± 4.0 GeV	200.0 ± 2.0 GeV	200.0 ± 1.5 GeV
$\tan\beta$	10.0 ± 2.0	10.0 ± 1.5	10.0 ± 0.6

20.2.9.3 Point 4

The squarks and sleptons are heavy at Point 4 because m_0 is very large. As a result, most of the measurements are controlled by gluino and gaugino masses, which have very little sensitivity to m_0. A number of possible methods to determine m_0 have been investigated [20-25]. The best approach seems to be to make a rough measurement of the squark mass by selecting events with at least five hard jets and large $E_{\mathrm{T}}^{\mathrm{miss}}$. The fraction of events with a large value of

$$E_{\mathrm{T}}^{\mathrm{sum}} = \sum_{i=1}^{5} p_{\mathrm{T},i}$$

is sensitive to the squark mass. The statistical errors are small; the main problem is to understand the systematic uncertainty on the relationship between the measured quantity and the squark mass. An estimate of this is included with the errors on the other measurements in Table 20-9.

The resulting fits for $\mu > 0$ are given in Table 20-10. As expected, $m_{1/2}$ is well determined. Since the Higgs mass becomes insensitive to $\tan\beta$ for large values, the errors on it are sensitive to those assumed for the Higgs mass. The violation of $e/\mu/\tau$ universality in gaugino decays is still very small for $\tan\beta = 10$, so the Higgs mass is probably the only way to determine $\tan\beta$ precisely. The errors on m_0 are larger and only improve slowly with increasing luminosity because the determination of the squark mass is limited by systematics. For low luminosity there is also a solution for $\mu < 0$ with $m_0 = 820 \pm 50$ GeV, $m_{1/2} = 190 \pm 4$ GeV, and $\tan\beta = 12.5 \pm 1.5$, but this solution does not exist for high luminosity. For all fits A_0 is essentially undetermined for the reasons already explained.

Table 20-11 Inputs for the minimal SUGRA model fit at Point 5. The numerical values are obtained from the formulas given in the referenced sections plus masses from ISAJET 7.37.

Quantity	Reference	Low-L	Ultimate
M_h	Section 19.2.2	92.9 ± 1.0 GeV	92.9 ± 0.2 GeV
$M_{ll}^{\max}$	Section 20.2.3	108.92 ± 0.50 GeV	108.92 ± 0.10 GeV
$M_{lq}^{\max}$	Section 20.2.4.3	478.1 ± 11.5 GeV	478.1 ± 5.0 GeV
$M_{lq}^{\max}/M_{llq}^{\max}$	Section 20.2.4.3	0.865 ± 0.060	0.865 ± 0.020
$M_{llq}^{\min}$	Section 20.2.6	271.8 ± 14.0 GeV	271.8 ± 5.4 GeV
$M_{hq}^{\max}$	Section 20.2.5	552.5 ± 10.0 GeV	552.5 ± 5.5 GeV
$M_{hq}^{\min}$	Section 20.2.6	346.5 ± 17.0 GeV	346.5 ± 17.0 GeV

Table 20-12 Results of a fit [20-29] of the minimal SUGRA model to the measurements in Table 20-11.

Parameter	Low-L	High-L	Ultimate
m_0	$100.0^{+4.1}_{-2.2}$ GeV	100.0 ± 1.4 GeV	100.0 ± 1.3 GeV
$m_{1/2}$	300.0 ± 2.7 GeV	300.0 ± 1.7 GeV	300.0 ± 1.5 GeV
$\tan\beta$	2.00 ± 0.10	2.00 ± 0.09	2.00 ± 0.05

20.2.9.4 Point 5

At Point 5 there are two good starting points, $\tilde{\chi}_2^0 \to \tilde{l}_R l$ and $\tilde{\chi}_2^0 \to \tilde{\chi}_1^0 h$, so there are many measurements that can be precisely expressed in terms of particle masses. These are summarised in Table 20-11 using masses from the same version of ISAJET that was used for the analyses described in Section 20.2.4.3 and Section 20.2.6. The statistical errors determined in those sections have been scaled appropriately with luminosity and then combined with the usual energy scale systematic errors.

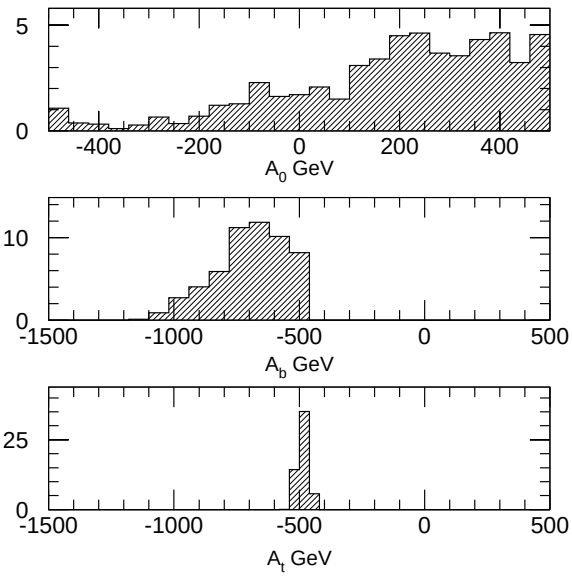

Figure 20-52 Allowed values of the GUT scale A_0 and the weak scale A_t and A_b for Point 5.

The resulting fits [20-29] are shown in Table 20-12. All three parameters are well determined, but A_0 is still essentially undetermined despite all the precise measurements. This can be understood by examining the distribution shown in Figure 20-52 of the values of A_0 and of the weak scale parameters A_t and A_b allowed by the fit. Evidently the weak scale parameters, which are what can actually be measured, are reasonably well determined but are simply insensitive to A_0.

Table 20-13 Inputs for the minimal SUGRA model fit at Point 6. The measurement listed below the heavy rule really determines a combination of masses and production dynamics; conservative (optimistic) errors for it are given.

Quantity	Reference	Low-L	Ultimate
M_h	Section 19.2.2	111.9 ± 1.0 GeV	111.9 ± 0.2 GeV
$M_{\tau\tau}^{\max}$	Section 20.2.8.2	59.6 ± 3.0 GeV	59.6 ± 1.2 GeV
$M_{\tilde{g}} - M_{\tilde{b}_1}$	Section 20.2.8.3	150 ± 20 GeV	150 ± 10 GeV
$M_{\tilde{g}}$	Section 20.2.8.3	540 ± 60 GeV	540 ± 30 GeV
$M_{\tilde{q}_R}$	Section 20.2.8.4	$498 \pm 50(25)$ GeV	$498 \pm 25(12)$ GeV

Table 20-14 Results of a fit of the measurements in Table 20-13 to the minimal SUGRA model. There are solutions for both signs of μ.

Parameter	Low-L	High-L	Ultimate
		$\mu < 0$	
m_0	236 ± 37 GeV	242 ± 28 GeV	242 ± 25 GeV
$m_{1/2}$	200 ± 14 GeV	196 ± 10 GeV	194 ± 6 GeV
$\tan\beta$	41 ± 3.9	44 ± 1.7	45 ± 1.7
A_0	0 ± 180 GeV	-60 ± 132 GeV	-50 ± 80 GeV
		$\mu > 0$	
m_0	228 ± 39 GeV	237 ± 26 GeV	218 ± 30 GeV
$m_{1/2}$	200 ± 15 GeV	197 ± 9 GeV	196 ± 8 GeV
$\tan\beta$	41 ± 3.7	44 ± 1.7	44 ± 1.1
A_0	80 ± 160 GeV	8 ± 124 GeV	63 ± 71 GeV

20.2.9.5 Point 6

The measurements discussed previously for Point 6 are summarised in Table 20-13. For the $\tilde{q}_R$ signature the error is almost entirely systematic, and the distribution shown in Figure 20-50 is featureless. Two error estimates are given in the table; the more conservative will be used except in the Ultimate fit. The errors at high luminosity for measurements involving τ's assume that hadronic τ decays can be identified and measured in the presence of pileup. This was not studied in Reference [20-34], but in Section 9.1.5.4 it is shown that τ identification and measurement are not significantly affected by high luminosity running.

The fit [20-33] was carried out as before extending the $\tan\beta$ range to $1 < \tan\beta < 60$. The upper limit was set because larger values lead to a negative squared mass for the $\tilde{\tau}_1$, breaking electromagnetic gauge invariance; it does not restrict the fit. The results are given in Table 20-14. There are nearly equivalent solutions for both signs of μ. This is to be expected: by a change of conventions, the sign of μ with $\tan\beta > 0$ can be traded for the sign of $\tan\beta$ with $\mu > 0$, and $\tan\beta \approx \pm\infty$ are equivalent [20-35]. The value of A_0 is also quite well determined, in contrast to

the points with lower $\tan\beta$. While Point 6 is certainly difficult, it is surprising how much can be measured. In part this is due to the fact that the masses have to be low to avoid $\tilde{\chi}_2^0 \to \tilde{\chi}_1^0 h$, leading to large event samples.

20.2.10 Non-universal SUGRA models

The fits in Section 20.2.9 all assume the minimal SUGRA parameters with just four real parameters plus $\mathrm{sgn}\mu$. While this simplicity is somewhat justified by the universality of gravity and by the need to satisfy limits based on precision low-energy tests, it is by no means necessary. Models of physics near the Planck scale can lead to qualitatively new signatures such as flavour mixing and *CP* violation in the slepton sector [20-31]. For example, it is possible to have a substantial rate for $\tilde{\chi}_2^0 \to \tilde{\mu}^{\pm} e^{\mp} \to \tilde{\chi}_1^0 \mu^{\pm} e^{\mp}$ at the LHC while still satisfying existing bounds on $\mu \to e\gamma$ and $\mu \to e$ conversion in the field of a nucleus. It is clear from Section 20.2.3 that this particular signature could be detected by ATLAS with good sensitivity.

A completely general SUGRA model has as many weak-scale parameters as the MSSM, so a general exploration is not possible without some experimental guidance. Since low-energy tests severely constrain flavour mixing and *CP*-violating phases, these are assumed to be absent, although there is no good justification for this assumption. This still leaves nineteen real parameters plus $\mathrm{sgn}\mu$, corresponding to the parameters of ISAJET. In this first exploration, three possible deviations from universality at the GUT scale have been considered: non-universal Higgs masses, non-universal $\underline{5}$ and $\underline{\overline{10}}$ sfermion masses, and non-universal third generation masses. Each case can be characterised by one additional parameter. In general these new parameters are less well constrained than the minimal ones. Only exploratory work was performed on a few of the many possible variants of the model. Due to the preliminary nature of the work, in most cases no explicit numerical conclusion is drawn, but it is shown that in all considered cases ATLAS is sensitive to the model parameters.

20.2.10.1 Nonuniversal Higgs masses

Additional Higgs bosons, some of them superheavy, are needed to break the GUT gauge group down to $SU(3) \times SU(2) \times U(1)$, so it makes sense to distinguish the Higgs bosons from the squarks and sleptons. For this case, the soft Higgs masses are taken to be equal but different from those of the other scalars at the GUT scale:

$$m_{H_u} = m_{H_d} = m_{0,H}$$
$$m_{\tilde{Q}} = m_{\tilde{q}_R} = m_{\tilde{L}} = m_{\tilde{l}_R} = m_0$$

The measurements for Point 5 were refit including $m_{0,H}^2 > 0$ in addition to the minimal SUGRA parameters. For the five-parameter fit, the error on $m_{1/2}$ is about 20% larger, while the errors on m_0 and $\tan\beta$ are almost the same [20-29]. However, the new parameter is poorly constrained,

$$m_{0,H} < 400 \text{ GeV (95\% CL)} \quad .$$

The fit is insensitive to the new parameter because the derived value of μ is large, about 500 GeV. The value of M_{H_u} at the weak scale is determined through the RGE's mainly by the top Yukawa coupling and the $\tilde{t}$ mass, not by M_{H_u} at the GUT scale. As a result the masses of the $\tilde{\chi}_1^0$, $\tilde{\chi}_2^0$, and h have little dependence on $m_{0,H}$ unless it is of order the heavy mass scale.

To determine $m_{0,H}$ it is necessary to measure the masses of the heavy Higgs bosons H and A, which vary by about 40 GeV over this range of $m_{0,H}$. Since at Point 5 these have small production cross sections and decay into $t\bar{t}$ more than 90% of the time, it seems difficult to detect them at the LHC.

20.2.10.2 Non-universal $\underline{5}$ and $\underline{10}$ sfermion masses

The second non-universal SUGRA possibility considered here is that the sfermions in the $\underline{5}$ and $\underline{10}$ representations of $SU(5)$ might have different masses:

$$m_{\tilde{d}_R} = m_{\tilde{L}} = m_{0,5}$$
$$m_{\tilde{Q}} = m_{\tilde{u}_R} = m_{\tilde{l}_R} = m_{H_u} = m_{H_d} = m_0$$

If the fit is redone for this case using only the information in Table 20-11, then only a poor limit is obtained on the new parameter:

$$m_{0,5} < 390 \text{ GeV (95\% C.L.)} \quad ;$$

the small error on $m_{1/2}$ about doubles and the errors on m_0 and $\tan\beta$ increase slightly. The reason for this poor limit is that only one of the four squarks of each generation is in the $\underline{5}$, and its mass is dominated by $m_{1/2}$.

The constraint on $m_{0,5}$ can be improved by using more information. If $m_{0,5} \lesssim 85$ GeV, then the decay $\tilde{\chi}_2^0 \to \tilde{l}_L l \to \tilde{\chi}_1^0 ll$ is kinematically allowed and produces a second edge in the dilepton mass distribution at

$$M_{ll}^{\max} = M_{\tilde{\chi}_2^0} \sqrt{1 - \frac{M_{\tilde{l}_L}^2}{M_{\tilde{\chi}_2^0}^2}} \sqrt{1 - \frac{M_{\tilde{\chi}_1^0}^2}{M_{\tilde{l}_L}^2}}$$

Near threshold, one of the leptons is very soft, so a low p_T threshold is essential. A sample of 200000 events was generated with ISAJET for $m_{0,5} = 75$ GeV [20-29]. Events were selected using the same jet and missing energy cuts as for the Point 5 analysis in Section 20.2.3 but requiring two muons with $p_T > 5$ GeV. The resulting $\mu^+\mu^-$ mass distribution, Figure 20-53, shows a clear second edge with an integrated luminosity of 10 fb^{-1}. This edge is almost invisible in the e^+e^- mass distribution with the standard cut $p_T > 10$ GeV.

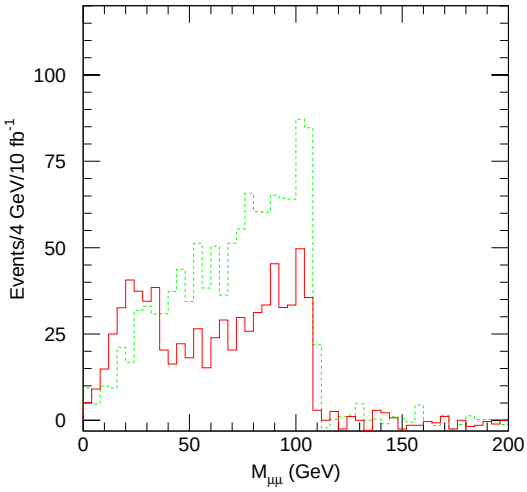

Figure 20-53 $\mu^+\mu^-$ mass distribution for modified Point 5 with $m_{0,5} = 75$ GeV (solid) and for Point 5 (dashed).

The slepton mass for $m_{0,5} = 75$ GeV differs from that for Point 5 by only 9 GeV. It would not be easy to distinguish these using the direct slepton production analysis described in Section 20.2.7.4 even with an integrated luminosity of 300 fb^{-1}. It should be possible at high

luminosity to use that analysis to distinguish $m_{0,5} = 150$ GeV, for which the $\tilde{l}_L$ is 24 GeV heavier than at Point 5. The rate of course becomes smaller for larger $m_{0,5}$; at some point one must rely on the absence of a direct slepton signal.

Direct $\tilde{l}_L^+\tilde{l}_L^-$ production can also give a four-lepton signature if one slepton decays via $\tilde{l}_L \to \tilde{\chi}_1^0 l$ and the other via $\tilde{l}_L \to \tilde{\chi}_2^0 l \to \tilde{l}'_L l' l \to \tilde{\chi}_1^0 l' l' l$. This branching ratio is too small to be observable at Point 5 but increases for larger $m_{0,5}$. One virtue of this signature is that the three-lepton mass has a kinematic endpoint at

$$M_{lll}^{\max} = \sqrt{1-\frac{M_{\tilde{l}_R}^2}{M_{\tilde{\chi}_2^0}^2}}\sqrt{M_{\tilde{l}_L}^2\left(1-\frac{M_{\tilde{\chi}_2^0}^2}{M_{\tilde{l}_L}^2}\right)+M_{\tilde{\chi}_2^0}^2\left(1-\frac{M_{\tilde{\chi}_1^0}^2}{M_{\tilde{l}_R}^2}\right)} = 128.0 \text{ GeV}, \qquad m_{0,5} = 125 \text{ GeV}.$$

A sample of 200000 events was generated [20-29] with $m_{0,5} = 125$ GeV and the other parameters the same as for Point 5. The main background comes from the strong production of gluinos and squarks, so a jet veto is required even with four leptons. The following cuts were made:

- no jet with $p_T > 40$ GeV and $|\eta| < 5$;
- at least four isolated leptons forming two opposite sign, same flavour pairs;
- $M_{ll} < 108$ GeV for at least one opposite sign, same flavour pair to be consistent with a $\tilde{\chi}_2^0$ decay.

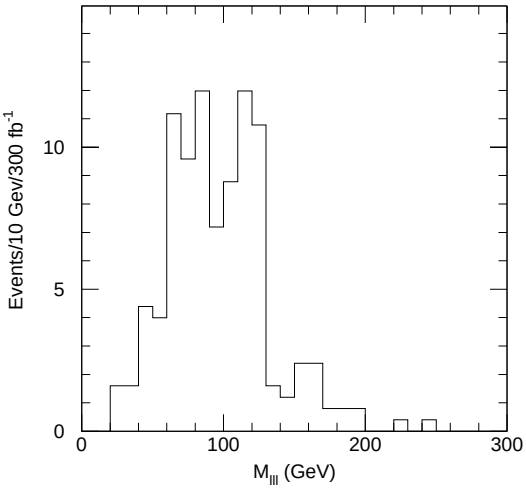

Figure 20-54 Three-lepton mass distribution in clean four-lepton events at Point 5 with $m_{0,5} = 125$ GeV.

After these cuts, the pair with $M_{ll} < 108$ GeV was combined with the lowest p_T additional lepton, since there is much more phase space for $\tilde{l}_L \to \tilde{\chi}_1^0 l$ than for $\tilde{l}_L \to \tilde{\chi}_2^0 l$. The resulting three-lepton mass distribution is shown in Figure 20-54 for an integrated luminosity of 300 fb^{-1}. The number of events is small even for the full luminosity of the LHC, but an endpoint at about the right position can be seen. Combining this signature with the two-lepton direct production signature would provide sensitivity to $m_{0,5} \approx 125$ GeV, much less than the limit from fitting only the measurements in Table 20-11.

20.2.10.3 Non-universal third generation masses

The third possibility considered here is that the sfermions of the third generation have different masses at the GUT scale:

$$m_{\tilde{t}_{L,R}} = m_{\tilde{b}_{L,R}} = m_{\tilde{\tau}_{L,R}} = m_{0,3},$$

with the rest of the scalar masses being m_0. Since the $\tilde{t}_{1,2}$ and $\tilde{b}_{1,2}$ masses are dominated by $m_{1/2}$, the main effect of changing $m_{0,3}$ is on the $\tilde{\tau}_{1,2}$ masses.

It is possible in principle to obtain information on the $\tilde{\tau}_1$ mass by measuring the visible $\tau\tau$ mass distribution, as was discussed for Point 6 in Section 20.2.8.2. For Point 5, however, the branching ratio for $\tilde{\chi}_2^0 \to \tilde{\tau}\tau$ is only 11.8%, opposed to 100% for Point 6, so extracting a $\tau\tau$ endpoint is

considerably more difficult than it is at Point 6. The signal seems to be lost in the fluctuations of the backgrounds from other sources [20-29]. If $\tan\beta$ is increased somewhat, then the $\tilde{\chi}_2^0 \to \tilde{\chi}_1^0 h$ mode is closed, the slepton modes dominate, and a signal can be extracted.

It is easier, although less direct, to get information on the $\tau\tau$ distribution by counting the number of like-flavour and unlike-flavour dileptons. Events were selected with

- $E_{\mathrm{T}}^{\mathrm{miss}} > \max(0.2M_{\mathrm{eff}}, 100\ \mathrm{GeV})$;
- at least four $R = 0.4$ jets with $p_{\mathrm{T}} > 100, 50, 50, 50\ \mathrm{GeV}$;
- two isolated electrons or muons with $p_{\mathrm{T}} > 10\ \mathrm{GeV}$ and $|\eta| < 2.5$.

The ratio of same-flavour to opposite-flavour dileptons with opposite sign,

$$R_{+-} = \frac{N(e^+e^-) + N(\mu^+\mu^-)}{N(e^\pm\mu^\mp)}$$

after these cuts is given in Table 20-15 for several values of $m_{0,3}$. This ratio is equal to one for two τ decays or for any other combination of two independent decays satisfying $e-\mu$ universality; it is greater than one for flavour-correlated decays such as $\tilde{\chi}_2^0 \to \tilde{l}l$. Since the $\tilde{\tau}_1$ is lighter for low values of $m_{0,3}$, the decay $\tilde{\chi}_2^0 \to \tilde{\tau}\tau$ is enhanced, reducing R_{+-}. For $m_{0,3} = 150\ \mathrm{GeV}$ the $\tilde{\tau}_1$ mass is 193 GeV. In this region the two-body decay $\tilde{\chi}_2^0 \to \tilde{\tau}\tau$ is not allowed; the τ branching ratios are determined by an interference between virtual slepton and Z exchange. Of course, the ratio R_{+-} is also sensitive to $\tan\beta$, so this measurement must be combined with other information such as the Higgs mass before any conclusion can be drawn.

Table 20-15 Values of R_{+-} for Point 5 with several values of $m_{0,3}$.

m_{03}	R_{+-}
30 GeV	2.61
70 GeV	3.86
Point 5	3.99
150 GeV	4.62
200 GeV	4.38

It would also be useful to obtain a measurement of single τ production by counting the number of leptons and hadronic τ decays. Since the jet multiplicity is substantial, this requires an algorithm for selecting hadronic τ's optimised for purity rather than for visible mass resolution as in Section 20.2.8. Presumably tight isolation cuts together with a displaced vertex should be required. This has not been studied in the framework of SUSY studies, but work along these lines is documented in Section 9.1.5.2

20.3 Gauge mediated SUSY breaking models

In Gauge Mediated SUSY Breaking (GMSB) models [20-13], SUSY breaking occurs in a separate sector, as in SUGRA models, but at a much lower scale, $F_m \ll (10^{10}\ \mathrm{GeV})^2$. It is then communicated to the MSSM particles through ordinary $SU(3)\times SU(2)\times U(1)$ gauge interactions at a messenger scale that is much lower than the Planck scale, $M_m \ll M_P$, and perhaps even close to the weak scale. This implies that all MSSM particles with the same Standard Model quantum numbers have the same mass at the scale M_m, so flavour changing neutral currents are suppressed. Since the gravitino $\tilde{G}$ gets its mass only through gravitational couplings at M_P, it is

much lighter than the $R = -1$ MSSM particles – generally much lighter than 1 GeV. The helicity-$1/2$ couplings of the gravitino are enhanced by factors of $1/M_{\tilde{G}}$, so all the other SUSY particles eventually decay into it.

The successful unification of coupling constants in the MSSM [20-12] is preserved if the messenger fields are chosen to be complete vector-like representations of $SU(5)$, *e.g.*, $5 + \bar{5}$ or $10 + \overline{10}$. In the minimal GMSB model considered here this is assumed, but the number N_5 of equivalent $5 + \bar{5}$ representations is left arbitrary. A single $10 + \overline{10}$ gives $N_5 = 3$; a combination of several representations can produce a non-integer effective N_5. It is also assumed that electroweak symmetry is broken radiatively through the large top Yukawa coupling as in minimal SUGRA model and that μ and $B\mu$ are generated. Finally, the gravitino can get mass not just from the messenger sector but from any other source of SUSY breaking, presumably in some more complex hidden sector. Then the parameters of the minimal GMSB model are [20-13]

$$\Lambda \equiv F_m/M_m, \qquad M_m, \qquad N_5, \qquad \tan\beta, \qquad \mathrm{sgn}\mu = \pm 1, \qquad C_{\mathrm{grav}}, \qquad \text{20-9}$$

where $C_{\mathrm{grav}} \geq 1$ is the ratio of the gravitino mass to its value if the only source of SUSY breaking is F_m; lifetimes for gravitino decay are proportional to C_{grav}^2. Gauginos get masses at one loop at the messenger scale, and scalars get squared masses at two loops, *e.g.*

$$\begin{aligned}
M_{\tilde{g}} &= \frac{\alpha_s}{4\pi}\Lambda N_5 \\
M_{\tilde{e}_L}^2 &= \frac{3\alpha_2^2}{32\pi^2}\Lambda^2 N_5 + \frac{3\alpha_1^2}{160\pi^2}\Lambda^2 N_5 \\
M_{\tilde{e}_R}^2 &= \frac{3\alpha_1^2}{40\pi^2}\Lambda^2 N_5 \\
M_{\tilde{u}_L}^2 &= \frac{\alpha_s^2}{6\pi^2}\Lambda^2 N_5 + \frac{3\alpha_2^2}{32\pi^2}\Lambda^2 N_5 + \frac{\alpha_1^2}{480\pi^2}\Lambda^2 N_5 \\
M_{\tilde{u}_R}^2 &= \frac{\alpha_s^2}{6\pi^2}\Lambda^2 N_5 + \frac{\alpha_1^2}{30\pi^2}\Lambda^2 N_5
\end{aligned}$$

Note that the gaugino and scalar masses are comparable, but gaugino masses are proportional to N_5 while scalar masses are proportional to $\sqrt{N_5}$.

In GMSB models the lightest SUSY particle is the gravitino with $M_{\tilde{G}} \ll 1$ GeV. The Next Lightest SUSY Particle (NLSP) is generally the $\tilde{\chi}_1^0$ if $N_5 = 1$ and a right-handed slepton if $N_5 > 1$, since these particles only have masses proportional to the small α_1 coupling. If $C_{\mathrm{grav}} \sim 1$, the NLSP will decay promptly to gravitinos via $\tilde{\chi}_1^0 \to \tilde{G}\gamma$ or $\tilde{l}_R \to \tilde{G}l$, while if $C_{\mathrm{grav}} \gg 1$ the NLSP will decay mainly outside the detector. (The $\tilde{l}_R$ must of course not be stable over the lifetime of the universe.) Thus there are four distinct cases for GMSB phenomenology, depending on whether the NLSP is a neutralino or a slepton and whether it has a short or a long lifetime.

One minimal GMSB model point for each case was selected for detailed study [20-36], forming two pairs differing only by the value of C_{grav} and hence by the lifetime of the NLSP. The parameters of these points are listed in Table 20-16; the corresponding masses from ISAJET [20-15] are given in Table 20-17. These points illustrate the main features expected in GMSB models: Point G1a gives events with two hard photons plus $E_{\mathrm{T}}^{\mathrm{miss}}$; Point G1b gives signatures qualitatively like SUGRA models; Point G2a gives multiple leptons; and Point G2b gives quasi-stable charged sleptons. Since the signatures are so different, each point will be discussed separately. Most of the results in this section are based on ISAJET and a simple particle-level simulation of

Table 20-16 Parameters of the four GMSB points considered in Section 20.3.

Point	Λ(TeV)	M_m(TeV)	N_5	tanβ	sgnμ	C_{grav}
G1a	90	500	1	5.0	+	1.0
G1b	90	500	1	5.0	+	10^3
G2a	30	250	3	5.0	+	1.0
G2b	30	250	3	5.0	+	5×10^3

Table 20-17 Masses in GeV for the particles at the GMSB points in Table 20-16 from ISAJET 7.37 [20-15]. Only the gravitino mass depends on C_{grav}.

Particle	Point G1	Point G2	Particle	Point G1	Point G2	Particle	Point G1	Point G2
$\tilde{g}$	747	713	$\tilde{u}_L$	986	672	$\tilde{e}_L$	326	204
$\tilde{\chi}_1^{\pm}$	223	201	$\tilde{u}_R$	942	649	$\tilde{e}_R$	164	103
$\tilde{\chi}_2^{\pm}$	469	346	$\tilde{d}_L$	989	676	$\tilde{\nu}_e$	317	189
$\tilde{\chi}_1^0$	119	116	$\tilde{d}_R$	939	648	$\tilde{\tau}_1$	163	102
$\tilde{\chi}_2^0$	224	204	$\tilde{t}_1$	846	584	$\tilde{\tau}_2$	326	204
$\tilde{\chi}_3^0$	451	305	$\tilde{t}_2$	962	684	$\tilde{\nu}_\tau$	316	189
$\tilde{\chi}_4^0$	470	348	$\tilde{b}_1$	935	643	h	110	107
			$\tilde{b}_2$	945	642	H	557	360
						A	555	358
						$H^{\pm}$	562	367

the ATLAS detector. It appears that the backgrounds are dominated by irreducible physics processes, so that the detector performance is not critical. Detailed GEANT-based studies have been performed for non-pointing photons at Point G1a and for quasi-stable sleptons at Point G2b.

20.3.1 GMSB Point G1a

At Point G1a the total SUSY cross section is 7.6 pb. The NLSP is the $\tilde{\chi}_1^0$, and it decays primarily to $\tilde{G}\gamma$ with $c\tau$ = 1.2 mm. SUSY events are therefore characterised by two hard isolated photons plus the usual jets, leptons, and missing transverse energy E_T^{miss} from the gravitinos and perhaps from neutrinos. The presence of two photons in almost every event renders the Standard Model backgrounds negligible and makes discovery trivial. In a small fraction (2.0%) of the events, the NLSP will undergo a Dalitz decay to $\tilde{G}e^+e^-$. The e^+ and e^- can be used to determine the decay vertex and so to make a precise measurement of the mean decay length. The mass of the $\tilde{\chi}_1^0$ can be determined as described in Section 20.3.1.1. If the polarisation of the $\tilde{\chi}_1^0$ can be neglected, as it is in the existing event generators, then its momentum distribution can be inferred from that of the photons and its proper lifetime determined. The polarisation is likely to be small since many channels contribute, but it has not been studied and could be the dominant uncertainty. This lifetime measurement is very important as it provides the only constraint on the true scale of SUSY breaking in all hidden sectors, not just the messenger sector.

For all the analyses in this subsection [20-36] events were selected to have:

- $M_{\text{eff}} > 400$ GeV;
- $E_{\text{T}}^{\text{miss}} > 0.1 M_{\text{eff}}$;
- two photons with $p_{\text{T}} > 20$ GeV and $|\eta| < 2.5$;
- at least two leptons with $p_{\text{T}} > 20$ GeV and $|\eta| < 2.5$ for electrons and $p_{\text{T}} > 5$ GeV and $|\eta| < 2.5$ for muons.

Jets were found using an $R = 0.4$ cone and requiring more than one charged track with $p_{\text{T}} > 1$ GeV to avoid counting τ's as jets. These cuts make the Standard Model background negligible; it remains so even for a γ/jet rejection of only 10^{-3}, much worse than is expected and is needed for $h \to \gamma\gamma$. Modes without leptons might of course also be useful.

20.3.1.1 Lepton and photon distributions

Events were selected with two photons and exactly two leptons satisfying the cuts listed above. Since GMSB models ensure flavour conservation, the leptons from

$$\tilde{\chi}_2^0 \to \tilde{l}^{\pm} l^{\mp} \to \tilde{\chi}_1^0 l^+ l^- \to \tilde{G} l^+ l^- \gamma$$

must be correlated in flavour, so the flavour subtracted combination $e^+e^- + \mu^+\mu^- - e^{\pm}\mu^{\mp}$ shown in Figure 20-55 selects this signal and removes both the SUSY and the small Standard Model background from two independent leptonic decays. This gives a dilepton mass distribution similar to that found for SUGRA Point 5 in Section 20.2.3 with a very sharp endpoint at

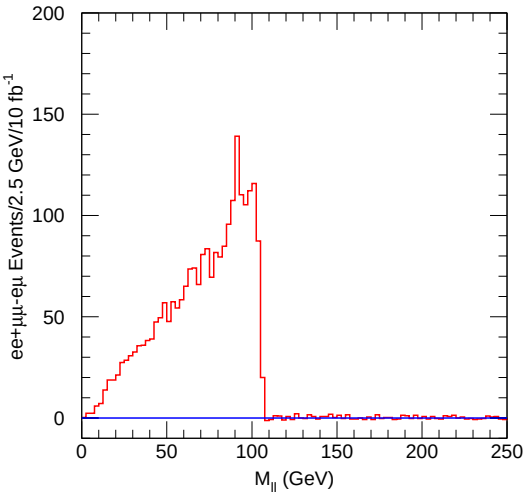

Figure 20-55 Flavour-subtracted dilepton distribution at Point G1a. The Standard Model background is not visible.

$$M_{ll}^{\max} = M_{\tilde{\chi}_2^0} \sqrt{1 - \frac{M_{l_R}^2}{M_{\tilde{\chi}_2^0}^2}} \sqrt{1 - \frac{M_{\tilde{\chi}_1^0}^2}{M_{l_R}^2}} \, .$$
$$= 105.1 \text{ GeV}$$

The other allowed two-body decay, $\tilde{\chi}_2^0 \to \tilde{\chi}_1^0 Z$, produces a small peak just visible in the figure. This does not directly measure masses and is not used here. It would be measurable with more luminosity, and the rate for it would then imply information about the Higgsino content of the two lightest neutralinos.

It is also useful to consider the whole 4-body decay chain, just as for the analysis of squark decay at Point 5 in Section 20.2.4.3. In this case the particles are leptons and photons, so the precision is much better. The sequence of three two-body decays implies that the $l^+l^-\gamma$ mass has an endpoint with a linear vanishing at

$$M_{ll\gamma}^{\max} = \sqrt{M_{\tilde{\chi}_2^0}^2 - M_{\tilde{\chi}_1^0}^2} = 189.7 \text{ GeV} \, .$$

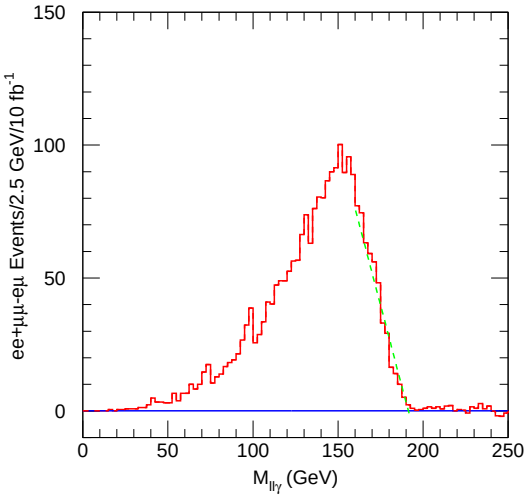

Figure 20-56 Flavour-subtracted distribution for the smaller $l^+l^-\gamma$ mass at Point G1a.

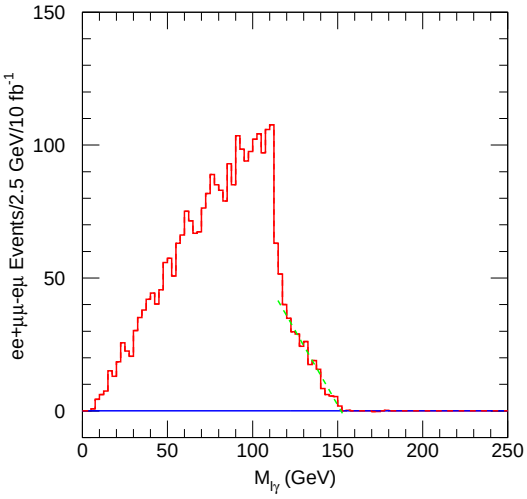

Figure 20-57 Flavour-subtracted $l^{\pm}\gamma$ distribution for the $l^+l^-\gamma$ combination below its endpoint.

Since at least one of the $l^+l^-\gamma$ masses must be less than this, the distribution of the smaller one vanishes at this point. The flavour-subtracted distribution for the smaller $l^+l^-\gamma$ mass is shown in Figure 20-56 together with a linear fit near the endpoint. The endpoint could be measured to about ± 0.5 GeV with 30 fb^{-1} and to the systematics limit of about ± 0.2 GeV with 300 fb^{-1}. The $l^{\pm}\gamma$ mass distribution from $\tilde{\chi}_2^0$ decays has a sharp edge like the dilepton one from pairing the photon and the 'right' lepton – that is, the second one, which is adjacent to the photon in the decay chain – at

$$M_{l\gamma}^{(1)} = \sqrt{M_{\tilde{l}_R}^2 - M_{\tilde{\chi}_1^0}^2} = 112.7 \text{ GeV}$$

plus an endpoint with a linear vanishing from pairing the photon and the 'wrong' lepton at

$$M_{l\gamma}^{(2)} = \sqrt{M_{\tilde{\chi}_2^0}^2 - M_{\tilde{l}_R}^2} = 152.6 \text{ GeV}\,.$$

In contrast to the squark case, the second endpoint is greater than the first one and so is also visible. Events were selected to have the mass of one $l^+l^-\gamma$ combination less than and the other greater than 189.7 GeV, so that only one combination is consistent with $\tilde{\chi}_2^0$ decay. The $l^{\pm}\gamma$ mass distribution for this $l^+l^-\gamma$ combination is shown in Figure 20-57. The errors on this edge and endpoint are estimated to be ± 0.2 GeV and ± 0.5 GeV with 30 fb^{-1}, reducing to ± 0.1 GeV and ± 0.2 GeV with 300 fb^{-1}.

The four measurements just described are sufficient to determine the $\tilde{\chi}_2^0$, $\tilde{l}_R$, and $\tilde{\chi}_1^0$ masses without any assumptions except for the neglect of the gravitino mass:

$$M_{\tilde{l}_R}^2 = \frac{(M_{l\gamma}^{(1)})^2 (M_{l\gamma}^{(2)})^2}{(M_{ll}^{\max})^2}$$

$$M_{\tilde{\chi}_1^0}^2 = M_{\tilde{l}_R}^2 - (M_{l\gamma}^{(1)})^2$$

$$M_{\tilde{\chi}_2^0}^2 = M_{\tilde{l}_R}^2 + (M_{l\gamma}^{(2)})^2$$

with the evident constraint

$$(M_{ll\gamma}^{\max})^2 = (M_{l\gamma}^{(1)})^2 + (M_{l\gamma}^{(2)})^2 .$$

This result demonstrates the power of identifying and using a multi-step decay chain even more clearly than the $\tilde{q}_L$ analysis at SUGRA Point 5, since in this case only leptons and photons are involved. Of course the rates and hence the errors are model dependent, as is the interpretation of the slepton as a $\tilde{l}_R$.

20.3.1.2 Reconstruction of $\tilde{G}$ momenta

Once the masses have been determined, the decay $\tilde{\chi}_2^0 \to \tilde{l}^{\pm} l^{\mp} \to \tilde{\chi}_1^0 l^+ l^- \to \tilde{G} l^+ l^- \gamma$ provides three mass constraints and hence a $0C$ fit for the gravitino momentum p,

$$(p + p_\gamma)^2 = M^2_{\tilde{\chi}_1^0}$$
$$(p + p_\gamma + p_{l_2})^2 = M^2_{l_R}$$
$$(p + p_\gamma + p_{l_2} + p_{l_1})^2 = M^2_{\tilde{\chi}_2^0}$$

assuming that the gravitino mass p^2 can be neglected. There is a two-fold ambiguity from assigning the order of the leptons – *i.e.*, which one appears in the second equation above – and another two-fold ambiguity from solving a quadratic equation. If this decay chain occurs twice in the same event, both gravitino momenta can be determined, and the best solution can be selected by comparing the vector sum of their reconstructed momenta with the missing transverse momentum. Thus, this long decay chain allows SUSY events to be fully reconstructed despite the presence of two missing particles.

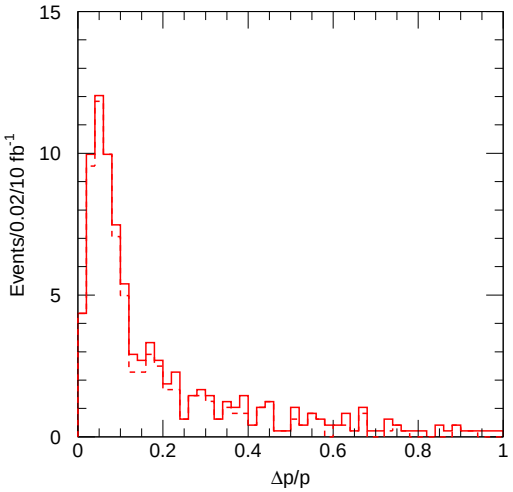

Figure 20-58 Fractional difference between reconstructed and generated gravitino momenta at Point G1a for $\chi^2 < 10$ (solid) and $\chi^2 < 1$ (dashed).

Events were required to have exactly four leptons and two photons satisfying the same cuts as before, with one and only one pairing into two opposite-sign, same-flavour $l^+l^-\gamma$ combinations consistent with $\tilde{\chi}_2^0$ decay. This eliminates any additional combinatorial background and gives a total of 16 solutions for the two gravitino momenta $\vec{p}_1$ and $\vec{p}_2$. These solutions can be found explicitly after straightforward algebra [20-36]. The gravitinos were assumed to give the $E_{\mathrm{T}}^{\mathrm{miss}}$ up to detector resolution effects. Therefore, the solution that minimised

$$\chi^2 = \left(\frac{E_x^{\mathrm{miss}} - p_{1x} - p_{2x}}{\Delta E_x^{\mathrm{miss}}}\right)^2 + \left(\frac{E_y^{\mathrm{miss}} - p_{1y} - p_{2y}}{\Delta E_y^{\mathrm{miss}}}\right)^2$$

was selected, where the errors were calculated using assumed calorimetric missing energy resolution

$$\Delta E_x^{\mathrm{miss}} = \Delta E_y^{\mathrm{miss}} = 0.6\sqrt{E_{\mathrm{T}}} + 0.03 E_{\mathrm{T}} .$$

This parametrisation gives resolution values which are a factor of two to three worse than the $E_{\mathrm{T}}^{\mathrm{miss}}$ resolution obtained from the full simulation studies described in Section 9.2.1.1. Events that satisfied $\chi^2 < 10$ were retained for further analysis.

The method was tested by comparing the reconstructed gravitino momenta with the generated momenta using the better of the two possible matches. The distribution for the fractional difference between the reconstructed and generated momenta,

$$\frac{\Delta p}{p} \equiv \frac{\left|\vec{p}_{\mathrm{recon}} - \vec{p}_{\mathrm{gen}}\right|}{\left|\vec{p}_{\mathrm{gen}}\right|} ,$$

is shown in Figure 20-58 for events with $\chi^2 < 10$. The peak is at about 10%, considerably larger than the typical lepton or photon resolution, and there is a substantial tail of events that presumably have missing energy from sources other than the gravitinos. The number of reconstructed events is quite small. Nevertheless, the fact that complete reconstruction with two missing particles is possible at all is interesting. A similar complete reconstruction is possible in principle for SUGRA Point 5 using the three mass constraints from decay chain $\tilde{q}_L \to \tilde{\chi}_2^0 q \to l_R^{\pm} l^{\mp} q \to \tilde{\chi}_1^0 l^+ l^- q$, but unfortunately the resulting errors are too large to be useful.

20.3.1.3 Reconstruction of gluinos and squarks

Events that are fully reconstructed as described in the previous section can be used to measure the squark and gluino masses using the decay chain $\tilde{q} \to \tilde{g} q \to \tilde{\chi}_2^0 \bar{q} q q$. It would probably be better to study these particles using partially reconstructed combinations of jets, leptons, and photons, as was done for several of the SUGRA points rather than using the small number of fully reconstructed events. This analysis mainly serves to illustrate further the possibility of full reconstruction; it is not used in the fit to determine the parameters of the model.

Events were selected to have two $\tilde{\chi}_2^0$'s fully reconstructed with $\chi^2 < 10$ and at least four jets with $p_T > 75$ GeV defined using a cone $R = 0.4$. Each reconstructed $\tilde{\chi}_2^0$ is then combined with two of the four hardest jets and then with a third. The resulting scatter plot of $M(\tilde{\chi}_2^0 jj)$ vs $M(\tilde{\chi}_2^0 jjj)$ has a broad peak near the gluino and squark masses. The two projections, each cut

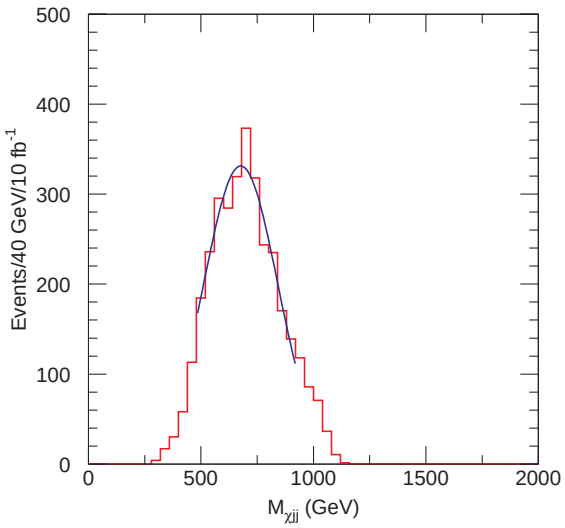

Figure 20-59 Distribution of $M(\tilde{\chi}_2^0 jj)$ for $800 < M(\tilde{\chi}_2^0 jjj) < 1000$ GeV at Point G1a.

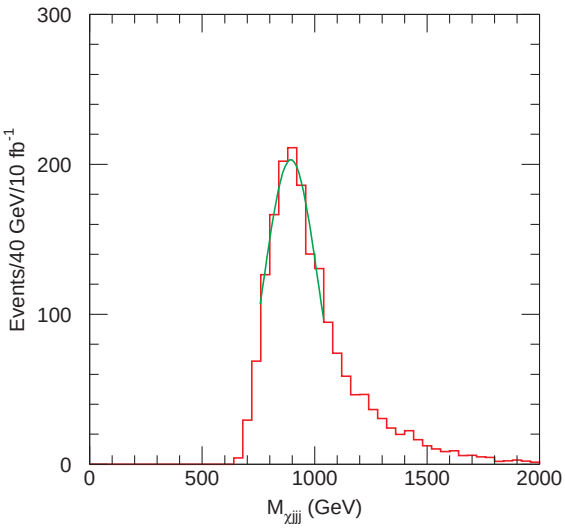

Figure 20-60 Distribution of $M(\tilde{\chi}_2^0 jjj)$ for $600 < M(\tilde{\chi}_2^0 jj) < 800$ GeV at Point G1a.

about the peak on the other axis, are shown in Figures 20-59 and 20-60 together with Gaussian fits to guide the eye. Even with the limited number of fully reconstructed events, the statistical errors on the peaks are quite small; the errors are likely to be dominated by systematic effects such as the jet energy scale.

20.3.2 GMSB Point G1b

The SUSY cross section at Point G1b is 7.6 pb, the same as at Point G1a. The NLSP, the $\tilde{\chi}_1^0$, is neutral and long-lived; most of them escape the detector, giving signatures that are qualitatively like those in SUGRA models. A qualitatively new feature is that the $\tilde{\chi}_1^0$ can occasionally decay in the tracking volume, giving rise to a photon that does not point to the interaction vertex. Since the ATLAS electromagnetic calorimeter provides directional information, it can measure such photons, giving information on the $\tilde{\chi}_1^0$ lifetime and hence on C_{grav}. Since this is the only source of information on the global scale of SUSY breaking, it is extremely important. It will be discussed in Section 20.3.2.4 after the other signatures.

20.3.2.1 Effective mass analysis

Discovery of SUSY in inclusive distributions at this point is similar to that for SUGRA models. Events were selected to have [20-36]

- at least four jets with $p_{\text{T, 1}} > 100$ GeV and $p_{\text{T, 2, 3, 4}} > 50$ GeV;
- $E_T^{\text{miss}} > \max(100\text{ GeV}, 0.2M_{\text{eff}})$, where M_{eff} is defined by Equation 20-5;
- transverse sphericity $S_{\text{T}} > 0.2$;
- no μ or isolated e with $p_{\text{T}} > 20$ GeV and $|\eta| < 2.5$.

With these cuts the signal exceeds the Standard Model background for $M_{\text{eff}} > 1000$ GeV by about a factor of five [20-36].

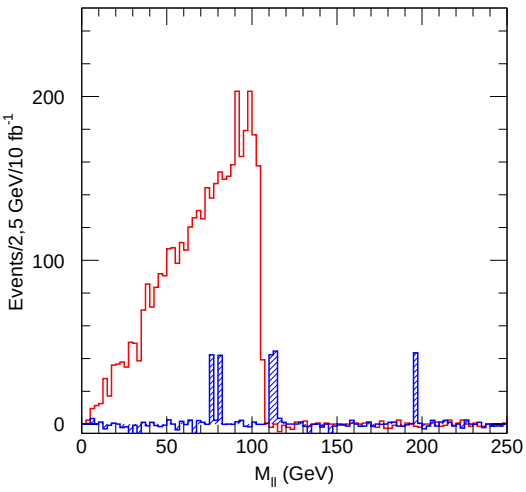

Figure 20-61 Flavour-subtracted dilepton distribution at Point G1b. The shaded histogram shows the Standard Model background; the fluctuations reflect the limited Monte Carlo statistics.

20.3.2.2 Dilepton distribution

At Point G1b the decay $\tilde{\chi}_2^0 \to \tilde{l}_R^{\pm} l^{\mp} \to \tilde{\chi}_1^0 l^+ l^-$ is allowed, but the $\tilde{\chi}_1^0$ is stable rather than decaying to $\tilde{G}\gamma$. Events were selected to have $M_{\text{eff}} > 1000$ GeV, $E_{\text{T}}^{\text{miss}} > 0.1M_{\text{eff}}$, and two and only two opposite-sign leptons with $p_{\text{T}} > 20$ GeV and $|\eta| < 2.5$. The resulting $e^+e^- + \mu^+\mu^- - e^{\pm}\mu^{\mp}$ dilepton distribution, shown in Figure 20-61 has an endpoint at 105.1 GeV, which of course is the same as for Point G1a. There is more Standard Model background than before because there are no photons in the signal events, but the background is still small; the spikes in the background curve in the figure are fluctuations that reflect the limited Monte Carlo statistics. Hence, the error on this endpoint should again be about 0.1%, limited by the absolute lepton energy scale. The sharp endpoint is characteristic of a sequential decay through a slepton.

There is also a small peak visible in the figure from Z decays which could be measured with more luminosity. This measurement would help to confirm the two body nature of the decay and potentially would provide information on the Higgsino content of the light neutralinos.

20.3.2.3 Reconstruction of gluinos and squarks

The $\tilde{\chi}_2^0 \to \tilde{l}_R^{\pm} l^{\mp} \to \tilde{\chi}_1^0 l^+ l^-$ decays reconstructed in the previous section come primarily from $\tilde{g} \to \tilde{\chi}_2^0 q\bar{q}$, where the gluino may be produced directly or from squark decay. To attempt to extract these signals, events were selected as before with the additional requirement of two hard jets with $p_T > 125$ GeV. The $e^+e^- + \mu^+\mu^- - e^{\pm}\mu^{\mp}$ dilepton pair was then combined with any two jets having $p_T > 25$ GeV. The resulting l^+l^-jj mass distribution, Figure 20-62, has a broad peak but no clear structure. It is, however, sensitive to the gluino mass: the same figure also shows as a dotted curve the distribution for a sample with the gluino mass increased from 747 GeV to 800 GeV. These could probably be distinguished statistically at high luminosity; the systematic errors need further study.

The branching ratio for $\tilde{g} \to \tilde{\chi}_2^0 b\bar{b}$ is 6.5%. The l^+l^-jj distribution using jets tagged as b's is shown in Figure 20-63. This has a structure that reflects the kinematic endpoint of this decay (for massless jets) at

$$\left[(M_{\tilde{g}} - M_{\tilde{\chi}_2^0})^2 + M_{ll}^2 + \frac{M_{\tilde{g}} - M_{\tilde{\chi}_2^0}}{2M_{\tilde{\chi}_2^0}} \left(M_{\tilde{\chi}_2^0}^2 - M_l^2 + \frac{(M_{\tilde{\chi}_2^0}^2 + M_l^2)(M_l^2 - M_{\tilde{\chi}_1^0}^2)}{2M_l^2} \left(1 + \frac{M_{\tilde{\chi}_2^0}^2 - M_l^2}{2M_{\tilde{\chi}_2^0} M_{\tilde{l}}} \right) \right) \right]^{1/2},$$

where M_{ll} is the value of the dilepton edge. For Point G1b this l^+l^-jj endpoint is at 629 GeV, while for a gluino mass of 800 GeV, it becomes 673 GeV. These values are approximately consistent with the structure of the solid and dashed curves in Figure 20-63. While the event rates are low, these curves could be distinguished statistically with higher luminosity; however, the impact of pileup on the analysis has not been studied.

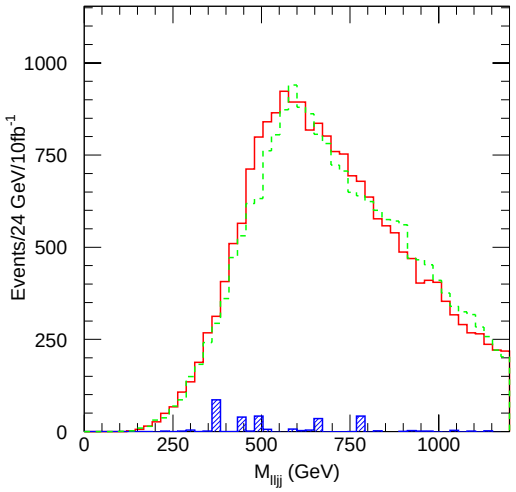

Figure 20-62 l^+l^-jj invariant mass distribution for Point G1b (solid curve) and for the gluino mass shifted to 800 GeV (dashed curve).

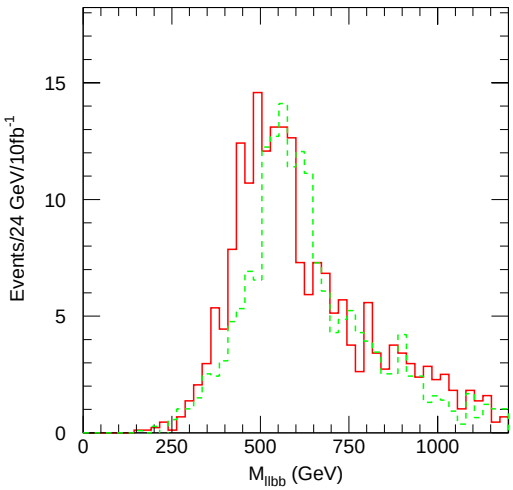

Figure 20-63 Same as Figure 20-62 for b-jets. The dashed curve is for the sample with $M_{\tilde{g}} = 800\text{GeV}$. No Standard Model event passed the cuts.

The endpoint of the dijet mass distribution should be sensitive to $M_{\tilde{g}} - M_{\tilde{\chi}_2^0}$, but the endpoint is not at all sharp due to the large combinatorial background. It is also possible to add another jet, thereby getting a handle on the squark mass. Again the rates are low, and while there is a difference in shape, there is not a clear kinematic endpoint. Since these analyses do not illustrate any new techniques, they will not be shown here, although they are used in the fitting described in Section 20.3.5.

20.3.2.4 Measurement of $\tilde{\chi}_1^0$ lifetime

If SUSY breaking occurs only in the messenger sector, then the $\tilde{\chi}_1^0$ lifetime is short, $c\tau \approx 1.1$ mm. It is possible, however, that SUSY breaking in the messenger sector is induced by higher order effects in some new interaction, giving a much longer lifetime. The parameter $C_{\text{grav}} = 1000$ assumed for Point G1b corresponds to $c\tau = 1.1$ km. Even though this decay length is large compared to the size of the tracking volume, it can still be measured by counting the number of non-pointing photons from the small number of $\tilde{\chi}_1^0 \to \tilde{G}\gamma$ that occur inside the detector.

The ATLAS electromagnetic calorimeter is particularly well suited for this because it has narrow strips in the first compartment that give good resolution in θ. As described in Section 4.4.2.2, the resolution for photons in the barrel that are close to pointing is

$$\Delta\theta \approx \frac{60 \text{ mr}}{\sqrt{E \text{ (GeV)}}} .$$

The resolution for non-pointing photons has been studied [20-37] for single photons from about 7500 $\tilde{\chi}_1^0 \to \tilde{G}\gamma$ decays and also for samples of 50 GeV photons generated at fixed angles. Two algorithms have been developed, which can reconstruct photons with reasonable accuracy for all values of $\Delta\theta$. These are described in Section 4.4.2.2.

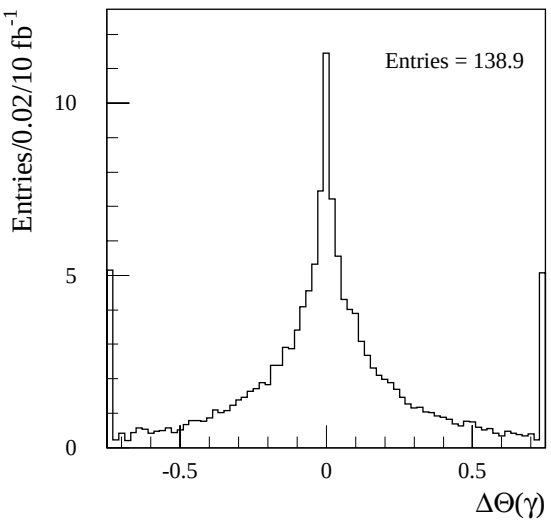

Figure 20-64 Non-pointing angle $\Delta\theta$ for photons in the barrel calorimeter from $\tilde{\chi}_1^0 \to \tilde{G}\gamma$ at Point G1b for the assumed lifetime $c\tau = 1.1$ km. The first and last bins contain the overflows.

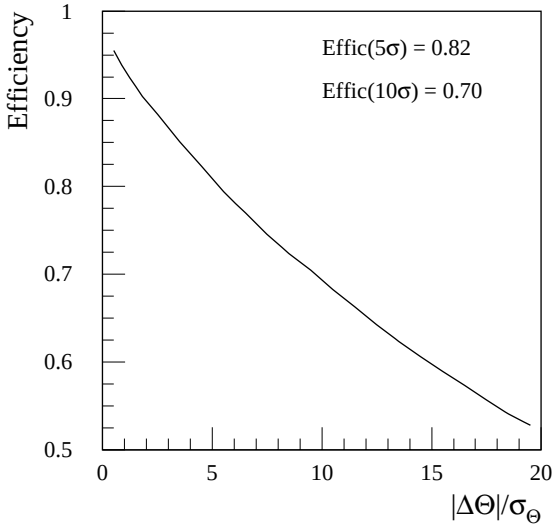

Figure 20-65 Efficiency vs significance for a photon from $\tilde{\chi}_1^0 \to \tilde{G}\gamma$ to be non-pointing at Point G1b.

For this analysis [20-37] it is assumed that the lifetime $c\tau$ is large compared to the length $L(\eta)$ inside of the tracker, so that the decay probability is given by $L(\eta)/(\beta\gamma c\tau)$ and the decays occur uniformly along the path length. For Point G1b a total of 152000 $\tilde{\chi}_1^0$ are produced corresponding to an integrated luminosity of 10 fb^{-1}. For the assumed $c\tau$ = 1.1 km, 180 of these will decay inside the tracking volume. The mean energy of these photons is 84.4 GeV. An analysis based on ATLFAST found that 77.3% of the photons hit the barrel calorimeter, and 82.5% of these have $p_T > 20$ GeV and are isolated.

The angular distribution of these photons relative to the nominal vertex direction, $\Delta\theta$, is shown in Figure 20-64 including the effect of the angular resolution. While the distribution peaks at zero, the angles are generally large compared to the resolution. This is reflected in the efficiency to detect an isolated photon as non-pointing as a function of the significance, shown in Figure 20-65. Requiring that $\Delta\theta$ be non-zero by 5σ gives an efficiency of 82%, or a total of 94 detected non-pointing photons, for an overall efficiency of 52%. Converting this rate to a measurement of a lifetime requires that the mass and momentum distribution of the $\tilde{\chi}_1^0$ be determined from other measurements. The rate for prompt photons in SUSY events has not been calculated but is expected to be of order α/π, so the background should be much less than one event.

If no non-pointing photons are detected for an integrated luminosity of 30 fb^{-1}, then the 95% confidence level lower limit on $\tilde{\chi}_1^0 \to \tilde{G}\gamma$ would be about $c\tau$ = 100 km, a factor of 10^8 longer than the value for $C_{grav} = 1$. Since

$$\Gamma(\tilde{X} \to \tilde{G}X) = \frac{1}{16\pi}\frac{M_{\tilde{X}}^5}{F^2}\left(1 - \frac{M_X^2}{M_{\tilde{X}}^2}\right)^4,$$

this corresponds to a value of F that is 10^4 times larger than that in the messenger sector. Of course this assumes that the $\Delta\theta$ resolution is really Gaussian. So far it has been studied only for single photons, not for complete events.

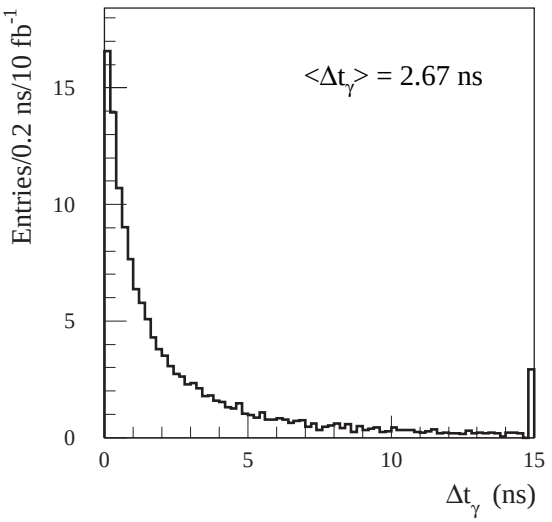

Figure 20-66 Time delay distribution in the EM calorimeter of photons from $\tilde{\chi}_1^0 \to \tilde{G}\gamma$ at Point G1b. The last bin contains the overflow.

The photons from $\tilde{\chi}_1^0 \to \tilde{G}\gamma$ will in general be delayed relative to prompt photons as shown in Figure 20-66. Both the velocity of the $\tilde{\chi}_1^0$ and the geometry of the path contribute to the delay. The mean delay, 2.67 ns, is long compared to the time resolution of about 100 ps for the ATLAS electromagnetic calorimeter. This provides an independent way to detect non-prompt photons and a cross-check on the whole analysis.

20.3.3 GMSB Point G2a

At Point G2a the NLSP is a charged slepton, the $\tilde{\tau}_1$. The splitting between the NLSP and the right-handed sleptons $\tilde{l}_R$ of the first two generations is small as is typical in GMSB models if $\tan\beta$ is not too large, so the decays $\tilde{l}_R^{\pm} \to \tilde{\tau}_1 \tau l^{\pm}$ are not kinematically allowed. The decays $\tilde{l}_R \to \tilde{\tau}_1 \nu_\tau \nu_l$ occur only through left-right mixing terms proportional to the lepton mass and are small even compared to gravitino decays. Hence the $\tilde{e}_R$, $\tilde{\mu}_R$ and $\tilde{\tau}_1$ are co-NLSP's that all decay directly to gravitinos with $c\tau$ = 52 μm. The SUSY production cross section is 23 pb, larger than

for Points G1a / b because the squarks are lighter, and all of these events decay through the sleptons to electrons, muons or τ's. Discovery of such a signal is obviously trivial, and there are many signatures to be studied.

20.3.3.1 Dilepton distributions

Neutralinos can decay via $\tilde{\chi}_i^0 \to \tilde{l}^{\pm} l^{\mp} \to \tilde{G} l^{+} l^{-}$ with substantial branching ratios to give opposite-sign, same-flavour dileptons. Since the neutralinos come mainly from the decay of squarks and gluinos, events were selected to have [20-36]

- at least four jets with $p_{\mathrm{T}} > 25$ GeV, $|\eta| < 2.5$, and having at least four tracks each with $p_{\mathrm{T}} > 1$ GeV;
- $M_{\mathrm{eff}} > 400$ GeV;
- $E_{\mathrm{T}}^{\boldsymbol{miss}} > 0.2 M_{\mathrm{eff}}$;
- Two opposite-charge leptons with $p_{\mathrm{T}} > 10$ GeV and $|\eta| < 2.5$.

The jet multiplicity cut is intended to remove τ's from the jet sample. The flavour-subtracted $e^+e^- + \mu^+\mu^- - e^{\pm}\mu^{\mp}$ dilepton mass was then formed to cancel backgrounds from two independent leptonic decays of charginos or from Standard Model processes. This distribution is shown in Figures 20-67 and 20-68 on two different scales. There are two separate edges, one from $\tilde{\chi}_1^0$ decay (31% branching ratio per flavour) at

$$\sqrt{M^2_{\tilde{\chi}_1^0} - M^2_{\tilde{l}_R}} = 52.1 \text{ GeV}$$

and a second from $\tilde{\chi}_2^0$ decay (23% branching ratio per flavour) at

$$\sqrt{M^2_{\tilde{\chi}_2^0} - M^2_{\tilde{l}_R}} = 175.9 \text{ GeV} \quad .$$

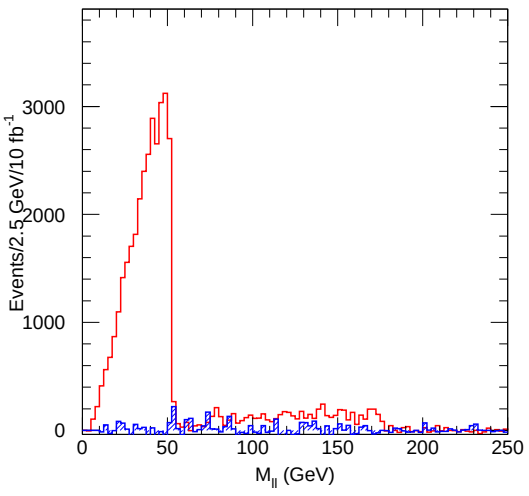

Figure 20-67 $e^+e^- + \mu^+\mu^- - e^{\pm}\mu^{\mp}$ dilepton distribution at Point G2a. The fluctuations in the Standard Model background (shaded) are due to Monte Carlo statistics; the true background is small.

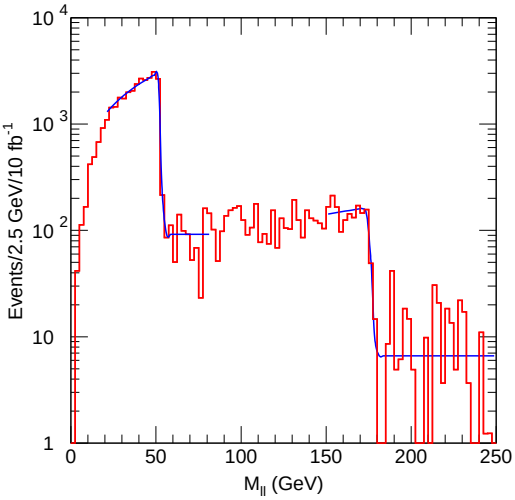

Figure 20-68 Same as Figure 20-67 on a logarithmic scale. Fits using the expected form, Equation 20-6, smeared with a Gaussian are also shown.

While the Standard Model background appears to be significant for the second edge, this is an artifact of the limited Monte Carlo statistics. In the region 60–170 GeV the background can be estimated to be 0 ± 60 events, compared to a total signal of about 4000 events. The statistics in these plots corresponds to about 10 fb^{-1}. A fit using the expected form of the distribution, Equation 20-6, smeared with a Gaussian gave

$$M = 52.266^{+0.058}_{-0.045}\ \text{GeV} \qquad \sigma = 0.86\ \text{GeV}$$

$$M = 175.46^{+0.21}_{-0.22}\ \text{GeV} \qquad \sigma = 6.5\ \text{GeV}$$

where the errors are determined using MINOS. Thus the errors on the upper edge are statistics limited even for design luminosity. Including systematic effects, the errors are estimated to be 0.07 and 0.27 GeV for 10 fb^{-1} and 0.05 and 0.18 GeV for 100 fb^{-1}. The upper edge seems wider than expected from detector resolution.

20.3.3.2 Detection of $\tilde{q}_R \to \tilde{\chi}_1^0 q$

Right-handed squarks are copiously produced both directly and through gluino decay, and they can decay via $\tilde{q}_R \to \tilde{\chi}_1^0 q \to \tilde{l}^{\pm} l^{\mp} q \to \tilde{G} l^{+} l^{-} q$. To select this mode, a dilepton pair with high p_T below the $\tilde{\chi}_1^0$ edge and two jets were required in addition to the cuts in the previous subsubsection:

- $M_{ll} < 52.2$ GeV and $p_{T,ll} > 75$ GeV;
- two jets with $p_T > 50$ GeV, $|\eta| < 2.5$, and at least four charged tracks each with $p_T > 1$ GeV.

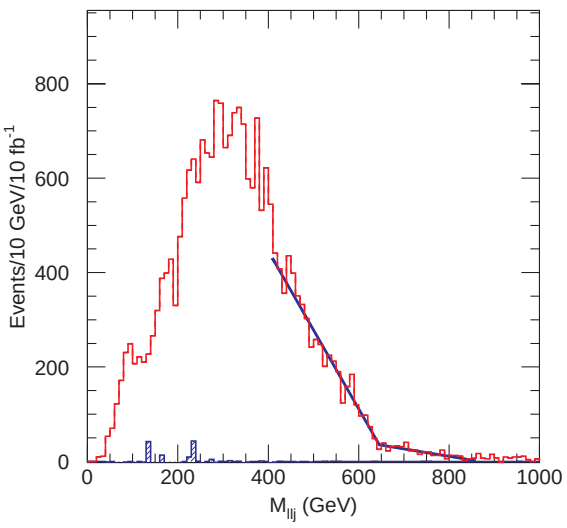

Figure 20-69 Distribution of the smaller llj mass for events with two leptons and four jets at Point G2a. The dashed line is a linear fit over 390-590 GeV. The Standard Model background is the hatched histogram.

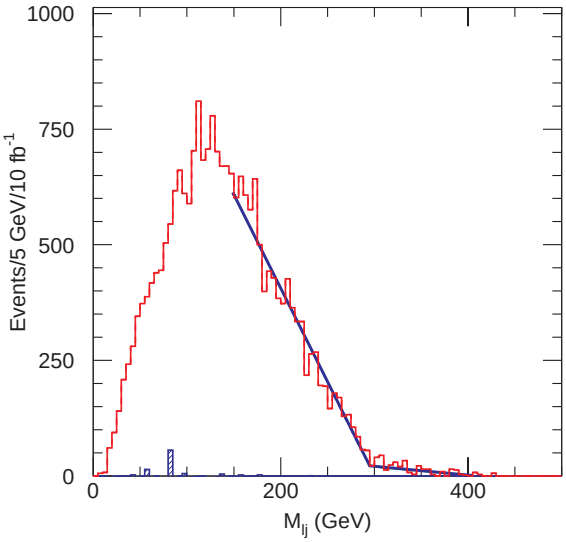

Figure 20-70 lj mass distribution for the same sample as in Figure 20-69. The dashed lines are linear fits over 150-280 GeV and 305-400 GeV.

Again the $e^+e^- + \mu^+\mu^- - e^\pm\mu^\mp$ combination is used to eliminate backgrounds. The dilepton pair was then combined with each of the two hardest jets in the event. Since one of these two should come from the squark decay, the combination with the smaller mass was selected as usual. Then the llq mass distribution, Figure 20-69, has a linear vanishing at the expected endpoint

$$M_{llq}^{\max} = \sqrt{M_{\tilde{q}_R}^2 - M_{\tilde{l}_R}^2} = 640.1 \text{ GeV}$$

while the lq mass distribution, Figure 20-70, shows the expected endpoint at

$$M_{lq}^{\max} = \sqrt{M_{\tilde{q}_R}^2 - M_{\tilde{\chi}_1^0}^2}\sqrt{1 - \frac{M_{\tilde{l}_R}^2}{M_{\tilde{\chi}_1^0}^2}} = 289.1 \text{ GeV} .$$

The ll, llj, and lj distributions from this three-step decay chain provide three measured endpoints from which the three masses involved can be determined assuming only that the gravitino mass is negligible:

$$M_{\tilde{l}_R} = \frac{M_{ll}\sqrt{M_{llq}^2 - M_{lq}^2 - M_{ll}^2}}{M_{lq}}$$

$$M_{\tilde{\chi}_1^0} = \sqrt{M_{ll}^2 + M_{\tilde{l}_R}^2}$$

$$M_{\tilde{q}_R} = \sqrt{M_{llq}^2 + M_{\tilde{l}_R}^2}$$

The determination of these masses depends only on the existence of the decay chain and does not assume the minimal GMSB or any other model, again reflecting the power of utilising multi-step decay chains. Of course the interpretation of the masses as those of the $\tilde{q}_R$, $\tilde{\chi}_1^0$, and $\tilde{l}_R$ is model dependent.

20.3.3.3 Detection of $\tilde{\chi}_1^\pm$

About 50% of the $\tilde{q}_L$ decays at this point occur through the $\tilde{\chi}_1^\pm$. While in general charginos are hard to reconstruct, the decay chain

$$\tilde{\chi}_1^+ \to \tilde{\nu} l^+ \to \tilde{\chi}_1^0 \nu l^+ \to \tilde{l}_R^\pm l^\mp \nu l^+ \to \tilde{G} l^+ l^- \nu l^+$$

has a combined branching ratio of 29% and gives a very nice trilepton signature. Events were selected to have at least three isolated leptons plus the same jets and other cuts described before. One pair of leptons was required to form an opposite-sign, same-flavour pair with $40 < M_{ll} < 52$ GeV, so that it is likely to have come from a $\tilde{\chi}_1^0$ decay. It was also required that there be no other opposite-sign, same-flavour pair with $M_{ll} < 175$ GeV, the

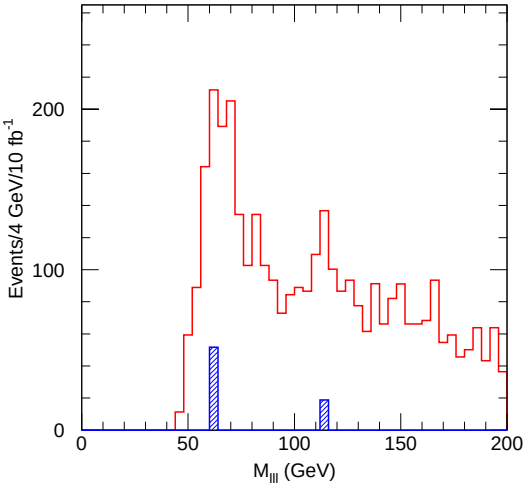

Figure 20-71 Trilepton mass distribution for chargino signal at Point G2a. The shaded histogram is the Standard Model background.

endpoint for $\tilde{\chi}_2^0$ decay. The lll mass distribution after these cuts is shown in Figure 20-71. If the three leptons come from the above chargino decay chain, then the distribution should vanish linearly at the kinematic endpoint

$$\sqrt{M^2_{\tilde{\chi}_1^\pm} - M^2_{\tilde{\nu}} + M^2_{\tilde{\chi}_1^0} - M^2_{\tilde{l}_R}} \; = \; 85.75 \text{ GeV} .$$

There is a lot of background, but nevertheless there is evidence for structure in the distribution at this point. While it seems hard to extract a precision measurement because of the background, this distribution does provide evidence for the existence of the chargino and a consistency check on the model.

20.3.4 GMSB Point G2b

At this point the NLSP is the $\tilde{\tau}_1$, which has $c\tau \approx 1\text{km}$ and so (almost) always decays outside the detector. Since the decay $\tilde{l}_R \to \tilde{\tau}_1 \tau l$ is not kinematically allowed, the $\tilde{e}_R$ and $\tilde{\mu}_R$ also are long-lived, decaying to gravitinos with about the same lifetime. Each event therefore contains two quasi-stable heavy particles which pass through the calorimeter and look essentially like muons in the detector except that they have $\beta < 1$, as shown in Figure 20-72. The slepton masses can be measured using the ATLAS muon system as a time-of-flight system, and the SUSY events can then be fully reconstructed [20-36]. It is again important to search for slepton decays in order to determine the true SUSY breaking scale. It should be possible to see such decays in the central tracker, but this is a difficult pattern recognition problem which has not yet been addressed. It would also be possible to detect $\tilde{e} \to \tilde{G}e$ using the same method as in Section 20.3.2.4. The NLSP could also be separated from the SM particles exploiting the dE/dx measurement in the TRT detector, using the algorithm described in Section 3.4.4 for charged hadrons. A full study taking into account the time delay of the NLSP in the TRT straws still remains to be performed.

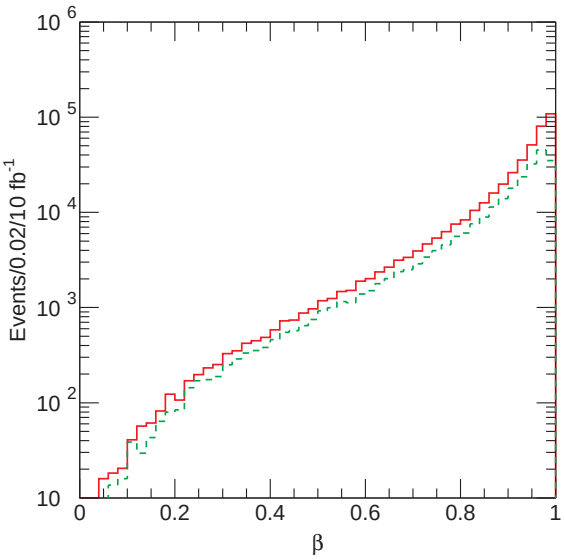

Figure 20-72 Generated slepton velocity distribution at Point G2b. The dashed curve shows the distribution for $\eta < 1$.

20.3.4.1 Trigger

The events at this point can be triggered using either the sleptons or the calorimeter information. The velocity distribution of the produced sleptons, shown in Figure 20-72, has a mean value of about 0.9. This implies that on average the sleptons reach the muon trigger chambers several nanoseconds late but still within the trigger acceptance [20-38]. One must of course be sure to record the hits from even very slow sleptons since these are the most useful for the time-of-flight measurement.

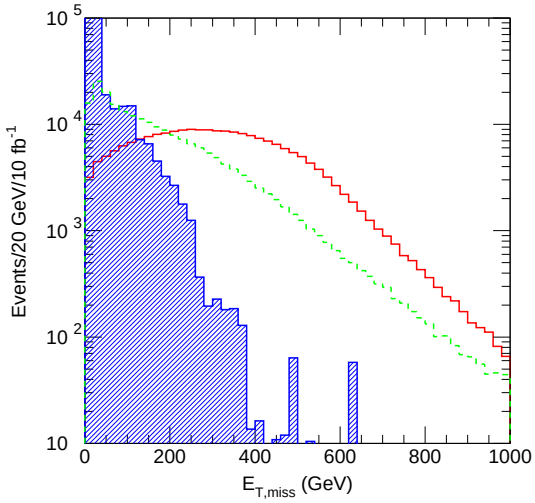

Figure 20-73 Calorimetric $E_{\mathrm{T}}^{\mathrm{miss}}$ distribution at Point G2b. The dashed curve shows the true $E_{\mathrm{T}}^{\mathrm{miss}}$ including sleptons, and the shaded histogram shows the Standard Model dimuon background.

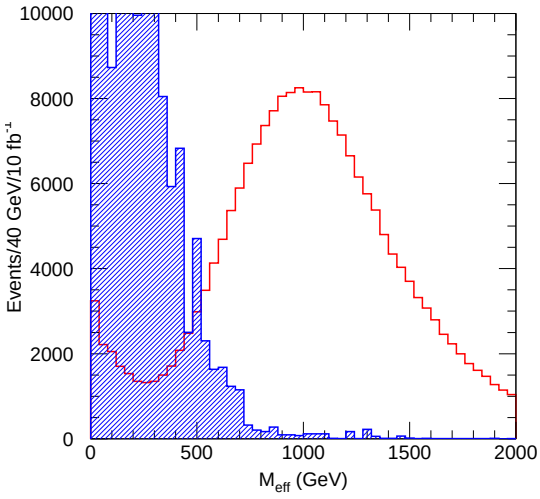

Figure 20-74 Effective mass distribution not including sleptons at Point G2b. The shaded histogram shows the Standard Model dimuon background.

The $E_{\mathrm{T}}^{\mathrm{miss}}$ as measured by the calorimeter, Figure 20-73, is large since the sleptons lose energy only by dE/dx. The $E_{\mathrm{T}}^{\mathrm{miss}}$ including the sleptons is much smaller, coming only from neutrinos produced in the cascade decays and from resolution effects. The typical effective mass, Figure 20-74, is also large, with a mean value of about 1000 GeV characteristic of gluino and squark production. However, there is also a peak at $M_{\mathrm{eff}} = 0$ from the direct production of sleptons and gauginos; it is necessary to rely on the muon trigger for these events.

20.3.4.2 Slepton mass determination

The mass of the sleptons can be measured using the muon system as a time-of-flight system: the precision chambers and trigger chambers together provide a time resolution of about 1ns [20-38]. This initial estimate has now been verified and refined [20-39] using DICE to fully simulate the response of the MDT chambers to slow tracks and ATRECON and MUONBOX to reconstruct them. An effective time resolution of 0.65 ns was obtained in this study (see Section 6.4). The momentum resolution for the $\tilde{\tau}_1$ at momenta $p \lesssim M$ is somewhat worse than the one for muons which was assumed in this analysis because of multiple scattering. This difference, however, does not affect the conclusions on $\tilde{\tau}_1$ mass measurement.

For each slepton with $|\eta| < 2.5$ the time delay relative to a particle with $\beta = 1$ to reach the outside of the muon system, taken to be a cyl-

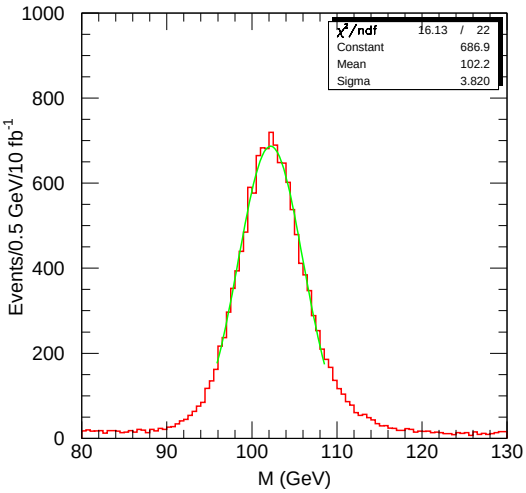

Figure 20-75 Reconstructed slepton masses at Point G2b for a 1ns time resolution and $\Delta t > 10\mathrm{ns}$.

inder with a radius of 10 m and a half-length of 20 m, was calculated using the generated momentum and was then smeared with a 1 ns Gaussian resolution. The resulting time delay Δt and measured momentum p were then used to calculate the mass. The resulting mass distribution is shown in Figure 20-75 for sleptons having $10 < \Delta t < 50$ ns. The fitted mean value agrees very well with the average, 102.2 GeV, for the generated mixture of sleptons. The width of the distribution results from a combination of the time and momentum resolutions; even for very large Δt it is not possible to resolve the $\tilde{\tau}_1$ and $\tilde{l}_R$ masses, 101.35 and 102.67 GeV. Because of this the upper limit on Δt is not critical; there would be little loss if it were restricted to one bunch crossing.

20.3.4.3 Reconstruction of $\tilde{\chi}_1^0$, $\tilde{\chi}_2^0$, and $\tilde{\chi}_4^0$

Since the $\tilde{l}_R$ are quasi-stable, the decays $\tilde{\chi}_i^0 \to \tilde{l}_R l$ can be fully reconstructed. Events were selected to have at least three electrons, muons, or quasi-stable sleptons with $|\eta| < 2.5$ and $p_T > 10\text{GeV}$. The two highest p_T particles among the sleptons and muons were assumed to be sleptons with the average slepton mass measured in the previous section; the rest were considered as muons. No time-of-flight cuts were made because the Standard Model background is already negligible. The sleptons were then combined with electrons or muons. The mass distribution for all $\tilde{l}_R^{\pm} l^{\mp}$ combinations is shown in Figure 20-76. There are two clear peaks at the $\tilde{\chi}_1^0$ and $\tilde{\chi}_2^0$ masses and a small peak at the $\tilde{\chi}_4^0$ mass. The rather strange shape of the $\tilde{\chi}_1^0$ peak results from the fact that the splitting between the $\tilde{\chi}_1^0$ and the $\tilde{l}_R$ is small, so the mass is dominated by the slepton rest mass.

The determination of the slepton masses can at this point be refined, since for events in the gaugino peaks the flavour of the slepton is tagged by that of the lepton. Events were selected within $\pm 5\text{GeV}$ of the $\tilde{\chi}_1^0$ peak, and the time-of-flight analysis in Section 20.3.4.2 was repeated. The resulting mass distribution, Figure 20-77, has a mean of 102.8 GeV, quite close to the 102.67 GeV mass of the $\tilde{e}_R$ and $\tilde{\mu}_R$, which are expected to be degenerate in GMSB models. The

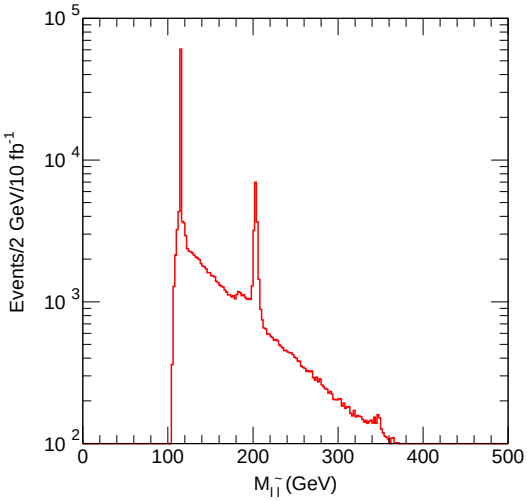

Figure 20-76 $\tilde{l}_R^{\pm} l^{\mp}$ mass distribution for Point G2b.

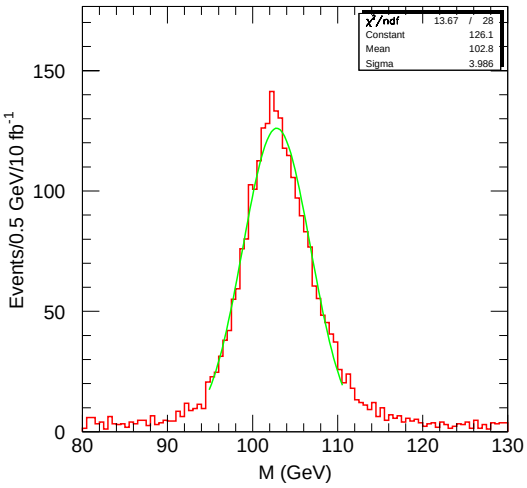

Figure 20-77 Same as Figure 20-75 for events within a $\pm 5\text{GeV}$ window of the $\tilde{\chi}_1^0$ peak in Figure 20-76.

statistical error is about $\pm 0.1\text{GeV}$ for 10fb^{-1}. The systematic error is expected to be at the 0.1% level. Thus it is possible to distinguish these masses from the average slepton mass measured previously, thereby constraining the $\tilde{\tau}_1$ mass as well.

20.3.4.4 Extraction of $\tilde{l}_L$ and $\tilde{\nu}$

Left-handed sleptons $\tilde{l}_L$ are produced mainly from decays of heavy gauginos although there is also some direct Drell-Yan production. They can decay via $\tilde{l}_L \to \tilde{\chi}_1^0 l \to \tilde{l}_R^{\pm} l^{\mp} l$. To reconstruct this process, events within $\pm 5\,\text{GeV}$ of the $\tilde{\chi}_1^0$ peak reconstructed in the previous section were selected, and the $\tilde{\chi}_1^0$ was combined with another lepton with $p_T > 10\,\text{GeV}$ and $|\eta| < 2.5$. The resulting mass distribution, Figure 20-78, shows a peak at the $\tilde{l}_L$ mass, 203 GeV, with a fitted width of 1.3 GeV. In addition to the resonance peak, there is also a low-mass structure in Figure 20-78. This results from $\tilde{\chi}_1^{\pm} \to \tilde{\nu} l \to \tilde{\chi}_1^0 \nu l \to \tilde{l}_R^{\pm} l^{\mp} \nu l$, which has a kinematic endpoint at

$$\sqrt{M^2_{\tilde{\chi}_1^{\pm}} - M^2_{\tilde{\nu}} + M^2_{\tilde{\chi}_1^0}} = 134\,\text{GeV}.$$

While this endpoint is clearly visible, there is a lot of background under it, so an accurate measurement will not be easy. Nevertheless, this structure will provide some measurement of a combination of the $\tilde{\nu}$ and $\tilde{\chi}_1^{\pm}$ masses.

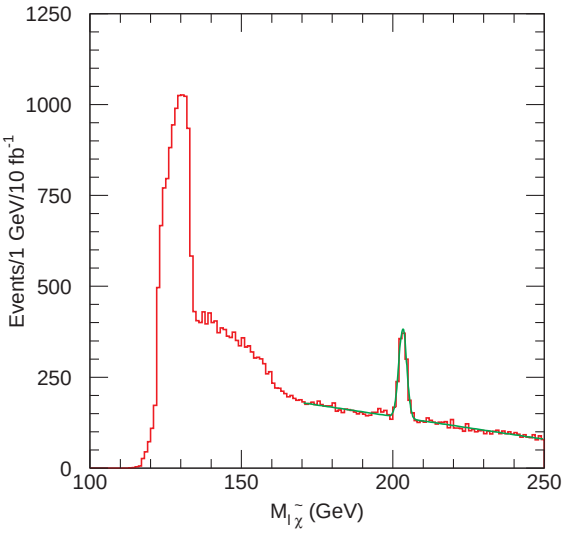

Figure 20-78 Mass distribution of a slepton and two leptons at Point G2b. The slepton and one lepton are required to be within $\pm 5\text{GeV}$ of the $\tilde{\chi}_1^0$ peak in Figure 20-76

20.3.4.5 Reconstruction of squarks

At Point G2b squarks are considerably lighter than gluinos. Direct production of squarks dominates, and the branching ratio for $\tilde{q}_R \to \tilde{\chi}_1^0 q$ is about 95%. Events were selected to have an $\tilde{l}^{\pm} l^{\mp}$ mass within $\pm 5\text{GeV}$ of the $\tilde{\chi}_1^0$ peak in Figure 20-76, and the $\tilde{l}^{\pm} l^{\mp}$ was then combined with each one of the four hardest jets in the event. The resulting $\tilde{\chi}_1^0 j$ mass distribution, Figure 20-79, shows a peak about 2% below the average $\tilde{q}_R$ mass of 648 GeV with a width of about 26 GeV. The statistical error on the mass is negligible; the mass shift could be corrected by applying the jet rescaling procedures described in Section 9.1.1.3 and the mass measured to about $\pm 1\%$, the systematic limit on the jet energy scale. The contribution of jets tagged as b's, shown as the dotted curve in the figure, is very small.

The branching ratio for $\tilde{q}_L \to \tilde{\chi}_2^0 q$ is about 25%. This decay can be reconstructed by in a similar way by selecting events with an $\tilde{l}^{\pm} l^{\mp}$ mass within $\pm 5\text{GeV}$ of the $\tilde{\chi}_2^0$ peak in Figure 20-76 and then combining the $\tilde{l}^{\pm} l^{\mp}$ with any of the four hardest jets. The resulting $\tilde{\chi}_2^0 j$ mass distribution, Figure 20-80, shows a peak about 3% below the average $\tilde{q}_L$ mass of 674 GeV. The figure also shows the distribution for the subset of events tagged as b's. (No correction to the b-jet energy scale was made.) In contrast to the $\tilde{\chi}_1^0 j$ case, there is a clear peak close to the average $\tilde{b}$ mass – 647 GeV with a splitting of only 9 GeV – which is significantly below the $\tilde{q}_L$ mass. While the de-

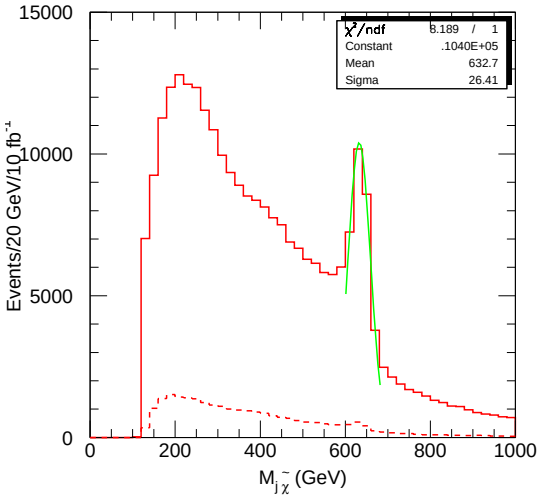

Figure 20-79 $\tilde{\chi}_1^0 j$ mass distribution at Point G1b. The $\tilde{l}^{\pm} l^{\mp}$ is required to be within $\pm 5\text{GeV}$ of the $\tilde{\chi}_1^0$ peak in Figure 20-76. The dashed curve is for jets which are tagged as b's.

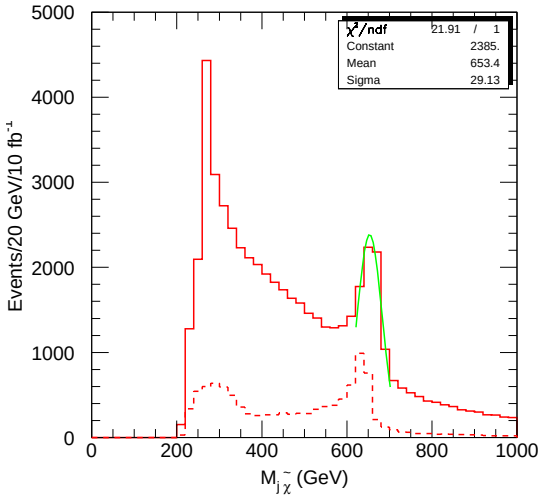

Figure 20-80 Same as Figure 20-79 but for $\tilde{\chi}_2^0 j$.

cay $\tilde{q}_R \to \tilde{\chi}_1^0 q$ is dominant, both the $\tilde{b}_1$ and the $\tilde{b}_2$ have branching ratios of only a few percent into $\tilde{\chi}_1^0$. The $\tilde{b}$ contribution explains the fact that the difference between the fitted masses in Figures 20-79 and 20-80 is a factor of two smaller than the $\tilde{q}_L - \tilde{q}_R$ mass difference.

20.3.4.6 Reconstruction of $\tilde{\tau}\tau$ decays

While $\tilde{\chi}_i^0 \to \tilde{\tau}\tau$ is more difficult to reconstruct than $\tilde{\chi}_i^0 \to \tilde{l}l$, it provides additional information, *e.g.*, about the Higgsino content of the neutralinos. The analysis described here is only a first pass: it uses generator information to identify the τ's and their visible decay products rather than the more sophisticated and realistic analysis used in Section 20.2.8. Hadronic τ's were selected with $p_T > 20$ GeV, $|\eta| < 2.5$, and either one or three charged tracks. A (perhaps optimistic) efficiency of 60%, the same as for b-tagging, was assumed and is included. The visible τ momentum was then combined with the slepton momentum. The resulting $\tilde{\tau}\tau$ distribution is shown in Figures 20-81 and 20-82 on two different scales. While the distribution does not show any mass peaks because of the missing neutrinos, it does have rather sharp endpoints at the $\tilde{\chi}_1^0$ and $\tilde{\chi}_2^0$ masses.

If there is only one ν_τ, then the true E_T^{miss} calculated from the calorimeter plus the sleptons can be used to determine the τ momentum. Only the τ with the highest p_T is used, and the angle between it and the E_T^{miss} direction is required to be $\Delta\phi < 0.1\pi$. The visible τ momentum is then scaled by a factor $1 + E_T^{miss}/E_{T,\tau}$, and the $\tilde{\tau}\tau$ mass is recomputed. This gives the dashed curves in Figures 20-81 and 20-82. As expected, including E_T^{miss} not only reduces the statistics but also worsens the resolution for the $\tilde{\chi}_1^0$, since the τ from $\tilde{\chi}_1^0$ is very soft. However, it produces a peak near the right position for the $\tilde{\chi}_2^0$. While this peak probably does not improve the mass resolution, it adds confidence that one is seeing a two-body resonance.

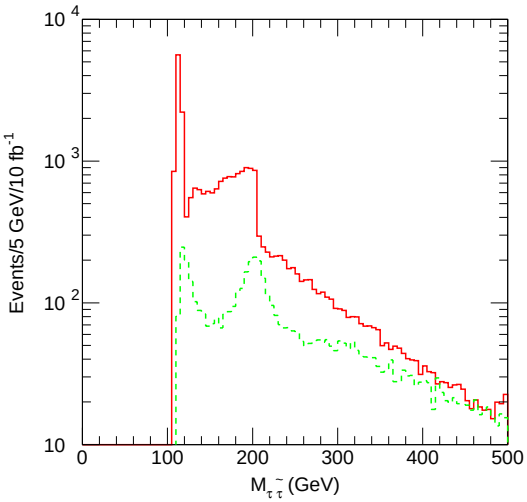

Figure 20-81 $\tilde{\tau}\tau$ invariant mass distribution at Point G2b. Solid curve: using visible τ momentum. Dashed curve: using $E_{\mathrm{T}}^{\mathrm{miss}}$ as described in the text.

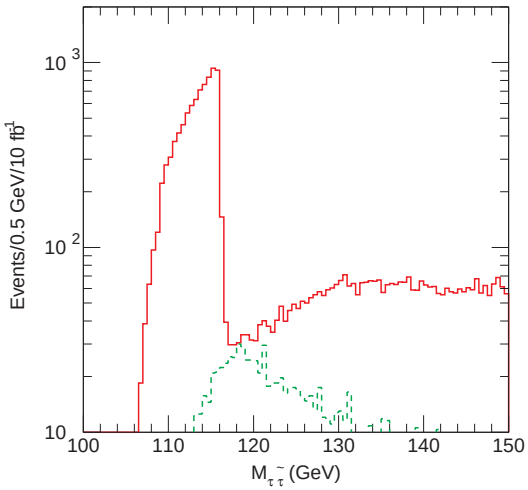

Figure 20-82 Same as Figure 20-81 on a finer scale.

20.3.4.7 Direct production of sleptons and gauginos

The peak at low M_{eff} in Figure 20-74 is due to the direct production of sleptons and gauginos. Studying this direct production does not lead to reconstruction of any new masses, but does contain information that could be used to constrain the SUSY model. Events were selected as in Section 20.3.4.3 and Figure 20-76 with the additional requirement $M_{\mathrm{eff}} < 100\ \mathrm{GeV}$, where the effective mass of course excludes the sleptons. The resulting $\tilde{l}l$ mass distribution, Figure 20-83,

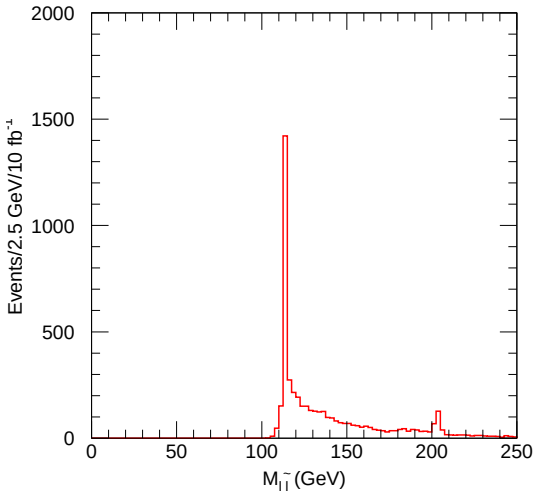

Figure 20-83 Same as Figure 20-76 with the additional requirement $M_{\mathrm{eff}} < 100\ \mathrm{GeV}$.

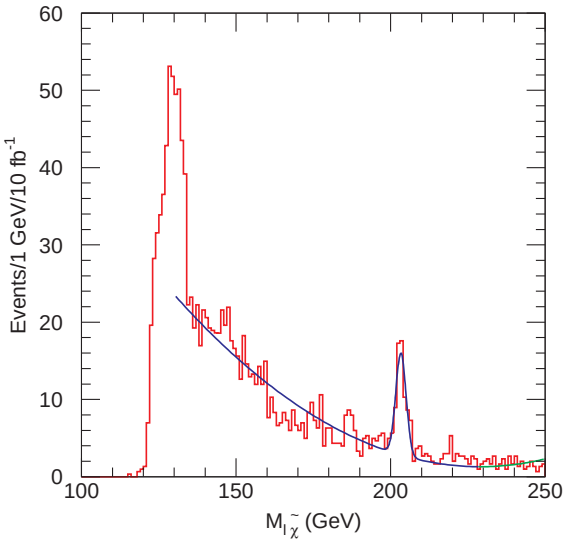

Figure 20-84 Combination of $\tilde{l}l$ from Figure 20-83 in the mass range 110–120 GeV with an additional lepton.

shows a strong $\tilde{\chi}_1^0$ peak and a small $\tilde{\chi}_2^0$ peak. The second peak is suppressed both by its larger mass and by the fact that its decay products can contribute to M_{eff}, causing part of the signal to be discarded.

Events from the $\tilde{\chi}_1^0$ peak in Figure 20-83 can be combined with a third lepton to reconstruct directly produced sleptons decaying via $\tilde{l}_L \to \tilde{\chi}_1^0 l \to \tilde{l}_R^{\pm} l^{\mp} l$. Events with $110 < M_{\tilde{l}l} < 120$ GeV were combined with another lepton having $p_{\mathrm{T}} > 10$ GeV and $|\eta| < 2.5$. Figure 20-84 shows the resulting mass distribution with a slepton peak having a fitted mass of 203.3 GeV and a width of 1.66 GeV. The low-mass feature from $\tilde{\chi}_1^{\pm} \to \tilde{\nu} l \to \tilde{\chi}_1^0 \nu l \to \tilde{l}_R^{\pm} l^{\mp} \nu l$ discussed previously is also visible. The number of events is much lower than in Figure 20-78, showing that the inclusive signals reconstructed in Section 20.3.4.4 are dominated by cascade decays, not by direct production.

20.3.5 Fitting GMSB parameters

In several of the GMSB cases considered a number of masses can be determined from the kinematic properties of the event without making use of a model. Nevertheless, it is still useful to make a global fit to determine the parameters of the minimal GMSB model. The method is similar to that described in Section 20.2.9. A scan is made over the ranges

$$\Lambda > 1000 \text{ GeV}$$
$$M_m \geq \Lambda$$
$$1 \leq N_5 \leq 10$$
$$1 < \tan\beta < 20$$

for both signs of μ. The upper limits on Λ and M_m are determined iteratively for each point. Once an approximate solution has been determined, the ranges are reduced and more points are scanned iteratively until the $\pm 1\sigma$ errors are determined. The signatures for the GMSB points are qualitatively different from any SUGRA model except for Point G1b; no minimal SUGRA solution was found for that point.

Results of the fits [20-36] for these four parameters are given for the same Low-L, High-L, and Ultimate scenarios as in Section 20.2.9 except that for the first two the theoretical error on the light Higgs mass is taken to be ± 3 GeV, somewhat more conservative than the value assumed in the SUGRA fits. The parameter C_{grav} is independent from the other parameters, and is determined in each case from the NLSP lifetime as already discussed. No study of the determination of non-minimal GMSB parameters has yet been made.

20.3.5.1 Point G1a

At Point G1a the presence of two prompt photons in almost every SUSY event strongly suggests a GMSB-like scenario. Besides the light Higgs mass there are four precisely measured combinations of leptons and photons, which are summarised in Table 20-18 with their estimated errors. The estimated error on $M_{ll}^{\max}$ at low luminosity may be a bit too small compared to the errors given in Section 20.2.3. The errors at high luminosity are dominated by systematic effects. These four observables can all be related to combinations of the masses involved, and they are sufficient to determine the parameters of the minimal model. The other measured quantities provide cross checks on the model but do not significantly constrain the parameters.

Table 20-18 Inputs for the minimal GMSB fit at Point G1a.

Quantity	Reference	Low-L	Ultimate
M_h	Section 19.2.2	(109.47 ± 3.0) GeV	(109.27 ± 0.2) GeV
$M_{ll}^{\max}$	Section 20.3.1.1	(105.1 ± 0.1) GeV	same
$M_{ll\gamma}^{\max}$	Section 20.3.1.1	(189.7 ± 0.3) GeV	(189.7 ± 0.2) GeV
$M_{l\gamma}^{(1)}$	Section 20.3.1.1	(112.7 ± 0.15) GeV	(112.7 ± 0.1) GeV
$M_{l\gamma}^{(2)}$	Section 20.3.1.1	(152.6 ± 0.3) GeV	(152.6 ± 0.2) GeV

Table 20-19 Results of the minimal GMSB fit at Point G1a. $\mathrm{sgn}\mu = +$ is unambiguously determined. Note that the errors in Reference [20-36] are too small by a factor of $\sqrt{2}$.

Parameter	Low-L	High-L	Ultimate
Λ	(90000 ± 1700) GeV	(90000 ± 890) GeV	same
M_m	(500000 ± 170000) GeV	(500000 ± 110000) GeV	same
N_5	1.00 ± 0.014	1.00 ± 0.011	same
$\tan\beta$	5.0 ± 1.3	5.0 ± 0.4	5.0 ± 0.14

The results of the fit are shown in Table 20-19. As expected, Λ, N_5, and $\mathrm{sgn}\mu$ are well determined even at low luminosity, while M_m is never very precisely determined because it enters only through the logarithmic running of masses in the renormalisation group equations. Since $\tan\beta$ is determined mainly from the Higgs mass, the errors on it do improve. Another handle on $\tan\beta$ might be provided by the large violation of $e/\mu/\tau$ universality at Point G1a, *e.g.*,

$$B(\tilde{\chi}_2^0 \to \tilde{e}e) = 25\%$$
$$B(\tilde{\chi}_2^0 \to \tilde{\tau}\tau) = 41\%$$

This has not yet been studied.

20.3.5.2 Point G1b

While the masses are the same at Point G1b as at Point G1a, the absence of $\tilde{\chi}_1^0 \to G\gamma$ decays leads to fewer measurements, which are summarised in Table 20-20. The measurement of the average slepton mass relies [20-36] on understanding the shape of a lepton-jet mass distribution, not just on kinematics. The gluino mass measurement nominally comes from an endpoint, but it also really requires understanding the shape of a distribution.

If the squark mass measurement is not included, then the fit is only able to constrain two combinations of parameters with any precision. For 30 fb^{-1},

- $\Lambda N_5 = (90000 \pm 880)$ GeV;
- $\tan\beta = 5.0^{+2.7}_{-1.8}$.

There is no independent information on Λ and N_5 because the position of the dilepton edge is independent of the slepton mass for $M_{\tilde{l}_R} = \sqrt{M_{\tilde{\chi}_1^0} M_{\tilde{\chi}_2^0}}$, and the equality holds to within 0.5 GeV at this point.

Table 20-20 Inputs for the minimal GMSB fit at Point G1b. The measurement below the horizontal rule determines a combination of masses and production dynamics.

Quantity	Reference	Low-L	Ultimate
M_h	Section 19.2.2	(109.47 ± 3.0) GeV	(109.27 ± 0.2) GeV
$M_{ll}^{\max}$	Section 20.3.2.2	(105.1 ± 0.1) GeV	same
$M_{\tilde{g}} - M_{\tilde{\chi}_2^0}$	Section 20.3.2.3	(523 ± 30) GeV	(523 ± 15) GeV
$\langle M_{\tilde{q}_L} \rangle$	[20-36]	(988 ± 50) GeV	same

If the squark mass measurement is included, then the fit gives for $30\ \text{fb}^{-1}$

- $\Lambda N_5 = (90000 \pm 880)$ GeV;
- $\Lambda = (90000 \pm 11500)$ GeV;
- $M_m < 7 \times 10^8$ GeV;
- $\tan\beta = 5.0^{+2.7}_{-1.8}$;

assuming $\text{sgn}\mu = +$, but there is also a solution for $\text{sgn}\mu = -$. This can be eliminated only if the slepton mass can be measured independently or the squark mass can be measured to ± 10 GeV. The errors decrease somewhat with higher luminosity, but the GMSB parameters remain poorly constrained.

The signatures for Point G1b are not qualitatively different from those of a SUGRA model. A fit to the measurements in Table 20-20 not including the squark mass gives for $30\ \text{fb}^{-1}$

- $m_0 = (100 \pm 20)$ GeV;
- $m_{1/2} = (295 \pm 6)$ GeV;
- $\tan\beta = 4.5 \pm 1.1$;
- $\text{sgn}\mu = +$;
- $A_0 = (250 \pm 200)$ GeV.

The fit has a probability of only 15%. The mean value of the squark mass is 760 GeV; GMSB models typically give a more spread-out spectrum than SUGRA ones. Hence the SUGRA fit can be ruled out by the squark measurement.

It may be possible to obtain a better determination of the parameters at this point, but doing so would require generating many samples of events and comparing the predicted distributions with the data. Thus, this point serves as a caution about drawing overly optimistic conclusions about the generality of the methods discussed in this chapter.

20.3.5.3 Point G2a

At Point G2a the prompt decay of the slepton provides well-measured multi-step decays. The measurements summarised in Table 20-21 are already limited by systematics for an integrated luminosity of $30\ \text{fb}^{-1}$; there is indeed not much improvement beyond $10\ \text{fb}^{-1}$. All of the measurements can be related precisely to combinations of masses, making the fit straightforward.

Table 20-21 Inputs for the minimal GMSB fit at Point G2a.

Quantity	Reference	Low-L	Ultimate
M_h	Section 19.2.2	(106.6 ± 3.0) GeV	(106.6 ± 0.2) GeV
$M_{ll}^{\max}$ (first edge)	Section 20.3.3.1	(52.21 ± 0.05) GeV	same
$M_{ll}^{\max}$ (second edge)	Section 20.3.3.1	(175.94 ± 0.18) GeV	same
$M_{llq}^{\max}$	Section 20.3.3.2	(640 ± 7) GeV	same
$M_{lq}^{\max}/M_{llq}^{\max}$	Section 20.3.3.2	0.450 ± 0.004	same

Table 20-22 Results of the minimal GMSB fit at Point G2a. $\mathrm{sgn}\mu = +$ is unambiguously determined. Note that the errors in Reference [20-36] are too small by a factor of $\sqrt{2}$.

Parameter	Low-L	High-L	Ultimate
Λ	(30000 ± 540) GeV	same	same
M_m	(250000 ± 60000) GeV	same	same
N_5	3.00 ± 0.05	same	same
$\tan\beta$	5.0 ± 1.0	5.0 ± 1.0	5.0 ± 0.06

The results of the fit are summarised in Table 20-22. Since there is accurate information on both sleptons and gauginos, Λ and N_5 are well determined even for low luminosity, and even M_m is determined to about 25%. The sign of μ is unambiguous. The reduced error on $\tan\beta$ for the Ultimate fit comes just from assuming no theoretical error on the Higgs mass.

20.3.5.4 Point G2b

At Point G2b the sleptons are stable; their masses can be determined by time of flight measurements and their momenta directly measured. This allows many different masses to be reconstructed directly as peaks in invariant mass distributions Even for an integrated luminosity of 10 fb^{-1} the errors are limited by the systematics of the detector energy scales, assumed to be 1% for jets and 0.1% for electrons and muons, so there is no need to summarise them here.

The results of the fit are summarised in Table 20-23. Again, Λ and N_5 are well determined. M_m is determined to less than $\pm 15\%$, and the error on $\tan\beta$ is limited by the uncertainty on the light Higgs mass. At least within the minimal GMSB model, the only question is how well C_{grav} could be measured or limited by looking for occasional slepton decays in the tracking system.

Table 20-23 Results of the minimal GMSB fit at Point G2b. $\mathrm{sgn}\mu = +$ is unambiguously determined. Note that the errors in Reference [20-36] are too small by a factor of $\sqrt{2}$.

Parameter	Low-L	High-L	Ultimate
Λ	(30000 ± 250) GeV	same	same
M_m	(250000 ± 32000) GeV	same	same
N_5	3.00 ± 0.02	same	same
$\tan\beta$	5.0 ± 0.3	5.0 ± 0.3	5.0 ± 0.03

The signature is straightforward in principle – the $\tilde{l}$ track ends, and an l track begins with a relative $p_T \sim M_{\tilde{l}}/2$, giving rise to 'kinks' – but the pattern recognition has not yet been studied. It however should be feasible at low luminosity.

20.4 *R*-Parity breaking models

The conservation of *R*-parity, defined as

$$R = (-1)^{3(B-L)+2S}$$

is an elegant way of imposing at the same time baryon (*B*) and lepton (*L*) number conservation in supersymmetric theories. However, there is no compelling theoretical reason why *R*-invariance should be a symmetry of the Lagrangian. It is therefore useful to investigate the phenomenological consequences of realistic models with broken *R*-parity.

In models with minimal field content, the *R*-violating superpotential can be written as

$$W_{RPV} = \lambda_{ijk} L_i L_j E^c_k + \lambda'_{ijk} Q_i L_j D^c_k + \lambda''_{ijk} U^c_i D^c_j D^c_k \ ,$$

where *L* and *E* are respectively isodoublet and isosinglet lepton, and *Q* and *D* are isodoublet and isosinglet quark superfields, and the indices *i,j,k* run over the three quark and lepton generations. The superscript *c* indicates charge conjugation. The terms in the superpotential explicitly violate baryon number (through the nine λ''_{ijk} couplings) and lepton number (by the nine λ_{ijk} and the 27 λ'_{ijk} couplings). In order to ensure proton stability, either *L* or *B* violating terms should be absent. Experimental limits on various *L*- and *B*-violating processes constrain the values of most of the λ couplings to a few 10^{-2} [20-14], but some of the couplings have bounds of order one.

Any additional term in the Lagrangian with a coupling bigger than 10^{-2} becomes competitive with the gauge couplings and affects the mass spectra and the branching ratios of the models, which will be very different from the *R*-conserving case. Such scenarios, for which no appropriate simulation tool was available for *pp* physics, are not considered further in this study. (Work on such scenarios has now started using HERWIG [20-40].) For lower values of the λ couplings, the only effect is the fact that the LSP becomes unstable, and decays to three *R*-even particles. The search strategies are thus drastically different with respect to *R*-parity conserving models, for which the basic signature is the E_T^{miss} from undetected $\tilde{\chi}_1^0$ in the final state.

For a value of the coupling constant $\lambda < 10^{-6}$ the LSP will decay outside the detector, thus giving a phenomenology identical to *R*-parity conserving models. For λ values between 10^{-2} and 10^{-6} the LSP will either decay with a displaced vertex in the detector, or at the interaction vertex. The studies in this section focus on the latter case, for which no additional information is available to disentangle the LSP decay products from the Standard Model background.

Given the requirements from proton decay lifetime, only one of the three terms in the superpotential is assumed to be non-zero for each given model study. Each of three cases presents a distinct $\tilde{\chi}_1^0$ decay pattern:

- $\tilde{\chi}_1^0 \to qqq$ for $\lambda''_{ijk} \neq 0$ giving six additional jets in the final state.
- $\tilde{\chi}_1^0 \to l^+ l^- \nu$ for $\lambda_{ijk} \neq 0$ giving four charged leptons per event and $E_{\text{T}}^{\text{miss}}$.
- $\tilde{\chi}_1^0 \to q\bar{q}l, q\bar{q}\nu$ for $\lambda'_{ijk} \neq 0$ giving four additional jets and two charged leptons or $E_{\text{T}}^{\text{miss}}$.

Each of the cases was studied separately, in general for each case assuming that the coupling constant is non zero only for one flavour combination at a time.

All the studies were performed within the minimal SUGRA model, with the $\tilde{\chi}_1^0$ forced to decay to the appropriate quark/lepton combination. The first step in the study was to verify that SUSY events can still be sorted out from the Standard Model background, even in the absence of the classic E_T^{miss} signature. This is straightforward for the *L*-violating couplings, which in most of the cases produce a high number of leptons in the final state, and requires a more careful analysis for the *B*-violating case. The next step was to study, for the five sample points in the SUGRA parameter space, the same exclusive decay chains that were studied for the *R*-conserving case. In general, the increased complexity of the events will make it more difficult to extract exclusive signatures from the SUSY combinatorial background. On the other hand, in many cases it will be possible to reconstruct the $\tilde{\chi}_1^0$ from its decay products, opening the possibility of the full reconstruction of the masses of the particles taking part in the identified decay chains.

20.4.1 Baryon number violation: $\chi_1^0 \rightarrow qqq$

This is potentially the most difficult case, as the decay of the $\tilde{\chi}_1^0$ into three jets destroys the $E_{\text{T}}^{\text{miss}}$ signature, and the increased jet multiplicity may not give a sufficient handle to extract the SUSY signal from the Standard Model background. The choice of a specific λ''_{ijk} as the dominant coupling only affects the final state signatures by changing the heavy quark multiplicity in the events. Two independent studies were performed using ISAJET [20-41] and HERWIG 6.0 [20-42], assuming that only the *R*-violating coupling λ''_{212} is different from zero, yielding the decay

$$\tilde{\chi}_1^0 \rightarrow cds$$

plus its complex conjugate. This particular choice of the non-zero coupling is motivated by the absence of significant experimental bounds [20-14] and by the decision to study a particularly difficult case where the high number of *c*-quarks in the final states increases the background to signatures based on the detection of *b*-quarks. HERWIG 6.0 contains a preliminary version of a simulation of all *R*-parity violating processes [20-40].

The general features of the model were studied using SUGRA Point 5 as an example. In Figures 20-85 and 20-86 the distributions of $E_{\text{T}}^{\text{miss}}$ and of the number of jets with $p_{\text{T}} > 15\text{GeV}$ are shown for the *R*-conserving case and the *R*-violating case at Point 5. The $E_{\text{T}}^{\text{miss}}$ signature has been significantly reduced, but the jet multiplicity is higher, as expected. The $\tilde{\chi}_1^0$ has a rather low mass, 112 GeV, and the jets from its decay will be rather soft and not well separated.

20.4.1.1 Inclusive signatures

The SUSY cross-section at SUGRA Point 5 is dominated by squark production either directly or from gluino decay. The final states will therefore be characterised by the presence of at least eight hadronic jets, and by a mass scale around 700 GeV. In order to have an estimate of the mass scale a variable can be defined:

$$m_{\text{T, cent}} = \sum_{(\eta < 2)} p_{\text{T}}^{\text{jet}} + \sum_{(\eta < 2)} p_{\text{T}}^{\text{lepton}} .$$

The distribution of $m_{\text{T, cent}}$ for events selected by requiring:

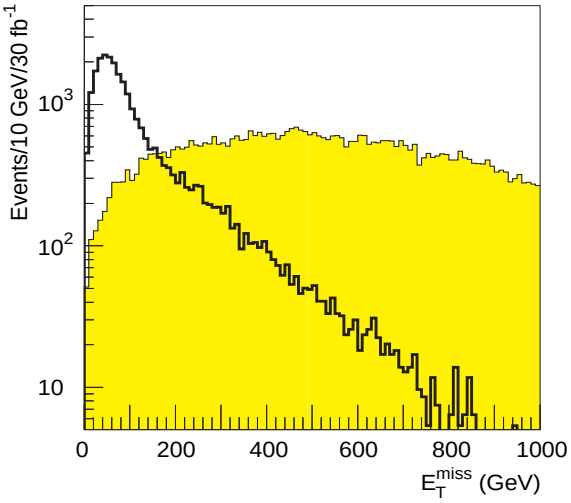

Figure 20-85 $E_{\mathrm{T}}^{\mathrm{miss}}$ distribution for SUGRA Point 5 in the case of *R*-parity conservation (shaded histogram) and *R*-parity violation (empty histogram).

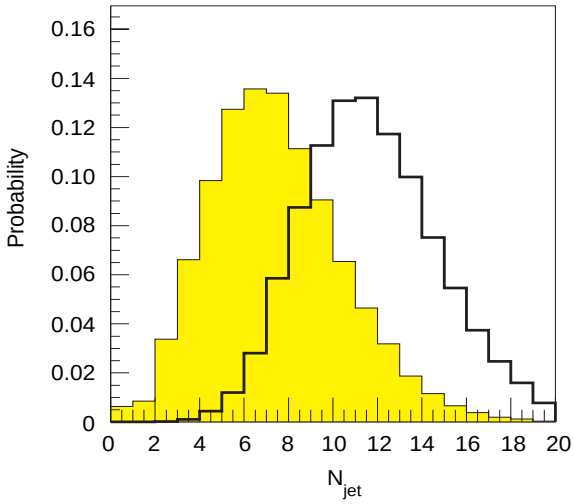

Figure 20-86 Total jet multiplicity ($p_{\mathrm{T}}^{\mathrm{jet}} > 15\mathrm{GeV}$) distribution for *R*-parity conservation (shaded) and *R*-parity violation at SUGRA Point 5. The jets are reconstructed using a topological algorithm based on joining neighbouring cells.

- at least eight jets with $p_{\mathrm{T}} > 50$ GeV;
- at least one jet with $p_{\mathrm{T}} > 100$ GeV;
- transverse sphericity > 0.2, thrust > 0.9;

is shown in Figure 20-87 for the SUSY signal, for QCD jets, and for other Standard Model backgrounds. A hard cut on the jet p_{T} is necessary to reduce the QCD multijet background, but it also reduces the efficiency for the jets from the $\tilde{\chi}_1^0$ decay. After the cuts described above, the signal is still dominated by the QCD background for all values of $m_{\mathrm{T,\,cent}}$.

The SUSY signal can therefore be separated from the SM background only by requiring the presence of at least one lepton in the event. If eight jets with $p_{\mathrm{T}} > 25$ GeV and a lepton with $p_{\mathrm{T}} > 15$ GeV are required, a cut on $m_{\mathrm{T,\,cent}} > 1000$ GeV will yield a signal over background ratio of 2.4. If two leptons are required, the ratio is greater than ten, and approximately 10000 events are expected for SUGRA Point 5, for an integrated luminosity of 30 fb^{-1}.

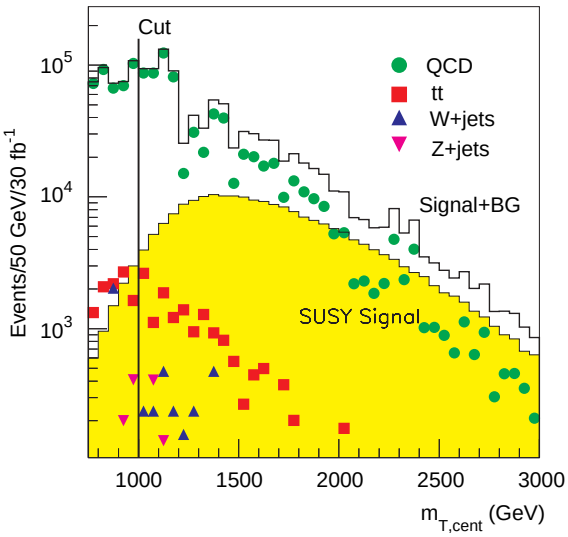

Figure 20-87 $m_{\mathrm{T,\,cent}}$ distribution for SUSY signal (shaded histogram), and for signal+background (full line histogram), after requiring at least eight jets with $p_{\mathrm{T}} > 50$ GeV. The different components of the background are also shown separately.

Another feature of SUGRA Point 5 is the presence of a large number of *b*-jets in the final state. Even by requiring four tagged *b*-jets, with no requirement on leptons, the signal cannot be extracted from the background. The high *b*-jet multiplicity can be used in combination with the requirement of one or more leptons in the final state to confirm a signal for new physics.

Abundant lepton production from $\tilde{\chi}_2^0$ decays is expected over a large part of the SUGRA parameter space, as shown in Figure 20-6. Therefore, it is expected that it will be possible to discover *B*-violating SUGRA models over a significant fraction of the parameter space with analyses similar to the one performed for Point 5.

20.4.1.2 Precision measurements

The di-lepton mass edge, produced from the decay $\tilde{\chi}_2^0 \to \tilde{l}^{\pm} l^{\mp} \to \tilde{\chi}_1^0 l^+ l^-$ is the starting point for exclusive analyses at SUGRA Point 5, and provides a very precise constraint on a combination of the masses of $\tilde{\chi}_1^0$, $\tilde{\chi}_2^0$ and $\tilde{l}_R$. In *R*-violating models the three masses involved can often be directly measured, but usually with limited statistical precision, and with the systematic uncertainties associated to the use of jets to reconstruct the invariant masses. The detection of the lepton edge provides moreover an easy way of selecting a pure SUSY sample for the reconstruction of exclusive final states.

Events were selected by requiring:

- at least eight jets with $p_T > 20\,\text{GeV}$;
- transverse sphericity > 0.2, thrust > 0.9;
- $m_{T,\,\text{cent}} > 1000\ \text{GeV}$;
- two opposite sign (OS), same flavour (SF) leptons, with $p_T > 10\ \text{GeV}$.

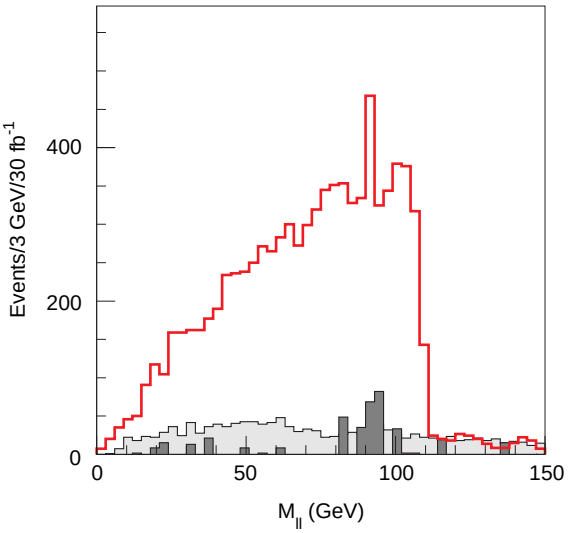

Figure 20-88 Distribution of the invariant mass formed by two OS-SF leptons after the selection described in the text for an integrated luminosity of $30\,\text{fb}^{-1}$. The cross-hatched distribution is the SM background, and the hatched distribution is the combinatorial background from OS-DF leptons.

The invariant mass spectrum of the two leptons is shown in Figure 20-88. For an integrated luminosity of $30\ \text{fb}^{-1}$ the expected SM background is about 400 events for 7500 SUSY events. The SUSY combinatorial background can be subtracted using the distribution of OS different flavour (DF) events, shown as a hatched histogram in the plot. The edge can be measured as $(109 \pm 0.30(\text{stat.}) \pm 0.11(\text{syst.}))\ \text{GeV}$, where the systematic error is given by the lepton energy scale.

The direct reconstruction of $\tilde{\chi}_1^0 \to qqq$ decays is problematic for two main reasons. First there is a high jet multiplicity, produced both from squark and gluino decays and from the presence of two $\tilde{\chi}_1^0 \to qqq$ decays in each event. Second, the $\tilde{\chi}_1^0$ mass is typically rather small over most of the accessible SUGRA parameter space – 122 GeV for Point 5. As an example, the softest jet from the harder (softer) $\tilde{\chi}_1^0$ has an average p_T of 35 (21) GeV. It is therefore necessary to keep a very low jet threshold in the analysis, thus increasing the probability of picking up a wrong jet from the underlying event.

The first step in the reconstruction is aimed at minimising the contribution from additional jets in the event. The high cross-section process with lowest jet multiplicity is $\tilde{q}_R\tilde{q}_L$ production, followed by the decays $q_R \to \tilde{\chi}_1^0 q$ and $q_L \to \tilde{\chi}_2^0 q$, with the $\tilde{\chi}_2^0$ decaying via $\tilde{\chi}_2^0 \to \tilde{l}_R^{\pm} l^{\mp} \to \tilde{\chi}_1^0 l^+ l^-$. The cuts used to select this process while minimising the QCD background were:

- one or two leptons with $p_T > 20$ GeV. If two, they should be OS-SF with $m_{ll} < 109$ GeV;
- at least eight jets with $p_T > 17.5$ GeV;
- no additional jets and no *b*-jets with $p_T > 25$ GeV;
- two central jets with $|\eta| < 2$, and $p_T^{jet1} > 200$ GeV, $p_T^{jet2} > 100$ GeV;
- $m_{T,\,cent} > 1000$ GeV;
- transverse sphericity > 0.2, thrust > 0.9.

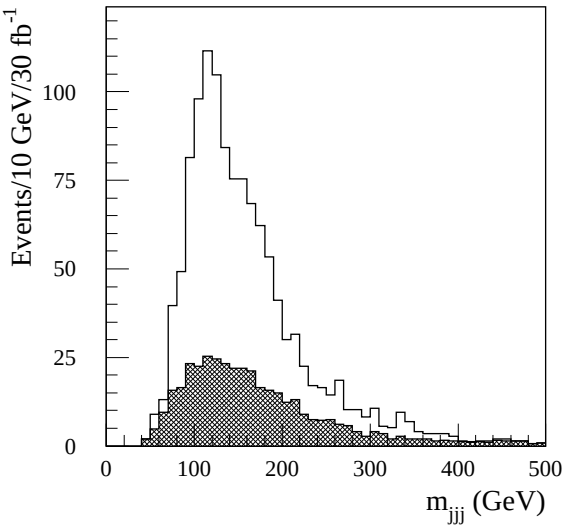

Figure 20-89 Distribution of the invariant mass for all 3-jet combinations passing the selection cuts described in the text for an integrated luminosity of 30 fb^{-1}. The cross-hatched distribution shows the SM background. The nominal value of $m_{\tilde{\chi}_1^0}$ is 122 GeV.

Pairs of three-jet combinations were then built from the jets in the event excluding the two leading ones. A series of cuts on the angular distance and on the transverse momentum of the jets was then applied, reducing the average number of combinations per event to 4.6. A given pairing of the six jets, $j_1 j_2 j_3$ and $j_4 j_5 j_6$, in order to be accepted was required to fulfil:

$$\Delta m_{jjj} = \left| m_{j_1 j_2 j_3} - m_{j_4 j_5 j_6} \right| < 20 \text{ GeV}.$$

In case more than one combination satisfied the requirement, the one with minimum Δm_{jjj} was retained. The resulting mass distribution is shown in Figure 20-89 superimposed to the QCD background for an integrated luminosity of 30 fb^{-1}. A very broad peak can be seen at the position corresponding to the $\tilde{\chi}_1^0$ mass, which corresponds also to the maximum of the QCD background. By using the Monte Carlo information, an efficiency of approximately 80% was found for reconstructing at least one $\tilde{\chi}_1^0$ correctly, and 25% for both.

In the second analysis, all unique pairs of masses passing the above cut were histogrammed, and the combinatorial background under the peak was estimated from the mass of all the neutralino candidates for which

$$\Delta m_{jjj} > 20 \text{ GeV}.$$

The upper plots in Figure 20-90 show the distribution of all neutralino candidates, and those in background sample, which is normalised in the region away from the peak, and the signal after background subtraction, for Point 5. The resulting signal peak has a fitted mean of 113 GeV, with a width of 15 GeV, 9 GeV below the true neutralino mass. This shift is due to the loss of energy from the cone used to define the jets, which is estimated in Section 9.1.2 to be approximately 10% at low p_T. Further work is in progress to optimise the mass estimate and resolution.

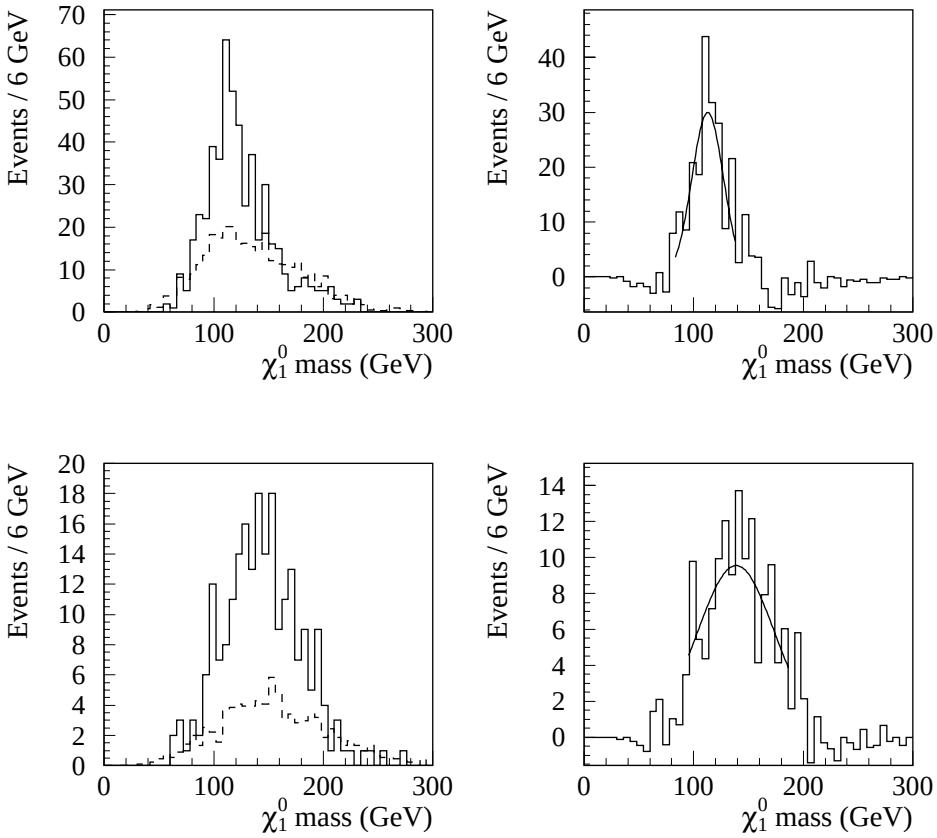

Figure 20-90 Distribution of three-jet combinations invariant masses obtained for $m_{\tilde{\chi}_1^0}$=122 GeV (upper plots) $m_{\tilde{\chi}_1^0}$=168 GeV (lower plots). The left hand plots show the $\tilde{\chi}_1^0$ candidates (solid histogram) and the combinatorial background (dashed histogram), while the left hand plots show the signal after background subtraction. The superimposed fit is to guide the eye to the peak.

The sensitivity of the peak position to the $\tilde{\chi}_1^0$ mass was studied generating a second event sample for SUGRA Point 1 with a $\tilde{\chi}_1^0$ mass of 168 GeV. The m_{jjj} distributions for this point, before and after background subtraction, are shown in Figure 20-90. The statistical precision is less as the cross-section is smaller. The fitted mass is $(140 \pm 4.2(\text{stat.}))$ GeV, compared to 151 GeV expected after energy loss from the jet cones. The shift is due to a small bias introduced by the cuts, which were optimised for Point 5. A data set with looser cuts is in production to study this effect.

From the fit to the background subtracted mass peak, the $\tilde{\chi}_1^0$ mass is expected to be measured with a statistical error of $\pm$ 3.1 GeV. The systematic uncertainties are similar to the ones studied for the top mass reconstruction in Chapter 18, with the difference that in this case the jet combinatorial is higher, the W mass constraint absent, and the $\tilde{\chi}_1^0$ is lighter than the top. The large available statistics of top events will allow a detailed study with of the systematic effects inherent in multijet mass reconstruction.

From the reconstructed $\tilde{\chi}_1^0$, using the decay chain $\tilde{\chi}_2^0 \rightarrow \tilde{l}_R^{\pm} l^{\mp} \rightarrow \tilde{\chi}_1^0 l^+ l^-$, the $\tilde{l}_R$ and $\tilde{\chi}_2^0$ peaks can be reconstructed. Events were selected by requiring:

- two reconstructed $\tilde{\chi}_1^0$ in a window 20 GeV wide centred on the fitted $\tilde{\chi}_1^0$ mass;

- two opposite sign, same flavour leptons with $p_T^{l1} > 15$ GeV, $p_T^{l2} > 10$ GeV, and $m_{ll} < 109$ GeV.

The momenta of the three jets were rescaled using the constraint of the measured $\tilde{\chi}_1^0$ mass.

Since the events used for the $\tilde{\chi}_1^0$ mass reconstruction were explicitly selected to enhance the contribution of $\tilde{q}_R\tilde{q}_L$ production, the hardest $\tilde{\chi}_1^0$ was assumed to come from the decay $q_R \to \tilde{\chi}_1^0 q$. Therefore, the $\tilde{l}_R$ mass was reconstructed by calculating the invariant mass of the softer $\tilde{\chi}_1^0$ with both leptons in the event. The distribution of the lower of these two masses is shown in Figure 20-91, for an integrated luminosity of 30 fb^{-1}. The statistics are rather low as the plot includes 119 events, but a clear peak at the nominal $\tilde{l}_R$ mass (157 GeV) is visible. The statistical uncertainty on the slepton mass was estimated to be ±5.1 GeV by comparing the observed peak with the peaks obtained varying the slepton mass by ±10 GeV.

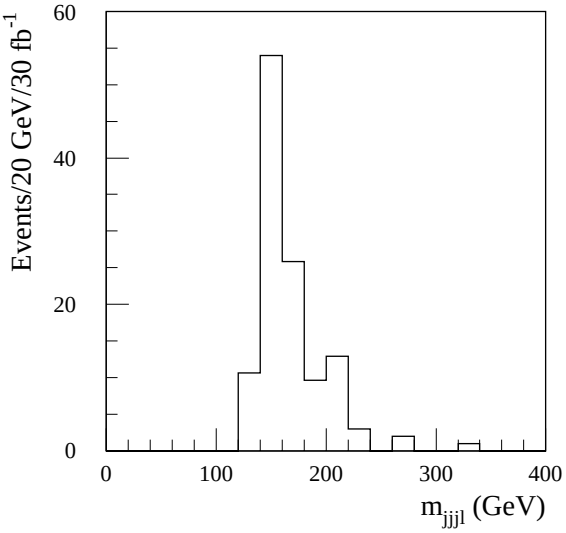

Figure 20-91 Distribution of the smaller invariant mass of the softer $\tilde{\chi}_1^0$ candidate with a lepton in the event. The distribution is peaked around the nominal $\tilde{l}_R$ mass of 157 GeV.

The $\tilde{\chi}_2^0$ is reconstructed by combining both sleptons with the softer $\tilde{\chi}_1^0$, after applying a cut around the $\tilde{l}_R$ peak. The resulting distribution (Figure 20-92) shows a peak at the nominal $\tilde{\chi}_2^0$ mass of 233 GeV. Within the statistical uncertainty, the peak position follows the $\tilde{\chi}_2^0$ mass, as

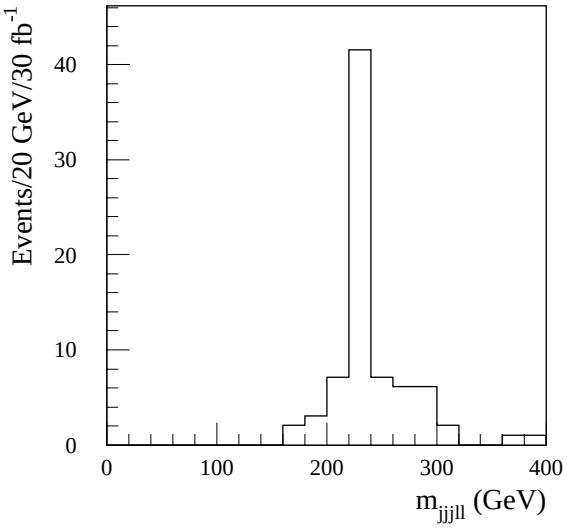

Figure 20-92 Distribution of the invariant mass of the softer $\tilde{\chi}_1^0$ with the two leptons in the event. The distribution is peaked around the nominal $\tilde{\chi}_2^0$ mass of 233 GeV.

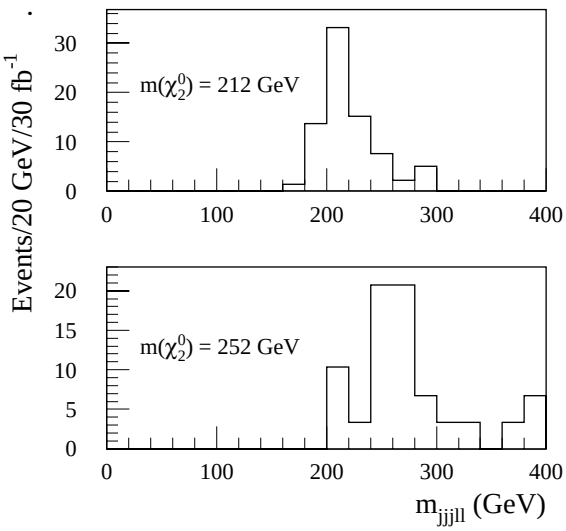

Figure 20-93 Distributions of the invariant mass off the softer $\tilde{\chi}_1^0$ with the two leptons in the event for two different values of the $\tilde{\chi}_2^0$ mass: 212 GeV (top plot) and 252 GeV (bottom plot).

shown in Figure 20-93, where the distributions for $\tilde{\chi}_2^0$ masses varied by ±20 GeV with respect to the nominal one are shown (top and bottom plot). From these distributions, the $\tilde{\chi}_2^0$ mass was measured to be $(233 \pm 4.1(\text{stat.}) \pm 2.3(\text{syst.}))$ GeV.

This same event sample can in principle be used for the direct reconstruction of both $\tilde{q}_R$ and $\tilde{q}_L$, by combining the hard jets in the event with the reconstructed $\tilde{\chi}_1^0$ and $\tilde{\chi}_2^0$ respectively. In practice, the number of fully reconstructed $\tilde{\chi}_2^0$ is too small to allow a meaningful $\tilde{q}_L$ reconstruction to be made. Therefore the analysis was focused on the reconstruction of the decay $q_R \to \tilde{\chi}_1^0 q$. The events were selected by requiring two reconstructed $\tilde{\chi}_1^0$ within 30 GeV of the measured $\tilde{\chi}_1^0$ mass, and a p_T of the leading jet larger than 300 GeV, in order to further enhance the fraction of $\tilde{q}_R$ decays in the sample. After these cuts 50% of the events contain a $\tilde{q}_R$.

The choice of the correct jet-$\tilde{\chi}_1^0$ combination was performed in two steps. First each of the two leading jets was combined with the softer $\tilde{\chi}_1^0$ and the leptons in the event, and the combination giving the lower mass was retained as the $\tilde{q}_L$. The remaining hard jet was then combined with the harder $\tilde{\chi}_1^0$. The invariant mass spectrum, shown in Figure 20-94, has a broad peak around 660 GeV, the nominal $\tilde{q}_R$ mass. By varying the $\tilde{q}_R$ mass, it was verified that the peak position does follow the $\tilde{q}_R$ mass, while it is insensitive to the value of the $\tilde{q}_L$ mass. From the invariant mass distribution, the squark mass is measured to be $(664 \pm 30(\text{stat.}) \pm 7(\text{syst.}))$ GeV.

The reconstruction of the $h \to b\bar{b}$ peak was straightforward at Point 1 and Point 5 for *R*-parity conserving models. In that case the Standard Model background was efficiently rejected by the $E_{\text{T}}^{\text{miss}}$ requirement. In the *B*-violating case, the $E_{\text{T}}^{\text{miss}}$ cannot be used, and the combined requirement of one lepton and two *b*-jets causes an unacceptable loss of statistics. Moreover, for the considered $\tilde{\chi}_1^0$ decay, which involves a *c*-quark, the SUSY background would also be big for realistic values of the probability to misidentify a *c*-jet for a *b*-jet. An explicit attempt at reconstruction shows that at Point 5 it is not possible to extract a significant $h \to b\bar{b}$ peak.

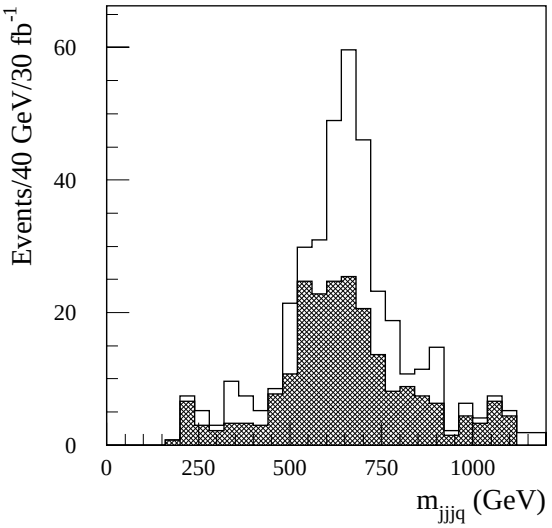

Figure 20-94 Invariant mass of the harder $\tilde{\chi}_1^0$ with the leading jet in the event. The cross-hatched distribution is for events which do not contain a $\tilde{q}_R$. The nominal $\tilde{q}_R$ mass is 660 GeV.

The SUSY events with abundant production of Higgs bosons in $\tilde{\chi}_2^0$ decays would anyway contain a large number of *b*-quarks from *h* decay, and the observed *b*-jet rate can be used to constrain the sign of μ.

All the analyses described above are valid only for SUGRA Point 5. The reconstruction of $\tilde{\chi}_1^0$ was attempted also for the other SUGRA points. At Points 1 and 2, the sparticles are heavier, so the production cross-section is lower. As shown above, applying the same reconstruction method as for Point 5 gave a peak in the three-jet invariant mass for the signal. The QCD background is 30% higher than the signal, thus rendering the detection of the three-jet peak more difficult. On the other hand, the higher energy of the jets from the $\tilde{\chi}_1^0$ decay as compared to Point 5 enhances the fraction of events in which the three jets can be reconstructed. A more detailed study based on the optimisation of the cuts for Points 1 and 2 is needed to assess the achievable precision of the $\tilde{\chi}_1^0$ mass measurement. At Point 3, the high production cross-section guarantees the discovery of SUSY, but the low $\tilde{\chi}_1^0$ mass (44 GeV) renders the direct reconstruction of the $\tilde{\chi}_1^0$

from hadronic jets impossible. At Point 4, the mass of the $\tilde{\chi}_1^0$ is 80 GeV, and the most promising channel is the electroweak production of chargino-neutralino pairs, which has a cross-section of 3.5 pb, followed by purely leptonic decays of the two gauginos, which gives final states with no jets from sparticle decays, except the ones from the two $\tilde{\chi}_1^0$. A detailed study is in progress to verify if the $\tilde{\chi}_1^0$ can be reconstructed in this case.

20.4.1.3 Constraints on the SUGRA parameters

The basic difference with respect to *R*-parity conserving SUSY is the possibility of direct mass measurements, albeit with very low statistics and limited precision. The studies performed up to now were based on a naive use of the standard jet algorithms. With these algorithms, a convincing reconstruction of the $\tilde{\chi}_1^0$, and subsequently of the particles decaying into it, seems possible only in the cases where the SUSY mass scale is low enough to guarantee a high production cross-section, and the $\tilde{\chi}_1^0$ is heavy enough to decay into an identifiable three-jet configuration. These conclusions could be modified by more detailed studies of jet reconstruction. On the other hand, the much increased jet multiplicity renders more difficult the extraction of signatures such as the $h \to b\bar{b}$ peak from the $\tilde{\chi}_2^0$ decay. Therefore the value of tan β, which is constrained by the Higgs mass measurement, would be accessible only if the direct production of the Higgs boson, *e.g.* in the $h \to \gamma\gamma$ channel, could be performed.

In conclusion, for *B*-violating SUGRA at Point 5, which was studied in detail, the parameters of the model should be constrained with a precision approximately equivalent, or somewhat better, to the one found in the *R*-conserving case except for tanβ, which requires a measurement outside SUSY final states.

20.4.2 Lepton number violation: $\chi_1^0 \to l^+ l \nu$

For this class of models, both $\tilde{\chi}_1^0$ in each event decay into three leptons, of which at least two are of different flavours since the λ_{ijk} couplings are antisymmetric. One lepton is neutral, and the other two have opposite charges, since the LSP is supposed to be neutral. The two charged leptons can either have the same flavour or different flavours. The relative weight of the two configurations is a function of the neutralino mixing matrix. For the studies presented here [20-43], the $\tilde{\chi}_1^0$ decay branching fractions are implemented in the simulation using the program described in [20-44]. This results in a dramatic increase in the number of leptons in the final state, and in the presence of a certain amount of $E_{\mathrm{T}}^{\mathrm{miss}}$. The standard model background is exceedingly small. In case one of the three subscripts of the λ_{ijk} takes the value three, one of the leptons is of the third generation, thus reducing the number of 'stable' leptons in the final state. In particular, if the *k* subscript takes the value three, all the events contain two τ's. In these cases the electron and muon multiplicity is significantly reduced, and there is a moderate increase of the $E_{\mathrm{T}}^{\mathrm{miss}}$.

20.4.2.1 Inclusive signatures

The high number of leptons in the final state renders the extraction of the SUSY signal from the Standard Model background very easy. The following selection criteria are sufficient to reduce the Standard Model background to a negligible level:

- at least three leptons with $p_{\mathrm{T}} > 20$ GeV (lepton = e, μ);

- $E_{\mathrm{T}}^{\mathrm{miss}} > 100\ \mathrm{GeV}$;
- $p_{\mathrm{T}} > 70\ \mathrm{GeV}$ for the leading lepton.

In order to study the reach of these selection criteria in the SUGRA parameter space, 1000 events were generated for each point in the $m_0 - m_{1/2}$ plane. The remaining parameters of the models were set to the values: tanβ=2, A=0, μ positive. The reach is conventionally expressed as the region in parameter space for which $S/\sqrt{B} > 5$, with S number of signal events and B number of background events after the cuts. The reach in the $m_0 - m_{1/2}$ plane for an integrated luminosity of $10\mathrm{fb}^{-1}$ is shown in Figure 20-95. The black squares represent the points for which $S/\sqrt{B} > 5$, and the white squares the points for which, due to the low statistics generated, the sensitivity could not be calculated.

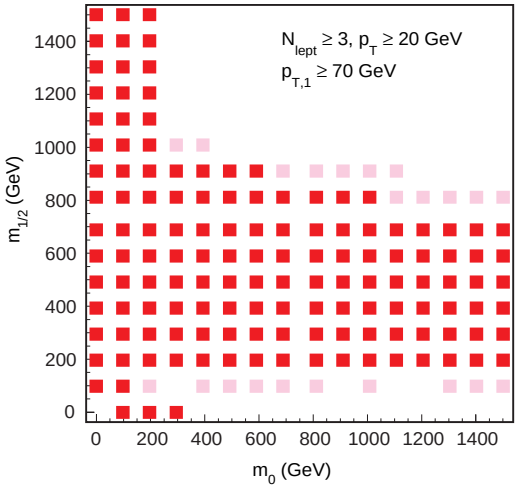

Figure 20-95 Reach in the $m_0 - m_{1/2}$ plane for a model with $\lambda_{123} = 10^{-3}$ for an integrated luminosity of $10\ \mathrm{fb}^{-1}$.

The mass scale of the SUSY events can be studied using a variable similar to the M_{eff} variable defined for the R-parity conserving case, modified to take into account the $\tilde{\chi}_1^0$ decay products:

$$M_{\mathrm{eff}} = \sum_{i=1}^{4} p_{\mathrm{T},i}^{jet} + \sum_{i=1}^{4} p_{\mathrm{T},i}^{lept} + E_{\mathrm{T}}^{\mathrm{miss}} .$$

10000 events were generated at 30 random points in the parameter space. For each of these points the correlation between the maximum of the M_{eff} distribution and M_{SUGRA} is shown in Figure 20-96, where M_{SUGRA} is defined as.

$$M_{\mathrm{SUGRA}} = \min(M_{\tilde{g}}, M_{\tilde{q}_R}, M_{\tilde{b}_1}, M_{\tilde{t}_1}) .$$

A good correlation is observed, with a ratio of approximately two.

A fundamental parameter for R-parity violating models is the strength of the different couplings λ_{ijk}. For the decay $\tilde{\chi}_1^0 \to l^+ l^- \nu$ the study of the lepton universality violation in the final state should give a hint on which coupling is dominant. To illustrate this, a study was performed for SUGRA Points 1, 3 and 5 and for two dominant couplings: λ_{122} and λ_{123}. For all three points, the number of events with zero electrons and four muons was compared

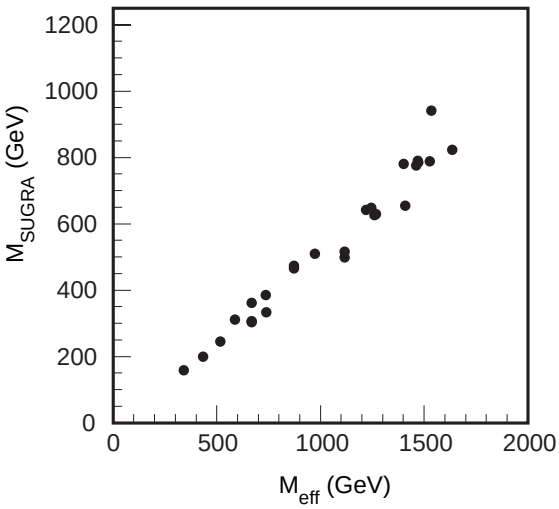

Figure 20-96 Correlation of the maximum of the M_{eff} distribution and M_{SUGRA} for 30 points in the SUGRA parameter space.

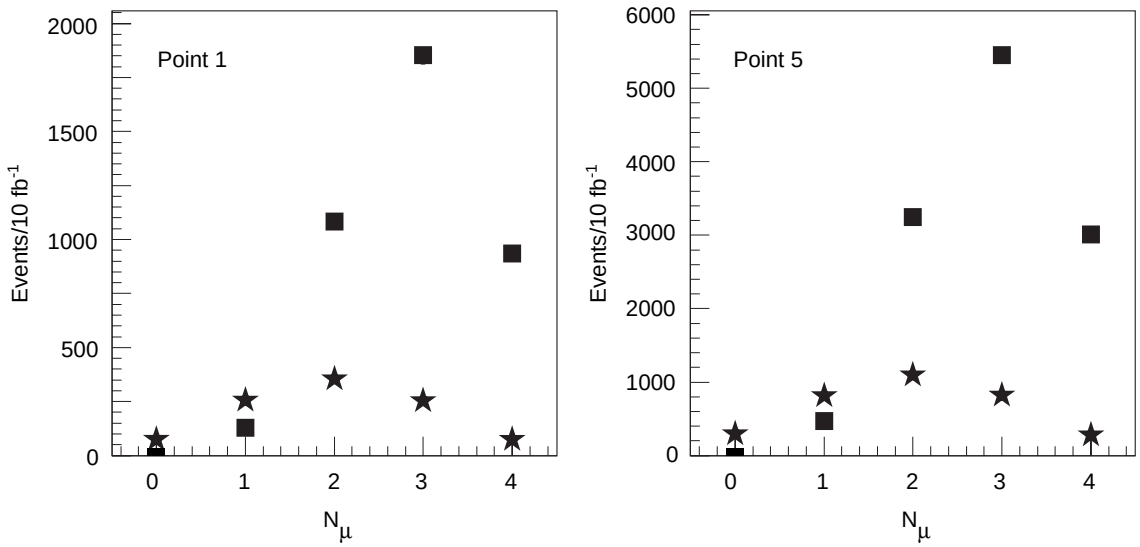

Figure 20-97 Distributions of the number of muons per event if the sum of the number of electrons and muons is equal to four, for two different active couplings for SUGRA Points 1, and 5. The full boxes are for $\lambda_{122} \neq 0$ and the stars for $\lambda_{123} \neq 0$.

to the number of events containing four electrons and zero muons. For $\lambda_{122} \neq 0$ the four-μ events dominate the four-electron events by roughly a factor of ten, whereas for $\lambda_{123} \neq 0$ the two topologies have approximately the same weight, and the overall statistics of four-lepton events is a factor between two and five lower than in the previous case. This is as expected from the index three in the coupling, which produces the decay of the $\tilde{\chi}_1^0$ into τ leptons. The pattern can be observed in Figure 20-97 where the number of muons per event is plotted for Points 1 and 5 for two dominant couplings. Only the events for which the sum of the number of electrons and muons is equal to four enter the plot.

20.4.2.2 Precision measurements

The study of detailed signatures was performed for three SUGRA Points: 1, 5, and 3, corresponding respectively to a high, medium and low mass scale. As already discussed in detail in the *R*-parity conserving sections, Points 1 and 5 both have a $h \rightarrow b\bar{b}$ signature. In addition Point 5 has also a lepton-based signature from slepton decay. Point 3 is interesting in this context because the abundant lepton production from $\tilde{\chi}_2^0$ decays can give a combinatorial background to the $\tilde{\chi}_1^0$ direct reconstruction.

Models with two different dominant *R*-violating couplings were studied: $\lambda_{122} \neq 0$ and $\lambda_{123} \neq 0$. In the first case, each $\tilde{\chi}_1^0$ decay contains two electrons or muons. For the $\lambda_{123} \neq 0$ coupling, each $\tilde{\chi}_1^0$ decay contains a τ lepton.

20.4.2.3 Points 1 and 5: $\lambda_{122} \neq 0$

The decay of the $\tilde{\chi}_1^0$ is in this case $\tilde{\chi}_1^0 \rightarrow \nu_{e(\mu)} + \mu^{\pm}(e^{\pm}) + \mu^{\mp}$. Each event contains at least four leptons. The signature for the $\tilde{\chi}_1^0$ decay is either a pair of Opposite Sign-Same Flavour leptons (OS-SF) or a pair of Opposite Sign-Different Flavour (OS-DF) leptons, with the relative ratio of the two modes determined by the neutralino mixing matrix.

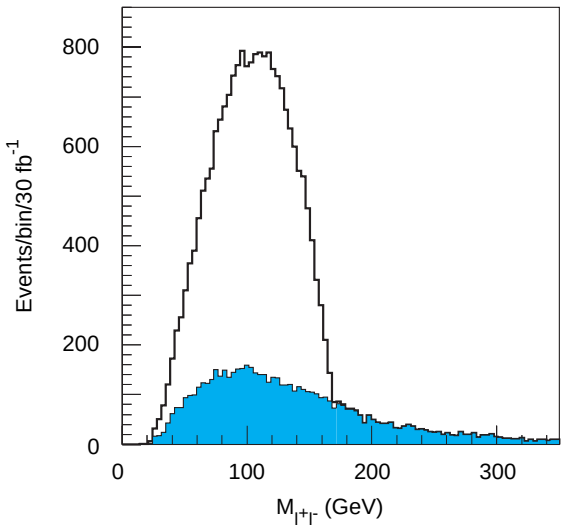

Figure 20-98 Invariant mass distribution for OS-DF lepton pairs at Point 1, for $\lambda_{122} \neq 0$ and for an integrated luminosity of 30 fb^{-1}. The combinatorial background is shown as a shaded histogram.

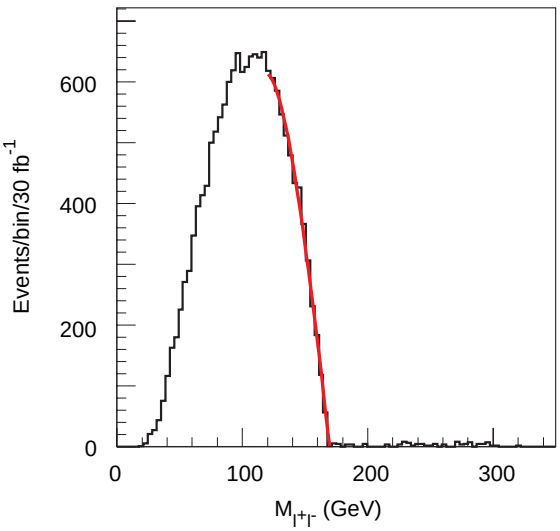

Figure 20-99 Same distribution as for Figure 20-98, after background subtraction. The polynomial fit to the end point is shown.

The events were selected by requiring:

- at least four leptons with $p_{\mathrm{T}} > 10$ GeV;
- $\cos\alpha_{ll'} \geq 0.5$, where $\alpha_{ll'}$ is the angle between any OS-DF lepton pair;
- $E_{\mathrm{T}}^{\mathrm{miss}} > 50$ GeV.

At Point 1 the production of lepton pairs is dominated by the $\tilde{\chi}_1^0$ decays. At Point 5 there is a significant contribution from the decay $\tilde{\chi}_2^0 \to \tilde{l}_R^{\pm} l^{\mp} \to \tilde{\chi}_1^0 l^+ l^-$, which produces OS-SF lepton pairs. Therefore an additional cut: $N_l^+ = N_l^-$ and $N_e = N_\mu$ was added for Point 5 to reduce the importance of this background.

The distribution of the invariant mass for the OS-DF lepton pairs after the above cuts is shown in Figure 20-98 for Point 1. There is a clear edge structure superimposed on the combinatorial background. After subtraction of the background parametrised with a Maxwellian function, the $\tilde{\chi}_1^0$ mass can be measured by fitting the resulting distribution near the end point with a polynomial function, as shown in Figure 20-99. The resulting values are: $m_{\tilde{\chi}_1^0} = (169.8 \pm 0.18)$ GeV for Point 1 and $m_{\tilde{\chi}_1^0} = (122.62 \pm 0.35)$ GeV for Point 5, where the error is the quadratic sum of the statistical error from the fit to the end point and of the 0.1% uncertainty in the lepton energy scale.

In the following, a reconstructed $\tilde{\chi}_1^0$ is defined as an OS-DF lepton pair with an invariant mass in the interval $(m_{\tilde{\chi}_1^0} - \Delta m_{\tilde{\chi}_1^0}, m_{\tilde{\chi}_1^0})$, where $m_{\tilde{\chi}_1^0}$ is the measured end point, and $\Delta m_{\tilde{\chi}_1^0}$ is 50 GeV for Point 1 and 30 GeV for Point 5.

To reconstruct the $h \to b\bar{b}$ peak from the decay $\tilde{\chi}_2^0 \to h\tilde{\chi}_1^0$ two additional requirements were applied:

- at least two b-jets with $p_{\mathrm{T}} > 30(40)$ GeV for Point 1 (Point 5) and $p_{\mathrm{T}} < 300$ GeV;
- $\cos\alpha_{bb} > 0.4(0.3)$ for Point 1 (Point 5), with α_{bb} the angle between the two b-jets.

The invariant mass distribution of the $b\bar{b}$ pairs is shown in Figure 20-100 for Point 1. The background is only from SUSY combinatorial, and it is larger than in the *R*-parity conserving case. This is due to the increase of the background from decays of third-generation squarks, which was suppressed by the lepton veto in the *R*-parity conserving case.

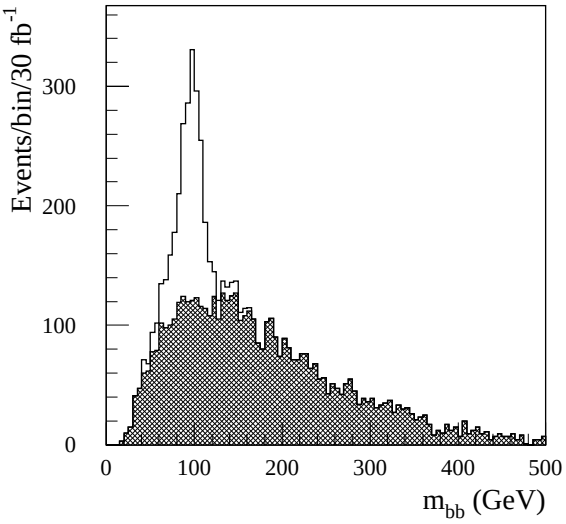

Figure 20-100 Invariant mass of $b\bar{b}$ pairs at Point 1 ($\lambda_{122} \neq 0$) for an integrated luminosity of $30\ \mathrm{fb}^{-1}$. The full line histogram is the signal+background, the hatched is the SUSY combinatorial background.

The reconstructed *h* peak was then combined with a reconstructed $\tilde{\chi}_1^0$ to form the $\tilde{\chi}_2^0$ mass. For this purpose the events were required to contain at least one reconstructed $\tilde{\chi}_1^0$, and a $b\bar{b}$ pair within ±15 GeV of the measured *h* mass. The angle α between the *h* and the $\tilde{\chi}_1^0$ candidates was required to satisfy the condition: $\cos\alpha > 0.7 (0.5)$ for Point 1 (Point 5).

A harder angular cut was applied at Point 1, as the $\tilde{\chi}_1^0$ and the *h* are expected to have a higher boost. The reconstructed $\tilde{\chi}_2^0$ mass is shown in Figures 20-101 and 20-102 for Points 1 and 5 respectively. From a fit to the peak, the following measurements were obtained: $m_{\tilde{\chi}_2^0} = (326.2 \pm 4.8)$ GeV for Point 1 and $m_{\tilde{\chi}_2^0} = (230.7 \pm 2.7)$ GeV for Point 5.

The $\tilde{q}_L$ has a branching fraction of 60% into $q\chi_1^+$ for both Points 1 and 5. The χ_1^+ in turn decays with 100% branching ratio to $W\tilde{\chi}_1^0$. This decay can be fully reconstructed by identifying the $q\bar{q}$ decay of the *W*. In events with a reconstructed $\tilde{\chi}_1^0$, light quark pairs were selected according to the following requirements:

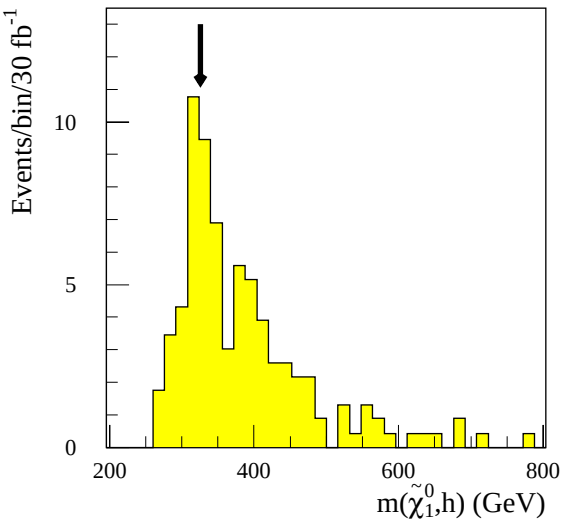

Figure 20-101 Invariant mass of a Higgs candidate with a $\tilde{\chi}_1^0$ for Point 1 ($\lambda_{122} \neq 0$) and an integrated luminosity of $30\ \mathrm{fb}^{-1}$. The distribution shows a peak at the expected position of the $\tilde{\chi}_2^0$ mass (326 GeV).

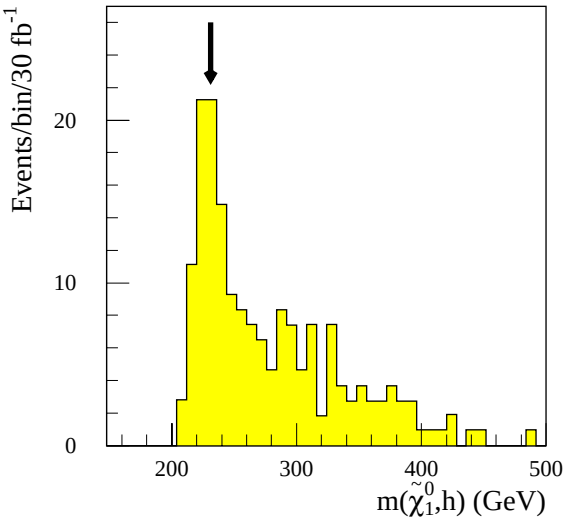

Figure 20-102 Invariant mass of a Higgs candidate with a $\tilde{\chi}_1^0$ for Point 5 ($\lambda_{122} \neq 0$) and an integrated luminosity of $30\ \mathrm{fb}^{-1}$. The distribution shows a peak at the expected position of the $\tilde{\chi}_2^0$ mass (233 GeV).

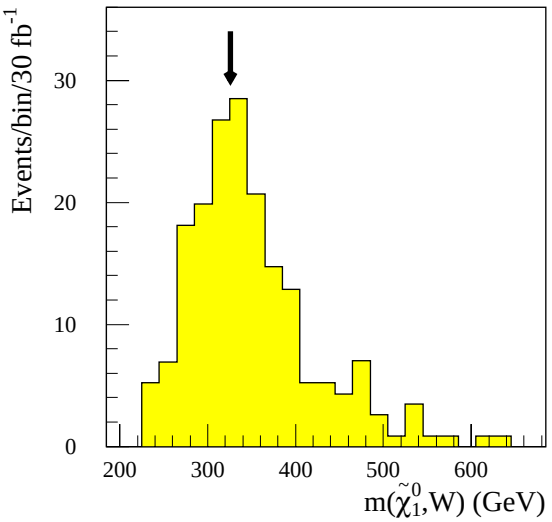

Figure 20-103 Invariant mass of a $W \to qq$ candidate with a $\tilde{\chi}_1^0$ candidate for Point 1 ($\lambda_{122} \neq 0$) and an integrated luminosity of $30\ \mathrm{fb}^{-1}$. The distribution shows a peak at the expected position of the $\tilde{\chi}_1^+$ mass (326 GeV).

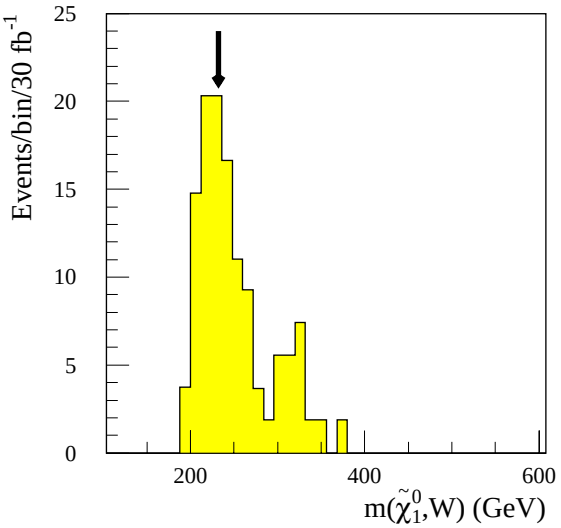

Figure 20-104 Invariant mass of a $W \to qq$ candidate with a $\tilde{\chi}_1^0$ candidate for Point 5 ($\lambda_{122} \neq 0$) and an integrated luminosity of $30\ \mathrm{fb}^{-1}$. The distribution shows a peak at the expected position of the $\tilde{\chi}_1^+$ mass (232 GeV).

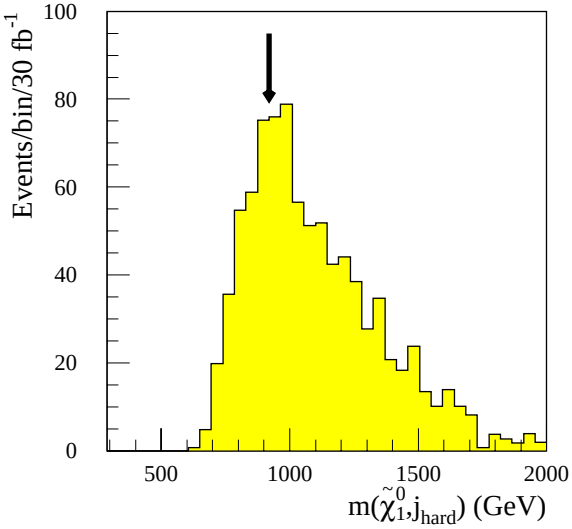

Figure 20-105 Invariant mass of $\tilde{\chi}_1^0$ with a hard jet in Point 1 ($\lambda_{122} \neq 0$) for an integrated luminosity of $30\ \mathrm{fb}^{-1}$. The expected positions of the mass of the right handed squark is shown.

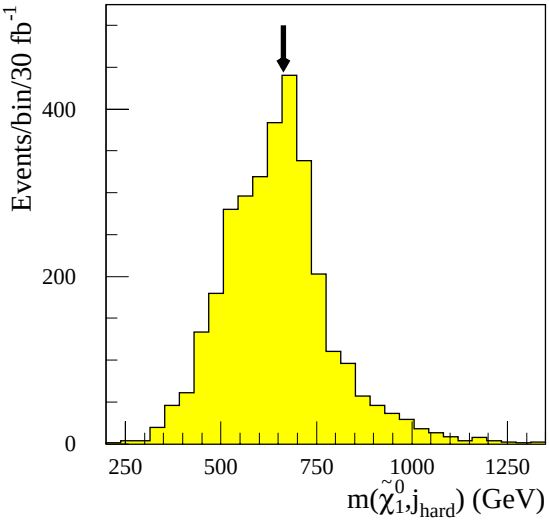

Figure 20-106 Invariant mass of $\tilde{\chi}_1^0$ with a hard jet in Point 5 ($\lambda_{122} \neq 0$) for an integrated luminosity of $30\ \mathrm{fb}^{-1}$. The expected positions of the masses of the right handed squark is shown.

- $p_T^{j1} > 100$ GeV and $p_T^{j2} < 600\ (350)$ GeV for Point 1 (Point 5);
- $\cos\alpha_{jj} > 0.9\ (0.8)$ for Point 1 (Point 5).

The invariant mass distribution of the two selected jets shows a clear peak around the W mass over a large combinatorial background. The W was selected by requiring an invariant mass within 15 GeV of the nominal W mass. The W candidate was then combined with the $\tilde{\chi}_1^0$ if the angle α between them satisfied the requirement $\cos\alpha > 0.85$. The resulting invariant mass is

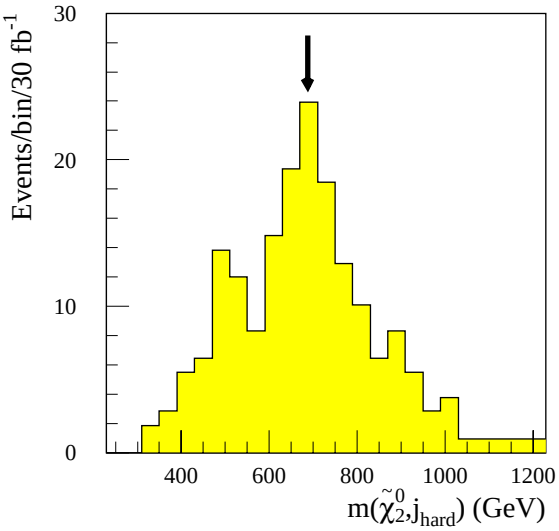

Figure 20-107 Invariant mass of a $\tilde{\chi}_2^0$ candidate with a hard jet at Point 5 ($\lambda_{122} \neq 0$). The position of the expected peak for the $\tilde{q}_L$ is shown.

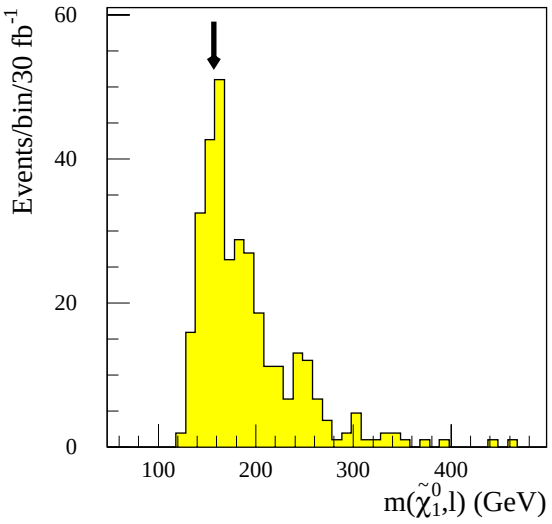

Figure 20-108 Invariant mass of the $\tilde{\chi}_1^0$ with a lepton at Point 5 ($\lambda_{122} \neq 0$). A peak at the expected position of the $\tilde{l}_R$ mass can be seen.

shown in Figures 20-103 and 20-104 for Points 1 and 5 respectively. A peak is visible at the value of the χ_1^+ mass, for both points. Due to the high combinatorial background under the selected W, the peak is very broad and the statistics is low. From the peak width and the number of events, an uncertainty on the χ_1^+ mass measurement of around 6 GeV for Point 1 and 4 GeV for Point 5 can be estimated.

Squark reconstruction can be attempted for $\tilde{q}_R$ by exploiting the decay $\tilde{q}_R \to q\tilde{\chi}_1^0$. Events were selected requiring at least one reconstructed $\tilde{\chi}_1^0$ and a hard jet. The hard jet was required not to give an invariant mass within 15 GeV of the Z or of the W mass combined with any other light jet in the event and to be in the same hemisphere as the $\tilde{\chi}_1^0$ candidate.

The invariant mass distributions are shown in figures Figures 20-105 and 20-106 for Points 1 and 5 respectively. The observed peaks are very broad, and suffer from contaminations from gluino and $\tilde{t}_1$ decays. In particular at Point 1 the $\tilde{q}_R$ mass is rather close to the gluino mass, and it is difficult to determine if the observed peak is actually due to $\tilde{q}_R$ decay. The situation looks clearer for Point 5, where the $\tilde{q}_R$ peak is clean, and has a good statistical significance. In order to extract a measurement from these distributions a detailed knowledge of the combinatorial background is necessary.

Given the low statistics of reconstructed $\tilde{\chi}_2^0$ (see Figures 20-101 and 20-102), the decay $\tilde{q}_L \to q\tilde{\chi}_2^0$ can only be reconstructed for Point 5. The events were required to include a reconstructed $\tilde{\chi}_2^0$ within 40 GeV of the measured $\tilde{\chi}_2^0$ peak, and a hard jet with $p_T > 100$ GeV which cannot be ascribed to a $W \to jj$ decay. The resulting invariant mass distribution is shown in Figure 20-107. The peak at the $\tilde{q}_L$ mass is clean and has a reasonable statistics, allowing the $\tilde{q}_L$ mass to be measured with a precision of about 15 GeV. The distribution presents an enhancement around 500 GeV, which, if statistically significant could be interpreted as a $\tilde{t}_1 \to \tilde{\chi}_2^0 t \to \tilde{\chi}_2^0 jjb$ decay where the three jets from the top decay are reconstructed as a single jet.

At Point 5 the right handed sleptons $\tilde{l}_R$ are produced in $\tilde{\chi}_2^0$ decays, and can be reconstructed from their dominant decay $\tilde{l}_R \to \tilde{\chi}_1^0 l$. Events were selected by requiring a $\tilde{\chi}_1^0$ candidate and an additional lepton. The lepton transverse momentum was required to be between 10 and

200 GeV, and the angle α between the $\tilde{\chi}_1^0$ and the lepton to satisfy the condition $\cos\alpha \geq 0.5$. The invariant mass distribution is shown in Figure 20-108. The peak is superimposed on a combinatorial background mainly coming from the decay chain $\tilde{\chi}_1^{\pm} \rightarrow \tilde{\chi}_1^0 W^{\pm} \rightarrow \tilde{\chi}_1^0 l^{\pm} \nu_l$. From a Gaussian fit to the peak the slepton mass is measured to be $m_{\tilde{l}_R} = (156.8 \pm 1.7)$ GeV.

20.4.2.4 Points 1 and 5: $\lambda_{123} \neq 0$

In this case there is always a τ lepton among the $\tilde{\chi}_1^0$ decay product. The clear OS-DF signature exploited for the case $\lambda_{122} \neq 0$ is therefore lost, and the direct reconstruction of the $\tilde{\chi}_1^0$ is very difficult. The aim of the analysis is in this case to check if the signatures studied in the *R*-parity conserving case are still valid.

At Point 5 the $\tilde{\chi}_2^0$ decay chain $\tilde{\chi}_2^0 \rightarrow \tilde{l}_R^{\pm} l^{\mp} \rightarrow \tilde{\chi}_1^0 l^+ l^-$ with the subsequent $\tilde{\chi}_1^0$ decay yields three leptons, among which an OS-SF and an OS-DF flavour pair can be formed. The lepton-lepton edge from the decay $\tilde{\chi}_2^0 \rightarrow \tilde{l}_R^{\pm} l^{\mp} \rightarrow \tilde{\chi}_1^0 l^+ l^-$ has a big combinatorial background from the additional leptons in the event. The events were selected in the same way as for the $\tilde{\chi}_1^0$ mass reconstruction, requiring the two OS-SF leptons to have $p_T > 15$ GeV, to be in the same hemisphere and to be unbalanced. The resulting invariant mass distribution of OS-SF lepton pairs is shown in Figure 20-109. An edge structure is visible above the combinatorial background. The precision with which this can be measured has not been investigated.

The OS-DF pairs with an invariant mass near the endpoint can be further combined with an OS lepton pair in the event, where one of the additional leptons comes from the $\tilde{\chi}_1^0$ decay, and the other one from the tau decay. If the mass of the OS-DF pair is rescaled to the value of the measured end point, the invariant mass distribution with the two additional leptons presents an edge which is sensitive the $\tilde{\chi}_2^0$ mass.

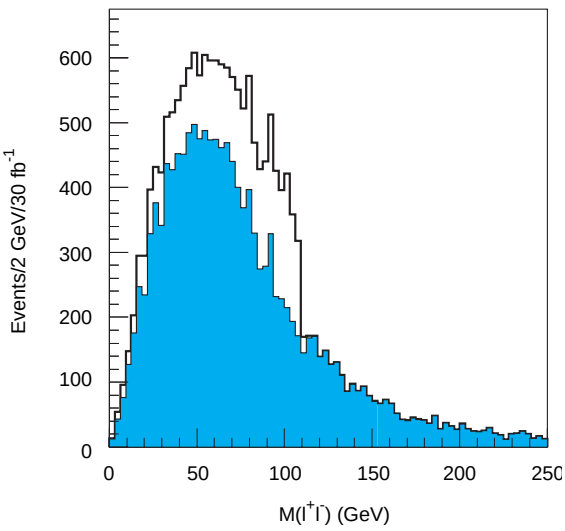

Figure 20-109 Invariant mass of OS-SF lepton pairs fat Point 5 ($\lambda_{123} \neq 0$) for an integrated luminosity of $30\ \mathrm{fb}^{-1}$. The full line histogram is signal+background and the shaded histogram the combinatorial background.

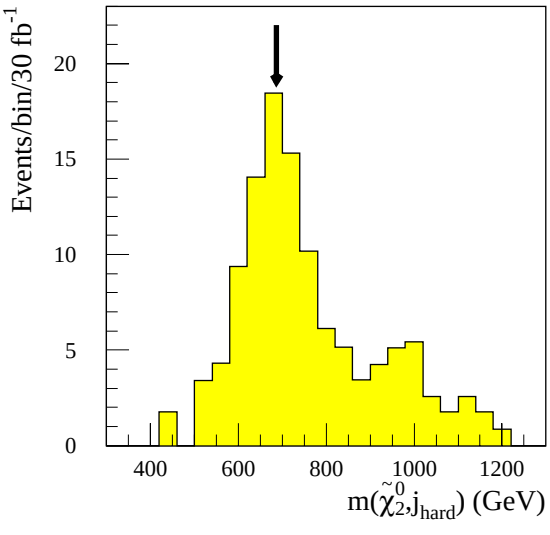

Figure 20-110 Invariant mass of the jet-$\tilde{\chi}_2^0$ combination as described in the text at Point 5 ($\lambda_{123} \neq 0$) for an integrated luminosity of $30\ \mathrm{fb}^{-1}$. The arrows shows the expected position of the $\tilde{q}_L$ mass.

By further combining the 4-lepton combinations with an invariant mass near the $\tilde{\chi}_2^0$ edge with a hard jet in the event, the distribution in Figure 20-110 is obtained which is peaked at the value of the $\tilde{q}_L$ mass.

20.4.2.5 Point 3: $\lambda_{122} \neq 0$

Point 3 has a much lower mass scale than the other points, and therefore a huge production cross-section. The dominant decay of the $\tilde{\chi}_2^0$ is the three-body decay $\chi_2^0 \to f\bar{f}\chi_1^0$, where f are ordinary fermions, yielding a large number of OS-SF lepton pairs in the final state. The $\tilde{\chi}_1^0$ decays $\tilde{\chi}_1^0 \to \nu_{e(\mu)} + \mu^{\pm}(e^{\pm}) + \mu^{\mp}$ yield both OS-DF and OS-SF pairs, with relative branching fractions 'a priori' different from those at point 5. There is a large violation of electron-muon universality in this case; the consequences of this have not been studied. The $\tilde{\chi}_1^0$ reconstruction is e performed by calculating the invariant mass of OS-DF pairs which have a lower background. Events were selected requiring at least four leptons with $p_T > 10$ GeV in the final state, and an E_T^{miss} greater than 50 GeV. The angle α_{ll} between the two leptons was required to satisfy the condition $\cos\alpha_{ll} \geq 0.85$.

The invariant mass distribution of the lepton pairs is shown in Figure 20-111 for an integrated luminosity of 10 fb^{-1}. The background is higher than in Point 5, and is mostly produced by the decays of $\tilde{t}_1$ and $\tilde{b}_1$ to charginos. The statistics is high, and the $\tilde{\chi}_1^0$ mass can be measured as $m_{\tilde{\chi}_1^0} = (44.8 \pm 0.1)$ GeV from a fit to the end point of the distribution after background subtraction. The quoted error includes the statistical error on the fit and a 0.1% uncertainty on the lepton energy scale. A detailed study on the modelling of the background is still needed in order to confirm that this precision is indeed achievable.

For the following steps in the reconstruction of the SUSY decay chains, a reconstructed $\tilde{\chi}_1^0$ is defined as an OS-DF lepton pair with invariant mass smaller than and within 10 GeV of the endpoint. The momenta of the two leptons are scaled up to the measured $\tilde{\chi}_1^0$ mass.

Information on the $\tilde{\chi}_2^0$ mass can be extracted using additional opposite-sign leptons in events with at least one reconstructed $\tilde{\chi}_1^0$. The invariant mass of the lepton pairs has a complex structure, with two edges superimposed: one at 45 GeV, and one at 42 GeV, corresponding to $m_{\tilde{\chi}_1^0}$ and $m_{\tilde{\chi}_2^0} - m_{\tilde{\chi}_1^0}$ respectively. The distribution is shown in Figure 20-112, where the full histogram shows the sum of the $\tilde{\chi}_1^0 \to l^+l^-\nu$ and of the $\tilde{\chi}_2^0 \to \tilde{\chi}_1^0 l^+l^-$ contributions, and the shaded histogram the distribution of the $\tilde{\chi}_1^0$ decay alone. Already from this distribution, the $\tilde{\chi}_1^0$-$\tilde{\chi}_2^0$ mass difference can be measured with a precision of about 1%, if the background can be adequately subtracted. Alternatively, a full reconstruction of the $\tilde{\chi}_2^0$ can be performed by calculating the invariant mass of a reconstructed $\tilde{\chi}_1^0$ with a lepton pair near the $m_{\tilde{\chi}_2^0} - m_{\tilde{\chi}_1^0}$ edge. From a gaussian fit to the distribution shown in Figure 20-113, the $\tilde{\chi}_2^0$ mass is measured as $m_{\tilde{\chi}_2^0} = (96.7 \pm 0.17)$, where the quoted error includes the statistical error on the fit, the statistical error on the $\tilde{\chi}_1^0$ mass measurement, and the systematic uncertainty on the lepton energy scale.

The most striking feature of Point 3 is the high number of b-jets in the final state. The dominant production mechanism is the decay chain $\tilde{g} \to \tilde{b}_1 + b \to \tilde{\chi}_2^0 + b + b$. A full reconstruction can be performed by using $\tilde{\chi}_2^0$ candidates defined as four-lepton combinations with an invariant mass within ±10 GeV of the $\tilde{\chi}_2^0$ peak shown in Figure 20-113. The b-jets from the decay $\tilde{b}_1 \to \tilde{\chi}_2^0 + b$ have typically a p_T in excess of 50 GeV, whereas the b-jets from the decay $\tilde{g} \to \tilde{b}_1 + b$ are much softer. Therefore events were selected requiring at least two b-jets with $p_T > 10$ GeV among which the ones with $p_T > 50$ GeV were labelled as 'hard' and the remaining ones as 'soft'.

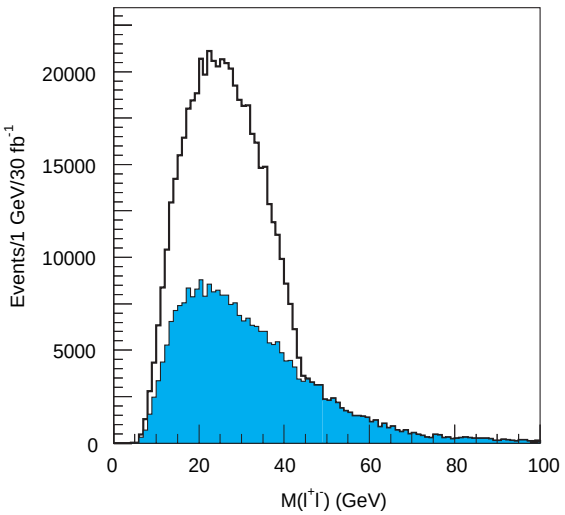

Figure 20-111 Mass of the OS-DF lepton pairs at Point 3 ($\lambda_{122} \neq 0$) for an integrated luminosity of $10\ \mathrm{fb}^{-1}$. The full line histogram is the signal+background, the shaded histogram the combinatorial background.

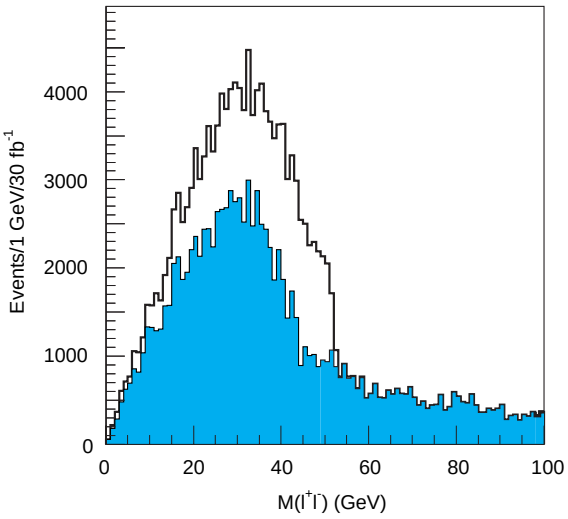

Figure 20-112 Invariant mass of the remaining OS lepton pairs after removal of the $\tilde{\chi}_1^0$ candidate at Point 3 ($\lambda_{122} \neq 0$) for an integrated luminosity of $10\ \mathrm{fb}^{-1}$.

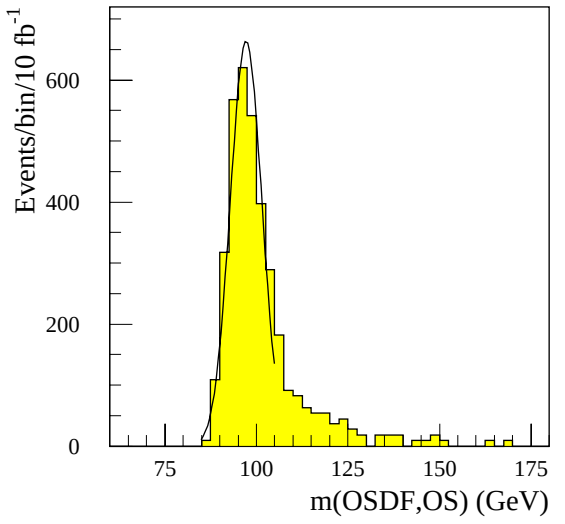

Figure 20-113 Invariant mass distribution of a $\tilde{\chi}_1^0$ and an OS lepton pair at Point 3 ($\lambda_{122} \neq 0$) for an integrated luminosity of $10\ \mathrm{fb}^{-1}$. The fitted peak gives a measurement of the $\tilde{\chi}_2^0$ mass.

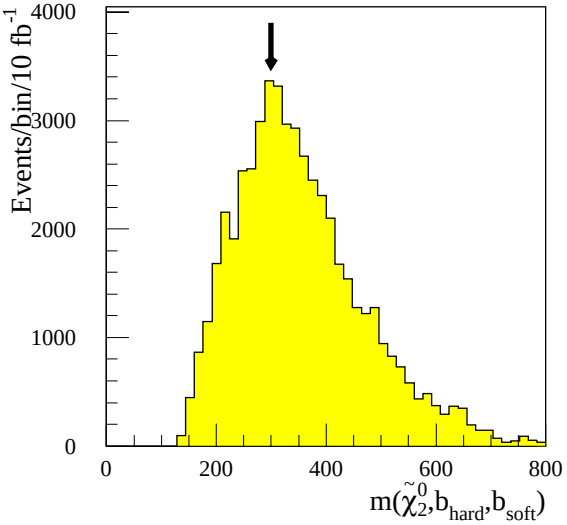

Figure 20-114 Invariant mass of a candidate $\tilde{\chi}_2^0$ with two *b*-jets at Point 3 ($\lambda_{122} \neq 0$) for an integrated luminosity of $10\ \mathrm{fb}^{-1}$. The position of the peak corresponds to the mass of the gluino.

The first step is to reconstruct a gluino peak by taking the invariant mass of a reconstructed $\tilde{\chi}_2^0$, a 'hard' *b*-jet, and a 'soft' *b*-jet. The distribution, shown in Figure 20-114, exhibits a broad peak around 300 GeV, which corresponds to the gluino mass. The events within ±10 GeV of the gluino peak were then selected, and the invariant mass of the $\tilde{\chi}_2^0$ with the 'hard' *b* was calculated if the angle α between them satisfied $\cos\alpha \geq 0.5$. The resulting mass distribution is shown in

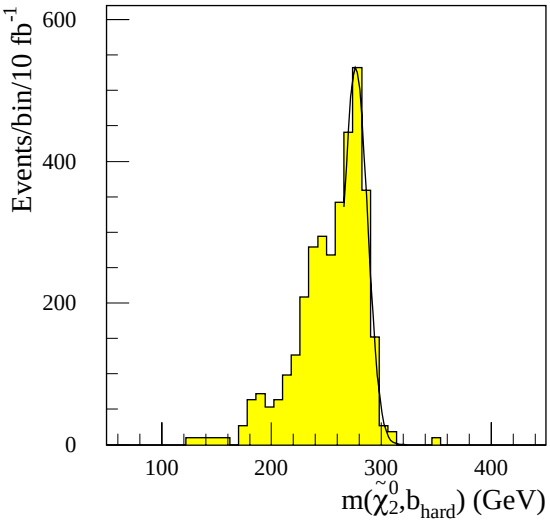

Figure 20-115 Invariant mass of the $\tilde{\chi}_2^0$ with a hard *b*-jet at Point 3 ($\lambda_{122} \neq 0$) for an integrated luminosity of 10 fb^{-1}. The events are selected requiring that the $\tilde{\chi}_2^0$-bb mass is near the gluino mass.

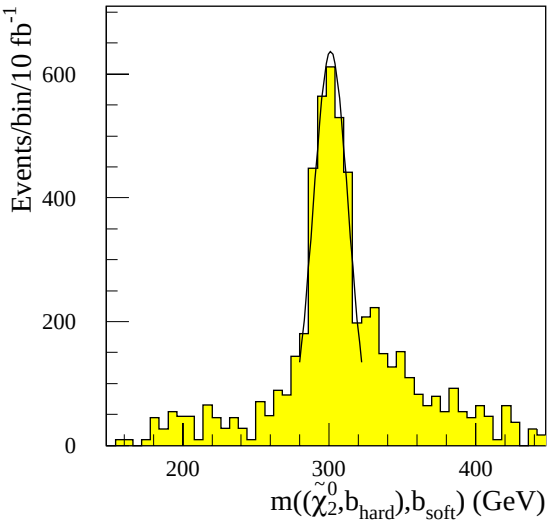

Figure 20-116 Invariant mass of the $\tilde{b}_1$ with the remaining soft b-jet in the event at Point 3 ($\lambda_{122} \neq 0$) for an integrated luminosity of 10 fb^{-1}. The fitted peak gives a measurement of the gluino mass.

Figure 20-115. From a gaussian fit to the observed peak the $\tilde{b}_1$ mass is measured to be $m_{\tilde{b}_1} = (276.6 \pm 3)$ GeV, where the error is dominated by the uncertainty in the *b*-jet energy scale. For the events within ±10 GeV of the $\tilde{b}_1$ peak, the invariant mass of the $\tilde{b}_1$ candidate with the soft *b*-jet can be calculated, as shown in Figure 20-116, yielding a measurement of the gluino mass: $m_{\tilde{g}} = (301 \pm 3)$ GeV.

20.4.2.6 Point 3: $\lambda_{123} \neq 0$

The direct reconstruction of $\tilde{\chi}_1^0$, as in Point 5, is rendered impossible by the presence of a tau lepton among the $\tilde{\chi}_1^0$ decay products. The possible measurements are therefore very similar to the *R*-parity conserving case, and will only be briefly summarised in the following. The mass difference $m_{\tilde{\chi}_2^0} - m_{\tilde{\chi}_1^0}$ can be measured from the end point of the invariant mass distribution of the OS-SF lepton pairs. The reconstruction of the $\tilde{g} \to \tilde{b}_1 + b \to \tilde{\chi}_2^0 + b + b$ decay chain follows the procedure described above for the $\lambda_{122} \neq 0$ case. The main difference is that no direct measurement of the $\tilde{\chi}_2^0$ mass is available, therefore one needs to assume a value for the $\tilde{\chi}_2^0$ mass in order to reconstruct gluino and $\tilde{b}_1$.

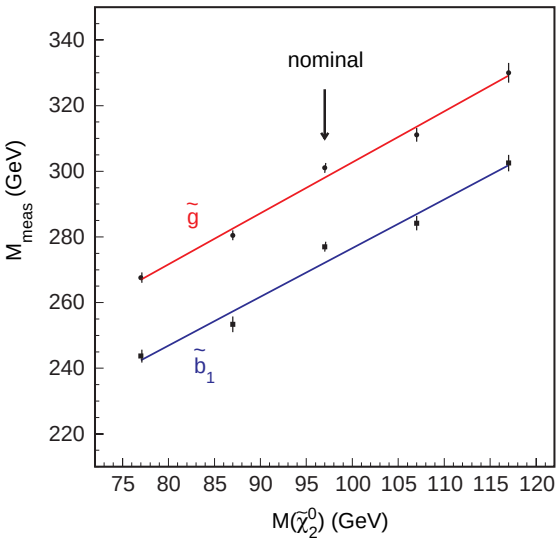

Figure 20-117 The dependence of the masses of $\tilde{b}_1$ and $\tilde{g}$ from the assumed value of the $\tilde{\chi}_2^0$ mass for Point 3 ($\lambda_{123} \neq 0$).

The distributions of the invariant masses for $\tilde{b}_1$ and gluino are very similar to the ones shown for $\lambda_{122} \neq 0$, once the $\tilde{\chi}_2^0$ mass is given. By repeating the analysis for different values of the $\tilde{\chi}_2^0$ mass a linear dependence, shown in Figure 20-117 was found between the $\tilde{b}_1$ and $\tilde{g}$ masses and the $\tilde{\chi}_2^0$ mass, which can be used as input to the fit of the fundamental parameters of the model.

20.4.2.7 Constraints on SUGRA parameters

For the $\tilde{\chi}_1^0$ decays involving only leptons of the first two generations, the invariant masses of the many lepton combinations available, and the fact that the neutrino is massless make it possible to perform a direct reconstruction of some supersymmetric decay chains with good precision. In this case, therefore, the SUGRA parameters are constrained with higher precision than in the *R*-parity conserving case. For *L*-violating couplings involving τ leptons, no advantage can be gained from direct $\tilde{\chi}_1^0$ reconstruction, and the high combinatorial background of leptons from the $\tilde{\chi}_1^0$ decay worsens in a significant way the precision of the measurements of edges in the invariant mass distribution of lepton pairs.

20.4.3 Lepton number violation: $\chi_1^0 \rightarrow q\bar{q}l$, $q\bar{q}\nu$

When one of the λ'_{ijk} is different from zero, each of the $\tilde{\chi}_1^0$ decays into two hadronic jets and a lepton, which can be either a charged lepton or a neutrino. The SUSY events will therefore exhibit a higher jet multiplicity than in the *R*-parity conserving case, with the presence of at least two additional leptons in each event. Two distinct final state phenomenologies appear in this case, depending on whether the lepton from the $\tilde{\chi}_1^0$ decay is a charged lepton or a neutrino. In the first case, one probably has the 'easiest' among all the possible *R*-parity violating signatures, as the two additional leptons per event allow easy separation from Standard Model backgrounds, and the two leptons can be taken as 'seeds' for the full reconstruction of the $\tilde{\chi}_1^0$. In case the lepton is a neutrino, there is some E_T^{miss} in the event, as shown in Figure 20-118, but hardly enough to guarantee the extraction of the signal from the background, and full reconstruction of $\tilde{\chi}_1^0$ is not possible.

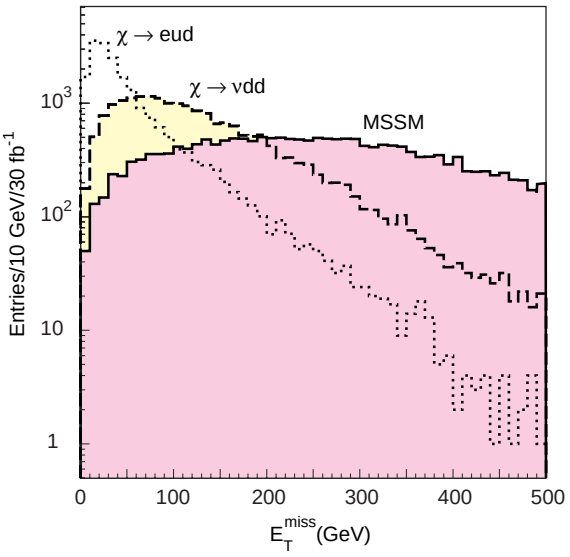

Figure 20-118 Comparison of the E_{T}^{miss} spectra for the *R*-parity conserving case, and for the decays into two jets and respectively a charged lepton or a neutrino.

For a given λ'_{ijk}, both the decays $\tilde{\chi}_1^0 \rightarrow q\bar{q}l$ and $\tilde{\chi}_1^0 \rightarrow q\bar{q}\nu$ exist, with a relative branching fraction which is determined by the neutralino mixing matrix and the SUSY mass spectrum in the considered point of parameter space. The branching fractions for the five SUGRA points were calculated for the case $\lambda'_{112} \neq 0$ [20-45]. The branching fraction into charged leptons varied between 75% (Point 3) and 35% (Point 5), thus giving for all points a significant number of events with one or two charged leptons from $\tilde{\chi}_1^0$ decays in the final state. For detailed studies [20-46]

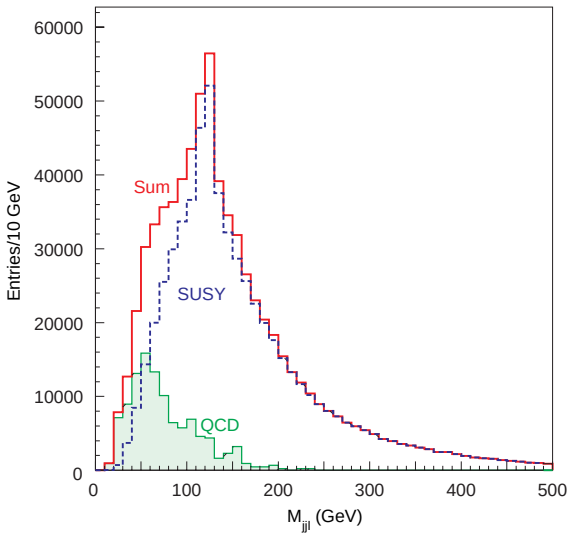

Figure 20-119 Invariant mass spectrum of *jjl* combination for SUSY (dashed), QCD (shaded), and both (full line).

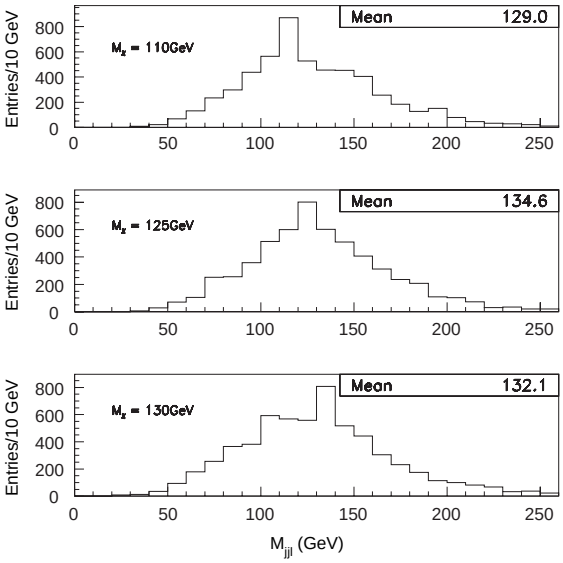

Figure 20-120 Invariant mass spectrum of *jjl* combinations for three values of the $\tilde{\chi}_1^0$ mass: 110 GeV (top), 125 GeV (middle), 130 GeV (bottom).

only decays to the first generation were considered, and the two cases, respectively with the decay in electron or neutrino, were considered separately, assuming in each case a 100% branching fraction.

20.4.3.1 Inclusive analysis

The SUSY signal can easily be extracted from the SM background by exploiting the high charged lepton multiplicity in the final state, in the case of $\tilde{\chi}_1^0 \to q\bar{q}l$ decays. This is true for all the five SUGRA points considered. For the decay $\tilde{\chi}_1^0 \to eu\bar{d}$, requiring a jet multiplicity greater than seven, with a hard leading jet, plus a single lepton with $p_T > 15$ GeV is enough to obtain signal-to-background ratios of better than ten. Similarly to the *B*-violating case, the variable $m_{T,\,cent}$ can be used to estimate the mass scale of the SUSY particles.

The decay $\tilde{\chi}_1^0 \to \nu q\bar{q}$ could be dominant in some corners of the parameter space. To take this into account, the extraction of the SUSY signal was explicitly studied for this decay. In general, the limited amount of E_T^{miss} in the events does not allow the separation of the signal from the Standard Model background in a convincing way just by requiring high jet multiplicity and E_T^{miss}. As already seen for *B*-violating couplings, a signal to background ratio adequate for discovery can be obtained requiring the presence of at least one lepton in the final state. These leptons are abundantly produced in the cascade decays of sparticles over a significant fraction of the SUGRA parameter space.

20.4.3.2 Precision measurements

The strategy for precision measurement when the decay $\tilde{\chi}_1^0 \to eu\bar{d}$ is dominant is radically different than in the *R*-parity conserving case. The starting point for the reconstruction of an exclusive decay chain is at the very bottom of the chain, where the presence of a charged lepton makes the reconstruction of at least one of the LSP reasonably easy.

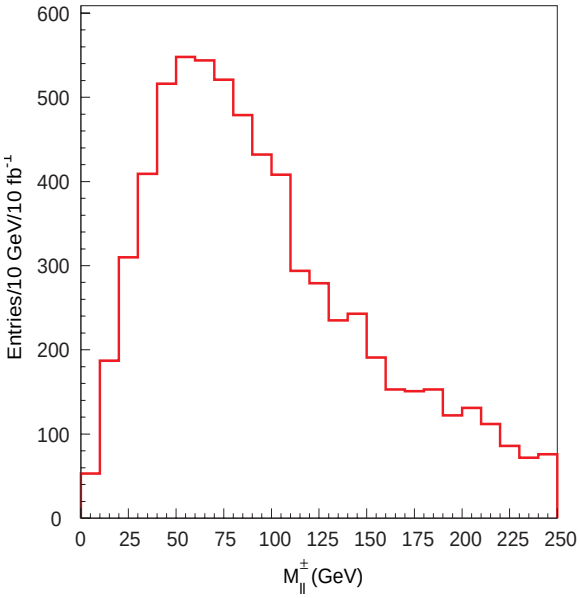

Figure 20-121 OS-SF lepton pairs invariant mass distribution (all leptons).

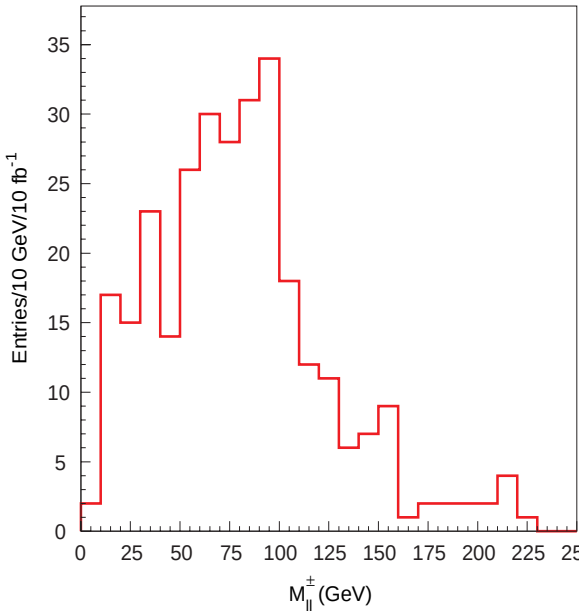

Figure 20-122 OS-SF lepton pairs invariant mass distribution (leptons not used for $\tilde{\chi}_1^0$ reconstruction).

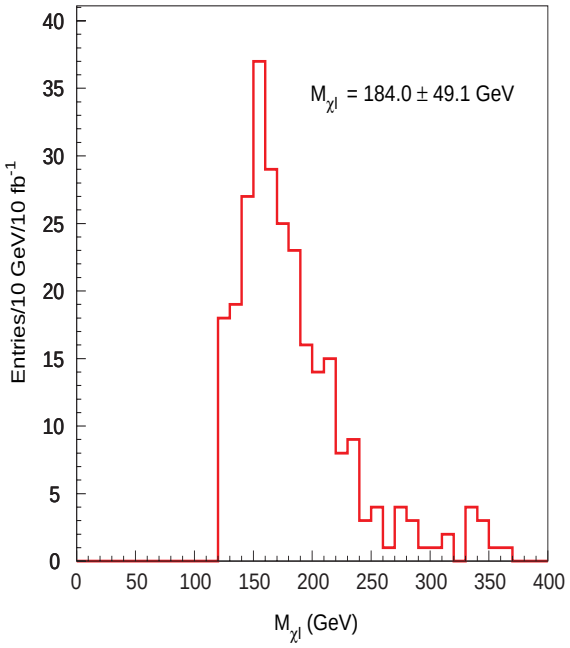

Figure 20-123 Minimum invariant mass distribution of the soft $\tilde{\chi}_1^0$ candidate combined with a lepton not used for $\tilde{\chi}_1^0$ reconstruction.

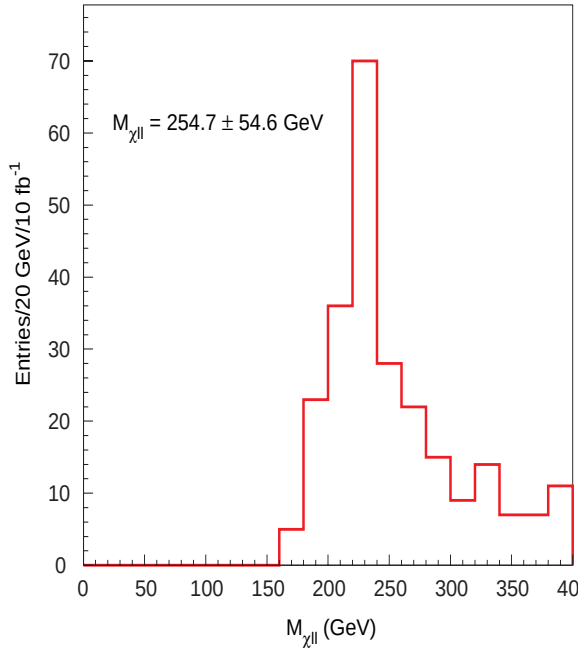

Figure 20-124 Invariant mass distribution of the soft $\tilde{\chi}_1^0$ candidate with two additional leptons. The peaks corresponds to the $\tilde{\chi}_2^0$ mass.

For SUGRA Point 5, the average p_T of the harder LSP is 320 GeV, and the decay particles have average p_T of 160, 55, and 105 GeV for the two jets, and the charged lepton respectively, allowing to reach a good efficiency in the reconstruction of the $\tilde{\chi}_1^0$.

The $\tilde{\chi}_1^0$ was reconstructed by first selecting the SUSY events with a set of loose cuts:

- at least six jets with $p_T > 20$ GeV, of which one with $p_T > 250$ GeV;
- at least one lepton with $p_T > 20$ GeV;
- transverse sphericity > 0.2, and thrust < 0.9.

Then the correct *jjl* combination was chosen, out of the combinatorial background from jets directly produced in squark and gluino decays. For the leading $\tilde{\chi}_1^0$, the ΔR distance between the two jets was required to be smaller than 1, and the distance between the leading (second) jet and the lepton was required to be smaller than 1 (1.5). All angular cuts were set at $\Delta R < 2$ for the reconstruction of the second $\tilde{\chi}_1^0$. The combinatorial background was further reduced by requiring that the leading jet has $p_T > 50$ GeV and the second jet has $p_T < 100$ GeV for the first $\tilde{\chi}_1^0$, and both jets have p_T smaller than 100 GeV for the second $\tilde{\chi}_1^0$. With these prescriptions 1.4 combination on average were found per event.

The invariant *jjl* mass, shown in Figure 20-119, exhibits a clear peak at the $\tilde{\chi}_1^0$ mass. The observed peak is not generated by the kinematic cuts, since one can see that the QCD background does not exhibit a peak in the same position. Moreover the reconstruction was performed for different values of the $\tilde{\chi}_1^0$ mass. The displacement of the peak position, shown in Figure 20-120, allows the $\tilde{\chi}_1^0$ mass to be determined with a precision of ±3 GeV. The same analysis was performed for SUGRA points 3 and 4, using the same angular and kinematic cuts. A peak, albeit degraded, is seen for Point 4, whereas at Point 3 the mass of the $\tilde{\chi}_1^0$ is small (44 GeV) and the reconstruction from the very soft jets and leptons is problematic.

Once the $\tilde{\chi}_1^0$ has been reconstructed, it is possible to go up the decay chain and reconstruct other sparticle masses. As usual, for SUGRA Point 5, the best decay chain for full exclusive reconstruction is $\tilde{q}_L \tilde{q}_R$ production, followed by the decays $\tilde{q}_L \to \tilde{\chi}_2^0 q$, $\tilde{\chi}_2^0 \to \tilde{l}_R^{\pm} l^{\mp} \to \tilde{\chi}_1^0 l^+ l^-$, and $q_R \to \tilde{\chi}_1^0 q$. This decay offers a large branching fraction, a low jet combinatorial background, and the characteristic edge in the two-lepton invariant mass from the $\tilde{\chi}_2^0$ decay to sleptons. In the case of the $\tilde{\chi}_1^0 \to eu\bar{d}$ decay, the edge is spoiled by the additional lepton combinatorics, as shown in Figure 20-121, where the two-lepton invariant mass is plotted for signal events. The situation can be improved by performing the $\tilde{\chi}_1^0$ reconstruction, and considering only the events with two *jjl* combinations with an invariant mass within 10 GeV of the $\tilde{\chi}_1^0$ mass. The invariant mass of the opposite-sign same-flavour lepton pairs, excluding the leptons used for the $\tilde{\chi}_1^0$ reconstruction, is shown in Figure 20-122. The edge at 100 GeV is present, albeit much less clean than in the *R*-parity conserving case.

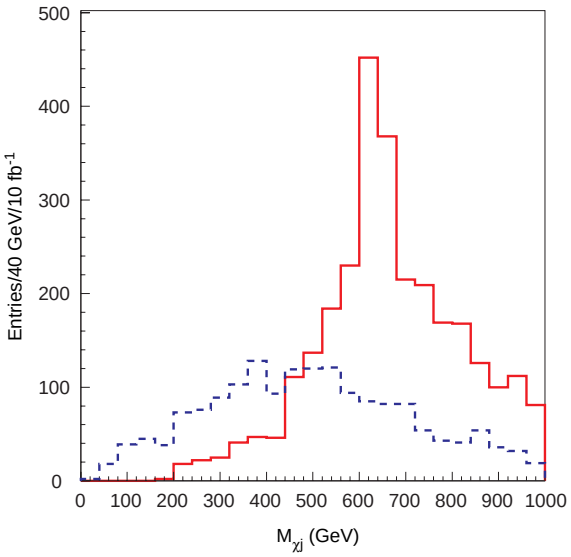

Figure 20-125 Invariant mass of the harder $\tilde{\chi}_1^0$ with the leading jet in the event. A broad peak can be seen around the nominal $\tilde{q}_R$ mass. The dashed distribution is the invariant mass of the softer $\tilde{\chi}_1^0$ with the second hardest jet in the event.

The events with two reconstructed $\tilde{\chi}_1^0$ can be used to reconstruct explicitly the $\tilde{l}_R$ mass by calculating the invariant mass of the $\tilde{\chi}_1^0$ with one of the two additional leptons. The problem is in this case the choice of the $\tilde{\chi}_1^0$ and of the lepton from the $\tilde{l}_R$ decay. The softer $\tilde{\chi}_1^0$ was used for the reconstruction, as it can be assumed that the harder one comes from the $\tilde{q}_R$ decay. The invariant

mass of the softer *jjl* combination was rescaled to the nominal $\tilde{\chi}_1^0$ mass, and the invariant mass with the remaining lepton was then calculated. The distribution of the lowest of the reconstructed invariant masses is shown in Figure 20-123. A peak can be seen corresponding to the slepton invariant mass of 157 GeV. By varying the slepton mass, a precision in the slepton mass measurement of ±15 GeV can be estimated. By further combining the reconstructed slepton with the remaining lepton, the $\tilde{\chi}_2^0$ can also be reconstructed. The distribution in Figure 20-124 was obtained by requiring the slepton candidate to have an invariant mass within 10 GeV of the slepton mass. The statistics, for an integrated luminosity of 10 fb^{-1} is limited, but a clear peak is observed at the nominal $\tilde{\chi}_2^0$ mass of 228GeV.

The mass of the $\tilde{q}_R$ can be measured through the decay $q_R \rightarrow \tilde{\chi}_1^0 q$, by calculating the invariant mass of one of the reconstructed $\tilde{\chi}_1^0$ with a hard jet. Events were selected by requiring two reconstructed $\tilde{\chi}_1^0$ with a mass within 10 GeV of the measured $\tilde{\chi}_1^0$ mass, and two hard central jets, within $|\eta| < 2$, and with a p_T respectively in excess of 300 and 100 GeV. The requirement of two hard jets is meant to preferentially select $\tilde{q}_L \tilde{q}_R$ production. Under the assumption that the SUSY sample is dominated by this process, the decay $q_R \rightarrow \tilde{\chi}_1^0 q$ can be expected to yield the harder $\tilde{\chi}_1^0$ and the leading jet. The mass combination of the two is presented in Figure 20-125, which does indeed show a convincing peak corresponding to the position of the $\tilde{q}_R$ mass. In the same plot the dotted line shows the invariant mass of the softer jet combined with the softer $\tilde{\chi}_1^0$ which, on the contrary, as expected does not show any clear peak structure.

As in *R*-parity conserving Point 5, the measurement of the lightest Higgs mass through the reconstruction of the $h \rightarrow b\bar{b}$ mass peak is necessary in order to constrain tanβ. The measurement is in this case more difficult due to the increased jet combinatorics from $\tilde{\chi}_1^0$ decay products when light jets are misidentified as *b*-jets. A narrow peak, albeit over a background much higher than in the *R*-conserving case, is obtained by selecting events with two reconstructed $\tilde{\chi}_1^0$, and excluding from the $b\bar{b}$ mass reconstruction jets which were used for the $\tilde{\chi}_1^0$. The situation would of course be worse, if the $\tilde{\chi}_1^0$ decays involved *c* or *b*-quarks. Likewise, in the case of SUGRA Point 1 the much reduced statistics, together with the big efficiency loss produced by the requirement of two reconstructed $\tilde{\chi}_1^0$ could greatly reduce the significance of the $h \rightarrow b\bar{b}$ peak.

20.4.3.3 Constraints on the SUGRA parameters

The case with $\lambda'_{ijk} \neq 0$ is intermediate between the two previously considered cases. If the $\tilde{\chi}_1^0$ decay involves a lepton from the first two generations, SUSY can be very easily discovered. The $\tilde{\chi}_1^0$, and hence full SUSY decay chains, can be reconstructed. This reconstruction is based on two jets, and therefore can be performed only for a sufficiently heavy $\tilde{\chi}_1^0$, so as to have observable jets. The precision of the mass measurement is limited. Therefore, the advantage of this scenario with respect to *R*-parity conservation is the possibility of performing model independent mass reconstructions, whereas little improvement is expected in constraining the SUGRA parameters. On the other hand, as it happens for the $\lambda_{ijk} \neq 0$ case, the precision in the measurement of the lepton-lepton edge in Point 5 is spoiled by the high lepton multiplicity in the final state.

20.5 Conclusion

If SUSY exists at the weak scale, then its discovery at the LHC should be straightforward. The SUSY cross section is dominated by gluinos and squarks, which are strongly produced with cross sections comparable to the Standard Model backgrounds at the same Q^2. Gluinos and squarks then decay via a series of steps into the LSP (which may itself decay if *R*-parity is vio-

lated). These decay chains lead to a variety of signatures involving multiple jets, leptons, photons, heavy flavours, W and Z bosons, and missing energy. The combination of a large production cross section and distinctive signatures makes it easy to separate SUSY from the Standard Model background. Therefore, the main challenge is not to discover SUSY but to separate the many SUSY processes that occur and to measure the masses and other properties of the SUSY particles. In most cases, the backgrounds from other SUSY events dominates the reducible Standard Model backgrounds due to the tails of the detector response. This fact justifies the use of particle level simulations for precision SUSY studies.

The number of free parameters for even the Minimal Supersymmetric Standard Model is very large, so it is impossible to investigate all cases. Since the background for SUSY is SUSY itself, one cannot just generate particular signals and compare them with known backgrounds. The approach followed here has been to investigate in detail the signatures for particular points in the parameter spaces of the minimal SUGRA, GMSB, and R-parity violating models. Methods such as looking for kinematic endpoints for mass distributions and using these to determine combinations of methods have proven generally useful. But each point has to some extent required inventing new analysis methods.

It seems clear that the points investigated here do not exhaust all possibilities even of the minimal SUSY models considered. Given the success in extracting precise measurements for these few points and the large number of SUSY events expected at the LHC, ATLAS is likely not just to discover SUSY if it exists but to make many precise measurements. The starting point in this study will be to look for characteristic deviations from the Standard Model. In SUGRA and some other models, there would be events with multiple jets and leptons plus large $E_{\mathrm{T}}^{\mathrm{miss}}$. In GMSB models, there would be events with prompt photons or quasi-stable sleptons. In R-parity violating models, there would be events with very high jet multiplicity and/or leptons. Any such signal would point to possible classes of models and would indicate the rough mass scale. The next step would be to use partial reconstruction methods like those described in this chapter to try to constrain as many combinations of masses as possible. A sharp dilepton edge like that in Figure 20-11 or a $h \rightarrow b\bar{b}$ peak is fairly unambiguous; so are some of the GMSB signatures. More complicated signatures, especially those involving complicated combinations of jets, would require much more work. These sorts of kinematical features represent only a small part of the total data. Given a SUSY signal, one would certainly generate large samples of events for many different models and compare many different distributions. This involves a huge effort, but one that would certainly be made given signals for new physics

The ultimate goal is to use all the measured quantities to determine the underlying SUSY model and to measure its parameters, just as the precision electroweak data has been fit in the Standard Model. The fits performed here have used minimal models with a small number of parameters. The fitting would clearly be more difficult for more complicated models. Even for simple models, it is not trivial to determine the masses and other parameters at a level of precision that matches many of the potential experimental measurements. Many corrections have to be included, and some can be quite important [20-47]. Fortunately – or rather unfortunately – we have many years to improve both the analysis techniques described here and the theoretical tools to interpret them.

20.6 References

20-1 J. Erler and P. Langacker, UPR-816-T, hep-ph/9809352 (1998).

20-2 S. Weinberg, Phys. Rev. **D13** (1976) 974, Phys. Rev. **D19** (1979) 1277;
L. Susskind, Phys. Rev. **D20** (1979) 2619.

20-3 Y. Gol'fand and E. Likhtam, JETP Lett. **13** (1971) 323;
P. Ramond, Phys. Rev. **D3** (1971) 2415;
A. Neveu and J.H. Schwartz, Nucl. Phys. **B31** (1971) 86;
J.L. Jervais and B. Sakita, Nucl. Phys. **B34** (1971) 632;
D. Volkov and V. Akulov, Phys. Lett. **B46** (1973) 109;
J. Wess and B. Zumino, Nucl. Phys. **B78** (1974) 39.

20-4 General reviews of SUSY include H.P. Nilles, Phys. Rep. **111** (1984) 1;
H.E. Haber and G.L. Kane, Phys. Rep. **117** (1985) 75;
J. Wess and J. Bagger, *Supersymmetry and Supergravity*, ISBN 0691085560 (1992);
S.P. Martin, hep-ph/9709356 (1997).

20-5 G.W. Anderson and D.J. Castano, hep-ph/9409419, Phys. Lett. **B347** (1995) 300.

20-6 M. Carena, *et al.*, hep-ex/9712022 (1997) and references therein.

20-7 ALEPH Collaboration, Eur. Phys. J. **C2** (1998) 417; Eur. Phys. J. **C1** (1998) 1;
DELPHI Collaboration, Eur. Phys. J. **C1** (1998) 1;
L3 Collaboration, Eur. Phys. J. **C4** (1998) 207;
OPAL Collaboration, Eur. Phys. J. **C2** (1998) 213.

20-8 ALEPH, DELPHI, L3, OPAL, and SLD Collaborations, CERN-PPE/97-154 (1997).

20-9 S.P. Martin, hep-ph/9602349, Phys. Rev. **D54** (1996) 2340.

20-10 S. Dimopoulos and D. Sutter, Nucl. Phys. **B452** (1995) 496.

20-11 L. Alvarez-Gaume, J. Polchinski, and M.B. Wise, Nucl. Phys. **B221** (1983) 495;
L. Ibanez, Phys. Lett. **118B** (1982) 73;
J. Ellis, D.V. Nanopolous, and K. Tamvakis, Phys. Lett. **121B** (1983) 123;
K. Inoue *et al.*, Prog. Theor. Phys. **68** (1982) 927;
A.H. Chamseddine, R. Arnowitt, and P. Nath, Phys. Rev. Lett. **49** (1982) 970.

20-12 For the form of the RGE's used here, see V. Barger, M.S. Berger, and P. Ohmann, hep-ph/9311269, Phys. Rev. **D49** (1994) 4908.

20-13 M. Dine, W. Fischler and M. Srednicki, Nucl. Phys. **B189** (1981) 575;
S. Dimopoulos and S. Raby, Nucl. Phys. **B192** (1981) 353;
C. Nappi and B. Ovrut, Phys. Lett. **113B** (1982) 175;
L. Alvarez-Gaume, M. Claudson, and M. Wise, Nucl. Phys. **B207** (1982) 961;
M. Dine and A. Nelson, Phys. Rev. **D48** (1993) 1227;
M. Dine, A. Nelson, and Y. Shirman, Phys. Rev. **D51** (1995) 1362;
M. Dine, *et al.*, Phys. Rev. **D53** (1996) 2658.

20-14 H. Dreiner, hep-ph/9707435 (1997).

20-15 H. Baer, F.E. Paige, S.D. Protopopescu, and X. Tata, hep-ph/9305342 (1993); *ibid.*, hep-ph/9804321 (1998).

20-16 S. Mrenna, hep-ph/9609360, Comput. Phys. Commun. **101** (1997) 232.

20-17 E. Richter-Was, D. Froidevaux, and L. Poggioli, 'ATLFAST 2.0: a fast simulation package for ATLAS', ATLAS Internal Note ATL-PHYS-98-131 (1998).

20-18 H. Baer, C.-H. Chen, F.E. Paige, and X. Tata, Phys. Rev. **D52** (1995) 2746; *ibid.*, Phys. Rev. **D53** (1996) 6241.

20-19 The present LEP preliminary limits, presented at the '99 winter conferences, are ALEPH: 90.2 GeV (ALEPH 99-007 CONF-99-003, March 1999);
DELPHI: 95.2 GeV (DELPHI 99-8 CONF-208);
L3: 95.2 GeV (L3 Notes 2382,2383, March 1999);
OPAL: 91.0 GeV (OPAL Note PN382, March 1999).

20-20 For a recent review, see M.S. Turner, astro-ph/9901168; to be published in *Proc. of Wein 98* (Santa Fe, 1998).

20-21 ATLAS Collaboration, Technical Proposal, CERN/LHCC/94-43 (1994).

20-22 I. Hinchliffe, F.E. Paige, M.D. Shapiro, J. Soderqvist, and W. Yao, Phys. Rev. **D55** (1997) 5520.

20-23 E. Richter-Was, D. Froidevaux, and J. Soderqvist, 'Precision SUSY measurements with ATLAS for SUGRA Points 1 and 2', ATLAS Internal Note ATL-PHYS-97-108 (1997).

20-24 I. Hinchliffe, F.E. Paige, E. Nagy, M.D. Shapiro, J. Soderqvist, and W. Yao, 'Precision SUSY measurements at LHC: Point 3', ATLAS Internal Note ATL-PHYS-97-109 (1997).

20-25 F. Gianotti, 'Precision SUSY measurements with ATLAS: SUGRA Point 4', ATLAS Internal Note ATL-PHYS-97-110 (1997).

20-26 G. Polesello, L. Poggioli, E. Richter-Was, and J. Soderqvist, 'Precision SUSY measurements with ATLAS for SUGRA Point 5', ATLAS Internal Note ATL-PHYS-97-111 (1997).

20-27 D. Froidevaux, D. Cavalli, F. Gianotti, I. Hinchliffe, F. Paige, G. Polesello, L. Poggioli, E. Richter-Was, S. Resconi, M. Shapiro, J. Soderqvist, and A. Weidberg, 'Precision SUSY measurements with ATLAS: Extraction of model parameters and conclusions', ATLAS Internal Note ATL-PHYS-97-112.

20-28 S. George and T. Hansl-Kozaneka, eds., 'ATLAS Trigger Menus', ATLAS Internal Note ATL-DAQ-98-121 (1998).

20-29 H. Bachacou, I. Hinchliffe and F.E. Paige, 'Measurements of masses in SUGRA models at LHC', Atlas Internal Note ATL-COM-PHYS-99-017.

20-30 F. James, *MINUIT Reference Manual*, CERN Program Library Long Writeup D506.

20-31 N. Arkani-Hamed, J.L. Feng, L.J. Hall, and H.-C. Cheng, hep-ph/9704205, Nucl. Phys. **B505** (1997) 3.

20-32 T. Tsukamoto, K. Fujii, H. Murayama, M. Yamaguchi, and Y. Okada, Phys. Rev. **D51** (1995) 3153.

20-33 I. Hinchliffe and F.E. Paige, 'Measurements for SUGRA Models with Large $\tan\beta$ at LHC', ATL-COM-PHYS-99-018.

20-34 Y. Coadou, I. Hinchliffe, J. Lozano-Bahilo, L.C. Loveridge, and M.D. Shapiro, 'Identification of hadronic Tau decays in ATLAS', ATLAS Internal Note ATL-PHYS-98-126.

20-35 X. Tata, private communication.

20-36 I. Hinchliffe and F.E. Paige, 'Measurements in Gauge Mediated SUSY Breaking Models at the LHC', hep-ph/9812233, ATL-PHYS-98-134.

20-37 L. Borissov, M. Leltchouk, F. Paige, J. Parsons, S. Rajogopalan, 'Study of non-pointing photon signatures of Gauge Mediated SUSY Breaking Models', Atlas Internal Note ATL-COM-PHYS-99-037 (1999).

20-38 A. Nisati, S. Petrarca, and G. Salvini, hep-ph/9707376, Mod. Phys. Lett. **A12** (1997) 2213; A. Nisati, 'Preliminary Timing Studies of the Barrel Muon Trigger System', ATLAS Internal Note ATL-DAQ-98-083 (1998).

20-39 G. Polesello and A. Rimoldi, 'Reconstruction of quasi-stable charged sleptons in the ATLAS muon spectrometer', Atlas Internal Note ATLAS-COM-MUON-99-008 (1999).

20-40 P. Richardson, private communication;
G. Corcella *et al.*, Cavendish HEP-99/03 (1999).

20-41 J. Soderqvist, 'Consequences of Baryonic R-parity Violation for Measurements of SUSY Particles using the ATLAS Detector', ATLAS Internal Note ATL-PHYS-98-122.

20-42 L. Drage, M.A. Parker, 'Measurement of the LSP mass in supersymmetric models with *R*-parity violation', Atlas Internal Note ATL-COM-PHYS-99-029.

20-43 A. Mirea and E. Nagy, 'Study of the determination of the SUGRA parameters using the ATLAS detector in the case of *L*-violating *R*-parity breaking', ATLAS Internal Note ATL-COM-PHYS-99-007.

20-44 A. Mirea, 'The program RPV_ISAJET, an extension of ISAJET for the case of R-parity violation', ATLAS Internal Note ATL-COM-PHYS-99-08.

20-45 E-J. Buis, 'Neutralino decay in SUGRA Point 4', ATLAS Internal Note ATL-COM-PHYS-99-20.

20-46 A. Connors, PhD Thesis, University of Birmingham (UK), 1998.

20-47 See for example D.M. Pierce, J.A. Bagger, K. Matchev, and R. Zhang, hep-ph/9606211, Nucl. Phys. **B491** (1997) 3.

21 Other physics beyond the Standard Model

21.1 Introduction

This chapter discusses signals for a variety of possible physics in extensions of the Standard Model. Technicolor models replace the elementary Higgs bosons of the Standard Model or SUSY with dynamical condensates. The simplest such models predict flavour changing neutral currents and other violations of precision electroweak data. Nevertheless, the basic idea of technicolor remains viable, although there is no 'standard' technicolor model. Technicolor solves the hierarchy problem if the mass scale is less than about 1 TeV, so it should be observable at the LHC. Excited quarks, leptoquarks, and contact interactions are not predictions of any specific model but are examples of possible new physics. New gauge bosons are typically predicted by any extension of the electroweak gauge group. Finally, monopoles might explain the quantisation of charge. The new energy regime opened up at the LHC makes it interesting to search for these and other types of new physics.

21.2 Search for technicolor signals

Technicolor theory (TC) provides a dynamical means of breaking electroweak symmetry [21-1]. It assumes the existence of technifermions possessing a technicolor charge and interacting strongly at a high scale. Chiral symmetry is broken by techniquark condensates giving rise to Goldstone bosons, the technipions, which are the longitudinal degrees of freedom of the *W* and Z gauge bosons. The theory has been extended (extended technicolor, or ETC) to allow the generation of mass for the known fermions [21-2]. In order to account for the absence of FCNC's, the coupling constant is required to 'walk', rather than 'run'. To achieve a walking α_{TC}, multiscale technicolor models contain several representations of the fundamental family, and lead to the existence of technihadron resonances accessible at LHC energies. Such models [21-3], and others [21-4] are constrained by precision electroweak data[21-5], but are not necessarily excluded [21-6][21-7]. However, the constraints from these measurements make it unnatural to have a large top quark mass. In top-colour-assisted technicolor (TC2) models [21-8][21-9], the top quark mass arises in large part from a new strong top-colour interaction, which is a separate broken gauge sector.

The search for technipions and associated ETC gauge bosons is discussed in recent references [21-3][21-10]. In this section, the possible observation of these resonances by using the ATLAS detector is investigated. In particular, the search for a (*I=1, J=1*) techni-rho resonance decaying to a pair of gauge bosons, or to a techni-pion and a gauge boson is presented. Single production of a technipion may be detected under particular conditions, if it decays to heavy quarks. A clean signal of another vector resonance can also be obtained from the process $p\,p \rightarrow \omega_T \rightarrow \pi_T^0\,\gamma$. Finally, the usefulness of forward jet tagging is discussed for studies of such resonances, when produced by gauge boson pair fusion. Although certain models, with a given set of parameters, are used as reference, the signals studied here can be considered generic in any model which predicts resonances. Therefore, results are presented in each case not only relative to the reference model, but also as lower limits on the $\sigma \times \mathrm{BR}$ required for observation of the resonance at the five standard deviation level.

The signals and backgrounds discussed in this note have been generated with PYTHIA 6.1 [21-11]. The trigger acceptance as well as the detector acceptance and resolution effects were simulated with the parametrised Monte Carlo program ATLFAST 1.53 [21-12], with default values of the parameters. In particular, jets were reconstructed with the cone algorithm, requiring a cone radius of 0.4 and a minimum E_T of 15 GeV. Low luminosity conditions ($L = 10^{33}$ cm^{-2} s^{-1}) were assumed for the energy resolution of jets. Leptons were required to be isolated, meaning that their electromagnetic clusters in the calorimeter were separated from other clusters by $\Delta R > 0.4$ and $E_T < 10$ GeV in a cone $\Delta R = 0.2$ around the lepton. Jets were identified as *b*-jets if a *b*-quark of $p_T > 5$ GeV was within a cone radius of 0.2 of the direction of the jet. For *b*-tagging efficiencies and rejection factors, 53% global efficiency and 91% global rejection of non-*b* jets are assumed.

21.2.1 Technicolor signals from $q\bar{q}$ fusion

The model adopted here is that of multiscale technicolor [21-13][21-14], with the technicolor group $SU(N_{TC})$, $N_{TC} = 4$ and two isotriplets of technipions. The mixing angle between the longitudinal gauge bosons and the technipions, $|\Pi_T> = \sin\chi \ |W_L> + \cos\chi \ |\pi_T>$, has the value $\sin(\chi)=1/3$, the decay constant of the mixed state $F_T = F_\pi \sin(\chi) = 82$ GeV, and the charge of the up-type (down-type) technifermion $Q_U = 1$, ($Q_D = 0$). This model is incorporated in PYTHIA6.1 [21-11]. It should be noted that the decay widths of the ρ_T and the ω_T depend upon $(Q_U^2 + Q_D^2)$ and upon the masses assumed. The branching ratios assumed in the present analysis do not account for possible decays to transversely polarised gauge bosons, recently calculated in [21-15].

The decay channels of a techni-rho (ρ_T) depend on the assumed masses of the techniparticles. Different 'typical' mass scenarios have been considered here. One case, $m_\rho = 220$ GeV and $m_\pi = 110$ GeV was chosen because it has been studied for the Tevatron [21-3][21-13]. Other cases are representative of what one may expect to probe at the LHC. It is also assumed in the present analysis that the π_T coupling (and therefore its decay) to the top quark is very small, as may be expected in TC2 theories. This is only an approximation. A more general case will be considered in the analysis of a $t\bar{t}$ resonance.

21.2.1.1 $\rho_T^\pm \to WZ \to l^\pm\nu\, l^+ l^-$

This decay could be the cleanest channel for detection of a technirho. The resonant production of *WZ* decaying to two leptons and two jets has been considered in the framework of the chiral Lagrangian model in Chapter 19.4.2. Table 21-1 shows the parameters assumed here for the techniparticles and the $\sigma \times$ BR in the multiscale model. The cross sections account for a preselection on the mass of the hard scattering subsystem ($\hat{m} > 150, 300, 600$ GeV for $m_{\rho T} = 220, 500$ and 800 GeV respectively.)

The only background which needs to be considered is the continuum production of *WZ* gauge bosons, with a cross section of 21 pb. The following cuts are applied:

- The lepton trigger serves as a preselection. At least three charged leptons are required here, ($E_T > 20$ GeV for electrons and $p_T > 6$ GeV for muons), two of which must have the same flavour and opposite charge[1].

1. The lepton detection efficiency was assumed to be 100%, the results in this section are slightly optimistic as an efficiency of 90% is expected.

Table 21-1 Masses and parameters for technicolor cases considered.

Case	$m\rho_T$ (GeV)	$m\pi_T$ (GeV)	$\Gamma\rho_T$ (GeV)	BR ($\rho_T \to WZ$)	σ(production), pb
(a)	220	110	0.93	0.13	80
(e)		110	67	0.014	7.1
(b)	500	300	4.5	0.21	4.4
(f)		500	1.1	0.87	4.4
(g)		110	130	0.013	0.82
(d)		250	77	0.022	0.74
(h)	800	300	52	0.032	0.80
(c)		500	7.6	0.22	0.77

- The invariant mass of the lepton pair with the same flavour and opposite sign should be close to the that of the Z: $m_{l^+l^-} = m_Z \pm 5$ GeV.
- The longitudinal momentum of the neutrino is calculated, within a two fold ambiguity, from the missing transverse energy and the momentum of the unpaired lepton assuming an invariant mass $m_{l\nu} = m_W$. Both solutions are given a weight of 0.5. Once the W and Z are reconstructed, their transverse momentum is required to be larger than 40 GeV.
- Only events for which the decay angle with respect to the direction of the WZ system (ρ_T) in its rest frame is $|\cos\hat{\theta}| < 0.8$ are accepted. This variable is sensitive to the polarisation of the ρ_T (see Figure 21-1).

Table 21-2 shows the significance for all the cases considered. The number of signal and background events is counted in mass regions around the ρ_T peak. The selected regions were [210-240]. [460-560] and [740-870] GeV for $m_{\rho T}$ = 220, 500 and 800 GeV respectively. No evident signal is observed for cases (e), (g) and (h) (see Figure 21-2), principally because the ρ_T resonance is wide. Table 21-2 shows also the lower limit on ($\sigma \times BR$) required for a 5σ significance, from which one could infer the potential of observability for a different assumed branching ratio. Since this signal is based only on lepton reconstruction, the significance can be expected to scale approximately as the square root of the integrated luminosity, even in the presence of pile-up.

Table 21-2 Expected significance for the signal $\rho_T^{\pm} \to W^{\pm}Z \to l^{\pm}\nu\, l^+l^-$, with 30 fb^{-1}. The mass bins used are given in the text.

case	(a)	(e)	(b)	(f)	(g)	(h)	(c)
$S/\sqrt{B}$	41.8	0.8	18	77	0.28	0.98	8.2
$\sigma \times$ BR (fb), model	160	1.04	13	54	0.15	0.36	0.25
$\sigma \times$ BR (fb), for 5σ significance	19	6.5	3.6	3.5	2.6	1.8	1.5

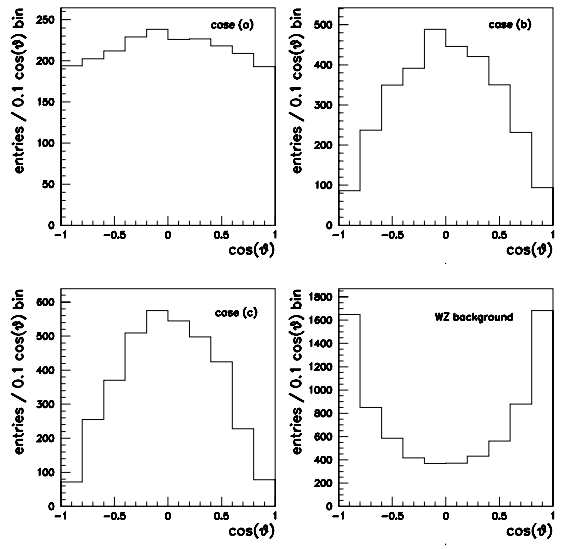

Figure 21-1 $\rho_T^{\pm} \rightarrow W^{\pm}Z \rightarrow l^{\pm}\nu\, l'^{+}l'^{-}$: Distribution of decay angles of the ρ_T candidates for three cases of ρ_T production and for *WZ* background.

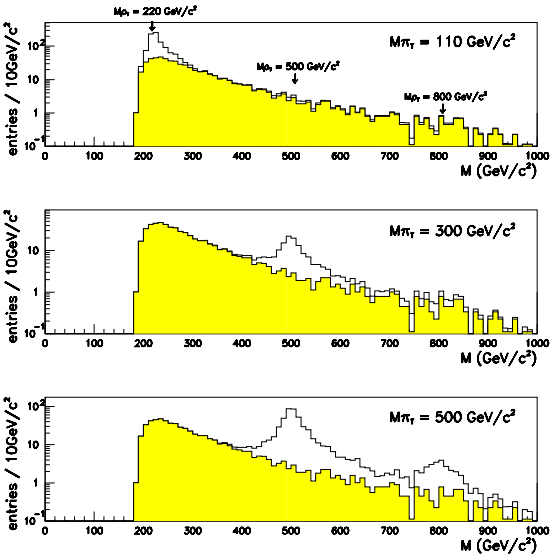

Figure 21-2 $\rho_T^{\pm} \rightarrow W^{\pm}Z \rightarrow l^{\pm}\nu\, l'^{+}l'^{-}$: Reconstructed $W^{\pm}Z^{0}$ invariant mass. The solid line is for the ρ_T signal and the filled area for the *WZ* background. The three diagrams show the different ρ_T for the cases (a) (e) (g), (b) (h), and (f) (c).

21.2.1.2 $\rho_T^{\pm} \rightarrow \pi_T^{\pm} Z \rightarrow b\, q\, l^{+}\, l^{-}$

Here, the technipion decays to *b* and *c* quarks (a *c*-quark jet will not be distinguished from a light quark jet in this analysis). Only cases (b), (c) and (d), defined in Table 21-1 are considered here. Given the parameters chosen for the model, the branching ratios $BR(\rho_T^{\pm} \rightarrow \pi_T^{\pm} Z^0)$ are 39.8%, 38.2% and 13.0% respectively. In all cases, $\pi_T^{\pm}$ decays to $c\bar{b}$ (or $b\bar{c}$) 92% of the time (assuming that the coupling to the top quark is negligible).

The principal backgrounds are: Z + jets (with $p_T > 100$ GeV, consisting of $qq \rightarrow gZ$, $qg \rightarrow qZ$ and $qq \rightarrow ZZ$), $t\bar{t}$ (with $p_T > 80$ GeV), and continuum WZ production (with $p_T > 30$ GeV). The cuts used in this analysis are the following:

- Two same flavour, opposite charge leptons required, with $p_T(l_1) > 60$ GeV and $p_T(l_2)$, 20 GeV. The invariant mass of the lepton pair should be close to the mass of the Z; i.e. $|m_{ll} - m_Z| < 5$ GeV.
- One identified *b*-jet is required. The highest p_T *b*-jet is assumed to come from the technipion decay. It must satisfy the conditions: $|\eta_b| < 2$ and $p_T{}^b > 100$ GeV.
- At least one jet, not identified as a *b*-jet, is required. The highest energy jet is the candidate. It must satisfy $|\eta_j| < 2$ and $p_T{}^j > 100$ GeV.
- The low mass regions are excluded: $m_{bj} > 150$ GeV and $m_{\mathrm{llbj}} > 300$ GeV. In the rest frame of the *llbj* system (the ρ_T), only events for which the angle of decay with respect to the direction of the ρ_T is $|\cos\hat{\theta}_{bj}| < 0.6$ are accepted. This angle is sensitive to the polarisation of the ρ_T.

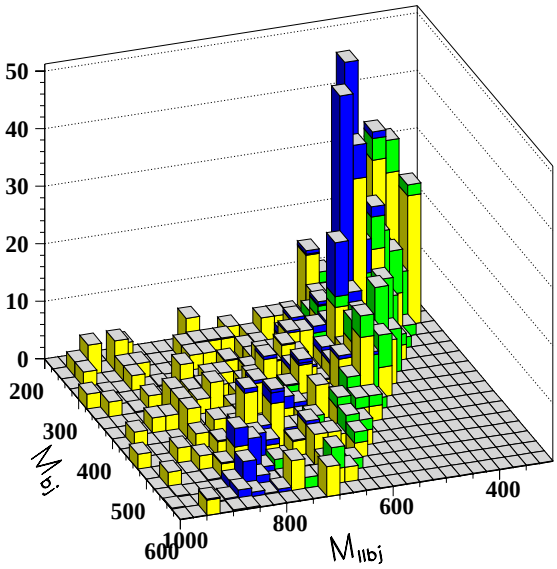

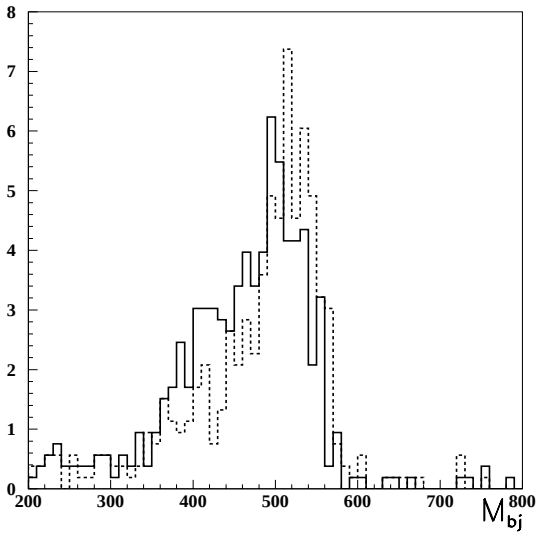

Figure 21-3 Reconstructed masses of ρ_T candidates and π_T candidates in the decay $\rho_T^{\pm} \rightarrow \pi_T^{\pm} Z \rightarrow b\ q\ l^+l^-$. The Z+jets background is in light shade, and the $t\bar{t}$ background in darker shade. The two cases (b) and (c) are shown in dark. Statistical fluctuations are overestimated.

Figure 21-4 $\rho_T \rightarrow \pi_T\ Z \rightarrow b\ q\ l^+\ l^-$: Comparison of reconstructed M_{bj} for jet cones of size $\Delta R = 0.4$ (full histogram) and $\Delta R = 0.7$ (dashed histogram). Case b is shown.

Figure 21-3 shows the signals and backgrounds expected with the above selection after three years of low luminosity running (integrated luminosity of 30 fb^{-1}). Because of the large weight of the backgrounds, statistical fluctuations are exaggerated in the figure. Cases (b) and (c) give clear signals above background, but case (d) is not resolved from background not only because of its small number of events, but also because of the larger width, 77 GeV, of the resonance.

A better mass resolution of the two jet system would considerably improve the signal to background ratio. The difference in the reconstructed masses $m_{\rho T}$ and $m_{\pi T}$ is better resolved than the individual masses separately, since uncertainties in jet pair mass measurement largely cancel. An improved jet pair resolution can be achieved by choosing a larger cone for jet reconstruction. Figure 21-4 shows the effect of selecting a value of $\Delta R = 0.7$ instead of $\Delta R = 0.4$. However, by doing so, one would become more susceptible to pile-up from minimum bias events, and other detector effects. In order to extract the significance of the signals (Table 21-3), the number of signal and background events are counted in mass regions around the signal peak in the following way: for cases (b), (c) and (d), the selected regions were $[m_{\rho T} - m_{\pi T}, m_{\pi T}]$ = [175-230,200-350], [250-350,350-600] and [420-620,190-280] respectively (in GeV). It was verified that the results do not change significantly if a cone of size $\Delta R = 0.7$ is used. The systematic error due to the uncertainty in the shape of the background is not included.

Table 21-3 $\rho_T \to \pi_T Z^0 \to bqll$: Number of signal / Z+jets / $t\bar{t}$ events around the mass peak (see text) of the signal after the application of cuts. The last two lines give the σ x BR predicted by the model with the assumed values of the parameters, as well as the $\sigma \times BR$ required for a 5σ significance, with 30 fb^{-1}.

	case (b): m(ρ_T)=500, m(π_T)=300 GeV	**case (c): m(ρ_T)=800, m(π_T)=500 GeV**	**case (d): m(ρ_T)=800, m(π_T)=250 GeV**
Number of events	115 / 148 / 17	48 / 43 / 2	11.5 / 49 / 0
$S/\sqrt{B}$	8.9	7.1	1.6
σ x BR model	0.104	0.018	0.0059
σ x BR for 5σ	0.058	0.013	0.018

21.2.1.3 $\rho_T^{\pm} \to W^{\pm} \pi_T^0 \to l \nu b \bar{b}$

With the multiscale technicolor model parameters used, the branching ratio $BR(\rho_T^{\pm} \to W^{\pm} \pi_T^0)$ = 36.3%, 38.2% and 13.2% for cases (b), (c) and (d) respectively. The π_T^0 decays 90% of the time to $b\bar{b}$ (assuming that the $t\bar{t}$ channel is closed, as in the TC2 model.). It is to be noted, however, that decay of a coloured neutral technipion to a pair of gluons may have a dominant branching ratio. This case has been analysed for Tevatron energy [21-16]. The backgrounds considered here are: $t\bar{t}$, W + *jets* (consisting of: $qq \to W$, $qq \to gW$, $qq \to WW$ and $qg \to qW$), Z+jets and WZ.

In the present analysis events are selected according to the following criteria:

- A preselection: one lepton having $p_T > 30$ GeV and two reconstructed b jets are required in the central region, $|\eta| < 2$. The most energetic b-jet must have $p_T > 100$ GeV and the other $p_T > 50$ GeV. The missing transverse energy should be $E_T^{miss} > 50$ GeV.
- Efficient reduction of the dominant tt background can be achieved by applying a jet veto. No extra jet, with $p_T > 40$ GeV, besides the two b-jets is allowed.
- The W is reconstructed from the lepton and E_T^{miss} four-momenta (the longitudinal momentum of the neutrino is calculated to give the correct W mass, up to a two-fold ambiguity). The two corresponding solutions for the reconstructed mass of the ρ_T must not differ significantly: $|m_{lvbb}(1) - m_{lvbb}(2)| < 80$ GeV This cut is found to be efficient at rejecting events which do not contain a W and for which the two solutions are very different. Only events having $m_{bb} > 150$ GeV and $m_{lvbb} > 300$ GeV are kept.
- For each of these solutions, the following cut is applied: in the rest frame of the $l\nu b\bar{b}$ system, the decay angle with respect to the direction of the ρ_T must be $|\cos\hat{\theta}_{lvbb}| < 0.6$. The importance of this cut is seen in Figure 21-5.

Figure 21-6 shows the signals and backgrounds expected with the above selection after 30 fb^{-1} of integrated luminosity. Both solutions are included in the histogram, with weight 0.5 each. Clear signals can be seen above background for some of the above cases, although poor m_{bb} resolution is obtained. These could be used to confirm discovery in the channel discussed above. The significance obtained for the signals is given in Table 21-4. Also shown in the table are the $\sigma \times BR$ required for a 5σ significance. The uncertainty in the shape of the background can be an important systematic error.

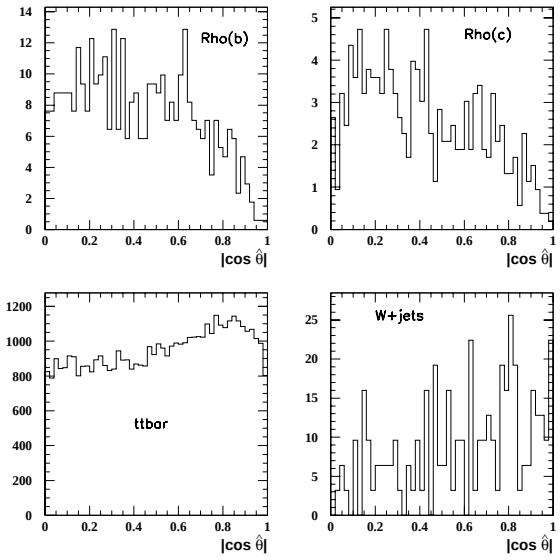

Figure 21-5 $\rho_T^{\pm} \to W^{\pm} \pi_T^0 \to l^+ \nu\ b\ \bar{b}$*:* Distribution of $|\cos\hat{\theta}_{lvbb}|$ for cases (b) and (c) as well for the $t\bar{t}$ and *W*+jets backgrounds.

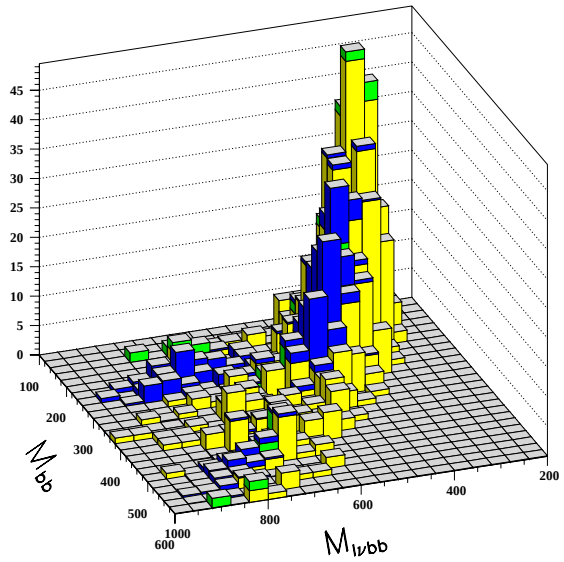

Figure 21-6 Reconstructed mass of the ρ_T candidates vs mass of the p_T candidates for the channel $\rho_T \to W^{\pm} \pi_T^0 \to l^+\nu\ b\bar{b}$. From lightest to darkest: *W* + jets background, $t\bar{t}$ background and the signals for three cases (b), (c) and (d). The statistical fluctuations are exaggerated.

Table 21-4 $\rho_T^{\pm} \to W^{\pm} \pi_T^0 \to l^+\nu\ b\ b$*:* Number of signal/ $t\bar{t}$ / (*W*+jets and *Z*+jets) events around the mass peak (see text), after the application of cuts. The last two lines give the $\sigma \times BR$ predicted by the model, with the assumed values of the parameters, as well as the $\sigma \times BR$ required for a 5σ significance of the signal, for an integrated luminosity of 30 fb^{-1}

	case (b) **m(ρ_T)=500, m(π_T)=300 GeV**	**case (c)** **m(ρ_T)=800, m(π_T)=500 GeV**	**case (d)** **m(ρ_T)=800, m(π_T)=250 GeV**
Number of events	86 / 165 / 5	24 / 118 / 10	12 / 5 / 0
$S/\sqrt{B}$	6.6	2.1	5.3
σ x BR (pb), model	0.336	0.064	0.021
σ x BR (pb), 5σ	0.255	0.15	0.02

21.2.1.4 $b\bar{b}$ resonance

Single production of pseudo-Goldstone bosons such at η_8 is observable, given a large enough cross section. Coloured technipions are, in particular, more likely to be detected since colour counting factors make their production cross section through *gg* fusion larger than for colour singlet ones. The decay to *gg* pairs compete, however, with the $b\bar{b}$ channel and may actually

dominate. Other $b\bar{b}$ resonances are predicted by topcolor models, where the topgluon splits into heavy quarks. The mass reach of such topgluons at the Tevatron (2 fb^{-1}) has been estimated at close to 1 TeV, depending on the width [21-17].

η_8 production is implemented in PYTHIA according to the one-family model [21-18][21-19]. The production mechanism is similar to a Standard Model Higgs boson via *gg* fusion, but is enhanced by the large number of techniquarks that can appear in the loop. This process is used here to estimate the observability of a generic $b\bar{b}$ resonance. The mass has been chosen to be 300 GeV, *i.e.* below the $t\bar{t}$ threshold. Generic vector resonances, such as a topgluon, of masses 500, 1000 and 2000 TeV are also studied. The backgrounds considered for this process are: hard QCD and $t\bar{t}$.

To extract the signal, the only selection was to require at least two identified *b*-jets with a minimum value of p_T in the region $|\eta| < 2$. For a 300 GeV resonance, LVL1 trigger J75 x 3 will be required (see Chapter 11.3.2), whereas for a 500 GeV resonance or above, single jet trigger J180 will suffice. (A prescaled single jet trigger could also be used.) Events having a third high p_T jet are rejected; the threshold is shown in Table 21-5 which also shows the required σ x BR for a 5 σ discovery limit. In this study, the assumed intrinsic widths of the resonances were very narrow. For a wider resonance, the intrinsic width must be added in quadrature with σ_m, shown in Table 21-5 and a new estimate of σ *x BR* can be obtained. In each case, the resonance would be seen as a small, but statistically significant peak, on top of a large, steeply falling, background.

Table 21-5 Discovery limits, after 30 pb^{-1}, for narrow $b\bar{b}$ resonances of different masses, after cuts on the minimum p_T of the reconstructed *b* jets, and a maximum p_T of any third jet. Also shown is the approximate width of the reconstructed resonance.

$m_{b\bar{b}}$	p_{Tmin} (b_1/b_2)	p_{T3} (max)	σ_m (GeV)	σ x BR (5σ) (pb)
300	75 / 75	100	37	13
500	180 / 50	50	60	7.0
1000	200 / 100	100	70	0.57
2000	300 / 200	100	160	0.11

21.2.1.5 $t\bar{t}$ resonances

The general case of $t\bar{t}$ resonances is discussed in Section 18.1.4.2. Here, the case of single production of a technipion, sufficiently massive to decay to $t\bar{t}$ pairs, $m_{t\bar{t}}$ = 500 GeV, is studied. Although the decay of a technipion to $t\bar{t}$ is highly suppressed in topcolor assisted technicolor models, other resonances, such as a topgluon are predicted in this model. As in Section 21.2.1.4 above, the process of η_8 production as implemented in PYTHIA is used here. An intrinsic width Γ (= 2.35 σ_m) of 57 GeV is assumed for this generic resonance.

The backgrounds considered are (i) *W*+jets (generated with $\hat{p}_T$ > 80 GeV) – Only events having at least one lepton and one *b*-jet (before *b*-tagging) have been generated for this analysis (ii) $t\bar{t}$, with a requirement of $\hat{p}_T$ > 80 GeV – Only events with one lepton have been generated; and (iii) hard QCD (with $\hat{p}_T$ > 80 GeV and $\hat{s}$ > (200 GeV)^2). The cuts applied at generator level do not affect significantly the results below.

The mass of the resonance is reconstructed by looking for the channel $t\dot{t} \rightarrow l\nu bbjj$. The following selection criteria are applied:

- One lepton is required for the trigger, with $p_T > 20$ GeV, within $|\eta| < 2$.
- Two b jets are required, with $p_T > 60$ GeV and 40 GeV respectively, and within $|\eta| < 2$. Two additional jets, not identified as b-jets are required, with $p_T > 50$ and 40 GeV, also within $|\eta| < 2$.
- E_T^{miss} must be greater than 20 GeV.

At that point, the W from the $t \to W\,b \to l\,\nu\,b$ decay is reconstructed, using E_T^{miss} and the lepton momentum. There is a two-fold ambiguity in the solution. There is also a two-fold ambiguity in assigning the two highest p_T b-jets to the two highest energy light-quark jets. These ambiguities are resolved by choosing the solution that gives top masses closest to the true mass of the top (175 GeV). The cut is then $160 < m_t^l < 195$ GeV and $160 < m_t^h < 220$ GeV, where m_t^l and m_t^l are the reconstructed masses of the top quarks for which the W decays leptonically and hadronically, respectively.

This simple procedure gives top-mass resolution as shown in Figure 21-7. The $t\bar{t}$ resonance mass is then reconstructed $t\bar{t}$ with a resolution of about 57 GeV. The required σ x BR for a 5σ discovery limit is then 9.9 pb, for an integrated luminosity of 30 fb^{-1}.

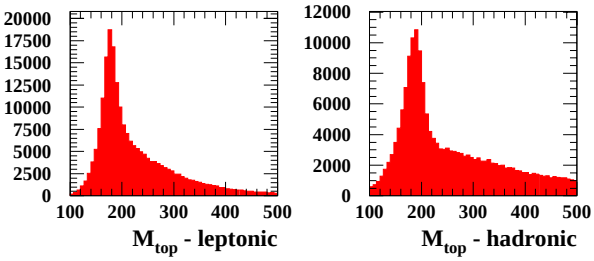

Figure 21-7 $t\bar{t}$ resonance: reconstructed masses of top in $t\bar{t}$ decays. The left histogram shows the mass of the top for which the W decays leptonically and the one on the right shows the mass of the other top, with leptonic decay of the W.

Table 21-6 shows the result of extending this study to larger masses. It shows the rates needed for these heavier cases to be found by ATLAS.

Table 21-6 Masses and natural widths assumed for the study of technicolor η_8 resonances. Also shown are the minimum values of $\sigma \times$ BR necessary for a 5σ discovery significance of $\eta_8 \to t\bar{t}$ for integrated luminosities of 10 fb^{-1} and 100 fb^{-1}.

m($t\bar{t}$)	$\Gamma(t\bar{t})$	$\sigma \times$ BR [pb]	
[GeV]	[GeV]	10 fb^{-1}	100 fb^{-1}
500	57	17.0	5.5
750	107	12.0	3.8
1000	152	5.0	1.6

21.2.1.6 $\omega_T \rightarrow \gamma \pi_T^0 \rightarrow \gamma b\bar{b}$

The ω_T^0 particle is a vector particle of isospin 0. One of its clean decay modes is $\omega_T \rightarrow \gamma \pi_T^0$. A search for this particle has been performed by CDF [21-20]. Here, two cases have been investigated: (i) $m_{\omega T}$ = 500 GeV, with width 0.32 GeV and m_π=300 GeV. The cross section for production is 0.51 pb, according to the model used here [21-13][21-14], as implemented in PYTHIA, and the branching ratio to $\gamma \pi_T^0$ is 87%.;(ii) $m_{\omega T}$ = 800 GeV, with width 1.0 GeV and m_π=500 GeV. The cross section for production is 0.093 pb, and the branching ratio to $\gamma \pi_T^0$ is 94%. This assumed branching ratio does not account for decays to transversely polarised gauge bosons [21-15].

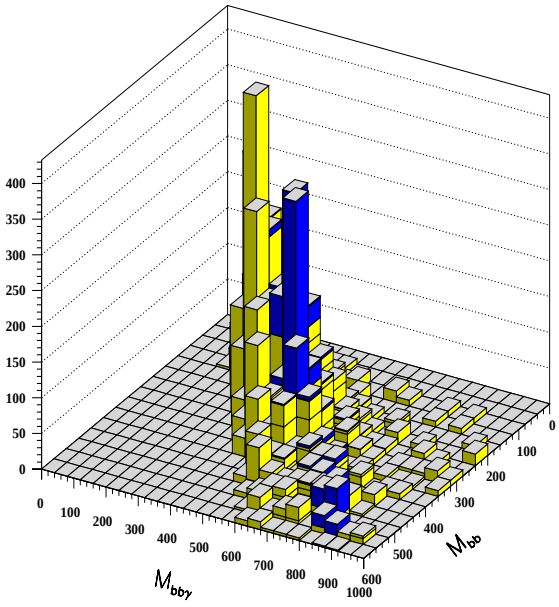

Figure 21-8 $\omega_T \rightarrow \gamma \pi_T^0 \rightarrow \gamma\, b\, b$*:* Reconstructed masses of $b\bar{b}$-jet system versus the mass of the $\gamma\, b\bar{b}$ system. Two scenarios are considered for the signal: ω_T of masses 800 GeV and 500 GeV decaying to π_T of masses 500 GeV and 300 GeV respectively. The signals are in dark shade. In light shade is the prompt photon background.

For the simulation of the background, a Monte Carlo program for $\gamma b\bar{b}$, provided by [21-21] was used. Also included are backgrounds from $qq \rightarrow \gamma g$, $qg \rightarrow \gamma q$ and $g\, g \rightarrow \gamma g$. Backgrounds from misidentified photon jets are not taken into account. The rejection that ATLAS obtains is large enough so that these backgrounds due to misidentification are small. (See the discussion of $h \rightarrow \gamma\gamma$ in Chapter 19.2.2)

To extract the signal, the selection criteria are:

- the presence of one photon with $p_T^\gamma > 50$ GeV within $|\eta| < 2$;
- the presence of two identified *b*-jets, each having $p_T > 40$ GeV and falling within $|\eta| < 2$;
- the difference in azimuthal angles between the two *b*-jets must be >2 radians, as they are expected to be mostly back to back for a heavy decaying system.

With these selection criteria, the signals that remain are shown in Figure 21-8. There is a significant signal for both masses of ω_T. Table 21-7 gives the observed significances and σ x BR required for a 5 σ significance after 30 fb^{-1} for both the lower and higher mass ω_T,in the mass windows [$250 < m_{bb} < 350$; $180 < m_{\gamma bb} < 220$}] and [$400 < m_{bb} < 600$; $280 < m_{\gamma bb} < 230$}] respectively.

21.2.2 Signals from vector boson fusion

Production of the ρ_T by vector boson fusion is potentially very interesting since it probes the coupling to gauge bosons and since the requirement of forward jets resulting from the scattered primary quarks provides a powerful method of background rejection.

Table 21-7 $\omega_T \to \gamma \pi_T^0 \to \gamma\, b\, b$**:** Number of signal/γ+jets events around the mass peak of the signal, for an integrated luminosity of 30 fb^{-1}. The σ *x BR* predicted by the model, with the assumed values of the parameters, and the σ x BR required for a 5σ significance of the signal are also shown.

	$m(\omega_T)$= 500 GeV	$m(\omega_T)$=800 GeV
Number of events	612 / 105	174 / 24
$S/\sqrt{B}$	60	35
$\sigma \times$ BR (pb), model	0.161	0.033
$\sigma \times$ BR (pb) 5σ	0.013	0.0046

As an example of this calculation, the same case as Section 21.2.1.3: $\rho_T^{\pm} \to W^{\pm} \pi_T^0 \to l\, \nu\, b\, \bar{b}$, ($l$ = μ, e) with $m_{\rho T}$ = 800 GeV and $m_{\pi T}$ = 500 GeV (case (c)) is considered here. For this process, $\sigma \times BR$ is about 2.5 fb [21-22]. Because it involves the $W Z \rho_T$ vertex, as well as the $\rho_T W \pi_T$ vertex, the cross section depends sensitively on the assumed value of the mixing angle sin χ between the longitudinal gauge boson and the technipion. The same background Monte Carlo samples as in Section 21.2.1.3 are used. The following cuts are applied on both the signal and background.

- The presence of at least one lepton (p_T > 20 GeV) and two reconstructed *b*-jets (p_T > 50 GeV) is required in the central region $|\eta| < 2$. The missing transverse energy must be greater than 20 GeV.
- Since the ρ_T is colour neutral, a central jet-veto ($|\eta| < 2$) helps reject the $t\bar{t}$ background.
- A forward and a backward jet are required, with p_T > 80 GeV and $1.5 < |\eta| < 3.5$ for the first jet and p_T > 50 GeV and $1 < |\eta| < 4$ for the second jet.

Given a $\sigma \times$ BR of only 2.5 fb, the resulting signal would be 2.6 events on a background of about 5.6, for an integrated luminosity of 30 fb^{-1}. This process of vector boson fusion with forward tagging of jets could complement the $q\bar{q}$ fusion process, but would not be a discovery channel unless the $\sigma \times$ BR is at least 10 fb.

21.2.3 Conclusion

The ATLAS detector will be sensitive to the new resonances predicted in technicolor theory, up to the TeV range. Although the parameter space is very large, the number of potential channels allows for combinations of signatures to help in understanding the nature of the resonances, and determine the possible existence of techniparticles.

21.3 Search for excited quarks

The replication of three generations of quarks and leptons suggests the possibility that they are composite structures made up of more fundamental constituents. The existence of such quark and lepton substructure leads one to expect a rich spectrum of new particles with unusual quantum numbers such as excited quarks and leptons, leptoquarks, diquarks, dileptons, *etc.* Since no satisfactory, theoretically consistent composite model yet exists, here the excited quarks are taken into account as composite particles. The regions of compositeness scale Λ are given as

- $\Lambda \gg \sqrt{\hat{s}}$, contact and anomalous interactions;
- $\Lambda \ll \sqrt{\hat{s}}$, resonance productions, excited quarks or di-quarks, pair or single production of new particles;
- $\Lambda \approx \sqrt{\hat{s}}$, model dependent interactions.

In this study, it is assumed that the compositeness scale Λ is less than the LHC energy. Gauge interactions are assumed to dominate over contact interactions when the masses of excited quarks are equal to the compositeness scale. Only, spin-1/2 excited states of the first generation, $q^* = u^*, d^*$ are considered. The coupling between excited (right-handed) quarks, ordinary (left-handed) quarks and gauge bosons is given by the effective Lagrangian of the magnetic moment type [21-23];

$$L = \frac{1}{2\Lambda}\bar{q}^*_R\sigma^{\mu\nu}\left(g_s f_s\frac{\lambda}{2}G^a{}_{\mu\nu} + gf\frac{\tau}{2}\cdot W_{\mu\nu} + g' f'\frac{Y}{2}B_{\mu\nu}\right)q_L$$

where $G^a_{\mu\nu}$, $W_{\mu\nu}$ and $B_{\mu\nu}$ are the field-strength tensors of the SU(3), SU(2) and U(1) gauge fields; λ_a, τ and Y are the corresponding gauge structure constants; and g_s, g and g' are the gauge coupling constants. Finally, f_s, f and f' are parameters determined by the composite dynamics.

The production of the first generation excited quarks u^*, d^* by quark-gluon fusion process $qg \to q^*$ is studied at the LHC [21-24]. Here, the quark from q^* decay was assumed to correspond to the leading jet with the highest transverse momenta in the event. The signal consists of a high energy jet resulting from the hadronisation of the final state quark and a photon which form a peak in photon+jet invariant mass distribution $m_{\gamma j}$.

CDF excludes the following mass ranges for the excited quarks: 80 GeV < m^* <460 GeV from $q^* \to q\gamma$, 150 GeV < m^* < 530 GeV from $q^* \to qW$ [21-25]. The D0 Collaboration has performed a search for excited quarks and excludes the mass range 200 GeV < m^* < 720 GeV [21-26]. Combining the all channels, CDF excludes the range 200 GeV < m^* < 760 GeV [21-27]. These exclusions are for the couplings $f = f' = f_s = 1$. Since the mass limit is sensitive to the choice of couplings, the excluded regions decrease slightly for smaller couplings.

21.3.1 The widths of excited quarks

An excited quark decays to a light quark and a gauge boson through the effective lagrangian above. Assuming $m^* > m_{W,Z}$ and neglecting ordinary quark masses, the partial decay widths for the various electroweak and QCD channels are ($V = W, Z$):

$$\Gamma(q^* \to qV) = \frac{1}{32\pi}g_V^2 f_V^2\frac{m^{*3}}{\Lambda^2}\left(1-\frac{m_V^2}{m^{*2}}\right)^2\left(2+\frac{m_V^2}{m^{*2}}\right),$$

$$\Gamma(q^* \to q\gamma) = \frac{1}{4}\alpha f_\gamma^2\frac{m^{*3}}{\Lambda^2} \text{ , and } \Gamma(q^* \to qg) = \frac{1}{3}\alpha_s f_s^2\frac{m^{*3}}{\Lambda^2}$$

with $f_Z = fT_3\cos^2\theta_W + f'\frac{Y}{2}\sin^2\theta_W$, $f_W = f/\sqrt{2}$ and $f_\gamma = fT_3 + f'Y/2$, where T_3 being the third component of the weak isospin, and Y being the hypercharge of q^*. Here, $g_W = e/\sin\theta_W$ and $g_Z = g_W/\cos\theta_W$ are the Standard Model W and Z coupling constants.

Table 21-8 The total decay width, Γ, of excited quarks into ordinary quarks and gauge bosons $V = g, W, Z, \gamma$ and relative branching ratios $BR = \Gamma(q^* \to qV)/\Sigma_V \Gamma(q^* \to qV)$ for $f = f' = f_s = 1$.

	$m^* = \Lambda =$ **1000 GeV**		$m^* = \Lambda =$ **3000 GeV**	
Decay mode	Γ **(GeV)**	BR	Γ **(GeV)**	BR
$d^* \to all$	37.3	1.0	102.	1.0
$d^* \to dg$	30.9	0.827	82.4	0.806
$d^* \to uW$	4.26	0.114	13.1	0.128
$d^* \to dZ$	1.98	0.0529	6.07	0.059
$d^* \to d\gamma$	0.22	0.0059	0.673	0.00666
$u^* \to all$	37.3	1.0	102.1	1.0
$u^* \to ug$	30.9	0.8267	82.4	0.806
$u^* \to dW$	4.26	0.114	13.01	0.128
$u^* \to uZ$	1.32	0.0353	4.05	0.0397
$u^* \to u\gamma$	0.87	0.0236	2.69	0.0264

The widths of an excited quarks decaying into a jet and a photon are small compared to the total widths as shown in Table 21-8. The total decay widths for the excited quarks (u^*, d^*) approximately 37 GeV and 102 GeV if the masses are set to $m^* = \Lambda = 1$ TeV and $m^* = \Lambda = 3$ TeV, respectively. Here, it is assumed that excited quarks (u^*, d^*) are degenerate in mass and the compositeness scale is chosen to be $\Lambda = m^*$. The total width is less than the di-jet mass resolution of ATLAS (See Chapter 9.3).

21.3.2 Simulation of the signal and backgrounds

The simulation of the excited quark signal (photon+jet) and relevant backgrounds was performed with ATLFAST [21-12]. Jets are formed within a cone of radius $\Delta R = 0.7$ and required to have transverse energy $E_T > 15$ GeV. Photons are considered isolated if they are separated from other jets by $\Delta R > 0.4$ and have maximum transverse energy $E_T < 10$ GeV deposition in cells in a cone $\Delta R = 0.2$ around the photon in $\eta - \phi$ space.

The processes $ug \to u^* \to u\gamma$, and $dg \to d^* \to d\gamma$ are considered.The main backgrounds from prompt photon production are given by the processes $q_i g \to q_i \gamma$, $q_i \bar{q}_i \to g\gamma$, $gg \to g\gamma$ which are referred to as background I. Backgrounds from single production of W/Z are given by $q_i \bar{q}_i \to Z\gamma$, $q_i \bar{q}_j \to W\gamma$ are referred to as background II.

The signal appears as a peak in the photon+jet invariant mass $m_{\gamma j}$. The partonic level information from PYTHIA-5.7 [21-11] for the decay products of excited quarks are shown in Figure 21-9 and Figure 21-10. The production cross sections times branching ratios for different coupling and mass of excited quarks are given in the Table 21-9. Hereafter, the cross section times branching ratio of the process is defined by σ. Photons and jets have sufficiently high transverse momenta and they are emitted predominantly in the barrel region, see Figure 21-10. The jet and photon are required to have $p_T^{\gamma, j} > 100$ GeV in the pseudorapidity range $|\eta^{\gamma, j}| < 2.5$. These cuts have approximately 30% acceptance.

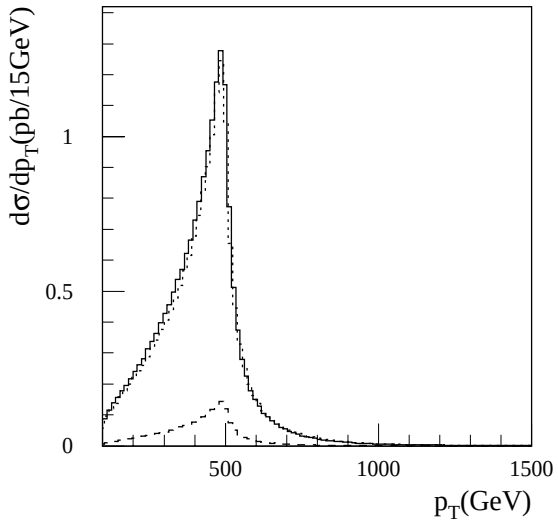

Figure 21-9 Transverse momentum distributions for excited quark signal with the scale $\Lambda = m^* = 1$ TeV and coupling $f = f' = f_s = 1$. Solid line denotes photon distributions while dotted and dashed lines are for *u*-quark and *d*-quark distributions, respectively.

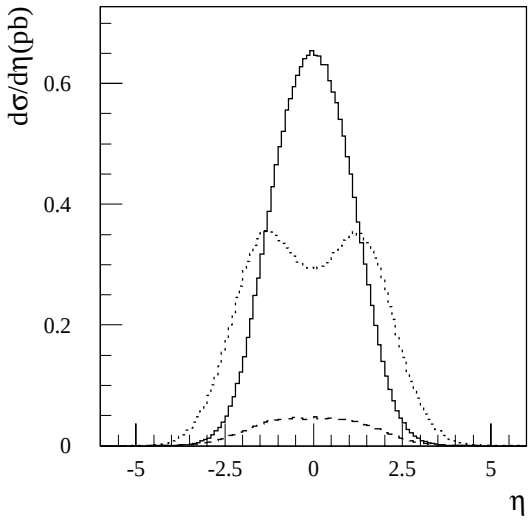

Figure 21-10 Pseudorapidity distributions for excited quark signal with the scale $\Lambda = m^* = 1$ TeV and coupling $f = f' = f_s = 1$. Solid line denotes photon distributions while dotted and dashed lines are for *u*-quark and *d*-quark distributions, respectively.

The main background is a prompt photon production associated with an energetic jet.

Table 21-9 The cross section times branching ratios, $\sigma(pb)$, for the signal at parton level are generated by PYTHIA-5.7. The values are given for the scale $\Lambda = m^*$ and the couplings for $f = f' = f_s$.

f	$m^* = 1000$ GeV	$m^* = 3000$ GeV	$m^* = 5000$ GeV
1.0	21.34	7.544×10^{-2}	1.335×10^{-3}
0.5	5.373	1.933×10^{-2}	3.334×10^{-4}
0.1	2.143×10^{-1}	8.303×10^{-3}	1.340×10^{-5}
0.05	5.352×10^{-2}	1.936×10^{-4}	3.361×10^{-6}
0.01	2.144×10^{-3}	7.747×10^{-6}	1.338×10^{-7}

Figure 21-11 and Figure 21-12 show the photon+jet invariant mass distribution for the backgrounds as well as the signal at different mass values and couplings

In order to evaluate the signal significance, the photon+jet invariant mass distribution is integrated around the excited quark masses. The bin width $\Delta m_{\gamma j}$ over which the integration is performed varies as the peak of the signal widens and is taken to be $\Delta m_{\gamma j} = 135$ GeV–$\Delta m_{\gamma j} = 690$ GeV for excited quark masses 1-6 TeV. In Table 21-10, we give the partial cross sections times branching ratios $\Delta\sigma$ for both signal, with the coupling parameters $f = f' = f_s = 1$, and the background. For smaller coupling parameters the bin width remains the same. We find an optimal cut on transverse momentum of the jets and photons, $p_T > 300$ GeV for the excited quark mass range 1-2 TeV, and $p_T > 1000$ GeV for the mass range 3-5 TeV. In

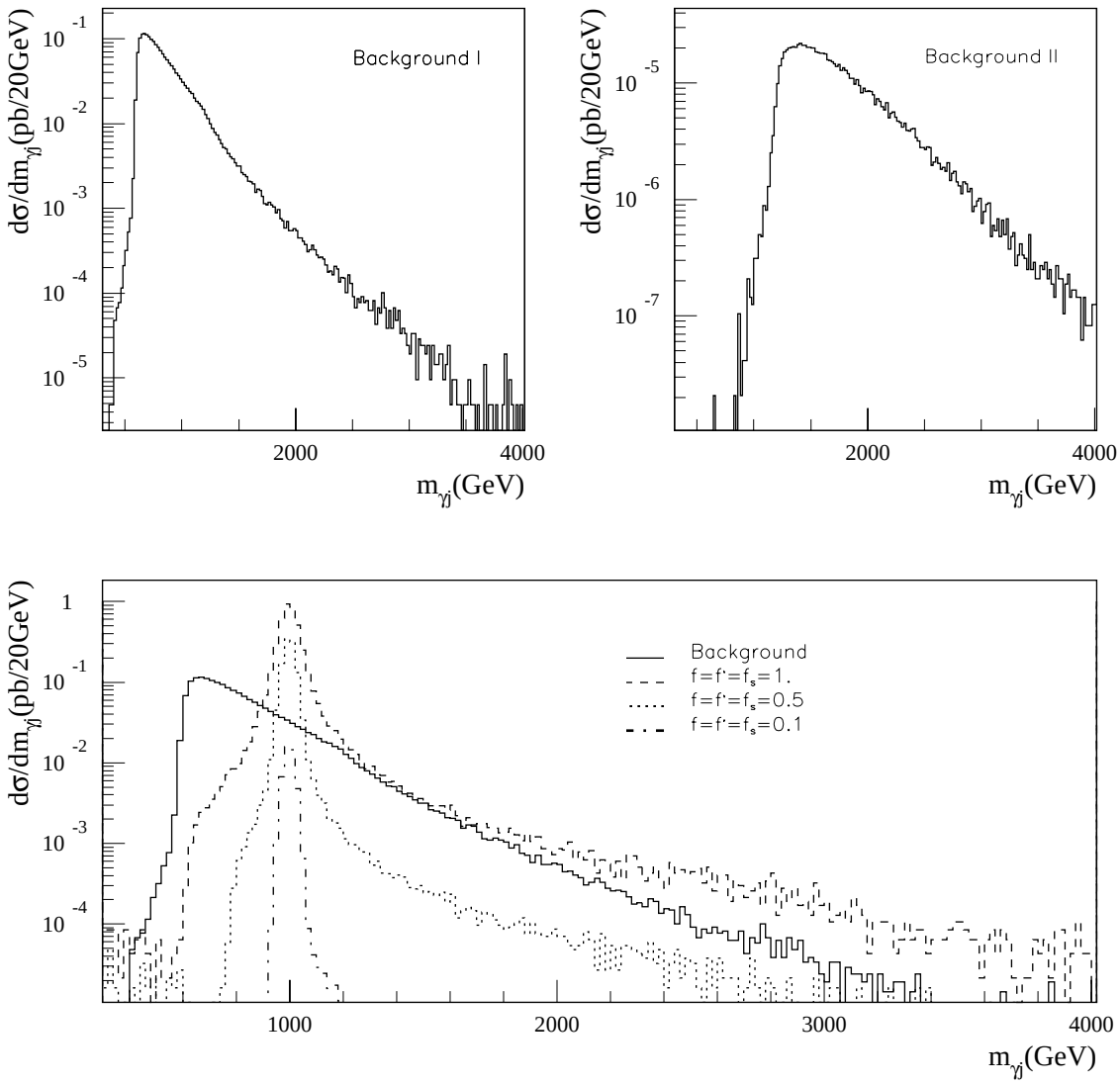

Figure 21-11 Invariant mass distributions for the excited quark signal, and backgrounds with the cuts $p_T > 300$ GeV, $|\eta| < 2.5$ for excited quark mass $m^* = 1000$ GeV. Upper figures show signal and background separately.

Figure 21-13, the expected $q^* \to q\gamma$ signal significances are defined for each mass point as $S/\sqrt{B}$ where S and B being the number of accepted signal and background events in the chosen mass bin for an integrated luminosity of 300 fb^{-1} at LHC.

Achievable mass limits for different coupling values are established by requiring at least 10 signal events and at least 5 standard deviation significance. The discovery reach for the excited quarks at LHC are presented in Figure 21-14 For a coupling $f = f' = f_s = 1$, it is possible to reach up to $m^* = 6.5$ TeV.

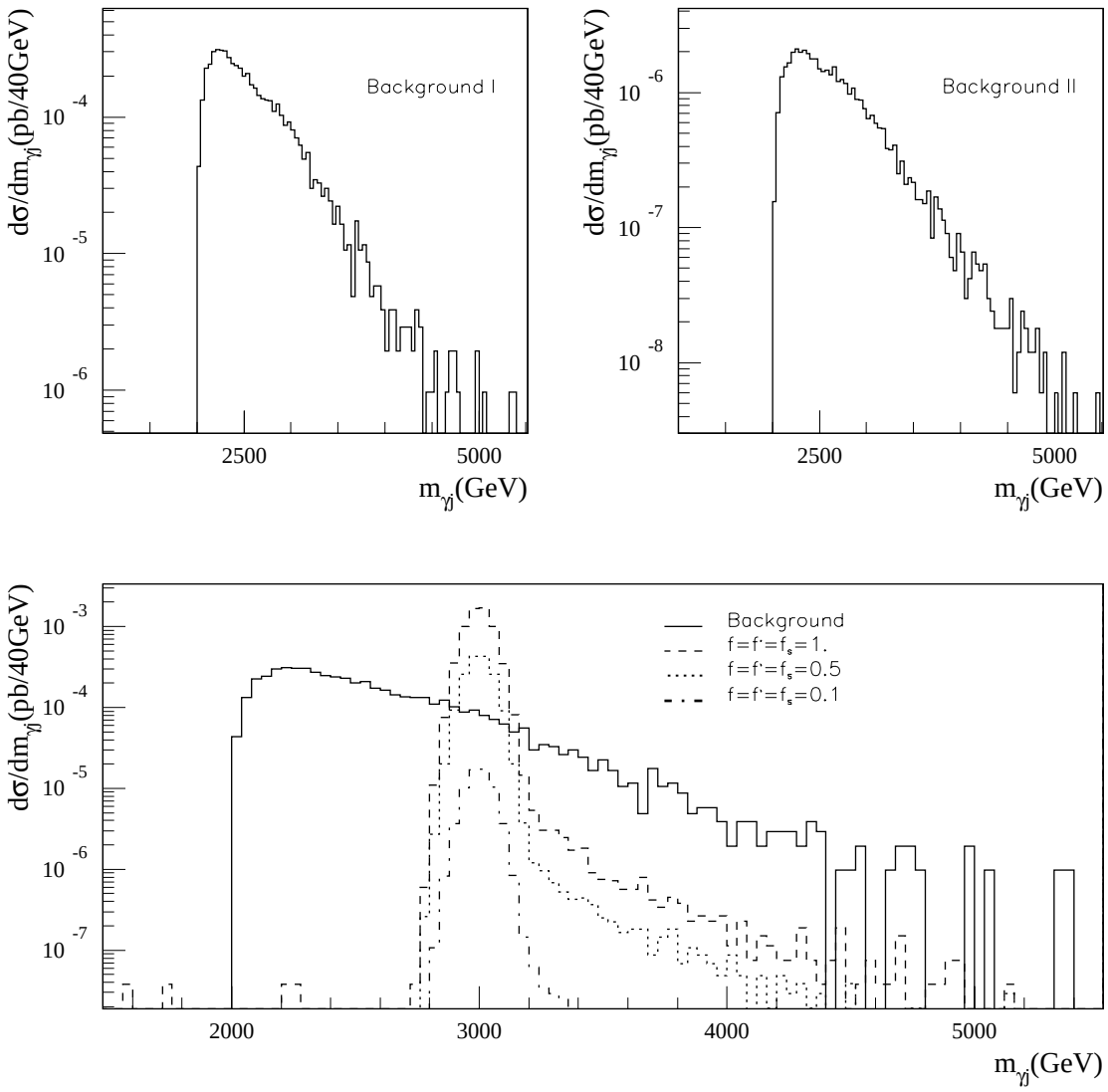

Figure 21-12 Invariant mass distributions for the excited quark signal, and backgrounds with the cuts $p_T > 1000$ GeV, $|\eta| < 1.5$ for the mass $m^* = 3000$ GeV. The upper figures show the background, the lower the signal and background combined

21.3.3 Conclusion

In conclusion, excited quarks are produced with large cross section at LHC. The results are presented for a complete analysis of the excited quark q^* production within the context of a composite model. The signal for d^* production and electromagnetic deexcitation is roughly a factor 8 smaller than for u^*. The excited quark signal (gamma+jet) was found to be dominant over prompt photon production background for the masses greater than 500 GeV. Both signal and background in the photon+jet invariant mass distribution are less by $O(\alpha/\alpha_s)$ relative to their values in the two-jet invariant mass distribution [21-27], but the signal(S)/background(B) ratio would is better in the photon+jet channel.

Table 21-10 Partial cross sections times branching ratios $\Delta\sigma$ for the signal and background are given for the bin width around the excited quark mass peak (within $\pm 2\sigma_m$). The couplings are assumed $f = f' = f_s = 1$, and transverse momentum and pseudorapidity cuts are applied for the optimisation.

m^* (GeV)	$\Delta m_{\gamma j}$ (GeV)	$\Delta\sigma^{signal}$ (pb)	$\Delta\sigma^{backg}$ (pb)
1000	135	3.552	2.312×10^{-1}
2000	255	1.245×10^{-1}	6.951×10^{-3}
3000	355	1.072×10^{-2}	6.125×10^{-4}
4000	490	1.285×10^{-3}	3.452×10^{-5}
5000	590	1.730×10^{-4}	7.553×10^{-6}
6000	690	2.414×10^{-5}	1.425×10^{-7}

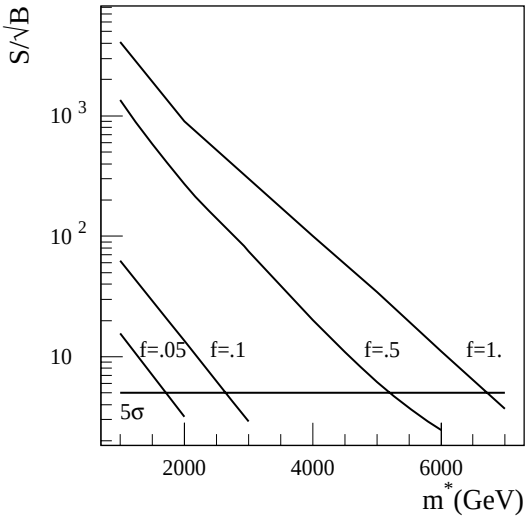

Figure 21-13 Excited quark signal significance for an integrated luminosity of 300 fb^{-1}.

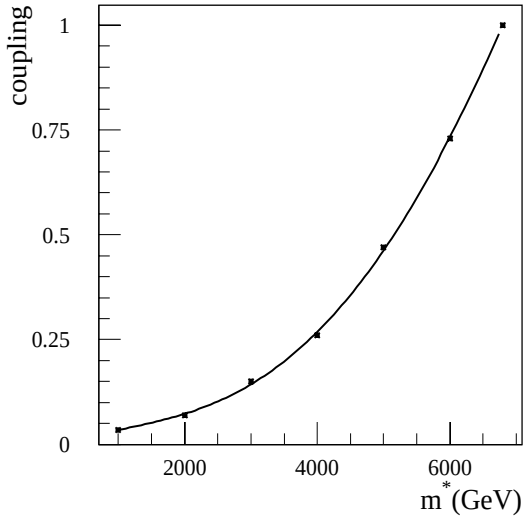

Figure 21-14 Excited quark discovery reach for an integrated luminosity of 300 fb^{-1}.

21.4 Leptoquarks

Leptoquarks (*LQ*s) are predicted in many extensions to the Standard Model, inspired by the symmetry between the quark and lepton generations [21-28]. These particles carry both lepton and baryon quantum numbers and hence couple to both leptons and quarks. Moreover, each fermion generation is associated with a different *LQ*. The various quantum numbers which characterise a given *LQ* are model-dependent, which precludes unique predictions of their properties.

This study considers only a scalar *LQ* of mass larger than 300 GeV and of charge *Q=+2/3* or *Q=-1/3*, which couple only to the first fermion generation. *LQ*s of mass less than this will be observed before LHC data taking begins. The parameter *k* which defines the coupling at the lep-

ton–quark–LQ vertex, is assumed to be unity [21-29]}. Single LQ [21-30] production and LQ pair-production [21-31] have both been studied. Studies have concentrated on the search for a first-generation LQ, assumed to decay 'democratically' 50% of the time to electron+jet.

Single LQ production proceeds via $q + g \rightarrow LQ + l$, where l is either an electron or a neutrino. In 25% of the cases, the final state will then consist of two electrons and one jet. The dominant background arises from Z+jets and top quark production. To minimise these backgrounds, the event selection required two electrons and one jet reconstructed with p_T>300 GeV and within $|\eta| \leq 2.5$ An additional requirement that the dilepton invariant mass be larger than 120 GeV completely eliminates the Z+jet background.

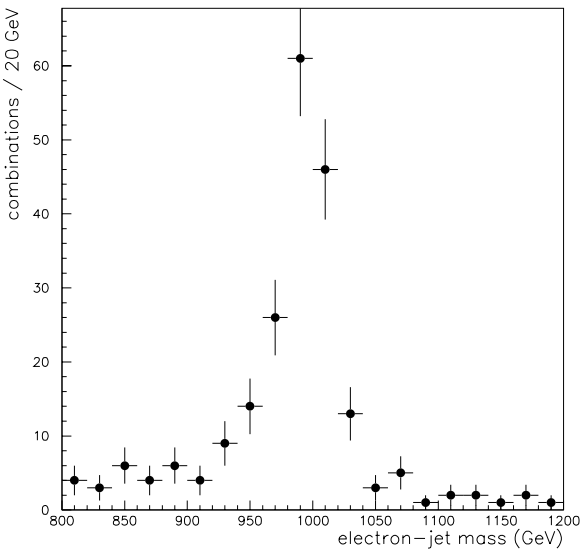

Figure 21-15 >The reconstructed electron+jet invariant mass distribution from pair production of LQ for 100 fb^{-1}.

Leptoquark pair production proceeds dominantly through gluon-gluon fusion, which does not involve any lepton–quark–LQ vertex and therefore is independent of the parameter k discussed above. In 25% of the events, the final state contains two electrons and two jets. The dominant background in this case is also from top pair production. It was reduced to a negligible level by requiring two electrons and two jets with $p_T > 200$ GeV and $|\eta| \leq 2.5$. In these events, both LQ masses were reconstructed above a small combinatorial background. After these cuts, the mass resolution is 27 GeV for m_{LQ} = 1 TeV and increases to 38 GeV for m_{LQ} = 1.5 TeV. Figure 21-15 shows the expected mass distribution for m_{LQ} = 1 TeV above the residual background which is due to top pair production The limit of sensitivity is around 1.5 TeV.

21.5 Compositeness

21.5.1 High-p_T jets

The observation of deviations from QCD predictions of jet rates will reveal new physics such as quark compositeness, the existence of axigluons or other new particles. Measuring the inclusive jet cross section and studying the di-jet mass spectrum and angular distributions are essential tests of QCD; see Chapter 15. The existence of a quark substructure would appear as an excess of high p_T jets compared to that predicted by QCD or as di-jet angular distributions that are more isotropic than that expected in a point-like quark theory. Di-jet angular distributions have been studied by the CDF [21-32] and D0 [21-33] experiments at a centre-of-mass (CM) energy of 1.8 TeV. The highest E_T reached so far at the Tevatron, 440 GeV, corresponds to a distance scale

of order 10^{-19}m. No evidence of quark substructure was found. Previous studies of the di-jet invariant mass spectrum reported by UA1 [21-34], UA2 [21-35] and by CDF [21-36] have also shown that data that were consistent with QCD predictions.

The effect of quark compositeness at the LHC is investigated in this section. To simulate a scenario with quark substructure the event generator PYTHIA-5.7 [21-11] has been used. More details can be found in [21-37]. A simple phenomenological approach is used. This adds contact interactions between quark constituents with a compositeness scale Λ [21-38], where the sign of the effective Lagrangian for a flavour diagonal definite chirality current is positive (destructive interference) or negative (constructive interference). The data simulated in the framework of the *Standard Model* (SM) are compared with those obtained assuming quark compositeness. The simulated event sample included the following hard-scattering final states: *qq*, *qg*, *gg*, $g\gamma$, $q\gamma$, and $\gamma\gamma$. The γ^*/Z, *W*, and $t\bar{t}$ production subprocesses were also enabled. A cut on the transverse momentum of the hard scattering subprocess was set to 600 GeV. Under these conditions, the contributions from the *qq*, *qg* and *gg* processes represent 97% of the cross-section. For the Q^2 scale in the hard scattering 2→2 process, $Q^2 = (m_{T1}{}^2 + m_{T2}{}^2)/2$ was used. Jets were reconstructed using ATLFAST with a cone size $\Delta R = 0.7$. All calorimeter cells with E_T>1.5 GeV are taken as possible initiators of clusters. The total E_T summed over all cells in a cone ΔR should be larger than 15 GeV. Jets were reconstructed down to $|\eta|$=5.0.

21.5.2 Transverse energy distributions of jets.

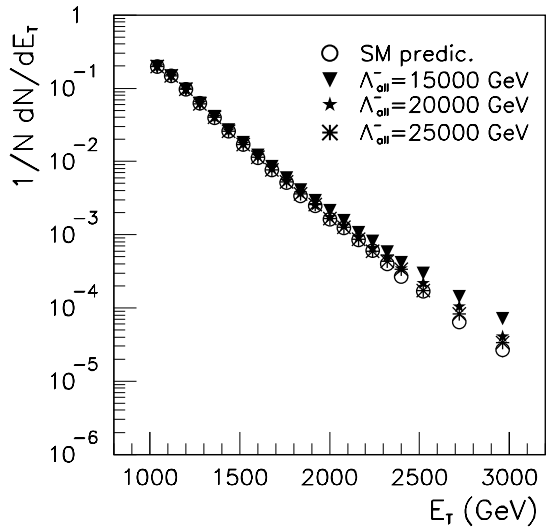

Figure 21-16 E_T distribution for two leading jets showing the Standard model prediction (open circles) and the effect of quark compositeness to the scales indicated. 30 fb^{-1} of integrated luminosity assumed.

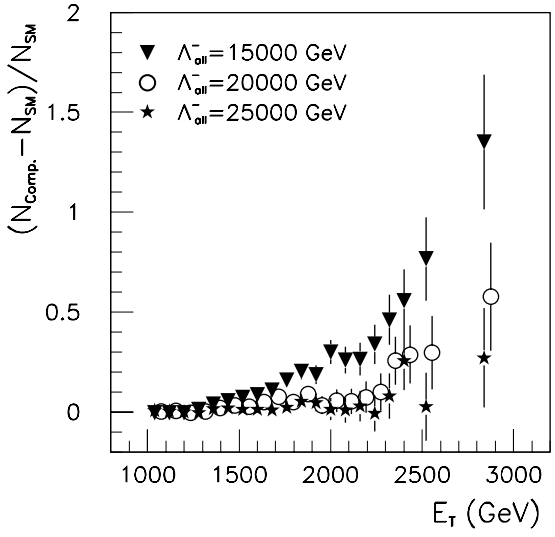

Figure 21-17 Difference of the standard model prediction and the effect of compositeness on the jet E_T distribution, normalised to the Standard Model rate. The errors correspond to 30 fb^{-1}

Figure 21-16 and Figure 21-17 show the effect of compositeness on the inclusive jet energy spectrum. The case of constructive interference is shown; the destructive case is similar. Only events with two jets of E_T> 400 GeV are included. Figure 21-17 shows the deviation from the Standard

Model prediction assuming that all quarks are composite. This figure emphasises that the deviation is significant only for the largest values of E_T Figure 21-18 and Figure 21-19 show the effects on the jet E_T distribution for 300 fb^{-1} of integrated luminosity and larger values of Λ.

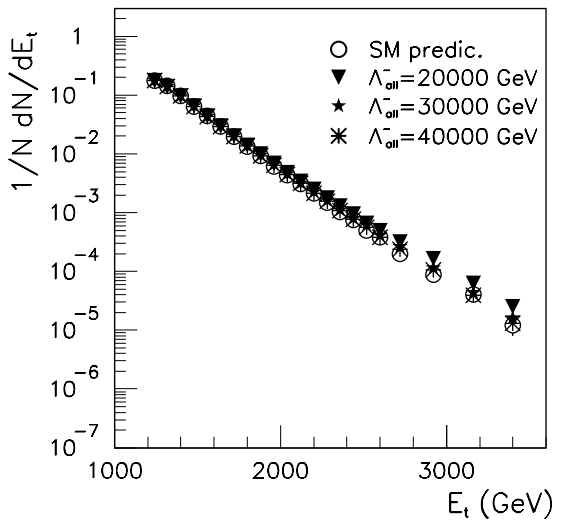

Figure 21-18 E_T distribution for two leading jets showing the Standard Model prediction (open circles) and the effect of quark compositeness to the scales indicated. 300 fb^{-1} of integrated luminosity assumed.

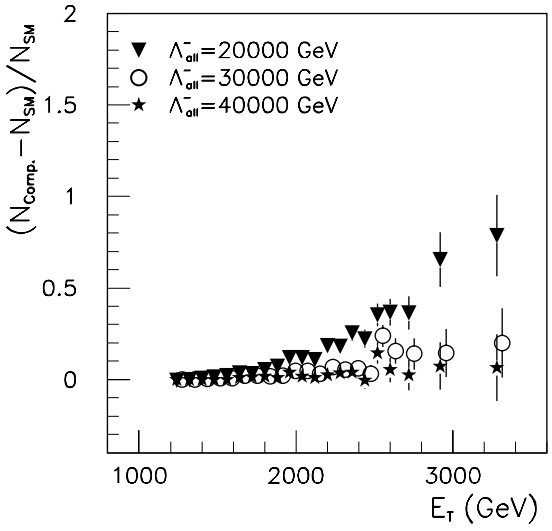

Figure 21-19 Difference of the Standard Model prediction and the effect of compositeness on the jet E_T distribution, normalised to the Standard model rate.The errors correspond to 300 fb^{-1}.

The effects of compositeness could be masked by uncertainties in the parton distribution functions (pdf's). Figure 21-20 shows a band corresponding to the results obtained with all the pdf's in PYTHIA 5.7 (except for DO1 and EHLQ1 which have large inconsistencies with present data, see also Figure 15-23). This figure should be compared to Figure 21-18. While the differences shown here are comparable to the effects of compositeness for $\Lambda > 15000$ GeV, the allowed range of pdf's will be further constrained by the time that LHC starts running. Furthermore, as will be shown below, the angular distributions are rather insensitive to pdf's.

The non-linear response of the hadron calorimeter can mask the true difference between the SM and a compositeness scenario, or fake a compositeness signal. To study this effect, the non-linearity of the jet E_T scale was parametrised by the relation [21-39]

$$E_{\mathrm{T}}(\mathrm{meas}) \;=\; E_{\mathrm{T}} \cdot \frac{1}{c(1 + (e/h - 1) \cdot b \cdot \ln E_{\mathrm{T}})}$$

where e/h = 1.36 and c is adjusted such that at 500 GeV the scale is unchanged. The parameter b controls the size of the non-linearity. After correction the residual uncertainty can be parametrised by this formula with b = 0.025 and corresponds to a 1.5% non-linearity at 3 TeV If no correction is made then b = 0.11 and there is a 5% on-linearity at 3 TeV. More details can be found in Section 9.1.1.3.

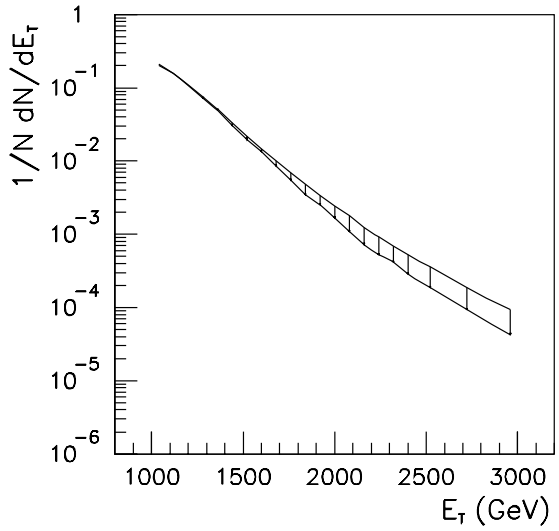

Figure 21-20 The jet E_T spectrum showing the uncertainty from present pdf's; 30 fb-1 assumed.

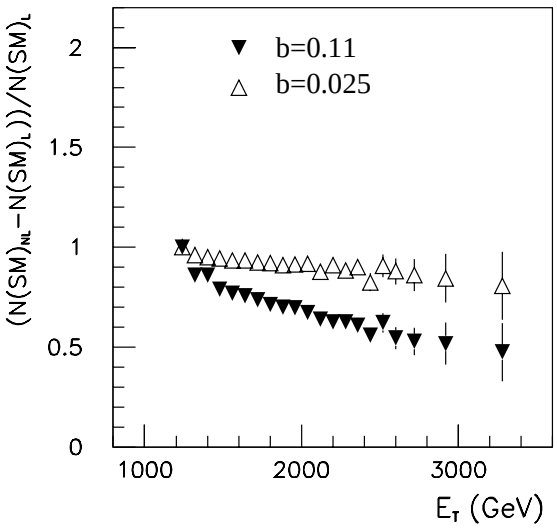

Figure 21-21 The fractional difference between the E_T spectrum measured by a linear and non-linear calorimeter. The curves are normalised at 1.25 TeV.

The effect of non-linearity shown in Figure 21-21. The figure shows the fractional deviation of the transverse energy spectrum as measured by a non-linear calorimeter to that expected from a linear one. The rates are normalised to be equal at 1.25 TeV. Two non-linearities are shown corresponding to b = 0.025 and b = 0.11. It can be seen by comparing this plot to that of Figure 21-19 that, in the worse case, the effect of a nonlinearity is similar in magnitude to that due to a composite scale of 20 TeV, and that if the 1.5% non linearity can be achieved then it is comparable to the 30 TeV case.

In order to assess the sensitivity of the E_T spectrum to the composite scale the event excess above some value of E_T is needed. If N is the number of events in the E_T spectrum, define

$$R = \left(\frac{N(E_T > E_T^0)}{N(E_T < E_T^0)}\right)_{comp} \Big/ \left(\frac{N(E_T > E_T^0)}{N(E_T < E_T^0)}\right)_{SM}$$

With the choice E_T^0 = 1500 GeV one can conclude that ATLAS is sensitive at 95% confidence to values of Λ as large as 25 (40) TeV for 30 (300) fb^{-1}. If this sensitivity is to be achieved then the calorimeter non-linearity must be understood at the 1.5% level.

21.5.3 Jet angular distributions.

The angular distribution of the jets are more sensitive to compositeness signals than the jet transverse energy spectrum and less susceptible to calorimeter non-linearities. The analysis was made in terms of an angular variable $\chi \equiv e^{|\eta_1 - \eta_1|}$, where $\eta_{1,2}$ are the pseudorapidities of the two leading jets. For the case of 2→2 parton scattering, it is related to the CM scattering angle Θ^* as follows:

$$\chi = \frac{1 + |\cos\Theta^*|}{1 - |\cos\Theta^*|}.$$

The di-jet angular distribution, *(1/N)(dN/dχ)*, was investigated in four di-jet invariant mass bins. For all di-jet invariant mass bins, the E_T -threshold for the highest E_T jet was 400 GeV. Table 21-11 shows the selection cuts for the highest E_T jet for the various invariant di-jet mass bins, to-

Table 21-11 Characteristics of the invariant mass of the high E_T jets.

Mass bin (GeV)	2000-2300	23-00-2800	2800-3400	>3400
E_T threshold(GeV)	400	400	400	400
No of events	18 562	15 781	7772	5228
Average m_{jj} (GeV)	2136	2512	3050	4048

gether with the average M_{jj} and the number of events per bin . The di-jet angular distributions for these di-jet mass bins are shown in Figure 21-22 for constructive interference. The destructive interference case is very similar [21-37]. From the figure, one can see that quark compositeness leads to an enhancement in the distribution at low values of χ in comparison to the SM prediction. The di-jet mass range above 3400 GeV is shows clearly the isotropic contributions to the di-jet angular distribution in *pp* interactions at LHC for Λ up to 8 TeV. The sensitivity is slightly greater for a constructive interference than for a destructive one.

Define R_χ as the fraction of events with $\chi > \xi_0$. In Figure 21-23 the dependence of R_χ on the scale Λ, is shown for the constructive and destructive cases, when either two or all quarks are composite; $\xi_0 = 5$ was used. It is clear, that there is not enough sensitivity to distinguish whether two or all quarks are composite.

R_χ is not very sensitive to the parton density function as illustrated in Figure 21-24, where the values of $R_\chi$are shown for the mass bin of M_{jj} above 3400 GeV. These predictions have been obtained for the cases when two or all quarks are composite. R_χ is also insensitive to the jet cone radius ΔR. Note that in the rest of the analysis, PYTHIA was used with the default structure function CTEQ2.

To study the sensitivity to the quark compositeness signal for higher scale Λ, an analysis was performed for an integrated luminosities of 30 fb^{-1} and 300 fb^{-1}. Figure 21-25 and Figure 21-26 show the deviation of the di-jet angular distribution from the Standard Model predictions.

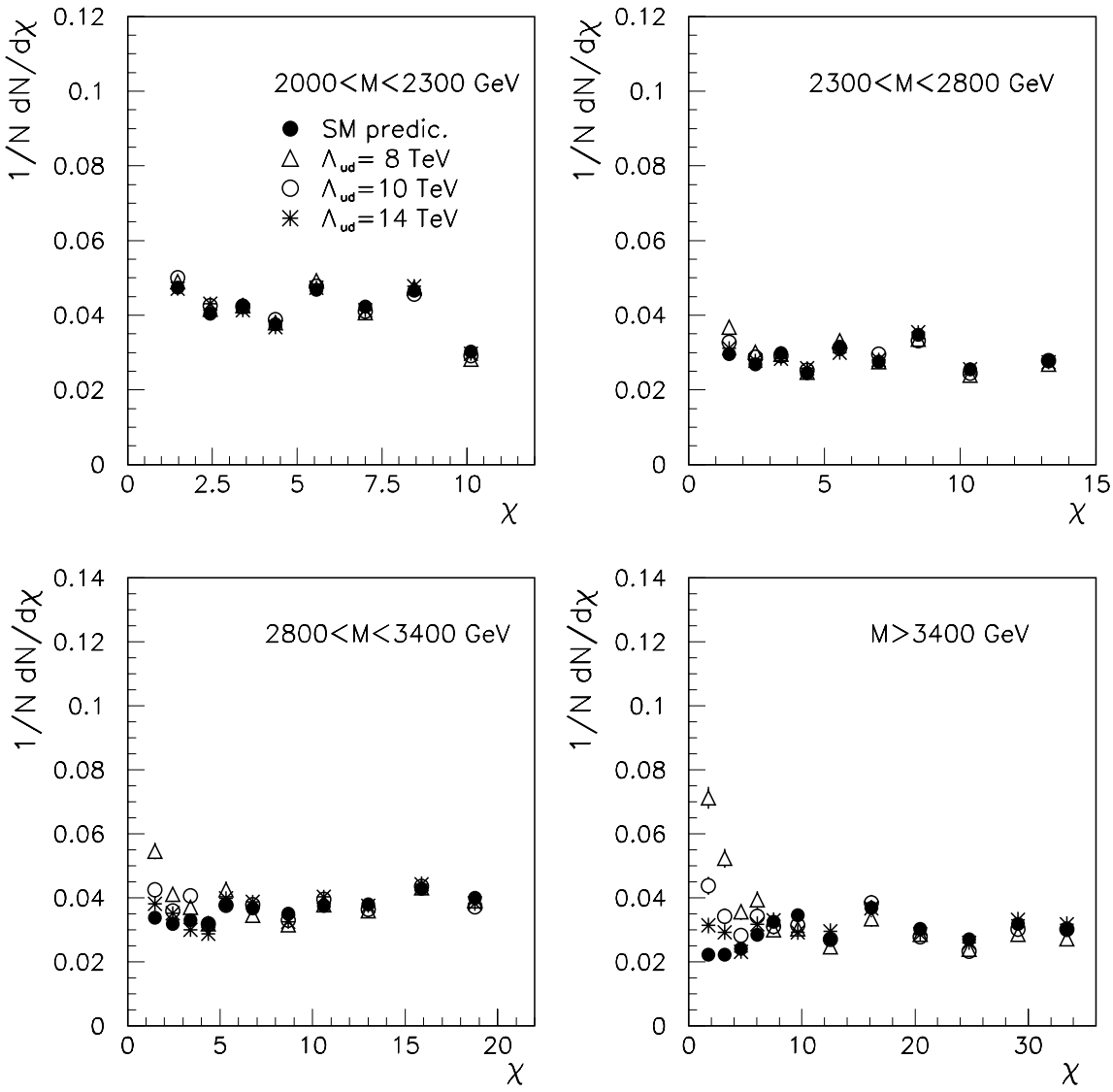

Figure 21-22 Di-jet angular distributions for various mass bins in case of constructive interference. Only quarks of the first two generations are assumed to be composite. The compositeness scale is taken to be 8, 10 and 14 TeV.

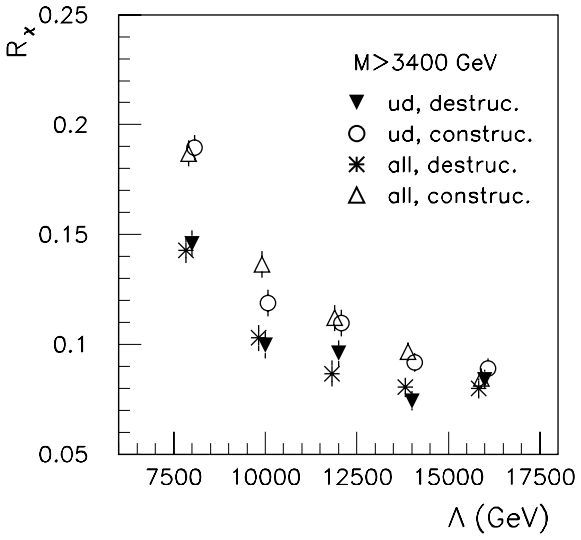

Figure 21-23 The dependence of R_χ on the scale Λ, for the constructive and destructive cases, when two or all quarks are composite.

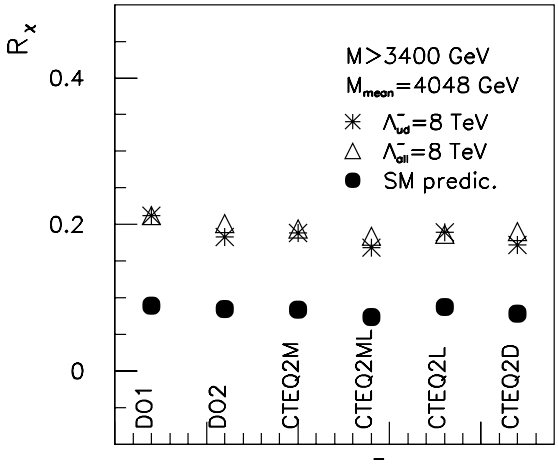

Figure 21-24 The dependence of R_χ on the parton density function.

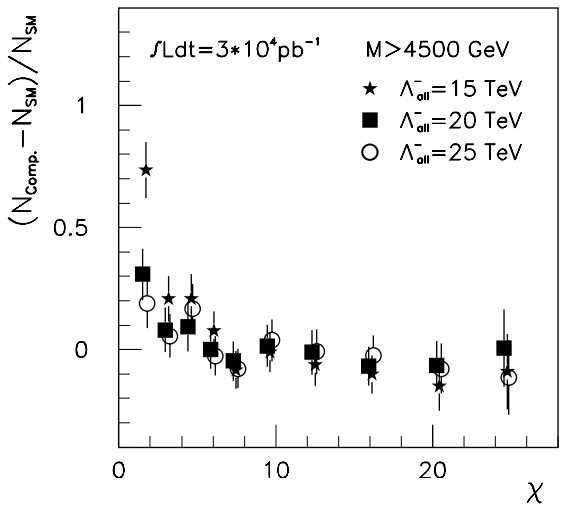

Figure 21-25 The di-jet angular distribution for di-jet mass above 4500 GeV for 30 fb^{-1}.

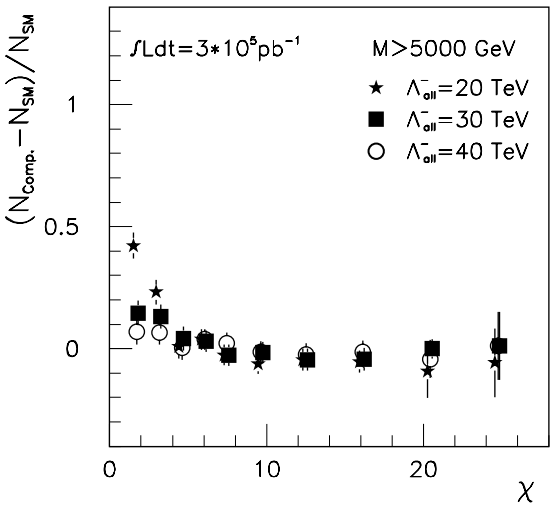

Figure 21-26 The di-jet angular distribution for di-jet mass above 5000 GeV for 300 fb^{-1}.

The sensitivity of the angular distributions to the calorimeter resolution has been studied [21-40]. In order to investigate the influence of a change of the constant term in the jet energy resolution on *(1/N)(dN/dχ). T*he constant term was varied by a factor of two. There is no significant impact on the di-jet angular distribution. Figure 21-27 compares the SM and composite quarks predictions with and without nonlinearity effects. Both non-linearities discussed above are shown on the figure. Even for the larger of these, the effect is negligible compared to the compositeness signal shown. For this choice of di-jet mass bin intervals and jet E_T, no fake signal is created and that the angular distribution is quite insensitive to the non-linearity.

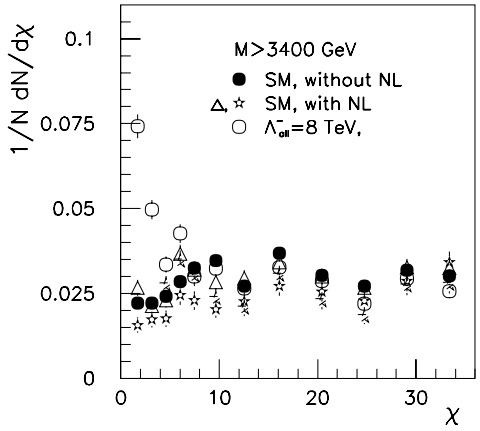

Figure 21-27 The jet angular distributions showing the effects of non-linearity.

In conclusion, the study shows that high mass di-jet angular distribution has an excellent discovery capability for quark compositeness. One month of LHC operation at 10^{33} $cm^{-2}s^{-1}$ allows discovering quark substructure if the constituent interaction constant is of the order of 14 TeV. An integrated luminosity of 300 fb^{-1} is needed to reach a 95% CL limit of 40 TeV.

21.5.4 Dilepton production

The production of dilepton pairs of large invariant mass can be used to probe models where leptons and quarks share constituents [21-38]. Events are selected with two isolated leptons of the same flavour and opposite charge, with $p_T > 400$ GeV and $|\eta| < 2.5$. The Standard Model rate is dominated by Drell-Yan pairs. A composite signal is revealed by an excess of events at large lepton pair invariant mass. If the invariant mass is greater than 1 TeV, the Standard model predicts a rate of 7 fb and the presence of compositeness with $\Lambda = 16$ TeV increases this by 6 fb For an integrated luminosity of 100 fb^{-1}, a sensitivity to $\Lambda < 30$ TeV is achievable at the 5σ level. Details can be found in [21-41].

21.6 Search for new gauge bosons and Majorana neutrinos

New gauge bosons arise from extensions of the Standard Model gauge group and are thus related to the generators of new symmetry groups [21-42]. Given the large number of possible models, a complete survey is not possible. Therefore, in the first part of this section, the discovery potential for new neutral and charged bosons (further referred to as *Z'* and *W'* respectively) will be reviewed. To do so, the prescriptions of a reference model [21-43], in which the couplings of *W'* and *Z'* to quarks and leptons are the same as for the standard *W* and *Z* bosons, and the *W'WZ* and *Z'WW* are suppressed by a factors of $(m(W)/m(W'))^2$ and $(m(Z)/m(Z'))^2$, will be followed.

In order to illustrate the capability for revealing the exact nature of new bosons, a detailed study was also performed in the framework of the Left-Right Symmetric Model, and is presented here.

21.6.1 Search for new vector bosons

21.6.1.1 Fermionic decays of *Z'* bosons

If the couplings of a new *Z'* boson to quarks and leptons are the same as those of a Standard Model *Z* boson and there is no significant *Z-Z'* mixing, then the decay width of the Z' boson grows linearly with its mass. This situation, which is probably the most favourable case, will be further referred to as a SM-like *Z'*. The discovery limits in the e^+e^-, $\mu^+\mu^-$ and jet-jet (*jj*) decay channels as a function of *m(Z')* are presented in Figure 21-28 [21-44]. The jets are required to have p_T greater than 300 GeV. Shown is the value of σB for the Z' relative to the value for a Standard Model *Z*, that is needed for a 5σ confidence level signal as a function of the mass of the *Z'*. As anticipated, the best sensitivity is obtained in the e^+e^- channel. The other decay channels, together with the measurement of the forward-backward asymmetry, are likely to provide some complementary information which are relevant to determine the couplings of the fermions to the *Z'* boson and to thereby help in specifying the origin of a new resonance. In the *jj* final state the signal to background ratio is rather small (between 10^{-3} and 10^{-2}), but a peak is visible [21-44].

21.6.1.2 Leptonic decays of W' bosons

Within the same model, the sensitivity to a possible signal from leptonic *W'* decays extends to masses of about 6 TeV [21-45]. For a value of *m(W')* = 4 TeV, Figure 21-29 shows the expected electron-neutrino transverse mass distribution for the signal above the dominant background from $W \rightarrow e\nu$ decays. For a transverse mass above 2.3 TeV and an integrated luminosity of 100 fb^{-1}, a clean signal of 160 events is expected above a background of 13 events from $W \rightarrow e\nu$ decays and a negligible contribution from top quark pair production and decay. With such a signal sample, the *W'* mass could be measured to an accuracy of about 50 GeV.

21.6.1.3 A study of $W' \rightarrow WZ$

In addition to the leptonic channels, a new W' charged boson could be observed via its decay into a *WZ* pair. Here, the three lepton decay channel *W' –> WZ -> (lν)(ll)* is considered for the mass range of *W'* from 500 GeV up to 3 TeV. To obtain the *W'* signal, the transverse mass distribution of three leptons and missing E_T is calculated. From the three leptons in the final state, the ones with opposite charges are paired in order to reconstruct the *Z* boson (when there are two possibilities, only the pair for which the invariant mass is the closer to *m(Z)* is selected). The transverse mass distribution of the remaining lepton and the missing E_T shows a Jacobian peak at *m(W)*.

The main background for this channel is the irreducible pair production and leptonic decays of *W* and *Z* gauge bosons *pp -> WZ -> (lν)(ll)*. In addition, there is a reducible background from *pp -> ZZ* with one misidentified lepton in the final state, as well as the reducible background from *pp -> tt -> WbWb*, where both *W* bosons decay into a *l*ν pair and where the third lepton comes from one of the *b* quarks. This background is significantly reduced when one requires three isolated leptons in the final state, since the soft lepton coming from the *b* quarks is non-isolated. The transverse mass distribution of the three leptons and the escaping neutrino are shown in Figure 21-30 for both the signal and the background. Even when no cut is applied, the *W'* signal can be seen clearly up to masses of 2.5 TeV.

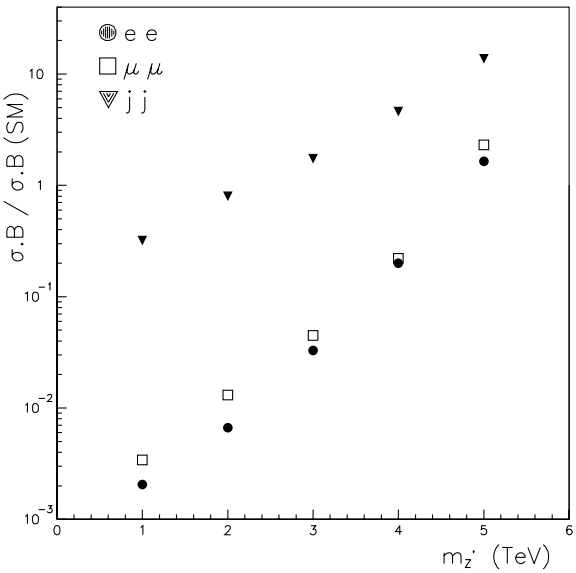

Figure 21-28 Discovery potential for a new Z' neutral boson with 100 fb^{-1} as a function of the *Z'* mass and the ratio of its coupling strength to that of a Standard Model *Z*.

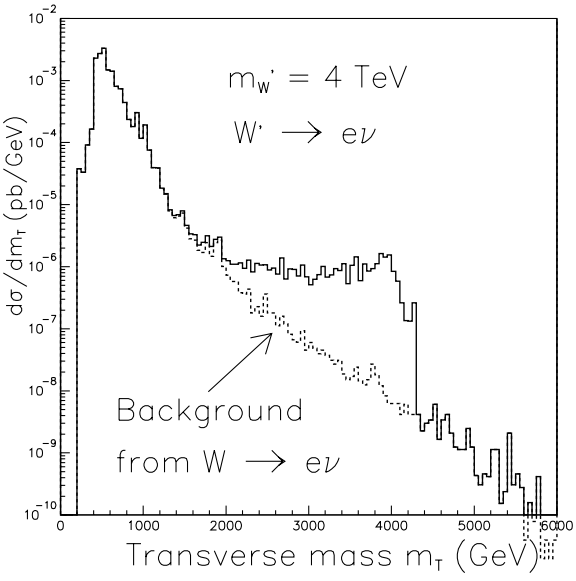

Figure 21-29 Expected transverse mass distribution for $W' \rightarrow e\nu$ decays above the dominant $W \rightarrow e\nu$ background, with m(W') = 4 TeV and for an integrated luminosity of 100 fb^{-1}.

Some additional cuts have been applied on the transverse momentum of the lepton, in order to further enhance the signal and reduce the background. The event rates and the corresponding statistical significances strongly depend on the coupling of *W'* to the *WZ* pair. In the following, a SM-like situation will be referred to when the coupling of *W'* to the *WZ* pair is equal to the Standard Model coupling of *W* to *WZ* reduced by a factor $(m(W)/m(W'))^2$: the corresponding cross section will be further denoted by $(\sigma B)_{SM}$. Table 21-12 shows the event rates for the signal and background in the three lepton final state; to the total background includes the contribution from top pair events

In order to accommodate different couplings from other possible models, the limiting value of the *W'WZ* coupling, corresponding to a significance of 5σ after 300 fb^{-1} has been determined. The cross section associated with this discovery limit will be further denoted by $(\sigma B)_{limit}$. In Figure 21-31, the ratio of the cross section leading to a 5σ significance to the cross section calculated with SM-like coupling for the *W'* boson is plotted as a function of *m(W')*, in the range between 500 GeV and 3 TeV. .

Table 21-12 Event rates for the signal and background for 300 fb^{-1}

$m_{W'}$ = 500 GeV			σ_{SM} **= 0.232 pb**		
m_T > 275 GeV	$W' \rightarrow WZ$	**B_{WZ}**	**B_{ZZ}**	**B_{total}**	$S/\sqrt{B}$
no cut	25446	5368	535	28736 *	150.1
$m_Z \mp 3\Gamma$ $p_{T\,l,\nu}$ > 50 GeV $p_{T\,Z}$ > 200 GeV	7884	341	16	357	417.4
$m_{W'}$ = 1000 GeV			σ_{SM} **= 1.506 10^{-2} pb**		

* Including $t\bar{t}$ background

Table 21-12 Event rates for the signal and background for 300 fb^{-1}

$m_{W'}$ = 500 GeV				σ_{SM} = 0.232 pb	
m_T > 495 GeV	$W' \to WZ$	B_{WZ}	B_{ZZ}	B_{total}	$S/\sqrt{B}$
no cut	1826	714	77	1552 *	46.4
$m_Z \mp 3\Gamma$ $p_{T\,l,\nu} > 50$ GeV $p_{T\,Z} > 450$ GeV	627	23	3	26	122.9
$m_{W'}$ = 2000 GeV				σ_{SM} = 7.099 10^{-4} pb	
m_T > 1140 GeV	$W' \to WZ$	B_{WZ}	B_{ZZ}	B_{total}	$S/\sqrt{B}$
no cut	67	20	2	22	14.28
$m_Z \mp 3\Gamma$ $p_{T\,l,\nu} > 50$ GeV $p_{T\,Z} > 700$ GeV	45	4	-	4	22.5
$m_{W'}$ = 2500 GeV				σ_{SM} = 2.498 10^{-4} pb	
m_T > 1425 GeV	$W' \to WZ$	B_{WZ}	B_{ZZ}	B_{total}	$S/\sqrt{B}$
no cut	20	6	1	7	5.66
$m_Z \mp 3\Gamma$ $p_{T\,l,\nu} > 50$ GeV	14	4	1	5	4.68
$m_{W'}$ = 3000 GeV				σ_{SM} = 7.652 10^{-5} pb	
m_T > 2119 GeV	$W' \to WZ$	B_{WZ}	B_{ZZ}	B_{total}	$S/\sqrt{B}$
no cut	5	1	-	1	3.24

* Including $t\bar{t}$ background

21.6.1.4 A study of *Z' → WW*

A similar study can be performed if a new *Z'* neutral boson couples to the standard *W* boson. To illustrate this, the $pp \to Z' \to WW \to (jj)(e\nu_e)$ is considered; the mass range of the *Z'* boson extends from 1 TeV to 3 TeV. To reconstruct the *Z'* signal, the hadronic and leptonic decays of the W bosons are treated separately.

Given the large transverse momentum of the *W* bosons, the two hadronic jets from their decays are very close and difficult to separate in the detector. After determining the radius ΔR_0 of the cone in which the two hadronic jets coming from the *W* boson are to be found, the invariant masses of all the hadronic clusters with a radius equal to ΔR_0 are calculated using the detailed calorimeter information. Note that as the mass of the *Z'* increases, ΔR_0 is reduced. The hadronic cluster for which the invariant mass is the closest to the value of *m(W)* is then assigned to the hadronic *W* decay.

For the leptonic *W* boson decay, the longitudinal momentum of the neutrino can be found by using its missing transverse energy and by solving a second order equation using the *W* mass as a constraint. The resulting $p_z(\nu_e)$, then permits a full reconstruction of the *W* boson momentum.

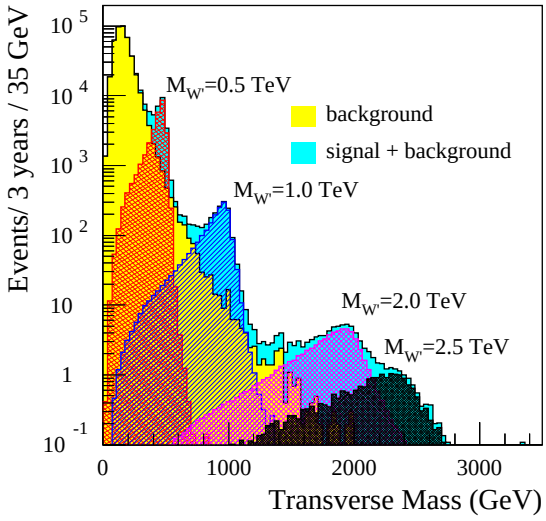

Figure 21-30 Transverse mass distribution of the three leptons and the escaping neutrino for the decay of a *W'* boson into a *WZ* pair and for the corresponding background, for an integrated luminosity of 300 fb^{-1}.

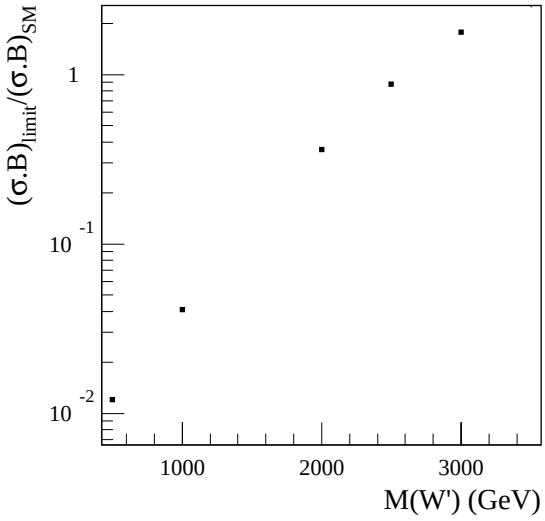

Figure 21-31 Discovery limit for a *W'* boson in the *WZ* decay channel as a function of the W' mass and the W' coupling to the *WZ* pair (see text), for an integrated luminosity of 300 fb^{-1}.

The major background for this channel is $pp \rightarrow W + jets$, where W decays into a $e\nu_e$ pair, while the additional jets give an invariant mass which is close to the W mass (this background depends on the value chosen for ΔR_0). In addition, the production of $t\bar{t}$ and WW pairs, where the W bosons have a large transverse momentum contribute. All these backgrounds can be reduced by the use of the following cuts:

- $E_T(W \rightarrow e\nu_e) > m(Z')/3$, $E_T(e) > m(Z')/10$, $E_T^{miss} > m(Z')/10$ and $m_T(e\nu_e) < 100$ GeV.
- $E_T(W \rightarrow jj) > m(Z')/3$ and $m(W)$ - 15 GeV $< m_{inv}(W \rightarrow jj) < m(W)$ + 15 GeV.
- $|\eta(W \rightarrow jj)| < 2$ and $|\eta(e)| < 2$.
- A veto on the jets in the $|\eta| < 2$ region: the events for which some jets, apart from the ones coming from the W boson, have a transverse energy greater than 25 GeV are rejected (this cut is very efficient in reducing the $t\bar{t}$ background).

The reconstructed mass of the Z' boson is shown in Figure 21-32, together with the contribution from the residual background.

As in the case of the $pp \rightarrow W' \rightarrow WZ$ process, the event rates and the corresponding statistical significance strongly depend on the coupling of the new Z' neutral boson to the WW pair. Here again, a SM-like situation is referred to when the coupling of Z' to the WW pair is equal to the Standard Model coupling of the Z boson to the WW pair reduced by a factor $(m(Z)/m(Z'))^2$. As in Section 21.6.1.3, the limiting value of the Z' WW coupling, corresponding to a significance of 5σ for 300 fb^{-1}, can be determined (see Figure 21-33).

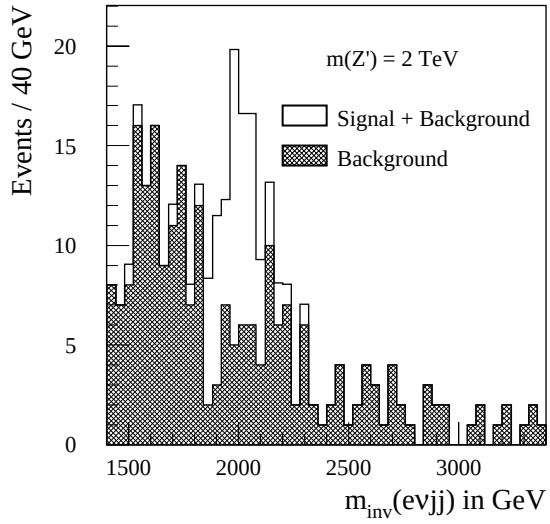

Figure 21-32 Invariant mass distribution of the two hadronic jets, the electron and the neutrino for the decay of a 2 TeV *Z'* boson into a *WW* pair and the corresponding background.

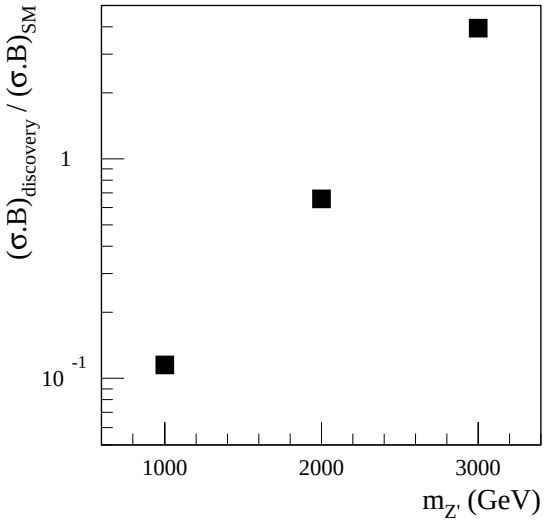

Figure 21-33 Discovery limit for a *Z'* boson in the *WW* decay channel as a function of the *Z'* mass and the *Z'* coupling to the *WW* pair (see text), for an integrated luminosity of 300 fb^{-1}.

21.6.2 Search for right-handed Majorana neutrinos

In the Standard Model, there are no right-handed neutrinos. As a result, given the Higgs structure of the theory, neutrinos are massless particles. However, no fundamental principle forbids them from acquiring masses and extensions to the Standard Model can have right-handed massive neutrinos.

An alternative model based on the $SU(2)_R x SU(2)_L x U(1)_{B-L}$ gauge group, restores the parity symmetry at high energy by using isospin doublets to describe both left-handed and right-handed fermions and by introducing three new heavy gauge bosons: W_R and Z' [21-46]. If neutrinos are Majorana particles, the Left-Right Symmetric Model also provides an explanation for the lightness of the left-handed neutrinos (further referred to as ν's) by introducing heavy right-handed neutrinos (further referred to as *N*'s) and using the See-Saw mechanism [21-47]. If the spontaneous breaking occurs at the TeV scale (as suggested by some supersymmetric extensions of the Left-Right Symmetric Model [21-48]), then the discovery of W_R boson and right-handed Majorana neutrinos, could be made via the process $pp \rightarrow W_R + X \rightarrow lN + X \rightarrow llqq + X$ [21-49].

PYTHIA 5.7 and JETSET 7.4 have been used in order to generate the $pp \rightarrow W_R$ events and the right-handed Majorana neutrinos have been implemented so that the decay chain above can be studied. In this study, the coupling constants and the CKM matrices are assumed to be identical for left-handed and right-handed fermions. Two extreme mass situations are considered, in which either the masses of N_e, N_μ and N_τ are equal or $m(N_e) \ll m(N_\mu)$ with both N_μ and N_τ heavier than the W_R boson. In the following, only the $N_e \rightarrow qqe$ decays will be studied in detail.

21.6.2.1 Reconstruction of W_R and N_e

Events with two isolated electrons and at least two hadronic jets in the final state are selected (the remnants of the *pp* collision and the gluons radiated by the quarks coming from N_e decays usually lead to a jet multiplicity which is greater than two). Then, one assumes that the two hadronic jets with highest transverse energies come from N_e. Since one does not know if a given electron comes from W_R or N_e, the two (ej_1j_2) combinations must be considered in order to reconstruct the right-handed Majorana neutrino. The W_R boson is reconstructed by calculating the invariant mass of the (eej_1j_2) system. Figure 21-34 shows the mass distributions which are obtained for the signal after these procedures.

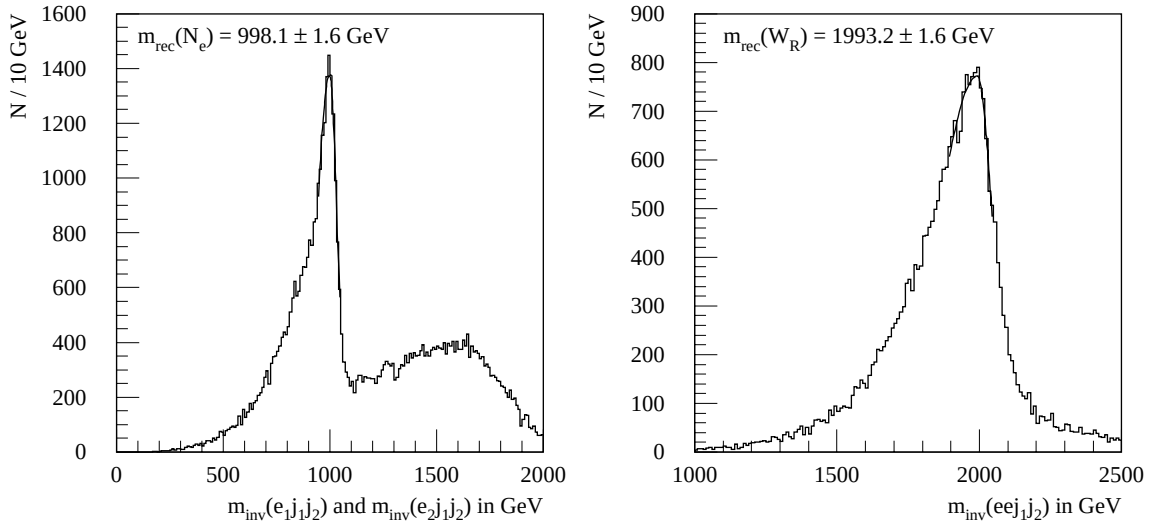

Figure 21-34 Reconstruction of N_e and W_R when their masses are respectively 1 and 2 TeV. The plots are given for an integrated luminosity of 300 fb^{-1} and when the three Majorana neutrinos are degenerate in mass. The peaks are fitted with an asymmetric Gaussian distribution.

The shape of the spectra are not symmetric, because of the final state radiation of hard gluons. As the asymmetry in the W_R and N_e mass distributions grows with $m(N_e)$, the following selection criteria will be further applied on the signal events

$$0.7m(N_e) \le m_{inv}(e_1 j_1 j_2) \le 1.1m(N_e) \text{ or } \quad 0.7m(N_e) \le m_{inv}(e_2 j_1 j_2) \le 1.1m(N_e)$$

$$(0.9 - 0.2r_W)m(W_R) \le m_{inv}(ee j_1 j_2) \le 1.1m(W_R)$$

where $r_W = (m(N_e))/(m(W_R))$. Note that when r_W is small, it becomes more difficult to extract a clean signal with two isolated electrons and at least two hadronic jets, since the decay products of the right-handed Majorana neutrino are very close to each other. In this case, one should look for signatures with one high-p_T isolated electron and one high-p_T hadronic jet.

21.6.2.2 Reduction of the background and discovery potential for W_R boson N_e

All the physics processes which lead to two isolated electrons and at least two hadronic jets in the final state are potential sources of background. In the framework of the Standard Model, the following processes are considered:

- $pp \rightarrow WW, WZ, ZZ$ (+ jets) $\rightarrow ee$ + jets,
- $pp \rightarrow t\bar{t} \rightarrow WWbb \rightarrow ee$ + jets,
- $pp \rightarrow Z/\gamma^*$ (+ jets) $\rightarrow ee$ + jets.

The two isolated electrons produced in these processes come either from a Z boson or from a WW pair. Their transverse energy is thus rather limited. The same applies for the two selected hadronic jets. Kinematical cuts at 200 GeV and 100 GeV are thus applied on $m_{inv}(ee)$ and on the transverse energy of j_1 and j_2. In a first step, the cuts that are used to reduce the background are $m_{inv}(ee) > 200$ GeV and $E_T(j_1,j_2) > 100$ GeV, when there are two isolated electrons and at least two hadronic jets in the final state (see full circles and squares). For events with one isolated electron and one hadronic jet which deposits a significant fraction of its energy in the electromagnetic calorimeter (see open circles and squares), one applies a kinematical cut at 1 TeV on the transverse energy of both the electron and the hadronic jet.

After 30 fb^{-1}, the $pp \rightarrow W_R \rightarrow e\ N_e$ channel will allow the discovery of the W_R boson and the right-handed Majorana neutrino N_e at the 5σ confidence level up to masses of 4.6 TeV and 2.8 TeV respectively (if there is no residual background in a given region of the (W_R;N_e) mass plane, one requires at least ten signal events for discovery). After 300 fb^{-1}, these discovery limits can be pushed up to 5.8 TeV for $m(W_R)$ and 3.4 TeV for $m(N_e)$, as it is shown on Figure 21-35a.

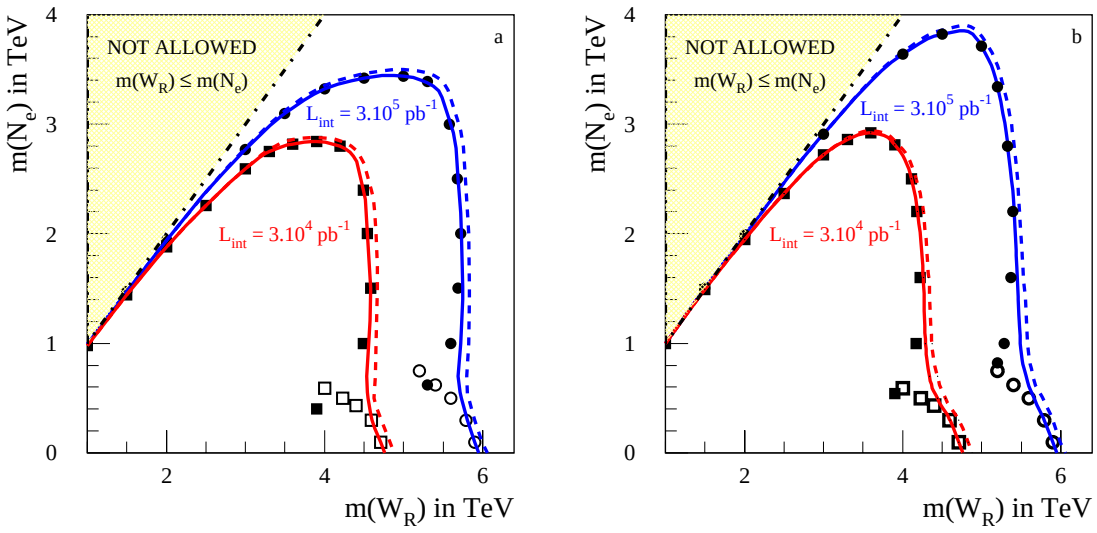

Figure 21-35 Discovery potential for W_R and N_e for 30 fb^{-1} and 300 fb^{-1}. Figures a and b correspond to two different sets of cuts (see text). The full lines correspond to $m(N_e) = m(N_\mu) = m(N_\tau)$ and the dashed lines correspond to $m(N_e) << m(N_\mu) << m(N_\tau)$ with $m(N_\mu)$ and $m(N_\tau)$ both larger than the W_R mass. The region marked NOT ALLOWED is not accessible using the analysis described here.

Also note that all the background processes lead to two electrons with opposite charges, while $pp \rightarrow W_R \rightarrow e\ N_e$ leads to two electrons with same-sign charges in half of the cases, due to the Majorana type of N_e. If one also requires that both isolated electrons have the same electric charge, then the background becomes negligible but, on the other hand, half of the signal is lost. After adding this cut, the discovery reach for W_R and N_e is modified, as shown in Figure 21-35b.

In addition to the $pp \rightarrow W_R \rightarrow e\ N_e$ process, one can also look at the $pp \rightarrow W_R \rightarrow \mu\ N_\mu$ channel, in order to further improve the sensitivity of ATLAS to the right-handed Majorana neutrinos. For simplicity, only the situation in which $m(N_e) = m(N_\mu) = m(N_\tau)$ is considered and, in order to suppress the background, one requires that the both leptons have the same-sign charge and one applies kinematical cuts at 200 GeV on $m_{inv}(ll)$ and 100 GeV on $E_T(j_1,j_2)$, where l is either an electron or a muon, and on the transverse energy of j_1 and j_2 (see Figure 21-36).

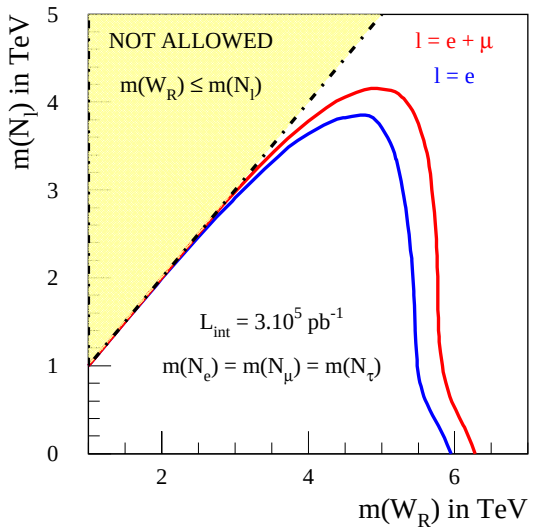

Figure 21-36 The discovery limit for the W_R boson and the right handed Majorana neutrino using the $pp \rightarrow W_R \rightarrow N\mu$ channel; 300 fb^{-1} assumed and $m(N_e)=m(N_\mu)=m(N_\tau)$. The cuts are the same as in Figure 21-35b.

21.6.2.3 Measurement of polarisation effects in $pp \rightarrow W_R \rightarrow e\ N_e$

If W_R and N_e are discovered, one can then identify the electron coming from W_R in order to measure polarisation effects. In the following, one will assume that the electron coming from N_e is the one for which $m_{inv}(ej_1j_2)$ is the closest to the reconstructed N_e mass. Once this assignment is done, the fraction of W_R bosons produced in a +1 or -1 helicity state can be determined in the following way. Let y and cosθ be the rapidity of the W_R boson and the emission angle of the electron coming from W_R with respect to the beam axis in the centre of mass of the boson. Once they have been measured, one can calculate $F(y)$ and $B(y)$ which are the number of events with $\cos\theta>0$ and $\cos\theta<0$ respectively. If A_{FB} is the variable that accounts for the forward-backward asymmetry, then the fraction $X(S_z=+1)$ of W_R bosons produced in the +1 helicity state is simply given by $X(S_z=+1) = 1/2\ (1 + 4/3\ |A_{FB}|)$. If $m(W_R) = 2$ TeV, then $X(S_z=+1)$ is 77% (71%) for positively charged (negatively charged) W_R bosons, on the generator level. Figure 21-37 shows that, after having suppressed the physics background and having reconstructed the W_R boson, one can account for the polarisation effects, provided that the electron assignment is 100% correct. In real life, it will not be the case, especially when r_W is close to 0.6-0.8: in this case, the invariant masses of $(e_1j_1j_2)$ and $(e_2j_1j_2)$ are very close, leading to some misidentification for the origin of the two electrons in the final state and thus to some misestimation of $X(S_z=+1)$.

21.6.2.4 Observability of the $pp \rightarrow Z' \rightarrow N_eN_e$ process

If W_R and N_e are discovered and if Z' is also observed, using the $pp \rightarrow Z' \rightarrow l^+l^-$ process, one can then search for signatures coming from $pp \rightarrow Z' \rightarrow N_eN_e$. In the framework of the Left-Right Symmetric Model, the Z' boson is about 1.7 times heavier than the W_R boson.

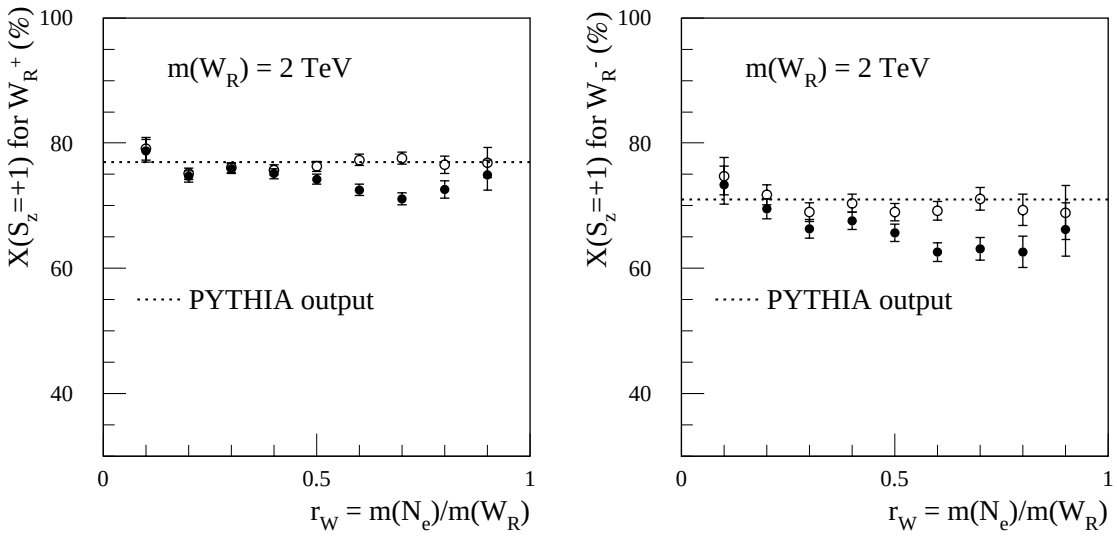

Figure 21-37 Measurement of polarisation effects in the $pp \rightarrow W_R \rightarrow e\,N_e$ process. The empty circles correspond to a perfect identification of the origin of the electrons and the full circles correspond to a realistic identification of the electrons. The plots are given for an integrated luminosity 300 fb^{-1}with $m(N_e) = m(N_\mu) = m(N_\tau)$. The cuts used to suppress the background are $m_{inv}(ee) >$ 200 GeV, $E_T(j_1,j_2) > 100$ GeV and charge(e_1) = charge(e_2).

If N_e is heavy enough, the final states to look for consist of two electrons and at least four hadronic jets. The assignment of the two electrons and the four hadronic jets to their correct N_e is achieved in the following way: for each of the six possible $(e_1 j_a j_b; e_2 j_c j_d)$ combinations $\delta m(abcd) = |m_{inv}(e_1 j_a j_b) - m_{inv}(e_2 j_c j_d)|$ is calculated and the one that minimises the value of $\delta m(abcd)$ is chosen. The Z' boson is then reconstructed by calculating the invariant mass of the two electrons and the four hadronic jets (see Figure 21-38). Note that, when $m(N_e) << m(Z')$, the decay products of the right-handed neutrino are not well separated in the detector and, as a result, a clean signal may be more difficult to extract.

All the processes that lead to final states with two electrons and at least four hadronic jets are potential sources of physics background. In addition to the Standard Model processes described in Section 21.6.2.2, one must take into account $pp \rightarrow W_R \rightarrow e\,N_e$. When requiring that the invariant masses of the two $(e_1 j_a j_b)$ and $(e_2 j_c j_d)$ selected combinations are very close, this background is suppressed, except if r_W is in the neighbourhood of 0.6-0.8; in this case, the electrons which are produced in the decays of W_R and N_e have similar energies and, once associated with four hadronic jets, they might fake a $N_e N_e$ pair. Thus, one must require either $m_{inv}(ee j_1 j_2) \geq 1.1 m(W_R)$ or $m_{inv}(ee j_1 j_2) \leq (0.9 - 0.2 r_W) m(W_R)$ in order to reduce the main background of the Left-Right Symmetric Model. Note that, by selecting the events with identical electric charges for the two electrons, one does not improve the sensitivity to the $pp \rightarrow Z' \rightarrow N_e N_e$ process.

In addition to the selection criterion on $m_{inv}(e_1 e_2 j_1 j_2)$, a cut at 200 GeV on $m_{inv}(ee)$ and a cut at 100 GeV on E_T of all four jets is applied. Once all the backgrounds are reduced, the $pp \rightarrow Z' \rightarrow N_e N_e$ process may be observed with 30 fb^{-1} of integrated luminosity, if the Z' and N_e masses are smaller than 3.2 TeV and 0.8 TeV respectively. If the integrated luminosity reaches 300 fb^{-1}, then these limits can be pushed up to 4.4 TeV for the Z' mass and 1.2 TeV for the N_e mass (see Figure 21-39).

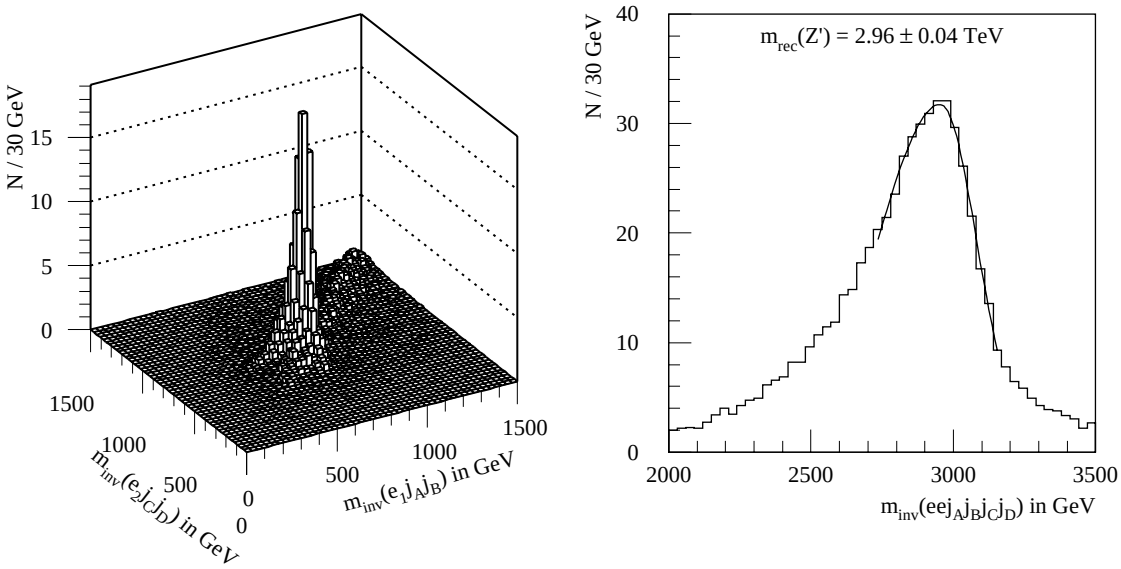

Figure 21-38 Reconstruction of N_e and Z' when their masses are respectively 0.75 and 3 TeV. The plots are given for an integrated luminosity of 300 fb^{-1} and when the three Majorana neutrinos are degenerated in mass. The *Z'* peak is fitted with an asymmetric Gaussian distribution.

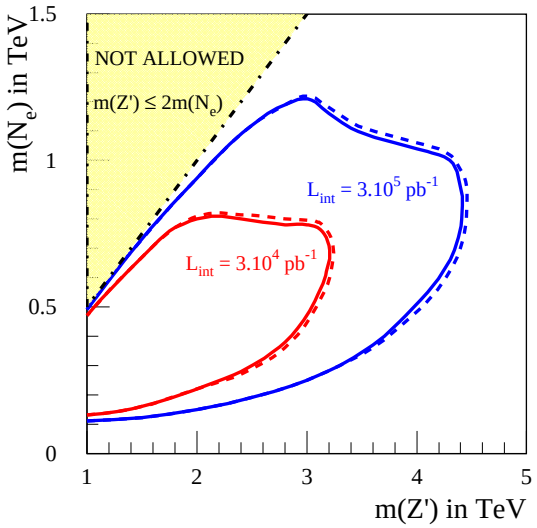

Figure 21-39 Observability of $pp \rightarrow Z' \rightarrow N_e N_e$ for 30 and 300 fb^{-1} of integrated luminosity. The full lines correspond to $m(N_e) = m(N_\mu) = m(N_\tau)$ and the dashed lines correspond to $m(N_e) << m(N_\mu) << m(N_\tau)$ with $m(N_\mu)$ and $m(N_\tau)$ both larger than the half of the *Z'* mass.

21.7 Monopoles

The pioneering Dirac paper [21-50] published in 1931 pointed out the possibility of the existence of particles with isolated magnetic charge (monopoles). A monopole restores the symmetry of the Maxwell's equations and explains the quantisation of the electric charge. Secondly, particles with the magnetic charges arise in gauge field theories as soliton like solutions to the field equa-

tions. Such solutions were found by Polyakov [21-51] and t'Hooft [21-52]. This type of monopoles, in realistic Grand Unification Theories have a mass of the order of the unification scale (~10^{16} GeV) and therefore cannot be discovered on the current or future accelerators. So, in the following discussion, Dirac's pointlike monopoles will be considered. Current constraints on monopoles are summarised in Table 21-13.

Table 21-13 Theoretical and experimental limits on monopole masses.

	Theory	Experiment
Charge	$eg = 2\pi n, \quad n = \pm 1, \pm 2, \ldots$	
Mass(M/n)	< *7000* TeV (cosmology) > *1.2* TeV *[21-55]* (deviation from Standard Model)	L3 ($Z \rightarrow \gamma\gamma\gamma$)[21-53] < *510* GeV ($J_M = 1/2$) D0[21-54] < *610* GeV ($J_M = 0$) < 810 GeV($J_M = 1/2$) < 1580 GeV ($J_M = 1$)

In this table, e and g denote electric and magnetic charge, respectively, and units are such that $\alpha_e \equiv e^2/(4\pi) \approx 1/137$ and $\alpha_g \equiv g^2/(4\pi) \approx 34n$. Limits on the monopole's mass was obtained in [21-55] for monopole spin $J_M = 1/2$. Experiments searching for monopoles in cosmic rays gives limits on their flux only. Note that the monopole mass always appears in calculations as ratio M/n, so in the following the monopole mass refer to this ratio.

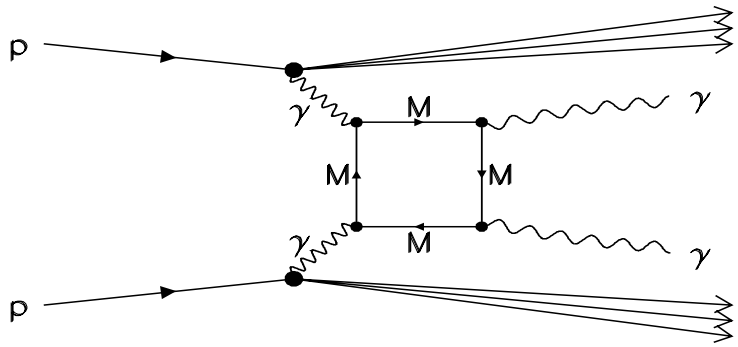

Figure 21-40 Schematic diagram for $\gamma\gamma$ production via the monopole loop.

The current best limit on monopole masses is obtained by the D0 experiment result [21-54], which relies on the method suggested in the paper Ginzburg and Schiller [21-56]. The main idea of this paper is based on observation that the interaction strength between monopole and photon is very strong and could give rise to photon-photon rescattering via the box diagram shown in Figure 21-40.The total cross section

$$\sigma_{pp \rightarrow \gamma\gamma X}(E, M, P, n) = 108P\left(\frac{nE}{M}\right)^8\left(\frac{N(E))}{N(1\text{TeV})}\right)^2\left(\frac{1TeV}{E}\right)^2 \text{fb}$$

shows strong dependence on the energy of incident particles (E) as well as on monopole mass. The numerical factor P reflects dependence of the cross section on monopole spin and equal 0.085, 1.39 and 159 for spin 0, 1/2 and 1, respectively.

The differential spectrum of produced photons as function of transverse momenta is shown on Figure 21-41. The predicted long tail in p_T distribution allows one to work in the region where expected background will be small. Even with p_T cut at 1 TeV about 60% of the signal will survive.

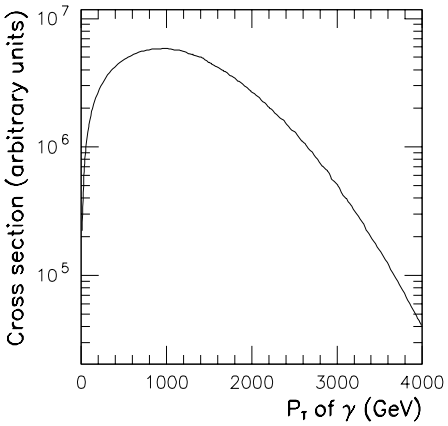

Figure 21-41 Theoretical prediction for transverse momenta spectra of photons.

There are a lot of processes which can obscure the signal. First, the same type of processes as shown on Figure 21-40 but with other particles in the loop. This has the same structure as the signal. Fortunately expected cross-section for these process about two orders of magnitude less than the monopole loop for mass region reachable at LHC. (see [21-56] and references therein). There are also processes where direct photons are produced by parton interactions. Finally, there are background processes from detector effects. These are:

- production of a photon and a hadron jet, mis-identified as electromagnetic one;
- production of two hadron jets both mis-identified as electromagnetic ones.

The probability to misidentify hadron jet as an electromagnetic one was taken to be 0.1% which is conservative but adequate for this analysis.

Monte Carlo estimation for background processes was made by ATLFAST with PYTHIA as event generator. Events were selected according to the following criteria:

- there are two isolated photons with E_T>50 GeV;
- no additional jet or muon with E_T>25 GeV;
- missing transverse energy less than *50* GeV.

To illustrate how monopole induced events will modify the distribution, Figure 21-42 shows the expected event rate for 100 fb^{-1} of integrated luminosity, assuming monopole mass equal to 10 TeV. They are shown as a function of S_T the scalar sum of photon transverse momenta. For a particular choice S_T>2 TeV The signal sensitivity, defined as $S/(\sqrt{B})$ as function of the monopole mass presented on Figure 21-43. It is clear that at LHC limits significantly in excess of the current ones will be set.

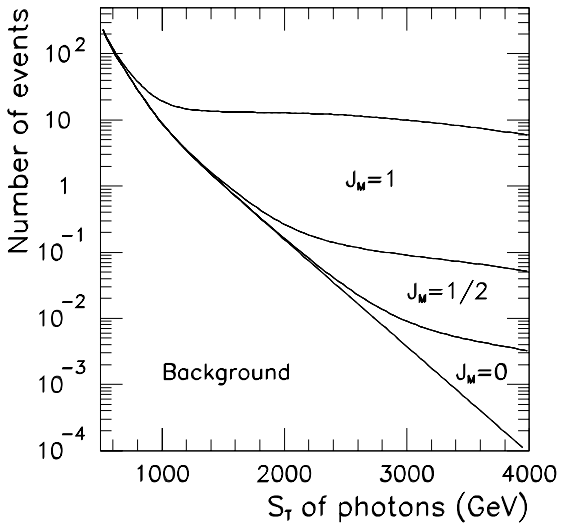

Figure 21-42 Expected number of events from background and background plus signal for 100 fb^{-1}. Mass of monopole as taken as $M/n = 10TeV$.

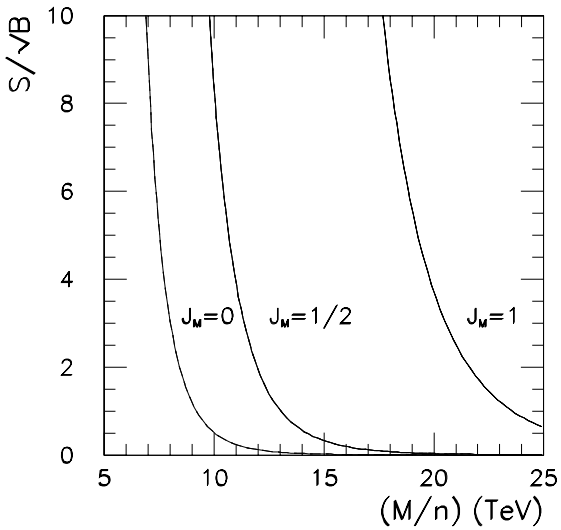

Figure 21-43 Signal sensitivity as function of monopole mass.

21.8 References

21-1 S. Weinberg, Phys Rev. **D19**, (1979) 1277;
L. Susskind, Phys. Rev. **D20** (1979) 2619.

21-2 S. Dimopoulos and L. Susskind, Nucl. Phys. **B155** (1979), 237;
E. Eichten and K. Lane, Phys. Lett. **B90** (1980) 125.

21-3 E. Eichten, K. Lane and J. Womersley, Phys.Lett. **B405** (1997) 305.

21-4 B.A. Dobrescu and J. Terning, Phys.Lett. **B416** (1998) 29.

21-5 M. Golden and L. Randall, Nucl. Phys. **B361** (1991) 3;
R.S. Chivukula *et al.*, hep-ph/9305232 or Phys.Lett. **B311** (1993) 157.

21-6 K. Lane, 27th International Conference on High Energy Physics (ICHEP), Glasgow, Scotland, 1994 (hep-ph/9409304).

21-7 M. Knecht and E. de Rafael, Phys.Lett. **B424** (1998) 335.

21-8 C. T. Hill, Phys. Lett. **266B** (1991) 419.

21-9 K. Lane and E. Eichten, Phys. Lett. **B352** (1995) 382.

21-10 R. Casalbuoni *et al.*, hep-ph/9809523;
T.L. Barklow *et al.*, hep-ph/9704217 (Working group summary report from the 1996 DPF/DPB Summer Study, 'New Directions in High Energy Physics' Snowmass, Colorado);
K. Cheung and R.M. Harris, Summary of New Interactions subgroup of New Phenomena group at Snowmass. To appear in the proceedings of DPF/DPB Summer Study on New Directions for High Energy Physics, Snowmass, Colorado, 1996;
R. Chivukula *et al.*, (in 'Electroweak Symmetry Breaking and New Physics at the TeV Scale', World Scientific, T. Barklow, ed., 1996).

21-11 T. Sjostrand, Comp. Phys. Commun. **82** (1994) 74. The most recent version is obtained from http://www.thep.lu.se/tf2/staff/torbjorn/Pythia.html

21-12 E. Richter-Was *et al.*, 'ATLFAST, a package for particle-level analysis'. ATLAS Internal Note PHYS-No-079(1996).

21-13 K. Lane, 'Electroweak and flavour dynamics at hadron colliders', hep-ph/9605257, 'Non-supersymmetric extensions of the Standard Mode', hep-ph/9610463

21-14 E. Eichten and K. Lane, Phys. Lett. **B388** (1996) 803.

21-15 K. Lane, 'Technihadron production and decay in low scale technicolour', hep-ph/9903369.

21-16 S. Mrenna and J. Womersley, Phys.Lett. **B451** (1999) 155.

21-17 R.M Harris.' Discovery mass reach for topgluons decaying into B-anti-B at the Tevatron'. hep-ph/9609316.

21-18 E. Eichten, I. Hinchliffe, K. Lane and C. Quigg, Rev. Mod. Phys. **56** (1984) 579; Rev. Mod. Phys. **58** (1985) 1065.

21-19 T. Appelquist and G. Triantaphyllou, Phys. Rev. Lett. **69** (1992) 2750.

21-20 F. Abe *et al.*, 'Search for a technicolor omega(T) particle in events with a photon and a b-quark jet at CDF',' hep-ex/9810031.

21-21 Thanks to M. Mangano for providing the Monte Carlo program for generation of $\gamma b\bar{b}$ background.

21-22 S. Slabospitsky, ATLAS note in preparation.

21-23 U. Baur, I. Hinchliffe and D. Zeppenfeld, Int. J. Mod. Phys. **A2**, (1987) 1285;
U. Baur, M. Spira and P. Zerwas, Phys. Rev **D42**, (1990) 815.

21-24 O. Cakir and R. Mehdiyev, 'A search for exited quarks at the CERN LHC', ATLAS Internal Note ATL-PHYS-99-002.

21-25 CDF Collaboration, F. Abe *et al.*, Phys. Rev. Lett. **72** (1994) 3004.

21-26 D0 Collaboration, I. Bertram, Report No. Fermilab-Conf-96/389-E, (1996).

21-27 CDF Collaboration, F. Abe *et al.*, Phys. Rev. **D55** (1997) R5263;
CDF Collaboration, F. Abe *et al.*, Phys. Rev. Lett. **74** (1995) 3538.

21-28 L.F.Abbott and E.Farhi Phys. Lett. **B101** (1981) 69; Phys. Lett. **B189** (1981} 547;
J. Pati and A. Salam, Phys. Rev. **D10** (1974) 275;
E. Witten, Nucl.Phys. **B258** (1985) 75;
M. Dine *et al.*, Phys.Lett. **B259** (1985) 519;
J. Breit, B.A.Ovrut and G. Segre, Phys.Lett. **B158** (1985})33;
S.Pakvasa, Int. J. Mod. Phys. **A2** (1987) 1317.

21-29 J.L. Hewett and S. Pakvasa Phys. Rev. D37 (1988) 3165.

21-30 E. Tsesmelis, 'Further Studies in Detecting Singly-produced Scalar leptoquarks with the ATLAS Detector', ATLAS Internal Note PHYS–NO–029 (1993).

21-31 A. d'Avella, 'Study of Scalar leptoquark pair production at LHC', ATLAS Internal Note PHYS–NO–026 (1993).

21-32 CDF Collaboration, F. Abe e*t al.*,Phys.Rev.Lett. **77** (1996) 5336.

21-33 D0 Collaboration, B. Abbott *et al.*,Phys.Rev.Lett. **80** (1998) 666.

21-34 UA1 Collaboration, C. Albajar *et al.*, Phys. Lett. **B209** (1988) 127.

21-35 UA2 Collaboration, J. Alitti *et al.*, Z. Phys. **C49** (1991) 17.

21-36 CDF Collaboration, F. Abe *et al.*, Phys. Rev **D41** (1990) 1722, Phys. Rev. Lett. **71** (1993) 2542.

21-37 Z.U. Usubov, 'A search for quark compositeness at the LHC', ATLAS Internal Note ATL-COM-PHYS-99-052 (1999).

21-38 E. Eichten, K. Lane and M. Peskin, Phys. Rev. Lett. **50** (1983) 811;
E. Eichten *et al.*, Rev. Mod. Phys. **56** (1984) 579.

21-39 M. Bosman, VI Int.Conf. on Calorimetry in HEP - Frascati, June 8-14, 1996, Frascati Physics series Vol.VI,(pp.299-310)

21-40 F. Ariztizabal *et al.*, Nucl. Instr. and Meth. **A349** (1994), 384.

21-41 E.C. Katsoufis, 'Searching for Quark-Lepton Compositeness at LHC', ATLAS Internal Note ATLAS-PHYS-NO-038 (1994).

21-42 J.C. Pati, and A.Salam, Phys. Rev. **D10** (1974) 275;
R.N. Mohapatra, and J.C. Pati, Phys. Rev.,.**D11** (1975) 566 and Phys. Rev. **D11** (1975) 2558;
G. Senjanovic, and R.N. Mohapatra:, Phys. Rev. **D12** (1975) 1502;
G. Senjanovic: Nucl. Phys. **B153** (1979) 334.

21-43 G. Altarelli, B. Mele, and M. Ruiz-Altaba: Z. Phys. **C45 (**1989) 109.

21-44 A. Henriques and L. Poggioli, 'Detection of the Z' vector boson in the jet decay mode ($Z' \rightarrow q\bar{q}$) (q) $\rightarrow jj$). Resolution and pile-up studies' ATLAS Internal Note PHYS-92-010 (1992).

21-45 M.C. Cousinou, 'Search for W' in the $l\nu$ channel', ATLAS Internal Note PHYS-94-059 (1994)

21-46 R.N. Mohapatra and G. Senjanovic, Phys. Rev. **D23** (1981) 165.

21-47 R.N. Mohapatra and P.B. Pal, 'Massive neutrinos in physics and astrophysics (World Scientific, Singapore, 1991);
C.W. Kim, A. Pevsner, 'Neutrinos in physics and astrophysics' (Harwood Academic Publishers, Switzerland, 1993).

21-48 R. Kuchimanchi and R.N. Mohapatra, Phys. Rev. **D48** (1993) 4352 and Phys. Rev. Lett. **75** (1995) 3989.

21-49 A. Datta and M. Guchait, D.P. Roy, Phys. Rev. **D47** (1993) 961;
J. Collot, and A. Ferrari, ATLAS Internal Note PHYS-98-124

21-50 P.A.M. Dirac, Proc. R. Soc., London, **A133** (1931) 60.

21-51 A.M. Polyakov, JETP Lett., **20** (1974) 194.

21-52 G. t'Hooft, Nucl. Phys., **B79** (1974) 276.

21-53 M. Acciarri *et al.*, Phys. Lett., **B345** (1995) 609.

21-54 B. Abbott *et al.*, Phys. Rev. Lett. **81** (1998) 524.

21-55 A. De Rujula, Nucl. Phys. **B435** (1995) 257.

21-56 L.F. Ginzburg and A. Schiller, Phys. Rev., **D57** (1998) 6599.

A Members of the ATLAS Collaboration

Armenia
Yerevan Physics Institute, Yerevan
Airapetian A., Grabsky V., Hakopian H., Vartapetian A.

Australia
Research Centre for High Energy Physics, Melbourne University, Melbourne
Dick B., Fares F., Guy L.P., Moorhead G.F., Sevior M.E., Taylor G.N., Tovey S.N.
University of Sydney, Sydney
Hashemi-Nezhad R., Peak L., Saavedra A., Ulrichs J.

Austria
Institut für Experimentalphysik der Leopold-Franzens-Universität Innsbruck, Innsbruck
Epp B., Ghete V. M., Girtler P., Kneringer E., Kuhn D., Nairz A., Rudolph G., Schaller M., Schweiger D.

Azerbaijan Republic
Institute of Physics, Azerbaijan Academy of Science, Baku
Abdinov O.B., Akhmedov A., Akhoundov A., Javadov N., Khalilzade F.T., Mekhdiyev R.R., Oussoubov Z., Rzayev H.J.

Republic of Belarus
Institute of Physics, National Academy of Sciences, Minsk
Baturitsky M.A., Bogush A.A., Gazizov A.Z., Gilevsky V.V., Kulchitsky Y., Kuzmin M.V., Levchuk M.I., Satsunkevich I.S.
National Centre of Particle and High Energy Physics, Minsk
Kuzhir P., Medvedev V., Pazin A., Prokoshin F., Soroko A., Starovoytov P.

Brazil
Universidade Federal do Rio de Janeiro, COPPE/EE/IF, Rio de Janeiro
Caloba L.P., Dos Anjos A., Gomes R., Maidantchik C.L., Marroquim F., Seixas J.M., Thome Z.D.

Canada
University of Alberta, Edmonton
Armstrong W.W., Burris W., Davis R., Gingrich D. M., Hewlett J.C., Holm L., Macpherson A.L., Mullin S., Pinfold J.L., Schaapman J., Soukup J., Wampler L.
Department of Physics, University of British Columbia, Vancouver
Axen D.
University of Carleton/C.R.P.P., Carleton
Armitage J., Dixit M., Estabrooks P., Losty M., Neuheimer E., O'Neil M., Oakham G.
Group of Particle Physics, University of Montreal, Montreal
Azuelos G., Leroy C., Marullo F., Mazini R., Roy P.
Department of Physics, University of Toronto, Toronto
Bailey D.C., Bhadra S., Martin J.F., Mayer J.K., Orr R.S., Sinervo P.K., Stairs G.G., Trischuk W.
TRIUMF, Vancouver
Astbury A., Birney P., Hodges T., Langstaff R., Oram C.
University of Victoria, Victoria
Dobbs M., Fincke-Keeler M., Fortin D., Keeler R., Lefebvre M., O'Neil D., Poffenberger P., Roney M., Sobie R.

CERN
European Laboratory for Particle Physics (CERN), Geneva
Aleksa M., Ambrosini G., Anderssen E., Anghinolfi F., Arnaud C., Bachy G., Barberio E., Benincasa G., Bergsma F., Bertinelli F., Bjorset L., Bloess D., Bock R., Bogaerts J., Boosten M., Bremer J., Burckhart D., Burckhart H.J., Butin F., Cataneo F., Chesi E., Chevalley J.L., Cobal M., Danielsson H., Dauvergne J.P., Dell'Acqua A., Dittus F., Dobinson R., Dobson M., Drevermann H., Dudarev A., Dydak F., Ellis N., Fabjan C.W., Farthouat P., Fassnacht P., Fernandez A., Flegel W., Francis D., Froidevaux D., Giancomini F.,

Gianotti F., Gildemeister O., Gschwendtner E.M., Hallgren B., Hansen J., Hatch M., Haug F., Hauser R., Hauviller C., Havet C., Heeley R., Henriques A., Hervas L., Hoffmann H.F., Hogbe-Nlend F., Hoimyr N., Jarp S., Jarron P., Jenni P., Jones R., Kantardjian G., Kaplon J., Klioutchnikova T., Knobloch J., Kulseth M., Lacasta C., Lasseur C., Lehraus I., Lemeilleur F., Lichard P., Linde F., Lopez J., Lozano J., Mandl M., Mapelli L., Martin B., Maugain J.-M., McLaren R.A., Meier D., Meinhard H., Mitsou V., Mornacchi G., Myers D., Nessi M., Nicquevert B., Niinikoski T., Onions C., Pailler P., Passardi G., Petersen J., Placci A., Poppleton A., Posch C., Poulard G., Price M., Riedler P., Roe S., Rohrbach F., Rudge A., Schaller M., Schmid P., Schuler G., Schwick C., Shears T., Simion S., Soulhat J., Spiwoks R., Stavrianakou M., Stavropoulos G., Szeless B., Tapprogge S., Tartarelli G.F., Ten Kate H., Teterin V., Tischhauser H., Treichel M., Tremblet L., Tuura L., Turala M., Unel G., Van der Bij H., Vincke H., von Boehn-Bucholz R., Voss R., Vreeswijk M., Vuillemin V., Weilhammer P., Werner P., Witzeling W., Wotschack J.

China

Institute of High Energy Physics, Academia Sinica, Beijing, University of Science and Technology of China, Hefei, University of Nanjing and University of Shandong
Chen C., Chen T-Y., Cheng S., Feng C., Fu Y., Kong F., Li H., Liu T., Lu W.D., Ma J.M., Meng X., Ouyang Q., Qi M., Tong G.L., Wang C., Xie Y.G., Xue L., Xu G.F., Yang B., Yang T., Ye B., Yu X.Q., Zhang B., Zhang N., Zhang Q.J., Zhao J.

Czech Republic

Academy of Sciences of the Czech Republic, Institute of Physics and Institute of Computer Science, Prague
Bohm J., Hakl F., Hrivnac J., Jirina M., Lednicky R., Lokajicek M., Mares J.J., Nemecek S., Rizek S., Sicho P., Simak V., Stastny J., Stedron M., Vanickova M., Vrba V., Weichert J., Zitek K.
Charles University, Faculty of Mathematics and Physics, Prague
Davidek T., Dolejsi J., Dolezal Z., Kucera M., Leitner R., Soustruznik K., Suk M., Tas P., Trka Z., Valkar S., Wilhelm I., Zdrazil M.
Czech Technical University in Prague, Faculty of Nuclear Sciences and Physical Engineering, Faculty of Mechanical Engineering, Prague
Jakubek J., Kubasta J., Ota J., Pospisil S., Sinor M., Sodomka J., Sopko B., Stekl I., Tomiak Z.

Denmark

Niels Bohr Institute, University of Copenhagen, Copenhagen
Dam M., Hansen J.D., Hansen J.R., Hansen P.

Finland

Helsinki Institute of Physics, Helsinki

France

Laboratoire d'Annecy-le-Vieux de Physique des Particules (LAPP), IN2P3-CNRS, Annecy-le-Vieux
Aubert B., Beaugiraud B., Billat C., Boniface J., Cailles M., Chollet-LeFlour F., Colas J., Duchesneau A., Dumont-Dayot N., Girard C., Gouanere M., Jezequel S., Kambara H., Lafaye R., Lesueur J., Masserot A., Massol N., Moynot M., Perrodo P., Perrot G., Prast J., Riccadonna X., Sauvage G., Thion J., Wingerter-Seez I., Zitoun R., Zolnierowski Y.
Université Blaise Pascal, IN2P3-CNRS, Clermont-Ferrand
Biscarat C., Chadelas R., Crouau M., Daudon F., Grenier P., Guicheney Ch., Hebrard C., Lefevre R., Montarou G., Pallin D., Podlyski F., Reinmuth G., Santoni C., Says L.P., Vazeille F.
Institut des Sciences Nucléaires de Grenoble, IN2P3-CNRS-Université Joseph Fourier, Grenoble
Andrieux M.L., Collot J., Dzahini D., Ferrari A., Hostachy J.Y., Martin Ph., Pouxe J., Rabier C., Rey-Campagnolle M., De Saintignon P., Stassi P.
Centre de Physique des Particules de Marseille, IN2P3-CNRS, Marseille
Bee C., Blanquart L., Breugnon P., Calvet D., Clemens J-C., Delpierre P., Dinkespiler B., Djama F., Duval P-Y., Etienne F., Fede E., Hallewell G., Henry-Couannier F., Hinz L., Karst P., Laugier D., Le Van Suu A., Martin L., Martin O., Meessen C., Mirea A., Monnier E., Mouthuy T., Nacasch R., Nagy E., Negroni S., Nicod D., Olivier C., Pralavorio P., Quian Z., Repetti B., Rondot C., Rousseau D., Rozanov A., Sauvage D., Tisserant S., Touchard F., Vacavant L., Valin I., Vigeolas E., Wielers M.

Laboratoire de l'Accélérateur Linéaire, IN2P3-CNRS, Orsay
Arnault C., Auge E., Barrand G., Belot G., Beney J. L., Blaquiere M., Bonivento W., Bourdarios C., Breton D., Chollet C., Coulon J-P., Cros Ph., De la Taille C., Delebecque P., Falleau I., Fallou A., Fournier D., Grivaz J-F., Imbert P., Jacquier Y., Mace G., Martin-Chassard G., Mencik M., Merkel B., Noppe J-M., Parrour G., Perus A., Petroff P., Puzo P., Richer J-P., Schaffer A-C., Seguin-Moreau N., Serin L., Tocut V., Vales F., Veillet J-J., Vernay E., Zerwas D.
LPNHE, Universités de Paris VI et VII, IN2P3-CNRS, Paris
Astesan F., Bertoli W., Canton B., David J., Fichet S., Fleuret F., Imbault D., Lacour D., Laforge B., Le Dortz O., Martin D., Poggioli L., Rossel F., Schwemling P.
CEA, DSM/DAPNIA, Centre d'Etudes de Saclay, Gif-sur-Yvette
Amadon A., Bauer F., Belorgey J., Berriaud C., Berthier R., Borgeaud P., Bystricky J., Cacaut D., Calvet D., Chalifour M., Chevalier L., Cloué O., Daël A., Delagnes E., Desages F., Durand D., Ernwein J., Gachelin O., Gallet B., Gastineau B., de Girolamo P., Guyot C., Hansl-Kozanecka T., Hubbard J.R., Huet M., Joudon A., Juster F.P., Kiourkos S., Kozanecki W., Laporte J.F., Le Coreller A., Le Dû P., Lesmond C., Lugiez F., Machefert F., Mandjavidze I., Mansoulié B., Mayri C., Molinié F., Mur M., Pabot Y., Pascual J., Perrin P., Ponsot P., Rey J.M., Rouger M., Schuller J.P., Schune Ph., Schwindling J., Sun Z., Taguet J.P., Teiger J., Thooris B., Tirler R., Van Hille H., Virchaux M.

Republic of Georgia
Institute of Physics of the Georgian Academy of Sciences and Tbilisi State University, Tbilisi
Chikovani L., Chiladze B., Djobava T., Gabunia L., Gogiberidze G., Grigalashvili T., Khelashvili A., Khorguashvili Z., Khubua J., Kipiani K., Koshtoev V., Liparteliani A., Metreveli Z., Mosidze M., Salukvadze R., Sopromadze D., Topchishvili L.

Germany
Physikalisches Institut, Universität Bonn, Bonn
Ackers M., Andre F., Andreazza A., Comes G., Fischer P., Geich-Gimbel C., Klasen V., Keil M., Kobel M., Kuhl T., Meuser S., Ockenfels W., Stockmanns T., Treis J., Wermes N.
Institut für Physik, Universität Dortmund, Dortmund
Geiser A., Goessling C., Huegging F., Wuestenfeld J., Wunstorf R.
Fakultät für Physik, Albert-Ludwigs-Universität, Freiburg
Baer Th., Chen J., Ebling D.G., Herten G., Irsigler R., Kollefrath M., Landgraf U., Lauxtermann S., Ludwig J., Mohr W., Paschhoff V., Rehmann V., Rolker B., Runge K., Schaefer F., Scherberger G., Schmid T., Webel M., Weber C.
Institut für Hochenergiephysik der Universität Heidelberg, Heidelberg
Geweniger C., Hanke P., Kluge E.-E., Mahboubi K., Meier K., Pfeiffer U., Putzer A., Schumacher C., Tittel K., Wunsch M.
Institut für Physik, Johannes-Gutenberg Universität Mainz, Mainz
Fuchs K., Geib K.H., Jakobs K., Kleinknecht K., Koepke L., Marschalkowski E., Merle K., Othegraven R., Quast G., Renk B., Schaefer U., Walkowiak W., Zeitnitz C.
Lehrstuhl für Informatik V, Universität Mannheim, Mannheim
Kornmesser K., Kugel A., Lay R. , Ludvig J., Maenner R., Noffz K-H., Ruehl S., Sessler M., Simmler H., Singpiel H.
Sektion Physik, Ludwig-Maximilian-Universität München, München
Chouridou S., Deile M., Kortner O., Hessey N.P., Schaile D., Staude A., Strohmer R., Trefzger T.
Max-Planck-Institut für Physik, München
Ackermann K., Aderholz M., Andricek L., Blum W., Bratzler U., Brettel H., Dietl H., Dulny B., Fent J., Gruhn C., Hauff D., Koffeman E., Kroha H., Lutz G., Manz A., Moser H.-G., Oberlack H., Ostapchuk A., Richter R., Richter R.H., Schacht P., Schael S., Soergel V., Stenzel H., Striegel D., Tribanek W.
Fachbereich Physik, Universität Siegen, Siegen
Holder M., Schoefer B., Ziolkowski M.
Fachbereich Physik, Bergische Universität, Wuppertal
Becks K.H., Braun H., Drees J., Gerlach P, Glitza K.W., Gregor I.M., Hamacher K., Kersten S., Lenzen G., Linder C., Thadome J., Wahlen H.

Greece
Athens National Technical University, Athens
Dris M., Filippas A., Fokitis E., Gazis E.N., Katsoufis E., Maltezos S., Papadopoulou T.
Athens University, Athens
Fasssouliotis D., Giokaris N., Ioannou P., Kourkoumelis C., Pancheluga V., Petridis A., Tatsis S., Tzanakos G.S., Vassiliou M.
Aristotle University of Thessaloniki, Thessaloniki
Bouzakis C., Chardalas M., Dedoussis S., Efstathiou K., Lagouri Th., Liolios A., Paschalias P., Petridou C., Sampsonidis D., Vichou I., Zamani M.

Israel
Department of Physics, Technion, Haifa
Dado S., Harel A., Landesman H., Lupu N., Robins S., Rozen Y., Tarem S.
Raymond and Beverly Sackler Faculty of Exact Sciences, School of Physics and Astronomy, Tel-Aviv University, Tel-Aviv
Abramowicz H., Alexander G., Bella G., Benary O., Dagan S., Etzion E., Grunhaus J., Oren Y.
Department of Particle Physics, The Weizmann Institute of Science, Rehovot
Breskin A., Chechik R., Duchovni E., Eisenberg Y., Gross E., Hass M., Karshon U., Lellouch D., Levinson L., Mikenberg G.

Italy
Dipartimento di Fisica dell' Università della Calabria e I.N.F.N., Cosenza
Ayad R., Capua M., Lagatta A., La Rotonda L., Schioppa M., Susinno G., Valdata-Nappi M.
Laboratori Nazionali di Frascati dell' I.N.F.N., Frascati
Bilokon H., Cerutti F., Chiarella V., Curatolo M., Dulach B., Esposito B., Ferrer M.L., Maccarrone G., Moccia S., Pace E., Pepe-Altarelli M., Spitalieri M., Zuffranieri F.
Dipartimento di Fisica dell' Università di Genova e I.N.F.N., Genova
Barberis D., Beccherle R., Caso C., Dameri M., Darbo G., Gagliardi G., Gemme C., Morettini P., Musico P., Olcese M., Osculati B., Parodi F., Pozzo A., Ridolfi G., Rossi L., Sette G.
Dipartimento di Fisica dell' Università di Lecce e I.N.F.N., Lecce
Creti P., Gorini E., Grancagnolo F., Palamara O., Petrera S., Primavera M.
Dipartimento di Fisica dell' Università di Milano e I.N.F.N., Milano
Acerbi E., Aleppo M., Alessandria F., Battistoni G., Broggi F., Caccia M., Camin D., Cavalli D., Costa G., Fanti.M., Ferrari A., LaBanca N., Lari T., Mandelli L., Mazzanti M., Meroni C., Perini L., Ragusa F., Resconi S., Rossi L., Sala P., Tartarelli G.F., Troncon C., Vanini S., Vegni G., Volpini G.
Dipartimento di Scienze Fisiche, Università di Napoli 'Federico II' e I.N.F.N., Napoli
Aloisio A., Alviggi M.G., Cevenini F., Chiefari G., De Asmundis R., Merola L., Napolitano M., Patricelli S.
Dipartimento di Fisica Nucleare e Teorica dell' Università di Pavia e I.N.F.N., Pavia
Cambiaghi M., Conta C., Ferrari R., Fraternali M., Lanza A., Livan M., Negri A., Polesello G., Rimoldi A., Vercesi V.
Dipartimento di Fisica dell' Università di Pisa e I.N.F.N., Pisa
Cavasinni V., Cologna S., Costanzo D., Del Prete T., Di Girolamo B., Flaminio V., Lami S., , Marrocchesi P.S., Mazzoni E., Paoletti R., Renzoni G., Roda C., Spano F., Suglia R., Usai G.
Dipartimento di Fisica dell' Università di Roma 'La Sapienza' e I.N.F.N., Roma
Bagnaia P., Bini C., Caloi R., Cardini A., Cavallari A., Ciapetti G., De Zorzi G., DiMattia A., Falciano S., Gauzzi P., Gentile S., Lacava F., Luci C., Luminari L., Marzano F., Mirabelli G., Nisati A., Petrolo E., Pontecorvo L., Veneziano S., Zanello L.
Dipartimento di Fisica dell' Università di Roma 'Tor Vergata' e I.N.F.N., Roma
Aielli G., Baranov S., Camarri P., Cardarelli R., Di Ciaccio A., Liberti B., Paoloni A., Santonico R.
Dipartimento di Fisica dell' Università di Roma 'Roma Tre' e I.N.F.N., Roma
Bacci C., Baroncelli A., Ceradini F., Farilla A., Iodice M., Orestano D., Pastore F., Spiriti E., Stanescu C.
Dipartimento di Fisica dell' Università di Udine, Gruppo collegato di Udine I.N.F.N. Trieste, Udine
Cauz D., D'Auria S., De Angelis A., Pauletta G., Santi L., Scuri B., Waldner F., del Papa C.

Japan
Department of Information Science, Fukui University, Fukui
Tanaka S.

Hiroshima Institute of Technology, Hiroshima
Asai M.
Department of Physics, Hiroshima University, Higashi-Hiroshima
Iwata Y., Ohsugi T.
KEK, National Laboratory for High Energy Physics, Tsukuba
Amako K., Arai Y., Fujii H., Haruyama T., Ikeno M., Iwasaki H., Kanzaki J., Kohriki T., Kondo T., Manabe A., Morita Y., Nomachi M., Ohska T.K., Sasaki O., Sasaki T., Terada S., Unno Y., Watase Y., Yamamoto A., Yasu Y.
Department of Physics, Faculty of Science, Kobe University, Kobe
Kawagoe K., Kurashige H., Nozaki M., Takeda H.
Department of Physics, Kyoto University, Kyoto
Sakamoto H., Sasao N.
Kyoto University of Education, Kyoto-shi
Takashima R.
Department of Electrical Engineering, Nagasaki Institute of Applied Science, Nagasaki
Nagasaka Y., Tanaka Y.
Naruto University of Education, Naruto-shi
Nagamatsu M., Yoshida H.
Department of Physics, Faculty of Science, Shinshu University, Matsumoto
Takeshita T.
International Centre for Elementary Particle Physics, University of Tokyo, Tokyo
Hasegawa Y., Homma K., Imori M., Kawamoto T., Kobayashi T.
Physics Department, Tokyo Metropolitan University, Tokyo
Fukunaga C., Hamatsu R.
Department of Applied Physics, Tokyo University of Agriculture and Technology, Tokyo
Emura T.

Morocco
Faculté des Sciences Aïn Chock, Université Hassan II, Casablanca, and Université Mohamed V, Rabat
Chakir H., Cherkaoui R., Goujdami D., El Kacimi M., Hoummada A., Saidi H., Sayouty E.

Netherlands
FOM - Institute SAF NIKHEF and University of Amsterdam/NIKHEF, Amsterdam
Bobbink G.J., Bos K., Boterenbrood H., Buis E.J., Dankers R.J., Daum C., Groenstege H., Hartjes F., Hendriks P., Heubers W., Kaan B., Kieft G.N.M., Kluit P., Kluit R., Massaro G.G.G., Meddeler G., Peeters S., Reichold A., Rewiersma P.A.M., Schuijlenburg H., Spelt J., Vermeulen J.C., Werneke P., Woudstra M., van Eijk B., van der Graaf H.
University of Nijmegen/NIKHEF, Nijmegen
Brouwer C., Crijns F.J.G.H., Dijkema J.A., De Jong S.J., Kittel W., Klok P.F., Lavrijsen W.T.L.P., Koenig A.C., Metzger W.J., Pols G.-J., Schotanus D.J., Wijnen Th.A.M.

Norway
University of Bergen, Bergen
Eigen G., Frodesen A.G., Klovning A., Stugu B.
University of Oslo, Oslo
Bugge L., Buran T., Dorholt O., Kristiansen H., Madsen R.A., Marshal A., Midttun G., Read A.L., Rohne O.M., Stapnes S., Strandlie A., Sundal B.

Poland
Henryk Niewodniczanski Institute of Nuclear Physics, Cracow
Blocki J., Bocian D., Gadomski S., Gornicki E., Godlewski J., Hajduk Z., Iwanski W., Kaczmarska A., Kisielewski B., Korcyl K., Madeyski B., Malecki P., Moszczynski A., Olszowska J., Piotrzkowski K., Richter-Was E., Sapinski M., Wolter M.
Faculty of Physics and Nuclear Techniques of the Academy of Mining and Metallurgy, Cracow
Dabrowski W., Grybos P., Idzik M., Jagielski S., Jelen K., Kiesilewska D., Koperny S., Kowalski T., Rulikowska-Zarebska E.

Portugal

Laboratorio de Instrumentação e Física Experimental de Partículas (University of Lisboa, University of Coimbra, University Católica-Figueira da Foz and University Nova de Lisboa), Lisbon
Amaral P., Amorim A., Carvalho J., Casarejos E., David M., Gomes A., Gomes J., Ivaniouchenkov I., Maio A., Maneira M., Martins J.P., Onofre A., Pinhao J., Santos J., Silva J., Varanda M., Wolters H.

Romania

Institute of Atomic Physics, National Institute of Physics and Nuclear Engineering, Bucharest
Alexa C., Arsenescu R., Badescu E., Boldea V., Caprini I., Caprini M., Constantin F., Constantinescu S., Dita P., Dita S., Micu A., Micu L., Niculescu M., Pantea D., Radu A.

Russia

Institute for Theoretical and Experimental Physics (ITEP), Moscow
Artamonov A., Epchtein V., Gorbunov P., Gurin R., Jemanov V., Khovansky V., Koutchenkov A., Kruchinin S., Maslennikov A., Ryabinin M., Shatalov P., Tsoukerman I., Zaitsev V., Zeldovich S.
P.N. Lebedev Institute of Physics, Moscow
Akimov A., Baranov S., Belov M., Blagov M., Fedorchuk R., Gavrilenko I., Kaioumov F., Komar A., Konovalov S., Kopytine M., Mouraviev S., Popov L., Shikanyan A., Shmeleva A., Snesarev A., Speransky M., Sulin V., Tikhomirov V., Vassilieva L., Yakimenko M.
Moscow Engineering and Physics Institute (MEPhI), Moscow
Bondarenko V., Dolgoshein B., Konstantinov A., Romaniouk A., Semenov S., Smirnov S., Sosnovtzev V.
Moscow State University, Institute of Nuclear Physics, Moscow
Bashindjagian G.L., Basiladze S.G., Berejnoi A., Erasov A.B., Grishkevich Y., Karmanov D.E., Kramarenko V.A., Larichev A.N., Melikhov D.I., Merkin M.M., Nikitin N.V., Rizatdinova F.K., Selikov A.V., Sivoklokov S.Yu., Smirnova L.N., Zverev E.G.
Budker Institute of Nuclear Physics (BINP), Novosibirsk
Batrakov A., Chekhtman A., Fedotov M., Gaponenko I., Klimenko S., Kollegov M., Kozlov V., Kuper E., Merzlyakov Y., Panin V., Shamov A., Telnov V., Tikhonov Y., Velikzhanin Y.
Institute for High Energy Physics (IHEP), Protvino
Amelin D.V., Ammosov V.V., Antipov Yu.M., Batarin V., Bogoliubsky M.Yu., Borissov A.A., Borissov E., Bozko N.I., Bryzgalov V.V., Chekulaev S.V., Denisov S.P., Dushkin A.Yu., Fakhroutdinov R., Fenyuk A.B., Gapienko V.A., Gilitsky Yu.V., Goryatchev V., Gouz Yu.P., Karyukhin A.N., Khokhlov Yu.A., Kirsanov M.M., Kiryunin A.E., Klyukhin V., Kojine A., Kononov A.I., Konstantinov V., Kopikov S.V., Korotkov V.A., Kostrikov M.E., Kostyukhin V.V., Kravtsov V.I., Kulemzin A., Kurchaninov L.L., Lapin V.V., Levitsky M.L., Los S., Maximov V., Miagkov A.G., Mikhailin V.N., Minaenko A.A., Moiseev A.M., Onuchin V.A., Pleskach A.V., Salomatin Yu.I., Senko V.A., Shein I., Soldatov A.P., Solodkov A.A., Solovianov O.V., Starchenko E.A., Sviridov Yu., Sytnik V.V., Tchmil V., Tchountonov A., Tikhonov V.V., Tsyupa Yu., Usenko E., Vorobiev A.P., Vovenko A.S., Zaets V.G., Zaitsev A.M., Zimin S., Zmouchhko V.
Petersburg Nuclear Physics Institute (PNPI), Gatchina, St. Petersburg
Fedin O., Filimonov V., Gavrilov G., Ivochkin V., Khomoutnikov V., Kolos S., Krivchitch A., Lochak I., Maleev V., Nadtochy A., Patritchev S., Prokofiev D., Riabov J., Schegelsky V., Soloviev I., Spiridenkov E., Zalite A.

JINR

Joint Institute for Nuclear Research, Dubna
Alexandrov I., Alexeev G., Alikov B., Anosov V., Astvatsaturov A., Azhgirei L., Backovic M., Baranov S., Boyko I., Budagov J., Chelkov G., Cheplakov A., Chirikov-Zorin I., Chlachidze G., Dedovich D., Dodonov V., Evtukhovich P., Fedorov A., Feshenko A., Flyagin V., Glagolev V., Golikov V., Golubykh S., Gongadze A., Gornushkin Y., Gostkin M., Iamburenko V., Ignatenko M., Juravlev N., Kakurin S., Kallinikov V., Kalinichenko V., Kazarinov M., Kazymov A., Kekelidze G., Khasanov A., Khomenko B., Khovansky N., Kotov S., Kotov V., Kovtun V., Krumstein Z., Kukhtin V., Kuznetsov O., Ladygin E.U., Lazarev A., Lebedev A., Ljablin M., Lomakin Y., Malyshev V., Malyukov S., Manjavidze D., Merekov Y., Minashvili I., Nikolenko M., Nozdrin A., Olshevski A., Peshekhonov V., Pisarev I., Podkladkin S., Pose R., Potrap I., Pukhov O., Romanov V., Rumyantsev V., Russakovich N., Ryabchenko K., Salihagic D., Savin I., Scheltckov A., Sedykh Y., Semenov A., Senchishin V., Shabalin D., Shalyugin A., Shigaev V., Shilov S.,

Simic M., Sissakian A., Snyatkov V., Sorokina J., Tchepournov V., Tkachev L., Tokmenin V., Topilin N., Tskhadadze E., Usov Y., Vertogradov L., Vinogradov V., Vorozhtsov S., Yarygin G., Zhuravlev V.

Slovak Republic
Bratislava University, Bratislava, and Institute of Experimental Physics of the Slovak Academy of Sciences, Kosice
Ban J., Bruncko D., Chochula P., Chytracek R., Dubnicka S., Dubnickova A., Ferencei J., Garabik R., Holik P., Jusko A., Kladiva E., Kocper B., Kubinec P., Kurca T., Luptak M., Masarik J., Povinec P., Rosinsky P., Stanicek J., Stavina P., Strizenec P., Sykora I., Tokar S., Vanko J.

Slovenia
Jozef Stefan Institute and Department of Physics, University of Ljubljana, Ljubljana
Cindro V., Filipcic A., Kramberger G., Mandic I., Mikuz M., Tadel M., Zontar D.

Spain
Institut de Física d'Altes Energies (IFAE), Universidad Autónoma de Barcelona, Bellaterra, Barcelona
Blanch O., Blanchot G., Bosman M., Cavalli-Sforza M., Crespo J.M., Dosil M., Fernandez E., Flix J., Korolkov I., Martinez M., Miralles Ll., Ostankov A., Pacheco A., Pena J.C., Zamora Y.
Physics Department, Universidad Autónoma de Madrid, Madrid
Barreiro F., Del Peso J., Hervas L., Labarga L.
Instituto de Física Corpuscular (IFIC), Universidad de Valencia, CSIC, Burjassot, Valencia and Instituto de Microelectronica de Barcelona, Campus Universidad Autonoma, Bellaterra, Barcelona
Ballester F., Bernabeu J., Camarena F., Campabadal F., Carrasco R., Castillo M.V., Costa M.J., Ferrer A., Fuster J., Garcia C., Gonzalez V., Gonzalez de la Hoz S., Higon H., Lopez J.M., Martinez C., Modesto P., Moreno A., Lozano M., Roldan J., Romance J.B., Ros E., Salt J., Sanchez J., Sanchis E., Santander J., Ullan M.

Sweden
Fysiska institutionen, Lunds universitet, Lund
Akesson T., Almehed S., Carling H., Danielson H., Eerola P., Egede Anderson U., Hedberg V., Jarlskog G., Korsmo H., Lorstad B., Lundberg B., Mjornmark U.
Royal Institute of Technology (KTH), Stockholm
Akerman D., Carlson P., Clement C., Leven S., Lund-Jensen B., Pearce M., Soderqvist J., Vanyashin A.
University of Stockholm, Stockholm
Berglund S., Bohm C., Engstrom M., Hellman S., Holmgren S-O., Johansson E., Jon-And K., Klereborn J., Sellden B., Silverstein S., Sjolin J., Yamdagni N.
Uppsala University, Department of Radiation Sciences, Uppsala
Bingefors N., Botner O., Brenner R., Bystrom O., Coadou Y., Damet J., Ekelof T., Gustafsson L., Hallgren A., Kullander S., Staaf P.

Switzerland
Laboratory for High Energy Physics, University of Bern, Bern
Beck H.P., Borer K., Hess M., Lehmann G., Mommsen R., Pretzl K.
Section de Physique, Université de Genève, Geneva
Bonino R., Clark A.G., Couyoumtzelis C., Demierre Ph., Efthymiopoulos I., Kowalewski R., La Marra D., Leger A., Perrin E., Vuandel B., Wu X.

Turkey
Department of Physics, Ankara University, Ankara
Atag A., Cakir O., Meric N., Sultansoy S., Turk I., Ulvi Yilmazer A.
Department of Physics, Bogaziçi University, Istanbul
Arik E., Celik O., Cetin S.A., Conka T., Hacinliyan A., Kurtulus O., Mailov A., Nurdan K., Tanoren B.

United Kingdom
School of Physics and Astronomy, The University of Birmingham, Birmingham
Bright-Thomas P., Charlton D.G., Dowell J.D., Garvey J., Hillier S.J., Homer R.J., Jovanovic P., Kenyon I.R., McMahon T.J., O'Neale S.W., Staley R.J., Watkins P.M., Watson A.T., Watson N.K., Wilson J.A.

Cavendish Laboratory, Cambridge University, Cambridge
Batley J.R., Carter J.R., Drage L., Goodrick M.J., Hill J.C., Munday D.J., Parker M.A., Robinson D., Wyllie K.H.
Department of Physics and Astronomy, University of Edinburgh, Edinburgh
Boyle O., Candlin D.J., Candlin E.R.S., Knowles I.G.
Department of Physics and Astronomy, University of Glasgow, Glasgow
Doyle A.T., Flavell A.J., Lynch J.G., Martin D.J., O'Shea V., Raine C., Saxon D.H., Skillicorn I.O., Smith K.M.
Department of Physics, Lancaster University, Lancaster
Brodbeck T.J., Chilingarov A., Henderson R.C.W., Hughes G., Jones R.W.L., Ratoff P.N., Sloan T., Smizanska M.
Department of Physics, Oliver Lodge Laboratory, University of Liverpool, Liverpool
Allport P.P., Booth P.S.L., Carroll L.J., Cooke P.A., Greenall A., Houlden M.A., Jackson J.N., Jones T.J., King B.T., Maxfield S.J., Moreton A., Smith N.A., Sutcliffe P., Turner P.R., Wells D.
Department of Physics, Queen Mary and Westfield College, University of London, London
Beck G.A., Carter A.A., Eisenhandler E.F., Hughes D.M., Kyberd P., Landon M., Lloyd S.L., Newman-Coburn D., Pentney J.M., Pritchard T.W., Thompson G.
Department of Physics, Royal Holloway and Bedford New College, University of London, Egham
Blair G.A., George S., Green B.J., Medcalf T., Strong J.A.
Department of Physics and Astronomy, University College London, London
Anderson B., Attree D., Butterworth J., Charalambous A., Clarke P., Cranfield R., Crone G., Fraser J., Hayes D., Hoare T., Jones T., Lane J., Postranecky M., Sherwood P., Wheeler S.
Department of Physics and Astronomy, University of Manchester, Manchester
Duerdoth I.P., Dunne P.W., Foster J.M., Freestone J., Hughes-Jones R.E., Ibbotson M., Kerr A., Kolya S.D., Loebinger F.K., Marshall R., Mercer D., Pater J., Snow S., Thompson R.J.
Department of Physics, Oxford University, Oxford
Buira-Clarke D., Cashmore R., Coe P., Hawes B.M., Hill J., Holmes A., Howell D., Huffman B.T., Kundu N., Loken J.G., Mitra A., Nickerson R.B., Reichold A.R., Renton P.B., Segar A.M., Wastie R.L., Weidberg A.R.
Rutherford Appleton Laboratory, Chilton, Didcot
Apsimon R.J., Baines J.T., Baynham D.E., Botterill D.R., Clifft R.W., Edwards M., English R.L., Fisher S.M., Gee C.N.P., Gibson M.D., Gillman A.R., Greenfield D., Hart J.C., Hatley R.W., Haywood S.J., Hill D.L., McCubbin N.A., Middleton R.P., Morrissey M.C., Murray W.J., Nichols A., Norton P.R., Payne B.T., Perera V.J.O., Phillips P.W., Pilling A., Saunders B.J., Shah T.P., Tappern G.J., Tyndel M., White D.J., Wickens F.J.
Department of Physics, University of Sheffield, Sheffield
Booth C.N., Buttar C.M., Combley F.H., Dawson I., Grigson C., Lehto M.H.

United States of America
State University of New York at Albany, New York
Alam S., Athar B., Mahmood A., Timm S., Wappler F., Zhichao L.
Argonne National Laboratory, Argonne, Illinois
Berger E.L., Blair R., Dawson J., Drake G., Guarino V., Hill N., May E.N., Nodulman L.J., Price L.E., Proudfoot J., Schlereth J.L., Stanek R., Wagner R.G., Wicklund A.B., Yoshida R.
University of Arizona, Tucson, Arizona
Cheu E., Embry T., Johns K., Loch P., Rutherfoord J., Savine A., Shaver L., Shupe M., Steinberg J., Tompkins D.
Department of Physics, The University of Texas at Arlington, Arlington, Texas
De K., Gallas E., Li J., Sosebee M., Stephens R., White A.
Lawrence Berkeley Laboratory and University of California, Berkeley, California
Barnett M., Bintinger D., Ciocio A., Einsweiler K., Gilchriese M., Haber C., Hinchliffe I., Joshi A., Loken S., Marchesini R., Meddeler G., Milgrome O., Niggli H., Palaio N., Richardson J., Shapiro M., Siegrist J., Spieler H., Trilling G.
Department of Physics, Boston University, Boston, Massachusetts
Ahlen S., Hazen E., Shank J., Simmons E., Whitaker J.S., Zhou B.

Brandeis University, Department of Physics, Waltham, Massachusetts
Behrends S., Bensinger J.R., Blocker C., Hashemi K., Kirsh L.E., Wellenstein H.
Brookhaven National Laboratory (BNL), Upton, New York
Alforque S., Barratt R., Citterio M., Gordeev A., Gordon H., Graf N., Gratchev V., Kandasamy A., Koehler J., Kotcher J., Lissauer D., Ma H., Makowiecki D., Murtagh M.J., Norton S., O'Connor P., Paige F., Polychronakos V., Protopopescu S., Radeka V., Rahm D.C., Rajagopalan S., Rescia S., Smith G., Sondericker J., Stephani D., Stumer I., Takai H., Tcherniatine V., Yu B.
University of Chicago, Enrico Fermi Institute, Chicago, Illinois
Anderson K., Bellerive A., Blucher E., Glenzinsky D., Merritt F., Oreglia M., Pilcher J., Pod E., Sanders H., Shochet M., Tang F., Teuscher R., Wu H.
Nevis Laboratory, Columbia University, Irvington, New York
Cartiglia N., Cunitz H., Dodd J., Gara J., Leltchouk M., Parsons J., Seman M., Shaevitz M., Sippach W., Willis W., Zhang L.
Department of Physics, Duke University, Durham, North Carolina
Ebenstein W.L., Goshaw A.T., Lee A.M., Oh S.H., Robertson W.J., Wang C.H.
Department of Physics, Hampton University, Virginia
Assamagan K.A., Baker O.K., McFarlane W.K.
Department of Physics, Harvard University, Cambridge, Massachusetts
Brandenburg G., Feldman G.J., Felt N., Franklin M.E.B., Huth J., Oliver J., Riegler W.
Indiana University, Bloomington, Indiana
Callahan J., Hanson G., Luehring F., Ogren H., Rust D.R.
University of California, Irvine, California
Fahlund T., Hackett C., Hall R., Lankford A.J., Pier S., Schernau M., Stoker D.
Massachusetts Institute of Technology, Department of Physics, Cambridge, Massachusetts
Haridas P., Osborne L.S., Paradiso J.A., Pless I.A., Taylor F.E., Wadsworth B.F.
University of Michigan, Department of Physics, Ann Arbor, Michigan
Ball R., Campbell M., Chapman J.W., Diehl E., Goldfarb S., Hou S., Kouba D., Levin D., McKee S., Neal H.A., Qian J., Schick H., Tarle G., Thun R., Weaverdyck C., Zhou B.
Michigan State University, Department of Physics and Astronomy, East Lansing, Michigan
Abolins M., Brock R., Bromberg C., Ermoline Y., Huston J., Linnemann J., Miller R., Pineiro B., Pope B.G., Richards R., Weerts H.
University of New Mexico, New Mexico Center for Particle Physics, Albuquerque
Gold M., Gorfine G., Hoeferkamp M., Seidel S.
Physics Department, Northern Illinois University, DeKalb, Illinois
Fortner M., Sirotenko V.I., Willis S.E.
Department of Physics, Ohio State University, Columbus, Ohio
Gan K.K., Honscheid K., Kagan H., Kass R.
Department of Physics and Astronomy, University of Oklahoma
Boyd R., Gutierrez P., McMahon T., Severini H., Skubic P., Snow J., Strauss M.
Department of Physics, University of Pennsylvania, Philadelphia, Pennsylvania
Dressnandt N., Keener P., Newcomer F.M., Van Berg R., Williams H.H.
University of Pittsburgh, Pittsburgh, Pennsylvania
Cleland W.E., Mcdonald J.E., Paolone V., Rabel J., Zuk G.
Department of Physics and Astronomy, University of Rochester, Rochester, New York
England D., Haelen T., Slattery P.
Institute for Particle Physics, University of California, Santa Cruz, California
Dorfan D., Dubbs T., Grillo A., Heusch C., Kashigin S., Litke A., Sadrozinski H., Seiden A., Spencer E., Webster A.
Department of Physics, Southern Methodist University, Dallas, Texas
Chou T.-M., Evans G., Stroynowski R., Ye J.
Department of Physics, High Energy Group, State University of New York at Stony Brook, Stony Brook, New York
Engelmann R., Grannis P., Hobbs J., Jung C.K., McCarthy B., Rijssenbeek M., Schamberger D., Yanagisawa C.
Tufts University, Medford, Massachusetts
Mann A., Milburn R., Napier A., Sliwa K.

High Energy Physics, University of Illinois, Urbana, Illinois
Errede D., Errede S., Haney M.J., Thaler J.
Department of Physics, Department of Mechanical Engineering, University of Washington, Seattle, Washington
Burnett T.H., Cook V., Daly C., Davisson R., Forbush D., Guldenmann H., Lubatti H.J., Mockett P.M., Rothberg J., Zhao T.
Department of Physics, University of Wisconsin, Madison, Wisconsin
Fasching D., Gonzalez S., Jared R.C., Pan Y.B., Scott I.J., Wu S.L., Yamartino J.M., Zobernig G.